الجمهورية الجزائرية الديمقراطية الشعبية

République Algérienne Démocratique et Populaire

وزراة التعليم العالي والبحث العلمي

Ministère de l'Enseignement Supérieur de la Recherche Scientifique

جامعة الشهيد حمة لخضر ـالوادي ـ

Université Echahid Hmma Lakhdar - D'El-oued –

مخبر استغلال وتثمين المصادر الطاقوية الصحراوية

Laboratoire d'Exploitation et de Valorisation Des Ressources Energétiques Sahariennes

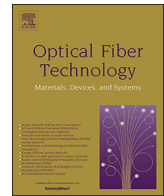# Publications Internationales du Laboratoire Période 2016-2019

Production Equipe 1

01   Design and modelling of all-normal dispersion $As_{39}Se_{61}$ photonic crystal fiber for flat-top coherent mid-infrared generation (**Abdelkader Medjouri, Djamel Abed**).

02   Design and optimization of As_2S_5 chalcogenide channel waveguide for coherent mid-infrared supercontinuum generation (**Abdelkader Medjouri, Djamel Abed, Omar Ziane, Lotfy Mokhtar Simohamed**).

03   Design of ZBLAN photonic crystal fiber with nearly zero ultra_flattened chromatic dispersion for supercontinuum generation

(Abdelkader Medjouri , El-Bachir Meraghni , Hadjer Hathroubi , Djamel Abed , Lotfy Mokhtar, Simohamed and Omar Ziane) .

04   Growth study of CdS thin films deposited by chemical bath

(A. Beggas, B.Benhaoua, A. Attaf and M. S. Aida).

05   Stable solar-pumped TEM_{00}-mode 1064 nm laser emission by a monolithic fused silica twisted light guide (**Said Mehellou , Dawei Liang , Joana Almeida , Rochdi Bouadjemine , Claudia R. Vistas ,Emmanuel Guillot , Ferhat Rehouma) .**

06   Mid-infrared broadband ultraflat-top supercontinuum generation in dispersion engineered Ge-Sb-Se chalcogenide photonic crystal fiber (**Abdelkader Medjouri, Djamel Abed**).

07   Numerical investigation of a broadband coherent super continuum generation in$Ga_8Sb_{32}S_{60}$chalcogenide photonic crystal fiber with all-normal dispersion. (**A.Medjouri, D. Abed, Z. Becer).**

08   Special glass for silver-sodium ion exchanged waveguides (**Ferhat Rehouma , Omar Bentouila).**

09   Stable TEM00-mode Nd:YAG solar laser operation by a twisted fused silica light-guide(**Bouadjemine , D. Liang , J. Almeida , S. Mehellou , C.R. Vistas , A. Kellou , E. Guillot)**

10   Thermal loading effects on Nd:YAG solar-laser performance in endpumping and side-pumping configurations: a review (**Said Mehellou, Ferhat Rehouma, Noureddine Hamrouni, Leila Bouras)**

11   Thermal stability and spectroscopic study of Ho3+/Yb3+ co-doped fluorophosphates glasses (**O. Bentouila , K.E. Aiadi , F. Rehouma , M. Poulain , F. Benhbirech)**

Design and modelling of all-normal dispersion $As_{39}Se_{61}$ chalcogenide photonic crystal fiber for flat-top coherent mid-infrared supercontinuum generation

Abdelkader Medjouri[a,*], Djamel Abed[b]

[a] *LEVRES Laboratory, University of EL Oued, 39000 El Oued, Algeria*
[b] *Department of Electronics and Telecommunications, Faculty of Sciences and Technology, University of Guelma, 24000 Guelma, Algeria*

A B S T R A C T

We report numerical investigation of mid-infrared supercontinuum (SC) generation in all-normal dispersion (ANDi) $As_{39}Se_{61}$ chalcogenide photonic crystal fiber (PCF). Numerical results, obtained by using the Finite-Difference Frequency-Domain (FDFD) method, indicate that desirable dispersion properties can be achieved by adjusting the air holes diameter and ANDi regime is obtained over the entire wavelength range with a PCF pitch and air holes diameter of 1.8 μm and 0.7 μm, respectively. Besides, the optimized design has a nearly zero dispersion wavelength of 3.45 μm and exhibits high Kerr nonlinearity of $5.89 \, w^{-1} \, m^{-1}$. By pumping 50 fs duration laser pulses at 3.45 μm, we demonstrate the generation of a broad, ultraflat-top and highly coherent SC spectrum extending from 2.43 μm to 4.85 μm at 4 dB spectral flatness and from 1.95 μm to 6.58 μm at 8 dB, by employing very low energy pulses of 50 pJ and 250 pJ, respectively. Owing to its remarkable optical characteristics, the proposed SC source based on $As_{39}Se_{61}$ chalcogenide glass PCF is found to be suitable for various potential mid-infrared applications such as optical coherence tomography, mid-infrared spectroscopy and metrology.

1. Introduction

Broadband light sources spanning the near and mid-infrared spectral region based on Supercontinuum (SC) generation process has been an attractive research topic during the last two decades [1]. As a fundamental feature of nonlinear optics, SC generation is defined as the substantial spectral broadening of laser pulses, occurred during its passing through nonlinear medium such as planar waveguides, optical fibers and Photonic Crystal Fibers (PCFs) [1]. Since the first experimental demonstration of continuum generation in bulk glass reported by R.R. Alfano et al. [2], SC has been increasingly involved in various photonic applications covering the visible and infrared wavelength ranges such as pulse compression, Coherent Anti-Stokes Raman Spectroscopy (CARS), telecommunications and atmosphere pollutants sensing [3]. Specifically, in broadband spectral imaging, mid-infrared SC sources are required to cover the molecular fingerprint spectral region where distinctive vibrational absorption features are exploited to identify the different molecules [4]. Moreover, ultra-flat and broadband SC sources are employed in mid-infrared Optical Coherence Tomography (OCT) systems for the analysis of polymers, ceramics and some

biochemical elements including phosphate, carbonate and collagen amide [5]. Compared to other mid-infrared light sources such as synchrotron radiation sources, quantum cascade lasers and thermal emitters, SC sources are preferred due to their suitable characteristics such as high coherence, high brightness, compactness and portability [6,7].

SC generation in optical waveguides usually requires pumping short (femtosecond) and high peak power laser pulses, where the drastic spectral broadening, occurring even over short propagation distances, is achieved through the contribution of several linear and nonlinear optical effects [8]. For waveguides with anomalous chromatic dispersion regime, the soliton dynamics including soliton fission, dispersive wave generation and Raman soliton self-frequency shifting are the main contributors to the SC formation and evolution [9]. Furthermore, SC generated by pumping in the normal regime of dispersion is achieved through the Self-Phase Modulation (SPM) and Optical Wave Breaking (OWB) mechanisms [10]. The main difference between the two regimes of pumping is the pulse-preserving aspect, high coherence and the spectral flat-top feature, which are substantially improved in the normal regime. This is explained by the fact that SPM and OWB are nonlinear self-seeded processes that preserve the optical pulses integrity

---

* Corresponding author.
  E-mail address: medjouri-abdelkader@univ-eloued.dz (A. Medjouri).

and the smoothness of their phase distribution [11]. Therefore, realizing SC sources with high brightness, high spectral flatness and high coherence requires a careful design of the optical waveguide to achieve both All Normal Dispersion (ANDi) and high nonlinearity and optimizing the initial laser pulses properties such as the pumping wavelength, the pulse duration and peak power [12]. Among various kinds of optical waveguides, PCFs have drawn a tremendous attention and are extensively used for the design of broadband light SC sources [13]. The main advantage of PCFs, compared to other optical waveguides, consists of their design flexibility through the adjustment of the cladding air holes lattice configuration, air holes diameters, photonic crystal pitch and the background glass [14]. Consequently, the chromatic dispersion properties can be easily engineered and high optical Kerr nonlinearity can be attained by controlling the PCFs opto-geometrical parameters [15]. Moreover, PCFs made of optical glasses with high nonlinear refractive index, such as chalcogenides and tellurite, are widely used to realize various nonlinear photonic applications [16–21].

Chalcogenide (ChG) glasses are non-oxide materials composed from the addition of metalloid elements such as Ge, As, Sb or Ga to one of the chalcogen elements S, Se, and Te [22,23]. ChG glasses have acquired an increasing interest because of the possibility of achieving glass systems with wide composition space and excellent resistance to crystallization, enabling to achieve suitable optical properties such as wide transparency window, spanning near-infrared and mid-infrared regions, high optical Kerr nonlinearities and high linear refractive indices [24]. Accordingly, ChG glasses have been recognized as an excellent candidate for the design of near and mid-infrared PCFs based SC light sources [1,22]. Recently, numerous theoretical and experimental works on the generation of coherent SC in the mid-infrared region employing ChG glass based ANDi PCFs have been reported [25–33]. P. Yan et al reported numerical investigation of coherent 2–5 μm bandwidth SC generated in As_2S_3 flat-top ANDi PCF achieved by pumping 610 W peak power 50 fs duration pulses in 2 cm length of the fiber [25]. M. R. Karim et al theoretically studied a dispersion engineered $Ge_{11.5}As_{24}Se_{64.5}$ based PCF for mid-infrared SC generation [26]. Ultraflat and coherent SC spanning 1.5 octaves is obtained by injecting 5 Kw peak power pulses at 3.1 μm in only 1 cm length of the optimized PCF design. Lai et al experimentally demonstrated coherent mid-infrared SC generated in four holes ChG $AsSe_2$-As_2S_5 multi-material optical fiber with ANDi profile [27]. The authors have shown that SC spectrum spanning the region from 2.2 μm to 3.3 μm is achieved in 2 cm long fiber pumped with 2.7 μm pulses obtained from an optical parametric oscillator. Furthermore, B. Siwicki et al presented a nano-structured graded index core fiber made of $As_{40}Se_{60}$-$Ge_{10}As_{23.4}Se_{66.6}$ glasses with flat and normal dispersion in the mid-infrared region [28]. They have numerically demonstrated that using 1 nJ pulses with a duration of 200 fs pumped at 6.3 μm, enable the generation of more than one octave spanning SC at 20 dB spectral flatness. Multi-material Triangular Core microstructured optical Fiber (TCF) using $Ge_{11.5}As_{24}Se_{64.5}$-$Ge_{11.5}As_{24}S_{64.5}$ ChG glass has been, also, investigated [29]. The ANDi regime is optimized by adjusting the core side length and SC extending up to 7 μm has been realized using 3 kW peak power 100 fs duration pulses launched at 4 μm into 10 mm of the TCF length. S. Xing et al experimentally studied linearly chirped mid-infrared SC generated in ANDi PCF made of AsSe-GeAsSe ChG system [30]. The authors have shown that launching at 2.070–2.080 μm, 2.9 Kw peak power and 79 fs duration optical pulses generates mid-infrared SC spanning a wavelength range with a bandwidth of 27.6 THz at 3 dB and 75.5 THz at 20 dB. Moreover, introducing a small defect into the PCF core has been used in the aim to control its chromatic dispersion profile and achieve ANDi regime [31]. In this respect, E. Wang et al theoretically studied ANDi As_2Se_3 based defected core PCF for flattened and broadband mid-infrared SC [32]. By injecting at 4.375 μm, 50 fs width and 4.25 Kw peak power pulses into 6 mm long PCF, flat and broadband SC extending from 3.866 μm to 5.958 μm at the spectral level of 3 dB is successfully generated. A more simple way to control the PCF

dispersion profile is through an appropriate adjusting of the cladding air holes radius. By employing this method, we have reported the design of a $Ga_8Sb_{32}S_{60}$ ChG glass based PCF, exhibiting ANDi profile for mid-infrared SC generation [33]. We have numerically shown that pumping at 4.5 μm, 50 fs width and 20 kW peak power into a 1 cm of the PCF length, generates coherent and broadband SC spectrum spanning the wavelength region from 1.65 μm to 9.24 μm at the 20 dB spectral flatness.

Recently, E.A. Anashkina et al. reported the design and the fabrication of tapered suspended core fibers made of $As_{39}Se_{61}$ ChG glass for mid-infrared wavelength conversion of ultra-short signals [34]. The As-Se glass system has excellent optical properties such as wide transparent window extending from 0.85 to 17.5 μm with an ultra-low optical loss in the range of 4–7 μm, high linear refractive index in the range of 2.75–2.81, high third-order nonlinear refractive index of $2.2 \times 10-17$ μm, high resistance to atmospheric moisture and excellent chemical stability [34]. The authors have experimentally demonstrated that wavelength conversion can be achieved for ultra-short optical pulses at the wavelength 1.57 μm. Moreover, numerical simulations on SC generation have been performed and broadband spectrum spanning the region from 1 μm to 10 μm has been achieved by pumping 100 pJ pulses at 2 μm. However, the generated SC spectrum is not smooth because of the anomalous dispersion regime exhibited by the proposed fibers. Besides, the proposed suspended core fiber in multimode, therefore, the output SC power is reduced due to an intermodal energy transfer caused by Four Wave Mixing (FWM) nonlinear coupling process between the different guided modes [35]. With simultaneously taking advantage of the excellent optical properties of the $As_{39}Se_{61}$ ChG glass and the design flexibility of PCFs, flat-top, broadband and highly coherent mid-infrared SC generation can be achieved by suitably engineering the PCF chromatic dispersion profile to exhibit ANDi regime.

In this paper, we theoretically investigate $As_{39}Se_{61}$ ChG glass based single mode triangular lattice PCF with a chromatic dispersion profile, engineered in order to generate broadband, coherent and ultraflat-top mid-infrared SC spectra. Aiming to achieve ANDi regime, the PCF cross section is specifically designed and optimized by suitably controlling the radius of the cladding air holes. Accordingly, the PCF linear and nonlinear optical parameters such as effective index, chromatic dispersion, effective mode area and Kerr nonlinear coefficient are computed by using the Finite-Difference Frequency-Domain (FDFD) method associated with the Perfectly Matched Layer (PML) absorbing boundary condition. Furthermore, nonlinear propagation of laser femtosecond pulses and spectral broadening inside the proposed $As_{39}Se_{61}$ PCF core is accurately modelled by numerically solving the Generalized Nonlinear Schrödinger Equation (GNLSE) and employing the fourth-order Runge-Kutta in the interaction picture method. Moreover, we analyze the impact of pulses initial characteristics (duration and peak power) and the seeded noise on the generated supercontinuum bandwidth and coherence, respectively.

2. Theory

2.1. Linear and nonlinear properties of the $As_{39}Se_{61}$ PCF

Aiming to numerically calculate the effective refractive index and the optical field distribution of the fundamental mode, we have employed the FDFD method [36]. By applying the PML boundary condition, the Maxwell's equations for both the electric E and the magnetic H fields, respectively, are expressed as following:

$$\begin{cases} ik_0 s\varepsilon_r E = \nabla \times H \\ -ik_0 s\mu_r H = \nabla \times E \end{cases} \tag{1}$$

$$s = \begin{bmatrix} s_y/s_x & & \\ & s_x/s_y & \\ & & s_y s_x \end{bmatrix} \tag{2}$$

where $s_x = 1 - \sigma_x/(i\omega\varepsilon_0)$ and $s_y = 1 - \sigma_y/(i\omega\varepsilon_0)$.

k_0 is the free space number, ε_r is the medium relative permittivity, μ_r is the medium relative permeability, σ represents the conductivity profile and ω is the angular frequency. Using a suitable meshing scheme for the PCF structure, the system of equations given above is transformed into a matrix eigenvalue problem. For a given excitation wavelength, a sparse matrix approach is applied to calculate the effective refractive index n_{eff} and find the mode optical field distribution [37]. The refractive index of As$_{39}$Se$_{61}$ ChG glass is approximated to that of As$_{38}$Se$_{60}$ [34]. The wavelength dependence of the As$_{38}$Se$_{60}$ ChG glass refractive index has been measured in the wavelength range from 1.5 μm to 12 μm, as reported by [38]. The refractive index values of the As$_{38}$Se$_{60}$ ChG glass are fitted and approximated by using a two-term Sellmeier model given by:

$$n = \sqrt{a_0 + \frac{a_1\lambda^2}{\lambda^2 - b_1^2} + \frac{a_2\lambda^2}{\lambda^2 - b_2^2}} \tag{3}$$

With $a_0 = 3.7464$, $a_1 = 3.9057$, $b_1 = 0.4073$ μm, $a_2 = 0.9466$ and $b_2 = 40.082$ μm [39]. Fig. 1 shows the evolution of the As$_{38}$Se$_{60}$ glass refractive index obtained from experimental measurements and the Sellmeier model. As it can be seen, an excellent agreement is found between the measured and the calculated values of the refractive index where the values of the summed squares of residuals and the root mean squared error are found to be 5.87×10^{-7} and 2.31×10^{-4}, respectively [39]. The chromatic dispersion, which include both the material dispersion and the waveguide dispersion, can be calculated from n_{eff} using the following equation:

$$D(\lambda) = -\frac{\lambda}{c}\frac{d^2 n_{eff}}{d\lambda^2} \tag{4}$$

where λ and c are the wavelength and the speed of light, respectively.

The Kerr nonlinearity coefficient γ is expressed as [12]:

$$\gamma = \frac{n_2\omega_0}{cA_{eff}} \tag{5}$$

With $n_2 = 2.2 \times 10^{-17}\ m^2/W$, is the nonlinear refractive index for As$_{39}$Se$_{61}$ ChG glass [34] and A_{eff} represents the effective mode area given by [35]:
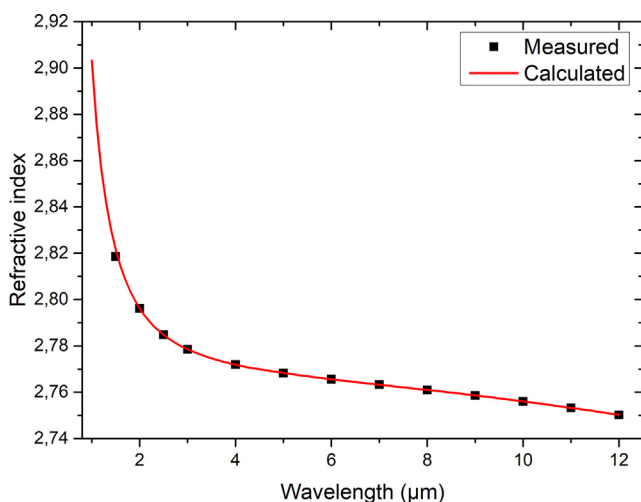

Fig. 1. Measured and calculated refractive index versus wavelength of the As$_{38}$Se$_{60}$ ChG glass.

$$A_{eff} = \frac{\left(\iint |E^2|\ dxdy\right)^2}{\iint |E|^4 dxdy} \tag{6}$$

where E represents the amplitude of the transverse electric field.

2.2. Modelling of SC generation

Nonlinear pulse propagation and SC spectral evolution inside optical fibers can be modeled by using the GNLSE. It describes the pulse evolution during its propagation within the PCF core, taking into account the different linear effects (optical loss and chromatic dispersion) and nonlinear effects (Kerr effect, Stimulated Raman Scattering and Self-steepening) [40]:

$$\frac{\partial\psi}{\partial z} + \frac{\alpha}{2}\psi + \left(\sum_{n\geq 2}\beta_n\frac{i^{n-1}}{n!}\frac{\partial^n}{\partial T^n}\right)\psi = i\gamma\left(1 + \frac{1}{\omega_0}\frac{\partial}{\partial t}\right) \times \left((1 - f_R)\psi\ |\psi|^2 \right.$$
$$\left. + f_R\psi\int_0^\infty h_R(\tau)|\psi(z, t - \tau)|^2 d\tau\right) \tag{7}$$

With $\psi(z, t)$ the complex envelope of the optical pulse field, z is the propagation distance and t is the retarded time. The left side of the GNLSE encompasses linear effects where α is the optical loss coefficient, $\beta_n = (d^n\beta/d\omega^n)_{\omega=\omega_0}$ are the dispersion coefficients calculated by a Taylor series expansion of the propagation constant and ω_0 is the pump pulses carrier frequency. The right side includes the nonlinear effects where pulse self-steepening effect is characterized by the shock term $\tau_{shock} = \frac{1}{\omega_0}$, γ is the Kerr nonlinearity coefficient, $h_R(t)$ is the Raman response function and f_R represents the Raman fractional contribution to the overall nonlinear response and it is equal to 0.1 for the As$_{39}$Se$_{61}$ ChG glass [34]. The Raman response function is described by a function representing two decaying harmonic oscillators with fractional contributions of f_a and f_b respectively [34,41]:

$$h_R(t) = f_a\tau_1(\tau_1^{-2} + \tau_2^{-2})exp\left(\frac{-t}{\tau_2}\right)sin\left(\frac{t}{\tau_1}\right)$$
$$+ f_b\tau_3(\tau_3^{-2} + \tau_4^{-2})exp\left(\frac{-t}{\tau_4}\right)sin\left(\frac{t}{\tau_3}\right) \tag{8}$$

With $f_a = 0.7$, $f_b = 0.3$, $\tau_1 = 23$ fs, $\tau_2 = 230$ fs, $\tau_3 = 20.5$ fs and $\tau_4 = 260$ fs.

Aiming to accurately solve the GNLSE, we have employed the fourth-order Runge-Kutta in the interaction picture method (RK4IP) [40]. This algorithm has been successfully implemented to study the Bose-Einstein condensates and is found suitable to describe optical pulses propagation due to the similarity between the GNLSE and the Gross-Pitaevskii equation [42]. Besides, the RK4IP method has shown high computational efficiency compared to other split-step schemes such as simple split-step, symmetric split-step RK2, and symmetric split-step RK4 [40,43]. The RK4IP method is based on the separation of the dispersion effects from the nonlinear effects by transforming the GNLSE into an interaction picture. This approach allow to use explicit techniques to find the solution and achieve high numerical accuracy [44,45].

The coherence properties of the SC generated in the proposed As$_{39}$Se$_{61}$ PCF are numerically evaluated through the calculation of the modulus of the complex degree of first-order coherence as follow [46]:

$$|g_{12}^{(1)}(\lambda)| = \left|\frac{<E_1^*(\lambda)><E_2(\lambda)>}{[<|E_1(\lambda)^2|><|E_2(\lambda)^2|>]^{1/2}}\right| \tag{9}$$

where the angle brackets represents an average over an ensemble of SC electric fields pairs, generated independently. For each of the SC generation simulation, we consider the addition of a quantum noise, generated based on the one photon per mode model [47]. Accordingly, we add a photon with a random phase to each frequency bin, where the amplitude of the noise seed is given in the frequency domain by the following expression [48]:

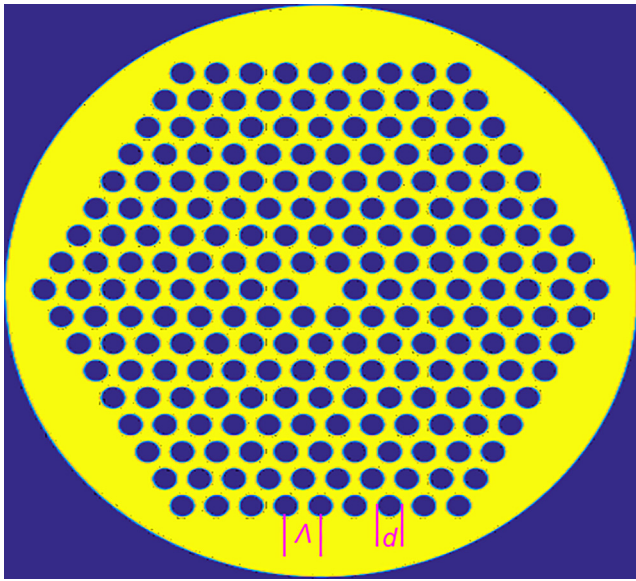$$\delta_{OPM}(\omega) = \sqrt{\frac{\hbar\omega}{\Delta\Omega}}exp(i2\pi\varphi(\omega)) \tag{10}$$

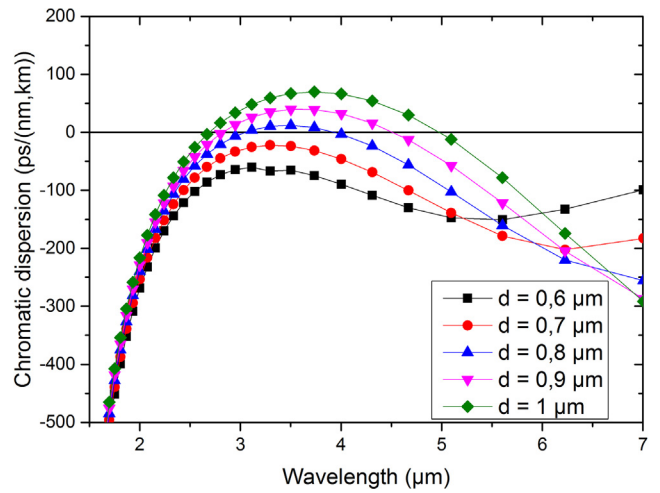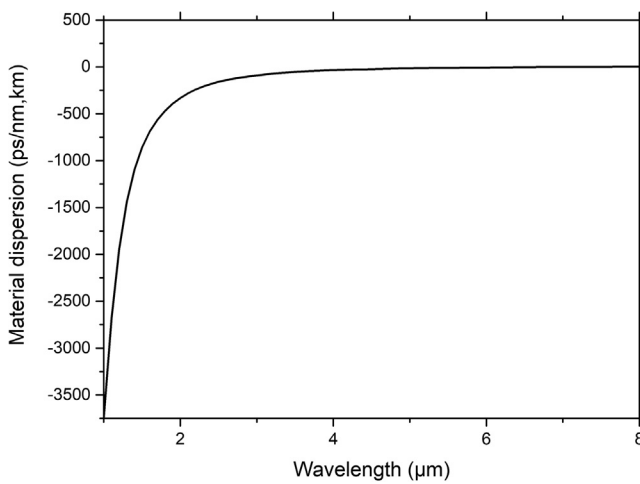**Fig. 2.** Cross sectional view of the proposed As$_{39}$Se$_{61}$ ChG glass PCF.

Fig. 3. Variation of the material dispersion with wavelengths of the As$_{39}$Se$_{61}$ ChG glass.

Fig. 4. Variation of the fundamental mode effective index with wavelengths for $\Lambda = 1.8\ \mu m$ and d varying from 0.6 μm to 1 μm with step of 0.1.

Fig. 5. Variation of the chromatic dispersion with wavelengths for $\Lambda = 1.8\ \mu m$ and d varying from 0.6 μm to 1 μm with step of 0.1.
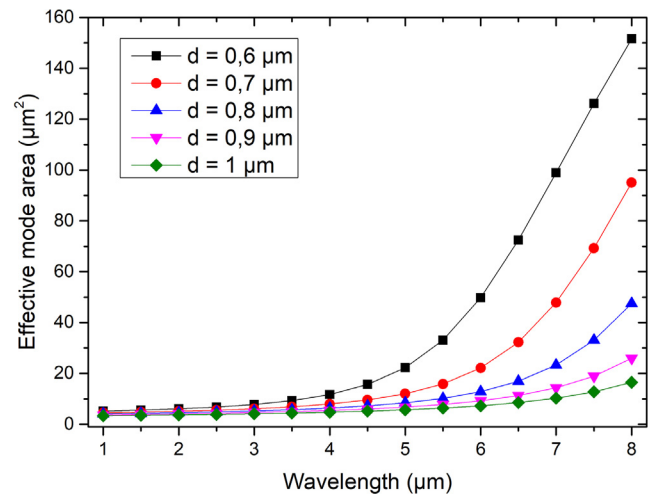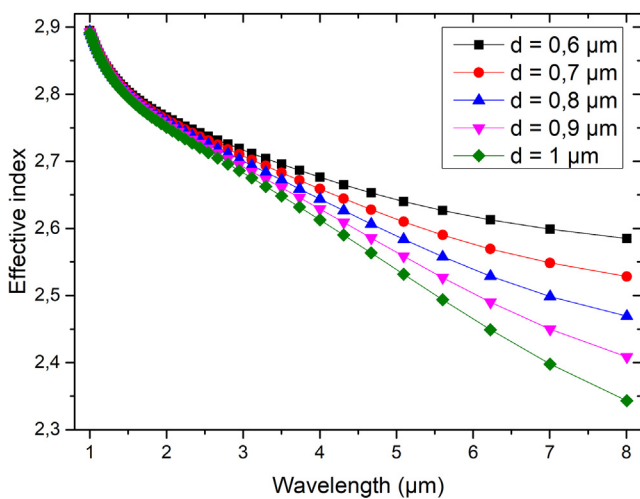

Fig. 6. Variation of the effective mode area with wavelengths for $\Lambda = 1.8$ μm and d varying from 0.6 μm to 1 μm with step of 0.1.
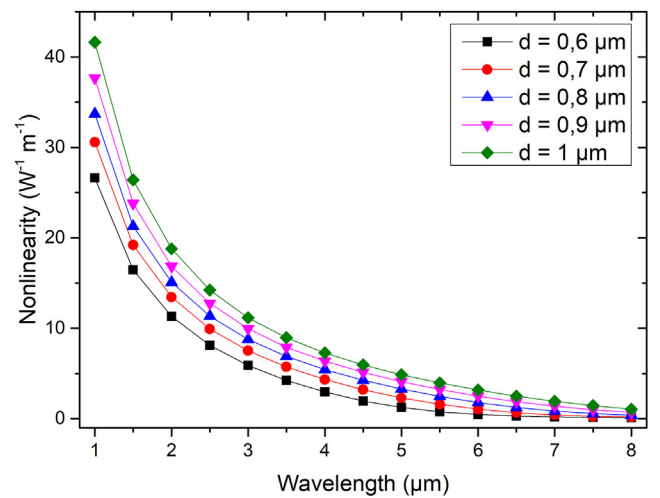

Fig. 7. Variation of the Kerr nonlinear coefficient with wavelengths for $\Lambda = 1.8$ μm and d varying from 0.6 μm to 1 μm with step of 0.1.

Table 1

β_n coefficients computed at 3.45 µm for As$_{39}$Se$_{61}$ PCF with $d = 0.7$ µm and $d = 0.8$ µm, respectively.

Coefficient	$d = 0.7$	$d = 0.8$
β_2	148.4 ps^2/km	-71.6 ps^2/km
β_3	-1.2 ps^3/km	0.324 ps^3/km
β_4	3.98×10^{-2} ps^4/km	2.82×10^{-2} ps^4/km
β_5	-5.64×10^{-4} ps^5/km	-5.03×10^{-4} ps^5/km
β_6	6.75×10^{-6} ps^6/km	8.59×10^{-6} ps^6/km
β_7	-8.12×10^{-8} ps^7/km	-1.57×10^{-7} ps^7/km
β_8	1.94×10^{-9} ps^8/km	2.65×10^{-9} ps^8/km
β_9	-4.68×10^{-11} ps^9/km	-2.36×10^{-11} ps^9/km

Here $\hbar$ is the reduced Planck constant, ω denotes the pulsation, $\Delta\Omega$ is the spectral bin size used for the simulations and $\varphi(\omega)$ is a random phase, uniformly distributed over the interval given by $[0, 2\pi]$.

3. Numerical results

3.1. PCF design and chromatic dispersion engineering

The proposed PCF cross section is depicted in Fig. 2. The structure is composed of eight rings of air holes arranged in a hexagonal configuration in As$_{39}$Se$_{61}$ based background glass. The solid core is obtained by the elimination of one air hole in the center of the structure. The pitch and the diameter of air holes are Λ and d, respectively. As mentioned previously, we aim to design As$_{39}$Se$_{61}$ glass based triangular lattice PCF with negative chromatic dispersion, allowing to generate flat-top and coherent supercontinua over a wide band of wavelengths. To that end, the PCF structure is optimized by carefully adjusting the air holes diameter and the pitch. Actually, the dispersion engineering of PCFs is fundamentally limited by the material dispersion of the PCF background glass [49]. Fig. 3 depicts the As$_{39}$Se$_{61}$ glass material dispersion obtained by deriving Eq. (3). It is clear to observe that the glass exhibits both negative and positive dispersion with a zero dispersion value at 7.55 µm. Sight to achieve ANDi regime over a wide band of wavelengths, the proposed As$_{39}$Se$_{61}$ PCF structure parameters are

carefully adjusted to engineer the waveguide dispersion and compensate the material dispersion. The structure optimization process is performed by considering different values of the cladding air-filling fraction. Fig. 4 gives the variation of the fundamental mode effective index with wavelengths for $\Lambda = 1.8$ µm and d varying from 0.6 µm to 1 µm with a step of 0.1 µm. Subsequently, the chromatic dispersion is calculated and its evolution with wavelengths is illustrated in Fig. 5. As it can be noticed, the chromatic dispersion depends strongly on the value of the air-filling fraction. From the figure, we observe that dispersion curve increases when d/Λ increases too with a peak value obtained around the wavelength 3.45 µm. Besides, ANDi regime with a peak close to the zero dispersion can be achieved for $d = 0.7$ µm. The nonlinear properties of the proposed PCF are then investigated. We have computed both the effective field mode area and the corresponding Kerr nonlinearity coefficient, where their variations versus wavelengths are shown in Figs. 6 and 7, respectively. Simulations results show that the proposed PCF exhibits high nonlinearity over the whole spectral range. Moreover, for the As$_{39}$Se$_{61}$ PCF with $d = 0.7$ µm, the effective mode area and Kerr nonlinear coefficient for the wavelength 3.45 µm, have been found to be 6.8 µm^2 and 5.89 w^{-1} m^{-1}, respectively.

3.2. SC generation in the As$_{39}$Se$_{61}$ PCF

Aiming to study femtosecond pulse propagation and SC formation in the proposed As$_{39}$Se$_{61}$ PCF, we have employed the GNLSE given by Eq. (7); which is implemented and solved using the RK4IP method. The laser pulses used in the simulations are modelled by a hyperbolic secant pulse centered at the pumping wavelength and are expressed as $\psi(t) = \sqrt{P_0}\,\text{sech}(t/T_0)$ where, P_0 is the peak power and T_0 is the pulse duration given by $T_0 = T_{FWHM}/1.76$ where T_{FWHM} is the Full Width at Half Maximum (FWHM) duration of the laser pulse. In order to ensure high numerical accuracy, pulse propagation simulations are performed by considering an integrator error of 0.001, temporal disctrization points of 2×10^{12} and the PCF length over which pulses propagate is segmented into 100 steps. Firstly, and sight to show the performance of pumping in the ANDi regime to generate high flatness SC spectra, we have considered SC generation in 1 cm length of the As$_{39}$Se$_{61}$ PCF with $d = 0.7$ µm (ANDi regime) and $d = 0.8$ µm (anomalous regime). For
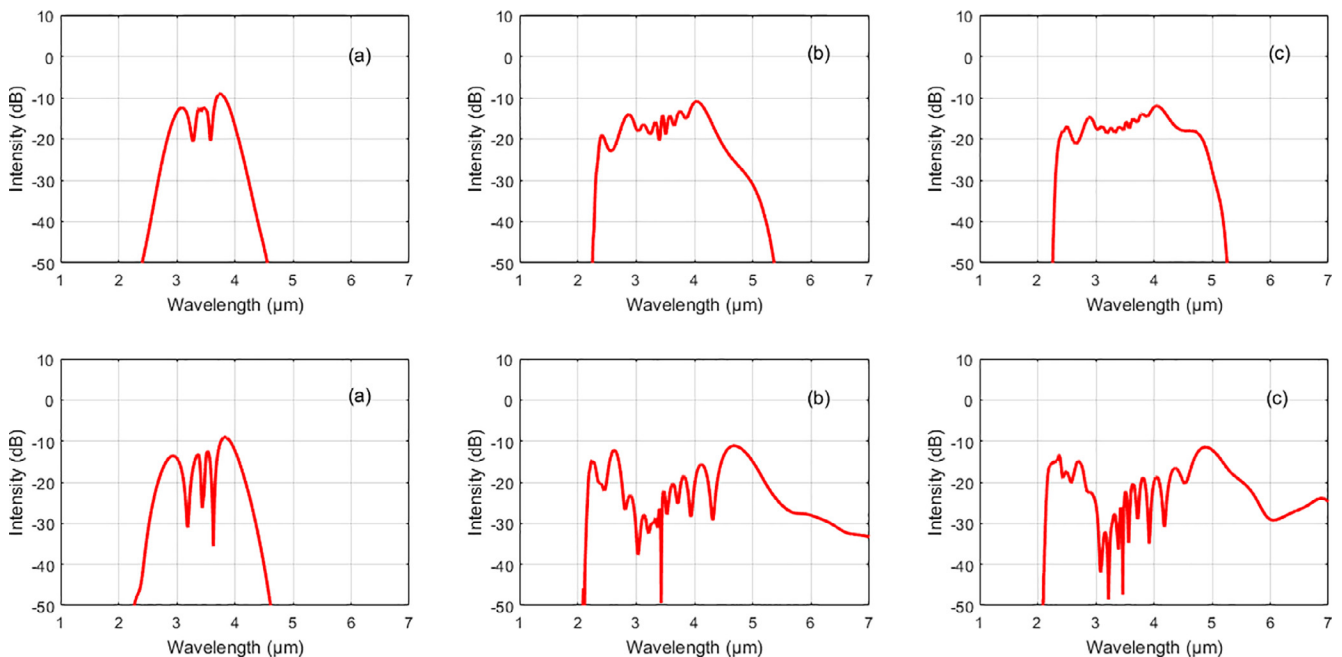
Fig. 8. SC spectrum after propagation over 2 mm (a), 6 mm (b) and 10 mm (c) of the As$_{39}$Se$_{61}$ PCF length with $d = 0.7$ µm (top) and $d = 0.8$ µm (bottom), respectively, for an input pulse with a total energy of 150 pJ.
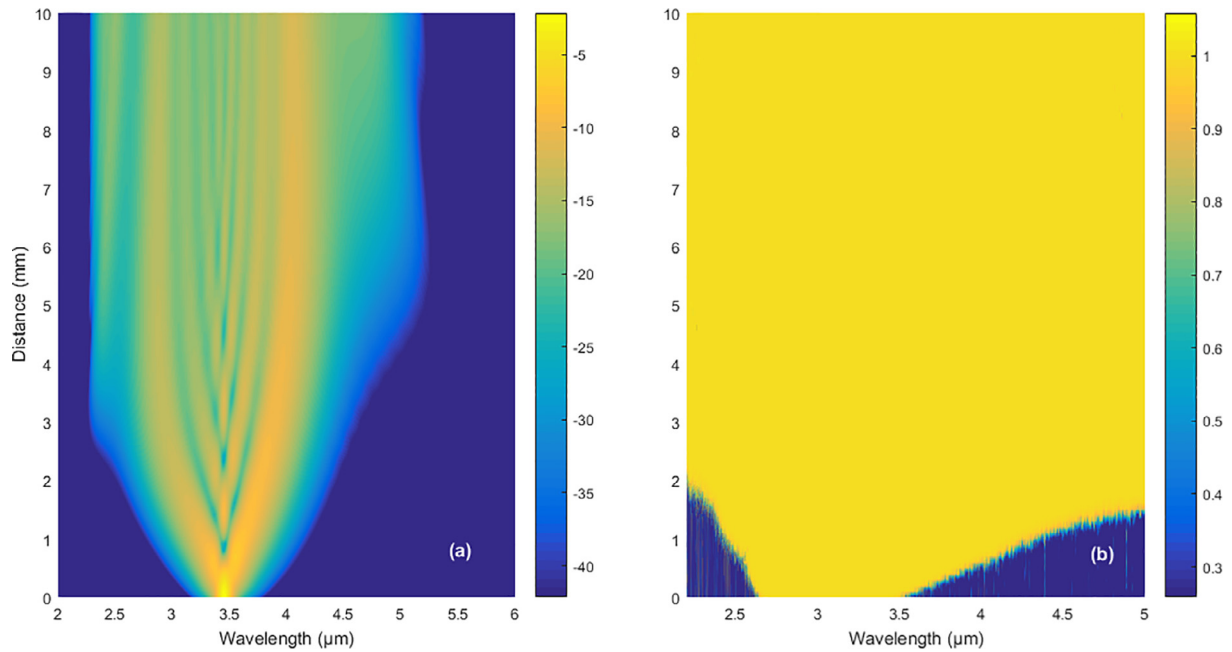
Fig. 9. Pulse spectral evolution with the propagation distance and the corresponding coherence of a 150 pJ laser pulse.
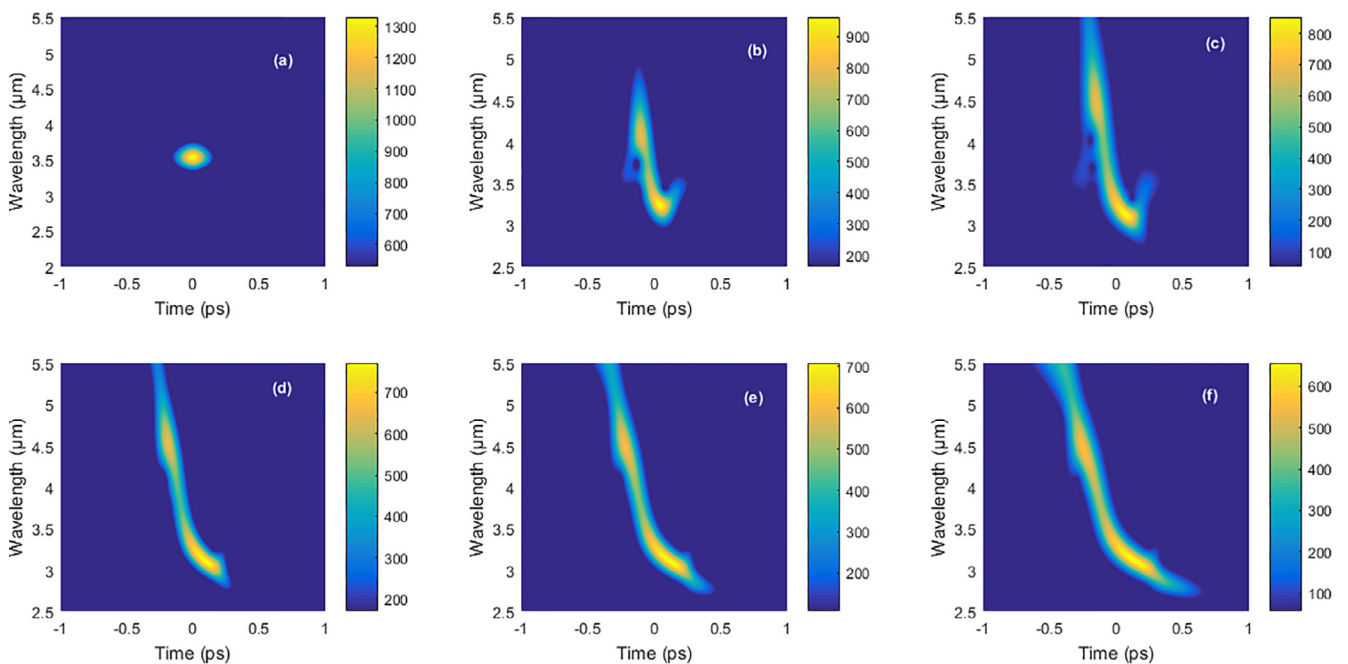

Fig. 10. Pulse spectrograms at the PCF input and after 2 mm, 4 mm, 6 mm, 8 mm and 10 mm of propagation, respectively, for an initially pumped pulse with a total energy of 150 pJ.

both two cases, we launch the pulse close to the zero dispersion wavelength at 3.45 μm. These optical pulses can be obtained by employing mid-infrared femtosecond laser fiber system, as reported in [50]. The light source, which is composed of a conventional femtosecond near-infrared laser and especially designed suspended core tungstate-telluride fiber, can be used to generate 100 fs duration optical pulses in the mid-infrared wavelengths range extending from 2 to 5 μm. The impact of the chromatic dispersion is accurately modelled through the Taylor series expansion coefficients of the propagation constant, expressed, up to the 9th order, at the pumping pulse frequency. Their values for both $d = 0.7$ μm and $d = 0.8$ μm designs, respectively, are given by Table 1.

We consider initial pumping at 3.45 μm of a laser pulse with a total energy of 150 pJ, corresponding to a peak power and T_{FWHM} duration of

0.88 kw and 150 fs, respectively. Fig. 8 depicts the output SC spectrum after propagation over 2 mm, 6 mm and 10 mm of the $As_{39}Se_{61}$ PCF length with $d = 0.7$ μm and $d = 0.8$ μm, respectively. Notwithstanding that SC generation achieved inside the PCF design with $d = 0.8$ μm is broader compared to that obtained with $d = 0.7$ μm, the output spectrum exhibits strong fluctuations among the generated spectral components even with small propagation lengths. By pumping in the ANDi regime, the output pulse SC spectrum shows smooth profile with small fluctuations within a spectral level of less than 10 dB. These spectral fluctuations are substantially reduced and SC extension to the mid-infrared region is achieved through the SPM and OWB mechanisms. Moreover, the output SC spectra, generated using the proposed $As_{39}Se_{61}$ PCF with $d = 0.7$ μm, are realized with high degree of coherence. Fig. 9
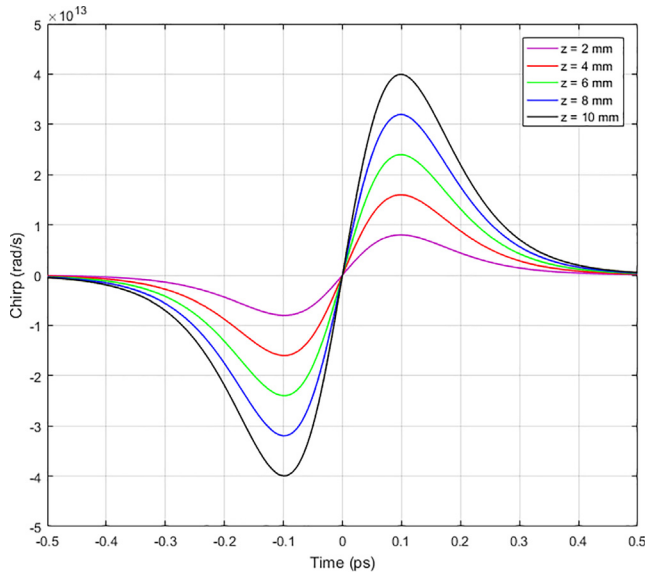
Fig. 11. Frequency chirp acquired by the pulse at different positions of the PCF length for an initially pumped pulse with a total energy of 150 pJ.

shows the pulse spectral evolution with the propagation distance and the corresponding coherence, calculated with 30 independent realizations at each distance point, of a 150 pJ laser pulse. Owing to the deterministic nature of the SPM and OWB mechanisms, the SC spectrum, achieved at each step of propagation length, is of high degree of coherence over the entire spectral band. The nonlinear optical process, namely SPM and OWB, which contribute to the pulses spectral broadening in the $As_{39}Se_{61}$ PCF with ANDi regime, can be effectively, investigated and confirmed, by employing a time-frequency representation of optical pulses, through the calculation of their spectrograms. Optical pulses spectrograms are calculated by applying Fourier transform to time gated parts of their electric component $E(t)$ as following:

$$S(\omega, \tau) = \left| \int_{-\infty}^{\infty} E(t)g(t - \tau)e^{-i\omega t}dt \right|^2 \tag{11}$$

where $g(t - \tau)$ is the gate function. This way of representation can be experimentally achieved by employing the cross correlation Frequency Resolved Optical Gating (XFROG) technique. Fig. 10 depicts the pulse spectrograms at the PCF input and after 2 mm, 4 mm, 6 mm, 8 mm and 10 mm of propagation, respectively, for an initially pumped pulse with a total energy and T_{FWHM} duration of 150 pJ and 150 fs, respectively. In the first stage of propagation, the pulse spectrum starts to broaden in a symmetrical fashion due to the SPM. The generated SC exhibits some spectral ripples on its top, as shown by the oscillatory structure in Fig. 9. The SPM induced frequency chirp acquired by the pulse during its propagation in the $As_{39}Se_{61}$ PCF is given by the following expression [51]:

$$\omega_c(z, t) = \frac{2\beta_2 z}{T_0^3}\left(\frac{\gamma P_0 T_0^2}{\beta_2} + 1\right)tanh\left(\frac{t}{T_0}\right)sech^2\left(\frac{t}{T_0}\right) \tag{12}$$

With z is the propagation distance. Fig. 11 depicts the frequency chirp in the propagating pulse for different values of z. The pulse leading edge (front part) experiences red shifting due to the negative frequency chirp from the center, while the trailing edge (back part) experiences blue shifting due to the positive frequency chirp. Moreover, the induced frequency chirp increases with propagation distance, leading to a substantial spectral broadening [3]. After few millimeters of propagation, the pulse undergoes OWB process, which occurs on the pulse leading and trailing edges. OWB associated with FWM are responsible for the creation of new frequencies through the overlapping of different pulse spectral components and the inducing of a sinusoidal beating between them [52]. The distance at which the OWB is first observed can be calculated by using the following formula [53,54]:

$$L_{OWB} = \sqrt{\frac{3\beta_2}{2\beta_2 + 2\gamma P_0 T_0^2}} \frac{T_0^2}{\beta_2} \tag{13}$$

For this simulation where $\beta_2 = 148.4 \ ps^2/km$, $\gamma = 5.89 \ w^{-1} \ m^{-1}$, $P_0 = 0.88 \ kW$ and $T_0 = 85 \ 22 \ fs$, the OWB distance is found to be 3.75 mm. Fig. 12 shows the pulse temporal evolution along the PCF length, with the dashed line indicating the onset of the OWB process, and the pulse spectrogram computed at the distance point of 3.75 mm. The pulse spectrum continues to extend toward short and long wavelengths, where new generated spectral wavelengths gain energy from the pulse
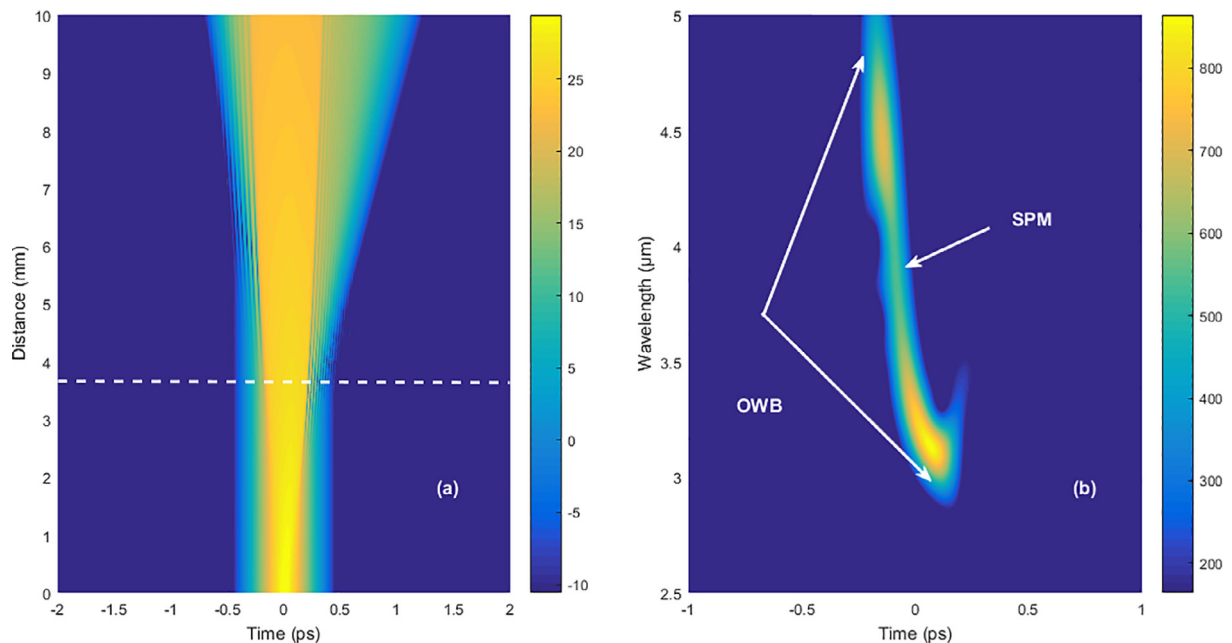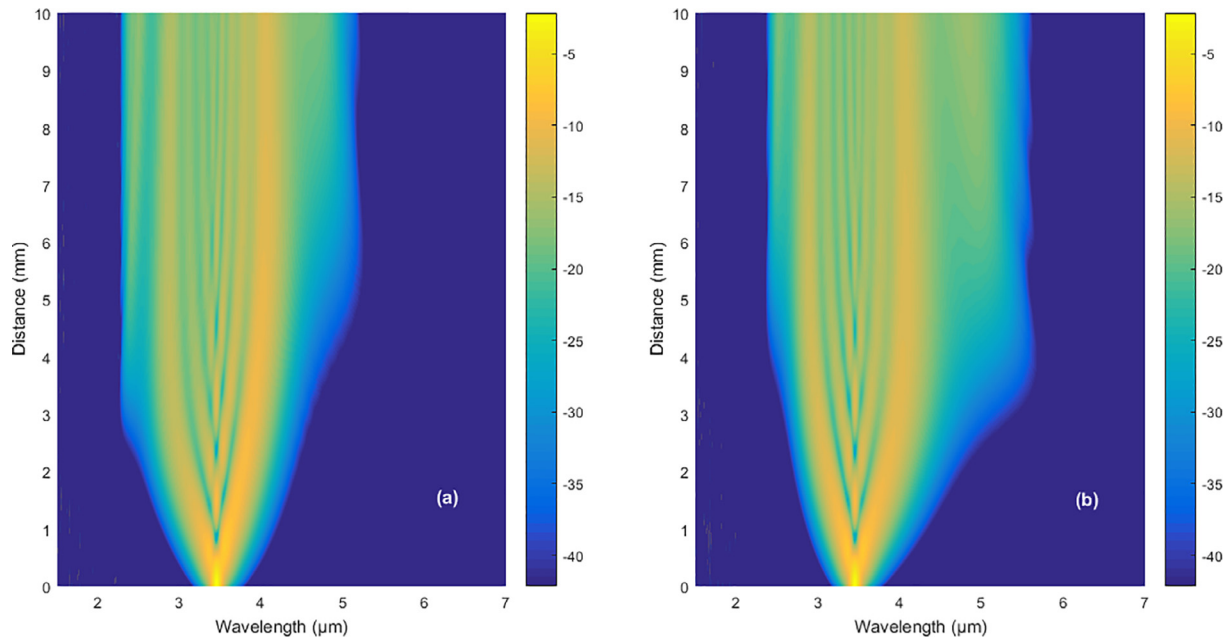

Fig. 12. Pulse temporal evolution along the PCF length and the pulse spectrogram computed at the distance point of 3.75 mm. The dashed line indicates the onset of the OWB process.

Fig. 13. Pulse spectral evolution with propagation distance with all nonlinear effects included (a) and without Raman stimulated scattering and pulse self-steepening (b).
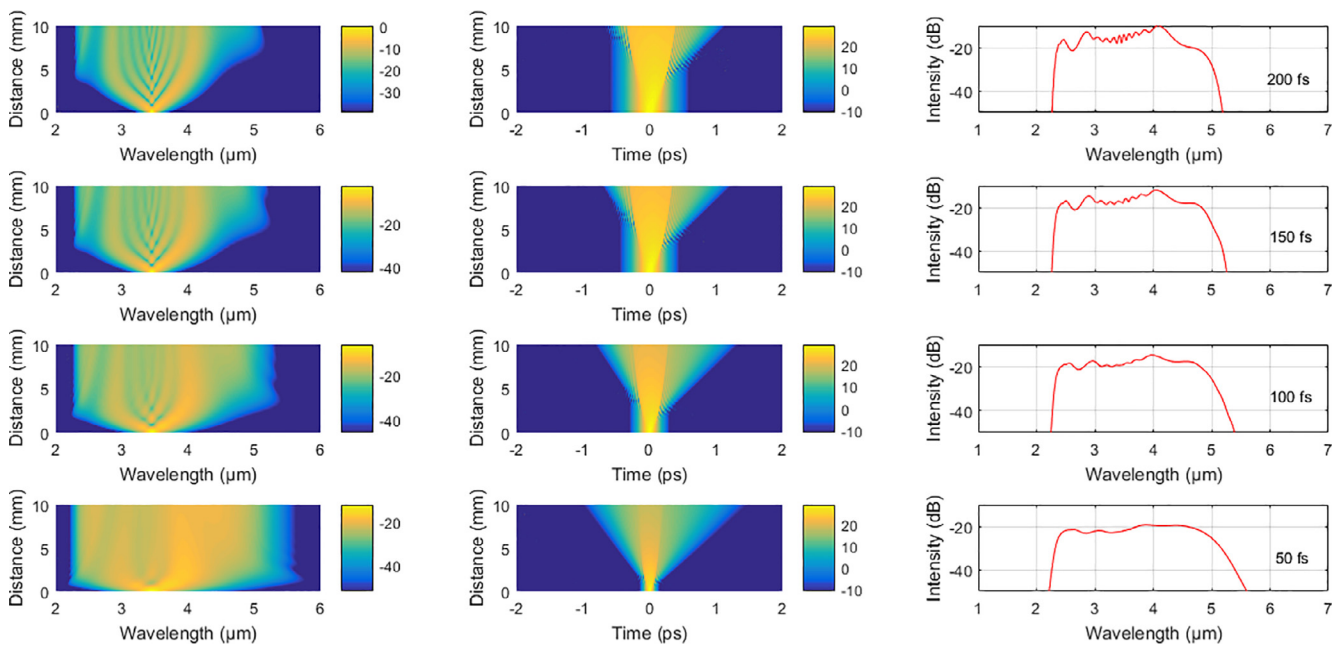

Fig. 14. Pulse spectral and temporal evolution with propagation distance and the output pulse spectrum after propagation over PCF length of 10 mm for pulse peak power of 0.88 kW and T_{FWHM} of 200 fs, 150 fs, 100 fs and 50 fs, respectively.

spectrum central part. Although we have employed the GNLSE to simulate SC generation, we have found that both Raman stimulated scattering and pulse self-steepening have no significant impact on the spectral broadening process. Fig. 13 shows the pulse spectral evolution with PCF length with all nonlinear effects included (13.a) and without including both the Raman stimulated scattering and pulse self-steepening (13.b). In order to optimize the spectral bandwidth of the generated SC, we have studied the impact of the initial parameters of the pumped laser pulses. We have performed a series of numerical simulations with various values of the pulse energy and duration. Firstly, the influence of the pulse duration T_{FWHM} is considered. Simulations are conducted with a pulse peak power of 0.88 kW and T_{FWHM} of 200 fs, 150 fs, 100 fs and 50 fs, respectively. Fig. 14 depicts the pulse spectral

and temporal evolution with propagation distance and the output pulse spectrum after propagation over PCF length of 10 mm. As can be seen, the decreasing of the input pulse duration has a beneficial impact on the spectrum width and flatness of the output pulse. In fact, the OWB length given by (13) is proportional to the pulse duration. Accordingly, when T_{FWHM} is reduced, the combined effect of OWB and FWM is shortly induced, which lead to substantially extend the generated SC bandwidth and enhance its flatness. Moreover, for a pulse duration of 50 fs (pulse energy of 50 pJ), broad SC spectra spanning the mid-infrared region and extending from 2.43 μm to 4.85 μm at the spectral level of 4 dB is achieved, along with smooth spectral profile. Furthermore, we have examined the impact of pulse peak power on the SC characteristics. Fig. 15 gives generated SC with a PCF length of 10 mm and the
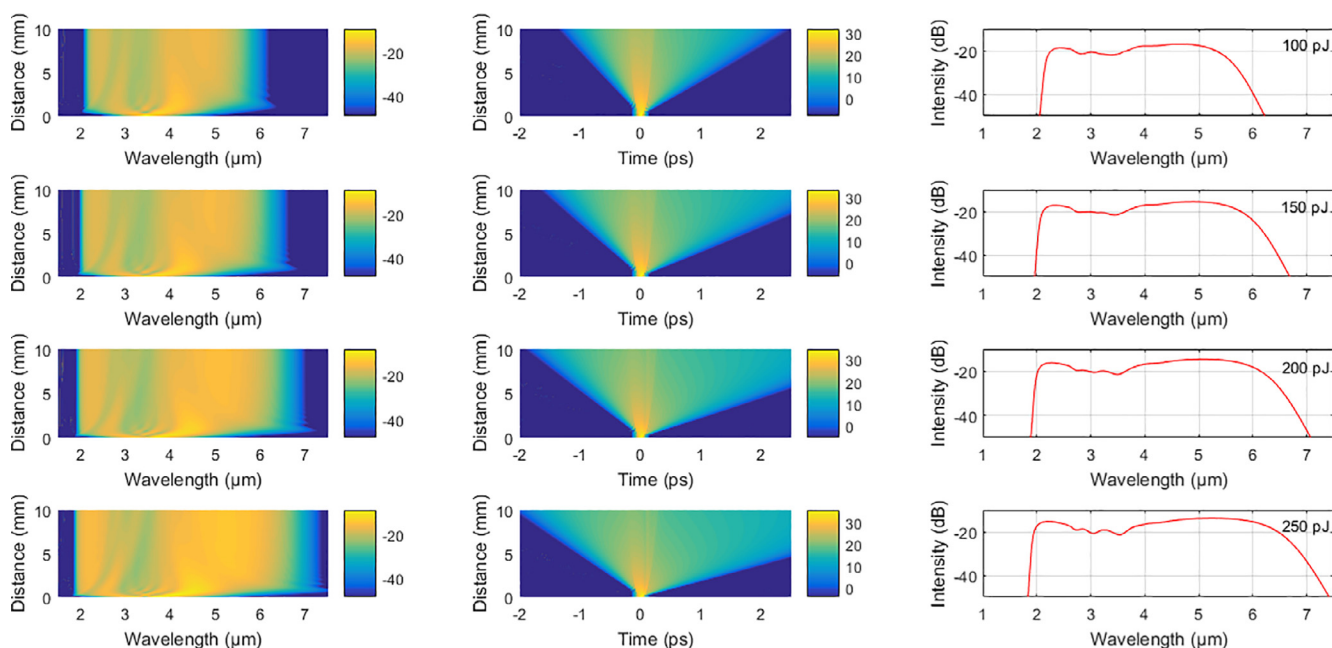
Fig. 15. Pulse spectral and temporal evolution with propagation distance and the output pulse spectrum after propagation over PCF length of 10 mm for pulse duration of 50 fs and total energy of 100 pJ, 150 pJ, 200 pJ and 250 pJ, respectively.
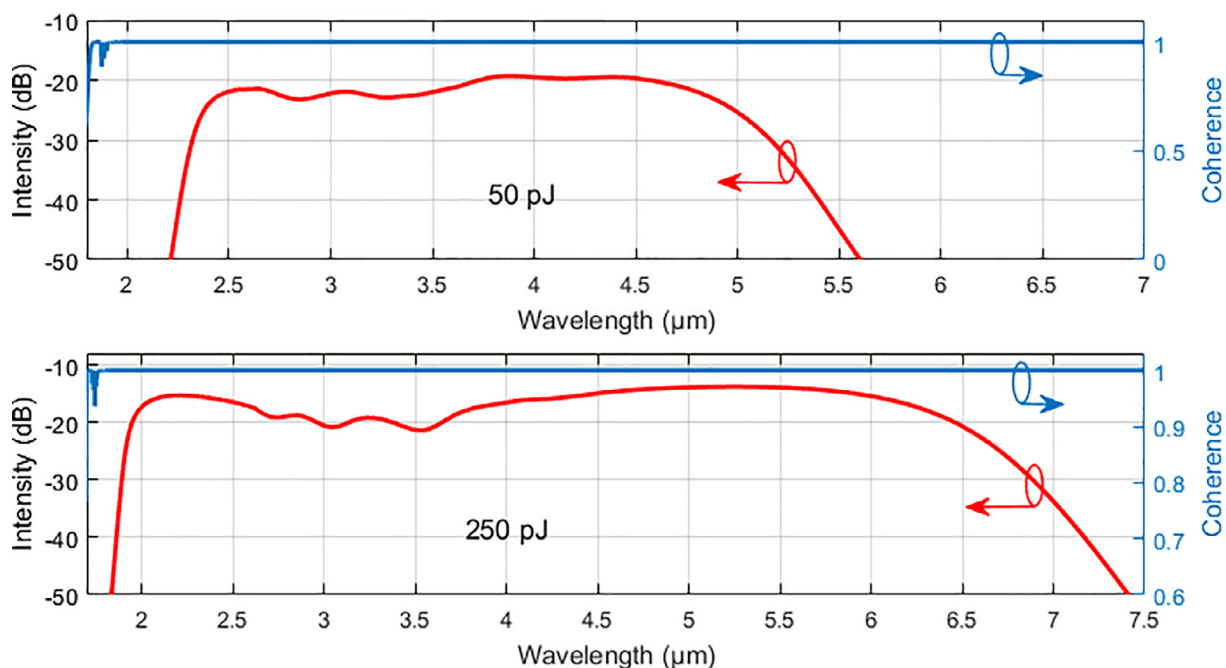

Fig. 16. SC generated in 1 cm $As_{39}Se_{61}$ PCF length and the corresponding coherence for an input pulse duration of 50 fs and total energy of 50 pJ and 250 pJ, respectively.

corresponding pulse spectral and temporal evolution with propagation distance. The pumped laser pulse has a T_{FWHM} of 50 fs and a peak power of 1.76 kW, 2.64 kW, 3.52 kW and 4.4 kW, which corresponds to pulse total energy of 100 pJ, 150 pJ, 200 pJ and 250 pJ, respectively. It is clearly to observe that the output pulse spectrum increases when the pulse peak power increases too and ultraflat-top broadband SC spanning the mid-infrared range from 1.95 μm to 6.58 μm at the spectral level of 8 dB is obtained with pulse energy of 250 pJ. Besides, and as is shown by Fig. 16, the generated SC in the ANDi $As_{39}Se_{61}$ based PCF exhibits high degree of coherence over the entire spectral range for both 50 pJ and 250 pJ pulses. The SC generated in our proposed ANDi $As_{39}Se_{61}$ ChG PCF by pumping 50 fs duration pulses with a total energy

of 50 pJ and 250 pJ, respectively, is compared to other obtained by various ChG based PCF designs. As presented in Table 2, the proposed $As_{39}Se_{61}$ PCF shows high potential to generate broadband and ultraflat-top mid-infrared SC using very low energy laser pulses.

4. Conclusion

In summary, we have studied an all-normal dispersion and highly nonlinear chalcogenide based PCF for coherent, broadband and ultra-flat-top mid-infrared SC generation. The proposed PCF consists of solid core made of $As_{39}Se_{61}$ ChG glass surrounded by eight rings of air holes arranged in hexagonal lattice. Numerical results indicate that targeted

Table 2

SC bandwidth and flatness generated in the proposed $As_{39}Se_{61}$ ChG PCF compared to selected PCF designs made of various types of ChG glass.

Reference	ChG glass	Pumping wavelength (μm)	Spectral flatness level	SC bandwidth (μm)
[25]	As_2S_3	3	10 dB	2–4.55
[26]	$AsSe_2$-As_2S_5	2.7	–	2.2–3.3
[53]	As_2S_5-Borosilicate	2.5	8 dB	1.05–5.05
[53]	As_2S_5-Borosilicate	2.5	20 dB	0.9–5.25
[55]	As_2S_3	2.8	20 dB	2.41–3.15
[56]	$As_{38.8}Se_{61.2}$	3.7	3 dB	2.9–4.57
[32]	As_2Se_3	4.37	3 dB	3.86–5.95
This work	$As_{39}Se_{61}$	3.45	4 dB	2.43–4.85
This work	$As_{39}Se_{61}$	3.45	8 dB	1.95–6.58

dispersion properties can be achieved simply by adjusting the air hole filling ratio in the cladding region and ANDi profile is obtained over the entire computational domain with a nearly zero dispersion wavelength of 3.45 μm. Besides, the proposed structure exhibits small effective mode area and high Kerr nonlinearity of 6.8 μm^2 and 5.89 w^{-1} m^{-1}, respectively, at the pumping wavelength (i.e. 3.45 μm). Furthermore, SC generation at 3.45 μm in the optimized design has been modelled through the GNLSE and using the RK4IP method. The impact of the input pulse peak power and duration on the output spectral bandwidth has been investigated. Simulations results have shown that broad and ultraflat-top SC spectrum extending from 2.43 μm to 4.85 μm at the 4 dB spectral level is successfully generated by using a 0.88 kW peak power 50 fs duration input pulse (corresponding to pulse energy of 50 pJ) in only 1 cm PCF length. Moreover, by increasing the pulse peak power to reach 4.4 kW (pulse energy of 250 pJ), perfectly coherent and ultraflat-top SC spectrum spanning the wavelength range from 1.95 μm to 6.58 μm at the 8 dB spectral level is successfully generated. Owing to its interesting properties, the proposed $As_{39}Se_{61}$ ChG glass PCF is found to be suitable for various potential mid-infrared applications such as optical coherence tomography, spectroscopy, material characterization and metrology.

References

[1] S. Dai, Y. Wang, X. Peng, P. Zhang, X. Wang, Y. Xu, A review of mid-infrared supercontinuum generation in chalcogenide glass fibers, Appl. Sci. 8 (2018) 707, https://doi.org/10.3390/app8050707.

[2] R.R. Alfano, S.L. Shapiro, Observation of self-phase modulation and small-scale filaments in crystals and glasses, Phys. Rev. Lett. 24 (1970) 592–596, https://doi.org/10.1103/PhysRevLett. 24.592.

[3] D. Faccio, J.M. Dudley, Frontiers in modern optics, Proceedings of the International School of Physics: Enrico Fermi, IOS press, The Netherlands, 2016.

[4] C.R. Petersen, N. Prtljaga, M. Farries, J. Ward, B. Napier, G.R. Lloyd, J. Nallala, N. Stone, O. Bang, Mid-infrared multispectral tissue imaging using a chalcogenide fiber supercontinuum source, Opt. Lett. 43 (5) (2018) 999–1002, https://doi.org/10.1364/OL.43.000999.

[5] A.V. Paterova, H. Yang, C. An, D.A. Kalashnikov, L.A. Krivitsky, Tunable optical coherence tomography in the infrared range using visible photons, Quantum Sci. Technol. 3 (2018) 025008, , https://doi.org/10.1088/2058-9565/aab567.

[6] F. Borondics, M. Jossent, C. Sandt, L. Lavoute, D. Gaponov, A. Hideur, P. Dumas, S. Février, Supercontinuum-based Fourier transform infrared spectromicroscopy, Optica 5 (4) (2018) 378–381, https://doi.org/10.1364/OPTICA.5.000378.

[7] C.R. Petersen, P.M. Moselund, L. Huot, L. Hooper, O. Bang, Towards a table-top synchrotron based on supercontinuum generation, Infrared Phys. Technol. 91 (2018) 182–186, https://doi.org/10.1016/j.infrared.2018.04.008.

[8] J.M. Dudley, J.R. Taylor, Supercontinuum Generation in Optical Fibers, Cambridge University Press, 2010 10.1017/CBO9780511750465.

[9] J.M. Dudley, G. Genty, S. Coen, Supercontinuum generation in photonic crystal fiber, Rev. Mod. Phys. 78 (2006) 1135–1184, https://doi.org/10.1103/RevModPhys. 78.1135.

[10] A.M. Heidt, A. Hartung, G.W. Bosman, P. Krok, E.G. Rohwer, H. Schwoerer, H. Bartelt, Coherent octave spanning near-infrared and visible supercontinuum generation in all-normal dispersion photonic crystal fibers, Opt. Express 19 (2011) 3775–3787, https://doi.org/10.1364/OE.19.003775.

[11] C. Huang, M. Liao, W. Bi, X. Li, L. Hu, L. Zhang, L. Wang, G. Qin, T. Xue, D. Chen, W. Gao, Ultraflat, broadband, and highly coherent supercontinuum generation in all-solid microstructured optical fibers with all-normal dispersion, Photonics Res. 6

[12] A. Medjouri, D. Abed, O. Ziane, L.M. Simohamed, Design and optimization of As_2S_5 chalcogenide channel waveguide for coherent mid-infrared supercontinuum generation, Optik 154 (2018) 811–820, https://doi.org/10.1016/j.ijleo.2017.10.135.

[13] J.M. Dudley, J.R. Taylor, Ten years of nonlinear optics in photonic crystal fibre, Nat. Photonics 3 (2009) 85–90, https://doi.org/10.1038/nphoton.2008.285.

[14] M. Yasin, S.W. Harun, H. Arof, Recent progress in optical fiber research, InTech (2011).

[15] Luc Thévenaz, Advanced Fiber Optics Concepts and Technology, EPFL press, Switzerland, 2012 10.5772/2428.

[16] Bikash Kumar Paula, Kawsar Ahmed, Si_7N_3 material filled novel heptagonal photonic crystal fiber for laser applications, Ceram. Int. 45 (2019) 1215–1218, https://doi.org/10.1016/j.ceramint.2018.09.307.

[17] Bikash Kumar Paul, Md. Golam Moctader, Kawsar Ahmed, Md. Abdul Khalek, Nanoscale GaP strips based photonic crystal fiber with high nonlinearity and high numerical aperture for laser applications, Results Phys. 10 (2018) 374–378, https://doi.org/10.1016/j.rinp.2018.06.033.

[18] S. Maheswaran, Bikash Kumar Paul, Md. Abdul Khalek, Sujan Chakma, Kawsar Ahmed, M.S. Mani Rajan, Design of Tellurite glass based quasi photonic crystal fiber with high nonlinearity, Optik 181 (2019) 185–190, https://doi.org/10.1016/j.ijleo.2018.12.033.

[19] Bikash Kumar Paul, Fahad Ahmed, Md. Golam Moctader, Kawsar Ahmed, Dhasarathan Vigneswarane, Silicon nano crystal filled photonic crystal fiber for high nonlinearity, Opt. Mater. 84 (2018) 545–549, https://doi.org/10.1016/j.optmat.2018.07.054.

[20] Bikash Kumar Paul, Md. Abdul Khalek, Sujan Chakma, Kawsar Ahmed, Chalcogenide embedded quasi photonic crystal fiber for nonlinear optical applications, Ceram. Int. 44 (2018) 18955–18959, https://doi.org/10.1016/j.ceramint.2018.07.134.

[21] Bikash Kumar Paul, Sujan Chakma, Md. Abdul Khalek, Kawsar Ahmed, Silicon nano crystal filled ellipse core based quasi photonic crystal fiber with birefringence and very high nonlinearity, Chin. J. Phys. 56 (2018) 2782–2788, https://doi.org/10.1016/j.cjph.2018.09.030.

[22] Y. Wu, M. Meneghetti, J. Troles, J.L. Adam, Chalcogenide microstructured optical fibers for mid-infrared supercontinuum generation: interest, fabrication, and applications, Appl. Sci. 8 (2018) 1637, https://doi.org/10.3390/app8091637.

[23] S. Wabnitz, B.J. Eggleton, All-optical Signal Processing: Data Communication and Storage Applications, Springer, 2015 10.1007/978-3-319-14992-9.

[24] B.J. Eggleton, B.L. Davies, K. Richardson, Chalcogenide photonics, Nat. Photonics 5 (2011) 141–148, https://doi.org/10.1038/nphoton.2011.309.

[25] P. Yan, R. Dong, G. Zhang, H. Li, S. Ruan, H. Wei, J. Luo, Numerical simulation on the coherent time-critical 2–5 mm supercontinuum generation in an As_2S_3 microstructured optical fiber with all-normal flat-top dispersion profile, Opt. Commun. 293 (2013) 133–138, https://doi.org/10.1016/j.optcom.2012.11.093.

[26] M.R. Karim, H. Ahmad, B.M.A. Rahman, All-normal dispersion chalcogenide PCF for ultraflat mid-infrared supercontinuum generation, IEEE Photonic Technol. Lett. 29 (21) (2017) 1792–1795, https://doi.org/10.1109/LPT.2017.2752214.

[27] L. Liu, T. Cheng, K. Nagasaka, H. Tong, G. Qin, T. Suzuki, Y. Ohishi, Coherent mid-infrared supercontinuum generation in all-solid chalcogenide microstructured fibers with all-normal dispersion, Opt. Lett. 41 (2) (2016) 392–395, https://doi.org/10.1364/OL.41.000392.

[28] B. Siwicki, A. Filipkowski, R. Kasztelanic, M. Klimczak, R. Buczyński, Nanostructured graded-index core chalcogenide fiber with all-normal dispersion-design and nonlinear simulations, Opt. Express 25 (11) (2017) 12984–12998, https://doi.org/10.1364/OE.25.012984.

[29] M.R. Karim, H. Ahmad, B.M.A. Rahman, Design and modeling of dispersion-engineered all-chalcogenide triangular-core fiber for mid-infrared region supercontinuum generation, J. Opt. Soc. Am. B 35 (2) (2018) 266–275, https://doi.org/10.1364/JOSAB.35.000266.

[30] S. Xing, S. Kharitonov, J. Hu, C.S. Brès, Linearly chirped mid-infrared supercontinuum in all-normal-dispersion chalcogenide photonic crystal fibers, Opt. Express 26 (15) (2018) 19627–19636, https://doi.org/10.1364/OE.26.019627.

[31] A. Medjouri, L.M. Simohamed, O. Ziane, A. Boudrioua, Z. Becer, Design of a circular photonic crystal fiber with flattened chromatic dispersion using a defected core and selectively reduced air holes: application to supercontinuum generation at 1.55 μm, Photonic Nanostruct. 16 (2015) 43–50, https://doi.org/10.1016/j.photonics.2015.08.004.

[32] E. Wang, J. Li, J. Li, Q. Cheng, X. Zhou, H. Jiang, Flattened and broadband mid-infrared super-continuum generation in As_2Se_3 based holey fiber, Opt. Quantum Electron. 51 (10) (2019), https://doi.org/10.1007/s11082-018-1722-7.

[33] A. Medjouri, D. Abed, Z. Becer, Numerical investigation of broadband coherent supercontinuum generation in $Ga_8Sb_{32}Se_{60}$ chalcogenide photonic crystal fiber with all-normal dispersion, Opto-Electron. Rev. 27 (1) (2019) 1–9, https://doi.org/10.1016/j.opelre.2019.01.003.

[34] E.A. Anashkina, V.S. Shiryaev, M.Y. Koptev, B.S. Stepanov, S.V. Muravyev, Development of As-Se tapered suspended-core fibers for ultra-broadband mid-IR wavelength conversion, J. Non-Cryst. Solids 480 (15) (2018) 43–50, https://doi.org/10.1016/j.jnoncrysol.2017.07.033.

[35] A. Ben Khalifa, A. Ben Salem, R. Cherif, Mid-infrared supercontinuum generation in multimode As2Se3 chalcogenide photonic crystal fiber, Appl. Opt. 56 (15) (2017) 4319–4324, https://doi.org/10.1364/AO.56.004319.

[36] Z. Zhu, T.G. Brown, Full-vectorial finite-difference analysis of microstructured optical fibers, Opt. Express 10 (2002) 853–864, https://doi.org/10.1364/OE.10.000853.

[37] S. Guo, F. Wu, S. Albin, H. Tai, R.S. Rogowski, Loss and dispersion analysis of microstructured fibers by finite-difference method, Opt. Express 12 (2004)

3341–3352, https://doi.org/10.1364/OPEX.12.003341.

[38] C. Caillaud, G. Renversez, L. Brilland, D. Mechin, L. Calvez, J.L. Adam, J. Troles, Photonic bandgap propagation in all-solid chalcogenide microstructured optical fibers, Materials 7 (9) (2014) 6120–6129, https://doi.org/10.3390/ma7096120.

[39] C. Caillaud, C. Gilles, L. Provino, L. Brilland, T. Jouan, S. Ferre, M. Carras, M. Brun, D. Mechin, J.L. Adam, J. Troles, Highly birefringent chalcogenide optical fiber for polarization-maintaining in the 3–8.5 μm mid-IR window, Opt. Express 24 (8) (2016) 7977–7986, https://doi.org/10.1364/OE.24.007977.

[40] J. Hult, A fourth-order Runge-Kutta in the interaction picture method for simulating supercontinuum generation in optical fibers, J. Lightwave Technol. 25 (12) (2007) 3770–3775, https://doi.org/10.1109/JLT.2007.909373.

[41] W. Yuan, 2–10 μm mid-infrared supercontinuum generation in As₂Se₃ photonic crystal fiber, Laser Phys. Lett. 10 (2013) 095107, , https://doi.org/10.1088/1612-2011/10/9/095107.

[42] W. Wüster, J.J. Hope, C.M. Savage, Collapsing Bose-Einstein condensates beyond the Gross-Pitaevskii approximation, Phys. Rev. A 71 (3) (2005) 033604, , https://doi.org/10.1103/PhysRevA.71.033604.

[43] K.J. Blow, D. Wood, Theoretical description of transient stimulated Raman scattering in optical fibers, IEEE J. Quantum Electron. 25 (12) (1989) 2665–2673, https://doi.org/10.1109/3.40655.

[44] A.A. Rieznik, A.M. Heidt, P.G. Konig, V.A. Bettachini, D.F. Grosz, Optimum integration procedures for supercontinuum simulation, IEEE Photonic Technol. Lett. 4 (2) (2012) 552–560, https://doi.org/10.1109/JPHOT.2012.2188281.

[45] M. Brehler, M. Schirwon, D. Goddeke, P.M. Krummrich, A GPU-accelerated fourth-order Runge-Kutta in the interaction picture method for the simulation of nonlinear signal propagation in multimode fibers, J. Lightwave Technol. 35 (17) (2017) 3622–3628, https://doi.org/10.1109/JLT.2017.2715358.

[46] J.M. Dudley, S. Coen, Numerical simulations and coherence properties of supercontinuum generation in photonic crystal and tapered optical fibers, IEEE J. Sel. Top. Quantum 8 (3) (2002) 651–659, https://doi.org/10.1109/JSTQE.2002.1016369.

[47] I.B. Gonzalo, R.D. Engelsholm, M.P. Sørensen, O. Bang, Polarization noise places severe constraints on coherence of all normal dispersion femtosecond

supercontinuum generation, Sci. Rep.-UK 8 (2018) 6579, https://doi.org/10.1038/s41598-018-24691-7.

[48] E. Genier, P. Bowen, T. Sylvestre, J.M. Dudley, P. Moselund, O. Bang, Amplitude noise and coherence degradation of femtosecond supercontinuum generation in all-normal-dispersion fibers, J. Opt. Soc. Am. B 34 (2) (2019) A161–A167, https://doi.org/10.1364/JOSAB.36.00A161.

[49] M. Klimczak, B. Siwicki, A. Heidt, R. Buczyński, Coherent supercontinuum generation in soft glass photonic crystal fibers, Photonics Res. 5 (6) (2017) 710–727, https://doi.org/10.1364/PRJ.5.000710.

[50] E.A. Anashkina, A.V. Andrianov, V.V. Dorofeev, A.V. Kim, Toward a mid-infrared femtosecond laser system with suspended-core tungstate–tellurite glass fibers, Appl. Opt. 55 (17) (2016) 4522–4530, https://doi.org/10.1364/AO.55.004522.

[51] T.S. Saini, N.P.T. Hoa, L. Xing, T.H. Tuan, T. Suzuki, Y. Ohishi, Chalcogenide W-type co-axial optical fiber for broadband highly coherent mid-IR supercontinuum generation, J. Appl. Phys. 124 (2018) 2131101, https://doi.org/10.1063/1.5062591.

[52] C. Finot, B. Kibler, L. Provost, S. Wabnitz, Beneficial impact of wave-breaking for coherent continuum formation in normally dispersive nonlinear fibers, J. Opt. Soc. Am. B 25 (2008) 1938–1948, https://doi.org/10.1364/JOSAB.25.001938.

[53] A. Ben Salem, M. Diouf, R. Cherif, A. Wague, M. Zghal, Ultraflat-top mid-infrared coherent broadband supercontinuum using all normal As₂S₅-borosilicate hybrid photonic crystal fiber, Opt. Eng. 55 (6) (2016) 066109, https://doi.org/10.1117/1.OE.55.6.066109.

[54] D. Anderson, M. Desaix, M. Lisak, M.L. Quiroga-Teixeiro, Wave-breaking in nonlinear optical fibers, J. Opt. Soc. Am. B 9 (1992) 1358–1361, https://doi.org/10.1364/JOSAB.9.001358.

[55] P.S. Maji, P.R. Chaudhuri, Design of all-normal dispersion based on multimaterial photonic crystal fiber in IR region for broadband supercontinuum generation, Appl. Opt. 54 (13) (2015) 4042–4048, https://doi.org/10.1364/AO.54.004042.

[56] M. Diouf, A. Ben Salem, R. Cherif, H. Saghaei, A. Wague, Super-flat coherent supercontinuum source in As₃₈.₈Se₆₁.₂ chalcogenide photonic crystal fiber with all-normal dispersion engineering at a very low input energy, Appl. Opt. 56 (2) (2017) 163–169, https://doi.org/10.1364/AO.56.000163.

Design and optimization of As 2 S 5 chalcogenide channel waveguide for coherent mid-infrared supercontinuum generation

4 authors, including:

Abdelkader Medjouri
El-Oued University, El oued, Algeria
20 PUBLICATIONS **41** CITATIONS

SEE PROFILE

Djamel Abed
Université 8 mai 1945 - Guelma
22 PUBLICATIONS **69** CITATIONS

SEE PROFILE

Omar Ziane
University of Science and Technology Houari Boumediene
**31** PUBLICATIONS **147** CITATIONS

SEE PROFILE

Some of the authors of this publication are also working on these related projects:

Project   Contribution à l'Etude et au Développement d'Antennes Miniatures et de Techniques Avancées pour les futurs Systèmes de communication sans fil View project

Project   PAPR Reduction in Multicarrier Modulation (MCM) Systems View project
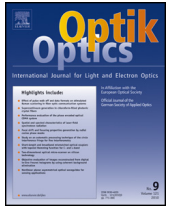
Full length article

Design and optimization of As$_2$S$_5$ chalcogenide channel waveguide for coherent mid-infrared supercontinuum generation

Abdelkader Medjouri [a],[*], Djamel Abed [b], Omar Ziane [c], Lotfy Mokhtar Simohamed [d]

[a] Laboratoire d'Exploitation et Valorisation des Ressources Sahariennes (LEVRES), Faculté des sciences exactes, Université Echahid Hamma Lakhdar EL Oued, BP 789, El Oued, 39000, Algeria
[b] Département d'électronique et télécommunications, Faculté des sciences et technologie, Université 8 mai 1945 Guelma, 24000, Guelma, Algeria
[c] Laboratoire d'Electronique Quantique (LEQ), Faculté de physique, USTHB, BP no. 32 El-Alia, Bab-Ezzouar, 16111, Alger, Algeria
[d] Laboratoire des Systèmes Electroniques Et Optroniques (LSEO), Ecole Militaire Polytechnique, 16111, Alger, Algeria

A R T I C L E   I N F O

A B S T R A C T

We numerically demonstrate mid-infrared supercontinuum generation in dispersion-engineered chalcogenide glass channel waveguide. The proposed ridge waveguide consists of arsenic pentasulfide (As$_2$S$_5$) strip deposited on magnesium fluoride (MgF$_2$) substrate and air acting as an upper cladding. The structure parameters are calculated and optimized by using the fully vectorial finite-difference in the frequency-domain (FDFD) method Results indicates that the proposed waveguide exhibits an all normal dispersion (ANDi) profile over a wide spectral range with a zero dispersion wavelength (ZDW) around 2 μm. By solving the generalized nonlinear Schrödinger equation, we demonstrate supercontinuum generation extending from the near infrared to the mid infrared region. Indeed, a broad and perfectly coherent ultra-flat supercontinuum spectrum spanning the region from 700 to 5200 nm is successfully generated by using a 25 kW peak power 100 fs input pulse pumped at 2.5 μm, in a waveguide of 5 mm length.

© 2017 Elsevier GmbH. All rights reserved.

1. Introduction

Supercontinuum (SC) generation refers to the considerable spectral broadening through the interaction of intense and short optical pulses with nonlinear materials such as solids, liquids and gases [1]. Since its discovery for the first time in the beginning of the 1970s [2], SC has attracted tremendous attentions due to its wide applications to metrology, pulse compression, optical communications, coherence tomography, spectroscopy and tunable multi-wavelength laser sources [3]. SC arises from a series of nonlinear processes depending on the waveguide chromatic dispersion regime where the femtoseconde pulses are injected. In the anomalous regime, SC generation is dominated by soliton-related propagation dynamics [4]. The generated spectra are broad, mainly due to the creation of new pulses resulting from the fundamental Soliton Fission (SF) process. However, these spectra are partially coherent due to their sensitivity to the noise-related pump

* Corresponding author.
  E-mail address: medjouri-abdelkader@univ-eloued.dz (A. Medjouri).

pulse intensity fluctuations [5]. In the normal regime, Self Phase Modulation (SPM) and Wave Breaking (WB) are responsible for the spectral broadening. The generated spectra are relatively narrower than in the anomalous dispersion regime, but highly coherent and smooth [6].

The nonlinear dynamics of spectral broadening results from the interplay between chromatic dispersion and nonlinearity [4]. These properties can be easily tailored in guiding medium rather than bulk. Thus, optical fiber based SC generation sources has been the target of many researchers, in particular due to the invention of photonic crystal fibers (PCF) [7]. Owing to their design flexibility, PCFs transverse structures can be optimized to tailor the chromatic dispersion and achieve high nonlinearity [8]. Recently, planar waveguides have gained much attention for on-chip SC sources due to their low cost, reduced size and high nonlinear parameter [9]. These waveguide based SC sources are of growing importance for photonic integrated circuits [10].

Chalcogenide (ChG) glasses are based on the chalcogen elements S, Se, and Te covalently bounded with glass forming materials such as As, Ge and Ga [11,12]. Thanks to their suitable optical properties, they have been widely used to design waveguide based mid-infrared SC sources [11]. Compared to silica, ChG exhibits higher optical Kerr nonlinearities, high refractive indices and wide transparency window covering near-infrared and mid-infrared [13]. Many ChG based waveguide structures have been reported aiming the generation of broad mid-infrared Zhang et al. reported mid-infrared SC generation from 1 μm to 7 μm in tapered As_2S_3 on MgF_2 rib waveguide pumped with 50 fs duration pulses at 1.55 μm with a pulse peak power of around 2 kW [14]. By using the same ChG glass, Lamont et al. reported SC spectrum spanning 750 nm in dispersion-engineered highly nonlinear chalcogenide planar waveguide by using 610 fs pulses with peak power of 68 W [15]. As_2Se_3 ChG glass based waveguide has been, also, considered. Saini et al. reported SC generation form 2 μm to 15 μm through a dispersion-engineered As_2Se_3 chalcogenide glass rib waveguide pumped with 50 fs pulses at a wavelength of 2.5 μm with a pulse peak power of around 1.1 kW [16]. Moreover, Alizadeh et al. reported SC spectrum extending from 1.5 μm to 12 μm over highly nonlinear rib waveguide employing a 100 W peak power 85 fs pulses pumped at 2.4 μm [17]. Furthermore, Karim et al. reported ultra-flat SC generation in 1 cm long all normal dispersion (ANDi) channel waveguide made using $Ge_{11.5}As_{24}Se_{64.5}$ ChG glass with various materials in the lower cladding [18]. In particular, when MgF_2 glass is used as a lower cladding, the authors have found that SC spectrum spanning from 1.6 μm to 6 μm can be produced by employing 3 kW peak power 85 fs width pulses pumped at 3.1 μm. Recently, SC generation in A_s2S_5 ChG glass PCF has been demonstrated numerically and experimentally. Compared to As_2S_3, the As_2S_5 glass exhibits higher transmission in the wavelength range extending from 0.5 μm to 9 μm combined with a shorter cut-off wavelength in the visible domain [19]. Gao et al. reported mid-infrared SC generation in a four-hole As_2S_5 ChG microstructured optical fiber [20]. A wide spectrum spanning from 1.37 μm to 5.65 μm has been achieved in a 4.8-cm-long fiber pumped at 2300 nm. In order to generate ultra-flat and coherent SC, Salem et al. studied a kind of hybrid As_2S_5-borosilicate PCF with ANDi regime [21]. A broadband and flat SC spectrum extending from 1 μm to 5 μm has been realized by pumping 28.16 kw peak power 50 fs pulses at 2.5 μm in only 4 mm fiber length. Nevertheless, and to the best of our knowledge, analyzing mid-infrared SC in As_2S_5 based planar geometries has been not achieved.

In this paper, we numerically investigate mid-infrared SC generation in a ridge waveguide consisting of As_2S_5 ChG glass strip deposited on MgF_2 substrate and air acting as an upper cladding. The propagation characteristics of the fundamental guided mode such as chromatic dispersion, effective mode area and nonlinearity are calculated by using a finite-difference in the frequency-domain (FDFD) method. The waveguide structure is optimized to exhibit an ANDi profile over the entire computational domain by properly adjusting its high and width. Furthermore, we demonstrate spectral broadening of an intense femtoseconde pulse pumped at 2.5 μm, by solving the Generalized Nonlinear Schrödinger Equation (GNLSE). The impact of pulse peak power on the generated spectra bandwidth is then examined. Additionally, we analyze the statistical properties of the SC source by calculating its first order spectral coherence in the aim to investigate its sensitivity to input pump noise.

2. Theoretical background

2.1. Structure of the proposed As_2S_5 ridge waveguide

The cross sectional view of the proposed ridge waveguide is given by Fig. 1. As mentioned in the previous section, the proposed ridge waveguide consists of As_2S_5 strip deposited on MgF_2 substrate, and air acting as an upper cladding. The parameters W and H are the core width and high, respectively. The wavelength dependent refractive index of the core and the cladding are given via the Sellmeier equation:

$$n(\lambda) = \sqrt{1 + \sum_{j=1}^{m} \frac{A_j \lambda^2}{\lambda^2 - \lambda_j^2}} \qquad (1)$$

Were the coefficients are given in Table 1 [19,22].

The variation of the refractive index with wavelength for both As_2S_5 and MgF_2 is depicted in Fig. 2. The large index contrast between the core and the cladding permits a strong light confinement inside the core whatever its wavelength. The inset Fig. 2 shows the optical field distribution at the excitation wavelength 1 μm and 4 μm respectively.
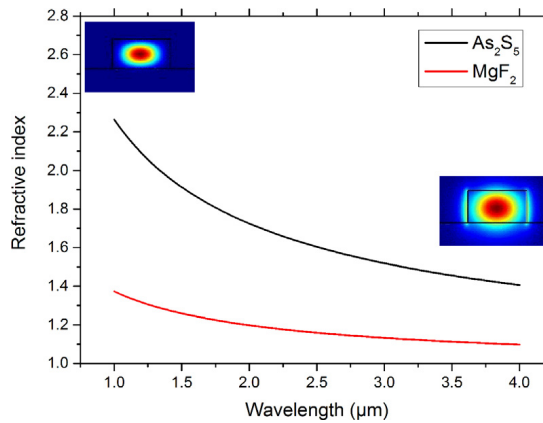
Fig. 1. Cross sectional view of the proposed As_2S_5 ridge waveguide where the width and the high of the channel are W and H, respectively. Inset simulated fundamental field profile at 2 μm.

Table 1
Sellmeier coefficients of As_2S_5 and MgF_2 glasses.

As_2S_5		MgF_2	
A_j	λ_j	A_j	λ_j
2.1361	0.3089	0.48755708	0.0433840
0.0693	15	0.39875031	0.09461442
1.7637	4.66×10^{-4}	2.3120353	23.793604

Fig. 2. Material refractive index versus wavelength of the As_2S_5 chalcogenide and MgF_2 glass.

2.2. Numerical method

In order to determine the fundamental guided mode and its optical properties, we have used the finite-difference frequency-domain (FDFD) method. Compared to the finite element method (FEM), the FDFD approach is easier and simpler to implement with a comparable accuracy [23].

The Maxwell's equations for the electric and magnetic field can be formulated as follow:

$$jk_0 s\varepsilon_r E = \nabla \times H$$
$$-jk_0 s\varepsilon_r H = \nabla \times E \tag{2}$$

$$s = \begin{bmatrix} s_y/s_x & & \\ & s_x/s_y & \\ & & s_x s_y \end{bmatrix} \tag{3}$$

Where: $s_x = 1 - \sigma_x/j\omega\varepsilon_0$ and $s_y = 1 - \sigma_y/j\omega\varepsilon_0$. σ, ω, E and H are the conductivity, the pulsation, the electric and the magnetic components of the propagating field, respectively.

Once an appropriate meshing is applied to the structure, the equations system given by (2) is transformed into a matrix eigenvalue problem and solved by employing a sparse matrix approach in order to obtain the effective refractive index n_{eff} and the optical field distribution of the fundamental mode.

As mentioned previously, the chromatic dispersion plays a critical role in the SC generation process. Since the material dispersion is directly included during the calculations by using formula (1), the total dispersion is calculated by taking the 2nd-order derivative of the mode effective index with respect to the wavelength:

$$D_w = -\frac{\lambda}{c}\frac{d^2 n_{eff}}{d\lambda^2}$$

(4)

Where λ and c are the wavelength and the speed of light, respectively.

The waveguide nonlinear coefficient (Kerr effect) is given by:

$$\gamma = \frac{2\pi}{\lambda}\frac{n_2}{A_{eff}}$$

(5)

Where $n_2 = 3 \times 10^{-18}$ m^2/W is the nonlinear refractive index of As$_2$S$_5$ [19]. A_{eff} is the mode effective area, given by:

$$A_{eff} = \frac{\left(\iint |E^2|dxdy\right)^2}{\iint |E|^4 dxdy}$$

(6)

2.3. SC generation modeling

Aiming to simulate the SC generation in the proposed As$_2$S$_5$ waveguide, the Generalized Nonlinear Schrödinger Equation (GNLSE) is numerically solved by using the Split Step Fourier Method (SSFM) [4]. This propagation equation governs the pulse evolution inside an optical waveguide with the contributions of the linear dispersion and the various nonlinear processes that lead to spectral broadening:

$$\frac{\partial A}{\partial z} + \frac{\alpha}{2}A - \sum_{k\geq 2}\frac{i^{k+1}}{k!}\beta_k\frac{\partial^k A}{\partial T^k} = i\gamma\left(1 + \frac{i}{\omega_0}\frac{\partial}{\partial T}\right)\left(A(z,t)\int_{-\infty}^{\infty}R\left(T'\right)\times |A\left(z,T-T'\right)|^2 dT'\right)$$

(9)

$A(z, t)$ is the temporal and longitudinal envelope of the pulse, α is the linear loss coefficient, β_k is the kth coefficient of the Taylor expansion of the propagation constant $\beta(\omega)$ centered around the carrier frequency ω_0, γ is the nonlinearity coefficient, $R(t)$ is the response function, which includes both instantaneous electronic and delayed Raman contributions. Its expression is given by [24]:

$$R(t) = (1 - f_R)\delta(t) + f_R h_R(t)$$

(10)

The Dirac delta function $\delta(t)$ represents the instantaneous electronic response, $h_R(t)$ is the Raman response function and f_R represents the fractional contribution of the delayed Raman response set to $f_R = 0.11$ [21,25]. The Raman response function is described by using the single Lorentzian model as follows:

$$h_r(t) = \frac{\tau_1^2 + \tau_2^2}{\tau_1 \tau_2^2}\exp(\frac{-t}{\tau_2})\sin(\frac{t}{\tau_1})$$

(11)

τ_1 and τ_2 are two adjustable parameters which are chosen to provide a good fit to the actual Raman gain spectrum [26]. τ_1 is related to the phonon frequency and τ_2 is related to the attenuation of the network of vibrating atoms [27]. Their values are set to be 15.2 fs and 230.5 fs, respectively [21].

3. Results and discussions

3.1. Structure optimization

As mentioned previously, we aim to optimize the waveguide structure exhibiting negative dispersion so that the generated SC is relatively coherent and noise insensitive over the entire bandwidth. In order to achieve all normal dispersion ($\beta_2 > 0$) over a wide wavelength range, the structural parameters of the proposed ridge waveguide are suitably adjusted. The impact of both the width (W) and the high (H) is carefully investigated through several numerical simulations. First, we analyzed the effect of W on the dispersion parameter. Fig. 3 shows the evolution of the chromatic dispersion with wavelength for the fundamental TE mode with W = 2 μm and H varying from 0.6 μm to 0.8 μm with step of 0.05 μm. From the figure we observe that dispersion curve increases when H increases too with a peak moving toward long wavelengths. Hence, ANDi regime with a peak close to the zero can be achieved for H laying between 0.6 μm and 0.65 μm. For this respect, we investigated the impact of changing W when H is set to 0.625 μm. Fig. 4 depicts the evolution of dispersion parameter for different values of W ranging from 1.8 μm to 2.4 μm with a step of 0.2 μm. As we can see, the curves shift upward, with an invariant peak, when W decreases. Moreover, the ANDi regime with a peak close to the zero can be obtained for H laying between 2.2 μm and 2.4 μm. Therefore, and from the above results, one can optimize the design of the proposed waveguide in order to achieve the desired ANDi profile over a wide range of wavelengths. For this purpose, we have calculated the chromatic
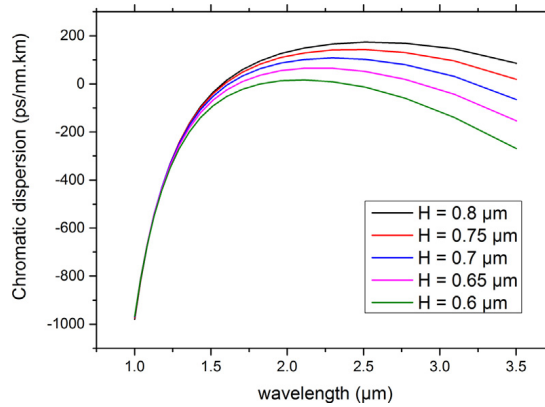
Fig. 3. Variation of the chromatic dispersion with wavelengths for W = 2 μm and H varying from 0.6 μm to 0.8 μm.
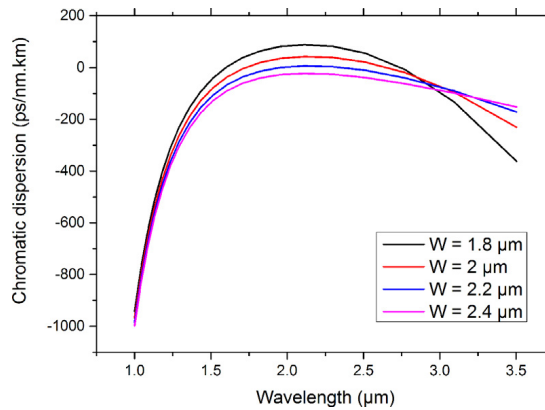
Fig. 4. Variation of the chromatic dispersion with wavelengths for H = 0.625 μm and W varying from 1.8 μm to 2.4 μm.
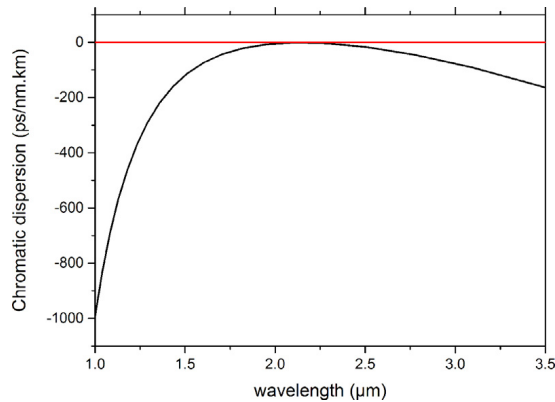
Fig. 5. Variation of the chromatic dispersion with wavelengths for H = 0.625 μm and W = 2.25 μm.

dispersion for the waveguide parameters W = 2.25 μm and H = 0.625 μm. As plotted in Fig. 5, the optimized design exhibits a negative dispersion over the whole wavelength range with a zero dispersion around 2 μm. Finally, we have computed both the effective mode area and the Kerr nonlinear coefficient. Their evolution against wavelength is depicted in Fig. 6 where we, clearly, observe that the waveguide exhibits high nonlinearity up to 22,500 w^{-1} km^{-1} at 3.5 μm. This is due to, jointly, the small effective mode area and the high nonlinear refractive index.

3.2. SC generation in the optimized design

SC generation was, then, carried out in the proposed chalcogenide waveguide with the optimized parameters. We consider the injection of a chirpless Gaussian pulse given by $A(0, t) = \sqrt{p_0} \exp\left(-t^2/2T_0^2\right)$ where, P_0 is the peak power and T_0 is the pulse duration related to the pulse Full Width Half Maximum (FWHM) as $T_0 = FWHM/1.763$. In order to generate broad SC, the pulse is pumped close to the zero dispersion at 2.5 μm. The chromatic dispersion and the nonlinear coefficient at the
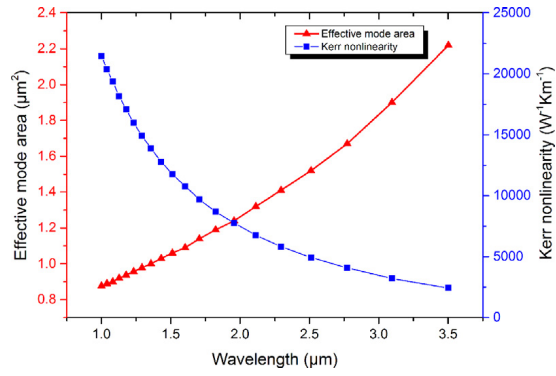
Fig. 6. Variation of the effective mode area and the corresponding nonlinear coefficient with wavelength for H = 0.625 μm and W = 2.25 μm.

Table 2
Terms of the Taylor series expansion of the propagation constant.

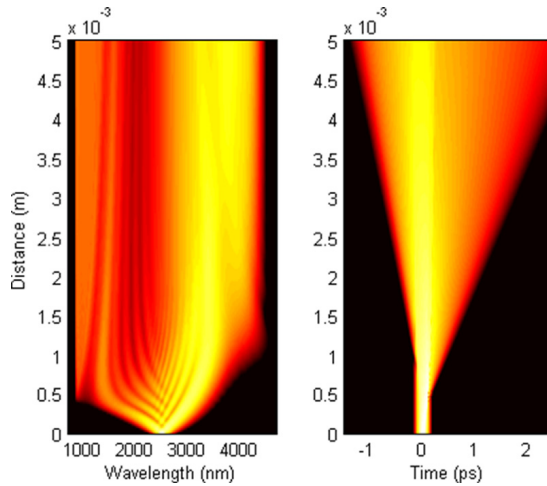| Coefficient	Valeur
β_2	0.0791 ps^2/km
β_3	−0.0012 ps^3/km
β_4	1.5202×10^{-5} ps^4/km
β_5	-1.4895×10^{-7} ps^5/km
β_6	1.4122×10^{-9} ps^6/km
β_7	-1.1137×10^{-11} ps^7/km
β_8	6.4771×10^{-14} ps^8/km
β_9	-2.4170×10^{-16} ps^9/km
β_{10}	4.3176×10^{-19} ps^{10}/km

Fig. 7. Spectral and temporal evolution over 5 mm waveguide length of a Gaussian pulse with a peak power and FWHM of 10 kW and 100 fs, respectively.

pump wavelength are −18 ps/nm.km and 5 W^{-1} m^{-1}, respectively. The Taylor series expansion coefficients, up to the 10th order, of the propagation constant have been calculated around the carrier frequency and their values are given in Table 2.

Firstly, and in the aim to provide a simple physical interpretation of pulse spectral broadening in our proposed design, we simulate the propagation of a Gaussian pulse with a peak power and FWHM of 10 kW and 100 fs, respectively. Therefore, the dispersion length L_D, the nonlinear length L_{NL} and the soliton order N can be calculated as following: $L_D = T_0^2/|\beta_2| = 0.0405$ m, $L_{NL} = 1/(\gamma P_0) = 2 \times 10^{-5}$ m and $N = \sqrt{L_D/L_{NL}} = 45$, respectively. For a waveguide length of 5 mm, Fig. 7 shows the spectral and temporal evolution of the SC generation process over the propagation distance. As we can see from the pulse spectral evolution, the initial stage of SC evolution is dominated by the SPM induced broadening. This can be, clearly, observed from the oscillatory structure that accompanies the generated spectra in the first few millimeters [28]. Furthermore, the SC spectra start to broaden asymmetrically due to the effect of WB. The distance where the WB is first observed is given by [29]:

$$z = \frac{L_D}{\sqrt{4e^{-3/2}N^2 - 1}} \tag{12}$$
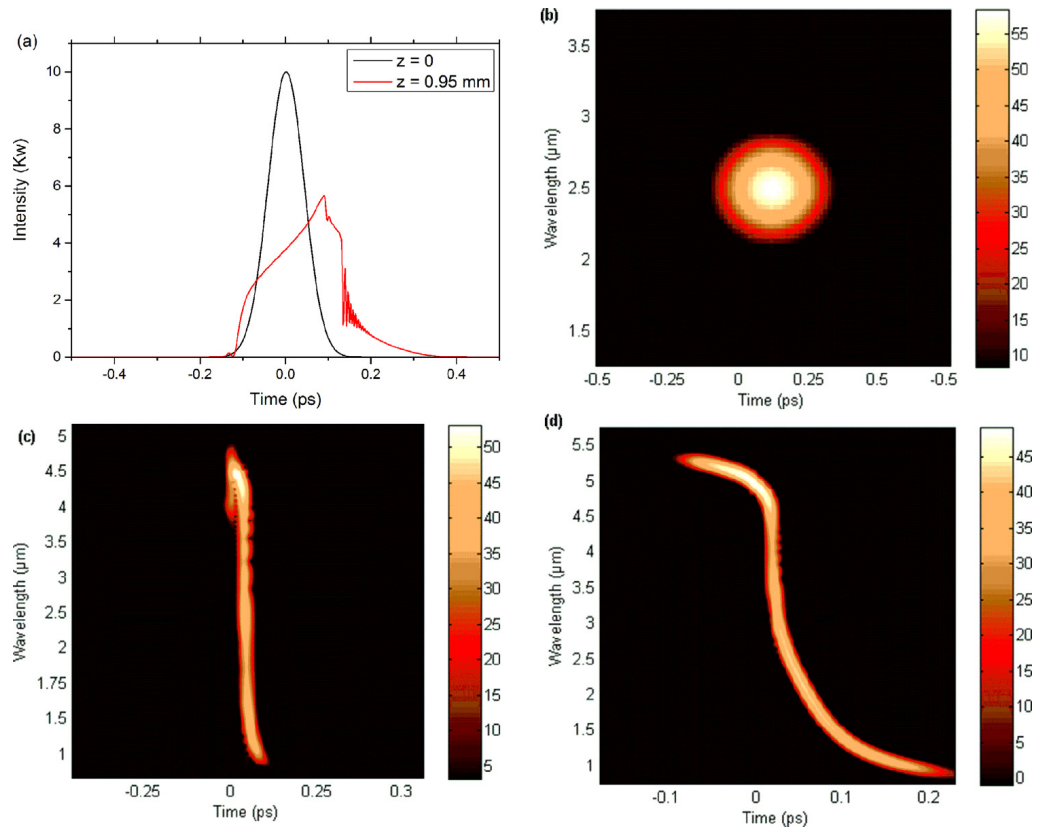
Fig. 8. (a) Pulse profiles at the input and after $z = 0.95$ mm of propagation. (b) Spectrogram of the initial pulse. (c) Spectrogram of the pulse at the onset of optical WB ($z = 0.95$ mm). (d) Spectrogram of the pulse after 5 mm propagation distance.

For this simulation, the distance is found to be 0.95 mm. Fig. 8(a) shows the pulse at the input as well as after 0.95 mm of propagation. Moreover, an overlap of two pulse components with different instantaneous frequencies results in sinusoidal beats between those frequencies [28]. These oscillations indicate the occurrence of WB [30]. With further propagation, WB fully develops by transferring energy from the pulse center wavelengths to the new frequency band around 3700 nm. The dynamics evolution of the propagating pulse can be clearly visualized by using a time-frequency analysis. Fig. 8(b)–(d) shows the calculated spectrograms of the initial pulse, at a propagation distance of 0.95 mm and of the output pulse, respectively. As we can see, after 0.95 mm propagation, the effect of WB on spectral broadening becomes important through the generation of sidelobes on both sides of the generated spectra. Furthermore, the effect of the initial pulse peak power on the output spectrum width is investigated. Simulations are performed with a pulse with a FWHM of 100 fs and a peak power of 10 kW, 15 kW, 20 kW and 25 kW, respectively. Fig. 9(a)–(d) shows the spectral evolution of the SC generation process over the propagation distance with different values of the peak power. As it can be seen, by increasing the initial peak power, the output spectrum width increases too, where the both sides of the pump wavelength are amplified stronger than the mid-section of the generated spectrum. Moreover, for a peak power of 25 kW, SC spectra extending to the mid infrared region and spanning 4500 nm in the range from 700 nm to 5200 nm is successfully obtained, along with smooth spectral profile. Finally, the coherence properties of SC spectra generated in our proposed waveguide has been investigated. Coherence of SC sources is of great interest for characterization of ultrafast or rarely occurring phenomena [31]. The coherence of the SC generated has been studied through a simple form of the first-order degree of coherence given by [32]:

$$|g_{12}(\omega)| = \frac{|\langle E(\omega) \rangle|^2}{\langle |E(\omega)|^2 \rangle} \tag{13}$$

The angular brackets stand for an ensemble average over separately generated SC spectra obtained from a large number of simulations. Each simulation is performed with different realization of input pulse shot noise modeled through the addition of a noise seed of one photon per mode with random phase on each spectral discretization bin [33]. The amplitude of the input noise is given by [34]:

$$A(\omega) = \sqrt{\hbar \omega / T_{span}} \exp(i 2\pi \varphi(\omega)) \tag{14}$$

Where $\hbar$ is the reduced Planck constant, ω is the pulsation, T_{span} is the temporal window used for the simulations and $\varphi(\omega)$ is a uniformly distributed random phase in the interval $[0, 2\pi]$. Besides, $|g_{12}(\omega)|$ is a positive number which lies in the interval [0-1], with a value of 1 denoting perfect coherence [4]. Fig. 10 shows the SC generated over 5 mm of the waveguide

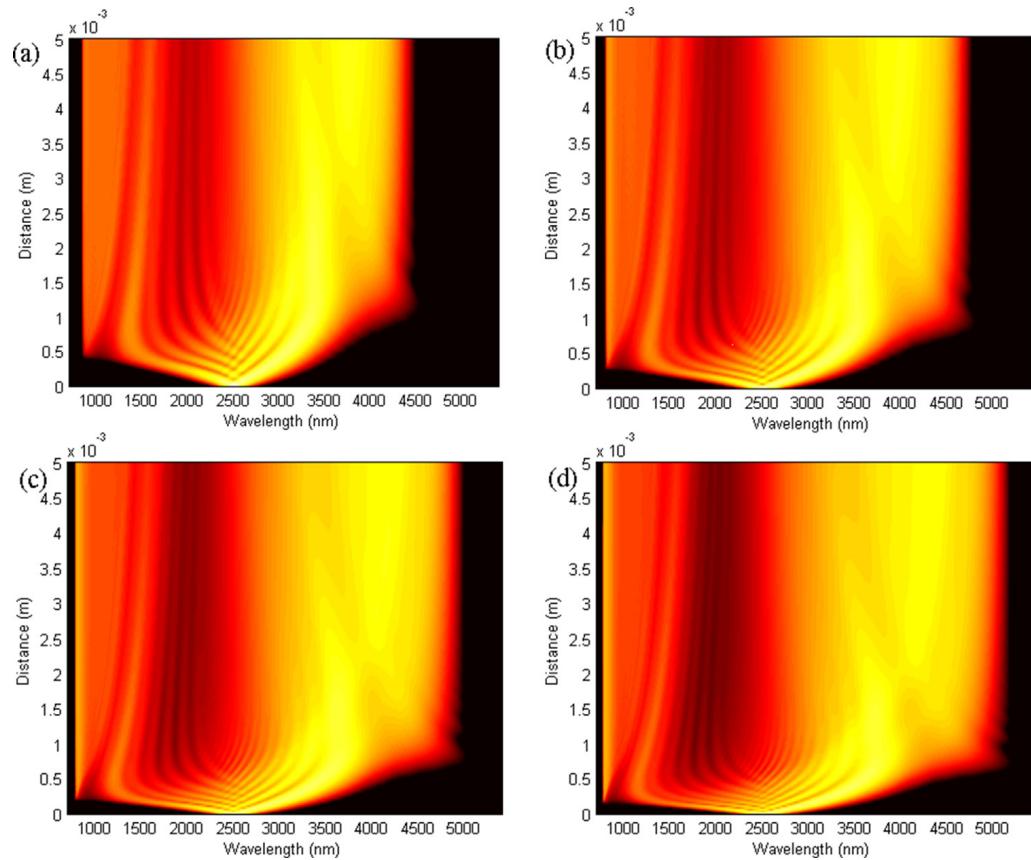**Fig. 9.** Spectral evolution over 5 mm waveguide length of a Gaussian pulse with a peak power of: (a) 10 kW, (b) 15 kW, (c) 20 kW and (d) 25 kW, respectively.
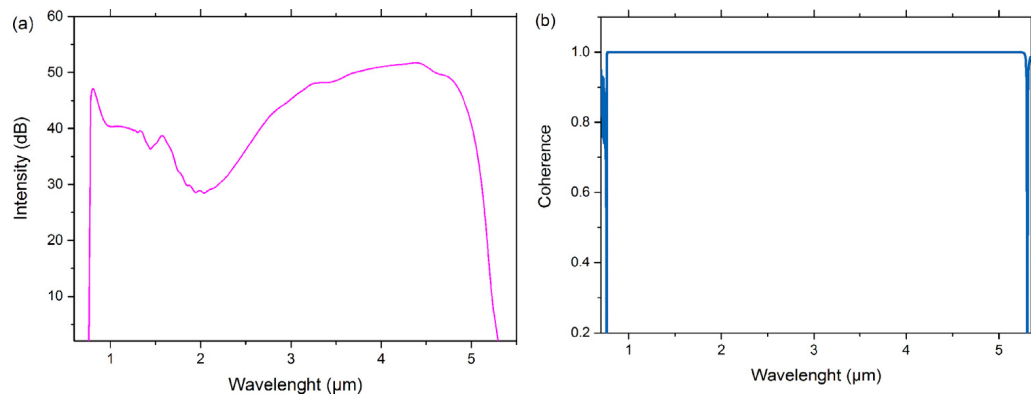
Fig. 10. (a) Generated SC spectrum with an input pulse with a peak power and FWHM of 25 kW and 100 fs, respectively. (b) Corresponding degree of coherence.

length employing a pulse with a peak power and FWHM of 10 kW and 100 fs, respectively and the corresponding first-order degree of coherence calculated from 50 independent realizations. As expected, the spectrum is perfectly coherent over the entire spectral range. This high spectral coherence is attained due to the elimination of soliton effects by pumping in the normal dispersion regime. Thereby, spectral broadening is mainly achieved through SPM which is a deterministic process that maintains the input pulses coherence [35].

Considering now the manufacturing process of the proposed As_2S_5 ChG waveguide. In order to fabricate ChG glass based planar waveguides, several methods have been employed to produce the ChG glass films and pattern them into micron-size low loss optical waveguides [36]. Among these techniques, the dry etching process has been, successfully, used to fabricate and characterize low loss rib waveguide with various ChG glasses [11,36]. By using this technique, we believe that our proposed As_2S_5 ChG ridge waveguide can be fabricated with the optimized design.

4. Conclusion

In conclusion, we have numerically demonstrated broadband and coherent SC generation in ANDi ridge waveguide. The proposed dispersion engineered waveguide consists of As_2S_5 ChG strip deposited on MgF_2 substrate and air acting as an upper cladding. The linear and nonlinear optical properties have been calculated and optimized by using a fully vectorial finite-difference in the frequency-domain (FDFD) method. The numerical results indicate that ANDi profile is obtained over the entire computational domain with a zero dispersion around 2 μm. Besides, the proposed structure exhibits high nonlinearity up to 22500 w^{-1} km^{-1} at 3.5 μm. Such high nonlinear coefficient is obtained due to the small effective mode area and the high nonlinear refractive index. Furthermore, the SC generation at 2.5 μm is simulated by solving the Non Linear Schrödinger Equation (GNLSE) and using the Split Step Fourier Method (SSFM). Since pumping is achieved in the normal regime of dispersion, simulations have shown that spectral broadening is realized due to SPM and WB. A broad and perfectly coherent ultra-flat SC spectrum extending from 700 to 5200 nm is successfully generated by using a 25 kW peak power 100 fs input pulse in only 5 mm waveguide length. Owing to its interesting properties, the proposed As_2S_5 ChG based waveguide is found to be suitable as an on-chip SC source for various applications such as gas sensing, frequency comb generation and ultrafast optical switching.

Acknowledgement

References

[1] R. Robert. Alfano, The Supercontinuum Laser Source: The Ultimate White Light, third edition, Springer, 2016, http://dx.doi.org/10.1007/978-1-4939-3326-6.
[2] R.R. Alfano, S.L. Shapiro, Observation of self-phase modulation and small-scale filaments in crystals and glasses, Phys. Rev. Lett. 24 (1970) 592–596, http://dx.doi.org/10.1103/PhysRevLett.24.592.
[3] J.M. Dudley, J.R. Taylor, Supercontinuum Generation in Optical Fibers, Cambridge University Press, 2010, http://dx.doi.org/10.1017/CBO9780511750465.
[4] J.M. Dudley, G. Genty, S. Coen, Supercontinuum generation in photonic crystal fiber, Rev. Mod. Phys. 78 (2006) 1135–1184, http://dx.doi.org/10.1103/RevModPhys.78.1135.
[5] A. Hartung, A.M. Heidt, H. Bartelt, Design of all-normal dispersion microstructured optical fibers for pulse-preserving supercontinuum generation, Opt. Express 19 (2011) 7742–7749, http://dx.doi.org/10.1364/OE.19.007742.
[6] Alexander M. Heidt, Alexander Hartung, Gurthwin W. Bosman, Patrizia Krok, Erich G. Rohwer, Heinrich Schwoerer, Hartmut Bartelt, Coherent octave spanning near-infrared and visible supercontinuum generation in all-normal dispersion photonic crystal fibers, Opt. Express 19 (2011) 3775–3787, http://dx.doi.org/10.1364/OE.19.003775.
[7] J.C. Knight, T.A. Birks, R.F. Cregan, P.St.J. Russell, J.-P. de Sandro, Photonic crystals as optical fibres – physics and applications, Opt. Mater. 11 (1999) 143–151, http://dx.doi.org/10.1016/S0925-3467(98)00040-8.
[8] Abdelkader Medjouri, Lotfy Mokhtar Simohamed, Omar Ziane, Azzedine Boudrioua, Zoubir Becer, Design of a circular photonic crystal fiber with flattened chromatic dispersion using a defected core and selectively reduced air holes: application to supercontinuum generation at 1.55 μm, Photonics Nanostruct. Fundam. Appl. 16 (2015) 43–50, http://dx.doi.org/10.1016/j.photonics.2015.08.004.
[9] D.-Y. Choi, S. Madden, D.A. Bulla, R. Wang, A. Rode, B. Luther-Davies, Submicrometer-thick low-loss As_2S_3 planar waveguides for nonlinear optical devices, IEEE Photonics Technol. Lett. 22 (2010), http://dx.doi.org/10.1109/LPT.2010.2040170, 594–497.
[10] Dong Yoon Oh, David Sell, Hansuek Lee, Ki Youl Yang, Scott A. Diddams, Kerry J. Vahala, Supercontinuum generation in on-chip silica waveguide, Opt. Lett. 39 (2014) 1046–1048, http://dx.doi.org/10.1364/OL.39.001046.
[11] A. Zakery, S.R. Elliot, Optical Nonlinearities in Chalcogenide Glasses and Their Applications, Springer, 2007, http://dx.doi.org/10.1007/978-3-540-71068-4.
[12] Stefan Wabnitz, Benjamin J. Eggleton, All-optical Signal Processing: Data Communication and Storage Applications, Springer, 2015, http://dx.doi.org/10.1007/978-3-319-14992-9.
[13] N. Granzow, M.A. Schmidt, W. Chang, L. Wang, Q. Coulombier, J. Troles, P. Toupin, I. Hartl, K.F. Lee, M.E. Fermann, L. Wondraczek, P. St. J. Russell, Mid-infrared supercontinuum generation in As_2S_3-silica nano-spike step-index waveguide, Opt. Express 21 (2013) 10969–10977, http://dx.doi.org/10.1364/OE.21.010969.
[14] Xiang Zhang, Hongyu Hu, Wenbo Li, Niloy K. Dutta, Mid-infrared supercontinuum generation in tapered As_2S_3 chalcogenide planar waveguide, J. Mod. Opt. 63 (2016) 1965–1971, http://dx.doi.org/10.1080/09500340.2016.1183055.
[15] Michael R.E. Lamont, Barry Luther-Davies, Duk-Yong Choi, Steve Madden, Benjamin J. Eggleton, Supercontinuum generation in dispersion engineered highly nonlinear (γ = 10/W/m) As_2S_3 chalcogenide planar waveguide, Opt. Express 16 (2008) 14938–14944, http://dx.doi.org/10.1364/OE.16.014938.
[16] Than Singh Saini, Ajeet Kumar, Ravindra Kumar Sinha, Design and modelling of dispersion-engineered rib waveguide for ultra broadband mid-infrared supercontinuum generation, J. Mod. Opt. 64 (2016) 143–149, http://dx.doi.org/10.1080/09500340.2016.1216190.
[17] Mohammad Reza Alizadeh, Mahmood Seifouri, Dispersion engineering of highly nonlinear rib waveguide for mid-infrared super continuum generation, Optik-Int. J. Light Electro Op. 140 (2017) 233–238, http://dx.doi.org/10.1016/j.ijleo.2017.04.056.
[18] M.R. Karim, H. Ahmad, B.M.A. Rahman, All-normal dispersion chalcogenide waveguides for ultraflat supercontinuum generation in the mid-infrared region, IEEE J. Quantum Electron. 53 (2017) 1–6, http://dx.doi.org/10.1109/JQE.2017.2677380.
[19] Tonglei Cheng, Ryo Usaki, Zhongchao Duan, Weiqing Gao, Dinghuan Deng, Meisong Liao, Yasuhire Kanou, Morio Matsumoto, Takashi Misumi, Takenobu Suzuki, Yasutake Ohishi, Soliton self-frequency shift and third-harmonic generation in a four-hole As_2S_5 microstructured optical fiber, Opt. Express 22 (2014) 3740–3746, http://dx.doi.org/10.1364/OE.22.003740.
[20] Weiqing Gao, Zhongchao Duan, Koji Asano, Tonglei Cheng, Dinghuan Deng, Morio Matsumoto, Misumi Takashi, Takenobu Suzuki, Yasutake Ohishi, Mid-infrared supercontinuum generation in a four-hole As_2S_5 chalcogenide microstructured optical fiber, Appl. Phys. B 116 (2014) 847–853, http://dx.doi.org/10.1007/s00340-014-5771-8.
[21] Amine Ben Salem, Mbaye Diouf, Rim Cherif, Ahmadou Wague, Mourad Zghal, Ultraflat-top mid infrared coherent broadband supercontinuum using all normal As_2S_5-borosilicate hybrid photonic crystal fiber, Opt. Eng. 55 (2016) 066109, http://dx.doi.org/10.1117/1.OE.55.6.066109.
[22] M.R. Karim, B.M.A. Rahman, Govind P. Agrawal, Mid-infrared supercontinuum generation using dispersion-engineered $Ge_{11.5}As_{24}Se_{64.5}$ chalcogenide channel waveguide, Opt. Express 23 (2015) 6903–6914, http://dx.doi.org/10.1364/OE.23.006903.

[23] Shangping Guo, Feng Wu, Sacharia Albin, Loss and dispersion analysis of microstructured fibers by finite-difference method, Opt. Express 12 (2004) 3341–3352, http://dx.doi.org/10.1364/OPEX.12.003341.

[24] Christian Agger, Christian Petersen, Sune Dupont, Henrik Steffensen, Jens Kristian Lyngsø, Carsten L. Thomsen, Jan Thøgersen, Søren R. Keiding, Ole Bang, Supercontinuum generation in ZBLAN fibers – detailed comparison between measurement and simulation, J. Opt. Soc. Am. B 29 (2012), http://dx.doi.org/10.1364/JOSAB.29.000635, 635–345.

[25] N. Granzow, S.P. Stark, M.A. Schmidt, A.S. Tverjanovich, L. Wondraczek, P. St.J. Russell, Supercontinuum generation in chalcogenide silica step-index fibers, Opt. Express 19 (2011) 21003–21010, http://dx.doi.org/10.1364/OE.19.021003.

[26] G.P. Agrawal, Nonlinear Fiber Optics, Academic Press, 2013.

[27] Karsten Rottwitt, Jørn H. Povlsen, Analyzing the fundamental properties of Raman amplification in optical fibers, J. Lightwave Technol. 23 (2005) 3597–3605, http://dx.doi.org/10.1109/JLT.2005.857776.

[28] Alexander M. Heidt, Pulse preserving flat-top supercontinuum generation in all-normal dispersion photonic crystal fibers, J. Opt. Soc. Am. B 27 (2010) 550–559, http://dx.doi.org/10.1364/JOSAB.27.000550.

[29] Christophe Finot, Bertrand Kibler, Lionel Provost, Stefan Wabnitz, Beneficial impact of wave-breaking for coherent continuum formation in normally dispersive nonlinear fibers, J. Opt. Soc. Am. B 25 (2008) 1938–1948, http://dx.doi.org/10.1364/JOSAB.25.001938.

[30] D. Anderson, M. Desaix, M. Lisak, M.L. Quiroga-Teixeiro, Wave breaking in nonlinear-optical fibers, J. Opt. Soc. Am. B 9 (1992) 1358–1361, http://dx.doi.org/10.1364/JOSAB.9.001358.

[31] Mariusz Klimczak, Grzegorz Soboń, Rafał Kasztelanic, Krzysztof M. Abramski, Ryszard Buczyński, Direct comparison of shot-to-shot noise performance of all normal dispersion and anomalous dispersion supercontinuum pumped with sub-picosecond pulse fiber-based laser, Sci. Rep. 6 (2016) 1–14, http://dx.doi.org/10.1038/srep19284.

[32] Goëry Genty, Ari T. Friberg, Jari Turunen, Chapter two-coherence of supercontinuum light, Progress Op. 61 (2016), http://dx.doi.org/10.1016/bs.po.2015.10.002.

[33] Michael H. Frosz, Validation of input-noise model for simulations of supercontinuum generation and rogue waves, Opt. Express 18 (2010) 14778–14787, http://dx.doi.org/10.1364/OE.18.014778.

[34] Charles Ciret, Simon-Pierre Gorza, Generation of ultra broadband coherent supercontinuum in tapered and dispersion managed silicon nanophotonic waveguides, J. Opt. Soc. Am. B 34 (2017) 1156–1162, http://dx.doi.org/10.1364/JOSAB.34.001156.

[35] L.E. Hooper, P.J. Mosley, A.C. Muir, W.J. Wadsworth, J.C. Knight, Coherent supercontinuum generation in photonic crystal fiber with all-normal group velocity dispersion, Opt. Express 19 (2011) 4902–4907, http://dx.doi.org/10.1364/OE.19.004902.

[36] Yinlan Ruan, Weitang Li, Ruth Jarvis, Nathan Madsen, Andrei Rode, Barry Luther-Davies, Fabrication and characterization of low loss rib chalcogenide waveguides made by dry etching, Opt. Express 12 (2004) 5140–5145, http://dx.doi.org/10.1364/OPEX.12.005140.

Accepted Manuscript

Title: Design of ZBLAN photonic crystal fiber with nearly zero ultra-flattened chromatic dispersion for supercontinuum generation

Author: Abdelkader Medjouri El-Bachir Meraghni Hadjer Hathroubi Djamel Abed Lotfy Mokhtar Simohamed Omar Ziane

Please cite this article as: A. Medjouri, E.-B. Meraghni, H. Hathroubi, D. Abed, L.M. Simohamed, O. Ziane, Design of ZBLAN photonic crystal fiber with nearly zero ultra-flattened chromatic dispersion for supercontinuum generation, *Optik - International Journal for Light and Electron Optics* (2017), http://dx.doi.org/10.1016/j.ijleo.2017.01.082

Design of ZBLAN photonic crystal fiber with nearly zero ultra-flattened chromatic dispersion for supercontinuum generation

Abdelkader Medjouri [1*], El-Bachir Meraghni [1], Hadjer Hathroubi [1], Djamel Abed [2], Lotfy Mokhtar Simohamed [3] and Omar Ziane [4].

[1]: Laboratoire d'Exploitation et Valorisation des Ressources Sahariennes (LEVRES), Faculté des sciences exactes, Université Echahid Hamma Lakhdar EL Oued, BP 789, El Oued, 39000, Algérie.

[2]: Laboratoire des Télécommunications, Faculté des Sciences et technologie, Université 8 mai 1945 Guelma, 24000, Guelma, Algérie.

[3]: Laboratoire des Systèmes Electroniques Et Optroniques (LSEO), Ecole Militaire Polytechnique, 16111, Alger, Algérie.

[4]: Laboratoire d'Electronique Quantique (LEQ), Faculté de physique, USTHB, BP no. 32 El-Alia, Bab-Ezzouar, 16111, Alger, Algérie.

[*] E-mail: medjouri-abdelkader@univ-eloued.dz

Abstract

In this paper, we present and numerically investigate Supercontinuum Generation (SCG) in ZBLAN circular lattice photonic crystal fiber with nearly zero ultra-flattened chromatic dispersion. The fiber dispersion properties are controlled by selectively liquid-filled and reduced air holes. The structure parameters have been optimized by using the fully vectorial finite-difference frequency-domain (FDFD) method combined with the perfectly matched layers (PML) boundary condition. Results indicates that a nearly zero ultra-flattened chromatic dispersion is obtained over a broad band of 300 nm centered around 1.55 µm with high nonlinearity and low confinement loss. Furthermore, SCG at 1.55 µm is demonstrated with the optimized design. By using a 3.2 Kw peak power 100 fs input secant-hyperbolic pulse, a symmetrical and relatively flat supercontinuum spectrum spanning 700 nm in the range 1200-1900 nm is successfully generated.

1

key words: ZBLAN; photonic crystal fiber; chromatic dispersion; supercontinuum generation; FDFD method.

1. Introduction

Supercontinuum Generation (SCG) is a well known nonlinear process that consists of the production of broadband light through the interaction of intense and short pulses, delivered by narrowband sources, with nonlinear materials [1, 2]. SCG, as an inherent aspect of nonlinear optics, has many applications such as metrology, pulse compression, optical communications, coherence tomography, spectroscopy and designing tunable ultrafast femto-second laser sources [1]. SC arises from a series of nonlinear processes such as self phase modulation (SPM), self-steepening, stimulated Raman scattering (SRS) and four wave mixing (FWM) [1]. In order to generate a smooth and broadband SC in optical fibers, a nearly zero chromatic dispersion around the targeted wavelength is required [3].

Photonic crystal fibers (PCFs) [4], also known as microstructured optical fibers or holey fibers are a class of optical fibers which enables the propagation of light in a way that it is not possible with conventional fibers. PCFs consist of a cladding formed by a morphological micrometer sized and periodic structure of air holes running along the longitudinal axis and a defect region in the center which acts as a solid core. Owing to their several and unique optical properties, PCFs have attracted widespread interest throughout the scientific community. Compared to

2

conventional optical fibers, PCFs can be designed with single mode behavior over a wide range of wavelengths [5], high birefringence [6], tailorable chromatic dispersion [7, 8], high nonlinearity [9] and so on. Due to these properties, many potential applications can be achieved, such as: dispersion compensating fibers [10, 11], polarization maintaining fibers [12], SCG [13], fiber based lasers [14], interferometry [15] and sensors [16].

PCFs with flattened chromatic dispersion have been the target of many researchers in the last few years. In order to achieve this property, many designs have been proposed and analysed. PCFs with different cladding geometries such as triangular, circular, octagonal and equiangular spiral have been widely studied [17-22]. Moreover, to improve the flatness of the aforementioned optical property over a wide range of wavelengths, two different ways are, in general, adopted: the first consists on using additional materials, either by doping the core with high index material such as germanium [23] and fluorine [24], or by infiltrating low index optofluids into selected air holes [3, 25].

Since its discovery in 1975 [26], ZBLAN (ZrF_4-BaF_2-LaF_3-AlF_3-NaF) heavy metal fluoride glass has been considered as an excellent alternative of the fused silica. In fact, the ZBLAN glass has a broadband transmission window extending from the ultra-violet to the mid infrared with a lower absorbing loss beyond 2 μm compared to the fused silica and a lower nonlinear coefficient compared to other soft glasses such

3

as tellurite or chalcogenide [26, 27]. Besides, ZBLAN based optical fibers can be easily drawn with high stability and high resistance to crystallization compared to other heavy metal fluoride glasses [28]. Furthermore, SC generation in ZBLAN optical fibers has been reported extensively with conventional step index fibers [29].

Recently, ZBLAN based PCFs have attracted more interest among the scientific community. A highly birefringent and low loss ZBLAN photonic quasi-crystal fiber has been proposed and numerically analyzed by W. Su el *al.* [27]. By introducing a rectangular array of four relatively small circular air holes in the core region, high birefringence up to 2.88×10^{-2} at 2 µm has been achieved. Moreover, the numerical modelling of the fundamental characteristics of ZBLAN-PCF have been reported for the 2-3 µm mid-infrared region [33]. Besides, the authors have shown the controllability of the chromatic dispersion by employing non-uniform air hole size. Furthermore, the investigation of SCG in ZBLAN based PCF has been considered. Xin Jiang et *al.* reported the first successful fabrication of solid core ZBLAN based PCF with hexagonal lattice [31]. By using a 4 cm length of the PCF, a supercontinua, spanning more than three octaves, has been demonstrated. More recently, Xin Jiang et *al.* reported the generation of broadband supercontinua, extending into the ultraviolet and mid-infrared regions, in a ZBLAN based PCF with six nanobore cores [32]. The SCG is experimentally demonstrated by exciting both the fundamental and the first higher order modes with long pulses at 1042 µm.

4

In this article, a ZBLAN based circular lattice photonic crystal fiber with a nearly zero ultra-flattened chromatic dispersion is proposed and numerically analyzed. To adjust the dispersion properties, the first inner air holes ring is filled with low index liquid and their radius is properly reduced. The propagation characteristics such as chromatic dispersion, confinement loss, effective mode area and nonlinearity are investigated by using a fully vectorial finite-difference frequency-domain (FV-FDFD) method combined with the perfectly matched layer (PML) as a boundary condition. SCG in the proposed ZBALN based PCF is then demonstrated through numerical simulations. The spectral broadening of a short and intense secant-hyperbolic pulse is investigated by solving the Generalized Nonlinear Schrödinger Equation (GNLSE) and using the Split Step Fourier Method (SSFM).

2. Theoretical background

2.1 Numerical method

The finite-difference frequency-domain (FDFD) method is a widely used approach for solving electromagnetic problems. Compared to the finite element method (FEM), the FDFD approach is easier and simpler to implement with a comparable accuracy [33]. Also, the FDFD method is based on a very general approach and it can be used to describe arbitrary structures whatever their design complexity. After introducing the PML boundary condition, the Maxwell's equations for the electric and magnetic field are given by [33]:

5

$$jk_0 s\varepsilon_r E = \nabla \times H$$

$$-jk_0 s\varepsilon_r H = \nabla \times E \tag{1}$$

$$s = \begin{bmatrix} s_y/s_x & & \\ & s_x/s_y & \\ & & s_x s_y \end{bmatrix} \tag{2}$$

where: $s_x = 1 - \dfrac{\sigma_x}{j\omega\varepsilon_0}$ and $s_y = 1 - \dfrac{\sigma_y}{j\omega\varepsilon_0}$. σ, ω, E, H are the

conductivity, the pulsation, the electric and the magnetic components of the

propagating field, respectively.

Once the meshing is applied to the structure, the equations system given by (1)

is transformed into a matrix eigenvalue problem and solved by employing a sparse

matrix approach to obtain the effective refractive index n_{eff} and the optical field

distribution of the fundamental mode [34].

2.2 Confinement loss

Theoretically, the light beam is totally confined into the PCF core due to the

infinite periodic structure (infinite cladding) around the centre. Practically, only a few

number of air holes rings form the cladding. Thereby, a fraction of the optical power

leaks out of the structure. This kind of losses is called the confinement loss and its

value can be calculated by using the formula [13]:

$$\alpha = 8.686 k_0 \, \text{Im}\left[n_{eff}\right] \tag{3}$$

6

In decibel per meter, where $\mathrm{Im}\lfloor n_{eff}\rfloor$ is the imaginary part of the effective refractive

index and k_0 is the free space wave number.

2.3 Chromatic dispersion

The control of chromatic dispersion in PCFs is a very important issue for

practical applications in dispersion compensation of optical communication systems

and nonlinear optics. As for standard fibre, the chromatic dispersion of a PCF is the

sum of the material dispersion D_m and the waveguide dispersion D_w:

$$D = D_m + D_w \tag{4}$$

The material dispersion D_m is derived from the following equation:

$$n_{ZBLAN}^2(\lambda) = 1 + \sum_{k=1}^{2} \frac{f_k \lambda^2}{\lambda^2 - \lambda_k^2} \tag{5}$$

Where $f_1 = 1.22514$, $f_2 = 1.52898$, $\lambda_1 = 0.08969$ μm and $\lambda_2 = 21.3825$ μm [35].

The waveguide dispersion is given by [10]:

$$D_w = -\frac{\lambda}{c} \frac{d^2 n_{eff}}{d\lambda^2} \tag{6}$$

Where λ and c are the wavelength and the speed of light, respectively.

2.4 Effective mode area

The effective mode area is a key factor in designing PCFs. It provides a

quantitative measurement of how much the mode field is confined within the PCF

core. It can be calculated using [13]:

7

$$A_{eff} = \frac{(\iint |E^2| dxdy)^2}{\iint |E|^4 dxdy}$$ (7)

Where E denotes the amplitude of the transverse electric field propagating inside the PCF.

An important parameter related to the effective mode area is the nonlinearity (Kerr effect). Its parameter is given by [36]:

$$\gamma = \frac{2\pi}{\lambda} \frac{n_2}{A_{eff}}$$ (8)

Where $n_2 = 5.4 \times 10^{-20} m^2 / W$ is the nonlinear refractive index of the ZBLAN glass [37].

3. Results and discussion

3.1 Structure optimization

The cross section of the proposed ZBLAN based PCF is given by Fig. 1. The structure is formed by five circular rings of air holes surrounding a solid core. The pitch and the diameters of the first inner ring and the cladding air holes are Λ, d_1 and d_2, respectively. Also, the core-neighbouring air holes ring is selectively filled with appropriate liquids of refractive indices n_L = 1.33, 1.34, 1.35, 1.36, 1.37. By solving the Maxwell's equation in the frequency domain, the optical field distribution of the fundamental mode and the correspondent effective index are obtained for a

8

given wavelength. For $\Lambda = 2.5\,\mu m$, $d_1 = 1.1$ µm, $d_2 = 0.76$ and $n_L = 1.35$, Fig. 2 shows the fundamental mode optical field distribution of the proposed PCF at 1.55 µm.

As it is mentioned in the introduction, to generate a relatively smooth and flat supercontinuum at 1.55 µm in high nonlinear PCF, the chromatic dispersion must be engineered through the optimization of the design to achieve a nearly zero value around the targeted wavelength. For this respect, the chromatic dispersion in our proposed PCF is firstly analyzed. Fig. 3 depicts its variation versus wavelength. The geometrical parameters of the structure are $\Lambda = 2.5\mu m$, $d_2/\Lambda = 0.88$, $d_1/\Lambda = 0.56$ (Fig. 3a) and $d_1/\Lambda = 0.64$ (Fig. 3b). As it can be observed, the chromatic dispersion can be tailored in the proposed PCF by modifying the value of the liquid index and the diameter of the inner air holes ring. Although, for a given wavelength, the chromatic dispersion decreases when the liquid refractive index increases. For the case where $d_1/\Lambda = 0.56$, the chromatic dispersion at 1.55 is 4.14 ps/nm.km for $n_L = 1.33$ and it decreases to -3.96 ps/nm.km for $n_L = 1.37$. For the case where $d_1/\Lambda = 0.64$, the chromatic dispersion at 1.55 is 6.95 ps/nm.km for $n_L = 1.33$ and it decreases to -4.79 ps/nm.km for $n_L = 1.37$. Besides, the closest value to the zero dispersion is obtained with $n_L = 1.35$. Moreover, the profile the chromatic dispersion can be adjusted by varying the liquid filled air holes radius. As it can be observed, chromatic dispersion with flattened shape can be achieved by slightly tuning the value

9

of d_1. For that purpose, we have calculated the chromatic dispersion for different values of d_1/Λ laying from 0.56 to 0.64. Fig. 4 shows the evolution of the chromatic dispersion with wavelength for $n_L = 1.35$, $\Lambda = 2.5\mu m$, $d_2/\Lambda = 0.88$ and d_1/Λ varying from 0.56 to 0.64 with a step of 0.016. As we can see, chromatic dispersion with the most flattened profile and the nearest value to zero was obtained for $d_1/\Lambda = 0.608$. Although, the chromatic dispersion fluctuation ΔD is approximately 1.05 ps/nm.km over a broad range of wavelengths varying from 1.39 μm to 1.71 μm.

The nonlinear properties of the proposed PCF is then investigated. The effective mode area is calculated as a first step where its variation with wavelength is depicted in Fig. 5. Due to the high fraction of air in the cladding region, the field is found to be highly confined in the core, which decrease the effective mode area. For $d_1/\Lambda = 0.608$ a very small effective mode area of about 10.14 μm^2 is obtained at 1.55 μm. Also, the proposed PCF exhibits high nonlinear coefficient over the wavelength bands that corresponds to the minimum dispersion. Around the wavelength 1.55 μm, a Kerr nonlinear coefficient of 21.6 W^{-1} Km^{-1} is obtained For $d_1/\Lambda = 0.608$.

Finally, the confinement loss is computed. The evolution of its factor with wavelength is plotted in Fig. 7 for $n_L = 1.35$, $\Lambda = 2.5\mu m$, $d_2/\Lambda = 0.88$ and d_1/Λ varying from 0.56 to 0.64. As it can be seen, the structure exhibits an ultra low loss over the computational wavelength range. In fact, the light beam is well confined within the core due the high air fraction presented in the cladding region

10

($d_2 / \Lambda = 0.88$). This explains the very small values of the confinement loss whatever

the value of the inner holes ring radius.

3.2 Supercontinuum generation

Until now, numerical investigations have shown that our proposed ZBLAN

based PCF with $\Lambda = 2.5 \mu m$, $d_2 / \Lambda = 0.88$, $d_1 / \Lambda = 0.608$ and $n_L = 1.35$ has a nearly

zero chromatic dispersion around 1.55 µm combined with high nonlinearity up to 21.6

$w^{-1}km^{-1}$ and an ultra low confinement. Therefore, SCG at 1.55 µm can be numerically

conducted. To simulate this nonlinear mechanism, the Generalized Nonlinear

Schrödinger Equation (GNLSE) is numerically solved by using the Split Step Fourier

Method (SSFM) where a short and intense pulse is initially launched [1]:

$$\frac{\partial A}{\partial z} + \frac{\alpha}{2} A - \sum_{k \geq 2} \frac{i^{k+1}}{k!} \beta_k \frac{\partial^k A}{\partial T^k} = i\gamma \left(1 + i\tau_{shok} \frac{\partial}{\partial T}\right) \left(A(z,t) \int_{-\infty}^{\infty} R(T') \times |A(z,T-T')|^2 \, dT'\right) \quad (9)$$

$A(z,t)$ is the temporal and longitudinal envelope of the pulse, α is the linear loss

coefficient, β_k is the kth coefficient of the Taylor expansion of the propagation

constant $\beta(\omega)$ centered around ω_0, γ is the nonlinearity coefficient, $R(t)$ is the

response function, which includes both instantaneous electronic and delayed Raman

contributions. Its expression is given by [29]:

$$R(t) = (1 - f_R)\delta(t) + f_R h_R(t) \quad (10)$$

where $f_R = 0.24$ is the Raman fraction, $\delta(t)$ is the Dirac function and $h_R(t)$ is the

Raman response function of the ZBLAN material. In order to model $h_R(t)$, the single

11

Lorentzian approximation has been widely used [38]. However, and through experimental measurements, an intermediate-broadening model, which results from the convolution of the Lorentzians and the Gaussians models has been recently proposed in the aim to give a better fit with the Raman gain spectrum [37]. Its mathematical expression is given by:

$$h_R(t) = \sum_1^8 A_i \exp\left(-\gamma_i t\right)\exp\left(-\Gamma_i^2 t^2/4\right)\sin\left(\omega_{v,i} t\right) \qquad (11)$$

where, A_i, $\omega_{v,i}$, γ_i and Γ_i are related to the peak intensity, Gaussian component position, Lorentzian and Gaussian full-width of half-maximum give by [37]:

I	A_i	$\omega_{v,i}$ (cm^{-1})	γ_i (cm^{-1})	Γ_i (cm^{-1})
1	8.48	54.43	58.67	23.46
2	17.12	102.91	82.40	32.96
3	51.78	169.95	115.27	46.11
4	155.69	275.91	160.76	64.30
5	62.12	377.35	137.90	55.16
6	107.05	504.77	184.62	73.85
7	27.69	576.43	38.50	15.40
8	17.83	648.44	135.84	54.34

Table. 1: Parameters used for the intermediate-broadening model [37].

The reason beyond using this complex model instead of the simple damping oscillation model is that the ZBLAN glass exhibits two major spectral peaks where the silica exhibits only one peak [37].

The input pulse is modeled using a secant-hyperbolic function given by :

$$A(0,t) = \sqrt{P}\sec h\left(\frac{t-t_0}{T_0}\right)\exp\left(\frac{-ic(t-t_0)^2}{2T_0^2}\right) \qquad (12)$$

12

Where, P is the peak power, T_0 is the width of the input pulse, t_0 is the center of the pulse and c is the chirp parameter. Modeling the input pulse as a secant-hyperbolic is widely used when simulating the SCG in optical fibers. However, simulations have shown that by using a Gaussian function, the same output spectrum can be obtained.

Since the pump wavelength is 1.55 μm, the Taylor coefficients of the propagation constant have been calculated at this pump wavelength, where, β_2, β_3, β_4, β_5, β_6, β_7, β_8 and β_9 are found to be, -4.9245×10^{-4} ps^2/km, -4.0503×10^{-6} ps^3/km, 1.8093×10^{-7} ps^4/km, -2.9811×10^{-10} ps^5/km, -4.6814×10^{-12} ps^6/km, 7.1503×10^{-14} ps^7/km, -6.6098×10^{-16} ps^8/km and 4.3340×10^{-18} ps^9/km, respectively. In order to simulate the propagation of the launched pulse, the well known Split Step Fourier Method (SSFM) has been employed. The peak power and the Full Width at Half Maximum (FWHM) of the chirpless pulse (c=0) are 3.2 Kw and 100 fs, respectively. A possible laser source for such pump can be a commercially available Ti:Saphire femto-second oscillator combined with an Optical Parametric Amplifier (OPA) to reach the required input peak power. Fig. 8 gives the evolution of the pulse spectrum with distance for a fiber length of 30 cm. As we can see, the spectrum of the secant-hyperbolic pulse broadens with the distance and a flat spectrum with a FWHM as high as 700 nm is successfully obtained around the pumping wavelength 1.55 μm.

13

The symmetrical shape of the spectral broadening is explained by the dominance of the Self Phase Modulation (SPM) nonlinear effect.

Considering now the manufacturing process of the proposed ZBLAN based PCF. Due to its physical and chemical properties such as the temperature range required to ensure both a suitable viscosity and stability against devitrivication, heat transfer efficiency and the thermal conductivity [31, 39, 40], drawing optical fibers made of ZBLAN has been exclusively done with step index fibers. However, an improved stack-and-draw technique has been recently used to fabricate microstructured optical fibers with ZBLAN [31, 32]. By using this technique, we believe that our proposed ZBLAN based PCF can be easily fabricated with the optimized design.

4. Conclusion

A ZBLAN based circular lattice photonic crystal fiber with a nearly zero ultra-flattened chromatic dispersion is proposed and its optical properties are numerically investigated by using a finite-difference frequency-method (FDFD) combined with the perfectly matched layer (PML). The near zero chromatic dispersion is achieved by selectively infiltrating a liquid with an appropriate refractive index into the first core-neighboring air holes ring and the flatness is obtained by appropriately reducing their radii. The numerical results indicate that a flattened chromatic dispersion with a fluctuation as small as 1.05 ps/nm km is obtained over a broad range of wavelengths

14

varying from 1.39 μm to 1.71 μm. Besides, the proposed structure exhibits high nonlinearity and ultra low confinement loss over a broad band of wavelengths. Furthermore, the supercontinuum generation at 1.55 μm is simulated by solving the Non Linear Schrödinger Equation (GNLSE) and using the Split Step Fourier Method (SSFM). By using 30 cm of fiber length, a supercontinuum spectra spanning 700 nm in the range 1200 nm to 1900 nm is successfully obtained by employing a 3.2 Kw peak power 100 fs input secant-hyperbolic pulse. Owing to its interesting properties, the proposed ZBLAN based PCF is found to be suitable for many applications such as spectroscopy, pulse compression, Dense Wavelength Division Multiplexing (DWDM) based telecommunication systems, ...etc.

References

[1] J.M. Dudley, G. Genty, S. Coen, Supercontinuum generation in photonic crystal fiber, Rev. Mod. Phys. 78 (2006) 1135-1184. http://dx.doi.org/10.1103/RevModPhys.78.1135

[2] Omar ZIANE, Soraya ZAIBA, Noureddine Melikechi, Continuum generation in water and carbon tetrachloride using a picosecond Nd-YAG laser pulse, Optics Communications 273 (2007) 200-206. http://dx.doi.org/10.1016/j.optcom.2006.12.014

[3] Majid Ebnali-Heidari, Hamed Saghaei, Farshid Koohi-Kamali, Mohammad Naser Moghadasi, Mohammad Kazem Moravvej-Farshi, Proposal for supercontinuum generation by optofluidic infiltrated photonic crystal fibers, IEEE Journal of Selected Topics in Quantum Electronics 20 (5) (2014) 4042-4048. http://dx.doi.org/10.1109/JSTQE.2014.2307313

[4] J.C. Knight, T.A. Birks, R.F Cregan, P.St.J. Russell, J.-P. de Sandro, Photonic crystals as optical fibres - physics and applications, Optical Materials. 11 (1999) 143–151. http://dx.doi.org/10.1016/S0925-3467(98)00040-8

[5] T. A. Birks, J. C. Knight, and P. St. J. Russell, Endlessly single-mode photonic crystal fiber, Opt. Lett. 22 (1997) 961–963. http://dx.doi.org/10.1364/OL.22.000961

[6] Abdelkader Medjouri, Lotfy Mokhtar Simohamed, Omar Ziane and Azzedine Boudrioua, Investigation of high birefringence and chromatic dispersion management in photonic crystal fibre with square air holes, Optik - International Journal for Light and Electron Optics 126 (2015) 2269-2274. : http://dx.doi.org/10.1016/j.ijleo.2015.05.119

15

[7] M.M. Haque, M. Shaifur Rahman, M. Selim Habib, M. Samiul Habib. A single mode hybrid cladding circular photonic crystal fiber dispersion compensation and sensing applications, Photon Nanostruct: Fundam Appl (2015) 63-70. http://dx.doi.org/10.1016/j.photonics.2015.01.006

[8] Partha Sona Maji and Partha Roy Chaudhuri, Design of all-normal dispersion based on multimaterial photonic crystal fiber in IR region for broadband supercontinuum generation, Applied Optics 54 (13) (2015) 4042–4048. http://dx.doi.org/10.1364/AO.54.004042

[9] Wei Su, Shuqin Lou, Hui Zou, Bolin Han, Design of a highly nonlinear twin bow-tie polymer photonic quasi-crystal fiber with high birefringence, Infrared Physics & Technology 63 (2014) 62–68. http://dx.doi.org/10.1016/j.infrared.2013.11.012

[10] M.M. Haque, M. Shaifur Rahman, M. Samiul Habib and S. M. A. Razak, Design and characterization of single mode circular photonic crystal fiber for broadband dispersion compensation, Optik - International Journal for Light and Electron Optics (2014) 2608-2611. http://dx.doi.org/10.1016/j.ijleo.2013.11.063

[11] T. A. Birks, D. Mogilevtsev, J. C. Knight, and P. St.J. Russell, Dispersion compensation using single-material fibers, IEEE Photonics Technol. Lett. 11 (06) (1999) 674–676. http://dx.doi.org/10.1109/68.766781

[12] Aihan Yin and Lei Xiong, Novel single-mode and polarization maintaining photonic crystal fiber, Infrared Physics & Technology 67 (2014) 148–154. http://dx.doi.org/10.1016/j.infrared.2014.07.014

[13] Partha Sona Maji, Partha Roy Chaudhuri, Supercontinuum generation in ultra-flat near zero dispersion PCF with selective liquid infiltration, Optik - International Journal for Light and Electron Optics 125 (2014) 5986–5992. http://dx.doi.org/10.1016/j.ijleo.2014.07.026

[14] Haili Yang , Shuangchen Ruan, Yongqin Yu, Hang Zhou, Erbium-doped photonic crystal fiber laser with 49 mW, Optics Communications 283 (2010) 3176–3179. http://dx.doi.org/10.1016/j.optcom.2010.04.021

[15] Sébastien Vergnole, Laurent Delage, François Reynaud, Laurent Labonté, Philippe Roy, Gilles Mélin, and Laurent Gasca, Test of photonic crystal fiber in broadband interferometry, App. Opt. 44 (13) (2005) 2496–2500. http://dx.doi.org/10.1364/AO.44.002496

[16] Rahul Kumar Gangwar, Vinod Kumar Singh, Refractive index sensor based on selectively liquid infiltrated dual core photonic crystal fibers, Photon Nanostruct: Fundam Appl. 15 (2015) 46-52. http://dx.doi.org/10.1016/j.photonics.2015.03.001

[17] Jingyuan Wang, Chun Jiang, Weisheng Hu, Mingyi Gao, Modified design of photonic crystal fibers with flattened dispersion, Optics & Laser Technology 38 (2006) 169–172. http://dx.doi.org/10.1016/j.optlastec.2004.11.016

[18] Abdelkader Medjouri, Lotfy Mokhtar Simohamed, Omar Ziane, Azzedine Boudrioua and Zoubir Becer, Design of a circular photonic crystal fiber with flattened chromatic dispersion using a defected core and selectively reduced air holes: Application to supercontinuum generation at 1.55 µm, Photonics and Nanostructures - Fundamentals and Applications 16 (2015) 43-50. http://dx.doi.org/10.1016/j.photonics.2015.08.004

16

[19] S. M. Abdur Razzak, Yoshinori Namihira, Proposal for highly nonlinear dispersion-flattened octagonal photonic crystal fibers, IEEE Photonics Technol. Lett. 20 (04) (2008) 249–251. http://dx.doi.org/10.1109/LPT.2007.912986

[20] Md. Asiful Islam, M. Shah Alam, Design optimization of equiangular spiral photonic crystal fiber for large negative flat dispersion and high birefringence, J. Lightwave Technol. 30 (2012) 3545–3551. http://dx.doi.org/10.1109/JLT.2012.2222349

[21] Xuyou Li, Zhenlong Xu, Weiwei Ling, Pan Liu, Design of highly nonlinear photonic crystal fibers with flattened chromatic dispersion, App. Opt. 53 (2014) 6682–6687. http://dx.doi.org/10.1364/AO.53.006682

[22] Jianfei Liao, Junqiang Sun, Mingdi Du, Yi Qin, Highly nonlinear dispersion-flattened slotted spiral photonic crystal fibers, IEEE Photonics Technol. Lett. 26 (2014) 380–383. http://dx.doi.org/10.1109/LPT.2013.2293661

[23] Y.L. Hoo, W. Jin, J. Ju, H.L. Ho, D.N. Wang, Design of photonic crystal fibers with ultra-low, ultra-flattened chromatic dispersion, Optics Communications 242 (2004) 327–332. http://dx.doi.org/10.1016/j.optcom.2004.08.030

[24] Richard Zeleny, Michal Lucki, Nearly zero dispersion-flattened photonic crystal fiber with fluorine-doped threefold symmetry core, Optical Engineering 52 (2013). http://dx.doi.org/10.1117/1.OE.52.4.045003

[25] Liang Tian, Li Wei, Feng Guoying, Numerical simulation of supercontinuum generation in liquid-filled photonic crystal fibers with a normal flat dispersion profile, Optics Communications 343 (2015) 196-202. http://dx.doi.org/10.1016/j.optcom.2014.07.080

[26] Michel Poulain, Marcel Poulain, Jacques Lucas and Pierre Brun, Verres fluores au tetrafluorure de zirconium proprietes optiques d'un verre dope au Nd^{3+}, Mat. Res. Bull. 10 (1975) 243-246. http://dx.doi.org/10.1016/0025-5408(75)90106-3

[27] Wei Su, Shuqin Lou, Hui Zou and Bolin Han, Highly birefringent ZBLAN photonic quasi-crystal fiber with four circular air holes in the core, Infrared Physics & Technology 66 (2014) 97-102. http://dx.doi.org/10.1016/j.infrared.2014.05.003

[28] Xiushan Zhu and N. Peyghambarian, High-power ZBLAN glass fiber lasers: review and prospect, Advances in OptoElectronics 2010 (2010). http://dx.doi.org/10.1155/2010/501956

[29] Christian Agger, Christian Petersen, Sune Dupont, Henrik Steffensen, Jens Kristian Lyngsø, Carsten L. Thomsen, Jan Thøgersen, Søren R. Keiding and Ole Bang, Supercontinuum generation in ZBLAN fibers—detailed comparison between measurement and simulation, J. Opt. Soc. Am. B 29 (2012) 635-345. http://dx.doi.org/10.1364/JOSAB.29.000635

[30] D. C. Tee, N. Tamchek and C. H. Raymond Ooi, Numerical modeling of the fundamental characteristics of ZBLAN photonic crystal fiber for communication in 2–3 μm midinfrared Region, IEEE Photonics Journal 8 (2016). 10.1109/JPHOT.2016.2536940

[31] Xin Jiang, Nicolas Y. Joly, Martin A. Finger, Fehim Babic, Gordon K. L. Wong, John C. Travers and Philip St. J. Russell, Deep-ultraviolet to mid-infrared supercontinuum generated in solid-core ZBLAN photonic crystal fibre, Nature Photonics (2015). 10.1038/nphoton.2014.320

17

[32] Xin Jiang, Nicolas Y. Joly, Martin A. Finger, Fehim Babic, Meng Pang, Rafal Sopalla, Michael H. Frosz, Samuel Poulain, Marcel Poulain, Vincent Cardin, John C. Travers, and Philip St. J. Russell, Supercontinuum generation in ZBLAN glass photonic crystal fiber with six nanobore cores, Optics Letters 41 (2016), 4245-4248. https://doi.org/10.1364/OL.41.004245

[33] Shangping Guo, Feng Wu and Sacharia Albin, Loss and dispersion analysis of microstructured fibers by finite-difference method, Optics Express 12 (2004) 3341-3352. http://dx.doi.org/10.1364/OPEX.12.003341

[34] Zhaoming Zhu and Thomas G. Brown, Full-vectorial finite-difference analysis of microstructured optical fibers, Optics Express 10 (2002) 853-864. http://dx.doi.org/10.1364/OE.10.000853

[35] Fuxi Gan, Optical properties of fluoride glasses: a review, Journal of Non-Crystalline Solids 184 (1995) 9-20. http://dx.doi.org/10.1016/0022-3093(94)00592-3

[36] Xuyou Li, Zhenlong Xu, Weiwei Ling, and Pan Liu, Design of highly nonlinear photonic crystal fibers with flattened chromatic dispersion, Applied Optics 53 (2014) 6682-6687. http://dx.doi.org/10.1364/AO.53.006682

[37] Xin Yan, Chihiro Kito, Shohei Miyoshi, Meisong Liao, Takenobu Suzuki and Yasutake Ohishi, Raman transient response and enhanced soliton self-frequency shift in ZBLAN fiber, J. Opt. Soc. Am. B 29 (2012) 238-243. http://dx.doi.org/10.1364/JOSAB.29.000238

[38] Xiaohong Hu, Yishan Wang, Wei Zhao, Zhi Yang, Wei Zhang, Cheng Li, and Hushan Wang, Nonlinear chirped-pulse propagation and supercontinuum generation in photonic crystal fibers, Applied Optics 49 (2010) 4984-4989. http://dx.doi.org/10.1364/AO.49.004984

[39] S. Aasland, and T. Grande, Crystallization of ZBLAN glass. J. Am. Ceram. Soc. 79 (1996) 2205–2206. 10.1111/j.1151-2916.1996.tb08961.x

[40] F. Smektala and M. Matecki, Stability study on heating and determination of critical cooling rates of fluorozirconate glasses. J. Non-Cryst. Solids 184 (1995) 314–3183. http://dx.doi.org/10.1016/0022-3093(94)00589-3

Figures captions

Fig. 1: Cross sectional view of the proposed ZBLAN based PCF where the pitch and the diameters of the first inner ring and the cladding air holes are Λ, d_1 and d_2, respectively.

Fig. 2: Field distribution of the fundamental mode at 1.55 μm.

Fig. 3: Variation of the chromatic dispersion with wavelengths for $\Lambda = 2.5 \mu m$, $d_2 / \Lambda = 0.88$, (a): $d_1 / \Lambda = 0.56$, (b): $d_1 / \Lambda = 0.64$ and n_L varying from 1.33 to 1.37.

Fig. 4: Variation of the chromatic dispersion with wavelength for $n_L = 1.35$, $\Lambda = 2.5 \mu m$, $d_2 / \Lambda = 0.88$ and d_1 / Λ varying from 0.56 to 0.64.

18

Fig. 5: Variation of the effective mode area with wavelength for n_L = 1.35, $\Lambda = 2.5\mu m$, $d_2/\Lambda = 0.88$ and d_1/Λ varying from 0.56 to 0.64.

Fig. 6: Variation of the nonlinear coefficient with wavelength for n_L = 1.35, $\Lambda = 2.5\mu m$, $d_2/\Lambda = 0.88$ and d_1/Λ varying from 0.56 to 0.64.

Fig. 7: Variation of the confinement loss with wavelength for n_L = 1.35, $\Lambda = 2.5\mu m$, $d_2/\Lambda = 0.88$ and d_1/Λ varying from 0.56 to 0.64.

Fig. 8: Evolution of a secant-hyperbolic pulse spectrum centered around 1.55 μm with a FWHM of 100 fs over a fiber length of 30 cm where $\Lambda = 2.5\mu m$, $d_2/\Lambda = 0.88$, $d_1/\Lambda = 0.608$ and $n_L = 1.35$.
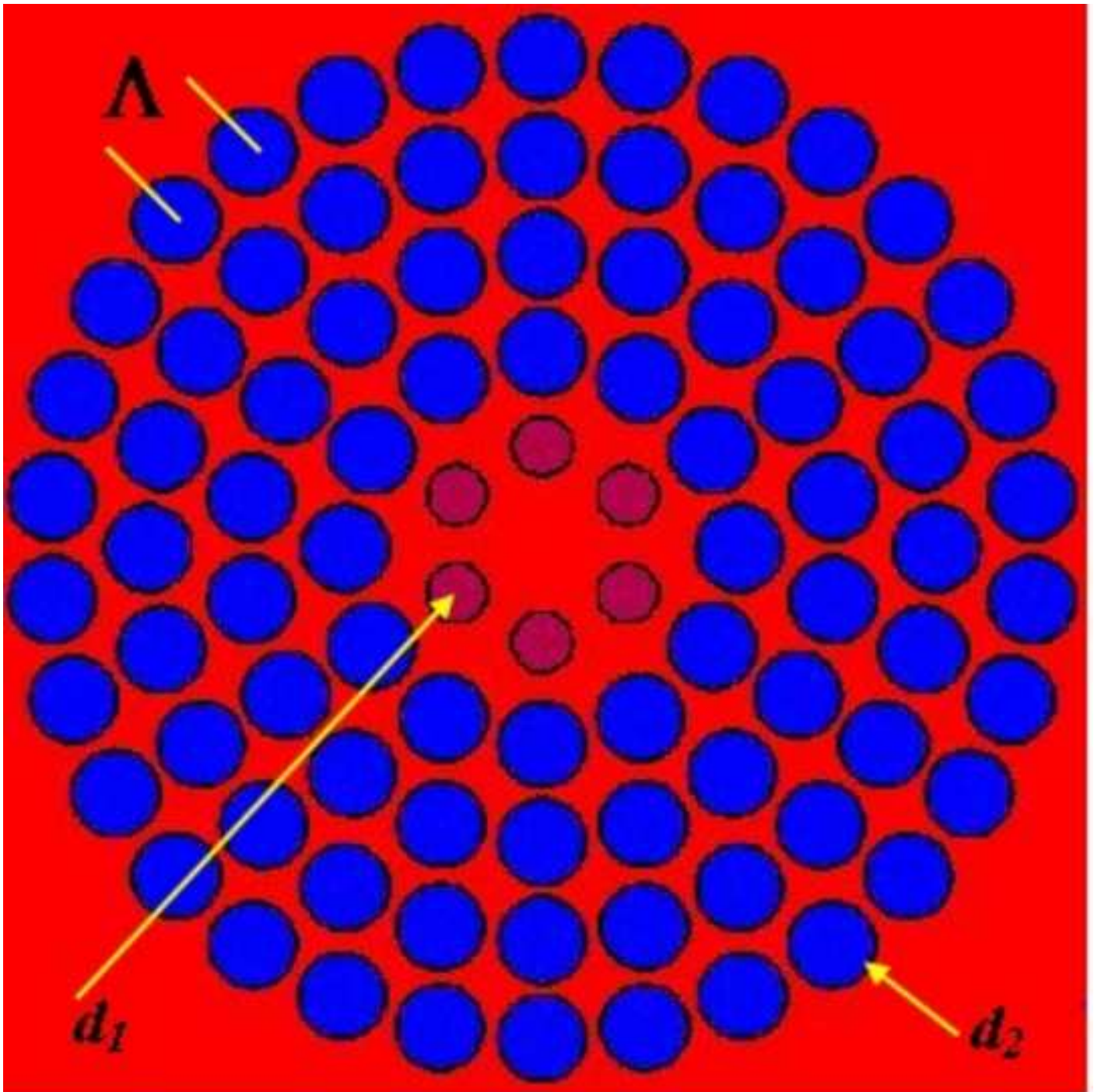
19
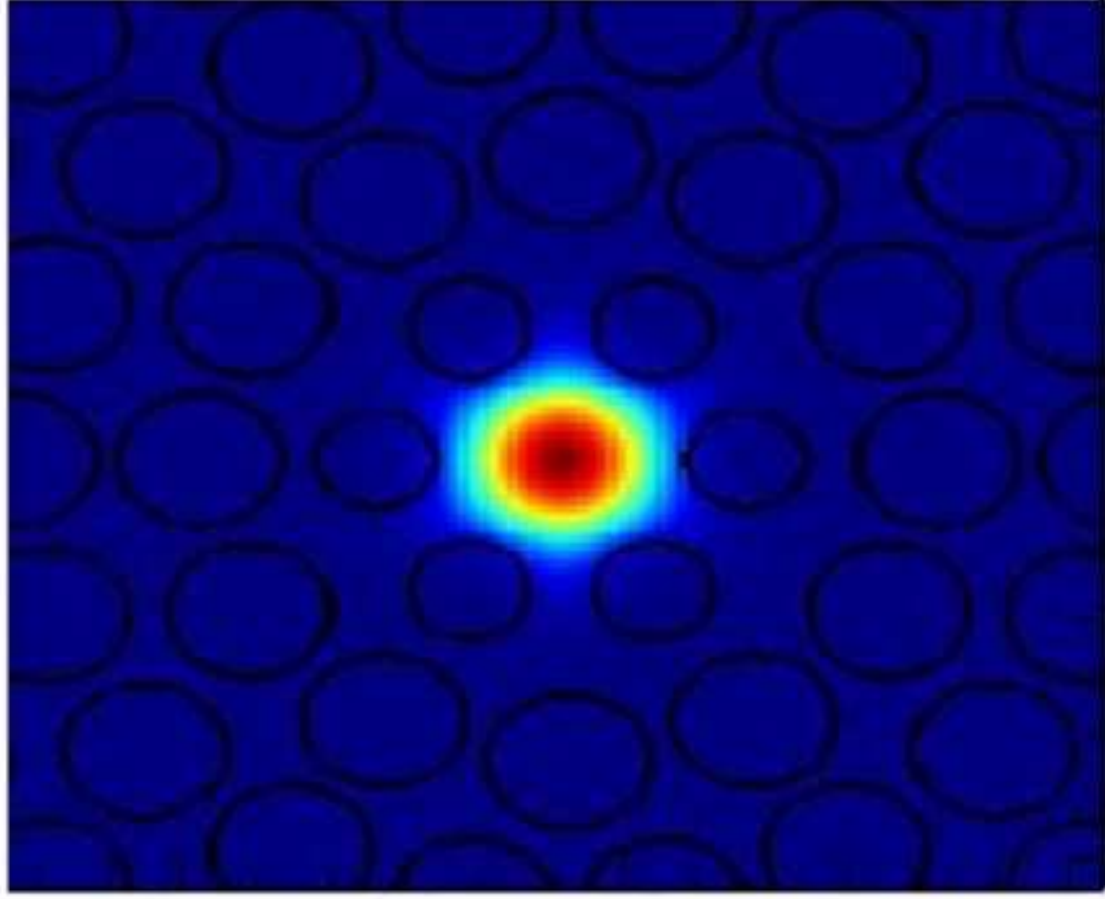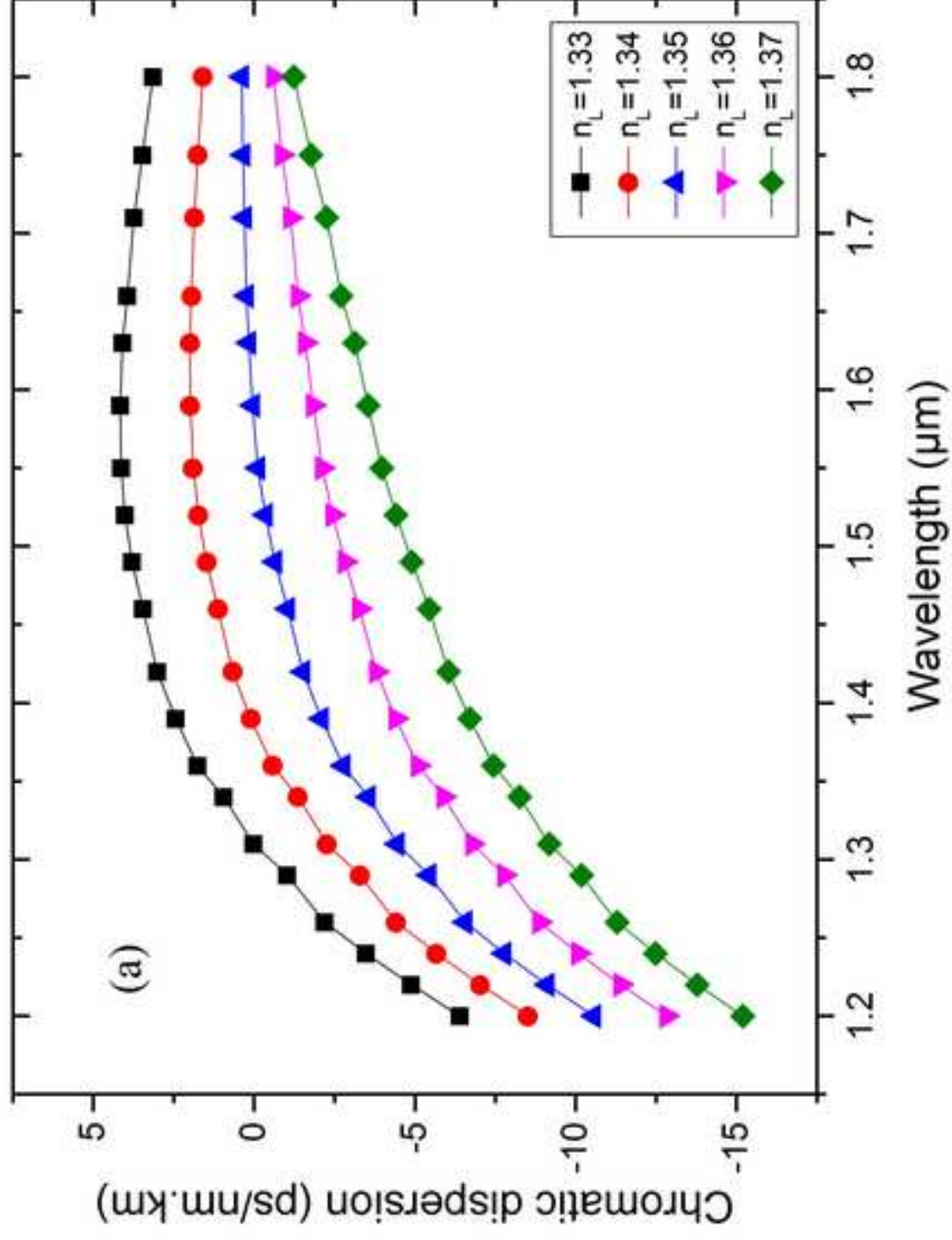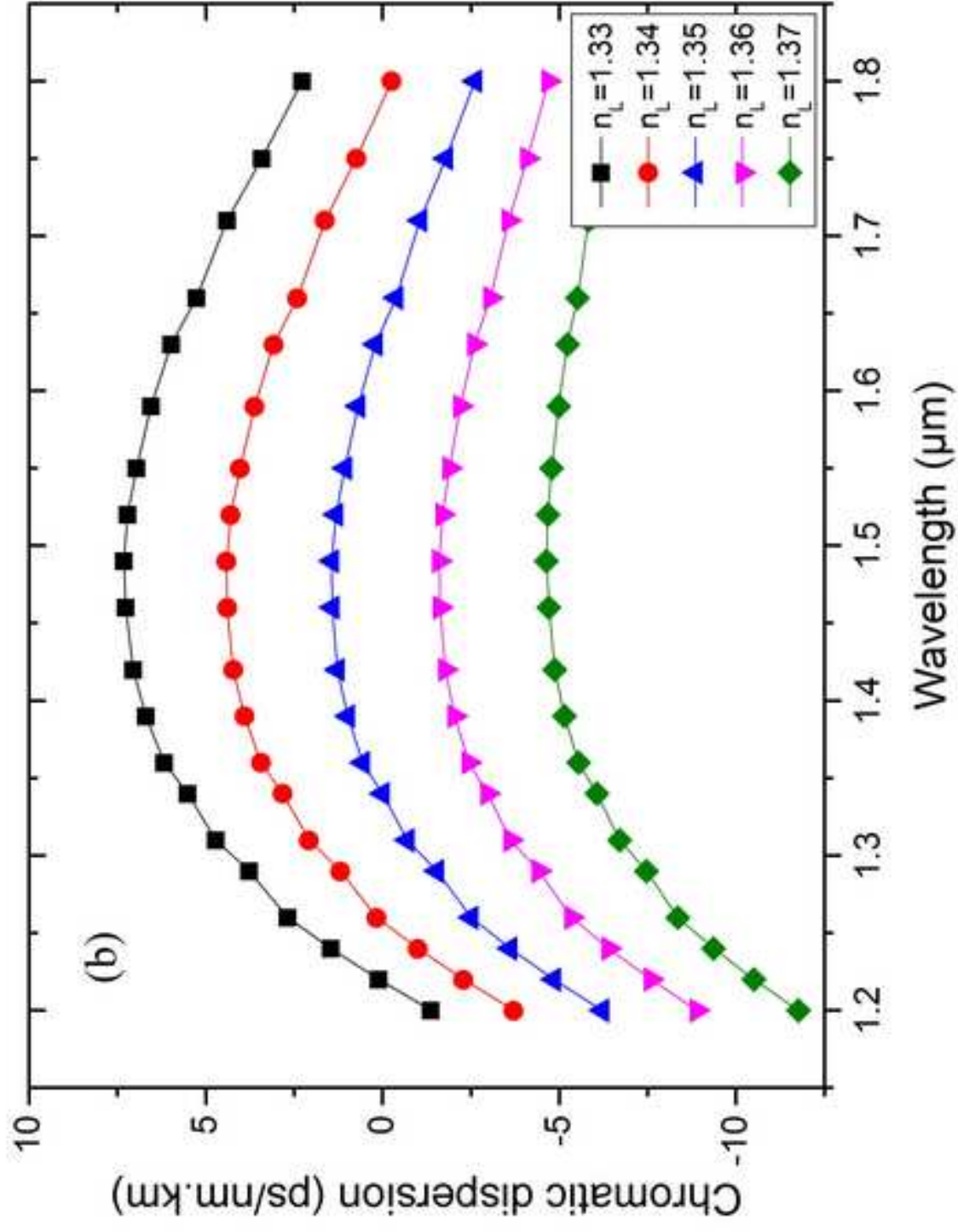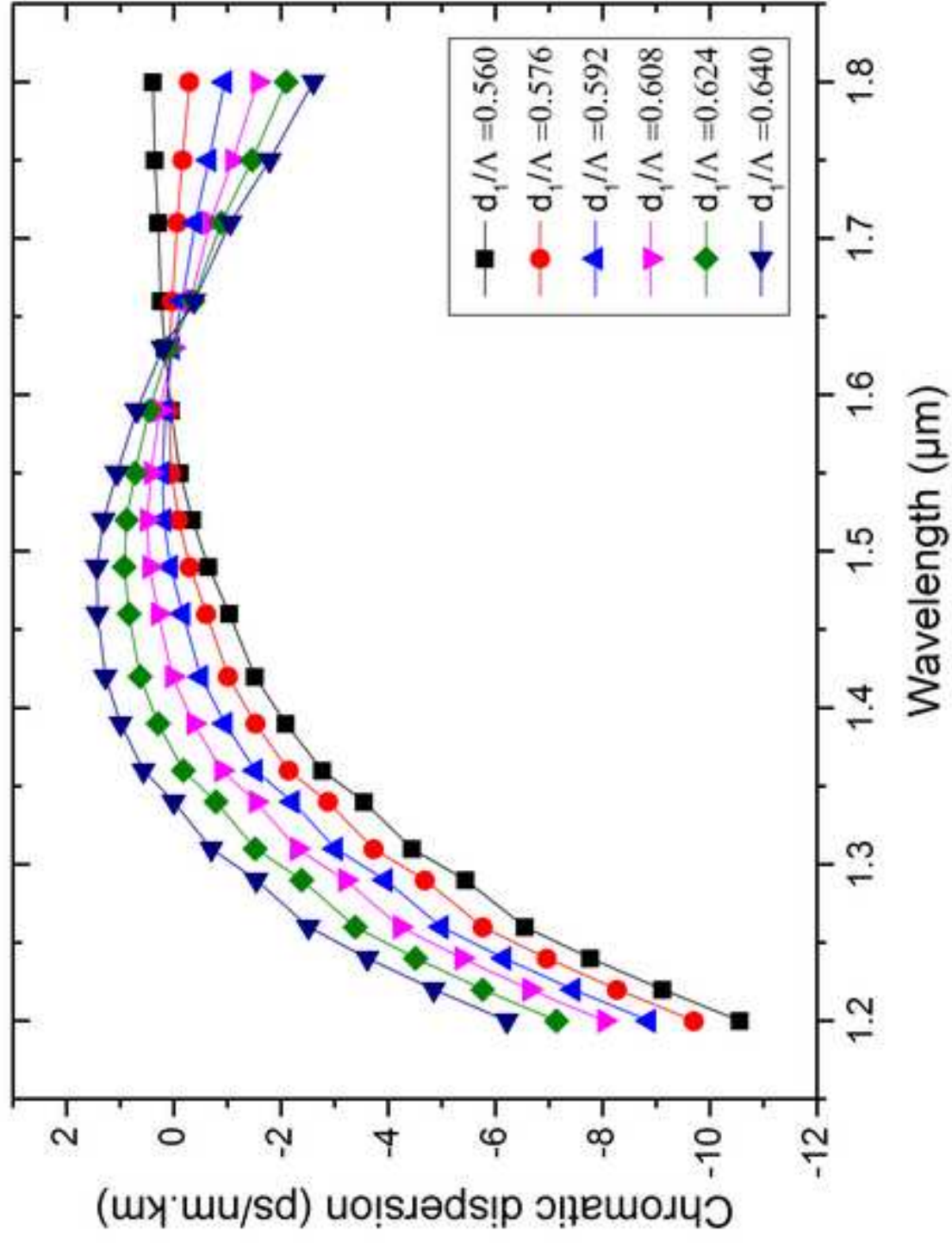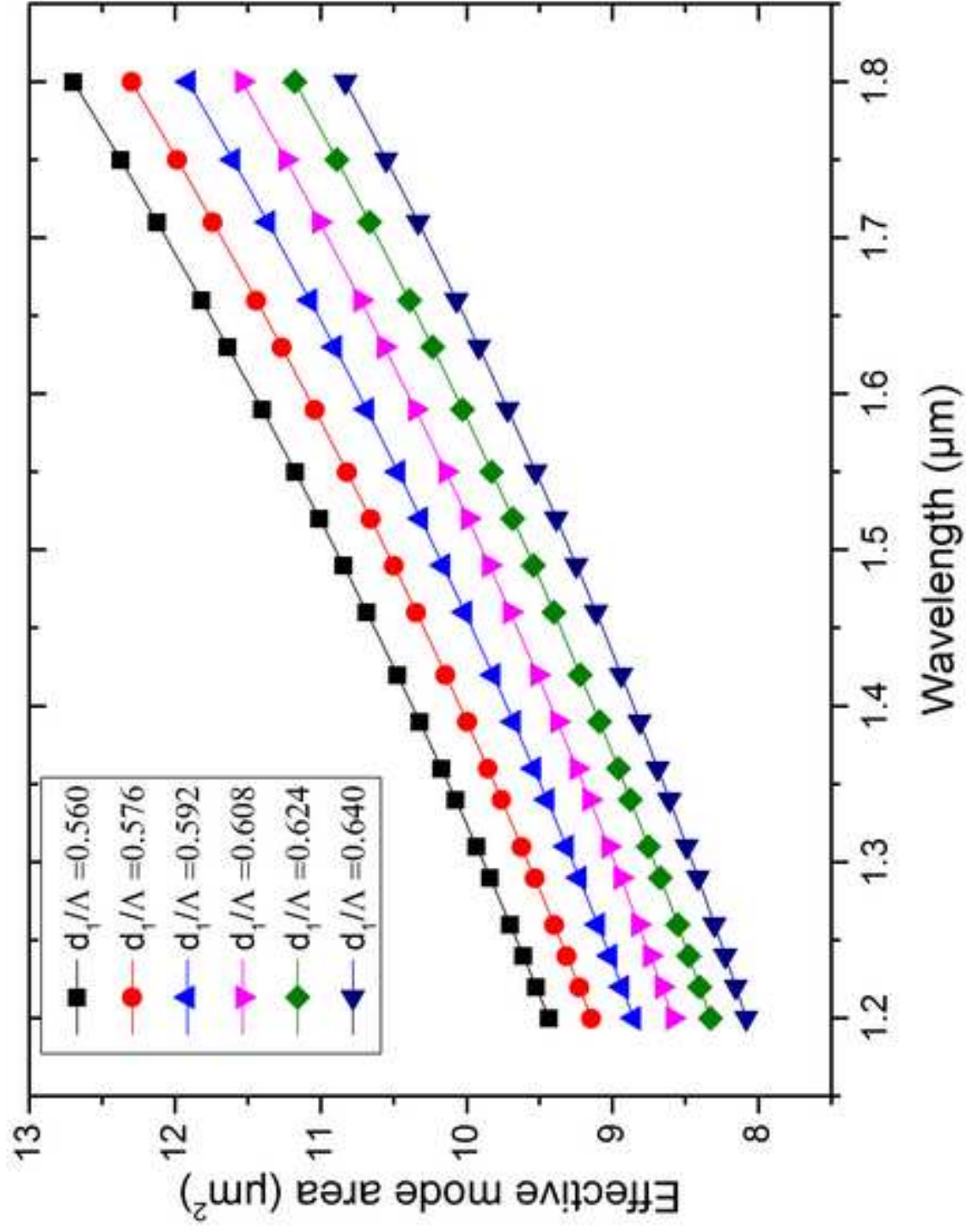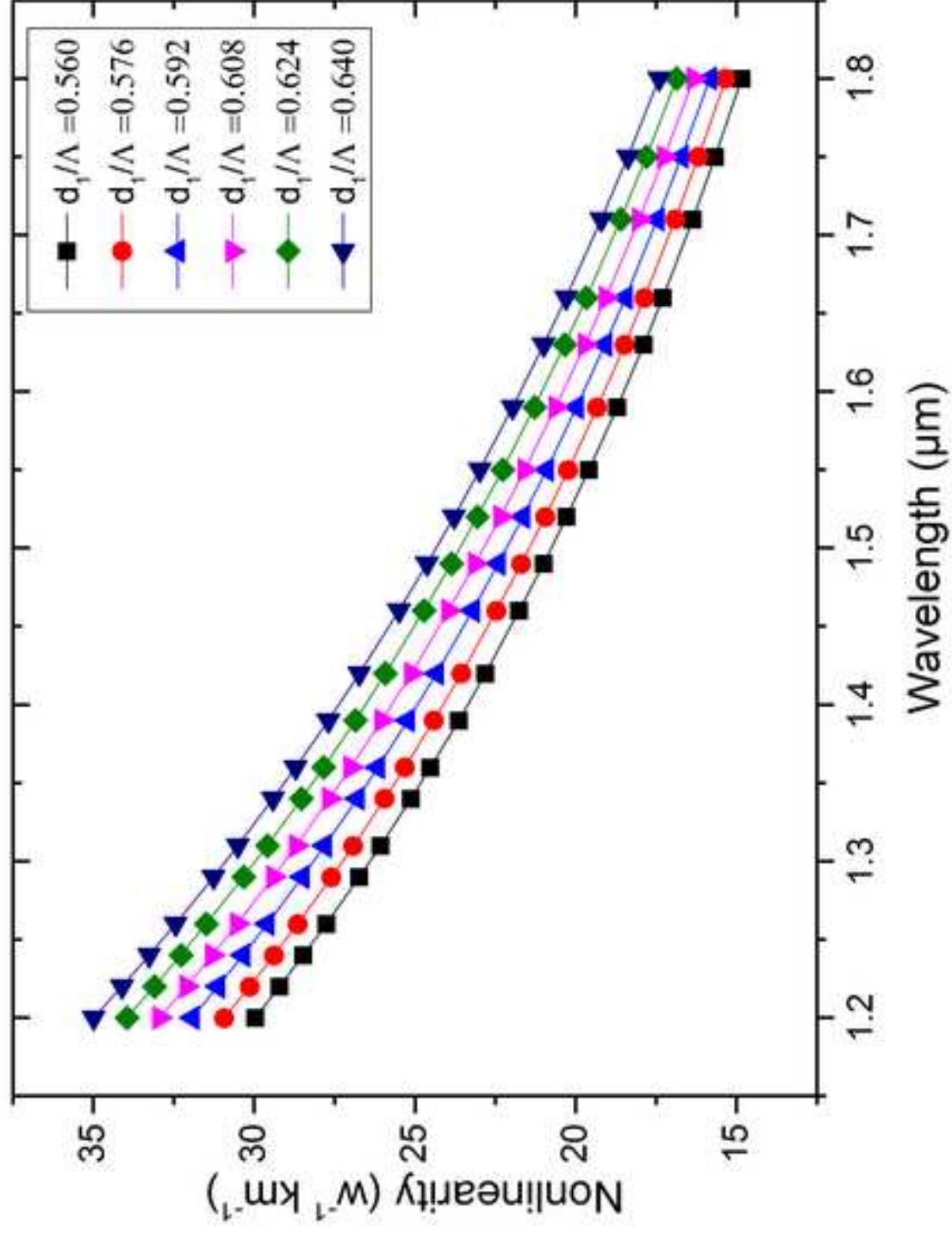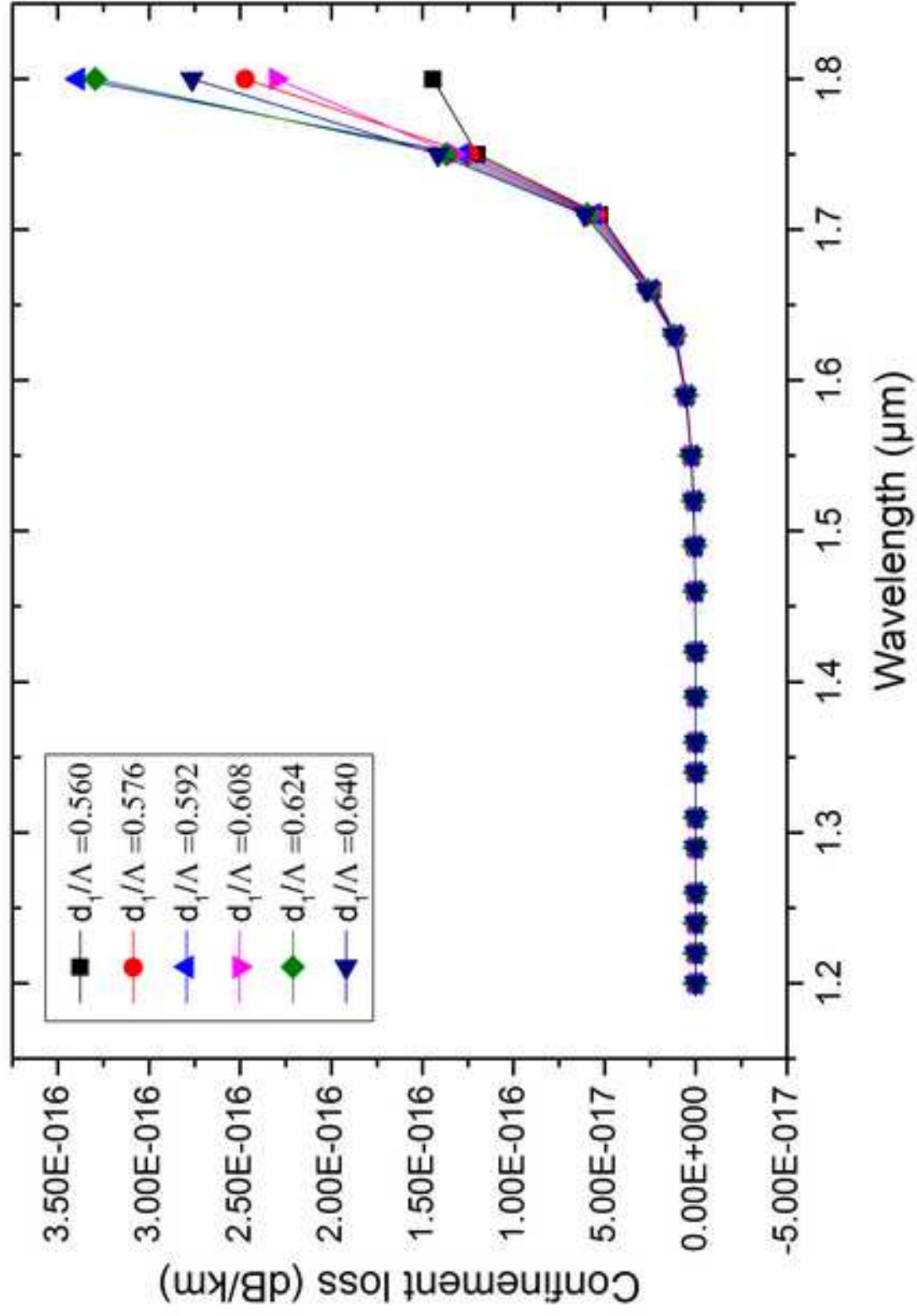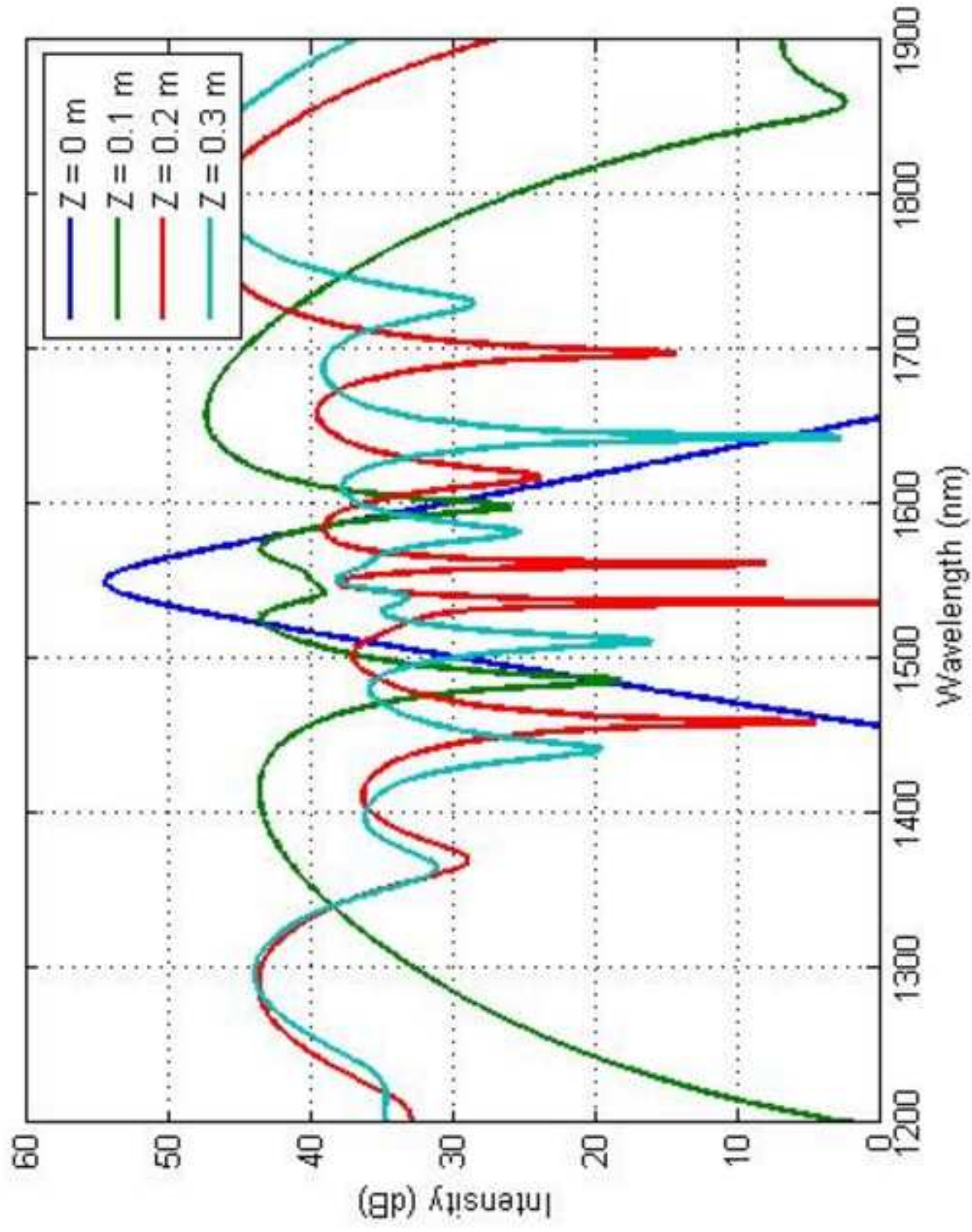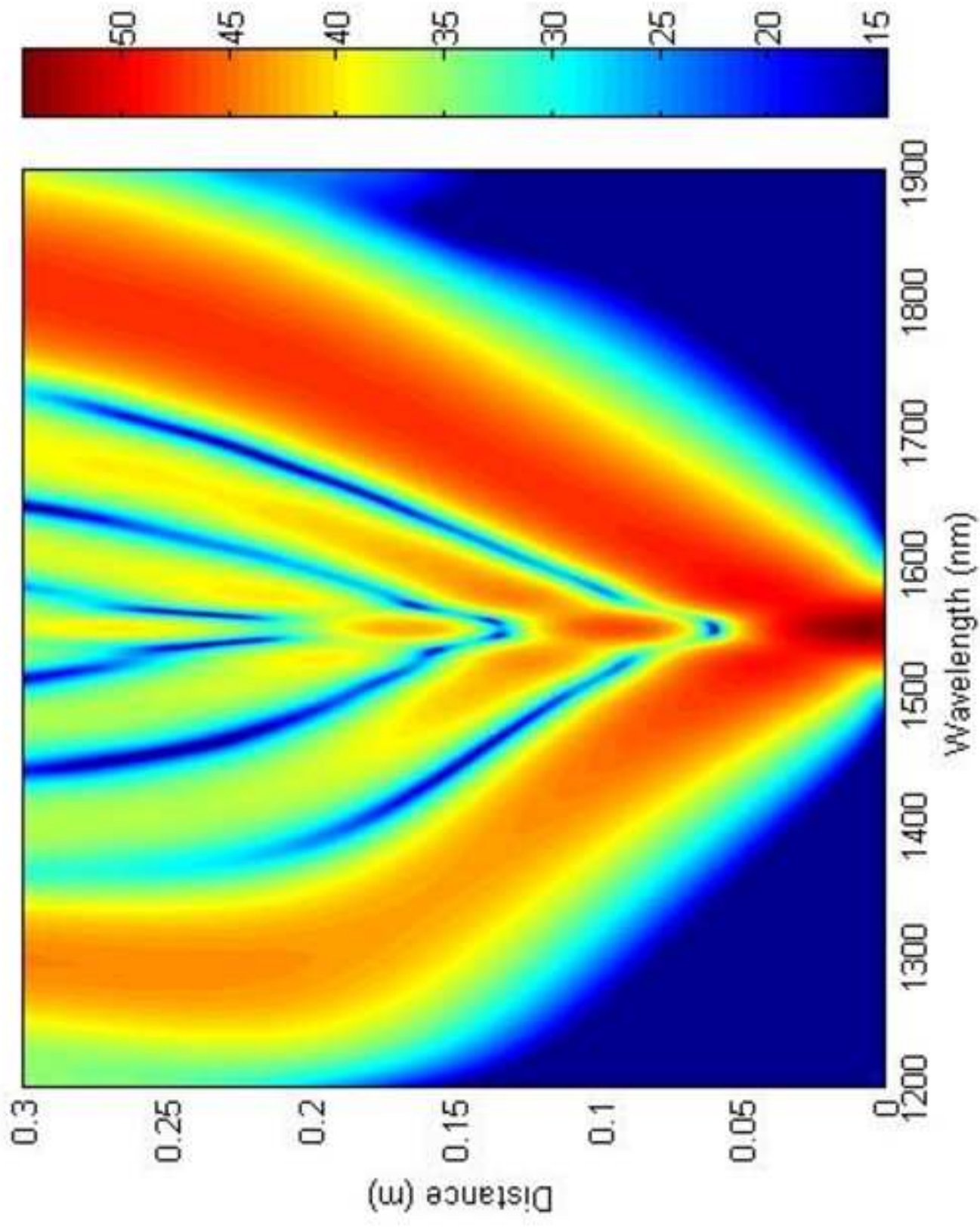
Accepted Manuscript

Title: Growth study of CdS thin films deposited by chemical bath

Author: A. Beggas B. Benhaoua A. Attaf M.S. Aida

Please cite this article as: A.Beggas, B.Benhaoua, A.Attaf, M.S.Aida, Growth study of CdS thin films deposited by chemical bath, Optik - International Journal for Light and Electron Optics http://dx.doi.org/10.1016/j.ijleo.2016.06.030

Growth study of CdS thin films deposited by chemical bath

A. Beggas[a,b] B.Benhaoua[a], A. Attaf[b] and M. S. Aida[c*]

[a]Lab. VTRS, Faculty of Science & Technology, Univ. El-Oued, El oued 39000, Algeria
[b]Faculty of Science, Univ. Biskra, Biskra 07000, Algeria
[c]Thin Films & Pasma Lab., Physics Dept., frères Mentouri University, 2500 Constantine, Algeria

Keywords: chalcogenides; thin films; chemical synthesis; FTIR; optical properties.

Abstract

CdS thin films were prepared by chemical bath deposition (CBD) technique. The bath solution is a mixture of Cadmium carbonate $CdCO_3$ and thioureaas source of Cadmium and Sulfur respectively, ammonia was used as complexing agent. In order to investigate the deposition time; films were prepared with two deposition times 45 and 90 min.X-raydiffraction, UV visible spectrophotometry and Fourier transform infrared techniques are used to investigate CdS thin films and the different steps of reactions leading to CdS product. Hexagonal CdS thin films were obtained with (002) preferred orientation and having crystallite size average in the range of 14.3 to 30.4 nmfor the two deposition times. CdS thin films transmittance is above 70% in visible region. Band gap energy was 2.46 and 2.42eV for both samples.Studies of different solutions and steps leading to the formation of CdS products were carried. The formation mechanism of CdS thin films was proposed based on FTIR results.

Corresponding author:: aida_salah2@yahoo.fr (**M.S.Aida** +213663 14 64 26)

1. Introduction

Cadmium Sulphide (CdS) is an important binary (II-VI) semiconductor material, widely used as an efficient window layer in thin films basedsolar cell structures due to its high transitivity and low resistivity [1]. CdS thin films are prepared by several methods such as: spray pyrolysis [2], sputtering [3], electro deposition [4], vacuum evaporation [5] and chemical bath deposition (CBD) [6]. Chemical bath deposition is simple, low temperature and low cost.It has been used in the deposition of CdS thin films since the 1960 [7]. Due to its high transitivityand low resistivity as mentioned above; today, the most important application of CdSthin films isin photovoltaic cells [8]. The chemical process of CBD to elaborate CdS thin films consists of the slow release of Cd^{+2} from cadmium saltand S^{-2} ions from thioureain chemical alkaline solution [9].A survey in the literature shows that during the years, different Cadmium sources have been used in this process to obtain Cd^{+2} from cadmium salt, such as Cadmium acetate [10], cadmium sulphate [11], cadmium chloride [12], cadmium nitrate [13] and cadmium iodide [14].While, thiourea is the most commonly used sulphur precursor [8]. Ammonia is used as complexing agent for the cadmium ions in the reaction solution. A large number of works were carried with the aim to prepare CdS thin films with good optoelectronic properties suitable for photovoltaic applications.

The aim of this work is firstly, to study the use of another saltsource of Cd^{+2} such as cadmium carbonate which, to our best knowledge, was not used until now. Secondly, to monitor all reactions steps leading to CdS thin films formation. In this study, XRD, UV-visible and FTIR techniques were used to investigate the structural and optical properties of CdS thin films and to identify the chemical reactions leading to CdS formation.

2

2. Experimental details

2. 1. CdS thin films elaboration

CdS thin films were grown on microscope glass slides (ref 217102) having dimension (75mm x 25 mm x 1.1mm). Before deposition, glass substrates were cleaned in acetone and deionized water, respectively. 50 ml ofsolution was prepared at room temperature, which was composed of 0.0015 M Cadmium carbonate ($CdCO_3$), 0.005 M thiourea ($CS(NH_2)_2$), 0.5 ml ammonium hydroxide 27% (NH_3, H_2O)as complexing agent and distilled water,for better dissolution of $CdCO_3$ a few drops of sulphuric acid were added.

The mixture was stirred during 30 minutes to obtain a homogeneous solution. Just after immersing the substratein the bath, thesolution temperature was fixed at55°C. CdS thin films were deposited with two deposition times of45 and 90 min. Structural properties of CdS thin films were carried out using X-ray diffractometer (XPERT-PRO X-ray diffractometer system), withCu Kα(λ=1.54060Å and energy incidence 40kv, 40 mA). Angle scanning (2θ) value wasbetween (20-70°). Optical transmittance spectra were obtained using UV-visible spectrophotometer (Shimadzu, model 1800) working in the range 200-900 nm.

2. 2. Chemical reactions and solution preparation

In order to have an insight on thechemical reactions leading to CdS thin films formation, two solutions were prepared separately, (i) solution A (0.0015 M Cadmium carbonate ($CdCO_3$), a few drops of sulphuric acid and distilled water) and (ii) solution B (A+ 0.5 ml ammonium hydroxide 27%). In conical flask the two solutions were constantly stirred for 30 mints, and then the precipitates were filtered out and calcinedunder air condition.(iii) C solution is prepared by mixing ammonia with thiourea. To investigate the calcined product, rest of both A and Bsolutions,and C solution,Fourier transform infrared (FT-IR)

3

measurements were carried out using (Shimadzu, model IR Affinity-1) working in the range (400-4000 cm^{-1}).

3. Results and discussion

3. 1. CdS thin films

Fig.1 shows X-ray diffraction patterns of CdS thin films, deposited with 45 and 90 min and named in the following as (CdS$_{45}$) and (CdS$_{90}$) respactively. As can be seen both films diffraction patterns exhibit peaks at 26.7°, assigned to the (002) of CdS hexagonal structure and much well with spatial group P63mc (186) having Joint Committee Powder Diffraction System card (JCPDS No: 77-2306). Two peaks appear at 24.9° and 28.4° corresponding to plans (100) and (101)respectively in the case of (CdS$_{90}$) whereas diffraction peak intensity increases with deposition time; this is a consequence of thickness increasing which leads to better crystallinity of CdS thin films. It is worth noting that CdS may crystallise in cubic or in hexagonal structure. However, for solar cell applications, hexagonal structured is preferred due to its thermodynamic stability [10].

The inter-planar spacing d_{hkl} can be calculated from the X-ray diffraction profiles using the Bragg condition:

$$n\lambda = 2d_{hkl}\sin\theta \qquad (1)$$

where$n$ is the order of diffraction, λ is the wavelength of the X-ray, θ is the diffraction angle. The calculated value of d_{hkl}-spacing are recapitulated in table 1 andmatched well with those of the JCPDS 77-2306 data for hexagonal CdS. Lattice constants can be determined using the relation for hexagonal systems:

$$\frac{1}{d_{hkl}^2} = \frac{4(h^2+hk+k^2)}{3a^2} + \frac{l^2}{c^2} \qquad (2)$$

4

where a and c are the lattice constants, hkl are the miller indices, the obtained values of a and c are0.4126 nm and0.6672nm respectively which are closely equal to standard ones of (JCPDS No: 77-2306 where a_0= 0.4136nm and c_0 = 0.6713nm).these values are illustrated in table 1

The crystallite size (D) can be found using the Scherer formula:

$$D = \frac{k\lambda}{\beta cos\theta} \qquad (3)$$

where k is a constant nearly equal to 0.9,λ is the wavelength of the X-ray, θ is the diffraction angle and β is the width full at half maximum (FWHM) usually measured in radian. The crystallite size is enhanced with deposition time; the estimated values were equal to 14.3 nm and 30.5 nm for CdS_{45} and CdS_{90} respectively.

3. 2 Optical properties

Fig.2. shows the optical transmittance spectra of CdS_{45} and CdS_{90} thin films.As can be seen, both films exhibit a high transmittancein the visible range; it is in order of 70% to 88% for CdS_{90} and 75% to 90% for CdS_{45}. The later has higher transmittance which may be due to its lower thickness. The band gap energy of thin films is one of the most important parameters for optical window applications. According to Tauc's relation [15], optical band gap (E_g)can be obtained by extrapolating the straight line portion,as shown in Fig.3, of the plot $(\alpha hv)^2$ versus hv to the energy axis $(\alpha hv)^2$= 0 (where α is the absorption coefficient and hv is the photon energy). E_g values are found to be 2.46eV and 2.42eV for CdS_{45} and CdS_{90} respectively.Those values are agreed with ones reported in literature [6, 10, 14].

3. 3. Reactions leading to CdS product

In order to investigate and toidentify the chemical reactions leading to the formation of the CdS product, different solutions A, B and C, as described in experimental details, were used for this purpose.

3. 3. 1. Fourier Transform Infra-Red Spectroscopy (FTIR)

Fourier transforms infrared spectra (FTIR) is a technique which is used to obtain information about the chemical bonding in a material by producing an infrared absorption spectrum.It can be used to determine the nature and the structure of compounds. In this work it is used to identify the chemical reactions leading to the formation of the CdS thin film. FTIR spectra, in 400-4000cm^{-1} range, of residual products and solutions by using KBr as support were released.

3. 3. 2. FTIR spectrum of cadmium carbonates (CdCO$_3$)

Fig.4. shows the FTIR spectrum in the wavenumber range (400-4000 cm^{-1}) of Cadmium Carbonate (CdCO$_3$) powder which was used as precursor in the present study.A broad absorption band centred at 3440 cm^{-1} and a small band, around 1620 cm^{-1}, are due to the -OH groups stretching vibration[16]. As mentioned in the figure,a strong broad absorption centred at about 1448 cm^{-1} is connected with the asymmetric stretching vibration which is attributed to the vibrations in CO$_3^{-2}$anion. Two absorption bands,strong sharp band at 852 cm^{-1}and at 718 cm^{-1} are assigned to the bending out plane vibrations of this anion [17].FTIR spectrum contains also peaks at1795cm^{-1} and 2472cm^{-1}which are expected for CdCO$_3$ [18].

3. 3. 3. FTIR spectrum of calcined products from A and B

The infrared spectrum for fine calcined powdered samples of A and B were obtained from FTIR in KBr as support in the range 400-4000cm^{-1} and compared with carbonate

6

cadmium one which are represented in Fig.5. It was noticed that all the three spectra are similar in shape. Nuance at around 3400 cm^{-1} maybe is due to the presence of different amount of humidity in the products. From this similarity one can inferredthat the precipitates in both A and B are only an amount of no dissociated carbonate cadmium.

FTIR spectrum of obtained solution after filtration from A (CdCO$_3$ with water and H$_2$SO$_4$) is represented in Fig.6. Peaks at 1054, 1080 and 1180 cm^{-1} indicate the presence of the coordinated SO$_4^{-2}$ion [19, 20], whereas peaks at1633 and 3443 cm^{-1}are due to -OH groups stretching vibration [21, 22]. The spectra show a peak around 2360 cm^{-1} is assigned to the antisymmetric stretching mode of CO$_2$ [23]. Peak at around 2083 cm^{-1} indicated the presence of CO [24] which may be formed from CO$_2$.From such observations a possible chemical reaction,to describe what has happened in the solution A to lead to free Cd^{+2}, can be written as follows:

$$CdCO_3 + H_2SO_4 \rightarrow Cd^{2+} + SO_4^{2-} + H_2O + CO_2 + CdCO_3(nodissociated) \qquad (4)$$
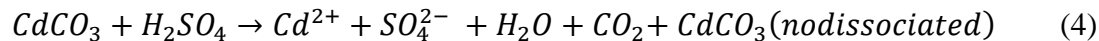
FTIR spectrum of the obtained solution after filtration from B (CdCO$_3$ with water, H$_2$SO$_4$ and NH$_3$) is represented in Fig.7. Peaks at 617, 670 and 3267 cm^{-1} confirm the presence of NH$_3$[25], peak at 462cm^{-1}is correlated to the Cd-Nbond [26], Peaks at 981 and 1103 cm^{-1} are attributed to SO$_4^{2-}$[27]. The presence of NH$_4^+$ is confirmed by the two peaks at 3046and 1400 cm^{-1}[28, 29], peaks at 3434 and 1633 cm^{-1}are due to the -OH groups stretching vibration[22, 23]. From all above resulting peaks evidence, the structure of the compound products are: SO$_4^{2-}$, NH$_4^+$ and cadmium tetramin [Cd(NH$_3$)$_4$]$^{2+}$ complex ion, which reduces the overall speed of reaction. It is worth noting the absence of such peaks at 3531, 3588and 3607 cm^{-1}[19, 23], which are related to the presence of Cd(OH)$_2$, confirming its non-existence in the final state.

From such observations a possible chemical reaction to describe what has happened in the solution B can be written as follows:

$$CdCO_3 + H_2SO_4 + 5NH_3$$
$$\rightarrow [Cd(NH_3)_4]^{2+} + SO_4^{2-}$$
$$+ CO_2 + NH_4^+ + +OH^- + CdCO_3(nodissociated) \qquad (5)$$
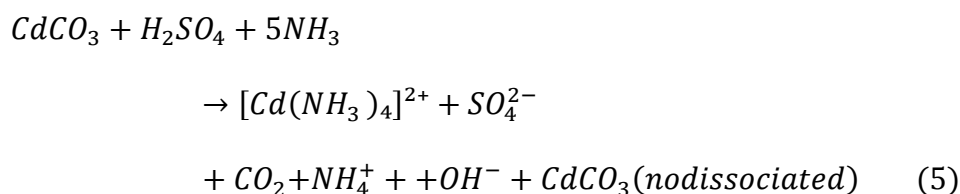
3. 3. 4. Effect of ammonia on B solution

In other hand, the FTIR of the products of the reaction between ammonia and thiourea CS $(NH_2)_2$ is given in Fig.8. The peaks obtained at 2065 cm^{-1} and 1083 cm^{-1} are assigned to N≡C and N-C respectively[30, 31], while peaks at 1627 and 3376cm^{-1} are assigned to NH$_2$[32],which means the formation of (NCNH$_2$). Peaks at 1400 and 1476 cm^{-1} indicate the presence of NH$_4^+$[28, 29], peaks around 1633 and 3434 cm^{-1}which overlap with NH$_2$ peak completely. The two peaks are assigned to H$_2$O[22, 23]. Then, it may be concluded that the reaction of thiourea and ammonia can be written leading to free S^{-2} ions as follows:

$$CS(NH_2)_2 + 2(NH_4^+ + OH^-) \rightarrow NCNH_2 + S^{-2} + 2NH_4^+ + 2H_2O \qquad (6)$$

The overall reaction can be written as follow:

$$CdCO_3 + H_2SO_4 + 6NH_3 + CS(NH_2)_2$$
$$\rightarrow CdS + SO_4^{2-} + H_2O + NCNH_2$$
$$+ CO_2 + 2NH_4^+ + 4NH_3$$
$$+ CdCO_3(nodissociated) \qquad (7)$$
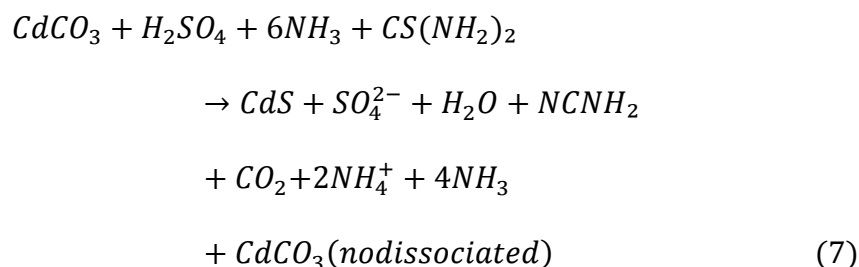
From the global equation, it's clear that the quantity of ammonia (NH$_3$) should be more sufficiently to ensure the transformation of Cd^{2+} into cadmium tetramin [Cd(NH$_3$)$_4$]$^{2+}$ (eq:5) and showing up (NH$_4^+$, OH$^-$ as if they formed from equilibrium of ammonia in

8

water: $NH_3 + H_2O \rightleftharpoons NH_4^+ + OH^-$) to make basic solution which is necessary for occurring reaction (6). The later combined with reaction (5) lead to CdS thin film formation as shown in schematic illustration (8) where chain of chemical and mechanism reaction may be proposed as follow:
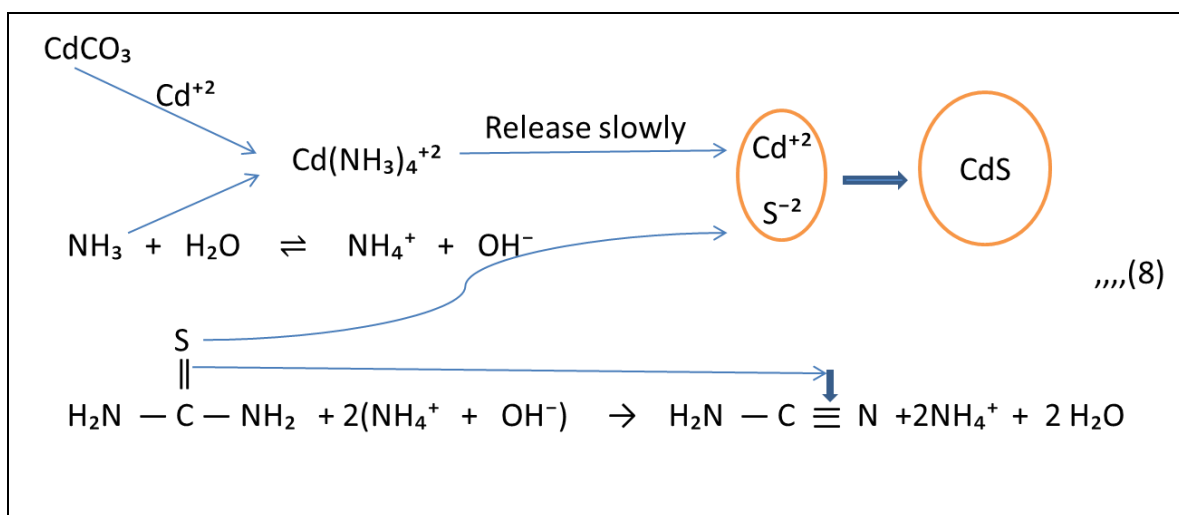
Schematic illustration of the formation process of CdS.

4. Conclusion

In this work CdS thin films were deposited by CBD method on glass substrate at 55°C heated solution containing cadmium carbonate as source of Cd^{+2} and ammonia as complexing agent and thiourea as source of S^{-2}. X-raysdiffraction results confirm that CdS thin films growth under hexagonal structure with (002) orientation with crystallite size average in 14.3-30.4 nm for both films. From optical studies elaborated CdS thin films exhibit transmittance over than 70% in visible range and band gap energy lies in therange of 2.46 to 2.42 eV with increasing films thickness.Composition analysis of different solutions leading to the formation of CdS products using FTIR analysis indicatesthat, for calcined precipitate and different steps solution, Cd^{+2} released from cadmium carbonate by the activation of sulphuric acid then complexes with NH_3 to form cadmium tetramin $[Cd(NH_3)_4]^{+2}$, while the S^{-2}released from thiourea by $(NH_4^+ + OH^-)$

9

action on it.Chain of chemical and mechanism reaction leading to CdS thin film formation were proposed.

10

References

[1] K. P. Chopra, S. R. Das. Thin Films Solar Cells, New York, 1979.

[2] I. K. Battisha, H. H. Afify, G. Abd El-Fattah and Y. Badr, Phizika, A11, (2002),31

[3] M. A. Islam, M. S. Hossein. , M. M Aliyu, P. Chelvanathan, Q. Huda, M. R. Karim, K. Sopian, N. Amin. Energy Procidia, Volume 33, (2013) 203-213.

[4] R.P. Raffaelle, H. Forsell, T. Potdevin, R. Fridefeld, J. G. mantovani, S. G. Bailey, S. M. Hubbard, E. M. Gordon and A. F. Hepp, Sol. Energy Mater. Sol. Cells 57(1999)167

[5] K. Senthil, D. Mangalaraj, Sa. K. Narayandass, Applied Surface Science 169-170 (2001) 476-479.

[6] A. I. Oliva, O. Solıs-Canto, R. Castro-Rodrıguez, P. Quintana, Thin Solid Films 391 (2001) 28-35.

[7] G. Kitaev, A. Uritskaya, S. Mokrushin, Russ. J. Phys. Chem. 39 (1965) 1101.

[8] G. Hodes, Chemical Solution Deposition of Semiconductor Films, New York, 2002.

[9]Q. Q. Liu, J. H. Shi, Z. Q. Li, D. W. Zhang, X. D. Li, Z. Sun, L. Y. Zhang, S. M. Huang, Physica B 405 (2010) 4360-4365

[10]K. S. Ramaiah, R. D. Pilkington, A. E. Hill, R. D. Tomlinson, A.K. Bhatnagar, Materials Chemistry and Physics 68 (2001) 22-30.

[11]H. Moualkia, S. Hariech, M. S. Aida, Thin Solid Films 518 (2009) 1259-1262

[12]Natalia S. Kozhevnikova, Andrey A. Rempel, Frank Hergert, Andreas Magerl, Thin Solid Films. 517(2009) 2586-2589.

[13] A. S. Z. Lahewil, Y. Al-Douri, U. Hashim, N. M. Ahmed, Procedia Engineering 53 (2013) 217-224

[14] T. Nakanishi, K. Ito, Solar Energy Materials and Solar Cells 35 (1994) 171-178

[15] J Tauc, R. Grigorovici, A. Vancu, Phys Stat. Sol, 15(1966)627-637.

[16] W. Hanke, K. Miiller, ZEOLITES, 1984, Vol 4, July 245

[17] M. Chávez Portillo, L. A. Chaltel Lima, U. Peña Rosas, G. Hernández Téllez, R. Gutiérrez Pérez, O. Portillo Moreno. Materials Letters. 120(2014) 130-132.

[18] C. S. Patterson, D. Carson, A. Phenix, H. Khanjian, K. Trentelman, J. Mass, C. Hirschmugl, e-Preservation Science (e-PS), (2013)10, 1-9

[19] G. Y. Zhang, D. Peak. Geochimica et Cosmo. Chimica Acta 71 (2007) 2158-2169

[20] S.V. Lalonde, L. T. Dafoe, S. G. Pemberton, M. K. Gingras, K. O. Konhauser, Chemical Geology 271 (2010) 44-51

[21]G. Della Ventura, F. Radica, F. Bellatreccia, C. Freda, M. CestelliGuidi, Phys. Chem. Minerals (2015) 42:735-745

[22]M. Ristic, S. Popovic, S. Music, Materials Letters 58 (2004) 2494–2499

[23] S. A. Sandford, F. Salama, L. J. Allamandola, L. M. Trafton, D. F. Lester, T. F. Ramseyer, Icarus, Volume 91, (1991), 125-144

[24] J. Sárkány, Topics in Catalysis Vol. 18, Nos. 3-4, February 2002

[25] K. Nakamoto, Infrared and Raman Spectra of Inorganic and Coordination Compounds, Sixth Edition (2009).

[26] Rahulkumar, K. Singh, R. Srivastava, M.N. Kamlasanan, J. Nano- Electron. Phys. 3 (2011) No1, P. 514-520

[27] L. Pejov, V. M. Petrusevski, Journal of Molecular Structure 482–483 (1999) 257–262

[28] D. Podsiadla, O. Czupinski, Journal of Molecular Structure 889 (2008) 251–258

[29]J. Regalbuto, Catalyst Preparation: Science and Engineering (2007)

[30] N. Kharasch, Organic Sulfur Compounds, volume 1, 1961

[31]L. Xia, R. L. McCreery, Journal of the Electrochemical Society, 146 (10) 3696-3701 (1999)

[32] J. T. J. Prakash, L. R. Nirmala, International Journal of Computer Applications (0975-8887) Volume 6- No.7, September 2010

Figure captions

Fig. 1. XRD spectra of CdS thin films deposited with different times.

Fig. 2. Optical transmission spectra of CdS thin films deposited with different times.

Fig. 3.Tauc's plot used for determination of optical band gap of CdS thin films.

Fig. 4.FTIR spectrum of Carbonate cadmium salt.

Fig. 5.FTIR spectrum of Carbonate cadmium and calcined powder samples obtained from A and B solutions (see text).

Fig. 6. FTIR spectrum of residual solution obtained from A.

Fig. 7. FTIR spectrum of residual solution obtained from B.

Fig. 8. FTIR of the products obtained from the reaction between ammonia and thiourea (solution C).

Table captions

Table. 1: Lattice parameters recapitulation

Fig. 1
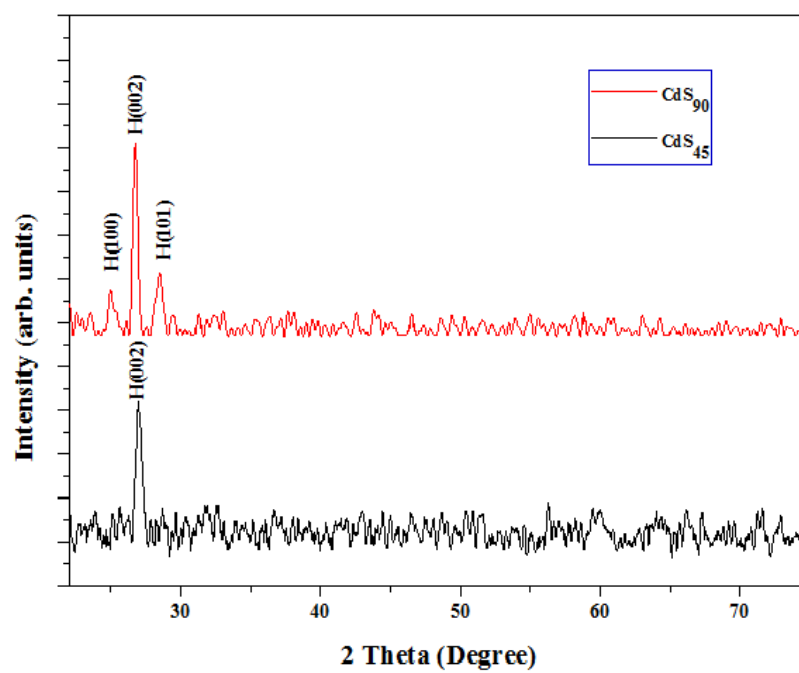
Fig.2
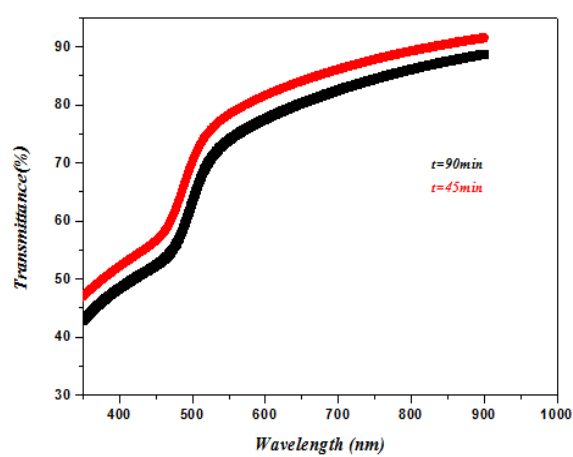
Fig.3

Fig.4

Fig. 5

Fig. 6

17
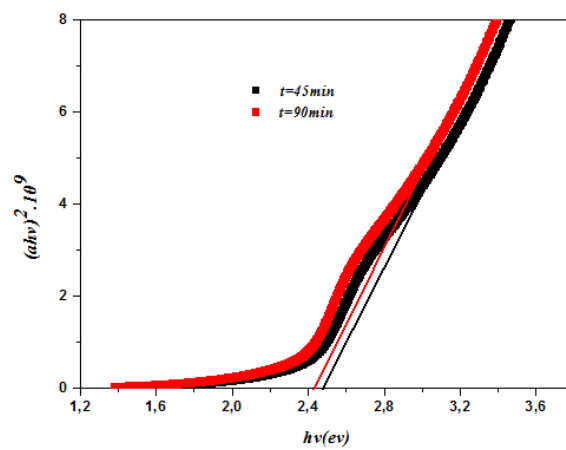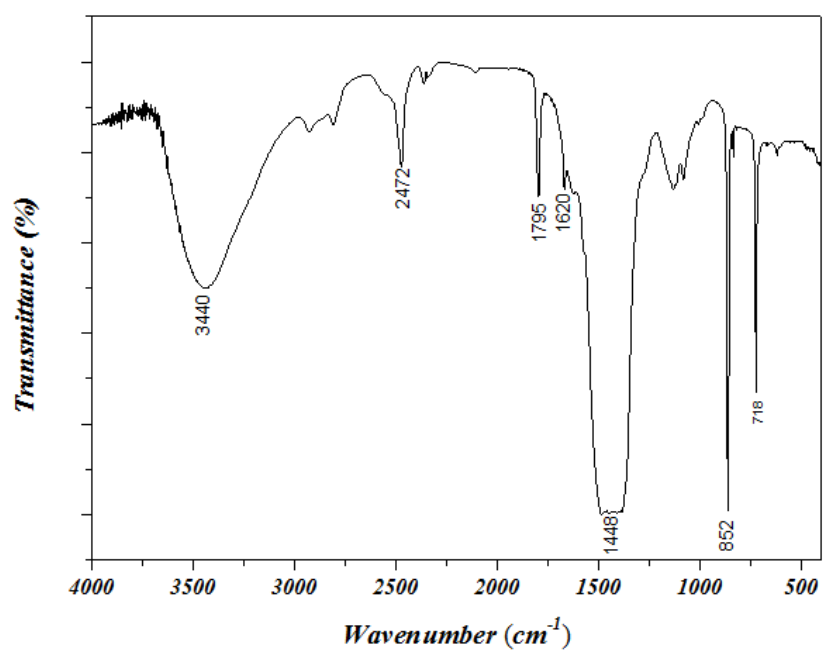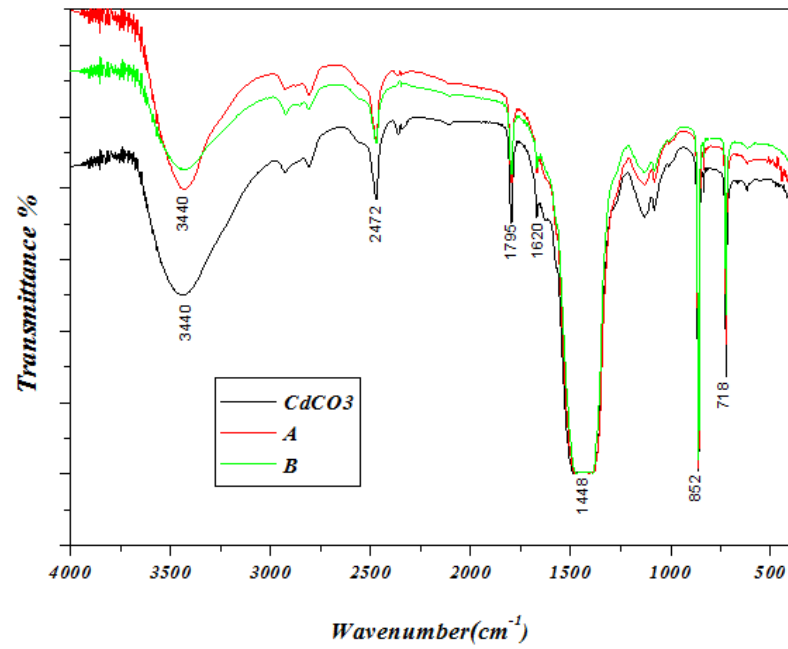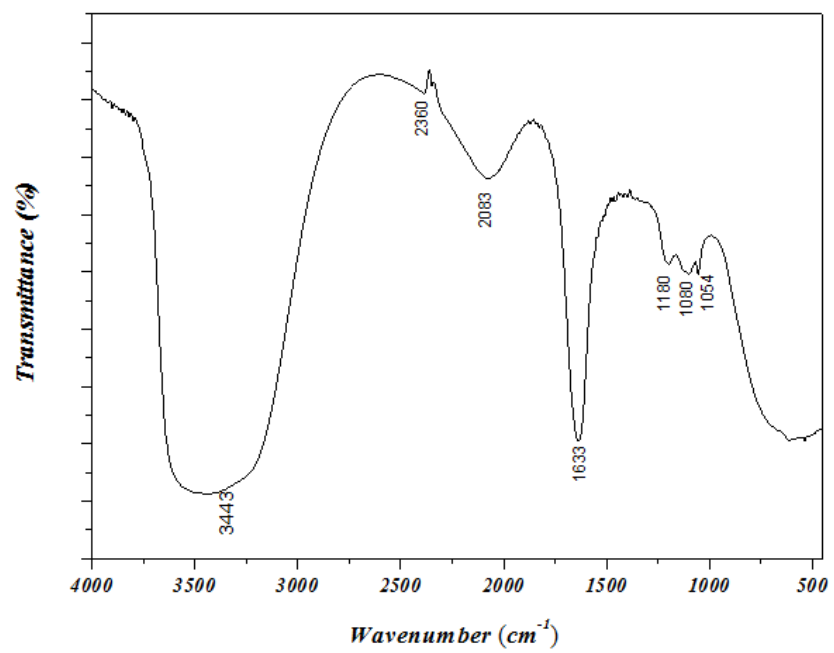
Fig. 7
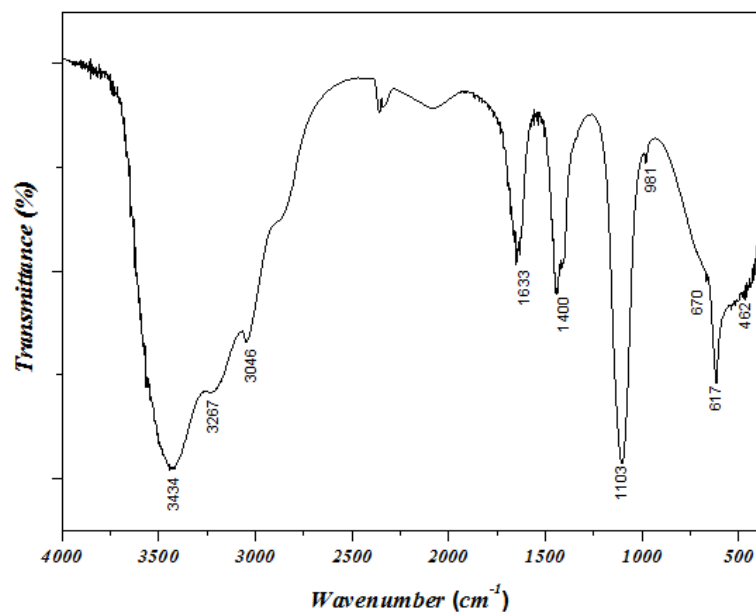
Fig. 8
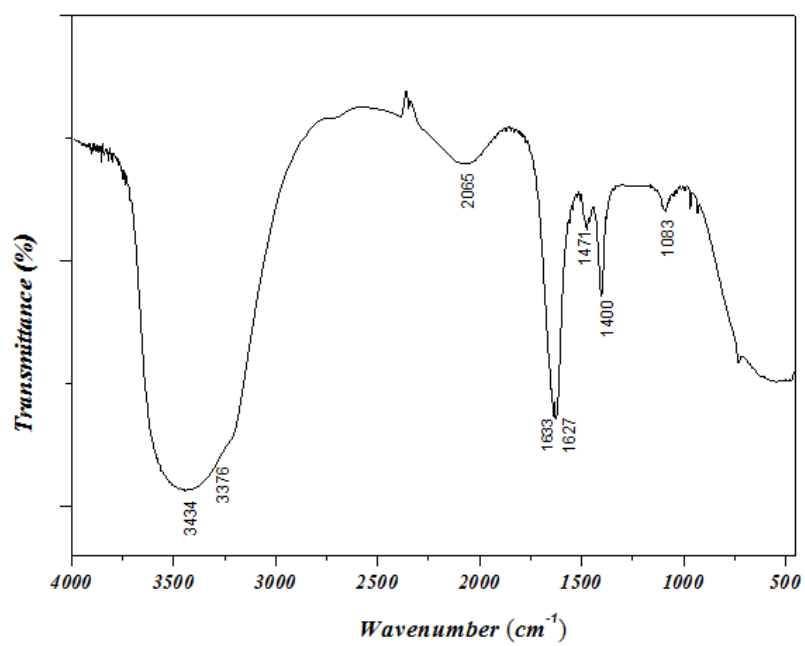
Table 1

Material	Lattice constants (nm)				$d_{(hkl)}$(nm) of plane			Grain size(nm)
	a	$\Delta a= a-a_0$	c	$\Delta c=c-c_0$	(100)	(002)	(101)	
H-CdS JCPDS card No: 77-2306	0.4136	---	0.6713	---	0.3583	0.3357	0.3160	---
CdS$_{45}$	0.4081	-0.0055	0.6624	-0.0089	---	0.3336	---	14.3
CdS$_{90}$	0.4126	-0.0010	0.6672	-0.0041	0.3573	0.3336	0.3140	30.5
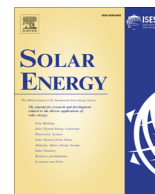
Stable solar-pumped TEM$_{00}$-mode 1064 nm laser emission by a monolithic fused silica twisted light guide

Said Mehellou [a,b,e], Dawei Liang [a,*], Joana Almeida [a], Rochdi Bouadjemine [a,c], Claudia R. Vistas [a], Emmanuel Guillot [d], Ferhat Rehouma [e]

[a] CEFITEC, Departamento de Física, FCT, Universidade Nova de Lisboa, 2829-516 Campus de Caparica, Portugal
[b] University of Ouargla, 30000, Algeria
[c] CDTA BP 17, Street 20 August 1956, Baba Hassan, Algiers 16000, Algeria
[d] PROMES-CNRS, 7 rue du Four Solaire, 66120 Font Romeu, Odeillo, France
[e] University of Echahid Hamma Lakhdar Eloued, 39000, Algeria

ABSTRACT

To improve TEM$_{00}$-mode solar-pumped laser output power stability, a monolithic fused silica twisted light guide was firstly produced and then combined with both a 2D-CPC (Compound Parabolic Concentrator) and a 2 V-shaped cavity to achieve uniform pumping along a 3 mm diameter, 50 mm length, 1.0 at.% Nd^{3+}:YAG rod through an heliostat-parabolic mirror system. Based on both refractive and total internal reflection principles, the light guide provided an effective solution to both guiding and redistributing highly concentrated solar radiations. A near-Gaussian profile focal spot was transformed into a uniform rectangular-shaped light column, facilitating further pump light coupling into the long and thin laser rod within the 2 V-shaped pump cavity. Optimum pumping parameters and solar laser output powers were found through both ZEMAX© non-sequential ray-tracing and LASCAD© laser cavity analysis codes. The light guide reduced considerably the thermal lensing effects of the solar laser. 2.7 W continuous-wave TEM$_{00}$-mode ($M_2 \leq 1.05$) 1064 nm solar laser emission with 2.3 W/m^2 collection efficiency and, more importantly, with 1.7% stability was finally achieved, being significantly more stable than the previous TEM$_{00}$-mode solar lasers.

© 2017 Elsevier Ltd. All rights reserved.

1. Introduction

Shortly after the invention of laser, the idea of directly converting free broad-band solar radiation into coherent narrow-band laser radiation appeared (Young, 1966). If lasers are needed in remote locations where sunlight is abundant and the other forms of energy are scarce, a solar laser would seem to be a natural choice. Broadband, temporally constant, sunlight can be converted into laser light, which can be a source of narrowband, collimated, rapidly pulsed, radiation with the possibility of obtaining extremely high brightness and intensity. Compared to other electrically powered lasers, solar lasers are much more simple and reliable due to the complete elimination of artificial pump sources and their associated electrical power generation and power conditioning equipment. Thus, direct excitation of large lasers by sunlight offers the prospect of a drastic reduction in the cost of coherent optical radiation for high average power applications, leading to numerous

environmental and economic benefits. The solar laser technology has therefore great potentials for various space applications, such as Earth, ocean, and atmospheric sensing, laser power beaming, free space communications (Guan et al., 2017). Powered by abundant solar energy, solar laser are also suitable for many terrestrial applications such as high temperature materials processing, magnesium–hydrogen energy cycle (Yabe et al., 2006). Many applications listed above can only be feasible with lasers of high-beam-quality, most preferably, in TEM$_{00}$-mode since it produces the smallest beam divergence, the highest power density and, hence, the highest brightness (Overton, 2013).

The growing importance of solar-pumped lasers has attracted considerable attention. Many studies have already been carried out to improve solar laser efficiencies (Young, 1966; Arashi et al., 1984; Weksler and Shwartz, 1988; Lando et al., 2003; Yabe et al., 2007; Ohkubo et al., 2009; Liang and Almeida (2011), Liang et al., 2013, 2016a,b, 2017; Payziyev et al., 2011; Payziyev and Makhmudov, 2016; Dinh et al., 2012; Almeida et al., 2012, 2013, 2015; Xu et al., 2014; Guan et al., 2017). Since the sunlight does not provide enough flux to initiate laser emission, additional

* Corresponding author.
E-mail address: dl@fct.unl.pt (D. Liang).

focusing optics are needed to both collect and concentrate the solar radiation to excite laser medium. Parabolic mirrors have long been explored to achieve tight focusing of incoming solar radiation (Young, 1966; Arashi et al., 1984; Weksler and Shwartz, 1988; Lando et al., 2003; Payziyev et al., 2011; Payziyev and Makhmudov, 2016; Almeida et al., 2012, 2013, 2015; Liang et al., 2013, 2015, 2016a,b, 2017). To maximize the solar radiation that impinges on the laser crystal, the 3D-CPC, the 2D-CPC and the V-shaped pump cavity are usually used as secondary and tertiary concentrators in solar lasers because they can either compress or wrap the concentrated solar radiations from their input aperture to the laser rod and give an additional concentration. Nevertheless, significant progresses in solar laser efficiency have been made in the last decade after the adoption of Fresnel lenses as primary solar concentrators (Yabe et al., 2007; Ohkubo et al., 2009; Liang and Almeida, 2011; Dinh et al., 2012; Xu et al., 2014; Guan et al., 2017). 30.0 W/m^2 collection efficiency, defined by the ratio between laser output power and primary concentrator area (Lando et al., 1995), was attained by pumping a 6 mm diameter, 100 mm 4 m^2 area large Fresnel lens (Dinh et al., 2012). However, very large $M_x^2 = M_y^2 = 137$ factors have been associated with this approach, resulting in very poor beam quality, only 0.0064 W value of the beam brightness figure of merit – defined as the ratio between laser power and the product of M_x^2 and M_y^2. Most recently, 31.5 W/m^2 multimode, 7.9 W/m^2 TEM$_{00}$-mode solar laser collection efficiencies were achieved (Liang et al., 2017) by using the heliostat-parabolic mirror system in the PROMES – CNRS (Procedes, Materiaux et Energie Solaire – Centre National de la Recherche Scientifique) in France, surpassing the previous record (Dinh et al., 2012) by the 4 m^2 Fresnel lens installed on a solar tracker. Even though Fresnel lenses have been preferred due to their simplicity, easy availability, and low cost, there still exist practical inconveniences, regarding to their use in solar lasers. The laser head pumped by the Fresnel lens solar concentration system moved together with the whole solar tracking structure (Yabe et al., 2007; Liang and Almeida, 2013), an optical fiber thus became necessary for the transportation of solar laser radiation to a fixed target position. This in turn affected negatively the efficiency of the whole solar laser system due to optical fiber transmission loss. The advantage of having an indoor laser head at the focus of a heliostat primary concentrator system has become much more obvious for applications such as material processing where a vacuum chamber should usually be installed nearby. Moreover, Fresnel lenses also cause a significant dispersion of solar radiation spectrum along its focal zone, hindering further efficient solar pump light concentration into the thin laser rod by both secondary and tertiary concentrators.
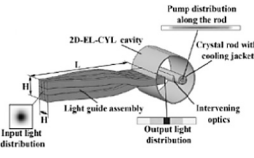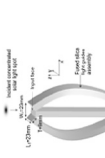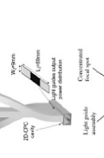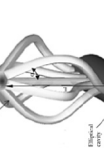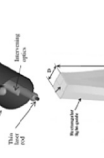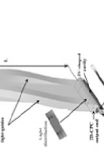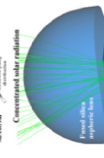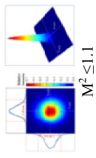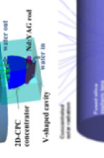
Because of its smooth intensity profile, low divergence and ability to be focused to a diffraction-limited spot, it is highly desirable to operate a solar-pumped laser in the lowest mode possible: TEM$_{00}$-mode. To achieve this, several pumping schemes have been built. TEM$_{00}$-mode solar lasers can have either side-pumping or end-pumping configurations (Arashi et al., 1984; Brauch et al., 1991). Although the most efficient laser systems have end-pumping approaches, the thermal lensing effects caused by non-uniform distribution of pump light in these pumping configurations affect negatively their efficiencies. Side-pumping configuration can present higher brightness as it allows a uniform absorption distribution along the rod axis and spreads the absorbed power within the laser medium, reducing the associated thermal loading problems. Besides, the free access to both rod ends permits the optimization of more laser resonator parameters, improving largely the laser beam quality and enabling the efficient extraction of solar laser in fundamental mode. Minimizing a laser rod volume reduces cost, and reducing the diameter makes the rod more resistant to thermal stress. Also, as the rod acts as an aperture, by pumping a small diameter laser rod, high-order res-

onator modes can be suppressed by large diffraction losses, and beam quality improves (Lando et al., 2003). For these reasons, we have been insisting on improving the TEM$_{00}$-mode solar laser power and beam profile by side-pumping small diameter rod (Liang and Almeida, 2013; Liang et al., 2015).

In order to clearly understand all the previous TEM$_{00}$-mode solar laser performances, research details are summarized in Table 1. Some literatures (Geraldes and Liang, 2008; Pereira and Liang, 2009; Liang and Pereira, 2009; Almeida and Liang, 2012) are merely numerical simulations for the improvement of fundamental mode solar laser output performance, while others already include experimental results (Liang and Almeida, 2013; Vistas et al., 2015; Almeida et al., 2015; Liang et al., 2015, 2016, 2017). Direct solar laser pumping configuration was firstly tested (Liang and Almeida, 2013; Vistas et al., 2015; Liang et al., 2015, 2017), where the concentrated solar radiation at the focus was efficiently coupled within the laser rod, through either a fused silica aspheric lens, or a semi-cylindrical lens or an ellipsoidal-shaped lens, allowing the efficient generation of fundamental mode laser power, resulting also, unfortunately, in stronger thermal lensing and a non-uniform distribution along the laser rod. Fused silica light guide with large rectangular cross section can be used in indirect pumping configuration, uniform pump light distribution was attained, but efficient light coupling from the light guide to the laser rod was affected (Almeida et al., 2015; Liang et al., 2015). 5.5 W continuous-wave TEM$_{00}$-mode 1064 nm laser power was registered (Almeida et al., 2015), however, serious laser beam stability problem was found with further increase in pump power, laser output power approached to a peak value and then dropped abruptly, meaning that the laser resonator operation had moved out of stability zone as the thermal lensing effect got stronger and finally the laser stopped oscillating. A more stable continuous-wave TEM$_{00}$-mode 1064 nm solar laser power of 4.4 W was also measured (Liang et al., 2015), but at the cost of relatively low collection efficiency of 1.91 W/m^2 (Liang et al., 2015). Most recently, 9.3 W continuous-wave TEM$_{00}$-mode 1064 nm solar laser power was measured, corresponding to 7.9 W/m^2 TEM$_{00}$-mode solar laser collection efficiency. However, most efficient end-side-pumping of a 4 mm diameter 35 mm length Nd^{3+}:YAG rod through a large aspheric lens has introduced a non-uniform absorbed pump light distribution, resulting in the TEM$_{00}$ – mode beam with only $M^2 \leq 1.2$. The beam stability was sensible to the variation of the thermal focal length of the rod. Also most recently, a non-symmetric fused silica twisted light-guide was used to achieve nearly uniform pumping along a 3 mm diameter and 50 mm length Nd:YAG single-crystal rod (Bouadjemine et al., 2017). 2.3 W continuous-wave fundamental mode 1064 nm solar laser power was measured, corresponding to 1.96 W/m^2 TEM$_{00}$ mode solar laser collection efficiency and 2.2 W laser beam brightness figure of merit. The non-symmetric twisted light guide in Table 1 provided a nearly uniform pump profile along the rod and further enhancements in both light guide architecture and solar laser collection efficiency are possible.
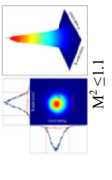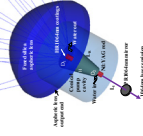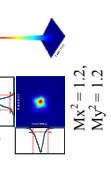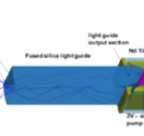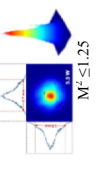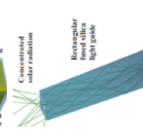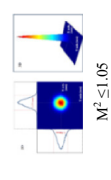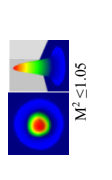
To improvement of the fundamental mode solar laser performance, the monolithic fused silica twisted light guide will be introduce in this paper. Based on the refractive and total internal reflection principles, the light guide, by serving also as a beam homogenizer, transformed the near Gaussian profile of the concentrated light spot at its large square input face into a uniform pump light distribution at its rectangular output end, facilitating further efficient light coupling into a long and thin laser rod. Fused silica was an ideal optical material for transmitting highly concentrated solar energy, it had a low coefficient of thermal expansion, and was resistant to scratching and thermal shock and it had a high optical purity 99.999%. To provide the desired form of the twisted light guide, two techniques were possible, shaping the light guide in

Table 1
TEM$_{00}$-mode solar laser performances.

Sources	Laser power (W)		Collection area (m²)	Rod diameter (mm)	Rod length (mm)	Pumping cavity	Active medium	Beam brightness figure of merit (W)	Slope efficiency	Light guide design	Collection efficiency (w/m²)	Beam profile	Beam stability
	Theoretical	Practical											
Geraldes and Liang (2008)	Parabolic mirror 2 Parabolic mirror 1.3	Nothing	1.82	2	40	2D-EL-CYL Side pumping 2D-DCPC Side pumping	Nd:YAG	Nothing	Nothing		1.10 0.71	Nothing	Nothing
Pereira and Liang (2009)	Parabolic mirror 11 Parabolic mirror 9	Nothing	6.85	3	80 110	2D-CPC Side pumping	1.1 at.% Nd:YAG	Nothing	Nothing		1.6 1.31	Nothing	Nothing
Liang and Pereira (2009)	Parabolic mirror 4.8 D = 14 mm aperture assembly	Nothing	1.82	2.5	70	Elliptical cavity with the intervening optics. Side pumping	1.1 at.% Nd:YAG	Nothing	Nothing		2.64	Nothing	Nothing
Almeida and Liang (2012)	Parabolic mirror 12.3 Parabolic mirror 8.8	Nothing	1.78	1.75 2.5	40	2 V-shaped Side pumping	Nd:YAG	0.61 0.63	Nothing		6.91 4.94	Nothing	Nothing
Liang and Almeida (2013)	Nothing	Fresnel lens 2.3	0.78	3	30	V-shaped Side pumping	1.0 at.% Nd:YAG	1.9	0.7%		2.93	$M^2 \leq 1.1$	Good stability
Vistas et al. (2015)	Nothing	Parabolic mirror 4	1.1	4	34	2 V-shaped Side pumping	1.0 at.% grooved Nd:YAG	3	Nothing		3.6	$M_x^2 \approx 1.2$, $M_y^2 \approx 1.1$	Poor stability

Table 1 (continued)

Sources	Laser power (W)		Collection area (m²)	Rod diameter (mm)	Rod length (mm)	Pumping cavity	Active medium	Beam brightness figure of merit (W)	Slope efficiency	Light guide design	Collection efficiency (w/m²)	Beam profile	Beam stability
	Theoretical	Practical											
Liang et al. (2016)	Nothing	Parabolic mirror 4.5	1.13	4	34	2 V-shaped Side pumping	1.0 at.% grooved Nd:YAG	Nothing	2.36%		4	$M^2 \leq 1.1$	Good stability
Liang et al. (2017)	Nothing	Parabolic mirror 7.9	1.18	4	35	Conical. shaped End-side-pumping	1.0 at.% Nd:YAG	6.45	Nothing		7.9	$Mx^2 = 1.2$, $My^2 = 1.2$	Poor stability
Almeida et al. (2015)	Nothing	Parabolic mirror 5.5	1.92	4	30	2 V-shaped Side pumping	1.1 at.% Nd:YAG	Nothing	1.27 %		2.84	$M^2 \leq 1.25$	Poor stability
Liang et al. (2015)	Nothing	Parabolic mirror 4.4	2.3	3	30	V-shaped Side pumping	1.0 at.% Nd:YAG	Nothing	0.81%		1.91	$M^2 \leq 1.05$	Good stability
Bouadjemine et al. (2017)	Nothing	Parabolic mirror 2.3	1.18	3	50	2D-CPC 2 V-shaped Side pumping	1.0 at.% Nd:YAG	2.2 W	Nothing		1.90	$M^2 \leq 1.05$	Very good stability

either high-temperature environment or directly sculpturing from a fused silica slab at room temperature. For the first technique, high-temperature environment (hydrogen flame, more than 1500 °C) and pure graphite moulds were needed for controlling the bending curvatures of the light guide for lamp-pumped lasers (Bernardes and Liang, 2006).

High temperature light guide shaping technique would be effective if each single curved light guide were produced separately, but the problem of water leakage would appear if several curved light guides were joined together. For cold production, direct glass sculpturing technique was chosen because it allowed the fabrication of the monolithic light guide at room temperature and hence avoiding water leakage problem. To the best of our knowledge, this is the first report of the successful sculpturing of a monolithic fused silica twisted light guide for solar laser research.

The radiation transmission and homogenization capacity of the monolithic light guide was combined with the light focusing properties of both the 2D-CPC concentrator and the 2 V-shaped cavity to provide efficient side-pumping to the 3mm diameter, 50 mm length Nd^{3+}:YAG rod. 2.7 W continuous-wave 1064 nm TEM_{00}-mode solar laser power with 2.3 W/m^2 collection efficiency was measured. More importantly, an excellent TEM_{00}-mode ($M^2 \leq 1.05$) beam profile with the beam stability of less than 1.7% were achieved simultaneously. The TEM_{00}-mode solar laser system composed of the heliostat-parabolic mirror system, the monolithic light guide, the solar laser head with both 2D-CPC concentrator and the 2 V-shaped pump cavity will be explained in Section 2. Numerical optimization of the solar laser design parameters and solar laser output performances by both ZEMAX© and LAS-CAD© numerical analysis codes will be explained in Section 3. The final test of the TEM_{00}-mode solar laser output performance, carried out in the PROMES-CNRS (Procedes, Materiaux et Energie Solaire – Centre National de la Recherche Scientifique) in France will be given in Section 4, followed by both discussions and conclusions.

2. Solar-pumped TEM_{00} mode Nd^{3+}:YAG laser by the heliostat-parabolic mirror system

2.1. Solar energy collection and concentration by the PROMES-CNRS heliostat-parabolic system

A large plane mirror (3.0 m × 3.0 m) with 36 small flat segments (0.5 m × 0.5 m each), mounted on a two-axis heliostat,

redirected incoming solar radiation towards the horizontal primary parabolic mirror. The reflected parallel solar rays illuminated everything in their way, including the shutter, the 2 m diameter, 850 mm focal length parabolic mirror, the doors and even the external walls of the laboratory. We actually used only the 1.4 m diameter central area of this mirror, as illustrated in Fig. 1. After discounting the shading effects of a shutter, an X-Y-Z axes positioning system, a multi-angle vise, a 0.3 m diameter central opening of the parabolic mirror and an asymmetrical solar laser cavity, as shown in Figs. 1 and 2, 1.18 m^2 effective collection area was calculated. All the mirrors were back-surface coated with silver, so only 59% of incoming solar radiation was effectively focused to the focal zone. There were several reasons contributing to such a low total reflectivity: (1) High iron contents glass substrate materials (10 mm thick for the parabolic mirror and 5 mm for the plane mirror) were used to build the mirrors. Considerable absorption loss can therefore occur, (2) there were no anti-reflection coatings on the front surfaces of these mirrors. For an average solar irradiance of 1000 W/m^2 in Odeillo, July 2016, more than 600 W solar power was focused into a near-Gaussian pump light spot with 11 mm full width at half maximum (FWHM).

2.2. Nd:YAG solar laser head with the monolithic fused silica twisted light guide

The solar laser head, composed by the fused-silica twisted light guide, the solar laser head with the secondary 2D-CPC concentrator, the tertiary 2 V-shaped pump cavity and the long and thin rod, was mechanically mounted to the laser resonant cavity, which was fixed on an X-Y-Z axis positioning system by using the multi-angle vise, as shown in Figs. 1 and 2. An accurate optical alignment in the focal zone was hence ensured. The thin Nd:YAG rod was actively cooled by water at 6 L/min flow rate.

2.3. Fused silica twisted light guide with tracking error compensation capacity

The concentrated solar radiation was firstly collected by the twisted fused silica light guide with 16 mm × 16 mm input face. It was then transmitted along 110 mm length, observing both refraction and total internal reflection principles, to its rectangular output end with 8 mm × 32 mm, as illustrated in Figs. 2 and 3. The twisted light guide provided a good solution for both transmitting and redistributing efficiently the concentrated solar radiation at
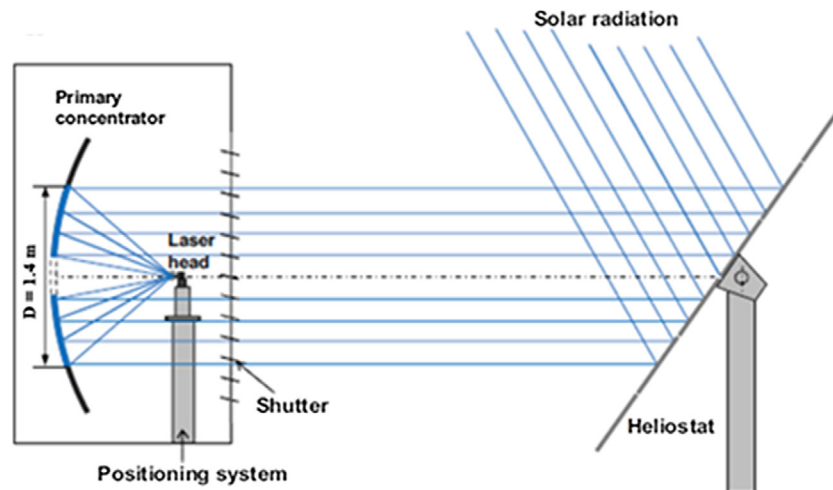
Fig. 1. Solar laser pumping scheme by the PROMES-CNRS solar energy collection and concentration system.

the focus. The near-Gaussian profile of the concentrated light spot incident on the input face of the light guide assembly was therefore transformed into a rectangular pump light column at the assembly output end. This ensured a homogenous pump light distribution along the output end of the guide. To produce the monolithic fused silica twisted light guide, composed of a lower straight part with rectangular cross section and two upper twisted parts with square cross-sections, as observed in Figs. 2 and 3. A fused silica slab of 99.999% optical purity, 35 mm × 35 mm square cross-section and 115 mm length, was cut, ground and polished to its final dimensions. The production of the twisted fused silica light-guide was a both time consuming and delicate job. The process was subdivided into three steps. The fused silica slab was firstly cut and sculpted by diamond tools and gradually ground into the shape of the twisted light-guide as optimized by both ZEMAX©

and LASCAD© numerical analysis codes. Secondly, the twisted light-guide was further dimensioned by coarse grinding paper. Finally, optically transparent input and output faces and side surfaces of the fused silica light guide, as shown in Fig. 2, was achieved by the final polishing

Heliostat orientation errors moved the center of the absorption distribution within the laser rod, resulting in less laser output power and a non-uniform beam profile, degrading the performance and quality of the laser output. The light guide with large input face was therefore essential to overcoming this problem, serving as a beam homogenizer by transforming the near-Gaussian profile of the concentrated light spot at its input face into a uniform pump light distribution at its output end, as shown in Fig. 3. By using a light guide with 16 mm × 16 mm square input face and 8 mm × 32 mm rectangular output end, the long and thin rod could
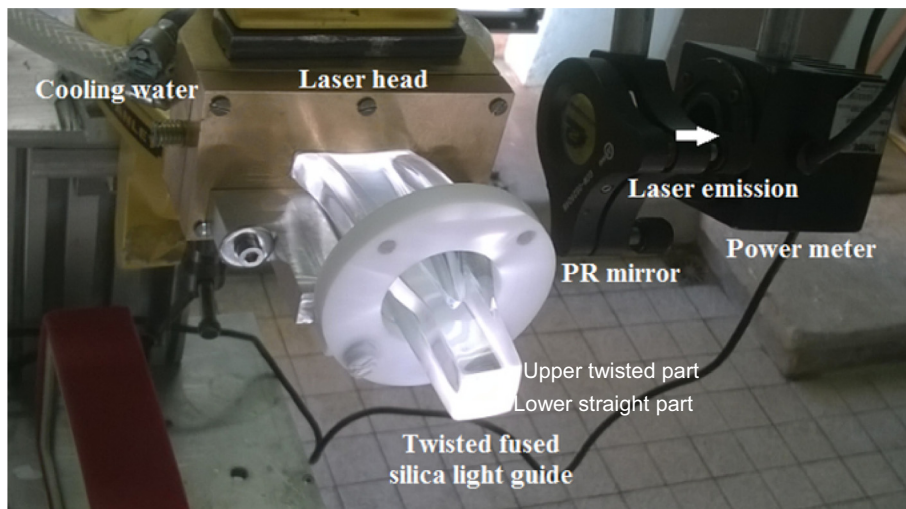
Fig. 2. Solar-pumped Nd:YAG laser head composed of the monolithic light guide, the solar laser head and the laser resonant cavity.
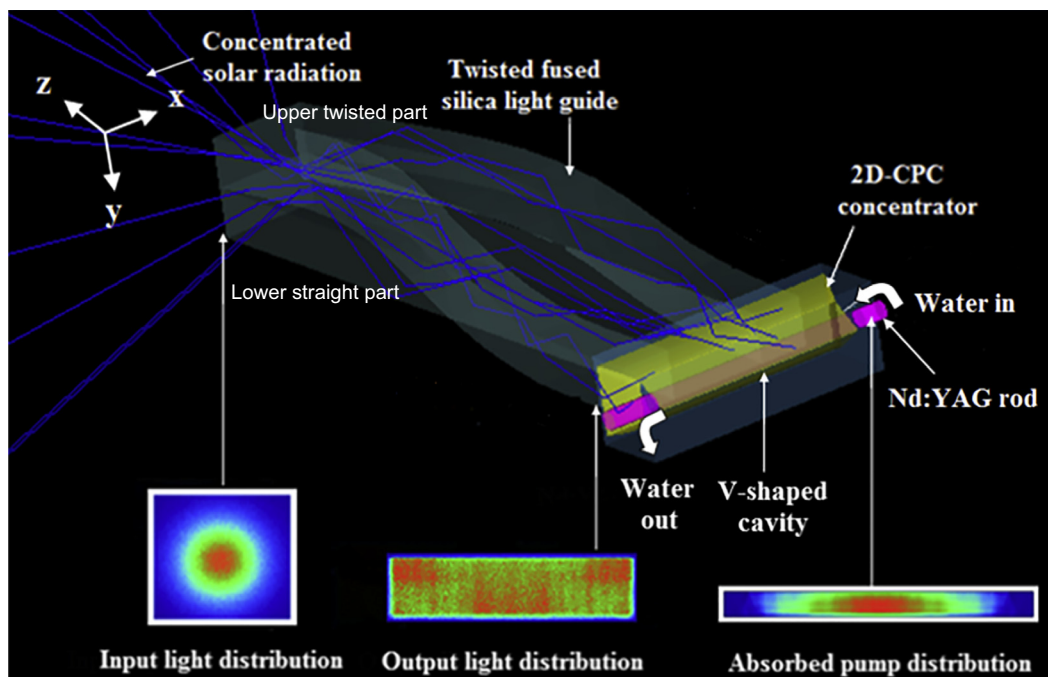
Fig. 3. 3D design of the solar laser head, composed of the monolithic twisted light guide, the 2D-CPC concentrator and 2 V-shaped pump cavity and the 3 mm diameter, 50 mm length Nd:YAG rod.

be pumped efficiently. The rod diameter was also a key parameter for achieving high transfer efficiency and reducing the heliostat orientation error dependent losses. For the focal distance of 0.85 m, a typical 0.2° orientation error corresponded to approximately 2.55 mm displacement in both X and Y axes. Fig. 4 gave pump light distribution at different sections along the light guide, the pump distribution along the laser rod and the output laser beam profile. Zero-orientation error corresponded to the optimum alignment between the heliostat and the primary parabolic concentrator.

Heliostat orientation error displaced the circular light spot away from the central point at the input face of the light guide. Zero orientation error occurred when the optimum alignment between the heliostat and the primary parabolic concentrator was achieved. Pump light in this case was efficiently transmitted and uniformly redistributed along the rod through the twisted light guide, resulting in 3.14 W numerically calculated TEM$_{00}$-mode solar laser

output power and an excellent Gaussian fundamental mode beam profile (detailed descriptions in Section 3). If the focal spot moved in the X-axis direction parallel to the laser rod axis, then the strong pump absorption distribution was shifted correspondingly along the rod in the axial direction, causing only a minor variation in both output laser power and beam profile. However, if the focal spot moved in the Y-axis direction perpendicular to the rod axis (the transversal shift), then the strong absorption distribution within the rod was shifted laterally in the direction perpendicular to the rod axis. For the displacement of the focal spot along either X-axis or Y-axis, more pump light coupling could be achieved through the lower straight part of the light guide, as shown in Fig. 4b and c, the output laser power was increased respectively to 3.19 W and 3.22 W in the LASCAD© analysis in Section 3. For the combined tracking errors of 2.55 mm in both X and Y axes, the focal spot was shifted obliquely from the center of the input face of the lower straight part of the light guide, then the homogeny of
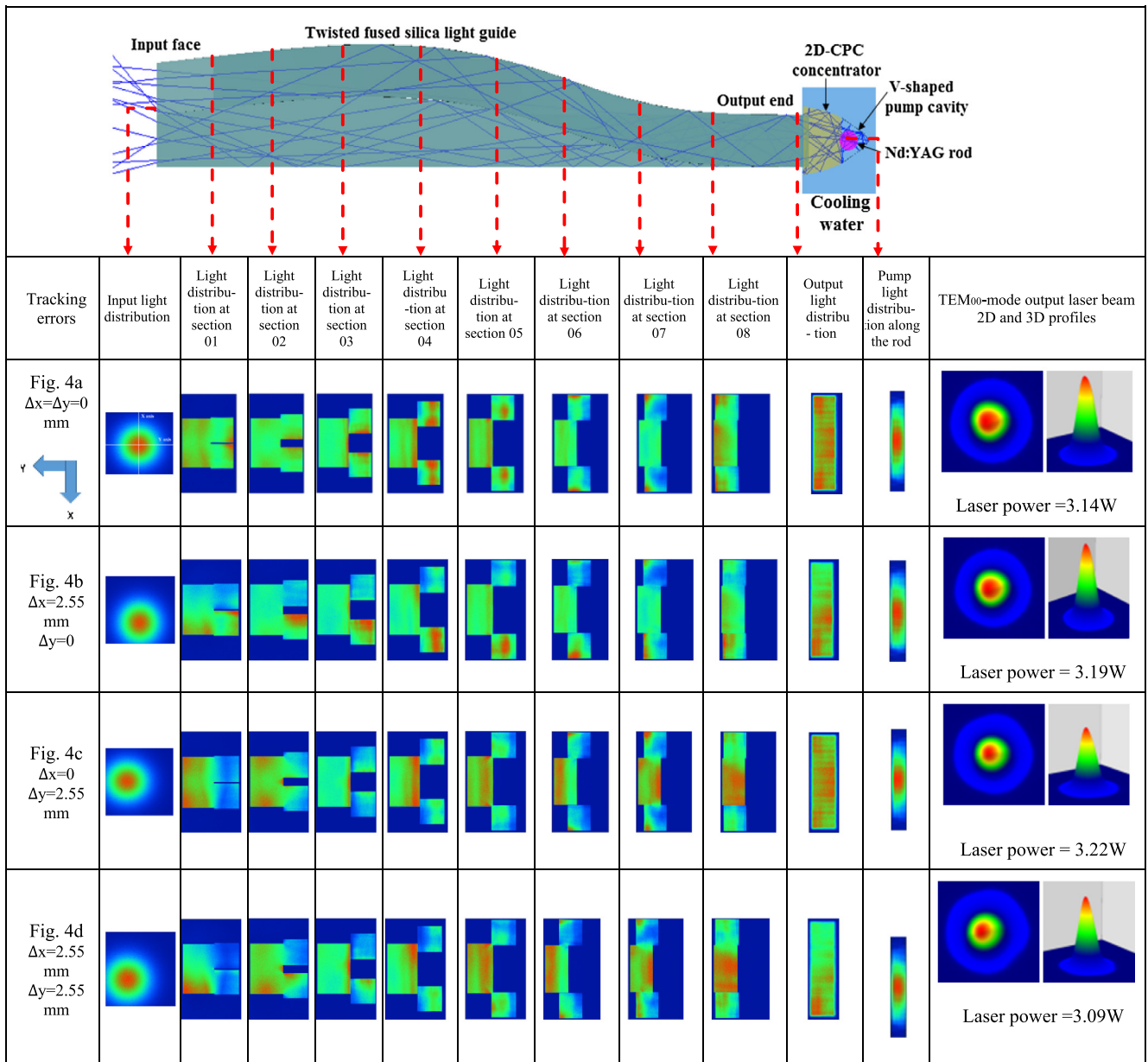
Fig. 4. Pump light distribution at different sections along the light guide, for the cases of (a) zero orientation error, (b) X-axis with 2.55 mm displacement, (c) Y-axis with 2.55 mm displacement and (d) combined X-Y axes with 2.55 mm displacement on both axes.

the pump light distribution within the rod was affected, causing a slight reduction in laser output power to 3.09 W and a little modification of the fundamental mode beam profile as shown in Fig. 4d and Section 3.

2.4. 2D-CPC secondary concentrator and the 2V-shaped pump cavity

The 2D-CPC concentrator had 11 mm × 36 mm rectangular large input aperture, 7 mm × 36 mm small output aperture and was 10 mm in height, as shown in Fig. 5. The 2D-CPC was used to convert the radiation from a large-area homogenous source emitting uniformly into a small angle, to a small-area homogenous output emitting uniformly into a large angle, thus the source étendue was preserved (Liang et al., 2013). This preservation implied that irradiance was higher at the output surface than at the entrance aperture, leading to a net concentration of the pump radiation.

The two-dimensional 2 V-shaped cavity had an entrance aperture of 7 mm × 36 mm and 5 mm depth. The 2 V-shaped cavity was composed of V-shaped reflectors, V_1 with 47.5° half-angle and V_2 with 14° half-angle relatively to V_1. This combination was much more effective in coupling highly concentrated light rays with different incidence angles into the laser rod as compared to using only a single V-shaped reflector. The inner walls of both V_1 and V_2 were bonded with a protected silver-coated aluminum foil with 94% reflectivity. Water material also ensured an efficient light coupling, while partially preventing both UV solarization and IR heating to the laser rod. By combining the light concentration capacity of both the 2D-CPC concentrator and the 2 V-shaped pump cavity with the light homogenization capacity of the twisted light guide, uniform pump power deposition within the laser rod was achieved. All the above optimized design parameters of the whole laser system were found by both non-sequential ray-tracing ZEMAX© and laser cavity design and analysis LASCAD© codes.

3. Numerical optimization for extracting the maximum TEM$_{00}$-mode laser power

3.1. Optical design parameters of the solar laser system by ZEMAX© analysis

The aforementioned optical design parameters in Section 2 were optimized through ZEMAX© non-sequential ray tracing software to obtain the most favorable absorbed pump flux distribution within the Nd^{3+}:YAG rod. The standard solar spectrum for one-and-a-half air mass (AM1.5) (ASTM Standard G173-03, 2012) was used as the reference data for consulting the spectral irradiance (W/m^2/nm) at each wavelength. The terrestrial solar irradiance of 1000 W/m^2 in Odeillo, France, was considered in ZEMAX© software. The effective pump power of the light source took into
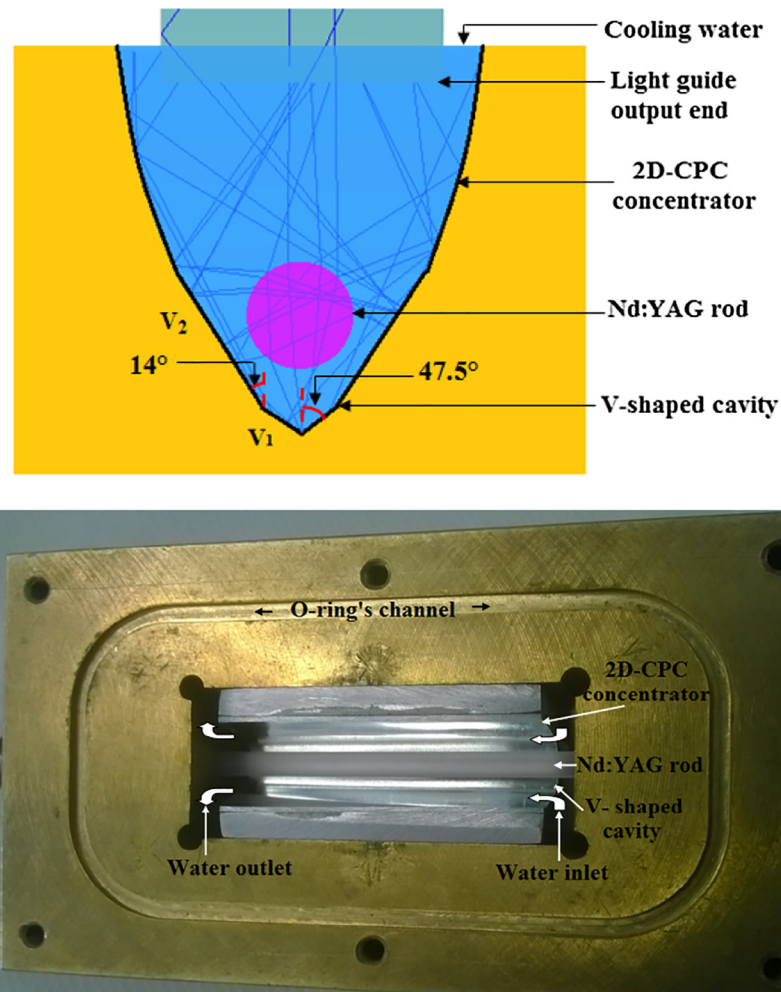
Fig. 5. (a) 2D-CPC concentrator and 2 V-shaped pump cavity, within which the 3 mm diameter, 50 mm length rod was efficiently pumped. (b) Photo of the pump cavity with the Nd^{3+}:YAG laser rod.

account the 16% overlap between the absorption spectrum of the Nd³⁺:YAG medium and the solar spectrum (Zhao et al., 2007). The half-angle of 0.27° subtended by the Sun was also considered in the analysis. The absorption spectrum of fused silica and water materials were included in ZEMAX© numerical data to account for absorption losses. For 1.0% Nd³⁺:YAG laser medium, 22 peak absorption wave lengths were defined in ZEMAX© numerical data. All the peak wavelengths and their respective absorption coefficients were added to the glass catalogue for Nd³⁺:YAG material in ZEMAX© software. Solar irradiance values for the 22 absorption peaks could be consulted from the standard solar spectra for AM1.5 and saved as source wavelength data. In raytracing, the laser rod was divided into a total of 18,000 zones. The path length in each zone was found. With this value and the effective absorption coefficient of 1.0% Nd³⁺:YAG material, the absorbed power within the laser medium was calculated by summing up the absorbed pump radiation of all zones. The 1.0 at.% Nd:YAG rod (inset of Fig. 3), was supplied by Chengdu Dong-Jun Laser Co., Ltd. Both end faces of the rod are antireflection (AR) coated for the laser emission wavelength (R < 0.2% @ 1064 nm).

3.2. Numerical analysis of TEM$_{00}$ – Mode solar laser operation by LASCAD© software

The absorbed pump flux data from the ZEMAX© analysis in Section 3.1 was then processed by LASCAD© software to study the laser beam parameters of Nd³⁺:YAG rod. The stimulated emission cross-section of 2.8×10^{-19} cm^{-1}, the fluorescence life time of 230 µs (Koechner, 1999) and a typical absorption and scattering loss $\alpha = 0.003$ cm^{-1} for the 1.0 at.% Nd³⁺:YAG medium were adopted. An averaged solar pump wavelength of 660 nm was also considered (Weksler and Shwartz, 1988). In LASCAD© analysis, the optical resonator was comprised of two opposing parallel mirrors at right angles to the axis of the laser medium, as shown in Fig. 5. The end mirror was high reflection coated (HR, 99.98%). The output coupler was partial reflection coated (PR) with the reflectivity variable between 85% and 99%, according to different laser rod diameter. L_1 and L_2 represent the separation length of the HR and PR mirrors to their nearest end face of the laser rod, respectively. The sum of absorption, scattering, and diffraction losses for laser emission wavelength within the active medium constituted the most important part of round-trip resonant cavity losses. Imperfect HR and AR coating losses of both laser medium and resonator cavity mirrors were also an important portion of the round-trip losses. For the laser rod of length $L_R = 50$ mm (Fig. 3). The amount of absorption and scattering losses was $2\alpha L_R = 3.0\%$. Assuming 0.4% of imperfect HR and AR coating loss, the round-trip losses increased to 3.4 %. The diffraction losses depended on rod diameter, resonator length and radius of curvature (ROC) of the resonator mirrors. Conventionally, lasers were designed to operate at the middle of thermally stable zones, where

the fundamental mode size was insensitive to thermal perturbation. The adoption of the asymmetric resonator configuration with concave end mirrors of large radius of curvature (ROC) has shown to provide a large spatial overlap between the fundamental mode and pump mode volume (Liang et al., 2015; Vistas et al., 2015). L_1 was a key parameter for achieving the optimum mode overlap. If L_1 increased, the fundamental mode size grown up, especially for high input power level. Thus, if we aimed to obtain efficient extraction of TEM$_{00}$-mode laser, the laser should operate close to the edge of the optically stable region, where the fundamental mode size was more sensitive to thermal focus fluctuations. With further increase in pump power, the fundamental mode size would grow up automatically to a value suitable for TEM$_{00}$-mode operation and very good beam quality was expected. An asymmetric optical resonator was an excellent configuration for achieving large spatial overlap between the fundamental mode volume and pump volume, improving thus the laser beam quality (Vistas et al., 2015). For efficient extraction of TEM$_{00}$-mode solar laser power from the absorbed solar pump power within the rod, large ROC = -5 m end mirrors were adopted. L_2 was fixed at 60 mm while L_1 varied between 500 mm and 515 mm Fig. 6. Nd³⁺:YAG rods with several diameter were studied to find the optimum TEM$_{00}$-mode laser beam parameters. The laser rod diameter played a crucial role on the beam quality factors and, consequently, on the extraction of TEM$_{00}$-mode solar laser power. Since the laser rod acted as an aperture, high order resonator modes was easily suppressed with small diameter rod due to large diffraction losses, improving thus the beam quality. The 3 mm diameter rod, pumped within the asymmetric resonator with $L_1 = 506.6$ mm, presented the beam quality factors, $M_x^2 = 1.1$ $M_y^2 = 1.1$. In this case, LASCAD© analysis gave a diffraction loss of 0.42%. The total round-trip loss of 3.4% + 0.42% = 3.82% was hence calculated, resulting in 3.14 W TEM$_{00}$-mode solar laser power, corresponding to 2.66 W/m² TEM$_{00}$-mode collection efficiency. Other TEM$_{00}$-mode solar laser powers with 2.5 mm displacement errors in X, or Y axis, or in both X and Y axes were also calculated correspondingly, as given in Fig. 4 in Section 2.

The TEM$_{00}$-mode laser beam profile attained with the 3 mm diameter rod, within the asymmetric resonator with $L_1 = 506.6$ mm and $L_2 = 60$ mm, are shown in Fig. 7. It has a near diffraction limited Gaussian distribution, leading to $M_x^2 = 1.1$ $M_y^2 = 1.1$ laser beam quality in the LASCAD© analysis.

3.3. Numerical analysis of input solar power dependent TEM$_{00}$ – Mode solar laser power and its beam profile by LASCAD© software

Both ZEMAX© and LASCAD© softwares were used to study the input solar power dependent TEM$_{oo}$-mode laser powers and beam profiles of both the conical-shaped end-side-pumped laser (Liang et al., 2017, Fig. 8a) and the side-pumped laser by the twisted light guide (Fig. 8b). In Fig. 8a, low-order mode solar laser beam profiles
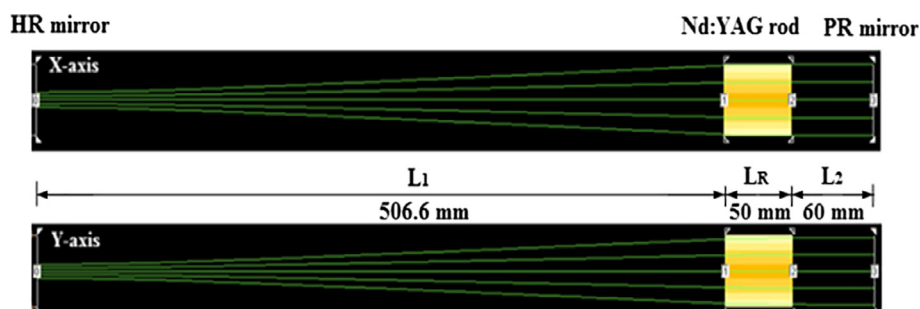
Fig. 6. Asymmetric laser resonant cavity for the efficient production of fundamental mode solar laser power. L_1 and L_2 represent the separation length of the high reflection (HR) mirror and partial reflection (PR) mirror, respectively, to the end face of the laser rod with length L_R.
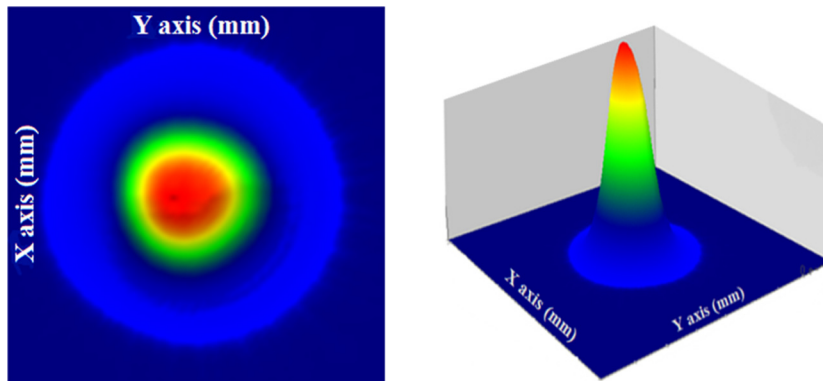
Fig. 7. Numerically simulated 2-D (a) and 3-D (b) TEM$_{00}$-mode laser beam profiles on the output mirror of the asymmetric laser resonator with ROC = −5 m for the 3 mm diameter rod.
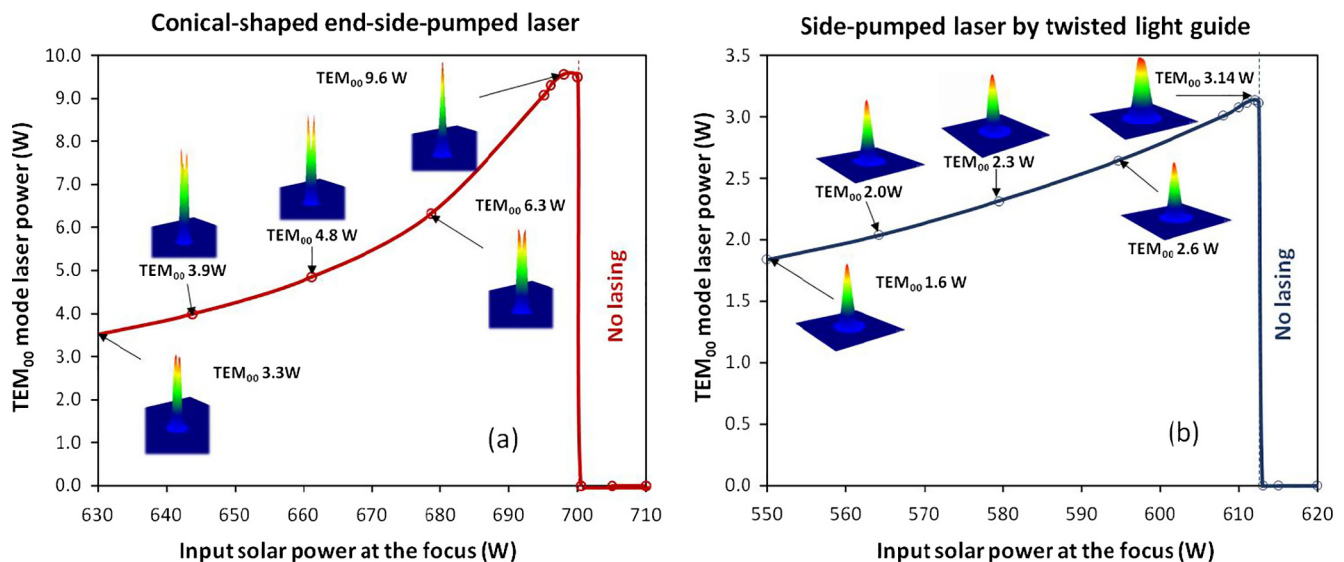
Fig. 8. Input solar power dependent TEM$_{oo}$-mode solar laser powers and beam profiles from both the conical-shaped end-side-pumped laser (Liang et al., 2017, Fig. 8a) and the side-pumped laser by the twisted light guide (Fig. 8b).

were changed to a Gaussian TEM$_{00}$-mode profile when input solar power at the focus approached 700 W, when the shutter was removed. 9.6 W fundamental mode laser power was numerically calculated. The TEM$_{00}$-mode solar power was found to be very sensitive to the variation of input solar power at the focus. Slight increase in input solar power above 700 W led to a shorter thermal length, causing the extinction of solar laser output power. Reduction in solar power alleviated considerably the thermal lensing effect, permitting either two-mode, or other low-order mode laser operation within the laser cavity, as shown in Fig. 8. Significant reduction in fundamental mode power, from 9.6 to 3.3 W were numerically calculated when solar power at the focus was reduced from 700 W to 630 W, as indicated by Fig. 8a, corresponding to 2.9 times reduction. For Fig. 8b, however, the Gaussian TEM$_{00}$-mode profile remained nearly stable when the input solar power at the focus was increased from 550 W to 612 W by controlling the shutter, demonstrating a remarkable laser beam profile stability until the input solar power level exceeded 612 W after which solar laser stopped lasing due to the thermal lensing effect. When the input solar power was reduced gradually from 612 W to 550 W, the numerically calculated TEM$_{00}$-mode laser power was gradually reduced from 3.14 W to 1.6 W, corresponding to 1.96 times reduction. From both Fig. 8a and b, it was clear that change in input solar power could cause much less variation in TEM$_{00}$-mode laser power

and its profile by the twisted light guide solution than by the conical-shaped end-side-pumped laser.

4. TEM$_{00}$-mode continuous-wave 1064 nm solar laser experiments

4.1. TEM$_{00}$-mode continuous-wave 1064 nm solar laser oscillation experiment

Based on the ZEMAX© and LASCAD© numerically optimized design parameters of the solar laser system, a prototype solar laser was built in Lisbon and tested in the PROMES – CNRS during the month of July 2016. The 3 mm diameter, 50 mm length Nd^{3+}: YAG was supplied by Altechna Co., Ltd. It had 1.0 % Nd^{3+} concentration. Both ends of the rod were anti-reflection (AR) coated (R < 0.2% @ 1064 nm). The resonator mechanics was designed to allow the displacement of the HR mirror, while maintaining the PR mirror at fixed L$_2$ = 60 mm, L$_R$ = 50 mm positions as shown in Fig. 9.

Direct solar irradiance was measured simultaneously during laser experiments with a Kipp & Zonen CH1 pyrheliometer on a Kipp & Zonen 2AP solar tracker. It varied between 970 and 1000 W/m^2 during the experiments. A CINOGY UV-NIR beam profiler – Cin Cam CMOS was used for monitoring the laser beam pro-
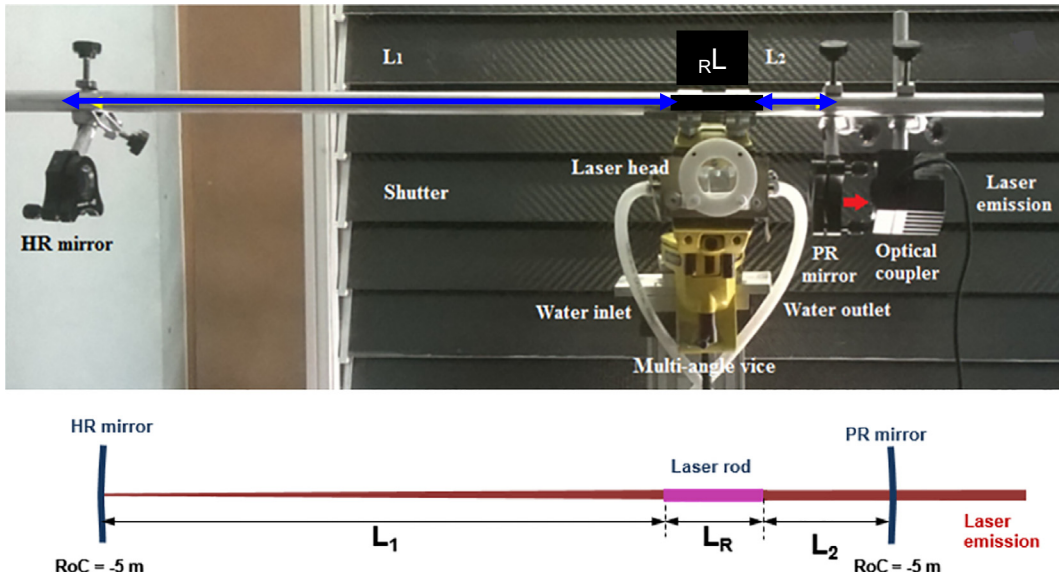
Fig. 9. The asymmetric laser resonant cavity for extraction of TEM$_{00}$-mode laser power.

file. To measure the beam diameters at $1/e^2$ width under high 1064 nm laser intensity, a PR1064 nm (95%), ROC = ∞ output mirror was added before the CMOS detector, acting as an extra laser beam attenuator and reducing the 1064 nm laser power to mW level for the detector. Laser power was measured simultaneously with a Thorlabs PM1100D power meter. The correspondingly input solar power at the focus was measured by a Molectron Power Max 500D power meter. The PROMES-CNRS heliostat parabolic mirror system collected about 610 W solar powers to its focal zone. By varying the rotation angle of the shutter, as indicated in Figs. 1 and 9, different inputs solar power levels at the focus and output TEM$_{00}$-mode laser power were respectively measured with Molectron Power Max 500D and Thorlabs PM1100D laser power meters, as shown in Fig. 10. The threshold solar power of 285 W was measured in the focal zone. For 1000 W/m^2 solar irradiance and 1.18 m^2 effective collection area (with the shutter totally opened), the asymmetric resonator with RoC = -5 m PR (94%) mirror fixed at L$_2$ = 85 mm and RoC = -5 m HR mirror placed at L$_1$ = 506.6 mm, offered the maximum TEM$_{00}$-mode solar laser power of 2.7 W. TEM$_{00}$-mode solar laser collection efficiency of 2.3 W/m^2 was hence calculated.
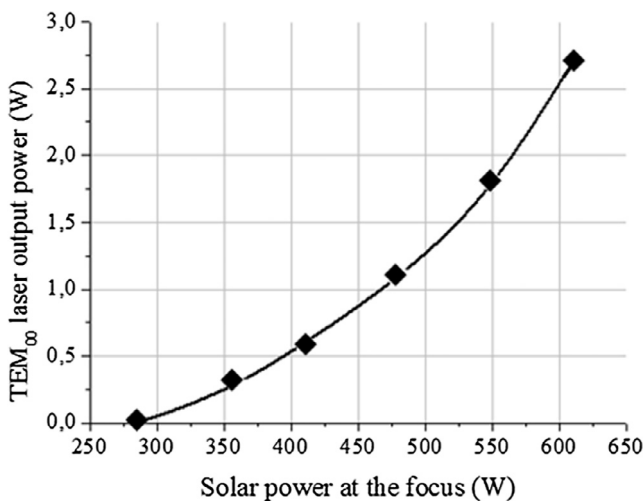
The thermal lens effect was a serious issue in solar laser systems, small diameter rods can minimize considerably this problem. The combination of both monolithic twisted light guide and small diameter Nd^{3+}:YAG rod have considerably overcome these thermal lensing problems, providing a uniform pumping distribution along the thin laser rod, which allows the generation of much more stable continuous-wave TEM$_{00}$-mode solar laser power with 2.3 W/m^2 collection efficiency. Since no aperture was used in the laser resonator besides the rod itself, oscillation of more than one mode occurred at low output powers due to the relatively small overlap between the fundamental mode volume and the pumped region. With the increase of pump power, and thus diffraction loss, only one mode of higher intensity become possible to oscillate. The twisted light-guide ensured more uniform pumping to the long and thin rod. This in turn, led to significantly reduced solar pumping intensity, and consequently less heat load, less thermal stress and working temperature, as compared to all the previous schemes (Liang et al., 2015, 2017; Almeida et al., 2015). Strong thermal lensing effects, which affected largely the TEM$_{00}$-mode laser power stability of previous solar lasers were not observed in our measurement. Therefore, the present prototype laser with twisted light-guide offered very good output power stability of 1.7% during the laser operation, considerably less than the previous prototype TEM$_{00}$-mode lasers with usually more than 10% laser beam stability. By improving polishing accuracy of the dimension of the twisted light guide, enhanced TEM$_{00}$-mode solar laser efficiency and stability can be achieved.

The slight discrepancy in laser beam diameters at $1/e^2$ along X and Y axis Fig. 11 can be justified by the slight pump profile misalignment due to the heliostat orientation error. Taking this factor into account, $M_x^2 \approx M_y^2 \leq 1.05$ were considered as adequate measured values for quantifying the laser beam quality. It was also interesting to note that the experimentally measured laser beam profile in Fig. 11 was slightly better than the numerically calculated profiles in Fig. 7. Due to the non-symmetry in the twisted light guide design, composed of the lower straight part and upper twisted parts as shown in Figs. 2 and 3, zero heliostat orientation error, and hence zero displacement on the input face of the twisted light guide meant neither the maximum TEM$_{00}$-mode solar laser power nor the most perfect profile, as explained in Section 2.3 and Fig. 4, the **TEM$_{00}$**-mode output laser beam 2D and 3D profiles in Fig. 11 represented most possibly the best one we measured with heliostat orientation errors.

Fig. 10. TEM$_{00}$-mode laser output power versus solar input power at the focus of the parabolic mirror for L$_1$ = 506.6 mm.
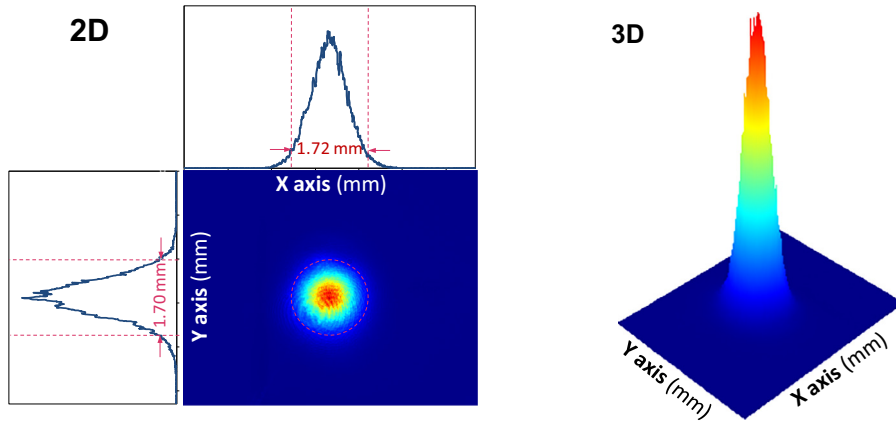
Fig. 11. 2D and 3D TEM$_{00}$-mode output laser beam 2D and 3D profiles, measured 50 mm away from the PR1064 nm mirror.
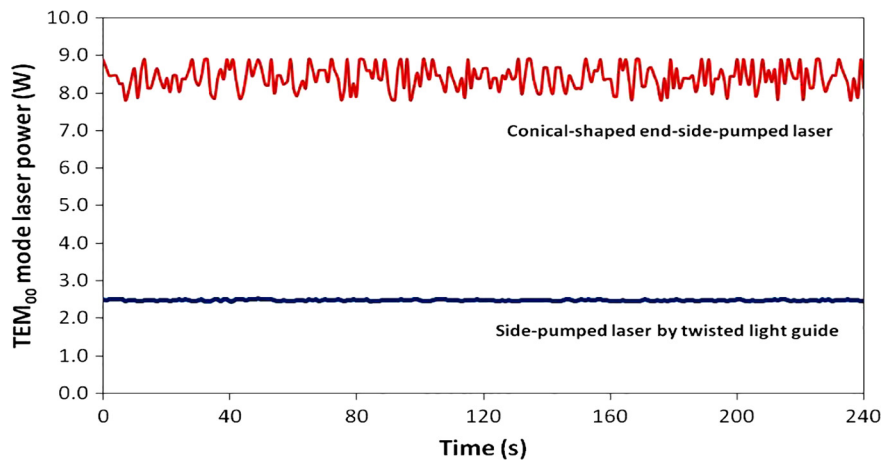
Fig. 12. Time dependent TEM$_{00}$-mode solar laser power variations of both the conical-shaped end-side-pumped laser (Liang et al., 2017) and the present side-pumped laser by the twisted light guide.

4.2. TEM$_{00}$-mode continuous-wave 1064 nm solar laser power stability experiment

Time dependent TEM$_{00}$-mode solar laser power variations of both the end-side-pumped laser (Liang et al., 2017, Fig. 12) and the side-pumped laser by the twisted light guide (Fig. 12) were measured by the PROMES-CNRS heliostat-parabolic mirror facility during the first two weeks of July in 2017.

For the side-pumped laser by the twisted light guide at 970 W/m^2 solar irradiance and 1.18 m^2 effective collection area, the asymmetric resonator with ROC = −5 m PR (94%) mirror fixed at L_2 = 85 mm and ROC = −5 m HR mirror placed at L_1 = 500 mm, similar to that shown in Fig. 9, 2.5 W TEM$_{00}$-mode solar laser power were measured during 240 s, with the maximum output power variation being less than 1.7%. The Gaussian fundamental mode profile was also found stable during the measurement. For the conical-shaped end-side-pumped laser (Liang et al., 2017) at 950 W/m^2 solar irradiance and 1.18 m^2 effective collection area, a − 5 m ROC output mirror with 94% reflectivity at L_1 = 430 mm similar to (Fig. 5 of Liang et al., 2017), provided the maximum TEM$_{00}$-mode laser output power of 8.9 W. Strong oscillation of 12% were observed during the measurement process of 240 s. The conical end-side-pumped configuration offered the maximum TEM$_{00}$-mode solar laser collection efficiency, but also suffered from a very strong thermal lensing effect. Much more than the 1.7% of the twisted light guide laser. Fig. 12 represented a favorable result in fundamental mode laser beam stability of less than 12% for the

conical-shaped end-side-pumped laser. During the measurement process, however, we found it not easy to maintain a perfect Gaussian mode profile due to the strong thermal lensing effect of this type of laser. Solar irradiance variation of less than 0.5%, cooling water temperature oscillation of less than 2 degree during the measurement were found sufficient to change a solar laser beam with Gaussian profile into a low-order mode beam with a two-mode, sometimes a four-mode or even a doughnut-shaped profiles.

5. Discussions

The main problem preventing wide spreading of solar lasers today is its low efficiency. Therefore, collection efficiency is generally regarded as a primary figure of merit for solar lasers. The second is thermal problem worsening the efficiency as well as the beam quality. Lasers for space missions generally require diffraction-limited beam quality. This is not easy to achieve when the heat load of the laser crystal is high. The heat load under direct solar pumping is very similar to that for pumping by arc lamps that were used before the advent of semiconductor lasers. The high heat load usually leads to very low efficiency, stability, and output power for diffraction-limited TEM$_{00}$-mode laser beams from both lamp-pumped and solar-pumped lasers.

The twisted fused silica light guide used in this work undoubtedly will be useful in further studies and developments in the field of solar-pumped lasers not only in TEM$_{00}$-mode operation but also

in increasing its overall efficiency by the use of solar-pumped laser acting as an amplifier. Improved pumping profile can be maintained by means of techniques like the twisted fused silica light guide. Since the twisted light guide is effective for transmitting, spreading and homogenizing the highly concentrated solar radiations from the focus of the primary concentrator to along a long and thin laser rod, high gain in pulse amplification can be achieved. The twisted fused silica light guide may provide an alternative solution to the Nd/Cr:YAG ceramic multi-amplifier active-mirror pulsed solar-pumped laser approach as reported by Saiki et al. (2017).

Finally, it is very important to notice that the results for multimode regime would be more important than the single mode collection efficiency reported here, which is just to confirm the high quality (uniformity) of pumping profile as a technique to characterize the twisted light guide. Besides, a low quality multimode solar laser can be used to pump another laser rod to obtain high quality TEM_{00}-mode solar laser output (Wittroch, 2013), offering a good solution for reaching high TEM_{00} mode laser collection efficiency.

6. Conclusions

The 2.7 W continuous-wave TEM_{00}-mode 1064 nm solar-pumped laser was pumped by the PROMES heliostat-parabolic mirror solar energy collection and concentration system. It was composed of the monolithic fused silica twisted light guide, the 2D-CPC concentrator and the 2 V-shaped pumping cavity, within which a 3 mm diameter, 50 mm length 1.0 at.% Nd:YAG rod was efficiently pumped. The adoption of the side-pumping configuration by employing the twisted light guide with square input face and rectangular output end enabled a uniform pumping profile along the rod. The present solar laser pumping approach also significantly enhanced its heliostat orientation error compensation capacity, as compared to that of the previous solar pumping approaches. The efficient extraction of TEM_{00}-mode solar laser was obtained by adopting an asymmetric laser resonator, since it offered a good overlap between the fundamental mode and the pumped region of the active medium. 2.7 W continuous-wave TEM_{00}-mode ($M_2 \leq 1.05$) 1064 nm solar laser emission with 2.3 W/m^2 collection efficiency and, more importantly, with 1.7% laser power stability was finally produced, being significantly more stable than the previous TEM_{00}-mode solar lasers.

References

Almeida, J., Liang, D., Guillot, E., 2012. Improvement in solar-pumped Nd:YAG laser beam brightness. Opt. Laser Technol. 44, 2115–2119.

Almeida, J., Liang, D., 2012. Design of a high brightness solar-pumped laser by light-guides. Opt. Commun. 285, 5327–5333.

Almeida, J., Liang, D., Guillot, E., Abdel-Hadi, Y., 2013. A 40 W continuous-wave Nd: YAG solar laser pumped through a heliostat: a parabolic mirror system. Laser Phys. 23, 065801–65806.

Almeida, J., Liang, D., Vistas, C.R., Guillot, E., 2015. Highly efficient end-side-pumped Nd:YAG solar laser by a heliostat–parabolic mirror system. Appl. Opt. 54, 1970–1977.

Almeida, J., Liang, D., Vistas, C.R., Bouadjemine, R., Guillot, E., 2015. 5.5 W continuous-wave TEM00-mode Nd:YAG solar laser by alight-guide/2 V-shaped pump cavity. Appl. Phy. B, Laser Opt. 121, 473–482.

Arashi, H., Oka, Y., Sasahara, N., Kaimai, A., Ishigame, M., 1984. A solar-pumped cw 18 W Nd:YAG laser. Jpn. J. Appl. Phys. 23, 1051–1053.

ASTM Standard G173-03, 2012. Standard Tables for Reference Solar Spectral Irradiances: Direct Normal, and Hemispherical on 37° Tilted Surface.

Bernardes, P.H., Liang, D., 2006. Solid-state laser pumping by light guides. Appl. Opt. 45, 3811.

Brauch, U., Muckenschnabel, J., Opower, H., Wittner, W., 1991. Space Power. 10, 285.

Bouadjemine, R., Liang, D., Almeida, J., Mehellou, S., Vistas, R.C., Kellou, A., Guillot, E., 2017. Stable TEM00-mode Nd:YAG solar laser operation by a twisted fused silica light-guide Opt. Laser Tecchnol. 97, 1–11.

Dinh, T.H., Ohkubo, T., Yabe, T., Kuboyama, H., 2012. 120 watt continuous-wave solar-pumped laser with a liquid light-guide lens and a Nd:YAG rod. Opt. Lett. 37, 2670–2672.

Guan, Z., Zhao, C.M., Yang, S.H., Wang, Y., Ke, J.Y., Zhang, H.Y., 2017. Demonstration of a free-space optical communication system using a solar-pumped laser as signal transmitter. Laser Phys. Lett. 055804. 4pp.

Geraldes, J.P., Liang, D., 2008. An alternative solar pumping approach by a light guide assembly elliptical-cylindrical cavity. Sol. Energy Mat. Sol. Cells 92, 836–843.

Koechner, W., 1999. Solid-State Laser Engineering. Springer- 543 Verlag, Berlin, Heidelberg, New York.

Lando, M., Jenkins, D.G., Bernstein, H., O'Gallagher, J.J., Winston, R., Lewandowski, A., 1995. High-brightness-solar-pumped Nd:YAG laser design. Proc. SPIE 2426, 478.

Lando, M., Kagan, J., Linyekin, B., Dobrusin, V., 2003. A solar-pumped Nd:YAG laser in the high collection efficiency regime. Opt. Commun. 222, 371–381.

Liang, D., Pereira, R., 2009. Maximizing TEM00-solar laser power by a light guide assembly-elliptical cavity. Opt. & Laser Technol. 41, 687–692.

Liang, D., Almeida, J., 2011. Highly efficient solar-pumped Nd:YAG laser. Opt. Express 19, 26399.

Liang, D., Almeida, J., 2013. Solar-pumped TEM00-mode Nd:YAG laser. Opt. Express 21, 25107–25112.

Liang, D., Almeida, J., Guillot, E., 2013. Side-pumped continuous-wave Cr:Nd:YAG ceramic solar laser. Appl. Phys. B. Lasers Optics 111, 305–311.

Liang, D., Almeida, J., Vistas, C.R., Guillot, E., 2015. Solar-pumped TEM00-mode Nd: YAG laser by a heliostat–parabolic mirror system. Sol. Energy Mater. Sol. Cells 134, 305–308.

Liang, D., Almeida, J., Vistas, C.R., Oliveira, M., Gonçalves, F., Guillot, E., 2016a. High-efficiency solar-pumped TEM00-mode Nd:YAG laser. Sol. Energy Mat. Sol. Cells 145, 397–402.

Liang, D., Almeida, J., Vistas, C.R., 2016a. 25 W/m² collection efficiency solar-pumped Nd:YAG laser by a heliostat-parabolic mirror system. Appl. Opt. 55, 1970–7717.

Liang, D., Almeida, J., Vistas, C.R., Guillot, E., 2017. Nd:YAG laser with 31.5 W/m² multimode and 7.9 W/m² TEM00-mode collection efficiencies. Sol. Energy Mat. Sol. Cells, 159–435.

Overton, G., 2013. Novel lasers: solar-pumped Nd:YAG lasers getting brighter. Laser Focus World Dez 9.

Ohkubo, T., Yabe, T., Yoshida, K., Uchida, S., Funatsu, T., Bagheri, B., Oishi, T., Daito, K., Ishioka, M., Nakayama, Y., Yasunaga, N., Kido, K., Sato, Y., Baasandash, C., Kato, K., Yanagitani, T., Okamoto, Y., 2009. Solar-pumped 80 W laser irradiated by a Fresnel lens. Opt. Lett. 34, 175.

Pereira, R., Liang, D., 2009. High conversion efficiency solar laser pumping by a light-guide/2D-CPC cavity. Opt. Commun. 282, 1385–1392.

Payziyev, S., Makhmudov, K., 2016. Solar pumped Nd:YAG laser efficiency enhancement using Cr:LiCAF frequency down-shifter. Opt. Commun. 380, 57–60.

Payziyev, Sh.D., Makhramudov, S.R., Kasimov, A.K., 2011. Transformation of concentrated sunlight into laser radiation on small parabolic mirror. J. Ren. Sustain. Energy. 3 (5). Article No. 053102–7.

Saiki, T., Fujiwara, N., Matsuoka, N., Nakatuka, M., Fujioka, K., Iiida, Y., 2017. Amplification properties of KW Nd/Cr:YAG ceramic multi-stage active-mirror laser using white-light pump source at high temperatures. Opt. Commun. 387 (15), 316–321.

Wittroch, U., 2013, Perspective of solar pumping of solid state laser for ESA mission, Contract Number: 400106760 <https://gsp.esa.int/gsp-study-view/-/wcl/gaUaMHco1QJ9/10192/perspective-of-solar-pumping-of-solid-state-lasers-for-esa-missions>.

Vistas, C.R., Liang, D., Almeida, J., 2015. Solar-pumped TEM00-mode laser simple design with a grooved Nd:YAG rod. Sol. Energy 122, 1325–1333.

Weksler, M., Shwartz, J., 1988. Solar-pumped solid-state lasers. IEEE J. Quantum Electron. 24, 1222–1228.

Xu, P., Yang, S., Zhao, C., et al., 2014. High-efficiency solar-pumped laser with a grooved Nd:YAG rod. Appl. Opt. 53, 3941–3944.

Yabe, T., Uchida, S., Ikuta, K., Yoshida, K., Baasandash, C., Mohamed, M.S., Sakurai, Y., Ogata, Y., Tuji, M., Mori, Y., et al., 2006. Demonstrated fossil-fuel-free energy cycle using magnesium and laser. Appl. Phys. Lett. 89, 261107.

Yabe, T., Ohkubo, T., Uchida, S., et al., 2007. High efficiency and economical solar energy pumped laser with Fresnel lens and chromium co-doped laser medium. Appl. Phys. Lett. 90, 261120.

Young, C.G., 1966. A sun-pumped CW one-watt laser. Appl. Opt. 5, 993–997.

Zhao, B., Zhao, C., He, J., Yang, S., 2007. The study of active medium for solar-pumped solid-state lasers. Acta Opt. Sin. 27, 1797–1801.
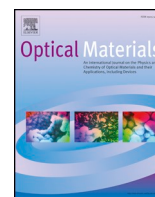
ELSEVIER

Mid-infrared broadband ultraflat-top supercontinuum generation in dispersion engineered Ge-Sb-Se chalcogenide photonic crystal fiber

Abdelkader Medjouri[a],[*], Djamel Abed[b]

[a] *LEVRES Laboratory, University of EL Oued, 39000, El Oued, Algeria*
[b] *Department of Electronics and Telecommunications, Faculty of Sciences and Technology, University of Guelma, 24000, Guelma, Algeria*

ARTICLE INFO

ABSTRACT

In this paper, we numerically demonstrate broadband, ultraflat-top and highly coherent mid-infrared Supercontinuum (SC) generation in an all-normal dispersion (ANDi) $Ge_{15}Sb_{15}Se_{70}$ chalcogenide Circular Lattice Photonic Crystal Fiber (CL-PCF). The propagation properties of the fundamental mode are computed with the Finite Difference Method (FDM). Numerical results show that ANDi regime is obtained over the entire mid-infrared wavelength range with a cladding pitch and air holes diameter of $\Lambda = 2\,\mu m$ and $d = 0.8\,\mu m$, respectively. Besides, the proposed CL-PCF exhibits small effective mode area and high Kerr nonlinearity up to $1.96\,W^{-1}\,m^{-1}$ at $3\,\mu m$. Ultrashort pulse propagation inside the CL-PCF core is modelled by using the Generalized Non-Linear Schrodinger Equation (GNLSE). Simulation results show that by pumping at $3\,\mu m$ laser pulses with a total energy of 0.6 nJ and duration of 50 fs, into 10 mm long of the CL-PCF, generates an ultrabroadband and highly coherent SC spanning the wavelength region from $1.86\,\mu m$ to $5.35\,\mu m$ within less than 3 dB spectral dynamics. By increasing the initial pulse energy to attain 1 nJ, the generated SC bandwidth increases too and reaches $4.53\,\mu m$ in the spectral range extending from $1.67\,\mu m$ to $6.2\,\mu m$ at 4 dB spectral level. Moreover, the proposed CL-PCF based SC source is found promising for application in Optical Coherence Tomography (OCT) with an axial resolution of $0.87\,\mu m$, achieved when pumping 1 nJ energy and 50 fs duration optical pulses.

1. Introduction

Over the past few years, high brightness laser sources based on Supercontinuum (SC) generation, covering the middle infrared spectral region extending from $2\,\mu m$ to $20\,\mu m$, have been the subject of huge research interest across various fields of both fundamental and applied sciences such as generation of few optical cycle pulses, metrology, biosensing, non-destructive testing and so on [1]. Particularly, the atmospheric transparent ($3–5\,\mu m$ and $8–12\,\mu m$) and the functional group ($3–5\,\mu m$) regions have drawn much attention for mid-infrared molecular absorption spectroscopy applications such as atmospheric pollutants monitoring, exhaled breath analysis, coherent anti-stokes Raman scattering imaging and mid-infrared optical biopsy for early cancers diagnostics [2–4]. This account for the fact that the fundamental rotational-vibrational absorption bands of various gases molecules are included in this spectral range [5,6]. Furthermore, high quality imaging of samples obtained by Optical Coherence Tomography (OCT) can be achieved when operating in the mid-infrared region [7]. Actually, the performance criteria of OCT systems, namely the penetration depth and the axial resolution, are limited by the light scattering losses occurred

when employing visible and near-infrared light sources [8]. In order to enhance its efficiency and achieve accurate results, OCT measurements can be performed by using broadband light sources operating at longer wavelengths located in the mid-infrared range [9].

The generation of broadband SC is achieved through the interaction of short and intense optical pulses with high nonlinear materials including solids, liquids and gases [10–12]. Moreover, the spectral broadening process can be realized by pumping femtosecond pulses in bulk structures, through the femtosecond filamentation nonlinear process, as well as in optical fibers, where the generation of new frequencies involves several linear and non-linear optical properties such as group velocity dispersion, Kerr nonlinearity and Stimulated Raman Scattering (SRS) [11,13]. The main advantage of optical fibers, compared to bulk structures, is the interaction length, which is several orders of magnitude larger than the confocal length of the focusing lens needed for beam coupling into bulk medium [9]. Besides, optical fibers enables a perfect control over the different nonlinear processes that contribute to the SC generation due to the suppression of filamentation and self-focusing, which are critical for SC generation in bulk geometries [14–18]. Nowadays, significant efforts are devoted to the design

---

* Corresponding author.
  E-mail address: medjouri-abdelkader@univ-eloued.dz (A. Medjouri).

and optimization of mid-infrared SC sources based on microstructured and Photonic Crystal Fibers (PCFs) [19]. The wavelength scale of the cladding microstructure combined with broad range of mid-infrared background materials, such as fluorides, tellurides and chalcogenides allow PCFs to exhibit unique laser pulses guiding features [20–23]. Particularly, all normal dispersion (ANDi) guiding regime can be achieved in optical waveguides by compensating the material dispersion with waveguide dispersion and this can be easily realized in PCFs through a suitable adjusting of the microstructure pitch and air holes diameters [20]. SC generated by pumping femtosecond laser pulses in PCFs exhibiting ANDi profile is highly beneficial for numerous applications such as OCT and optical metrology, since it allows to generate broadband, flat-top and coherent SC through the elimination of noisy processes such as modulation instability, soliton collisions and SRS [24]. Therefore, pulses spectral broadening in ANDi PCFs results from the contribution of Self-Phase Modulation (SPM), in the initial stage, followed by the generation of new frequencies via the Optical Wave Breaking (OWB) mechanism [25,26].

In the last few years, chalcogenide (ChG) glasses have attracted a widespread interest for the design of waveguide and fiber based mid-infrared SC sources [27]. ChG glasses are multicomponent inorganic materials that are mainly composed of chalcogen elements from group XVI, including Sulphur (S), Selenium (Se), Tellurium (Te) with the addition of other elements from group XV such as Arsenic (As) and Antimony (Sb) and group XIV such as Germanium (Ge) and Silicon (Si) [28]. The key advantages of ChG rely to their several attractive optical properties such as high linear refractive index, high nonlinear refractive index, low phonon energy and large optical transparency extending from the visible to $20 \mu m$ [29]. These beneficial features of ChG glass combined with the high flexibility of PCFs design have been, recently, exploited and several numerical and experimental demonstrations of efficient mid-infrared and coherent SC sources, realized by pumping femtosecond laser pulses, have been reported [20,30–36]. E. Wang et al. investigated, via numerical simulations, the SC generation in holey PCF made of As_2Se_3 ChG glass [30]. The PCF total chromatic dispersion is adjusted by introducing a small defect into the solid core and ANDi regime is obtained over the entire spectral range. Moreover, the authors have shown that pumping 4.25 kW peak power and 50 fs duration optical pulses at $4.37 \mu m$ generates broadband and flat-top SC spanning the region from $3.86 \mu m$ to $5.95 \mu m$ at the spectral level of 3 dB. H. P. T. Nguyen et al. reported numerical study of coherent and mid-infrared SC generation, achieved by using cascaded ANDi tellurite and ChG fibers [31,32]. The authors have demonstrated that pumping 200 fs duration and 100 kW peak power pulses at $2 \mu m$, corresponding to total energy of 22.7 nJ, generates broadband SC extending from $0.78 \mu m$ to $8.3 \mu m$ at 10 dB. Furthermore, SC generation in all-solid ChG glass PCFs exhibiting ANDi regime has been, also, investigated. Lai et al. reported experimental demonstration of highly coherent SC in the mid-infrared region, obtained by using a hybrid four holes PCF composed of $AsSe_2$ and As_2S_5 ChG materials [33]. By pumping 200 fs laser pulses at $2.7 \mu m$ in 2 cm of the PCF length, broadband SC extending from $2.2 \mu m$ to $3.3 \mu m$ has been generated. S. Xing et al. demonstrated linearly chirped SC generation by pumping at $2.07–2.08 \mu m$ 79 fs width and 2.9 kW peak power pulses in all-solid ANDi AsSe-GeAsSe PCF [34]. Their results show that broadband and perfectly coherent SC having a bandwidth of 27.6 THz and 75.5 THz is realized at the spectral flatness of 3 dB and 20 dB, respectively. Moreover, M. R. Karim et al. reported numerical simulations of mid-infrared SC generation in a kind of dispersion engineered multi-material ChG triangular core PCF [35]. The proposed structure is composed of $Ge_{11.5}As_{24}Se_{64.5}$ ChG core surrounded by $Ge_{11.5}As_{24}S_{64.5}$ ChG cladding running along the PCF length. The authors have shown that pumping optical pulses with 100 fs duration and 3 kW peak power at $4 \mu m$ into 10 mm of the PCF length generates a $7 \mu m$ bandwidth coherent SC. T. S. Saini et al. reported numerical investigation of mid-infrared SC generation in As_2Se_3 ChG glass ANDi Triangular-Core Graded-Index (TCGI) PCF [36]. The ANDi

regime is achieved by gradually reducing the air holes diameter of the different cladding rings. The authors have shown that pumping 50 fs duration and 3.5 kW peak power laser pulses at $4.1 \mu m$ into 5 mm of the PCF length, generates a coherent and broadband SC spanning the region from $2 \mu m$ to $15 \mu m$. A simple and straightforward method to engineer the chromatic dispersion profile of PCFs and ensure ANDi regime, through a careful adjustment of the cladding air hole fraction, has been reported in [20,37]. We have studied a hexagonal lattice PCF made of $Ga_8Sb_{32}S_{60}$ and $As_{39}Se_{61}$ ChG glass, respectively. In the first design, we have shown, via numerical simulations, that pumping 1.06 nJ pulses at $4.5 \mu m$ into 1 cm of the PCF length, generates a broadband SC spanning the spectral region from $1.65 \mu m$ to $9.24 \mu m$ with a spectral flatness of 20 dB. In the second design, numerical results indicate that coherent SC extending from $2.43 \mu m$ to $4.85 \mu m$ at 4 dB and from $1.95 \mu m$ to $6.58 \mu m$ at 8 dB can be achieved by pumping at $3.45 \mu m$ optical pulses with a total energy of 50 pJ and 250 pJ, respectively.

Among various compositions of ChG glasses, the $Ge_{15}Sb_{15}Se_{70}$ system is found to be an excellent candidate for mid-infrared nonlinear optics. A growing interest is paid to this ChG glass due to its numerous advantageous characteristics including broad spectral transmittance spanning the region from $2 \mu m$ to $12 \mu m$, large third order nonlinearity, high laser damage threshold of about $3674 \, GW/cm^2$ and suitability for fiber drawing thanks to its excellent thermal stability against crystallization [38,39]. Besides, the $Ge_{15}Sb_{15}Se_{70}$ glass is environment friendly due to the absence of highly toxic elements such as Arsenide [40]. Within this scope, B. Zhang et al. used a two-stage rode-in-tube technique to fabricate a step index fiber with a core and cladding made of $Ge_{15}Sb_{15}Se_{70}$ and $Ge_{20}Se_{80}$ ChG glasses, respectively [38]. The authors demonstrated SC generation spanning the range from $2.2 \mu m$ to $12 \mu m$ by pumping at $4.485 \mu m$ 330 fs duration pulses into 11 cm of the fiber length. Furthermore, M. A. Khamis et al. designed and optimized a kind of W type index fiber for mid-infrared SC generation beyond $10 \mu m$ [41]. The fiber structure consists of a core made of $Ge_{15}Sb_{15}Se_{70}$ surrounded by double cladding made of $Ge_{20}Se_{80}$ and $Ge_{20}Sb_5Se_{75}$ glasses, respectively. The authors have shown, via numerical modelling, that pumping 330 fs duration and 1 kW peak power pulses at $6.3 \mu m$, generates a broadband SC extending from $3.7 \mu m$ to $12 \mu m$. Recently, Y. Yuan et al. reported the fabrication of a four holes suspended-core fiber based on $Ge_{15}Sb_{15}Se_{70}$ ChG glass for SC generation [42]. The preform has been fabricated by employing a Computerized Numerical Control (CNC) precision mechanical drilling technique. They experimentally demonstrated the generation of broadband SC spanning the region from $1.5 \mu m$ to $12 \mu m$ at the spectral flatness level of 30 dB by pumping 23 mW pulses close to the zero dispersion wavelength into 14 cm fiber length. The common feature of the studies on SC generation reported in [38,41,42] is the anomalous regime of chromatic dispersion at which pulses are pumped. Indeed, the realized SC spectra are broadband, due to the soliton dynamics process, but exhibits substantial spectral fluctuations and strong shot-to-shot variations. These limitations can be suppressed by exploiting PCFs versatility and achieve ANDi regime through a careful design of their microstructure.

The present work reports on the design and optimization of a Circular Lattice PCF (CL-PCF) made of $Ge_{15}Sb_{15}Se_{70}$ ChG glass for mid-infrared SC generation. The CL-PCF dispersion profile is engineered and ANDi regime is achieved by controlling the cladding photonic crystal parameters. The propagation characteristics including the guided mode effective index, the chromatic dispersion, the mode effective area and the Kerr nonlinear parameter are calculated by using a Finite Difference Method (FDM) and employing an Anisotropic Perfectly Matched Layer (APML) scheme as boundary condition. Moreover, we perform a series of numerical simulations to investigate SC generation in the optimized design and analyze the impact of the laser pulse duration and peak power and the effect of the quantum noise on the SC bandwidth and coherence, respectively. The propagation of optical pulses inside the CL-PCF is analyzed by solving the Generalized Non-Linear Schrodinger Equation (GNLSE) and employing a fourth order Runge Kutta in the
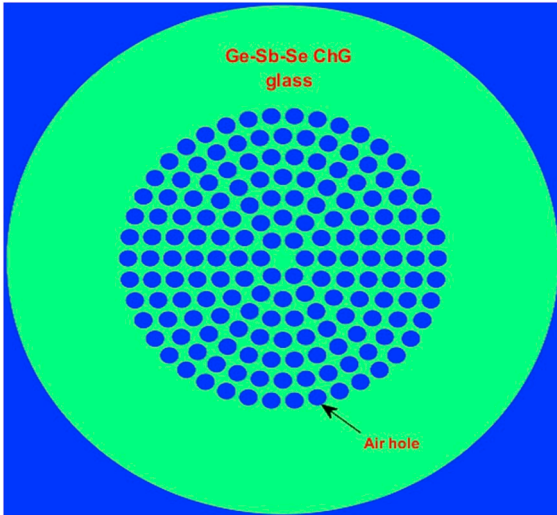
Fig. 1. Cross sectional view of the proposed $Ge_{15}Sb_{15}Se_{70}$ ChG glass CL-PCF.

Interaction Picture (RK4IP) method.

2. Theoretical background

Fig. 1 depicts the schematic cross section of the proposed CL-PCF. The solid core is made of $Ge_{15}Sb_{15}Se_{70}$ ChG glass and the cladding is formed by seven rings of air holes arranged in a circular configuration. The air holes diameter and pitch are denoted by d and Λ, respectively. CL-PCFs have been widely used for various linear and nonlinear applications such as sensing [43], optical communication [44], transmission of optical angular momentum modes [45] and SC generation [46]. The dispersive properties of optical glasses are often modelled through the Sellmeier formula. Therefore, the frequency dependence of the $Ge_{15}Sb_{15}Se_{70}$ ChG glass refractive index is given by:

$$n_{Ge-Sb-Se} = \sqrt{1 + \frac{A_1\lambda^2}{\lambda^2 - B_1} + \frac{A_2\lambda^2}{\lambda^2 - B_2}} \quad (1)$$

With $A_1 = 6.0072$, $A_2 = 1.3076$, $B_1 = 0.09138$ μm^2, and $B_2 = 1718.1854$ μm^2 [38]. Fig. 2 shows the evolution against wavelengths of the $Ge_{15}Sb_{15}Se_{70}$ ChG glass refractive index and the corresponding material chromatic dispersion, respectively. As we can see, the glass exhibits flat anomalous dispersion curve over a wide range of wavelengths, which can be compensated and achieve the targeted ANDi regime by meticulously adjusting the CL-PCF geometrical parameters.

Sight to compute the different wave-guiding properties of the proposed CL-PCF, we have employed a two dimensional version of the FDM [47]. This method is fast, straightforward and provides highly accurate results, which make it advantageous over several other computational methods such as Plane Wave Expansion Method (PWEM), Finite Element Method (FEM), Beam Propagation Method (BPM) and Localized Function Method (LFM) [48]. Moreover, the FDM can be, effectively implemented for solving both of the Helmholtz equation and Maxwell's equations, where the material dispersion and loss can be easily included during calculations [47,48]. In order to compute the guided modes in the proposed CL-PCF, the Maxwell's equations with APML boundaries are expressed in the frequency domain as follow:

$$\begin{cases} ik_0 s\varepsilon_r E = \nabla \times H \\ -ik_0 s\mu_r H = \nabla \times E \end{cases} \quad (2)$$

$$s = \begin{bmatrix} s_y/s_x & & \\ & s_x/s_y & \\ & & s_y s_x \end{bmatrix} \quad (3)$$

Where: $s_x = 1 - \sigma_x/(i\omega\varepsilon_0)$ and $s_y = 1 - \sigma_y/(i\omega\varepsilon_0)$.

k_0 is the free space number, ε_r is the medium relative permittivity, μ_r is the medium relative permeability, σ is the material conductivity parameter and ω is the optical pulsation. The CL-PCF structure is discretized by employing a two dimensional Yee-cell scheme and the curl equations given by (2) are transformed to a matrix eigenvalue problem for both the electric and magnetic fields. Finally, sparse matrix technique is used to reduce the computation task and the different characteristics of fundamental guided mode HE_{11} including the propagation constant and the mode field profile are determined. Besides, the leaky (tunneling) modes of the CL-PCF are perfectly eliminated and absorbed in the outer APML layer.

The Kerr nonlinearity parameter is computed as follow

$$\gamma = \frac{n_2 \omega_0}{c A_{eff}} \quad (4)$$

A_{eff} is the effective mode area and n_2 is the nonlinear refractive index of the $Ge_{15}Sb_{15}Se_{70}$ glass. The frequency dependence of n_2 is calculated using a modified form of the Miller's semi-empirical rule, which describe the relation between the linear and nonlinear susceptibilities [49]. Fig. 3 depicts the variation of the nonlinear refractive index against wavelengths. Thanks to its high linear refractive index, the $Ge_{15}Sb_{15}Se_{70}$ glass exhibits large third order nonlinearity in the mid-infrared region, which allow the generation of broadband SC with very low energy optical pulses.

As mentioned previously, SC generation in optical fibers involves

Fig. 2. Variation of the refractive index and the material dispersion with wavelengths of the $Ge_{15}Sb_{15}Se_{70}$ ChG glass.
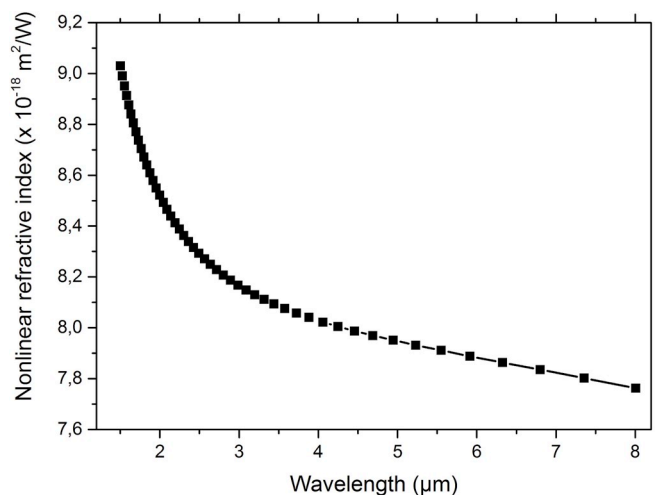
Fig. 3. Variation of the nonlinear refractive index with wavelengths of the $Ge_{15}Sb_{15}Se_{70}$ ChG glass.

several linear and nonlinear effects. For single-mode and single-polarization propagation, we employ a scalar form of the GNLSE. It governs the evolution of the pulse envelope function $\psi(z, t)$ with the contribution of all the optical effects as well as the interaction between them [50]:

$$
\frac{\partial \psi}{\partial z} = -\frac{\alpha}{2}\psi - \left(\sum_{n \geq 2} \beta_n \frac{i^{n-1}}{n!} \frac{\partial^n}{\partial T^n}\right)\psi + i\gamma\left(1 + \frac{1}{\omega_0}\frac{\partial}{\partial t}\right)
$$
$$
\times \left((1 - f_R)\psi |\psi|^2 + f_R \psi \int_0^\infty h_R(\tau) |\psi(z, t - \tau)|^2 d\tau\right) \tag{5}
$$

Linear effects contain the optical loss coefficient α and the chromatic dispersion, represented by the Taylor expansion coefficients $\beta_n = (d^n\beta/d\omega^n)_{\omega=\omega_0}$. Nonlinear effects include the Kerr nonlinearity parameter γ, the characteristic time scale of pulses self-steepening $\tau_0 = \frac{1}{\omega_0}$ and the delayed Raman response function $h_R(t)$ given by the following expression [46–53]:

$$
h_R(t) = \frac{\tau_1^2 + \tau_2^2}{\tau_1 \tau_2^2}exp\left(\frac{-t}{\tau_2}\right)sin\left(\frac{t}{\tau_1}\right) \tag{6}
$$

Where τ_1 = 15.5 fs and τ_2 = 230.5 fs are the Raman oscillation period and the decay time, respectively. The fractional contribution of the delayed Raman response to the overall nonlinear response of the $Ge_{15}Sb_{15}Se_{70}$ glass is given by f_R = 0.031 [51].

The GNLSE is commonly solved by using the Split Step Fourier Method (SSFM) [54]. In this pseudo-spectral technique, the linear and nonlinear terms are independently integrated and the results are combined to obtain the final solution. Another alternative to solve the GNLSE is based on the fourth order Runge Kutta in the Interaction Picture (RK4IP) method [55]. This method has been originally proposed to model the dynamics of Bose-Einstein condensates by solving the Gross-Pitaevskii equation [56]. Compared to the SSFM, the RK4IP method provides higher computational accuracy for both small and large step size with a local error of 5th order, which make it preferable for modelling pulses propagation in single mode, birefringent and multimode optical fibers [57–60]. In the RK4IP method, we define the dispersion and the nonlinear operators as follow:

$$
\hat{D} = -\frac{\alpha}{2}\psi - \left(\sum_{n \geq 2} \beta_n \frac{i^{n-1}}{n!} \frac{\partial^n}{\partial T^n}\right)\psi \tag{7}
$$

$$
\hat{N} = i\gamma\left(1 + \frac{1}{\omega_0}\frac{\partial}{\partial t}\right) \times \left((1 - f_R)\psi |\psi|^2 + f_R \psi \int_0^\infty h_R(\tau) |\psi(z, t - \tau)|^2 d\tau\right) \tag{8}
$$

The pulse envelope function ψ is transformed into an interaction picture representation ψ_I as follow:

$$
\psi_I = exp(-(z - z')\hat{D})\psi \tag{9}
$$

z' is the separation between the normal and the interaction pictures of ψ. The evolution of ψ_I with distance is expressed by:

$$
\frac{\partial \psi_I}{\partial z} = \hat{N}_I \psi_I \tag{10}
$$

With:

$$
\hat{N}_I = exp(-(z - z')\hat{D})\hat{N}exp(-(z - z')\hat{D}) \tag{11}
$$

$\hat{N}_I$ is the interaction picture representation of the nonlinear operator. The integration over one spatial step h, which advances $\psi(z, t)$ to $\psi(z + h, t)$ is written as:

$$
\psi_I = exp\left(\frac{h}{2}\hat{D}\right)\psi(z + h, t) \tag{12a}
$$

$$
k_1 = exp\left(\frac{h}{2}\hat{D}\right)[h\hat{N}\psi(z + h, t)]\psi(z + h, t) \tag{12b}
$$

$$
k_2 = h\hat{N}(\psi_I + k_1/2)[(\psi_I + k_1/2)] \tag{12c}
$$

$$
k_3 = h\hat{N}(\psi_I + k_2/2)[(\psi_I + k_2/2)] \tag{12d}
$$

$$
k_4 = h\hat{N}\left[\left(\frac{h}{2}\hat{D}\right)(\psi_I + k_3)\right] \times exp\left(\frac{h}{2}\hat{D}\right)[\psi_I + k_3] \tag{12e}
$$

$$
\psi(z + h, t) = exp\left(\frac{h}{2}\hat{D}\right)\left[\psi_I + \frac{k_1}{6} + \frac{k_2}{3} + \frac{k_3}{3}\right] + \frac{k_4}{6} \tag{12f}
$$

At each spatial step, eight Fast Fourier Transforms (FFTs) are required to compute four times the nonlinear operator $\hat{N}$ and the exponential dispersion operator $exp\left(\frac{h}{2}\hat{D}\right)$.

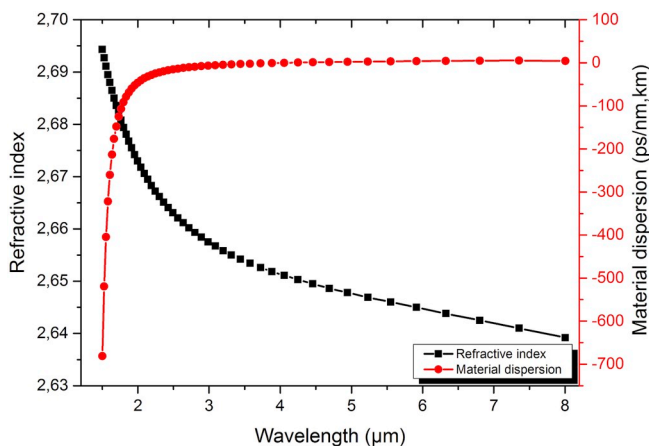Temporal coherence is a key parameter for many quantitative techniques. It allows the characterization of shot-to-shot spectral fluctuations of the generated SC [61]. The frequency dependence of coherence is evaluated by calculating the modulus of the complex degree of first order coherence as follow [20]:

$$
|g_{12}^{(1)}(\lambda, t_1 - t_2 = 0)| = \left|\frac{E_1^*(\lambda, t_1)E_2(\lambda, t_2)}{[|E_1(\lambda, t_1)^2||E_2(\lambda, t_2)^2|]^{1/2}}\right| \tag{13}
$$

The coherence is perfect if $|g_{12}^{(1)}| = 1$, which indicates that the electric fields of different realizations have an equal phase. Besides, we set $t_1 - t_2 = 0$ in order to address uniquely the wavelength dependence of coherence. Moreover, the coherence is assessed by considering a large number of numerical simulations with different random noise seed. Hereof, a semi-classical quantum noise based on One Photon Per Mode (OPPM) model is used [25]. For each numerical simulation of SC generation, the noise signal is added to the initial optical pulse in the frequency domain, and its expression is given by [25]:

$$
N_{OPPM}(\omega) = \sqrt{\frac{\hbar\omega}{\Delta\Omega}} exp(i2\pi\phi_m(\omega)) \tag{14}
$$

Where $\hbar$ is the reduced Planck constant, ω is the optical pulsation, $\Delta\Omega$ is the spectral bin size and $\phi(\omega)$ is a random phase uniformly distributed in the interval [0-2π].

3. Numerical results and discussion

In this study, our goal is to design and optimize a $Ge_{15}Sb_{15}Se_{70}$ ChG glass based CL-PCF in the aim to exhibit ANDi regime over the whole mid-infrared wavelength range. Afterwards, the SC generation is investigated and its characteristics including bandwidth, flatness and coherence are analyzed and optimized through a judicious adjustment of the initial optical pulse peak power and duration.

3.1. Geometrical optimization of the $Ge_{15}Sb_{15}Se_{70}$ CL-PCF

Aiming to realize ANDi profile, the CL-PCF geometrical parameters are tuned to down shift the dispersion of the $Ge_{15}Sb_{15}Se_{70}$ ChG glass [62]. Looking toward achieving this task, the design parameters of the proposed CL-PCF are rigorously adjusted through multiple numerical simulations considering different values of the air-filling fraction d/Λ. We consider a pitch with a fixed value of 2 μm and air holes diameter varying from 0.8 μm to 1.4 μm with a step of 0.2 μm. Accordingly, Maxwell's equations given by (2) are solved at each excitation wavelength from the range of 1 μm–8 μm and the fundamental guided mode characteristics are determined. Fig. 4 shows the variation of the mode effective index with wavelengths for different values of d. As seen from the figure, changing the air-filling fraction in the cladding has a strong impact on the fundamental mode guiding properties. The evolution of the calculated chromatic dispersion against wavelengths, for different air holes sizes is depicted in Fig. 5. The results clearly show the
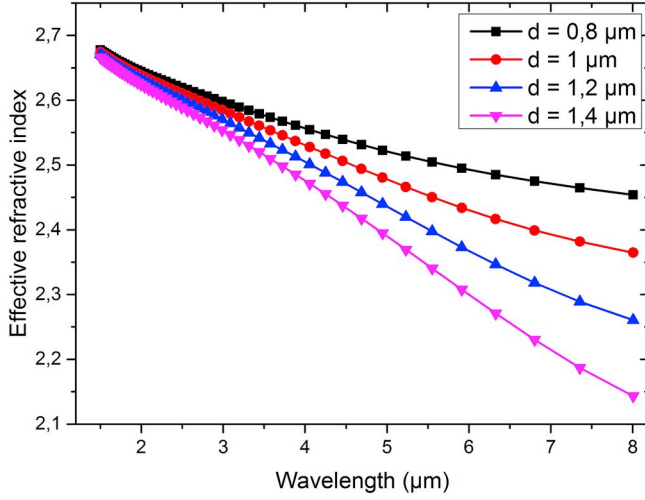
Fig. 4. Variation of the fundamental mode effective index with wavelengths for $\Lambda = 2\,\mu m$ and d varying from 0.8 μm to 1.4 μm with a step of 0.2 μm.
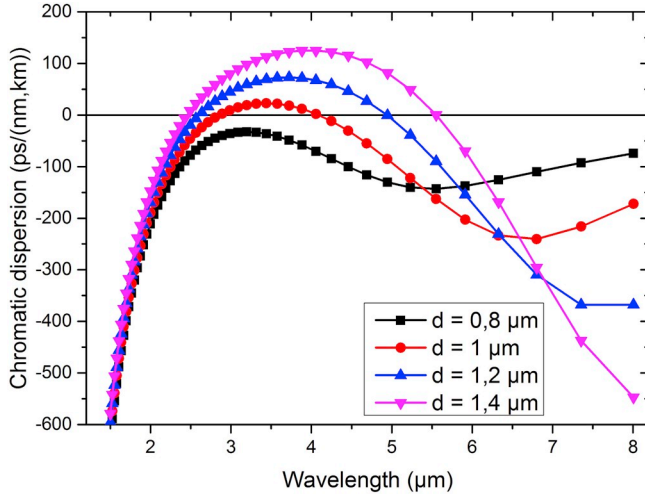
Fig. 5. Variation of the chromatic dispersion with wavelengths for $\Lambda = 2\,\mu m$ and d varying from 0.8 μm to 1.4 μm with a step of 0.2 μm.
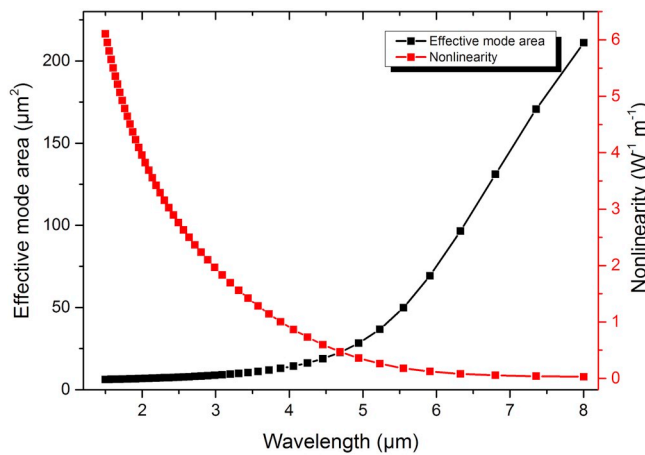
Fig. 6. Variation of the effective mode area and the Kerr nonlinear coefficient with wavelengths for $\Lambda = 2\,\mu m$ and $d = 0.8\,\mu m$.

influence of the variation of the value of d on the dispersion profile of the proposed CL-PCF. Besides, when d is reduced, the dispersion profile is down shifted and ANDi regime is successfully obtained for $d = 0.8\,\mu m$

(corresponding to air-filling fraction of $d/\Lambda = 0.4$) with a peak value of -35 ps/nm.km at the wavelength 3 μm. Furthermore, the fundamental mode effective area and the corresponding Kerr nonlinearity are calculated for $\Lambda = 2\,\mu m$ and $d = 0.8$, and their evolution versus wavelengths is depicted in Fig. 6. The CL-PCF shows high nonlinear parameter due to the reduced field mode area and the high nonlinear refractive index of the $Ge_{15}Sb_{15}Se_{70}$ ChG glass, and a Kerr coefficient of $1.96\,W^{-1}\,m^{-1}$ is obtained at the pump wavelength 3 μm.

3.2. SC generation in the $Ge_{15}Sb_{15}Se_{70}$ CL-PCF

Once the CL-PCF structure is optimized and ANDi regime is achieved, we have investigated SC generation by employing very low energy femtosecond laser pulses. The temporal shape of pulses is mathematically modelled through a hyperbolic secant function expressed as $\psi(t) = \sqrt{P_0}\,\mathrm{sech}(t/T_0)$ where, P_0 is the peak power and T_0 is the pulse duration given by $T_0 = T_{FWHM}/1.76$ where T_{FWHM} is the Full Width at Half Maximum (FWHM) temporal width of the optical pulse. The pulse energy is related to its peak power and FWHM as follow: $E = 0.88P_0 T_{FWHM}$. We consider the pumping at the wavelength 3 μm where the chromatic dispersion is close to the zero value. Such optical pulses can be generated using a degenerate sync-pumped subharmonic Optical Parametric Amplifier (OPA) as reported in Ref. [63]. The material loss is calculated from the experimental measurements of the Ga-Sb-S glass system transmission spectra [38]. For a sample thickness of 5.65 mm, the $Ge_{15}Sb_{15}Se_{70}$ ChG glass exhibits a good transparency of about 65% in the 1.5–10 μm wavelength range and hence an optical loss coefficient of 0.33 dB/mm is obtained. In order to precisely model the contribution of chromatic dispersion on pulses spectral broadening, we have computed its Taylor expansion coefficients β_n up to the 9th order at the central wavelength 3 μm. The calculated values of β_2 to β_9 are 170.5 ps²/km, 0.1363 ps³/km, 1.4268×10^{-2} ps⁴/km, -2.1377×10^{-4} ps⁵/km, 3.5763×10^{-6} ps⁶/km, -3.2604×10^{-8} ps⁷/km, -1.3991×10^{-9} ps⁸/km, 1.8872×10^{-11} ps⁹/km, respectively. Sight to accurately model pulses propagation inside the CL-PCF core, we have carefully adjusted the different parameters of numerical simulations. The GNLSE is solved by considering a local error of 10^{-3}, which is required to ensure stable numerical results and allow studying the different physical processes that contribute to the SC generation [55]. The CL-PCF length, over which pulses propagate, is segmented into 100 steps. Nevertheless, the implemented RK4IP algorithm employs an efficient adaptive step size method, which is required to, effectively, track the balance between the linear and nonlinear optical effects and achieve high computational accuracy [64,65]. Finally, the simulation temporal window is set to be 10 ps and both of the time and frequency windows are discretized into 2^{12} bins. Firstly, and in order to identify the different mechanisms that are involved in the extreme spectral broadening of laser pulses, we have carried out a first simulation with an input pulse with a total energy of 800 pJ, corresponding to peak power and duration of 4.7 kW and 150 fs, respectively. Therefore, the corresponding dispersion length L_D, the nonlinear length L_{NL} and the soliton order N are computed as follow [37]: $L_D = T_0^2/|\beta_2| = 0.0425\,m$, $L_{NL} = 1/(\gamma P_0) = 1.08 \times 10^{-4}\,m$ and $N = \sqrt{L_D/L_{NL}} = 20$, respectively. Fig. 7 depicts pulse temporal and spectral evolution over 1 cm of the CL-PCF length and the input and the output pulse profiles in the time and frequency domains, respectively. In the initial stage of the spectral broadening, the SPM plays the major role by generating, simultaneously, red-shift and blue-shift wavelength components near the leading and trailing pulse spectrum edges, respectively [66]. The generated SC is symmetric and shows an oscillatory structure in its top where the most intense peaks are located in its both wings. The instantaneous frequency shift (chirp) experienced by optical pulses due to SPM can be calculated as follow [20,67]:

$$\omega_c(z, t) = \frac{2\beta_2 z}{T_0^3}\left(\frac{\gamma P_0 T_0^2}{\beta_2} + 1\right)tanh\left(\frac{t}{T_0}\right)sech^2\left(\frac{t}{T_0}\right)$$

(15)
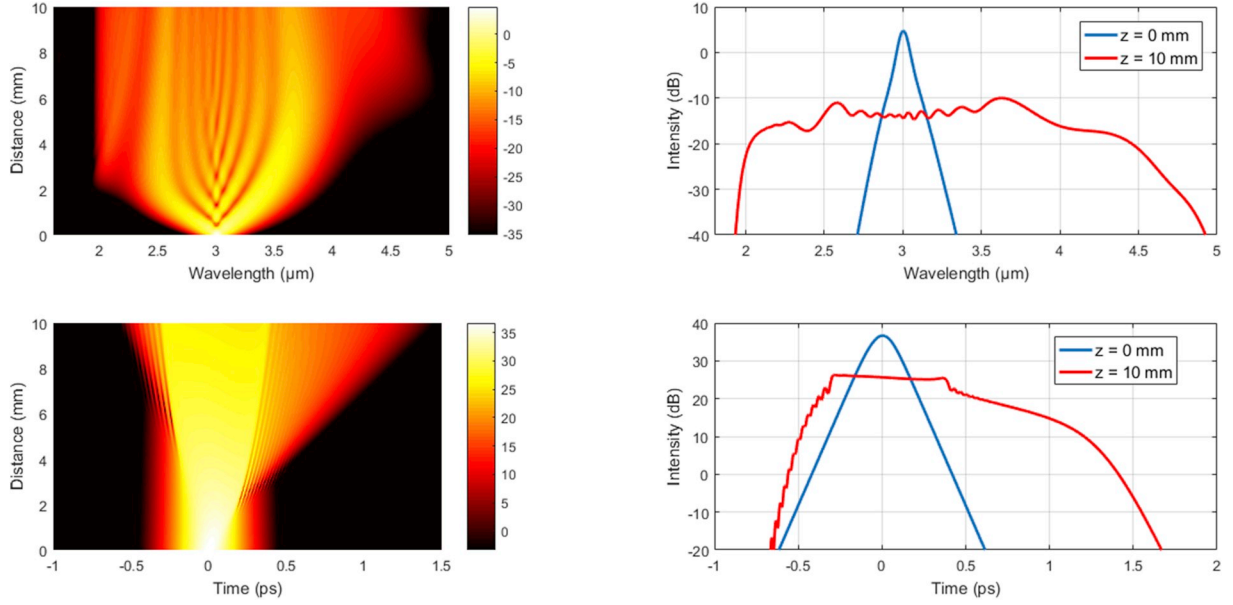
Fig. 7. Pulse spectral and temporal evolution with propagation distance and the input and output pulse spectral and temporal profiles for an initial T_{FWHM} of 150 fs and total energy of 800 pJ.
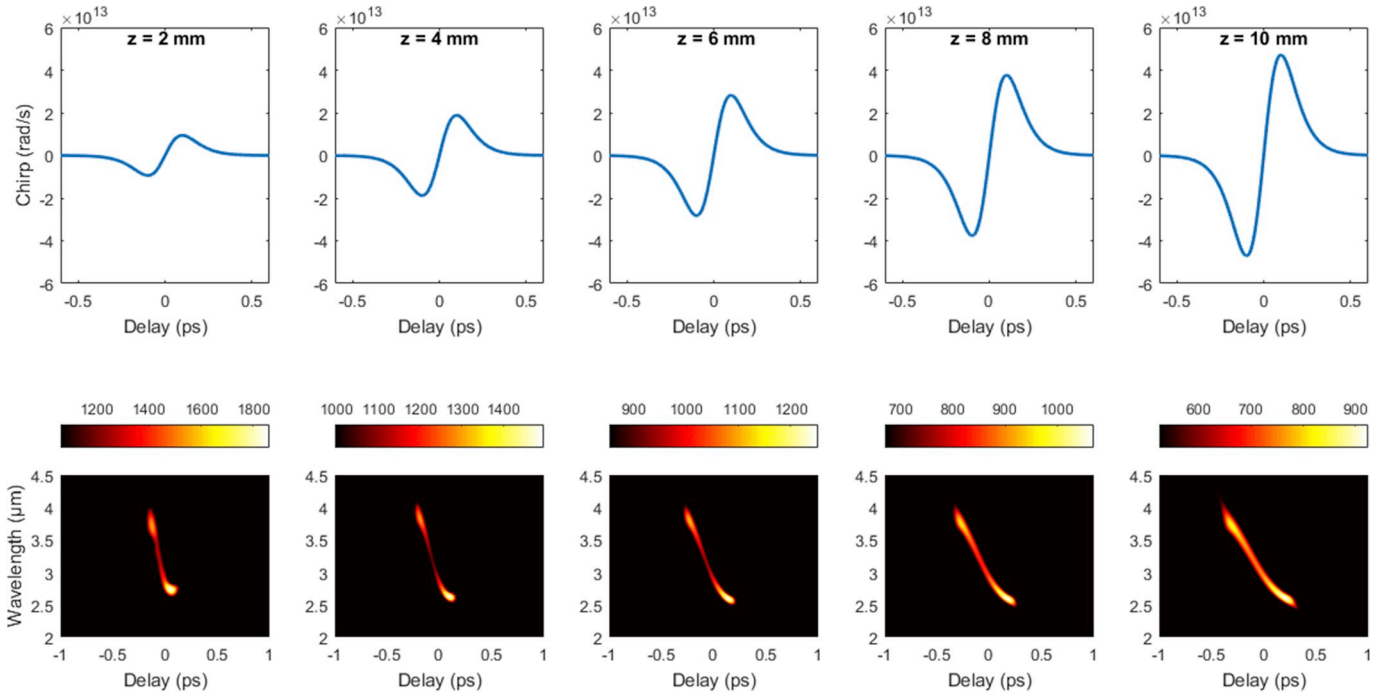
Fig. 8. Pulse spectrograms and the calculated frequency chirp after 2 mm, 4 mm, 6 mm, 8 mm and 10 mm of propagation, respectively, for an initially pumped pulse with a duration and total energy of 150 fs and 800 pJ.

Where z is the propagation distance. Fig. 8 gives the computed pulse spectrogram and the SPM induced chirp after the propagation over 2 mm, 4 mm, 6 mm, 8 mm and 10 mm of the fiber length, respectively. As it can be seen, SPM introduces a linear variation with time to the pulse instantaneous frequency, which lead to the typical S-shape of pulse spectrogram and preserve its integrity (no fission is occurred) [68]. Soon afterwards, OWB mechanism arises due to the self-steepening and third order dispersion [66]. It results from the overlapping of the optical pulse chirped middle section with the unchirped section, which trigger the generation of new wavelength components through the Four Wave Mixing (FWM) process [69,70]. Moreover, OWB starts to appear at the distance Z_{OWB} given by Ref. [71]:

$$L_{OWB} = \sqrt{\frac{3\beta_2}{2\beta_2 + 2\gamma P_0 T_0^2}} \frac{T_0^2}{\beta_2}$$

(16)

In our simulation we have $\beta_2 = 170.5 \, ps^2/$km, $\gamma = 1.96 \, w^{-1} \, m^{-1}$, $P_0 = 4.7$ kW and $T_0 = 85.22$ fs, hence, the OWB distance is found to be 2.63 mm. Besides the occurrence of OWB has a beneficial impact since it enhances the flatness of the generated SC central part, obtained as a result of a nearly linear dissemination of the instantaneous frequency over the output pulse [66]. Furthermore, the coherence properties of the generated SC are evaluated. Fig. 9 shows the evolution of $|g_{12}^{(1)}|$ with propagation distance, calculated from an ensemble of 20 independent numerical realizations. Both of the deterministic nature and noise
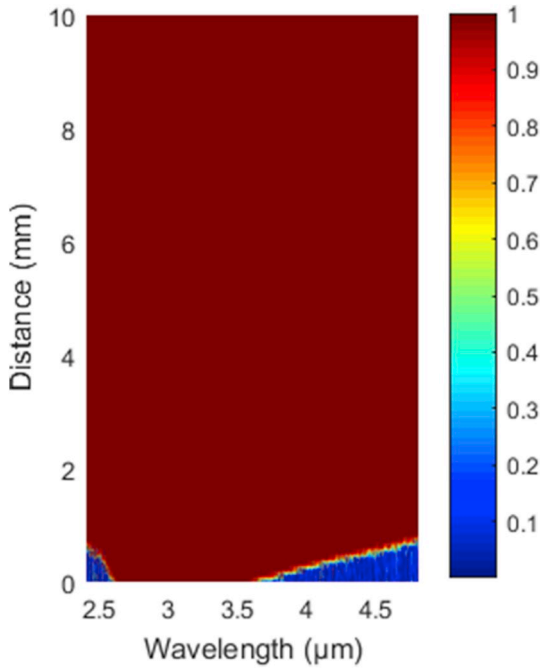
Fig. 9. Evolution of coherence with the propagation distance for an initial T_{FWHM} of 150 fs and total energy of 800 pJ.

insensitivity of SPM and OWB allow the generation of highly coherent SC across the entire wavelength range. According to the obtained results, intrapulse Raman scattering has no determining impact on the SC generation process. To endorse this assumption, we have simulated SC generation and suppressing the Raman contribution from the GNLSE. Fig. 10 depicts the pulse spectral and temporal evolution with distance and the output pulse spectral and temporal profiles with and without taking into account the Raman term. During the SC formation, the intrapulse Raman scattering is suppressed by SPM and OWB due to the short pulse duration and the short propagation distance [72]. The impact of the initial pulse parameters on the generated SC bandwidth and

flatness is investigated. The influence of pulse duration is firstly studied. Fig. 11 gives the output pulse spectrogram, the generated SC and the calculated coherence for an initial pulse with a total energy of 800 pJ and duration of 150 fs, 100 fs and 50 fs, respectively. As shown in the figure, when the pulse duration is decreased, the ripples on the top of the output spectrum are vanished and the generated SC broadens to reach a bandwidth of 4.05 μm spanning the region from 1.75 μm to 5.8 μm at the spectral flatness of 3.5 dB. Furthermore, the effect of varying the pulse energy is examined. Fig. 12 shows the output pulse spectrogram, the generated SC and the calculated coherence for an initial pulse with duration of 50 fs and total energy of 600 pJ, 800 pJ and 1 nJ, respectively. By increasing the input pulse energy, the generated SC bandwidth increases too with a negative impact on the spectrum flatness. Hence, a SC bandwidth of 3.49 μm extending from 1.86 μm to 5.35 μm at a spectral flatness less than 3 dB is achieved with a pulse energy of 600 pJ. When the pulse energy is increased to reach 1 nJ, the SC spectrum is extended to a wider range spanning the region from 1.67 μm to 6.2 μm (4.53 μm) at 4 dB spectral dynamics.

A comparison of the achieved SC performance with respect to other SC sources realized with various designs of ChG based ANDi PCFs, is summarized in Table 1. It is clear that our proposed $Ge_{15}Sb_{15}Se_{70}$ CL-PCF shows high potentiality to generate broadband and ultraflat-top mid-infrared SC, realized by pumping very low energy laser pulses.

Owing to its remarkable properties, the SC laser source based on the proposed $Ge_{15}Sb_{15}Se_{70}$ ChG glass CL-PCF is found suitable for numerous applications, notably for OCT imaging systems [78]. OCT is an interferometric non-destructive probing technique that has been widely used in various medical fields for early disease diagnosis in cardiology, ophthalmology and dermatology [79,80]. A key factor for characterizing an OCT system performances is the axial resolution, which is related to the coherence length of the SC source as follow [79]:

$$L_c = 0.441 \frac{\lambda_c^2}{\Delta \lambda} \tag{17}$$

Where λ_c and $\Delta\lambda$ are the central wavelength and spectral bandwidth of the light source, respectively. Accordingly, high axial resolution is realized by employing ultrabroadband SC source operating at short wavelengths. Fig. 13 depicts the evolution of the generated SC
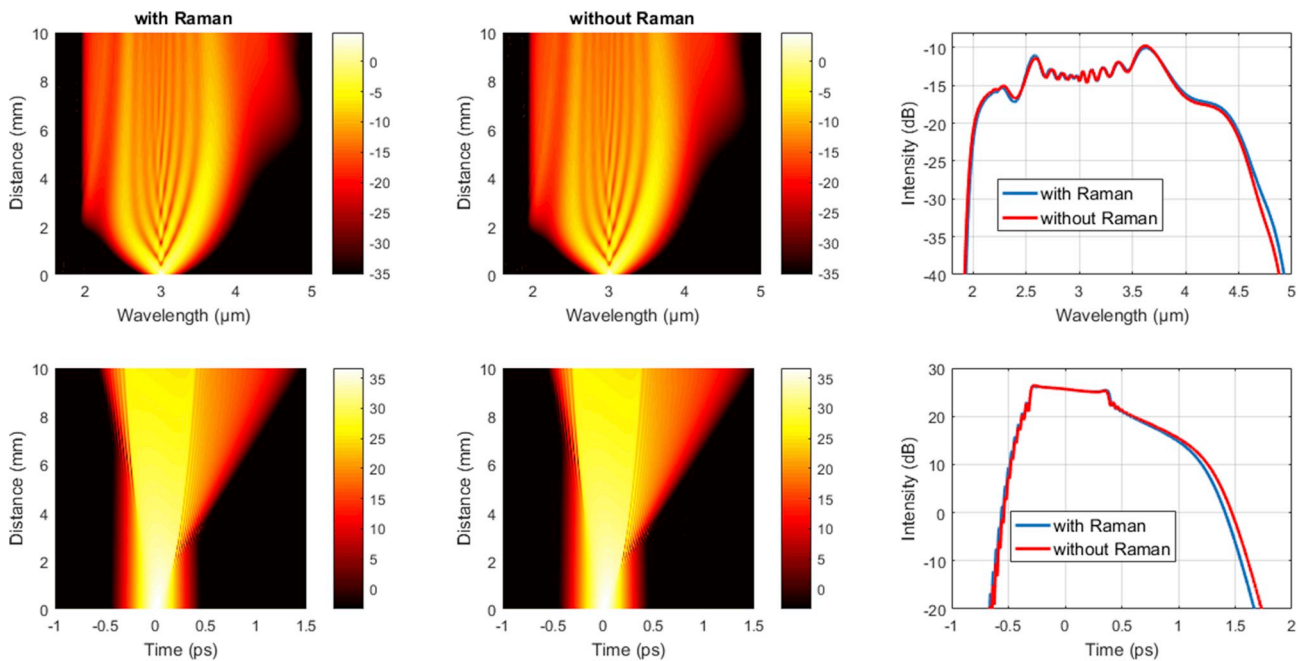
Fig. 10. Pulse temporal and spectral evolution with propagation distance and the output pulse spectral and temporal profiles with all nonlinear effects included and without stimulated Raman scattering term.
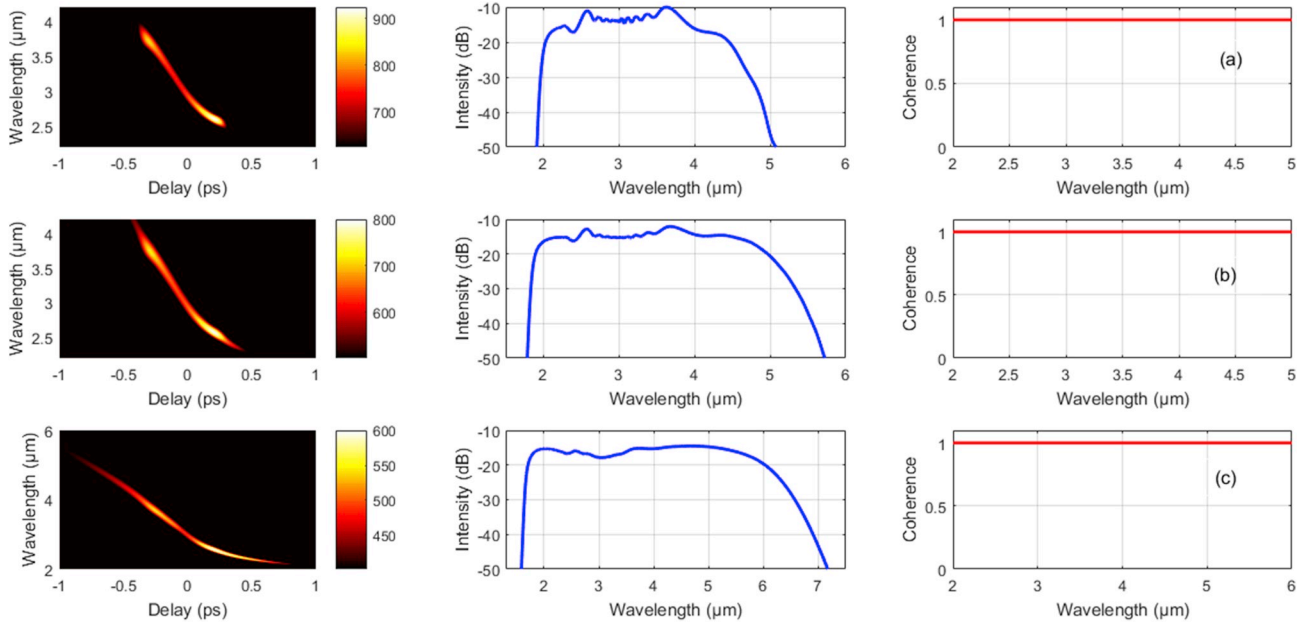
Fig. 11. Pulse spectrogram and output spectrum after propagation over CL-PCF length of 10 mm and the corresponding coherence for an input pulse with a total energy of 800 pJ and T_{FWHM} of 150 fs (a), 100 fs (b) and 50 fs (c), respectively.
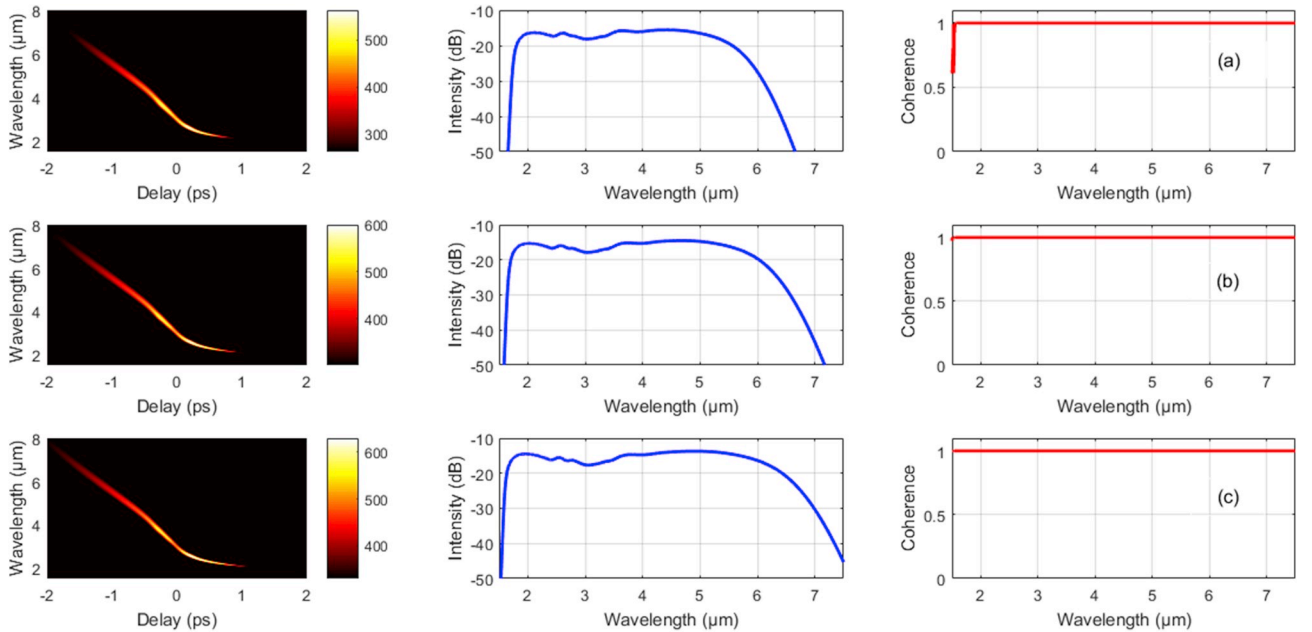
Fig. 12. Pulse spectrogram and spectrum after propagation over CL-PCF length of 10 mm and the corresponding coherence for an input pulse with T_{FWHM} of 50 fs and a total energy of 600 pJ (a), 800 pJ (b) and 1 nJ (c), respectively.

bandwidth and the corresponding coherence length with pumping pulse energy, for an input pulse duration of 50 fs. We clearly observe that the coherence length decreases when the spectral bandwidth of the SC source increases. Moreover, ultrahigh resolution depth is achieved with a coherence length of 0.87 μm for an input pulse energy of 1 nJ. Besides, the flattened shape of the optimized SC source ensures high image contrast through the suppression of side lobes, which make it advantageous compared to other broadband sources such as multiplexed Super-Luminescent Diodes (SLDs) [79].

4. Conclusion

In this work, we have numerically investigated mid-infrared SC generation in normally dispersive CL-PCF made of non-toxic $Ge_{15}Sb_{15}Se_{70}$ ChG glass. The chromatic dispersion is engineered through a fine adjustment of the cladding air-filling fraction and ANDi regime over the mid-infrared region is obtained with a cladding pitch and air holes diameter of $\Lambda = 2$ μm and d = 0.8 μm, respectively. Besides, the proposed CL-PCF exhibits low effective mode area and high Kerr nonlinearity coefficient up to 1.96 $W^{-1} m^{-1}$ at 3 μm. The SC generation has been simulated in the optimized design by solving the GNLSE and employing the RK4IP method. We have identified the SPM and OWB as the main contributors to the SC generation process. Moreover, numerical results show that pumping 0.6 nJ energy and 50 fs duration laser pulses at 3 μm, generates highly coherent, ultraflat and broadband SC spanning the region from 1.86 μm to 5.35 μm with spectral level less

Table 1

Comparison of the SC generated in the proposed $Ge_{15}Sb_{15}Se_{70}$ ANDi CL-PCF against other recent ChG PCF designs.

Reference	Chalcogenide material	Pump wavelength (µm)	Spectral flatness	SC bandwidth (µm)
[30]	As_2Se_3	4.37	3 dB	3.86–5.95
[20]	$As_{39}Se_{61}$	3.45	4 dB	2.43–4.85
[34]	GeAsSe-AsSe	2.08	3 dB	1.92–2.34
[73]	$Ge_{11.5}As_{24}Se_{64.5}$	3.1	10 dB	2–5.5
[74]	As_2S_5-Borosilicate	2.5	8 dB	1.05–5.05
[75]	$As_{38.8}Se_{61.2}$	3.7	3 dB	2.9–4.57
[76]	As_2Se_3	4.357	20 dB	3.89–4.92
[77]	As_2S_3-Borosilicate	2.8	20 dB	2.41–3.15
The present work	$Ge_{15}Sb_{15}Se_{70}$	3	< 3 dB	1.86–5.35
The present work	$Ge_{15}Sb_{15}Se_{70}$	3	4 dB	1.67–6.2
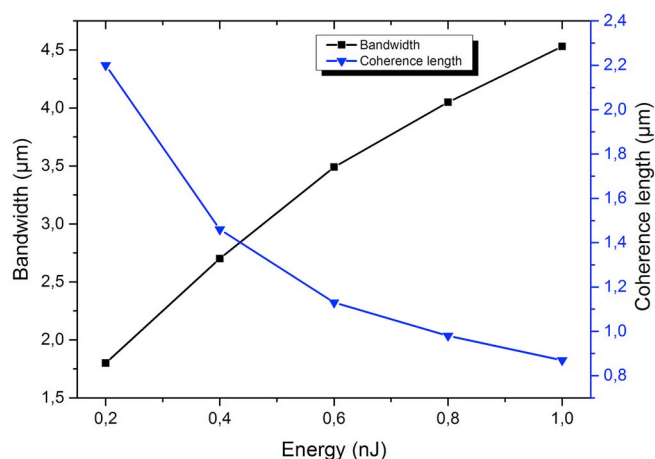
Fig. 13. Evolution of the generated SC bandwidth and coherence length with the input pulse enrgy.

than 3 dB. By increasing the initial energy to reach 1 nJ, the generated SC bandwidth increases too and reach 4.53 µm in the wavelength range extending from 1.67 µm to 6.2 µm at the spectral level 4 dB. Furthermore, we have shown that our proposed SC source has a potential application for OCT imaging systems. We have theoretically demonstrated that our broadband SC source design with the spectral bandwidth of 4.53 µm achieves high-resolution depth with a coherence length as low as 0.87 µm.

Declaration of competing interest

The authors declare that they have no known competing financial interests or personal relationships that could have appeared to influence the work reported in this paper.

References

[1] A. Dubietis, A. Couairon, G. Genty, Supercontinuum generation: introduction, J. Opt. Soc. Am. B. 36 (2019) SG1, https://doi.org/10.1364/josab.36.000sg1.

[2] M. Vainio, L. Halonen, Mid-infrared optical parametric oscillators and frequency combs for molecular spectroscopy, Phys. Chem. Chem. Phys. 18 (2016) 4266–4294, https://doi.org/10.1039/c5cp07052j.

[3] A.B. Seddon, B. Napier, I. Lindsay, S. Lamrini, P.M. Moselund, N. Stone, O. Bang, M. Farries, Prospective on using fibre mid-infrared supercontinuum laser sources for in vivo spectral discrimination of disease, Analyst 143 (2018) 5874–5887, https://doi.org/10.1039/c8an01396a.

[4] M. Falconieri, M. Marrocco, C. Merla, S. Gagliardi, F. Rondino, M. Ghezelbash, Characterization of supercontinuum generation in a photonic crystal fiber for uses in multiplex CARS microspectroscopy, J. Raman Spectrosc. (2019) 1–9, https://doi.org/10.1002/jrs.5599.

[5] A. Lemière, F. Désévédavy, B. Kibler, P. Mathey, G. Gadret, J.C. Jules, C. Aquilina, P. Béjot, F. Billard, O. Faucher, F. Smektala, Mid-infrared two-octave spanning supercontinuum generation in a Ge-Se-Te glass suspended core fiber, Laser Phys. Lett. 16 (2019) 075402 https://doi.org/10.1088/1612-202X/ab2053.

[6] D. Grassani, E. Tagkoudi, H. Guo, C. Herkommer, F. Yang, T.J. Kippenberg, C.S. Brès, Mid infrared gas spectroscopy using efficient fiber laser driven photonic chip-based supercontinuum, Nat. Commun. 10 (2019), https://doi.org/10.1038/s41467-019-09590-3.

[7] N.M. Israelsen, C.R. Petersen, A. Barh, D. Jain, M. Jensen, G. Hannesschläger, P. Tidemand-Lichtenberg, C. Pedersen, A. Podoleanu, O. Bang, Real-time high-resolution mid-infrared optical coherence tomography, Light Sci. Appl. 8 (2019), https://doi.org/10.1038/s41377-019-0122-5.

[8] M. Jensen, I.B. Gonzalo, R.D. Engelsholm, M. Maria, N.M. Israelsen, A. Podoleanu, O. Bang, Noise of supercontinuum sources on spectral domain optical coherence tomography, J. Opt. Soc. Am. B. 36 (2019) A154, https://doi.org/10.1364/JOSAB.36.00A154.

[9] A.V. Paterova, H. Yang, C. An, D.A. Kalashnikov, L.A. Krivitsky, Tunable optical coherence tomography in the infrared range using visible photons, Quantum Sci. Technol. 3 (2018), https://doi.org/10.1088/2058-9565/aab567.

[10] A. Robert, R. Alfano, The Supercontinuum Laser Source: the Ultimate White Light, third ed., Springer, 2016, https://doi.org/10.1007/978-1-4939-3326-6.

[11] J.M. Dudley, J.R. Taylor, Supercontinuum Generation in Optical Fibers, Cambridge university press, 2010, https://doi.org/10.1017/CBO9780511750465.

[12] A.I. Adamu, Md S. Hbib, C.R. Petersen, J.E.A. Lopez, B. Zhou, A. Schülzgen, M. Bache, R. Amezcua-Correra, O. Bang, C. Markos, Deep-uv to mid-IR supercontinuum generation driven by mid-IR ultrashort pulses in a gas-filled hollow-core fiber, Sci. Rep. 9 (1) (2019) 4446, https://doi.org/10.1038/s41598-019-39302-2.

[13] A. Dubietis, A. Couairon, Ultrafast Supercontinuum Generation in Transparent Solid-State Media, Springer, 2019, https://doi.org/10.1007/978-3-030-14995-6.

[14] A. Marcinkevičiūtė, V. Jukna, R. Šuminas, N. Garejev, G. Tamošauskas, A. Dubietis, Femtosecond filamentation and supercontinuum generation in bulk silicon, Opt. Lett. 44 (2019) 1343–1346, https://doi.org/10.1364/ol.44.001343.

[15] M. Vengris, N. Garejev, G. Tamošauskas, A. Čepėnas, L. Rimkus, A. Varanavičius, V. Jukna, A. Dubietis, Supercontinuum generation by co-filamentation of two color femtosecond laser pulses, Sci. Rep. 9 (2019) 9011, https://doi.org/10.1038/s41598-019-45357-y.

[16] T.S. Saini, N.P.T. Hoa, L. Xing, T.H. Tuan, T. Suzuki, Y. Ohishi, Chalcogenide W-type co-axial optical fiber for broadband highly coherent mid-IR supercontinuum generation, J. Appl. Phys. 124 (2018) 213101, https://doi.org/10.1063/1.5062591.

[17] T.S. Saini, T.H. Tuan, L. Xing, N.P.T. Hoa, T. Suzuki, Y. Ohishi, Coherent mid-infrared supercontinuum spectrum using a step-index tellurite fiber with all-normal dispersion, Appl. Phys. Express 11 (2018) 102501, https://doi.org/10.7567/APEX.11.10250.

[18] T.S. Saini, N.P.T. Hoa, T.H. Tuan, X. Luo, T. Suzuki, Y. Ohishi, Tapered tellurite step-index optical fiber for coherent near-to-mid-IR supercontinuum generation: experiment and modeling, Appl. Opt. 58 (2) (2019) 415–421, https://doi.org/10.1364/AO.58.000415.

[19] S. Dai, Y. Wang, X. Peng, P. Zhang, X. Wang, Y. Xu, A review of mid-infrared supercontinuum generation in chalcogenide glass fibers, Appl. Sci. 8 (2018) 707, https://doi.org/10.3390/app8050707.

[20] A. Medjouri, D. Abed, Design and modelling of all-normal dispersion $As_{39}Se_{61}$ chalcogenide photonic crystal fiber for flat-top coherent mid-infrared supercontinuum generation, Opt. Fiber Technol. 50 (2019) 154–164, https://doi.org/10.1016/j.yofte.2019.03.021.

[21] J. Troles, L. Brilland, C. Caillaud, J.-L. Adam, Original designs of chalcogenide microstuctured optical fibers, Adv. Device Mater. 3 (2017) 7–13, https://doi.org/10.1080/20550308.2017.1312053.

[22] C. Markos, J.C. Travers, A. Abdolvand, B.J. Eggleton, O. Bang, Hybrid photonic-crystal fiber, Rev. Mod. Phys. 89 (4) (2017) 045003, , https://doi.org/10.1103/RevModPhys.89.045003.

[23] H.P.T. Nguyen, T.H. Tong, T.S. Saini, X. Luo, T. Suzuki, Y. Ohishi, Highly coherent supercontinuum generation in a tellurite all-solid hybrid microstructured fiber pumped at 2 micron, Appl. Phys. Express 4 (12) (2019) 059401, , https://doi.org/10.7567/1882-0786/ab0aac.

[24] I.B. Gonzalo, R.D. Engelsholm, M.P. Sørensen, O. Bang, Polarization noise places severe constraints on coherence of all-normal dispersion femtosecond supercontinuum generation, Sci. Rep. 8 (2018) 6579, https://doi.org/10.1038/s41598-018-24691-7.

[25] E. Genier, P. Bowen, T. Sylvestre, J.M. Dudley, P. Moselund, O. Bang, Amplitude noise and coherence degradation of femtosecond supercontinuum generation in all-normal-dispersion fibers, J. Opt. Soc. Am. B. 36 (2019) A161, https://doi.org/10.1364/JOSAB.36.00A161.

[26] S. Rao D. S, R.D. Engelsholm, I.B. Gonzalo, B. Zhou, P. Bowen, P.M. Moselund, O. Bang, M. Bache, Ultra-low-noise supercontinuum generation with a flat near-zero normal dispersion fiber, Opt. Lett. 44 (2019) 2216, https://doi.org/10.1364/OL.44.002216.

[27] C. Goncalves, M. Kang, B.-U. Sohn, G. Yin, J. Hu, D. Tan, K. Richardson, New candidate multicomponent chalcogenide glasses for supercontinuum generation, Appl. Sci. 8 (2018) 2082, https://doi.org/10.3390/app8112082.

[28] D. Jayasuriya, C.R. Petersen, D. Furniss, C. Markos, Z. Tang, M.S. Habib, O. Bang, T.M. Benson, A.B. Seddon, Mid-IR supercontinuum generation in birefringent, low loss, ultra-high numerical aperture Ge-As-Se-Te chalcogenide step-index fiber, Opt. Mater. Express. 9 (2019) 2617, https://doi.org/10.1364/ome.9.002617.

[29] A. Viswanathan, S. Thomas, Tunable linear and non linear optical properties of GeSeSb chalcogenide glass with solute concentration and with silver doping, J. Alloy. Comp. 798 (2019) 424–430, https://doi.org/10.1016/j.jallcom.2019.05.261.

[30] E. Wang, J. Li, J. Li, Q. Cheng, X. Zhou, H. Jiang, Flattened and broadband mid-infrared super-continuum generation in As_2Se_3 based holey fiber, Opt. Quant. Electron. 51 (2019) 1–13, https://doi.org/10.1007/s11082-018-1722-7.

[31] H.P.T. Nguyen, K. Nagasaka, T.H. Tuan, T.S. Saini, X. Luo, T. Suzuki, Y. Ohishi, Highly coherent supercontinuum in the mid-infrared region with cascaded tellurite and chalcogenide fibers, Appl. Opt. 57 (2018) 6153, https://doi.org/10.1364/ao.57.006153.

[32] K. Nagasaka, L. Liu, T.H. Tuan, T. Cheng, M. Matsumoto, H. Tezuka, T. Suzuki, Y. Ohishi, Numerical investigation of highly coherent mid-infrared supercontinuum generation in chalcogenide double-clad fiber, Opt. Fiber Technol. 36 (2017) 82–91, https://doi.org/10.1016/j.yofte.2017.03.002.

[33] L. Liu, T. Cheng, K. Nagasaka, H. Tong, G. Qin, T. Suzuki, Y. Ohishi, Coherent mid-infrared supercontinuum generation in all-solid chalcogenide microstructured fibers with all-normal dispersion, Opt. Lett. 41 (2016) 392, https://doi.org/10.1364/ol.41.000392.

[34] S. Xing, S. Kharitonov, J. Hu, C.-S. Brès, Linearly chirped mid-infrared supercontinuum in all-normal-dispersion chalcogenide photonic crystal fibers, Opt. Express. 26 (2018) 19627, https://doi.org/10.1364/oe.26.019627.

[35] M.R. Karim, H. Ahmad, B.M.A. Rahman, Design and modeling of dispersion-engineered all-chalcogenide triangular-core fiber for mid-infrared-region supercontinuum generation, J. Opt. Soc. Am. B 35 (2018) 266, https://doi.org/10.1364/josab.35.000266.

[36] T.S. Saini, A. Kumar, R.K. Sinha, Broadband mid-infrared supercontinuum spectra spanning 2-15 μm using As_2Se_3 chalcogenide glass triangular-core graded-index photonic crystal fiber, J. Light. Technol. 33 (18) (2015) 3914–3920, https://doi.org/10.1109/JLT.2015.2418993.

[37] A. Medjouri, D. Abed, Z. Becer, Numerical investigation of a broadband coherent supercontinuum generation in $Ga_8Sb_{32}S_{60}$ chalcogenide photonic crystal fiber with all-normal dispersion, Opto-Electron. Rev. 27 (2019) 1–9, https://doi.org/10.1016/j.opelre.2019.01.003.

[38] B. Zhang, Y. Yu, C. Zhai, S. Qi, Y. Wang, A. Yang, X. Gai, R. Wang, Z. Yang, B. Luther-Davies, Y. Xu, High brightness 2.2–12 μm mid-infrared supercontinuum generation in a nontoxic chalcogenide step-index fiber, J. Am. Ceram. Soc. 99 (2016) 2565–2568, https://doi.org/10.1111/jace.14391.

[39] H. Ou, S. Dai, P. Zhang, Z. Liu, X. Wang, F. Chen, H. Xu, B. Luo, Y. Huang, R. Wang, Ultrabroad supercontinuum generated from a highly nonlinear Ge–Sb–Se fiber, Opt. Lett. 41 (2016) 3201, https://doi.org/10.1364/ol.41.003201.

[40] W.H. Wei, L. Fang, X. Shen, R.P. Wang, Crystallization kinetics and thermal stability in Ge-Sb-Se glasses, Phys. Status Solidi B. 250 (2012) 59–64, https://doi.org/10.1002/pssb.201248284.

[41] M.A. Khamis, R. Sevilla, K. Ennser, Design of W-type index chalcogenide fiber for highly coherent mid-IR supercontinuum generation, J. Light. Technol. 36 (2018) 5388–5394, https://doi.org/10.1109/JLT.2018.2873589.

[42] Y. Yuan, K. Xia, Y. Wang, Z. Liu, N. Zhang, J. Su, L. Jiang, P. Zhang, S. Dai, Precision fabrication of a four-hole $Ge_{15}Sb_{15}Se_{70}$ chalcogenide suspended-core fiber for generation of a 15-12 μm ultrabroad mid-infrared supercontinuum, Opt. Mater. Express. 9 (2019) 2196, https://doi.org/10.1364/ome.9.002196.

[43] J. Lou, T. Cheng, S. Li, High sensitivity photonic crystal fiber sensor based on dual-core coupling with circular lattice, Opt. Fiber Technol. 48 (2019) 110–116, https://doi.org/10.1016/j.yofte.2018.12.023.

[44] J. Han, E. Liu, J. Liu, Circular gradient-diameter photonic crystal fiber with large mode area and low bending loss, J. Opt. Soc. Am. A 36 (2019) 533–539, https://doi.org/10.1364/JOSAA.36.000533.

[45] H. Pakarzadeh, V. Sharif, Control of orbital angular momentum of light in opto-fluidic infiltrated circular photonic crystal fibers, Opt. Commun. 438 (2019) 18–24, https://doi.org/10.1016/j.optcom.2019.01.007.

[46] A. Medjouri, L.M. Simohamed, O. Ziane, A. Boudrioua, Z. Becer, Design of a circular photonic crystal fiber with flattened chromatic dispersion using a defected core and selectively reduced air holes: application to supercontinuum generation at 1.55 μm, Photonics Nanostructures - Fundam, Appl 16 (2015) 43–50, https://doi.org/10.1016/j.photonics.2015.08.004.

[47] Z. Zhu, T. Brown, Full-vectorial finite-difference analysis of microstructured optical fibers, Opt. Express. 10 (2002) 853–864 doi:https://doi.org/10.1364/OE.10.000853.

[48] S. Guo, F. Wu, S. Albin, H. Tai, R.S. Rogowski, Loss and dispersion analysis of microstructured fibers by finite-difference method, Opt. Express. 12 (2004) 3341–3352, https://doi.org/10.1364/opex.12.003341.

[49] T. Wang, X. Gai, W. Wei, R. Wang, Z. Yang, X. Shen, S. Madden, B. Luther-Davies, Systematic z-scan measurements of the third order nonlinearity of chalcogenide glasses, Opt. Mater. Express. 4 (2014) 1011–1022, https://doi.org/10.1364/ome.4.001011.

[50] T. Huang, Q. Wei, Z. Wu, X. Wu, P. Huang, Z. Cheng, P. Shum, Ultra-flattened normal dispersion fiber for supercontinuum and dissipative soliton resonance generation at 2 μm, IEEE Photonics J 0655 (2019) 7101511, https://doi.org/10.1109/jphot.2019.2915265.

[51] M.R. Karim, B.M.A. Rahman, G.P. Agrawal, Dispersion engineered $Ge_{11.5}As_{24}Se_{64.5}$ nanowire for supercontinuum generation: a parametric study, Opt. Express. 22 (2014) 31029–31040, https://doi.org/10.1364/oe.22.031029.

[52] W. Gao, M. El Amraoui, M. Liao, H. Kawashima, Z. Duan, D. Deng, T. Cheng, T. Suzuki, Y. Messaddeq, Y. Ohishi1, Mid-infrared supercontinuum generation in a suspended-core As_2S_3 chalcogenide microstructured optical fiber, Opt. Express. 21 (2013) 9573–9583, https://doi.org/10.1364/OE.21.009573.

[53] C.R. Petersen, R.D. Engelsholm, C. Markos, L. Brilland, C. Caillaud, J. Trolès, O. Bang, Increased mid-infrared supercontinuum bandwidth and average power by tapering large-mode-area chalcogenide photonic crystal fibers, Opt. Express 25 (2017) 15336–15348, https://doi.org/10.1364/OE.25.015336.

[54] G. Agrawal, Nonlinear Fiber Optics, Elsevier, 978-0-12-397023-7, 2013.

[55] J. Hult, A fourth-order Runge-Kutta in the interaction picture method for simulating supercontinuum generation in optical fibers, J. Light. Technol. 25 (2007) 3770–3775, https://doi.org/10.1109/JLT.2007.909373.

[56] C.M. Savage, N.P. Robins, J.J. Hope, Bose-Einstein condensate collapse: a comparison between theory and experiment, Phys. Rev. A 67 (2003) 014304, , https://doi.org/10.1103/PhysRevA.67.014304.

[57] M. Brehler, M. Schirwon, D. Göddeke, P.M. Krummrich, A GPU-accelerated fourth-order Runge-Kutta in the interaction picture method for the simulation of nonlinear signal propagation in multimode fibers, J. Light. Technol. 35 (2017) 3622–3628, https://doi.org/10.1109/JLT.2017.2715358.

[58] A.A. Rieznik, A.M. Heidt, P.G. König, V.A. Bettachini, D.F. Grosz, Optimum integration procedures for supercontinuum simulation, IEEE Photonics J 4 (2012) 552–560, https://doi.org/10.1109/JPHOT.2012.2188281.

[59] P. Balla, G.P. Agrawal, Nonlinear interaction of vector solitons inside birefringent optical fibers, Phys. Rev. A 98 (2018) 1–9, https://doi.org/10.1103/PhysRevA.98.023822.

[60]] M. Brehler, M. Schirwon, P.M. Krummrich, D. Göddeke, Simulation of nonlinear signal propagation in multimode fibers on multi-GPU systems, http://arxiv.org/abs/1901.01895, (2019).

[61] G. Genty, M. Surakka, J. Turunen, A.T. Friberg, Complete characterization of supercontinuum coherence, J. Opt. Soc. Am. B. 28 (2011) 2301–2309, https://doi.org/10.1364/josab.28.002301.

[62] G. Dhanu Krishna, V.P. Mahadevan Pillai, K.G. Gopchandran, Design of low dispersion and low loss photonic crystal fiber: defected core circular-octagon hybrid lattices, Opt. Fiber Technol. 51 (2019) 17–24, https://doi.org/10.1016/j.yofte.2019.04.015.

[63] M.W. Haakestad, A. Marandi, N. Leindecker, K.L. Vodopyanov, Five-cycle pulses near λ = 3 μm produced in a subharmonic optical parametric oscillator via fine dispersion management, Laser Photonics Rev. 7 (6) (2013) L93–L97, https://doi.org/10.1002/lpor.201300112.

[64] A.M. Heidt, Efficient adaptive step size method for the simulation of supercontinuum generation in optical fibers, J. Light. Technol. 27 (2009) 3984–3991 https://doi.org/10.1109/JLT.2009.2021538.

[65] J. Wen, L. Duan, C. Ma, W. Fan, Numerical simulation and analysis of femtosecond pulse evolution in liquid-core photonic crystal fiber based on adaptive step-size methods, Opt. Quant. Electron. 51 (2019) 184, https://doi.org/10.1007/s11082-019-1906-9.

[66] N. Zhang, X. Peng, Y. Wang, S. Dai, Y. Yuan, J. Su, G. Li, P. Zhang, P. Yang, X. Wang, Ultrabroadband and coherent mid-infrared supercontinuum generation in Te-based chalcogenide tapered fiber with all-normal dispersion, Opt. Express. 27 (2019) 10311–10319, https://doi.org/10.1364/OE.27.010311.

[67] C. Finot, F. Chaussard, S. Boscolo, Simple guidelines to predict self-phase modulation patterns, J. Opt. Soc. Am. B 35 (2018) 3143–3152, https://doi.org/10.1364/josab.35.003143.

[68] C.V. Lanh, V.T. Hoang, V.C. Long, K. Borzycki, K.D. Xuan, V.T. Quoc, M. Trippenbach, R. Buczyński, J. Pniewski, Optimization of optical properties of photonic crystal fibers infiltrated with chloroform for supercontinuum generation, Laser Phys. 29 (2019) 075107 https://doi.org/10.1088/1555-6611/ab2115.

[69] C. Finot, B. Kibler, L. Provost, S. Wabnitz, Beneficial impact of wave-breaking for coherent continuum formation in normally dispersive nonlinear fibers, J. Opt. Soc. Am. B. 25 (2008) 1938–1948, https://doi.org/10.1364/josab.25.001938.

[70] W.J. Tomlinson, R.H. Stolen, A.M. Johnson, Optical wave breaking of pulses in nonlinear optical fibers, Opt. Lett. 10 (1985) 457–459, https://doi.org/10.1364/OL.10.000457.

[71] D. Anderson, M. Desaix, M. Lisak, M.L. Quiroga-Teixeiro, Wave breaking in non-linear-optical fibers, J. Opt. Soc. Am. B. 9 (1992) 1358–1361.

[72] L. Liu, T. Cheng, K. Nagasaka, H. Tong, G. Qin, T. Suzuki, Y. Ohishi, Coherent mid-infrared supercontinuum generation in all-solid chalcogenide microstructured fibers with all-normal dispersion, Opt. Lett. 41 (2016) 392–395, https://doi.org/10.1364/ol.41.000392.

[73] M.R. Karim, H. Ahmad, B.M.A. Rahman, All-normal dispersion chalcogenide PCF for ultraflat mid-infrared supercontinuum generation, IEEE Photonics Technol. Lett. 29 (21) (2017) 1792–1795, https://doi.org/10.1109/LPT.2017.2752214.

[74] A. Ben Salem, M. Diouf, R. Cherif, A. Wague, M. Zghal, Ultraflat-top mid-infrared coherent broadband supercontinuum using all normal As_2S_5-borosilicate hybrid photonic crystal fiber, Opt. Eng. 55 (6) (2016) 066109, , https://doi.org/10.1117/1.OE.55.6.066109.

[75] M. Diouf, A. Ben Salem, R. Cherif, H. Saghaei, A. Wague, Super-flat coherent supercontinuum source in $As_{38.8}Se_{61.2}$ chalcogenide photonic crystal fiber with all-normal dispersion engineering at a very low input energy, Appl. Opt. 56 (2) (2017) 163–169, https://doi.org/10.1364/AO.56.000163.

[76] J. Li, F. Zhao, Z. Hui, Mid-infrared supercontinuum generation in dispersion-engineered highly nonlinear chalcogenide photonic crystal fiber, Mod. Phys. Lett. B 33 (19) (2019), https://doi.org/10.1142/S0217984919502117.

[77] P. S Maji, P.R. Chaudhuri, Design of all-normal dispersion based on multimaterial photonic crystal fiber in IR region for broadband supercontinuum generation, Appl. Opt. 54 (13) (2015) 4042–4048, https://doi.org/10.1364/AO.54.004042.

[78] P. Wachulak, A. Bartnik, H. Fiedorowicz, Optical coherence tomography (OCT) with 2 nm axial resolution using a compact laser plasma soft X-ray source, Sci. Rep. 8 (2018) 8494, https://doi.org/10.1038/s41598-018-26909-0.

[79] X. Ji, A. Klenner, X. Yao, Y. Gan, A.L. Gaeta, C.P. Hendon, M. Lipson, Chip-based frequency combs sources for optical coherence tomography, Opt. Express. 27 (2019) 19896–19905 https://doi.org/10.1364/OE.27.019896.

[80] M.G.O. Gräfe, M. Gondre, J.F. de Boer, Precision analysis and optimization in phase decorrelation OCT velocimetry, Biomed. Opt. Express. 10 (2019) 1297–1314, https://doi.org/10.1364/BOE.10.001297.

Numerical investigation of a broadband coherent supercontinuum generation in $Ga_8Sb_{32}S_{60}$ chalcogenide photonic crystal fiber with all-normal dispersion

A. Medjouri [a],*, D. Abed [b], Z. Becer [a]

[a] LEVRES Laboratory, Faculty of Exact Sciences, University of Echahid Hamma Lakhdar EL Oued, BP 789, El Oued, 39000, Algeria
[b] Department of Electronics and Telecommunications, Faculty of Sciences and Technology, University of 8 mai 1945 Guelma, 24000, Guelma, Algeria

ABSTRACT

All normal dispersion (ANDi) and highly nonlinear chalcogenide glass photonic crystal fiber (PCF) is proposed and numerically investigated for a broad, coherent and ultra-flat mid-infrared supercontinuum generation. The proposed PCF consists of a solid core made of $Ga_8Sb_{32}S_{60}$ glass surrounded by seven rings of air holes arranged in a triangular lattice. We show by employing the finite difference frequency domain (FDFD) method that the $Ga_8Sb_{32}S_{60}$ PCF dispersion properties can be engineered by carefully adjusting the air holes diameter in the cladding region and ANDi regime is achieved over the entire range of wavelengths with a zero chromatic dispersion around 4.5 μm. Moreover, we demonstrate that injecting 50 fs width and 20 kW peak power laser pulses (corresponding to a pulse energy of 1.06 nJ) at a pump wavelength of 4.5 μm into a 1 cm long ANDi $Ga_8Sb_{32}S_{60}$ PCF generates a broad, flat-top and perfectly coherent SC spectrum extending from 1.65 μm to 9.24 μm at the 20 dB spectral flatness. These results make the proposed $Ga_8Sb_{32}S_{60}$ PCF an excellent candidate for various important mid-infrared region applications including mid-infrared spectroscopy, medical imaging, optical coherence tomography and materials characterization.

© 2019 Association of Polish Electrical Engineers (SEP). Published by Elsevier B.V. All rights reserved.

1. Introduction

Supercontinuum (SC) generation refers to the substantial spectral broadening obtained by using ultrafast laser pulses propagating in nonlinear medium [1]. Since the first experimental observation of the white light continuum in a borosilicate glass sample in the beginning of the 1970s [2], SC has become a significant scientific success and has found numerous applications including ultrafast laser spectroscopy, frequency comb generation, optical communications, optical coherence tomography (OCT), metrology and nonlinear optical pulse compression [3]. Under femtosecond pumping, the generation of spectrally continuous radiation results from the contribution of several linear and nonlinear processes and is strongly related to the dispersion profile exhibited by the optical waveguide [4]. When pumping in the anomalous regime of dispersion, soliton dynamics, dispersive wave generation and Raman self-frequency shifting are responsible for the SC process [5]. The generated spectra are ultra-wide, as a result of appearing of new optical pulses created from the fission of the fundamental Soliton. Nevertheless, the SC spectra are not completely coherent because

of their sensitivity to the noise amplification and, hence, shot-to-shot fluctuations [6]. On the other hand, achieving SC generation by pumping optical pulses at the normal dispersion regime can be triggered by self phase modulation (SPM) and the pulse spectrum extends toward longer wavelengths because of the optical wave breaking (OWB) mechanism. The generated SC spectra are narrow compared to that produced with the anomalous dispersion regime, but exhibit smooth profile and high degree of coherence [7].

Dynamics of a supercontinuum formation results from the interplay between a plethora of linear and nonlinear optical effects which come together to produce the spectral broadening of laser pulses, commonly over short propagation lengths [8]. Even though bulk media provide some interesting features related to the strong spatiotemporal coupling, guiding medium such as optical fibers is much more interesting as their optical properties can be adjusted, notably with the invention of photonic crystal fibers (PCFs) [9]. The main advantage of PCF resides in its versatility in terms of morphology, application and glass used for its fabrication [10]. Therefore, PCFs geometries can be optimized to, simultaneously, engineer the dispersion properties and increase the Kerr nonlinearity [11].

Chalcogenide (ChG) glasses are compound that contain at least one of the chalcogen elements S, Se, and Te combined with the other elements such as Sb, Ge, As, Ga, etc. [12,13]. ChG glasses are of great interest due to the possibility of producing glass systems with large

* Corresponding author.
  E-mail address: medjouri-abdelkader@univ-eloued.dz (A. Medjouri).

composition space and good resistance to crystallization which yield to achieve excellent optical properties such as high refractive indices, high Kerr nonlinearities, and broad transparency window extending from near-infrared to mid-infrared wavelengths [14,15]. Owing to these excellent optical properties, ChG glasses have been extensively employed to design mid-infrared SC laser sources based on PCF exhibiting all-normal chromatic dispersion (ANDi) profile [12]. Yan *et al.* numerically investigated coherent SC generation extending from 2 to 5 μm by pumping 50 fs duration 1 kW peak power laser pulses in As_2S_3 ChG glass PCF [16]. The authors have optimized the PCF dispersion profile by controlling the air hole diameters of inner layers. By using a similar approach, T.S. Saini *et al.* reported SC spectra spanning 1.9–10 μm by pumping at 4.5 μm, 50 fs width 0.7 kW peak power laser pulses in As_2Se_3 ChG glass triangular-core PCF [17]. Furthermore, Diouf *et al.* reported a coherent super-flat SC source in hexagonal lattice PCF made of $As_{38.8}Se_{61.2}$ ChG [18]. Dispersion and nonlinear parameters of the proposed PCF are engineered by adjusting the air holes diameter in the aim to achieve both ANDi regime and high Kerr nonlinearities. They have numerically shown that coherent SC spectrum extending from 2.9 to 4.575 μm at a 3 dB spectral flatness level can be achieved by launching a 0.05 nJ energy laser pulses pumped at a central wavelength of 3.7 μm into a 5 cm ANDi PCF length. A. Ben Salem *et al.* reported SC generation in a kind of hybrid PCF composed of As_2S_5 ChG glass and borosilicate [19]. The authors have shown that coherent and ultra-flat SC spectra spanning from 1 to 5 μm can be obtained by injecting at 2.5 μm, 50 fs pulses with 28.16 kW peak power through 4 mm PCF length. Mid-infrared SC extending from 1.5 to 12.2 μm has been, also, reported in $AsSe_2$ ChG based PCF by Diouf *et al.* [20]. The authors have shown that such broadband spectra can be obtained by pumping 100 fs pulses with a peak power of 11.44 kW at 3.5 μm. Karim *et al.* used a hexagonal lattice PCF made using $Ge_{11.5}As_{24}Se_{64.5}$ glass in the aim to generate super-flat and broadband SC in ANDi regime [21]. The results, obtained via numerical simulations, indicate that by pumping at 3.1 μm laser pulses with a 50 fs width and a 5 kW peak power, a SC extended up to 6 μm can be obtained. Moreover, Karim *et al.* reported a coherent SC generation spanning beyond 15 μm with a 1 cm all-chalcogenide dispersion-engineered triangular core fiber (TCF) by using a pump at 4 μm with a peak power of 5 kW [22]. The proposed TCF is composed of a solid core of $Ge_{11.5}As_{24}Se_{64.5}$ ChG glass surrounded by a cladding made of $Ge_{11.5}As_{24}S_{64.5}$ ChG glass.

Recently, a novel Ga–Sb–S ChG glass system has been proposed for mid-infrared applications [23]. The Ga–Sb–S based ChG glass has excellent optical properties such as broad transparency wavelength range extending from 0.8 to 14 μm, high linear refractive index laying in the range of 2.62–2.70, high third-order nonlinear refractive index up to 12.4×10^{-14} cm²/W at the wavelength of 1.55 μm, large solubility and low phonon energy when doping with rare earth [23]. Besides, Ga-based glasses combined with heavy metals exhibit smaller multi-photon spectra which is suitable for the design of lasers and other photonic applications [24]. Boruah *et al.* proposed and numerically investigated optical properties of low bend loss PCF based on $Ga_8Sb_{32}S_{60}$ ChG glass for mid-infrared nonlinear applications [25]. The proposed structure is found to be highly nonlinear and insensitive to microbending which makes it an excellent candidate for nonlinear applications such as SC generation. Ga–Sb–S ChG glass system has been, also, considered to design a rib waveguide for an on-chip mid-infrared SC generation [24]. The waveguide geometry consists of a $Ga_8Sb_{32}S_{60}$ ChG glass core surrounded by a layer of MgF_2 glass which act as an upper and lower cladding material. By pumping at 2.8 μm optical pulses with a 497 fs duration and a 6.4 kW peak power, mid-infrared SC spanning the spectral band extending from 1 to 9.7 μm can be, successfully, achieved [24]. However, the generated spectra are not smooth because of the anomalous dispersion regime exhibited by
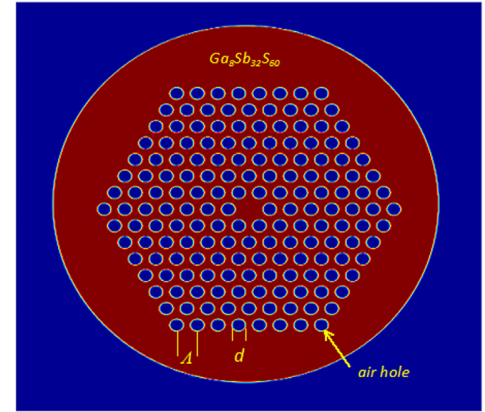
Fig. 1. Cross sectional view of the proposed $Ga_8Sb_{32}S_{60}$ ChG glass PCF.

the proposed rib waveguide. To overcome this critical limitation, ANDi regime can be achieved in PCF through a proper adjustment of its air holes diameter.

In this work, we report on a numerical modelling of a mid-infrared SC generation in a dispersion engineered hexagonal lattice PCF with a background material made of $Ga_8Sb_{32}S_{60}$ ChG glass. To achieve a broadband, coherent and flat-top SC in the mid-infrared region, the proposed $Ga_8Sb_{32}S_{60}$ PCF is specifically designed with ANDi profile and nearly-zero chromatic dispersion wavelength in the mid-infrared region. This characteristics can be fulfilled with appropriately controlling the cladding air holes diameter. For that purpose, the finite-difference frequency-domain (FDFD) method is employed to compute the PCF linear and nonlinear properties such as chromatic dispersion, field mode area and Kerr nonlinear coefficient. The spectral broadening occurring due to the propagation of high peak power and femtosecond laser pulses inside the proposed PCF is simulated by solving the generalized nonlinear schrödinger equation (GNLSE). Furthermore, the influence of pulses' characteristics and the seeded noise on the generated SC bandwidth and coherence is, respectively, investigated.

2. Theory

2.1. Design and parameters computation of the $Ga_8Sb_{32}S_{60}$ PCF

Figure 1 depicts the cross section of our proposed PCF. The structure is formed by a solid core made of $Ga_8Sb_{32}S_{60}$ ChG glass surrounded by seven rings of air holes arranged in a triangular lattice and running along the PCF length. The number of rings has been chosen to prevent the confinement loss which arises due to the optical tunnel effect. The air holes pitch and diameter are Λ and d, respectively. The refractive index of $Ga_8Sb_{32}S_{60}$ ChG glass is calculated by using the Sellmeier dispersive model as [25]:

$$n = \sqrt{1 + \frac{a_1\lambda^2}{\lambda^2 - b_1^2} + \frac{a_2\lambda^2}{\lambda^2 - b_2^2}}. \tag{1}$$

Where: $a_1 = 6.2563$, $b_1 = 0.3425$ μm, $a_2 = 2.9444$ and $b_2 = 34.28$ μm.

In order to compute the fundamental mode effective index and find the corresponding optical field distribution, the finite-difference frequency-domain (FDFD) method has been used. After applying the PML boundary condition, the Maxwell's equations for the electric field E and magnetic field H are given by [26]:

$$\begin{cases} ik_0 s\varepsilon_r E = \nabla \times H \\ -ik_0 s\mu_r H = \nabla \times E \end{cases} \tag{2}$$

$$s = \begin{bmatrix} s_y/s_x & 0 & 0 \\ 0 & s_x/s_y & 0 \\ 0 & 0 & s_y s_x \end{bmatrix}. \tag{3}$$

Where: $s_x = 1 - \sigma_x/(i\omega\varepsilon_0)$ and $s_y = 1 - \sigma_y/(i\omega\varepsilon_0)$.

k_0 is the free space number, ε_r is the medium relative permittivity, μ_r is the medium relative permeability, σ is the conductivity profile and ω is the angular frequency. Once an adequate meshing is introduced to the structure, the Maxwell's equations system is converted into a matrix eigenvalue problem. For a given excitation wavelength, a sparse matrix method is used to compute the mode effective refractive index n_{eff} and its optical field profile [27].

The chromatic dispersion is a key parameter in the propagation of short optical pulses and their nonlinear interactions in optical fibers [4]. The PCF chromatic dispersion coefficient is evaluated from the fundamental mode effective index as follows:

$$D(\lambda) = -\frac{\lambda}{c} \frac{d^2 n_{eff}}{d\lambda^2}. \tag{4}$$

Where λ and c are the wavelength and the speed of light, respectively.

The field effective area of the propagating mode plays a crucial role in designing PCFs. It gives a measurement of the light transmitting area regarding the PCF nonlinear response. It can be calculated using [28]:

$$A_{eff} = \frac{\left(\iint |E^2| \, dxdy\right)^2}{\iint |E|^4 dxdy}. \tag{5}$$

Where E denotes now the amplitude of the transverse electric field that propagates within the PCF.

The PCF Kerr nonlinearity coefficient is defined as [5]:

$$\gamma = \frac{n_2 \omega_0}{c A_{eff}}. \tag{6}$$

Where $n_2 = 12.4 \times 10^{-14} \, cm^2/W$ at $1.55 \, \mu m$ for $Ga_8Sb_{32}S_{60}$ ChG glass [23].

2.2. Modelling of nonlinear pulse propagation in PCFs

Ultra-court pulse propagation and SC generation in PCFs can be modelled by the generalized nonlinear schrödinger equation (GNLSE) [5]. This propagation's equation describes the pulse evolution inside an optical fiber with the mutually combined effects of chromatic dispersion and the various nonlinear processes. Its expression is given by:

$$\frac{\partial A}{\partial z} + \frac{\alpha}{2} A - \sum_{k \geq 2} \frac{I^{k+1}}{k!} \beta_k \frac{\partial^k A}{\partial T^k} = i\gamma \left(1 + \frac{i}{\omega_0} \frac{\partial}{\partial T}\right)$$

$$\left(A(z,T) \int_{-\infty}^{\infty} R(T') \times |A(z, T-T')|^2 dT'\right). \tag{7}$$

$A(z,T)$ is the temporal envelope of the pulse electric field, α is the propagation loss coefficient, β_k is the kth Taylor series expansion coefficient of the propagation constant $\beta(\omega)$ computed at the center carrier frequency ω_0 of the pumping pulse, γ is the Kerr nonlinearity coefficient, $R(T)$ is the nonlinear response function, that contains both instantaneous electronic (Kerr effect) and delayed (Raman scattering) contributions. Its expression is given by Ref. 5:

$$R(t) = (1 - f_R)\delta(t) + f_R h_R(t). \tag{8}$$

$\delta(t)$ is the Dirac delta function that represents the instantaneous electronic response, $h_R(t)$ is the Raman response function and f_R represents the Raman fractional contribution to the overall nonlinear response. Given that, the $Ga_8Sb_{32}S_{60}$ ChG glass Raman response

and fractional contribution are unknown, we have employed those of the As_2Se_3 ChG glass [24]. Accordingly, the value of f_R is set to be 0.115 and the Raman response is given by the following expression [17]:

$$h_R(t) = \frac{\tau_1^2 + \tau_2^2}{\tau_1 \tau_2^2} exp\left(\frac{-t}{\tau_2}\right) sin\left(\frac{t}{\tau_1}\right) \Theta(t). \tag{9}$$

This single Lorentzian model is characterized by two parameters τ_1 and τ_2 which are appropriately adjusted to provide an excellent fit to the real Raman gain spectrum [29]. τ_1 is related to the phonon frequency and τ_2 is related to the network attenuation of vibrating atoms [30]. Their values are set to be of 23.1 fs and 195 fs, respectively [17].

Finally, the statistical properties of the generated SC are investigated. Aiming to analyze their sensitivity to the input noise present on the pump pulses. Coherence of SC sources refers to a measure of correlations among their spectral intensities and is required to characterize ultrafast or rarely occurring phenomena [31]. The analysis can be performed by calculating the modulus of the first-order degree of coherence described as the ratio of the mean spectral field squared to the mean spectral intensity as following [32]:

$$|g_{12}(\omega)| = \frac{|<E(\omega)>|^2}{<|E(\omega)|^2>}. \tag{10}$$

Where $E(\omega)$ is the output pulse spectrum. The degree of coherence is calculated considering an ensemble average over a large number of independent realizations of the generated SC spectra. The input pulse noise is seeded into each of these simulations based on the one photon per mode model [33]. The spectral amplitude of the input noise $A(\omega)$ can be expressed as [34]:

$$A(\omega) = \sqrt{\frac{\hbar\omega}{T_{span}}} exp(i2\pi\varphi(\omega)). \tag{11}$$

Where $\hbar$ is the reduced Planck constant, ω is the angular pulsation, T_{span} is the temporal window employed for the numerical simulations and $\varphi(\omega)$ is a randomly generated phase, uniformly distributed in the interval $[0, 2\pi]$. Besides, $|g_{12}(\omega)|$ is lying in the interval $[0–1]$, with a value of 1 indicating perfect coherence [5].

3. Numerical results

3.1. Dispersion engineering of the proposed PCF

As stated previously, our target is to design $Ga_8Sb_{32}S_{60}$ ChG glass based hexagonal lattice PCF exhibiting ANDi regime so that the resulting SC is flat and coherent over a broad spectral range. For this purpose, the geometrical parameters of the proposed PCF are suitably adjusted. In fact, the material dispersion of the background glass is a fundamental limit when engineering the PCF chromatic [35]. Figure 2 depicts the material dispersion of $Ga_8Sb_{32}S_{60}$ ChG glass derived from Eq. (1). As it can be seen, the glass exhibits both normal and anomalous dispersion with a zero dispersion wavelength at $5.25 \, \mu m$. Through a careful adjusting of the lattice pitch and the air holes diameter, the material dispersion can be adjusted by waveguide dispersion and ANDi regime can be, then, achieved. We optimize the proposed PCF structure considering a constant pitch Λ and different values of air holes diameter. Figure 3 depicts the evolution of the fundamental mode chromatic dispersion with wavelengths for $\Lambda = 2.5 \, \mu m$ and d varying from $0.6 \, \mu m$ to $1.2 \, \mu m$ with step of $0.2 \, \mu m$. As it can be observed, the total chromatic dispersion profile is strongly affected by the value of the air filling fraction. When d/Λ increases, the dispersion curve increases too and a maximum value obtained around the wavelength of $4.5 \, \mu m$. Besides, ANDi regime can be achieved with a peak close to the zero
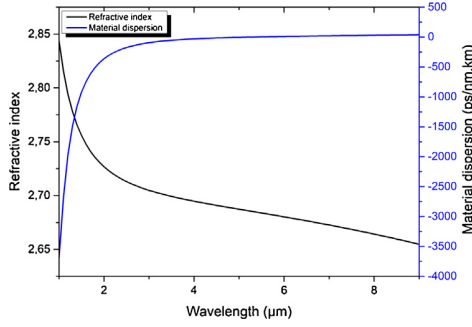
Fig. 2. Refractive index and corresponding material dispersion versus wavelength of the $Ga_8Sb_{32}S_{60}$ ChG glass.
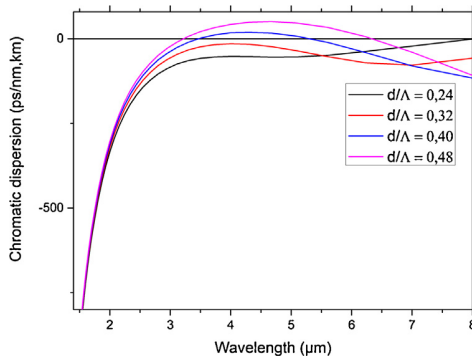
Fig. 3. Variation of the chromatic dispersion with wavelengths for $\Lambda = 2.5\,\mu m$ and d varying from $0.6\,\mu m$ to $1.2\,\mu m$ with step of 0.2.
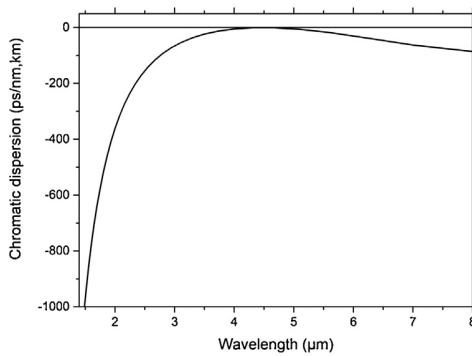
Fig. 4. Variation of the chromatic dispersion with wavelengths for $d/\Lambda = 0.352$.

for d/Λ laying between 0.32 and 0.40. Further numerical investigations have shown that such required dispersion profile can be ensured with $d/\Lambda = 0.352$, corresponding to an air hole diameter of $d = 0.88\,\mu m$. As depicted in Fig. 4, the PCF design with optimized air holes diameter exhibits a negative dispersion over the entire spectral range with zero dispersion wavelength around $4.5\,\mu m$. Finally, we have calculated the effective field mode area and the corresponding Kerr nonlinearity and their variations with wavelengths are depicted in Fig. 5. By using the Miller' rule, the nonlinear refractive index of the $Ga_8Sb_{32}S_{60}$ ChG glass has been reduced to $n_2 = 10.6 \times 10^{-14}\,cm^2/W$, corresponding to the central wavelength $4.5\,\mu m$ [36]. Simulations results show that the proposed $Ga_8Sb_{32}S_{60}$ PCF exhibits extreme high nonlinearity over the whole spectral range. Moreover, the effective field mode area and the corresponding Kerr nonlinear coefficient for the wavelength of $4.5\,\mu m$ have been found to be of $15.23\,\mu m^2$ and $970\,w^{-1}\,km^{-1}$, respectively.
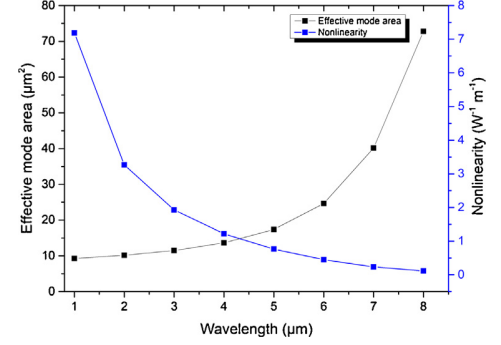
Fig. 5. Variation of the effective mode area and the corresponding nonlinear coefficient with wavelength for $d/\Lambda = 0.352$.

Table 1
Taylor series expansion coefficients of the propagation constant.

Coefficient	Value
β_2	$0.2121\,ps^2/km$
β_3	$-0.0027\,ps^3/km$
β_4	$3.5188 \times 10^{-05}\,ps^4/km$
β_5	$-1.8685 \times 10^{-07}\,ps^5/km$
β_6	$5.7195 \times 10^{-10}\,ps^6/km$
β_7	$-7.8881 \times 10^{-13}\,ps^7/km$

3.2. Simulation of mid-infrared SC in the proposed PCF

For studying SC generation in our proposed PCF with the optimized design, we numerically solve the GNLSE equation given by Eq. (7). Optical pulses propagating within the $Ga_8Sb_{32}S_{60}$ PCF core are modelled by a chirpless Gaussian pulse given by $A(0, t) = \sqrt{P_0}exp\left(-t^2/2T_0^2\right)$ where, T_0 is the pulse duration and P_0 is the peak power. Aiming to generate broad SC, laser pulses are pumped at $4.5\,\mu m$, corresponding to the zero chromatic dispersion wavelength. A possible light source for these pulses is based on phase-matched difference-frequency mixing (DFM) in Gallium Selenide (GaSe) crystal of near-infrared signal and idler pulses obtained from a parametric system [37]. The light source is capable of providing optical pulses with μ-joule energy level in the mid-infrared wavelengths range extending from 3 to $20\,\mu m$ with very short durations of 50 fs at the wavelength of $5\,\mu m$. In order to accurately model the dispersion variation over a large spectral bandwidth, the Taylor series expansion coefficients up to the 7th order of the propagation constant have been computed around the center carrier frequency and their corresponding values are given in Table 1. The propagation loss is neglected from Eq. (7) since pulse propagation is considered in only few millimeters PCF length piece.

Firstly, and aiming to give a simple explanation of SC formation mechanisms in the proposed $Ga_8Sb_{32}S_{60}$ PCF, we consider the injection of a Gaussian pulse with a total energy of 0.53 nJ, corresponding to FWHM and a peak power of 100 fs and 5 kW, respectively. Accordingly, the dispersion length L_D, the nonlinear length L_{NL} and the soliton order N can be computed as following: $L_D = T_0^2/\left|\beta_2\right| = 0.047\,m$, $L_{NL} = 1/(\gamma P_0) = 20.60 \times 10^{-5}\,m$ and $N = \sqrt{L_D/L_{NL}} = 15$, respectively. Figure 6 depicts the pulse temporal and spectral evolution over the propagation distance. In the first few millimeters, the SC process is initiated by the SPM and the pulse spectrum extends symmetrically toward shorter and longer wavelengths. Furthermore, the SC spectrum begin to broaden asymmetrically because of the OWB effect. It arises on the pulse leading and trailing edges where the spectrum sidebands are obtained from mixing the overlapping frequency components generated by the SPM [38]. Consequently, OWB is responsible for the creation of the extreme frequencies on both sides of the pulse spec-
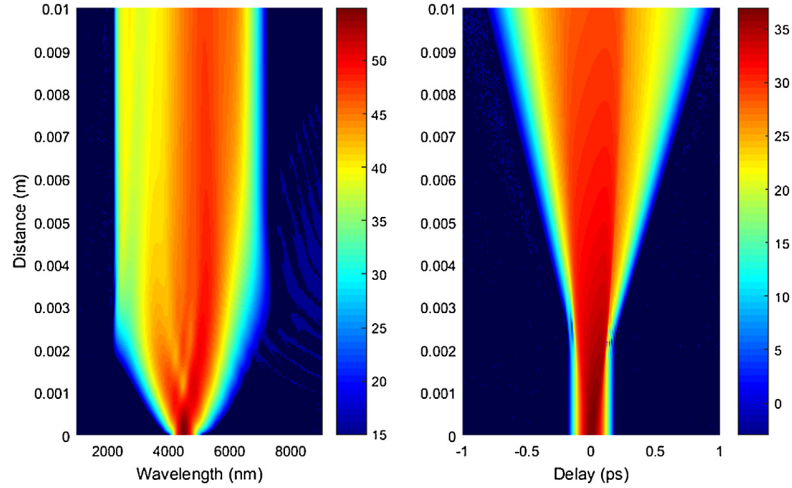
Fig. 6. Gaussian pulse spectral and temporal evolution over 1 cm PCF length where the peak power and FWHM are 5 kW and 100 fs, respectively.
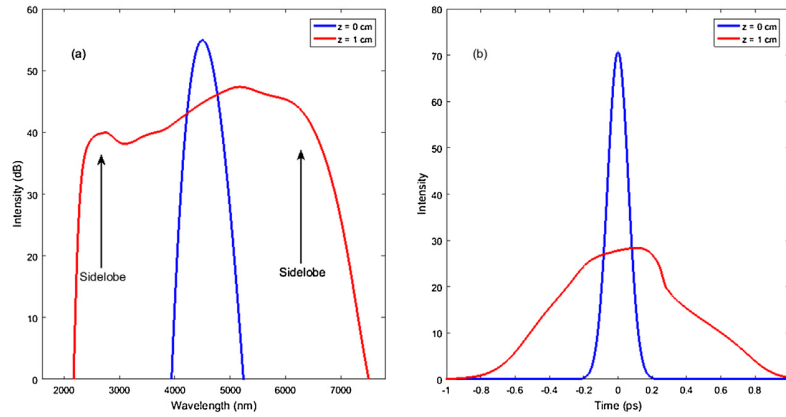
Fig. 7. Pulse spectral (a) and temporal (b) profiles at the input and after z = 1 cm of propagation.

trum and for the uniform spectral and temporal profiles of the pulse spectrum at the PCF output [1]. Figure 7 shows the pulse temporal and spectral profiles at the PCF input and after 1 cm of propagation length. The propagation length where the OWB arises is given by [39]:

$$z = \frac{L_D}{\sqrt{4e^{-1.5}N^2 - 1}} \tag{12}$$

Accordingly, the OWB starts to occur at the distance of 3.3 mm. Figure 8 shows the pulse temporal profile at the input and after 3.3 mm of propagation and the spectrogram of the output pulse. Upon further propagation, the pulse spectrum extends on both sides by transferring energy from its center wavelengths to the new generated frequency band. Sight to enhance the generated SC bandwidth, we have studied the impact of the pumped pulses initial conditions. Firstly, the impact of the pulse peak power is investigated. Numerical simulations are conducted with a 100 fs pulse duration with a peak power of 5 kW, 10 kW, 15 kW and 20 kW, respectively. As it can be seen from Fig. 9, the output pulse spectrum width increases with the initial peak power. Besides, smooth SC spectra extending to the mid infrared region and spanning 6.9 μm in the range from 1.7 μm to 8.6 μm at 20 dB is successfully obtained for a peak power of 20 kW. The effect of the initial pulse duration on the output spectrum bandwidth is, then, studied. We consider an initially injected pulse with a peak power of 20 kW and various FWHM durations. Figure 10 depicts the output pulse spectrum

after propagation over PCF length of 1 cm where the FWHM is set to be 100 fs, 75 fs and 50 fs, respectively. When the pulse FWHM is reduced, the generated SC spectrum extends toward the mid-infrared region and large bandwidth spanning of 7.59 μm from 1.65 μm to 9.24 μm at 20 dB is successfully achieved when pumping with 50 fs FWHM pulses. The SC sensitivity to the input noise is, then, analyzed. The coherence of SC spectra generated in our proposed PCF is investigated by considering the optimized parameters of the input pulse. Figure 11 shows the SC generated after 1 cm of propagation in the PCF using a pulse with a peak power and FWHM of 20 kW and 50 fs, respectively and the corresponding first-order degree of coherence calculated from 100 independent realizations. As it can be seen, the generated spectrum exhibits smooth profile with perfect spectral coherence over the entire spectral range. In fact, the spectral broadening is achieved mainly due to SPM which is a deterministic process that preserves the coherence of input optical pulses [40]. Finally, the influence of the material loss on the SC spectral bandwidth is examined. Figure 12 depicts the output SC spectrum for a laser pulse with a peak power and FWHM of 20 kW and 50 fs, respectively, without loss and after introducing an optical attenuation with a coefficient of 1.24 dB/mm, calculated from the transmission spectra of the Ga-Sb-S glass system [23]. Compared to the case where the loss is neglected, the generated SC spectrum bandwidth at the spectral flatness level of 20 dB is reduced only by 0.29 μm. Besides, this spectral narrowing can be compensated by increasing the input pulses peak power.
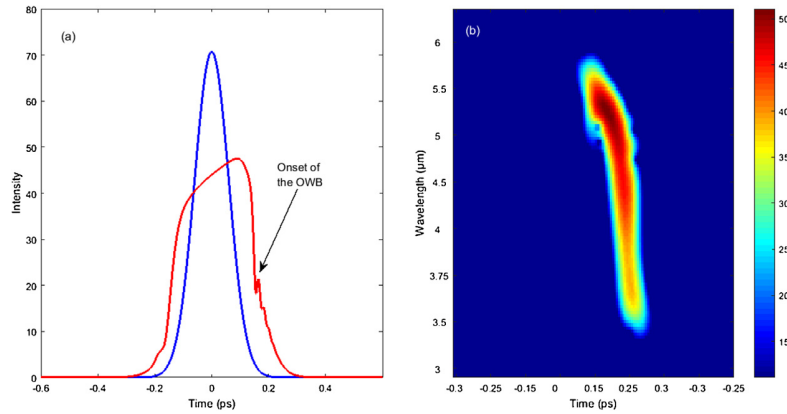
Fig. 8. (a) Pulse profiles at the input and after *z* = 3.3 mm of propagation. (b) Spectrogram of the output pulse.
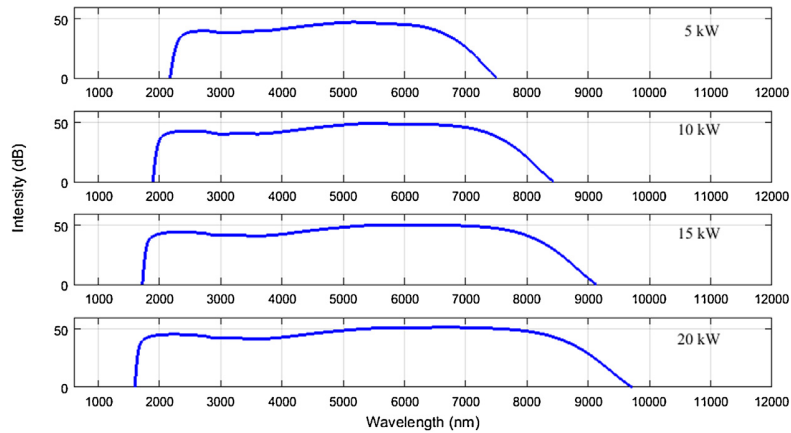
Fig. 9. Generated SC spectrum in 1 cm PCF length with an input pulse FWHM of 50 fs and various values of the peak power.
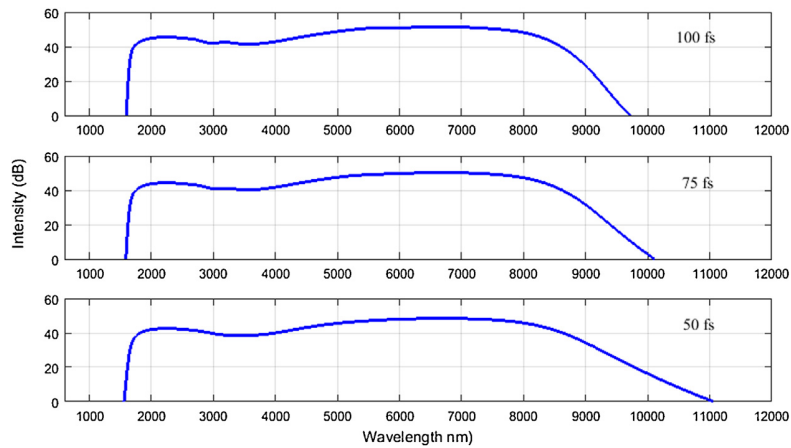
Fig. 10. Generated SC spectrum in 1 cm PCF length with an input pulse peak power of 20 kW and various values of FWHM.

The numerical results presented in this paper are compared to recently published works reporting mid-infrared SC generation in ANDi ChG based PCFs (Table 2). Although the comparison is performed by considering a spectral flatness of 20 dB level, it reveals the potential of our proposed $Ga_8Sb_{32}S_{60}$ ChG glass based PCF to generate coherent, broadband and ultra-flat SC spectra.

Also, it is worth noting that the SC is generated in our PCF with a simple design compared to more complex structures such as multi-material PCFs [19,22], PCF with different air holes diameters [17] or nanostructured graded-index fiber [43].

The broadband SC generated in our proposed $Ga_8Sb_{32}S_{60}$ glass PCF makes it a promising candidate for multiple nonlinear applications, especially in OCT [44]. Visible and near-infrared OCT has been widely used as non-invasive and non-contact cross-sectional imaging technique for biological tissues, material characterization, dimensional measurement etc. [45]. Recently, mid-infrared OCT systems have been reported for the analysis of ceramics, polymers
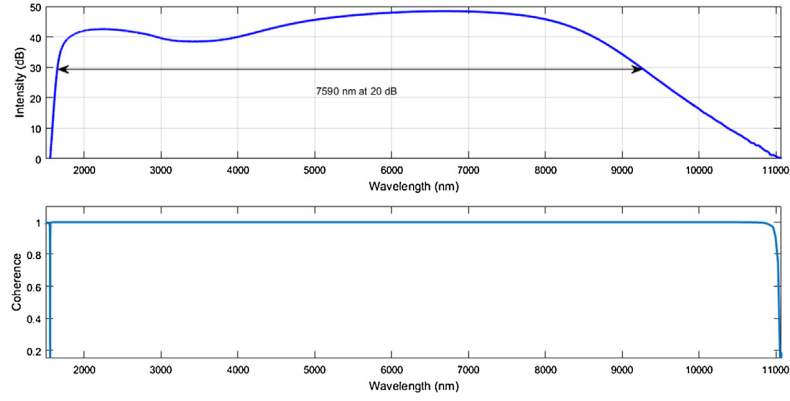
Fig. 11. SC generated with an input Gaussian pulse peak power and FWHM of 20 kW and 50 fs, respectively and the calculated degree of coherence.
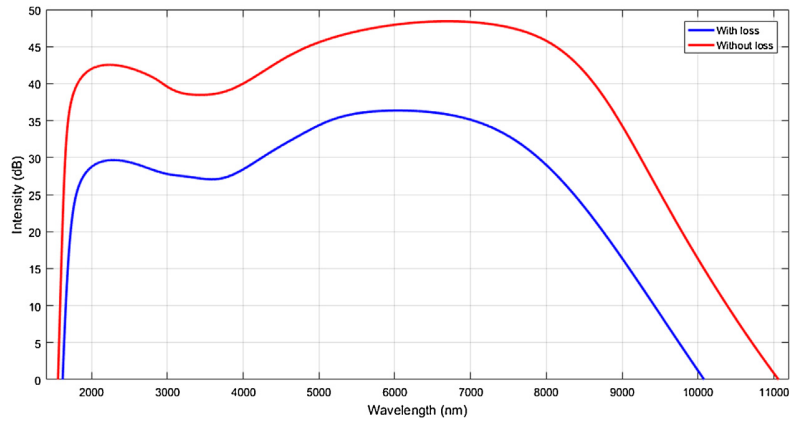
Fig. 12. SC generated with an input Gaussian pulse peak power and FWHM of 20 kW and 50 fs, respectively with and without introducing optical material loss.

Table 2

Comparison of the SC bandwidth at 20 dB generated with the proposed $Ga_8Sb_{32}S_{60}$ based PCF with that reported in selected ANDi ChG based PCF designs.'.

Reference	ChG glass	Pump wavelength (μm)	SC bandwidth (μm)
[17]	As_2Se_3	4.5	2 - 8
[18]	$As_{38.8}Se_{61.2}$	3.7	2.8 – 4.8
[19]	As_2S_5 – borosilicate	2.5	0.9 – 5.25
[21]	$Ge_{11.5}As_{24}Se_{64.5}$	3.1	2 - 5.5
[22]	$Ge_{11.5}As_{24}Se_{64.5}$ - $Ge_{11.5}As_{24}S_{64.5}$	4	2.5 - 7
[41]	As_2S_3 - borosilicate	2.8	2.4 – 3.1
[42]	As_2S_3	2.5	1-7.5
[43]	$As_{40}Se_{60}$ - $Ge_{10}As_{23.4}Se_{66.6}$	6.3	3.5 – 8.5
Proposed PCF	$Ga_8Sb_{32}S_{60}$	4.5	1.65 - 9.24

and some biochemical species such as collagen amide, carbonate and phosphate [46,47]. For an OCT system, an axial resolution is a key specification. Its value is determined by the coherence length of the light source given by [48]:

$$L_c = \frac{2\ln 2}{\pi} \frac{\lambda_0^2}{\Delta\lambda}. \tag{13}$$

Where λ_0 and $\Delta\lambda$ are the source center wavelength and spectral bandwidth, respectively. As it can be noticed from Eq. (13), the coherence length is inversely proportional to the optical source spectral bandwidth and, therefore, broadband optical sources are needed to design OCT systems with improved axial resolution [48]. In our simulations, we have found that pumping 1.06 nJ pulses at a central wavelength of 4.5 μm into a 1 cm long PCF generates a broad SC with the spectral width $\Delta\lambda = 7.59$ μm. Therefore, the coherence length is 1.18 μm and, hence, high resolution OCT imaging system can be ensured for the mid-infrared fingerprint region. Besides, the ultra-flatness of the generated SC prevents the creation of side lobes

in the interferogram and ensures the required high quality of axial resolution [47].

Considering now the fabrication possibilities of the proposed PCF. A key factor for fiber manufacturing is related to the thermal stability of the host glass. Thermal stability is defined as the difference ΔT between the crystallization temperature T_c and the glass transition temperature T_g which has to be higher than 100^0 C [49,50]. According to the experimental results reported in [23], the glass transition and crystallization temperatures of the $Ga_8Sb_{32}S_{60}$ glass are found to be $T_g = 240^0$ C and $T_c = 357^0$ C, leading to a thermal stability of $\Delta T = T_g - T_c = 117^0$ C. For that reason, the $Ga_8Sb_{32}S_{60}$ chalcogenide glass system is found suited for fibers fabrication.

4. Conclusions

In summary, we have studied ANDi and highly nonlinear chalcogenide glass based PCF for coherent, broadband and flat-top mid-infrared SC generation. The proposed PCF consists of a solid

core made of $Ga_8Sb_{32}S_{60}$ ChG glass surrounded by seven rings of air holes arranged in a hexagonal lattice. Numerical results indicate that targeted dispersion properties can be achieved simply by controlling the air hole diameters in the cladding and ANDi profile is achieved over a wide range of wavelengths with a zero dispersion wavelength located around 4.5 μm. Moreover, the proposed PCF exhibits Kerr nonlinearity as high as 970 $w^{-1} km^{-1}$ at the pumping wavelength (i.e., 4.5 μm). Furthermore, SC generation at 4.5 μm in the optimized design has been analyzed. The impact of input pulse peak power and duration on output spectral bandwidth have been investigated. Simulations' results have shown that broadband and perfectly coherent flat-top SC spectrum spanning the wavelength range from 1.65 μm to 9.24 μm at the 20 dB spectral level is successfully generated by using a 50 fs duration 20 kW peak power laser pulse (corresponding to pulse energy of 1.06 nJ) in only 1 cm PCF length. Owing to its interesting properties, the proposed $Ga_8Sb_{32}S_{60}$ glass PCF is found to be suitable for potential mid-infrared applications such as optical coherence tomography, mid-infrared spectroscopy, metrology and material characterization.

CRediT authorship contribution statement

A. Medjouri: Conceptualization, Investigation, Writing - original draft, Writing - review & editing. **D. Abed:** Writing - original draft, Writing - review & editing. **Z. Becer:** Writing - original draft.

References

[1] R.R. Alfano, The Supercontinuum Laser Source: the Ultimate White Light, 3rd edition, Springer, 2016, http://dx.doi.org/10.1007/978-1-4939-3326-6.

[2] R.R. Alfano, S.L. Shapiro, Observation of self-phase modulation and small-scale filaments in crystals and glasses, Phys. Rev. Lett. 24 (1970) 592–596, http://dx.doi.org/10.1103/PhysRevLett.24.592.

[3] D. Faccio, J.M. Dudley, Frontiers in modern optics, in: Proceedings of the International School of Physics, Enrico Fermi, IOS Press, The Netherlands, 2016.

[4] J.M. Dudley, J.R. Taylor, Supercontinuum Generation in Optical Fibers, Cambridge University Press, 2010, http://dx.doi.org/10.1017/CBO9780511750465.

[5] J.M. Dudley, G. Genty, S. Coen, Supercontinuum generation in photonic crystal fiber, Rev. Mod. Phys. 78 (2006) 1135–1184, http://dx.doi.org/10.1103/RevModPhys.78.1135.

[6] A. Hartung, A.M. Heidt, H. Bartelt, Design of all-normal dispersion microstructured optical fibers for pulse-preserving supercontinuum generation, Opt. Express 19 (2011) 7742–7749, http://dx.doi.org/10.1364/OE.19.007742.

[7] A.M. Heidt, A. Hartung, G.W. Bosman, P. Krok, E.G. Rohwer, H. Schwoerer, H. Bartelt, Coherent octave spanning near-infrared and visible supercontinuum generation in all-normal dispersion photonic crystal fibers, Opt. Express 19 (2011) 3775–3787, http://dx.doi.org/10.1364/OE.19.003775.

[8] M. Yasin, Sulaiman Wadi Harun, H. Arof, Recent progress in optical fiber research, InTech (2012), http://dx.doi.org/10.5772/2428.

[9] R. Thomson, C. Leburn, D. Reid, Ultrafast Nonlinear Optics, Springer, 2013, http://dx.doi.org/10.1007/978-3-319-00017-6.

[10] L. Thévenaz, Advanced fiber optics concepts and technology, EPFL press, Switzerland, 2011.

[11] Philip St.J. Russell, Photonic-crystal fibers, J. Lightwave Technol. 24 (12) (2006) 4729–4749, http://dx.doi.org/10.1109/JLT.2006.885258.

[12] A. Zakery, S.R. Elliot, Optical Nonlinearities in Chalcogenide Glasses and Their Applications, Springer, 2007, http://dx.doi.org/10.1007/978-3-540-71068-4.

[13] S. Wabnitz, B.J. Eggleton, All-optical Signal Processing: Data Communication and Storage Applications, Springer, 2015, http://dx.doi.org/10.1007/978-3-319-14992-9.

[14] N. Granzow, M.A. Schmidt, W. Chang, L. Wang, Q. Coulombier, J. Troles, P. Toupin, I. Hartl, K.F. Lee, M.E. Fermann, L. Wondraczek, P.St.J. Russell, Mid-infrared supercontinuum generation in As_2S_3-silica "nano-spike" step-index waveguide, Opt. Express 21 (2013) 10969–10977, http://dx.doi.org/10.1364/OE.21.010969.

[15] B.J. Eggleton, B.L. Davies, K. Richardson, Chalcogenide photonics, Nat. Photonics 5 (2011) 141–148, http://dx.doi.org/10.1038/nphoton.2011.309.

[16] P. Yan, R. Dong, G. Zhang, H. Li, S. Ruan, H. Wei, J. Luo, Numerical simulation on the coherent time-critical 2–5 mm supercontinuum generation in an As_2S_3 microstructured optical fiber with all-normal flat-top dispersion profile, Opt. Commun. 293 (2013) 133–138, http://dx.doi.org/10.1016/j.optcom.2012.11.093.

[17] T.S. Saini, A. Kumar, R.K. Sinha, Broadband mid-IR supercontinuum generation in As_2Se_3 based chalcogenide photonic crystal fiber: a new design and analysis, Opt. Commun. 345 (2015) 13–19, http://dx.doi.org/10.1016/j.optcom.2015.02.049.

[18] M. Diouf, A. Ben Salem, R. Cherif, H. Saghaei, A. Wague, Super-flat coherent supercontinuum source in $As_{38.8}Se_{61.2}$ chalcogenide photonic crystal fiber with all-normal dispersion engineering at a very low input energy, Pure Appl. Opt. J. Eur. Opt. Soc. Part A 56 (2) (2017) 163–169, http://dx.doi.org/10.1364/AO.56.000163.

[19] A. Ben Salem, M. Diouf, R. Cherif, A. Wague, M. Zghal, Ultraflat-top mid-infrared coherent broadband supercontinuum using all normal As_2S_5-borosilicate hybrid photonic crystal fiber, Opt. Eng. 55 (6) (2016), 066109, http://dx.doi.org/10.1117/1.OE.55.6.066109.

[20] M. Diouf, R. Cherif, A. Ben Salem, A. Wague, Ultra-broadband, coherent mid-IR supercontinuum expanding from 1.5 to 12.2 μm in new design of $AsSe_2$ photonic crystal fibre, J. Mod. Optic. 64 (13) (2017) 1335–1341, http://dx.doi.org/10.1080/09500340.2017.1288830.

[21] M.R. Karim, H. Ahmad, B.M.A. Rahman, All-normal dispersion chalcogenide PCF for ultraflat mid-infrared supercontinuum generation, IEEE Photonics Technol. Lett. 29 (21) (2017) 1792–1795, http://dx.doi.org/10.1109/LPT.2017.2752214.

[22] M.R. Karim, H. Ahmad, B.M.A. Rahman, Design and modeling of dispersion-engineered all-chalcogenide triangular-core fiber for mid infrared-region supercontinuum generation, J. Opt. Soc. Am. B 35 (2) (2018) 266–275, http://dx.doi.org/10.1364/JOSAB.35.000266.

[23] A. Yang, M. Zhang, L. Li, Y. Wang, B. Zhang, Z. Yang, D. Tang, Ga–Sb–S Chalcogenide Glasses for Mid-Infrared Applications, J. Am. Ceram. Soc. 99 (1) (2016) 12–15, http://dx.doi.org/10.1111/jace.14025.

[24] T.S. Saini, U.K. Tiwari, R.K. Sinha, Rib waveguide in Ga-Sb-S chalcogenide glass for on-chip mid-IR supercontinuum sources: design and analysis, J. Appl. Phys. 122 (2017) 053104, http://dx.doi.org/10.1063/1.4997541.

[25] J. Boruah, T.S. Saini, R.K. Sinha, Low bend loss photonic crystal fiber in Ga–Sb–S-based chalcogenide glass for nonlinear applications: design and analysis, J. Nanophotonics 11 (3) (2017), 036002, http://dx.doi.org/10.1117/1.JNP.11.036002.

[26] S. Guo, F. Wu, S. Albin, H. Tai, R.S. Rogowski, Loss and dispersion analysis of microstructured fibers by finite-difference method, Opt. Express 12 (2004) 3341–3352, http://dx.doi.org/10.1364/OPEX.12.003341.

[27] Z. Zhu, T.G. Brown, Full-vectorial finite-difference analysis of microstructured optical fibers, Opt. Express 10 (2002) 853–864, http://dx.doi.org/10.1364/OE.10.000853.

[28] A. Medjouri, L.M. Simohamed, O. Ziane, A. Boudrioua, Analysis of a new circular photonic crystal fiber with large mode area, Optik 126 (2015) 5718–5724, http://dx.doi.org/10.1016/j.ijleo.2015.09.035.

[29] G.P. Agrawal, Nonlinear Fiber Optics, 5th edition, Academic Press, 2013.

[30] K. Rottwitt, J.H. Povlsen, Analyzing the fundamental properties of Raman amplification in optical fibers, J. Lightwave Technol. 23 (2005) 3597–3605, http://dx.doi.org/10.1109/JLT.2005.857776.

[31] M. Klimczak, G. Soboń, R. Kasztelanic, K.M. Abramski, R. Buczyński, Direct comparison of shot-to-shot noise performance of all normal dispersion and anomalous dispersion supercontinuum pumped with sub-picosecond pulse fiber-based laser, Sci Rep-Uk 6 (2016) 1–14, http://dx.doi.org/10.1038/srep19284.

[32] G. Genty, A.T. Friberg, J. Turunen, Chapter two-Coherence of supercontinuum light, Prog. Optics 61 (2016), http://dx.doi.org/10.1016/bs.po.2015.10.002.

[33] M.H. Frosz, Validation of input-noise model for simulations of supercontinuum generation and rogue waves, Opt. Express 18 (2010) 14778–14787, http://dx.doi.org/10.1364/OE.18.014778.

[34] C. Ciret, S.P. Gorza, Generation of ultra-broadband coherent supercontinuum in tapered and dispersion managed silicon nanophotonic waveguides, J. Opt. Soc. Am. B 34 (2017) 1156–1162, http://dx.doi.org/10.1364/JOSAB.34.001156.

[35] M. Klimczak, B. Siwicki, A. Heidt, R. Buczyński, Coherent supercontinuum generation in soft glass photonic crystal fibers, Photonics Res 5 (6) (2017) 710–727, http://dx.doi.org/10.1364/PRJ.5.000710.

[36] R.W. Boyd, Nonlinear Optics, 3rd edition, Academic Press, 2008.

[37] R.A. Kaindl, M. Wurm, K. Reimann, P. Hamm, A.M. Weinerand, M. Woerner, Generation, shaping, and characterization of intense femtosecond pulses tunable from 3 to 20 μm, J. Opt. Soc. Am. B 17 (12) (2000) 2086–2094, http://dx.doi.org/10.1364/JOSAB.17.002086.

[38] W.J. Tomlinson, R.H. Stolen, A.M. Johnson, Optical wave breaking of pulses in nonlinear optical fibers, Opt. Lett. 10 (9) (1985) 457–459, http://dx.doi.org/10.1364/OL.10.000457.

[39] C. Finot, B. Kibler, L. Provost, S. Wabnitz, Beneficial impact of wave-breaking for coherent continuum formation in normally dispersive nonlinear fibers, J. Opt. Soc. Am. B 25 (2008) 1938–1948, http://dx.doi.org/10.1364/JOSAB.25.001938.

[40] L.E. Hooper, P.J. Mosley, A.C. Muir, W.J. Wadsworth, J.C. Knight, Coherent supercontinuum generation in photonic crystal fiber with all-normal group velocity dispersion, Opt. Express 19 (2011) 4902–4907, http://dx.doi.org/10.1364/OE.19.004902.

[41] P.S. Maji, P.R. Chaudhuri, Design of all-normal dispersion based on multimaterial photonic crystal fiber in IR region for broadband supercontinuum generation, Pure Appl. Opt. J. Eur. Opt. Soc. Part A 54 (13) (2015) 4042–4048, http://dx.doi.org/10.1364/AO.54.004042.

[42] M. Kalantari, A. Karimkhani, H. Saghaei, Ultra-Wide mid-IR supercontinuum generation in As_2S_3 photonic crystal fiber by rods filling technique, Optik 158 (2018) 142–151, http://dx.doi.org/10.1016/j.ijleo.2017.12.014.

[43] B. Siwicki, A. Filipkowski, A. Kasztelanic, A. Klimczak, A. Buczyński, Nanostructured graded-index core chalcogenide fiber with all-normal dispersion– design and nonlinear simulations, Opt. Express 25 (11) (2017) 12984–12998, http://dx.doi.org/10.1364/OE.25.012984.

[44] L. Froehly, J. Meteau, Supercontinuum sources in optical coherence tomography: A state of the art and the application to scan-free time domain correlation techniques and depth dependant dispersion compensation, Opt. Fiber Technol. 18 (2012) 411–419, http://dx.doi.org/10.1016/j.yofte.2012.08.001.

[45] R. Su, M. Kirillin, E.W. Chang, E. Sergeeva, S.H. Yun, L. Mattsson, Perspectives of mid-infrared optical coherence tomography for inspection and micrometrology of industrial ceramics, Opt. Express 22 (13) (2014) 15804–15819, http://dx.doi.org/10.1364/OE.22.015804.

[46] A.V. Paterova, H. Yang, C. An, D.A. Kalashnikov, L.A. Krivitsky, Tunable optical coherence tomography in the infrared range using visible photons, Quantum Sci. Technol. 3 (2018), 025008, http://dx.doi.org/10.1088/2058-9565/aab567.

[47] C.S. Colley, J.C. Hebden, D.T. Delpy, A.D. Cambrey, R.A. Brown, E.A. Zibik, W.H. Ng, L.R. Wilson, J.W. Cockburn, Mid-infrared optical coherence tomography, Rev. Sci. Instrum. 78 (2007), 123108, http://dx.doi.org/10.1063/1.2821609.

[48] W. Drexler, J.G. Fujimoto, Optical Coherence Tomography: Technology and Applications, Springer, 2015, http://dx.doi.org/10.1007/978-3-319-06419-2.

[49] H. Takebe, D.J. Brady, D.W. Hewak, K. Morinaga, Thermal properties of Ga_2S_3-based glass and their consideration during fiber drawing, J. Non-Cryst. Solids 258 (1-3) (1999) 239–243, http://dx.doi.org/10.1016/S0022-3093(99)00540-2.

[50] V.A.G. Rivera, D. Manzani, Technological Advances in Tellurite Glasses Properties, Processing, and Applications, Springer, 2017, http://dx.doi.org/10.1007/978-3-319-53038-3.

Special glass for silver-sodium ion exchanged waveguides

2 authors:

F. Rehouma
Echahid Hamma Lakhdar University, El Oued, Algeria
52 PUBLICATIONS   **57** CITATIONS

SEE PROFILE

Omar Bentouila
Université Kasdi Merbah Ouargla
15 PUBLICATIONS   **1** CITATION

SEE PROFILE

Some of the authors of this publication are also working on these related projects:

Solar Laser View project

Modeling of Thulium doped fluorophosphate glasses lasers View project

Special glass for silver-sodium ion exchanged waveguides

Ferhat Rehouma [a], Omar Bentouila [b],*

[a] Laboratoire d'Exploitation et de Valorisation des ressources Energétiques Sahariennes (LEVRES), Faculty of Exact Sciences, El Oued University, 39000 El Oued, Algeria
[b] Équipe Optoélectronique, Laboratoire LENREZA, Kasdi Merbah Ouargla University, 30000 Ouargla, Algeria

A B S T R A C T

In the present paper, we report an experimental study on a special glass developed for Ag^+-Na^+ ion-exchange. The glass composition and the influence of each element of the composition on the diffusion parameters were studied. Some parameters of exchange are determined, as well as the diffusion coefficient, refractive index variation, propagation and coupling losses. Such parameters can determine the fabrication conditions of integrated devices. The obtained waveguides have low coupling and propagation losses. The behavior of the fabricated waveguides at low temperatures is tested. It observed that, at these temperatures the diffusion is not negligible, which can affect the life time of the components. In order to improve this parameter, a modification of the amount of some elements of the glass composition is necessary, specially the alumina.

© 2018 The Authors. Production and hosting by Elsevier B.V. on behalf of King Saud University. This is an open access article under the CC BY-NC-ND license (http://creativecommons.org/licenses/by-nc-nd/4.0/).

1. Introduction

Ion exchange in glass is a suitable technique which is widely applied to modify the surface composition and properties of the glass surface without changing the bulk glass properties (Guldiren et al., 2016). This technique is usually used to fabricate glass waveguide owing to their benefits compared with other fabrication techniques (Wang et al., 2015). Waveguides made by ion-exchange on glass substrates are good candidates for passive integrated optics applications (Ramaswamy and Srivastava, 1988; Opilski et al., 2000). In addition, the integrated waveguide fabricated by this technology is a process well suited to industrial production. The quality and the performances of such waveguides depend strongly on the glass composition and on the type of the dopant ions (Ag^+, K^+, Tl^+, $Cs^{+,}$ etc.), which determine the diffusion parameters of the exchange (Rehouma and Aiadi, 2008). Some conditions are required on glass to use it in this technology. It must contains enough of alkaline oxides in order to create an important variation of refractive index, low intrinsic losses, the refractive index of the material is close to that of the silicon, chemical durability, no bubbles and high degree of homogeneity, easy diffusion of the ions, simple production, the fusion temperature is higher than the diffusion temperature and finally a low Haven ratio.

In this work, we report an experimental study on a special glass developed for Ag^+-Na^+ ion-exchange. The study includes the glass composition, and the influence of each element of the composition on the diffusion parameters. The fabrication parameters, the characterization of the fabricated waveguides on this glass and its performances are presented. The results are discussed in order to improve this composition.

2. Experimental

2.1. Glass's composition and characteristics

The glass used in this study contains SiO_2 as network former oxide with quantity in weight (%) of 61–64%. This amount gives the glass strength and high transparency in the visible and near infrared ranges. The alumina (Al_2O_3) is introduced as network intermediate oxide with 11–13%. The intermediate oxide, contribute to the glass strength, causes an elevation of refractive index. The existence of this quantity in the glass permits to increase the electrical conductivity, the chemical durability of glass and the diffusion efficiency in the material. As network modifier oxides, Na_2O, Li_2O, MgO and CaO are introduced with 12–14, 0.5–1, 3–4 and 3–5% respectively. The addition of alkaline oxides (Na_2O and Li_2O) permits to reduce the elaboration temperature,

the viscosity and the chemical durability of glass. Moreover, the presence of alkaline oxides increases the dilatation coefficient, the electrical conductivity and the refractive index. The *MgO* and *CaO* improve also the chemical resistance of glass and reduce the electrical conductivity. The introduction of B_2O_3, in this case (4–6%), increases the chemical resistance and decreases the dilatation coefficient. It should be noted, that the composition do not contains *FeO, As₂O₃* or *Sb₂O₃* since these elements cause the reduction of silver ions leading to excessive losses in the substrate. The glass samples, with size of 6 cm, were prepared starting from high purity powders according the weight (%) composition mentioned above by melt-quenching method. This method includes a series of classical steps: mixing of starting materials, melting, fining, casting and annealing (Murugasen et al., 2015). The refractive index of this glass is nearly of 1.51 (λ = 0.8 µm) and the temperature of fusion (Tg) is in order of 560 °C.

2.2. Ion-exchanged waveguide's parameters

In order to design optical waveguides made by ion-exchange in this glass, it is important to characterize the diffusion properties of cations in the substrate. The kinetic of diffusion is obtained by analysis of the refractive index profile of planar waveguides calculated by the inverse WKB method from the effective index of multimode structures (Hocker and Burns, 1975; Kaul and Thyagarajan, 1984; Ding et al., 2004).

The diffusion coefficient and ionic mobility are deduced from this experiment by fitting numerically the index profiles by finite difference program. Such program simulates the differential equation (Fick's law) which governs the diffusion kinetic of the two cations. The diffusion coefficient D (µm²/min) is determined experimentally for two different concentrations (2% and 10% Molar fraction) of silver in a molten bath of Sodium Nitrate (NaNO₃). The measurements of D were performed for different temperatures varying from 250 to 350 °C (Table 1). The time of diffusion is a few seconds for each operation.

The refractive index variation (Δn) after the thermal exchange depends also on the silver concentration in the molten bath. The experimental results are given in the table 2.

We assume that $D(T)$ has temperature dependence given by the following law:

$$D(T) = D_0 e^{-\frac{\Delta E}{RT}} \tag{1}$$

Where D_0 is the frequency factor, ΔE is the activation energy and R is the gas constant.

The Fig. 1 illustrates the variation of D as a function of temperature (°C).

A glass waveguide elaborated with a silver concentration of 10% has a diffusion coefficient which is equal to 0.00002 µm²/min at 80 °C, which is not negligible. That is to say that it takes about 9 days for Ag^+ ion move over a distance of 1 µm ($x = 2\sqrt{Dt}$) into
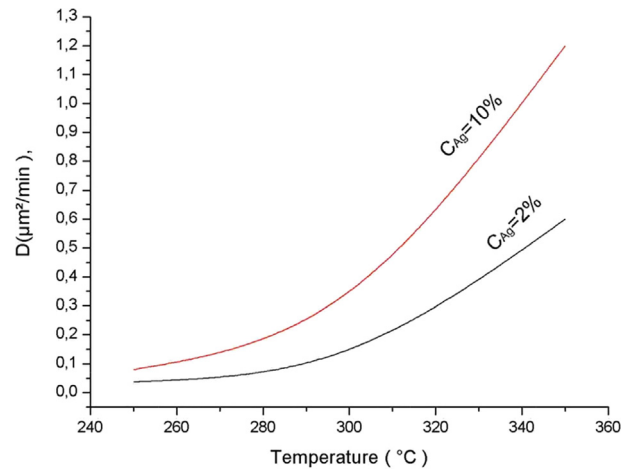
Fig. 1. The variation of *D* as function of silver concentration and temperature.

the glass. This aspect is confirmed by heating the fabricated planner waveguides in a furnace, at low temperature (100 °C), for several days (until 750 h). It observed that the variation of refractive index of the fundamental mode, decrease from 0.055 to 0.047.

The diffusion of K^+ is also tested, by immersing the glass substrate in a molten bath of KNO₃. The temperature of the exchange is more than 400 °C, for a time of diffusion more than four hours. From the obtained planner waveguides, the diffusion coefficient D and Δn are determined experimentally. D depends on the temperature of diffusion. For T varies from 390 to 460 °C, D changes from 0.012 to 0.065 µm²/min. The refractive index variation depends only on the kind of the dopant. In this case, it is about 0.0125. This glass is not well-suited for K^+ exchange due to the qualities of the obtained buried waveguides (Tervonen et al., 2011).

A channel-waveguides are made by two-step exchange process (Rehouma et al., 1995). During the first step, a surface channel-waveguide is fabricated by purely thermal exchange between the *Ag⁺* cations of the bath and the *Na⁺* cations present in the glass, through a mask previously deposited on the glass surface. This mask is then removed; the waveguide is buried below the surface by application of an external electric field across the substrate, during the second step. The obtained waveguides, 3 cm of length, are well compatible with optical fiber. The insertion losses (input, output coupling and propagation losses) of such waveguides are less than 0.8 dB. These losses were divided as follow: 0.4 dB in input and output coupling losses (Rehouma et al., 2007), less than 0.39 dB (0.13 dB/cm) in propagation losses (at λ= 0.785 µm) (Rehouma and Aiadi, 2008). The propagation losses are measured by the Cut back method (Cai et al., 2013; Kaminow and Stulz, 1978).

3. Discussions

We can draw several remarks from the results. Firstly, the important quantity of *Na₂O* in the studied glass is responsible of the considerable variation of the refractive index of the exchanged waveguides (Inácio et al., 2013; Rehouma, 1994). The diffusion coefficient (*D*) of the external cations into glass depends on the concentration of *Al₂O₃* and *Na₂O* of the glass in the one hand (Mendez and Morse, 2007), on the other hand, it depends on the concentration of silver in the molten bath and its temperature (Rehouma and Aiadi, 2008). *D* is important, in spite of the existence of *B₂O₃* in the glass. This parameter remains important even at low temperature (60–100 °C), which affects on the lifetime of the fabricated integrated devices. It will be preferable to have a value of

Table 1
The variation of D as function of silver concentration and temperature.

Temperature (°C)	250	300	350
D(µm²/min), C_{Ag} = 2%	0.037	0.15	0.6
D(µm²/min), C_{Ag} = 10%	0.08	0.35	1.2

Table 2
variation of refractive index as function of AgNO₃ concentration in molten bath.

Concentration of AgNO₃ (molar fraction%)	0.2	0.4	0.5	1	5	10	14
Δn at the glass surface (x10^{-2})	1.02	1.91	2.1	2.9	5.85	6.95	7.33

activation energy 23 kcal/mol in order to extend the stability of the components over 20 years. To improve this factor, a reduction of Al_2O_3 and replace it by an alkaline oxide like K_2O is necessary (Tomozawa, 1993). A saturation of Δn is obtained for a silver concentration about 10% in the bath. It means economically, is not advised to use more than this concentration in order to obtain a maximum of Δn. The temperature of the exchange (300–400 °C) is largely less than the T_g of the glass, then the fabrication condition has no affect on the substrate. The transparency and the homogeneity of the material are demonstrated by the obtained low losses propagation. Its refractive index (1.51) is nearly close to that of optical fiber (1.46), but the addition of small quantity of fluoride (less than 4%) can reduce significantly this parameter (García-Bellés et al., 2017; Rabinovich, 1983).

4. Conclusions

This study shows that this composition of glass is well adapted for silver-sodium ion-exchange. A good qualities and performances of the fabricated waveguides were obtained in terms of propagation and coupling losses. The factor of stability of the components must be taken in consideration for a future evolution of this composition.

References

Cai, Z., Qiu, W., Shao, G., Wang, W., 2013. A new fabrication method for all-PDMS waveguides. Sensors Actuators, A Phys. 204, 44–47. https://doi.org/10.1016/j.sna.2013.09.019.

Ding, Y., Cao, Z.Q., Shen, Q.S., 2004. Determination of optical waveguide refractive-index profiles with the inverse analytic transfer matrix method. Opt. Quantum Electron. 36, 489–497. https://doi.org/10.1023/B:OQEL.0000025769.11690.2d.

García-Bellés, A., Clausell, C., Barba, A., Pomeroy, M.J., Hampshire, S., 2017. Effect of fluorine and nitrogen content on the properties of Ca-Mg-Si-Al-O-(N)-(F) glasses. Ceram. Int. 43, 4197–4204. https://doi.org/10.1016/j.ceramint.2016.12.046.

Guldiren, D., Erdem, I., Aydin, S., 2016. Influence of silver and potassium ion exchange on physical and mechanical properties of soda lime glass. J. Non. Cryst. Solids 441, 1–9. https://doi.org/10.1016/j.jnoncrysol.2016.03.007.

Hocker, G., Burns, W., 1975. Modes in diffused optical waveguides of arbitrary index profile. IEEE J. Quantum Electron. 11, 270–276. https://doi.org/10.1109/JQE.1975.1068610.

Inácio, P., Barreto, B., Horowitz, F., Correia, R.R.B., Pereira, M.B., 2013. Silver migration at the surface of ion-exchange waveguides: a plasmonic template. Opt. Mater. 3, 390. https://doi.org/10.1364/OME.3.000390.

Kaminow, I.P., Stulz, L.W., 1978. Loss in cleaved Ti-diffused LiNbO3 waveguides. Appl. Phys. Lett. 33, 62–64. https://doi.org/10.1063/1.90191.

Kaul, A.N., Thyagarajan, K., 1984. Inverse WKB method for refractive index profile estimation of monomode graded index planar optical waveguides. Opt. Commun. 48, 313–316. https://doi.org/10.1016/0030-4018(84)90306-7.

Mendez, A., Morse, T., 2007. Specialty Optical Fibers Handbook. Academic Press.

Murugasen, P., Sagadevan, S., Shajan, D., 2015. Preparation, techniques and tools used for investigating glasses: an overview. Int. J. Chem. Sci. 13, 693–713.

Opilski, A., Rogoziński, R., Gut, K., Błachut, M., Opilski, Z., 2000. present state and perspectives involving application of ion exchange in glass. Opto-Electronics Rev. 8, 117–127.

Rabinovich, E.M., 1983. Structural role of fluorine in silicate glasses. Phys. Chem. Glas. 24, 54–56.

Ramaswamy, R.V., Srivastava, R., 1988. Ion-Exchanged Glass Waveguides: A Review. J. Light. Technol. 6, 984–1000. https://doi.org/10.1109/50.4090.

Rehouma, F., 1994. Study of silver ion exchange in aluminoborosilicate glass (Doctoral dissertation). Institut National Polytechnique de Grenoble, France.

Rehouma, F., Aiadi, K.E., 2008. Glasses for ion-exchange technology. Int. J. Commun. 1, 148–155. https://doi.org/10.1007/978-94-009-4376-6_12.

Rehouma, F., Aiadi, K.E., Meftah, M.T., 2007. Integrated structure for dual role: measuring the fiber – Guide coupling losses and sensing the external medium variations. J. Optoelectron. Adv. Mater. 9, 2351–2353.

Rehouma, F., Persegol, D., Kevorkian, A., 1995. A new fabrication method for waveguides with controlled surface-interaction length. Sensors Actuators B. Chem. 29, 406–409. https://doi.org/10.1016/0925-4005(95)01715-1.

Tervonen, A., West, B.R., Honkanen, S., 2011. Ion-exchanged glass waveguide technology: a review. Opt. Eng. 50, 71107. https://doi.org/10.1117/1.3559213.

Tomozawa, M., 1993. Alkali ionic transport in mixed alkali glasses. J. Non. Cryst. Solids 152, 59–69. https://doi.org/10.1016/0022-3093(93)90444-3.

Wang, F., Chen, B., Pun, E.Y.B., Lin, H., 2015. Alkaline aluminum phosphate glasses for thermal ion-exchanged optical waveguide. Opt. Mater. (Amst) 42, 484–490. https://doi.org/10.1016/j.optmat.2015.02.007.

Full length article

Stable TEM$_{00}$-mode Nd:YAG solar laser operation by a twisted fused silica light-guide

CrossMark

R. Bouadjemine [a,b,c], D. Liang [a,*], J. Almeida [a], S. Mehellou [a,d], C.R. Vistas [a], A. Kellou [c], E. Guillot [e]

[a] CEFITEC, Departamento de Física, FCT, Universidade Nova de Lisboa, 2829-516 Campus de Caparica, Portugal
[b] CDTA BP 17, Cité 20 Aout 1956, Baba Hassan, Alger 16000, Algeria
[c] Faculté de Phsique, USTHB BP 32 El-Alia, Bab-Ezzouar, Alger 16000, Algeria
[d] Faculté de Phsique Université de Ouargla, 30000, Algeria
[e] PROMES-CNRS, 7 rue du Four Solaire, 66120 Font Romeu, Odeillo, France

ARTICLE INFO

ABSTRACT

To improve the output beam stability of a TEM$_{00}$-mode solar-pumped laser, a twisted fused silica light-guide was used to achieve uniform pumping along a 3 mm diameter and 50 mm length Nd:YAG rod. The concentrated solar power at the focal spot of a primary parabolic mirror with 1.18 m^2 effective collection area was efficiently coupled to the entrance aperture of a 2D-CPC/2V-shaped pump cavity, within which the thin laser rod was pumped. Optimum solar laser design parameters were found through ZEMAX© non-sequential ray-tracing and LASCAD© laser cavity analysis codes. 2.3 W continuous-wave TEM$_{00}$-mode 1064 nm laser power was measured, corresponding to 1.96 W/m^2 collection efficiency and 2.2 W laser beam brightness figure of merit. Excellent TEM$_{00}$-mode laser beam profile at M$^2 \leq 1.05$ and very good output power stability of less than 1.6% were achieved. Heliostat orientation error dependent laser power variation was considerably less than previous solar laser pumping schemes.

© 2017 Elsevier Ltd. All rights reserved.

1. Introduction

The idea of solar-pumped lasers appeared [1] no long after the invention of laser. The conversion of free sunlight into laser light by direct solar pumping is of increasing importance because broadband, temporally constant, sunlight is converted into laser light, which can be a source of narrowband, collimated, rapidly pulsed, radiation with the possibility of obtaining extremely high brightness and intensity. This type of renewable laser is unique since it does not require any artificial pumping source along with its associated electrical power generation and conditioning equipment. Solar-pumped lasers are hence very useful for space applications [2] such as atmospheric and ocean sensing; laser power beaming; deep space communications; orbital space debris removal. Powered by abundant solar energy, solar laser has also large potentials for terrestrial applications such as high temperature materials processing and magnesium–hydrogen energy cycle [3–5], where high brightness solar laser beam can play an important role. Brightness is the most significant parameters for a laser beam. It is given by the laser power divided by the product of the beam spot area and its solid angle divergence. This product is proportional to the
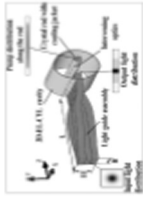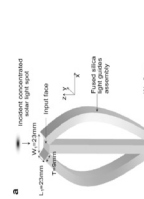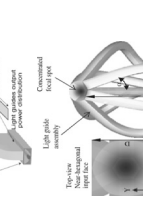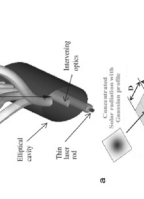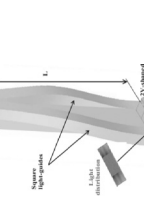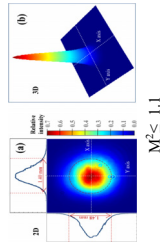
square of beam quality factor M^2. Brightness figure of merit is thus defined as the ratio between laser power and the product of M$_x^2$ and M$_y^2$. Many applications require operation of a solar laser at its fundamental mode: e.g. TEM$_{00}$-mode, since this mode produces the smallest beam divergence, the highest power density, the highest brightness [6] and also the highest stability [7]. Furthermore, the radial profile of TEM$_{00}$-mode is smooth. This property is important at high power levels, since multimode operation leads to the random occurrence of local maxima in intensity, which might exceed the damage threshold of the optical components in a resonator [6].

Since the first demonstration of 1-W solar-pumped laser by Young in 1966 [1], researchers have exploited both parabolic mirrors and Fresnel lenses to attain enough solar flux at the focal point. Many pumping schemes have been proposed to improve solar laser output performance [8–28]. Even though parabolic mirrors have long been explored to achieve tight focusing of incoming solar radiation, the adoption of a Fresnel lens as a primary solar concentrator in the last decade has boosted significantly solar laser efficiency. Considerable solar laser collection efficiency – defined as the ratio between laser output power and primary concentrator area – have been achieved, reaching 30 W/m^2 when pumped through a 4 m^2 area Fresnel lens in 2012 [14]. The thermal lensing effects caused by non-uniform distribution of pump light have,
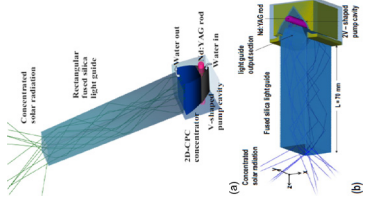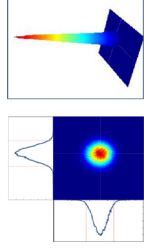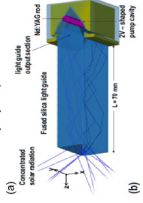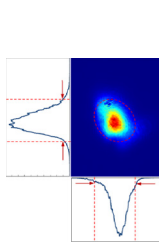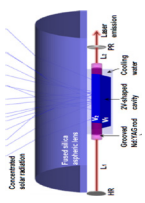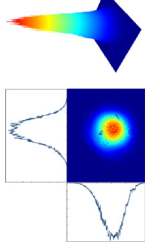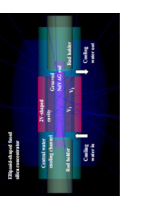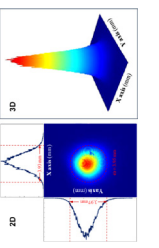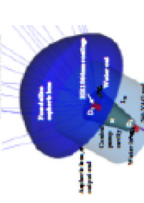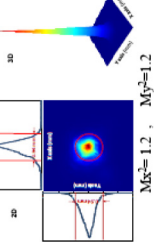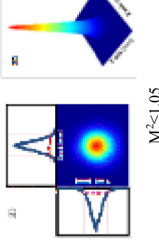
* Corresponding author.
  E-mail address: dl@fct.unl.pt (D. Liang).

Table 1
TEM$_{00}$-mode solar laser pumping schemes with thin laser rods.

	Effective collection area	Configuration pumping	Shape light-guide	Laser rod	Power laser TEM$_{00}$-mode (W)		Collection efficiency (W/m^2)	Beam profile	Beam stability
					Theoretical	Practical			
Geraldes et al. [21]	Parabolic mirror (NA)	Side pumping Twisted fused silica light-guide/2D-EL-CYL pump cavity/intervening optics		Nd:YAG D = 2.5 mm	2	NA	NA	NA	NA
		Side pumping Twisted fused silica light-guide/2D-DCPC/intervening optics			1.4	NA	NA	NA	NA
Pereira et al. [22]	Parabolic mirror 6.85 m^2	Side pumping Twisted fused silica light-guide/2D-CPC pump cavity		Nd:YAG L = 80 mm, D = 3 mm	10.5	NA	11	NA	NA
Liang et al. [23]	Parabolic mirror 1.82 m^2	Side pumping Twisted fused silica light-guide/Elliptical cavity with intervening optics			4.8	4.8	NA	NA	NA
Almeida et al. [24]	Parabolic mirror 1.77 m^2	Side pumping Twisted fused silica light-guide/2DCPC/2V pump cavity		Nd:YAG D = 2.5 mm	8.8	NA	4.97	NA	NA
Liang et al. [15]	Fresnel lens 0.78 m^2	Side pumping Direct pumping Aspheric fused silica lens/2D-CPC/V-shape pumping cavity		Nd :YAG D = 3 mm L = 30 mm	NA	2.3	2.93	$M^2 \leq 1.1$	Moderate stability

Reference	Collector	Pumping scheme	Laser medium				Beam quality	Stability
Liang et al. [17]	Parabolic mirror (CNRS) 2.3 m²	Side pumping rectangular fused silica light-guide/2D-CPC/V pump cavity	Nd:YAG D = 3 mm L = 30 mm		4.4	1.9	$M_x^2 = 1.05$, $M_y^2 = 1.05$	Good stability
Almeida et al. [20]	Parabolic mirror (CNRS) 1.92 m²	Side pumping Single fused silica light-guide/2 V pumping cavity	Nd:YAG D = 4 mm L = 30 mm		5.5	2.84		Reduced stability
Vistas et al. [19]	Parabolic mirror (FCT) 1.11 m²	Side pumping Direct pumping Semi cylindrical fused silica lens/2 V pump cavity	Grooved Nd:YAG D = 3.5 mm L = 34 mm	25.5	4.0	3.6	$M_x^2 = 1.25$, $M_y^2 = 1.14$	Poor stability
Liang et al. [25]	Parabolic mirror (CNRS) 1.13 m²	Side pumping Direct pumping ellipsoid-shaped fused silica/2 V pump cavity	Grooved Nd:YAG D = 4 mm L = 34 mm	4.6	4.5	4	$M_x^2 = 1.2$, $M_y^2 = 1.1$	Poor stability
Liang et al. [28]	Parabolic mirror (CNRS) 1.18 m²	End-side pumping Direct pumping	Nd:YAG D = 4.5 mm L = 35 mm	9.8	9.3	7.9	$M_x^2 = 1.1$, $M_y^2 = 1.1$	Poor stability
Present work	Parabolic mirror (CNRS) 1.18 m²	Side pumping Twisted fused silica light-guide/2D-CPC/2 V pump cavity	Nd:YAG D = 3 mm L = 50 mm	2.7	2.3	1.94	$M_x^2 = 1.2$, $M_y^2 = 1.2$ $M^2 \leq 1.05$	Very good stability

however, contributed to low laser beam brightness when the laser rod was end-side-pumped by the Fresnel lens [13,14]. Even though Fresnel lenses have been preferred due to its simplicity, easy availability and low-cost [11–15], there are still a few inconveniences regarding to their use in solar laser research. Fresnel lenses cause the dispersion of the solar radiation spectrum along its focal zone, impairing the most efficient pump light concentration to laser rod. The solar laser head pumped by a Fresnel lens [11–15] moved together with the whole solar tracking structure; thus, an optical fiber was required for the transportation of solar laser radiation to a fixed target position, diminishing therefore the efficiency of the whole laser system due to the transmission loss of the optical fiber. The advantage of having a stationary laser head at the focus of a primary collector is more pronounced for applications like material processing where a vacuum chamber should be conveniently installed near the laser head. We have, therefore, insisted on improving solar laser efficiency and beam brightness by heliostat-parabolic mirror systems in recent years [16–20,25,27]. Most recently, we have achieved $31.5 \, W/m^2$ multimode, $7.9 \, W/m^2$ TEM_{00}-mode solar laser collection efficiency by using the heliostat-parabolic mirror system in the PROMES – CNRS (Procedes, Materiaux et Energie Solaire – Centre National de la Recherche Scientifique) [28], surpassing the previous records by Fresnel lens [14,15].

The utilization of two-dimensional compound parabolic secondary concentrator (2D-CPC) and three-dimensional compound parabolic concentrator (3D-CPC) tertiary pumping cavity further boosted up the solar laser power level [13–17,25]. Despite the small overlap between Nd:YAG absorption spectrum and solar emission spectrum, Nd:YAG single-crystal material has been demonstrated as an excellent material under solar pumping because of its superior thermal conductivity, high quantum efficiency and mechanical strength characteristics compared to other host materials [7–29]. Side-pumping configuration presents high brightness since it allows the uniform distribution of absorbed solar pump power along the rod axis and spreads the power within the laser medium, reducing the associated thermal loading problems [18,25]. Besides, the free access to both rod ends permits the optimization of more laser resonator parameters, improving largely the laser beam quality and enabling the efficient extraction of solar laser in fundamental mode. Also importantly, as the rod acts as an aperture within a laser resonator, by pumping a small diameter laser rod, high-order resonator modes can be suppressed by large diffraction losses, and beam quality improves. For these reasons, we have concentrated our efforts on side-pumping small diameter rods through heliostat-parabolic mirror system in recent years [15,17,25].

Heliostat orientation error is a critical factor influencing the resonator stability of a solar laser. It moves the center of the absorption distribution inside the crystal, resulting in both less output power and a non-uniform beam profile. To minimize this problem, a single fused silica light-guide with large square input/output ends was proposed [16,17,20]. Pump light uniformity at the output end of the square light-guide was achieved. The transfer efficiency from the focal spot to the laser rod was, however, reduced due to the inefficient light coupling between the large output end of the light guide and the laser rod. Besides, in solar lasers, thermal focusing of a laser rod greatly modifies the modes, and the pump-induced fluctuations of the focal length may strongly perturb the laser output, even preventing any practical or reliable use of the laser [19,20]. Efficient exploitation of the rod volume of a solar laser operating in the fundamental mode requires the solution of following problems: the TEM_{00}-mode volume in the rod has to be maximized, but the resonator should remain as insensitive as possible to focal length and alignment perturbations. Early solutions proposed the compensation of the thermal lens by a convex

mirror, or by negative lenses ground at the ends of the rod, that exactly eliminate the focusing effect of the rod. With these methods, high power in a single-mode beam was obtained [6]. This compensation technique, however, was effective only for one particular value of the focal length.

Since 2008, many solar laser pumping schemes [21–24] were proposed and prototypes [15,17,19,20,25,28] built to generate TEM_{00}-mode laser emission, as listed in Table 1. The most efficient method was related to the direct pumping of a laser rod in the focal zone through either an aspheric lens [15,28], or a cylindrical lens [19] or an ellipsoidal lens [25]. For the PROMES heliostat-parabolic mirror system, a fused silica semi-cylindrical lens was combined with a 2V-shaped pumping cavity to provide efficient side-pumping along a grooved Nd:YAG rod. 4.0 W continuous-wave TEM_{00}-mode ($Mx^2 = 1.2$ and $My^2 = 1.1$) 1064 nm solar laser power at $3.6 \, W/m^2$ collection efficiency were obtained [19]. An ellipsoid-shaped fused silica lens was also combined with a 2V-shaped pumping cavity to provide efficient side-pumping along the same grooved rod. 4.5 W continuous-wave TEM_{00}-mode ($M^2 \leq 1.1$) 1064 nm solar laser power was achieved at collection efficiency of $4.0 \, W/m^2$ [25]. However, poor laser beam stability was found due to the strong thermal lensing effect in both cases [19,25]. Most recently, 9.3 W continuous-wave TEM_{00}-mode 1064 nm solar laser power was measured, corresponding to $7.9 \, W/m^2$ TEM_{00}-mode solar laser collection efficiency [28]. However, most efficient end-side-pumping of a 4 mm diameter 35 mm length Nd:YAG rod through a large aspheric lens has inevitably resulted in non-uniform absorbed pump light distribution, resulting in the TEM_{00}-mode laser beam with reduced quality of $M^2 \leq 1.2$. The laser beam stability was also sensible to the thermal lensing conditions, which depends heavily on the orientation accuracy of the heliostat. Indirect solar laser pumping through a single or a twisted fused silica light-guide [16,17,20–24] was considered to be an effective solution to solar laser beam stability problem. Even though optimum light-guide solar laser pumping parameters were found through ZEMAX© and LASCAD© numerical analysis codes, no prototypes lasers were built to validate these proposals until 2012 [21–24]. A rectangular fused silica light-guide and a 2D-CPC concentrator were combined to further compress the concentrated solar radiation from the focal spot of the PROMES parabolic mirror into a thin laser rod within a V-shaped pumping cavity. 4.4 W continuous-wave TEM_{00}-mode ($M^2 \leq 1.05$) 1064 nm solar laser power was finally produced, attaining 4.0 W laser beam brightness figure of merit [17]. The output laser beam stability was also improved. However, only $1.9 \, W/m^2$ TEM_{00}-mode solar laser collection efficiency was attained. Another rectangular fused silica light-guide was used to couple the concentrated solar power at the focus of the PROMES parabolic mirror into a thin laser rod within a 2V-shaped pumping cavity. 5.5 W continuous-wave TEM_{00}-mode solar laser power and $2.86\% \, W/m^2$ collection efficiency were obtained [20]. However, both output laser beam quality at $M^2 \leq 1.25$ and its stability was quite limited, as shown in Table 1. It is also interesting to note that the prototype with the 2D-CPC/V-shaped pump cavity gave better TEM_{00}-mode laser beam stability than that with only single 2V-shaped pump cavity.

To improve the laser beam stability of the solar-pumped laser by the heliostat–parabolic mirror system, a twisted fused silica light guide side-pumping scheme is proposed here. Based on the refractive and total internal reflection principles, the twisted light-guide transformed the concentrated light spot with near-Gaussian profile at its input face into a uniform rectangular pump light distribution at its output end, facilitating further pump light coupling to the entrance aperture of the 2D-CPC/2V-shaped pump cavity, where the long and thin Nd:YAG rod was efficiently pumped. The prototype solar laser was built in Lisbon and tested in the PROMES during the month of July, 2016. By pumping the

3 mm diameter, 50 mm length rod within the 2D-CPC/2V-shaped cavity, 2.3 W continuous-wave TEM_{00}-mode ($M^2 \leq 1.05$) 1064 nm stable laser emission was achieved, corresponding to 1.96 W/m^2 collection efficiency. The TEM_{00}-mode laser output power was significantly more stable than other solar pumping approaches as listed in Table 1.

2. Stable solar-pumped TEM00-mode Nd:YAG laser system

2.1. Solar energy collection and concentration by the PROMES-CNRS heliostat – parabolic mirror system and the solar-pumped Nd:YAG laser with the twisted light guide

A large plane mirror with 36 small flat segments (0.5 m × 0.5 m each), mounted on a two-axis heliostat, redirected the incoming solar radiation towards the horizontal axis primary parabolic mirror with 2 m diameter, 60° rim angle and 850 mm focal length, as shown in Fig. 1. All the mirrors were back-surface silver coated. Due to iron impurities within the glass substrates of both plane and parabolic mirrors (with 5 mm and 10 mm thickness respectively), only 59% of incoming solar radiation was effectively focused to the focal zone. A shutter with motorized blades regulated the incoming solar power from the heliostat. After considering all the shading effects such as the spaces between the heliostat plane mirrors, the shutter blades, the X-Y-Z axis positioning system, the laser resonant cavity and its mechanical fixture, an effective collection area of 2.65 m^2 was calculated when the shutter was totally opened. On high solar insolation days, more than 1400 W solar power could be focused into a near-Gaussian light spot with 11 mm full width at half maximum (FWHM). We

Fig. 1. Solar laser pumping scheme by the PROMES heliostat – parabolic mirror system.

actually limited the maximum solar power at the focus by masking the external annular area of the 2.0 m diameter parabolic mirror as explained in Section 4.2.

The TEM_{00}-mode solar laser system, composed by the twisted fused silica light guide, the 2D-CPC/2V-shaped pump cavity with the long and thin Nd:YAG rod, were mechanically mounted to the laser resonant cavity, which was then fixed on the X-Y-Z axis positioning system, as shown in Fig. 1, through a multi-angle vice, as shown in Fig. 2. Accurate optical alignment of the laser head in the focal zone was ensured by adjusting the X-Y-Z axes of the positioning system. Both the Nd:YAG rod and pump cavity were actively cooled by water at 6 L min^{-1} flow rate.

2.2. Description of the twisted fused silica light-guide and 2D-CPC/2V-shaped pump cavity

The concentrated solar radiation from the PROMES parabolic mirror was firstly collected by the twisted fused silica light-guide with 19.4 mm × 16.6 mm input face, 119.3 mm length and 8.3 mm × 38.6 mm rectangular output end, as illustrated in Figs. 3 and 6 (see more details in Section 4). The 2D-CPC/2V-shaped cavity had an entrance aperture of 11 mm × 35 mm and was 10 mm in depth. The hollow 2D-CPC had 11 mm input aperture, 7 mm output aperture, 6.5 mm height and 45° acceptance angle. The 2V-shaped cavity was composed of two plane reflectors $V_1 + V_2$, where the reflector V_1 was mounted at $\alpha_1 = 107°$ full-angle and the reflector V_2 at $\alpha_2 = 48°$ half-angle, as shown in Fig. 3. In ZEMAX© analysis, the 2D-CPC/2V-shaped cavity combination was found more efficient for coupling the light rays of different angles from the twisted light-guide to the laser rod, as compared to the single V-shaped reflector. The inner walls of both 2D-CPC and 2V-shaped reflectors were bonded with a protected silver-coated aluminum foil with 94% reflectivity. Cooling water also ensured an efficient light coupling from the light guide to the laser cavity and partially prevented both UV solarization and IR heating to the laser rod. By combining the light concentration features of the 2D-CPC/2V-shaped pump cavity with the homogenization capacity of the twisted light-guide, relatively uniform pump power deposition within the laser rod was achieved.

In ZEMAX© analysis, eight detectors were used along the light guide to exam the light distribution at different sections along the light guide. The numerically calculated transfer efficiency, the absorbed pump power by the laser rod, and finally the calculated TEM_{00}-mode laser powers and profiles by LASCAD© analysis, with or without heliostat orientation errors, are given in Table 2.

Heliostat orientation errors moved the center of the absorption distribution within a laser rod, resulting in less laser output power and a non-uniform laser beam profile. The twisted light-guide was therefore essential to overcoming this problem, serving as a beam
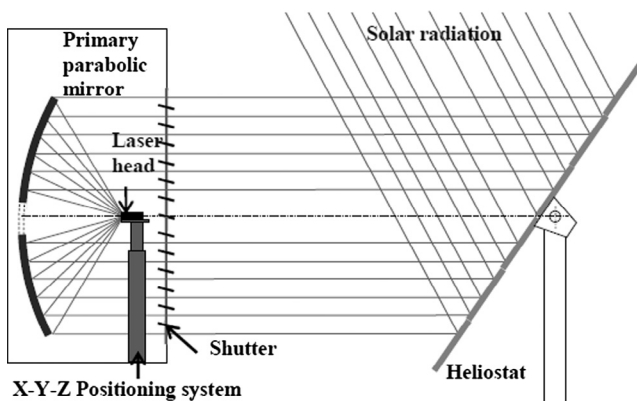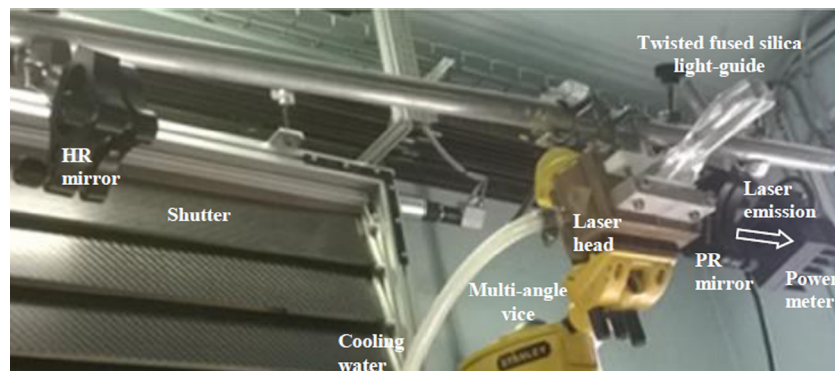
Fig. 2. Solar laser system with the twisted fused silica light-guide and asymmetric laser resonant cavity for the extraction of TEM_{00}-mode laser power.
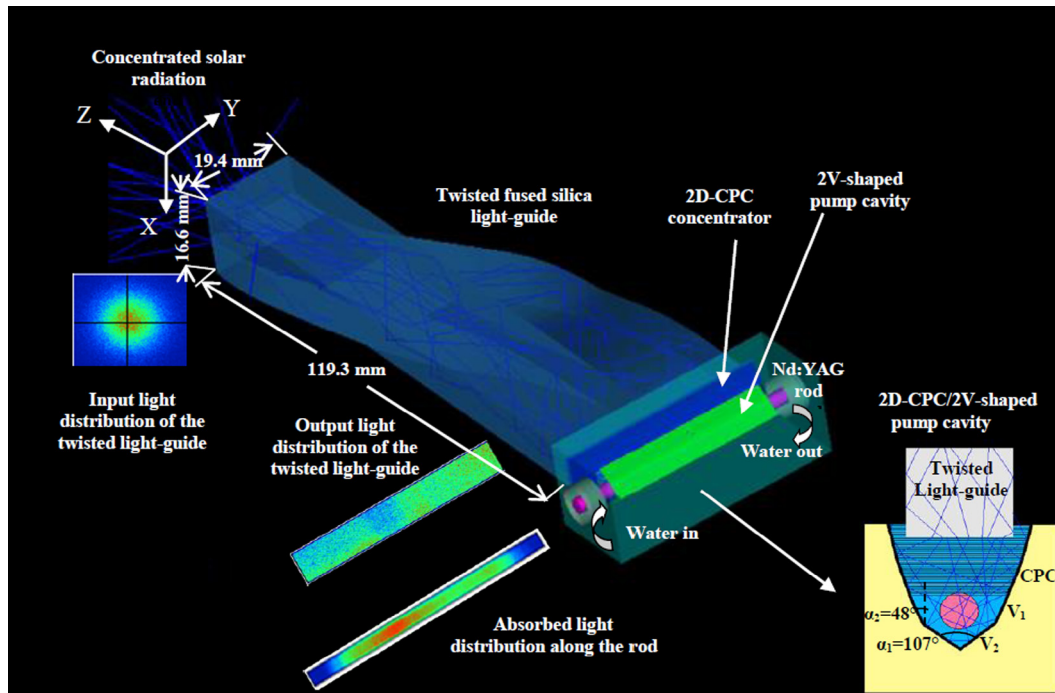
Fig. 3. Design of twisted light guide solar-pumped Nd:YAG laser head.

homogenizer by transforming the near-Gaussian profile of the concentrated light spot at its input face into a uniform pump light distribution at its output end. The light distributions along the twisted light-guide, the absorbed pumped light distribution along the laser rod and consequently the output laser beam profiles were all listed in both Fig. 3 and Table 2. By ZEMAX© ray tracing code, 73.4% transfer efficiency was calculated for zero orientation error. A typical 2 mrad heliostat orientation error could cause 2.55 mm displacement of focal spot, shifting it away from the center of the input face. The displacement of the focal spot along X-axis caused a slight improvement in transfer efficiency to 73.7%, since more light could be coupled to the output end by the curved part of the light-guide. Also, for the 2.55 mm displacement in Y-axis, 73.7% transfer efficiency was attained. With 2.55 mm orientation errors in both X and Y-axes, the transfer efficiency was finally reduced to 73.3%. For zero orientation error, 41.7 W absorbed pump power was calculated by the ZEMAX© code. For 2.55 mm displacement in either X or Y axis, 39.9 W and 41.3 W was also calculated respectively. For 2.55 mm displacement in both X and Y axis, 39.7 W absorbed pump power was finally calculated. It was interesting to note that high transfer efficiency did not necessarily mean high absorption efficiency by the laser rod, since the angles of the exiting light rays from the light guide output end also influenced strongly the final absorption efficiency of the laser rod. Orientation error dependent TEM$_{00}$-mode laser beam profiles and output powers in Table 2 will be discussed in Section 3.

3. Numerical optimization of the laser system and TEM$_{00}$-mode power by ZEAMAX© and LASCAD© codes

3.1. ZEAMAX© optimization of the optical parameters of the laser system

ZEMAX© non-sequential ray-tracing code was used to optimize all the design parameters of the twisted light-guide solar laser. The standard solar spectrum for one-and-a-half air mass (AM1.5) [30] was used as the reference data for consulting the spectral irradiance (W/m^2/nm) at each wavelength. The terrestrial solar irra-

diance of 1000 W/m^2 was considered in the ZEMAX© analysis. The half-angle of 0.27° subtended by the Sun was also considered. The effective pump power of the light source was 189 W for the parabolic mirror with 1.4 m diameter. It took into account of parameters such as the 16% overlap between the Nd:YAG absorption spectrum and the solar spectrum, the reflection and absorption losses of both the heliostat and the parabolic mirror, the shading effects of the shutter, the mechanical support unit and the laser head. The absorption spectrum of fused silica and water were also included in the ZEMAX© numerical data to account for absorption losses. For a 1.1 at.% Nd^{3+}-doped YAG single-crystal medium, 22 absorption peaks were defined in the ZEMAX© numerical data. All the peak wavelengths and their respective absorption coefficients were added to the glass catalog in the ZEMAX software [18]. Solar irradiance values for the above-mentioned 22 peak absorption wavelengths were consulted from the standard solar spectra for AM1.5 and saved as source wavelength data. During ray-tracing, the active medium was divided into a total of 18,000 zones. The path length in each zone was found. With this value and the effective absorption coefficient, the absorbed power within the laser medium was calculated by summing up the absorbed pump radiation of all zones. The absorbed pump flux data from the ZEMAX© numerical analysis was then processed by LASCAD software to study the laser beam parameters of the Nd:YAG single-crystal rod.

3.2. Extracting the maximum TEM$_{00}$-mode solar laser power by LASCAD© code

In LASCAD© analysis, the optical resonator as given in Fig. 4 was comprised of two opposing parallel mirrors at right angles to the axis of the active medium. One end mirror R$_1$ was high-reflection coated with 99.8% reflectivity (HR1064 nm). The other output mirror R$_2$ was partial reflection coated (PR1064 nm). The amount of feedback was determined by the reflectivity of the PR mirror. The asymmetric optical resonator was already found to be a good configuration for achieving fundamental mode laser operation [17,20], as shown in Fig. 4. The absorbed pump-flux data from the ZEMAX©

Table 2
Orientation error dependent transfer efficiency of the twisted light-guide and TEM$_{00}$-mode laser power.

Input/output face area	Input face 19.4 mm × 16.6 mm Length of light-guide L = 119.3 mm Output end 38.6 mm × 8.3 mm										
	Distribution of pump light at different section along the light-guide / Transfer efficiency								%	Distribution of absorbed pump power along the rod	3D TEM00-mode laser beam profile and laser power
	Detector 1 input face	Detector2 0.12 L	Detector3 0.2 L	Detector 4 0.37 L	Detector5 0.54 L	Detector6 0.75 L	Detector7 0.87L	Detector 8 output face	%		
without tracking error	113.6 W							83.4W	73.4	41.7W	2.64 W
With tracking error — ΔX = 2.55 mm	113.6 W							83.8W	73.7	39.9 W	2.70 W
With tracking error — ΔY = 2.55 mm	113.6 W							83.8W	73.7	41.3 W	2.67 W
With tracking error — ΔX = ΔY = 2.55 mm	113.6 W							83.3W	73.3	39.7 W	2.57 W
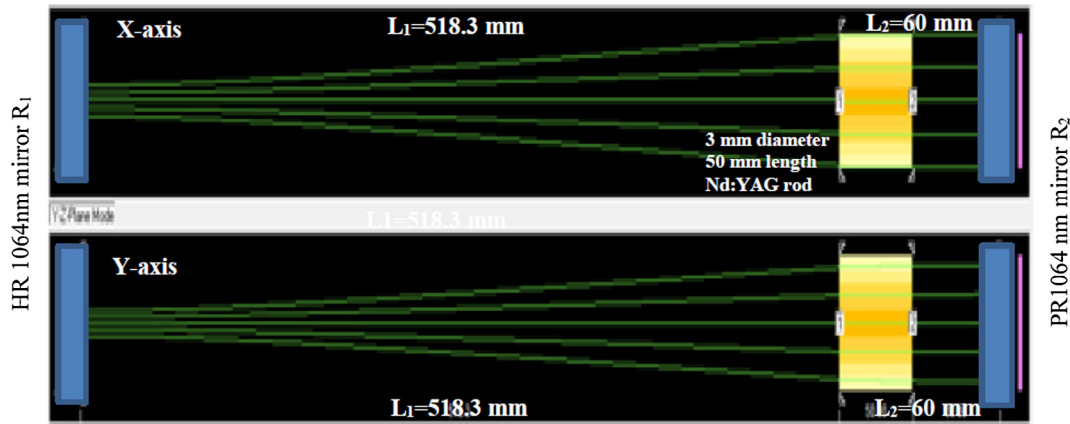
Fig. 4. Asymmetric laser resonant cavity for extracting the maximum TEM$_{00}$-mode solar laser power.
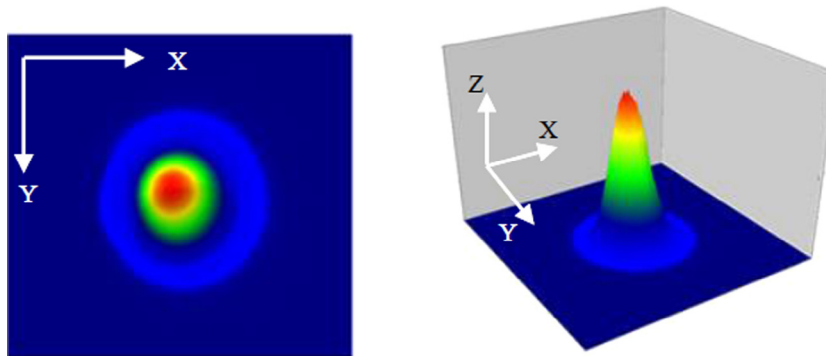
Fig. 5. Numerically calculated 2D, and 3D TEM$_{00}$-mode laser beam profiles on the output mirror of the asymmetric laser resonator without orientation error.

analysis in Section 3.1 was processed by LASCAD© software. By considering 3.88% diffraction loss calculated from the LASCAD© analysis, 2.6 W TEM$_{00}$-mode solar laser power was numerically attained. The resonant cavity with -5 m RoC end mirror R_1 (HR 99.8%) positioned at L_1 = 518.3 mm, another -5 m RoC output mirror R_2 (with 94% reflectivity) positioned at L_2 = 60 mm, and total resonant cavity length $L_T = L_1 + L_2 + L_{rod} = 628.3$ mm extracted the maximum TEM$_{00}$-mode laser power from the 3 mm diameter, 50 mm length rod.

The numerically calculated 2D and 3D TEM$_{00}$-mode laser beam profiles on the output mirror of the asymmetric laser resonator with RoC = -5 m without tracking error is given in Fig. 5. Using LASCAD© analysis, 2.64 W TEM$_{00}$-mode continuous-wave laser power was achieved, as indicated in Table 2. The numerical simulation of laser beam pattern with orientation error was slightly shifted from the center, as shown in Table. 2. 2.7 W TEM$_{00}$ mode continuous-wave laser power was obtained for the 2.55 mm shift in X-axis. Also, 2.67 W continuous-wave TEM$_{00}$-mode laser power was obtained for the 2.55 mm shift in Y-axis. For orientation errors in both X and Y-axes, the worst TEM$_{00}$-mode laser power of 2.57 W was numerically obtained. 2% laser beam stability was therefore calculated for 2.55 mm shift along either X or Y axis. For the worst case, 5% beam stability was numerically calculated when there were 2.55 mm shifts in both X and Y axis.

4. TEM$_{00}$-mode continuous-wave solar laser oscillation experiments

4.1. Production of both the twisted fused silica light-guide and the solar laser head

Fused silica was an ideal optical material for solar laser pumping since it was transparent over the Nd:YAG absorption spectrum.

It had a low coefficient of thermal expansion and it was resistant to scratching and thermal shock. The twisted fused silica light-guide with 19.4 mm × 16.6 mm input face, 119.3 mm length and 8.3 mm × 38.6 mm rectangular output face, as shown in Fig. 6d, was produced directly from the fused silica slab of 99.999% optical purity and 40 mm × 17 mm × 120 mm dimensions, as shown in Fig. 6a. The production of the twisted light-guide was both time consuming and delicate. The process was subdivided into three steps. The fused silica slab in Fig. 6a was firstly sculpted by diamond tools and ground into the shape of twisted light-guide, as shown in Fig. 6b. Secondly, the twisted light-guide was then polished by coarse grinding paper, and finally to transparent surfaces, as shown in both Fig. 6c and d, by fine polishing paper and suspension liquid.

After the successful production of the light-guide, another important step was to manufacture the laser head according to the final dimension of output end of the twisted light-guide, as optimized by both ZEMAX© and LASCAD© analysis in the previous section. All mechanicals pieces of laser head were designed with Solid Works software, as shown in Fig. 7.

4.2. Experimental results of TEM$_{00}$-mode solar laser oscillation

Based on the numerically optimized design parameters of the solar laser system by both ZEMAX© and LASCAD© codes, the prototype solar laser was built in Lisbon and tested in PROMES – CNRS during July, 2016. The 3 mm diameter, 50 mm length thin Nd:YAG rod was supplied by Altechna Co., Ltd. It had 1.1% Nd^{3+} concentration. Both ends of the rod were anti-reflection (AR) coated (R < 0.2% @ 1064 nm). The resonator mechanics were designed to allow the displacement of the HR mirror, while maintaining the PR mirror at fixed L_2 = 60 mm position, as shown in Fig. 2. Direct
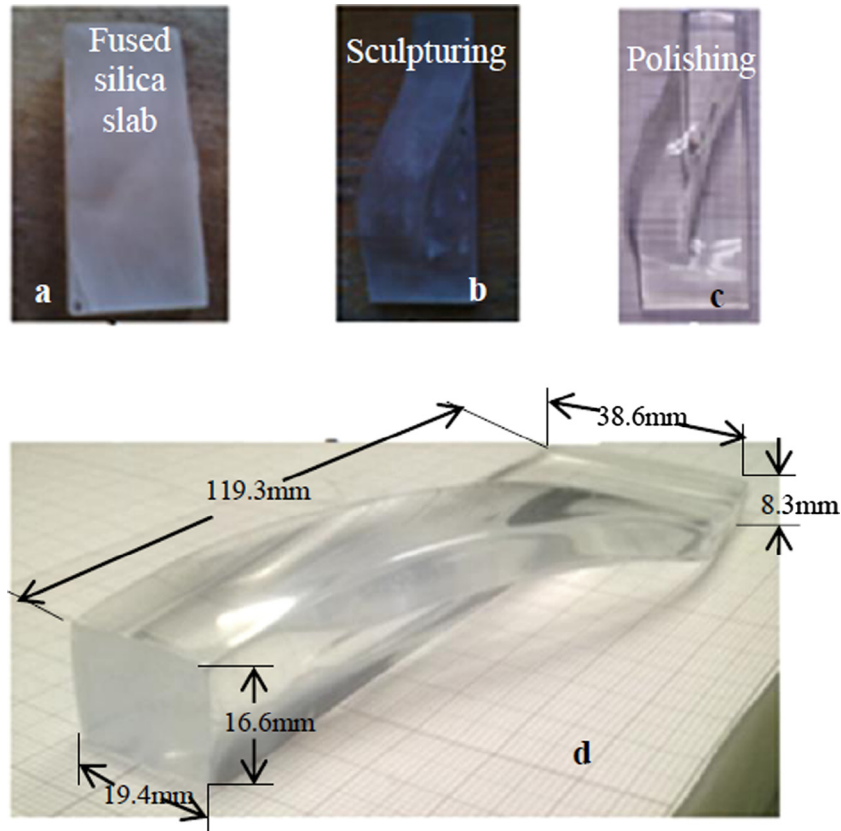
Fig. 6. Photos of different production steps of the fused silica twisted light-guide. (a) Fused silica slab. (b) Sculpturing the twisted light-guide from the slab. (c) Grinding and polishing of the twisted light-guide. (d) Twisted fused silica light guide with final dimensions.
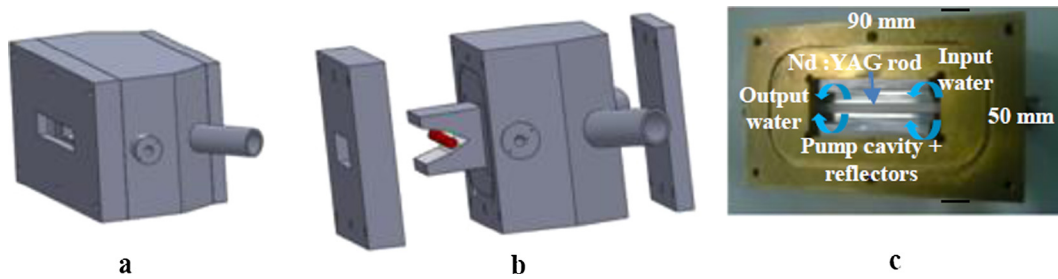
Fig. 7. 3D Design of laser head: (a) assembled view, (b) side view, (c) manufactured laser head in copper, laser cavity in aluminum, inner wall of reflector bonded with a protected silver-coated aluminum and the thin laser rod.

solar irradiance was measured simultaneously during laser experiments with a Kipp & Zonen CH1 pyrheliometer on a Kipp & Zonen AP solar tracker. It varied between 970 and 1000 W/m^2 during the experiments. A CINOGY UV-NIR beam profiler – CinCam CMOS was used for monitoring the laser beam profile.

To measure the beam diameters at $1/e^2$ width under high 1064 nm laser intensity, a PR1064 nm (95%), ROC = ∞ output mirror was added before the CMOS detector, acting as an extra laser beam attenuator to reduce the 1064 nm laser power to mW level for the detector. Laser power was measured simultaneously with a Thorlabs PM1100D power meter. The input solar power at the focus was measured by a Molectron PowerMax 500D power meter.

To reduce the maximum input solar power at the focus, we limited the input solar power at focus by masking the external annular area of the 2.0 m diameter parabolic mirror so that only its 1.4 m diameter central circular area was utilized. After discounting the shading effects of the heliostat solar mirror, the
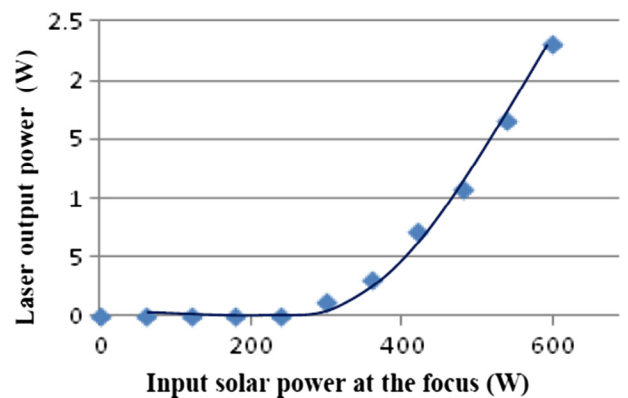
Fig. 8. TEM$_{00}$-mode continuous-wave 1064 nm solar laser power output versus solar input power at the focus.
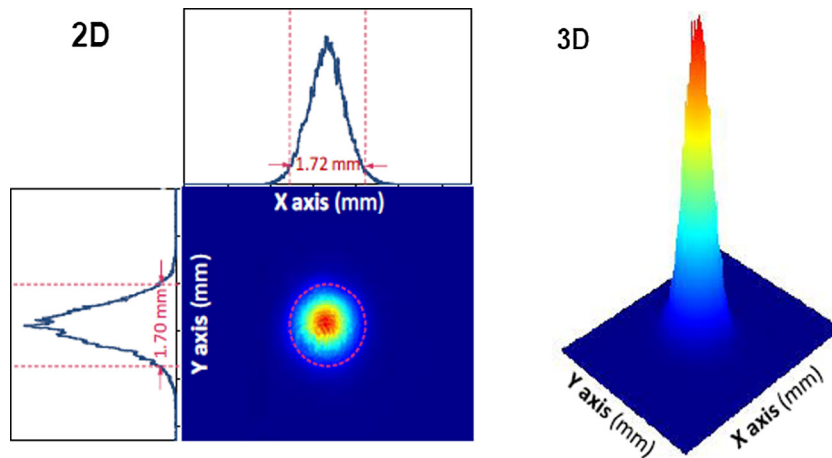
Fig. 9. TEM_{00}-mode output laser beam 2D and 3D profiles.

shutter, the X-Y-Z axes positioning system, the multi-angle vise and the 0.3 m diameter central opening on the parabolic mirror and the solar laser head, 1.18 m^2 effective solar energy collection area was calculated. For 1000 W/m^2 solar irradiance and 1.18 m^2 effective collection areas, 600 W was measured at the focal spot with the shutter totally opened. The asymmetric resonator with RoC = −5 m PR (94%) output mirror R_2 was fixed at L_2 = 60 mm and RoC = −5 m HR mirror R_1 placed at L_1 = 518.3 mm. Laser started to oscillate at an input power of 276 W, corresponding to approximately 46% of the total solar power of focal spot. The maximum TEM_{00}-mode continuous-wave 1064 nm laser power of 2.3 W was measured, as shown in Fig. 8, corresponding to the collection efficiency of 1.94 W/m^2. Since no aperture was used in the laser resonator besides the rod itself, oscillation of more than one mode occurs at low output powers due to the relatively small overlap between the fundamental mode volume and the pumped region. With the increase of pump power and also diffraction loss, only one mode of higher intensity become possible to oscillate. The previous TEM_{00}-mode laser schemes demonstrated poor stability [19,25]. The single light-guide/2D-CPC/V-shaped pump cavity [27] offered better TEM_{00}-mode laser beam stability than that with single light-guide/2V-shaped pump cavity [20]. Our twisted light-guide ensured more uniform pumping to the long and thin Nd: YAG rod. This in turn, led to significantly reduced solar pumping intensity, and consequently less heat load, less thermal stress and working temperature, as compared to all the previous schemes [19,20,25,27,28]. Strong thermal lensing effects, which affected largely the TEM_{00}-mode laser power stability of previous solar lasers were not observed in our measurement. Therefore, the present prototype laser with twisted light-guide offered better output stability of 1.6% during the laser operation, considerably than the previous prototype TEM_{00}-mode lasers with usually more than 10% laser beam stability. In future, by improving polishing accuracy of the dimension of the twisted light guide, enhanced TEM_{00}-mode solar laser efficiency and stability can hopefully be achieved.

The slight discrepancy in laser beam diameters at $1/e^2$ along X and Y-axis in Fig. 9 could be justified by the slight pump profile misalignment due to heliostat orientation error. Taking this factor into account, $Mx^2 \approx My^2 \leq 1.05$ were considered as adequate measured values for quantifying the laser beam quality. Relatively good solar laser beam figure of merit of 2.2 W was therefore calculated.

5. Conclusion

The twisted light-guide acted as a beam homogenizer by transforming the Gaussian profile of the concentrated light spot at its input end into a rectangular uniform pump light distribution at its output end, suitable for pump light coupling to the entrance aperture of the 2D-CPC/2V-shaped pump cavity, where the long and thin Nd:YAG rod was efficiently pumped. The twisted fused silica light-guide was firstly optimized by both ZEMAX© non-sequential ray-tracing and LASCAD© laser cavity analysis, this side-pumping solar laser with the twisted light-guide was firstly built in Lisbon, and then tested in the PROMES – CNRS heliostat-parabolic solar energy collection and concentration system. 2.3 W continuous-wave TEM_{00} 1064 nm laser power ($M^2 \leq 1.05$) was achieved, corresponding to 1.96 W/m^2 collection efficiency and 2.2 W laser beam brightness figure of merit. Very good laser power stability of 1.6% was achieved, significantly better than that of the previous prototypes. By improving polishing accuracy of the twisted light-guide dimensions, more uniform pump light absorption along the laser rod and consequently higher solar laser efficiency and stability can be expected.

Acknowledgements

References

[1] C. Young, Appl. Opt. 5 (1966) 993.
[2] Space Solar Power: Limitless Clean Energy from Space, National Space Society, March 26, 2013.
[3] T. Yabe, S. Uchida, K. Ikuta, K. Yoshida, C. Baasandash, M.S. Mohamed, Y. Sakurai, Y. Ogata, M. Tuji, Y. Mori, Y. Satoh, Y. Ohkubo, M. Murahara, A. Ikesue, M. Nakatsuka, T. Saiki, S. Motokoshi, C. Yamanaka, Appl. Phys. Lett. 89 (2006) 261107.
[4] T. Yabe, B. Bagheri, T. Ohkubo, S. Uchida, K. Yoshida, T. Funatsu, T. Oishi, K. Daito, M. Ishioka, N. Yasunaga, Y. Sato, C. Baasandash, Y. Okamoto, K. Yanagitani, J. Appl. Phys. 104 (2008) 083104.
[5] M. Oliveira, D. Liang, J. Almeida, C.R. Vistas, F. Gonçalves, R. Martins, Sol. Energy Mater Sol. Cells 155 (2016) 430.
[6] W. Koechner, Solid-state Laser Engineering, vol. 5, Springer-Verlag, Berlin, Heidelberg, 2006, pp. 227–238.
[7] Y. Wang, J. Liu, Q. Liu, Y. Li, K. Zhang, Opt. Express 18 (2010) 12044.
[8] M. Weksler, J. Shwartz, IEEE J. Quantum Electron. 24 (1988) 1222.
[9] R. Benmair, J. Kagan, Y. Kalisky, Y. Noter, M. Oron, Y. Shimony, A. Yogev, Opt. Lett. 15 (1990) 36.

[10] M. Lando, J. Kagan, B. Linyekin, V. Dobrusin, Opt. Commun. 222 (2003) 371.
[11] T. Yabe, T. Ohkubo, S. Uchida, M. Nakatsuka T. Funatsu, A. Mabuti, A. Oyama, Y. Nakagawa, T. Oishi, K. Daito, B. Behgol, Y. Nakayama, M. Yoshida, S. Motokoshi, Y. Sato, C. Baasandash, Appl. Phys Lett. 90 (2007) 261120.
[12] T. Ohkubo, T. Yabe, K. Yoshida, S. Uchida, T. Funatsu, B. Bagheri, T. Oishi, K. Daito, M. Ishioka, Y. Nakayama, N. Yasunaga, K. Kido, Y. Sato, C. Baasandash, K. Kato, T. Yanagitani, Y. Okamoto, Opt. Lett. 34 (2009) 175.
[13] D. Liang, J. Almeida, Opt. Express 19 (2011) 26399.
[14] T.H. Dinh, T. Ohkubo, T. Yabe, H. Kuboyama, Opt. Lett. 37 (2012) 2670.
[15] D. Liang, J. Almeida, Opt. Express 21 (2013) 25107.
[16] J. Almeida, D. Liang, E. Guillot, Opt. Laser Technol. 44 (2012) 2115.
[17] D. Liang, J. Almeida, C.R. Vistas, E. Guillot, Sol. Energy Mater. Sol. Cells 134 (2015) 305.
[18] D. Liang, J. Almeida, E. Guillot Appl. Phys. B – Laser Opt. 111 (2013) 305.
[19] C.R. Vistas, D. Liang, J. Almeida, E. Guillot, Opt. Commun. 366 (2016) 50.
[20] J. Almeida, D. Liang, C.R. Vistas, R. Bouadjemine, E. Guillot, Appl. Phys. B – Laser Opt. 121 (2015) 473.
[21] J.P. Geraldes, Dawei Liang, Sol. Energy Mater. Sol. Cells 92 (2008) 836–843.
[22] R. Pereira, D. Liang, Opt. Commun. 282 (2009) 1385.
[23] D. Liang, R. Pereira, Opt. Laser Technol. 41 (2009) 687.
[24] J. Almeida, D. Liang, Opt. Commun. 285 (2012) 5327.
[25] D. Liang, J. Almeida, C.R. Vistas, M. Oliveira, F. Gonçalves, E. Guillot, Sol. Energy Mater. Sol. Cells 145 (2016) 397.
[26] J. Almeida, D. Liang, Opt. Commun. 333 (2014) 219.
[27] D. Liang, J. Almeida, C.R. Vistas, Appl. Opt. 55 (2016) 7712.
[28] D. Liang, J. Almeida, C.R. Vistas, E. Guillot, Sol. Energy Mater. Sol. Cells 159 (2017) 435.
[29] D. Liang, J. Almeida, D. Garcia, Proc. SPIE 8785 (2013), 87859Y-1.
[30] Standard Tables for Reference Solar Spectral Irradiances: Direct Normal, and Hemispherical on 37° Tilted Surface, ASTM Standard G173-03, 2012.

Thermal stability and spectroscopic study of Ho^{3+}/Yb^{3+} co-doped fluorophosphates glasses

O. Bentouila [a],*, K.E. Aiadi [a], F. Rehouma [b], M. Poulain [c], F. Benhbirech [a]

[a] Équipe Optoélectronique, Laboratoire LENREZA, Université Kasdi Merbah-Ouargla, 30000 Ouargla, Algeria
[b] Université d'El-Oued, B.P 789 El-Oued R.P, 39000 El-Oued, Algeria
[c] Matériaux Photoniques, UMR Sciences Chimiques, Université de Rennes 1, F-35042 Rennes, France

A B S T R A C T

Holmium/Ytterbium co-doped fluorophosphate glasses with compositions (80-x-y) NaPO$_3$-10SrF$_2$-10ZnF$_2$- xHoF$_3$- yYbF$_3$ (x = 1 and y = 0.5, 1, 1.5 and 2 mol%) were prepared by melt-quenching technique. The stability criteria indicate that these glasses exhibit a good resistance against devitrification. Densities of glasses were determined and showed an almost linear variation with increase of YbF$_3$ content. Spectroscopic parameters of Ho^{3+} such as radiative transition probability, branching ratio, spectroscopic quality factor, integrated emission cross section and radiative lifetime, were calculated on the basis of Judd-Ofelt analysis. The results showed that these glasses could be proposed as suitable lasing materials.
© 2017 The Authors. Production and hosting by Elsevier B.V. on behalf of King Saud University. This is an open access article under the CC BY-NC-ND license (http://creativecommons.org/licenses/by-nc-nd/4.0/).

1. Introduction

Rare earth ions doped glasses have a potential application in different fields as a solid state lasers, optical fiber amplifiers and waveguide lasers. Rare earth ions are used as doping agents because of their various transitions in the visible and infrared regions and their insensitivity to the matrix in which are introduced. Up to now, a variety of glassy materials such as silicate (Bai et al., 2011), phosphate (Rivera-López et al., 2011; Hraiech et al., 2013), fluoride (Mortier et al., 2007; Reichert et al., 2015), chalcogenide (Li et al., 2016; Ari et al., 2017), tellurite (Meruva et al., 2014; Costa et al., 2015; Sajna et al., 2016), germanate (Fan et al., 2011, 2015) and halogeno-phosphates glasses (Babu and Ratnakaram, 2016; Galleani et al., 2017) have been investigated as host materials for rare earth ions in the aim to developing of optical devices. Among different glassy host materials, halogeno-phosphates glasses offer significant advantages. They are easily prepared by introducing selected metal halides (fluoride in our

case) into polyphosphate glasses. These glasses exhibit low phonon energy than that of phosphate glasses and a less complex fabrication route than that of fluoride glasses and can accept a high concentration of rare earth ions which can improve or induce new optical properties (Poulain et al., 1992; Kenyon, 2002; Dwivedi et al., 2010; Polishchuk et al., 2011; Galleani et al., 2017).

Solid state lasers operating at 2 µm wavelength has attracted so much attention in recent years owing to their potential applications in several fields such as eye safe laser radars, remote sensing, military, atmospheric pollution detection, medical surgery, etc (Tian et al., 2010; Wu et al., 2012; Ryabochkina et al., 2017). Efficient 2 µm emission required an appropriate rare earth ions and host materials. 2 µm laser emission can be achieved in some rare earth ions such as Ho^{3+} with the transition $^5I_7 \rightarrow ^5I_8$ (Fan et al., 2015) However, Ho^{3+} ions have no corresponding absorption energy levels to be pumped directly by the commercial 800 nm or 980 nm laser diode (LD). Thus, Co-doping with other rare earth ions such as Tm^{3+} (Seshadri et al., 2014; Chen et al., 2016) and Yb^{3+} (Żmojda et al., 2012; Pandey et al., 2016) ions can sensitize efficiently Ho^{3+} to achieve 2 µm emission. Yb^{3+} is frequently chosen as a sensitizer because this ion has a strong absorption band around 980 nm, and the Yb^{3+}: $^2F_{5/2}$ level is close to the Ho^{3+}: $^5I_6$ level which can provide an efficient energy transfer from Yb^{3+} to Ho^{3+} ions.

A several number of recent studies reporting the spectroscopic properties of Ho^{3+} doped glasses and Ho^{3+} doped glasses sensitized with either Tm^{3+},Yb^{3+} or Er^{3+} are available in the literature

Production and hosting by Elsevier

(Babu and Ratnakaram, 2016; Bai et al., 2011; Chen et al., 2016; Gandhi et al., 2010; Hemming et al., 2014; Rai et al., 2003; Satyanarayana et al., 2010). Furthermore, to our knowledge, there are few number of investigations on Ho^{3+}/Yb^{3+} co-doped fluorophosphate glasses (Gámez et al., 2009; Tian et al., 2010; Wang et al., 2011). In this work we report thermal and spectroscopic studies of a new composition of fluorophosphate glasses co-doped Ho^{3+}/Yb^{3+} with doping concentration of Yb^{3+} varied from 0.5 mol% up to 2 mol% while the doping concentration of Ho^{3+} is kept constant at 1 mol%.

2. Experimental

2.1. Glass preparation

Samples of fluorophosphate glasses with general formula (in mol%): $(80-x-y)$ $NaPO_3$-$10SrF_2$-$10ZnF_2$- $xHoF_3$- $yYbF_3$ $(x = 1$ and $y = 0.5$, 1, 1.5 and 2 mol%) were prepared using high-purity of $NaPO_3$, SrF_2, ZnF_2, HoF_3 and YbF_3 powder. The doping concentration of the rare earth was set at 1 mol% for Ho^{3+} ions and varying from 0.5 to 2 mol% for Yb^{3+} ions. A stoichiometric mixture of the starting materials (about 10 g) is placed in a platinum crucible and melted at 900 °C for 15 min. The melts were cast on preheated brass molds at a temperature 10 °C below the glass transition temperature. Thermal annealing of the samples is performed for several hours, in order to eliminate the internal stresses of mechanical or thermal origins created during quenching, following by a slow cooling to room temperature. After annealing, the glass samples were cut and polished. The samples obtained after polishing have parallel faces allowing the optical characterization. In the other hand, some local defects, such as scratches and unevenness, are difficult to avoid.

2.2. Measurements

The characteristic temperatures (temperature of glass transition T_g and temperature of onset crystallization T_x) were determined by differential scanning calorimetry (DSC) using *DSC TA Instrument* with a programmed heating rate of 10 °C/min. The accuracy on the temperature is about ±2 °C. Density was measured by Archimedean method with an accuracy of ±0.001. Refractive index was measured by an Abbe refractometer with a mean error ±0.001. Absorption spectra were recorded at room temperature using a double beam spectrophotometer UV–Vis – Near IR CARY 5G brand operating between 200 and 3000 nm with a spectral resolution of 0.1 nm.

3. Results

3.1. Glass samples

Fig. 1 shows all the samples: non-doped, doped with Ho^{3+} only and co-doped H^{3+}/Yb^{3+}. Compositions of glass samples were presented in Table 1.
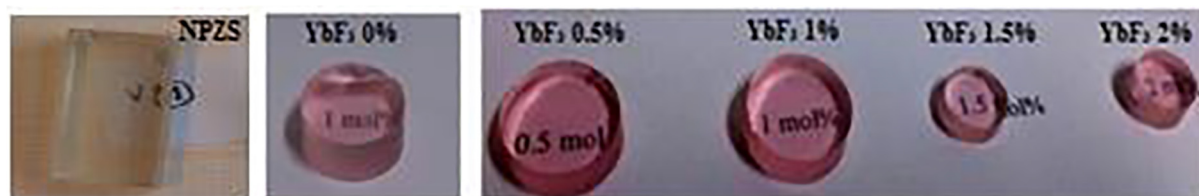
3.2. Thermal properties, density and refractive index

Fig. 2 represents the DSC curves of the samples:j without any doping ions (dash-dotted line), doped with Ho^{3+} only (dotted line) and Ho^{3+}/Yb^{3+} co-doped (with 1 mol%YbF_3, solid line). Glass transition temperature T_g for NPSZ_HYy series still situated around 250 °C and the crystallization onset T_x around 450 °C.

The values of refractive index and the density of glass samples were presented in Table 2. The results show a small almost linear variation of refractive index and density with the variation of YbF_3 content.

3.3. Absorption spectra and Judd-Ofelt analysis

The absorption spectra are shown in Fig. 3. We can count ten absorption bands centered at 1957, 1155, 642, 538, 486, 472, 448, 418, 386 and 360 nm corresponding to the optical transitions of the Ho^{3+} ion from its ground state $^5I_8$ to the different excited states: $^5I_7$, $^5I_6$, $^5F_5$, $^5F_4$, $^5F_3$, $(^5F_2, {}^3K_8)$, $^5G_6$, $^5G_5$, $^5G_4$ and $^3H_6$ respectively. We can also observe an absorption band at 980 nm correspond to the transition $^2F_{7/2}$ to $^2F_{5/2}$ of the Yb^{3+} ion in the four co-doped samples.

The different spectroscopic parameters of the trivalent rare-earth ions in various hosts can be calculated by the application of the theory proposed by Judd (Judd, 1962) and Ofelt (Ofelt, 1962). The detailed assumptions of the theory have been described in original articles. A brief summary of the theory will present below taking into account only the formulas necessary to determine the different spectroscopic parameters.

The intensities of intraconfigurational *f-f* transitions of trivalent rare earths observed in the absorption spectra can be described by the oscillator strengths f_{mes} of each $J \rightarrow J'$ transition. The majority of these transitions are induced electric dipole transitions, although a few magnetic dipole transitions are also present. From the absorption spectra, we can calculate the oscillator strength f_{mes}, which is proportional to the band absorption intensity, from the value of the absorption coefficient $\alpha(\lambda)$ at a particular wavelength λ according to the formula:

$$f_{mes} = \frac{mc^2}{\pi e^2 N} \int \frac{\alpha(\lambda) d\lambda}{\lambda^2} \tag{1}$$

where m is the electron mass, c is the celerity of the light in the vacuum and e is the electron charge.

On the other side, the oscillator strength can be given in term of the electric dipole line strength S_{ed}:

$$f_{cal} = \frac{8\pi^2 mc}{3h(2J+1)\lambda} \frac{(n^2+2)}{9n} S_{ed} \tag{2}$$

$$S_{ed} = e^2 \sum_{k=2,4,6} \Omega_k \left| \left\langle J' \left\| U^{(k)} \right\| J \right\rangle \right|^2 \tag{3}$$

where Ω_k $(k = 2, 4$ and 6) are known as Judd-Ofelt parameters. These parameters are dependent on both the chemical environment and the lanthanide ion (de Sá et al., 2000). The factor $(n^2 + 2)/9n$ takes

Fig. 1. Fluorophosphates glass Samples.

Table 1
Compositions of glass samples.

Name of the sample	Glass compositions (mol%)				
	$NaPO_3$	SrF_2	ZnF_2	HoF_3	YbF_3
NPZS	80	10	10	0	0
NPZS_H1	79	10	10	1	0
NPZS_HY0.5	79.5	10	10	1	0.5
NPZS_HY1	78	10	10	1	1
NPZS_HY1.5	77.5	10	10	1	1.5
NPZS_HY2	77	10	10	1	2
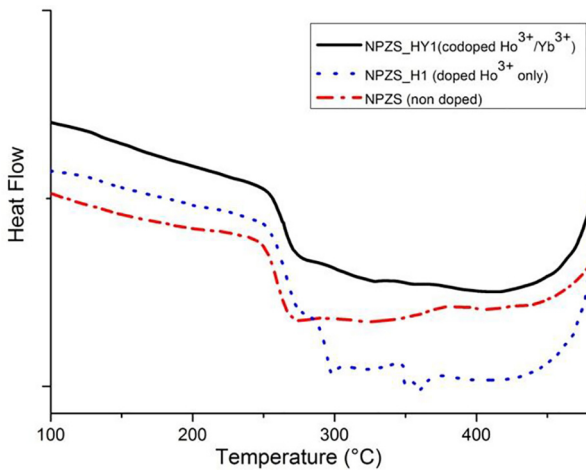
Fig. 2. DSC Curves of the non-doped, Ho^{3+} doped and Ho^{3+}/Yb^{3+} co-doped glass samples.

Table 2
Refractive index and density of glass samples.

Samples	Refractive index ±0.001	Density (g/cm^3) ±0.001
NPZS	1.494	2.772
NPZS_H1	1.495	2.803
NPZS_HY0.5	1.493	2.820
NPZS_HY1	1.494	2.859
NPZS_HY1.5	1.495	2.883
NPZS_HY2	1.496	2.904

Fig. 3. Absorption spectra of NPZS_HY samples.

into account the fact that the rare earth ion is not in a vacuum, but in a dielectric medium, n being the refractive index of this medium. $U^{(k)}$ are the components of the reduced tensorial operator which are independent of ligand field. The values of $U^{(k)}$ are usually considered to be host invariant and they are tabulated (Carnall et al., 1968, 1965). h is the Planck's constant and λ is the average wavelength of the transition.

The values of the Ω_k are empirically determined by comparing the computed values starting from the formula (2) with the values obtained from the absorption spectra at ambient temperature of the oscillator strengths (formula (1)). If q is the number of the absorption bands considered in experiments, the resolution of a system of q equation to 3 unknown factors, by a least square approximation, makes it possible to obtain the values of the parameters Ω_k. These parameters are expressed in cm^2. A measure of the accuracy of the fit is given by the root mean square deviation (RMS):

$$RMS = \sqrt{\frac{\sum (f_{cal} - f_{mes})^2}{q - 3}} \tag{4}$$

The values of Judd-Ofelt parameters obtained are used to calculate the line strength of the transitions between the initial state J and the final state J' using the Eq. (3). The probabilities of the radiative transitions are given by the equation:

$$A_{rad}(J, J') = \frac{64\pi^4}{3h(2J+1)\lambda^3} \left[\frac{n(n^2+2)^2}{9} \right] S_{ed} \tag{5}$$

The branching ratios can be to obtain from the probabilities of radiative transitions A_{rad} by the equation:

$$\beta = \frac{A_{rad}(J, J')}{\sum_{J'} A_{rad}(J, J')} \tag{6}$$

The radiative lifetime of the level J is given by:

$$\tau_{rad} = \frac{1}{\sum_{J'} A_{rad}(J, J')} \tag{7}$$

Table 3
Measured and calculated oscillator strength for Ho^{3+} ions in NPSZ_HY samples.

Transition: $^5I_8 \rightarrow$	λ(nm)	Oscillator strength f ($\times 10^{-6}$)									
		NPZS_H1		NPZS_HY0.5		NPZS_HY1		NPZS_HY1.5		NPZS_HY2	
		f_{mes}	f_{cal}	f_{mes}	f_{cal}	f_{mes}	f_{cal}	f_{mes}	f_{cal}	f_{mes}	f_{cal}
$^5I_7$	1957	1.1951	1.30792	1.2529	1.5595	1.2983	1.5987	1.3064	1.8003	1.2161	1.4308
$^5I_6$	1155	0.5946	0.96128	0.6883	1.1498	0.6651	1.1765	0.6861	1.3338	0.6485	1.051
$^5F_5$	642	2.3739	2.57079	2.6415	3.0311	2.6752	3.1015	2.6738	3.3458	2.6391	2.8484
$^5F_4$	538	3.3668	2.79476	4.5804	3.3199	4.8053	3.4026	5.6358	3.7506	3.9579	3.0808
$^5F_3$	486	0.8187	1.04389	0.3176	1.2556	0.4405	1.2903	0.3395	1.4719	0.6037	1.1409
$^5F_2, ^3K_8$	474	0.5251	0.64620	0.6064	0.7773	0.1951	0.7987	0.3039	0.9112	0.4084	0.7063
$^5G_6$	448	12.4917	12.70179	13.331	13.625	12.587	12.869	13.473	13.743	13.006	13.292
$^5G_5$	418	2.3285	2.42021	2.5453	2.7951	2.5716	2.8468	2.5617	2.8813	2.5005	2.719
$^5G_4$	386	0.3533	0.32203	0.7069	0.3781	0.6512	0.3865	0.8467	0.4116	0.7537	0.3579
$^3H_6$	362	3.4714	2.37699	4.0711	2.5256	3.8578	2.3779	3.9563	2.5319	3.9731	2.484
RMS ($\times 10^{-6}$)		±0.511		±0.8946		±0.9261		±1.1160		±0.7466	

Table 4
Judd-Ofelt parameters ($\Omega_k \times 10^{-20}$cm^2) of Ho^{3+} doped NPSZ_HY samples and other glasses.

Sample	Ω_2	Ω_4	Ω_6	Ω_4/Ω_6	Trend
NPZS_H1 (present work)	3.03	2.26	1.72	1.31	$\Omega_2 > \Omega_4 > \Omega_6$
NPZS_HY0.5 (present work)	3.13	2.62	2.07	1,26	$\Omega_2 > \Omega_4 > \Omega_6$
NPZS_HY1(present work)	2.83	2.66	2.12	1,25	$\Omega_2 > \Omega_4 > \Omega_6$
NPZS_HY1.5(present work)	3.09	2.69	2.42	1,11	$\Omega_2 > \Omega_4 > \Omega_6$
NPZS_HY2(present work)	3.07	2.54	1.88	1,35	$\Omega_2 > \Omega_4 > \Omega_6$
Halogeno-phosphate (Bentouila et al., 2013)	2.44	1.40	1.31	1.07	$\Omega_2 > \Omega_4 > \Omega_6$
Phosphate (Reisfeld and Hormadaly, 1976)	5.20	2.72	1.87	1.45	$\Omega_2 > \Omega_4 > \Omega_6$
Germanate (Fan et al., 2015)	4.70	1.63	0.81	2.01	$\Omega_2 > \Omega_4 > \Omega_6$
Fluoride (Florez et al., 2006)	1.56	3.72	2.86	1,30	$\Omega_2 < \Omega_6 < \Omega_4$
Tellurite (Rai et al., 2003)	4.98	0.99	2.96	0.33	$\Omega_4 < \Omega_6 < \Omega_2$

Table 5
Predicted radiative transition probability, integrated emission cross-section and radiative lifetimes for $^5I_7 \rightarrow \, ^5I_8$ transition of Ho^{3+} ions in NPSZ_HY samples and other glasses.

Sample	A_{rad}(s)	β(%)	Σ ($\times 10^{-20}$ m)	τ_{rad} (ms)
NPZS_H1 (present work)	57,357	1000	1519	17,435
NPZS_HY0.5 (present work)	68.47	100	1.56	14.60
NPZS_HY1 (present work)	70.21	100	1.60	14.24
NPZS_HY1.5 (present work)	79.25	100	1.80	12.61
NPZS_HY2 (present work)	63.00	100	1.43	15.87
Fluorophosphate (Tian et al., 2010)	73.55	100	–	13.60
Germanate (Fan et al., 2011)	97.84	100	–	10.22
Fluoride (Florez et al., 2006)	109.93	100	–	9.09

Another important term, integrated emission cross-section (in m), which is particularly useful to determine the possibility of lasing in glass, is defined as:

$$\Sigma = \frac{\lambda^2}{8\pi \, cn^2} A_{rad}(J, J') \qquad (8)$$

When the value of the integrated emission cross-section is close to or greater than $\sim 10^{-20}$ m, there is a possibility of lasing (Watekar et al., 2008).

The results obtained from the Judd-Ofelt analysis are reported in Tables 3–5.

4. Discussions

4.1. Thermal stability

Determination of glass transition temperature (T_g) and onset crystallization (T_x) is interesting for many reasons: in practical terms, T_g is a measure of approximate upper use temperature for a given composition, and annealing of glass samples is carried out somewhat below T_g. In addition, T_g is an important factor for laser glass. It is reported that a glass with high T_g has a good thermal stability to resist thermal damage at high pumping power (Xu et al., 2011a,b). T_x defines a safe upper limit for processing the melt if crystallization is to be avoided. From the DSC curves, one can observe that there is no crystallization peak till T = 450 ± 2°C for all samples, T_g is about 247 ± 2 °C and T_x is about 460 ± 2 °C for the glass sample without any doping ions and for glasses containing HoF$_3$ and YbF$_3$, the vitreous transition still situated around 250 °C and crystallization onset around 450 °C. One can notice that the glass transition temperature is shifted upwards high temperatures and the onset crystallization is shifted downwards low temperatures by addition of HoF$_3$ and YbF$_3$, results in agreement with previous works (Imanieh et al., 2014). As the changes of T_g and T_x is largely depending on the major mixing elements, because the temperature is closely related to the bonding force among the constituent elements, one can explain the shifting of T_g and T_x by structure arrangement of glass due to participation of Yb^{3+} and Ho^{3+} ions and enhanced glassy network structure

(Chen et al., 2014). However, it has been observed that with high concentration of rare-earth, the glass became impossible to pour due to its high instability and during the pouring it could be crystallize to become opaque (Dantelle et al., 2005). Thus, an optimization of rare earth content is necessary to obtain a transparent glass.

The quantity $\Delta T = T_x - T_g$, known as the supercooled liquid region, defined as the temperature gap between T_g and T_x. It has been used as a rough measure of the glass forming ability of a melt, i.e., of resistance against crystallization during casting (Wang, 2008). Large ΔT means strong inhibition to processes of nucleation and crystallization (Park et al., 2010; Xu et al., 2011a,b). For this reason, it is frequently used as an assessment criterion to determine the stability of glass. To achieve a large working range during operations such as fiber fabrication or the preparation of bulk glass articles, it is desirable to have ΔT as large as possible. We find that all glass samples have relatively a large value of ΔT ($\sim 200\,°C$) close to the value obtained for fluorophosphate glasses (Tian et al., 2010; Chen et al., 2014), which is significantly higher than that of other kinds of rare earth doped fluorophosphate glasses such as Tm^{3+} (Liao et al., 2007). This result means that all our glass samples are stable against crystallization.

From the analysis of DSC curve, we can conclude that thermal properties of our glass samples are good for fiber drawing.

4.2. Absorption spectra and Judd-Ofelt analysis

Absorption spectra of the Ho^{3+} and Ho^{3+}/Yb^{3+} co-doped glass samples are shown in Fig. 3. The spectroscopic properties of our glass samples were determined using the Judd-Ofelt model. The *f-f* transitions are considered to be electric dipole in nature, because the magnetic dipole oscillator strength (f_{md}) will be relatively small (Sooraj Hussain et al., 2006). For that reason in the present work, these magnetic dipole line strengths have not been considered. Measured and calculated oscillator strength for Ho^{3+} ions in NPSZ_HY samples were presented in Table 3.The low RMS values suggest the good agreement between calculated and experimental oscillator strengths of Ho^{3+} ions in our glasses samples which indicates the validity of the Judd-Ofelt model for predicting the spectroscopic properties of Ho^{3+}.

The Judd-Ofelt parameters Ω_k ($k = 2, 4, 6$) are mainly depend on the host glass composition. These parameters can provide versatile information regarding the rare earth in glass structure. Some empirical correlations of the Judd-Ofelt parameters and the local structure of the rare earth ions have been reported in literature (Jacobs and Weber, 1976; Ebendorff-Heidepriem et al., 1998; Malta and Carlos, 2003). Generally, Ω_2 is an indicator of the covalency of the rare earth-ligand bonds (short-range effect), and it is hypersensitive to the compositional changes in the host materials. Ω_2 is also related with the symmetry of ligand field in the glass host. According to previous studies (Ebendorff-Heidepriem and Ehrt, 1999), Ω_2 increase with the increasing of covalency and asymmetry at the rare earth sites. The values for Ω_4 and Ω_6 provide some information of the rigidity of the host materials (Wang, 2008). They depend on bulk properties such as viscosity and dielectric constant of the media (long-range effects). They are also affected by the vibronic transitions of the rare earth ions bound to the ligand atoms. In the present work, the Judd-Ofelt parameters Ω_λ are calculated and compared with those of various Ho^{3+} doped glasses, the results were presented in Table 4. One can observe, from the values of Ω_2 of our samples, that the covalent environment for Ho^{3+} is slightly decreased with increasing of Yb^{3+} amount in glasses. The observed Ω_2 values of our samples are located between the higher side to the values reported for ionic glasses (for fluoride glasses, $\Omega_2 \sim 2 \times 10^{-20}\,cm^2$) and those of the covalent glasses (for phosphates $\Omega_2 \sim 5 \times 10^{-20}\,cm^2$). Theoretically, the polarizability of oxide ions is higher than that of fluorine ions, resulting in the

increasing covalence of the bonds between rare earth ions and surrounding ligand from fluoride to phosphate glasses due to substitution of fluorine ions by oxygen ions. As fluorophosphate glasses has both O^{2-} and F^- ions, the value of Ω_2 is larger than that of fluoride glass and smaller than that of phosphate glass (Tian et al., 2010). However, the observed lower values of Ω_2 parameter for Ho^{3+}/Yb^{3+} co-doped NPSZ_HY glasses compared by those of phosphate glasses indicates that the ligand asymmetry around the rare earth ions in Ho^{3+}/Yb^{3+} co-doped NPSZ_HY glasses is weaker than those in phosphate glasses. Additionally, a larger modifier ion in phosphate glass gives rise to a larger average between P-O-P chains causing the increasing average Ho-O distance to increase. Such increase in the bond lengths produces weaker local field near rare earth ions and lead to lower value of Ω_2 (Rao et al., 2012).

According to the theory of Jacobs and Weber (Jacobs and Weber, 1976), the rare earth emission intensity can be characterized uniquely by Ω_4 and Ω_6 parameters. Thus, we used the so-called spectroscopic quality factor (Ω_4/Ω_6). This factor is important in predicting the behavior of various lasing transitions in a given matrix. Based on this factor, it is found that the NPZS_HYy glasses appear to be better optical glasses. Moreover, it is noticed that the values of Judd-Ofelt parameters of our sample glasses follows the trend $\Omega_2 > \Omega_4 > \Omega_6$ in consistent with that one observed for halogeno-phosphate, phosphate and germanate glasses; nevertheless, it differs from those of fluoride and tellurite glasses.

Table 5 presents the predicted radiative transition probability A_r, branching ratios β, integrated emission cross-section and radiative lifetimes τ_{rad} for $^5I_7 \rightarrow\,^5I_8$ transition of Ho^{3+} ions in NPSZ_HY samples. The results show that the values A_{rad} of the $^5I_7$ level of Ho^{3+} were 68.4, 70.2, 79.2 and 63.0 s^{-1}, which are similar to the value found for fluorophosphates glass and smaller than that of germanate and fluoride glasses. It is reasonable to obtain such result because the radiative transition probability is proportional to $n(n^2 + 2)^2/9$ (Eq. (5) in Section 3.3) and the refractive index of fluorophosphates glasses is usually less then germanate and fluoride glasses. It is evident to find also that the radiative lifetimes of the $^5I_7$ level of Ho^{3+} for NPZS_HYy glasses are greater than those of germanate and fluoride glasses. Further, the radiative lifetimes values for Ho^{3+}/Yb^{3+} co–doped NPZS_HYy glasses are found to be smaller than that for individually Ho^{3+} doped NPZS_H1 glass. This result, which may be explained by the crucial contribution of phonon subsystem, is in agreement with those found by Gandhi et al. (2010) for the measured lifetime of blue, green and red transitions.

The values of the integrated emission cross-sections obtained are greater than $\sim 10^{-20}\,m$, which indicates a possibility of lasing with these glasses. But it must be mentioned that lasing can be specifically determined only if emission cross-section and fluorescence lifetime are taken into account.

5. Conclusions

A series of Ho^{3+}/Yb^{3+} co-doped new fluorophosphate glasses have been investigated and characterized. All the prepared samples exhibit a high thermal stability against crystallization compared with other kinds of rare earth doped fluorophosphate glasses. From the absorption spectra, Judd-Ofelt parameters are obtained and discussed. The spectroscopic properties of Ho^{3+} in these glasses, such as radiative transition probabilities, integrated emission cross-sections and radiative lifetimes, were calculated and compared with other glasses. Spectroscopic quality factor (Ω_4/Ω_6) and the integrated emission cross-section were found greater than 1 and about $10^{-20}\,m$ respectively, which indicates better properties of these glasses as lasing materials. Ho^{3+}/Yb^{3+} co–doped fluorophosphate glasses have predicted radiative lifetimes smaller than that for individually Ho^{3+} doped

fluorophosphate glass which may be explained by the crucial contribution of phonon subsystem. Consequently, these results indicate these glasses appear as a potential lasing materials and offer prospects for photonics applications.

References

Ari, J., Starecki, F., Boussard-Plédel, C., Doualan, J.-L., Quétel, L., Michel, K., Braud, A., Camy, P., Chahal, R., Bureau, B., Ledemi, Y., Messaddeq, Y., Nazabal, V., 2017. Rare-earth-doped chalcogenide glasses for mid-IR gas sensor applications. Proc. SPIE 10100, 101000Q. https://doi.org/10.1117/12.2251529.

Babu, S., Ratnakaram, Y.C., 2016. Emission characteristics of holmium ions in fluorophosphate glasses for photonic applications. AIP Conf. Proc. 1731, 1–4. https://doi.org/10.1063/1.4947833.

Bai, G., Guo, Y., Tian, Y., Hu, L., Zhang, J., 2011. Light emission at 2 μm from Ho-Tm-Yb doped silicate glasses. Opt. Mater. (Amst) 33, 1316–1319. https://doi.org/10.1016/j.optmat.2011.03.033.

Bentouila, O., Aiadi, K.E., Rehouma, F., Poulain, M., 2013. Spectroscopic studies of rare earth-doped halogeno-phosphate glasses. J. Optoelectron. Adv. Mater. 15.

Carnall, W.T., Fields, P.R., Wybourne, B.G., 1965. Spectral intensities of the trivalent lanthanides and actinides in solution. I. Pr 3+, Nd 3+, Er 3+, Tm 3+, and Yb 3+. J. Chem. Phys. 42, 3797–3806. https://doi.org/10.1063/1.1695840.

Carnall, W.T., Fields, P.R., Rajnak, K., 1968. Spectral intensities of the trivalent lanthanides and actinides in solution. II. Pm 3+, Sm 3+, Eu 3+, Gd 3+, Tb 3+, Dy 3+, and Ho 3+. J. Chem. Phys. 49, 4412–4423. https://doi.org/10.1063/1.1669892.

Chen, H., Chen, F., Wei, T., Liu, Q., Shen, R., Tian, Y., 2014. Ho3+ doped fluorophosphate glasses sensitized by Yb3+ for efficient 2 μm laser applications. Opt. Commun. 321, 183–188. https://doi.org/10.1016/j.optcom.2014.01.072.

Chen, R., Tian, Y., Li, B., Jing, X., Zhang, J., Xu, S., Eckert, H., Zhang, X., 2016. Thermal and luminescent properties of 2 μm emission in thulium-sensitized holmium-doped silicate-germanate glass. Photonics Res. 4, 214–221. https://doi.org/10.1364/PRJ.4.000214.

Costa, F.B., Yukimitu, K., Nunes, L.A.O., Andrade, L.H. da C., Sandro Marcio Lima, J.C., Moraes, S., 2015. Characterization of Nd3 + -doped Tellurite Glasses with Low OH Content. Mater. Res. 18;2–7. https://doi.org/10.1590/1516-1439.320614.

Dantelle, G., Mortier, M., Vivien, D., Patriarche, G., 2005. Nucleation efficiency of erbium and ytterbium fluorides in transparent oxyfluoride glass-ceramics. J. Mater. Res. 20, 472–481. https://doi.org/10.1557/JMR.2005.0051.

de Sá, G., Malta, O., de Mello Donegá, C., Simas, A., Longo, R., Santa-Cruz, P., da Silva, E., 2000. Spectroscopic properties and design of highly luminescent lanthanide coordination complexes. Coord. Chem. Rev. https://doi.org/10.1016/S0010-8545(99)00054-5.

Dwivedi, Y., Bahadur, A., Rai, S.B., 2010. Spectroscopic study of Sm: Ce ions co-doped in barium fluoroborate glass. J. Non. Cryst. Solids 356, 1650–1654. https://doi.org/10.1016/j.jnoncrysol.2010.06.013.

Ebendorff-Heidepriem, H., Ehrt, D., Bettinelli, M., Speghini, A., 1998. Effect of glass composition on Judd-Ofelt parameters and radiative decay rates of Er3+ in fluoride phosphate and phosphate glasses. J. Non. Cryst. Solids 240, 66–78. https://doi.org/10.1016/S0022-3093(98)00706-6.

Ebendorff-Heidepriem, H., Ehrt, D., 1999. Tb3+ f–d absorption as indicator of the effect of covalency on the Judd-Ofelt Ω2 parameter in glasses. J. Non. Cryst. Solids 248, 247–252. https://doi.org/10.1016/S0022-3093(99)00243-4.

Fan, J., Fan, Y., Yang, Y., Chen, D., Calveza, L., Zhang, X., Zhang, L., 2011. Spectroscopic properties and energy transfer in Yb3+–Ho3+ co-doped germanate glass emitting at 2.0 μm. J. Non. Cryst. Solids 357, 2431–2434. https://doi.org/10.1016/j.jnoncrysol.2010.11.085.

Fan, X., Kuan, P., Li, K., Zhang, L., Li, D., Hu, L., 2015. Spectroscopic properties and quenching mechanism of 2 μm emission in Ho3+ doped germanate glasses and fibers. Opt. Mater. Express 5, 1356–1365. https://doi.org/10.1364/OME.5.001356.

Florez, A., Oliveira, S.L., Flórez, M., Gómez, L.A., Nunes, L.A.O., 2006. Spectroscopic characterization of Ho3+ ion-doped fluoride glass. J. Alloys Compd. 418, 238–242. https://doi.org/10.1016/j.jallcom.2005.12.088.

Galleani, G., Santagneli, S.H., Messaddeq, Y., de Oliveira, M., Eckert, H., 2017. Rare-earth doped fluoride phosphate glasses: structural foundations of their luminescence properties. Phys. Chem. Chem. Phys. 19, 21612–21624. https://doi.org/10.1039/C7CP03927A.

Gámez, M.A.M., Kiryanov, A.V., Lucio, J.L., Wiechers, C., Kumar, G.A., 2009. Near-IR emission from holmium-ytterbium co-doped alkali bismuth gallate and fluorophosphate fiber glass preforms. J. Alloys Compd. 473, 500–504. https://doi.org/10.1016/j.jallcom.2008.06.025.

Gandhi, Y., Rao, M.V.R., Rao, C.S., Srikumar, T., Kityk, I.V., Veeraiah, N., 2010. Influence of aluminum ions on fluorescent spectra and upconversion in codoped CaF2-Al2O3-P2O 5-SiO2: Ho3+ and Er3+ glass system. J. Appl. Phys. 108. https://doi.org/10.1063/1.3464257.

Hemming, A., Simakov, N., Haub, J., Carter, A., 2014. A review of recent progress in holmium-doped silica fibre sources. Opt. Fiber Technol. 20, 621–630. https://doi.org/10.1016/j.yofte.2014.08.010.

Hraiech, S., Ferid, M., Guyot, Y., Boulon, G., 2013. Structural and optical studies of Yb3+, Er3+ and Er3+/Yb3+ co-doped phosphate glasses. J. Rare Earths 31, 685–693. https://doi.org/10.1016/S1002-0721(12)60343-3.

Imanieh, M.H., Martín, I.R., Gonzalez-Platas, J., Eftekhari Yekta, B., Marghussian, V.K., Shakhesi, S., 2014. Behavior of Yb 3+ and Er 3+ during Heat Treatment in Oxyfluoride Glass Ceramics 2014. https://doi.org/10.1155/2014/171045.

Jacobs, R.R., Weber, M.J., 1976. Dependence of the 4 F 3/2→ 4 I 11/2 induced-emission cross section for Nd 3+ on glass composition. IEEE J. Quantum Electron. 12, 102–111. https://doi.org/10.1109/JQE.1976.1069101.

Judd, B.R., 1962. Optical absorption intensities of rare-earth ions. Phys. Rev. 127, 750–761. https://doi.org/10.1103/PhysRev. 127.750.

Kenyon, A.J., 2002. Recent developments in rare-earthdoped materials for optoelectronics. Prog. Quant. Elec. 26, 225–284. https://doi.org/10.1016/S0079-6727(02)00014-9.

Li, L., Bian, J., Jiao, Q., Liu, Z., Dai, S., Lin, C., 2016. GeS2–In2S3–CsI Chalcogenide Glasses Doped with Rare Earth Ions for Near- and Mid-IR Luminescence. Sci. Rep. 6, 37577. https://doi.org/10.1038/srep37577.

Liao, M.S., Fang, Y.Z., Sun, H.T., Hu, L.L., 2007. Stability against crystallization and spectroscopic properties of Tm3+ doped fluorophosphate glasses. Opt. Mater. (Amst) 29, 867–872. https://doi.org/10.1016/j.optmat.2006.01.012.

Malta, O.L., Carlos, L.D., 2003. Intensities of 4f–4f transitions in glass materials. Quim. Nova 26, 889–895. https://doi.org/10.1590/S0100-40422003000600018.

Meruva, S., Carlos, B.L., Alberto Peres, F.J.J., 2014. Optical characterization, luminescence properties of Er 3+ and Er 3+ /Yb 3+ co-doped tellurite glasses for broadband amplification 8961, 896132. https://doi.org/10.1117/12.2037000.

Mortier, M., Bensalah, A., Dantelle, G., Patriarche, G., Vivien, D., 2007. Rare-earth doped oxyfluoride glass-ceramics and fluoride ceramics: Synthesis and optical properties. Opt. Mater. (Amst) 29, 1263–1270. https://doi.org/10.1016/j.optmat.2005.12.014.

Ofelt, G.S., 1962. Intensities of Crystal Spectra of Rare-Earth Ions. J. Chem. Phys. 37, 511–520. https://doi.org/10.1063/1.1701366.

Pandey, A., Kroon, R.E., Kumar, V., Swart, H.C., 2016. Impact of ytterbium on photoluminescence from the modifier in TeO2-ZnO:Ho3+ glass. Phys. B Condens. Matter 480, 137–140. https://doi.org/10.1016/j.physb.2015.08.017.

Park, E.S., Na, J.H., Kim, D.H., 2010. Abnormal behavior of supercooled liquid region in bulk-forming metallic glasses. J. Appl. Phys. 108. https://doi.org/10.1063/1.3465310.

Polishchuk, S.A., Ignat'eva, L.N., Marchenko, Y.V., Bouznik, V.M., 2011. Oxyfluoride glasses (A review). Glas. Phys. Chem. 37, 1–20. https://doi.org/10.1134/S108765961101010X.

Poulain, M., Soufiane, A., Messaddeq, Y., Aegerter, M.A., 1992. Fluoride glasses: synthesis and properties. Brazilian J. Phys. 22, 205–217.

Rai, S.B., Singh, A.K., Singh, S.K., 2003. Spectroscopic properties of Ho3+ ions doped in tellurite glass. Spectrochim. Acta Part A Mol. Biomol. Spectrosc. 59, 3221–3226. https://doi.org/10.1016/S1386-1425(03)00178-1.

Rao, P.R., Venkatramaiah, N., Gandhi, Y., Kumar, V.R., Kityk, I.V., Veeraiah, N., 2012. Role of modifier oxide in emission spectra and kinetics of Er-Ho codoped Na 2SO 4-MO-P 2O 5 glasses. Spectrochim. Acta - Part A Mol. Biomol. Spectrosc. 86, 472–480. https://doi.org/10.1016/j.saa.2011.10.071.

Reichert, F., Moglia, F., Metz, P.W., Arcangeli, A., Marzahl, D.-T., Veronesi, S., Parisi, D., Fechner, M., Tonelli, M., Huber, G., 2015. Prospects of Holmium-doped fluorides as gain media for visible solid state lasers. Opt. Mater. Express 5, 88. https://doi.org/10.1364/OME.5.000088.

Reisfeld, R., Hormadaly, J., 1976. Optical intensities of holmium in tellurite, calibo, and phosphate glasses. J. Chem. Phys. 64, 3207–3212. https://doi.org/10.1063/1.432659.

Rivera-López, F., Babu, P., Basavapoornima, C., Jayasankar, C.K., Lavín, V., 2011. Efficient Nd3+→Yb3+ energy transfer processes in high phonon energy phosphate glasses for 1.0 μm Yb3+ laser. J. Appl. Phys. 109, 1–11. https://doi.org/10.1063/1.3580475.

Ryabochkina, P.A., Chabushkin, A.N., Lyapin, A.A., Lomonova, E.E., Zakharov, N.G., Vorontsov, K.V., 2017. Tunable 2 μ m ZrO 2 –Y 2 O 3 –Ho 2 O 3 solid-state laser. Laser Phys. Lett. 14, 55807. https://doi.org/10.1088/1612-202X/aa69a5.

Sajna, M.S., Thomas, S., Jayakrishnan, C., Joseph, C., Biju, P.R., Unnikrishnan, N.V., 2016. NIR emission studies and dielectric properties of Er3+-doped multicomponent tellurite glasses. Spectrochim. Acta Part A Mol. Biomol. Spectrosc. 161, 130–137. https://doi.org/10.1016/j.saa.2016.02.039.

Satyanarayana, T., Kalpana, T., Ravi Kumar, V., Veeraiah, N., 2010. Role of Al coordination in barium phosphate glasses on the emission features of Ho3+ion in the visible and IR spectral ranges. J. Lumin. 130, 498–506. https://doi.org/10.1016/j.jlumin.2009.10.021.

Seshadri, M., Ferencz Junior, J.A.P., Ratnakaram, Y.C., Barbosa, L.C., 2014. Spectroscopic properties of Ho 3+, Tm 3+, and Ho 3+ /Tm 3+ doped tellurite glasses for fiber laser applications. Proc. SPIE 8961, 896139. https://doi.org/10.1117/12.2036876.

Sooraj Hussain, N., Ali, N., Dias, A.G., Lopes, M.A., Santos, J.D., Buddhudu, S., 2006. Absorption and emission properties of Ho3+ doped lead-zinc-borate glasses. Thin Solid Films 515, 318–325. https://doi.org/10.1016/j.tsf.2005.12.085.

Tian, Y., Zhang, L., Feng, S., Xu, R., Hu, L., Zhang, J., 2010. 2 μm Emission of Ho3+-doped fluorophosphate glass sensitized by Yb3+. Opt. Mater. (Amst) 32, 1508–1513. https://doi.org/10.1016/j.optmat.2010.06.012.

Wang, X., 2008. Investigation of thermal stability and spectroscopic properties in Er3+/Yb3+ co-doped niobic tungsten tellurite glasses. Spectrochim. Acta Part A Mol. Biomol. Spectrosc. 70, 99–103. https://doi.org/10.1016/j.saa.2007.07.013.

Wang, M., Yu, C., He, D., Feng, S., Li, S., Zhang, L., Zhang, J., Hu, L., 2011. Enhanced 2 μm emission of Yb-Ho doped fluorophosphates glass. J. Non. Cryst. Solids 357, 2447–2449. https://doi.org/10.1016/j.jnoncrysol.2010.11.073.

Watekar, P.R., Ju, S., Han, W.T., 2008. Optical properties of Ho-doped alumino-germano-silica glass optical fiber. J. Non. Cryst. Solids 354, 1453–1459. https://doi.org/10.1016/j.jnoncrysol.2007.08.068.

Wu, C.T., Ju, Y.L., Chen, F., Jin, G.Y., 2012. Research on 2-μm solid-state lasers. Laser Phys. 22, 635–647. https://doi.org/10.1134/S1054660X12040275.

Xu, R., Tian, Y., Hu, L., Zhang, J., 2011a. 2μm spectroscopic investigation of Tm3+-doped tellurite glass fiber. J. Non. Cryst. Solids 357, 2489–2493. https://doi.org/10.1016/j.jnoncrysol.2010.11.059.

Xu, R., Tian, Y., Hu, L., Zhang, J., 2011b. Broadband 2 μm emission and energy-transfer properties of thulium-doped oxyfluoride germanate glass fiber. Appl. Phys. B Lasers Opt. 104, 839–844. https://doi.org/10.1007/s00340-011-4461-z.

Żmojda, J., Dorosz, D., Kochanowicz, M., Miluski, P., Dorosz, J., 2012. Yb 3+ /Ho 3+ -codoped antimony-silicate optical fiber 8454, 845414. https://doi.org/10.1117/12.2000174.

Production Equipe 2

01   Short Communication Effect of Annealing in Physical Properties of NiO Nanostructure Thin Film **(M. Ghougali1, O. Belahssen, A. Chala)**

02   Effect of Iron Doping on Physical Properties of NiO Thin Films **(O. Belahssen, M. Ghougali, A. Chala)**

03   N-Ferrocenymethyl-N-phenylacetamide **(Abdelhamid Khelef, Mohammed Sadok Mahboub and Touhami Lanez)**

04   Spectroscopic Characterizations of Sand Dunes Minerals of El-Oued (Northeast Algerian Sahara) by FTIR, XRF and XRD Analyses

   (Nassima Meftah & Mohammed Sadok Mahboub)

05   Structural, Optical and Electrical Properties of NiO Nanostructure Thin Film

   (M. Ghougali, O. Belahssen , A. Chala)

06   SYNTHESIS AND STRUCTURE REFINEMENT OF $Ca_{0.5}Sr_{0.5}FeO_2$ SOLID SOLUTION **(Soria ZEROUAL, Mohammed Sadok MAHBOUB, Ali BOUDJADA)**

Short Communication

Effect of Annealing in Physical Properties of NiO Nanostructure Thin Film

M. Ghougali[1,2,3], O. Belahssen[1,2,*], A. Chala[1,2]

[1] *Material Sciences Department, Faculty of Science, University of Biskra, Algeria*
[2] *Physic Laboratory of Thin Films and Applications (LPCMA), University of Biskra, Algeria*
[3] *Laboratory of exploitation and valorization the azalea energetics sources (LEVRES), Faculty of exact Science, University of El-Oued, Algeria*

Nickel oxide was deposited on highly cleaned glass substrates using spray pneumatic technique. The effect of precursor molarity on structural, optical and electrical properties has been studied. The XRD lines of the deposited NiO were enhanced with increasing precursor molarity due to the improvement of the films crystallinity. It was shown that the average of the crystalline size of the deposited thin films was calculated using Debye–Scherer formula and found 46.62 for as-deposited sample and 119.89 nm for the annealed one. The optical properties have been discussed in this work. The absorbance (*A*), the transmittance (*T*) and the reflectance (*R*) were measured and calculated. Band gap energy is considered one of the most important optical parameter, therefore measured and found ranging ranging 3.64 for as-deposited sample and 2.98 eV for the annealed one. The NiO thin film reduces the light reflection for visible range light. The increase of the electrical conductivity to maximum value of 0.09241 $(\Omega \cdot cm)^{-1}$ can be explained by the increase in carrier concentration of the films. A good electrical conductivity of the NiO thin film is obtained due to the electrically low sheet resistance. NiO can be applied in different electronic and optoelectronic applications due to its high band gap, high transparency and good electrical conductivity.

Keywords: NiO thin films, XRD, Optical constants, Electrical conductivity.

1. INTRODUCTION

Nickel oxide (NiO) is the most investigated metal oxide and it has attracted considerable attention because of its low cost material, and also for its applications in several fields such as a catalyst, transparent conducting oxide, photodetectors, electrochromic, gas sensors, photovoltaic devices, electrochemical supercapacitors, heat reflectors, photo-electrochemical cell, solar cells and many opto- electronic devices [1–11]. NiO is an IV group and it can be used as a transparent p-type semi-conductor layers, it has a band gap energy ranging from 3.45 eV to 3.85 eV [12]. Band gap energy is significant to adjust the energy level state of NiO.

The reduction in particle size to nanometer scale results more interesting prosperities in compared with their bulk properties [13]. Therefore, there are several techniques have been used for synthesis and manipulation of nanostructures NiO such as the thermal evaporation, sputtering, pulse laser ablation, thermal decomposition, electrochemical deposition and spray methods etc. Among of these techniques, spray has some advantages such as high purity of raw materials and a homogeneous solution hence easy control over the composition of the deposited films.

In this work, a low cost spray pneumatic technique was used to prepare pure NiO nanoparticles thin films with 0.15 mol L^{-1} precursor molarity. The structural properties of the produced nickel oxide thin films have been examined. The absorption, transmittance and reflectance spectra of the produced thin films for the NiO are also measured in range between 300-900 nm.

Moreover, the optical band gap is determined as a function of the precursor concentrations.

2. EXPERIMENTAL DETAILS

2.1 Preparation of Samples

NiO thin films were prepared onto a highly cleaned glass substrates using sol-gel spay pneumatic technique. Nickel nitrate was dissolved in 50 ml of water as a solvent and chloride acid was used as a stabilizer for the all samples in this work. The produced mixture was stirred at 60 °C for 2 h in order to obtain a clear and homogenous solution then the mixture was cooled down at room temperature and placed at dark environment for 48 h. The glass substrates were cleaned by detergent and by alcohol mixed with deionized water.

2.2 Deposition of Thin Films

The coating was dropped into glass substrates at 480 °C that sprayed during 2 min by pneumatic nebulizer system which transforms the liquid to a stream formed with uniform and fine droplets, followed by the films dried on hot plate at 120 °C for 10 min in order to evaporate the solvent.

2.3 Devices and Measurements

The X-ray diffraction (XRD) spectra of the NiO were measured to verify the structure. (XRD) was measured by using BRUKER-AXS-8D diffractometer with Cu Kα radiation (λ = 1.5406 Å) operated at 40 KV and 40 mA

---

*belahssenokba@gmail.com

in the scanning range of (2θ) between 20° and 80°. The spectral dependence of the NiO transmittance (T) and the absorbance (A), on the wavelength ranging 300-1100 nm are measured using an ultraviolet–visible spectrophotometer (Perkin-Elmer Lambda 25). The reflectance (R) was calculated by the well-known equation as ($T + R + A = 1$). Whereas the electrical conductivity of the films was measured in a coplanar structure of four golden stripes on the deposited film surface; the measurements were performed with Keithley model 2400 low voltage source meter instrument.

3. RESULTS AND DISCUSSIONS

3.1 Structural Properties

Fig. 1 shows the spectra of the grown NiO nanoparticles with 2 XRD lines, showing the broadening of the peak which is a characteristic of the formation of nanoparticles. The X-ray diffraction was used in this work in order to understand the structure of the as-deposited and the annealed NiO thin.
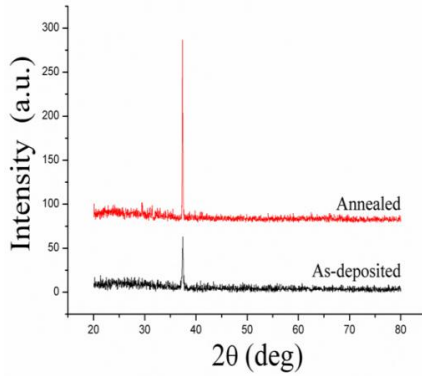
Fig. 1 – XRD patterns of the as-deposited and annealed NiO thin films

The indexed peak (111) at $2\theta = 37.1°$ correspond to the cubic structure of NiO nanoparticles which are consistent with the JCPDS (No.47-1049). Fig. 1 shows that the diffraction intensity increased for annealed sample; it shows that the best crystalline quality of the film is achieved for this annealed sample. The crystalline size was calculated using the well-known Debye–Scherrer for(1)

$$D = \frac{0.9}{\beta \cos \theta}$$

where λ is the wavelength of the X-rays used (1.5406 Å), β is the full width at half maximum (FWHM) and θ is the diffraction angle.

The increasing of the diffraction peaks may indicate to the resulted of the NiO in good crystallinity [15]. The crystalline size is found in the range of 46.62 nm for as-deposited sample and 119.89 nm for annealed one. The changing in the crystallites size leads to the changes in optical properties i.e. band gap energy increased with decreasing crystallites size as shown in Fig. 2.

3.2 Optical Properties

Fig. 2 shows the optical absorption spectra of NiO

nanoparticles. The absorption spectra of as-deposited sample show that the absorption edge is slightly shifted towards shorter wavelength when compared to the annealed one. The absorption edge of annealed sample is shifted to longer wave-lengths. This shift predicts that there is a decrease in band gap value ($E_g = 2.98$ eV), which is due to an enlargement in particle size ($D = 119.89$ nm). The fundamental absorption, which corresponds to the electron transition from the valance band to the conduction band, can be used to determine the nature and value of the optical band gap. The optical absorption study was used to determine the optical band gap of the nanoparticles, which is the most familiar and simplest method.
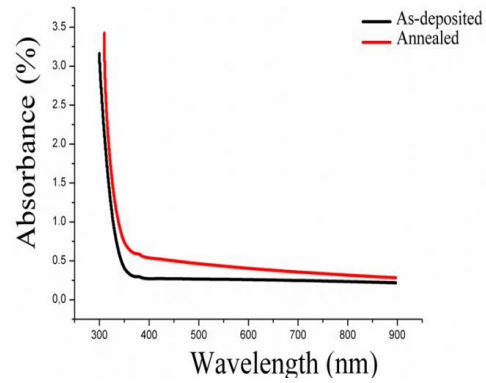
Fig. 2 – Absorbance spectra of the as-deposited and annealed NiO thin films $D = \dfrac{0.9}{\beta \cos \theta}$

The absorption coefficient (α) and the incident photon energy ($h\nu$) are related by the expression [16]:

$$\left(\alpha h\nu\right) = C\left(h\nu - E_g\right)^n \qquad (2)$$

where α is the absorption coefficient, C is a constant, $h\nu$ is the photon energy, ν is the frequency of the incident radiation, h is the Planck's constant, exponent n is 0.5 for direct band allowed transition ($h\nu = 1239/\lambda$(nm)(eV)) and E_g the band gap energy of the semiconductor.

As it was shown in Fig. 3a typical variation of ($\alpha h\nu$)^2 as a function of photon energy ($h\nu$) of NiO nanoparticles Eq. (2), used for deducing optical band gap E_g. The optical band gap values have been determined by extrapolating the linear portion of the curve to meet the energy axis ($h\nu$) [17]. The band gap values were given in Table 1.

For a transmittance study (Fig. 4), the as-deposed NiO showed high transmittance, averaged in the wavelength (λ) of 300-900 nm. Suppression of light reflection at a surface is an important factor to absorb more photons in semiconductor materials.

The reflectance profiles of NiO coated as deposited and annealed are shown in Fig. 5. The averaged reflectance values were significantly lower than 0.203 %. Moreover, NiO coating drives a substantially suppressed reflectance under 0.20 % in 400 nm $< \lambda <$ 900 nm. This notifies that the NiO coating is an efficient design scheme to intro-duce the incident light into substrate.

3.3 Electrical Properties

The elecrtical properties of the NiO films are summarized in Table. 1. The as-deposited films have good conductivity 0.04125 $(\Omega \cdot cm)^{-1}$, after annealing the conductivity increase at 0.09241 $(\Omega \cdot cm)^{-1}$. The increase

Table 1 – Structural, optical and electrical parameters of as-deposited and annealed NiO thin film

Sample	Crystallite size (nm)	Band gap energy (eV)	Conductivity $(\Omega \, cm)^{-1}$
As-deposed	46.62	3.64	0.04125
Annealed	119.89	2.98	0.09241
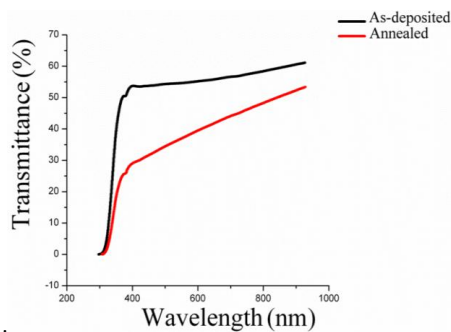
Fig. 3 – Transmission spectra of the as-deposited and annealed NiO thin films
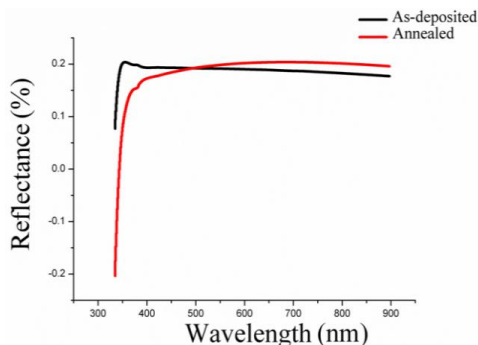
Fig. 4 – Reflectance profiles of the as-deposited and annealed NiO thin films

of the electrical comductivity can be explained by the increase in the carrier concentration. Patil et. al [18] have reported that the increase of the electrical conductivity is due to the increase in activation energy. This was explained by the crystal structure of the film which is increased, leading to a reduced concentration of structural defects such as dislocations and grain boundaries. Thus, the decrease of the concentration of crystal defects leads in the increase of free carrier concentration. The improvement of crystal quality reduces the carrier scattering from structural defects, leading to higher mobility.

4. CONCLUSION

The spray pneumatic technique has been successfully employed to deposit NiO thin films with 0.15 mol·L^{-1} concentration precursor on glass substrates. The films showed cubic crystal structure with preferential orientation according to the direction (111). It has found that the crystallite size increase from 46.62 nm for the as-deposited sample to 119.89 nm for the annealed one. We have observed an improvement in the films crystallinity for the annealed sample where the peak at position 37.1° corresponding to the (111) plans is very sharp, the film obtained for the annealed sample has higher and sharper diffraction peak indicating an improvement in peak intensity compared to the as-deposited film. The band gap value of NiO films decreased from 3.64 eV for the as-deposited sample to 2.98 eV for the annealed one. The high transmittance, low reflectance under 0.20 %, widened band gap and good conductivity obtained for NiO thin films make them promising candidate for optoelectronic devices as well as window layer in solar cell applications.

REFERENCES

1. M.A. Abbasi, Z.H. Ibupoto, A. Khan, O. Nur, M. Willander, *Mater. Lett.* **108**, 149 (2013).
2. M.D. Irwin, D.B. Buchholz, A.W. Hains, R.P.H. Chang, T.J. Marks, *Proceedings of the National Academy of Sciences* ID No 0711990105, **105** (2008).
3. M. Ghougali, O. Belahssen, A. Chala, *J. Nano- Electron. Phys.* **8** No 4, 04059 (2016).
4. J. Kim, J.-H. Yun, Y.C. Park, W.A. Anderson, *Mater. Lett.* **75**, 99 (2012).
5. M.-J. Park, J.-Y. Jung, S.-M. Shin, J.-W. Song, Y.-H. Nam, D.-H. Kim, *Thin Solid Films* **599**, 54 (2016).
6. K.C. Wang, P.S. Shen, M.H. Li, S. Chen, M.W. Lin, P. Chen, *ACS Appl. Mater. Interfaces* **6**, No.15, 11851 (2014).
7. S. Benramache, O. Belahssen, H. Ben Temam, *J. Semicond.* **35**, No.7, 073001 (2014).
8. J.H. Yun, J. Kim, Y.C. Park, S.J. Moon, W.A. Anderson, *Thin Solid Films* **547**, 17 (2013).
9. A. Alshahrie, I.S. Yahia, A. Alghamdi, P.Z. Al Hassan, *Optik* **127**, 5105 (2016).
10. S. Ahn, A.H. Tuan, S. Kim, C. Park, C. Shin, Y.J. Lee,

Mater. Lett. **132**, 06 (2014).
11. O. Belahssen, H. Ben Temam, S. Lakel, B. Benhaoua, S. Benramache, S. Gareh, *Optik* **126**, 1487 (2015).
12. D. Zaouk, Y. Zaatar, R. Asmar, *Microelectron. J.* **37**, 1276 (2006).
13. A.A. Al-Ghamdi, W.E. Mahmoud, .J. Yaghmour, F.M. Al-Marzouki, *J. Alloy. Compd.* **486**, 9 (2009).
14. B.D. Cullity, *Elements of X-ray Diffraction* (Addison-Wesley Publishing Co. Inc.: New York: 1976).
15. R. Charma, A.D. Acharya, S. Moghe, B. Shrivastava, M. Gangrade, V. Shripathi, V. Ganesan, *Mater. Sci. Semicond. Process.* **23**, 42 (2014).
16. R. Sharma, A.D. Acharya, S.B. Shrivastava, M.M. Patidarc, M. Gangradec, T. Shripathic, V. Ganesan, *Optik* **127**, 4661 (2016).
17. P.M. Ponnusamy, S. Agilan, N. Muthukumarasamy, T.S. Senthil, G. Rajesh, M.R. Venkatraman, D. Velauthapillai, *Mater. Character.* **114**, 166 (2016).
18. P.S. Patil, L.D. Kadam, *Appl. Surf. Sci.* **199**, 211 (2002).

Effect of Iron Doping on Physical Properties of NiO Thin Films

O. Belahssen[1,2,*], M. Ghougali[1,2,3], A. Chala[1,2]

[1] *Material Sciences Department, Faculty of Science, University of Biskra, Algeria*
[2] *Physic Laboratory of Thin Films and Applications (LPCMA), University of Biskra, Algeria*
[3] *Laboratory of exploitation and valorization the azalea energetics sources (LEVRES), Faculty of exact Science, University of El-Oued, Algeria*

Nickel-iron oxide was deposited on highly cleaned glass substrates using spray pneumatic technique. The effect of iron percentage on structural, optical and electrical properties has been studied. The crystalline size of the deposited thin films was calculated using Debye-Scherer formula and found in the range between 8.8 and 27.6 nm. The optical properties have been discussed in this work. The absorbance (A), the transmittance (T) and the reflectance (R) were measured and calculated. Band gap energy is considered one of the most important optical parameter, therefore measured and found ranging between 3.81 and 3.98 eV. The NiO:Fe thin film reduces the light reflection for visible range light. The increase of the electrical conductivity to maximum value of $0.470 \ 10^{-4}$ (Ω cm)$^{-1}$ for 6 % Fe can be explained by the increase in carrier concentration of the films. A good electrical conductivity of the NiO:Fe thin film is obtained due to the electrically low sheet resistance. NiO:Fe can be applied in different electronic and optoelectronic applications due to its high band gap, high transparency and good electrical conductivity.

Keywords: NiO thin films, XRD, Optical constants, Electrical conductivity.

1. INTRODUCTION

Nickel oxide (NiO) is the most investigated metal oxide and it has attracted considerable attention because of its low cost material, and also for its applications in several fields such as a catalyst, transparent conducting oxide, photodetectors, electrochromic, gas sensors, photovoltaic devices, electrochemical supercapacitors, heat reflectors, photo-electrochemical cell, solar cells and many opto- electronic devices [1-9]. NiO is an IV group and it can be used as a transparent p-type semiconductor layers, it has a band gap energy ranging from 3.45 eV to 3.85 eV [10]. Band gap energy is significant to adjust the energy level state of NiO.

Several techniques have been used for synthesis and manipulation of nanostructures NiO:Fe such as the thermal evaporation, sputtering, pulse laser ablation, thermal decomposition, electrochemical deposition and sol–gel methods etc. Among of these techniques, sol-gel has some advantages such as high purity of raw materials and a homogeneous solution hence easy control over

In this work, a low cost spray pneumatic technique was used to prepare pure NiO:Fe nanoparticles thin films with various iron percentages. The structural properties of the produced nickel oxide doped iron thin films have been examined. The absorption, transmittance and reflectance spectra of the produced thin films for the NiO:Fe are also measured in range between 300-1100 nm. Moreover, the optical band gap is determined as a function of the iron percentages.

2. EXPERIMENTAL DETAILS

2.1 Preparation of Samples

NiO:Fe thin films were prepared onto a highly cleaned glass substrates using spay pneumatic tech-

nique. Nickel nitrate was dissolved in 50 ml of water as a solvent, iron nitrate was dissolved in 50 ml of water too and chloride acid was used as a stabilizer for the all samples in this work. The precursor molarity and iron nitrate concentration are 0.20 mol L^{-1}. The produced mixture was stirred at 60 °C for 2 h in order to obtain a clear and homogenous solution then the mixture was cooled down at room temperature and placed at dark environment for 48 h. The glass substrates were cleaned by detergent and by alcohol mixed with deionized water.

2.2 Deposition of Thin Films

The coating was dropped into glass substrates at 480 °C that sprayed during 2 min by pneumatic nebulizer system which transforms the liquid to a stream formed with uniform and fine droplets.

2.3 Devices and Measurements

The X-ray diffraction (XRD) spectra of the NiO:Fe were measured to verify the structure. X-ray diffraction (XRD) was measured by using BRUKER-AXS-8D diffractometer with Cu Kα radiation ($\lambda = 1, 5406$ Å) operated at 40 kV and 40 mA in the scanning range of (2θ) between 20° and 80°. The spectral dependence of the NiO:Fe transmittance (T) and the absorbance (A), on the wavelength ranging 300-1100 nm are measured using an ultraviolet-visible spectrophotometer (Perkin-Elmer Lambda 25). The reflectance (R) was calculated by the well-known equation as ($T + R + A = 1$). Whereas the electrical conductivity of the films was measured in a coplanar structure of four golden stripes on the deposited film surface; the measurements were performed with Keithley model 2400 low voltage source meter instrument.

* belahssenokba@gmai.com

3. RESULTS AND DISCUSSIONS

3.1 Structural Properties

The X-ray diffraction was used in this work in order to understand the structure of the deposited NiO:Fe thin films with different iron percentages. XRD patterns of all the deposited samples of Nickel-Iron Oxide thin films are shown in figure 1. From the figure, it can be noticed that all the patterns exhibit diffraction peaks around $2\theta \sim 37°$, referred to (111) favorite direction which is in agreement with the Joint Committee of Powder Diffraction Standards (JCPDS) card number 47-1049. The position of the peaks leads to the conclusion that the films are, in nature, with a cubic crystalline structure, which is in agreement with other reports [11, 12].
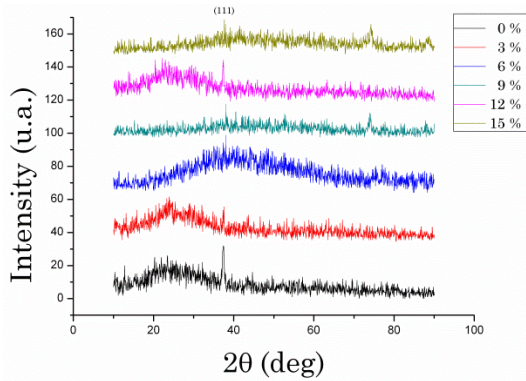
Fig. 1 – XRD patterns of the deposited NiO:Fe thin films on glass substrate at different iron percentages

The lattice constant a of Fe doped NiO thin films, is calculated using equation (1):

$$d_{(hkl)} = \frac{a}{\sqrt{\left(h^2 + k^2 + l^2\right)}}, \qquad (1)$$

where (h, k, l) is the Miller indices of the planes and d_{hkl} is the interplanar spacing.

It can be observed that no peaks correspond to the Fe doping exist in the XRD patterns. In fact, doping with low concentration impurities does not result in the appearance of new XRD peaks, but instead leads to a shift in the lattice parameters of the host material. This shift may arise from the strain induced when the dopant is incorporated into the crystal lattice [13]. The strain ε values in the films were estimated from the observed shift, in the diffraction peak between their positions in the XRD spectra via the formula (2):

$$\varepsilon = \frac{a - a_0}{a_0} \cdot 100 \qquad (2)$$

where ε is the mean strain in NiO:Fe thin films (Table 1), a is the lattice constant of NiO:Fe thin films and a_0 the lattice constant of bulk (standard $a_0 = 0, 4177$ nm).

The crystalline size was calculated using Debye-Scherer formula [14]:

$$D = \frac{0.9\lambda}{\beta \cos\theta} \qquad (3)$$

where β is the full width at half maximum (FWHM) and θ is the diffraction angle.

The crystallite size of the NiO:Fe thin films were calculated using the well-known Deby-Scherer's formula Eq. (3), the average of the NiO:Fe thin films ranging between 8.8 and 27.6 nm. The changing in the crystallites size leads to the changes in optical properties.

Fig. 2 shows the variation of the crystallite size and mean strain as a function of percentage of Fe. The crystallite size increases when the stain decreases and inversely.

The changing in the crystallites size leads to the changes in optical properties i.e. band gap energy increases with decreasing crystallites size as shown in Fig. 3.
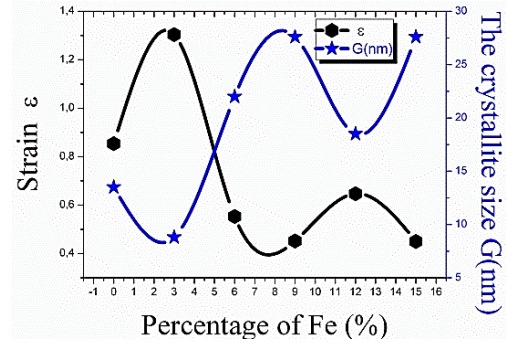
Fig. 2 – The variation of crystallite size and mean strain of Fe doped NiO thin films as a function of the percentage of Fe
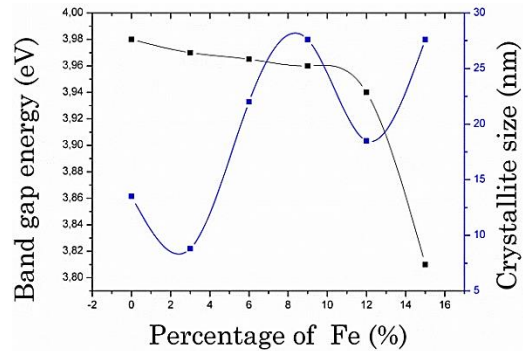
Fig. 3 – The variation of crystallite size and band gap energy of NiO:Fe thin films as a function of the percentage of Fe

3.2 Optical Properties

Fig. 4 shows the optical absorption spectra of NiO:Fe nanoparticles. The absorption spectra of 6 % Fe show that the absorption edge is slightly shifted towards shorter wavelength when compared to other absorption spectra. The absorption edge of a degenerate semiconductor is shifted to shorter wavelengths with increasing carrier concentration. This shift predicts that there is an increase in band gap value ($E_g = 3.965$ eV). The fundamental absorption, which corresponds to the electron transition from the valance band to the conduction band, can be used to determine the nature and value of the optical band gap. The optical absorption study was used to determine the optical band gap of the nanoparticles, which is the most familiar and simplest method.

Table 1 – Structural, optical and electrical parameters of NiO:Fe thin film at different iron percentages

Percentage Fe (%)	Crystallite size (nm)	Strain ε (%)	Band gap energy (eV)	Conductivity 10^{-4} $(\Omega\,cm)^{-1}$
0	13.5	0.854	3.980	0.366
3	8.8	1.304	3.970	0.295
6	22.0	0.553	3.965	0.470
9	27.6	0.452	3.960	0.303
12	18.5	0.647	3.940	0.283
15	27.6	0.450	3.810	0.279
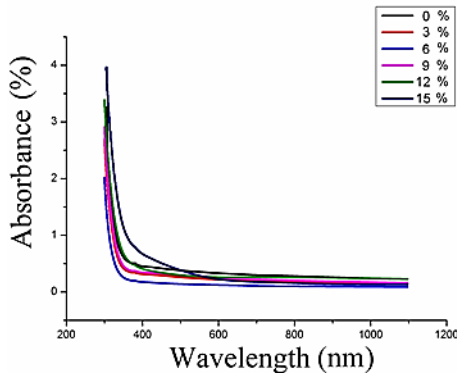
Fig. 4 – Absorbance spectra of NiO samples for different percentage of Fe

The absorption coefficient (α) and the incident photon energy ($h\upsilon$) are related by the expression 2 [12]:

$$(\alpha h\upsilon) = C\left(h\upsilon - E_g\right)^n \qquad (2)$$

where α is the absorption coefficient, C is a constant, $h\upsilon$ is the photon energy, υ is the frequency of the incident radiation, h is the Planck's constant, exponent n is 0.5 for direct band allowed transition ($h\upsilon = 1239/\lambda$(nm) (eV)) and E_g the band gap energy of the semiconductor.
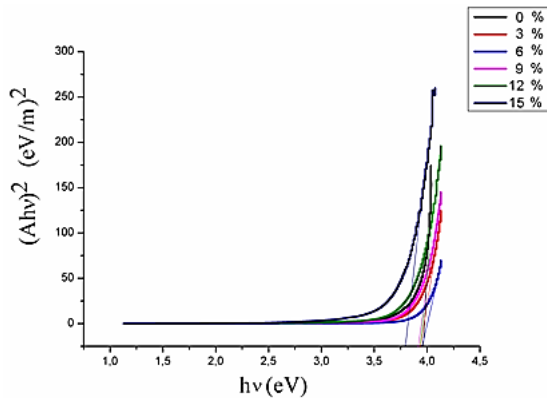
Fig. 5 – Plot of $(\alpha h\upsilon)^2$ versus incident photon energy ($h\upsilon$) of NiO:Fe nanoparticles for different percentage of Fe

As it was shown in (Fig. 5) a typical variation of $(\alpha h\upsilon)^2$ as a function of photon energy ($h\upsilon$) of NiO:Fe nanoparticles Eq. (2), used for deducing optical band gap E_g, The optical band gap values have been determined by extrapolating the linear portion of the curve to meet the energy axis ($h\upsilon$) [15]. The band gap values were given in Table 1.
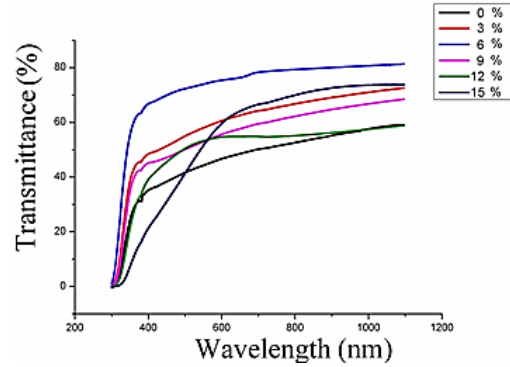
Fig. 6 – Transmission spectra of NiO:Fe samples for different percentage of Fe

For a transmittance study (Fig. 6), the NiO:Fe layer showed very high transmittance of 80 % for 6 % iron concentration, averaged in the wavelength (λ) of 300-1100 nm. Suppression of light reflection at a surface is an important factor to absorb more photons in semiconductor materials. We obtained the reflectance profiles of NiO:Fe coated (Fig. 7). The averaged reflectance values (300-1100 nm) were significantly lower than 20 %. Moreover, NiO:Fe coating drives a substantially suppressed reflectance under 20 % in 500 nm < λ < 1100 nm. This notifies that the NiO:Fe coating is an efficient design scheme to introduce the incident light into substrate.
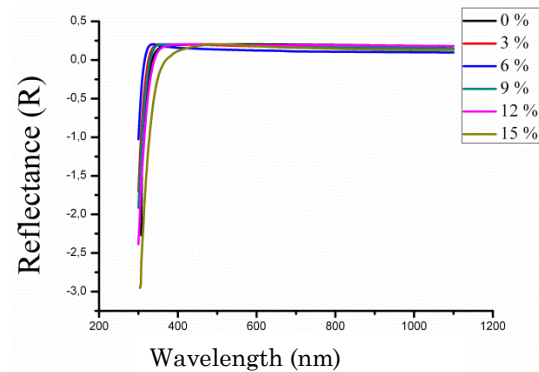
Fig. 7 – Reflectance profiles of NiO;Fe thin film for different percentage of Fe

3.3 Electrical Properties

The electrical properties of the NiO:Fe films are summarized in Table I. Fig. 8 shows the variation of the electrical conductivity σ of NiO:Fe thin films as a function as percentage of Fe. As can be seen, deposited films have good conductivity. The maximum recorded value was 0.470 10^{-4} $(\Omega\,cm)^{-1}$ for the NiO:Fe thin film depos-

ited using 6 % iron concentration. The increase of the electrical conductivity can be explained by the increase in the carrier concentration. Patil et al. [16] have reported that the increase of the electrical conductivity is due to the increase in activation energy with increasing film thickness. This was explained by difference in the experimental conditions of spraying solution, spray rate and cooling of the substrates during decomposition. However, with 0.20 mol L^{-1} precursor molarity, the crystal structure of the film is significantly improved and the grain size is increased, leading to a reduced concentration of structural defects such as dislocations and grain boundaries. Thus, the decrease of the concentration of crystal defects leads in the increase of free carrier concentration. The improvement of crystal quality reduces the carrier scattering from structural defects, leading to higher mobility.
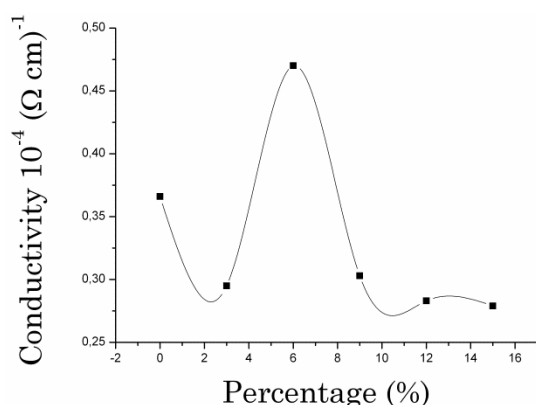
Fig. 8 – Variation of the electrical conductivity of NiO:Fe thin films as a function of the percentage of Fe

4. CONCLUSION

The spray pneumatic technique has been successfully employed to deposit NiO:Fe thin films with different iron concentrations on glass substrates. All the films showed cubic crystal structure with preferential orientation according to the direction (111). The maximum crystallite size was found (27.06 nm). We have observed an improvement in the films crystallinity at 0.10 mol L^{-1} precursor molarity where the peak at position 37.1° corresponding to the (111) plans is very sharp, the film obtain at this concentration has higher and sharper diffraction peak indicating an improvement in peak intensity compared to other films. The band gap value of NiO:Fe films was found from 3.810 eV to 3.980 eV. The high transmittance (80 %), low reflectance under 20 %, widened band gap and good conductivity (0.470 10^{-4} $(\Omega\ cm)^{-1}$) obtained for NiO:Fe thin films make them promising candidate for optoelectronic devices as well as window layer in solar cell applications.

AKNOWLEDGEMENTS

REFERENCES

1. M.A. Abbasi, Z.H. Ibupoto, A. Khan, O. Nur, M. Willander, *Mater. Lett.* **108**, 152 (2013).
2. M.D. Irwin, D.B. Buchholz, A.W. Hains, R.P.H. Chang, T.J. Marks, *Proc. National Academy Sci.* **105**, art. No 0711990105 (2008).
3. M. Ghougali, O. Belahssen, A. Chala, *J. Nano- Electron. Phys.* **8** No 4, 04059 (2016).
4. J. Kim, J.-H. Yun, Y.C. Park, W.A. Anderson, *Mater. Lett.* **75**, 99 (2012).
5. M.-J. Park, J.-Y. Jung, S.-M. Shin, J.-W. Song, Y.-H. Nam, D.-H. Kim, *Thin Solid Films* **599**, 54 (2016).
6. K.C. Wang, P.S. Shen, M.H. Li, S. Chen, M.W. Lin, P. Chen, *ACS Appl. Mater. Interf.* **6**, 11851 (2014).
7. J.H. Yun, J. Kim, Y.C. Park, S.J. Moon, W.A. Anderson, *Thin Solid Films* **547**, 17 (2013).
8. S. Ahn, A.H. Tuan, S. Kim, C. Park, C. Shin, Y.J. Lee, *Mater. Lett.* **132**, 332 (2014).
9. M. Ghougali, O. Belahssen, A. Chala, *J. Nano- Electron. Phys.* **9** No 3, 03043 (2017).
10. D. Zaouk, Y. Zaatar, R. Asmar, *Microelectron. J.* **37**, 11 (2006).
11. A.R. Balu, V.S. Nagarethinam, N. Arunkumar, M. Suganya, *J. Electron. Dev.* **13**, 739 (2012).
12. R. Sharma, A.D. Acharya, S.B. Shrivastava, M.M. Patidarc, M. Gangradec, T. Shripathic, V. Ganesan, *Optik* **127**, 4661 (2016).
13. J. Daniel Bayan, Daniel R. Gametin, *Prog. Inorgan. Chem.* **47** (2005).
14. B.D. Cullity, *Elements of X-ray Diffraction* (Addison-Wesley Publishing Co. Inc.: New York: 1976).
15. P.M. Ponnusamy, S. Agilan, N. Muthukumarasamy, T.S. Senthil, G. Rajesh, M.R. Venkatraman, D. Velauthapillai, *Mater. Character.* **114**, 166 (2016).
16. P.S. Patil, L.D. Kadam, *Appl. Surf. Sci.* **199**, 211 (2002).

N -Ferrocenymethyl- N -phenylacetamide

3 authors:

Abdelhamid Khelef
El-Oued University
23 PUBLICATIONS   **27** CITATIONS

SEE PROFILE

Mohammed Sadok Mahboub
El-Oued University
14 PUBLICATIONS   **7** CITATIONS

SEE PROFILE

Touhami Lanez
El-Oued University
178 PUBLICATIONS   **346** CITATIONS

SEE PROFILE

Some of the authors of this publication are also working on these related projects:

Elaboration and caracterisation of Bi based superconductors View project

Copper Corrosion Inhibition using Organic and Inorganic Inhibitors View project

N-Ferrocenymethyl-N-phenylacetamide

Abdelhamid Khelef,[a] Mohammed Sadok Mahboub[b] and Touhami Lanez[a]*

[a]VTRS Laboratory, Department of Chemistry, Faculty of Exact Sciences, University of El-Oued, PO Box 789, El-Oued 39000, Algeria, and [b]LEVRES Laboratory, Department of Physics, Faculty of Exact Sciences, University of El-Oued, PO Box 789, El-Oued 39000, Algeria. *Correspondence e-mail: lanezt@gmail.com

In the title compound, [Fe(C_5H_5)($C_{14}H_{14}NO$)], the asymmetric unit comprises two unique molecules. The two cyclopentadienyl (Cp) rings of each ferrocene residue are nearly parallel to one another. In each substituted Cp ring, the CH_2 group carries an N-phenylacetamide residue. In the crystal, C—H···O hydrogen bonds stack molecules along a.

3D view

Chemical scheme
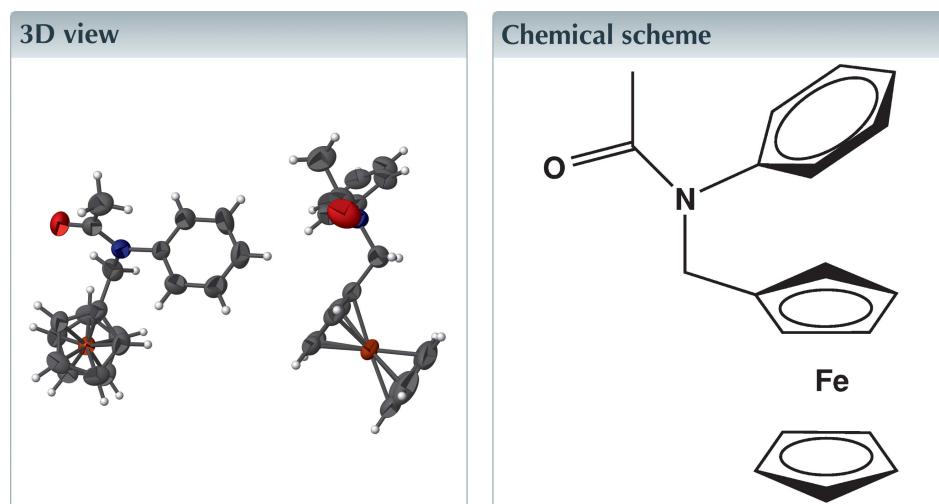
Structure description

Ferrocene and its derivatives are known to be of considerable interest, because of their use in organic synthesis (Khand *et al.*, 1989), catalysis (Szarka *et al.*, 2004), materials science (Uno & Dixneuf, 1998), asymmetric synthesis (Torres *et al.*, 2002), medicinal chemistry (Chavain *et al.*, 2009) and electrochemistry (Ahmedi & Lanez, 2011; Khelef & Lanez, 2015). As a continuation of our research related to ferrocene derivatives (Khelef *et al.*, 2012; Rahim *et al.*, 2012), we report the synthesis and structural characterization of the title compound.

The asymmetric unit of title compound comprises two crystallographically independent molecules, A and B (Fig. 1). The two cyclopentadienyl (Cp) rings of each ferrocene residue are nearly parallel to one another, the dihedral angle between the mean planes of Cp1/Cp2 is 3.2 (2)° and Cp3/Cp4 is 2.6 (2)° (Cp1 = C1A–C5A, Cp2 = C6A–C10A, Cp2 = C1B–C5B and Cp4 = C6B–C10B). The Cp rings are essentially parallel and the Fe···centroid distances are 1.648 (3) (Cp1), 1.640 (3) (Cp2), 1.652 (3) (Cp3) and 1.645 (3) Å (Cp4). The [Cg1···Fe1···Cg2] angle is 178.16 (2)° and [Cg3···Fe2···Cg4] angle is 179.21 (2)° [Cg1, Cg2, Cg3 and Cg4 are the centroids of the Cp1, Cp2, Cp3 and Cp4 rings, respectively].

In each molecule one of the Cp rings is substituted by an amide group which is essentially perpendicular to the substituted cyclopentadienyl ring [torsion angles C14A—N1—C11A—C10A and C14B—N2—C11B—C10B are 93.3 (4) and −93.3 (4)°, respec-

OPEN ACCESS
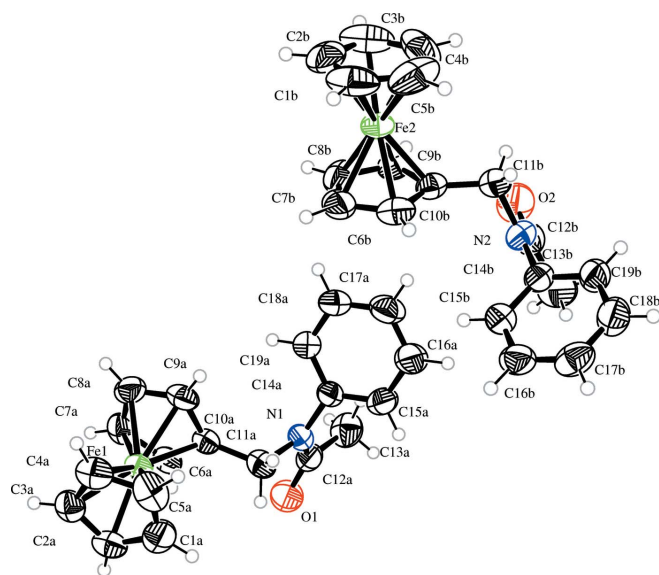
Figure 1
The molecular structure of the title compound, showing the atomic numbering scheme and 50% probability displacement ellipsoids.

tively]. In the methanoyl group, the N and O atoms are coplanar [the C11A—N1—C12A—O1 torsion angle is $-0.6\,(5)°$ and the C11B—N2—C12B—O2 torsion angle is $-2.9\,(6)°$]. In the crystal, C—H···O hydrogen bonds, Table 1, combine to stack the molecules along the *a* axis, Fig. 2.

Synthesis and crystallization

N-ferrocenylmethylaniline was obtained as described in the literature (Osgerby & Pauson, 1961). To a 250 ml round-bottom flask equipped with a reflux condenser and a magnetic
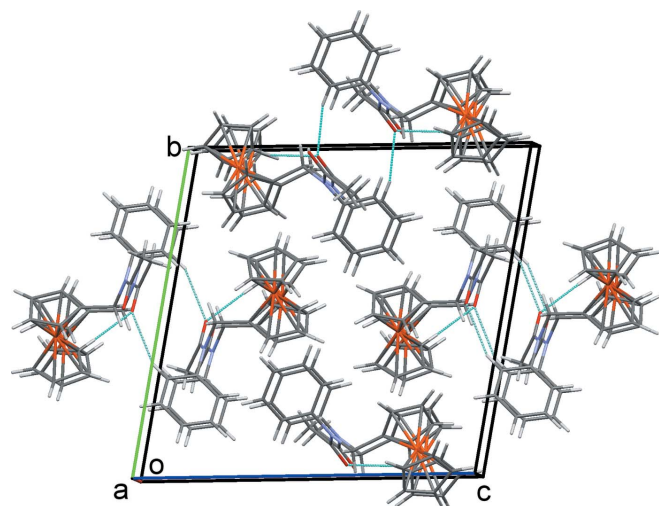
Figure 2
The crystal packing of the title compound, viewed along the *b* axis, with hydrogen bonds drawn as dashed lines.

Table 1
Hydrogen-bond geometry (Å, °).

D—H···A	D—H	H···A	D···A	D—H···A
C15A—H15A···O1^i	0.93	2.56	3.456 (5)	162
C19B—H19B···O2^{ii}	0.93	2.55	3.421 (5)	157
C15A—H15A···O1^i	0.93	2.56	3.456 (5)	162
C19B—H19B···O2^{ii}	0.93	2.55	3.421 (5)	157

Symmetry codes: (i) $-x-1, -y+2, -z+1$; (ii) $-x, -y+1, -z+2$.

stirrer a suspension of *N*-ferrocenylmethylaniline (6 g, 20 mmol) in 50 ml of dry toluene was added under a nitrogen atmosphere. The resulting suspension was heated at 50°C until all the solid materials had dissolved completely. 50 ml of anhydride acetic acid was then added and the resulting mixture was vigorously stirred under reflux for 20 min. The reaction mixture was then poured into water; the organic layer was separated, washed twice with water, dried over $MgSO_4$ and evaporated. The residue was recrystallized from a mixture of ethanol–water to yield *N*-ferrocenymethyl-*N*-phenyl-acetamide as orange needles (yield: 5.6 g, 81.5%; m.p. 116–117°C). The compounds gave clean ^1H and ^{13}C NMR spectra in $CDCl_3$. NMR ^1H (300 MHz, $CDCl_3$) 1.75 (*s*, 3H, CH_3), 4.03 (*s*, 4H, C_5H_4), 4.08 (*s*, 5H, C_5H_5), 4.61 (*s*, 2H, CH_2), 6.99 (*d*, 2H, *ortho*-C_6H_5), 7.28–7.35 (*m*, 3H, *meta*- and *para*-C_6H_5). NMR ^{13}C (75 MHz, $CDCl_3$) 22.83 (1C, CH_3), 48.40 (1C, CH_2), 68.13, 69.89 and 83.13 (5C, C5H4), 68.55 (5C, C_5H_5), 127.87, 128.55, 129.43, 142.84 (6C, C_6H_5), 169.74 (1C, CO).

Table 2
Experimental details.

Crystal data	
Chemical formula	[Fe(C₅H₅)(C₁₄H₁₄NO)]
M_r	333.2
Crystal system, space group	Triclinic, $P\bar{1}$
Temperature (K)	298
a, b, c (Å)	7.344 (1), 14.831 (1), 15.267 (1)
α, β, γ (°)	79.094 (10), 79.627 (10), 87.508 (10)
V (Å^3)	1606.1 (3)
Z	4
Radiation type	Mo $K\alpha$
μ (mm^{-1})	0.94
Crystal size (mm)	$0.3 \times 0.1 \times 0.1$
Data collection	
Diffractometer	Nonius KappaCCD
No. of measured, independent and observed [$I > 2\sigma(I)$] reflections	8635, 5157, 3765
R_{int}	0.039
$(\sin\theta/\lambda)_{max}$ (Å^{-1})	0.588
Refinement	
$R[F^2 > 2\sigma(F^2)]$, $wR(F^2)$, S	0.042, 0.115, 1.02
No. of reflections	5157
No. of parameters	398
H-atom treatment	H-atom parameters constrained
$\Delta\rho_{max}, \Delta\rho_{min}$ (e Å^{-3})	0.37, −0.28

Computer programs: *COLLECT* (Nonius, 1998), *SIR92* (Altomare *et al.*, 1993), *SHELXL2014* (Sheldrick, 2015), *ORTEP-3 for Windows* (Farrugia, 2012), *Mercury* (Macrae *et al.*, 2008), *WinGX* (Farrugia, 2012).

Refinement

Crystal data, data collection and structure refinement details are summarized in Table 2.

References

Ahmedi, R. & Lanez, T. (2011). *J. Fundam. Appl. Sci.* **3**, 183–193.

Altomare, A., Cascarano, G., Giacovazzo, C. & Guagliardi, A. (1993). *J. Appl. Cryst.* **26**, 343–350.

Chavain, N., Davioud-Charvet, E., Trivelli, X., Mbeki, L., Rottmann, M., Brun, R. & Biot, C. (2009). *Bioorg. Med. Chem.* **17**, 8048–8059.

Farrugia, L. J. (2012). *J. Appl. Cryst.* **45**, 849–854.

Khand, I. U., Lanez, T. & Pauson, P. L. (1989). *J. Chem. Soc. Perkin Trans. 1*, pp. 2075–2078.

Khelef, A. & Lanez, T. (2015). *Der Pharma Chem.* **7**, 318–323.

Khelef, A., Terki, B., Mahboub, M. S. & Lanez, T. (2012). *Acta Cryst.* E**68**, m647.

Macrae, C. F., Bruno, I. J., Chisholm, J. A., Edgington, P. R., McCabe, P., Pidcock, E., Rodriguez-Monge, L., Taylor, R., van de Streek, J. & Wood, P. A. (2008). *J. Appl. Cryst.* **41**, 466–470.

Nonius (1998). *COLLECT*. Nonius BV, Delft, The Netherlands.

Osgerby, J. M. & Pauson, P. L. (1961). *J. Chem. Soc.* pp. 4600–4604.

Rahim, O., Khelef, A., Terki, B., Mahboub, M. S. & Lanez, T. (2012). *Acta Cryst.* E**68**, m1318.

Sheldrick, G. M. (2015). *Acta Cryst.* C**71**, 3–8.

Szarka, Z., Kuik, Á., Skoda-Földes, R. & Kollár, L. (2004). *J. Organomet. Chem.* **689**, 2770–2775.

Torres, J. C., Pilli, R. A., Vargas, M. D. A., Violante, F., Garden, S. J. & Pinto, A. C. (2002). *Tetrahedron*, **58**, 4487–4492.

Uno, M. & Dixneuf, P. H. (1998). *Angew. Chem. Int. Ed.* **37**, 1714–1717.

full crystallographic data

N-Ferrocenymethyl-*N*-phenylacetamide

Abdelhamid Khelef, Mohammed Sadok Mahboub and Touhami Lanez

N-Ferrocenymethyl-*N*-phenylacetamide

Crystal data

[Fe(C_5H_5)($C_{14}H_{14}NO$)]	$Z = 4$
$M_r = 333.2$	$F(000) = 696$
Triclinic, $P\bar{1}$	$D_x = 1.378$ Mg m^{-3}
Hall symbol: -P 1	Mo $K\alpha$ radiation, $\lambda = 0.71073$ Å
$a = 7.344$ (1) Å	Cell parameters from 5157 reflections
$b = 14.831$ (1) Å	$\theta = 2.8$–24.7°
$c = 15.267$ (1) Å	$\mu = 0.94$ mm^{-1}
$\alpha = 79.094$ (10)°	$T = 298$ K
$\beta = 79.627$ (10)°	Needle, orange
$\gamma = 87.508$ (10)°	$0.3 \times 0.1 \times 0.1$ mm
$V = 1606.1$ (3) Å^3	

Data collection

Nonius KappaCCD diffractometer	3765 reflections with $I > 2\sigma(I)$
Radiation source: fine-focus sealed tube	$R_{int} = 0.039$
CCD scans	$\theta_{max} = 24.7°$, $\theta_{min} = 2.8°$
8635 measured reflections	$h = -8 \rightarrow 8$
5157 independent reflections	$k = -17 \rightarrow 17$
	$l = -15 \rightarrow 17$

Refinement

Refinement on F^2	Hydrogen site location: inferred from neighbouring sites
Least-squares matrix: full	H-atom parameters constrained
$R[F^2 > 2\sigma(F^2)] = 0.042$	$w = 1/[\sigma^2(F_o^2) + (0.0489P)^2 + 0.6059P]$ where $P = (F_o^2 + 2F_c^2)/3$
$wR(F^2) = 0.115$	
$S = 1.02$	$(\Delta/\sigma)_{max} = 0.001$
5157 reflections	$\Delta\rho_{max} = 0.37$ e Å^{-3}
398 parameters	$\Delta\rho_{min} = -0.28$ e Å^{-3}
0 restraints	Extinction correction: *SHELXL2014* (Sheldrick, 2015), Fc*=kFc[1+0.001xFc$^2\lambda^3$/sin(2θ)]$^{-1/4}$
0 constraints	Extinction coefficient: 0.0049 (12)

Special details

Geometry. All e.s.d.'s (except the e.s.d. in the dihedral angle between two l.s. planes) are estimated using the full covariance matrix. The cell e.s.d.'s are taken into account individually in the estimation of e.s.d.'s in distances, angles and torsion angles; correlations between e.s.d.'s in cell parameters are only used when they are defined by crystal symmetry. An approximate (isotropic) treatment of cell e.s.d.'s is used for estimating e.s.d.'s involving l.s. planes.

Fractional atomic coordinates and isotropic or equivalent isotropic displacement parameters (Å²)

	x	*y*	*z*	U_{iso}*/U_{eq}
Fe2	0.46219 (6)	0.43859 (3)	0.69245 (3)	0.04595 (17)
Fe1	0.06009 (6)	0.92687 (3)	0.17945 (3)	0.04206 (17)
O1	−0.5391 (4)	0.9627 (2)	0.3939 (2)	0.0854 (10)
C14A	−0.2433 (5)	0.8074 (2)	0.5143 (2)	0.0462 (8)
N2	0.1143 (4)	0.6002 (2)	0.8775 (2)	0.0570 (8)
C10B	0.2785 (5)	0.5231 (2)	0.7548 (2)	0.0473 (8)
N1	−0.3111 (4)	0.8744 (2)	0.44649 (18)	0.0524 (7)
O2	−0.1384 (5)	0.5145 (2)	0.8928 (2)	0.0918 (10)
C3A	0.2181 (5)	0.9949 (3)	0.0637 (3)	0.0555 (9)
H3A	0.2196	0.9852	0.0051	0.067*
C10A	−0.1303 (4)	0.8808 (2)	0.2910 (2)	0.0445 (8)
C7A	−0.1331 (5)	0.8472 (3)	0.1509 (3)	0.0578 (10)
H7A	−0.1637	0.8476	0.0943	0.069*
C1B	0.7309 (6)	0.4029 (3)	0.6688 (5)	0.0860 (16)
H1B	0.8239	0.4413	0.6337	0.103*
C14B	0.2045 (5)	0.6821 (2)	0.8845 (2)	0.0510 (9)
C11A	−0.1712 (6)	0.9246 (3)	0.3737 (2)	0.0610 (10)
H11A	−0.0575	0.9277	0.3969	0.073*
H11B	−0.215	0.987	0.3565	0.073*
C5A	0.2862 (6)	0.9844 (3)	0.2041 (3)	0.0702 (12)
H5A	0.3401	0.9666	0.2554	0.084*
C9B	0.1873 (5)	0.4692 (3)	0.7081 (3)	0.0560 (10)
H10B	0.0918	0.4282	0.7341	0.067*
C6B	0.4137 (5)	0.5750 (2)	0.6887 (3)	0.0600 (10)
H8B	0.4938	0.6167	0.7	0.072*
C8B	0.2676 (6)	0.4892 (3)	0.6154 (3)	0.0670 (12)
H6B	0.2336	0.4638	0.5695	0.08*
C15B	0.2566 (6)	0.7485 (3)	0.8087 (3)	0.0630 (10)
H15B	0.2272	0.7424	0.7534	0.076*
C19A	−0.1770 (6)	0.7239 (3)	0.4957 (3)	0.0623 (10)
H19A	−0.1825	0.7092	0.4397	0.075*
C16A	−0.1674 (7)	0.7642 (3)	0.6620 (3)	0.0860 (15)
H16A	−0.1669	0.7775	0.7191	0.103*
C15A	−0.2392 (6)	0.8279 (3)	0.5980 (3)	0.0701 (12)
H15A	−0.2843	0.8842	0.6116	0.084*
C11B	0.2372 (6)	0.5234 (3)	0.8542 (3)	0.0638 (10)
H11C	0.1794	0.4658	0.8854	0.077*
H11D	0.3526	0.5274	0.8757	0.077*
C19B	0.2455 (5)	0.6916 (3)	0.9662 (3)	0.0593 (10)
H19B	0.2109	0.6467	1.0174	0.071*
C16B	0.3528 (6)	0.8243 (3)	0.8152 (3)	0.0693 (12)
H16B	0.3899	0.8686	0.7639	0.083*
C7B	0.4077 (6)	0.5539 (3)	0.6044 (3)	0.0683 (12)
H7B	0.4833	0.5783	0.5502	0.082*
C17B	0.3936 (5)	0.8344 (3)	0.8966 (3)	0.0687 (11)

H17B	0.458	0.8855	0.901	0.082*
C13B	−0.1921 (6)	0.6659 (3)	0.9251 (3)	0.0840 (14)
H13D	−0.1149	0.7167	0.9247	0.126*
H13E	−0.2758	0.6843	0.8833	0.126*
H13F	−0.2614	0.6468	0.985	0.126*
C18B	0.3386 (6)	0.7683 (3)	0.9719 (3)	0.0715 (12)
H18B	0.3646	0.7755	1.0276	0.086*
C18A	−0.1024 (6)	0.6619 (3)	0.5591 (3)	0.0678 (11)
H18A	−0.0554	0.606	0.5452	0.081*
C12B	−0.0721 (6)	0.5868 (3)	0.8974 (3)	0.0661 (11)
C13A	−0.6325 (5)	0.8459 (3)	0.5234 (3)	0.0755 (12)
H13A	−0.5703	0.7993	0.5603	0.113*
H13B	−0.6982	0.8867	0.5602	0.113*
H13C	−0.7184	0.8176	0.4966	0.113*
C5B	0.6691 (9)	0.3963 (4)	0.7606 (5)	0.108 (2)
H5B	0.7128	0.4286	0.7991	0.13*
C12A	−0.4920 (6)	0.8994 (3)	0.4496 (3)	0.0603 (10)
C3B	0.5097 (7)	0.3011 (3)	0.7083 (5)	0.0904 (17)
H3B	0.4254	0.2576	0.7046	0.108*
C17A	−0.0971 (6)	0.6820 (3)	0.6423 (3)	0.0712 (12)
H17A	−0.0463	0.6403	0.6851	0.085*
C2B	0.6325 (7)	0.3434 (4)	0.6386 (4)	0.0820 (14)
H2B	0.6478	0.3336	0.5793	0.098*
C4B	0.5260 (8)	0.3308 (5)	0.7846 (4)	0.104 (2)
H4B	0.4566	0.3118	0.842	0.125*
C6A	−0.2156 (4)	0.9027 (2)	0.2139 (2)	0.0473 (8)
H6A	−0.3095	0.946	0.2058	0.057*
C9A	0.0048 (5)	0.8118 (2)	0.2743 (3)	0.0565 (10)
H9A	0.0823	0.7844	0.3139	0.068*
C2A	0.1019 (5)	1.0569 (3)	0.1067 (3)	0.0598 (10)
H2A	0.0129	1.0951	0.0821	0.072*
C8A	0.0022 (6)	0.7917 (3)	0.1888 (3)	0.0643 (11)
H8A	0.0774	0.7489	0.1617	0.077*
C4A	0.3312 (5)	0.9501 (3)	0.1231 (3)	0.0606 (10)
H4A	0.4205	0.9056	0.1111	0.073*
C1A	0.1441 (6)	1.0510 (3)	0.1936 (3)	0.0699 (12)
H1A	0.0884	1.0849	0.2368	0.084*

Atomic displacement parameters (Å²)

	U^{11}	U^{22}	U^{33}	U^{12}	U^{13}	U^{23}
Fe2	0.0372 (3)	0.0402 (3)	0.0616 (3)	0.0043 (2)	−0.0144 (2)	−0.0080 (2)
Fe1	0.0369 (3)	0.0396 (3)	0.0473 (3)	−0.00241 (19)	−0.0069 (2)	−0.0021 (2)
O1	0.109 (2)	0.079 (2)	0.0712 (19)	0.0397 (18)	−0.0356 (17)	−0.0112 (17)
C14A	0.0495 (19)	0.043 (2)	0.0428 (19)	0.0045 (15)	−0.0064 (14)	−0.0025 (16)
N2	0.071 (2)	0.0462 (18)	0.0552 (19)	0.0011 (15)	−0.0074 (15)	−0.0164 (15)
C10B	0.047 (2)	0.041 (2)	0.058 (2)	0.0054 (15)	−0.0164 (16)	−0.0133 (17)
N1	0.0625 (19)	0.0486 (18)	0.0406 (16)	0.0073 (14)	−0.0026 (13)	−0.0021 (14)

O2	0.107 (3)	0.076 (2)	0.091 (2)	−0.0400 (19)	−0.0019 (18)	−0.0184 (18)
C3A	0.053 (2)	0.058 (2)	0.055 (2)	−0.0172 (18)	−0.0041 (17)	−0.0073 (19)
C10A	0.0441 (19)	0.0402 (19)	0.0457 (19)	−0.0021 (14)	−0.0062 (14)	−0.0005 (15)
C7A	0.063 (2)	0.058 (2)	0.049 (2)	−0.0259 (19)	−0.0017 (17)	−0.0067 (19)
C1B	0.049 (3)	0.053 (3)	0.140 (5)	0.005 (2)	−0.009 (3)	0.014 (3)
C14B	0.056 (2)	0.045 (2)	0.051 (2)	0.0004 (16)	−0.0041 (16)	−0.0131 (17)
C11A	0.077 (3)	0.051 (2)	0.051 (2)	−0.0078 (19)	−0.0100 (19)	−0.0004 (18)
C5A	0.059 (3)	0.090 (3)	0.065 (3)	−0.030 (2)	−0.021 (2)	−0.005 (2)
C9B	0.0389 (19)	0.056 (2)	0.078 (3)	0.0079 (16)	−0.0175 (18)	−0.021 (2)
C6B	0.053 (2)	0.040 (2)	0.084 (3)	0.0015 (16)	−0.0076 (19)	−0.009 (2)
C8B	0.069 (3)	0.079 (3)	0.064 (3)	0.036 (2)	−0.031 (2)	−0.032 (2)
C15B	0.081 (3)	0.052 (2)	0.052 (2)	0.002 (2)	−0.0035 (19)	−0.0068 (19)
C19A	0.087 (3)	0.048 (2)	0.050 (2)	0.006 (2)	−0.0067 (19)	−0.0074 (18)
C16A	0.139 (4)	0.065 (3)	0.070 (3)	0.020 (3)	−0.061 (3)	−0.017 (2)
C15A	0.101 (3)	0.050 (2)	0.066 (3)	0.019 (2)	−0.031 (2)	−0.019 (2)
C11B	0.086 (3)	0.047 (2)	0.062 (2)	0.008 (2)	−0.022 (2)	−0.0129 (19)
C19B	0.071 (3)	0.055 (2)	0.051 (2)	−0.0111 (19)	−0.0023 (18)	−0.0106 (19)
C16B	0.081 (3)	0.048 (2)	0.068 (3)	−0.001 (2)	0.010 (2)	−0.004 (2)
C7B	0.071 (3)	0.061 (3)	0.062 (3)	0.026 (2)	−0.001 (2)	−0.002 (2)
C17B	0.061 (3)	0.056 (3)	0.087 (3)	−0.0099 (19)	0.006 (2)	−0.023 (2)
C13B	0.070 (3)	0.075 (3)	0.095 (4)	−0.001 (2)	0.009 (2)	−0.009 (3)
C18B	0.081 (3)	0.074 (3)	0.061 (3)	−0.012 (2)	−0.006 (2)	−0.020 (2)
C18A	0.084 (3)	0.045 (2)	0.068 (3)	0.013 (2)	−0.008 (2)	−0.004 (2)
C12B	0.078 (3)	0.062 (3)	0.054 (2)	−0.012 (2)	0.0000 (19)	−0.007 (2)
C13A	0.057 (3)	0.089 (3)	0.079 (3)	0.010 (2)	−0.006 (2)	−0.021 (3)
C5B	0.113 (5)	0.096 (4)	0.160 (6)	0.060 (4)	−0.102 (5)	−0.075 (4)
C12A	0.078 (3)	0.056 (2)	0.051 (2)	0.019 (2)	−0.0197 (19)	−0.019 (2)
C3B	0.065 (3)	0.046 (3)	0.155 (6)	0.001 (2)	−0.034 (3)	0.008 (3)
C17A	0.087 (3)	0.054 (3)	0.076 (3)	0.006 (2)	−0.038 (2)	0.000 (2)
C2B	0.088 (4)	0.076 (3)	0.090 (4)	0.046 (3)	−0.035 (3)	−0.030 (3)
C4B	0.092 (4)	0.126 (5)	0.067 (3)	0.054 (4)	−0.003 (3)	0.024 (3)
C6A	0.0379 (18)	0.048 (2)	0.051 (2)	−0.0018 (15)	−0.0074 (14)	0.0028 (17)
C9A	0.053 (2)	0.047 (2)	0.061 (2)	0.0054 (16)	−0.0079 (17)	0.0093 (18)
C2A	0.058 (2)	0.045 (2)	0.070 (3)	−0.0051 (17)	−0.0093 (19)	0.0036 (19)
C8A	0.070 (3)	0.043 (2)	0.071 (3)	−0.0047 (18)	0.013 (2)	−0.011 (2)
C4A	0.038 (2)	0.059 (2)	0.080 (3)	−0.0057 (16)	−0.0078 (18)	−0.003 (2)
C1A	0.071 (3)	0.061 (3)	0.075 (3)	−0.027 (2)	0.011 (2)	−0.021 (2)

Geometric parameters (Å, °)

Fe2—C5B	2.006 (4)	C5A—H5A	0.93
Fe2—C1B	2.008 (4)	C9B—C8B	1.413 (5)
Fe2—C4B	2.019 (5)	C9B—H10B	0.93
Fe2—C3B	2.030 (4)	C6B—C7B	1.389 (6)
Fe2—C6B	2.031 (4)	C6B—H8B	0.93
Fe2—C9B	2.031 (3)	C8B—C7B	1.403 (6)
Fe2—C10B	2.034 (3)	C8B—H6B	0.93
Fe2—C2B	2.037 (4)	C15B—C16B	1.381 (6)

Fe2—C7B	2.038 (4)	C15B—H15B	0.93
Fe2—C8B	2.041 (4)	C19A—C18A	1.376 (5)
Fe1—C9A	2.022 (3)	C19A—H19A	0.93
Fe1—C5A	2.024 (4)	C16A—C17A	1.368 (6)
Fe1—C10A	2.026 (3)	C16A—C15A	1.385 (5)
Fe1—C1A	2.028 (4)	C16A—H16A	0.93
Fe1—C6A	2.028 (3)	C15A—H15A	0.93
Fe1—C4A	2.038 (3)	C11B—H11C	0.97
Fe1—C8A	2.040 (4)	C11B—H11D	0.97
Fe1—C2A	2.040 (4)	C19B—C18B	1.377 (5)
Fe1—C7A	2.041 (4)	C19B—H19B	0.93
Fe1—C3A	2.044 (4)	C16B—C17B	1.366 (6)
O1—C12A	1.224 (4)	C16B—H16B	0.93
C14A—C19A	1.372 (5)	C7B—H7B	0.93
C14A—C15A	1.374 (5)	C17B—C18B	1.373 (6)
C14A—N1	1.435 (4)	C17B—H17B	0.93
N2—C12B	1.363 (5)	C13B—C12B	1.515 (6)
N2—C14B	1.439 (4)	C13B—H13D	0.96
N2—C11B	1.478 (4)	C13B—H13E	0.96
C10B—C6B	1.417 (5)	C13B—H13F	0.96
C10B—C9B	1.423 (5)	C18B—H18B	0.93
C10B—C11B	1.495 (5)	C18A—C17A	1.366 (6)
N1—C12A	1.359 (5)	C18A—H18A	0.93
N1—C11A	1.478 (4)	C13A—C12A	1.510 (5)
O2—C12B	1.216 (5)	C13A—H13A	0.96
C3A—C4A	1.396 (5)	C13A—H13B	0.96
C3A—C2A	1.402 (5)	C13A—H13C	0.96
C3A—H3A	0.93	C5B—C4B	1.413 (8)
C10A—C6A	1.409 (5)	C5B—H5B	0.93
C10A—C9A	1.420 (5)	C3B—C2B	1.337 (7)
C10A—C11A	1.506 (5)	C3B—C4B	1.347 (8)
C7A—C8A	1.398 (5)	C3B—H3B	0.93
C7A—C6A	1.421 (5)	C17A—H17A	0.93
C7A—H7A	0.93	C2B—H2B	0.93
C1B—C2B	1.357 (7)	C4B—H4B	0.93
C1B—C5B	1.379 (8)	C6A—H6A	0.93
C1B—H1B	0.93	C9A—C8A	1.397 (5)
C14B—C19B	1.369 (5)	C9A—H9A	0.93
C14B—C15B	1.377 (5)	C2A—C1A	1.401 (6)
C11A—H11A	0.97	C2A—H2A	0.93
C11A—H11B	0.97	C8A—H8A	0.93
C5A—C4A	1.406 (6)	C4A—H4A	0.93
C5A—C1A	1.414 (6)	C1A—H1A	0.93
C5B—Fe2—C1B	40.2 (2)	C4A—C5A—H5A	126.2
C5B—Fe2—C4B	41.1 (2)	C1A—C5A—H5A	126.2
C1B—Fe2—C4B	67.4 (2)	Fe1—C5A—H5A	125.4
C5B—Fe2—C3B	66.6 (2)	C8B—C9B—C10B	107.8 (4)

C1B—Fe2—C3B	65.69 (19)	C8B—C9B—Fe2	70.1 (2)
C4B—Fe2—C3B	38.9 (2)	C10B—C9B—Fe2	69.58 (19)
C5B—Fe2—C6B	110.1 (2)	C8B—C9B—H10B	126.1
C1B—Fe2—C6B	114.67 (18)	C10B—C9B—H10B	126.1
C4B—Fe2—C6B	136.1 (3)	Fe2—C9B—H10B	125.8
C3B—Fe2—C6B	174.9 (2)	C7B—C6B—C10B	109.2 (4)
C5B—Fe2—C9B	143.4 (3)	C7B—C6B—Fe2	70.3 (2)
C1B—Fe2—C9B	175.3 (2)	C10B—C6B—Fe2	69.7 (2)
C4B—Fe2—C9B	113.4 (2)	C7B—C6B—H8B	125.4
C3B—Fe2—C9B	111.81 (18)	C10B—C6B—H8B	125.4
C6B—Fe2—C9B	68.21 (15)	Fe2—C6B—H8B	126.2
C5B—Fe2—C10B	112.9 (2)	C7B—C8B—C9B	108.2 (4)
C1B—Fe2—C10B	143.6 (2)	C7B—C8B—Fe2	69.8 (2)
C4B—Fe2—C10B	109.84 (19)	C9B—C8B—Fe2	69.3 (2)
C3B—Fe2—C10B	135.9 (2)	C7B—C8B—H6B	125.9
C6B—Fe2—C10B	40.81 (14)	C9B—C8B—H6B	125.9
C9B—Fe2—C10B	41.00 (13)	Fe2—C8B—H6B	126.6
C5B—Fe2—C2B	66.5 (2)	C14B—C15B—C16B	119.8 (4)
C1B—Fe2—C2B	39.2 (2)	C14B—C15B—H15B	120.1
C4B—Fe2—C2B	65.7 (2)	C16B—C15B—H15B	120.1
C3B—Fe2—C2B	38.4 (2)	C14A—C19A—C18A	120.7 (4)
C6B—Fe2—C2B	144.9 (2)	C14A—C19A—H19A	119.7
C9B—Fe2—C2B	136.39 (19)	C18A—C19A—H19A	119.7
C10B—Fe2—C2B	174.3 (2)	C17A—C16A—C15A	120.9 (4)
C5B—Fe2—C7B	135.2 (3)	C17A—C16A—H16A	119.6
C1B—Fe2—C7B	111.34 (18)	C15A—C16A—H16A	119.6
C4B—Fe2—C7B	175.5 (3)	C14A—C15A—C16A	119.5 (4)
C3B—Fe2—C7B	145.2 (2)	C14A—C15A—H15A	120.2
C6B—Fe2—C7B	39.93 (16)	C16A—C15A—H15A	120.2
C9B—Fe2—C7B	68.19 (16)	N2—C11B—C10B	113.1 (3)
C10B—Fe2—C7B	68.36 (15)	N2—C11B—H11C	109
C2B—Fe2—C7B	116.37 (19)	C10B—C11B—H11C	109
C5B—Fe2—C8B	175.0 (3)	N2—C11B—H11D	109
C1B—Fe2—C8B	136.1 (2)	C10B—C11B—H11D	109
C4B—Fe2—C8B	143.6 (3)	H11C—C11B—H11D	107.8
C3B—Fe2—C8B	116.1 (2)	C14B—C19B—C18B	119.3 (4)
C6B—Fe2—C8B	67.48 (17)	C14B—C19B—H19B	120.3
C9B—Fe2—C8B	40.60 (15)	C18B—C19B—H19B	120.3
C10B—Fe2—C8B	68.47 (14)	C17B—C16B—C15B	120.3 (4)
C2B—Fe2—C8B	112.73 (17)	C17B—C16B—H16B	119.8
C7B—Fe2—C8B	40.24 (17)	C15B—C16B—H16B	119.8
C9A—Fe1—C5A	107.14 (17)	C6B—C7B—C8B	108.2 (4)
C9A—Fe1—C10A	41.06 (13)	C6B—C7B—Fe2	69.8 (2)
C5A—Fe1—C10A	114.86 (16)	C8B—C7B—Fe2	70.0 (2)
C9A—Fe1—C1A	128.96 (18)	C6B—C7B—H7B	125.9
C5A—Fe1—C1A	40.85 (17)	C8B—C7B—H7B	125.9
C10A—Fe1—C1A	106.73 (15)	Fe2—C7B—H7B	125.9
C9A—Fe1—C6A	68.28 (14)	C16B—C17B—C18B	119.3 (4)

C5A—Fe1—C6A	148.24 (17)	C16B—C17B—H17B	120.3
C10A—Fe1—C6A	40.66 (13)	C18B—C17B—H17B	120.3
C1A—Fe1—C6A	116.23 (16)	C12B—C13B—H13D	109.5
C9A—Fe1—C4A	116.56 (15)	C12B—C13B—H13E	109.5
C5A—Fe1—C4A	40.48 (16)	H13D—C13B—H13E	109.5
C10A—Fe1—C4A	148.34 (15)	C12B—C13B—H13F	109.5
C1A—Fe1—C4A	68.09 (16)	H13D—C13B—H13F	109.5
C6A—Fe1—C4A	170.28 (15)	H13E—C13B—H13F	109.5
C9A—Fe1—C8A	40.21 (15)	C17B—C18B—C19B	121.0 (4)
C5A—Fe1—C8A	129.55 (19)	C17B—C18B—H18B	119.5
C10A—Fe1—C8A	68.57 (14)	C19B—C18B—H18B	119.5
C1A—Fe1—C8A	167.65 (19)	C17A—C18A—C19A	120.2 (4)
C6A—Fe1—C8A	68.23 (15)	C17A—C18A—H18A	119.9
C4A—Fe1—C8A	109.49 (16)	C19A—C18A—H18A	119.9
C9A—Fe1—C2A	167.78 (16)	O2—C12B—N2	121.2 (4)
C5A—Fe1—C2A	68.18 (17)	O2—C12B—C13B	121.8 (4)
C10A—Fe1—C2A	129.41 (14)	N2—C12B—C13B	117.1 (4)
C1A—Fe1—C2A	40.30 (16)	C12A—C13A—H13A	109.5
C6A—Fe1—C2A	109.33 (15)	C12A—C13A—H13B	109.5
C4A—Fe1—C2A	67.81 (15)	H13A—C13A—H13B	109.5
C8A—Fe1—C2A	151.25 (17)	C12A—C13A—H13C	109.5
C9A—Fe1—C7A	67.68 (16)	H13A—C13A—H13C	109.5
C5A—Fe1—C7A	168.53 (18)	H13B—C13A—H13C	109.5
C10A—Fe1—C7A	68.54 (14)	C1B—C5B—C4B	106.4 (5)
C1A—Fe1—C7A	150.29 (18)	C1B—C5B—Fe2	70.0 (3)
C6A—Fe1—C7A	40.89 (14)	C4B—C5B—Fe2	69.9 (3)
C4A—Fe1—C7A	131.44 (16)	C1B—C5B—H5B	126.8
C8A—Fe1—C7A	40.06 (16)	C4B—C5B—H5B	126.8
C2A—Fe1—C7A	118.96 (16)	Fe2—C5B—H5B	124.9
C9A—Fe1—C3A	149.96 (15)	O1—C12A—N1	121.0 (4)
C5A—Fe1—C3A	67.63 (16)	O1—C12A—C13A	121.3 (4)
C10A—Fe1—C3A	168.82 (14)	N1—C12A—C13A	117.7 (3)
C1A—Fe1—C3A	67.51 (16)	C2B—C3B—C4B	110.1 (5)
C6A—Fe1—C3A	132.00 (14)	C2B—C3B—Fe2	71.1 (3)
C4A—Fe1—C3A	40.00 (14)	C4B—C3B—Fe2	70.1 (3)
C8A—Fe1—C3A	119.04 (16)	C2B—C3B—H3B	124.9
C2A—Fe1—C3A	40.14 (14)	C4B—C3B—H3B	124.9
C7A—Fe1—C3A	111.33 (15)	Fe2—C3B—H3B	125.4
C19A—C14A—C15A	119.4 (3)	C18A—C17A—C16A	119.3 (4)
C19A—C14A—N1	120.8 (3)	C18A—C17A—H17A	120.3
C15A—C14A—N1	119.8 (3)	C16A—C17A—H17A	120.3
C12B—N2—C14B	124.7 (3)	C3B—C2B—C1B	108.7 (5)
C12B—N2—C11B	118.9 (3)	C3B—C2B—Fe2	70.5 (3)
C14B—N2—C11B	116.2 (3)	C1B—C2B—Fe2	69.2 (3)
C6B—C10B—C9B	106.6 (3)	C3B—C2B—H2B	125.6
C6B—C10B—C11B	127.5 (3)	C1B—C2B—H2B	125.6
C9B—C10B—C11B	125.8 (3)	Fe2—C2B—H2B	126.2
C6B—C10B—Fe2	69.5 (2)	C3B—C4B—C5B	106.7 (5)

C9B—C10B—Fe2	69.42 (19)	C3B—C4B—Fe2	71.0 (3)
C11B—C10B—Fe2	125.9 (2)	C5B—C4B—Fe2	68.9 (3)
C12A—N1—C14A	124.2 (3)	C3B—C4B—H4B	126.6
C12A—N1—C11A	118.7 (3)	C5B—C4B—H4B	126.6
C14A—N1—C11A	116.9 (3)	Fe2—C4B—H4B	125
C4A—C3A—C2A	108.8 (4)	C10A—C6A—C7A	108.0 (3)
C4A—C3A—Fe1	69.8 (2)	C10A—C6A—Fe1	69.60 (19)
C2A—C3A—Fe1	69.8 (2)	C7A—C6A—Fe1	70.0 (2)
C4A—C3A—H3A	125.6	C10A—C6A—H6A	126
C2A—C3A—H3A	125.6	C7A—C6A—H6A	126
Fe1—C3A—H3A	126.4	Fe1—C6A—H6A	126
C6A—C10A—C9A	107.0 (3)	C8A—C9A—C10A	108.8 (3)
C6A—C10A—C11A	126.2 (3)	C8A—C9A—Fe1	70.6 (2)
C9A—C10A—C11A	126.8 (3)	C10A—C9A—Fe1	69.61 (19)
C6A—C10A—Fe1	69.74 (18)	C8A—C9A—H9A	125.6
C9A—C10A—Fe1	69.32 (19)	C10A—C9A—H9A	125.6
C11A—C10A—Fe1	124.6 (2)	Fe1—C9A—H9A	125.8
C8A—C7A—C6A	108.1 (3)	C1A—C2A—C3A	107.6 (3)
C8A—C7A—Fe1	70.0 (2)	C1A—C2A—Fe1	69.4 (2)
C6A—C7A—Fe1	69.1 (2)	C3A—C2A—Fe1	70.0 (2)
C8A—C7A—H7A	126	C1A—C2A—H2A	126.2
C6A—C7A—H7A	126	C3A—C2A—H2A	126.2
Fe1—C7A—H7A	126.6	Fe1—C2A—H2A	126
C2B—C1B—C5B	108.1 (5)	C9A—C8A—C7A	108.1 (3)
C2B—C1B—Fe2	71.6 (3)	C9A—C8A—Fe1	69.2 (2)
C5B—C1B—Fe2	69.8 (3)	C7A—C8A—Fe1	70.0 (2)
C2B—C1B—H1B	126	C9A—C8A—H8A	125.9
C5B—C1B—H1B	126	C7A—C8A—H8A	125.9
Fe2—C1B—H1B	124.3	Fe1—C8A—H8A	126.5
C19B—C14B—C15B	120.2 (4)	C3A—C4A—C5A	107.8 (4)
C19B—C14B—N2	119.4 (3)	C3A—C4A—Fe1	70.2 (2)
C15B—C14B—N2	120.3 (3)	C5A—C4A—Fe1	69.2 (2)
N1—C11A—C10A	113.1 (3)	C3A—C4A—H4A	126.1
N1—C11A—H11A	109	C5A—C4A—H4A	126.1
C10A—C11A—H11A	109	Fe1—C4A—H4A	126.1
N1—C11A—H11B	109	C2A—C1A—C5A	108.0 (4)
C10A—C11A—H11B	109	C2A—C1A—Fe1	70.3 (2)
H11A—C11A—H11B	107.8	C5A—C1A—Fe1	69.4 (2)
C4A—C5A—C1A	107.7 (4)	C2A—C1A—H1A	126
C4A—C5A—Fe1	70.3 (2)	C5A—C1A—H1A	126
C1A—C5A—Fe1	69.7 (2)	Fe1—C1A—H1A	125.8
C19A—C14A—N1—C12A	110.5 (4)	C2B—C1B—C5B—C4B	−0.8 (5)
C15A—C14A—N1—C12A	−71.6 (5)	Fe2—C1B—C5B—C4B	60.8 (3)
C19A—C14A—N1—C11A	−75.3 (4)	C2B—C1B—C5B—Fe2	−61.7 (3)
C15A—C14A—N1—C11A	102.6 (4)	C14A—N1—C12A—O1	173.5 (3)
C12B—N2—C14B—C19B	84.9 (5)	C11A—N1—C12A—O1	−0.6 (5)
C11B—N2—C14B—C19B	−89.9 (4)	C14A—N1—C12A—C13A	−7.0 (5)

C12B—N2—C14B—C15B	−98.1 (4)	C11A—N1—C12A—C13A	178.9 (3)
C11B—N2—C14B—C15B	87.2 (4)	C19A—C18A—C17A—C16A	0.3 (7)
C12A—N1—C11A—C10A	−92.1 (4)	C15A—C16A—C17A—C18A	−1.6 (8)
C14A—N1—C11A—C10A	93.3 (4)	C4B—C3B—C2B—C1B	−0.6 (5)
C6A—C10A—C11A—N1	93.3 (4)	Fe2—C3B—C2B—C1B	58.9 (3)
C9A—C10A—C11A—N1	−88.7 (4)	C4B—C3B—C2B—Fe2	−59.5 (3)
Fe1—C10A—C11A—N1	−177.6 (2)	C5B—C1B—C2B—C3B	0.9 (5)
C6B—C10B—C9B—C8B	0.0 (4)	Fe2—C1B—C2B—C3B	−59.7 (3)
C11B—C10B—C9B—C8B	−180.0 (3)	C5B—C1B—C2B—Fe2	60.6 (3)
Fe2—C10B—C9B—C8B	−59.9 (2)	C2B—C3B—C4B—C5B	0.1 (5)
C6B—C10B—C9B—Fe2	59.8 (2)	Fe2—C3B—C4B—C5B	−60.0 (3)
C11B—C10B—C9B—Fe2	−120.1 (3)	C2B—C3B—C4B—Fe2	60.1 (3)
C9B—C10B—C6B—C7B	−0.4 (4)	C1B—C5B—C4B—C3B	0.5 (5)
C11B—C10B—C6B—C7B	179.6 (3)	Fe2—C5B—C4B—C3B	61.3 (3)
Fe2—C10B—C6B—C7B	59.4 (3)	C1B—C5B—C4B—Fe2	−60.8 (3)
C9B—C10B—C6B—Fe2	−59.8 (2)	C9A—C10A—C6A—C7A	0.1 (4)
C11B—C10B—C6B—Fe2	120.2 (3)	C11A—C10A—C6A—C7A	178.4 (3)
C10B—C9B—C8B—C7B	0.4 (4)	Fe1—C10A—C6A—C7A	59.7 (2)
Fe2—C9B—C8B—C7B	−59.1 (3)	C9A—C10A—C6A—Fe1	−59.6 (2)
C10B—C9B—C8B—Fe2	59.6 (2)	C11A—C10A—C6A—Fe1	118.7 (3)
C19B—C14B—C15B—C16B	0.9 (6)	C8A—C7A—C6A—C10A	−0.1 (4)
N2—C14B—C15B—C16B	−176.2 (4)	Fe1—C7A—C6A—C10A	−59.4 (2)
C15A—C14A—C19A—C18A	−1.7 (6)	C8A—C7A—C6A—Fe1	59.3 (2)
N1—C14A—C19A—C18A	176.3 (4)	C6A—C10A—C9A—C8A	0.0 (4)
C19A—C14A—C15A—C16A	0.3 (7)	C11A—C10A—C9A—C8A	−178.3 (3)
N1—C14A—C15A—C16A	−177.7 (4)	Fe1—C10A—C9A—C8A	−59.9 (3)
C17A—C16A—C15A—C14A	1.3 (8)	C6A—C10A—C9A—Fe1	59.9 (2)
C12B—N2—C11B—C10B	91.5 (4)	C11A—C10A—C9A—Fe1	−118.4 (3)
C14B—N2—C11B—C10B	−93.3 (4)	C4A—C3A—C2A—C1A	0.4 (4)
C6B—C10B—C11B—N2	82.3 (5)	Fe1—C3A—C2A—C1A	59.4 (2)
C9B—C10B—C11B—N2	−97.7 (4)	C4A—C3A—C2A—Fe1	−59.1 (2)
Fe2—C10B—C11B—N2	173.0 (2)	C10A—C9A—C8A—C7A	−0.1 (4)
C15B—C14B—C19B—C18B	0.3 (6)	Fe1—C9A—C8A—C7A	−59.4 (3)
N2—C14B—C19B—C18B	177.3 (4)	C10A—C9A—C8A—Fe1	59.3 (2)
C14B—C15B—C16B—C17B	−1.1 (6)	C6A—C7A—C8A—C9A	0.1 (4)
C10B—C6B—C7B—C8B	0.7 (4)	Fe1—C7A—C8A—C9A	58.9 (3)
Fe2—C6B—C7B—C8B	59.7 (3)	C6A—C7A—C8A—Fe1	−58.8 (2)
C10B—C6B—C7B—Fe2	−59.0 (2)	C2A—C3A—C4A—C5A	−0.2 (4)
C9B—C8B—C7B—C6B	−0.7 (4)	Fe1—C3A—C4A—C5A	−59.2 (3)
Fe2—C8B—C7B—C6B	−59.5 (3)	C2A—C3A—C4A—Fe1	59.1 (2)
C9B—C8B—C7B—Fe2	58.9 (3)	C1A—C5A—C4A—C3A	−0.1 (4)
C15B—C16B—C17B—C18B	0.2 (6)	Fe1—C5A—C4A—C3A	59.8 (3)
C16B—C17B—C18B—C19B	0.9 (7)	C1A—C5A—C4A—Fe1	−59.9 (3)
C14B—C19B—C18B—C17B	−1.2 (6)	C3A—C2A—C1A—C5A	−0.4 (4)
C14A—C19A—C18A—C17A	1.4 (7)	Fe1—C2A—C1A—C5A	59.4 (3)
C14B—N2—C12B—O2	−177.5 (4)	C3A—C2A—C1A—Fe1	−59.8 (2)
C11B—N2—C12B—O2	−2.9 (6)	C4A—C5A—C1A—C2A	0.3 (4)
C14B—N2—C12B—C13B	2.5 (6)	Fe1—C5A—C1A—C2A	−60.0 (3)

C11B—N2—C12B—C13B	177.2 (3)		C4A—C5A—C1A—Fe1	60.3 (3)

Hydrogen-bond geometry (Å, º)

D—H⋯A	D—H	H⋯A	D⋯A	D—H⋯A
C15A—H15A⋯O1[i]	0.93	2.56	3.456 (5)	162
C19B—H19B⋯O2[ii]	0.93	2.55	3.421 (5)	157
C15A—H15A⋯O1[i]	0.93	2.56	3.456 (5)	162
C19B—H19B⋯O2[ii]	0.93	2.55	3.421 (5)	157

Symmetry codes: (i) $-x-1, -y+2, -z+1$; (ii) $-x, -y+1, -z+2$.

ORIGINAL PAPER

Spectroscopic Characterizations of Sand Dunes Minerals of El-Oued (Northeast Algerian Sahara) by FTIR, XRF and XRD Analyses

Nassima Meftah[1] · Mohammed Sadok Mahboub[1,2]

Abstract

This paper investigates the chemical and crystal structural properties of sand dunes of El-Oued region from the northeast Sahara of Algeria. By using of Fourier-transform infrared (FT-IR) spectroscopy, X-ray fluorescence (XRF) and X-ray diffraction (XRD) we show that El-Oued sand dunes are composed mainly of 97.6% α-quartz (SiO_2) and 0.56% calcite ($CaCO_3$). Very low concentrations of some oxides as Al_2O_3, Fe_2O_3, MgO and trace elements impurities were also found. The calculated crystallinity index CI = 0.975 confirm the highly crystalline nature of quartz. From the X-ray diffraction data, structural parameters of quartz and calcite minerals were determined. Quartz grains were found to have a hexagonal crystal structure with lattice parameters of a = b = 4.907 Å and c = 5.401 Å and calcite grains have a trigonal crystal structure with a = b = 4.977 Å and c = 17.04 Å. The calculated lattice parameters were similar to those of standard references. The crystallite sizes of quartz and calcite were estimated to be nanometric.

1 Introduction

In recent years, the interest in raw materials has increased due to their physico-chemical properties and also their availability. Sand of particular interest; it is widely used in industry and nanotechnology [1]. The sand in its raw state is used in various fields: as building materials, thermal energy reservoir medium, water filtering material and in bricks and ceramic manufacture [2–4]. Sand is defined as loose granular material derived from weathering and natural disintegration of rocks and other materials on the earth's surface and has grains ranging from 0.0625 to 2 mm in diameter [5]. The compositions and texture of sand grains are controlled by the chemical and physical processes such as wind action, fluvial and marine processes, weathering, precipitation, and air temperature [6]. The sand can acquire various colors ranging from light red to black due to the presence of certain chemical compounds [7]. Although the components of sand grains depend on the local rock sources and conditions, the main mineral constituents of sand are quartz (SiO_2), feldspar ($KAlSi_3O_8$, $NaAlSi_3O_8$, $CaAl_2Si_2O_8$) and carbonates. In addition, it contains considerable concentrations of aluminum oxide (Al_2O_3) and iron oxide (Fe_2O_3), as well as small amounts of heavy materials [8, 9]. Furthermore, sand represents the most promising resource of quartz (silicon dioxide) material compared to crystalline hard rocks. Today, high-purity quartz has become a vital mineral, with its particular physicochemical properties being employed in a wide range of nanotechnologies such as glass fabrication, optics and microelectronics, semiconductors and telecommunications [10–12]. Also, quartz contains Silicon (Si), which can be exploited in various fields, including medicine, sensor and biosensing, photonics, microelectronics, energy technologies and solar silicon applications [13–16]. Extracting quartz from sand or extracting silicon from quartz and determining its suitability for different industrial applications require knowledge of the physical and chemical properties of the quartz. Several investigations have been undertaken on sand dunes from different regions of the world. Howari et al. [17] have studied the geomorphology and mineralogy of different dune types in the east Abu Dhabi using Landsat 7 ETM+ data sets. Trabelsia et al. [18] identified the physicochemical proprieties of Douiret

✉ Nassima Meftah
    meftahnassima@yahoo.fr

1   Department of physics, Faculty of Exact Sciences, University of El-Oued, 39000 El-Oued, Algeria

2   LEVRES Laboratory, Faculty of Exact Sciences, University of El-Oued, 39000 El-Oued, Algeria

Fig. 1 Map of Algeria (http://www.primap.com/wsen/Maps/MapCollection/NationalMaps/Algeria-Satellite-4000x3816.html) showing El-Oued region location and the dune from which the analyzed samples are taken

sand in order to promoted the production of silica gel. Elipe and Lopez-Querol [19] characterized and improved aeolian sand for its potential use in construction. However, the existance of impurities on Tihimatine Quartz, Algeria has been characterized [20]. Also, some researchers have evaluated the quartz sand occurrences of the Santa Maria Eterna formation, in northeastern Brazil, as a potential source of raw material for silica glass production [21]. Bennefi et al. [22] investigated the morphology, mineralogy, geochemistry, and provenance of sand dunes in Saudi Arabia. Adnani et al. [23] have studied the color differences of sand dunes and then investigated sand's origin and transport pathways. The heat effect on the composition of dunes sand of Ouargla region (Algeria) using XRD and FTIR has been studied [24]. Recently, a study has characterized the desert sand of the United Arab Emirates which will be used as a thermal energy storage medium in particle solar receiver technology [25] and other researchers carried out a mineralogical analysis of sand roses and sand dunes samples from two different regions of South Algeria [26].
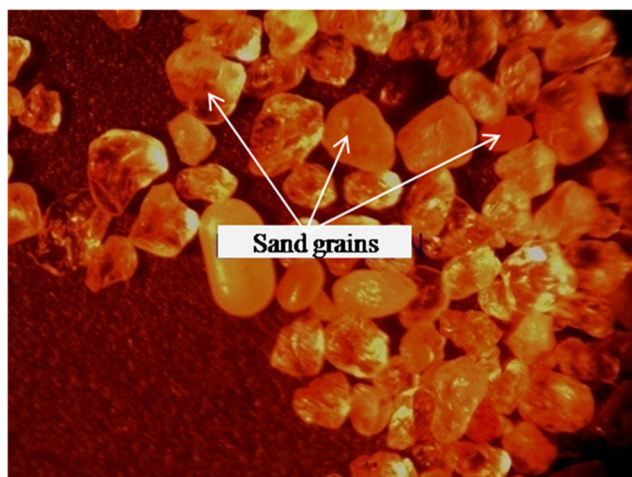
Several studies have characterized the Algerian sand dunes, but a very limited number thereof addressed the microscopic and crystallographic properties of sand dune minerals.

Algerian Sahara has enormous quantities of sand dunes (about a quarter of its total area). Moreover, it has very large sunny areas making it a potential reservoir of solar energy.

The El-Oued region is situated in the northeast Sahara of Algeria and is entirely covered by sand dunes. However, quartz in its sand dunes, which has a great economic importance, has not been characterized up to now. We assume that a good knowledge of the physico-chemical properties of El-Oued sand and its components can contribute to exploiting this natural resource, in particular for the production of solar energy.

The aim of this study is to identify the minerals of El-Oued sand dunes, assess the presence of pure quartz in the sand dunes of this region and determine some crystal structural properties of sand components, by using nondestructive instrumentation such as Fourier-transform infrared spectroscopy (FT-IR), X-ray fluorescence (XRF) and X-ray diffraction (XRD).

2 Materials and Methods

2.1 Geology Setting

El Oued region is located in northeast of Algeria Sahara has border with Tunisia from the east (Fig. 1). Its geographical coordinates are: latitude of 33°27′20″ North, longitude of 7°11′ 0″ East. This region is very sunny and its southern half is covered by the Grand Erg Oriental, a vast region of uninterrupted sand dunes, and the rest is a mixture of sandy desert with scarce vegetation, scattered oases, and salt lakes. In order to ensure the quality of the results, samples were collected from unmodified pristine dunes and away from engineering

Fig. 2 Micrograph of the El-Oued sand dunes

Table 1 Physicochemical properties of the El-Oued sand sample

	Bulk density (g/ml)	pH	Porosity (%)	Conductivity (μS/cm)	TDS (mg/l)
Sand sample	1.6	9.3	34.09	130.1	59

construction areas. About seventy-five samples were collected from dunes located at the south of El Oued (33°8′54″ north, 6°5′ 37.7 ″ east). Samples were picked up from different faces of the dune, from the top to bottom and at different depths. To homogenize the sampling protocol, equal weights well-mixed samples were obtained.

2.2 Sample Preparation

As a first preparation step before XRD, XRF and FT-IR analysis, the sand was crushed by using a glass mortar. Before FT-IR analysis, 2 mg of the crushed sand were mixed carefully with 198 mg of dry potassium bromide (KBr). The mixture was then compressed to form a pellet of 13 mm diameter and 1 mm thickness. A Shimadzu FTIR-8300 machine running under the spectral range (400–4000 cm^{-1}) was used to identify the constituent bonds of the sand samples. For X-ray fluorescence measurements, the crushed sample was compressed under high pressure for few minutes to form a measurable pellet. A Philips MagiX Pro-XRF instrument was used to carry out the measurements. To determine the crystallographic parameters of the sand samples we used X-rays powder diffraction by an AXRD Benchtop Powder Diffractometer. At room temperature, the diffractometer worked with a wavelength $\lambda_{CuK\alpha1}$ = 1.54 A° under a voltage of 30 KeV and a current intensity of 20 mA. The data sets were collected from the scans with 2θ running from 20° to 80°.

3 Results and Discussion

Our sand sample has a beige color and its grains have shapes ranging from round to elongate to irregular as shown in the optical microscope image (Fig. 2). Some physicochemical properties of examined sand are presented in the Table 1. The low porosity of 34.09% confirms that the El-Oued sand belongs to the fine class. The alkaline nature of the sample (pH > 7) suggests the accessibility of exchangeable cations as Ca^{2+}, Mg^{2+}, K^+, Na^+ and a high content of carbonate ions in sand. Also, the high value of the conductivity and the total dissolved solids (TDS) strongly depend on the presence of dissolved salt (e.g. NaCl, Na_2SO_4, $MgSO_4$, ...) in the sand [27].

3.1 Analysis by Fourier-Transform Infrared(FTIR)

The infrared absorption spectrum of the El-Oued sand dune samples is illustrated in Fig. 3. From the FT-IR spectrum we can identify the main component of our samples. Table 2 summarizes the functional groups found in the sand. In the range of the high wavenumbers we see a high intensity absorption band at 3429 cm^{-1} which is due to stretching vibrations of hydroxyl groups (OH) [28, 29], a less intense band has been observed at 1616 cm^{-1}, which is due to the twisting of H-O-H [30]. Also, three absorption bands have been observed at wavenumbers of 2511 cm^{-1}, which are due to $(CO_3)^{-2}$

Fig. 3 FTIR absorption spectrum of El-Oued sand dunes
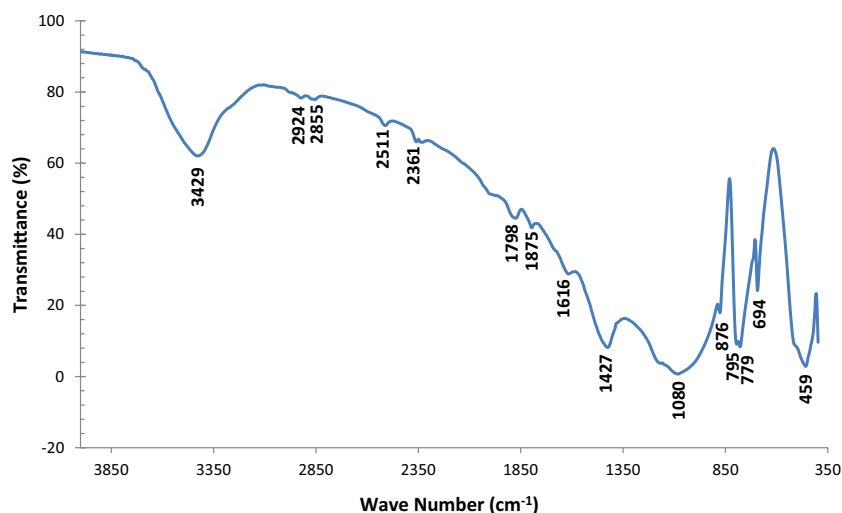
Table 2 The main bands of IR absorption and associated bond vibration of El-Oued sand

Band (cm^{-1})	Bond (Vibration mode)	Compound
3429	H-O-H (stretching vibration)	Water
2924	C-H (stretching vibration)	Organic Carbon
2855	C-H (stretching vibration)	Organic Carbon
2511	$(CO_3)^{-2}$ (asymmetrical stretch and symmetrical stretching)	Calcite
1875		Quartz
1798	$(CO_3)^{-2}$ (plane bending and symmetrical stretching combination mode)	Calcite
1616	H–OH (stretching)	Water
1427	$(CO_3)^{-2}$ (asymmetrical stretching)	Calcite
1080	Si–O–Si (symmetrical stretching)	Quartz
876	$(CO_3)^{-2}$ (out-of-plane bending)	Calcite
779	Si–O (symmetrical stretching)	Quartz
694	Si–O–Si (symmetrical bending)	Quartz
459	Si–O–Si (asymmetrical bending)	Quartz

asymmetrical and symmetrical stretching mode vibrations [8]. The 1427 cm^{-1} wavenumber feature is due to doubly degenerate asymmetric stretching mode vibration, and the 876 cm^{-1} one corresponds to the C=O stretching mode vibration [8]. These bands confirm the presence of calcite in our samples [31, 32]. A sharp absorption band at 1080 cm^{-1} has been observed and seems to fit with symmetrical stretching of Si–O–Si bond [33]. In the spectrum range of 1080–400 cm^{-1} a strong band has been observed. Symmetrical bands at 795 and 779 cm^{-1} have been observed and correspond to Si-O symmetrical bending vibration. These peaks confirm the presence of quartz [33]. In addition, we observed other bands at 694 and 459 cm^{-1} which coincide with Si–O–Si symmetrical and asymmetrical bending, respectively. The presence of Si-O and O-Si-O vibrations in our sample again confirm the presence of quartz. The 694 cm^{-1} band indicates that the quartz in our samples is crystalline [34]. Thus, FT-IR absorption spectrum exhibits only an absorption band characterizing quartz (SiO$_2$) and calcite (CaCO$_3$) compounds in our sand samples.

We notice that the quartz of the El-Oued sand samples does not contain other impurities suggesting a high degree of purity for this sand quartz. In contrast, Beddiaf et al. [28] and Maazouzi et al. [35] found that the Western Erg sand and the Ouargla sand in the Algerian Sahara have a considerable amount of Al_2O_3 and Fe_2O_3. The presence of the double absorption at 795 and 779 cm^{-1} is an indicator of the presence of the quartz in α-phase [36, 37]. The crystallinity index (CI) of quartz in our sample is calculated by measuring the ratio between the absorbance of the bands 795 and 779 cm^{-1} (A_{795}/A_{779}), where the absorbance A_α at wavenumber α is defined as [38]:

$$A_\alpha = -\log T_\alpha \tag{1}$$

where T_α is the transmittance at wavenumber α.

We found that the degree of crystallinity of sand quartz is equal to 0.975. Since the crystallinity index is inversely proportional to crystallinity of materials [39, 40], the calculated ratio

Table 3 Chemical analysis of El-Oued sand dunes sample by X-ray fluorescence

The concentrations in (%) of oxides		The concentrations in (ppm) of trace elements	
SiO$_2$	97.63	Cl	425
MgO	0.613	Zn	44.0
CaO	0.564	Ba	21.0
Na$_2$O	0.542	Sr	6.00
Al$_2$O$_3$	0.327	Nb	5.00
CO$_2$	0.105	Bi	5.00
K$_2$O	0.0677	Ge	3.00
Fe$_2$O$_3$	0.042		
SO$_3$	0.037		
P$_2$O$_5$	0.0138		
TiO$_2$	0.0053		
MnO	0.0021		

Fig. 4 The XRD pattern of El-Oued sand dunes
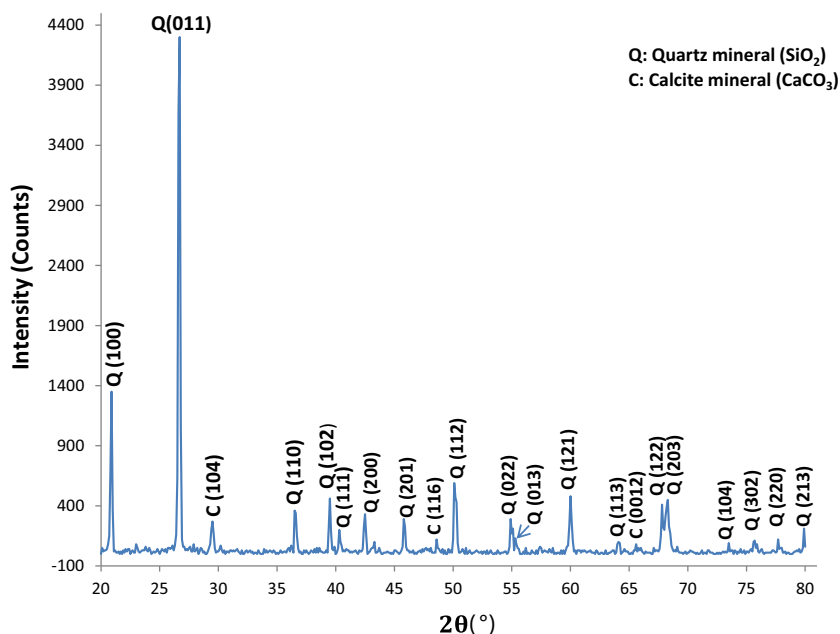
indicates that El-Oued sand quartz has a highly crystalline nature.

3.2 Chemical Analysis by X-Ray Fluorescence (XRF)

The chemical compositions of El-Oued sand dunes obtained by XRF measurements are summarized in Table 3. We show that

Table 4   Indexed Powder XRD Pattern for El-Oued Sand

Peaks	$2\theta(°)$	Intensity(a.u)	Mineral	(d_{hkl})cal (Å)	hkl
#1	20.89	1350	Quartz	4.434	100
#2	26.69	4300	Quartz	3.335	011
#3	29.49	270	Calcite	3.024	104
#4	36.59	340	Quartz	2.452	110
#5	39.49	460	Quartz	2.279	102
#6	40.29	200	Quartz	2.235	111
#7	42.49	330	Quartz	2.125	200
#8	45.79	290	Quartz	1.979	201
#9	48.60	120	Calcite	1.871	116
#10	50.09	590	Quartz	1.819	112
#11	54.90	290	Quartz	1.670	022
#12	55.30	130	Quartz	1.659	013
#13	60.10	270	Quartz	1.548	121
#14	64.09	100	Quartz	1.451	113
#15	65.59	80	Calcite	1.421	0012
#16	67.79	410	Quartz	1.381	122
#17	68.29	450	Quartz	1372	203
#18	73.49	90	Quartz	1.287	104
#19	75.69	110	Quartz	1.255	302
#20	77.69	120	Quartz	1.228	220
#21	79.89	210	Quartz	1.199	213

our sample has a high concentration (97.63%) of silica, low concentration of calcium oxide (0.56%) and very low percentage of aluminum oxide and iron oxide. A small amounts of MgO (0.61%) and Na_2O (0.54%) have been noticed. Also, very low levels for others oxides were found in the sand dunes sample. Furthermore, as shown in Table 3, the El-Oued sand contain insignificant amount of other trace elements, such as bromine (Br), germanium (Ge), bismuth (Bi), niobium (Nb), strontium (Sr), zinc (Zn), barium (Ba) and chlorine (Cl). These results confirm that El-Oued sand dunes consist mainly of quartz with minor calcite and very low quantities of Fe_2O_3, Al_2O_3, Na_2O, SO_3, MgO and TiO_2. The very low concentrations of these oxides suggest the purity of the El-Oued sand quartz. The light color of the sample results from the concentrations relatively considerable of magnesium (Mg) and sulfur (S) in the El-Oued sand dunes [34]. As well as the presence of Mg, Ca and K cations contributed to increase the pH and the conductivity of sand.

3.3 Analysis by X-Ray Diffraction (XRD)

The XRD pattern of the sand samples is shown in Fig. 4. As is evident, the diffraction peaks are related to the planes (100), (011), (110), (102), (111), (200), (201), (112), (022), (013), (121), (113), (122), (203), (104), (302), (213) and (220). According to the JCPDS (N° 46–1045) standard pattern [41], these XRD peaks correspond to quartz with a hexagonal crystalline structure and belonging to the space group P3$_2$21 (154).

We observed that the (011) peak has the highest intensity indicating preferred orientation. Further, three other peaks have been observed at $2\theta = 29.49°$, 48.6° and 65.59° which are related to (104), (116) and (0012) planes respectively. These planes fit calcite ($CaCO_3$) compound as reported by JCPDS (N° 47–1743) with a rhombohedral

Table 5 Lattice parameters a, c and crystalline size D of quartz and calcite of El-Oued sand dunes

Mineral	Standard lattice parameters (Å)	Calculated lattice parameters (Å)				FWHM (°)	Crystalline sizes (nm) (D)
		a	$\Delta a = a_0\text{-}a$	c	$\Delta c = c_0\text{-}c$		
Quartz (SiO_2)	$a_0 = 4.910$ [a] $c_0 = 5.400$ [a]	4.907	0.003	5.401	−0.001	0.2	42.64
Calcite ($CaCO_3$)	$a_0 = 4.989$ [b] $c_0 = 17.061$ [b]	4.977	0.012	17.04	0.021	0.3	28.6

[a] data from JCPDS (N° 46–1045)

[b] data from JCPDS (N° 47–1743)

crystal system belonging to $R\overline{3}c$ (167) space group. We note that the majority of the crystallographic planes are due to quartz SiO_2 (Table 4), with the presence of three planes belonging to calcium carbonate $CaCO_3$.

The XRD results agreed with XRF and FTIR spectroscopy data confirming that the dominant phase in the sand dunes of El-Oued is quartz (SiO_2).

The d_{hkl} inter-planar spacing has been calculated from the X-ray diffraction profile using the Bragg law:

$$2d_{hkl}sin\theta = n\lambda \tag{2}$$

where θ is the diffraction angle, λ is the used wavelength of X-rays and n is the order of diffraction. We note that the calculated value of d_{hkl}-spacing (Table 4) matched very well with those of the standard JCPDS data. From Table 4 the spacing distances d_{hkl} of 4.43, 3.33 and 2.45 (Å) affirm the presence of the α-quartz phase in our sand [28, 33]. The α-quartz is the most stable phase of quartz at room temperature. The lattice constants a, b and c, for the hexagonal phase structure were determined from XRD results using the following equation:

$$\frac{1}{d_{hkl}^2} = \frac{4}{3}\left(\frac{h^2 + hk + k^2}{a^2}\right) + \frac{l^2}{c^2} \tag{3}$$

where (h k l) are the Miller indexes and 'a' and 'c' are the lattice constants.

The calculated and standard JCPDS lattice constants for quartz and calcite are indicated in Table 5. As we can see, the calculated lattice parameters for the quartz (a = b = 4.907 Å and c = 5.401 Å) agree well with the standard values (a_0 and c_0).

Since impurities in the crystal lattice would affect the d-spacing between lattice planes and therefore the lattice parameters, the above agreements confirm the high degree of purity of quartz of the El-Oued sand dunes. We can further calculate the crystallite sizes D of the quartz and calcite of our sand from the strongest peaks by using Scherrer's formula [42]:

$$D = \frac{0.96\,\lambda}{\beta cos\theta} \tag{4}$$

where D is the crystallite size, λ (=1.54 Å) is the wavelength of X-rays, β is the width full at half maximum (FWHM) of the most intense diffraction peak, usually measured in radian and θ is the Bragg angle.

The crystallite size of quartz D = 42.64 nm is very large compared to calcite size D = 28.6 nm, but remain less than 100 nm which makes it of great interest to the nanometric industries and nanotechnologies.

4 Conclusion

The sand dunes of El-Oued region were characterized using FTIR spectroscopy, XRF and XRD analysis. We found that the El-Oued sand mainly consists of about 97.63% quartz in α-phase, minor calcite mineral (about 0.56%) and very low concentrations of other oxides (Al_2O_3, Fe_2O_3, Na_2O, MgO) and some trace elements. The low quantities of the impurities bear witness to the high purity of the quartz sand of El-Oued region. The degree of crystallinity of our sand quartz has been estimated to CI = 0.975, which supports the high crystalline nature of the quartz. The XRD analysis corroborate that our sand is very rich in quartz with hexagonal crystal structure and belonging to space group $P3_221$ (154). Furthermore, the sand has some calcite with trigonal crystal system and $R\overline{3}c$ (167) space group. We estimated the crystallite size of quartz to D = 42.64 nm, which demonstrates the nanometric aspect of the El-Oued sand quartz.

References

1. Götze J; Möckel R (ed.) (2012) Quartz: Deposits, mineralogy and analytics. Springer Science & Business Media, Verlag Berlin Heidelberg

2. Al-Ansary M, Pöppelreiter MC, Al-Jabry A, Iyengar SR (2012) Geological and physiochemical characterization of construction sands in Qatar. Int J Sustain Built Environ 1, 64°C84. https://doi.org/10.1016/j.ijsbe.2012.07.001

3. Diago M, Iniesta AC, Delclos T, Shamim T, Calvet N (2015) Characterization of desert sand for its feasible use as thermal energy storage medium. Energy Procedia 75:2113–2118

4. Hamoda MF, Al-Ghusain I, Al-Mutairi NZ (2004) Sand filtration of wastewater for tertiary treatment and water reuse. Desalination 164(3):203–211

5. Pettijohn FJ, Potter PE, Siever R (1974) Sand and sandstone. Springer science and business media, Verlag Berlin Heidelberg

6. El-Baz F (1992) Origin and evolution of sand seas in the great Sahara and implications to petroleum and ground-water exploration. In proceedings of the 1st. Conference on the geology of the Arab world, Cairo University, Cairo

7. Jallad KN, Espada-Jallad C (2008) Spectroscopic characterization of geological materials from the United Arab Emirates. Arab J Geosci 1(2):119–127

8. Gnanasaravanan S, Rajkumar P (2013) Characterization of minerals in natural and manufactured sand in Cauvery River belt, Tamilnadu, India. Infrared Phys Technol 58:21–31

9. Pye K, & Tsoar H (2008) Aeolian sand and sand dunes. Springer science & business media, Verlag Berlin Heidelberg

10. Dal Martello E, Bernardis S, Larsen RB, Tranell G, Di Sabatino M, & Arnberg L (2011a) Electrical fragmentation as a novel refining route for hydrothermal quartz for SoG-Si production. Miner Eng. https://doi.org/10.1016/j.powtec.2012.02.055

11. Haus R, Prinz S, Priess C (2012) Assessment of high purity quartz resources. Quartz: deposits, mineralogy and analytics. Springer, Berlin, Heidelberg, pp 29–51

12. Moore P (2005) High-purity quartz. Ind Miner 8:54-57

13. Hernandez-Montelongo J, Muñoz-Noval A, García-Ruíz JP, Torres-Costa V, Martin-Palma RJ, Manso-Silvan M (2015) Nanostructured porous silicon: the winding road from photonics to cell scaffolds. A review. Front Bioeng biotechnol 3:60

14. Lührs AK, Geurtsen W (2009) The application of silicon and silicates in dentistry: a review. Biosilica in evolution, morphogenesis, and Nanobiotechnology. Springer, Berlin, Heidelberg, pp 359–380

15. Mangolini L (2013) Synthesis, properties, and applications of silicon nanocrystals. J Vac Sci Technol B Nanotechnol Microelectron 31(2):020801

16. Müller A, Ghosh M, Sonnenschein R, Woditsch P (2006) Silicon for photovoltaic applications. Mater Sci Eng B 134(2–3):257–262

17. Howari FM, Baghdady A, Goodell PC (2007) Mineralogical and geomorphological characterization of sand dunes in the eastern part of United Arab Emirates using orbital remote sensing integrated with field investigations. Geomorphology 83:67–81

18. Trabelsi W, Benzina M, Bouaziz S (2009) Physico-chemical characterization of the Douiret sand (Southern Tunisia): valorisation for the production of silica gel. Phys Procedia 2(3):1461–1467

19. Elipe MG, Lopez-Querol S (2014) Aeolian sands: characterization, options of improvement and possible employment in construction–the state-of-the-art. Constr Build Mater 73:728–739

20. Boussaa SA, Kheloufi A, Zaourar NB (2017) Characterization of impurities present on Tihimatine (Hoggar) quartz, Algeria. J Afr Earth Sci 135:213–219

21. Dos Santos MFM, Fujiwara E, Schenkel EA, Enzweiler J, Suzuki CK (2015) Quartz sand resources in the Santa Maria Eterna formation, Bahia, Brazil: a geochemical and morphological study. J S Am Earth Sci 62:176–185

22. Benaafi M, Abdullatif O (2015) Sedimentological, mineralogical, and geochemical characterization of sand dunes in Saudi Arabia. Arab J Geosci 8(12):11073–11092

23. Adnani M, Azzaoui MA, Elbelrhiti H, Ahmamou M, Masmoudi L, Chiban M (2016) Yerdi sand dunes (Erfoud area, southeastern of Morocco): color, composition, sand's provenance, and transport pathways. Arab J Geosci 9(5):366

24. Mechri ML, Chihi S, Mahdadi N, Beddiaf S (2017) Study of heat effect on the composition of dunes sand of Ouargla (Algeria) using XRD and FTIR. Silicon 9(6):933–941

25. Diago M, Iniesta AC, Soum-Glaude A, Calvet N (2018) Characterization of desert sand to be used as a high-temperature thermal energy storage medium in particle solar receiver technology. Appl Energy 216:402–413

26. Zouaouid K, Gheriani R (2018) Mineralogical analysis of sand roses and sand dunes samples from two regions of South Algeria. Silicon:1–9

27. Corwin DL, Yemoto K (2017) Salinity: Electrical Conductivity and Total Dissolved Solids. Methods Soil Anal 2(1) https://doi.org/10.2136/msa2015.0039.

28. Beddiaf S, Chihi S, Leghrieb Y (2015) The determination of some crystallographic parameters of quartz, in the sand dunes of Ouargla, Algeria. J Afr Earth Sci 106:129–133

29. Saikia BJ, Parthasarathy G (2010) Fourier transform infrared spectroscopic characterization of kaolinite from Assam and Meghalaya, northeastern India. J Mod Phys 1(04):206–210

30. Boussaa S, Kheloufi A, Zaourar NB, Kerkar F (2016) Valorization of Algerian sand for photovoltaic application. Acta Phys Pol A 130(1)

31. Boev B, Jovanovski G, Makreski P (2009) Minerals from Macedonia. XX. Geological setting, lithologies, and identification of the minerals from Rzanovo Fe-Ni deposit. Turkish. J Earth Sci 18(4):631–652

32. Ersoy B, Dikmen S, Yildiz A, Gören R, Elitok Ö (2013) Mineralogical and physicochemical properties of talc from Emirdağ, Afyonkarahisar, Turkey. Turkish. J Earth Sci 22(4):632–644

33. Saikia BJ, Parthasarathy G, Sarmah NC (2008) Fourier transform infrared spectroscopic estimation of crystallinity in SiO_2 based rocks. Bull Mater Sci 31(5):775–779

34. Mahdadi N, Chihi S, Bouguettaia H, Beddiaf S, Mechri ML (2017) Chromatic classification of Ouargla (Algeria) dunes sand: determination of Main compositions and color causes, by using XRD, FTIR and XRF. Silicon 9(2):211–221

35. Maazouzi A, Kettab A, Badri A, Zahraoui B, Khelfaoui R (2014) Algerian sahara sand dunes characterization. Silicon 6(3):149–154

36. Anbalagan G, Prabakaran AR, Gunasekaran S (2010) Spectroscopic characterization of Indian standard sand. J Appl Spectrosc 77(1):86–94

37. Van der Marel HW, Beutelspacher H (1976) Atlas of infrared spectroscopy of clay minerals and their admixtures. Elsevier Publishing, Amsterdam

38. Hlavay J, Jonas K, Elek S, Inczedy J (1978) Characterization of the particle size and the crystallinity of certain minerals by IR spectrophotometry and other instrumental methods: II, investigations on quartz and feldspar. Clays Clay Miner 26(2):139–143

39. Nayak PS, Singh BK (2007) Instrumental characterization of clay by XRF, XRD and FTIR. Bull Mater Sci 30(3):235–238

40. Suresh G, Ramasamy V, Ponnusamy V (2011) Mineralogical and Thermoluminescence characterizations of the river sediments from Tamilnadu, India. Nat Resour Res 20(4):389–399

41. File, P D (1997) JCPDS International Center for Diffraction Data: Swarthmore

42. Scherrer P (1918) Nachrichten von der Gesellschaft der Wissenschaften zu Göttingen, Mathematisch-Physikalische Klasse. Vol. 2, 98–100

Structural, Optical and Electrical Properties of NiO Nanostructure Thin Film

M. Ghougali[1,2,3], O. Belahssen[1,2,*], A. Chala[1,2]

[1] *Material Sciences Department, Faculty of Science, University of Biskra, Algeria*
[2] *Physic Laboratory of Thin Films and Applications (LPCMA), University of Biskra, Algeria*
[3] *Laboratory of exploitation and valorization the azalea energetics sources (LEVRES), Faculty of exact Science, University of El-Oued, Algeria*

Nickel oxide was deposited on highly cleaned glass substrates using spray pneumatic technique. The effect of precursor molarity on structural, optical and electrical properties has been studied. The XRD lines of the deposited NiO were enhanced with increasing precursor molarity due to the improvement of the films crystallinity. It was shown that the crystalline size of the deposited thin films was calculated using Debye-Scherer formula and found in the range between 9 and 47 nm. The optical properties have been discussed in this work. The absorbance (A), the transmittance (T) and the reflectance (R) were measured and calculated. Band gap energy is considered one of the most important optical parameter, therefore measured and found ranging between 3.64 and 3.86 eV. The NiO thin film reduces the light reflection for visible range light. The increase of the electrical conductivity to maximum value of 0.0896 $(\Omega \text{ cm})^{-1}$ can be explained by the increase in carrier concentration of the films. A good electrical conductivity of the NiO thin film is obtained due to the electrically low sheet resistance. NiO can be applied in different electronic and optoelectronic applications due to its high band gap, high transparency and good electrical conductivity.

Keywords: NiO thin films, XRD, Optical constants, Electrical conductivity.

1. INTRODUCTION

Nickel oxide (NiO) is the most investigated metal oxide and it has attracted considerable attention because of its low cost material, and also for its applications in several fields such as a catalyst, transparent conducting oxide, photodetectors, electrochromic, gas sensors, photovoltaic devices, electrochemical supercapacitors, heat reflectors, photo-electrochemical cell, solar cells and many opto- electronic devices [1-7]. NiO is an IV group and it can be used as a transparent p-type semiconductor layers, it has a band gap energy ranging from 3.45 eV to 3.85 eV [8]. Band gap energy is significant to adjust the energy level state of NiO.

The reduction in particle size to nanometer scale results more interesting prosperities in compared with their bulk properties [9]. Therefore, there are several techniques have been used for synthesis and manipulation of nanostructures NiO such as the thermal evaporation, sputtering, pulse laser ablation, thermal decomposition, electrochemical deposition and sol-gel methods etc. Among of these techniques, sol-gel has some advantages such as high purity of raw materials and a homogeneous solution hence easy control over the composition of the deposited films. In this work, a low cost sol-gel/spray pneumatic technique was used to prepare pure NiO nanoparticles thin films with various precursor concentrations. The structural properties of the produced nickel oxide thin films have been examined. The absorption, transmittance and reflectance spectra of the produced thin films for the NiO are also measured in range between 300-1100 nm. Moreover, the optical band gap is determined as a function of the precursor concentrations.

2. EXPERIMENTAL DETAILS

2.1 Preparation of Samples

NiO thin films were prepared onto a highly cleaned glass substrates using sol-gel spay pneumatic technique. Nickel nitrate was dissolved in 50ml of water as a solvent and chloride acid was used as a stabilizer for the all samples in this work. The produced mixture (Sol) was stirred at 60 °C for 2 h in order to obtain a clear and homogenous solution then the mixture was cooled down at room temperature and placed at dark environment for 48 h to have the final (Gel). The glass substrates were cleaned by detergent and by alcohol mixed with deionized water.

2.2 Deposition of Thin Films

The coating was dropped into glass substrates at 480 °C that sprayed during 2 min by pneumatic nebulizer system which transforms the liquid to a stream formed with uniform and fine droplets, followed by the films dried on hot plate at 120 °C for 10 min in order to evaporate the solvent.

2.3 Devices and Measurements

The X-ray diffraction (XRD) spectra of the NiO were measured to verify the structure. X-ray diffraction (XRD) was measured by using BRUKER-AXS-8D diffractometer with Cu Kα radiation (λ =1, 5406Å) operated at 40 KV and 40 mA in the scanning range of (2θ) between 20° and 80°. The spectral dependence of the NiO transmittance (T) and the absorbance (A), on

---

* belahssenokba@gmail.com

the wavelength ranging 300-1100 nm are measured using an ultraviolet-visible spectrophotometer (Perkin-Elmer Lambda 25). The reflectance (*R*) was calculated by the well-known equation as ($T + R + A = 1$). Whereas the electrical conductivity of the films was measured in a coplanar structure of four golden stripes on the deposited film surface; the measurements were performed with keithley model 2400 low voltage source meter instrument.

3. RESULTS AND DISCUSSIONS

3.1 Structural Properties

Fig. 1 shows the spectra of the grown NiO nanoparticles with 4 XRD lines, showing the broadening of the line which is a characteristic of the formation of nanoparticles. The X-ray diffraction was used in this work in order to understand the structure of the deposited NiO thin films with different precursor concentrations.
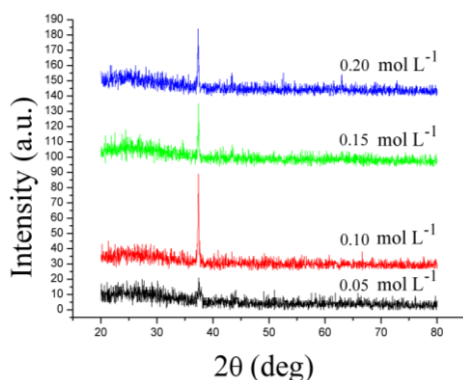
Fig. 1 – XRD patterns of the deposited NiO thin films on glass substrate at different precursor concentrations

The indexed peak (111) at $2\theta = 37.1°$ correspond to

the cubic structure of NiO nanoparticles which are consistent with the JCPDS (No.47-1049). Figure shows that the diffraction intensity increased for precursor molarity 0.10 mol L^{-1}; it shows that the best crystalline quality of the film is achieved for this precursor molarity. The crystalline size was calculated using Debye-Scherrer formula [10]:

$$D = \frac{0,9\lambda}{\beta \cos \theta} \qquad (1)$$

where λ is the wavelength of the X-rays used (1.5406 Å), β is the full width at half maximum (FWHM) and θ is the diffraction angle.

The increasing of the diffraction peaks may indicate to the resulted of the NiO in good crystallinity [11]. The crystallite size of the NiO thin films were calculated using the well-known Debye-Scherer's formula Eq. (3.1), the average of the NiO thin films ranging between 9.72 and 46.62 nm. The changing in the crystallites size leads to the changes in optical properties i.e. band gap energy increased with decreasing crystallites size as shown in Fig. 2.
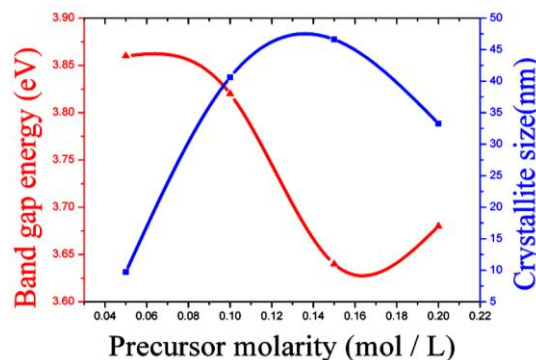
Fig. 2 – The variation of crystallite size and band gap energy NiO thin films as a function of the precursor molarity

Table 1 – Structural, optical and electrical parameters of NiO thin film at different precursor molarity

Precursor molarity (mol L^{-1})	Crystallite size (nm)	Band gap energy (eV)	Conductivity (Ω cm)$^{-1}$
0.05	9,72	3,86	0.03306
0.10	40,61	3,82	0.08961
0.15	46,62	3,64	0.04125
0.20	33,29	3,68	0.00698

3.2 Optical Properties

Fig. 3 shows the optical absorption spectra of NiO nanoparticles. The absorption edge of 0.05 mol/L was found to be at 326 nm and of 0.20 mol/L was found to be at 343 nm. The absorption spectra of 0.05 mol/L show that the absorption edge is slightly shifted towards shorter wavelength when compared to other precursor concentration. The absorption edge of a degenerate semiconductor is shifted to shorter wavelengths with increasing carrier concentration. This shift predicts that there is an increase in band gap value ($E_g = 3.86$ eV), which is due to the reduction in particle size ($D = 9.72$ nm). The fundamental absorption, which corresponds to the electron transition from the valance band to the conduction band, can be used to determine

the nature and value of the optical band gap. The optical absorption study was used to determine the optical band gap of the nanoparticles, which is the most familiar and simplest method.

The absorption coefficient (α) and the incident photon energy ($h\upsilon$) are related by the expression [12]:

$$(\alpha h\upsilon) = C(h\upsilon - Eg)^n \qquad (2)$$

where α is the absorption coefficient, C is a constant, $h\upsilon$ is the photon energy, υ is the frequency of the incident radiation, h is the Planck's constant, exponent n is 0.5 for direct band allowed transition $\left(h\upsilon = 1239 / \lambda \,(\text{nm})° (\text{eV})\right)$ and E_g the band gap energy of the semiconductor.
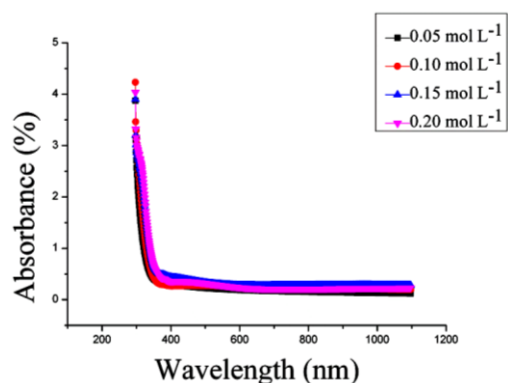
Fig. 3 – Absorbance spectra of NiO samples for different precursor molarity
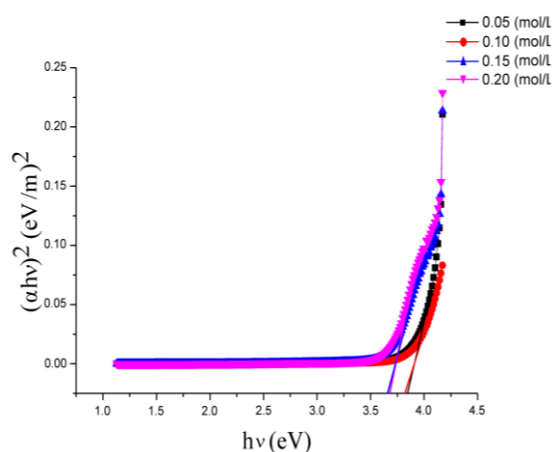

Fig. 4 – Plot of $(\alpha h\nu)^2$ versus incident photon energy ($h\nu$) of NiO nanoparticles

As it was shown in (Fig. 4) a typical variation of $(\alpha h\nu)^2$ as a function of photon energy ($h\nu$) of NiO nanoparticles Eq. (2), used for deducing optical band gap Eg, The optical band gap values have been determined by extrapolating the linear portion of the curve to meet the energy axis ($h\nu$) [13]. The band gap values were given in Table 1.
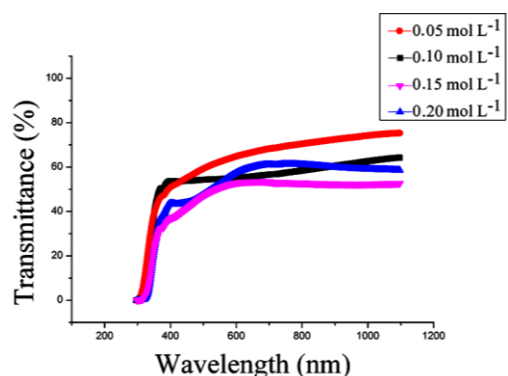
Fig. 5 – Transmission spectra of NiO samples for different precursor molarity

For a transmittance study (Fig. 5), the NiO layer showed very high transmittance of 75.36 %, averaged in the wavelength (λ) of 300-1100 nm. Suppression of light

reflection at a surface is an important factor to absorb more photons in semi-conductor materials. We obtained the reflectance profiles of NiO-coated (Fig. 6). The averaged reflectance values (300-1100 nm) were significantly lower than 0.203 %. Moreover, NiO-coating drives a substantially suppressed reflectance under 0.20 % in 500 nm $< \lambda < $ 1100 nm. This notifies that the NiO-coating is an efficient design scheme to introduce the incident light into substrate.
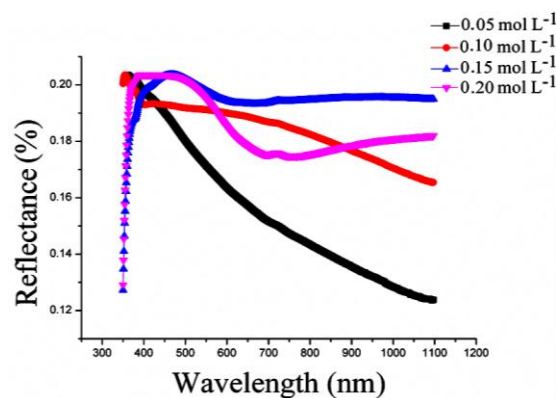
Fig. 6 – Reflectance profiles of NiO thin film for different precursor molarity

3.3　Electrical Properties

The electrical properties of the NiO films are summarized in Table 1. Fig. 7 shows the variation of the electrical conductivity σ of NiO thin films as a function as precursor molarity. As can be seen, deposited films have good conductivity. The maximum recorded value was 0.0896 (Ω cm)$^{-1}$ for the NiO thin film deposited using the molarity 0.10 mol L^{-1}. The increase of the electrical conductivity can be explained by the increase in the carrier concentration. Patil et al. [14] have reported that the increase of the electrical conductivity is due to the increase in activation energy with increasing film thickness. This was explained by difference in the experimental conditions of spraying solution, spray rate and cooling of the substrates during decomposition. However, with 0.10 mol L^{-1} precursor molarity, the crystal structure of the film is significantly improved and the grain size is increased, leading to a reduced concentration of structural defects such as dislocations and grain boundaries. Thus, the decrease of the concentration of crystal defects leads in the increase of free carrier concentration. The improvement of crystal quality reduces the carrier scattering from structural defects, leading to higher mobility.

4.　CONCLUSION

The spray pneumatic technique has been successfully employed to deposit NiO thin films with different concentrations precursor on glass substrates. All the films showed cubic crystal structure with preferential orientation according to the direction (111). The maximum crystallite size was found (46.62 nm). We have observed an improvement in the films crystallinity at 0.10 mol L^{-1} precursor molarity where the peak at position
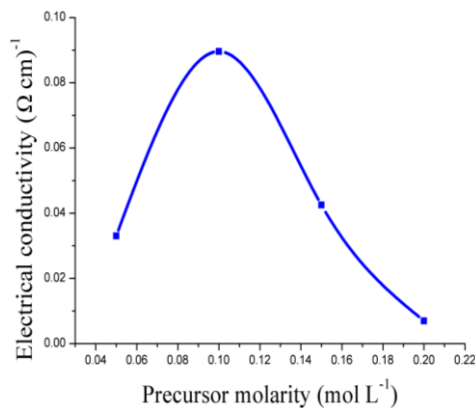
Fig. 7 – Variation of the electrical conductivity of NiO thin films with the precursor molarity

37.1° corresponding to the (111) plans is very sharp, the film obtained at this concentration has higher and sharper diffraction peak indicating an improvement in

peak intensity compared to other films. The band gap value of NiO films was found from 3.64 eV to 3.86 eV. The high transmittance (75.36 %), low reflectance under 0.20 %, widened band gap and good conductivity $(0.0896\ (\Omega\ cm)^{-1})$ obtained for NiO thin films make them promising candidate for optoelectronic devices as well as window layer in solar cell applications.

REFERENCES

1. M.A. Abbasi, Z.H. Ibupoto, A. Khan, O. Nur, M. Willander, *Mater. Lett.* **108**, 152 (2013).
2. M.D. Irwin, D.B. Buchholz, A.W. Hains, R.P.H. Chang, T.J. Marks, *Proceedings of the National Academy of Sciences*, art. No 0711990105, **105** (2008).
3. J. Kim, J.-H. Yun, Y.C. Park, W.A. Anderson, *Mater. Lett.* **75**, 99 (2012).
4. M.-J. Park, J.-Y. Jung, S.-M. Shin, J.-W. Song, Y.-H. Nam, D.-H. Kim, *Thin Solid Films* **599**, 54 (2016).
5. K.C. Wang, P.S. Shen, M.H. Li, S. Chen, M.W. Lin, P. Chen, *ACS Appl. Mater. Interfaces* **6**(15), 11851 (2014).
6. J.H. Yun, J. Kim, Y.C. Park, S.J. Moon, W.A. Anderson, *Thin Solid Films* **547**, 17 (2013).
7. S. Ahn, A.H. Tuan, S. Kim, C. Park, C. Shin, Y.J. Lee, *Mater. Lett.* **132**, 06 (2014).
8. D. Zaouk, Y. Zaatar, R. Asmar, *Microelectron. J.* **37**,5 (2006).
9. A.A. Al-Ghamdi, W.E. Mahmoud, .J. Yaghmour, F.M. Al-Marzouki, *J. Alloy. Compd.* **486**, 1 (2009).
10. B.D. Cullity, *Elements of X-ray Diffraction* (Addison-Wesley Publishing Co. Inc.: New York: 1976).
11. R. Charma, A.D. Acharya, S. Moghe, B. Shrivastava, M. Gangrade, V. Shripathi, V. Ganesan, *Mater. Sci. Semicond. Process.* **23**, 42 (2014).
12. R. Sharma, A.D. Acharya, S.B. Shrivastava, M. M. Patidarc, M. Gangradec, T. Shripathic, V. Ganesan, *Optik* **127**(1), 11 (2016).
13. P.M. Ponnusamy, S. Agilan, N. Muthukumarasamy, T.S. Senthil, G. Rajesh, M.R. Venkatraman, D. Velauthapillai, *Mater. Charact.* **114**, 166 (2016).
14. P.S. Patil, L.D. Kadam, *Appl. Surf. Sci.* **199**, 1 (2002).

SYNTHESIS AND STRUCTURE REFINEMENT OF Ca 0.5 Sr 0.5 FeO 2 SOLID SOLUTION

Article *in* UPB Scientific Bulletin, Series B: Chemistry and Materials Science · August 2016

3 authors:

Zeroual Soria
El-Oued University
4 PUBLICATIONS   **3** CITATIONS

SEE PROFILE

Mohammed Sadok Mahboub
El-Oued University
14 PUBLICATIONS   **7** CITATIONS

SEE PROFILE

Ali Boudjada
42 PUBLICATIONS   **57** CITATIONS

SEE PROFILE

Some of the authors of this publication are also working on these related projects:

Elaboration and caracterisation of Bi based superconductors View project

Iododurene View project

SYNTHESIS AND STRUCTURE REFINEMENT OF $Ca_{0.5}Sr_{0.5}FeO_2$ SOLID SOLUTION

Soria ZEROUAL[1], Mohammed Sadok MAHBOUB[2], Ali BOUDJADA[3]

*$Ca_{0.5}Sr_{0.5}FeO_2$ solid solution has been prepared by the reacting of $Ca_{0.5}Sr_{0.5}FeO_{2.5}$ brownmillerite with CaH_2 at 553 K. The crystal structure of $Ca_{0.5}Sr_{0.5}FeO_2$ phase has been refined by the Rietveld method from X-ray powder diffraction data. In the present study, we have successfully synthesized a stable Oxoferrate $Ca_{0.5}Sr_{0.5}FeO_2$ phase, where no phase separation was observed. The structure is tetragonal, space group P4/mmm, a=3.95718 (9) Å and c=3.39839 (13) Å. The Final structure refinement values of the Rietveld parameters are: R_p=1.15%, R_{wp}=1.75% and χ^2=2.72. The structure of $Ca_{0.5}Sr_{0.5}FeO_2$ consists of a stacking sequence of infinite FeO_2 layers with square-planar coordinated iron (II) lattices separated by alternating Ca/Sr atoms in the **c** direction. This structure might be promising candidates for applications as membrane in solid oxide fuel cells (SOFC).*

1. Introduction

Among candidate for the ionic conductor materials we can quote $SrFeO_{2.5}$ compound exhibit fast oxygen transport and high electron conductivity even at low temperatures [1-5]. It became an interesting field of research, such as: ceramic membranes for oxygen separation and electrodes of solid oxide fuel cells (SOFCs), electrocatalysis, battery electrodes and sensor materials [6-13]. Controversy, the isomorphic $CaFeO_{2.5}$ unlike $SrFeO_{2.5}$ compound shows inability to the electrochemical intercalation of oxygens [2,14-17]. It seems that the order of the FeO_4 tetrahedra plays an important role in explaining the chemical reactivity in Brownmillerite compounds according to Paulus *et al.* [18]. Deepened study of $Ca_{1-x}Sr_xFeO_{2.5}$ is required, considering their important function as a key to better understanding of the ionic conduction mechanism in perovskite-related oxides. A few years ago, Tsujimoto *et al.* [19] reported on the synthesis of the first ternary earth alkaline oxoferrate (II), $SrFeO_2$, by the reduction of perovskite-related $SrFeO_{2.875}$ precursor at 553 K with CaH_2. In their study, Tassel *et al.* [20] have observed that the $Ca_{1-x}Sr_xFeO_2$-phases persists up to 960 K for $SrFeO_2$ and

---

[1] PhD Researcher, LEVRES Laboratory, Department of Physics, Faculty of Exact Sciences, University of El-Oued, Algeria, e-mail: zersoraya@yahoo.com

[2] PhD Researcher, LEVRES Laboratory, Department of Physics, Faculty of Exact Sciences, University of El-Oued, Algeria, Corresponding author, e-mail: mmsad1@yahoo.fr

[3] Professor, Laboratoire de Cristallographie, Unité de Recherche de Physique, Faculté des Sciences Exactes, Université Constantine 1, Algeria, e-mail: boudjada_ali@yahoo.fr

630 K at least for $CaFeO_2$. They have concluded that the infinite layer (IL) iron oxide is thermodynamically stable against substitution as well as temperature. Recently, we have reported for the first time a new synthesis method using a mirror furnace (*MF*) for pure $Ca_{0.5}Sr_{0.5}FeO_{2.5+\delta}$ compound [21]. Based on the relationship between structure and physical properties, we will report in this contribution the synthesis and structural characterization of $Ca_{0.5}Sr_{0.5}FeO_2$ obtained by X Ray Powder Diffraction (XRPD) in order to check the stability of our sample synthesized by a new technique so-called "mirror furnace method".

2. Experimental

2. 1. Synthesis method

$Ca_{0.5}Sr_{0.5}FeO_2$ powder was obtained by a solid state reaction through mixing $Ca_{0.5}Sr_{0.5}FeO_{2.5+\delta}$ prepared according to [21] and CaH_2 in a 1:2 molar ratio, ground inside an argon-filled glovebox. The mixture was inserted into a Pyrex tube. The sealed tube was inserted in a furnace for 6 days at 553 K. The unreacted CaH_2 and byproduct CaO were removed from the product by washed it in a solution of methanol and 0.1 M of NH_4Cl.

2. 2. X-ray Powder diffraction

Powder X-ray diffraction data were performed at room temperature on a Brucker D8 Advance diffractometer (Bragg–Brentano configuration) equipped with Johanson Ge (111) monochromator and a LynxEye position sensitive detector. The datasets were collected in the range of $20° \leq 2\theta < 120°$ using $CuK_{\alpha1}$ radiation at step size of $2\theta = 0.016°$ and a fixed counting time of 15 s/step.

2. 3. EDS spectroscopy

The energy dispersive X-ray spectroscopy (EDS) analysis was carried out for $Ca_{0.5}Sr_{0.5}FeO_{2.5+\delta}$ sample using a JEOL (JSM-6400) scanning electron microscope equipped with an EDAX (Oxford Link INCA) micro-analytical system, intended for the observation of dry and conducting samples.

3. Result and discussion

A quantitative analysis of the precursor $Ca_{0.5}Sr_{0.5}FeO_{2.5+\delta}$ by the energy dispersive X-ray spectroscopy (EDS) analysis was used to check the chemical composition. Small amount of the sample's size is observed on a holey carbon film supported by a copper grid. EDS analysis indicates a Ca:Sr ratio of 0.5:0.5 in $Ca_{0.5}Sr_{0.5}FeO_{2.5+\delta}$, which is consistent with the expected stoichiometry, within the limit of experimental error (Table 1).

The EDS spectrum confirms the desired compound (Fig. 1). XRD powder pattern of the final product $Ca_{0.5}Sr_{0.5}FeO_2$, is isomorphic to those of the parent

structure for $SrFeO_2$ [19]. An additional peak was detected at $2\theta = 32.7°$, thus indicating the presence of a small amount of unreacted phase.

Table 1

Compositions of $Ca_{0.5}Sr_{0.5}FeO_{2.5+\delta}$ extracted by theoretical calculation and EDS analysis

Element	Ca	Sr	Fe
Theoretical composition (% wt.)	12.55	27.43	34.97
Experimental sample composition (% wt.)	12.86	28.04	36.82
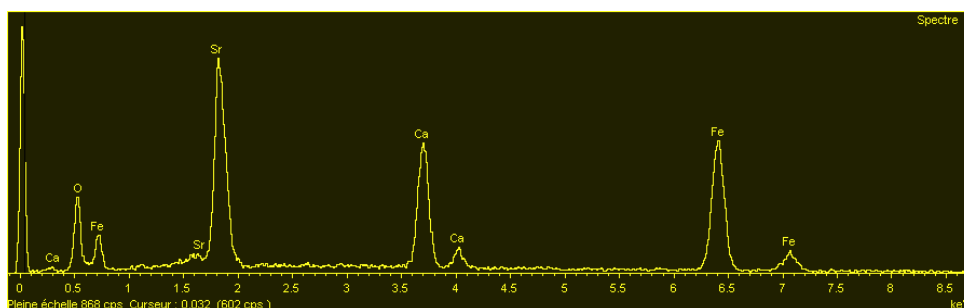
Fig. 1. EDS analysis of initial product $Ca_{0.5}Sr_{0.5}FeO_{2.5+\delta}$

We have found that this peak corresponds to the (141) more intense reflection of the starting Brownmillerite $Ca_{0.5}Sr_{0.5}FeO_{2.5}$ not reacted. The Rietveld refinement of the XRD data was carried out with *FULLPROF* [22] in the *P4/mmm* space group. The background in rietveld refinement was fitted with a linear interpolation function, and pseudo-voight function was employed to model the peak shapes. No splitting peaks were observed, which allowed to us indexing the diffraction pattern in this tetragonal space group. This situation indicates that a no phase separation takes place and the ''miscibility gap'' problem resolved in $Ca_{0.5}Sr_{0.5}FeO_{2.5+\delta}$ solid solution [21] does not arise again. There is no decomposition to form Ca- and Sr-enriched microdomains. We started the refinement with the lattice parameters and initial atomic positions, referring to those quoted by Tassel *et al.* [20]. After careful treatment, the structure refinement leads to rather good match between the experimental and calculated XRD pattern (Fig. 2). The Rietveld refinement leads to confidence reliability factors quite satisfactory. The refinement parameters are listed in Table 2.

Final atomic positions, isotropic displacement factors are given in Table 3 and interatomic distances in Table 4. A possibility of disorder for Ca (Sr) atom was checked.
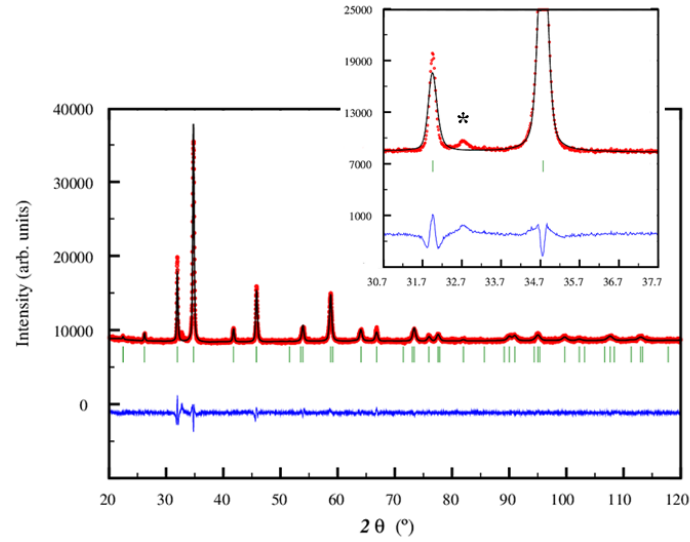
Fig. 2. Observed, calculated and difference X-ray diffraction plots for $Ca_{0.5}Sr_{0.5}FeO_2$. The intense reflection of unreacted $Ca_{0.5}Sr_{0.5}FeO_{2.5}$ is marked is marked

Table 2

Crystallographic data for $Ca_{0.5}Sr_{0.5}FeO_2$

System	*Tetragonal*
Space group	$P4/mmm$
Lattice parameters	a= 3.95718 (9) Å
	c = 3.39839 (13) Å
Volume of unit cell	53.216 (1) Å^3
Z	1
D_x	4.72 (1) Mg m^{-3}
λ	1.54056 Å
R_p (%)	1.15
R_{wp} (%)	1.75
R_{exp} (%)	1.06
χ^2	2.72
N^o of parameters refined	45

where:

$$R_p = \frac{\sum y_i(obs) - y_i(cal)}{\sum y_i(obs)} \qquad (1)$$

$$R_{wp} = \left\{ \frac{\sum w_i(y_i(obs) - y_i(cal))^2}{\sum w_i(y_i(obs))^2} \right\} \qquad (2)$$

$$R_{exp} = [(N - P)/\sum w_i y_{oi}^2]^{1/2} \qquad (3)$$

$$\chi^2 = {R_{wp}}/{R_{exp}} \qquad (4)$$

Refining both the atomic occupation number and displacement parameters revealed that the ratio of Ca:Sr = 0.51: 0.49. Refinement in both possible tetragonal space groups $P42_12$ and $P\text{-}42_1m$ not successful.

Table 3

Atomic coordinates, isotropic displacement parameters and BVS of $Ca_{0.5}Sr_{0.5}FeO_2$

Atom	x	y	z	Uiso*/Ueq (Å^2)	Occ.	BVS
Ca	1/2	1/2	1/2	0.0056 (8)	0.512	2.127
Sr	1/2	1/2	1/2	0.0056 (8)	0.488	2.127
Fe	0	0	0	0.0122 (11)	1.000	2.065
O	1/2	0	0	0.0148 (18)	1.000	2.096

Table 4

Interatomic Distances and Torsion angles for $Ca_{0.5}Sr_{0.5}FeO_2$ (Å, °)

Fe - O x 4	1.9786(6)	O – Fe - O x 2	180.00
(Ca, Sr) - O x 6	2.6081(8)	O – Fe - O x 4	90.00

We note that the mean Fe-O distance in the structure of $Ca_{0.5}Sr_{0.5}FeO_2$ solid solution is 1.98 Å, which is comparable with the mean Fe-O (octahedral site) distance of 1.97 Å in $CaFeO_{2.5}$ [23-24], and 2.06 Å in $SrFeO_{2.5}$ [25], due to the effect of the partial replacement of Ca by Sr in the crystal structure. On the other hand, the mean (Ca, Sr)-O distance in the title structure is 2.61 Å which are significantly larger than the Ca-O bond value of 2.55 Å in $CaFeO_{2.5}$ [23] and 2.59 Å in $CaFeO_2$ [20], but smaller than the bond values of 2.63 Å [25] or 2.65 Å [23] for Sr-O bond in $SrFeO_{2.5}$ and 2.65 Å in $SrFeO_2$ [19], indicating that calcium and strontium occupy the same position (static disorder). In this structure, the Fe^{2+} ions are fourfold coordinated by oxygen in the planes, and no apical oxygen are present. The Fe atoms with their immediate environment consisting of Oxygen atoms form square planes that are repeated in an infinite way on both *a* and *b* directions to form infinite $(FeO_2)_\infty$ layers (Fig. 3a). These layers are separated by A = $(Ca_{0.5}Sr_{0.5})$ atoms (Fig. 3b).

Therefore, the structure consists of a stacking sequence of these infinite layers (IL) of square lattices FeO_2 in the *c* direction (Fig. 4). Four equal Fe–O distances form a perfect square planes, because all atoms situated in special position. In this new architecture all of the apical O atoms have been selectively removed upon reduction. We are therefore facing a new phase "$Ca_{0.5}Sr_{0.5}FeO_2$" with an unusual coordination in this type of oxides formed by square planes around the iron to form infinite $(FeO_2)_\infty$ layers. In other hand, the very small U_{iso} values of all atoms indicates the stability of this structure. It is isostructural with the superconducting copper oxide $SrCuO_2$ [26]. The structure is plotted using Balls & Sticks -1.80beta structural visualization program [27].

The calculated Bond Valence Sum (BVS) of each ion [28-29] [Sr/Ca: 2.127, Fe: 2.065, O: 2.096] are in agreement with the expected valence state of Sr/Ca $^{2+}$, Fe^{2+} and O^{2-} respectively. Likewise, the perfect square planes formed by

four equal Fe-O bond mentioned above might contribute to the fact that the BVS value of the Ca^{2+}, Sr^{2+}, Fe^{2+} and O^{2-} ions given in Table 3 with values very close to the expected formal oxidation states of each ion.

(a)

(b)
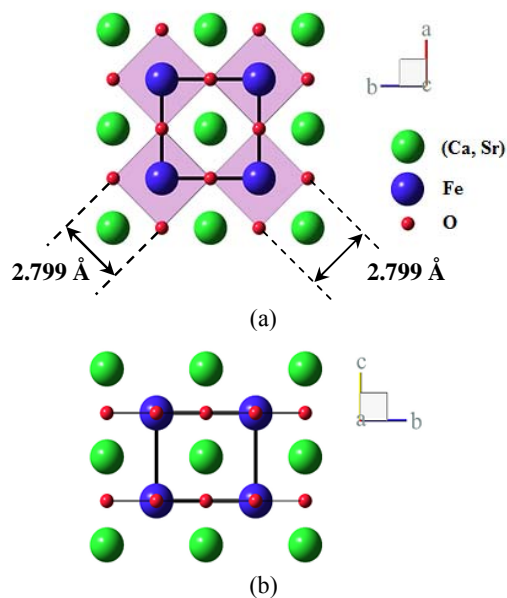
Fig. 3. Structure view of $Ca_{0.5}Sr_{0.5}FeO_2$ at: (a) c axis (b) a axis
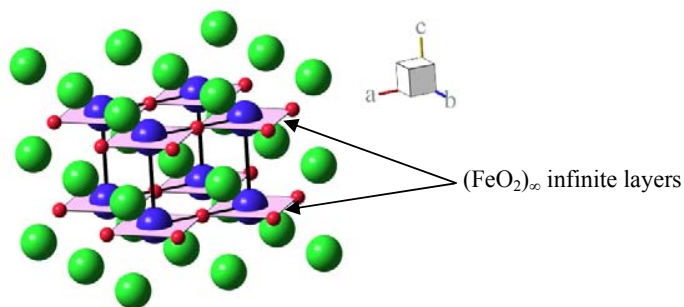
Fig. 4. Perspective view of the crystal structure $Ca_{0.5}Sr_{0.5}FeO_2$

Crystallographic data for the structure reported here have been deposited under FIZ Deposition No. CSD- 430786. These data can be obtained free of charge from FIZ Karlsruhe, D-76344, Eggenstein-Leopoldshafen, Germany, E-mail: crysdata@fiz-karlsruhe.de.

4. Conclusions

The influences of reduction of homogenous $Ca_{0.5}Sr_{0.5}FeO_{2.5+\delta}$ brownmillerite prepared by a mirror furnace technique were investigated. Synthesis and structure refinement of Oxoferrate $Ca_{0.5}Sr_{0.5}FeO_2$ phase have been reported here. The sample was characterized by powder X-ray diffraction. A stable structure of $Ca_{0.5}Sr_{0.5}FeO_2$ consists of a stacking sequence of infinite FeO_2 layers with square-planar coordinated iron (II) lattices separated by alternating Ca/Sr atoms in the **c** direction. There is no decomposition to form Ca- and Sr-enriched microdomains. Calculated Bond Valence Sum (BVS) of Sr/Ca^{2+}, Fe^{2+} and O^{2-} ions are in agreement with the expected valence state. This compound might be promising candidate for important technological applications such as membrane in solid oxide fuel cells. So, further studies are needed to investigate the ionic diffusion in this type of structure.

R E F E R E N C E S

[1]. *M.V. Patrakeev, I.A. Leonidov, V.L. Kozhevnikov, & V.V. Kharton*, Ion–electron transport in strontium ferrites: relationships with structural features and stability, Solid State Sci., **vol. 6**, no. 9, 2004, pp. 907-913.

[2]. *A. Nemudry, M. Weiss, I. Gainutdinov, V. Boldyrev, & R. Schöllhorn*, Room Temperature Electrochemical Redox Reactions of the Defect Perovskite $SrFeO_{2.5+x}$, Chem. Mater., **vol. 10**, no. 9, 1998, pp. 2403-2411.

[3]. *C. Haavik, E. Bakken, T. Norby, S. Stølen, T. Atake, & T. Tojo*, Heat capacity of $SrFeO_{3-\delta}$; δ= 0.50, 0.25 and 0.15 - configurational entropy of structural entities in grossly non-stoichiometric oxides, Dalton trans. 2003, no. 3, pp. 361-368.

[4]. *C.A.J. Fisher, M. Saiful Islam*, Mixed ionic/electronic conductors $Sr_2Fe_2O_5$ and $Sr_4Fe_6O_{13}$: atomic-scale studies of defects and ion migration, J. Mater. Chem., **vol. 15**, no. 31, 2005, pp. 3200-3207.

[5]. *H. D'Hondt, A.M. Abakumov, J. Hadermann, A.S. Kalyuzhnaya, M.G. Rozova, E.V. Antipov, & G. Van Tendeloo*, Tetrahedral Chain Order in the $Sr_2Fe_2O_5$ Brownmillerite, Chem. Mater., **vol. 20**, no. 22, 2008, pp. 7188-7194.

[6]. *H.J.M. Bouwmeester, A.J. Burggraaf*, In Fundamentals of Inorganic Membrane Science and Technology; Burggraaf, A.J.L. Cot (Eds.), Elsevier: Amsterdam, 1996, pp. 435.

[7]. *C.H. Chen, H.J.M. Bouwmeester, R.H.E. van Doorn, H. Kruidhof, & A.J. Burggraaf*, Oxygen permeation of $La_{0.3}Sr_{0.7}CoO_{3-\delta}$, Solid State Ionics, **vol. 98**, no. 1-2, 1997, pp. 7-13.

[8]. *S.P.S. Badwal, F.T. Ciacchi*, Ceramic Membrane Technologies for Oxygen Separation, Adv. Mater., **vol. 13**, no. 12-13, 2001, pp. 993-996.

[9]. *J.P.P. Huijsmans*, Ceramics in solid oxide fuel cells, Curr. Opin. Solid State Mater. Sci., **vol. 5**, no. 4, 2001, pp. 317-323.

[10]. *P.V. Hendriksen, P.H. Larsen, M. Mogensen, F.W. Poulsen, & K. Wiik*, Prospects and problems of dense oxygen permeable membranes, Catal. Today, **vol. 56**, no. 1-3, 2000, pp. 283-295.

[11]. *A.F. Sammells, M. Schwartz, R.A. Mackay, T.F. Barton, & D.R. Peterson*, Catalytic membrane reactors for spontaneous synthesis gas production, Catal. Today, **vol. 56**, no. 1-3, 2000, pp. 325-328.

[12]. *B.C.H. Steele*, Oxygen ion conductors and their technological applications, Mater. Sci. Eng. B, **vol.13**, no. 2, 1992, pp. 79-87.

[13]. *H.Y. Tu, Y. Takeda, N. Imanishi, & O. Yamamoto*, $Ln_{1-x}Sr_xCoO_3$(Ln = Sm, Dy) for the electrode of solid oxide fuel cells, Solid State Ionics, **vol. 100**, no. 3-4, 1997, pp. 283-288.

[14]. *E. Goldberg, A. Nemudry, V. Boldyrev, & R. Schöllhorn*, Model for anomalous transport of oxygen in nonstoichiometric perovskites: 1. General formulation of the problem, Solid State Ionics, **vol. 110**, 1998, no. 3-4, pp. 223-233.

[15]. *A. Nemudry, A. Rogatchev, I. Gainutdinov & R. Schöllhorn*, Reactivity of the perovskite system $Ca_{1-x}Sr_xFeO_{2.5}$ in topotactic electrochemical oxidation at ambient temperature, J. Solid State Electrochem. , **vol. 5**, no. 7-8, 2001, pp. 450-458.

[16]. *A. Wattiaux, L. Fournès, A. Demourgues, N. Bernaben, J.C. Grenier & M. Pouchard*, A novel preparation method of the $SrFeO_3$ cubic perovskite by electrochemical means, Solid State Commun., **vol. 77**, no. 7, 1991, pp. 489-493.

[17]. *A. Piovano, G. Agostini, A.I. Frenkel, T. Bertier, C. Prestipino, M. Ceretti, W. Paulus, & C. Lamberti*, Time Resolved in Situ XAFS Study of the Electrochemical Oxygen Intercalation in $SrFeO_{2.5}$ Brownmillerite Structure: Comparison with the Homologous $SrCoO_{2.5}$ System, J. Phys. Chem. C, **vol. 115**, no. 4, 2011, pp. 1311-1322.

[18]. *W. Paulus, H. Schober, S. Eibl, M. Johnson, T. Berthier, O. Hernandez, M. Ceretti, M. Plazanet, K. Conder, & C. Lamberti*, Lattice Dynamics To Trigger Low Temperature Oxygen Mobility in Solid Oxide Ion Conductors, J. Am. Chem. Soc., **vol. 130**, no. 47, 2008, pp. 16080-16085.

[19]. *Y. Tsujimoto, C. Tassel, N. Hayashi, T. Watanabe, H. Kageyama, K. Yoshimura, M. Takano, M. Ceretti, C. Ritter & W. Paulus*, Infinite-layer iron oxide with a square-planar coordination, Nature, **vol. 450**, no. 7172, 2007, pp. 1062-1065.

[20]. *C. Tassel, T. Watanabe, Y. Tsujimoto, N. Hayashi, A. Kitada, Y. Sumida, T. Yamamoto, H. Kageyama, M. Takano, & K. Yoshimura*, Stability of the Infinite Layer Structure with Iron Square Planar Coordination, J. Am. Chem. Soc., **vol. 130**, no. 12, 2008, pp. 3764-3765.

[21]. *M.S. Mahboub, S. Zeroual, & A. Boudjada*, Synthesis of homogeneous $Ca_{0.5}Sr_{0.5}FeO_{2.5+\delta}$ compound using a mirror furnace method, Mater. Res. Bull., **vol. 47**, no. 2, 2012, pp. 370-374.

[22]. *J. Rodriguez-Carvajal*, FULLPROF: http://www.ill.eu/ sites/fullprof/, (2001).

[23]. *P. Berastegui, S-G. Eriksson, & S. Hull*, A neutron diffraction study of the temperature dependence of $Ca_2Fe_2O_5$, Mater. Res. Bull., **vol. 34**, no. 2, 1999, pp. 303-314.

[24]. *E.F. Bertaut, P. Blum, & A. Sagnières*, Structure du Ferrite Bicalcique et de la Brownmillerite, Acta Cryst., **vol. 12**, no. 2, 1959, p. 149.

[25]. *C. Greaves, A.J. Jacobson, B.C. Tofield & B.E.F. Fender*, A Powder Neutron Diffraction Investigation of the Nuclear and Magnetic Structure of $Sr_2Fe_2O_5$, Acta Cryst. B, **vol. 31**, no. 3, 1975, pp. 641-646.

[26]. *X. Zhou, C. Dong, F. Wu, H. Chen, G. Che, Y. Yao, & Z. Zhao*, High-Temperature X-Ray Diffraction Study on Stability of the Infinite-Layer $SrCuO_2$, J. Solid State Chem., **vol. 112**, no. 1, 1994, pp. 211-213.

[27]. *T.C. Ozawa, S.J. Kang*, "Balls & Sticks: Easy-to-Use Structure Visualization and Animation Creating Program", J. Appl. Cryst., **vol. 37**, no. 4, 2004, pp. 679.

[28]. *N.E. Brese, M. O'Keeffe*, Bond-valence parameters for solids, Acta Cryst. B, **vol. 47**, no. 2, 1991, pp. 192–197.

[29]. *I.D. Brown, D. Altermatt*, Bond-valence parameters obtained from a systematic analysis of the Inorganic Crystal Structure Database, Acta Cryst. B, **vol. 41**, no. 4, 1985, pp. 244–247.

Production Equipe 03

01   A Review of Studies on Geothermal Energy System Applied on Sub- Saharan Climate Regions**(Abdelmalek Atia, Abdessamia Hadjadj, Boubaker Benhaoua and Nacer Lebbihiat, Abdelhafid Brima)**

02   A Review on the Application of Enhanced Oil/Gas Recovery through CO2 Sequestration **(Abdelmalek Atia and Kamal Mohammedi)**

03   Compressive Strength of Dune Sand Reinforced Concrete **(Mani Mohammed , Kriker Abdelouahed and Belferrag Allaoua)**

04   Contribution To The Experimental Study Of The Hydraulic Jump In Trapezoidal Channel With Positive Slope (**A. Ghomri, F. Riguet, S. Khechana**)

05   Failure of a Vertical Drainage System Installed to Fight the Rise of Groundwater in El-Oued Valley (SE Algeria): Causes and Proposed Solutions**(Salim Khechana, Abdelmonem Miloudi, Ali Ghomri, El Habib Guedda & El-Fadel Derradji**

06   Lattice Boltzmann investigation of thermal effect on convective mixing at the edge of solvent chamber in CO 2 -VAPEX process **(Abdelmalek Atia and Kamal Mohammedi)**

07   Optimisation multi-objectif de la structure d'une machine d'usinage agile de type delta linéaire **(Khaled Mansouri , Idir Belaidi , Abdelmalek Atia)**

08   PEM fuel cell as an alternative solution for clean energy production **(Khelaifa Khaoula, Abdelmalek Atia, Hocine Ben Moussa, Ferdjani Abdelfettah and Yahia Abdennour)**

09   Pore-scale study based on lattice Boltzmann method of density driven natural convection during CO2 injection project **(Abdelmalek Atia, Kamal Mohammedi)**

10   Qualité des eaux destinées à la consommation humaine et à l'utilisation agricole (Cas des eaux souterraines d'Oued-Souf, SE algérien) **(Salim KHECHANA1 & El-Fadel DERRADJI)**

11   State of the art on enhanced oil recovery with CO_2 sequestration for low carbon industry **(A.Atia , K. Mohammedi)**

12   STUDY OF THE WORKABILITY AND MECHANICAL STRENGTH OF CONCRETE IN THE FACE OF UPWELLING (CASE OF THE EL OUED REGION OF ALGERIA) **(T. Djedid, A. Guettala, M. Mani)**

13   Thermal Lattice Boltzmann Model for Natural Convection in an Inclined Cavity Packed with Porous Material **(Atia Abdelmalek and Mohammedi Kamal)**

A review of studies on geothermal energy system applied on sub-saharan climate regions

Article *in* Water and Energy International · August 2017

5 authors, including:

ABDELMALEK ATIA
El-Oued University
20 PUBLICATIONS **7** CITATIONS

Hadjadj Abdessamia
El-Oued University
6 PUBLICATIONS **0** CITATIONS

Benhaoua Boubaker
El-Oued University
98 PUBLICATIONS **720** CITATIONS

Nacer Lebbihiat
El-Oued University
3 PUBLICATIONS **0** CITATIONS

Some of the authors of this publication are also working on these related projects:

green house gaz reduction View project

Elaboration des électrodes transparents collectrices en couches minces à base d'oxyde d'étain View project

A Review of Studies on Geothermal Energy System Applied on Sub-Saharan Climate Regions

ABDELMALEK ATIA, ABDESSAMIA HADJADJ, BOUBAKER BENHAOUA AND NACER LEBBIHIAT
Mechanical Engineering Department, Univ. El-Oued, Algeria

ABDELHAFID BRIMA
Laboratoire de Génie Mécanique, Université de Biskra, Alegria

ABSTRACT

Due to fossil fuel reserves diminishing, electrical energy costs increasing, air pollution and global warming, properly designed geothermal heat exchangers offer a sustainable alternative to reduce the need for conventional compressor-based air conditioning systems, ground-air heat exchangers have been recognized as being among the most energy efficient systems for space heating and cooling in residential buildings and agricultural facilities and horticultural facilities. This paper aims to give an overview of the implementation of Ground Heat Exchanger (GHE) for passive air conditioning for any applications. The overview switches focus to systems which utilize the ground as a heat source; this covers general definitions and the most factors influencing on GHE performances; which need to be considered from ground thermal properties to piping materials. Also, this article includes a literature review of the main scientific research that implemented in low-Temperature geothermal energy like Algerian climate, in order to reduce the energy needs and greenhouse gas emission.

Keywords - geothermal energy, Ground Heat Exchanger, Algerian climate, low-Temperature gradient.

1. INTRODUCTION

In the context of today's global energy consumption is increasing and diminishing fossil fuel reserves, which used abusively, these energies are resulting air pollution and global warming which may have adverse effects on the physical, economic, social and political equilibrium of our planet[1].

The concerns associated with the global growth of energy usage can be significantly reduced through the use of renewable energy sources. Renewable energy which is environmentally friendly energy source techniques utilize the natural resources, which are continuously replenished through natural resources, geothermal energy is one of the important renewable energies sources, which can be utilized to provide electricity and space heating / cooling[1-4]. The potential of geothermal energy can be harnessed through a number of techniques, all of which attempt to utilize the thermal energy stored within the earth[5, 6]. Refreshing by geothermal energy is a technique traditionally used in our region of Sahara; People build their houses under the ground to be comfortable in the summer.

The achievement of indoor thermal comfort whilst minimizing energy consumption in buildings is a key challenge in desert climates. The desert climate can be classified as hot and arid and such conditions exist in a number of areas throughout the world. One such area is South Algeria, with an average ambient temperature around 45°C during summer months. In general, most people feel comfortable indoors when the temperature is between 22-26°C, and relative humidity is within the range of 30-50%[7,8].

The principle of GHE is simple in which the renewal air is passed into a buried tube before enters in the house. In winter, the air is thus preheated because the ground is warmer than the outside air. In summer, the air is refreshed because it is the opposite phenomenon that occurs[9-11].

Two principal types of ground heat exchangers are mostly used: horizontal and vertical heat exchangers. Many research has interested in the development of the geothermal heat exchangers such as Hollmuller et al[12] in a theoretical and experimental study used the air / ground exchanger to heat and refresh buildings. This study is based on a compilation of measurements collected and a simulation carried out using a developed numerical model, The authors conclude the importance of diffuse coupling between the exchanger and the building, the temperature at the outlet of the exchanger is within the comfort interval. Al-Ajmi et al[13] they carried out study on the cooling potential of earth–air heat exchangers for domestic buildings in a desert climate which they concluded that there is potential for of earth–air heat exchangers systems to make a useful contribution to energy saving in Kuwait, and in similar desert climate locations. Moummi et al[14] have established theoretical and experimental study on refreshing by geothermal energy in Biskra area, the authors found a promising vector in climate

engineering as a renewable energy source will have to be a questionably exploited industrially. Benhammou et al[15] presented study on simulation and characterization of a geothermal air exchanger for refreshing buildings operating in the climatic conditions of southern Algeria (Adrar), the authors conclude that many parameters influencing the GHE behaviour such as the burial depth in the ground, length, diameter and flow velocity. Mebarki et al[16] carried out study on the air conditioning system integrating a Canadian well in the arid zones, case of Bechar, The results obtained by the authors make it possible to fully understand the functional of the air-ground heat exchanger during the seasons. Naili et al[17] performed In-field performance analysis of ground source cooling system with horizontal ground heat exchanger in Tunisia, the authors shows the effect of various parameters such as mass flow rate of circulating water, length and buried depth and they conclude that the thermal potential in Tunisia offers a good exploitation of horizontal ground source heat exchanger.

As horizontal geothermal heat exchanger requires a large area to be implanted, we have constructed new geometry, which consist to a conical basket. This configuration allows to decrease the area of installation of the geothermal heat exchanger and to assure the maximum of heat transfer from the soil to its surface due to the conical shape of the basket. Most research activities in this field of spiral geometry are numerical. A few experimental works are conducted. Boughanmi et al in 2015[18] presented thermal performance of a conic basket heat exchanger coupled to a geothermal heat pump for greenhouse cooling under Tunisian climate in which they concluded that this new shape of conic basket is practically feasible and giving good performance. However the same author Boughanmi et al in 2016[19] studied the evaluation of soil thermal potential under Tunisian climate using a new conic basket geothermal heat exchanger, in this study, the thermal potential of sandy soil is evaluated using a new conical basket geothermal heat exchanger (CBGHE). Energetic efficiencies variations of this novel heat exchanger are determined.

The main objective of this study is to present the previous researches have been investigated the refreshing techniques by the low gradient geothermal energy using the air-to-ground exchanger (GHE), such as the scientific researchers have been carried out in Algerian climate. Additional to that, the geothermal background and the main factors influencing on GHE behaviour will be discussed in this paper.

2. MAIN FACTORS INFLUENCING ON GHE BEHAVIOUR

In literature review of previous studies, we found several factors that affecting the behaviour of geothermal heat exchanger. Soil properties and moisture content such as the heat capacity, thermal conductivity and thermal diffusivity should take in consideration during the GHE implementation, because those factors have an important influence on the behaviour of the GHE[12, 20-22]. Also, the ground loop such as

length, diameter and physical properties, have a consistent effect[12,23]. Additional to all these factors, the climatic conditions play a principal role in GHE performances[20].

Besides the selection of mechanical components, the ground-loop length is the primary focus of ground source heat system design. Despite this, few investigations have considered the long-term influence of ground-loop characteristics on ground behaviour or with regard to system optimization[24]. To date, the design of ground-loops is non-standardized, leading to range of ground-loop configurations, installation depths, pipe diameters and materials being used[20]. The following paragraphs present the main factors of the ground-loop influencing on the geothermal heat exchanger.

The conduit of the well may consist of a single tube laid in a meander or loop around the building or be organized in the form of a network of parallel tubes installed between collectors in order to increase the flow of air circulating in the well[9]. However, the length of the tubes determines the exchange surface and the residence time of the air in the tubes. In a first approximation, the temperature profile of the air in the tubes is asymptotic. The optimum length of the exchanger will depend on the flow in the pipes. Indeed, the bibliography shows that for low flows, the minimum temperature is reached rather quickly, and that after a certain length, the exchanger no longer tempers the air: It has reached its limit of effectiveness. On the other hand, when flow increases, the tube length increases too in order to establish the ground temperature[23]. Therefore, an increase in the diameter of the tubes results in an increase in the exchange surface, but the experience demonstrated that doesn't necessarily increasing the heat exchange, this is due to the air circulating in the center of the pipe will no longer be in contact with the pipe wall's and its temperature will be little influenced by the temperature of the ground. The choice of the material properties is important because it is directly affects the soil / well thermal exchanges. The use of compact walls with high thermal conductivity must be favored because it allows to increase the exchanges and thus to reduce the length of the well[19]. Some other factors have low influence on the behaviour of the GHE, These include the internal roughness of the pipes, the overall geometry of the ground loop and the operating regime of the GHE[23].

3. STATE OF ART ON GROUND HEAT EXCHANGER

Several experimental and theoretical researchers have been carried out on the GHE system in literature. Al-Ajmi et al[13] carried out study on the cooling potential of earth–air heat exchangers for domestic buildings in a desert climate, a theoretical model of an earth–air heat exchanger (EAHE) was developed for predicting the outlet air temperature and cooling potential of these devices in a hot, arid climate. A sub-soil temperature model adapted for the specific conditions in Kuwait is presented and its output compared with measurements in two locations, a typical meteorological year for Kuwait was prepared and

used to predict the cooling loads of the air-conditioned dwelling with and without the assistance of the EAHE. A typical Kuwaiti domestic building of dimensions 10 m x 10 m x 3 m was defined for testing EAHE performance. The building materials (walls, roof and floor) are in accord with the prevailing building materials and practices in the region. The building is assumed to have two windows each of area 1 m^2 in the North/South direction. The simulation carried out by Al Ajmi et al for the period from May to September, which is the most arid and the hottest time of the year in Kuwait. The simulation conducted for the case of the building being cooled by air-conditioning both with and without assistance from the EAHE. The peak heat removal rate from the building with air-conditioning alone was calculated to be 4370 W while that with air conditioning and EAHE assistance was 2670 W. The peak cooling load reduction due to the operation of the EAHE was thus 1700 W (mid-July). The indoor temperature of the building for the "free running" condition (that is, without air conditioning) showed a reduction of 2.8°C in the peak hours through use of the EAHE system as illustrated in Figure 1. Al Ajmi et al[13] concluded that there is potential for EAHE systems to make a useful contribution to energy saving in Kuwait, and in similar desert climate locations.

Fig. 1 : Indoor air temperature of the building during the period May–September for the "free-running" situation, with and without EAHE assistance[13]

N. Moummi et al[25] presented theoretical and experimental study on refreshing by geothermal energy in Biskra area, This technique, called Canadian's well, uses air/ground heat exchanger system. They investigated the air temperature evolution at the outlet of the heat exchanger.

The authors verified experimentally first the mathematical models that have been established, which give the best evolution of the air temperature in the exchanger as a function of the different structural parameters (diameter, length, flow, ground temperature, depth). The experimental tests bench was mounted on site at the University of Biskra. It is a network of four trays with a total length of about 60 m. The inner diameter of the pipe is 110 mm which is placed at a depth of 3 m under a slope of 2%.

In the second stage, a synthesis and comparison study was taken place between the theoretical results developed and those obtained experimentally from the measurements as shown in Fig 2.
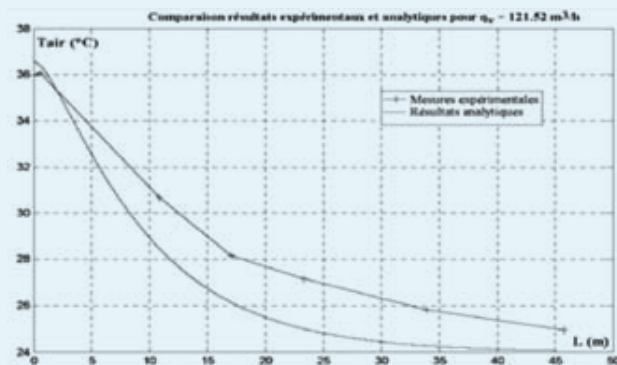
Fig. 2 : Variation of the air temperature versus the length of the exchanger[25]

At the end of this study and based on the results obtained, the authors found a promising vector in climate engineering as a renewable energy source can be exploited industrially. However the experimental results compared to the analytical results allowed the authors to conclude that the presented model can be improved. Indeed, experimentally the temperature of the fluid continuously decreases with the length of the exchanger.

Benhammou et al they implemented study on simulation and characterization of a geothermal air exchanger for refreshing buildings operating in the climatic conditions of southern Algeria (Adrar). The authors obtained very encouraging results which indicate that this low-priced technique can cover an important part of our needs in domestic cooling. This study also permitted them to exanimate the influence of several parameters of the exchanger on its daily average efficiency and on the temperature of air cooled in the outlet of the exchanger.

This heat exchanger constructed from a polyethylene pipe of 40 m length and 16 cm diameter, buried at a depth of 3 m from the ground surface. The average air velocity in the pipe is taken to be 3.5 m/s Figures 3-6 shows the influence of different parameters on the functional of the air-to-ground exchanger[15].

Fig. 3 : Variation of the cooled air temperature versus the time for the month of July

Fig. 4 : Variation of the cooled air temperature versus the time for the month of September

Fig. 5 : Variation of the cooled air temperature and daily average efficiency versus depth

Fig. 6 : Variation of the cooled air temperature and daily average efficiency versus the pipe longer

Based on this study the authors concluded that the temperature of the cooled air at the outlet of the exchanger is lower when the burial depth in the ground greater. Similarly, when the exchanger is longer the temperature of the cooled air is lower; however the flow velocity has such an important effect on the functional of the geothermal exchanger. The temperature of the cooled air increases linearly with the speed of the air. Therefore, it is better to choose a speed neither very low nor very high. Concerning the diameter of the buried pipe, they found that there is an optimum diameter of 10 cm for which the temperature of the cooled air is minimal and the daily efficiency of the exchanger is maximal.

Mebarki et al[16] carried out study on the air conditioning system integrating a Canadian well in the arid zones, case of Bechar. In this work, they studied the performance of an air-ground heat exchanger with a view to perform an analytical modeling. They first validated the model of the ground temperature and air temperature in the heat exchanger, and then analyzed the influence of several parameters, namely depth, diameter and length of the pipe on the temperature inside the exchanger, the authors exanimated the influence of several parameters on the functional of the air-to-ground heat exchanger, furthermore they compared their results with some work already implemented[13,25]. The results obtained by the authors make it possible to fully understand the functional of the air-ground heat exchanger during the seasons.

Beloufi et al[9] Investigated the thermal performances of an earth air heat exchanger (EAHE) under transient conditions in cooling mode. They carried out their experiments in south Algeria at the University of Biskra. They constructed a PVC pipe of 53.16 m long and 110 mm diameter buried at 3 m depth to be used. The experimental setups were tested under monitoring of 71 hours in continuous operation mode with high inlet temperatures. Therefore, a mathematical model was presented for EAHE by using the finite differences method. They found that the continuous operation mode have no significant effect on the outlet air temperature and thus on the EAHE performances during operating period. Results of the theoretical predictions were validated with the measured air temperatures along the EAHE and showed acceptable matching between numerical and experimental results.

H. Boughanmi et al[19] studied the evaluation of soil thermal potential under Tunisian climate using a new conic basket geothermal heat exchanger, they designed geothermal heat exchangers system composed of two conic baskets serially connected. Both heat exchangers are made in polyethylene high-density material and have a length of 3 m each one. They used for greenhouse cooling and heating through a geothermal heat pump. Its conical geometry is selected to reduce the operation cost and the exploited area, compared to vertical and horizontal geothermal heat exchangers often used. It also assures the maximum of heat exchange with the soil. The aim of this study is to determine the

thermal performance of one Conic Basket Geothermal Heat Exchanger (CBGHE), buried at 3 m deep, in the exploitation of the soil thermal potential, in summer. A rate of heat exchange with the soil is determined and the global heat exchange of the CBGHE is assessed. Its energy and efficiencies are also evaluated using both first and second law of thermodynamic. Figure 7 present the results obtained by the authors. This study allows determining the optimal exchange surface of the CBGHE which should be used to assure the maximal exploitation of the soil thermal potential for eventual use in greenhouse heating and cooling.

Fig. 8 : Picture of the CBGHE after filling by water

Fig. 7 : Heat exchange rate versus time for different mass flow rate[19].

In May 2017 we have constructed geothermal heat exchanger with conical basket configuration designed, installed and tested in El-Oued region, Algeria, in which the CBGHE was immersed in a water well of 5 meters depth, the aim of this work is to evaluate the main parameters influencing the CBGHE and understanding its behaviour with experimental and analytical analyzes, the experiments are conducted between the 1st and the 9th May 2017, the influence of several parameters such as air flow rate, length, inlet temperature and buried depth were studied, the obtained results are very encouraging and confirming the feasibility of using the CBGHE for cooling and heating buildings in Algerian Sahara. (Figure 8)

The Experimental measurements carried out on this CBGHE which have 30 m long and at velocity of 10 m/s shows as described in Figure 9 that when the temperature difference between the ambient air and the water well increases the gained temperature gap between the inlet and the outlet air of the exchanger increases too. Moreover, we found that the corresponding temperature differences between the ambient air and the cooled air at the outlet of the exchanger for inlet air temperature of 42°C and 33.4°C are respectively 13.9°C and 7.6°C. This is due to the fact that when the temperature of the ambient air is greater than that of the water well, the thermal losses towards the tube walls are also great. This causes its temperature to drop considerably.

Fig. 9 : Exchanger outlet air temperature versus the inlet air temperature

4. CONCLUSION

The research presented in literature cover a number of topics which can be divided into three categories, namely; analytical, numerical and experimental investigations, the provided literature review containing the notable research advances within the GHE field in which intended for refreshing buildings in summer and warming in winter, the presented work summaries the main research that including the main factors influencing the GHE behaviour, most of the discussed studies conducted in our country and some of them carried out in foreign countries which have approximately similar climate such as Tunisia and Kuwait. Based on the presented literature review and throughout the results obtained by the cited authors, a promising vector in climate engineering as a renewable energy source can be exploited in Algerian desert, more research and investigation will be required in the future for the development of the GHE system.

W & E INTERNATIONAL (WATER RESOURCES SECTION)

REFERENCES

1. T. Plaksina and C. White, "Modeling coupled convection and carbon dioxide injection for improved heat harvesting in geopressured geothermal reservoirs," Geothermal Energy, vol. 4, 2016.

2. M.S.S. Sanjeev Jakhar and N. Gakkhar, "Parametric modeling and simulation of photovoltaic panels with earth water heat exchanger cooling," Geothermal Energy, vol. 4, 2016.

3. J. Busby and R. Terrington, "Assessment of the resource base for engineered geothermal systems in Great Britain," Geothermal Energy, vol. 5, 2017.

4. I. Akhmadullin and M. Tyagi, "Numerical analysis of downhole heat exchanger designed for geothermal energy production," Geothermal Energy, vol. 5, 2017.

5. M. J. Swenka, An energy and cost analysis of residential ground-source heat pumps in Iowa: ProQuest, 2008.

6. L.J. Taylor, "Development of a low temperature geothermal organic rankine cycle standard," 2015.

7. S. Ouali, "Étude géothermique du sud de l'Algérie," 2005.

8. A. Sehli, A. Hasni, and M. Tamali, "The potential of earth-air heat exchangers for low energy cooling of buildings in South Algeria," Energy Procedia, vol. 18, pp. 496-506, 2012.

9. Y. Belloufi, A. Brima, R. Atmani, N. Moummi, and F. Aissaoui, "Theoretical and experimental study of air refresh by a geothermal heat exchanger air/ground," LARHYSS Journal ISSN 1112-3680, pp. 121-137, 2016.

10. J. Sobti and S. K. Singh, "Earth-air heat exchanger as a green retrofit for Chandīgarh—a critical review," Geothermal Energy, vol. 3, 2015.

11. T. S. Bisoniya, "Design of earth–air heat exchanger system," Geothermal Energy, vol. 3, 2015.

12. P. Hollmuller, "Utilisation des échangeurs air/sol pour le chauffage et le rafraîchissement des bâtiments: mesures in situ, modélisation analytique, simulation numérique et analyse systémique," University of Geneva, 2002.

13. F. Al-Ajmi, D. Loveday, and V.I. Hanby, "The cooling potential of earth–air heat exchangers for domestic buildings in a desert climate," Building and Environment, vol. 41, pp. 235-244, 2006.

14. N. Moummi, H. Benfatah, N. Hatraf, A. Moummi, and S. Youcef-Ali, "Le rafraîchissement par la géothermie: étude théorique et expérimentale dans le site de Biskra," 2014.

15. M. Benhammou and B. Draoui, "Simulation et caractérisation d'un échangeur géothermique à air destiné au rafraîchissement des bâtiments fonctionnant dans les conditions climatiques du sud de l'Algérie," Revue des Energies Renouvelables, vol. 15, pp. 275-284, 2012.

16. B. Mebarki, B. Draoui, S. Abdessemed, A. Keboucha, S. Drici, and A. Sahli, "Etude d'un système de climatisation intégrant un puits canadien dans les zones arides, cas de Béchar," Revue des Energies Renouvelables, vol. 15, pp. 465-478, 2012.

17. N. Naili, I. Attar, M. Hazami, and A. Farhat, "Experimental analysis of horizontal ground heat exchanger for Northern Tunisia," 2012.

18. H. Boughanmi, M. Lazaar, S. Bouadila, and A. Farhat, "Thermal performance of a conic basket heat exchanger coupled to a geothermal heat pump for greenhouse cooling under Tunisian climate," Energy and Buildings, vol. 104, pp. 87-96, 2015.

19. H. Boughanmi, M. Lazaar, A. Farhat, and A. Guizani, "Evaluation of soil thermal potential under Tunisian climate using a new conic basket geothermal heat exchanger: Energy and exergy analysis," Applied Thermal Engineering, vol. 113, pp. 912-925, 2017.

20. B.D.P. Hepburn, "An investigation of the behaviour of the ground in response to energy extraction," Cardiff University, 2013.

21. P. Le Feuvre, "An investigation into ground source heat pump technology, its UK market and best practice in system design," Strathclyde University, 2007.

22. Y. Belloufi, A. Brima, S. Zerouali, R. Atmani, F. Aissaoui, A. Rouag, et al., "Numerical and experimental investigation on the transient behaviour of an earth air heat exchanger in continuous operation mode."

23. M. Saadeddine, "Identification et analyse des principaux facteurs influant le comportement thermique d'un échangeur air/sol enterré," 2013.

24. C.S.A. Chong, G. Gan, A. Verhoef, R.G. Garcia, and P. L. Vidale, "Simulation of thermal performance of horizontal slinky-loop heat exchangers for ground source heat pumps," Applied energy, vol. 104, pp. 603-610, 2013.

25. N. Moummi, H. Benfatah, N. Hatraf, A. Moummi, and S. Y. Ali, "Le rafraîchissement par la géothermie: étude théorique et expérimentale dans le site de Biskra," Revue des Energies Renouvelables, vol. 13, pp. 399-406, 2010.

We are IntechOpen,
the world's leading publisher of
Open Access books
Built by scientists, for scientists

4,400
Open access books available

117,000
International authors and editors

130M
Downloads

Our authors are among the

154
Countries delivered to

TOP 1%
most cited scientists

12.2%
Contributors from top 500 universities

CLARIVATE ANALYTICS

BOOK
CITATION
INDEX

INDEXED

WEB OF SCIENCE™

Selection of our books indexed in the Book Citation Index
in Web of Science™ Core Collection (BKCI)

Interested in publishing with us?
Contact book.department@intechopen.com

Numbers displayed above are based on latest data collected.
For more information visit www.intechopen.com

A Review on the Application of Enhanced Oil/Gas Recovery through CO_2 Sequestration

Abdelmalek Atia and Kamal Mohammedi

Abstract

Global warming is considered as one of very important problems in the last few years. This phenomenon is caused primarily by increase in greenhouse gases such as carbon dioxide (CO_2). Natural events and human activities are believed to be the principal sources of this problem. A promising long-term solution for mitigating global heating is to inject CO_2 into oil field geological formations for combination between CO_2 sequestration and enhanced oil recovery. This chapter aims to give an extensive literature survey and examines research papers that focus on EOR-CO_2 processes and projects that have been tested in the field.

Keywords: CO_2 sequestration, EOR, global warming, energy

1. Introduction

The growing concern over the climate change caused by global warming due to a high emission of greenhouse gases (essentially carbon dioxide (CO_2)) has increased the interest in finding various techniques to resolve this problem. The injection of this gas for enhanced oil recovery has been tested with full success in several fields over the world.

Traditionally, oil recovery operations have been subdivided into three stages: primary, secondary, and tertiary as shown in **Figure 1**. Historically, these stages described the production from a reservoir in a chronological sense. Primary production, the initial production stage,
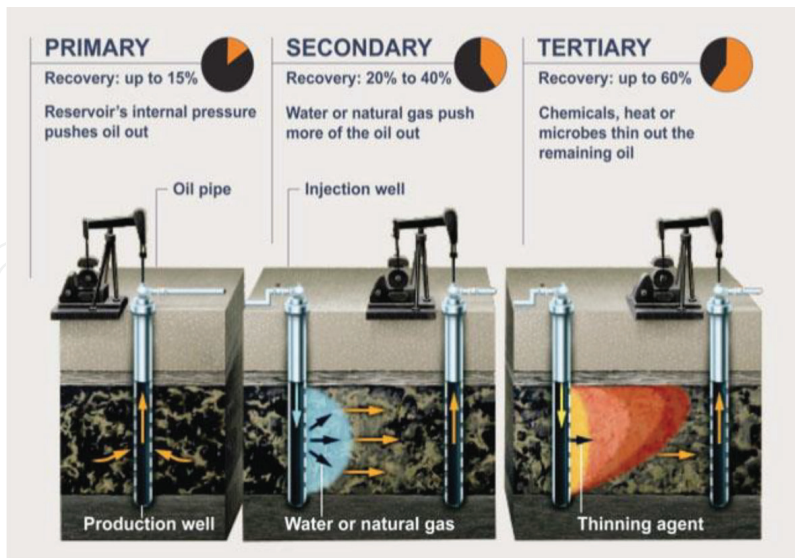
Figure 1. Oil recovery stages [1].

resulted from the displacement energy naturally existing in a reservoir; the driving energy may be derived from the expansion of the gas cap or an active aquifer, from the liberation and expansion of dissolved gas, from gravity drainage, or from a combination of all these mechanisms. Secondary recovery, the second stage of operations, usually was implemented after primary recovery declined. Traditional secondary production processes are gas injection, water flooding, or water alternative gas injection (WAG). Tertiary recovery or enhanced oil recovery (EOR) is a term used to describe a set of processes intended to increase the production of oil beyond what could normally be extracted when using conventional oil production techniques, while traditional oil production (primary and secondary stage) can recover up to 35–45% of the original oil in place (OOIP). The application of an EOR technique is typically performed toward what is normally perceived to be the end of the life of an oil field, and tertiary production used miscible gases (e.g., CH_4, CO_2), chemicals, and/or thermal energy to displace additional oil (5–15%).

2. Carbon dioxide properties

Carbon dioxide is formed from the combination of two elements: carbon and oxygen. It is produced from the combustion of coal or hydrocarbons. CO_2 is a colorless, odorless, and non-toxic stable compound found in a gaseous state at standard conditions. In petroleum engineering application, it can be in a gas or a liquid state depending on the PVT conditions. **Table 1** gives the main properties of carbon dioxide. The phase diagram (**Figure 2**) of CO_2 is

Property	Value
Molecular weight	44 g/mol
Critical temperature	31°C
Critical pressure	73.77 bar
Critical density	467.6 kg/m^3
Triple point temperature	−56.5°C
Triple point pressure	5.18 bar
Boiling (sublimation) point (1.013 bar)	−78.5°C
Critical Z factor	0.274
Solid phase	
Density of carbon dioxide snow at freezing point	1562 kg/m^3
Latent heat of vaporization (1.013 bar at sublimation point)	571.1 kJ/kg[1]
Liquid phase	
Vapor pressure (at 20°C)	58.5 bar
Liquid density (at −20°C and 19.7 bar)	1032 kg/m^3
Viscosity (at STP)	99 µPa s
Characteristics of CO_2 gas phase	
Gas density	2.814 kg/m^3
Gas density (according to STP)	1.976 kg/m^3
Specific volume (according to STP)	0.506 m^3/kg
C_p (according to STP)	0.0364 kJ/(mol K)
C_v (according to STP)	0.0278 kJ/(mol K)
C_p/C_v	1.308
Viscosity (according to STP)	13.72 µPa s
Thermal conductivity (according to STP)	14.65 mW/(m K)
Enthalpy (according to STP)	21.34 kJ/mol
Entropy (according to STP)	117.2 J mol/K

Note: STP stands for standard temperature and pressure, which are 0°C and 1.013 bar.

Table 1. Carbon dioxide properties [3].

also a key data since we can inject it under different temperature and pressure conditions. The three phases are shown in this diagram, with the triple and critical point. Above the critical point, the CO_2 is considered as a supercritical fluid.
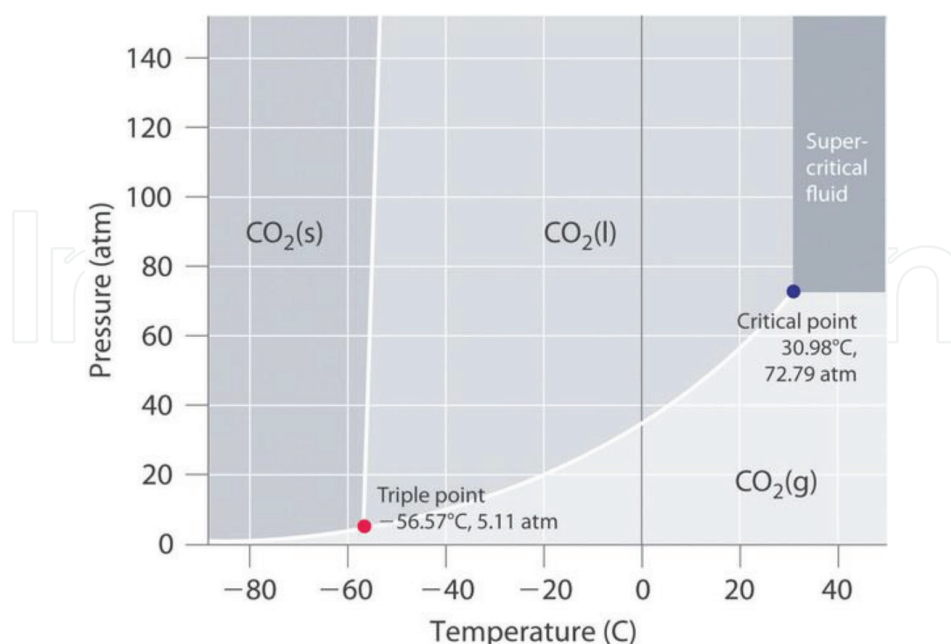
Figure 2. CO_2 phase diagram [2].

3. Carbon capture and storage

Carbon dioxide is the most important greenhouse gas, because it is emitted into the atmosphere in large quantities [4]. Carbon capture and storage (CCS) has been recognized as a new project around the world that should help mitigate CO_2 emissions significantly. The idea behind CCS is simple and can be divided into three steps: capture of CO_2 (e.g., from a fossil fuel power plant), transportation of the captured CO_2, and permanent storage into different geological formations (e.g., saline aquifer and oil and reservoirs), with the aim of isolating CO_2 from the atmosphere [5] (**Figure 3**).

Several scenarios describing the emission of greenhouse gases and models for the estimation of their influence on the global climate have been examined by the members of several association interests by this subject like the Intergovernmental Panel on Climate Change (IPCC) and the International Energy Agency (IEA). Based on the assumptions of IPCC, the climate model global temperature increases between 1 and 6°C were predicted by the year 2100, while some regions might benefit from higher temperatures [6]. The IEA Agency estimates that CCS projects should contribute to about 15–20% of the total greenhouse gas emissions mitigation by 2050, and without the application of CCS, the overall costs to halve CO_2 emissions by 2050 would rise by 70% [5]. It has been estimated that geological formations worldwide are able to store more than 10,000 Gt of carbon dioxide; this huge quantity is large compared to the cumulated anthropic emissions of carbon dioxide [3].
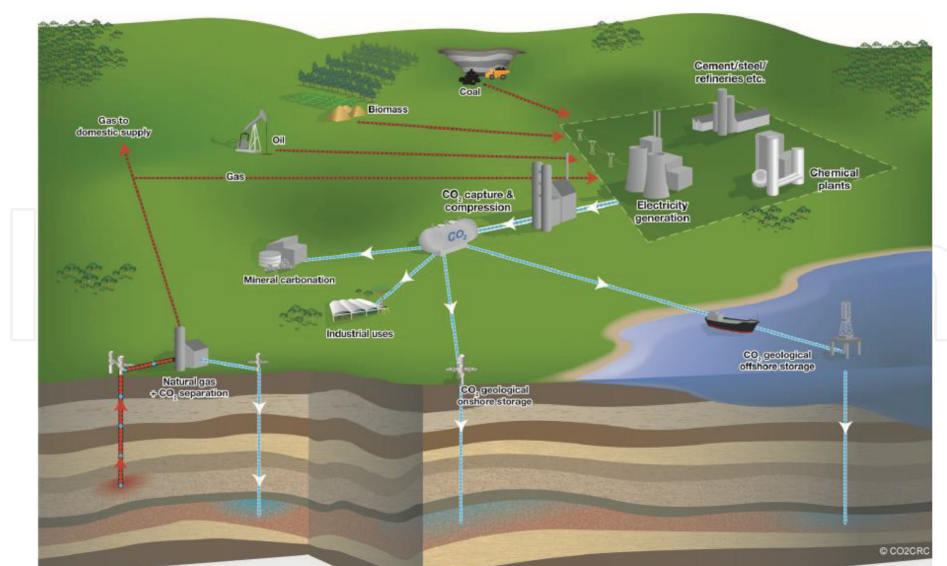
Figure 3. A schematic diagrams of possible CCS projects [5].

4. EOR methods

Many EOR methods have been used in the past, with varying degrees of success, for the recovery of light and heavy oils, as well as tar sands. There are two main categories of EOR: thermal and non-thermal methods (include gas and chemical methods). Each main category includes some individual processes [7].

Thermal methods are primarily intended for heavy oils and tar sands; these methods recover the oil by introducing heat into the reservoir. Thermal method is based on a set of displacement mechanisms to enhance oil recovery. The most important mechanism is the reduction of crude oil viscosity with increasing temperature [8]. However, the viscosity reduction is less for lighter crude oil. Therefore, thermal methods have had limited success in the field of light crudes.

Non-thermal methods (gas and chemical methods) are normally used for light oils <100 cp. In a few cases, they are applicable to heavy oils <2000 cp, which are unsuitable for thermal methods.

Gas methods, particularly carbon dioxide (CO_2), recover the oil mainly by injecting gas into the reservoir. Gas methods sometimes are called miscible process or solvent methods. The reservoir geology and fluid properties determine the suitability of a process for a given reservoir. Currently, gas methods account for most EOR production and are very successful especially for the reservoirs with low permeability, high pressure, and lighter oil [9].

Vapor extraction (VAPEX) is among the gas methods (**Figures 4** and **5**). It is a promising technique for the recovery of heavy oils and bitumen in reservoirs where thermal methods,
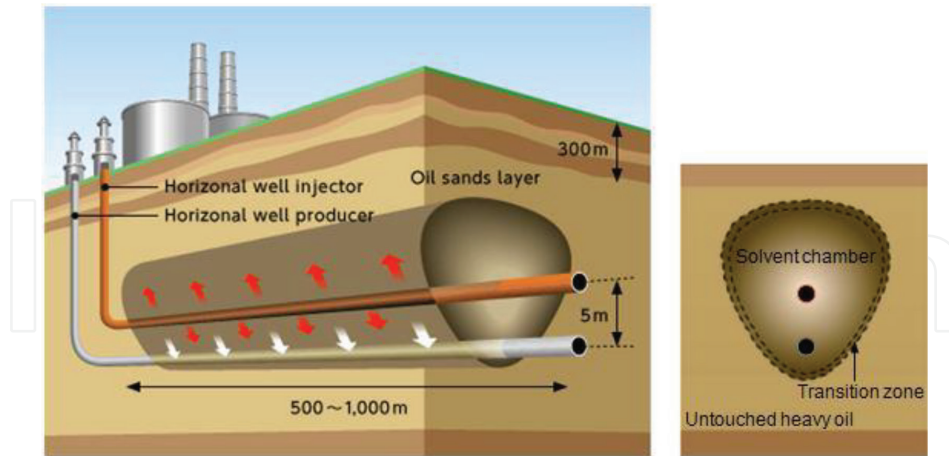
Figure 4. The VAPEX heavy oil recovery process [11].
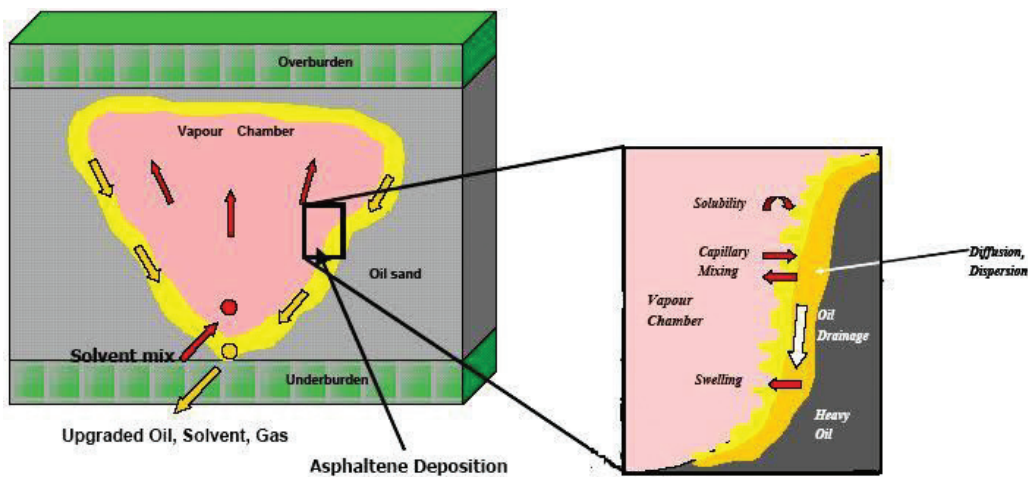
Figure 5. Mechanism involved in the VAPEX process [12].

such as steam-assisted gravity drainage (SAGD), cannot be applied. In the VAPEX process, a pair of horizontal injector-producer wells is employed. The gaseous hydrocarbon solvent (propane, butane, or a mixture of them) is injected into the deposit from the top well, and the diluted oil drains are gravitated downward to the bottom producing well. Recently, an attractive option was developed using CO_2 as a solvent in the VAPEX process. The high solubility and viscosity reduction potential of CO_2 could provide improvement to VAPEX performance. It also creates new opportunities for CO_2 sequestration [10].

Chemical methods include polymer floods, surfactant flooding, alkaline flooding, and so on. The mechanisms of chemical methods are dependent on the chemical materials added into the reservoir. The chemical methods may provide one or several effects: interfacial tension
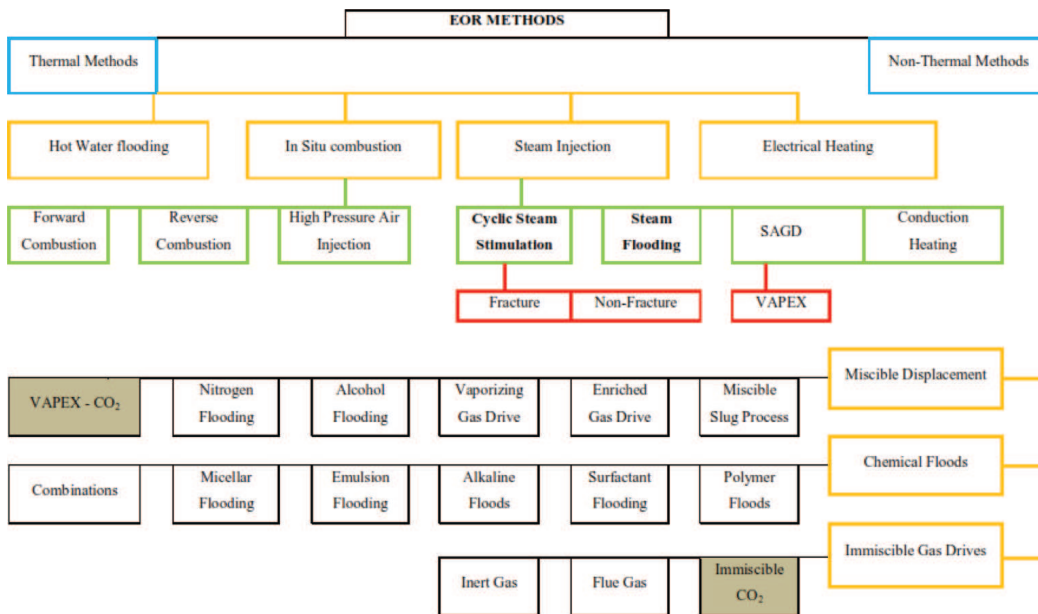
Figure 6. Classification of EOR methods.

reduction, viscosity reduction, wettability alteration, and mobility control. Meanwhile, there are many researchers on the background of EOR process; for a detailed review of enhanced oil recovery, we refer the interested reader to Thomas [7], and general classifications of these methods are shown in **Figure 6**.

5. Oil recovery by CO_2 injection

5.1. CO_2-EOR: definition and advantages

The combustion and flaring of fossil fuels produce large quantities of CO_2. The Intergovernmental Panel on Climate Change stresses the need to control anthropogenic greenhouse gases in order to mitigate the climate change that is adversely affecting the planet. Moreover, in some fields, the hydrocarbon gases produced along with the oil are re-injected into the reservoir to enhance oil production. Nevertheless, in some fields, the hydrocarbon gas is sold, and the gas itself is considered as a source of energy. An attractive option is the use of CO_2 as one of the main components of the solvent mixture for EOR process.

Enhanced oil recovery using CO_2 is an attractive oil recovery process that involves the injection of CO_2 to oil reservoirs and produce petroleum substances that would otherwise remain unrecoverable [13]. Typically, only around one-third of the oil is produced after primary and secondary oil recovery methods. Much of the remaining oil are trapped by capillary forces as disconnected drops, surrounded by water, or as a continuous phase at low saturation with gas occupying the larger fraction of the pore space. EOR operations

using carbon dioxide have been practiced for more than 50 years; the results revealed that 6–15% of original oil in place can be recovered by these kinds of processes [14].

The low saturation pressure of CO_2 compared to CH_4 or N_2 and its low price compared with other hydrocarbon solvents are the incentives for the use of CO_2 in the EOR process. Moreover, a mixture of hydrocarbon solvents with CO_2 may be less likely to precipitate asphaltene, which is a great problem in enhanced oil recovery [15]. Furthermore, at high pressures, CO_2 density has a density close to that of a liquid and is greater than that of either nitrogen (N_2) or methane (CH_4), which makes CO_2 less prone to gravity segregation compared with N_2 or CH_4 [16].

5.2. Oil recovery mechanisms by CO_2 dissolution

When CO_2 is injected into the reservoir, it interacts physically and chemically with rocks and fluids that are present in the reservoir, creating favorable mechanisms that can make enhancement in oil recovery. Among these mechanisms include a high dissolution of CO_2 into crude oil via mass transfer followed by the following aspects: an increase of oil density, a reduction of the viscosity of the original crude oil, vaporization of intermediate components of the oil, a reduction of CO_2-oil interfacial tension, oil swelling, a reduction of water–oil interfacial tension, and an improvement of reservoir permeability [17].

The main scenario followed by CO_2 sequestration is the mechanism of fluid density increasing caused by the dissolution and mixing of injected CO_2 into fluid. In the past, there are a set of studies that have not taken the effect of density increase from mixing into account; this mechanism in the modeling of CO_2 injection has been ignored [18–21]. However, as shown in other studies, this may not be true; CO_2 has an effect on the density of fluid that is present in the reservoir [22, 23]. Its dissolution and mixing leads to density increase followed by density-driven natural convection phenomena. There are several published studies which reported that this phenomenon has a significant enhancement in hydrocarbon recovery and sequestration potential [24–27].

5.3. Literature review on EOR/EGR-CO_2

CO_2 storage studies started almost two decades ago. Despite this fact, still vast areas of research have not been covered in detail in the area of coupled enhanced oil recovery with CO_2 sequestration [28].

DeRuiter et al. [22] studied the solubility and displacement of heavy crude oils with CO_2 injection; they have found that the oils exhibit an increase in density due to CO_2 solubility. The two samples in their study with API gravities of 18.5 and 14 exhibited an increase in density upon CO_2 dissolution.

Morel et al. [29] and Le Romancer et al. [30] studied the effects of diffusion of nitrogen (N_2) and CO_2 on light oil using an outcrop core system. During 2010, Jamili et al. [31] simulated these previous experiments. These authors reported that diffusion was the main mass transfer mechanism between the matrix and fracture during nitrogen (N_2) injection. On the other side, CO_2 experiments conducted have shown that both diffusion and convection were important mechanisms.

Mehrotra and Svrcek [32–34] during the 1980s reported extensive experimental data on the dissolution of carbon dioxide on different bitumen samples in Alberta reservoirs. Their experimental data confirm a higher solubility of carbon dioxide in bitumen, and they found that this solubility increases as the injection pressure increases.

Darvish et al. [35] performed a set of experiments of CO_2 injection in an outcrop chalk core saturated with oil and was surrounded by an artificial fracture at reservoir conditions. These authors observed the production of gas enriched with methane at an early stage. Next, the amount of intermediate components increased in the production stream, and during the end of the experiments, the heavier components were recovered. Their results were also confirmed by simulation study performed by Moortgat et al. [36].

Malik and Islam [37] conclude that in the Weyburn field of Canada, horizontal injection wells have showed to be efficient for CO_2-flooding process to improve oil recovery while increasing the CO_2 storage potential. Besides employing horizontal wells, Jessen et al. [38] have applied different well control techniques including completion equipment for both injection and production wells, at the same time improving the amount of injected and stored CO_2 as well as enhancing oil recovery.

Recently, Li-ping et al. [39] conducted an evaluation study around Ordos Basin in Yulin city of China; this Basin was divided into 17 reservoirs and is considered as the first largest low-permeability proliferous onshore basin in China with proved reserves more than 10^9 t. These authors conclude that Ordos Basin has good geographical and geological conditions for CO_2 storage, and it has nine reservoirs suitable for CO_2 immiscible flooding and eight reservoirs suitable for CO_2 miscible flooding. The average incremental oil recovery ratios for immiscible and miscible flooding are 6.44 and 12%, respectively.

The booming development and production of shale gas largely depend on the extensive application of water-based hydraulic fracturing treatments. Hence, high water consumption and formation damage are two issues associated with this procedure. More recently, Pei et al. [40] investigated the feasibility of using CO_2 for reservoir fracturing and enhanced gas recovery (EGR) in order to reduce water usage and resource degradation, guarantee the environmental sustainability of unconventional resource developments, and create new opportunity for CO_2 storage. This study shows that this proposed CO_2-EGR process was mostly like to be successful in the Barnett shale reservoir, but there are some scientific and engineering questions that need to be further investigated to push the proposed technology to be applicable in practice.

Song investigated the effect of operational schemes, reservoir types, and development parameters on both the amount of incremental oil produced and CO_2 stored in high water cut oil reservoirs during CO_2 water-alternating-gas (WAG) flooding by running a compositional numerical simulator. The author's study shows that the five-spot pattern is more suitable for WAG flooding. Appropriately expanding well spacing improves the economic efficiency, even though the recovery factor decreases slightly. In addition, oil price, rather than CO_2 injection cost, is considered as the parameter that impacts the economic efficiency of WAG flooding more significantly [41].

Er et al. [42] investigated the effect of injection flow rate of CO_2 on oil recovery using synthetic micro-scale fractured system saturated by normal decane (n-C_{10}). The authors concluded that

for immiscible CO_2 displacement, the amount of oil trapped in the system was reduced as well as increasing injection rates of carbon dioxide. They also observed that for miscible CO_2 conditions, higher CO_2 injection rates yielded faster oil recovery.

Coal bed methane is also tested for enhanced gas recovery and CO_2 storage; Blue Creek and Pocahontas are two fields of coal bed methane in USA. Pashin et al. [43] employed a diverse suite of well testing and monitoring procedures designed to determine the heterogeneity, capacity, injectivity, and performance of mature Blue Creek coal bed methane reservoirs. A total of 516 m³ of water and 252 t of CO_2 were injected into coal in a battery of slug tests. The author's results demonstrate that significant injectivity exists in this reservoir and that reservoir heterogeneity is a critical factor to consider when implementing CO_2-enhanced methane recovery programs. Based on the study by Grimm et al. [44], CO_2-CBM project can be conducted in the stratigraphic interval below the Hensley Shale where this confinement horizon is greater than 183 m below the surface and is above the level of hydraulic fracturing in CBM wells.

6. Conclusion

With the decline of oil production and apparition of global warming problem caused by excessive emission of carbon dioxide during the last decades, it is believed that EOR/EGR-CO_2 technologies will play a key role to meet the energy demand and better mitigation of climate change in the years to come. If we investigate at the great number of studies cited in this study, the subject of EOR-CO_2 is being very important. Several physical and chemical mechanisms are associated with CO_2 injection, and the most important mechanism is the dissolution of carbon dioxide into fluid formation. It has been accepted from previous studies that the dissolution of CO_2 increases fluid density, which results in a downward density-driven convection and consequently greatly enhances oil recovery and CO_2 potential sequestration.

Author details

Abdelmalek Atia[1]* and Kamal Mohammedi[2]

*Address all correspondence to: abdelmalek-atia@univ-eloued.dz

1 University of El Oued, Levres Lab, Algeria

2 MESOnexTeam-URMPE, UMBB, Algeria

References

[1] Maugeri L. Squeezing more oil from the ground. Scientific American. 2009;**301**:56-63

[2] Whitson CH, Brulé MR. Phase behavior. In: Henry L, editor. Doherty Memorial Fund of AIME. Society of Petroleum Engineers; Richardson Texas; 2000

[3] Metz B, Davidson O, de Coninck H, Loos M, Meyer L. Carbon dioxide capture and storage. IPCC Special; 2005

[4] Bielinski A. Numerical simulation of CO_2 sequestration in geological formations. Hydraulic Engineering Institute of Stuttgart University; 2007

[5] Nikoosokhan S. Stockage géologique du dioxyde de carbone dans les veines de charbon: du matériau au réservoir. Thèse de doctorat, Université Paris Est; 2012

[6] Griggs DJ, Noguer M. Climate change 2001: The scientific basis. Contribution of working group I to the third assessment report of the intergovernmental panel on climate change. Weather. 2002;**57**:267-269

[7] Thomas S. Enhanced oil recovery—An overview. Oil & Gas Science and Technology-Revue de l'IFP. 2008;**63**:9-19

[8] Liu S. Alkaline Surfactant Polymer Enhanced Oil Recovery Process. Vol. 69; Doctoral dissertation, Rice University; 2008

[9] Lake LW. Enhanced Oil Recovery. Prentice Hall. 1989;**1**(43):17-39

[10] Zadeh AB. Use of CO_2 in Vapex: Experimental and Modeling Study. Canada: University of Calgary; 2013

[11] Jia X. Enhanced Solvent Vapour Extraction Processes in Thin Heavy Oil Reservoirs. Canada: Faculty of Graduate Studies and Research, University of Regina; 2014

[12] Upreti S, Lohi A, Kapadia R, El-Haj R. Vapor extraction of heavy oil and bitumen: A review. Energy & Fuels. 2007;**21**:1562-1574

[13] Abedini A. Mechanisms of Oil Recovery During Cyclic CO2 Injection Process: Impact of Fluid Interactions, Operating Parameters, and Porous Medium. Canada: Faculty of Graduate Studies and Research, University of Regina; 2014

[14] Hustad C-W, Austell JM, Roggenkamp M, Hammer U. Mechanisms and incentives to promote the use and storage of CO_2 in the North Sea. In: European Energy Law Report I, Intersentia. 2004. pp. 355-380

[15] Javaheri M, Abedi J. The effect of heavy oil viscosity reduction by solvent dissolution on natural convection in the boundary layer of VAPEX. Transport in Porous Media. 2013;**99**: 307-326

[16] Bui LH. Near Miscible CO_2 Application to Improve Oil Recovery. USA: University of Kansas; 2010

[17] Klins MA. Carbon Dioxide Flooding: Basic Mechanisms and Project Design; U.S. Department of Energy; 1984

[18] Bangia V, Yau F, Hendricks G. Reservoir performance of a gravity-stable, vertical CO_2 miscible flood: Wolfcamp reef reservoir. Wellman unit. SPE Reservoir Engineering. 1993; **8**:261-269

[19] Cardenas RL, Alston R, Nute A, Kokolis G. Laboratory design of a gravity-stable miscible CO_2 process. Journal of Petroleum Technology. 1984;**36**:111-118

[20] Johnston J. Weeks Island gravity stable CO_2 pilot. In: SPE Enhanced Oil Recovery Symposium; 1988

[21] Palmer F, Nute A, Peterson R. Implementation of a gravity-stable miscible CO_2 flood in the 8000 foot sand, Bay St. Elaine Field. Journal of Petroleum Technology. 1984;**36**:101-110

[22] DeRuiter R, Nash L, Singletary M. Solubility and displacement behavior of a viscous crude with CO_2 and hydrocarbon gases. SPE Reservoir Engineering. 1994;**9**:101-106

[23] Ashcroft SJ, Isa MB. Effect of dissolved gases on the densities of hydrocarbons. Journal of Chemical & Engineering Data. 1997;**42**:1244-1248

[24] Atia A, Mohammedi K. Pore-scale study based on lattice Boltzmann method of density driven natural convection during CO_2 injection project. Chinese Journal of Chemical Engineering. 2015;**23**(10):1593-1602

[25] Farajzadeh R, Ranganathan P, Zitha PLJ, Bruining J. The effect of heterogeneity on the character of density driven natural convection of CO_2 overlying a brine layer. Advances in Water Resources. 2011;**34**:327-339

[26] Javaheri M, Abedi J. Modelling of mass transfer boundary layer instability in the CO-Vapex process. In: Canadian International Petroleum Conference; 2008

[27] Li Z, Dong M, Shirif E. Natural convection—An underlying mechanism in CO-VAPEX process. In: Canadian International Petroleum Conference; 2004

[28] Ghomian Y. Reservoir simulation studies for coupled CO_2 sequestration and enhanced Oil Recovery. Doctoral dissertation, Texas University; 2008

[29] Morel D, Bourbiaux B, Latil M, Thiebot B. Diffusion effects in gasflooded light-oil fractured reservoirs. SPE Advanced Technology Series. 1993;**1**:100-109

[30] Le Romancer J, Defives D, Kalaydjian F, Fernandes G. Influence of the diffusing gas on the mechanism of oil recovery by gas diffusion in fractured reservoir. In: IEA Collaborative Project on Enhanced Oil Recovery Workshop and Symposium; Bergen Norway; 1994. pp. 28-31

[31] Jamili A, Willhite GP, Green D. Modeling gas-phase mass transfer between fracture and matrix in naturally fractured reservoirs. SPE Journal. 2011;**16**:795-811

[32] Mehrotra AK, Svrcek WY. Correlations for properties of bitumen saturated with CO_2, CH_4 and N_2, and experiments with combustion gas mixtures. Journal of Canadian Petroleum Technology. 1982;**21**(6):94-104

[33] Mehrotra AK, Svrcek WY. Measurement and correlation of viscosity, density and gas solubility for Marguerite Lake bitumen saturated with carbon dioxide. AOSTRA Journal of Research. 1984;**1**:51-62

[34] Mehrotra A, Svrcek W. Viscosity, density and gas solubility data for oil sand bitumens: Part I: Athabasca bitumen saturated with CO and C_2H_6. AOSTRA Journal of Research. 1985; **1**:263-268

[35] Darvish GR, Utne SA, Holt T, Kleppe J, Lindeberg E. Reservoir conditions laboratory experiments of CO2 injection into fractured cores (SPE99650). In: 68th EAGE Conference & Exhibition; 2006

[36] Moortgat J, Firoozabadi A, Farshi MM. A new approach to compositional modeling of CO2 injection in fractured media compared to experimental data. In: SPE Annual Technical Conference and Exhibition; 2009

[37] Malik QM, Islam M. CO_2 injection in the Weyburn field of Canada: Optimization of enhanced oil recovery and greenhouse gas storage with horizontal wells. In: SPE/DOE Improved Oil Recovery Symposium; 2000

[38] Jessen K, Kovscek AR, Orr FM. Increasing CO_2 storage in oil recovery. Energy Conversion and Management. 2005;**46**:293-311

[39] Li-ping H, Ping-ping S, Xn-wei L, Qi-Chao G, Cheng-sheng W, Fangfang L. Study on CO_2 EOR and its geological sequestration potential in oil field around Yulin city. Journal of Petroleum Science and Engineering. 2015;**134**:199-204

[40] Pei P, Ling K, He J, Liu Z. Shale gas reservoir treatment by a CO_2-based technology. Journal of Natural Gas Science and Engineering. 2015;**26**:1595-1606

[41] Song Z, Li Z, Wei M, Lai F, Bai B. Sensitivity analysis of water-alternating-CO_2 flooding for enhanced oil recovery in high water cut oil reservoirs. Computers & Fluids. 2014;**99**: 93-103

[42] Er V, Babadagli T, Xu Z. Pore-scale investigation of the matrix− fracture interaction during CO_2 injection in naturally fractured oil reservoirs. Energy & Fuels. 2009;**24**:1421-1430

[43] Pashin JC, Clark PE, McIntyre-Redden MR, Carroll RE, Esposito RA, Oudinot AY, et al. SECARB CO_2 injection test in mature coalbed methane reservoirs of the Black Warrior Basin, Blue Creek Field, Alabama. International Journal of Coal Geology. 2015;**144**:71-87

[44] Grimm RP, Eriksson KA, Ripepi N, Eble C, Greb SF. Seal evaluation and confinement screening criteria for beneficial carbon dioxide storage with enhanced coal bed methane recovery in the Pocahontas Basin, Virginia. International Journal of Coal Geology. 2012;**90**:110-125

Compressive strength of dune sand reinforced concrete

Mani Mohammed, Kriker Abdelouahed, and Belferrag Allaoua

Compressive Strength of Dune Sand Reinforced Concrete

Mani Mohammed [1, a)], Kriker Abdelouahed [1, b)] and Belferrag Allaoua [1, c)]

[1]University KASDI Merbah of Ouargla,Laboratory of Exploitation and Valorization of Natural Resources in Arid Areas (E.V.R.N.Z.A.), Ouargla 30000, Algeria

a) m.mani39@gmail.com
b)a_kriker@yahoo.fr
c) belallaoua67@yahoo.fr

Abstract. Many areas of south Algeria suffer from the problem of accumulation of sand on constructions. In fact, the phenomenon of sand silting causes technical and economical problems. Besides, these areas and other regions in Algeria suffer from the problem of unavailability of suitable sand for building. The use of dune sand offers an alternative solution for construction. In the same context, many researches confirm the possibility of using dune sand in the composition of concrete. In this paper, concrete made with dune sand was studied. For correction of the granulometry of dune sand by river sand, the rates of 50% DS + 50% RS and 40% DS + 60% RS were used. Also, two types of fibers were used, with 45 and 30 mm lengths, and diameters of 1 and 0.5 mm respectively. The percentage of the used fibers in the sand concrete was 1% and 1.5%. In this work an improvement of the compressive strength for the metal fibers reinforced sand concrete compared to plain concrete was obtained.

INTRODUCTION

Generally the Saharan areas suffer from the silting phenomenon in particular on basic infrastructures, causing economic and environmental damages.

The lack of construction sand especially in Saharan areas has a negative impact on the sand cost. Thereby, the abundance of dune sand in south of Algeria can contribute to solving this problem. Several researches were realized, studying concrete with normalized sand and dune sand. Many of them [1-4]revealed that dune sand present a low fineness modulus. For this, a granulometric correction of dune sand is necessary.

Several studies have shown the improvement of the compressive strength of the metal fibers reinforced concrete compared to the plain concrete[5-7]. In the same context Ramli and Thanon Dawood[8] concluded that the use of the steel fiber increases the compressive strength and that the best improvement is obtained when the steel fiber is 1.25% of the mortar mix. This is due according to the authors, to the mechanical bond between the cement paste and the steel fiber. Also Yazici et al.[9]attest that theusage of steel fiber in concrete increases the compressive strength of concrete by about 4 to19%.

The aim of this work is to inspect the effects of granulometric correction of dune sand and metal fibers incorporation in dune sand concrete.

MATERIALS

Sand

Two type of sand were used in this work, dune sand (DS) and river sand (RS) extracted from deposits located in Ouargla (South Algeria). Table 1 presents physical proprieties of sands used.

TABLE 1. Physical properties of sands used.

Type	Absorption (%)	Sand equivalent (SE) (%)	Fineness modulus (FM) (%)	Specific density (kg/m³)	Apparent density (kg/m³)
Dune sand	0.086 ± 0.003	98% ± 0.26	1.07 ± 0.01	2612 ± 3.60	1521 ± 6.60
River sand	0.080 ± 0.003	83% ± 0.55	2.80 ± 0.20	2608 ± 3.25	1668 ± 5.60
50% RS + 50% DS	0.083 ± 0.002	85% ± 0.45	2.08 ± 0.05	2610 ± 9.60	1594 ± 5.60
60% RS + 40% DS	0.082 ± 0.002	87% ± 0.33	2.25 ± 0.09	2610 ± 5.80	1609 ± 7.30

Cement

The used cement is a CPJ CEM II / A 42.5 from Ain Touta Algeria. The results of experience on this type of cement are given according to technical card [10] as shown in the Table 2.

TABLE 2. Physical result tests on used cement [10].

Specific density (kg/m3)	Apparent density (kg/m3	Primary hardening (min)	Final hardening (min)
3034	2120	128	184

Fiber

The used fibers were industrial metal fibers (Granitex). Two different metal fiber types were selected: corrugated fiber (F1), and hooked ends fiber (F2) (Fig.1).

The above mentioned fibre types have lengths of 45 and 30 mm, diameters of 1.0 and 0.5 mm and aspect ratios of 45 and 60 respectively for F1 and F2.

The properties of the selected metal fibres, used for the mixtures, are shown in Table 3.

(a)	(b)

FIGURE 1. Used metal fibers. (a): F1 Corrugated metal fibers, (b): F2 Hooked ends metal fibers.

TABLE 3. Physical and mechanical properties of used fibers [11].

Fibers	Length (mm)	Diameter (mm)	Tensile strength (MPa)
F1	45	1	1100-800
F2	30	0.5	600-800

SAND CONCRETE FORMULATION

For the formulation of plain concrete and metal fiber reinforced sand concrete, the proportions for a standardized mortar were used according to EN 196. In other word, one part of cement, three parts of sand for all the mixtures with and without fibers. For the determination of the amount of water LCPC maniabilimeter was used [12, 13].

TABLE 4. Mixtures proportions (1 m³).

Mixtures	Fibers (%)	W/C	Fibers (kg)	Water (l)	Cement (kg)	Sand(kg)
100% DS	0.00	0.60	-	276.52	460.86	1382.61
	1.00	0.60	78.50	271.30	452.16	1356.49
	1.50	0.60	117.75	268.68	471.81	1343.43
50% DS+50%RS	0.00	0.55	-	255.27	464.13	1392.39
	1.00	0.55	78.50	250.48	455.43	1366.29
	1.50	0.55	117.75	248.09	451.08	1353.24
40% DS+60%RS	0.00	0.55	-	255.27	464.13	1392.39
	1.00	0.55	78.50	250.48	455.43	1366.29
	1.50	0.55	117.75	248.09	451.08	1353.24

MECHANICAL TESTING

Compressive strength of sand concrete was measured according to the standard EN 196-1. The rupture in compression of the specimens was realized according to the device shown in Fig.1, six specimens were used for each testing by using the following equation:

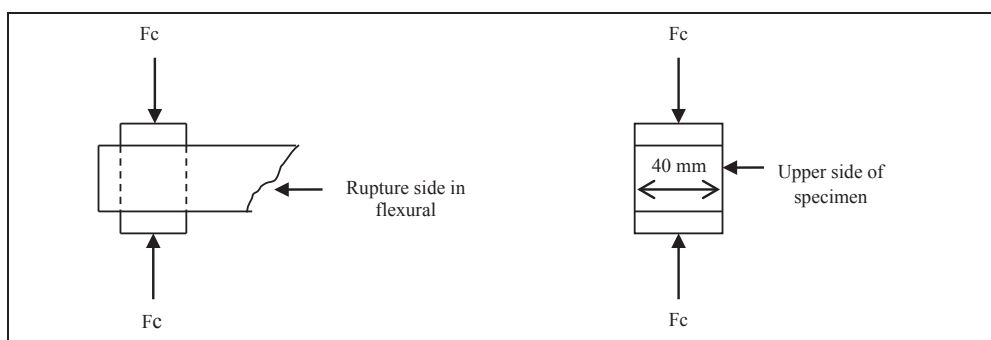**FIGURE 2.** Device of rupture in compression.

$$Rc = \frac{F_c}{b^2}$$

(1)

Rc: compressive strength (MPa)
F_c : load of rupture (N)
b^2 : cross-sectional area (b = 40 mm)

RESULTS AND DISCUSSION

Effect of Granulometric Correction

Figure 3 shows the results of the compressive strength of plain concretes made with various sands 100% DS, 50% DS + 50% RS and 40% DS + 60% RS.
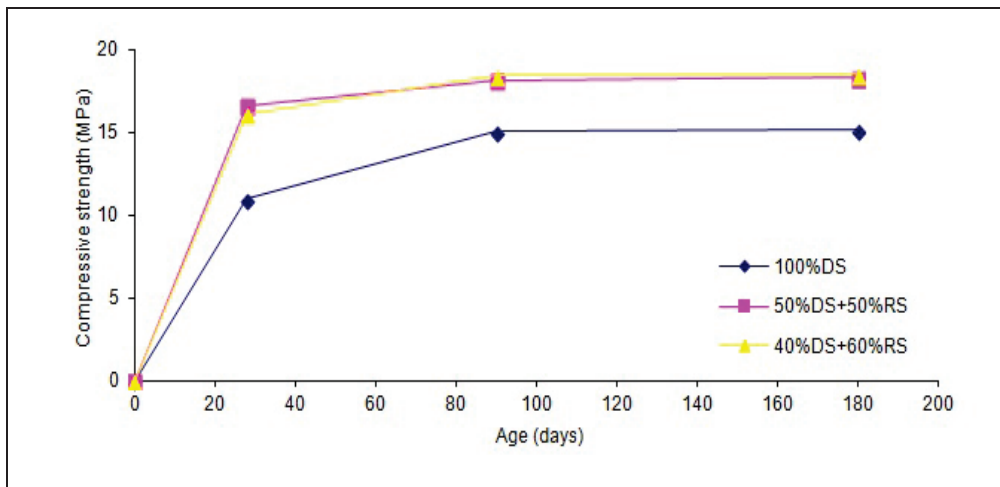
FIGURE 3. Compressive strength of plain concretes as a function of age.

The effect of the granulometric correction on the compressive strength of concretes is given in Fig. 3. These results show that there is an increase in the compressive strength of concretes made with proportions 50% DS + 50% RS and 40% DS + 60% RS compared to plain concrete made with 100% dune sand. This increase in compressive strength was respectively of 20.51% and 21.89%. It is due to the correction of dune sand granulometry by river sand having a fineness modulus of 2.8.

Effect of Metal Fibers

Figure 4 indicates the results of the compressive strength of metal fiber reinforced sand concrete of fiber volume fraction 1% of F1.
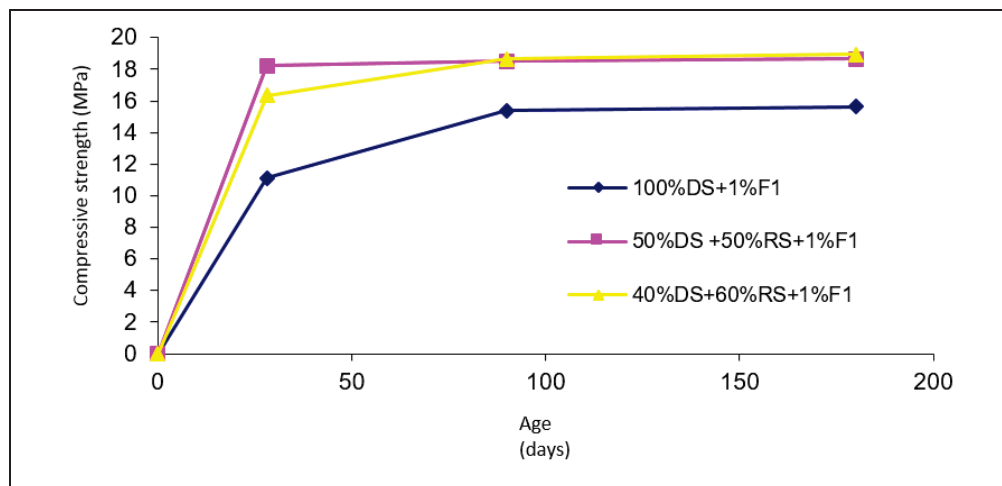
FIGURE 4. Compressive strength of reinforced concrete as a function of age (1% F1).

Figure 5 shows the compressive strength of metal fiber reinforced sand concrete of fiber volume fractions 1.5% (F1).
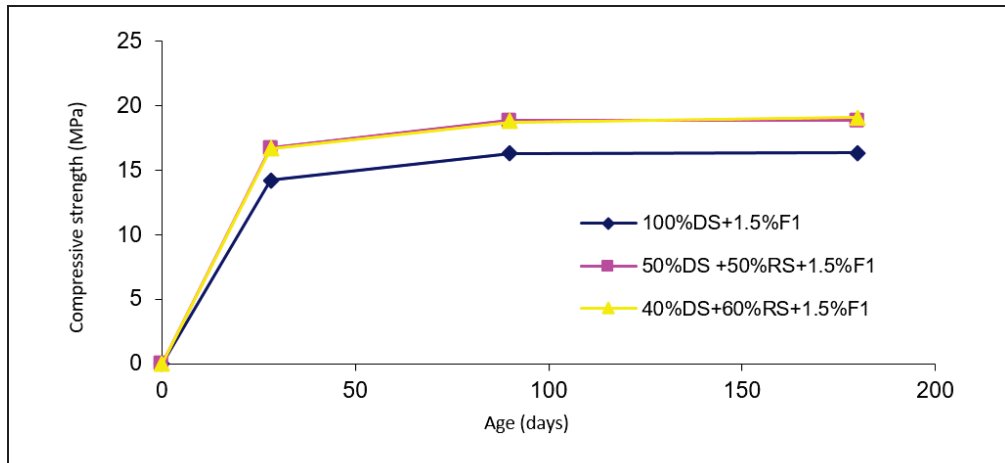
FIGURE 5. Compressive strength of reinforced concrete as a function of age (1.5% F1).

Figure 6 shows the compressive strength of metal fiber reinforced sand concrete of fiber volume fractions 1.5% (F2).
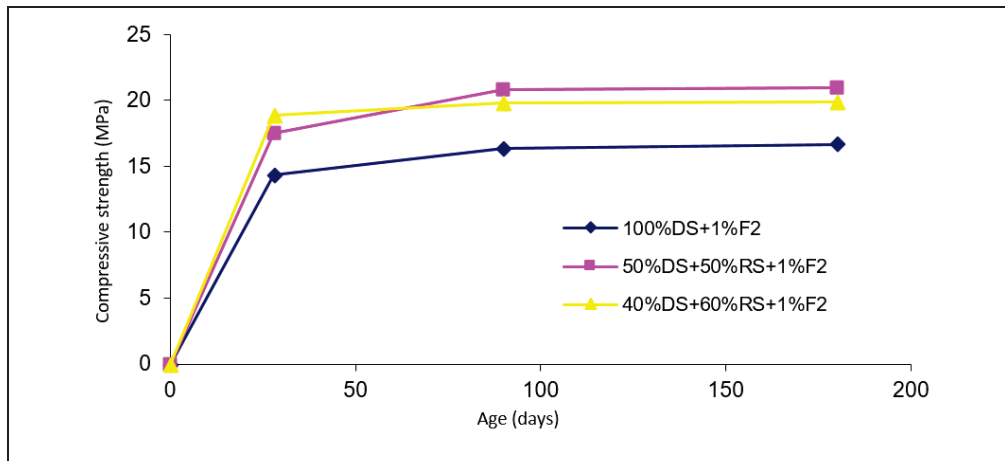
FIGURE 6. Compressive strength of reinforced concrete as a function of age (1% F2).

Figure 7 shows the compressive strength of metal fiber reinforced sand concrete of fiber volume fractions 1.5% (F2).
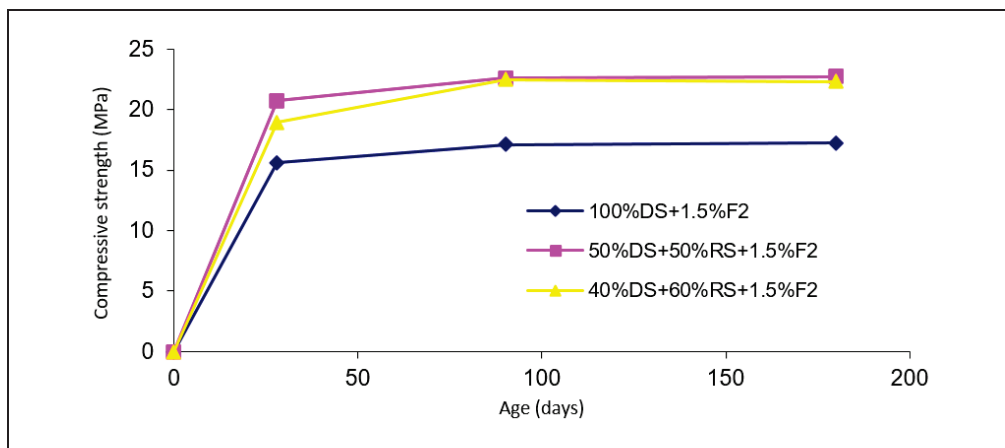
FIGURE 7. Compressive strength of reinforced concrete as a function of age (1.5% F2).

The results shown in Figs. 4, 5, 6 and 7 indicate that the metal fiber reinforced sand concretes made with dune sand and river sand (50% DS + 50% RS and 40% DS + 60% RS), have the best compressive strength compared to metal fiber reinforced dune sand concrete with fiber volume fraction of 1% and 1.5%. However, the difference of the compressive strength of concretes prepared with (50% DS + 50% RS) and those of (40% DS + 60% RS) is insignificant for all mixtures with and without fibers.

Figure 8 indicates the compressive strength of metal fiber reinforced dune sand concrete (100% DS) of fiber volume fractions 1% and 1.5% (F1 and F2).
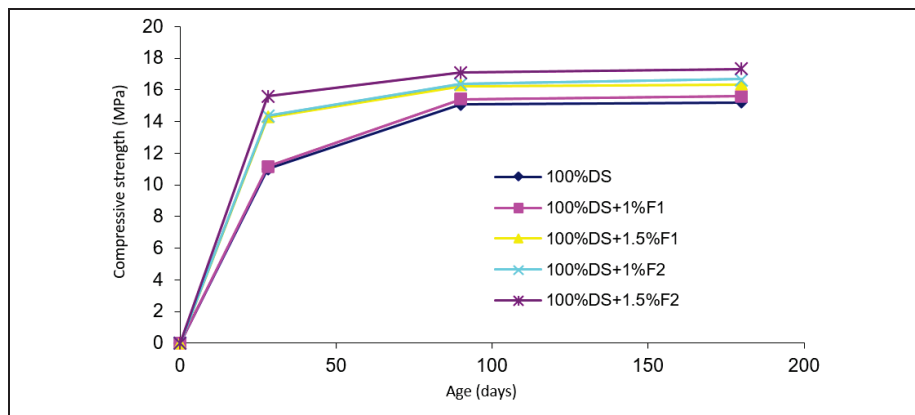
FIGURE 8. Compressive strength of reinforced concrete as a function of age for mixtures made with 100% DS (F1+F2).

According to the experimental results shown in Fig. 8, an increase in the compressive strength of metal fiber reinforced dune sand concretes was obtained compared to the plain concrete. This improvement is significant especially for the concretes reinforced by fibers F2 having length of 30 mm and a diameter of 0.5 mm with fiber volume fraction of 1% and 1.5%. This increase is respectively of 9.6% and 13.6%. For the reinforced concretes made with fibers F1 (lf = 45 mm, df = 1 mm), an improvement in compressive strength of 2.76% and 7.5% was obtained respectively with volume fraction of 1% and 1.5%. The best result of dune sand concrete was obtained by the mixture made with fiber F2 and a fiber volume fraction of 1.5%.

Figure 9 shows the compressive strength of metal fiber reinforced sand concrete (50% DS + 50% RS) of fiber volume fractions 1% and 1.5% (F1 and F2).

FIGURE 9. Compressive strength of reinforced concrete as a function of age for mixtures made with 50% DS+50% RS (F1+F2).

Figure10 shows the compressive strength of metal fiber reinforced sand concrete (40% DS + 60% RS) of fiber volume fractions 1% and 1.5% (F1 and F2).

FIGURE 10. Compressive strength of reinforced concrete as a function of age for mixtures made with 40% DS+60% RS (F1+F2).

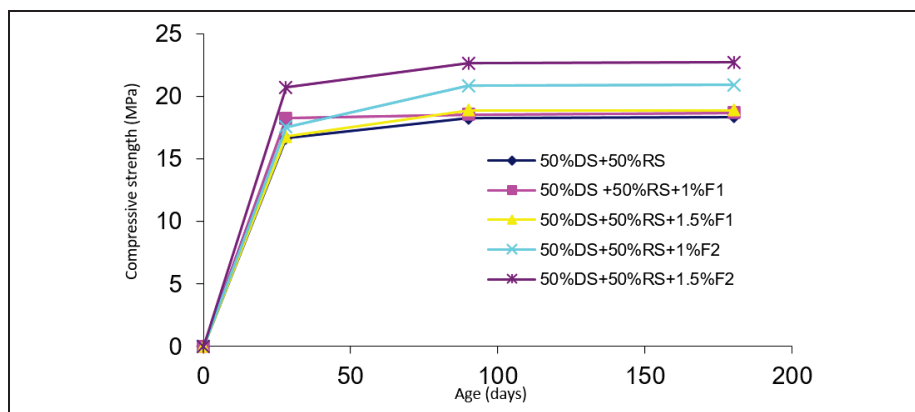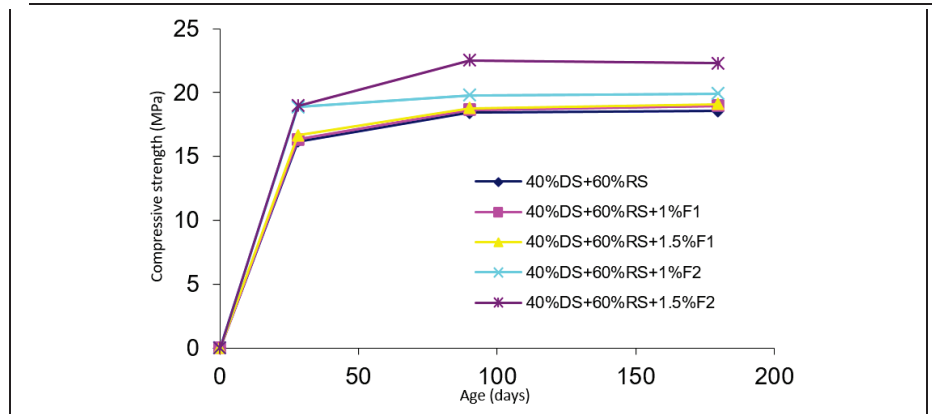Figures 9 and 10 show the results of compressive strength of the concretes made with the proportions 50% DS + 50% RS and 40% DS + 60% RS reinforced by metal fibers F1 and F2. An improvement in the compressive strength of all mixtures reinforced with metal fibers compared to the plain concrete was obtained. Same as that of the dune sand concrete, the best result was obtained by the mixtures made with fibers F2 and fiber volume fraction of 1.5%.

Several authors attest that the reinforcement of concrete with metal fibers improves the compressive strength with increase of fiber volume fraction. Indeed, Belferrag et al.[3] concluded that the mixtures having a fiber volume of 1.5%, presented a better improvement of the compressive strength compared to those of 1%. In the same context, Ait Tahar[6] found that improvement in compressive strength with fiber volume fractions of 1%, 2% and 3% is respectively of 21.7%, 39% and 52% compared to plain concrete.

ECONOMIC BENEFITS

The use of dune sand in the confection of concrete reduces the needed quantity of river sand with an amount ranging between 40% and 50%. It can also reduce the phenomenon of desertification.

CONCLUSION

Based on the experimental results, the following conclusions can be drawn:

- Improvement of compressive strength of concretes made with 50% DS + 50% RS and 40% DS + 60% RS was observed compared to plain concrete (100% DS);
- The addition of metal fibers F1 and F2, improves compressive strength of sand concrete;
- The increase of fiber volume fraction in sand concrete, improves compressive strength;
- The best result of compressive strength was obtained for the mixtures, made with fiber F2 and volume fraction of 1.5%;
- Improvement of compressive strength is affected by the type of fiber.

REFERENCES

1. A. Tafraoui, "Contribution à la valorisation du sable de dune de l'erg occidental (Algérie). Application aux nouveaux bétons, " Ph.D. thesis, University of Toulouse France, 2009.
2. S. El Euch Khay, A. Neji and J. Loulizi, Shrinkage properties of compacted sand concrete used in pavements, Constr. Build. Mater. **24**, 1790–1795 (2010).
3. A. Belferrag, A. Kriker and M.E. Khenfer, Improvement of the compressive strength of mortar in the arid climates by valorization of dune sand and pneumatic waste metal fibers, Constr. Build. Mater. **40**, 847–853 (2013).
4. A. Belferrag, A. Kriker, S. Abboudi and S. Tié-Bi, Effect of granulometric correction of dune sand and pneumatic waste metal fibers on shrinkage of concrete in arid climates, J. Clean. Prod. **112**, 3048–3056 (2016).

5. R. D. Neves and J.C.O. de Almeida, Compressive behavior of steel fiber reinforced concrete, Struct.Concr. **6** (2005).

6. K. Ait-Tahar, Mode de rupture par flexion des poutres composites en béton de fibres, Annales du Bâtiment et des Travaux Publics **4** (2001).

7. K. Holschemacher, T. Mueller and Y. Ribakov, Effect of steel fibres on mechanical properties of high-strength concrete, Mater. Design. **31**, 2604–2615 (2010).

8. M. Ramli and E. Thanon Dawood, High-strength flowable mortar reinforced by steel fiber, SJCE. XIX, 10–16 (2011).

9. Yazıcı S., Inan G. and Tabak V., Effect of aspect ratio and volume fraction of steel fiber on the mechanical properties of SFRC, Constr. Build. Mater. **21**, 1250–1253 (2007).

10. fiche technique de cimenterie Ain-touta ; Algeria 2003.

11. Fiche de qualité "Fibres de renforcement", SIKA, Egypte, 2003.

12. O. Emile, Technologie des matériaux de construction (Entreprise Moderne d'Edition, Paris, 1978).

13. A. Kriker, G. Debicki , A. Bali, M.M. Khenfer and M. Chabanni, Mechanical properties of date palm fibres and concrete reinforced with date palm fibres in hot-dry climate, Cement Concrete Comp. **27**, 554–564 (2005).

Research Article

CONTRIBUTION TO THE EXPERIMENTAL STUDY OF THE HYDRAULIC JUMP IN TRAPEZOIDAL CHANNEL WITH POSITIVE SLOPE

A. Ghomri[*,1,2], F. Riguet[1,2], S. Khechana[2]

[1]Laboratoire de Recherche en Hydraulique Souterraine et de Surface, Université Biskra
[2]Laboratoire d'exploitation et de valorisation des ressources energétiques sahariènnes, université d'El Oued

ABSTRACT

The purpose of this study is to study experimentally the hydraulic jump evolving in a symmetric trapezoidal channel with a positive slope, requires the use of an experimental protocol, and to find experimental relations linking the characteristics of the formed projection. The experimental study investigated the variation of the relative height $S = s / h_1$ of the threshold as a function of the Froude F1 number of the incident flow, for five distinct values of the slope of the channel.

Keywords : Hydraulic jump, trapezoidal channel, damping basin, trapezoidal channel with positive slope, suddenly varied flow.

---

1. INTRODUCTION

L'étude du ressaut hydraulique évoluant dans un canal trapézoïdal symétrique à un angle d'ouverture de 72,68° à pente positive, nécessite l'utilisation d'un protocole expérimental, afin d'estimer d'une part le coefficient de correction k évoqué dans l'étude théorique, et d'autre part de trouver des relations

empiriques liant les caractéristiques que l'on ne peut évaluer théoriquement.

Dans cette présente recherche nous allons aborder d'abord la description des essais effectués pour cette étude. Nous décrirons en premier lieu le protocole expérimental, constitué du canal trapézoïdal, des appareils et instruments utilisés pour la mesure des caractéristiques du ressaut hydraulique.

Nous passerons à la procédure expérimentale suivie par des essais en second lieu,et en dernier lieu nous exposerons enfin les résultats obtenus.

1.2. PROTOCOLE EXPERIMENTAL

Le canal de mesures (figure 1 et photo 1) qui nous a servi de banc d'essai est de section trapézoïdale, il est constitué essentiellement par une structure métallique rigide, sur laquelle est fixé latéralement, des deux cotés une série de 6 panneaux transparents en plexiglas permettant les   prises de vue et observations. Ces panneaux sont reliés entre eux par collage au silicone. L'étanchéité est assurée par des joints en caoutchouc et par le silicone. Un vérin manuel est utilisé pour varier la pente du canal (photo 5).

Le banc d'essais est constitué d'un grand canal rectangulaire dans lequel est inséré un canal de mesure de section trapézoïdale, caractérisé par une largeur de base 20cm, de longueur 6m et un angle d'inclinaison des parois latérales de 72,68° ; relier à un bassin d'accumulation par le moyen d'une conduite circulaire de 115 mm de diamètre. Celle-ci est reliée à une boite métallique fermée (photo 2), sur laquelle est insérée une ouverture en tôle de section trapézoïdale (photo 3) débouchant dans le canal. Le rôle de ce dernier est de générer un écoulement incident à grande vitesse. La section de sortie de celle-ci est variable et sa hauteur correspondra à la hauteur initiale h_1 du ressaut.L'ensemble fonctionne en circuit fermé dans lequel et insérée une pompe axiale (photo 4) débitant jusqu'à 44 l/s.

Le réglage des débits volumes s'effectue par manipulation de la vanne et sont mesurés à l'aide d'un débitmètre à affichage numérique (voir photographies cidessous).

Fig.1. Schéma simplifié du canal de mesure de section trapézoïdale, ayant servi à l'expérimentation**.**

Photo 1: Photographie du canal de mesure utilisé.

Photo 2: Photographie de la boite en charge.   Photo 3: Photographie d'une série de convergent

Photo 4**:** Photographie d'une Pompe centrifuge   Photo 5: Photographie d'un vérin manuel

Photo6: Photographie de la série de seuil   Photo7: convertisseur du débitmètre électromagnétique

Photo 8: écran d'affichage des débits

1.3. Description des essais

L'étude expérimentale s'est intéressée au ressaut hydraulique contrôlé par seuil mince dans un canal trapézoïdal à pente positive. Les caractéristiques étudiées sont: le débit volume Q, la hauteur initiale h_1, mesurée au pied de ressaut, la hauteur finale h_2, mesurée au droit de la longueur du rouleau, la hauteur s du seuil, l'angle d'inclinaison α du canal par rapport à l'horizontale, la longueur Lr du rouleau, mesurée à la fin de la formation du ressaut et la longueur Lj du ressaut, mesurée dans le même endroit de la hauteur finale h_2.

Celles-ci sont formulées sous forme adimensionnelle pour composer les rapports suivants: le nombre de Froude F_1 de l'écoulement incident, le rapport $Y = h_2/h_1$ des hauteurs conjuguées du ressaut, la hauteur relative $S = s/h_1$ du seuil, la longueur relative $\lambda j = Lj/h_1$ du ressaut, et le coefficient de forme du canal $M = mh_1/b$.

L'expérimentation a été menée sous cinq hauteurs initiales : h_1 (mm) = 20 ; 30 ; 40 ; 50 et 60mm. Pour chaque hauteur h_1 choisie, on donne au canal cinq positions d'inclinaison d'angle α correspondant chacune a une valeur bien déterminée de la pente positive, de sorte que la tangente de l'angle d'inclinaison α par rapport à l'horizontale, prend les valeurs suivantes (en %) : 0 ; 0,5 ; 1 ; 1,5 et 2. Une gamme assez pratique de nombres de Froude incident a été

ainsi obtenue: $1 < F_1 < 14$.

Des seuils de différentes hauteurs's' ont été testés (photo 6), afin d'observer leur influence sur le contrôle du ressaut; vingt-sept seuils ont ainsi été confectionnés, dont la hauteur s varie entre 3 cm et 26 cm.

Pour une hauteur h_1 et pour une hauteur s et une position x du seuil de l'écoulement incident, l'augmentation du débit volume Q, provoque l'apparition d'un ressaut.

Le couple de valeur (Q, h_1) permet le calcul du nombre de Froude F_1 de l'écoulement incident. L'accroissement de F_1 entraîne à la fois le déplacement du ressaut vers l'aval ainsi l'augmentation de sa longueur du rouleau Lr et du ressaut Lj. La distance Δx sur laquelle le ressaut s'étend augmente également et pour ramener le pied de celui-ci dans sa position initiale, c'est à dire à environ 5 cm de la sortie du convergent, la hauteur s du seuil situé à l'extrémité aval du canal doit être augmenté. Ainsi à chaque valeur du nombre de Froude F_1 correspondent une valeur de la longueur Lj du ressaut et une valeur de la hauteur s du seuil.

Les photos 9 et 10 illustrent deux configurations typiques de ressaut contrôlé par seuil mince en canal trapézoïdale symétrique, respectivement à pente nulle et incliné d'un angle α par rapport à l'horizontal, pour la même hauteur initiale h_1 = 30mm et à débit volume croissant.

Figure 2: Schéma simplifier d'un ressaut hydraulique évoluant dans un canal à pente positive

Photo 9:Photographie d'un ressaut hydraulique   photo10:Photographie d'un ressaut hydraulique

Contrôlé à pente nulle F_1 =6, 63; s =7 cm;   contrôlé à pente positive F_1 =8, 96;
Lj =110 cm; h_2 =13,7 cm ; tang(α)=0   s =17cm; Lj =164 cm h_2 =20,8 cm ; tang(α)=0,01

Pour obtenir les résultats expérimentaux, nous avons suivis les étapes suivantes:

Mesure de l'angle d'inclinaison α par rapport à l'horizontal;

Mesure de la longueur Lr du rouleau;

Mesure de la longueur Lj du ressaut;

Mesure de la hauteur géométrique s du seuil;

Mesure de la hauteur conjuguée aval h_2 du ressaut;

Mesure du débit volume ;

$$F_1 = \sqrt{\frac{Q^2[b(1+2M)]}{g[bh_1(1+M)]^3}}$$

Calcul du nombre de Froude F_1 de l'écoulement incident, par application de la relation

2. RESULTS ET DISCUSSION

Les figures (3-7) montrent la variation de la hauteur relative s/h_1 du seuil en fonction du nombre de Froude F_1, pour cinq angles d'inclinaison α distincts, tels que :tang (α) = 0.00, 0.005, 0.01, 0.015, 0.02.
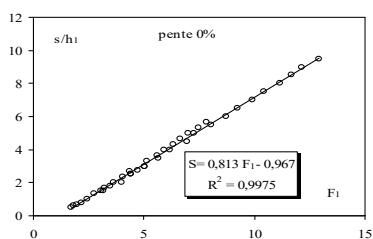
Figure 3 : Variation du rapport s/h_1 en function du nombre de Froude F_1,pour tang(α) = 0. o) points expérimentaux (—) Courbes d'ajustement
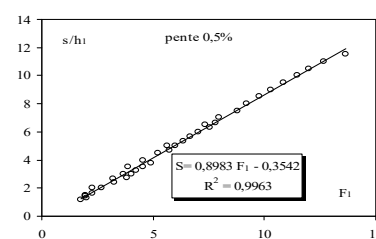
Figure 4: Variation du rapport s/h_1 en fonction du nombre de Froude F_1,pour tang(α) =0,005 o) points expérimentaux (—) Courbes d'ajustement
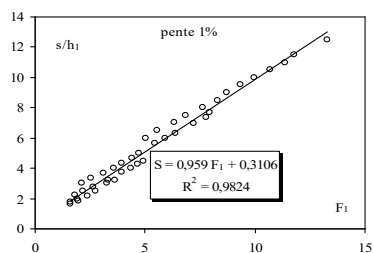
Figure 5: Variation du rapport s/h_1 en fonction du nombre de Froude F_1, pour tang(α) = 0,01. (o) Points expérimentaux (—) Courbesd'ajustement
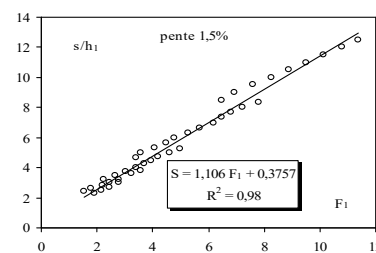
Figure 6 : Variation du rapport s/h_1 en fonction du nombre de Froude F_1, pour tang (α) = 0,015.(o) Points Expérimentaux (—) Courbes d'ajustement
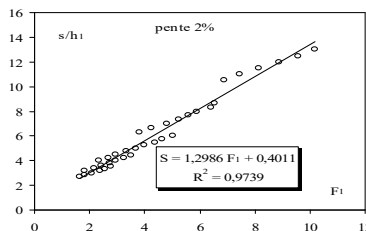
Figure 7 : Variation du rapport s/h_1 en fonction
du nombre de Froude F_1, pour $\tan(\alpha) = 0,02$.
(o) points expérimentaux ;   (—) Courbes d'ajustement

Selon les figures(3-7), l'ajustement des mesures expérimentales a montré que la   variation du rapport s/h_1 en fonction du nombre de   Froude F_1 de l'écoulement incident suit une loi de type   linéaire de la   forme $s/h_1 = a (F_1) + b$.

Le tableau 1 représente les paramètres a et b pour les cinq valeurs de pente considérées.

Tableau 1 : Valeurs des paramètres a et b .

Ce tableau montre clairement que les paramètres a et b sont fonction de la pente du canal et augmente progressivement avec l'augmentation de $\tan(\alpha)$.

Les figures 8 et 9 montre l'ajustement statistique des couples de valeurs (a, $\tan(\alpha)$) et (b, $\tan(\alpha)$) par la méthode des moindre carrés.

Tableau 1 : Valeurs des paramètres a et b .

tang (α)	a	b
0,000	0,81	-0,97
0,005	0,89	-0,35
0,010	0,96	-
0,015	1,11	0,38
0,020	1,30	0,40
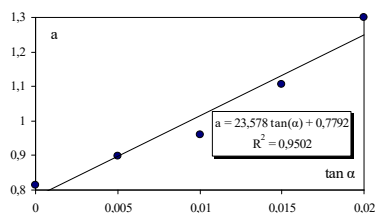
Figure 8 : Variation du paramètre 'a' en fonction de $\tan(\alpha)$.
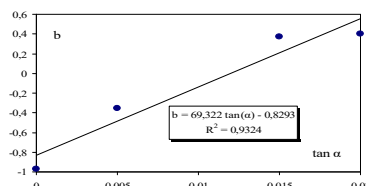
Figure 9 : Variation du paramètre 'b' en fonction de $\tan(\alpha)$.
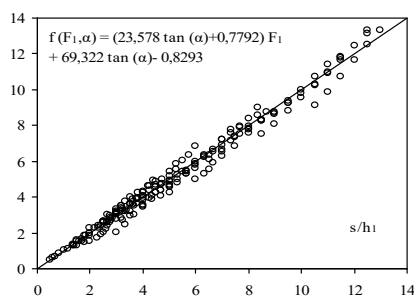
Figure 10. Variation de la relation $f(F_1, \alpha)$ en fonction de la hauteur relative s/h_1 du seuil. (o) Points expérimentaux. (—) Première bissectrice d'équation: $f(F_1, \alpha) = s/h_1$.

La figure 10 montre que les points se répartissent de manière quasi uniforme autour de la première bissectrice.

Les figures 8 et 9 montrent clairement que la variation de a et de b en fonction de la pente (tang(α)) du canal suit une loi linéaire pour les deux paramètres, selon les relations suivantes:

$\quad$ a=23,578 tang (α) + 0,7792 ; $\qquad$ (1)

$\quad$ b=69,322 tang (α) - 0,8293; $\qquad$ (2)

En remplaçant les paramètres a et b par leurs expressions respectives dans la relation $s/h_1 = a(F_1) + b$ on obtient la relation générale : **$s/h_1 = (23{,}578\ \text{tang}\ (\alpha) + 0{,}7792)\ F_1 + 69{,}322\ \text{tang}\ (\alpha) - 0{,}829$** $\qquad$ **(3)**

$\qquad$ **avec $\quad 1{,}52 < F_1 < 13{,}64 ; \qquad 0 \leq \text{tang}\ (\alpha) \leq 0.02$**

La figure 10 confirme que la relation (3) représente un assez bon ajustement pour la détermination de la hauteur relative s/h_1 du seuil, connaissant le nombre de Froude incident F_1, et l'inclinaison (α) du canal.

3. CONCLUSION

Cette présente recherche a été consacrée à l'étude expérimentale du ressaut hydraulique dans un canal de section droite trapézoïdal à pente positive variable. Nous avons décrit dans un premier temps, le modèle physique qui nous a servi de banc d'essai, ainsi que les instruments et l'appareillage utilisé pour la mesure des caractéristiques du ressaut hydraulique, moyennant quelques schémas et des photographies. Dans un second temps, nous avons expliqué la procédure expérimentale suivie pendant les essais. Passant en troisième temps aux résultats expérimentaux, cinq (05) hauteurs initiales h1 ont été testées vingt (20) seuils s de hauteurs différentes et cinq (05) inclinaisons du canal par rapport à l'horizontale. Une large gamme des nombres de Froude incidents a été ainsi obtenue. L'étude expérimentale s'est intéressée, à la

variation de la hauteur relative S = s/h$_1$ du seuil en fonction du nombre de Froude F$_1$ de l'écoulement incident, pour cinq valeurs distinctes de la pente du canal. Cinq nuages de points distincts, correspondant chacun à une valeur bien déterminée de la pente du canal. L'ajustement des mesures expérimentales a montré que la variation du rapport S en fonction du nombre de Froude F$_1$ de l'écoulement incident suit une loi de type linéaire de la forme s/h$_1$= a (F$_1$) + b, régissant le ressaut hydraulique qui s'évolue en canal trapezoidal à pente posirive.

5. REFERENCES

[1] Achour, B., Debabeche, M., (2003), Ressaut contrôlé par seuil dans un canal profilé en U, J. Hydraulic Research, vol. 41, N0.3,pp.319-325.

[2] Achour, B., Debabeche, M., (2003), Control of Hydraulic jump by sill in a triangular channel, J. Hydraulic Research, Vol. 41, No. 3, pp. 97-103

[3] Anderson, V., M. (1978). Undular hydraulic jump, Proc., ASCE, J. Hydraulic Division, Vol. 104(HY8), pp. 1185-1188, discussion 1979, 105 (HY9), 1208-1211, 1980,106(HY7), 1252-1254.

[4] Debabeche, M., (2003), Le ressaut hydraulique dans les canaux prismatiques, Doctorat d'état, Département d'Hydraulique, Université de Biskra.

[5] Debabeche, M., (2008), Les écoulements brusquement variés, cours de 1ère année magister, polycopié, Université de Biskra.

[6] Debabeche, M., Achour, B., Effect of sill in the hydraulic jump in a triangular channel, J. Hydraulic Research Vol. 45, No. 1, (2007), pp. 135–139.

[7] Debabeche, M., Cherhabil, S., Hafnaoui, A. et Achour, B. (2009), Hydraulic jump in a sloped triangular channel, Can. J. Civ; Eng. 36: 2009, 655-658

[8] Ghomri, A., Debabeche, M., Riguet, F., Etude semi théorique du ressaut hydraulique évoluant en canal profilé en U, à fond rugueux, Revues des sciences fondamentales et appliquées, centre universitaire d'Oued Souf, N° 1 , 2009, pp. 41-56.

[9] Ghomri, A., Debabeche, M., Riguet, F., Etude expéimentale du ressaut hydraulique évoluant dans un canal en U à fond rugueux, Revues des sciences fondamentales et appliquées, centre universitaire d'Oued Souf, N° 1 , 2009, pp.80-103.

[10] Ghomri, A., Riguet, F. , Debabeche, M. Riguet, F, Journal of Fundamental and Applied Sciences, Université Hamma Lakhdar El Oued, N° 4(2) , 2012, pp.1-15.

[11] Hager, W.H., Wanoschek, R (1989), Hudraulic jump in trapezoidal channel, J. hydraulic research, Vol. 27, 1989, N.3.

Failure of a Vertical Drainage System Installed to Fight the Rise of Groundwater in El-Oued Valley (SE Algeria): Causes and Proposed Solutions

5 authors, including:

Salim Khechana
université d'El Oued
17 PUBLICATIONS   20 CITATIONS

SEE PROFILE

Abdelmonem Miloudi
El-Oued University
6 PUBLICATIONS   3 CITATIONS

SEE PROFILE

Ali Ghomri
El-Oued University
13 PUBLICATIONS   7 CITATIONS

SEE PROFILE

El Habib Guedda
El-Oued University
25 PUBLICATIONS   14 CITATIONS

SEE PROFILE

Some of the authors of this publication are also working on these related projects:

Call for Papers: The 1st IEEE International Conference on Communications, Control Systems and Signal Processing CCSSP 2020 View project

effect of electron energy distribution on atomic data View project

Failure of a Vertical Drainage System Installed to Fight the Rise of Groundwater in El-Oued Valley (SE Algeria): Causes and Proposed Solutions

Salim Khechana, Abdelmonem Miloudi, Ali Ghomri, El Habib Guedda & El-Fadel Derradji

🐎 Springer

Springer

CrossMark

TECHNICAL ARTICLE—PEER-REVIEWED

Failure of a Vertical Drainage System Installed to Fight the Rise of Groundwater in El-Oued Valley (SE Algeria): Causes and Proposed Solutions
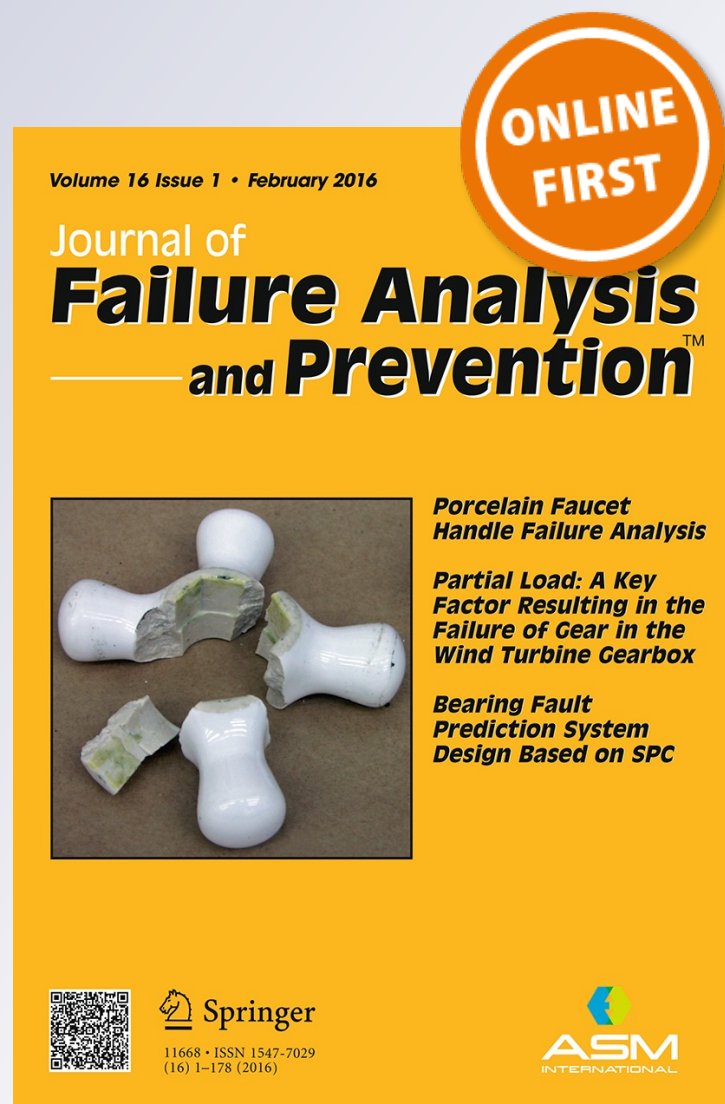
Salim Khechana · Abdelmonem Miloudi · Ali Ghomri · El Habib Guedda · El-Fadel Derradji

Abstract El-Oued Valley suffers from the problem of rising groundwater which affects agricultural and urban areas and degrades all aspects of the socioeconomic life of its inhabitants. This problem, which appeared in the 1980s, is primarily a result of overexploitation of deep groundwater, lack of sanitation network, and discharge of wastewater directly into the unconfined aquifer. To solve this problem, a megaproject was carried out, based on the principle of sewerage, to drain and evacuate excess water after treatment to a discharge site 70 km north of the region. In this project, the blade of groundwater above elevation of 60 m should be drained through wells of a vertical drainage system. However, the expected results have not been achieved in most affected cities, where the groundwater level continues to rise. Herein, we propose a solution to this problem, based on a new explanation of the hydrogeological structure of the unconfined aquifer that drives the rising groundwater to the surface. The main part of this research is based on interpretation of well tests carried out in wells of the vertical drainage system.

Keywords El-Oued Valley · Rising groundwater · Unconfined aquifer · Vertical drainage system · Hydrogeological structure · Well tests

S. Khechana (✉) · A. Miloudi · A. Ghomri · E. H. Guedda
Faculty of Sciences and Technology, El-Oued University, P.O.B 789, 39000 El-Oued, Algeria
e-mail: khechana-salim@univ-eloued.dz

E.-F. Derradji
Laboratory of Geology, Badji Mokhtar University, P.O.B 12, 23000 Annaba, Algeria
e-mail: derradji_d@yahoo.fr

Introduction

Groundwater is an important source of fresh water for humans, animals, and plants on Earth [1]. Unfortunately, several Algerian regions, especially those located in the Sahara, today face problems related to quantitative and qualitative aspects of water resources, mainly due to rising groundwater from aquifers, which is harmful to agriculture and habitats [2]. This problem has negative consequences for the environment and health, as shown by Photos 1 and 2 [3].

To date, hydrogeological studies analyzing this rising groundwater phenomenon have assumed that the aquifer is homogeneous and formed only by sands characterized by high hydraulic conductivity [4]. However, in reality, the aquifer is heterogeneous, consisting of layers of clay, marl, and gypsum.

The failure to account for such heterogeneity has led to misinterpretation of pumping test results, in turn influencing the design of well tubes and the position of their screens.

This paper reports new understanding on the rising groundwater phenomenon in El-Oued Valley, based on analysis of well test data, which indicates that the unconfined aquifer is composed of two layers, probably separated by lenses of clay and sometimes sandy clay.

Methods and Materials

Geological and Hydrogeological Data of Study Area

The study zone is located in southeast Algeria (Fig. 1), in the center of a large synclinal basin; it is known as low Sahara because of its low altitude. It occupies an area of

Photo 1 Backfilling of rising groundwater by home waste—degradation of urban area and impact on inhabitants in terms of health and environment due to contamination

Photo 2 Groundwater rising to the surface in agriculture area—reeds replace dead palm trees, leading to a decrease in agricultural output
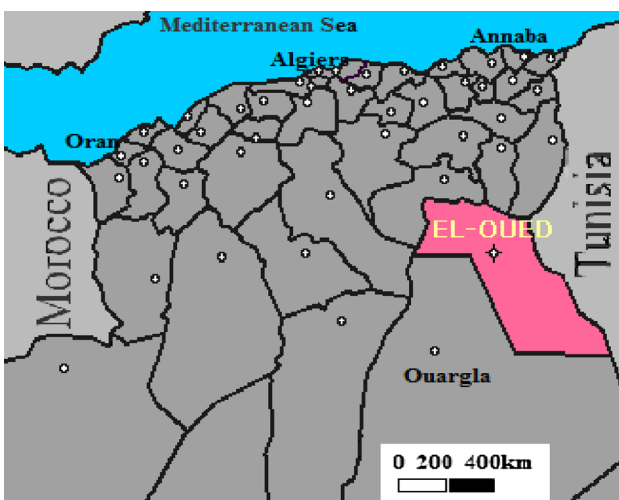
Fig. 1 Location of study area (Wilaya of El-Oued)

11,738 km^2 and includes over 500,000 inhabitants. It is bounded by the following Lambert coordinates system [5]:

- $X = 275,200/322,000$
- $Y = 3,665,000/3,743,000$

The geology of the El-Oued region has not been extensively studied by researchers, and not in sufficient detail to understand the internal structure of superficial layers. A review of all existing geological work is summarized in Cretenet's report [5]. Figure 2 shows a geological cross-section (AB in geological card) established by the National Agency of Water Resources [6].

All geological cross-sections carried out by the Direction of Water Resources (DWR) based on logs from deep boreholes pay little attention to the surface layers and do not have sufficient accuracy to determine the basis of the unconfined aquifer [7]. Close to the study area, the depth of clay and gypsum layers is greater than 60 m (Fig. 3).

Geophysical prospecting (by electrical soundings) along line CD with length of 500 m was carried out by the National Company of Geophysics (NCG) in the region, showing that there are three distinct fields [8]:

- Sands and gravels with high resistivity
- Clayey sands and sandy clay with intermediate resistivity
- Clay with low resistivity

The clay depth in Oued-Souf varies between 10 and 100 m, and the thickness of the unconfined aquifer ranges between 0 and 60 m [9].

Causes of Rising Groundwater

One can summarize two causes of the rising groundwater:

(a) *Overexploitation of deep aquifers (Pontian and Albian aquifer).* Before 1980, the water balance of groundwater was in equilibrium and advocated by all users. The problem emerged in the early 1980s following growing water demand by different (domestic, agricultural, and industrial) users, requiring use of deep aquifers characterized by high flows (approximately 200 l/s for the Pontian aquifer and 400 l/s for the Albian aquifer).

(b) *The sanitation systems applied (septic tanks or cesspools).* Before completion of this project, the area was devoid of a sewerage system; the majority of residents used traditional systems for evacuating wastewater, allowing sewage infiltration into the water table. Use of nonstandardized tanks is a

principal cause of the rising groundwater, because of their numbers and the incredible amount of water they carry directly into the water table.

Consequences of Rising Groundwater

The implications of rising groundwater are diverse:

(a) *On the economy*. Rising water often causes pollution that causes the death of thousands of palm trees, which symbolize the wealth of the region (Photo 2), being the main source of livelihood for the people of El-Oued. This situation causes abandonment of oases, and even farming activities by individuals. Owners are forced to look for another source of livelihood, and large cities are often their main

destinations, leading to other social problems such as rising unemployment rates and the demand for housing and education.

(b) *On public health and the environment*. These impacts are even more harmful because they alter human life and the natural wealth of the region (hydric and landscape). Some residents take advantage of the degraded state of flooded areas, using them to reject their domestic waste. These flooded areas have therefore unfortunately been transformed into "dustbins" and have become a source of harm that threatens citizens and harms their quality of life (Photo 2), due to the proliferation of mosquitoes and the spread of unwanted odors from polluted water and garbage, especially when burned.

(c) *On habitat*. Rising groundwater has caused the destruction of several houses.

Solutions Implemented to Solve the Problem of Rising Groundwater

El-Oued Valley has a very important reservoir of groundwater, in the form of three aquifers: the unconfined aquifer and two confined deep aquifers [10]. Table 1 summarizes the aquifer systems in the region [11].

Many efforts have been made to fight the rising groundwater, the most important among them being a megaproject named "sewerage of wastewater and drainage of residual, rainfall, and irrigation water in El-Oued Valley," planned and funded by the Ministry of Water Resources and implemented by national and international companies.

Fig. 2 Geological map of study area (extract from map of northern Sahara, G. Busson 1970)

Fig. 3 Geological cross-section extracted from lithological logs of drills [6]
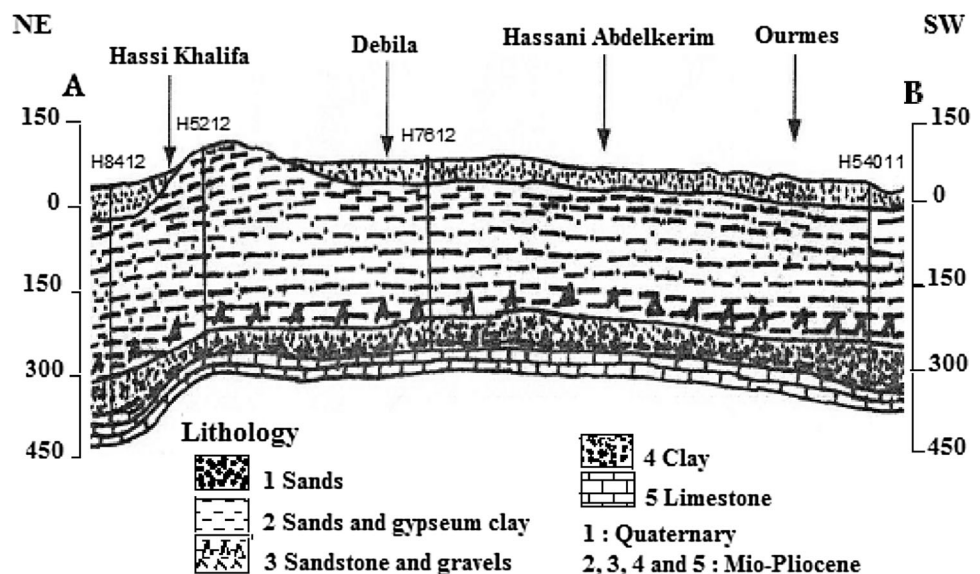
Table 1 Aquifer systems in El-Oued Valley

Hydrogeological nature	Lithological nature	Stage		Era
Unconfined aquifer	Sands	Quaternary		
Impermeable Layer	Clay			
Pontian aquifer				
1st layer of sand	Sands	Pliocene		Tertiary
Semipermeable layer	Gypsum clay			
2nd layer of sand	Sands, gravels	Pontian	Miocene	
Impermeable layer	Clay, lagoonal marls	Middle	Eocene	
Limestone aquifer (permeable)	Limestone cracked	Less		
		Cretaceous (Senonian)	Cretaceous	Secondary carbonate
Semipermeable	Evaporites, clays	Lagoon Senonian		
Impermeable layer	Clay, marl	Cenomanian		
Albian aquifer	Sands and sandstone	Albian		

A general overview of this project is presented in Fig. 4, indicating that it is essentially based on four plans [12]:

Sewerage Plan

Before inception of this project, there was no sewerage network in the region. Two types of wastewater collection are used: a sewerage system with a network of 750 km and a self-cleaning system.

Purification Plan

Four purification stations have been proposed in the region. The treatment type chosen is airy lagoon.

Evacuation Plan

All treated wastewater with drainage water will be forwarded through a transfer collector, oriented south–north to 70 km north of the valley.

Drainage Plan

The proposed drainage scheme is a vertical drainage system composed of a network of 58 wells, connected to 34 km of pipes and having depths between 21 and 40 m (Fig. 5). The wells are equipped with submersible pumps and can extract 6 l/s at a separation of 500 m; the drained water is led to the existing pumping station (ST10), from where it is sent on for final discharge (70 km to the north of the region).

Depending on the water balance, the excess water is estimated at 22,185 l/day [4]. The objective of this system is to drain this excess, such that the water table is at 1 m depth in the lowest area (Chott and Sidi-Mestour Cities), to ensure self-sewerage and increase the purifying power of soil.

Each drainage well contains, from bottom to top, 2 m of full tube, 8 m of strainer (screen), with the rest of the well being a full tube (with length depending on the topographic level of the well) so that the bottom of all drains is at an elevation of 48 m (Fig. 5).

Failure of Existing Drainage System

After 2 years of operation, the expected results of the vertical drainage system have not been achieved, with groundwater continuing to rise in the same cities, while the flow rates of some drains are very low.

The management of the drainage project lacked a tool to understand the cause of the failure of the vertical drainage system in most cities affected by this phenomenon (Chott and Sidi-Mestour Cities). To address this, we performed well tests in three drains of the vertical drainage system.

Description of Well Tests

Accurate analysis of well tests carried out in the unconfined aquifer in the El-Oued region is considerably hindered by difficulties in describing the internal structure of this reserve with precision [4, 10]. The spatial distribution of the various domains that are heterogeneous and have different permeability frequently seems strongly unpredictable, if not totally random [10]. However, knowledge of such structures is needed to determine the flow path in different zones and understand whether there are tight limits or imposed flow [13].

To determine the limits of the unconfined aquifer and whether there are anomalies in the internal structures of the ground, we carried out well tests of the drainage system

Fig. 4 Representation of project "sewerage of wastewater and drainage of residual, rainfall, and irrigation water in El-Oued Valley"

PUST : Purification Station
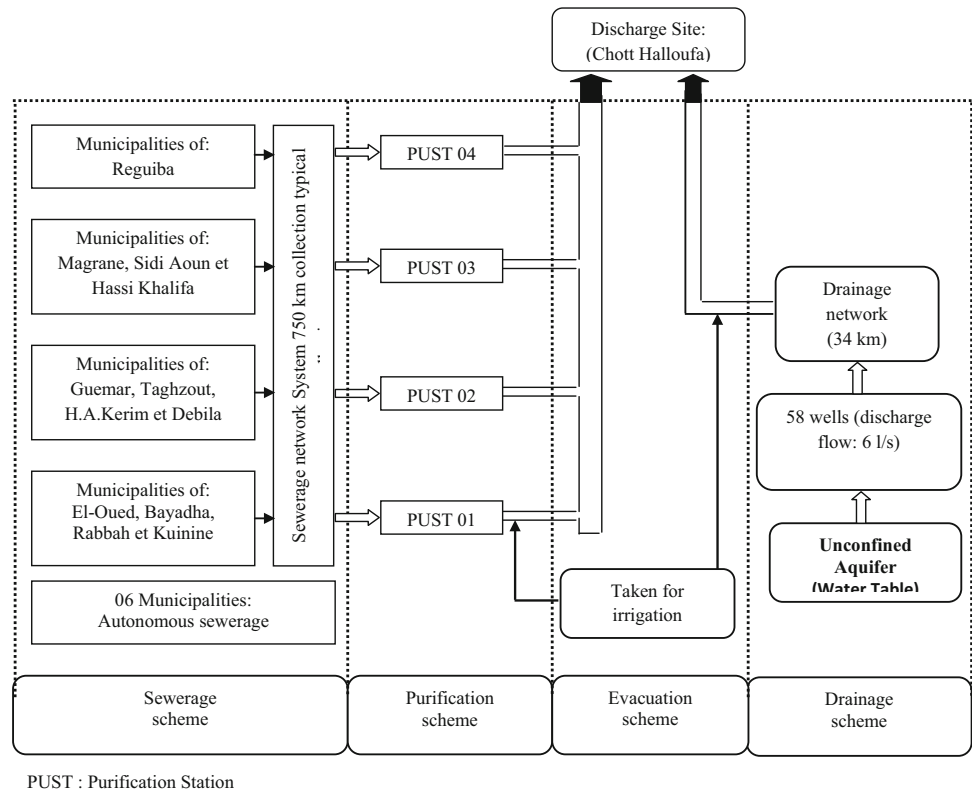
(D05, D20, and D53) in the winter of 2014 with duration of 24 h, recovery time of 12 h, and pumping rates of 2.8, 2.5, and 5.10 l/s, respectively. We chose these drains because of their low rates (less than 6 l/s) measured at the end of the drilling operation and their locations in the cities most affected by the problem of rising groundwater.

The response of the hydraulic head to the pumping was observed at the same drains and at two sumps (SD5 and SD20) in the vicinity of D5 and D20 (Fig. 6). After the 24 h of the well test, we proceeded to pump in the sumps (SD5 and SD20), using an emerged pump, while the depth of water was observed in the nearby well (D5 and D20).

The descent and ascent curves during the well tests are shown in Fig. 7.

Variation of Piezometric Levels

At the beginning of pumping, the water level in the pumping wells fell rapidly [14].

At well D05, the static water level was 1.34 m and the pumping rate was 2.8 l/s. The drawdown reached over 6.5 m after 3 min of pumping and 6.96 m after 1440 min (24 h). The water level at well D05 thus showed an immediate response to pumping, with fast drawdown in a reduced time (3 min), after which the drawdown reached only 0.51 m in the remaining pumping time. Two minutes after stopping pumping, the water level had risen rapidly

up to 6.5 m, after which it showed a steady increase with time.

At a distance of 12 m from drain D05, sump SD05 was used as an observation point. The response of the hydraulic head in SD05 was very slow, and the water level had decreased by only 1–2 cm even after 4 h since pumping had started.

During pumping in sump SD05, we did not record any change in the water level of well D05.

At well D20, the static water level was 0.35 m and the pumping rate was 2.5 l/s. The drawdown reached over 11.70 m after 7 min of pumping and 12.61 m after 1440 min (24 h). The water level at well D20 showed an immediate response to pumping with fast drawdown in a reduced time, after which the drawdown showed a steady increase with time (reaching 0.91 m in the remaining pumping time). Five minutes after stopping pumping, the water level had risen rapidly up to 6.28 m, after which it showed a steady increase with time.

At a distance of 17 m from well D20, sump SD20 was used as an observation point. The response in SD20 was very slow too, with only 1–3 cm of drawdown being recorded even after 4 h since the start of pumping.

During the pumping in sump SD20, we also did not record any change in the water level of drain D20.

At well D53, the static water level was 7.10 m and the pumping rate was 5.10 l/s. Drawdown reached over 7 m

Fig. 5 Plan of existing vertical drainage network
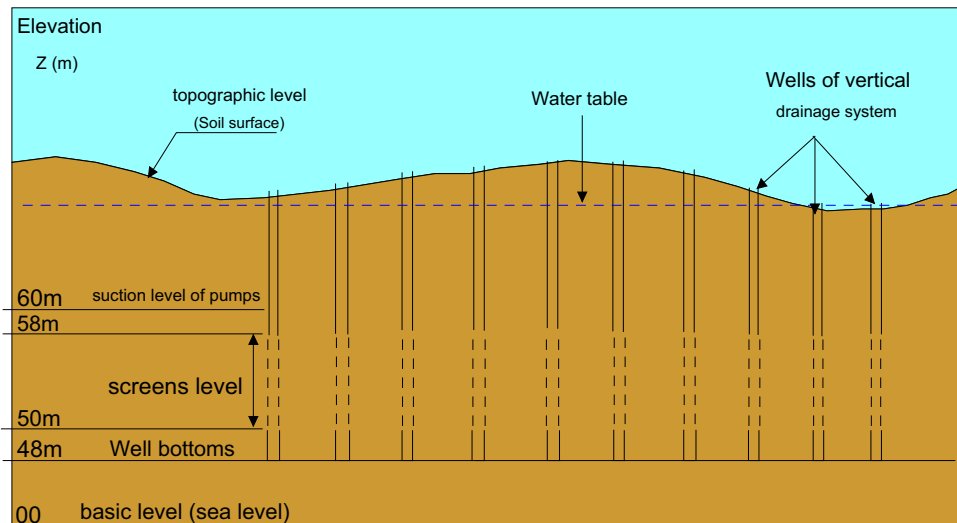
after 3 min of pumping and 7.47 m after 1440 min (24 h). The water level at well D53 thus showed an immediate response to pumping with fast drawdown in a reduced time (3 min), after which the drawdown showed a steady increase with time (reaching only 0.51 m in the remaining pumping time). Two minutes after stopping pumping, the water level had risen rapidly up to 7.75 m, then the residual drawdown showed a decrease with time.

Discussion and Interpretation of Results

One can divide the curves of the well tests into two parts:

- *The descent curve*. This curve shows two phases:

The first results from the effect of the well capacity, characterizing the aquifer–well couple and yielding an empty well without the water aquifer [15].

The second part of the curve is a steady increase in the drawdown versus time [16], which allows us to draw a line of slope C that reflects the presence of an unlimited aquifer [13].

According to Theis [17], the transmissivity T can be calculated as

$$T = \frac{0.183Q}{C},$$

where Q is the pumping rate (l/s) and C is the slope of the drawdown line.

After numerical calculation, we found that:

At well D05, $Q = 3$ l/s and $C_{05} = 4.2$, yielding $T = 0.183Q/C_{05} = 2.18 \times 10^{-4}$ m²/s.
At well D20, $Q = 2.5$ l/s and $C_{20} = 4$, yielding $T = 0.183Q/C_{20} = 1.14 \times 10^{-4}$ m²/s.
At well D53, $Q = 5.10$ l/s and $C_{53} = 3.9$, yielding $T = 0.183Q/C_{53} = 2.39 \times 10^{-4}$ m²/s.

- The increasing curve shows two distinct phases:

A first phase in which a rapid rise of water level is observed due to the phenomenon of postproduction and the recovery of the hydraulic head in the pumping well [18].

A second phase, in which the steady increase in the water level indicates a normal rise in the water table, where the residual drawdown is [17]

$$s' = \frac{Q}{4\pi T} \times \log\left(\frac{t + t'}{t'}\right) \;\Rightarrow\; s' = \frac{Q}{4\pi S} \times \log\left(1 + \frac{t}{t'}\right).$$

When analyzing the recovery data, the drawdown $(h_0 - h)$ is referred to as the residual drawdown (s') and is expressed as the difference between the original water level before the start of pumping and the water level measured at a time (t') after the cessation of pumping [19]. Recovery data were transformed according to the following equation:

$$T = \frac{Q}{4\pi C}.$$

It is generally known that the transmissivity or hydraulic conductivity as estimated from well tests is much lower than obtained from pumping tests [20]. In pumping tests carried out in 2002 by the National Sanitation Office (NSO), the values of transmissivity were between 1.54×10^{-3} m²/s at the northern site and 8.3×10^{-3} m²/s at the southern site. The average transmissivity was 3.77×10^{-3} m²/s [4].

The water level in the sumps did not change during pumping in the wells, and likewise pumping in the sumps did not show any influence on the groundwater level in the drainage wells, despite the small distance between them (12 or 17 m). This confirms the existence of a sealed limit separating the two aquifers [13]: the first aquifer is below, providing water pumped from the drainage wells, while the second lies on top, containing the water that appears in
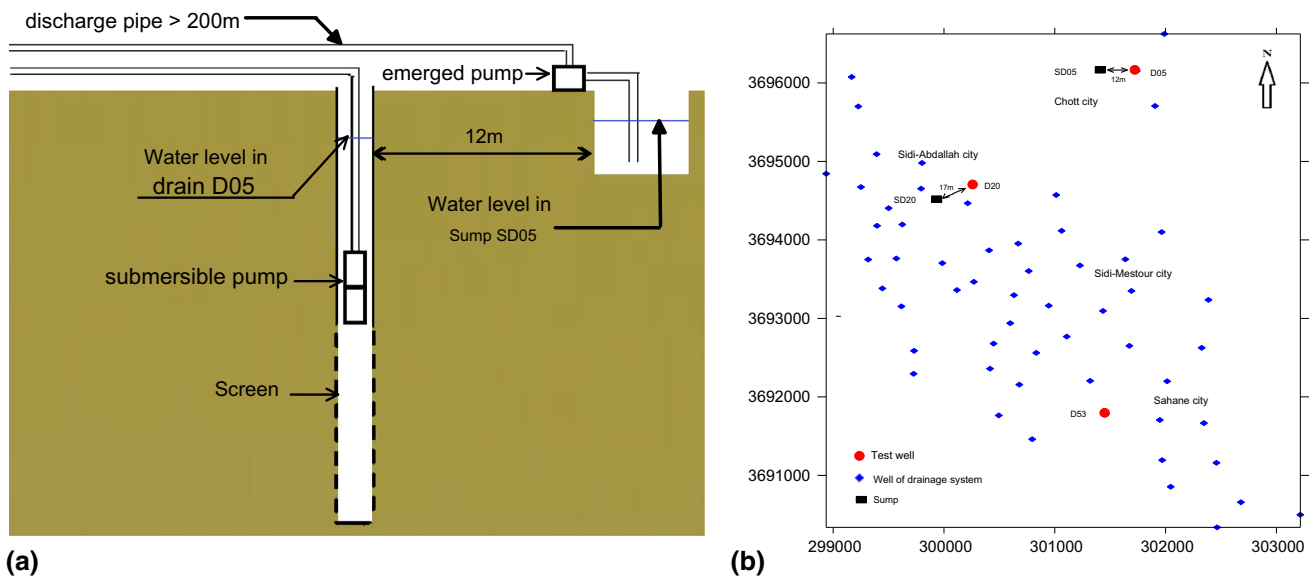
Fig. 6 Location of wells and sumps: (**a**) pumping and discharge system in sumps and wells, and (**b**) location of wells and sumps and distances between them
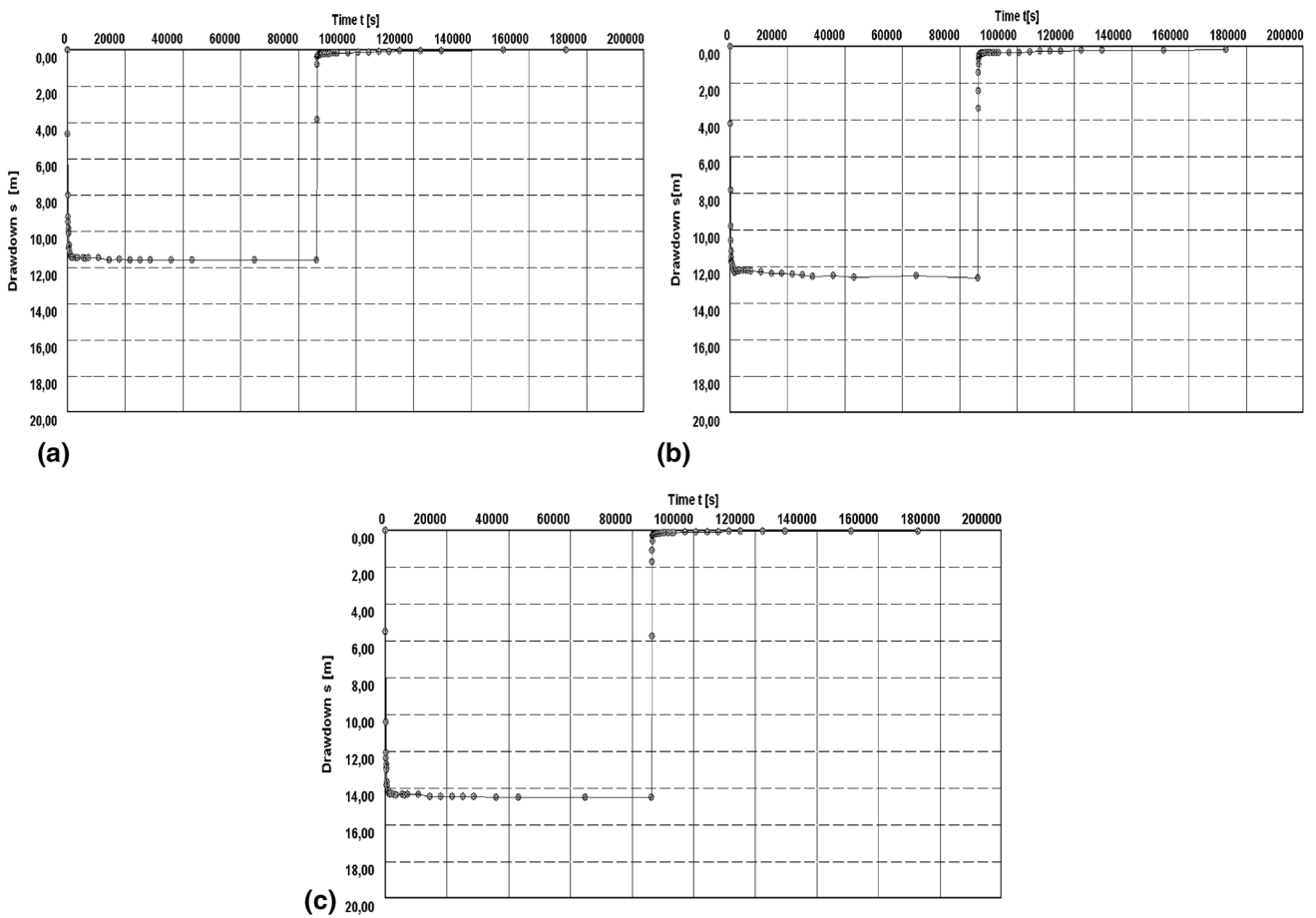
Fig. 7 Drawdown and residual drawdown observed in (**a**) D05, (**b**) D20, and (**c**) D53
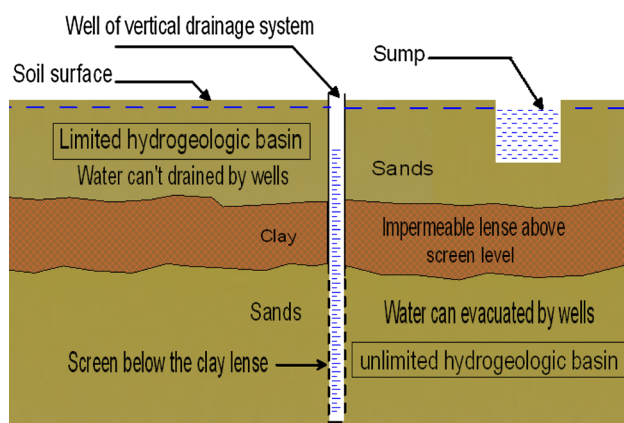
Fig. 8 Internal structural of unconfined aquifer and failure of drainage wells to evacuate rising groundwater

the sumps (SD05 and SD20). This sealing is probably due to:

– The existence of a fault between the wells and sumps, which appears unlikely due to the predominance of sandy formations characterizing this inactive seismic area
– The presence of impermeable or semipermeable formations (sandy clays, clayey sands) resulting in compartmentalization of a multilayer aquifer, as shown in Fig. 8

The existence of two discontinuous aquifers is confirmed by:

– The constancy of the water level in drains D05 and D20 following continuous pumping in sumps SD05 and SD20, respectively
– The constancy of the water level in the sumps following continuous pumping in the wells.

Conclusions and Recommendations

Rising groundwater is a known problem in El-Oued Valley, affecting the life of inhabitants. The local authorities have supported implementation of a megaproject primarily based on the principle of disposal of surplus water through a vertical drainage system composed of 58 drains.

After 2 years of operation of this system, the water in the unconfined aquifer still rises to the surface in most affected cities (Chott and Sid Mestour).

To address this situation and understand the cause of the failure of this system, we carried out well tests in these cities. The interpretation of these well tests is based on the observation of the water level in the same wells as well as nearby sumps, showing discontinuity between the water pumped from wells and sumps. This allows us to state that

the unconfined aquifer in the region is not homogeneous, but rather has some heterogeneity and is intercalated by clay lenses at shallow depths. These clay lenses act as a substrate that supports domestic wastewater to rise to the surface, especially in the cities lacking a sewerage system.

The drainage wells exhibiting low rates probably have an incorrectly positioned strainer (screen), corresponding to the clay layer. This is due to the predetermination of the screen depth for all wells (elevation Z between 50 and 58 m) as shown in Fig. 5.

So, the main error leading to the failure of the vertical drainage system is the assumption that the aquifer is homogeneous and formed only by sands.

In this context, we propose to install a horizontal drainage system in the cities where the groundwater continues to rise, to connect the discharged water to the existing station (ST10) to be sent onto the final rejection site. In the same context, we recommend:

– Realization of geophysical prospecting to determine the limits of the superficial layers, especially clay lenses
– Replacement of the vertical drainage system by another horizontal one in the most affected cities to evacuate the excess water and avoid land subsidence, which is considered the most damaging result of the large drawdown [21]
– Installation of a pumping station at the center of El-Oued (the most affected area) to permit realization of experimental pumping tests, being designed, built, and equipped according to research programs focused on hydrodynamics and groundwater resources [22]

This new system could greatly reduce the costs of pumping, especially the electrical energy required to operate the existing vertical drainage network [5], returning the water table to its original level before the occurrence of the problem, which could increase the purifying power of soil and contribute to local development of the region. The design and size of such a horizontal drainage system will be considered in future research.

References

1. P. Li, H. Qian, W. Jianhua, H. Liu, X. Lyu, H. Zhang, Determining the optimal pumping duration of transient pumping tests for estimating hydraulic properties of leaky aquifers using global curve-fitting method: a simulation approach. Environ. Earth Sci. (2013). doi:10.1007/s12665-013-2433-9
2. DE (Department of Environment, El Oued), Report "damage of rising groundwater and pollution of superficial aquifer in El-Oued", 2009
3. S. Khechana, E. Derradji, Management of water resources in a hyper-arid area: strategy and issues (Case of Oued-Souf Valley-South Eastern of Algeria). J. Water Resour. Prot. **4**(11), 922–928 (2012). doi:10.4236/jwarp.2012.411108

4. J.M. Burri, P. Burri, Study of sewerage wastewater, stormwater and irrigation and additional measures against the rising groundwater in Oued-Souf valley, First Campaign of Hydrogeological Measurements, 2001

5. J.-N. Cretenet, Study of sewerage wastewater, stormwater and irrigation and additional measures against the rising groundwater in Oued-Souf valley, Mission I, 2004

6. National Agency of Water Resources (NAWR), Regional Directorate of Ouargla, Summary report of rising groundwater in Oued Souf region. Ministry of Infrastructure and Planning Land, National Agency of Water Resources, 1999

7. J.M. Burri, P. Burri, Study of sewerage wastewater, stormwater and irrigation and additional measures against the rising groundwater in Oued-Souf valley, Mission II, 2004

8. National Company of Geophysics (NCG), Topographic study of the Souf region. Technical Report. Wilaya of El-Oued, Hydraulic Department. Branch of Hydrogeology and Topography, 1990

9. National Company of Geophysics (NCG), Topographic Study of the Souf region. Coordinates of piezometers. Wilaya of El-Oued, Hydraulic Department. Branch of Hydrogeology and Topography, 1991

10. HDW (Hydraulic Department of El-Oued), Water resources in El-Oued region, 2010

11. S. Khechana et al., Hydrochemical characteristics of groundwater in Oued-Souf valley (SE Algerian). Eur. J. Sci. Res. EJSR **62**(2), 1 (2011)

12. S. Khechana et al., La gestion intégrée des ressources en eau dans la vallée d'Oued-Souf : Enjeux d'adaptation d'une nouvelle stratégie. Revue des Sciences Fondamentales et Appliquées, http://www.univ-eloued.dz/rsfa, **2**(2)

13. G. Castany, *Méthodes et principes en hydrogéologie*, Edition Dunod, ISBN: 2-04-01122-9 (Bordas, Paris, 1982)

14. J.-Y. Lee et al., Combined performance of pumping and tracer tests: a case study. Geosci. J. **7**(3), 237–241 (2003)

15. M. Bonnet, P. Suzanne, P. Umgemach, Interprétation des pompages en régime transitoire. L'effet de puits et la post-production. 86e congr. Ass. Advancement Sc., Bordeaux et Chron. hydro., B.R.G.M., Orleans, vol. 12, 113–116

16. K.E. Murray, L.S. Yosko, Multi-observation well aquifer test case study: is recovery coincident with the cessation of pumping? Environ. Earth Sci. **68**, 1955–1965 (2013). doi:10.1007/s12665-012-1883-9

17. C.V. Theis, The relationship between the lowering of the piezometric surface and the rate and duration of discharge of a well using groundwater storage. Trans. Am. Geophys. Union **16**, 519–524 (1935)

18. G.P. Kruseman, N.A. de Ridder, *Analysis and Evaluation of Pumping Test Data*, 2nd edn. (International Institute for Land Reclamation and Improvement, Wagningen, 1990)

19. L. Chengpeng et al., Interpretation of a short-duration pumping test in the mixed flow karst system using a three-reservoir model. Carbonates Evaporites **28**, 149–158 (2013)

20. J.J. Butler Jr, J.M. Healey, Relationship between pumping-test and slug-test parameters: scale effect or artifact? Groundwater **36**(2), 305–313 (1998)

21. C.-H. Liu, Y.-W. Pan, J.-J. Liao, W.-C. Hung, Estimating coefficients of volume compressibility from compression of strata and piezometric changes in a multiaquifer system in west Taiwan. Eng. Geol. (2004). doi:10.1016/j.enggeo.2004.04.007

22. J.-P. Faillat, C. Drogue, Influence of scale effects, heterogeneity and connectivity of fractured aquifers on the behaviour of drill-holes in shield zone (West Africa). J. Hydrol. **90**, 159–182 (1987)

Lattice Boltzmann investigation of thermal effect on convective mixing at the edge of solvent chamber in CO 2 -VAPEX process

2 authors, including:

Kamal Mohammedi
University M'Hamed Bougara of Boumerdes
150 PUBLICATIONS **814** CITATIONS

Some of the authors of this publication are also working on these related projects:

Project   Solar Fuels In Algeria View project

Project   green house gaz reduction View project

Lattice Boltzmann investigation of thermal effect on convective mixing at the edge of solvent chamber in CO_2-VAPEX process

by

Abdelmalek Atia and Kamal Mohammedi
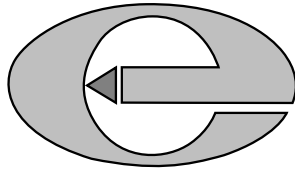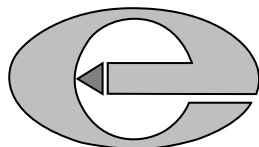
Lattice Boltzmann investigation of thermal effect on convective mixing at the edge of solvent chamber in CO$_2$-VAPEX process

Abdelmalek Atia[1, 2, *] and Kamal Mohammedi[2]

[1]*Mechanical Engineering Departement, Faculty of sciences and technology,*
The University of Hamma Lakhdar, El-oued 39000, Algeria
[2]*Laboratory of Energetic, Mechanics and Engineering, Faculty of sciences of Engineer,*
The University of M'hamed Bougara, Boumerdes 35000, Algeria
[*]*E-mail: abdelmalek-atia@univ-eloued.dz*

Abstract

The high viscosity of heavy oil is a serious problem for the recovery efficiency of this resource by conventional methods. Since a few past years, the vapour extraction process (VAPEX) has emerged as a promising technology for the recovery of heavy oils and bitumen in reservoirs where thermal methods, such as steam-assisted gravity drainage cannot be applied. Recently, the use of CO$_2$ as a solvent is believed to make the VAPEX process more economical and environmentally and technically attractive. Convective mixing at the edge of the solvent chamber enhances mass and heat transfer rates which increases oil mobility and production rate. The objective of this study is to analysis the influence of the main controlling parameters, such as buoyancy ratio and Prandtl number on the flow patterns and mass transfer mechanism, in order to understand the thermal effect on the dissolution of carbon dioxide through natural convection at the boundary layer of solvent chamber of CO$_2$-VAPEX process. The numerical results obtained by lattice Boltzmann method show that the flow structure and the mass transfer mechanism are strongly depend on the buoyancy ratio and Prandtl number. So, the performances of CO$_2$-VAPEX process are strongly influenced by thermal effect; and we found that it has negative consequences on this process.

Key words: Thermal lattice Boltzmann, VAPEX, Convective mixing, CO$_2$, Mass transfer

1. Introduction

As the total production and reserve of conventional oil is declining, a major thrust of oil industries throughout the world is on the exploitation of heavy oil and bitumen reservoirs (Ayub, 2009). The quantity of these resources is about six trillion barrels of oil, which is about six times the total conventional oil reserve (Upreti *et al.*, 2007). A major part of these resources are located in Venezuela, Russia, Canada, and the United States. These reservoirs typically have relatively high permeability (often between 1 and 5 Darcy) with oil viscosities between 1000 and 35,000 cP (Zhao *et al.*, 2014). Under these conditions, productions by the conventional primary recovery techniques are extremely limited. Hence, in-situ processes have to

be used to reduce the viscosity of the oil in-place and mobilize it. Currently, steam-assisted gravity drainage (SAGD), a thermal method, is a popular method for the recovery of heavy oil and bitumen and has been successfully applied in several fields. Despite of this success, it suffers from inherent disadvantages in reservoirs with such things as thin reservoirs, excess heat loss due a bottom water zone, low thermal conductivity of the rock matrix and low porosity, which make this process economically unfeasible (Karmaker and Maini, 2003). In cases where SAGD cannot be applied, VAPEX is the most promising technique for recovering these resources in an economically viable and environmentally responsible way (Roopa and Dawe, 2010; Kok *et al*., 2007; Kok *et al*., 2009; Batohie and Dawe, 2012). The VAPEX process (Fig. 1) is analogous to steam assisted gravity drainage (SAGD) processes but solvent instead of steam, it usually involves two horizontal wells, with a production well located directly below the injection well. The vaporized solvents are injected through the injection well and form a chamber of solvent vapour around the well, Figure 1. The solvents mix with heavy oil, reducing its viscosity so that the diluted oil can drain down along the solvent/oil interface to the production well with the aid of gravity (Xu *et al*., 2012). Incorporating CO_2 in the solvent mixture could provide improvement to VAPEX performance; it is beneficial both environmentally and in terms of recovery, since it is more soluble than other hydrocarbon solvents in heavy oil, its low price compared to other solvents, On the other hand it creates new opportunities for CO_2 sequestration (Javaheri and Abedi, 2013). Hydrocarbon solvents that are used in VAPEX process reduce oil viscosity significantly (Shu, 1984). They all decrease the density of heavy oils when they are dissolved into them. However, CO_2 can increase the density of the heavy oils (Ashcroft and Isa, 1997). The increase in density of the draining edge of the solvent chamber allows forming a gravitationally unstable diffusive boundary layer. This can lead to convective mixing that can increase the rate of solvent's diffusion into oil, followed by a higher oil production rate leading to a significant improvement in the performance of VAPEX.

Li *et al*. 2004 have studied the likelihood of the onset of natural convection in CO_2–oil contact region of CO_2-Vapex process using convective instability theory. Javaheri and co-workers (Javaheri and Abedi, 2008; Javaheri and Abedi, 2013)
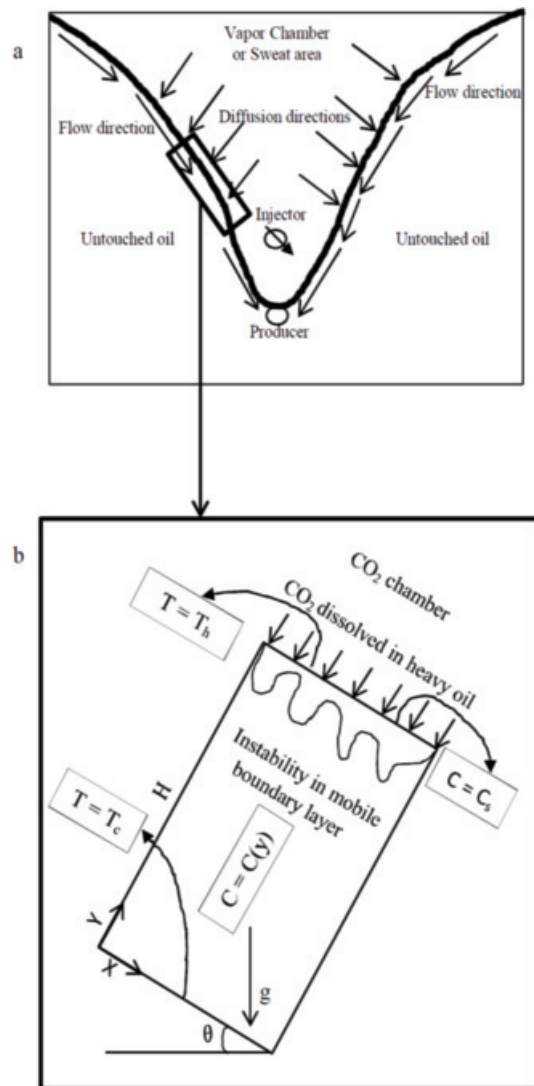
Fig. 1. (a) Schematic representation of the VAPEX process, (b) cross section of the boundary layer in CO_2-VAPEX process.

numerically investigated natural convection with constant viscosity and viscosity reduction with solvent dissolution at the boundary layer of CO_2-VAPEX process, respectively.

This work is to investigate the influence of the main controlling parameters, such as buoyancy ratio and Prandtl number, in order to understand the thermal effect on the natural convection within the contact region between CO_2 and heavy oil via lattice Boltzmann method.

2. Mathematical modelling
2.1. Macroscopic equations for thermo-solutal convection in porous media

The physical problem considered in the present study is a two-dimensional inclined rectangular

cavity reservoir shown in Figure 1. The porosity is considered to be constant and the permeability is assumed to be homogeneous and isotropic, the porous matrix is assumed to be rigid, in local thermodynamic equilibrium and saturated with an incompressible and Newtonian fluid with negligible viscous dissipation. Boundary conditions are no fluid flow across all boundaries and no solute fluxes across lateral and bottom boundaries at any time. Also there is no heat flux across the lateral boundaries while the top and bottom boundaries are maintained at isothermal cold and hot temperatures, respectively. We assume the constant concentration condition at the top boundary, to handle the dissolution of carbon dioxide into heavy oil. The heat flux produced by the concentration gradient (Dufour effect) and the mass flux produced by the temperature gradient (Soret effect) are neglected. The flow is driven by a combined buoyancy effect due to both concentration and temperature variations. Further, we assume that all thermo-physical properties are constant, except for the effect of density variations, which is approximated by the Boussinesq approximation. Based on the above assumptions, equations of continuity, momentum (the Brinkman-Forchheimer equation), heat and solute concentration, and the equation of state (density variation) are stated below:

$$\nabla.\mathbf{u} = 0 \tag{1}$$

$$\partial_t \mathbf{u} + (\mathbf{u}.\nabla)\left(\frac{\mathbf{u}}{\varepsilon}\right) = -\frac{1}{\rho}\nabla(\varepsilon p) + \nu_e \nabla^2 \mathbf{u} + \mathbf{F} \tag{2}$$

$$\partial_t T + \frac{\mathbf{u}}{\sigma}.\nabla T = \frac{\alpha_e}{\sigma}\nabla^2 T \tag{3}$$

$$\partial_t C + \frac{\mathbf{u}}{\varepsilon}.\nabla C = D\nabla^2 C \tag{4}$$

$$\rho(T,C) = \rho_0(1 + \beta_c(C - C_0) + \beta_T(T - T_0)) \tag{5}$$

$$\beta_C = \frac{1}{\rho_0}\left[\frac{\partial\rho}{\partial C}\right]_T \quad and \quad \beta_T = \frac{1}{\rho_0}\left[\frac{\partial\rho}{\partial T}\right]_C \tag{6}$$

Where ε is the porosity of the medium, ν_e is the effective viscosity, D is the molecular diffusivity of the solvent into oil, and β_C and β_T are the coefficient of density variation with CO_2 concentration and temperature, respectively. C_0 and T_0 are the reference concentration and temperature,

respectively. $\sigma = \left[\varepsilon(\rho c)_f + (1-\varepsilon)(\rho c)_s\right]/(\rho c)_f$ is the specific heats ratio, where $(\rho c)_f$ and $(\rho c)_s$ are the specific heat of fluid and solid matrix, respectively. $\alpha_e = \lambda_e/(\rho c)_f$ is the effective thermal diffusivity of the porous medium, $\lambda_e = \varepsilon\lambda_f + (1-\varepsilon)\lambda_s$ is the equivalent thermal conductivity, where λ_f and λ_s are the thermal conductivity of fluid and solid matrix, respectively. $\mathbf{F}$ represents the total body force due to the presence of porous media and other external force, and can be expressed as:

$$\mathbf{F} = -\frac{\varepsilon\nu}{k}\mathbf{u} - \frac{1.75}{\sqrt{150\varepsilon k}}|\mathbf{u}|\mathbf{u} + \varepsilon\mathbf{G} \tag{7}$$

Where ν is the kinematic viscosity and k is the permeability of porous media. $\mathbf{G}$ is the gravitational buoyancy force, it's approximately given by:

$$\mathbf{G} = g(\vec{x}.\sin\theta + \vec{y}.\cos\theta)\left(\beta_c(C - C_0) + \beta_T(T - T_0)\right) \tag{8}$$

Where g is the gravity and θ is the angle of the mobile oil layer with the horizontal. The double natural convection governed by above equations is characterized by several non-dimensional parameters, such as buoyancy ratio N, Prandtl number Pr, Lewis number Le, solutal Rayleigh number and thermal Rayleigh number, which are defined by:

$$N = \frac{\Delta\rho_C}{\Delta\rho_T}, \ \mathrm{Pr} = \frac{\nu}{\alpha_e}, \ Le = \frac{\alpha_e}{\varepsilon D},$$
$$Ra_C = \frac{gkH\Delta\rho_C\cos\theta}{\varepsilon\mu D}, \ Ra_T = \frac{gkH\Delta\rho_T\cos\theta}{\mu\alpha_e} \tag{9}$$

Where $\Delta\rho_c$ is the difference between the densities of pure heavy oil and saturated heavy oil by CO_2, $\Delta\rho_T$ is the difference between the densities of heavy oil at reference and maximum temperature.

2.2. *Thermal LB-model for convective mixing flow in CO2-VAPEX process*

The Lattice Boltzmann method (LBM) is a recently developed method for simulating fluid flows and modeling physics in fluids (Mohamadm, 2011). Unlike conventional computational methods which are based on discretisation of macroscopic governing equations, LBM is an approach based on

the mesoscopic kinetic equation (Boltzmann equation) for fluids. In the present work a D2Q9 model is used, which has the following set of discrete velocities (Bayat *et al.*, 2012): $e_0 = 0$, and $e_i = \lambda_i \left(\cos\theta_i, \sin\theta_i \right) c$, with $\lambda_i = 1$, $\theta_i = (i-1)\pi/2$ for $i = 1 - 4$ and $\lambda_i = \sqrt{2}$, $\theta_i = (i-5)\pi/2 + \pi/4$ for $i = 5 - 8$.

Where $c = \delta x/\delta t$ is the particle velocity and δx and δt are the lattice grid spacing and time step, respectively.

The dynamics of the flow is described by a distribution function f, which follows the Lattice Boltzman equation (Guo *et al.*, 2009):

$$f_i\left(x + e_i\delta t, t+\delta t\right) = f_i\left(x, t\right) - \frac{f_i\left(x, t\right) - f_i^{eq}(\rho, \mathbf{u})}{\tau_f} \ (i = 0, 1, 2....8) \quad (10)$$

τ_f is the dimensionless relaxation time related to the effective viscosity v_e as $v_e = (\tau_f - 0.5)\delta x^2/3\delta t$ (Inamuro *et al.*, 2002).

$f_i^{eq}(\rho, \mathbf{u})$ is the equilibrium distribution function at location x and time t along the ith direction, which is chosen to recover the macroscopic Navier-Stokes equations:

$$f_i^{eq}(\rho, \mathbf{u}) = \omega_i\rho\left[1 + \frac{c_i.\mathbf{u}}{c_s^2} + \frac{1}{2}\frac{(c_i.\mathbf{u})^2}{\varepsilon c_s^4} - \frac{1}{2}\frac{\mathbf{u}^2}{\varepsilon c_s^2}\right] \quad (11)$$

Where $c_s = c/\sqrt{3}$ is the sound speed, wi are the weight coefficients with $\omega_0 = 4/9$, $\omega_{1-4} = 1/9$ and $\omega_{5-8} = 1/36$ in D2Q9 model. To simulate heat transfer within the boundary layer of CO_2-VAPEX process, we have used another distribution function $T_i(x, t)$:

$$T_i\left(x + e_i\delta t, t+\delta t\right) = T_i\left(x, t\right) - \frac{T_i\left(x, t\right) - T_i^{eq}(\rho, \mathbf{u})}{\tau_T} \ (i = 0, 1, 2....8) \quad (12)$$

Where τ_T is the dimensionless relaxation time related to the thermal diffusivity as follow $\alpha_e = \sigma(\tau_T - 0.5)\delta x^2/3\delta t$. $T_i^{eq}(C, \mathbf{u})$ is the equilibrium distribution function at location x and time t along

the ith direction, which is chosen to recover the macroscopic thermal advection-diffusion equation:

$$T_i^{eq}(C, \mathbf{u}) = \omega_i T\left[1 + \frac{c_i.\mathbf{u}}{\sigma c_s^2}\right] \quad (13)$$

In order to simulate the transport of dissolved CO_2, we have added new distribution function $C_i(x, t)$:

$$C_i\left(x + e_i\delta t, t+\delta t\right) = C_i\left(x, t\right) - \frac{C_i\left(x, t\right) - C_i^{eq}(\rho, \mathbf{u})}{\tau_C} \ (i = 0, 1, 2....8) \quad (14)$$

Where τ_C is the dimensionless relaxation time related to the solute diffusivity by $D = (\tau_C - 0.5)\delta x^2/3\delta t$ (Inamuro *et al.*, 2002). $C_i^{eq}(C, \mathbf{u})$ is the equilibrium distribution function at location x and time t along the ith direction, which is chosen to recover the macroscopic solutal advection-diffusion equation:

$$C_i^{eq}(C, \mathbf{u}) = \omega_i C\left[1 + \frac{c_i.\mathbf{u}}{\varepsilon c_s^2}\right] \quad (15)$$

The macroscopic quantities, fluid density, temperature and concentration, are defined as

$$\rho = \sum_{i=0}^{8} f_i, \quad T = \sum_{i=0}^{8} T_i \ \text{ and } \ C = \sum_{i=0}^{8} C_i, \text{ respectively.}$$

The fluid velocity $\mathbf{u}$ is calculated using a temporal velocity $\mathbf{v}$ to consider the effects of porous media (Seta *et al.*, 2006):

$$\mathbf{u} = \frac{\mathbf{v}}{c_0 + \sqrt{c_0^2 + c_1|\mathbf{v}|}} \quad (16)$$

Where $\mathbf{v} = \sum_{i=0}^{8} \left(e_i f_i/\rho\right) + \frac{\delta t}{2}\varepsilon\mathbf{G}$, $c_0 = \frac{1}{2}\left(1 + \varepsilon\frac{\delta t}{2}\frac{v}{k}\right)$

and $c_1 = \varepsilon\frac{\delta t}{2}\frac{1.75}{\sqrt{150\varepsilon^3 k}}$.

3. Numerical results and discussion

In this section, we will be discussed the predicted numerical results in terms of the effect of buoyancy ratio and Prandtl number on the CO_2

concentration contours, instantaneous CO_2 molar flux and the variation of total CO_2 inventory at the top boundary. From the simulated concentration field, the instantaneous mass flux $N_{ins,\,t}$ across the interface at time t can be estimated by (Fu *et al.*, 2013):

$$N_{ins,t} = \frac{(C_{avg,t+\Delta t} - C_{avg,t})V}{A\,\Delta t} \qquad (17)$$

Where *A* is the left Interfacial area, and *V* is the total liquid volume.

We found from literature that the viscosity of heavy oil decreased by 20~50 times when it was diluted by carbon dioxide (Srivastava *et al.*, 1999). Therefore, the viscosity of tested heavy oil (Plover Lake oil) will be in the range of 4 ~150 mPa.s (Li *et al.*, 2004). All other parameters for oil and formation proprieties that used in our simulations are cited in table 1 (Zhao *et al.*, 2014; Mozaffari *et al.*, 2013; Chi *et al.*, 2014; Dunn *et al.*, 1989).

Figure 2 shows the concentration profiles obtained for two different buoyancy ratio, when it increase (decreasing of thermal effect), the instabilities grow faster and the fingers become numerous. Also, it can be seen that the sweep area by CO_2 dissolution becomes much higher. This implies that we can get more quantity of dissolved CO_2 into heavy oil when we limit the thermal effect. This idea becomes more evident in the evolution of CO_2 dissolving molar flux and total CO_2 inventory shown in Figures 3. Figure 3-(a) shows that the variation of instantaneous molar flux decreased sharply at first and then increased slowly with time indicating the onset of natural convection, after that it become stable nearly followed by a clearly decreasing. These situations can be interpreted as follow: the mass transfer of CO_2 from the top boundary is only controlled by molecular diffusion at early stage, and then it can be known as being dominated by natural convection, the decreasing indicates that the computational domain is nearly saturated with dissolved CO_2 after the fingers reach the bottom boundary. It can be seen from Figure 3-(b) that the amount of dissolved CO2 is generally linear with time during the convection-dominated period, which indicates that the instantaneous molar flux of CO_2 is approximately stable during this stage; also it appears from this figure that the total CO_2 inventory decrease sharply when the thermal

Table 1.
Values of parameters used for lb simulation model

Parameters	Tests	
	buoyancy ratio $N = \dfrac{\Delta\rho_C}{\Delta\rho_T}$	Prandtl number $\text{Pr} = \dfrac{\nu}{\alpha_e}$
	Fluid properties	
$\mu\,(\text{mPa.s})$[1]	5	**5, 10**
$\rho\,(\text{Kg}/\text{m}^3)$[1]	993	993
$D\,(\text{m}^2/\text{s})$[1]	1×10^{-9}	1×10^{-9}
$\lambda_f\left(W/m.C^0\right)$[2]	0.133	0.133
$(\rho c)_f\left(J/m^3.C^0\right)$[3]	2.079E + 6	2.079E + 6
$\beta_c\,(\text{Kg/mol})$[1]	8.24E − 3	8.24E − 3
$C_s\left(\text{mol}/\text{m}^3\right)$[1]	1.82E + 3	1.82E + 3
$\Delta\rho_C\,(\text{Kg}/\text{m}^3)$[1]	14.99	14.99
$\beta_T\left(1/C^0\right)$[4]	7.2E − 4	7.2E − 4
$\Delta\rho_T\,(\text{Kg}/\text{m}^3)$	7.495, 1.499	7.495
Boundary layer formation properties		
Porosity[5]	0.35	0.35
Permeability (Darcy)[5]	1800	1800
$\theta\,(°)$[1]	30	30
$(\rho c)_s\left(J/m^3.C^0\right)$[2]	2.6E + 6	2.6E + 6
$\lambda_s\left(W/m.C^0\right)$[2]	7.64	7.64

[1](Li *et al.*, 2004)
[2](Zhao *et al.*, 2014)
[3](Mozaffari *et al.*, 2013)
[4](Chi *et al.*, 2014)
[5](Dunn *et al.*, 1989)

effect is dominant. The above results and interpretations confirmed by Figures 4 and 5 that present the second test (Prandtl number); we show nearly the same results when the thermal effect is considered. We can say that the thermal effect is considered as a negative buoyancy force works as an adiabatic temperature for rising and stopping the moving interface layer.

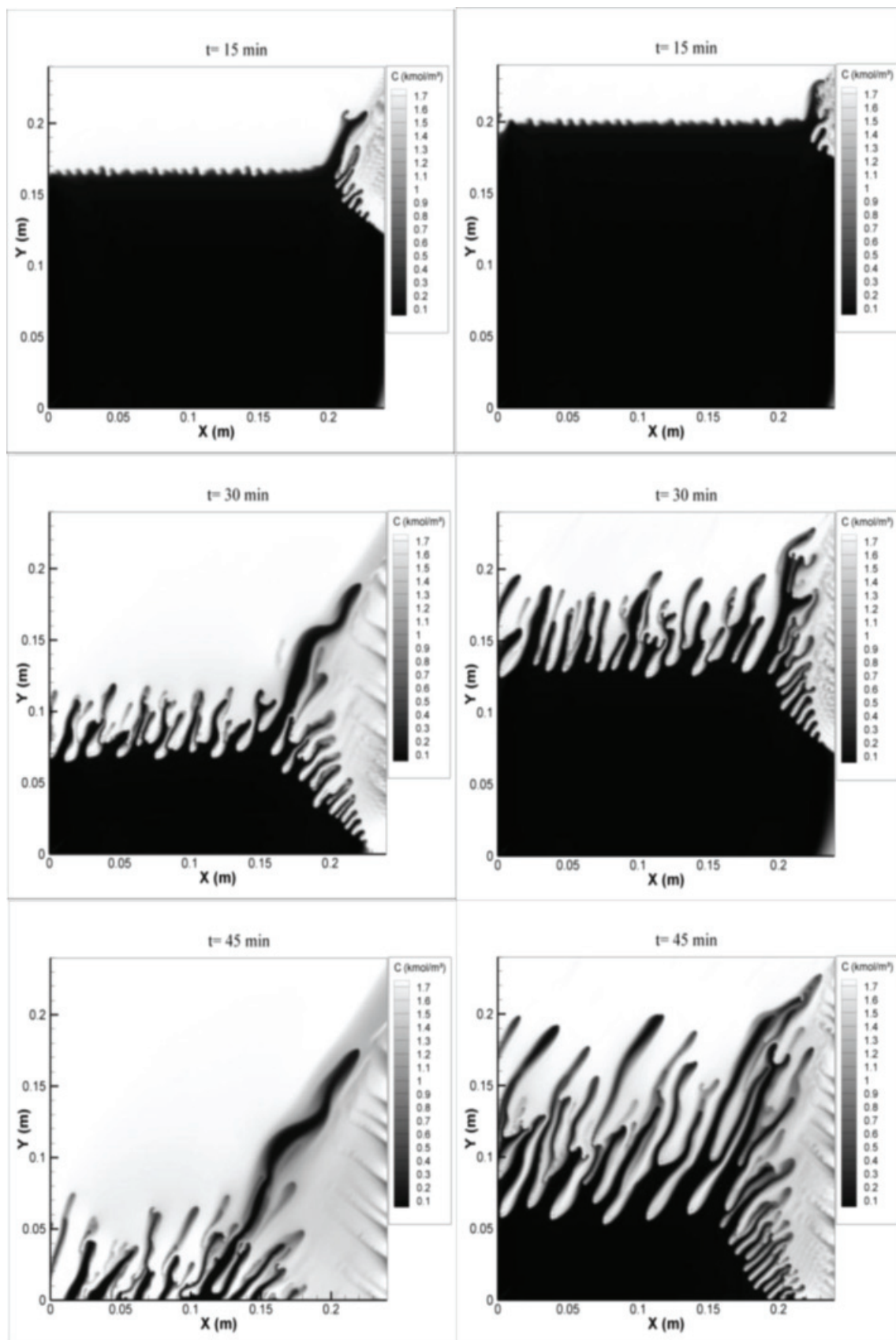Fig. 2. Simulated distribution of dissolved CO_2 at different time instants for different buoyancy ratio: left N = 10; right N = 2.
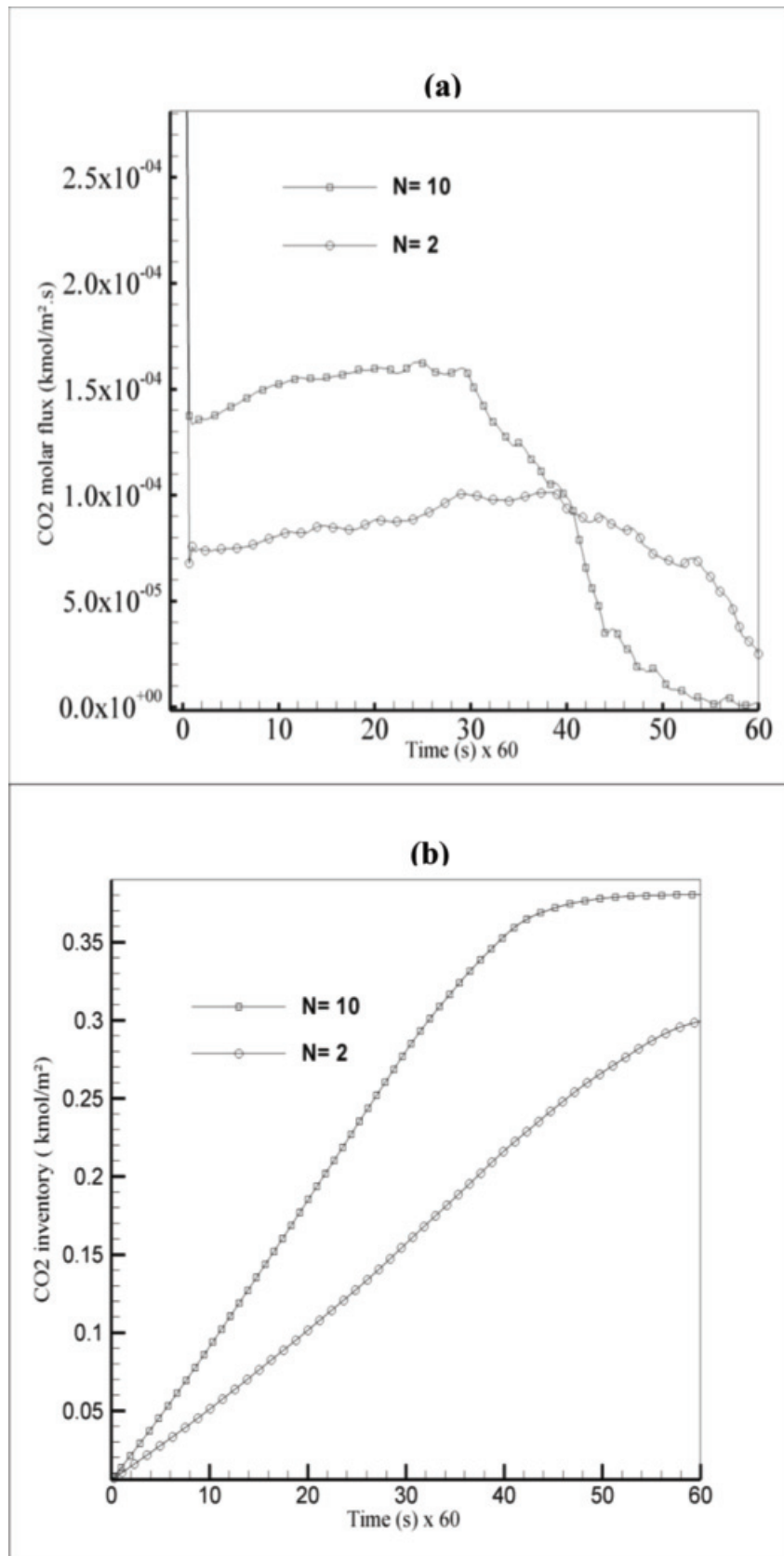
Fig. 3. Variation of CO_2 molar flux (a) and Variation of the dissolved CO_2 inventory (b) at the top boundary for different buoyancy ratio.
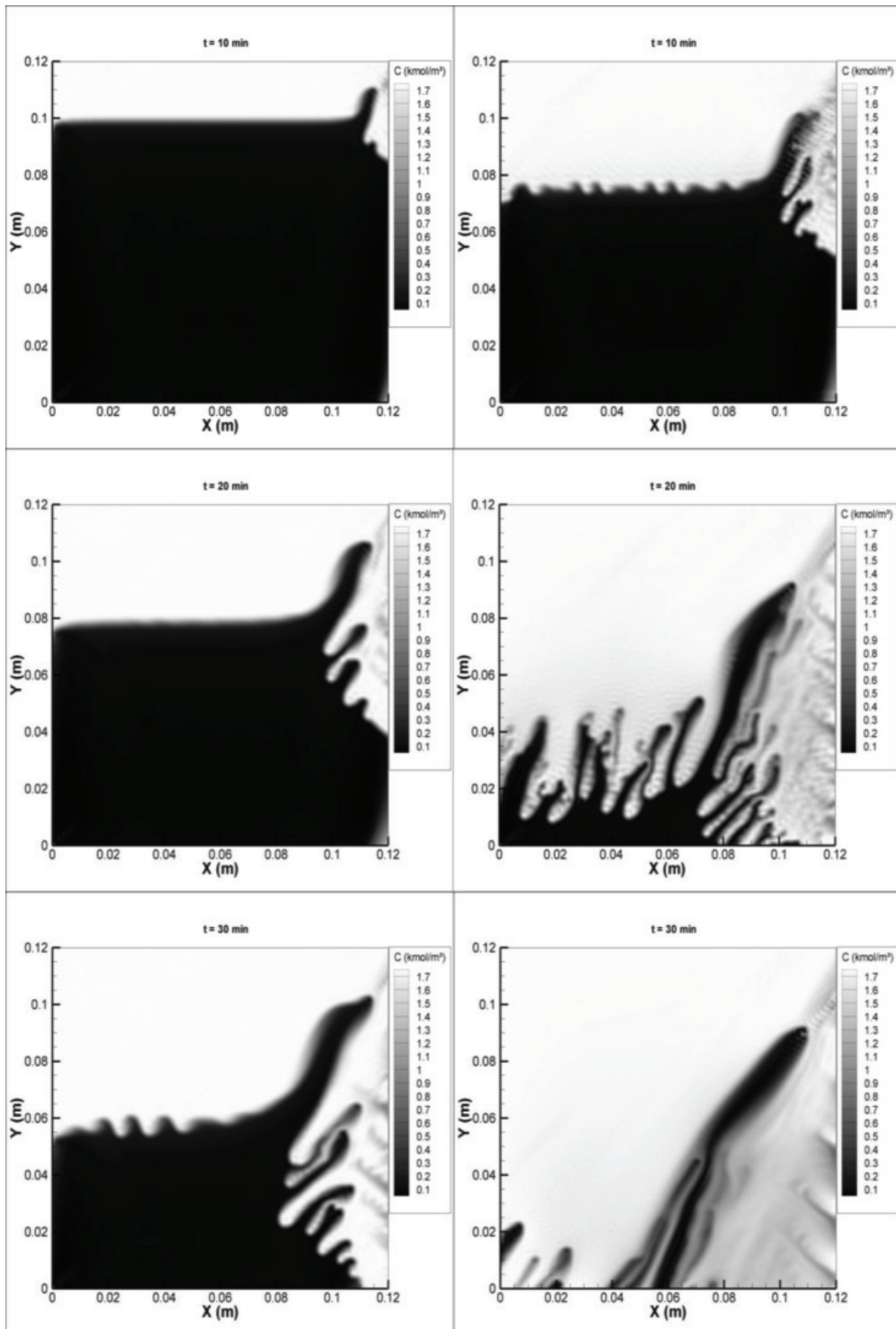
Fig. 4. Simulated distribution of dissolved CO_2 at different time instants for different. Prandtl number: left Pr = 4.86; right Pr = 2.43.
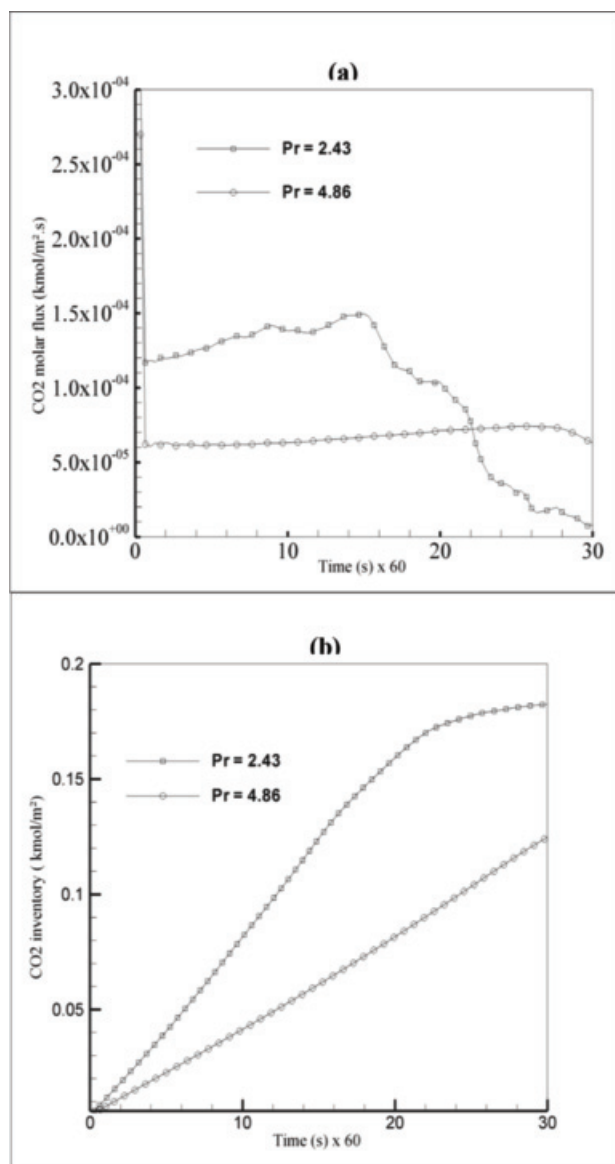
Fig. 5. Variation of CO_2 molar flux (a) and Variation of the dissolved CO_2 inventory (b) at the top boundary for different Prandtl number.

4. Conclusion

In this paper, a thermal LB model with a three distribution functions has been used to simulate thermo-solutal natural convection flow within the diluted mobile oil boundary layer of CO_2-VAPEX. The key point of this article lies to the application of thermal lattice Boltzmann model for CO_2-VAPEX process at first time in order to understand the thermal effect on this process, the predicted results with the proposed model showed that the thermal effect has negative consequences on CO_2-VAPEX process. Hence, the performances of this process can improve by limiting the thermal effect. This

improvement leads to huge quantity of CO_2 dissolved into heavy oil followed by enhancement of flow rate of CO_2-VAPEX process. Current study has not considered the role of Duffour number effect, Sorret number effect and viscosity variation effect on double-diffusive natural convection within boundary layer of CO_2-VAPEX process. A research project, which aims to investigate double-diffusive natural convection (heat and mass transfer) with a complete model during CO_2-VAPEX process, is being conducted at the future time.

References

Ashcroft S.J., Mustafa B.I., 1997. Effect of dissolved gases on the densities of hydrocarbons. *Journal of Chemical & Engineering Data* **42(6)**,1244–1248.

Ayub M., 2009. The role of capillarity in the VAPEX process. *Petroleum Science and Technology* **27(10)**, 1020–1032.

Batohie G., RA D., 2012. Modeling the VAPEX and SAGD side wall process with a wax heating experiment. *Energy Sources, Part A: Recovery, Utilization, and Environmental Effects* **34(5)**, 439–446.

Bayat M., Abadi A., Jamialahmadi M., 2012. The application of the lattice boltzmann method for permeability prediction of porous media: investigating the effects of viscosity and grid resolution. *Petroleum science and technology* **30(13)**, 1324–1334.

Chi G.X., Li Z.H., Kathryn B., 2014. Numerical modeling of hydrocarbon generation in the Douglas Formation of the Athabasca basin (Canada) and implications for unconformity-related uranium mineralization. *Journal of Geochemical Exploration* **144**, 37–48.

Dunn S.G., Nenniger E.H., Rajan V.S.V., 1989. A study of bitumen recovery by gravity drainage using low temperature soluble gas injection. *The Canadian Journal of Chemical Engineering* **67(6)**, 978–991.

Bo F., Liu B.T., Yuan X.G., Chen S.Y., Yu K.T., 2013. Modeling of Rayleigh convection in gas-liquid interfacial mass transfer using lattice Boltzmann method. *Chemical Engineering Research and Design* **91(3)**, 437–447.

Guo Z.L., Han H.F., Shi B.C., Zheng C.G., 2009. Theory of the lattice boltzmann equation: lattice boltzmann model for axisymmetric flows. *Physical Review E* **79(4)**, 46–708.

Inamuro T.J., Masato Y.S., Hiroshi I., Riki M., Fumimaru O., 2002. A lattice Boltzmann method for a binary miscible fluid mixture and its application to a heat-transfer problem. *Journal of Computational Physics* **179(1)**, 201–215.

Javaheri M., Abedi J., 2008. Modelling of mass transfer boundary layer instability in the CO-Vapex process. Canadian International Petroleum Conference, 17–19 June. Calgary, Alberta.

Javaheri, M., Jalal A., 2013. The effect of heavy oil viscosity reduction by solvent dissolution on natural convection in the boundary layer of VAPEX. *Transport in porous media* **99(2)**, 307–326.

Karmaker K, Brij B.M., 2003. Applicability of vapor extraction process to problematic viscous oil reservoirs. SPE Annual Technical Conference and Exhibition, 5–8 October. Denver, Colorado.

Kok M.V., Yildirim Y., Akin S., 2007. Application of vapex process for light crude oil. *Energy Sources, Part A: Recovery, Utilization, and Environmental Effects* **30(1)**, 20–26.

Li Z., Dong M., Shirif E., 2004. Natural convection-an underlying mechanism in CO-VAPEX process. Canadian International Petroleum Conference. Calgary, Alberta.

Mohamad A.A., 2011. Lattice Boltzmann method: fundamentals and engineering applications with computer codes. Springer, London.

Mozaffari S., Mohammad N., Mohammad R.E., Leili S., Emad R., Amir H.M., 2013. Numerical modeling of steam injection in heavy oil reservoirs. *Fuel* **112**, 185–192.

Roopa I., Dawe R.A., 2010. A laboratory study of recovery with carbon dioxide around critical conditions of trinidad's heavy oil and tar sands. *Petroleum Science and Technology* **28(15)**, 1544–1554.

Seta T., Eishun T.S., Kenichi O., 2006. Lattice Boltzmann simulation of natural convection in porous media. *Mathematics and Computers in Simulation* **72(2)**, 195–200.

Srivastava R.K., Sam S.H., Dong M.Z., 1999. Comparative Effectiveness of CO2 Produced Gas and Flue Gas for Enhanced Heavy-Oil Recovery. *SPE Reservoir Evaluation & Engineering* **2(03)**, 238–247.

Upreti S.R., Lohi A., Kapadia R.A., El-Haj R., 2007. Vapor extraction of heavy oil and bitumen: A review. *Energy & Fuels* **21(3)**,1562–1574.

Xu S.X., Zeng F.H., Gu Y.G., Knorr K.D., 2012. Upscaling study of vapor extraction process through numerical simulation. *Transport in porous media* **95(3)**, 697–715.

Zhao David W., Wang Jacky, Gates Ian D., 2014. Thermal recovery strategies for thin heavy oil reservoirs. *Fuel* **117**, 431–441.

multiobjective optimization of an agile machining type linear delta structure Journal of Materials and Engineering Structures « JMES » ISSN 2170-127X

3 authors:

Khaled Mansouri
El-Oued University
5 PUBLICATIONS   **0** CITATIONS

SEE PROFILE

Idir Belaidi
University M'Hamed Bougara of Boumerdes
117 PUBLICATIONS   **151** CITATIONS

SEE PROFILE

ABDELMALEK ATIA
El-Oued University
20 PUBLICATIONS   **7** CITATIONS

SEE PROFILE

Some of the authors of this publication are also working on these related projects:

Call for Papers: The 1st IEEE International Conference on Communications, Control Systems and Signal Processing CCSSP 2020 View project

feasibility and realization of geothermal heat exchanger View project

Journal of Materials and Engineering Structures

Research Paper

Optimisation multi-objectif de la structure d'une machine d'usinage agile de type delta linéaire

Multiobjective optimization of an agile machining type linear delta structure

Khaled Mansouri [a,b,*], Idir Belaidi [a], Abdelmalek Atia [b]

[a] University Mhamed Bougara of Boumerdès, LAMI Lab, Boumerdès, Algeria

[b] University Echahid Hamma Lakhdar of El Oued, LEVRES Lab, El Oued, Algeria

R E S U M E

La conception d'architectures innovantes de machines agiles dédiées à l'usinage à très grande vitesse (UTGV) nécessite la mise en œuvre de modèles analytiques et numériques pour l'optimisation du comportement cinématique, statique et dynamique de la machine, avec prise en considération des déformations élastiques et leur compensation au niveau de la commande de la machine. Dans le contexte d'une optimisation multi-objectif, il s'agit dans une première partie d'identifier les paramètres et variables inhérents à chaque élément constitutif d'une machine de type robot DELTA, dont le but d'optimiser les éléments essentiels de sa structure. Ceci nécessite une formulation du problème multi-objectif en exprimant les fonctions objectifs, les contraintes et les espaces de recherche correspondants, ainsi que la résolution du problème par l'utilisation de méthodes et outils mathématiques performants (Algorithmes génétique…).

A B S T R A C T

The innovative architectures design of agile machines dedicated to the machining at high speed requires the implementation of analytical and numerical models for the optimization of the kinematic, static and dynamic behavior of the machine, taking into account the elastic deformations and their compensation at level of machine control. In the context of multi-objective optimization, the first part is to identify the parameters and variables inherent to each constituent element of a DELTA robot type machine, the purpose is to optimize the essential elements of its structure. This requires a formulation of the multi-objective problem by expressing the objective functions, the constraints and the corresponding search spaces, as well as the resolution of the problem by the use of high-performance mathematical methods and tools (genetic algorithms, etc.).

RESEARCH REVIEW of
Sciences and Technologies

1 Introduction

Le robot delta est un robot parallèle qui est construit à l'aide de mécanismes en forme de parallélogramme et la plate-forme mobile possède trois degrés de liberté en translation et une rotation par rapport à la base [1]. Le robot est venu d'abord en 1986 par l'intermédiaire d'un brevet d'invention de l'Organisation Mondiale de la Propriété Intellectuelle [2]. Après que de nombreuses études ont été versées dans le robot delta et ses architectures. Pierrot et al. ont donné les équations correspondant à différents modèles tels que la cinématique directe et inverse ainsi que la dynamique inverse [3]. Codourey a étudié la modélisation dynamique et l'évaluation de la matrice de masse des robots Delta basées sur une application directe du principe du travail virtuel [4]. Récemment, les topologies ont été conçus pour plusieurs versions de machines à cinématique parallèle [5-7]. La synthèse dimensionnelle reste une étape importante de la conception optimale des robots parallèles parce que les critères de performance d'un robot donné sont très sensibles à leur géométrie. Parmi toutes les mesures cinématiques, l'espace de travail est l'un des principaux indices importants dans la conception d'un robot parallèle [1, 8, 9].

La plupart des travaux réalisés dans ce domaine étaient dédiés à l'optimisation d'un seul objectif, or la plupart des applications réelles intègrent plusieurs objectifs souvent contradictoires à optimiser simultanément. Pendant longtemps, les approches de résolution multi-objectif consistaient principalement à les transformer en problèmes mono-objectifs. Depuis quelques années, l'approche Pareto définie initialement dans des travaux en économie au 19éme siècle a été utilisée dans les sciences pour l'ingénieur. Cette approche a l'avantage de traiter les problèmes multi-objectifs sans transformation, sans favoriser un objectif par rapport à un autre.

Maximisation de l'espace de travail seulement ne garantit pas une conception optimale, car il est possible de provoquer des indésirables performances cinématique (et / ou dynamique) de robot au sein de son espace de travail. Alors que, pour surmonter ce problème, le concepteur doit tenir compte de l'un des nombreux indices de performance (problème multi-objectif) qui ont été proposés pour l'estimation et l'évaluation des performances des robots [10, 11]. Les approches de résolution multi-objectif consistaient principalement à les transformer en problèmes mono-objectifs. Depuis quelques années, l'approche Pareto définie initialement dans des travaux en économie a été utilisée dans les sciences pour l'ingénieur. Cette approche a l'avantage de traiter les problèmes multi-objectifs sans transformation, sans favoriser un objectif par rapport à un autre.

Dans ce travail, et dont le but de trouver une structure parallèle optimisé de type Delta, Nous donnons une formulation du problème multi-objectif en exprimant les fonctions objectif, les contraintes et les espaces de recherche correspondants, ainsi que la résolution du problème par l'utilisation de méthodes et outils mathématiques performants (Algorithmes génétique…).

2 Description et modélisation du robot delta

2.1 Géométrie de robot Delta

Les modèles géométriques direct et inverse sont les relations qui expriment la situation de l'organe terminal du robot (la nacelle dans le cas présent) en fonction de la configuration du mécanisme (coordonnées articulaires) et inversement [11].

Dans le cas de l'architecture Delta l'orientation reste constante (le paramétrage de l'orientation de la nacelle est inutile car cette dernière reste parallèle à un plan de référence) et seulement trois actionneurs sont utilisés. Nous devons alors résoudre un système de trois équations à trois inconnues [11, 12].

Les paramètres géométriques de robot Delta sont présentés dans (Fig.1).

Coordonnées des points P_i dans le repère fixe :

$$\begin{bmatrix} P_1 & P_2 & P_3 \end{bmatrix} = \begin{bmatrix} R & -\dfrac{R}{2} & -\dfrac{R}{2} \\ 0 & R\dfrac{\sqrt{3}}{2} & -R\dfrac{\sqrt{3}}{2} \\ 0 & 0 & 0 \end{bmatrix} \tag{1}$$

Coordonnées des points B_i dans le repère mobile R_n :

$$\begin{bmatrix} B_1 & B_2 & B_3 \end{bmatrix} = \begin{bmatrix} r & -\dfrac{r}{2} & -\dfrac{r}{2} \\[2mm] 0 & r\dfrac{\sqrt{3}}{2} & -r\dfrac{\sqrt{3}}{2} \\[2mm] 0 & 0 & 0 \end{bmatrix} \tag{2}$$

Composantes des vecteurs u_i dans le repère fixe :

$$\begin{bmatrix} u_1 & u_2 & u_3 \end{bmatrix} = \begin{bmatrix} 0 & 0 & 0 \\ 0 & 0 & 0 \\ 1 & 1 & 1 \end{bmatrix} \tag{3}$$
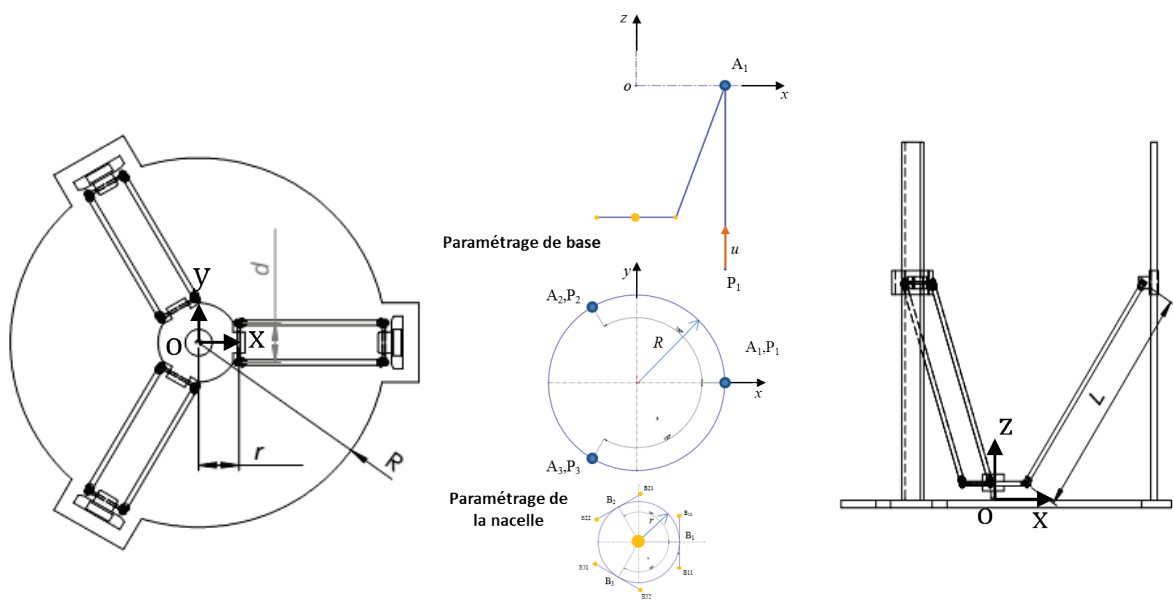
Fig. 1 Paramètres géométriques

Pour calculer le vecteur des variables articulaires q (les coordonnés suivant z des points A)**,** nous écrivons que chacun des segments A_iB_i, pour $1 < i < k$ $(k = 3)$ a une longueur constante l_i. Ce qui nous donne le système de trois équations

$$A_iB_i^{\,2} - l_i^{\,2} = 0 \; / \; l_i = L \tag{4}$$

$$\overrightarrow{A_iB_i} = \overrightarrow{A_iP_i} + \overrightarrow{P_iO} + \overrightarrow{OB_i} \tag{5}$$

$$\overrightarrow{A_iB_i} = \begin{bmatrix} 0 \\ 0 \\ -q_i \end{bmatrix} + \begin{bmatrix} -x_P \\ -y_P \\ 0 \end{bmatrix} + \begin{bmatrix} x + x_{B_i/R_n} \\ y + y_{B_i/R_n} \\ z + z_{B_i/R_n} \end{bmatrix} = \begin{bmatrix} x + x_{B_i/R_n} - x_P \\ y + y_{B_i/R_n} - y_P \\ z + z_{B_i/R_n} - q_i \end{bmatrix} \tag{6}$$

L'équation (4) devient :

$$\left(x - \left(x_P - x_{B_i/R_n}\right)\right)^2 + \left(y - \left(y_P - y_{B_i/R_n}\right)\right)^2 + \left(z + z_{B_i/R_n} - q_i\right)^2 - L^2 = 0 \tag{7}$$

En utilisant les paramètres définis par les équations (1, 2, 3), nous obtenons l'expression analytique du modèle géométrique inverse :

$$\begin{cases} q_1 = z + \sqrt{L^2 - (r - R + x)^2 - y^2} \\ q_2 = z + \sqrt{L^2 - \left((R-r)\dfrac{1}{2} + x\right)^2 - \left((r-R)\dfrac{\sqrt{3}}{2} + y\right)^2} \\ q_3 = z + \sqrt{L^2 - \left((R-r)\dfrac{1}{2} + x\right)^2 - \left((R-r)\dfrac{\sqrt{3}}{2} + y\right)^2} \end{cases} \tag{8}$$

Pour obtenir l'expression analytique du modèle géométrique direct, nous devons résoudre le système suivant par rapport aux variables *x, y* et *z*.

$$\begin{cases} (r - R + x)^2 + y^2 + (z - q_1)^2 = L^2 \\ \left((R-r)\dfrac{1}{2} + x\right)^2 + \left((r-R)\dfrac{\sqrt{3}}{2} + y\right)^2 + (z - q_2)^2 = L^2 \\ \left((R-r)\dfrac{1}{2} + x\right)^2 + \left((R-r)\dfrac{\sqrt{3}}{2} + y\right)^2 + (z - q_3)^2 = L^2 \end{cases} \tag{9}$$

Le système peut se réécrire :

$$\begin{cases} \left(A^2 + C^2 + 1\right)z^2 + 2\big((C(D - (R-r)) + A \times B - q_1)\big)z + \left(B^2 + (D - (R-r))^2 + q_1^2 - L^2\right) = 0 \\ y = Az + B \\ x = Cz + D \end{cases} \tag{10}$$

Avec : $A = \dfrac{(q_2 - q_3)}{\sqrt{3}(r - R)}$, $B = \dfrac{q_3^2 - q_2^2}{\sqrt{3}(r - R)}$, $C = \dfrac{2(q_2 - q_1) - A\sqrt{3}(r - R)}{3(R - r)}$, $D = \dfrac{q_1^2 - q_2^2 - B\sqrt{3}(r - R)}{3(R - r)}$

La première équation du système admet deux solutions qui correspondent à deux positions de la nacelle. La solution correspondant à la machine étudiée est la position basse. Il faut donc conserver la plus petite des deux solutions de l'équation polynomiale. Connaissant *z*, nous pouvons ensuite calculer *x* et *y* de manière unique.

2.2 Modélisation cinématique

Le modèle cinématique établit la relation entre la vitesse de la nacelle en translation et en rotation que nous noterons $\dot{x}$ et $\dot{q}$ (vitesse linéaire des actionneurs) pour une position et une orientation données de la nacelle.

Pour la barre numéro *i*, nous avons :

$$V_{A_i} . A_i B_i = V_{B_i} . A_i B_i \tag{11}$$

L'écriture pour l'ensemble des *k* barres nous donne l'écriture matricielle :

$$J_q \dot{q} = J_x \dot{x} \tag{12}$$

Avec

$$J_q = \begin{bmatrix} A_1 B_1 . u_1 & 0 & 0 \\ 0 & A_2 B_2 . u_2 & 0 \\ 0 & 0 & A_3 B_3 . u_3 \end{bmatrix} \tag{13}$$

et
$$J_x = \begin{bmatrix} (A_1B_1)_x & (A_1B_1)_y & (A_1B_1)_z \\ (A_2B_2)_x & (A_2B_2)_y & (A_2B_2)_z \\ (A_iB_i)_x & (A_iB_i)_y & (A_iB_i)_z \end{bmatrix} \tag{14}$$

Le modèle cinématique inverse est l'expression de $\dot{q}$ en fonction de $\dot{x}$. L'écriture du modèle cinématique inverse à partir de (12) est alors :

$$\dot{q} = J_q^{-1} J_x \, \dot{x} \tag{15}$$

Soit en posant $J = J_x^{-1} J_q$

$$\dot{q} = J^{-1} \dot{x} \tag{16}$$

Où J est appelée la matrice Jacobienne.

Le modèle cinématique direct est l'expression de $\dot{x}$ en fonction de $\dot{q}$. Compte tenu des notations précédentes et de l'équation (14), le modèle cinématique direct s'écrit :

$$\dot{x} = J \, \dot{q}$$

Dans le cas de l'architecture choisie, les matrices J_x et J_q s'écrivent :

$$J_x = \begin{bmatrix} r - R + x & y & z - q_1 \\ \dfrac{1}{2}(R-r) + x & \dfrac{\sqrt{3}}{2}(r-R) + y & z - q_2 \\ \dfrac{1}{2}(R-r) + x & \dfrac{\sqrt{3}}{2}(R-r) + y & z - q_3 \end{bmatrix} \tag{17}$$

$$J_q = \begin{bmatrix} z - q_1 & 0 & 0 \\ 0 & z - q_2 & 0 \\ 0 & 0 & z - q_3 \end{bmatrix} \tag{18}$$

2.3 Performance dynamique

Pour pouvoir écrire le modèle dynamique, nous établissons :

- La relation entre $\ddot{q}$ et $\ddot{x}$

- La relation entre un effort appliqué sur la nacelle et l'effort résultant sur les moteurs.

- Les masses en mouvement.

Nous recherchons l'expression de $\ddot{q}$ (accélération des moteurs) en fonction de $\ddot{x}$ (accélération désirée de la nacelle). En réalité cette accélération est également fonction de $\dot{x}$, $\dot{q}$, x et q. La connaissance de cette relation nous permet de déterminer les caractéristiques requises concernant l'accélération des moteurs en fonction des performances en accélération demandées à la nacelle. L'expression recherchée s'obtient en dérivant le modèle cinématique par rapport au temps. En dérivant l'équation (16), nous obtenons :

$$\ddot{q} = J^{-1}\ddot{x} + J_q^{-1}\left(\dot{J}_x - \dot{J}_q J^{-1}\right)\dot{x} \tag{19}$$

Pour l'arrangement de l'architecture Delta que nous avons retenue, les matrices $\dot{J}_x$ et $\dot{J}_q$, s'expriment analytiquement :

$$\dot{J}_x = \begin{bmatrix} \dot{x} & \dot{y} & \dot{z} - \dot{q}_1 \\ \dot{x} & \dot{y} & \dot{z} - \dot{q}_2 \\ \dot{x} & \dot{y} & \dot{z} - \dot{q}_3 \end{bmatrix} \tag{20}$$

et
$$
\dot{J}_q = \begin{bmatrix} \dot{z} - \dot{q}_1 & 0 & 0 \\ 0 & \dot{z} - \dot{q}_2 & 0 \\ 0 & 0 & \dot{z} - \dot{q}_3 \end{bmatrix}
$$
(21)

Nous constatons que l'accélération des moteurs est composée de la somme de deux termes :

- $J^{-1}\ddot{x}$ L'accélération des actionneurs due à l'accélération de la nacelle.

- $\left(\dot{J}_x - \dot{J}_q J^{-1} \right)\dot{x}$ L'accélération des actionneurs due au déplacement de la nacelle à une vitesse constante. Ce terme traduit le non linéarité de la relation entre la vitesse des actionneurs et la vitesse de la nacelle.

Nous calculons dans un premier temps la relation qui relie l'effort de poussée des moteurs aux efforts appliqués sur la nacelle du point de vue statique.

$$
F_{mot} = {}^t J \, F_{nac}
$$

$$
F_{nac} = \begin{bmatrix} F_x \\ F_x \\ F_z \end{bmatrix} \text{ et } F_{mot} = \begin{bmatrix} F_{mot1} \\ F_{mot2} \\ F_{mot3} \end{bmatrix}
$$

- F_{mot} Effort de poussée des moteurs

- ${}^t J$ Transposée de la matrice jacobienne définie dans modèle cinématique

F_{nac} Torseur des efforts appliqués sur la nacelle.

Masses en mouvement :

La pratique montre que, pour simplifier les calculs, la masse de chaque barre de fixation peut être répartie pour une moitié sur la nacelle et pour l'autre moitié sur la glissière, tandis que son inertie est négligée. Cette simplification est représentée sur la Fig.2.
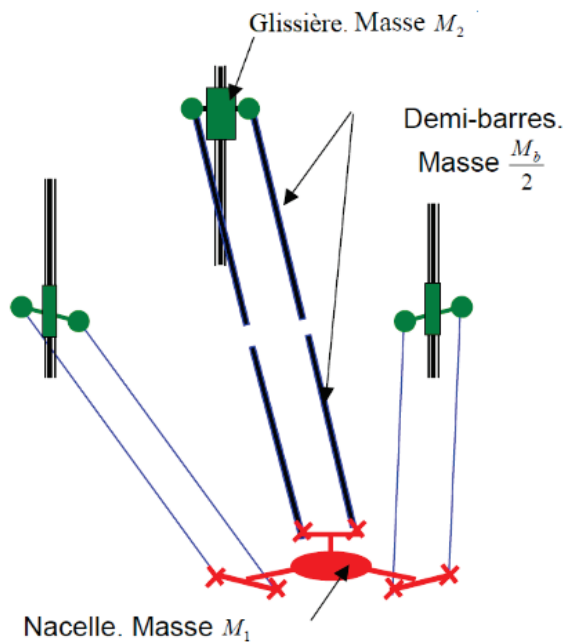

Fig. 2   Répartition de la masse des barres

La simplification proposée ci-dessus nous donne les masses corrigées :

Masse corrigée de la nacelle :

$$M_{nac} = M_1 + 6\frac{M_b}{2} = M_1 + 3M_b \tag{22}$$

Masse corrigée de chaque glissière :

$$M_{mot} = M_2 + 2\frac{M_b}{2} = M_2 + M_b \tag{23}$$

La matrice masse du robot est donnée par

$$M = J^{-T}\left(M_{nac}J^TJ + \frac{1}{2}M_{mot}\sum_{i=1}^{3}J_{m,i}^TJ_{m,i}\right)J^{-1} \tag{24}$$

3 Formulation du problème d'optimisation

Plusieurs critères ont été proposés afin de comparer différents mécanismes par rapport à leur géométrie, leur architecture ou leurs dimensions. Ces critères peuvent être de plusieurs natures :

- Géométrique (encombrement de la machine, course des actionneurs, ratio encombrement de la machine par rapport à son volume de travail, volume de travail)

- Cinématiques (transformation des vitesses, isotropie, absence de singularités)

- Dynamiques (poussée des moteurs, efforts dans la structure, capacité d'accélération)

- Autres (rigidité de la machine, précision, facilité d'étalonnage)

Dans notre travail, le problème d'optimisation multi-objectif (conception optimale) de robots parallèles peut être résumé comme suit:

Trouver la meilleure dimension des paramètres géométriques du robot qui assure l'obtention de critères de performance par rapport à des contraintes différentes.

3.1 Critères de performance

3.1.1 Performance cinématique

Par les performances cinématiques, nous entendons la dextérité cinématique et statique. La dextérité cinématique est définie par l'aptitude du la nacelle du robot à effectuer avec une grande précision et facilité des déplacements arbitraires autour d'un point dans l'espace de travail, et la dextérité statique est définie par l'aptitude du la nacelle du robot à appliquer des forces et moments dans toutes les directions de l'espace de travail.

Pour mesurer la performance cinématique, nous pouvons utiliser l'indice d'isotropie (conditionnement de matrice Jacobienne)

$$c = cond\left(J\right) = \frac{\sigma_{max}}{\sigma_{min}} \tag{25}$$

L'indice d'isotropie cinématique est retenu comme indice de mesure des performances cinématiques du robot parallèle, parce que l'isotropie est une propriété importante dans les applications qui exigent de la précision (par exemple l'usinage).

3.1.2 Espace de travail :

L'espace de travail E est l'un des facteurs les plus importants pour la conception de robots parallèles [13-15]. Théoriquement, c'est l'ensemble de l'espace de configuration que l'organe terminal peut atteindre. Cet espace est défini par ses limites qui sont imposées par les articulations (active et passive), les longueurs des segments et par les collisions internes.

Par conséquent, le problème que nous posons ici est le suivant :

Quel est le meilleur dimensionnement (vecteur des paramètres géométriques optimisés) d'un robot parallèle (robot Delta) qui permet d'avoir le plus grand espace de travail habile ?

Le but de ce travail est de trouver un vecteur de paramètres géométriques P* qui maximise l'espace de travail du robot parallèle E_{dex} tout en respectant une contrainte fondée sur un critère cinétostatique (exemple : le nombre de conditionnement de la matrice jacobienne). Par conséquent, la fonction objectif est:

$$E_{dex} = \left\{ Point \in E_T \ .^{\cdot} CondJ \le CondJ_{max} \right\}$$

D'où

$$e_t = \frac{n_p\left(E_{dex}\right)}{n_p\left(E_T\right)} \tag{26}$$

3.1.3   *Performance dynamique :*

Pour mesurer la performance cinématique, nous calculons le conditionnement de la matrice masse du robot

$$cm = cond\left(M\right) \tag{27}$$

Il est à noter que les indice d'isotropie cinématique et dynamique dépendent largement de la configuration et des paramètres géométriques du robot. Nous utilisons les indices globaux η_J et η_M (très souvent utilisés pour comparer les différentes structures), qui sont définies par les moyennes des indices locaux sur l'espace de travail accessible.

$$\eta_J = \frac{\int cj\, dE}{\int dE} \tag{28}$$

$$\eta_M = \frac{\int cm\, dE}{\int dE} \tag{29}$$

3.2 *Variables et contraintes :*

3.2.1   *Limite de l'espace de travail et variables de conception*

- Limites des variables articulaires

$$q_{es} = \ q_{i\,min} \le q_i \le q_{i\,max}$$

- Limites des variables de conception

$$\left(X_{c,i}\right)_{min} \le \ X_{c,i} \le \left(X_{c,i}\right)_{max} , \ i = 1,\dots,n$$

$$X_c = \left\{L,\ R,\ r,\ D\right\}$$

- R : Rayon de la base fixe
- r : Rayon de la nacelle
- L : Longueur des barres
- D_b : Diamètre de section des barres

- Limites cinématiques articulaires :

$$\left|\dot{q}_j\right| \le \left(\dot{q}_j\right)_{max} , j=1,2,3 \text{ et } \left|\ddot{q}_j\right| \le \left(\ddot{q}_j\right)_{max} , j=1,2,3$$

- Limites de forces extérieures :

Les forces extérieures agissent sur la nacelle, qui sont les forces de coupes, ne doivent pas dépasser une limite donnée.

$$\left| \left(F_{ext} \right)_j \right| \leq \left(F_{ext} \right)_{max} , j=1,2,3$$

3.2.2   Rigidité des barres :

Comme nous l'avons présenté précédemment, toutes les articulations sont considérées parfaitement rigides.

Par construction, les barres sont sollicitées uniquement en traction-compression. Ces sollicitations restent suffisamment petites pour que les problèmes liés au flambement ne soient pas présents.

La déformation d'une de ces barres est :

$$Df_b = \frac{F_b L}{SE} \tag{30}$$

Avec :

- F_b : Effort de traction-compression dans la barre

- L : Longueur initiale de la barre

- S : Surface d'une section droite de la barre

- E : Module d'Young du matériau avec lequel sont réalisées les barres

Cette déformation ne doit pas dépasser une valeur admissible trop petite $Df_b \leq (Df_b)_{ad}$ pour éviter une grande erreur de déplacement de la nacelle, qui risque d'influer négativement sur la rigidité de la machine.

3.2.3   L'absence de la configuration singulière

Les configurations singulières sont des postures particulières de l'organe terminal où la rigidité naturelle des manipulateurs parallèles subit une grande détérioration.

On peut aussi introduire les singularités en abordant sommairement la notion d'équilibre mécanique d'un robot parallèle. Pour un manipulateur parallèle nous notons τ le vecteur des forces articulaires et $\mathcal{F}$ le torseur des efforts externes appliqués sur l'organe terminal. Pour un torseur $\mathcal{F}$ appliqué sur le plateau mobile, le système mécanique est en équilibre s'il existe des forces articulaires dont l'action sur la plate-forme est l'opposée de $\mathcal{F}$. Si ce n'est pas le cas, l'organe terminal du manipulateur va se déplacer jusqu'à ce qu'une nouvelle position d'équilibre soit atteinte. Or il existe une relation bien connue entre τ et $\mathcal{F}$:

$$\mathcal{F} = J^{-t}\tau \tag{31}$$

Où J^{-t} est la transposée de la matrice Jacobienne cinématique inverse. L'équation précédente décrit un système linéaire en terme de composantes du vecteur τ qui admettra en général une solution en τ pour tout $\mathcal{F}$ (solution qui conduit donc à un équilibre mécanique du système) sauf dans le cas où la matrice J^{-t} est dégénérée : dans ce cas le système linéaire n'admet pas de solution et le système mécanique n'est plus en équilibre.

Donc on prend comme contrainte :

$$\left| J^{-t} \right| \neq 0$$

Pour éliminer cette contrainte il suffit d'éviter les singularités parallèles et en séries.

- Singularité en séries ($\left| J_q \right| = 0$)

c'est à dire
$$|J_q| = 0 \Rightarrow (z - q_1)(z - q_2)(z - q_3) = 0$$
$$\Rightarrow (z = q_1) \vee (z = q_2) \vee (z = q_3)$$

Cette singularité apparaît lorsque l'un ou deux ou même trois parallélogrammes deviennent perpendiculaires aux directions des actionneurs linéaires. En d'autres termes, ces configurations sont obtenues lorsque. $L = R - r$ Pour les éliminer, il est nécessaire de choisir. $L > R - r$

- Singularité parallèle ($|J_x| = 0$)

$|J_x| = 0$, signifie que les trois vecteurs $(B_1 - A_1)^t$, $(B_2 - A_2)^t$, $(B_3 - A_3)^t$ sont coplanaires. Pour les éliminer, il faut de choisir $L > R - r$.

3.2.4   Forces des Moteurs :

Les forces fournies par les moteurs doivent être compatibles avec les limites de performances attendues (vitesses, accélérations et charge autorisées) en tout point de l'espace de travail.

L'expression des forces des moteurs est donnée par :

$$F_{mot} = M_{mot}\ddot{q} + M_{nac} \, {}^tJ\ddot{x} + {}^tJ \, F_{ext} \tag{32}$$

avec

$$F_{mot} \leq (F_{mot})_{ad}$$

- $M_{mot}\ddot{q}$: composante de l'effort moteur due à l'accélération de la masse (M_{mot}) de la partie mobile des moteurs (glissière + liaison rotule). Tous les moteurs sont identiques (modularité).

- ${}^tJ \, F_{ext}$: Composante de l'effort moteur due aux efforts extérieurs (principalement les efforts de coupe) appliqués à la nacelle.

- ${}^tJF_{nac,acc,D} = M_{nac} \, {}^tJ\ddot{x}$: Composante de l'effort moteur due à l'accélération de la masse de la nacelle (M_{nac})).

4   Procédure algorithmique développée

L'approche numérique que nous avons utilisée pour résoudre notre problème d'optimisation multi-objectif utilisant l'algorithme génétique NSGA II (Non dominated Sorting Genetic Algorithm II) est représentée sur la Fig.3.

4.1 Données de l'algorithme génétique et les caractéristiques du robot

Table 1- Données de l'algorithme NSGA II

Paramètres	Valeurs
Taille de la population	**200 Individus**
Nombre de générations	**700 générations**
Nombre de fonctions objectif	**03**
Nombres de contraintes	**02**
Pression de sélection	**1.9**
Type de mutation	**mutation réelle**
Probabilité de mutation	**0.2**
Type de codage	**Codage réelle**
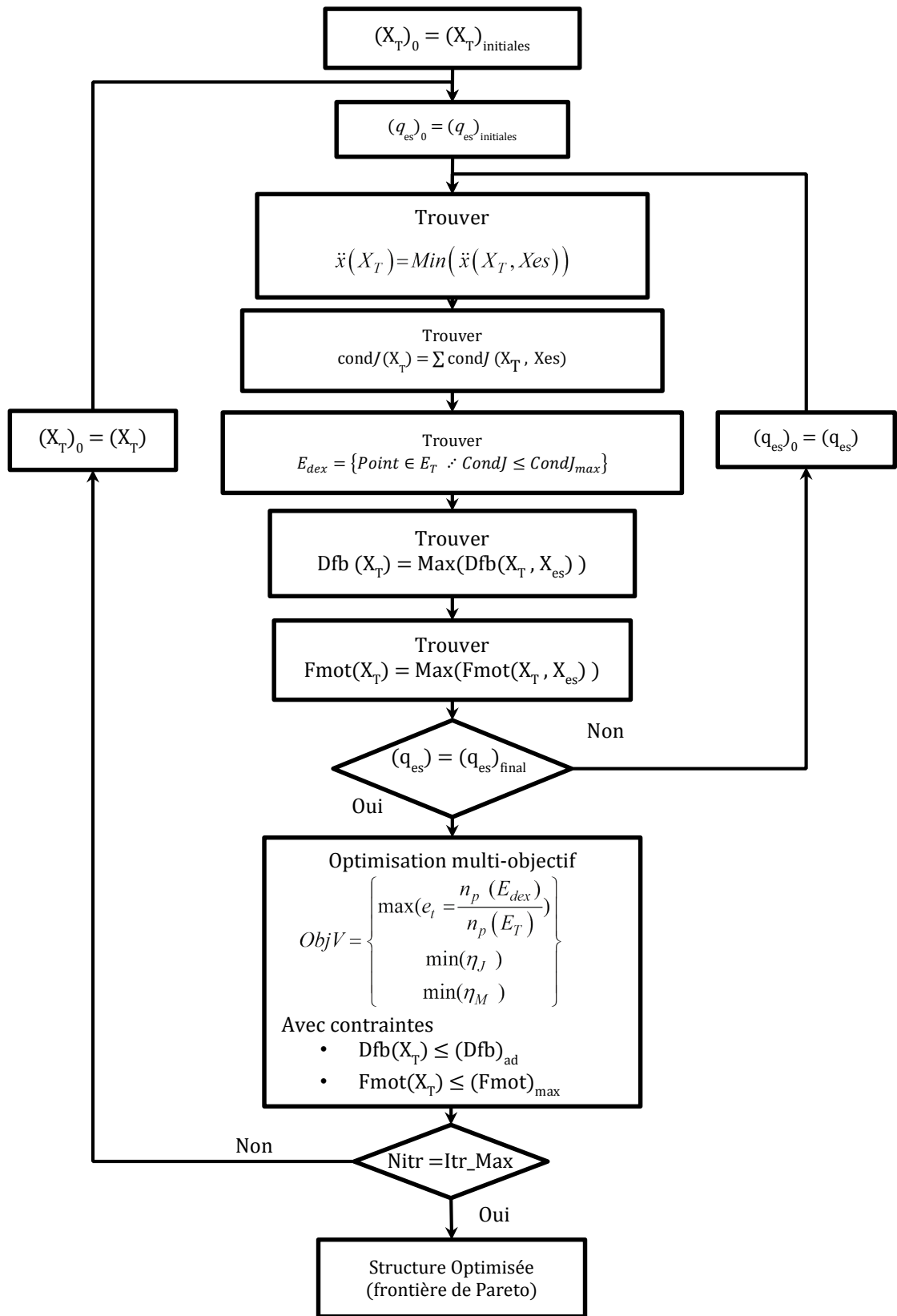
Fig. 3 Procédure algorithmique développée

Table 2- Caractéristiques du robot

Paramètre		Valeur	
		Min	Max
	q(m)	0	0.6
	R(m)	0.5	0.7
	r(m)	0.1	0.3
	L(m)	0.8	1.7
Espace de recherche	D_b (m)	0.01	0.05
	$\left|\dot{q}_j\right|_{max}$ (m/s)	0.2	
	$\left|\ddot{q}_j\right|_{max}$ (m/s²)	0.2	
	$(F_{ext})_{max}$ (N)	1000	
	$CondJ_{max}$	4	
	(M₁) Masse de Nacelle (kg)	20	
	(M₂) Masse de Moteur (kg)	10	
Paramètres du robot	$(Df_b)_{ad}$ (mm)	0.1	
	$(F_{mot})_{ad}$ (N)	9000	

5 Résultats et discussions

Matlab est utilisé comme une plateforme pour l'implémentation des algorithmes génétiques NSGA II, avec les paramètres représentés dans la Table 1. La Fig.4 représente les meilleurs compromis obtenus entre les différentes fonctions objectif. Fig.5 représente l'effet de la longueur des barres L sur les fonctions objectives. Nous remarquons qu'il y a un antagonisme entre les performances (cinématiques et dynamiques) et l'espace de travail dextre. Nous notons que plus les performances indiquées sont élevées, plus l'espace de travail sera petit et vice-versa.

(a)   *(b)*
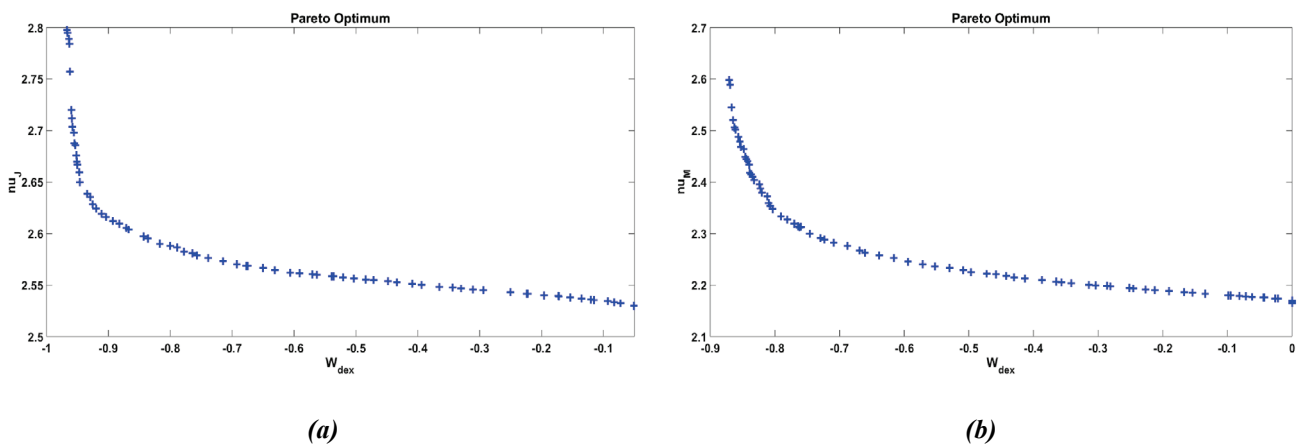
Fig. 4 La frontière de Pareto des solutions, (a) frontière de Pareto entre l'espace de travail dextérité et η_J, (b) frontière de Pareto entre l'espace de travail dextérité et η_M

(a)

(b)

(c)

Fig. 5 Effet de la valeur de (L) sur les fonctions objectif, (a) l'espace de travail dextérité en fonction de(L), (b) et η_J en fonction de (L), (c) η_M en fonction de (L)
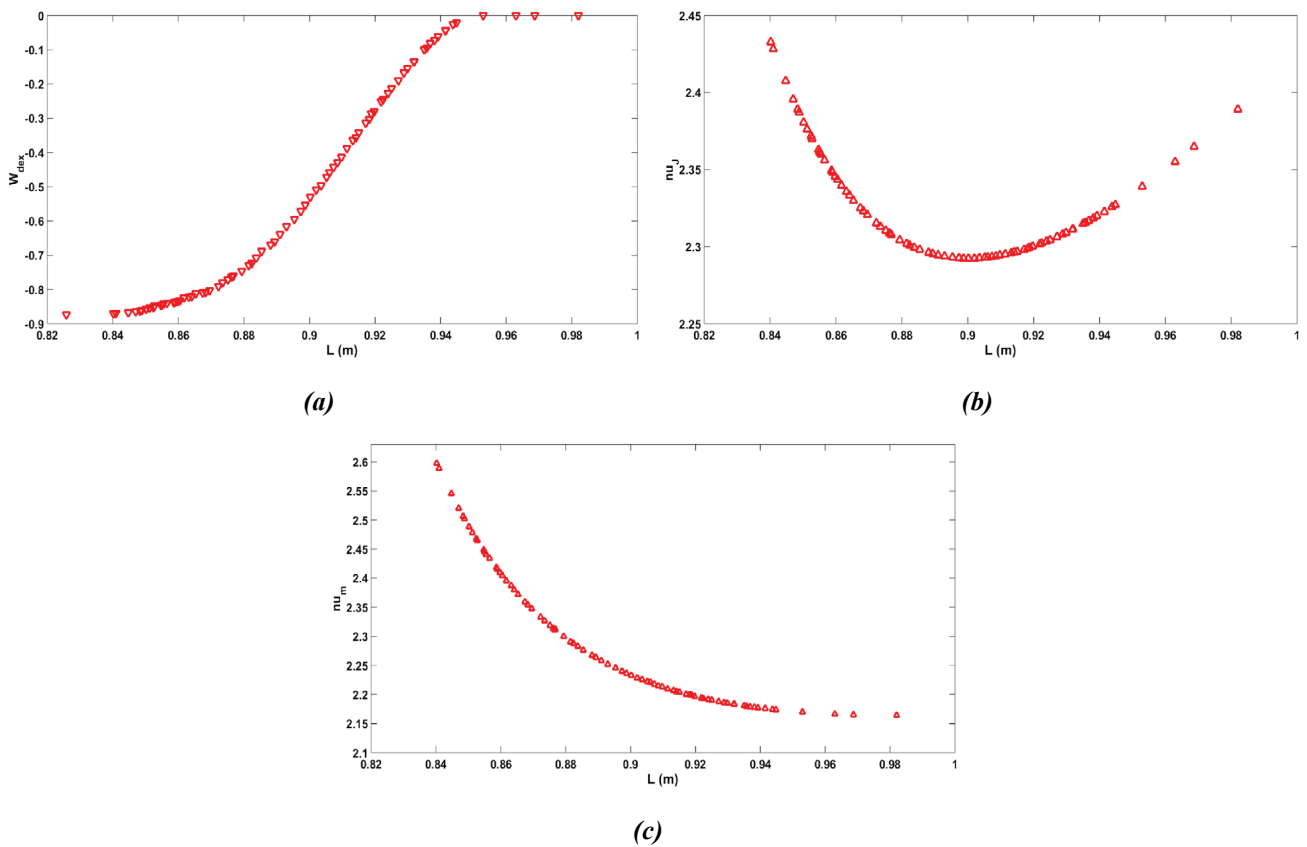
Le choix des paramètres géométriques optimisés du compromis obtenu entre les différents objectifs qui contient les meilleures solutions, il sera fait selon l'ordre d'importance des critères (préférences du concepteur).

Après avoir pris en compte de plusieurs critères de performance dans la méthodologie développée, nous présentons son impact sur le l'espace de travail dextérité (optimisé par critère cinétostatique : le conditionnement de la matrice jacobienne inverse), nous pouvons choisir, pour préférer avoir de meilleures performances cinématiques et dynamiques, les valeurs de fonctions objectif optimisées suivantes :

Table 3- Valeurs optimisées chisies

e_t	η_J	η_M	R(m)	r (m)	L(m)
60%	2,3	2,25	0,7	0,15	0,9

Fig.6 présente l'espace de travail dextérité avec les paramètres géométriques (R=0.7 ; r=0.15 ; L=0.9), où (Cond(J) < CondJ$_{max}$ =3) dans l'espace (xyz) et dans les trois plans (xy), (xz), (yz), pour une meilleure visualisation.

Fig.7 présente l'espace de travail dextérité avec les paramètres géométriques (R=0.7 ; r=0.15 ; L=1.3), où (Cond(J) < CondJ$_{max}$ =3) dans l'espace (xyz) et dans les trois plans (xy), (xz), (yz),

Les Fig.8 et Fig.9 présentent successivement l'évolution du conditionnement de la matrice Jacobienne et de l'évolution du conditionnement de la matrice Masse dans un plan de l'espace de travail (z=0), avec les paramètres géométriques (R=0.7 ; r=0.15 ; L=0.9)

Représentation de l'espace de travail

Fig. 6 Espace de travail de robot Delta (R=0.7 ; r=0.15 ; L=0.9), Points en vert : Cond(J) <= CondJ_max , Points en rouge : Cond(J) > CondJ_max
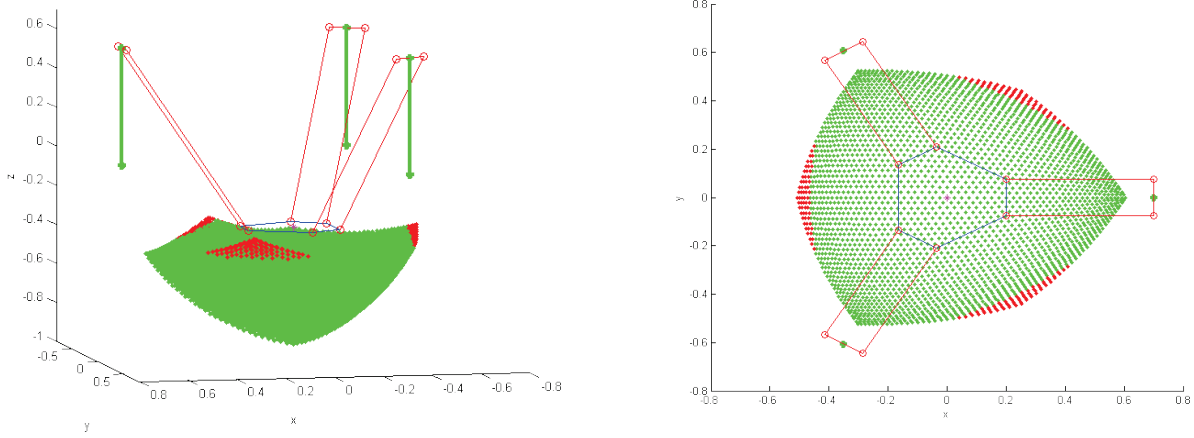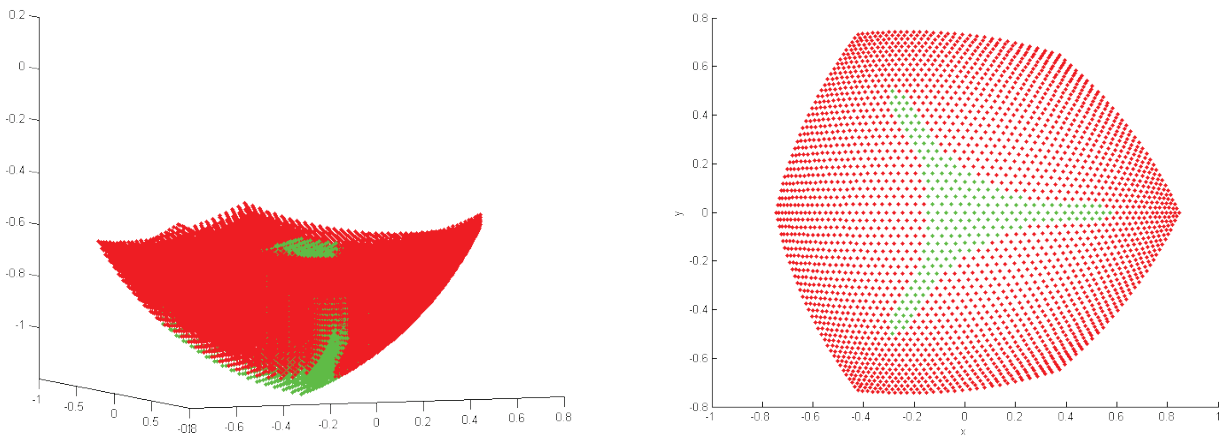

Fig. 7 Espace de travail de robot Delta (R=0.7 ; r=0.15 ; L=1.3),Points en vert : Cond(J) <= CondJ_max ,Points en rouge : Cond(J) > CondJ_max
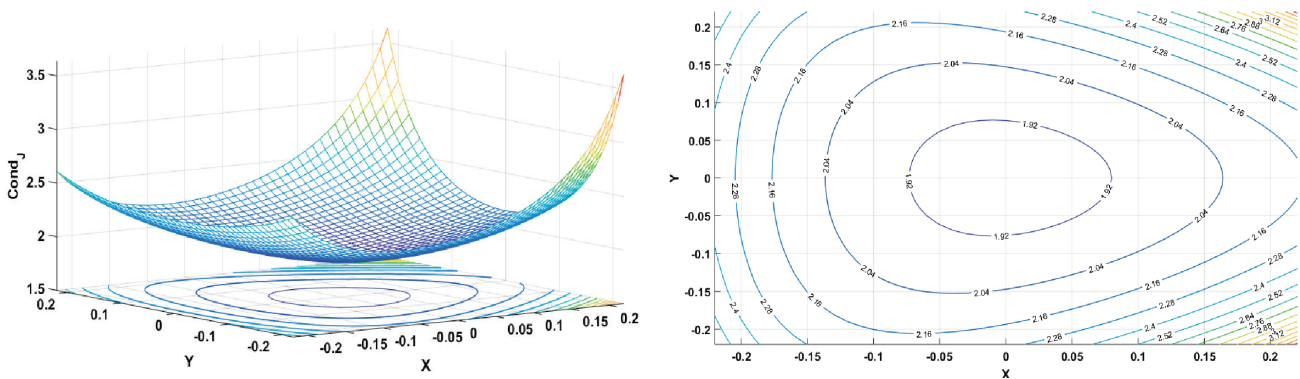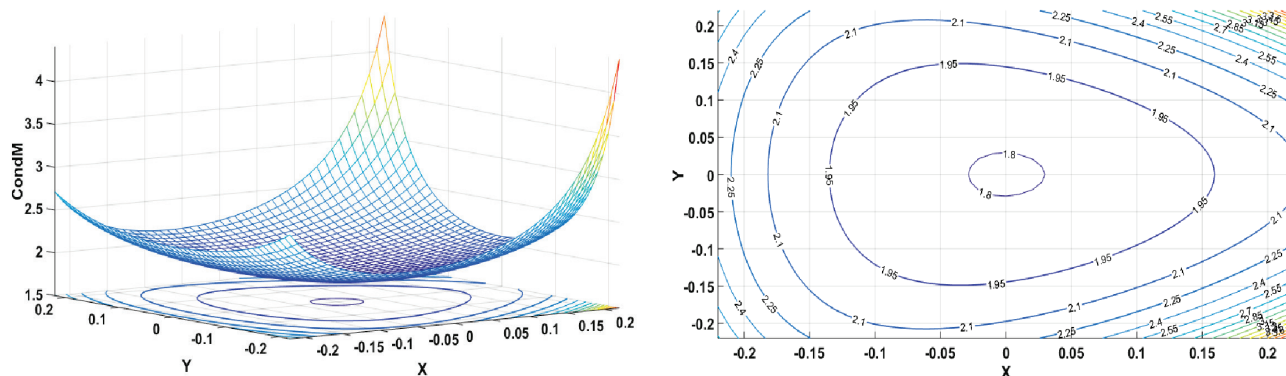

Fig. 8 Représentation de l'évolution du Conditionnement de la matrice Jacobienne dans un plan de l'espace de travail (z=0)

Fig. 9 Représentation de l'évolution du Conditionnement de la matrice Masse dans un plan de l'espace de travail (z=0)

6   Conclusion

Dans ce travail, nous avons présenté une méthodologie de conception dimensionnelle des robots parallèles, fondée sur une approche d'optimisation multi-objectif des différents critères de performance, tels que la rigidité, les performances cinématiques et dynamiques, ainsi que l'espace de travail dextérité à l'aide des algorithmes génétiques. . Pour sa résolution (Approche de la résolution), nous avons choisi l'algorithme génétique NSGA – II.

L'approche proposée permet de déterminer une bonne approximation du compromis (front de Pareto) entre les différents critères de performance qui sont parfois antagonistes, avec leurs vecteurs associés de paramètres géométriques optimisés, ce qui est très difficile à obtenir avec les méthodes classiques, qui ne peuvent pas prendre en compte tous ces critères simultanément. Le front de Pareto obtenu regroupe les meilleures solutions, notre choix de la solution est fait dans le but d'avoir un grand espace de travail dextérité, qui se traduit par le vecteur de paramètres géométriques [R=0.7 ; r=0.2 ; L=0.9].

REFERENCES

[1]- R. Clavel, DELTA, a fast robot with parallel geometry. In Proceedings of the 18th International Symposium on Industrial Robots, New York, Springer-Verlag, 1988, pp. 91-100.

[2]- R. Clavel, Device for displacing and positioning an element in space. Patent, WO1987/003528, 1987.

[3]- F. Pierrot, C. Reynaud, A. Fournier, DELTA: a simple and efficient parallel robot. Robotica 8(2) (1990) 105-109. doi:10.1017/S0263574700007669.

[4]- A. Codourey, Dynamic modelling and mass matrix evaluation of the DELTA parallel robot for axes decoupling control. In Proceedings of IEEE/RSJ International Conference on Intelligent Robots and Systems, Osaka, Japan, 1996, pp. 1211-1218. doi:10.1109/IROS.1996.568973.

[5]- M.-O. Demaurex, The Delta robot within the industry. In Parallel Kinematic Machines, Ed. Springer, 1999, pp. 395-399, doi:10.1007/978-1-4471-0885-6_28.

[6]- F. Holy, K. Steiner, Machining system with movable tool head. Patent US6161992A, 2000.

[7]- O Company, F. Pierrot, Modeling and Preliminary Design Issues of a 3-axis Parallel Machine-Tool. Mech. Mach. Theory 37(11) (2002) 1325-1345. doi:10.1016/S0094-114X(02)00040-X

[8]- J.-P. Merlet, Parallel robots. Solid Mechanics and its Applications vol. 74, Ed. Springer, 2001. doi:10.1007/978-94-010-9587-7

[9]- E.F. Fichter, D.R. Kerr, J. Rees-Jones, The Gough-Stewart platform parallel manipulator: A retrospective appreciation. P. I. Mech. Eng. C-J. Mec. 223(1) (2009) 243-281. doi:10.1243/09544062JMES1137.

[10]- R. Kelaiaia, O. Company, A. Zaatri, Multiobjective optimization of a linear Delta parallel robot. Mech. Mach. Theory 50(2012) 159-178. doi:10.1016/j.mechmachtheory.2011.11.004.

[11]- X.-J. Liu, J. Wang, K.-K. Oh, J. Kim, A New Approach to the Design of a DELTA Robot with a Desired Workspace. J. Intell. Robot. Sys. 39(2) (2004) 209-225. doi:10.1023/B:JINT.0000015403.67717.68.

[12]- O. Company, Machines-outils rapides à structure parallèle. Méthodologie de conception, applications et nouveaux concepts. Thèse de doctorat, Universite Montpellier II, France, 2000.

[13]- A. Kosinska, M. Galicki, K. Kedzior, Determination of parameters of 3-dof spatial orientation manipulators for a specified workspace. Robotica 21(2) (2003) 179-183. doi:10.1017/S0263574702004447.

[14]- E. Ottaviano, M. Ceccarelli, Optimal design of CaPaMan (Cassino Parallel Manipulator) with a specified orientation workspace. Robotica 20(2) (2002) 159-166. doi:10.1017/S026357470100385X

[15]- R.E. Stamper, L.-W. Tsai, G.C. Walsh, Optimization of a three DOF translational platform for well-conditioned workspace. In: Proceedings of International Conference on Robotics and Automation, Albuquerque, NM, USA, 1997, pp. 3250-3255. doi:10.1109/ROBOT.1997.606784

PEM fuel cell as an alternative solution for clean energy production

Khelaifa Khaoula[1], Abdelmalek Atia[1,*], Hocine Ben Moussa[2], Ferdjani Abdelfettah[1] and Yahia Abdennour[1].

[1] Univ. El-Oued ,Levres Lab, Algeria
[2]Univ. Batna,Algeria

*Corresponding author: abdelmalek-atia@univ-eloued.dz;Tel.: +213 550 31 59 60

ARTICLE INFO	ABSTRACT/RESUME
	Abstract:Due to the energy crisis and the rising level of pollution around the world, a new source of clean energy is the fuel cell, as it has no production other than water and heat. PEMFC (Proton Exchange Membrane Fuel Cell) is an electrochemical device that are designed to directly convert, with high efficiency, the chemical energy from the reaction of the fuel (hydrogen in case of PEMFC) and an oxidant (oxygen) into electricity. This study aims to setup a state of the art on PEM Fuel Cell.

I-Introduction

Increasing levels of pollution and possible anthropogenic global warming resulting   from the combustion of fossil fuels have urged scientists to consider alternative energy conversion and power generation systems that could satisfy the global energy demands in more environmental-friendly ways[1]. Wind, tidal, solar and hydrogen based renewable energy systems are some of the potential areas in this regard. Hydrogen-based renewable energy systems such as fuel cells offer a promising pathway with the prospect of low- to zero-emissions during power   generation for sub-watt to megawatt applications in transportation, manufacturing and communications.

The combination of high efficiency, environmental benefits and versatility make fuel cells a suitable power generation device for both terrestrial and space applications. Despite these potential benefits, the commercial deployment of fuel cells faces many challenges such as, high operating cost and a lack of existing hydrogen infrastructure.

The fuel cell was first demonstrated by Lawyer-cum-inventor William Grove in 1839, but no further significant research was carried out in this field until the late 1940s. The first commercial application of a fuel cell was in space and military systems[2]. Among the different types of fuel cells, the polymer electrolyte membrane (PEM) fuel cell is considered a promising approach due to its low operating temperature and simple design configuration. The basic operating principle of a fuel cell is simple, but involves the coupling of complex transport phenomena such as species transport by convection and diffusion, heat transfer, charge balance and electrochemical kinetics[3]. These transport phenomena lead to certain efficiency losses in the fuel cell that affect its overall performance. The performance of a fuel cell can be investigated in two ways; either by experimental techniques or by numerical simulations. Experimental methods have limitations when investigating the complex interaction of transport phenomena taking place inside the fuel cell, whereas numerical modelling provides a better insight into the problem. Furthermore, it is not possible to perform detailed in-

634

situ measurements of a fuel cell during its operation because of its reactive environment. The complex experimental setup of the fuel cell system has stimulated efforts to develop sophisticated numerical models of the fuel cell that can simulate and predict the coupled transport of reactant and product species, heat transfer and charge balance along the fuel cell domain.

A several scientific papers were performed on PEM Fuel Cell system and its application. Theses researches were contributedsignificantly on the improvement of the PEMFC performances and uses.

Sudarshan L *et all*[4]are used identification black box approach system to develop more realistic mathematical model for dynamic behaviour inside a polymer electrolyte membrane (PEM) fuel cell. The performance of each model structure was validated with the data from a $25\,cm^2$ active area practical PEMFC. Their devellped model models can be used to predict polarization behavior under different loading conditions in PEMFC system.

Nanofluid adoption as an alternative coolant for PEMFC thermo-electrical performances improvement was studied by IrnieZakaria et all [5]. In this articl, Thermo-physical properties of 0.1, 0.3 and 0.5% volume concentration of Al_2O_3 nanoparticles dispersed in water was used.Theirresultwas depicted that the cooling rate improved up to 187% with the addition of 0.5% volume concentration of Al_2O_3 nanofluids to the base fluid of water. The obtained improvement was interpreted by the excellent thermal conductivity property of nanofluids as compared to the base fluid.

Horng-Wen Wu et all [6] was performed a numerical study on the effect of flow field designchnagement by the arrangement pattern of the protrusive gas diffusion layer (GDL) on the cell performance for a full-scale serpentine channel. This paper showed that the arrangement pattern of protrusive GDL affects the electric power, pressure drop, and the net power of the PEM fuel cell. In different paper, Horng-Wen Wu [7] is reviewed the transport phenomana and performance modeling of proton exchange membrane (PEM) fuel cells during the past few years. He defined the PEM fuel cell as a set of distinct devices and a series of transport phenomanenthrough gas porous channels, electric power production through membrane electrode assembly and electrochemical reactions. It can be conclude from thispaperthat there are a lot findings and enhancement of PEMFC system performance through numerical modelling and simulation studies.

The PEM fuel cell is exposed to different mechanical stresses due to the different assembly procedures, operational and environmental working conditions. Ahmed MohmedDafalla and Fangming Jiang [8] are carried out a review research on the mentioned problem. These stresses include the compressive clamping stress, hygrothermal stress,

freeze-thaw stress, and the stress due to vibration conditions. The review depicted that the combination of these stresses may be lead to PEMFC performance degradation and structural damage. As consequence, avoiding generated stress are necessary for improving PEM fuel cell permanence and durability.

A numerical simulation using Matlab–Simulink environment was performed by Z.Abdin et all [9]. The adopted model was based on parameters with direct physical meaning, with the aim to get empirically describion on the characteristics of the fuel cell. The impact of different parametres namely pressure, temperature, humidification and reactant partial pressure on cell performance are studied. The proposed simplifying assumptions led to fairly light in computational demand of the adopted model and it getout a result with well corcordance with experimental data especially at high current density.

This paperaims to review PEM fuel cell system, itsworkingprincipalsandits applications.
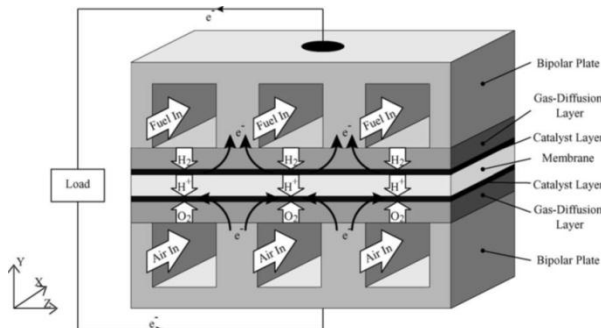
II. Fuel Cell Types

There are different types of the fuel cell systems have been investigated by researchers to improve their performance and promote their commercialization. Theses classes of fuel cells have emerged as viable power systems for the present and near future applications. Each type of fuel cell has some merits and drawbacks. A brief description of the major types of fuel cells is presented in the following sections.

II.1 Polymer Electrolyte Membrane (PEM) Fuel Cell

The polymer electrolyte membrane (PEM) fuel cell is regarded as one of the most promising types of fuel cells due to its simplicity and low operating temperature. This type of fuel cells generally operate between 50 to 100 °C, which makes them suitable for automotive and mobile applications [1].In this type of fuel cells, the electrolyte is a solid polymer which contains mobile protons. The major drawback of the low operating temperature of PEM fuel cells is the low electrochemical reaction rate, which can be addressed using sophisticated catalysts and electrodes.

A lot of research has been done on various aspects of PEM fuel cells. The standard single PEM fuel cell is a combination of two endplates as current collectors, two gas diffusion layers, two catalyst layers and a proton exchange membrane Generally, the hydrogen is fed in from anode side channel and split in the catalyst layer into protons and electrons. The protons pass through the membrane to the cathode catalyst where they combine with the oxygen fed in from the cathode-side channel and electrons from the external electric circuit to form

635

Algerian Journal of Environmental Science and Technology
April edition. Vol 4.Nº 1. (2018)
ISSN   : 2437-1114
www.aljest.org

water. The movement of the electrons in the external circuit is the current generated.

Figure 1.*Schematic of a PEM fuel cell[3]*

II.2 Phosphoric Acid Fuel Cell

This type of fuel cells uses liquid phosphoric acid as an electrolyte. Hydrogen is introduced at the anode side and is oxidized to produce positively charged protons and negatively charged electrons. The ionic conductivity of the phosphoric acid is low at low temperatures. Furthermore, it solidifies at temperatures below 40 °C, which makes the initial start-up difficult and restricts the continuous operation of this type of fuel cells . Phosphoric acid fuel cells operate at a temperature of around 220 °C and can tolerate carbon monoxide, which is not acceptable for many other types of fuel cells. Moreover, In this type of fuel cells, the hydrogen fuel problem can be solved by reforming natural gas (CH₄, methane) to hydrogen and carbon dioxide, but the equipment required for this adds considerable cost, complexity and size to the fuel cell system[10].

II.3 Solid Oxide Fuel Cell

Solid oxide fuel cells are made up of four layers, three of which are ceramic. Ceramics do not become ionically active until they reach at very high temperature and therefore the solid oxide fuel cell is only operational in the region of 800-1200 ºC. Oxygen gas enters at the cathode side while fuel enters at the anode side. Light hydrocarbon fuels such as methane, propane and butane are mostly used as fuels in this type of fuel cell. Oxygen is reduced into oxygen ions at the cathode side. These oxygen ions then diffuse through the solid oxide electrolyte to the anode where they electro-chemically oxidize the fuel. This type of fuel cell is generally suitable for large industrial applications because of its high operating temperature range. Due to such high

temperatures, a fast reaction rate can be achieved without using any expensive catalysts[11].

II.4 Molten Carbonate Fuel Cell

This type of fuel cell is a mixture of molten alkali metal carbonates, usually a binary mixture of lithium and potassium, or lithium and sodium carbonates. It should be operate at 650 °C in order toliquefy the carbonate salts and achieve high ion mobility through the electrolyte.Unlike other types of fuel cells; molten carbonate fuel cells do not necessitate any external reformer to extract hydrogen from energy-dense fuels. Due to its high operating temperature, the fuels are converted into hydrogen within the fuel cell itself by internal reforming[12].
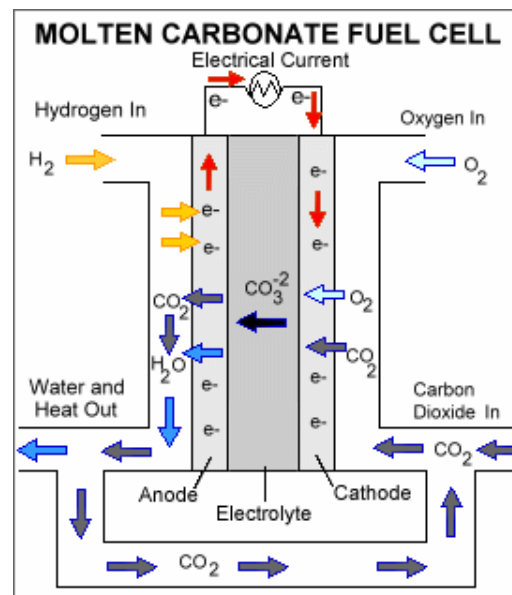
Figure 2.*molten carbonate fuel cells working princible[3]*

III. PEM Fuel Cell operating principles

PEM fuel cells consist of three major components: a negatively charged electrode (cathode), a positively charged electrode (anode) and a membrane electrode assembly. The membrane electrode assembly consists of a current collector, a porous gas diffusion layer, a catalyst layer and an electrolyte membrane. The operating principle of a PEMFC is simple and can be considered to be the opposite of electrolysis in wicth the electric current is passed through water to produce hydrogen and oxygen, however in a PEM fuel cell, hydrogen and oxygen gases are passed at either side of the polymer

636

electrolyte membrane where hydrogen is split into its elementary constituents - the positively charged proton ions and the negatively charged electrons.

The potential difference between anode and cathode attracts the protons from anode to cathode causing them to travel through the electrolyte membrane, whereas the electrons travel first through an external circuit and then to the membrane catalyst layer interface at the cathode side where they react with the reduced oxygen atoms, following this, the reduced oxygen atoms react with the protons diffusing through the membrane to produce heat and water as by-products [13].The electrochemical reactions for the PEM fuel cell can be stated as follows:
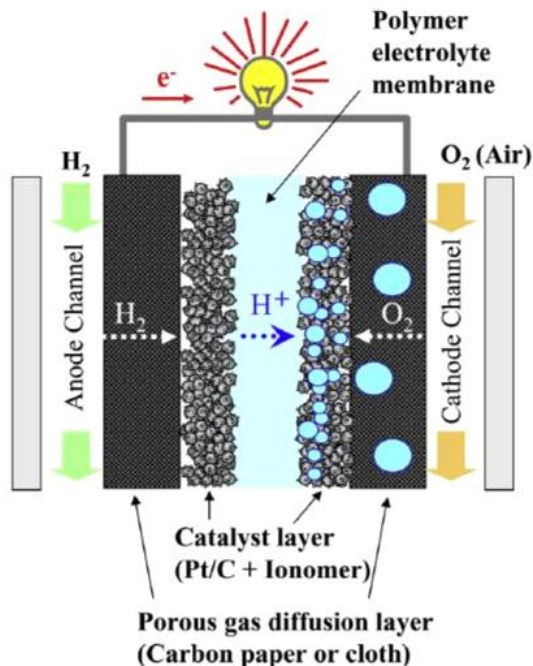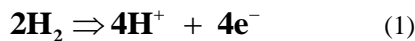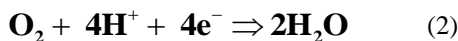

Figure 3.*Schematic view of a PEM fuel cell and its operating principles[14]*

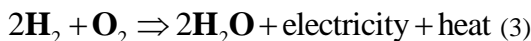At the catalyst layer, the hydrogen splits into hydrogen protons and electrons according to:

$$2H_2 \Rightarrow 4H^+ + 4e^- \tag{1}$$

Cathode Reaction:

$$O_2 + 4H^+ + 4e^- \Rightarrow 2H_2O \tag{2}$$

The overall reaction is exothermic and can be written as:

$$2H_2 + O_2 \Rightarrow 2H_2O + electricity + heat \tag{3}$$

IV. PEM Fuel Cell Components

A PEM fuel cell consists of four major components. The following sections briefly describe these components and their role in the operation of the fuel cell.

IV.1 Polymer Electrolyte Membrane

The polymer electrolyte membrane is the heart of a PEM fuel cell. It has two main functions; firstly, it works as a gas separator, preventing the reactant gases from directly reacting with each other; secondly, it acts as the proton conductor. Typically, the electrolyte membrane consists of a Perfluroinated polymer backbone with Sulphonyl acid side chains [15].Nafion® membranes by Du-Pont are typically used as the de-facto standard for most of the polymer electrolyte fuel cells.

However, there are also other variants of electrolyte membranes, such as Flemion® and Aciplex® membranes, which are well known in the fuel cell industry [16]. Membranes have to be hydrated so as to sustain their protonic conductivity. It is therefore necessary for the membrane to retain a certain amount of water content so as to maintain its ability to transfer protons. This depends on two phenomena; firstly, that of the chemical affinity for water in hydrophobic regions of the membrane, which enables the membrane to absorb and retain water; secondly, that of the electro-osmotic drag phenomena, whereby each hydrogen ion is accompanied by one or two molecules of water [17].The requirement to keep the membrane hydrated restricts PEM fuel cell operation at higher temperatures. In general, to achieve high efficiency, the membrane must possesses the following properties [18, 19]
a) High proton conductivity to support high currents with minimum resistive losses and zero electronic conductivity.
b) Adequate mechanical strength and durability.
c) Chemical stability under operating conditions.
d) Extremely low fuel or oxygen by-pass to minimize crossover current.
e) Reasonable production cost which is compatible with intended application.

IV.2 Gas Diffusion Layer (GDL)

The gas diffusion layer enables efficient distribution of the reactant and product species along the fuel cell domain. The gas diffusion layer is made up of a sufficiently porous and electrically conductive material. Materials of a typical gas diffusion layer include carbon paper or carbon cloth with typical thicknesses of 100- 300 μm[2]. The GDL is intentionally porous to increase the wetted surface area by hundreds and even thousands times the geometric surface area [13].

The gas diffusion layer is characterized by its thickness, hydrophobic nature and dry resistance to flow and electric properties [20]. Performance of the PEM fuel cell is immensely influenced by the reactant/product species distribution along the gas diffusion layer since it can lead to issues such as water flooding and poor concentration distribution.

637

To facilitate excess water removal from the fuel cell and minimize water flooding, the hydrophobicity of the GDL is increased by impregnating it with a hydrophobic material. The amount of hydrophobic agent used is a sensitive parameter as excess impregnation can result in the blockage of surface pores and thus a reduction of the GDL porosity [21].

IV.3 Catalyst Layer

A fine layer of catalyst, usually the noble metal platinum (Pt), is applied to both faces of the electrolyte membrane. A catalyst loading of 0.1-0.3 mg/cm2 per membrane catalyst layer is typically used. The thickness of the catalyst layer is usually in the range 5-15 μm[22]. Due to the high cost of platinum, it must be used sparingly in order to reduce the overall cost of the PEM fuel cell[23].The catalyst layer breaks the bonds between the atoms of the reactant species and promotes higher reaction rates. At the anode side, the hydrogen molecules are absorbed onto the surface of the catalyst and the bonds between the hydrogen atoms are stretched and weakened so that they eventually break. A similar mechanism occurs on the cathode side where the reduction of oxygen is promoted by the action of the catalyst.
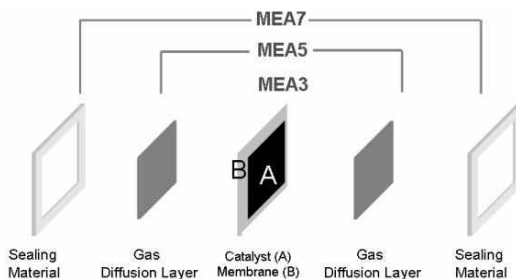
Figure 4.fuel cell catalyst construction[16]

IV.4 Gas Flow Channel (Bipolar / End Plates)

The interconnection between the fuel cells in a stack is achieved using conductive plates. When machined on both sides, they are normally called bipolar plates. Plates which are fitted at the edges of the fuel cell stack and are machined on one side only are termed end plates. The term electrode plates will be used here to refer to the bipolar and end plates. These plates are an important component of any fuel cell system because they assist the supply of fuel and oxidant to the reactive sites, remove reaction products, collect produced current and provide structural support [24]. Usually, when the electrode plates are made of graphite; they represent about 60

% of the total weight of PEMFC, 30% of its total cost and 80% of its total volume. Hence,the designs of the electrode plates play a significant role in the weight and cost of a fuel cell. The essential requestsof these plates are [2]:

- High values of electronic and thermal conductivity;
- High mechanical strength;
- Impermeability to reactant gases;
- Resistance to corrosion;
- Low cost of production.

Bipolar plates are usually constructed from graphite. However, graphite is porous, fragile, and needs to be thick for the required strength, leading to an increase in weight, size and cost. As such, alternative materials have been under intense study by various researchers [25]. Different design topologies, i.e. straight, serpentine or spiral shapes have been used by the researchers to achieve the aforementioned functions efficiently with the aim of obtaining high performance and economic advantages. Around a 50% increase in fuel cell performance has been reported just by improving the distribution of the gas flow fields [26]. Bipolar/end plates typically have fluid flow channels stamped on their surfaces. Flow channel geometry at both the anode and cathode sides can be different from each other depending on their design requirements. The essential requirements for the bipolar plates with respect to physio-chemical characteristics are the uniform distribution of the reactant species over the active surface of the electrode to minimize the concentration over potential. The choice of flow field configuration strongly affects the performance of a PEM fuel cell, especially in terms of water management and distribution of reactant species. Due to this, the effective design and optimization of the gas flow fields and the bipolar plates remains a very important issue for cost reduction and performance improvement of the PEM fuel cell. The different types of flow field configurations that have been used by researchers are discussed in the following sections.

a) Serpentine Shaped Gas Flow Channel

The serpentine shaped gas flow channel configuration is a common option for many fuel cell designers. In this design configuration, only one flow path exists for the reactant gases across the flow field plate and any liquid water accumulating in the channel is quickly pushed out of the cell. Watkins *et al.*[27]studied the optimization of serpentine shaped flow channels. This type of flow field configuration

638

results in high pressure losses and therefore needs a high pressure flow.
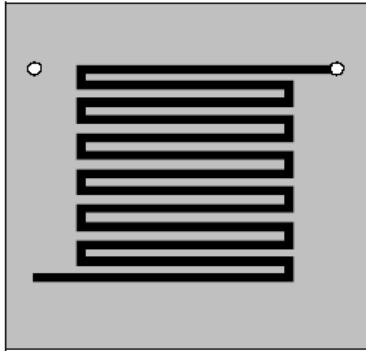

Figure 5.*Serpentine shaped gas flow channel configuration [27]*

b) Parallel/Straight Shaped Gas Flow Channel

Pollegri*et al.*[24]introduced the concept of a parallel/straight type gas flow channel configuration. This type of flow field has an advantage over the serpentine shaped channels due to the lower pressure losses; on the other hand, a major drawback is that different paths exist across the bipolar plate for the reactant gases, potentially causing ineffective water removal because of the uneven flow distribution of the reactant flow through the fuel cell domain**.**
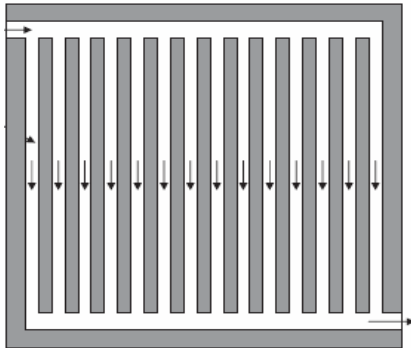

Figure 6.*Parallel gas flow channel configuration [24]*

c) Spiral Shaped Gas Flow Channel

Kaskimies et al. [27] proposed a spiral shaped gas flow field configuration. This configuration combines the effective water removal of the single channel geometry with the advantage of having channels containing fresh and depleted cathode gas side by side, leading to better distributions of oxygen and water. However, the manufacturing cost of this type of flow field configuration is significantly higher.
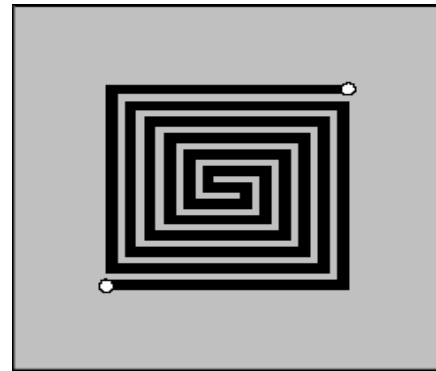

Figure 7.*Spiral flow field configuration [26]*

V- Conclusion

This paper reviewed the existing literature on PEM type fuel cells, mainly focusing upon the important type, components and reactions taking place inside its domain. Different materials for bipolar/end plates were also discussed in this research. PEM fuel cells have undeniable advantages, system performance, good dynamics and low operating temperature. Regardless of the problem of availability and supply of hydrogen, many points remain to be addressed (cost, mass and volume, service life, thermal management, fluidic management).

If we look to the great number of studies interest by PEM fuel cell system, we can conclude that this subject is being very important in Clean Technologies and Environmental Sciences.

VI- References

1. A. Atia and K. Mohammedi, "State of the art on enhanced oil recovery with CO2 sequestration for low carbon industry," *Algerian J. Env. Sc. Technology,* vol. 3, 2017.
2. V. Mehta and J. S. Cooper, "Review and analysis of PEM fuel cell design and manufacturing," *Journal of Power Sources,* vol. 114, pp. 32-53, 2003.
3. J. Larminie, A. Dicks, and M. S. McDonald, *Fuel cell systems explained* vol. 2: J. Wiley Chichester, UK, 2003.
4. S. L. Chavan and D. B. Talange, "System identification black box approach for modeling performance of PEM fuel cell," *Journal of Energy Storage,* vol. 18, pp. 327-332, 2018.
5. I. Zakaria, W. Mohamed, W. Azmi, A. Mamat, R. Mamat, and W. Daud, "Thermo-electrical performance of PEM fuel cell using Al 2 O 3 nanofluids," *International Journal of Heat and Mass Transfer,* vol. 119, pp. 460-471, 2018.
6. H.-W. Wu, G.-J. Shih, and Y.-B. Chen, "Effect of operational parameters on transport and performance of a PEM fuel cell with the best protrusive gas diffusion layer arrangement," *Applied Energy,* vol. 220, pp. 47-58, 2018.
7. H.-W. Wu, "A review of recent development: Transport and performance modeling of PEM fuel cells," *Applied Energy,* vol. 165, pp. 81-106, 2016.

639

8.   A. M. Dafalla and F. Jiang, "Stresses and their impacts on proton exchange membrane fuel cells: A review," *International Journal of Hydrogen Energy,* 2017.

9.   Z. Abdin, C. Webb, and E. M. Gray, "PEM fuel cell model and simulation in Matlab–Simulink based on physical parameters," *Energy,* vol. 116, pp. 1131-1144, 2016.

10.   M. Watanabe, K. Tsurumi, T. Mizukami, T. Nakamura, and P. Stonehart, "Activity and stability of ordered and disordered Co-Pt alloys for phosphoric acid fuel cells," *Journal of The Electrochemical Society,* vol. 141, pp. 2659-2668, 1994.

11.   R. M. Ormerod, "Solid oxide fuel cells," *Chemical Society Reviews,* vol. 32, pp. 17-28, 2003.

12.   A. L. Dicks, "Molten carbonate fuel cells," *Current Opinion in Solid State and Materials Science,* vol. 8, pp. 379-383, 2004.

13.   A. R. Balkin, "Modelling a 500W polymer electrolyte membrane fuel cell," *University of Technology, Sydney,* 2002.

14.   S. Tsushima and S. Hirai, "In situ diagnostics for water transport in proton exchange membrane fuel cells," *Progress in Energy and Combustion Science,* vol. 37, pp. 204-220, 2011.

15.   S. Haufe and U. Stimming, "Proton conducting membranes based on electrolyte filled microporous matrices," *Journal of Membrane Science,* vol. 185, pp. 95-103, 2001.

16.   M. Mustafa, "Design and manufacturing of a (PEMFC) proton exchange membrane fuel cell," Coventry University, 2009.

17.   K. Kreuer, "On the development of proton conducting polymer membranes for hydrogen and methanol fuel cells," *Journal of membrane science,* vol. 185, pp. 29-39, 2001.

18.   M. Rikukawa and K. Sanui, "Proton-conducting polymer electrolyte membranes based on hydrocarbon polymers," *Progress in Polymer Science,* vol. 25, pp. 1463-1502, 2000.

19.   B. Smitha, S. Sridhar, and A. Khan, "Solid polymer electrolyte membranes for fuel cell applications—a review," *Journal of membrane science,* vol. 259, pp. 10-26, 2005.

20.   E. Ramunni and M. Kienberger, "Gas-diffussion electrodes for polymeric membrane fuel cell," ed: Google Patents, 2000.

21.   D. Bevers, R. Rogers, and M. Von Bradke, "Examination of the influence of PTFE coating on the properties of carbon paper in polymer electrolyte fuel cells," *Journal of power sources,* vol. 63, pp. 193-201, 1996.

22.   M. S. Wilson and S. Gottesfeld, "Thin-film catalyst layers for polymer electrolyte fuel cell electrodes," *Journal of applied electrochemistry,* vol. 22, pp. 1-7, 1992.

23.   R. Fernandez, P. Ferreira-Aparicio, and L. Daza, "PEMFC electrode preparation: influence of the solvent composition and evaporation rate on the catalytic layer microstructure," *Journal of power sources,* vol. 151, pp. 18-24, 2005.

24.   X. Li and I. Sabir, "Review of bipolar plates in PEM fuel cells: Flow-field designs," *International journal of hydrogen energy,* vol. 30, pp. 359-371, 2005.

25.   A. Kumar and R. G. Reddy, "Materials and design development for bipolar/end plates in fuel cells," *Journal of Power Sources,* vol. 129, pp. 62-67, 2004.

26.   D. S. Watkins, K. W. Dircks, and D. G. Epp, "Fuel cell fluid flow field plate," ed: Google Patents, 1992.

27.   D. S. Watkins, K. W. Dircks, and D. G. Epp, "Novel fuel cell fluid flow field plate," ed: Google Patents, 1991.

Accepted Manuscript

Pore-scale study based on lattice Boltzmann method of density driven natural convection during CO_2 injection project

Abdelmalek Atia, Kamal Mohammedi

Please cite this article as: Abdelmalek Atia, Kamal Mohammedi, Pore-scale study based on lattice Boltzmann method of density driven natural convection during CO_2 injection project, (2015), doi: 10.1016/j.cjche.2015.07.010

2014-0408

CO_2 注入时密度差引起的自然对流 Boltzmann 网格法中孔喉尺度的研究
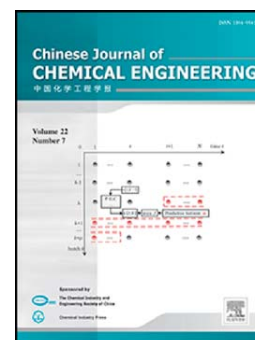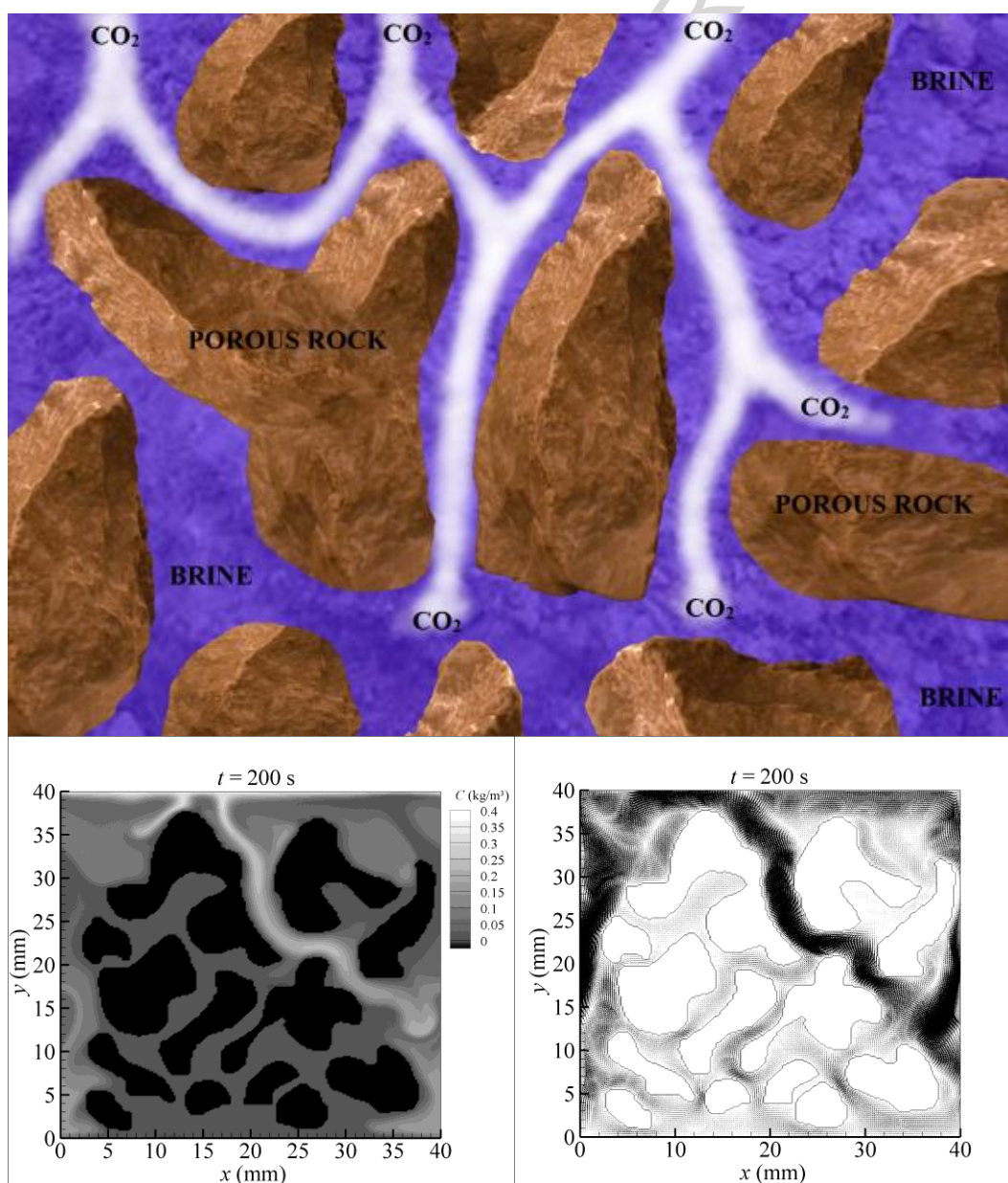
Graphic abstract

Fluid Dynamics and Transport Phenomena

Pore-scale study based on lattice Boltzmann method of density driven natural convection during CO_2 injection project

Abdelmalek Atia[1,2,*] , **Kamal Mohammedi**[1]

[1] Univ. Boumerdes, LEMI Lab, Algeria

[2] Univ. El-Oued , LEVRES Lab, Algeria

[*] To whom correspondence should be addressed. E-mail: abdelmalek-atia@univ-eloued.dz

Abstract Saline aquifers are chose for geological storage of greenhouse gas CO_2 because of their storage potential. In almost all cases of practical interest, CO_2 is present on top of the liquid and CO_2 dissolution leads to a small increase in the density of the aqueous phase. This situation results in the creation of negative buoyancy force for downward density-driven natural convection and consequently enhances CO_2 sequestration. In order to study CO_2 injection at pore-level, an isothermal Lattice Boltzmann Model (LBM) with two distribution functions is adopted to simulate density-driven natural convection in porous media with irregular geometry obtained by image treatment. The present analysis showed that after the onset of natural convection instability, the brine with a high CO_2 concentration infringed into the underlying unaffected brine, in favor of the migration of CO_2 into the pores structure. With low Rayleigh numbers, the instantaneous mass flux and total dissolved CO_2 mass are very close to that derived from penetration theory (diffusion only), but the fluxes are significantly enhanced with high *Ra* number. The simulated results show that as the time increases, some chaotic and recirculation zones in the flow appear obviously, which promotes the renewal of interfacial liquid, and hence enhances dissolution of CO_2 into brine. This study is focused on the scale of a few pores, but shows implications in enhanced oil/gas recovery with CO_2 sequestration in aquifers.

Keywords Lattice Boltzmann method, Density driven, Pore-scale, CO_2, Mass transfer

1. Introduction

The growing concerns over the global warming due to the increase in the global concentration of greenhouse gases in the atmosphere has increased the interest in examining various techniques to reduce the emission of these gases. A main component of greenhouse gases is carbon dioxide (CO_2).

A promising long term solution for mitigating global heating is to inject CO_2 into geological formations; either for CO_2 sequestration or enhanced oil/gas recovery. A suitable choice of geological formations for CO_2 sequestration includes coal beds, depleted petroleum and gas reservoirs, deep-sea sediments, and deep saline aquifers. In many practical cases, geological storage of CO_2 is accomplished by injecting it in supercritical phase into a porous rock formation below the earth surface which is already saturated with a liquid (water or oil) [1,2]. The great concern on geological CO_2 trapping is the long-term fate and security of the stored CO_2. More specifically, researchers are concerned with preventing potential leakage of CO_2 from underground reservoirs, which might be caused by fractures in cap rock or abandoned oil/gas wells [3]. Therefore, the analysis of CO_2 dissolution phenomena in underground geological formations is of great importance in CO_2 injection projects.

In most CO_2 injection studies over the world, the carbon dioxide is injected in the supercritical phase. The supercritical density of CO_2 is about 70% of water density, and the kinematic viscosity is 0.1–0.25 of water [4]. Hence, it is expected that when CO_2 is injected into the porous formation, initially it accumulates under low-permeability cap rock and subsequently dissolves into the formation liquid by molecular diffusion [5]. As a result, the saline density aquifer increases and eventually the CO_2–brine interface become unstable. For favorable conditions, density driven natural downward convection occurs and CO_2–saturated brine moves downward and is replaced by underlying unaffected brine, which enhances the mass transfer of CO_2. Numerous experimental and theoretical studies on the density-driven natural convection process in porous media [2,6-8] are available. Rapaka *et al.* studied the effect of anisotropy in the permeability fields on density-driven natural convection [9]. Li and Dong reported experimental studies of carbon dioxide diffusion in porous media under reservoir conditions [10]. They presented a new method for measuring the effective CO_2 diffusion coefficient in oil-saturated porous media under reservoir conditions. The investigation of the effect of heterogeneity on density-driven natural convection of CO_2 overlying a brine layer was studied by Farajzadeh *et al.* [11]. The spectral method has been used to generate permeability heterogeneity fields. Chen *et al.* investigated experimentally the velocity distribution in Rayleigh convection in the gas–liquid mass transfer of acetone volatilization in acetone-ethyl acetate binary system via particle image velocimetry (PIV) [12].

During the past two decades, Lattice Boltzmann Method (LBM) has been demonstrated to have the advantages in clear mathematical and physical meanings, easy implementation of the boundary conditions in complex geometry like real porous structure, high computational efficiency, numerical accuracy and easy parallelization. LBM has been successfully applied to the simulation of fluid flow including single- and multiphase flows [13,14], natural convection caused by temperature gradient [15,16], and double diffusive natural convection in a cavity with a hot square obstacle inside [17], Rayleigh convection generated by a local high concentration gradient in the gas–liquid mass transfer process of CO_2 absorption into liquid ethanol [18,19], density driven natural convection in anisotropic and heterogeneous saline aquifers [4]. Cheng *et al.* [3] have simulated the density driven

natural convection in simple fractured porous media at pore scale by using LBM. However, in real porous media the geometry is rather irregular and complex.

In this study, a two-dimensional LBM with a double distribution model is implemented for simulating density driven natural convection of CO_2 in porous medium of irregular geometry. The density driven natural convection was manipulated by a high concentration gradient area at the top boundary. The complicated coupling between pore geometry, dissolution of CO_2, and density-driven natural convection was investigated. The simulated results are used to investigate the velocity, concentration fields, the instantaneous mass flux and total dissolved CO_2 mass.

2. Problem Definition and mathematical Model

2.1. Pore-level view of CO_2 injection project

Figure 1 shows a schematic of pore-level image during CO_2 injection in saline aquifers. Porous rocks in the geological formation have a wide range of pore scales. Injected CO_2 accumulates under the low permeability cap rock and slowly diffusion into brine. The density of CO_2- saturated brine is slightly increased, as a results the density driven natural convection occurs and downward. However, there is little pore-scale investigation of the process coupling density driven natural convection and CO_2 dissolution in real porous structure. In the following sections, the LB method will be described for the pore-level study.

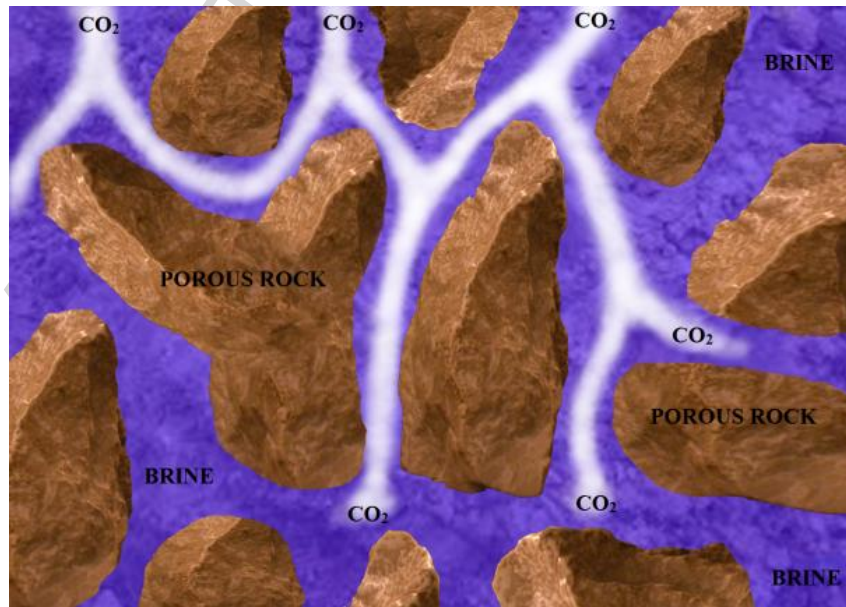Fig. 1. Schematic illustration of pore-level CO_2 injection, dissolution and natural convection

2.2. Problem statement

The two-dimensional computational domain of the problem is shown in Fig. 2. The geometry is considered as a porous structure packed with irregular grains retrieved by image processing and filled with quiescent brine. The domain has a total dimension of 200×200 non-dimensional lattice

unit with a resolution of 0.2 mm per unit. Thus, the domain dimension $(h \times h)$ in the real system is 0.04×0.04 m^2. The thermal effect of absorption of CO_2 is assumed to be isothermal. Also, the chemical interactions and diffusion between rocks / fluids are neglected, so the dissolved CO_2 acts as a conservative solute tracer. The top boundary of this domain is CO_2-brine free interface. The bottom boundary is considered as solid wall. Because the natures of velocity and concentration distributions are complex and random in the density driven natural convection process, we simulate a simple case where the top boundary is a free surface with a constant concentration corresponding to the solubility of carbon dioxide.
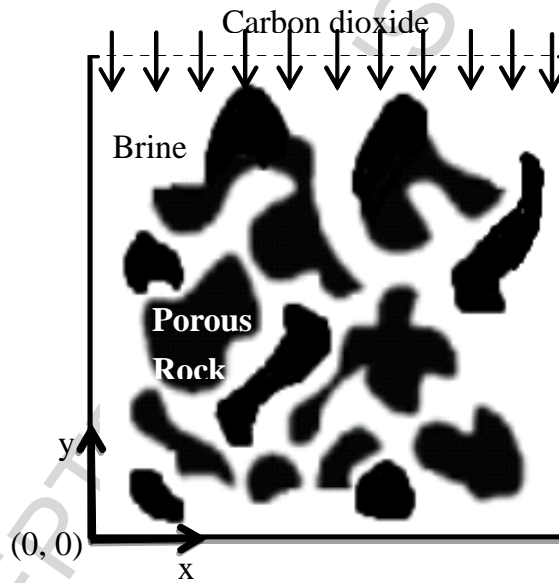
Fig. 2. Geometry of the computational domain of porous structure

The physical properties of the brine and the saturated brine-CO_2 are given in Table 1. In the simulation, an interfacial concentration value of 0.4 kg/m^3 at the CO_2-brine interface was taken.

Table 1 Physical properties of pure brine and saturated brine-CO_2 at T=296.15 K, P=101.0 kPa

$\rho_{\text{brine}}^{(1)}$, kg/m^3	$\Delta\rho^{(1)}$, kg/m^3	$C_s^{(1)}$, kg/m^3	$D^{(2)}$(m^2/s)	$\mu^{(2)}$, Pa·s
1000	10	10	1.85×10^{-9}	0.93×10^{-3}

Note: (1) From [4], (2) from [20].

2.3. LBM model with double distribution functions

Unlike macroscale differential approaches based on traditional Navier-Stokes equations, the LBM discretizes the fluid into particles which are individually sited on every node of a lattice system. At the end of each time step, the particles move and collide with others, and the distribution probability of particle density at a node after the collision obeys the Boltzmann equation. The underlying concept of the LBM is to incorporate the essential physics of the problem into the

5

simplified kinetic equation such that the correct macroscopic behavior of the fluid is recovered [18]. A D2Q9 (9 velocity vectors in 2-D space) lattice model was adopted in this study. The LB equation for fluid flow is written as [21]

$$f_i\left(\boldsymbol{x}+\boldsymbol{e}_i\delta t,t+\delta t\right)=f_i\left(\boldsymbol{x},t\right)-\frac{f_i\left(\boldsymbol{x},t\right)-f_i^{\,eq}\left(\rho,\mathbf{u}\right)}{\tau_f} \quad (i=0,1,2....8) \tag{1}$$

where $f_i\left(\boldsymbol{x},t\right)$ is the volume-averaged distribution function for the particle at lattice location $\boldsymbol{x}$ and time t traveling along the i-th direction; $\boldsymbol{e}_i$ is the lattice velocity vector corresponding to direction i, which is defined as

$$\boldsymbol{e}_i=c\begin{cases} 0 & \text{for } i=0 \\ \left(\cos\left[(i-1)\dfrac{\pi}{2}\right],\sin\left[(i-1)\dfrac{\pi}{2}\right]\right) & \text{for } i=1,2,3,4 \\ \sqrt{2}\left(\cos\left[(i-5)\dfrac{\pi}{2}+\dfrac{\pi}{4}\right],\sin\left[(i-5)\dfrac{\pi}{2}+\dfrac{\pi}{4}\right]\right) & \text{for } i=5,6,7,8 \end{cases} \tag{2}$$

In the above equations, $c=\delta x/\delta t$, where δx and δt are the lattice spacing and the time step, respectively, are both equal to one in LB method. τ_f is the dimensionless relaxation time related to the kinematic viscosity v as $v=(\tau_f-0.5)\delta x^2/3\delta t$ [22].

$f_i^{\,eq}(\rho,\mathbf{u})$ is the equilibrium distribution function at location $\boldsymbol{x}$ and time t along the i-th direction, which is chosen to recover the macroscopic Navier-Stokes equations:

$$f_i^{\,eq}(\rho,\mathbf{u})=\omega_i\rho\left[1+\frac{\boldsymbol{c}_i\boldsymbol{u}}{c_s^2}+\frac{1}{2}\frac{(\boldsymbol{c}_i\boldsymbol{u})^2}{c_s^4}-\frac{1}{2}\frac{\boldsymbol{u}^2}{c_s^2}\right] \tag{3}$$

where $c_s=c/\sqrt{3}$ is the sound speed, ω_i are the weight coefficients with $\omega_0=4/9$, $\omega_{1-4}=1/9$, $\omega_{5-8}=1/36$ in the D2Q9 model. ρ and $\mathbf{u}$ are the macroscopic fluid density and velocity, respectively:

$$\rho=\sum_{i=0}^{8}f_i \tag{4}$$

$$\rho\mathbf{u}=\sum_{i=0}^{8}f_i\mathbf{e}_i \tag{5}$$

The pressure can be calculated by $p=c_s^2\rho$. In order to simulate the transport of dissolved CO_2, another distribution function $g_i\left(\boldsymbol{x},t\right)$ is used:

$$g_i\left(\boldsymbol{x}+\mathbf{e}_i\delta t,t+\delta t\right)=g_i\left(\boldsymbol{x},t\right)-\frac{g_i\left(\boldsymbol{x},t\right)-g_i^{\text{eq}}(\rho,\mathbf{u})}{\tau_{\text{s}}}\ (i=0,1,2....8) \tag{6}$$

where τ_{s} is the dimensionless relaxation time related to the solute diffusivity by $D=(\tau_{\text{s}}-0.5)\delta x^2/3\delta t$ [22]. $g_i^{\text{eq}}(C,\mathbf{u})$ is the equilibrium distribution function at location $\boldsymbol{x}$ and time t along the i-th direction, which is chosen to recover the macroscopic advection−diffusion equation:

$$g_i^{\text{eq}}(C,\mathbf{u})=\omega_iC\left[1+\frac{\boldsymbol{c}_i\cdot\boldsymbol{u}}{c_s^2}+\frac{1}{2}\frac{(\boldsymbol{c}_i\cdot\boldsymbol{u})^2}{c_s^4}-\frac{1}{2}\frac{\boldsymbol{u}^2}{c_s^2}\right] \tag{7}$$

where C is the macroscopic concentration of dissolved CO_2 calculated by

$$C=\sum_{i=0}^{8}g_i \tag{8}$$

The main governing dimensionless parameters controlling density driven natural convection are the Rayleigh (Ra) and Schmidt (Sc) numbers, defined as

$$Ra=\frac{h^3g\Delta\rho}{D\mu} \tag{9}$$

$$Sc=\frac{\upsilon}{D} \tag{10}$$

One of the important characterizing parameter for density driven natural convection is the critical time, defined as the minimum time for the onset of instability at the interface and marked as t_{cr}. We can define the dimensionless critical time as $t_{\text{cr}}^*=t_{\text{cr}}/t_{\text{c}}$, where t_{c} is the characteristic time and calculated by

$$t_{\text{c}}=\sqrt{\rho_{\text{brine}}h/g\Delta\rho} \tag{11}$$

One of the key components for the application of the lattice Boltzmann method to physical problems is the correct conversion from physical world units to lattice units to and vice versa. Because it is not possible to directly input the variables and therefore, scaling has to be applied. The fluid viscosity has to be scaled first, we can choose any value less than 0.1 [23]. Having in hand the real values of fluids physical proprieties and the model parameters, we can define the domain high $h\left[\text{m}\right]$, the fluid kinematic viscosity $v\left[\text{m}^2/\text{s}\right]$, the strength of external force (gravity) $g\left[\text{m/s}^2\right]$, the fluid density $\rho\left[\text{kg/m}^3\right]$, the size of an LBM lattice $\Delta x\left[\text{m}\right]$ (resolution dependent). These parameters are used to set a reasonable time step size $\Delta t\left[\text{s}\right]$ and limit the mass difference in the simulation $\Delta m\left[\text{kg}\right]$. The values of the LBM simulation are dimensionless and they should be converted to the dimensionless values The following steps show how the physical units (with a subscript $'\text{p}'$) are transformed to lattice units (with a subscript $'\text{l}'$): lattice time:

$t_1 = t_p / \Delta t$, lattice gravity: $g_1 = g_p(\Delta t^2 / \Delta x)$, lattice density difference: $\Delta \rho_1 = \Delta \rho_p(\Delta x^3 / \Delta m)$, lattice diffusion number: $D_1 = D_p(\Delta t / \Delta x^2)$.

2.4. Implementation of external forces

Initially, dissolved CO_2 migrates downward mainly by pure diffusion, which implies that the dissolved CO_2 slightly increases the brine density. The well-known assumption of Boussinesq approximation is adopted to assume that material properties are independent of CO_2 concentration except the density. Thus, only the body force, buoyancy or gravity, caused by density difference is considered as the external force in the system. The density difference, which was assumed to vary linearly with the concentration difference caused by the mass transfer, is the only source [18]. In this problem, the exerted body force can be written as

$$\rho \mathbf{g} = \rho_0 \mathbf{g} + \rho_0 \mathbf{g} \beta C \tag{12}$$

where ρ is the saline aquifer density, ρ_0 is the density of pure water, and β is the expansion coefficient, which is defined as $\beta = (\Delta \rho / \Delta C) / \rho_0$. It is noticed that only the second term on the right-hand side of Eq. (12) contributes to density variation. The first term on the right-hand side of Eq. (12) is the same for all nodes, thus we can put it into the pressure term as $-\rho_0 g \mathbf{e}_y$. After inserting β into Eq. (12), the body force term can be reduces to

$$\mathbf{F} = \rho \mathbf{g} = -\frac{\Delta \rho}{\Delta C} C g \mathbf{e}_y \tag{13}$$

where $\Delta \rho$ is the increment of saline aquifer density when the difference between the concentrations of pure brine and the concentration of saturated brine-CO_2 reaches the maximum value ΔC. The dimensionless form of the body force is defined as follow

$$\mathbf{F}(\theta) = -\Delta \rho g \theta \mathbf{e}_y \tag{14}$$

This implies that the body force is linearly proportional to the local dimensionless concentration, $\theta = C / \Delta C$, with $0 \leq \theta \leq 1$. Incorporating the body force into the model, the velocity in the equilibrium distribution function $\boldsymbol{u}^*$ and flow velocity $\tilde{\boldsymbol{u}}$ is modified as follows [24]:

$$\boldsymbol{u}^* = \boldsymbol{u} + \tau_f \frac{\mathbf{F} \Delta t}{\rho} \tag{15}$$

$$\tilde{\boldsymbol{u}} = \boldsymbol{u} + \frac{\mathbf{F} \Delta t}{2\rho} \tag{16}$$
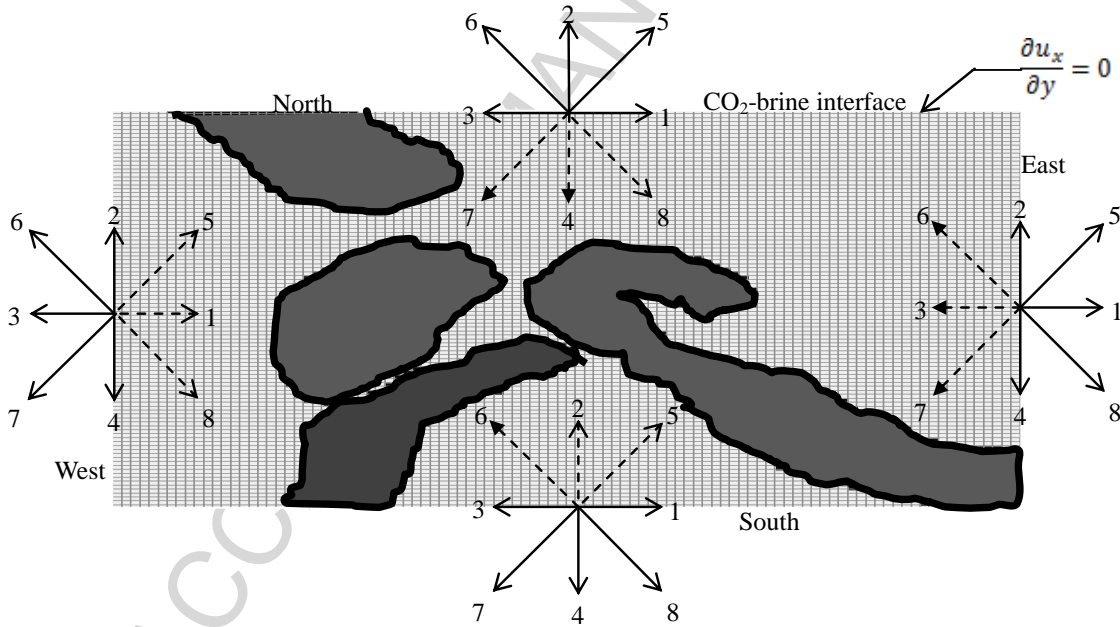
2.5. Boundary conditions

In the LB method, distribution functions out of the domain are known from the streaming process. The unknown distribution functions are those towards the domain [25]. Fig. 4 shows the

8

unknown distribution functions, which are needed to be determined, as dotted lines.

The bounce-back boundary is employed on the south boundary and brine-rock interface for the flow field and the concentration field, which means that incoming boundary populations equal to out-going populations after the collision. For instance for south boundary, the following conditions are imposed:

$$f_5(x,y) = f_7(x,y)$$
$$f_2(x,y) = f_4(x,y) \qquad (17)$$
$$f_6(x,y) = f_8(x,y)$$

where f_i represents the distribution function after collision and streaming, similarly for concentration field.

Fig. 4. Boundary conditions with domain classification: (1) fluid lattice (light gray nodes); (2) inner solid lattice (gray nodes) and (3) boundary solid-fluid interface (black nodes)

A periodic boundary condition was used at the west and east boundaries for the flow field and the concentration field, which means that entering distribution functions at west boundary, are the same as the distribution functions leaving from east boundary and vice versa. For instance for west boundary, the following conditions are imposed:

$$f_{5\,west}(x,y) = f_{5\,east}(x,y)$$

$$f_{1\,west}(x,y) = f_{1\,east}(x,y) \qquad (18)$$

$$f_{8\,west}(x,y) = f_{8\,east}(x,y)$$

We use the same boundary condition for concentration field. We use the mirror symmetric

9

boundary [26] to treat the CO_2-brine free interface. This type of boundary condition can ensure that the gradient of horizontal velocity along the vertical direction equals to zero, i.e.

$$
\begin{aligned}
&f_i(x,m) = f_i(x,m-1) \qquad\qquad i = 0,1,3 \\
&f_2(x,m) = f_4(x,m-1), \; f_4(x,m) = f_2(x,m-1) \\
&f_6(x,m) = f_7(x,m-1), \; f_7(x,m) = f_6(x,m-1) \\
&f_5(x,m) = f_8(x,m-1), \; f_8(x,m) = f_5(x,m-1)
\end{aligned}
\tag{19}
$$

where m is the number of nodes in the y direction.

The constant concentration boundary [27] is used on the north boundary to handle the dissolution of CO_2 into brine, which is described below:

$$
\begin{aligned}
\tilde{C} &= \frac{C - (f_0 + f_1 + f_2 + f_3 + f_5 + f_6)}{\omega_4 + \omega_7 + \omega_8} \\
f_4 &= \omega_4 \tilde{C} \\
f_7 &= \omega_7 \tilde{C} \\
f_8 &= \omega_8 \tilde{C}
\end{aligned}
\tag{20}
$$

where $\tilde{C}$ denotes the residual amount of concentration needed to satisfy the specified constant concentration condition C at the current lattice node.

3. Model validation

The LB model described above was validated with experimental study performed by Fu *et al*. [18] by simulating under the same operating conditions the 2D Rayleigh convection generated by a local high concentration gradient in the gas–liquid mass transfer process during CO_2 absorption into liquid ethanol. The height and width of the computational domain are equal to 100 (in the lattice unit); with a resolution of 0.4 mm. Thus, the domain dimension in the real system is equal to $40 \times 40\,\mathrm{mm}^2$. For boundary conditions, the bounce-back boundary is employed on the south boundary, and periodic boundary on the east and west boundaries for the flow field and the concentration field. On the north boundary, we used the mirror symmetric boundary for fluid flow and the constant concentration boundary for solute transport. The predicted distribution of vertical velocity along vertical line during the absorption process at $x = 20\,\mathrm{mm}$ for different time instants is presented in Fig. 5. It can be seen from this figure that simulated results coincide quite well with the experimental results. The minor discrepancies between the present simulation and experimental measurements can be attributed to the measurements uncertainties and simulation accuracy. Figure 6 shows the simulated and experimental transient streamlines results after 120 s, 140 s and 160 s, respectively. These figures show the agreement between simulation and experimental results of circulation flows obtained by particle image velocimetry technique.

10
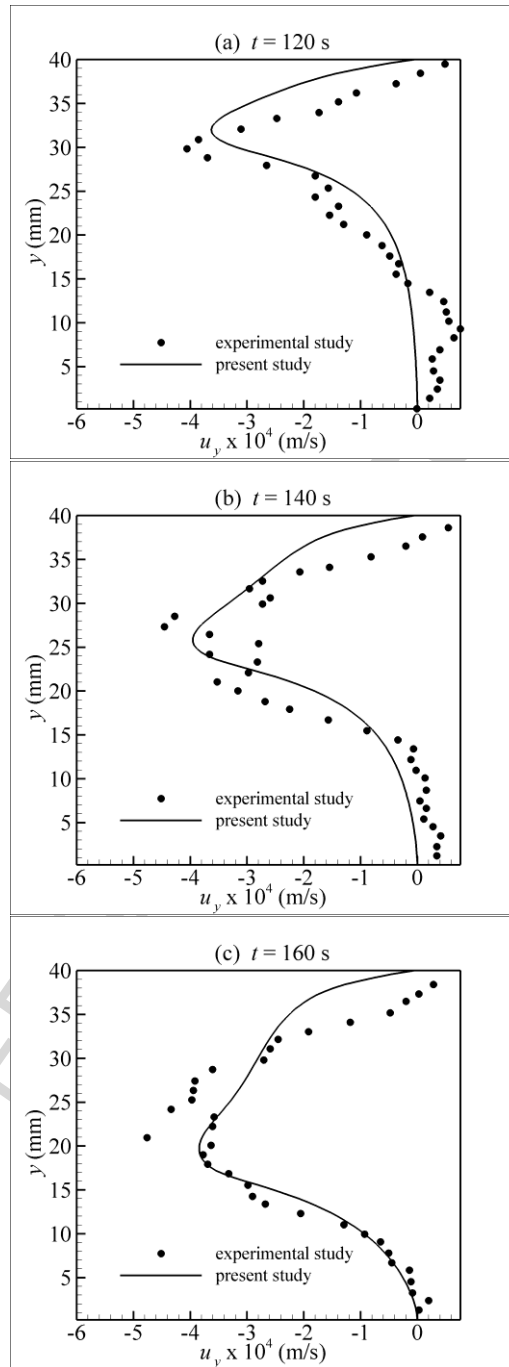
Fig. 5. Comparison between simulated (continuous line) and experimental (black points) results for distribution of vertical velocity along vertical line at $x = 20\,\text{mm}$ **for different time instants**
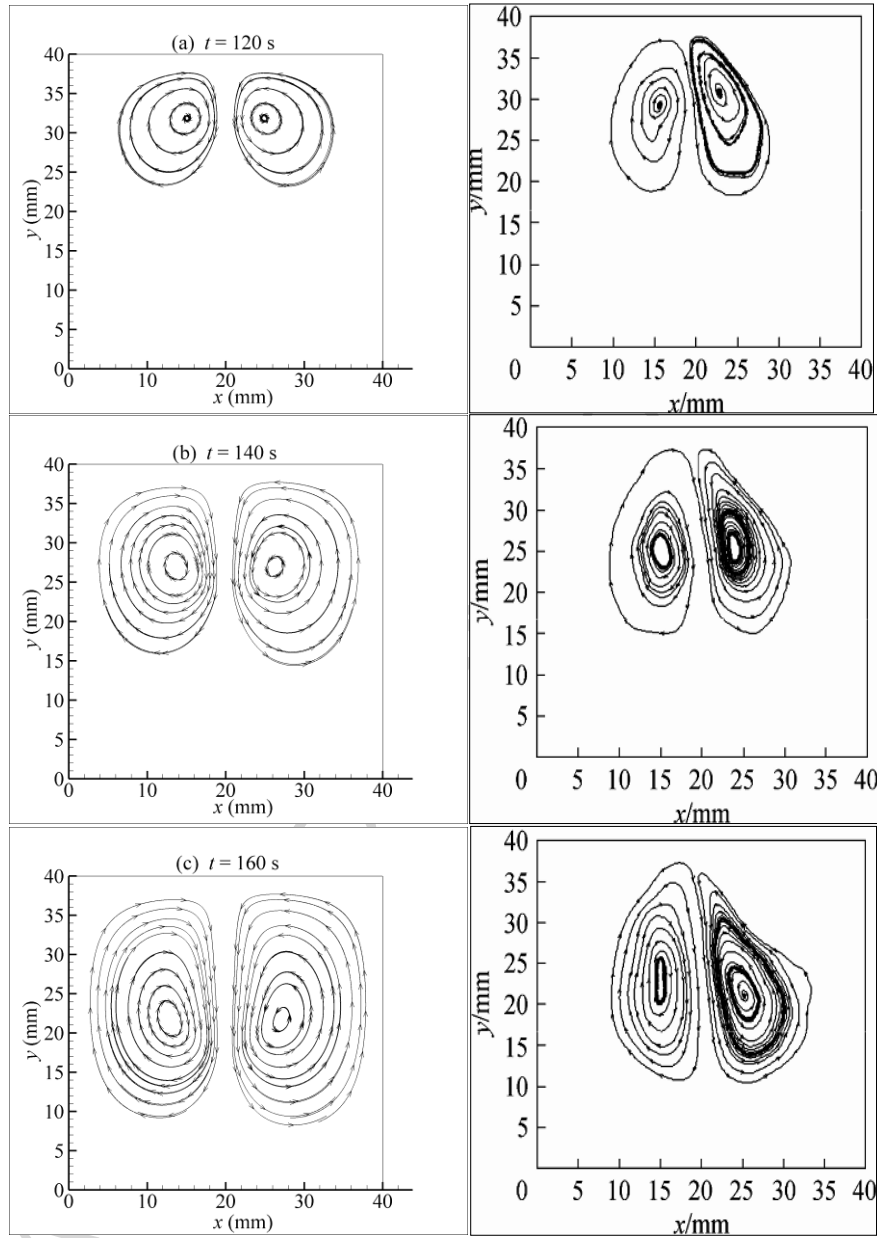
Fig. 6. Transient simulated streamlines of present study (left) and transient experimental streamlines (right) for different time instants.

2. Simulation Results and Discussion

As described in Section 2.4, the brine density was assumed to be linearly proportional to the concentration of CO_2 caused by mass transfer process at the interface. Hence, saline aquifer density near the top was higher than that near the bottom. Thus, the density driven natural convection will be obvious and develop if the Rayleigh number is higher than the critical number. Under the real physical proprieties listed in Table 1, the Schmidt number will be around 500, however, this value present some numerical instability. Hence we set $Sc = 100$ to avoid this problem. In addition, the computational domain has a total dimension of 200×200 and we set $\nu = 0.1$ for LB simulation. The simulation results of the temporal-spatial of solute concentration contours at different times are

illustrated in Fig. 7, representing the density driven natural convection of CO_2 in porous structure. It can be seen that in the early stage, the dissolved CO_2 migrated into the porous medium mainly by diffusion and the liquid density near the interface is increased. In this scenario, the density of the brine at the interface increases and becomes unstable and tended to move downward.

The density driven natural convection could be observed at $t = 50$ s. After that, CO_2 continues to diffuse and intrude into the underlying unaffected brine. This process increased the interfacial area between dissolved CO_2 plume and unaffected brine, which is favorable to enhance the migration of dissolved CO_2 into the porous structure. The density driven natural convection reached the bottom of the domain at about $t = 200$ s, after that it began to spread into the porous structure, as shown in Figs. 7g, 7h and 7i.
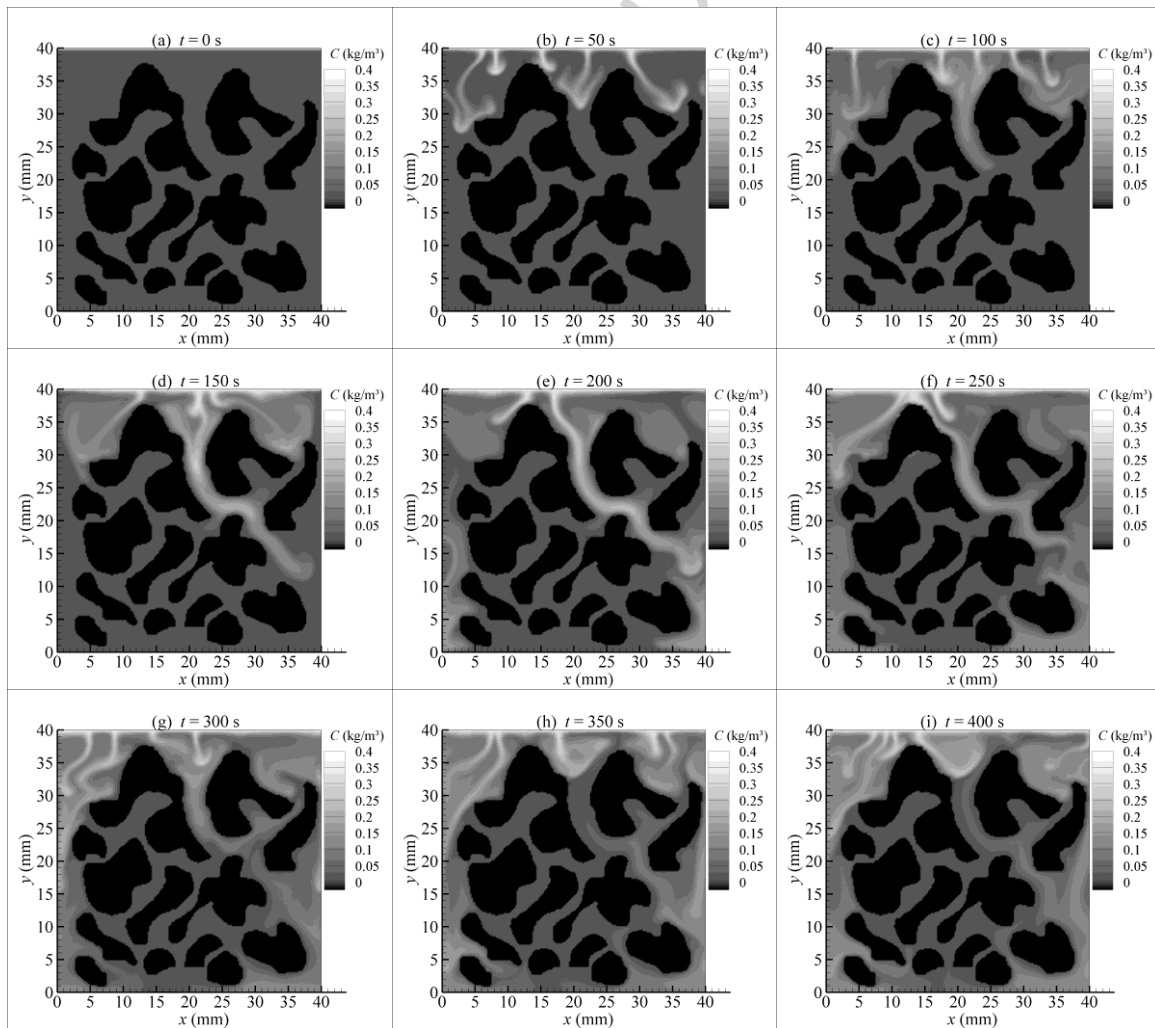
Fig. 7. Simulated of temporal-spatial cloud map of solute concentration at different times

The transient velocity vectors in the porous structure are shown in Fig. 8. It can be seen in the early stage, that there are several pairs of vortex cells with diverse rotational directions and different sizes is formed in the brine. Also, with time going on, the flow fields became more disordered. As a result, the vortex centers continue moving downwards and impel the continuum mixing and

exchange between the saturated brine and unaffected liquid by interfacial vicinity and promote the mass transfer process. Hence, we can conclude that in reality, the density driven natural convection during a CO_2 injection project is able to produce obvious irregular motion of this geometry type.
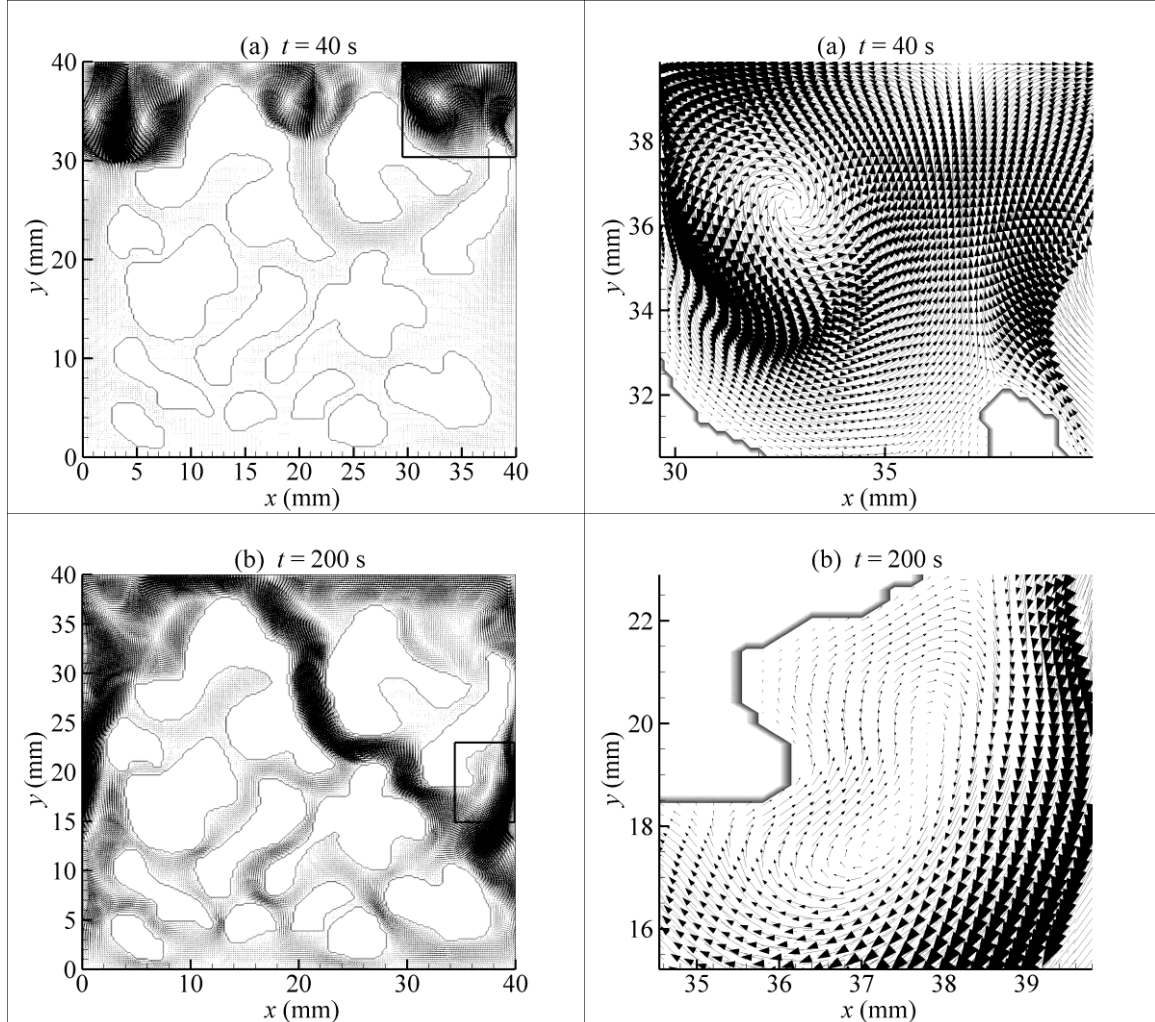
Fig. 8. Simulated transient velocity vectors at different times with enlarged map of rectangular zone

The critical time for the occurrence of density driven natural convection as function of Rayleigh number is presented in Fig. 9. t_{cr} decreases when Ra is increased. Specifically, for the case $Ra = 5.7 \times 10^{12}$, $t_{cr} \approx 30$ s. Several other Ra numbers were used in the simulations. The shape of the $t_{cr} - Ra$ curve was similar to the result obtained by Chen et al. [3], who investigated the relationship between the critical time and Ra number in fractured porous media.
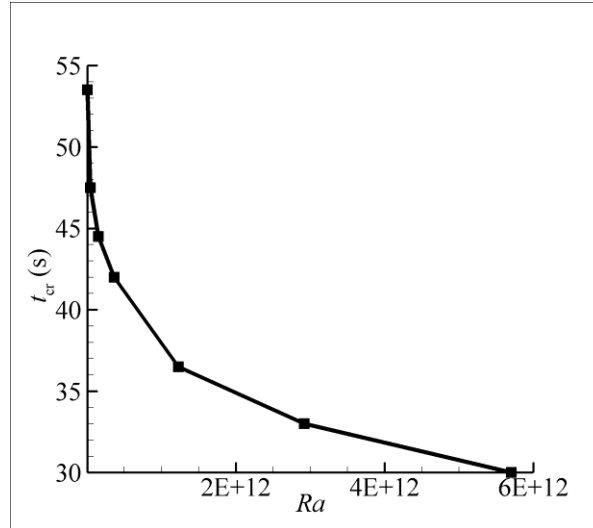
Fig. 9. Critical time for the onset of instability as a function of Rayleigh number for $\mu = 0.93 \times 10^{-3}$ **Pa.s ,**

$D = 1.85 \times 10^{-9}$ **m^2/s and $\Delta \rho = 10$ kg/m^3**

The simulated dimensionless critical time is presented as function of block size, as shown in Fig. 10. It can be observed that there is a nearly linear relationship between $t_{cr}^{*-1/2}$ and block size for our problem.
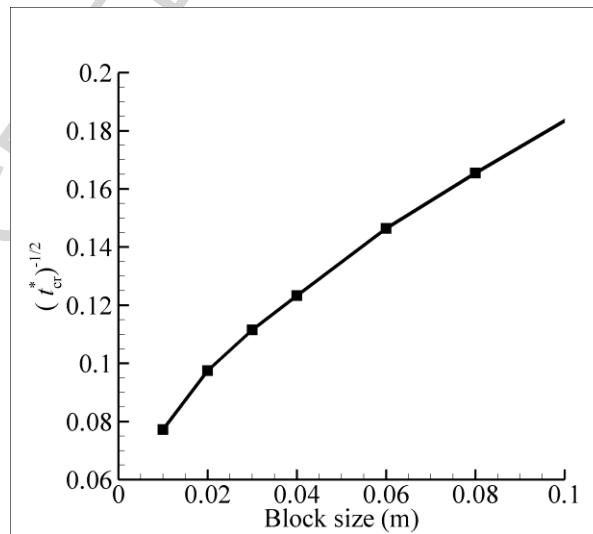
Fig. 10. Dimensional critical time as function of block size (grid 200×200) for $\mu = 0.93 \times 10^{-3}$ **Pa.s ,**

$D = 1.85 \times 10^{-9}$ **m^2/s and $\Delta \rho = 10$ kg/m^3**

Figure 11 show the transient behavior of velocity vectors for different values of block size at $t = 200$ s on a grid of 200×200). As can be seen, a set of circulation flow is formed in the liquid bulk. Also, it can be noted that the geometrical morphology of porous media is invariant with variation of block size and the flow patterns are geometrically similar to Fig. 8.

15
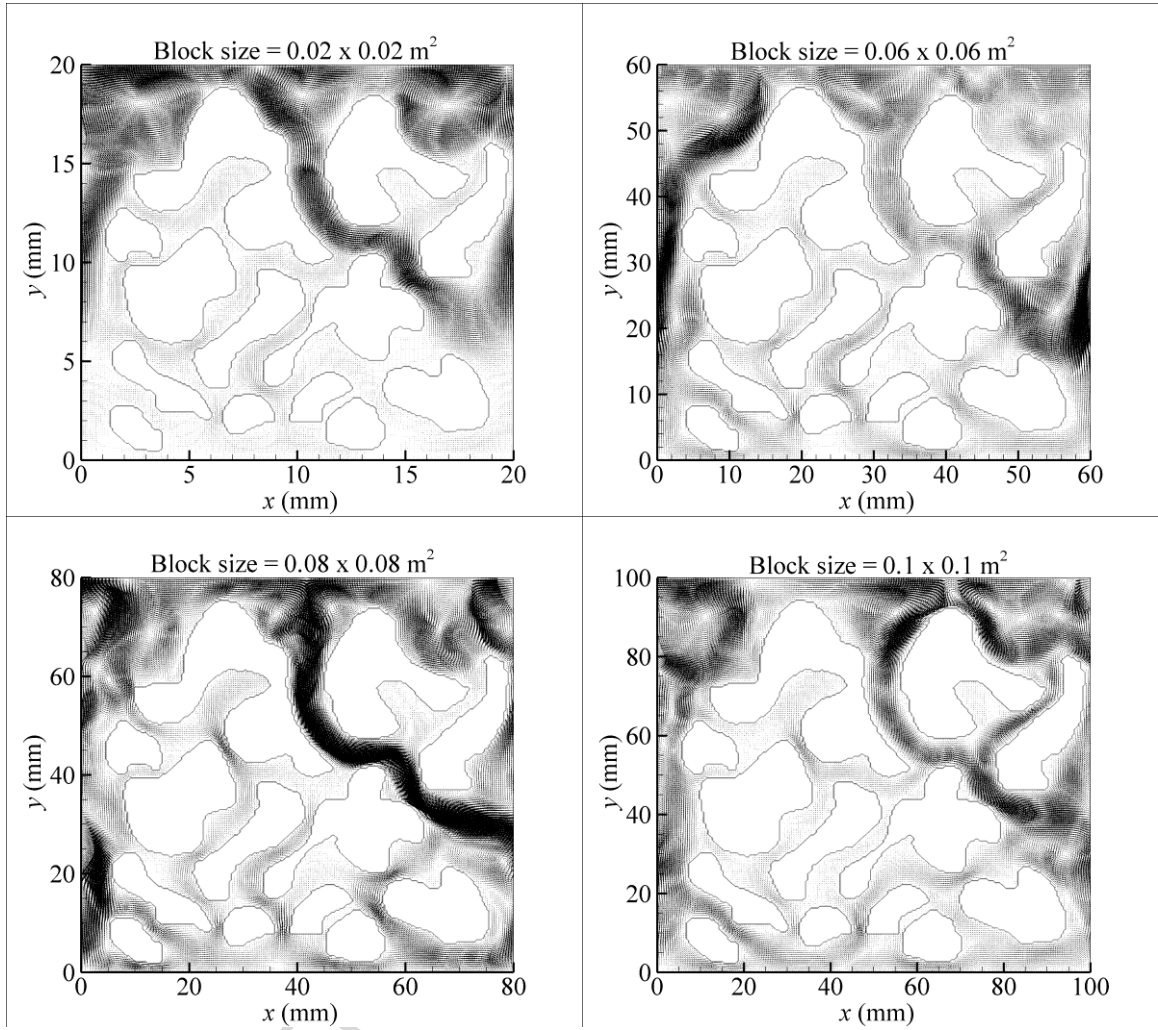
Fig. 11. Transient velocity vectors for different values of block size at 200 s (grid 200×200)

The effect of Rayleigh number on interfacial mass transfer can be presented quantitatively by the instantaneous mass flux and dissolved CO_2 mass into the porous structure. From the simulated concentration field, the instantaneous mass flux $N_{\text{ins},t}$ across the interface at time t under the condition of $C_I = 0.4$ kg/m^3 can be estimated by

$$N_{\text{ins},t} = \frac{(C_{\text{avg},t+\Delta t} - C_{\text{avg},t})V}{A_I \Delta t} = \frac{(C_{avg,t+\Delta t} - C_{\text{avg},t})h}{\Delta t} \tag{21}$$

The instantaneous mass flux through the top boundary per unit cross-sectional area along the vertical direction can be obtained by penetration theory, and can be written as [28]

$$N_{\text{ins},t} = (C_I - C_0)\sqrt{\frac{D}{\pi t}} \tag{22}$$

The total dissolved CO_2 mass accumulated after time t per unit cross-sectional area can be obtained by integrating Eq. (22) to yield

16

$$M_t = 2(C_I - C_0)\sqrt{\frac{Dt}{\pi}} \qquad (23)$$

The variation of instantaneous mass flux across the interface with time for different Rayleigh number by penetration theory and simulated concentration is shown in Fig. 12. In all cases the instantaneous mass flux along the vertical direction across the interface decreased clearly before 40 s where the interfacial mass transfer only proceeds by molecular diffusion. It can be found that the simulation results agree very well with the values predicted by the penetration theory within that time period, and then increased slowly with time at the onset of density driven natural convection. Following that, the instantaneous mass flux across the interface after 40 s is very close to the one derived from penetration theory with decreasing Rayleigh number, but it is above that derived from penetration theory with increasing Rayleigh number. As a result, the interfacial mass transfer proceeded in the combined manners of both density driven natural convection and molecular diffusion at high Rayleigh number. Therefore, the interfacial mass transfer flux is enhanced with increasing of Rayleigh number.
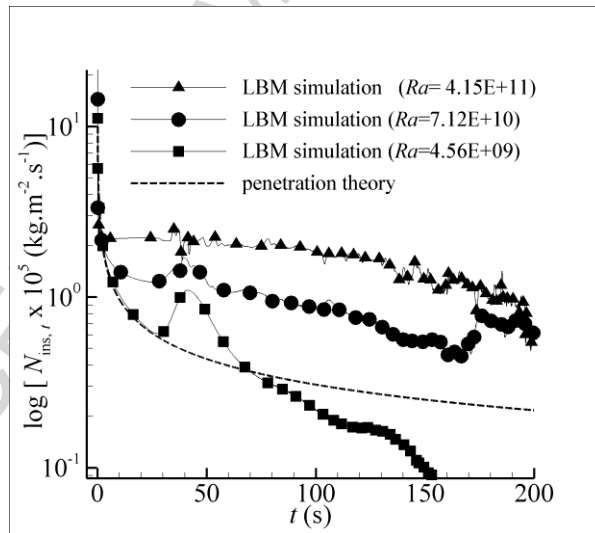
Fig. 12. Variation of instantaneous mass flux $N_{ins,t}$ with time for LBM simulation and penetration theory at

$C_I = 0.4$ **kg·m^3 for different Rayleigh number**

Figure 13 shows the effect of Rayleigh number on dissolved CO_2 mass per unit interface area as a function of time. In the case of $Ra = 4.56 \times 10^9$, the dissolved CO_2 mass is close to that obtained by analytical solution, or the diffusion dominated transport of dissolved CO_2. When Ra was increased to 7.12×10^{10}, the dissolved CO_2 mass in the system was enhanced, because of the intensive downward convection due to the density difference. However, in this case, the dissolved CO_2 mass in the porous structure does not exceed $0.001\,\mathrm{kg \cdot m^{-2}}$ over that by combined diffusion-convection and diffusion-only. As Ra was increased to 4.15×10^{11}, the difference in the

total dissolved CO_2 mass became significant. This implies that the highly disordered fluid motion greatly enhanced the dissolution of CO_2 at the different regions of unaffected brine.
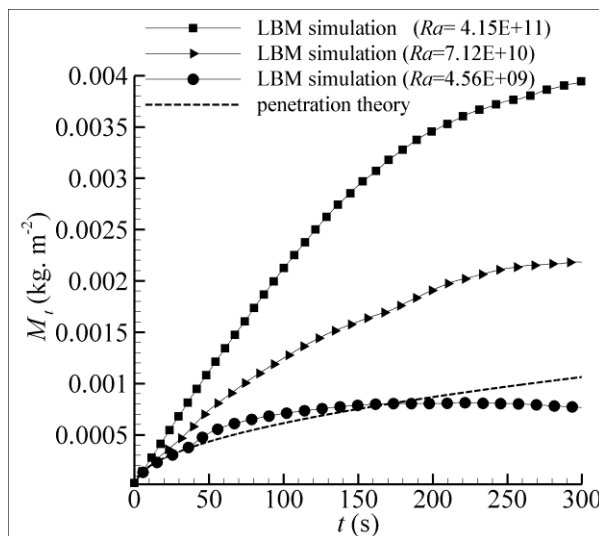
Fig. 13. Variation of dissolved CO_2 mass with time at C_1 =0.4 kg·m^3 for different Rayleigh number.

6. Conclusions

In this study, the LB model with a double distribution functions has been used to simulate density driven natural convection in a porous medium with a complex geometry. The LB model was verified by experimental study performed by Fu et al [18], by simulating the Rayleigh convection generated by a local high concentration gradient in the gas–liquid mass transfer process during CO_2 absorption into quiescent liquid ethanol. The key point for this study lies in the integration of irregular geometry obtained by image treatment in order to investigate real systems. The simulated results with the adopted LBM model show that the density driven natural convection will not occur until a critical time, and this time decreases with increasing Rayleigh number. When critical time is reached, the onset of convective instability will make the brine with a high CO_2 concentration intruded into the underlying brine by circulation flows with high velocity and vortexes, which increases the interfacial mass transfer and mixing between rich brine by CO_2 and poor brine, consequently in favor of the migration of CO_2 into the fracture of porous structure. It was also demonstrated that our adopted LBM simulation approach can effectively capture the instantaneous mass flux across the interface and total dissolved CO_2 mass, and the mass transfer rate and dissolved mass are effectively enhanced by increasing Rayleigh number. Pore-scale simulation by lattice Boltzmann method is considered as a promising tool for studying the coupling between CO_2 dissolution, mass transport, and heterogeneity of pore geometry. Specifically, the effect of density driven natural convection during geological storage of CO_2 on underground petro-physical and chemical properties should be investigated.

18

Nomenclature

A_I Interfacial area, m^2

C CO_2 concentration in the brine, $kg \cdot m^{-3}$

C_0 Initial CO_2 concentration in the brine, $kg \cdot m^{-3}$

C_I Interfacial concentration, $kg \cdot m^{-3}$

C_s Saturation of CO_2 concentration in the brine, $kg \cdot m^{-3}$

ΔC Difference between the concentrations of pure brine and saturated brine, $kg \cdot m^{-3}$

c Lattice velocity set to unity

$\boldsymbol{e}_i$ Discrete velocity vector for D2Q9

D Diffusion coefficient of CO_2 in the brine, $m^2 \cdot s^{-1}$

$\boldsymbol{F}$ Body force per unit volume of density driven natural convection, $N \cdot m^{-3}$

f_i Density distribution function of the brine

f_i^{eq} Equilibrium distribution function of the brine

g Acceleration due to gravity, $m \cdot s^2$

g_i Concentration distribution function of the CO_2

g_i^{eq} Equilibrium distribution function of the CO_2

h The high of the computational domain, m

$N_{\text{ins},t}$ Mass flux per unit area, $kg \cdot m^{-2} s^{-1}$

M_t Total dissolved CO_2 mass per unit area, $kg \cdot m^{-2}$

p Pressure, Pa

Ra Rayleigh number $(= h^3 g \Delta \rho / D \mu)$

Sc Schmidt number $(= \upsilon / D)$

t Time, s

Δt Time interval set to 0.1 s

δt Lattice time step size

t_c Characteristic time, s

t_cr Critical time for the onset instability, s

t_cr^{*} Dimensionless Critical time for the onset instability, s

$\boldsymbol{u}$ Macroscopic velocity, $m.s^{-1}$

$\boldsymbol{u}^{*}$ Modified velocity in the equilibrium distribution function, ms^{-1}

$\tilde{\boldsymbol{u}}$ Modified flow velocity, ms^{-1}

V Liquid volume, m^3

x Position vector, m

x Coordinate in horizontal direction

δx Lattice space step size

y Coordinate in vertical direction

Greek letters

β Expansion coefficient

μ Dynamic viscosity, Pa.s

ν Kinematic viscosity, $m^2.s^{-1}$

θ Dimensionless concentration

ρ Macroscopic density, $kg.m^{-3}$

ρ_0 Macroscopic density of pure water, $kg.m^{-3}$

$\Delta\rho$ Difference between the densities of pure brine and saturated brine by CO_2, $kg.m^{-3}$

τ_f Dimensionless relaxation time related to the kinematic viscosity

τ_s Dimensionless relaxation time related to the solute diffusivity

ω_i Weight factor

Subscripts

avg   Average

eq   Equilibrium

I   Interface

i Discrete direction (i =0, 1, ⋯, 9)

ins   Instantaneous

l   Lattice units

p   Physical units

0   Initial

References

[1]   B. Metz, O. Davidson, H. De Coninck, M. Loos, and L. Meyer, IPCC special report on carbon dioxide capture and storage. Prepared by Working Group III of the Intergovernmental Panel on Climate Change, *Cambridge University Press, United Kingdom and New York, USA* 4 (2005) 195-276.

[2]   R. Farajzadeh, H. Salimi, P. L. Zitha, and H. Bruining, Numerical simulation of density driven natural convection in porous media with application for CO_2 injection projects, *Int. J. Heat Mass Transfer* 50 (25) (2007) 5054-5064.

[3]   C. Chen and D. Zhang, Pore scale simulation of density driven convection in fractured porous media during geological CO_2 sequestration, *Water Resour. Res.* 46 (11) (2010).

[4]   C. Chen, L. Zeng, and L. Shi, Continuum scale convective mixing in geological CO_2 sequestration in anisotropic and heterogeneous saline aquifers, *Adv. Water. Resour.* 53 (2013) 175-187.

[5]   E. Lindeberg and D. Wessel-Berg, Vertical convection in an aquifer column under a gas cap of CO_2, *Energy Convers. Manage.* 38 (1997) S229-S234.

[6]   H. Hassanzadeh, M. Pooladi‐Darvish, and D. W. Keith, Scaling behavior of convective mixing with application to geological storage of CO_2, *AlChE J.* 53 (5) (2007) 1121-1131.

[7] G. S. Pau, J. B. Bell, K. Pruess, A. S. Almgren, M. J. Lijewski, and K. Zhang, High resolution simulation and characterization of density driven flow in CO_2 storage in saline aquifers, *Adv. Water. Resour.* 33 (4) (2010) 443-455.

[8] K. Pruess, Numerical modeling studies of the dissolution diffusion convection process during CO_2 storage in saline aquifers, *Lawrence Berkeley National Laboratory* (2008).

[9] S. Rapaka, R. J. Pawar, P. H. Stauffer, D. Zhang, and S. Chen, Onset of convection over a transient base state in anisotropic and layered porous media, *J. Fluid Mech.* 641 (2009) 227-244.

[10] Z. Li and M. Dong, Experimental study of carbon dioxide diffusion in oil-saturated porous media under reservoir conditions, *Ind. Eng. Chem. Res.* 48 (20) (2009) 9307-9317.

[11] R. Farajzadeh, P. Ranganathan, P. L. J. Zitha, and J. Bruining, The effect of heterogeneity on the character of density driven natural convection of CO_2 overlying a brine layer, *Adv. Water. Resour.* 34 (3) (2011) 327-339.

[12] W. Chen, S. Chen, X. Yuan, H. Zhang, B. Liu, and K. Yu, PIV Measurement for Rayleigh Convection and Its Effect on Mass Transfer, *Chin. J. Chem. Eng.* 22 (10) (2014) 1078-1086.

[13] Q. Kang, D. Zhang, and S. Chen, Displacement of a two-dimensional immiscible droplet in a channel, *Physics of Fluids (1994-present)* 14 (9) (2002) 3203-3214.

[14] C. Pan, M. Hilpert, and C. Miller, Lattice Boltzmann simulation of two phase flow in porous media, *Water Resour. Res.* 40 (1) (2004).

[15] A. Mohamad, M. El-Ganaoui, and R. Bennacer, Lattice Boltzmann simulation of natural convection in an open ended cavity, *Int. J. Therm. Sci.* 48 (10) (2009) 1870-1875.

[16] T. Seta, E. Takegoshi, and K. Okui, Lattice Boltzmann simulation of natural convection in porous media, *Math. Comput. Simulat.* 72 (2) (2006) 195-200.

[17] M. Nazari, L. Louhghalam, and M. H. Kayhani, Lattice Boltzmann simulation of double diffusive natural convection in a square cavity with a hot square obstacle, *Chin. J. Chem. Eng.* 23 (1) (2015) 22-30.

[18] B. Fu, X. Yuan, B. Liu, S. Chen, H. Zhang, A. Zeng, and G. Yu, Characterization of Rayleigh convection in interfacial mass transfer by lattice Boltzmann simulation and experimental verification, *Chin. J. Chem. Eng.* 19 (5) (2011) 845-854.

[19] W. Chen, S. Chen, X. Yuan, H. Zhang, and K. Yu, Three dimensional simulation of interfacial convection in CO_2 ethanol system by hybrid lattice Boltzmann method with experimental validation, *Chin. J. Chem. Eng.* 23 (2) (2015) 356-365.

[20] F. Takemura and A. Yabe, Rising speed and dissolution rate of a carbon dioxide bubble in slightly contaminated water, *J. Fluid Mech.* 378 (1999) 319-334.

[21] Z. Guo, H. Han, B. Shi, and C. Zheng, Theory of the lattice Boltzmann equation: lattice Boltzmann model for axisymmetric flows, *Phys. Rev. E* 79 (4) (2009) 046708.

[22] T. Inamuro, M. Yoshino, H. Inoue, R. Mizuno, and F. Ogino, A lattice Boltzmann method for a binary miscible fluid mixture and its application to a heat transfer problem, *J. Comput. Phys.* 179 (1) (2002) 201-215.

[23] A. Mohamad, Lattice Boltzmann Method, Springer, (2011).

[24] J. Buick and C. Greated, Gravity in a lattice Boltzmann model, *Phys. Rev. E* 61 (5) (2000) 5307.

[25] A. Mohamad and A. Kuzmin, A critical evaluation of force term in lattice Boltzmann method: natural convection problem, *Int. J. Heat Mass Transfer* 53 (5) (2010) 990-996.

[26] Y. Shi, T. Zhao, and Z. Guo, Finite difference based lattice Boltzmann simulation of natural convection heat transfer in a horizontal concentric annulus, *Comput. Fluids* 35 (1) (2006) 1-15.

[27] M. C. Sukop and D. T. Thorne, Lattice Boltzmann modeling: an introduction for geoscientists and engineers, Springer, (2007).

[28] E. L. Cussler, Diffusion: mass transfer in fluid systems, Cambridge university press, (2009).
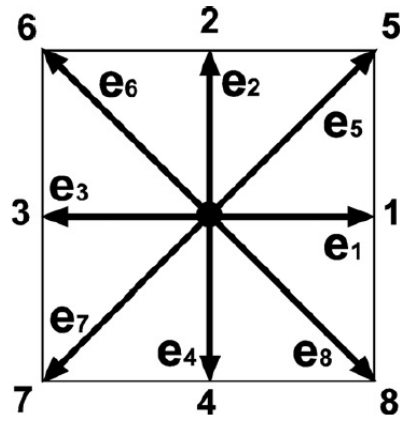
Fig. 3. Two-dimensional nine-velocity (D2Q9) model

Qualité des Eaux Destinées à la Consommation Humaine et à l'Utilisation Agricole : Cas des Eaux Souterraines d'Oued-Souf , se Algérien

2 authors:

Salim Khechana
université d'El Oued
17 PUBLICATIONS **20** CITATIONS

SEE PROFILE

Derradji El Fadel
Badji Mokhtar - Annaba University
51 PUBLICATIONS **92** CITATIONS

SEE PROFILE

Some of the authors of this publication are also working on these related projects:

Gestion et vulnérabilité des eaux à la pollution dans l'extrême Nord-Est algérien View project

CONTRIBUTION TO THE EXPERIMENTAL STUDY OF THE HYDRAULIC JUMP IN TRAPEZOIDAL CHANNEL WITH POSITIVE SLOPE View project

Qualité des eaux destinées à la consommation humaine et à l'utilisation agricole (Cas des eaux souterraines d'Oued-Souf, SE algérien)

Salim KHECHANA[1*] & El-Fadel DERRADJI [2]

[1] *Faculté des Sciences et Technologie, Université d'El-OuedB.P. 789 El-Oued 39000 – Algérie.*
[2] *Laboratoire de Géologie, Université Badji Mokhtar- AnnabaB.P. 12 Annaba 23000 – Algérie.*

ملخص

أصل مياه التموين بالشرب والسقي في غور وادي سوف من مياه المركب النهائي (CT)، الذي يعاني كثرة التبذير، خاصة في السنوات الأخيرة، عند ظهور مشكل صعود مياه الطبقة السطحية. في هذه الدراسة، قمنا بتقييم نوعية مياه المركب النهائي (CT)، من خلال تفسير نتائج التحاليل الفيزيوكيميائية لعينات أخذت من أبراج المياه المتواجدة عبر منطقة الدراسة. بحسب هذه التحاليل، تبين أن النوعية الكيميائية لهذه المياه غير صالحة للاستهلاك البشري ولا للاستعمال الفلاحي بحسب المعايير الدولية.

الكلمات المفتاحية: *غور وادي سوف — مياه طبقة المركب النهائي — تحاليل فيزيوكيميائية — الاستهلاك البشري — الاستعمال الفلاحي.*

Résumé

Les eaux destinées à l'alimentation de la population et d'irrigation dans la vallée d'Oued Souf ont comme origine la nappe du Complexe Terminal (CT), et souffrent de trop de gaspillage, surtout les dernières années, sous l'influence de l'apparition du phénomène de la remontée des eaux de la nappe phréatique. Dans ce travail, on a évalué la qualité des eaux du CT, grâce à l'interprétation des résultats des analyses physico-chimiques des échantillons pris des châteaux d'eau à travers le territoire de la région d'étude. D'après ces analyses, il apparaît que la qualité chimique des eaux en question est médiocre à mauvaise pour la consommation humaine et impropre à l'utilisation agricole.

Mots clés: *Vallée d'Oued-Souf– Nappe du Complexe Terminal (CT) - Analyses physico chimiques - Consommation humaine- Utilisation agricole.*

Abstract

Water of drinking supply and irrigation water in Oued Souf valley come from groundwater of the Complex Terminal (CT), which suffers, excess use, especially in recent years, under the influence of the rising groundwater phenomenon. In this work, we assess the water quality of CT, through the interpretation of physico-chemical analysis results of water samples taken from water reservoirs throughout the territory of the study area. The present data indicate that the quality of the water in question is not suitable neither for human consumption nor for agricultural use.

Keywords: *Oued Souf Valley- Groundwater of Complex Terminal (CT) - Physico-chemical analyzes - Human consumption - Agricultural use.*

Auteur correspondant : khechana_salim@yahoo.fr

1. INTRODUCTION

La vallée d'Oued Souf (Sud-Est algérien) possède un réservoir d'eau souterraine très important, constitué de trois nappes souterraines: la nappe phréatique, la nappe du Complexe Terminal (CT) et la nappe du Continental Intercalaire (CI) [1]. La nappe phréatique a connu le problème de la remontée des eaux, qui a des conséquences néfastes sur le plan environnemental et sanitaire [2], ceci a conduit à l'utilisation des eaux des nappes profondes (CT et CI) pour satisfaire les besoins en eau potable et d'irrigation.

L'utilisation accrue et incontrôlée des eaux du CT, plus particulièrement dans le secteur agricole, a dépassé de loin les normes de l'apport d'eau par hectare [3]. Ainsi, le gaspillage de ces eaux est également remarqué par la dotation journalière par habitant très élevée, dépassant largement les normes de consommation (204 l/j/hab) [4].

Dans cette optique, on a réalisé ce travail pour déterminer le faciès chimique des eaux de la nappe du CT, les origines de chimisme, ses potabilités et ses aptitudes à l'irrigation, en vue de mieux les gérer.

2. PRESENTATION DU MILIEU

2.1 Situation géographique

La vallée de Oued-Souf est une unité de ressource en eau située au Sud-Est algérien (Fig.1) au centre d'une grande cuvette synclinale, appelée aussi région du Bas-Sahara à cause de sa faible altitude. Elle occupe une superficie de 11738 km^2 et représente administrativement 18 communes et englobe une population de l'ordre de 500 000 habitants (en 2009) selon la Direction des Statistiques de la Wilaya [5]. La région d'El Oued est caractérisée par la production de dattes qui, avec celle de Biskra, sont parmi les régions les plus réputées au monde. La variété de dattes la plus connue en Europe est celle de Déglat-Nour. La région d'étude est limitée par les coordonnées Lambert suivantes [6]:

X = 275 200 / 322 000   •
Y = 3 665 000 / 3743 000

2.2 Les ressources hydriques disponibles

Malgré l'absence des ressources de surface, la vallée de Oued Souf dispose d'une réserve hydraulique très importante, présentée sous forme de trois nappes souterraines :
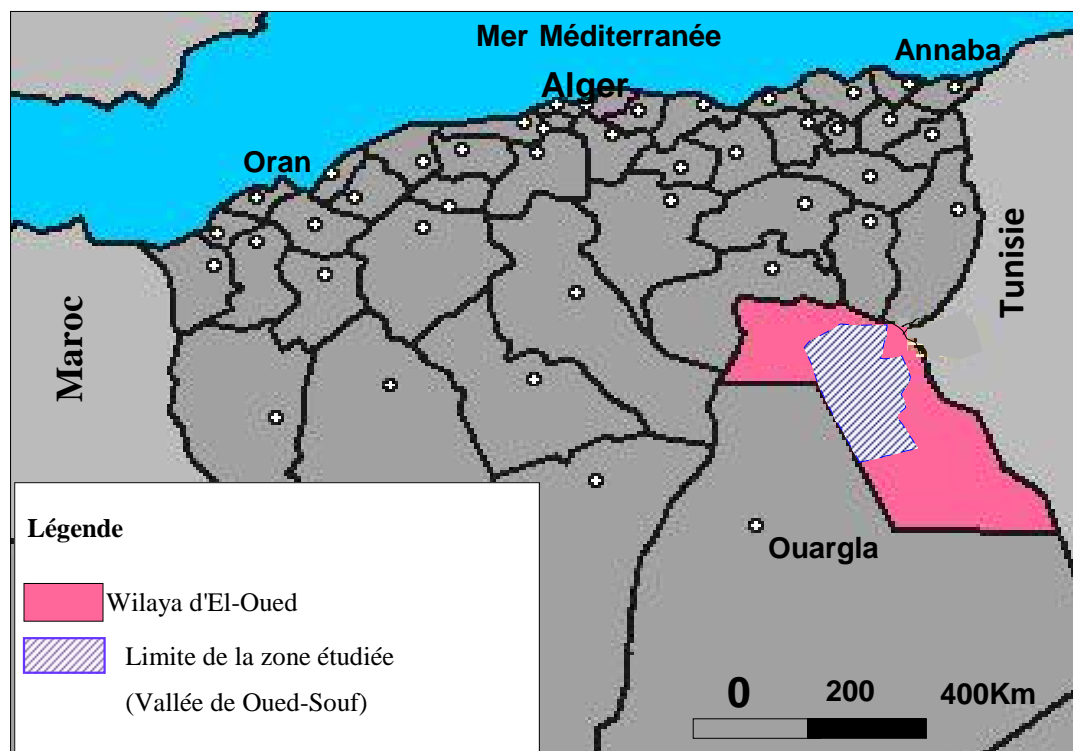

Figure 1. Situation géographique de la zone d'étude

la nappe de l'Albien (ou Continental Intercalaire CI), la nappe du Complexe Terminal (CT) et la nappe phréatique [7]. Le tableau 1 récapitule les systèmes aquifères de la région d'El-Oued.

3. MATERIEL ET METHODES

3.1 Echantillonnage

Afin de mener à bien notre travail et atteindre les objectifs souhaités, nous avons procédé à un échantillonnage selon l'axe Rabbah, El-Oued,

Kouinine, Guemar et Réguiba, c'est à dire selon le sens d'écoulement des eaux de la nappe du Complexe Terminal (CT), à partir des forages destinés à la consommation humaine (Fig. 2). Les prélèvements ont été effectués manuellement pendant le mois de mars 2012 à partir de 26 châteaux d'eau, avec la condition que la javellisation soit arrêtée et la conduite vidangée pour que l'échantillon soit représentatif de l'eau du forage.

Tableau 1. Récapitulatif des systèmes aquifères de la région d'El-Oued [4]

Nature hydrogéologique		Nature lithologique	Etage		Ere
Nappe phréatique		Sables	Quaternaire		
Niveau imperméable		Argiles			
1ère nappe des sables	Nappe de Complexe Terminal (CT)	Sables	Pliocène		Tertiaire
Semi-perméable		Argiles gypseuses			
2ème nappe des sables		Sables grossiers, graviers	Pontien	Miocène	
Niveau imperméable		Argiles lagunaires, marnes	Moyen	Eocène	
Nappe des calcaires (perméables)		Calcaire fissuré	Inférieur		
			Sénonien carbonaté	Crétacé	Secondaire
Semi-perméable		Evaporites, argiles	Sénonien lagunaire		
Niveau imperméable		Argiles, marnes	Cénomanien		
Nappe de Continental Intercalaire (CI)		Sables et grès	Albien		
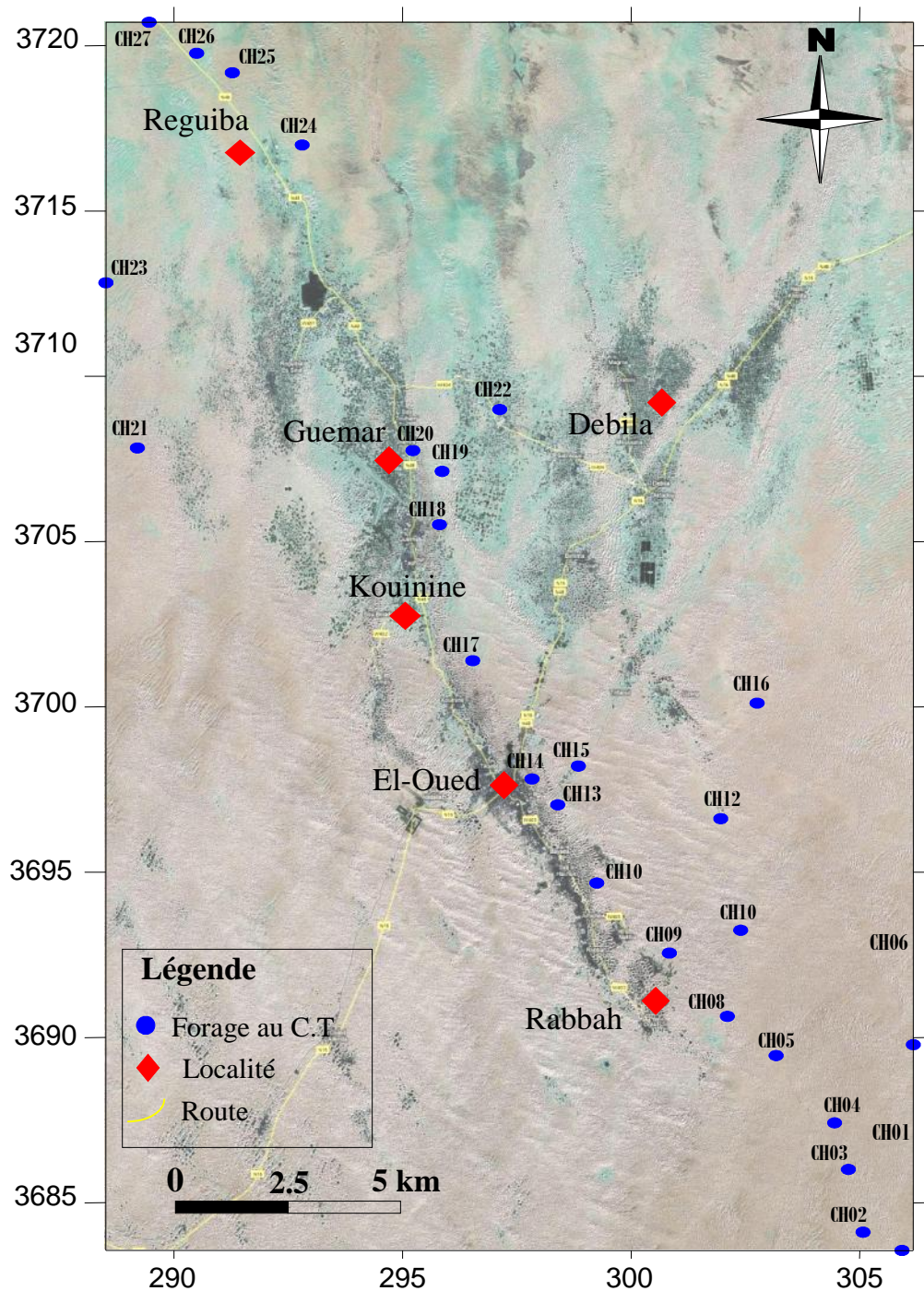
Figure 2. Carte d'inventaire des forages de prélèvement

Les échantillons ont été prélevés dans des bouteilles bien lavées, d'une capacité de 1 litre, sans rajouter aucune substance conservatrice pour éviter toutes contaminations [8].
La fiche de l'échantillon comporte : l'identité du préleveur, la date et l'heure du prélèvement, la ville ou l'établissement que l'eau alimente, l'origine et la température de l'eau.

3.2 Mode opératoire

Les paramètres physiques concernant la qualité des eaux (T°, conductivité et pH) sont mesurés sur terrain (in situ) à l'aide d'une valise multi–paramètres (marque : 350i). La dureté totale des échantillons est déterminée par complexométrie (par titrage avec l'acide éthylène-diamine-tétracétique, EDTA). La

mesure de l'alcalinité est basée sur la neutralisation d'un certain volume de l'échantillon par l'acide sulfurique (N/50). Les chlorures sont déterminés par la méthode de Mohr et les sulfates par spectrophotométrie à une longueur d'onde = 420 nm pour une suspension obtenue par réaction des sulfates avec le chlorure de baryum. Le sodium et le potassium sont dosés par photométrie à émission de flamme sur appareil JENWAY PFP7.

Tous les résultats sont comparés avec les normes de l'organisation mondiale de la santé (OMS) [9].

4. RESULTATS ET DISCUSSION :

Les résultats des analyses physico-chimiques des eaux du complexe terminal (26 forages) sont portés sur le tableau 2. Pour tous les échantillons, la balance ionique est inférieure 7%.

4.1 Le faciès chimique

4.1.1 Diagramme de Piper

Le report de 26 forages d'eau sur le diagramme de Piper (Fig. 3) montre que tous les points analysés sont caractérisés par des eaux de type sulfaté sodique [10]. Ce faciès indique une dissolution évaporitique riche en sels et en gypse [11].

4.1.2 Digramme de Schoeller-Berkaloff

Le diagramme de Schoeller-Berkaloff permet la représentation de plusieurs analyses sur le même graphique. Si les concentrations sont identiques, on trouve une superposition des droites obtenues et dans le cas contraire, on remarque un décalage relatif de ces dernières.

D'après la figure 4 (a et b) on constate toujours l'existence d'une même famille d'eau qui est celle des eaux sulfatées, avec la prédominance du faciès sulfaté sodique.

4.2 Etude des rapports caractéristiques et origine des éléments dominants

4.2.1 Origine des éléments Na$^+$ et Cl$^-$

Pour avoir une idée sur les éléments dominants, une représentation graphique a été effectuée sur une échelle logarithmique, avec en abscisses la teneur exprimée en milliéquivalents des chlorures, et en ordonnées celle du sodium [12]. L'examen de la figure 5.a permis de remarquer que la majorité des points d'eau se

trouve au-dessous de la droite d'une pente égale à 1. Dans ce cas, ce sont les chlorures qui l'emportent sur le sodium à cause d'un excès de dissolution de cet élément dû à l'écoulement souterrain important et à la température élevée de ces eaux [13-14].

4.2.2 Origine du calcium

Le faciès calcique a été étudié à l'aide de deux diagrammes, à cause de sa double origine : carbonatée et évaporitique [15]. Les figures 5.b et 5.c montrent que l'ensemble des points se trouve dans le domaine évaporitique, ce qui vérifie que l'élément Ca^{++} provient de la dissolution des calcaires fissurés et des évaporites d'âge Sénonien (Tab. 1).

4.2.3 Le rapport Ca^{++} / Mg^{++}

La figure 5.d montre l'existence de deux ensembles de points :

Un ensemble où le rapport est supérieur à 1, donc le calcium prédomine, c'est le cas de la plupart des points d'eau analysés, cela est dû à la dissolution des formations gypseuses [16].

Un ensemble où le rapport est inférieur à 1, le magnésium prédomine, il concerne quelques échantillons analysés. Le faciès magnésien indique la présence d'argiles ou de dolomies riches en magnésium [17].

4.3 Aptitude des eaux à la potabilité

Afin de définir la potabilité des eaux souterraines, nous nous basons sur les normes de l'O.M.S (Organisation Mondiale de la Santé) et ceux du D.H.T (Degré Hydrométrique Total).

4.3.1 Selon l'O.M.S

Ces normes définissent deux types de concentrations maximales (Tab. 3) qui traduisent les limites de potabilité. On distingue :

- Une concentration maximale acceptable à partir de laquelle une eau provoque une certaine réticence chez les consommateurs.
- Une concentration maximale admissible qui correspond à la quantité maximale de substance à tolérer et dont la teneur supérieure peut être dangereuse à la santé.

L'examen du tableau 3, montre que tous les échantillons analysés ont des teneurs en SO$_4^-$, Ca^{++}, Na$^+$ et Cl$^-$ supérieures aux normes maximales admissibles

Tableau 2 : Résultats des analyses physico-chimiques des eaux du CT (mars 2012).

| Nom	SO_4^{--} (mg/l)	NO_3^- (mg/l)	Ca^{++} (mg/l)	Mg^{++} (mg/l)	Cl^- (mg/l)	HCO_3^- (mg/l)	Na^+ (mg/l)	K^+ (mg/l)	pH	T °C	CE (ms /cm)
CH01	841.41	31.18	310	190.80	1065	42.70	701.27	30.73	7.41	22.60	4.38
CH02	615.53	30.12	364	117.60	1579.75	45.14	713.92	30.12	7.55	22.50	4.38
CH03	508.24	29.35	404	120	1100.50	41.48	713.92	30.73	7.34	22.50	4.46
CH04	776.47	29.21	288	156	1242.50	46.36	688.61	32.56	7.30	22.50	4.31
CH05	728.47	29.24	312	208.8	1100.50	40.26	726.58	28.9	7.28	22.50	4.27
CH06	824.47	30.12	316	148.8	1065	43.92	562.03	31.95	7.55	22.50	4.47
CH08	485.65	35.83	248	151.20	1029.50	46.36	713.92	27.07	7.67	22.60	3.97
CH09	660.71	30.85	232	216	1217.65	46.36	663.29	27.68	7.38	22.50	3.96
CH10	417.88	30.68	302	85.20	656.75	47.58	308.86	45.37	7.17	22.30	2.69
CH11	423.07	30.78	352	115.20	1189.25	42.70	594.94	29.51	7.37	22.40	4.32
CH12	807.53	31.59	274	164.40	1100.50	45.14	701.27	28.90	7.57	22.20	4.33
CH13	649.41	27.67	278	133.20	1189.25	43.92	701.27	26.46	7.41	22.50	4.10
CH14	550.59	28.26	314	181.20	1118.25	48.80	688.61	31.34	7.51	22.50	4.32
CH15	680.47	28.88	256	153.60	390.50	47.58	625.32	28.90	7.71	22.10	3.95
CH16	663.53	27.96	352	98.40	1189.25	45.14	625.32	28.90	7.39	22.10	3.98
CH17	494.12	29.94	304	115.20	1153.75	43.92	663.29	27.07	7.47	22.30	3.99
CH18	504.28	28.29	428	26.40	1118.25	42.70	579.11	27.07	7.55	22.50	4.07
CH19	545.36	31.07	328	204	1792.75	45.14	579.11	28.90	7.37	23	4.58
CH20	434.67	27.60	274	140.40	1029.50	46.36	612.66	24.63	7.42	22.60	3.66
CH21	895.06	31.22	380	103.20	1118.25	46.36	726.58	28.29	7.28	22.50	4.57
CH22	745.41	29.87	290	111.60	1029.50	43.92	701.27	26.46	7.34	22.50	4.29
CH23	646.59	29.90	332	172.80	1136	46.36	713.92	28.90	7.33	22.30	4.34
CH24	671.25	29.90	364	85.20	1189.25	45.14	579.11	27.68	7.38	22.50	4.35
CH25	578.82	33.60	250	188.40	958.50	46.36	688.61	27.68	7.26	22.60	4.37
CH26	835.77	31.11	416	96	1153.75	46.36	675.95	28.90	7.3	22.50	4.38
CH27	784.76	29.87	314	151.20	1065	43.92	594.94	27.07	7.34	22.30	4.33
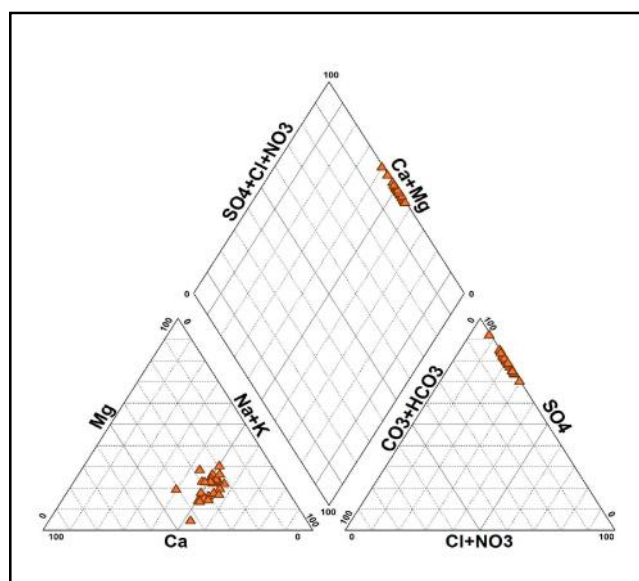
Figure 3: Diagramme de Piper des eaux de la nappe du CT
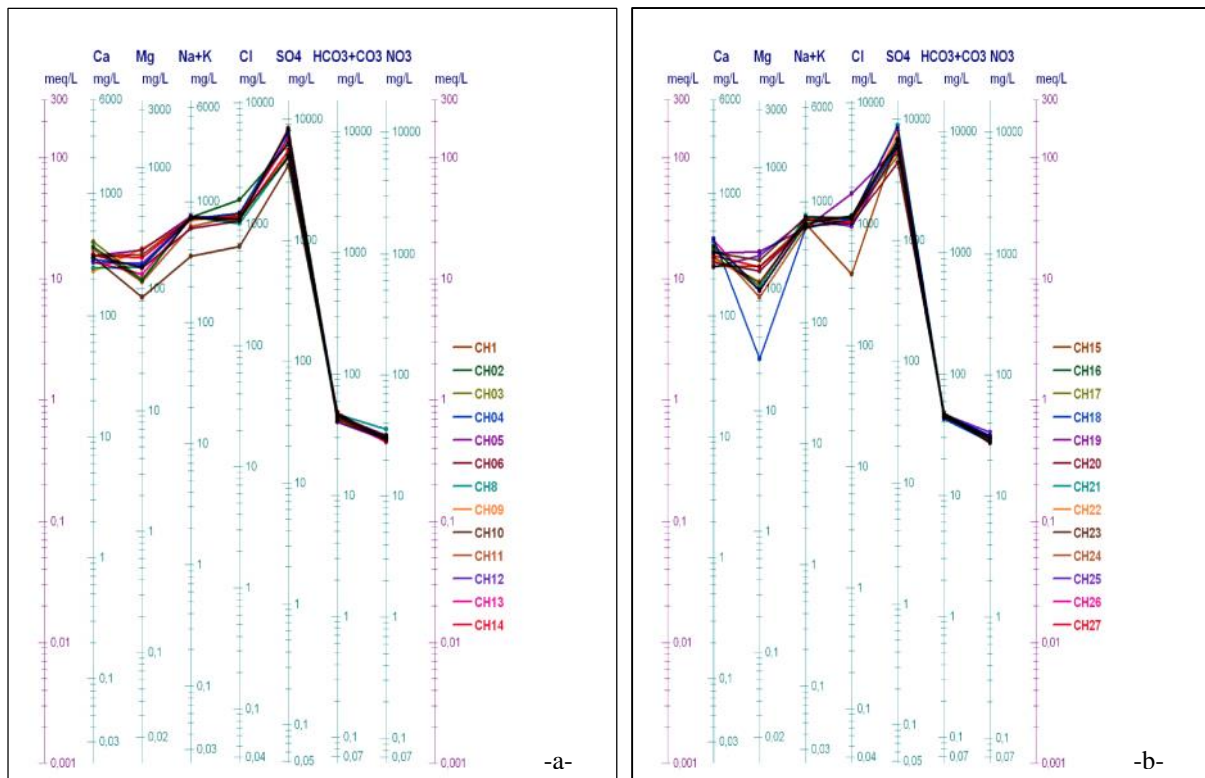(Région d'Oued Souf, mars 2012)

Figure 4: Diagramme de Schoeller Berkaloff des eaux de la nappe du CT (Région d'Oued Souf, mars 2012).
a: Diagramme de Schoeller Berkaloff des eaux de 13 forages (du CH 1 à CH 14) ; b : Diagramme de Schoeller Berkaloff des eaux de 13 forages (du CH 15 à CH 27).
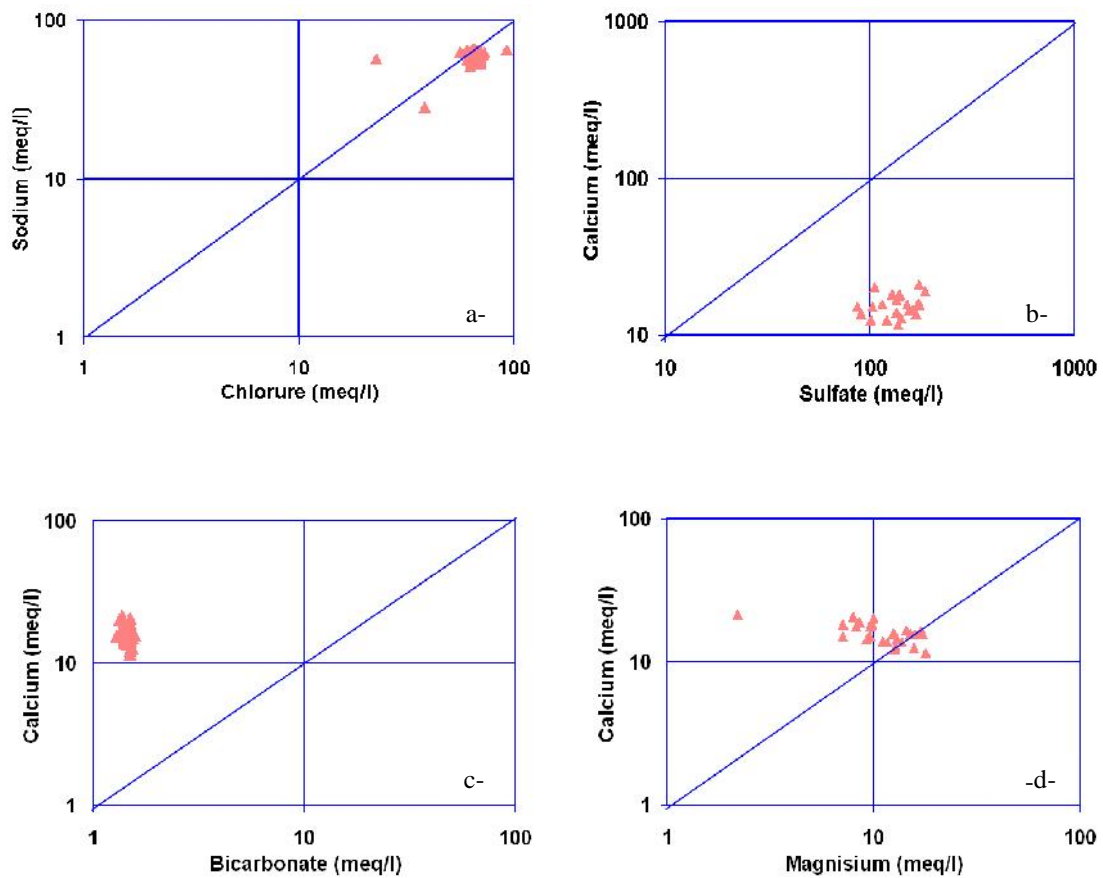

Figure 5 : Les rapports caractéristiques
a : le rapport Na^+/Cl^- ; b: le rapport Ca^{++}/SO_4^- ; c: le rapport Ca^{++}/HCO_3^- ; d: le rapport Ca^{++}/Mg^{++}

Tableau 3 : Normes de potabilité de l'O.M.S [9].

Eléments chimiques	Concentration maximale acceptable (mg/l)	Concentration maximale admissible (mg/l)	Pourcentage des échantillons ayant une concentration inférieure à la concentration maximale admissible
Calcium	75	200	00
Magnésium	50	150	50
Sodium	150	250	00
Sulfates	200	500	00
Chlorures	200	400	00
Nitrates	50	100	100

Pour le magnésium, 50 % des eaux ont des teneurs inférieures aux normes. Cependant, pour les nitrates, elles restent toutes inférieures aux normes maximales admissibles.

En résumé, d'après les analyses physico-chimiques effectuées sur terrain et au laboratoire en mars 2012 pour les 26 forages de la nappe du Complexe Terminal alimentant les quatre daïras d'El Oued, Rabbah, Guemar et Reguiba, on constate ce qui suit (Tab. 2):

- La température varie entre 22.1 °C et 23 °C, elle est conforme aux normes (20 °C- 25 °C);
- Le pH varie entre 7.175 et 7.71, il est conforme aux normes (6.5- 8.5);
- Les valeurs de la conductivité électrique varient entre 2690 µs/cm et 4580µs/cm, elles dépassent la norme admise (200 à 1000µs/cm), pour toute la région d'étude;
- Les teneurs en calcium (Ca^{++}) varient entre 232 mg/l et 428 mg/l dépassant la norme qui est de 100 à 140 mg/l. Par contre pour le magnésium 50% des forages ont des teneurs conformes à la norme;
- Les concentrations en chlorures (Cl^-) dans les forages varient entre 656.75 mg/l et 1792.75 mg/l dépassant la norme (500 mg/l), excepté le forage de Sidi Mestour (390.5 mg/l);
- Les concentrations en sulfates (SO_4^{--}) oscillent entre 4178.82 et 8950 mg/l dépassant la norme préconisée qui est de 400 mg/l;
- En ce qui concerne le sodium (Na^+), les concentrations oscillent entre 308 et 726 mg/l dépassent la norme (200 mg/l);

- Les concentrations en potassium (K^+) varient entre 24 et 45 mg/l dépassant largement la norme qui est 12 mg/l;
- Malgré l'activité agricole intense dans la région, les concentrations en nitrates ($NO3^-$) restent conformes à la norme (50 mg/l), et varient entre 27 et 35 mg/l, ceci s'explique par la nature captive de la nappe du Complexe Terminal qui assure sa protection contre toute contamination anthropique [18].

4.3.2 Selon le degré hydrométrique total (D.H.T)

Le degré hydrométrique ou la dureté d'une eau correspond à la somme des concentrations en calcium et en magnésium [19].

DHT = r Ca^{++} + r Mg^{++} (en méq/l).
DHT = (r Ca^{++} + r Mg^{++}) * 5 (en degré français °F).

Le tableau 4 montre que la totalité des eaux analysées (100%) sont très dures, le D.T.H est supérieur à 54 °F. Cette dureté a des conséquences plus ou moins néfastes telle que la consommation excessive du savon, la mauvaise cuisson des légumes secs et le goût inacceptable, ce qui oblige les citoyens à acheter l'eau à des propriétaires.

Nous pouvons donc dire que les eaux souterraines de la nappe du Complexe Terminal d'Oued Souf sont de qualité chimique médiocre à mauvaise et impropres à la consommation selon les normes de l'OMS.

4.4 Aptitudes des eaux à l'irrigation

L'abondance de sodium dans l'eau d'irrigation peut provoquer également la

dispersion et la destruction de la structure du sol [20], si la teneur en sodium est au moins trois fois supérieure à celle du calcium. Dans de telles conditions, il peut devenir extrêmement difficile de satisfaire les besoins en eau de la culture [21]. Le risque est déterminé à partir de la valeur du sodium absorbable « Sodium Absorption Ratio » (S.A.R) pour une même conductivité, le risque est d'autant plus grand que le coefficient est plus élevé. Le S.A.R est donné par la formule ci-dessous, il est utilisé en combinaisons avec la conductivité électrique de l'eau.

$$SAR = \frac{Na^+}{\sqrt{\dfrac{Ca^{++} + Mg^{++}}{2}}}$$

Où tous les éléments sont exprimés en méq/l

Par sa qualité bactériologique, l'eau souterraine doit être destinée prioritairement à l'AEP, malheureusement ce n'est pas le cas pour la nappe du Complexe Terminal d'Oued Souf à cause de sa qualité impropre [6]. Afin d'estimer l'influence de ces eaux sur le sol et sur certaines cultures pratiquées dans la région, nous allons essayer d'évaluer leur aptitude à l'irrigation.

Pour classer ces eaux, nous avons utilisé la méthode de Richards. Le tableau 5 récapitule les résultats obtenus après l'interprétation du diagramme de Richards (Fig.6).

Les eaux de la région d'étude appartiennent à deux classes selon le diagramme de Richards [22] :

- La classe $S_2 C_4$ avec un pourcentage de 38.46%. Celle-ci est caractérisée par des eaux de mauvaise qualité. L'eau est fortement minéralisée pouvant convenir à l'irrigation de certaines espèces (concombre) bien tolérantes au sel, sur des sols bien drainés et lessivés.
- La classe $S_3 C_4$ avec un pourcentage de 61.54, caractérisée par des eaux de très mauvaise qualité, parce que le SAR et la conductivité sont à leur maximum [23 et 24].

Tableau 4 : Dureté des eaux en °F [9].

D.H.T (en °F)	0 -7	7 - 22	22 - 32	32 - 54	> 54
Qualification de l'eau	Douce	Modérément douce	Assez douce	Dure	Très dure
Pourcentage des points	0	0	0	0	100

Tableau 5 : Résultats obtenus après interprétation du diagramme de Richards

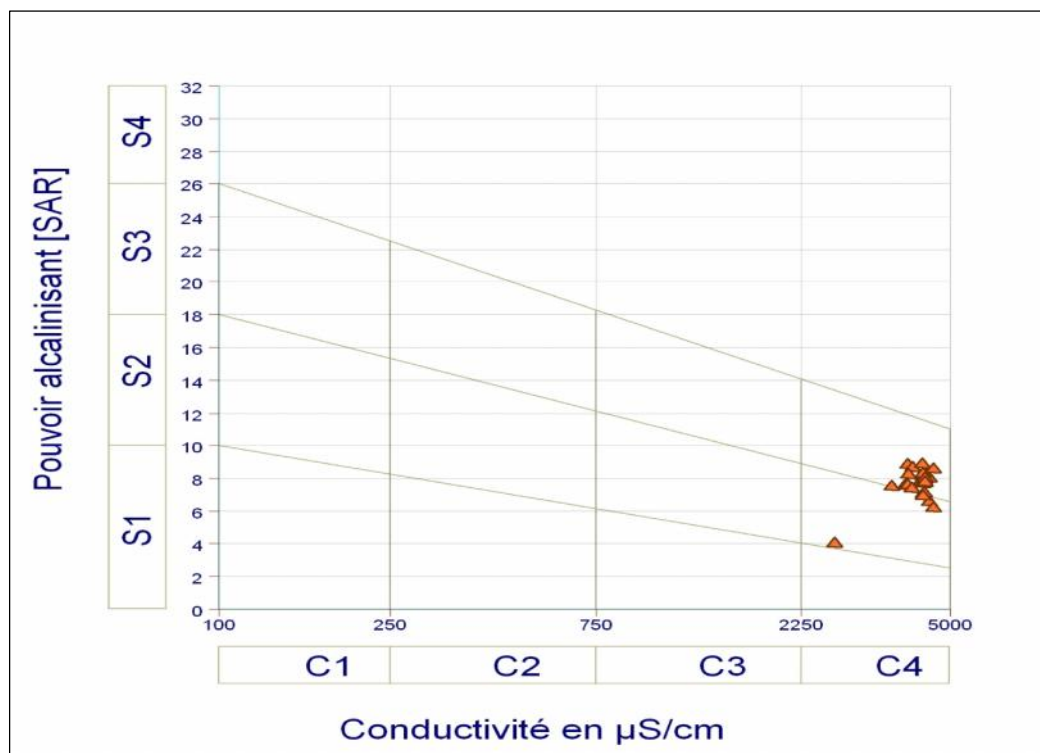| Classes		Pourcentage des points d'eau (%)
Admissible	$S_1 C_3$	00
	$S_2 C_3$	00
Médiocre	$S_1 C_4$	00
	$S_2 C_4$	00
Mauvaise	$S_2 C_4$	38.46
Très mauvaise	$S_3 C_4$	61.54

Figure 6 : Diagramme de Richards: classification des eaux d'irrigation en fonction du S.A.R
(Nappe du Complexe Terminal de la région d'Oued Souf, mars 2012)

5. CONCLUSION

La région d'Oued Souf possède une potentialité hydrique très importante, présentée sous forme de trois nappes souterraines : la nappe du Complexe Terminal (CT), la nappe du Continental Intercalaire (Albien) et la nappe phréatique (libre). La quasi-totalité des eaux destinée à l'alimentation de la population sont celles du CT qui ont de forts débits (dépassant les 14 000m^3/j [25]) ce qui traduit une consommation excessive de cette nappe

Au cours de ce travail, on a pu définir la qualité des eaux de la nappe du CT, du point de vu potabilité et aptitude à l'irrigation. D'après l'interprétation des analyses physico-chimiques, ces eaux sont trop salées et la concentration des éléments majeurs dépasse de loin les normes de potabilité de l'OMS, ce qui nous laisse confirmer la mauvaise qualité de ces eaux pour la consommation humaine.
La classification des eaux du CT selon le diagramme de Richards montre qu'elles ont des conductivités très fortes et sont impropres pour les utilisations agricoles.
Cette situation a conduit les habitants de la région d'Oued Souf à acheter les eaux des citernes (eaux traitées ou provenant des régions voisines) pour leur propre consommation et n'utiliser les eaux de robinet (de CT) que pour le lavage et l'arrosage des espaces verts et des jardins. Ainsi, la dotation journalière devient très élevée (dépassant les 200 litres/jour/habitants [25]), ce qui a pour conséquence une mauvaise gestion de cette ressource rare et vulnérable.

REFERENCES

[1] DHW (Direction d'Hydraulique de la Wilaya d'El-Oued)., 2010. Ressources en eau de la région d'El-Oued, 6p.

[2] DE (Direction de l'Environnement d'El-Oued), 2009, Rapport «dégâts de la remontée des eaux et pollution de la nappe superficielle d'El-Oued », 19p.

[3] DSA (Direction Des Services Agricoles de la Wilaya d'El-Oued)., 2010. L'irrigation par les forages de la nappe du Complexe Terminal (CT), p.4-11.

[4] Khechana S. & Derradji F., 2012. Management of Water Resources in a Hyper-Arid Area: Strategy and Issues (Case of Oued-Souf Valley-South Eastern of Algeria), *Journal of Water Resource and Protection*, Vol.4 No.11, 922-928.

[5] DS (Direction de la Statistique de la wilaya d'El Oued), 2009., Recensement de l'année 2008 pour la wilaya d'El-Oued, 2p.

[6] Burri J.M. & Burri P., 2004. Vallée du Souf : Etudes d'assainissement des eaux résiduaires, pluviales et d'irrigation, Mesures complémentaires de lutte contre la remontée de la nappe phréatique, Mission II. 111p.

[7] Khechana S., Derradji F. & Derouiche A., 2010. La gestion intégrée des ressources en eau dans la vallée d'Oued-Souf : enjeux d'adaptation d'une nouvelle stratégie, *Revue des Sciences Fondamentale et Appliquées*, Vol.2 No.2, 22-36.

[8] Tiri A. & Boudoukha A., 2010. Hydro chemical analysis and assessment of Surface water quality in Koudiat Medouar reservoir, Algeria. *European Journal of Scientific Research*, Vol.41 No.2, .273-285

[9] WHO (World Health Organization)., 1993. "Guidelines for drinking water quality", (2nd edition), Volume 1, Geneva, WHO, pp. 130.

[10] Piper A. M., 1944. "A graphic procedure in the geochemical interpretation of water analyses". *Transactions American Geophysical Union*, 25, 914-928.

[11] Rouabhia A., 2006. Vulnérabilité et risques de pollution des eaux souterraines de la nappe des sables Miocènes de la plaine d'El Ma El Abiod nord-est algérien. Thèse de Doctorat en hydrogéologie. Université d'Annaba, Algérie 189p.

[12] Khechana S., Derradji E.F. & Mega N., 2011. Hydro chemical characteristics of groundwater from the Valley of Oued Souf (SE Algerian), *European Journal of Scientific Research*, Vol.62 No.2, 207-215.

[13] Olivier H., Séverin P., Nicolas C., Jean D., Christelle B. & Jean-Luc S., 2006. Origine des eaux des émergences karstiques chlorurées du Languedoc-Roussillon, *Comptes Rendus Géoscience,* 338, 703–710.

[14] Romain S. & François-David V., 2010. Remobilisation of deep Na-Cl waters by a regional flow system in the Alps: Case study of Saint-Gervais-les-Bains (France), *Surface geosciences, Comptes Rendus Geoscience, 342*, 151–161.

[15]. Bernard S., Gil M. & Annie M., 1990. Origine des substances dissoutes dans les eaux des sources thermales et des forages de la région Asal-Ghoubbe (République de Djibouti), *Journal of Volcanology and Geothermal Research*, 43, 333-352.

[16] Lucia F., Mohamed K., Kamel Z., Ahmed M. & Gian M., 2001. Origine de la minéralisation et comportement hydrogéochimique d'une nappe phréatique soumise à des contraintes naturelles et anthropiques sévères : exemple de la nappe de Djebeniana (Tunisie), *Comptes Rendus Académie des Sciences Paris, Sciences de la Terre et des planètes,* 332, 665–671.

[17] Youssef H., Jacques M., Jacky M., Lhoussaine B. & Pierre C.,1999. Use of the Bd/Cl ratio to determine the origin of the salinity of groundwater an example from the Souss plain (Morocco), *Académie des sciences / Elsevier.*

[18] J.-N. Cretenet., 2003. Vallée du Souf : Etudes d'assainissement des eaux résiduaires, pluviales et d'irrigation, Mesures complémentaires de lutte contre la remontée de la nappe phréatique, Mission II, 60p.

[19] Rosset R., Ben Amor M. & Ghorbel A., 1997. Caractérisation du pouvoir incrustant des eaux d'irrigation du Cap Bon par chronoéléctrogravimétrie, *Comptes Rendus Académie des sciences Paris,* 325, p.727-732.

[20] Suyama H., Benes S.E., Robinson P.H., Grattan S.R., Grieve C.M. & Getachew G., 2007. Forage yield and quality under irrigation with saline-sodic drainage water, *Greenhouse evaluation. agricultural water management,* 88, 159–172.

[21] Papaioannoua A., Plageras P., Dovriki E., Minas A., Krikelis V., Nastos P.Th., Kakavas K., & Paliatsos A.G., 2007. Groundwater quality and location of productive activities in the region of Thessaly (Greece), *Journal of Desalination,* 213, 209–217.

[22] Richard L.A., 1954. "Diagnosis and improvement of saline and alkali soils". *Agricultural handbook* 60. Washington, DC: USDA, 160p.

[23] Wilcox L.V., 1948. "The quality of water for irrigation use". *Technical Bulletin 962.Washington, U.S. Department of Agriculture*, 40p.

[24] Wilcox. L.V., 1955. "Classification and use of irrigation waters". Circular 969. Washington, U.S. Department of Agriculture, 19p.

[25] ADE (Algérien Des Eaux),. 2010. Compte-rendu d'enquête sur les exploitations et les demandes d'AEP dans la Wilaya d'El-Oued, 4p.

State of the art on enhanced oil recovery with CO 2 sequestration for low carbon industry ARTICLE INFO ABSTRACT/RESUME

Article · January 2017

2 authors:

ABDELMALEK ATIA
El-Oued University
20 PUBLICATIONS **7** CITATIONS

SEE PROFILE

Kamal Mohammedi
University M'Hamed Bougara of Boumerdes
150 PUBLICATIONS **813** CITATIONS

SEE PROFILE

Some of the authors of this publication are also working on these related projects:

feasibility and realization of geothermal heat exchanger View project

Call for Papers: 1st IEEE International Conference on Communications, Control Systems and Signal Processing CCSSP 2020 View project

State of the art on enhanced oil recovery with CO_2 sequestration for low carbon industry

A.Atia[1,2*] , K. Mohammedi[2]

[1] Univ. El-Oued , LEVRES Lab, Algeria
[2] Univ. Boumerdes, LEMI Lab, Algeria

*Corresponding author: abdelmalek-atia@univ-eloued.dz; Tel.: +213 550 31 59 60; Fax: +213 32 22 30 13

ARTICLE INFO	ABSTRACT/RESUME
	Abstract: *The growing concerns over the global warming due to the increase in the global concentration of greenhouse gases in the atmosphere has increased the interest in examining various techniques to reduce the emission of these gases and for low carbon dioxide industry. A main component of greenhouse gases is carbon dioxide (CO2). A promising long term solution for mitigating global heating is to inject CO2 into geological formations; either for CO2 sequestration or enhanced oil recovery, or a combination between the two solutions. A suitable choice of geological formations for CO2 injection includes petroleum and gas reservoirs, water formation leg of the oil/gas reservoir or separate deep saline aquifers, deep-sea sediments and coal beds. This study aims to setup a state of the art on this problem.*

I. Introduction

The combustion and flaring of fossil fuels produces large quantities of CO2. The Intergovernmental Panel on Climate Change stresses the need to control anthropogenic greenhouse gases in order to mitigate the climate change that is adversely affecting the planet. Moreover, in some fields the hydrocarbon gases produced along with the oil are re-injected to the reservoir to enhance oil production. Nevertheless, in some fields the hydrocarbon gas is sold and the gas itself is considered as source of energy. An attractive option is the use of CO2 as one of the main components of the solvent mixture for EOR process.

Enhanced oil recovery using CO2 is an attractive oil recovery process that involves the injection of CO2 to oil reservoirs and produce petroleum substances that would otherwise remain unrecoverable . Typically only around one third of the oil is produced after primary and secondary oil recovery methods. Much of the remaining oil are trapped by capillary forces as disconnected drops, surrounded by water, or as a continuous phase at low saturation with gas occupying the larger fraction of the pore space. An efficiency EOR process must mobilise these dispersed oil and form an oil bank that can move towards the production wells. This needs to be accomplished both on the microscale, at the pore level, and also on the macro-scale affecting the largest possible volume of the reservoir. EOR operations using CO2 have been practiced for more than 50 years, the results revealed that $6-15\%$ of original oil in-place can be recovered by these kind of processes .

The low saturation pressure of CO2 compared to CH4 or N2, its low price compared with other hydrocarbon solvents are the incentives for the use of CO2 in the EOR process. Moreover, a mixture of hydrocarbon solvents with CO2 may be less likely to precipitate asphaltene, which is a great problem in enhanced oil recovery . Furthermore at high pressures, CO2 density has a density close to that of a liquid and is greater than that of either nitrogen (N2) or methane (CH4), which makes CO2 less prone to gravity segregation compared with N2 or CH4 .

II. CO_2 injection schemes for EOR projects

CO_2 is introduced in a reservoir through a number of injector wells perforated around a producer well.

As an injected phase, CO_2 can be injected into the oil zone through various schemes including miscible and immiscible continuous CO_2 injection, cyclic CO_2 injection, CO_2-flue gas mixture injection, water-alternating-CO_2 injection, carbonated water injection . Parameters such as the type of crude oil, thermodynamic conditions of the reservoir, petro-physical and geo-mechanical properties of the reservoir rock, and the extension of the oil zone have a significant effect on the performance of CO_2-EOR processes .

Under favourable reservoir temperature and pressure conditions and crude oil composition, carbon dioxide can become miscible with petroleum, i.e. the crude oil and CO_2 form a single homogenous phase (Figure 1). As a result of this interaction, the volume of oil swells, its viscosity is reduced, and surface tension effects diminish, improving the ability of the oil to flow out of the reservoir. When CO_2 is directly miscible with oil the interface between the two phases ceases to exist and theoretically the oil recovery factor reaches unity . However, Carbon dioxide can be not instantaneously miscible with oil at first contact, miscibility conditions develop dynamically in the reservoir through mass transfer of components as a result of repeated contacts between oil and injected carbon dioxide during the flow, via a process known as multiple contact miscibility (MCM), the pressure at which multiple contact miscibility takes place is called Minimum Miscibility Pressure (MMP). For a miscible CO_2 flood, the pressure should be above the MMP.
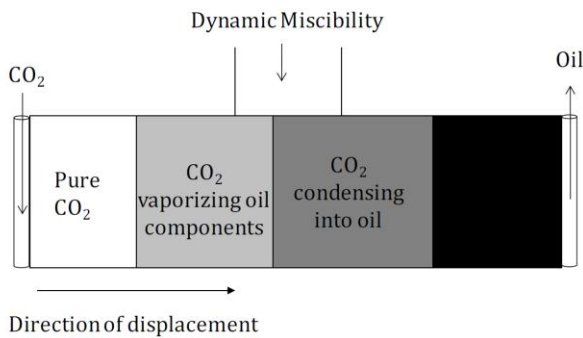

Figure 1. *One dimensional schematic showing how CO2 becomes miscible with crude oil*

If the reservoir pressure is lower than the MMP between the crude oil and CO2, the CO2 injection is classified as an immiscible solvent injection. In this case, the CO2 although not fully miscible with oil, it can still partially dissolve in it causing some swelling and reducing oil viscosity. More importantly, in immiscible displacement, the role of CO2 is similar to that of water in secondary oil recovery processes, i.e. to maintain reservoir pressure. The use of CO2 to maintain reservoir pressure has been considered in limited number of

projects when the permeability of the reservoir formation is too low or geologic conditions do not favour the use of water.

Cyclic CO2 injection, which is also known as a CO2 huff-and-puff process, has been investigated through experimental and simulation studies as well as field tests as an EOR technique for more than 30 years . Cyclic CO2 injection was initially proposed as an alternative to cyclic steam stimulation for heavy crude oils. However, It is reported that the cyclic CO2 injection process has wider applications in light oil reservoirs . In this process, after the injection of CO2 into the reservoir, the well is close for a period of time called soaking period, depending on the pressure and temperature reservoir conditions and reservoir rock and fluid properties. Then, the oil production is initiated by converting the injection well to a production well. The injected carbon dioxide has the ability to change the reservoir rock and fluid properties in terms of rock wettability and relative mobility, leading to enhance the hydrocarbon production recovery. Several operating parameters including characteristics of reservoir rock, crude oil proprieties, pressure, soaking period, injection time and number of cycles influence the performance of this technique. Although a set of studies have been reported on this process, there remains a lack of experimental work to illustrate the influence of the aforementioned parameters on the recovery performance on CO2 injection process.

It is reported in the literature that there are also two types of CO2 injection in CO2-EOR processes: the water alternating gas (WAG) method and the gravity stable gas injection (GSGI) method. In WAG injection, CO2 is injected first to dissolve into oil through mass transfer for swelling the oil and improving its fluidity. Then, water is used to displace the oil bank towards the production well. A schematic of the process is shown in Figure 2.
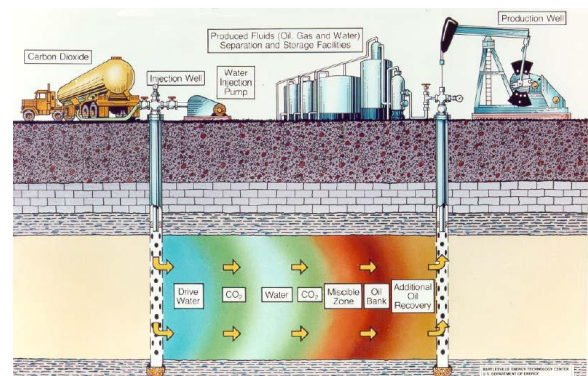
Figure 2. *A schematic of a WAG miscible CO2-EOR process*

Another method for introducing CO_2 in the reservoir is to inject it in the crest, called gravity

stable gas injection (Figure 3). The injected carbon dioxide creates an artificial gas cap, pushing oil downwards and towards the rim of the reservoir where the producing wells are located. CO_2 (which can be miscible or immiscible to oil) is used for maintaining reservoir pressure and for stabilising displacements via gravity drainage to increase sweep. WAG has an advantage over GSGI in that it can be performed on a small field; while in general, GSGI is applied in the whole oil reservoir. Hence GSGI projects are likely to recover more oil and store larger CO_2 volumes
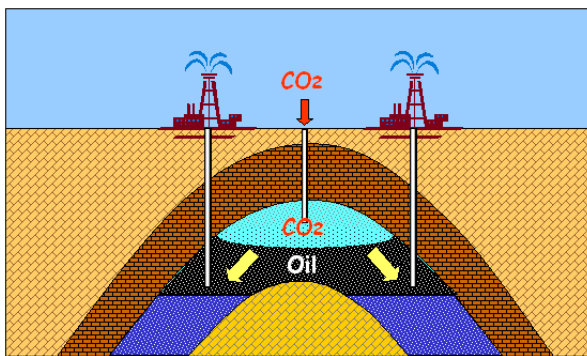

Figure 3. *A schematic of the GSGI immiscible displacement in CO2-EOR process*

III. On-going CO2-EOR projects

The first project of CO2 -EOR at industrial scale was started in 1972 in SACROC field in the USA . A large number of CO2 - EOR projects have started since then. Based on the 2014 EOR survey by the Oil and Gas Journal there are more than 140 of CO2-EOR projects worldwide. Nearly all of them are miscible CO2-EOR projects were implemented in the USA [30]. Table 1 shows the production of active CO2-EOR projects and their production rates in 2014 with the outlook of these projects in 2020 for United State by region . These projects produced cumulatively approximately 300000 barrels of oil per day at the start of year 2014 by injecting over than 68 million tonnes of CO2 per year. This rate of oil production has grown steadily for the past 30 years. Given the new volumes of CO2 supplies and the numerous announced CO2-EOR projects, A. Kuuskraa and M.Wallace envision strong growth in near-term oil production and CO2 utilization from CO2-EOR, their analysis shows that incremental oil production from CO2-EOR operations is likely to double to 638000 barrels of oil per day in 2020.

Table 1. *Projected CO2-EOR production*

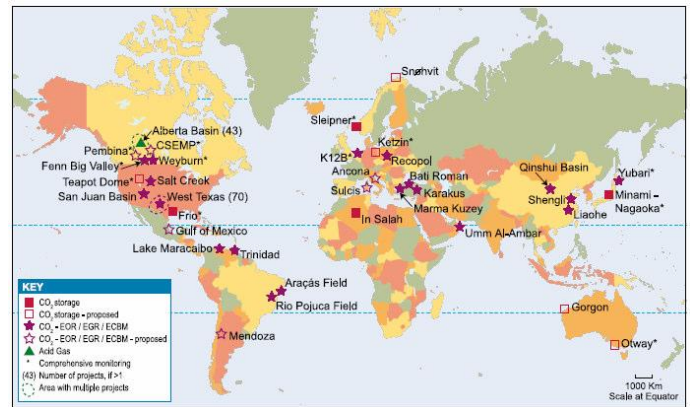| Region	CO₂-EOR production rates (bbl/day) (1 bbl = 159 l)	
	2014	**2020**
Permian Basin	199000	323000
Gulf Coast	47000	152000
Rocky Mountains	39000	103000
Midcontinent	14000	59000
Other	1000	1000
Total	**300000**	**638000**

Figure 4. *Location of sites where activities relevant to CO2 storage are planned or under way*

The use of CO2 injection for oil recovery has been slow to catch some exception on outside of the US. One notable exception is Weyburn oil field, where in Canada and Apache have field-wide CO2-EOR projects. Additional exceptions include the injection of CO2 into Bati Raman heavy oil field in Turkey and the use of CO2 in a series of heavy oil fields in Trinidad. Recently, the interests have emerged several CO2 injection projects in Algeria (In Salah Gas), Abu Dhabi, Brazil, China, Malaysia, the North Sea, and other areas for purpose of enhanced oil recovery or CO2 storage, Fig 4.

In Salah Gas is a joint venture of Sonatrach, British Petroleum (BP), and Statoil, which started in July 2004, for producing natural gas to sale in Europe. The natural gas contains up to 10% of CO2 concentration, which has to be reduced to 0.3% before the gas is sold. Hence, 1 million tonnes/year of CO2 is produced and re-injected into the Krechba Carboniferous Sandstone reservoir via two horizontal wells at a depth of 1900 metres for

combined between CO2 geological storage and enhanced gas recovery. The height of this geological formation is 20m, its porosity is 16% and its permeability is 10 md, fig 5. This joint venture is the first industrial-scale project in the world to store CO2 in the water leg of a gas reservoir .
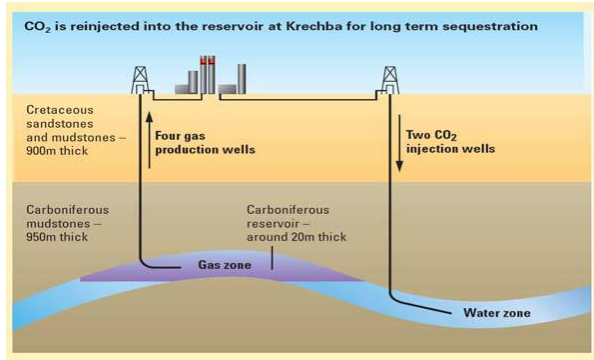
Figure 5. Schematic of CO2 storage strategy at Krechba field (In Salah Gas project) .

IV. Conclusion

With the decline of oil production and apparition of global warming problem caused by excessive emission of carbon dioxide during the last decades, it is believed that EOR-CO2 technologies will play a key role to meet the energy demand and better mitigation of climate change in years to come. If we look to the great number of studies interest by EOR-CO2 projects problem, we can conclude that this subject is being very important in Clean Technologies and Environmental Sciences.

V. References

1. A. Abedini, "Mechanisms of Oil Recovery during Cyclic CO2 Injection process: Impact of Fluid Interactions, operating parameters, and Porous Medium," Faculty of Graduate Studies and Research, University of Regina, 2014.

2. C.-W. Hustad, J. M. Austell, M. Roggenkamp, and U. Hammer. Mechanisms and incentives to promote the use and storage of CO2 in the North Sea. European Energy Law Report I, Intersentia. (2004). 355-380.

3. M. Javaheri and J. Abedi. The effect of heavy oil viscosity reduction by solvent dissolution on natural convection in the boundary layer of VAPEX. Transport in porous media. 99, (2013). 307-326.

4. L. H. Bui, "Near miscible CO2 application to improve oil recovery," University of Kansas, 2010.

5. N. Mosavat and F. Torabi. Performance of secondary carbonated water injection in light oil systems. Industrial & Engineering Chemistry Research. 53, (2013). 1262-1273.

6. R. Farajzadeh, Enhanced transport phenomena in CO2 sequestration and CO2 EOR: TU Delft, Delft University of Technology, 2009.

7. G. Thomas and T. Monger-McClure. Feasibility of cyclic CO2 injection for light-oil recovery. SPE Reservoir Engineering. 6, (1991). 179-184.

8. E. Tzimas, A. Georgakaki, C. Garcia-Cortes, and S. Peteves, Enhanced oil recovery using carbon dioxide in the European energy system: Publications Office, 2005.

9. S. Goodyear, I. Hawkyard, J. Masters, C. Woods, A. Jayasekera, and E. Balbinski. Subsurface issues for CO 2 flooding of UKCS reservoirs. Chemical engineering research and design. 81, (2003). 315-325.

10. M. W. Vello A. Kuuskraa. CO2-EOR set for growth as new CO2 supplies emerge. Oil & Gas Journal. 112, (2014)

11. B. Metz, O. Davidson, H. De Coninck, M. Loos, and L. Meyer. IPCC special report on carbon dioxide capture and storage. Prepared by Working Group III of the Intergovernmental Panel on Climate Change. Cambridge University Press, United Kingdom and New York, USA. 4, (2005). 195-276.

12. D. Abdelhakim and K. Baddari, "A Riveting Review of Worldwide Industrial Geological Carbon Capture and Storage Projects with the Junction of CO2 Emissions in Algeria," in North Africa Technical Conference and Exhibition, 2012.

13. I. W. Wright, "The In Salah gas CO2 storage project," in IPTC 2007: International Petroleum Technology Conference, 2007.

STUDY OF THE WORKABILITY AND MECHANICAL STRENGTH OF CONCRETE IN THE FACE OF UPWELLING (CASE OF THE EL OUED REGION OF ALGERIA)

T. Djedid[*1], A. Guettala[2], M. Mani[1]

[1]Laboratoire d'exploitation et valorisation des ressources énergétiques sahariennes « LEVRES » Université d'El Oued, Algérie

[2]Laboratoire de Recherche en Génie Civil « LRGC » Université Mohamed Khider Biskra, BP 145 RP, 07000 Biskra, Algérie

ABSTRACT

The objective of this study is to explore the effect of partial and total substitution of river sand by crushing sand in ordinary concrete. Various mixtures were tested to evaluate the properties of fresh and hardened concrete exposed to the water rising from the water table. The river sand was substituted by the limestone sand for the following proportions (0%, 30%, 40%, 50%, 60%, 70%, and 100%). The results showed that, the presence of limestone sand greatly improves the properties of strengh and workability. It was noted that these properties were much higher in the presence of crushed limestone sand compared to silica sand in the concrete. The optimal percentage of river sand substitution by crushed limestone sand is 50%.

Keywords: River Sand, Crushed Limestone Sand, Mechanical Strength, Workability, rising water.

Author Correspondence, e-mail: tarek-djedid@univ-eloued.dz

1. INTRODUCTION

Le béton est le matériau de construction le plus largement utilisé par l'homme dans le monde. Il est classé le deuxième après l'eau comme la substance la plus utilisée sur la planète. Il est obtenu en mélangeant le ciment, l'eau et les agrégats dans des proportions requises. Le sable est l'un des principaux constituants du béton faisant environ 35% du volume du béton utilisé dans l'industrie de la construction des bâtiments, des infrastructures et des ouvrages d'art, ces derniers exige de gros approvisionnements en matériaux. Jusqu'à présent, les sables les plus couramment utilisés pour la confection des bétons entrant dans ces ouvrages sont les sables roulés alluvionnaires. Mais les prélèvements excessifs de ces sables ont fortement contribué à l'épuisement des ressources et ont provoqué des retombés néfastes sur l'environnement [1].

Comme plusieurs régions du monde, la zone d'El oued vive cette situation et doivent aujourd'hui chercher des matériaux de substitution pour faire face à la demande croissante en sables ,qu'ils ont transportés en grandes quantités surtout au nord du pays (Algérie) aprés l'interdiction d'exploitation du sable de la mer. L'importance d'utiliser les sables de carrières concassés comme substitut avec les sables alluvionnaires est d'exploiter ces présieuses ressources car ils sont disponibles en quantités suffisantes, à prix raisonnables, par conséquant ils contribuent à améliorer les caractéristiques de la durabilité et / ou retarder le plus possible l'effet de substances chimiques nocives issus de la rémontée des eaux sur le béton d'enrobage. Notons que certains travaux ont déjà été menés dans ce contexte, Les résultats obtenus ont révélé que différents matériaux locaux valorisés répondent bien aux exigences des normes et peuvent être utilisés pour l'élaboration des bétons hydrauliques et des mortiers. Çelik *et* Marar [2] ont utilisé des poussières provenant du concassage des roches calcaires pour remplacer le sable en béton pour des proportions allant jusqu'à 30%. Ils ont conclu que lorsque le taux de poussières augmente, le volume d'air et l'ouvrabilité réduit. Kenai et al [3] a constaté que l'ajout jusqu'à 15% des fines calcaires n'influent pas sur les performances de résistance du béton de calcaire. Ilangovan [4] a signalé que les déchets de carrière pouvaient être utilisés comme agrégats fins dans le béton et ont également constaté que la poussière de carrière réduisait le coût sans affecter la résistance du béton. Hudson [5] a conclu que, en raison de particules irrégulières de sable de concassage, l'ouvrabilité de béton réduit. En raison de

l'espace élevé des vides dans le sable concassé, l'exigence d'eau est également élevée, ce qui réduit la résistance du béton. Shukla et al [6] ont confirmé que le remplacement du sable par la poussière de pierre réduit l'ouvrabilité du béton, alors que la résistance à la compression et à la résistance à la traction du béton augmente jusqu'à 40% de substitution du sable par la poussière de pierre de concassage. Sahu et al [7] ont constaté que le béton fabriqué avec la substitution du sable naturel de la rivière par des déchets de poussière de pierre concassée peut atteindre la même résistance à la compression, une résistance à la traction comparable et un module de rupture comme le béton témoin. Topçu et al [6] ont évolué en augmentant la résistance à la compression et à la flexion lors de la substitution du sable par du calcaire de moins de 2 mm de grain. Salvador Villalobos et al [6] ont révélé que le pourcentage optimal de sable concassé au sable naturel est soit 1: 1,5 ou 1,5: 1 et a indiqué que le volume des vides est réduit de 41 à 46% lorsqu'il est mélangé avec du sable naturel. Ainsi, la teneur en ciment et la teneur en eau peuvent être réduites en mélangeant avec le sable naturel. Ilangovan et al [8] ont signalé que le remplacement complet de sable naturel avec la poussière de carrière en béton est possible avec un traitement adéquat de la poussière de carrière avant l'utilisation et a également constaté que la compression, la flexion, la traction et les propriétés de durabilité du béton en poudre de pierre de carrière sont près de 10% de plus que le béton conventionnel. Shahul Hameed et Sekar [9] ont délibéré les propriétés du béton vert contenant de la poussière de pierre de carrière et de la poudre de boue de marbre comme agrégat fin. Ils ont conclu que la résistance à la compression, la résistance à la traction et aux propriétés de durabilité du béton en poudre de pierre de carrière sont près de 14% de plus que le béton conventionnel. Vinay Chandwani et al [10] ont constaté que le taux le plus élevé de substitution de sable de concassage par le sable de rivière affecte l'ouvrabilité du béton et qu'une réduction considérable de la résistance à la compression était perceptible à plus de 50% de remplacement de sable de concassage.

L'objectif de cette recherche est de clarifier et d'interpréter l'effet de la substitution partiel et total de sable de rivière avec le sable de carrière de Hassi Messaoud (Sud Est de L'algérie) sur l'ouvrabilité et la resistance des bétons ordinaires immergés pendant 6 mois dans les eaux remontées de la nappe phréatique, Selon les normes, ces eaux sont agressives [11]. En

cherchant le niveau optimal de substitution qu'on a obtenu dans cette étude après la consultation de la résistance à la compression, la résistance à la flexion, ainsi que les critères d'ouvrabilité (cône d'abrams).

2. MATÉRIAUX ET METHODES

2.1 Ciment

Le ciment utilisé dans ce travail est CEMI42.5 NA 442 provenant de la cimenterie de Tebessa (El Maa labiod) (Groupe industriel des ciments d'Algérie), dont les caractéristiques physico-chimiques et minéralogique sont indiquées dans le tableau 1.

2.2 Granulats

Deux types de sable ont été utilisés au cours de cette expérimentation, le premier est un sable de rivière (SR) provient de la sablière d'Asila (sur la route qui relie El meghier et still), et le deuxième est un sable concassé (SC) ramené des déchets de carrière Ben Brahim (Hassi Messoud). Leurs distributions granulométriques sont illustrées sur la figure (1).

Le SR présente une distribution de taille de particules continue allant de 0,08 à 5 mm avec une fraction de grains inférieure à 0,08 mm est environ 1% (figure1). Le SC présente également une distribution de taille de particules continue avec un diamètre de grain maximal d'environ 5 mm, mais la proportion de grains de moins de 0,08 mm est environ 17% (figure1). Il convient de noter que cette proportion de fines grains reste acceptable [12]. De manière schématique, la distribution granulométrique du sable concassé est légèrement plus étalée que celle du sable de la rivière (figure 1). De plus, les grains SR présentent des formes arrondies (figure 2a) tandis que les grains SC présentent des formes angulaires (figure 2b). Le tableau (2) énumère l'ensemble des caractéristiques physiques pour les deux types de sable.

Il révèle que la densité de SC et la densité de SR sont égaux. D'autre part le module de finesse de SR est de 2,29, mais SC est de 2,62, ce qui signifie que SC est légèrement plus grossier. Les valeurs de l'équivalent de sable ont signalé que les deux sables sont acceptables pour la construction. L'analyse minéralogique par DRX, nous montre la nature siliceuse de SR, et la nature essentiellement calcaire de SC (figure 3).

Tableau 1. Caractéristiques physico-chimiques et minéralogique du ciment

Composition Chimique (%)										
SiO2	Fe$_2$O$_3$	AlO$_2$	SO$_3$	CaO	K$_2$O	Cl	Na$_2$O	PAF	RI	CaO Libre
20.16	5.54	4.54	2.66	62.97	0.34	0.001	0.18	0.87	0.97	0.69

Composition Minéralogique (%)			
C$_3$S	C$_2$S	C$_3$A	C$_4$AF
68.84	6.98	2.58	17.69

Caractéristiques physiques				
Consistance %	Début de prise (min)	Fin de prise (min)	Finesse (cm^2/g)	P.S(g/cm^3)
25.59	177	280	3275	3.22
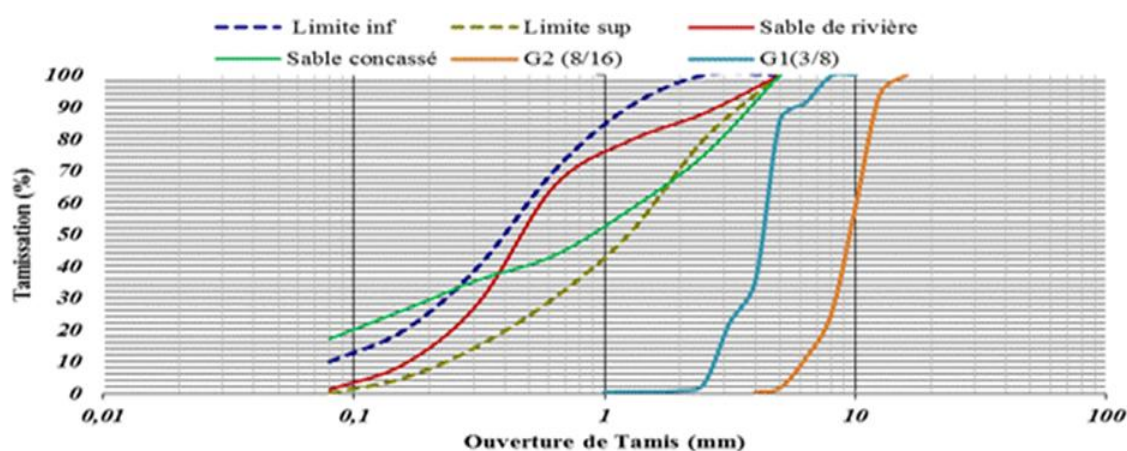
Fig.1. Analyse granulométrique des granulats étudiés

Tableau 2. Propriétés physico-mécanique de granulats utilisés

Caractéristiques physiques	SR	SC	G1(3/8)	G2(8/16)
Densité spécifique (g/cm^3)	2.55	2.55	2.72	2.45
Densité apparente (g/cm^3)	1.65	1.44	1.25	1.22
Compacité (%)	62	56	46	50
Porosité (%)	38	44	54	50
Indice des vides (%)	61	78	117	100
Module de finesse	2.29	2.62	-	-
Equivalent du sable (visuel)	71.37	80.87	-	-
Equivalent du sable (piston)	72.65	82.60	-	-
Coefficient d'absorption (%)	2.13	4.1	2.38	3
Coefficient d'aplatissement (%)	-	-	17	14
Propreté superficielle (%)	-	-	98.84	99.95
Teneur en eau (%)	1.73	0.6	0.45	0.45
L.A	-	-	24	25

L'observation par Microscope Electronique à Balayage MEB de SC et SR montre clairement la forme angulaire de texture rugueuse du premier et la forme arrondis de la deuxième

(figure2). Enfin, il convient de noter que la différence fondamentale entre ces deux sables réside donc dans la nature, dans la forme du grain et de la proportion d'éléments fins.

Deux types des graviers sont utilisés G1 (3/8) et G2 (8/16) de la même source minéralogique que SC (figure1), dont les caractéristiques physico-mécaniques sont indiquées au tableau (2).

2.3 Adjuvent

Le plastifiant réducteur d'eau utilisé est SIKA PLAST BV40+ pour hautes résistances mécaniques, non chloré, à base de polycarboxylates modifiés, de densité 1.04 ± 0.015 et de PH $= 4.7 \pm 1$, conforme à la norme NF EN 934-2. Le pourcentage autorisé par le fabricant est de $0.3 - 1.5\%$ de poids de ciment selon les performances recherchées.

L'idée était de développer un béton dense à partir d'un squelette granulaire compact d'un pourcentage adéquat de substitution de sable de concassage, du ciment et de l'eau et répond aux exigences de résistance, de durabilité et de maniabilité.

2.4 Procédure d'essai

2.4.1 Composition des bétons

La méthode employée pour cette formulation est la méthode graphique de Dreux Gorise [13].

La composition utilisée est celle du béton normal de classe C 30/37 préparé selon la norme NF P18-405 [14]. Sept différents mélanges ont été utilisés C0, C1, C2, C3, C4, C5, C6 de pourcentage de substitution de SR avec SC respectivement :(0, 30, 40, 50, 60, 70, 100)%.

La valeur de E/C est fixée de 0.5, le dosage de ciment utilisé est de 400 kg/m^3. LeTableau 3 indique les différentes proportions des matériaux utilisés.
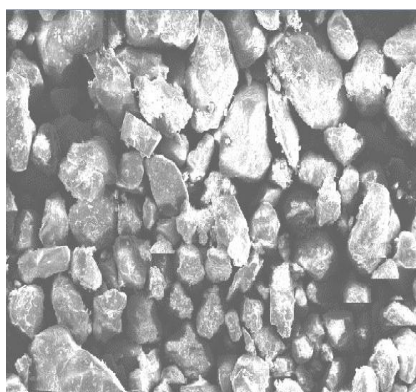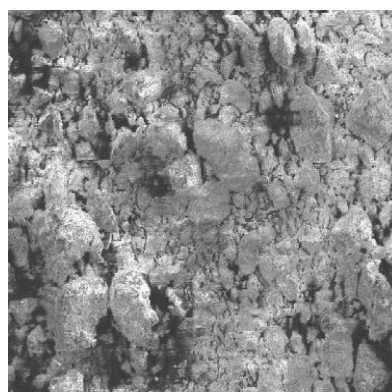

(a)   (b)

(b) Fig.2. Photos prises au MEB de deux sables utilisés (a: sable de rivière, b : sable de carrière)

2.4.2 Confection des éprouvettes

Deux types de moules ont été utilisés, cubes de 100×100×100 mm pour la résistance à la compression, prismes de 70×70×280 mm pour la résistance à la flexion, Le matériau est coulé en deux couches. Chacune des couches est mise en place par 25 chocs dans le but d'éliminer les bulles d'air emprisonnées [15].

| (a) | (b) |
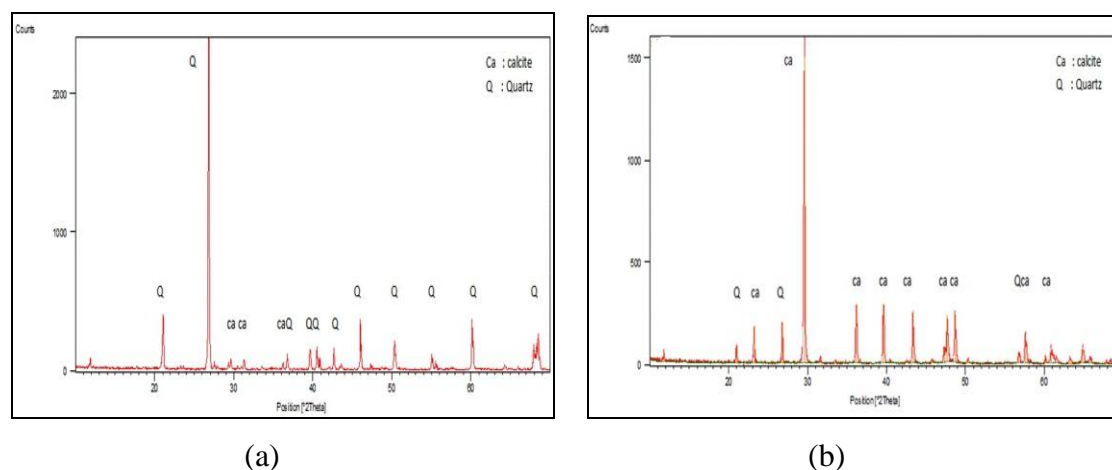
Fig.3. Analyse par DRX de deux sables utilisés : (a) SR, (b) SC

Tableau 3. Proportions des matériaux utilisés dans la confection de béton (par rapport au poids de ciment)

Type de béton	Ciment	SR	SC	G1(3/8)	G2(8/16)	Plastifiant(%)
C0	1	1.63	0.00	0.23	2.45	1.5
C1	1	1.12	0.48	0.28	2.38	1.5
C2	1	0.99	0.66	0.28	2.34	1.5
C3	1	0.82	0.82	0.28	2.34	1.5
C4	1	0.66	0.99	0.28	2.34	1.5
C5	1	0.51	1.19	0.28	2.30	1.5
C6	1	0.00	1.69	0.27	2.19	1.5

Tableau (4). Composition physico- chimiques de l'eau remontée

PH	T°C	Sal%	Ca^{+2} mg/l	Mg^{+2} mg/l	NH_4^+ mg/l	Cl^- mg/l	RS mg/l	HCO_3^- mg/l	NO_3^- mg/l	NO_2^- mg/l	SO_4^{-2} mg/l
7.35	16-22	0.77	324.684	143.399	0.6	1425.21	10400	488	3.792	0.039	1119

2.4.3 Méthode de cure

Après l'élaboration des éprouvettes, ils sont conservés dans les eaux remontées de la nappe phréatique (figure 4), on a noté que cet environnement est d'agressivité chimique modérée [11]. La composition physico-chimique de ces eaux est illustrée au tableau (4).

Dans le but d'accélérer la cinétique de dégradation, des cycles de mouillage-séchage ont été réalisés. Le Bureau de réclamation des États-Unis a suivi depuis vingt ans les changements dimensionnels des éprouvettes cylindriques de béton soumis séparément à des cycles d'immersion-séchage et à une immersion continue. Les résultats montrent qu'une année de l'immersion alternative est équivalente à huit ans d'immersion continue [16,17].

2.4.4 Protocol et suivis

Les éprouvettes cubiques et prismatiques sont soumises jusqu'au jour d'écrasement à huit cycles périodiques des mouillage-séchage comme il est indiqué ci-après :

Du 1er – 4ème cycle : Toutes les éprouvettes sont mouillées six jours et séchées un jour dans un étuve de (60°C), pendant un mois (soit 4 cycles, chaque cycle = 7 jours)

Du 5ème – 6ème cycle : Toutes les éprouvettes sont mouillées 14 jours et séchées un jour dans un étuve de (60°C), pendant un mois (soit 2 cycles, chaque cycle = 15 jours)

7ème cycle : Toutes les éprouvettes sont mouillées 29 jours et séchées un jour dans un étuve de (60°C), pendant un mois (soit 1 cycle = 30 jours)

8ème cycle : Toutes les éprouvettes sont mouillées 59 jours et séchées un jour dans un étuve de (60°C), pendant deux mois (soit 1 cycle = 60 jours).

3. RESULTATS ET DISCUSSION

3.1. Effet de la substitution sur les propriétés du béton frais

Les détails des mélanges des bétons étudiés, ainsi que les résultats de l'ouvrabilité obtenus au cours de cette expérimentation (Tableau 3, 5) nous montrent que lorsqu'on augmente la teneur en sable concassé de nature minéralogique quasi-totalement $CaCO_3$, le mélange devient plus difficile à maitriser (Tableau 5) et un besoin d'eau sera nécessaire pour atteindre la plasticité souhaitée. Contrairement au cas du sable de rivière, où le mélange devient presque fluide (4.1% d'absorption pour SC au lieu de 2.13% pour SR). Une fois que le ciment est presque

totalement hydraté, l'excès d'eau rend les grains de ciment plus éloignés, la cohésion agrégats-pâte est affaiblie et donc le matériau devient plus fluide [18]. De plus les résultats indiquent que pour un rapport E/C égale à 0.5 et l'ajout d'un plastifiant bien déterminé, les mélanges qui ont des taux de substitution entre (0-50%) deviennent plus réalisables que plus de 50% (Figure 6). Cela s'explique sans doute que la forme ronde et la texture de surface lisse du sable naturel de rivière réduisent le frottement inter-particules afin que la maniabilité soit presque élevée. Les particules de sable concassé sont de forme angulaire et leur texture de surface rugueuse améliore le frottement interne dans le mélange. Pour cette raison, la maniabilité est réduite [19]. L'incorporation d'un plastifiant réducteur d'eau sera nécessaire dans notre cas pour conserver une meilleur maniabilité, une bonne hydratation de ciment et une résistance élevée [20, 12, 21]. Le dosage performant de ce dernier est de 1.5% de poids de ciment en raison de la grande densification obtenue (Tableau 5, Figure 5) (seuil supérieur autorisé par le fabriquant). Cette densification a été augmentée d'un pourcentage de 1.40% dans le cas d'un 50% de substitution par rapport au béton de 100% sable siliceux (référence), et diminuée de 1.49% dans le cas d'un béton à 100% sable concassé par rapport à la référence. Cela pourrait etre dû à un pourcentage idéal de fines (9.75%), qui remplissent les vides et assurent une meilleur interface entre la pâte et les granulats dans le mélange du béton à 50% de substitution, en le rendant plus compact. Au-delà de cette valeur la densité diminue. Ce constat est confirmé par Lohani et al. [22]. Selon Bertrandy et Coquillat [23] pour une consistance plastique, le taux de fillers optimal semble se situer entre 8 et 12 % dans le sable de concassage. En outre, La présence d'une courbe granulométrique régulière du sable combiné (50% SR - 50% SC) ayant un module de finesse (MF = 2.49) diminue les interstices entre les particules des granulats du mélange de béton homogénéisé, comparant à des bétons de totalité SR ou SC qui ont de MF respectivement 2.29 et 2.62 (Tableau2). Notez que, le module de finesse ne peut pas être utilisé seul pour décrire la granulométrie d'un granulat, mais il est valable pour indiquer des petites variations dans le cas de granulats élaborés à partir d'une même source [24].

Fig.4. Conservation des éprouvettes dans l'eau rémontée
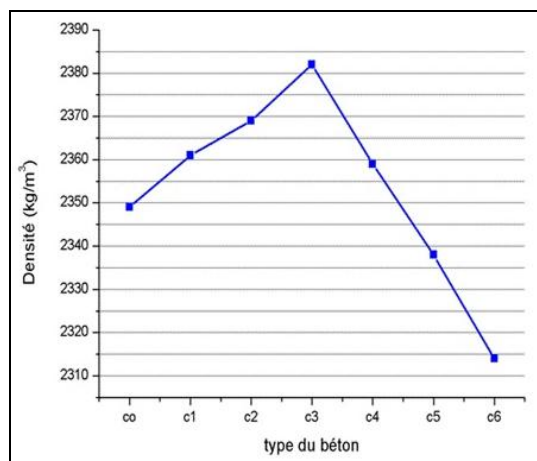
Fig.5 . Densité du béton frais selon différentes compositions
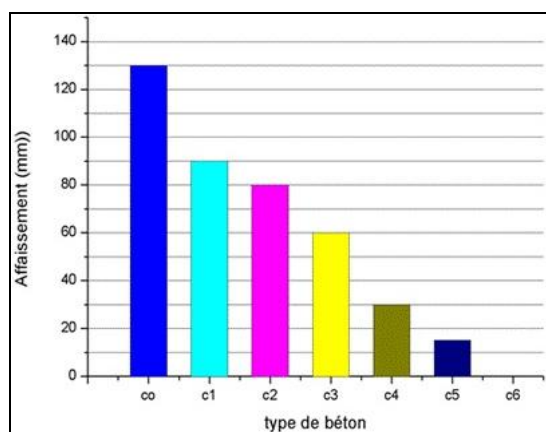
Fig.6. Valeurs d'affaissements en fonction de type du béton

3.2. Effet de la substitution sur la résistance mécanique

La résistance mécanique (à la compression et à la flexion) a été déterminée selon les normes EN 12390-3 [25], EN 12390-5 [26] respectivement et a également été exécutée pour différents échantillons de béton façonné avec différents pourcentages de substitution de sable de rivière avec du sable de carrière. Les résultats (figure 7, 8, Tableau 6) montrent que la résistance mécanique augmente avec l'augmentation du pourcentage de substitution jusqu'au 50%, au-delà de cette valeur la résistance chute jusqu'à la substitution complète.

L'évolution de la résistance mécanique au cours du temps est due à la bonne hydratation de matériaux cimentaires, malgré l'existence du béton dans un environnement agressif. Cela explique qu'une concentration plus élevée de cristaux de portlandite ainsi qu'une

concentration plus faible de silicate de calcium hydraté (C-S-H) sont formés à la zone de transition interfaciale entre les agrégats et la pâte, et que le pourcentage de pores capillaires est minimal, surtout le béton C3 comparant aux autres formulations étudiées. Plusieurs auteurs stipulent que La porosité capillaire est fortement influencée par : le rapport eau/ciment, la distribution granulométrique du matériau cimentaire et le degré d'hydratation [20]. Enfin le module de finesse du sable combiné du mélange C3 est optimisé par rapport à ceux du mélange C0 , C6 (Tableau 2).

il convient également de noter que le béton de sable de calcaire de 50% de substitution par le sable alluvionnaire résiste mieux et surtout à la flexion lorsqu'il est immergé dans l'eau remontée de la nappe phréatique comparant au béton de autres pourcentages de remplacement.

Tableau 5. Propriétés des bétons frais et durcis et optimisation de plastifiant

Plastifiant BV40+ (%)	Mélange du Béton frais				Béton durci
	N°	E/C	Affaissement mm	Densité kg/m³	Résistance à la compression à 28 jours (MPA)
1.5	C0	0.5	130	2349	20.21
1.5	C1	0.5	90	2361	23.18
1.5	C2	0.5	80	2369	26.72
1.5	C3	0.5	60	2382	30.77
1.5	C4	0.5	30	2359	28.35
1.5	C5	0.5	15	2338	26.03
1.5	C6	0.5	00	2314	24.58
0.5	C3	0.5	10	2325	
1.0	C3	0.5	30	2330	
1.5	C3	0.5	60	2382	

Tableau 6. Résistance mécanique de différentes compositions étudiées

	Résistance à la compression (MPA)				Résistance à la flexion (MPA)			
Age (jours)	28	60	90	180	28	60	90	180
C0	20.21	23.60	24.95	27.54	3.55	5.71	6.12	7.72
C1	23.18	24.97	26.55	29.56	4.69	6.33	7.55	9.14
C2	26.72	31.35	33.12	34.44	6.73	8.57	9.06	10.33
C3	30.77	33.50	36.53	38.60	7.96	9.03	10.61	11.31
C4	28.35	31.90	34.70	36.87	6.90	8.78	9.80	11.14
C5	26.03	30.79	33.05	33.80	6.53	7.35	8.74	10.24
C6	24.58	28.17	29.27	31.41	6.32	7.34	7.93	9.36

3.2. 1　La résistance à la compression

La　Figure 7 et le Tableau 7 ont indiqués que la résistance à la compression de 50% de substitution gagne 52.25% à 28 jours par contre elle gagne 40.16% à 180 jours par rapport au béton témoin (100% à base de sable siliceux). Les résultats prouvent aussi que la substitution globale de SR par SC améliore la résistance à la compression de 21.62% à 28 jours et 14.05% à 180 jours. Ces résultats ont été confirmés par plusieurs chercheurs, Adams et al. [27], déclaraient que le remplacement du sable naturel par 50% du sable de concassage dans le béton présente une meilleure résistance à la compression. Priyanka et al. [28], confirmaient que le remplacement de 50% de sable naturel par le sable artificiel, dans le mélange du mortier, présente une résistance à la compression élevée avec un rapport E/C égale 0.5. V. Chandwani et al. [10], ont constaté qu'une réduction considérable de la résistance à la compression était perceptible à plus de 50% de remplacement de sable de concassage. Toutefois il est connu que les bétons conçus avec des granulats totalement concassés génèrent une surface spécifique plus développée et demandent plus d'eau que les granulats roulés ce qui affecte la résistance. Benabed et al. [29], a conclu que lorsque le pourcentage de fines dépasse 15%, (dans notre cas 17.12%) la résistance chute. Ceci est probablement dû en raison d'insuffisante de la pâte de ciment pour enrober toutes les particules des agrégats fins ce qui conduit par conséquent à une diminution de la résistance à la compression.
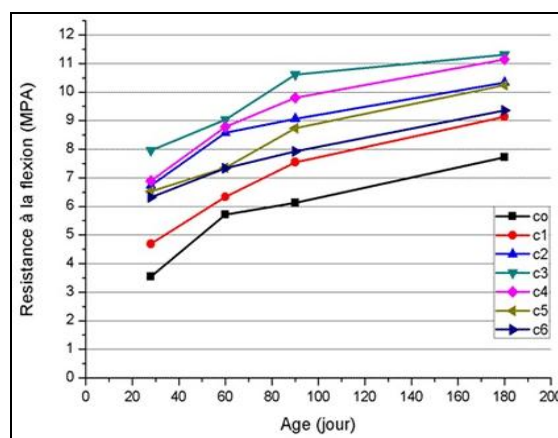
3.2. 2   La résistance à la flexion

La Figure 8 et le Tableau 7 ont affirmés que la résistance à la flexion de 50% de substitution gagne 124.23% à 28 jours par contre elle gagne 46.50% à 180 jours par apport au béton témoin. Les résultats montrent que la substitution globale de SR par SC améliore la résistance à la flexion de 78.03% à 28 jours et 21.24% à 180 jours. Par conséquent, la résistance à la flexion du béton avec des granulats de calcaire est meilleure que celle du sable de la rivière (figure 8). Shanumugapriya et al. [30], ont montré que la résistance à la flexion du béton à haute performance augmente avec l'augmentation du pourcentage de la fumée de silice dans le ciment. Pour un béton contenant 50% de sable artificiel, la résistance est optimale. Cependant, le taux d'augmentation de la résistance à la flexion est de13.2% à l'âge de 28 jours pour le béton avec 50% de sable artificiel et 5% de fumée de silice. Puneeth G T et al. [31], ont déclaré que l'échantillon de béton avec 15% de remplacement du ciment par fumée de silice présentait une résistance à la flexion supérieure à celle du béton conventionnel. La résistance a augmenté jusqu'à 12,5% par rapport à celle du l'échantillon de béton conventionnel après une période de durcissement de 28 jours. En outre, la résistance à la flexion est plus élevée pour le béton composé de 100% de la poudre de pièrre concassée comme une substitution du sable naturel, avec une évolution de la résistance à la flexion de l'ordre de 162% par rapport au béton de sable naturel [32].

Le tableau 7 résume l'évolution de la résistance mécanique avec l'âge par rapport au béton témoin (C0) (en pourcentage).
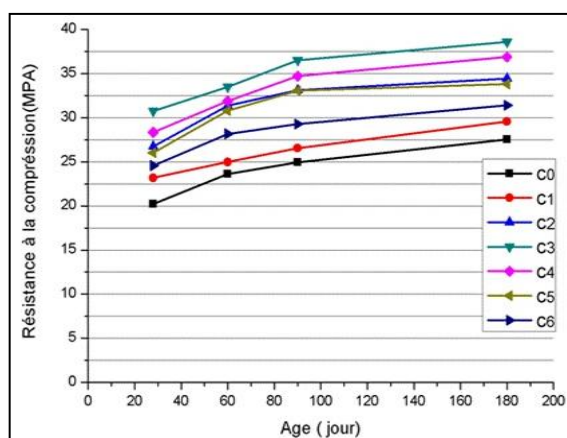
Fig.7. Résistance à la compression des bétons conservés dans l'eau remontée

Fig.8. Résistance à la flexion des bétons conservés dans l'eau remontée

Tableau 7. Évolution de la résistance mécanique des différentes compositions avec l'âge comparé de C0

Age (jours)	Évolution de la Résistance à la compression (%)				Évolution de la Résistance à la flexion (%)			
	28	**60**	**90**	**180**	**28**	**60**	**90**	**180**
C0	/	/	/	/	/	/	/	/
C1	14.70	5.80	6.41	7.33	32.11	10.86	23.37	18.39
C2	32.21	32.84	32.75	25.05	89.58	50.09	48.04	33.81
C3	52.25	41.95	46.41	40.16	124.23	58.14	73.37	46.50
C4	40.28	35.17	39.08	32.39	94.37	53.77	60.13	44.30
C5	28.80	30.47	32.46	22.73	83.94	28.72	42.81	32.64
C6	21.62	19.36	17.31	14.05	78.03	28.55	29.58	21.24

4. CONCLUSION

Après cette étude on peut aboutir à la synthèse suivante :

Un taux de substitution compris entre 0 et 50% de sable de rivière par le sable de carrière concassé dans le béton ordinaire donne une maniabilité acceptable. Sa consistance varie de plastique à très plastique, par conséquent plus de 50% de substitution le mélange devient moins réalisable et la consistance apparait ferme. De plus la densité à l'état frais a été améliorée lorsqu'on commence de substituer le sable alluvionnaire par le sable concassé. Elle atteint un point d'inflexion de 50% de remplacement. Une réduction graduelle de celle-ci est remarquée jusqu'à la substitution complète.

Dans l'eau remontée de la nappe phréatique, la présence du sable de calcaire améliore la résistance à la compression pour tous les pourcentages de substitution, en particulier de 50%. Elle gagne en conséquence de 52.25% à 28 jours et de 40.16% à 180 jours. Il a noté également que l'incorporation du sable de calcaire dans l'élaboration des éléments soumis à la flexion est très important parce que la résistance a évolué de 124.23% à 28 jours, mais le pourcentage d'évolution de la résistance a reculé de 2.67 fois après la période de dégradation accélérée (180 jours).

Le pourcentage optimal de substitution de sable de rivière par le sable de calcaire concassé est de 50%.Ainsi qu'un pourcentage optimisé des fines de la même formulation (9.75%) assure

une meilleure interface entre la pâte et les granulats dans le mélange en le rendant plus compact.

Dans l'eau remontée de la nappe phréatique, le matériau calcaire est bénéfique pour augmenter la durée de vie des structures et pour préserver l'environnement.

5. REFERENCES

[1] Imène Joudi-Bahri. "Influence des sables fillérisés calcaires sur les propriétés des bétons courants et superplastifiés. Un exemple tunisien", Thèse de doctorat. Université de Lorraine, 2012.p.3.

[2] Celik, T., Marar, K. Effects of crushed stone dust on some properties of concrete. Cement Concrete Res., 1996, 26 (7),1121-1130.

[3] Kenai S, Menadi B, Ghrici M. Performance of limestone cement mortar. In: Eight CANMET/ACI international conference on recent advances in concrete technology; 2006. p. 39.

[4] Ilangovan, R. Studies on strength and behaviour of concreteby using quarry dust as fine aggregate. In: Proceedings of AllIndia Seminar on Materials and Machines for Construction. NewAge International., 2000, pp. 99 -102.

[5] Hudson BP. Manufactured sand for concrete.The Indian concrete journal,1997: pp:237-240

[6] Shodhganga.inflibnet.ac.in/bitstream/10603/.../7/07_ chapter2.pdf

[7] Sahu, A.K., Sunil Kumar Sachan, A.K. Quarry stone waste as fine aggregate for concrete. Indian Concrete J., 2003, 845-848.

[8] R. Ilangovana., N. Mahendrana and K. Nagamanib. Strength And Durability Properties Of Concrete Containing Quarry Rock Dust As Fine Aggregate, ARPN Journal of Engineering and Applied Sciences., 2008, vol. 3, no. 5.

[9] Shahul Hameed, M., Sekar, A.S.S. Properties of green concrete containing quarry rock dust and marble sludge powder asfine aggregate. ARPN J. Eng. Appl. Sci., 2009, 4 (4), 83-89.

[10] Vinay Chandwania, Sanjay Mundraa, P.R. Sindhib, Ravindra Nagara, Vinay Agrawalaa. Crushed rock sand-An economical and ecological alternative to natural sand to optimize

concrete mix .Engineering and Material Sciences., 2016, 345-347.

[11] NF EN 206-1 Béton — Partie 1: Spécification, performances, production et conformité, AFNOR, French standard, from European standard EN 206 Concrete-Performance, production and conformity, 2004.

[12] Menadi B, Kenai S, Khatib J, Aït-Mokhtar A. Strength and durability of concrete incorporating crushed limestone sand. Constr Build Mater.,(2009), 23:625-633.

[13] Dreux G., Jean FESTA. Nouveau guide du béton et de ses constituants. Edition Eyrolles. Juin; 1998. p. 416.

[14] NF P18-405 Bétons- Essais d'information Confection et conservation des éprouvettes, Décembre 1981.

[15] NF EN 12390-2. Essais pour béton durci - Partie 2: confection et conservation des éprouvettes pour essais de résistance, Octobre 2001.

[16] Kamali S, Gerard B, Moranville M. Modelling the leaching kinetics of cement based materials-inluence of materials and environment. Cem Concr Compos 2003;25:451–8.

[17] Agostini F, Lafhaj Z, Skoczylas F, Loodsveldt H. Experimental study of accelerated leaching on Hollow cylinders of mortar. Cem Concr Res 2007;37:71–8.

[18] Gmira A. Etude texturale et thermodynamique d'hydrates modeles du Ciment, These de Doctorat, Université d'Orleans, France; 2003. p. 212.

[19] Swapnil S. Fate. Concrete with Smart Material (Manufactured Crushed Sand)-A Review. IOSR Journal of Mechanical and Civil Engineering (IOSR- JMCE) e-ISSN: 2278-1684, p-ISSN: 2320-334X PP 27-29.

[20] Neville AM. Properties of concrete. Fourth edition, Longman, England,1995, pp.844.

[21] Aquino Carlos, Inoue Masumi, Miura Hiroaki, Mizuta Maki, Okamoto Takahisa. The effects of limestone aggregate on concrete properties. Construction and Building Materials. ,2010, 24: 2363-2368.

[22] Lohani T.K, Padhi M, Dash K.P, Jena S, Optimum utilization of Quarry dust as partial replacement of sand in concrete, Int. Journal of Applied Sciences and Engineering Research, 2012; V 1, pp:391-404.

[23] Bertrandy R., Coquillat G. Les calcaires dans les bétons hydrauliques, CEBTP., 1992,

pp. 6-13.

[24] Neville Adam M. Proprietes des betons. Edition Eyrolles; 2000. p. 824.

[25] NF EN 12390-3. Essai pour beton durci – Partie 3: resistance a la compression des eprouvettes, Fev. 2003.

[26] NF EN 12390-5. Essai pour beton durci – Partie 5: resistance a la flexion sur eprouvettes, October 2001.

[27] Adams JM, Rajesh AM, Brightson P, Anand MP. Experimental Investigation on The Effect Of M-Sand In High Performance Concrete, American Journal of Engineering Research (AJER), 2013; V 02, pp: 46-51.

[28] Priyanka AJ, Dilip KK. Effect of replacement of natural sand by manufactured sand on the properties of cement mortar. International Journal Of Civil And Structural Engineering, 2013; V 3, pp: 621-628.

[29] Benabed B, Kadri EH, Azzouz L, Kenai S. Properties of self-compacting mortar made with various types of sand, Cement and Concrete Composites, 2012; V 34, pp:1167–1173.

[30] Shanmugapriya T, Uma RN, Optimization of partial replacement of M-sand by natural sand in high performance concrete with silica fume. International Journal of Engineering Sciences & Emerging Technologies, 2012; V 2, pp: 73-80.

[31] Puneeth G T., Mamatha A. An experimental investigation on the strength of concrete by partial replacement of cement with micro silica and naturel sand with manufactured sand.International Journal of Civil and Structural Engineering Research ISSN 2348-7607 (Online) Vol. 3, Issue 2, pp: (52sand-57).

[32] Anitha-selva SSD, Gayathri R, Swathi G, Prince AG.Experimental Investigation On Quarry Dust Concrete With Chemical Admixture, International Journal of Latest Research in Science and Technology, 2013; V 2, pp:91–94.

Thermal Lattice Boltzmann Model for Natural Convection in an Inclined Cavity Packed with Porous Material

2 authors:

ABDELMALEK ATIA
El-Oued University
20 PUBLICATIONS **7** CITATIONS

SEE PROFILE

Kamal Mohammedi
University M'Hamed Bougara of Boumerdes
150 PUBLICATIONS **814** CITATIONS

SEE PROFILE

Some of the authors of this publication are also working on these related projects:

Modeling and Simulation of central receiver solar thermal power plants View project

GreenAlInd Project: Improvement of Energy and Environmental Performances of Algerian Industry. View project

Thermal Lattice Boltzmann Model for Natural Convection in an Inclined Cavity Packed with Porous Material

Atia Abdelmalek[1] and Mohammedi Kamal[2]

1. Mechanical Engineering Departement, Faculty of Sciences and Technology, University of Hamma Lakhdar, El-oued 39000, Algeria

2. Laboratory of Energetic, Mechanics and Engineering, Faculty of Sciences of Engineer, University of M'hamed Bougara, Boumerdes 35000, Algeria

Abstract: In the present work, the LBM (Lattice-Boltzmann method) is used to simulate natural convection in an inclined open ended square cavity filled with porous material. The cavity is submitted to heating and cooling from two opposite sides with constant temperatures. The double-population approach is used to simulate hydrodynamic and thermal fields. The effect of a porous medium is taken into account by introducing the porosity into the equilibrium distribution function and adding a force term to the evolution equation. The Brinkman-Forchheimer equation, which includes the viscous and inertial terms, is applied to predict the heat transfer and fluid dynamics in the non-Darcy regime. The present model is validated with the previous literature. A comprehensive parametric study of natural convective flows is performed for various values of inclined angle.

Key words: Lattice boltzmann method, natural convection, porous cavity, Brinkman-Forchheimer equation.

1. Introduction

There is no need to say that LBM (Lattice Boltzmann Method) are in high pace development and have become a powerful method for simulation fluid flow and transport problems for single and multiphase flows [1, 2]. In this work, the method is applied for natural convection in open ended porous cavities.

Natural convection has lots of applications in both nature and engineering, such as the cooling of electronic devices and heat transfer improvement in heat exchanger apparatuses and petroleum reservoirs. Because cavities and slots are benchmark test cases, many researches using LBM [3, 4]. Natural convection in a square cavity and its fluid flow is a classical problem in mechanical engineering. Mohamad et al. [5] presented a detailed analysis of natural convection problem to use LBM; they demonstrated the abilities of the LBM in simulating natural convection. Open cavities are 2-D cavity that has an open side. These kinds of cavities have special

physics in open side because of outgoing of flow from this side. Some research papers have been published on studies of buoyant flows and their heat transfer in open cavities [6]. Mohamad et al. [7] presented natural convection in an open ended cavity and slots, they analyzed the effect of aspect ratio of cavity on heat transfer rate. They presented a good procedure for simulating open boundaries in LBM.

Research on natural convection in enclosure packed with a porous medium is motivated by its wide applications in engineering, such as drying processes, chemical catalytic reactors and solar power collectors. Several models have been introduced for natural convection heat transfer in porous media. An excellent and comprehensive review has been given by Nield and Bejan [8]. The buoyancy-driven convection in a porous cavity is analyzed by D. Gao et al. [9]. A. Haghshenas et al. [4] studied numerically the steady natural convection in a square cavity filled with a porous medium via LBM.

2. Thermal Lattice Boltzmann Method

The thermal Lattice Boltzmann model utilizes two

Corresponding author: Atia Abdelmalek, D.Sc. candidate, research fields: modelling and simulation in mechanical engineering. E-mail: abdelmalek-atia@univ-eloued.dz.

distribution functions, f and g, for the flow and temperature fields, respectively. In this approach the fluid domain is discredited in uniform Cartesian cells. Each cell holds a fixed number of distribution functions. For this work the D2Q9 model has been used. This model is shown in Fig. 1.

For the D2Q9 lattice, the nine velocities $\vec{c}_i$ and their corresponding weights w_i are calculated from Ref. [10]:

$$\vec{c}_i = c \begin{cases} 0 \ for \ i = 0 \\ \left(\cos\left[(i-1)\frac{\pi}{2}\right], \sin\left[(i-1)\frac{\pi}{2}\right] \right) \ for \ i = 1,2,3,4 \\ \sqrt{2}\left(\cos\left[(i-5)\frac{\pi}{2}+\frac{\pi}{4}\right], \sin\left[(i-5)\frac{\pi}{2}+\frac{\pi}{4}\right] \right) \ for \ i = 5,6,7,8 \end{cases} \tag{1}$$

And the weighting factors are given by:

$$w_0 = \frac{4}{9}, w_1 = w_2 = w_3 = w_4 = \frac{1}{9},$$

and $w_5 = w_6 = w_7 = w_8 = \frac{1}{36}$ (2)

It is to be noted that in the above equations, $c = \frac{\Delta x}{\Delta t}$, and the weights satisfy the relation $\sum_{i=1}^{9} w_i = 1$.

The Lattice Boltzmann equation with an external force F can be written respectively for the fluid flow and temperature distribution as follows:

The $f(r,t)$ and $g(r,t)$ are calculated by solving the Lattice Boltzmann equation. By using BGK model, the general form of Lattice Boltzmann equation with an added force term can be written as:

For the flow field:

$$f_i(r + c_i\Delta t, t + \Delta t) =$$
$$f_i(r,t)[1 - \omega_v] + \omega_v f_i^{eq}(r,t) + \Delta t. \mathrm{F}_i \tag{3}$$

For the temperature field:

$$g_i(r + c_i\Delta t, t + \Delta t) =$$
$$g_i(r,t)[1 - \omega_T] + \omega_T g_i^{eq}(r,t) \tag{4}$$

where, Δt denotes lattice time step, c_i is the discrete lattice velocity in direction i, F_i is the total body force in direction of lattice velocity, $\omega_v = \frac{\Delta t}{\tau_v}$ and

$\omega_T = \frac{\Delta t}{\tau_T}$ denotes the non-dimensional relaxation time for the flow and temperature fields. The kinetic viscosity v and the thermal diffusivity α are defined in terms of their respective relaxation times, i.e.

$v = c_s^2(\tau_v - 1/2)$, and $\alpha = c_s^2(\tau_T - 1/2)$, respectively. The local equilibrium distribution for flow and temperature fields is as follows respectively.

$$f_i^{eq} = w_i\rho \left[1 + \frac{c_i.u}{c_s^2} + \frac{1}{2}\frac{(c_i.u)^2}{\epsilon c_s^4} - \frac{1}{2}\frac{u^2}{\epsilon c_s^2} \right] \tag{5}$$

where, ϵ is the porosity of the material.

$$g_i^{eq} = w_i T \left[1 + \frac{c_i.u}{c_s^2} + \frac{1}{2}\frac{(c_i.u)^2}{c_s^4} - \frac{1}{2}\frac{u^2}{c_s^2} \right] \tag{6}$$

In LBM Eqs. (3) and (4) are solved in two important steps that are called collision and streaming step. Collision step is as follows for flow field and temperature field respectively [10]:

$$f_i(r, t + \Delta t) = f_i(r,t)[1 - \omega_v] +$$
$$\omega_v f_i^{eq}(r,t) + \Delta t. \mathrm{F}_i \tag{7}$$
$$g_i(r, t + \Delta t) = g_i(r,t)[1 - \omega_T] + \omega_T g_i^{eq}(r,t) \tag{8}$$

Streaming step can be written as follows:

$$f_i(r + c_i\Delta t, t + \Delta t) = f_i(r, t + \Delta t) \tag{9}$$
$$g_i(r + c_i\Delta t, t + \Delta t) = g_i(r, t + \Delta t) \tag{10}$$

Macroscopic variable can be calculated in terms of these variables, with the following formula:

Flow density:

$$\rho = \sum_{i=0}^{9} f_i \tag{11}$$

Momentum:

$$\rho u = \sum_{i=0}^{9} f_i c_i \tag{12}$$

Temperature:

$$T = \sum_{i=0}^{9} g_i \tag{13}$$

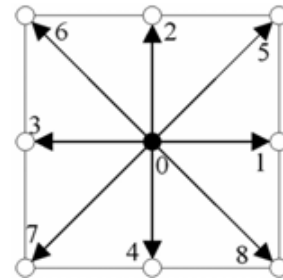The total body is added as an extra source term to Eq. (14),

Fig. 1   Lattice arrangements for 2-D problems, D2Q9.

$$F_i = w_i \rho \left(1 - \frac{w_v}{2}\right)\left[\frac{3c_i \cdot F}{c^2} + \frac{9uF:c_i c_i}{\epsilon c^4} - \frac{3uF}{\epsilon \cdot c^2}\right] \quad (14)$$

where, $F = F_{buoyancy\ force} + F_{porous\ material}$.

With the Boussinesq approximation the buoyancy force modeled as:

$$F_{buoyancy\ force} =$$
$$\epsilon g \beta (T - T_m)(cy_i cos\varphi + cx_i sin\varphi) \quad (15)$$

where, $T_m = (T_h + T_c)/2$.

$$F_{porous\ material} = -\frac{\epsilon v}{K}u - \frac{\epsilon 1.75}{\sqrt{150\epsilon K}}|u|u \quad (16)$$

where, g, β, ϵ, K , and T_m are gravitational acceleration, thermal expansion coefficient, porosity of the medium, permeability and reference temperature.

3. Position of the Problem and Boundary Conditions

The studied configuration is sketched in Fig. 2. It consists of a square cavity of length H with two partially heated walls, located on two opposite walls, and maintained at constant temperatures T_h and T_c ($T_h > T_c$), respectively. The cavity is inclined at an angle φ with respect to the horizontal and filled with porous material; the east side is considered as open ended.

The distribution functions out of the domain are known from the streaming process. The unknown distribution functions are those toward the domain. Fig. 3 shows the unknown distribution function, which needs to be determined, as dotted lines [7].

Flow:

Bounce back boundary condition is used on the solid boundaries (west, north and south boundaries). At the east open boundary, the following condition is used,

$$f_{6\,n} = f_{6\,n-1},\ f_{3\,n} = f_{3\,n-1}, f_{7\,n} = f_{7\,n-1} \quad (17)$$

where, n is the lattice on the boundary and n-1, is the lattice inside the cavity adjacent to the boundary.

Temperature:

Bounce back boundary condition (adiabatic) is used on the north and south of the boundaries. Temperature at the west wall is known, Tw = 1.0. Since we are using D2Q9, the unknown are $g1, g5\ and\ g8$, which are evaluated as,
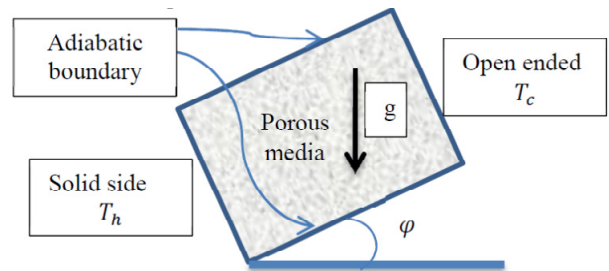
Fig. 2   Studied configuration.
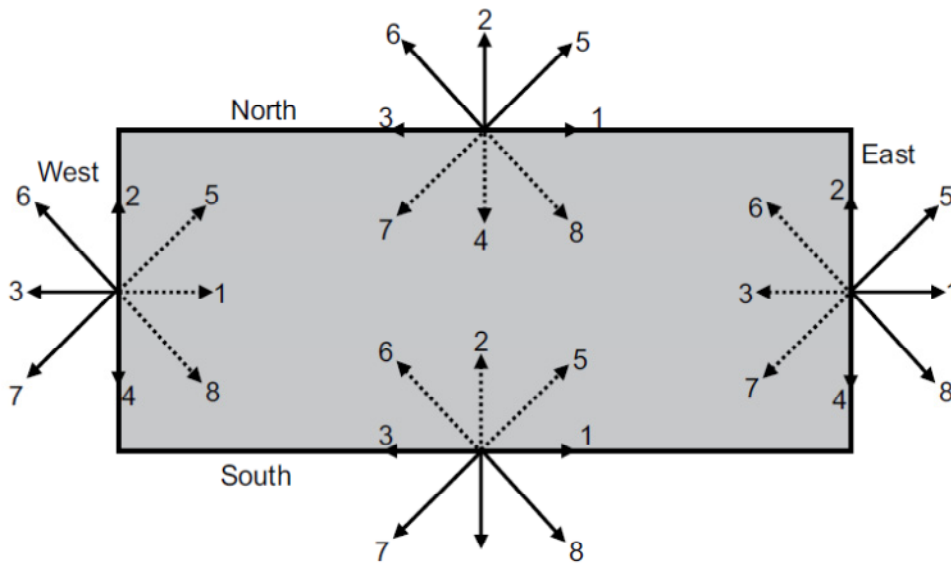
Fig. 3   Domain boundaries and direction of streaming velocities.

$$g1 = Tw * (w1 + w3) - g3$$
$$g5 = Tw * (w5 + w7) - g7 \qquad (18)$$
$$g8 = Tw * (w8 + w6) - g6$$

The boundary condition for east wall needs special treatment, since prior to solution, the advected velocity direction is not known. It is assumed that if the flow is penetrating into the cavity $(u < 0)$, then the temperature should be ambient, T = 0, and if the flow leaving the cavity $(u > 0)$, it is assumed that there is no heat diffusion, i.e., gradient of temperature is negligible.

For east boundary, the distributions function, $g6, g3$ and $g7$, are evaluated as,

$$if\ u < 0\ then:$$
$$g6, n = 0 - g8, n$$
$$g3, n = 0 - g1, n \qquad (19)$$
$$g7, n = 0 - g5, n$$
$$if\ u > 0\ then:$$
$$g6, n = g6, n - 1$$
$$g3, n = g3, n - 1 \qquad (20)$$
$$g7, n = g7, n - 1$$

4. Results and Discussion

In this work the problem of natural convection heat transfer in an inclined open ended cavity packed with porous material is simulated. The cavity has two horizontal insulated walls, a west wall with constant temperature and an open east side. The temperature of west wall is equal to unity that is more than the ambient zero temperature. One point must be noticed that this temperature is dimensionless in Lattice scale. In the present study to simulate natural convection in inclined cavity, the gravity acceleration (g) is rotated counter clockwise. The negative values of rotating angel mean rotation is clockwise. To validate the numerical method, two different cases are tested:

(1) Natural convection in an open-ended cavity without porous medium, and without rotating angel.

(2) Natural convection in an open-ended cavity with porous medium, and without rotating angel.

The results are compared with the findings of Mohamad et al. [7] for case (1) and of A. Haghshenas et al. [4] for case (2).

Tables 1 and 2 summarize the average Nusselt numbers obtained by the present work and compared with the previous literature.

As it can be seen from these tables, in each case, the results are considerably consistent with those in the literature and these comparisons.

Hence, it is concluded that LBM with the suggested boundary condition at the opening of the cavity can produce reliable results.

Figs. 4 and 5 show streamlines and isotherms, respectively, comparison between the present study and that presented by Mohamad et al. [7] for Ra = 10^4. The flow enters from the lower half portion of the cavity and leaves from the upper half of the opening.

Now, the problem of natural convection heat transfer in an inclined open porous cavity was solved for different angles, when Rayligh number is fixed to 10^4, Prantdl number (Pr) is fixed to 0.71, porosity is fixed to 0.4, and Darcy number is fixed to 0.01. Streamline and Temperature contours are plotted and average Nusselt number on closed west wall is investigated.

Figs. 6 and 7 Streamline and Temperature contours are plotted for different rotation angle, the effect of rotation on Streamline and Temperature contours can be seen obviously.

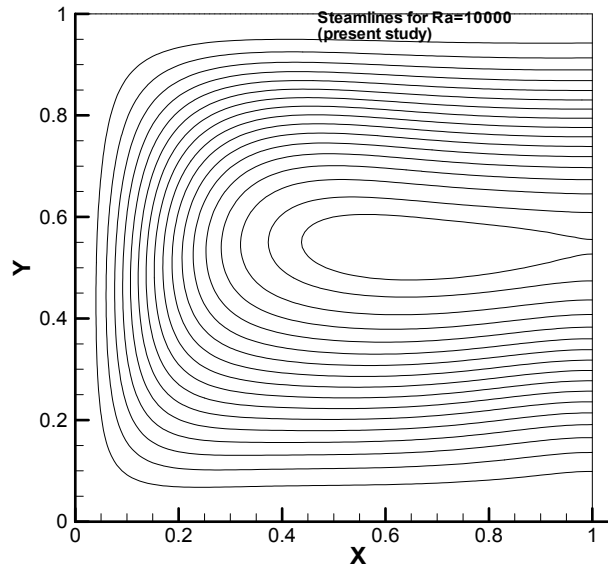**Table 1 Average Nusselt number comparison for differents Rayligh number and Pr = 0.71 (case 1).**

Ra	Mohamad et al. (FV)	LBM (present)
10^4	3.264	3.249202
10^5	7.261	7.061324
10^6	14.076	14.045800

Table 2 Average Nusselt number comparison for differents Rayligh number and Pr = 1.0, Da = 0.01 and $\varepsilon = 0.4$ (case 2).

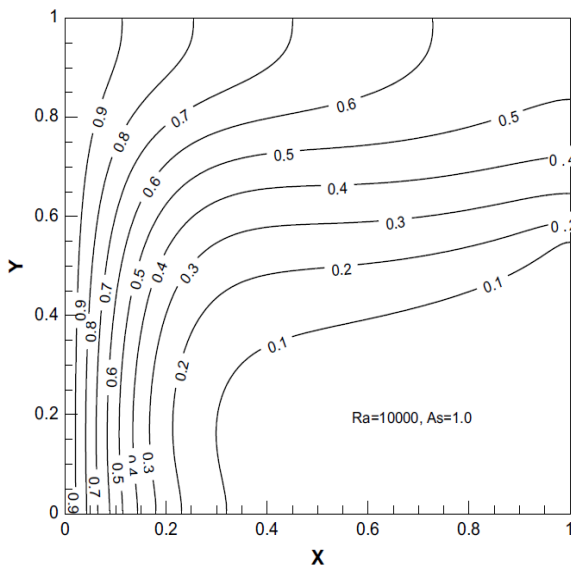| Ra	A. Haghshenas et al. (LBM)	LBM (present)
10^4	1.541	1.678586
10^5	4.294	4.327931
10^6	9.432	9.598819
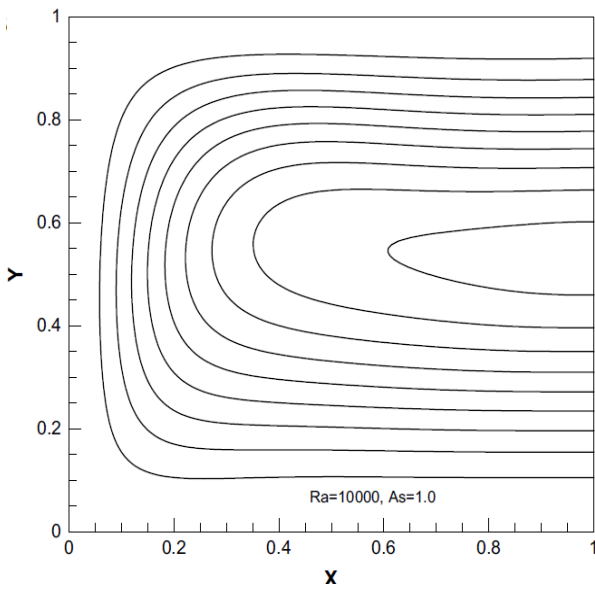
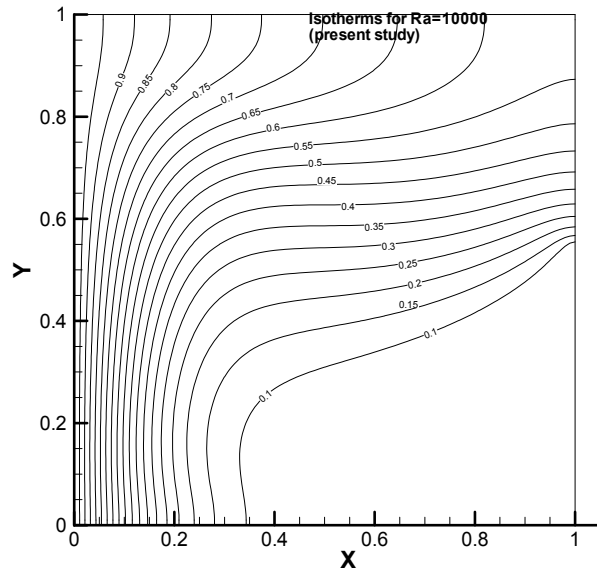(a) Mohamad et al. [7]   (b) Present study

Fig. 4   Streamlines for Ra = 10^4 and aspect ratio of 1.0.

(a) Mohamad et al. [7]   (b) Present study

Fig. 5   Isotherms for Ra = 104 and aspect ratio of 1.0.

Table 3 shows that rotation angle has low effect on average Nusselt in the low Rayligh number (Ra = 10^4).

5. Conclusion

In the present work, simulations of flow and temperature fields that arise due to natural convection in an open-ended inclined square cavity filled with a porous medium have been carried out. The double-population approach, the LBM were employed. The influence of rotation angle was considered by adding a force term to the evolution equation. To predict the heat transfer and fluid dynamics in the non-Darcy regime, the Brinkman-Forchheimer equation was applied. The numerical method was validated by two different cases and a good agreement
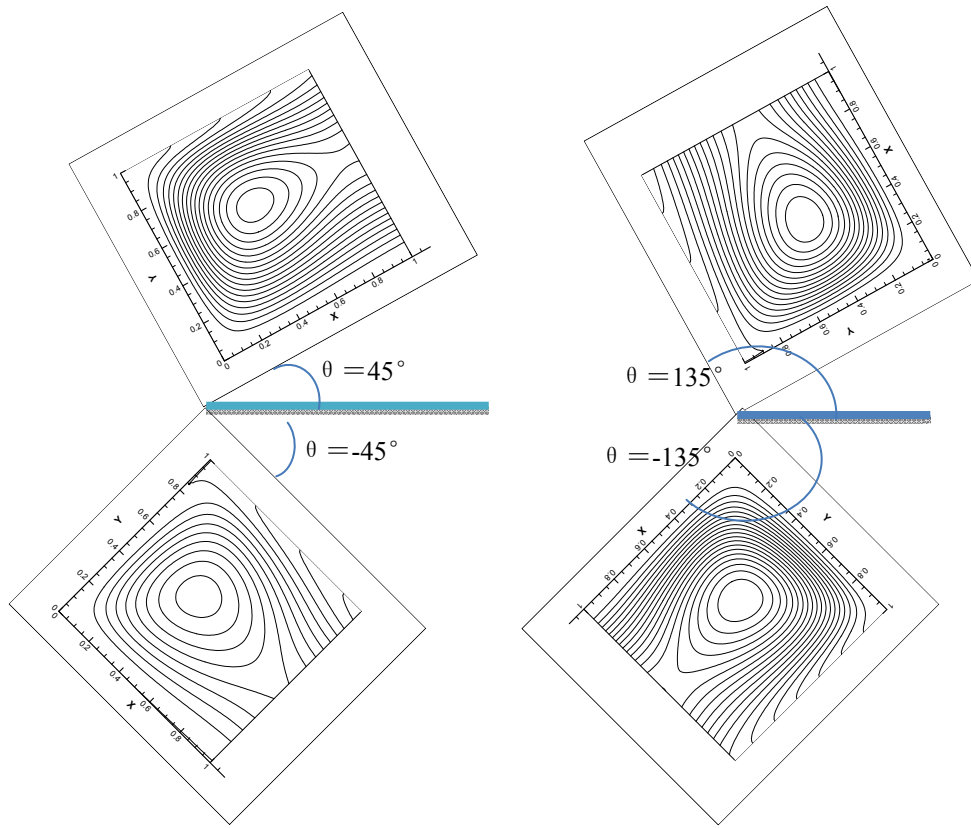
Fig. 6   Streamlines for different rotation angle.
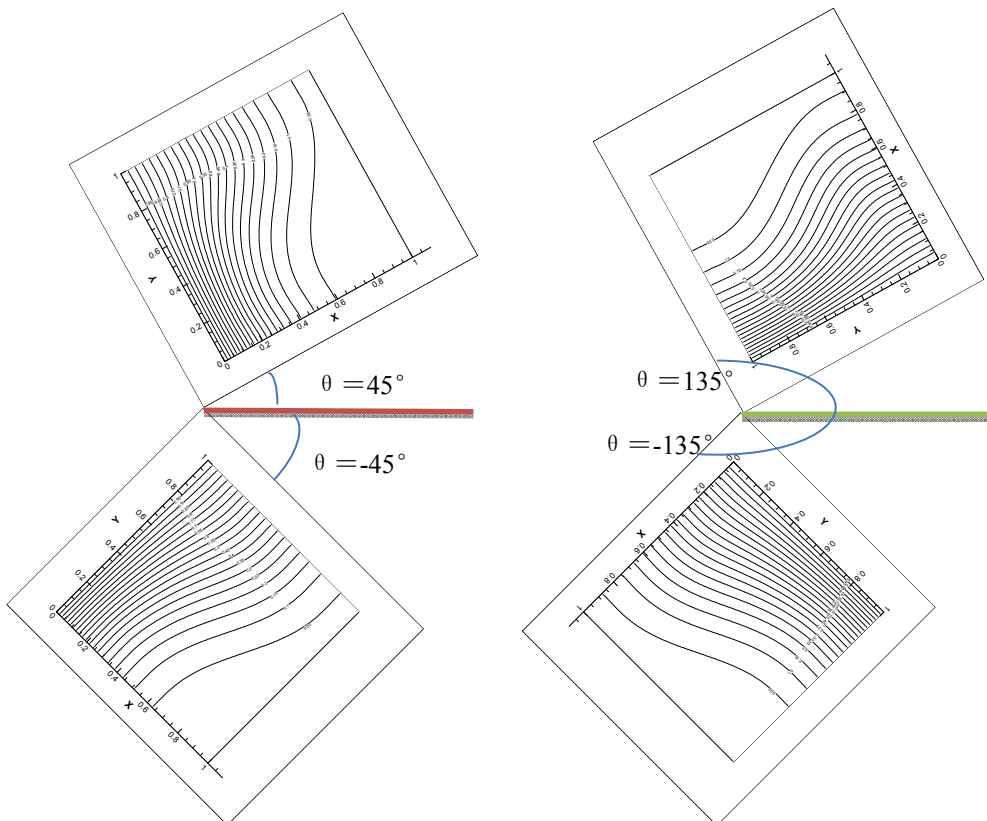
Fig. 7   Isotherms for different rotation angle.

Table 3   Average Nusselt number comparison for different rotation angle.

θ	Nu
45°	2.312473
−45°	2.294909
135°	2.312482
−135°	2.294900

was observed. It was found that, for low Rayleigh numbers, the average Nusselt number is almost independent of rotation angle.

References

[1]   Mohamad, A. 2007. "Applied Lattice Boltzmann Method for Transport Phenomena, Momentum." *The Canadian Journal of Chemical Engineering* 85 (6): 946-7.

[2]   Succi, S. 2001. *The Lattice Boltzmann Equation: For Fluid Dynamics and Beyond*: Oxford University Press.

[3]   Fattahi, E., Farhadi, M., and Sedighi, K. 2010. "Lattice Boltzmann Simulation of Natural Convection Heat Transfer in Eccentric Annulus." *International Journal of Thermal Sciences* 49: 2353-62.

[4]   Haghshenas, A., Nasr, M. R., and Rahimian, M. 2010. "Numerical Simulation of Natural Convection in an Open-Ended Square Cavity Filled with Porous Medium by Lattice Boltzmann Method." *International Communications in Heat and Mass Transfer* 37: 1513-9.

[5]   Mohamad, A., and Kuzmin, A. 2010. "A Critical Evaluation of Force Term in Lattice Boltzmann Method, Natural Convection Problem." *International Journal of Heat and Mass Transfer* 53: 990-6.

[6]   Polat, O., and Bilgen, E. 2002. "Laminar Natural Convection in Inclined Open Shallow Cavities." *International Journal of Thermal Sciences* 41: 360-8.

[7]   Mohamad, A., El-Ganaoui, M., and Bennacer, R. 2009. "Lattice Boltzmann Simulation of Natural Convection in an Open Ended Cavity." *International Journal of Thermal Sciences* 48: 1870-5.

[8]   Nield, D. A., and Bejan, A. 2006. *Convection in Porous Media:* Springer.

[9]   Gao, D., and Chen, Z. 2011. "Lattice Boltzmann Simulation of Natural Convection Dominated Melting in a Rectangular Cavity Filled with Porous Media." *International Journal of Thermal Sciences* 50: 493-501.

[10] Mohamad, A. A. 2011. *Lattice Boltzmann Method: Fundamentals and Engineering Applications with Computer Codes:* Springer.

Production Equipe 04

01   A PV powered shunt active power filter for power quality improvement
(Ayoub Benzahia, Rabhi Boualaga , Ammar Moussi, Laid Zellouma, Memich Meriem,Bouziane Chaima)

02   An investigation on combined operation of five-level shunt active power filter with PEM fuel cell **(Amar Benaissa, Boualaga Rabhi, Mohamed Fouad Benkhoris, Laid Zellouma)**

03   Anti-Windup Proportional Integral Strategy For Shunt Active Power Filter Interfaced By Photovoltaic System Using Technique Of Direct Power Control
(Abdelbasset Krama, Laid Zellouma, Boualaga Rabhi)

04   Design And Experimental Investigation Of Predictive Direct Power Control Of Three-Phase Shunt Active Filter With Space Vector Modulation Using Anti-Windup PI Controller Optimized By PSO **(Abdelbasset Krama, Laid Zellouma, Amar Benaissa, Boualaga Rabhi, Mansour Bouzidi, Mohamed Fouad Benkhoris)**

05   Direct Sliding Mode Control Of Doubly Fed Induction Generator Driven By A Wind Turbine With A Svm Inverter Using Simulink **(Youcef Bekakra, Djilani Ben Attous, Laid Zellouma)**

06   Filtering Of Harmonics In Dc Traction Substation System **(Y .Djeghader, L.Zellouma)**

07   Flatness-based adaptive neurofuzzy control of Induction Generators using output feedback
 (G. Rigatos ,Siano , Z. Tir, M. Assad)

08   Fuzzy logic based speed control of indirect field oriented controlled Double Star Induction Motors connected in parallel to a single six-phase inverter supply

     (Zoheir Tir, Om P. Malik, Ali M. Eltamaly)

09   Fuzzy logic field oriented control of double star induction motor drive
(Zoheir Tir, Youcef Soufi, Mohammad Naser Hashemnia, Om P. Malik Khoudir Marouani)

10   Improvement of Power Quality Using Hybrid Power Filter with Fuzzy Logic Controller
(Yacine Djeghader, Laid Zellouma)

11   Optimizing of IP speed controller using particle swarm optimization for FOC of an induction motor **(Youcef Bekakra, Djilani Ben Attous)**

12   Real-Time Implementation of High Performance Control Scheme for Grid-Tied PV System for Power Quality Enhancement Based on MPPC-SVM Optimized by PSO Algorithm **(Abdelbasset Krama , Laid Zellouma , Boualaga Rabhi , Shady S. Refaat and Mansour Bouzidi)**

13   Simulation And Real Time Implementation Of Three Phase Four Wire Shunt Active Power Filter Based On Sliding Mode Controller**(LAID ZELLOUMA, BOUALAGA RABHI, ABDELBASSET KRAMA, AMAR BENAISSA, M.F. BENKHORIS)**

14   Sliding Mode Control of DFIG Driven by Wind Turbine with SVM Inverter
(Youcef Bekakra, Djilani Ben Attous and Hocine Bennadji)

15   Using Hybrid Power Filter To Mitigate Currents And Voltages Harmonics In Three Phase System **(Y. DJEGHADER, L.ZELLOUMA)**

An investigation on combined operation of five-level shunt active power filter with PEM fuel cell

Amar Benaissa[1] · Boualaga Rabhi[2] · Mohamed Fouad Benkhoris[3] · Laid Zellouma[4]

Abstract In this paper, a proton exchange membrane PEM fuel cell power plant is used to improve the filtering performance of the conventional active power filter, as well as simultaneously contribute with the electric grid to supply the power to the load. The five-level inverter is used as a shunt active power filter, taking advantages of the multilevel inverter such as low harmonic distortion and reduced switching losses. It is capable of compensating power factor, current harmonics and can also make the interface between renewable energy sources and the electric grid, injecting the energy generated by PEM fuel cell to the load. The active power filter control strategy is based on the use of self tuning filters for reference current generation and a fuzzy logic current controller. The MATLAB Fuzzy Logic Toolbox is used for implementing the fuzzy logic control algorithm. The obtained results show that the PEM fuel cell contributes successfully to supply simultaneously the load with the electric grid and produced a sinusoidal supply current with low harmonic distortion and in phase with the line voltage.

Keywords Proton exchange membrane (PEM) fuel cell · Active power filter · Harmonics isolator · Self-tuning filter · Fuzzy logic control · PWM control

✉ Amar Benaissa
  benaissa_am@yahoo.fr

[1] LAADI Laboratory, University of Djelfa, Djelfa, Algeria

[2] LMSE Laboratory, University of Biskra, Biskra, Algeria

[3] IREENA-CRTT Laboratory, Department of Electrical Engineering, Ecole Polytech Nantes, University of Nantes, 44600 Saint Nazaire, France

[4] LEVRES Laboratory, University of El-Oued, El-Oued, Algeria

1 Introduction

The use of static converters in industrial activities and public consumers leads to an increase in harmonic injection in the network and a lower power factor. This causes various problems in power systems and in domestic appliances such as equipment overheating, capacitor blowing, motor vibration, excessive neutral currents and low power factor.

Active power filter involving two levels voltage source inverters [1] have been widely studied and used to eliminate harmonics and compensate reactive power [2,3]. Due to power handling capabilities of power semiconductors, these active power filters are limited in medium power applications. Then, hybrid topologies have been proposed to achieve high power filters [4,5].

Recently, the interest in using multilevel inverters for high power drives, reactive power and harmonics compensation has increased [6,7]. Multilevel pulse width modulation inverters can be used as active power filter for high power applications solving the problem of power semiconductor limitations. The use of neutral-point-clamped (NPC) inverters allows equal voltage shearing of the series-connected semiconductors in each phase.

A DC–DC converter can be used to adjust the output voltage value of the renewable energy sources (PEMFC) [8], to the voltage value of the DC-side capacitors of the five-level shunt active filters. The available energy is then managed by the active filter controller [9].

The performances of different reference current generation strategies under balanced, sinusoidal, alternating current (AC) voltages conditions are well referenced [10,11], such as the so-called p–q theory and Synchronous Reference Frame Theory (SRF) which provide similar performances. Differences arise when one works under distorted and unbalanced AC voltage which is the case in real conditions, where

the mains voltages are distorted that decreases filter performances [12].

In this paper, the reference current generation for shunt active power filter control under distorted voltage conditions is based on the use of self-tuning filters (STF).

The STF is used to extract the fundamental component directly from electrical signals in the α–β reference frame under distorted voltage conditions [13].

The controller is the main part of the active power filter operation and has been a subject of many researches in recent years [14,15]. Conventional PI voltage and current controllers have been used to control the harmonic current and DC voltage of the shunt APF. However, they require precise linear mathematical model of the system, which is difficult to achieve under parameter variations, nonlinearity and load disturbances. These limitations are overridden by using fuzzy logic techniques.

In the conventional APF, a required active power is taken from the electrical grid to regulate the DC side of the inverter.

The novelty of this work is in the following aspects:

– a renewable source of energy (PEMFC) is able not only to exempt the electrical grid of the required power to regulate the DC side of the APF, but also to contribute with it to supply the load.
– A five-level shunt active power filter is capable simultaneously to compensate the power factor, the harmonic currents, and also inject the energy generated by the proton exchange membrane PEM fuel cell to the load.

The performance of the proposed system is evaluated through computer simulations. The obtained results show that the PEM fuel cell contributes successfully to supply simultaneously the load with the electric grid and produced a sinusoidal supply current with low harmonic distortion and in phase with the line voltage.

2 Proposed system

The proposed configuration of APF and grid-connected PEM fuel cell generation system is shown in Fig. 1. The PEM fuel cell model is based on simulating the relationship between output voltage and partial pressures of hydrogen, oxygen, and water. The PEMFC power plant consists of 680 cells connected in series. The DC–DC boost converters drain the energy from PEMFC and feed the DC bus capacitor based on hysteresis controller. In this paper, the DC bus voltage (DC–DC converter output) is $V_{dc} = 800$ V. The DC bus is connected to a five-level inverter. Through this converter, the energy generated by the PEMFC is transferred to the three-phase utility grid (400 V/60 Hz) or the AC loads. An R–L filter has been used at the output of the five-level inverter to filter the switching frequency harmonics.

A novel reference current generation strategy, which is based on generalized instantaneous reactive power theory, has been proposed for the five-level shunt active power filter. Also, this strategy adjusts the active and reactive power delivered to the utility grid. However, the proposed

Fig. 1 Proposed configuration
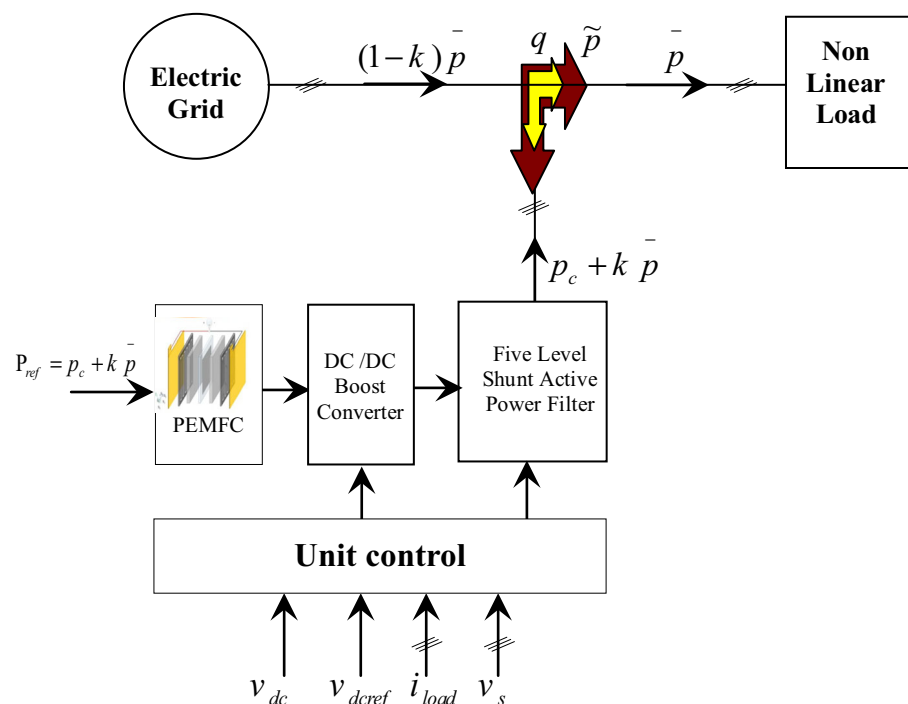
system can provide the power factor correction, harmonic elimination, and reactive power compensation, and simultaneously inject the power available from the PEMFC into the grid.

The power reference strategy of the DC–AC inverter provides suitable power transfer between the AC source and PEMFC through the five-level active power filter. The reference active power of the PEMFC is specified by the power you need to regulate the DC side of the five-level APF and a part of active power necessary to feed the load ($p_c + k * \hat{p}$).

2.1 PEM fuel cell model

In Ref. [16], Padulles et al. introduced a model for the SOFC. The model has been modified to simulate a PEM fuel cell [17]. This model is based on simulating the relationship between the output voltage and partial pressures of hydrogen, oxygen, and water. A detailed model of the PEM fuel cell is shown in Fig. 2.

The simulated characteristics of PEM fuel cell stack voltage for the fixed values of input fuel pressures for single cell is shown in Fig. 3. It can be seen that at low current level, the ohmic loss becomes less significant and the increase in output voltage is mainly due to activity of slowness of chemical reactions. So, this region is also called active polarization. At very high current density, the voltage fall down significantly because of the reduction of gas exchange efficiency. This is mainly due to overflooding of water in catalyst and this region is also called concentration polarization. Intermediate between the active region and concentrations region, there is a linear slope which is mainly due to internal resistance offered by various components of the fuel cell. This region is generally called as ohmic region [18,19].
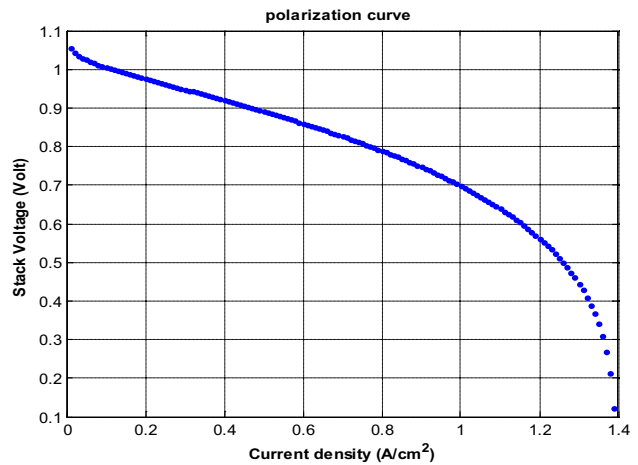
Fig. 3 Characteristic curve of PEM fuel cell single stack

Fig. 2 PEM fuel cell model
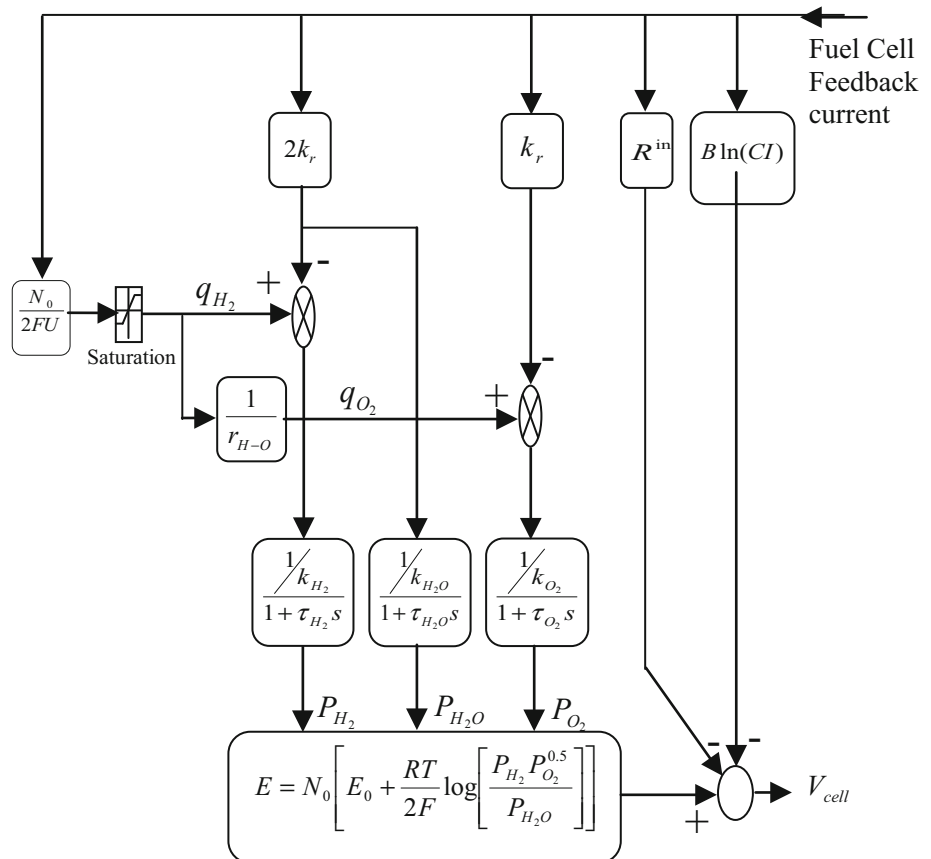
2.2 Design of DC/DC boost converter

The increase in load power decreases the FC output voltage according to the model dynamics. Therefore, a boost type DC–DC converter is used at the FC system bus to maintain 800 V output voltage. The topology of the boost type DC–DC converter is given in Fig. 4. In the converter, the gate signal of the IGBT is obtained using a band hysteresis controller-based system which determines the duty cycle according to the load side voltage.

Based on the state averaging method, the resulting model of the boost converter is [20] :

$$\frac{\mathrm{d}I_{\mathrm{cell}}}{\mathrm{d}t} = -\frac{1-k}{L_{\mathrm{dc}}}V_{\mathrm{dc}} + \frac{1}{L_{\mathrm{dc}}}V_{\mathrm{cell}} \tag{1}$$

$$\frac{\mathrm{d}V_{\mathrm{dc}}}{\mathrm{d}t} = \frac{1-k}{C_{\mathrm{dc}}}I_{\mathrm{cell}} - \frac{1}{C_{\mathrm{dc}}R}V_{\mathrm{dc}}, \tag{2}$$

where k is the duty cycle and $R = \frac{V_{\mathrm{dc}}}{I_l}$.

Based on linearization of states equation around an equilibrium point, the output voltage V_{dc} can be written in steady state as follows:

$$V_{\mathrm{dc}} = \frac{V_{\mathrm{cell}}}{1-k}. \tag{3}$$

The hysteresis controller is designed to adjust the duty cycle to regulate the output voltage around his reference.

The hysteresis control scheme, used for the control of the DC–DC converter, is shown in Fig. 5, where the switching logic is formulated as follows:

If $V_{\mathrm{dc}} < (V_{\mathrm{dc}}^* - \mathrm{HB})$ switch is OFF ($S_w = 0$),
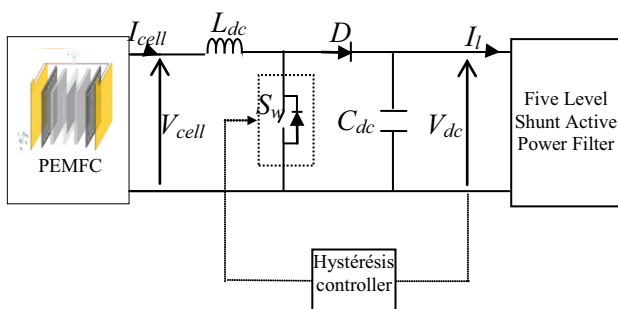
Fig. 4 Typical structure of DC–DC boost converter with feedback control
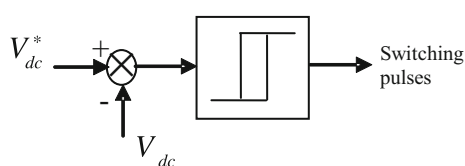
Fig. 5 Hysteresis band voltage controller

If $V_{\mathrm{dc}} > (V_{\mathrm{dc}}^* + \mathrm{HB})$ switch is ON ($S_w = 1$),

where HB denotes the predefined hysteresis band.

The selection of components like boost inductor value and capacitor value is very important to reduce the ripple generation for a given switching frequency. However, large inductance tends to increase the startup time slightly while small inductance allow the coil current to ramp up to higher levels before the switch turns off [20].

$$V_{\mathrm{dc}} = V_{\mathrm{cell}}\frac{T}{t_{\mathrm{off}}} = \frac{V_{\mathrm{cell}}}{1-k}, \tag{4}$$

where $t_{\mathrm{off}} = (1-k)T$ and $t_{\mathrm{on}} = kT$. Assuming a lossless circuit, the average input current is

$$I_{\mathrm{cell}} = \frac{I_l}{1-k}. \tag{5}$$

Then,

$$\Delta I_{\mathrm{cell}} = \frac{V_{\mathrm{cell}}(V_{\mathrm{dc}} - V_{\mathrm{cell}})}{f L_{\mathrm{dc}} V_{\mathrm{dc}}} = \frac{V_{\mathrm{cell}}k}{f L_{\mathrm{dc}}}, \tag{6}$$

where ΔI_{cell} is the peak-to-peak ripple current of inductor L_{dc}. When the switch S_w is on, the capacitor supplies the load current for $t = t_{\mathrm{on}}$. The average capacitor current during this time t_{on} is $I_{c\mathrm{dc}} = I_l$ and the peak-to-peak ripple voltage of the capacitor is

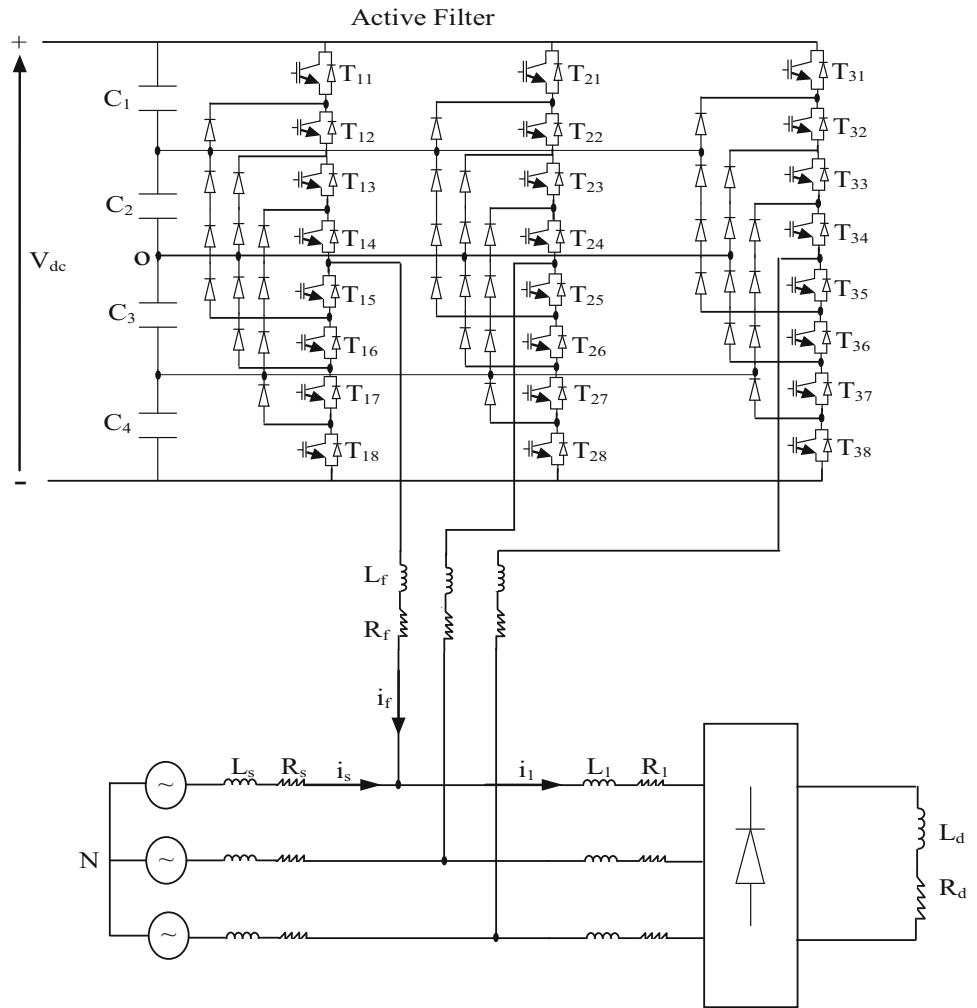$$\Delta V_{C\mathrm{dc}} = \frac{I_l k}{f C_{\mathrm{dc}}}. \tag{7}$$

The size of the reactive elements of the boost converter can be determined from the rated voltage, current ripple, voltage ripple, and switching frequency of the converter based on the equations from (4), (6), and (7).

2.3 Shunt active filter configuration

Figure 6 presents the shunt active filter topology based on a three-phase voltage source inverter, using IGBT switches, connected in parallel with the AC three-phase three-wire system through three inductors. The capacitors are used on the DC side to smooth the DC terminal voltage. A three-phase diode rectifier supplying an R–L load represents the nonlinear load. The main task of the proposed shunt APF is to reduce the harmonic currents and to compensate for the reactive power. The structure in Fig. 6 describes this shunt APF based on a three-phase five-level VSI. To produce an inverter (active filter) of N levels, $N - 1$ capacitors are required.

Where the voltage across each capacitor is equal to $V_{\mathrm{dc}}/(N-1)$, V_{dc} is the total voltage of the DC source. Each pair of switches (T_{11}, T_{15}) form a commutation cell, and the switch pairs are ordered in a complementary way.

Active Filter

Table 1 Five voltage values

K_i	T_{il}	T_{i2}	T_{i3}	T_{i4}	T_{i5}	T_{i6}	T_{i7}	T_{i8}	V_{io}
1	1	1	1	1	0	0	0	0	$V_{dc}/2$
1/2	0	1	1	1	1	0	0	0	$V_{dc}/4$
0	0	0	1	1	1	1	0	0	0
−1/2	0	0	0	1	1	1	1	0	$-V_{dc}/4$
−1	0	0	0	0	1	1	1	1	$-V_{dc}/2$

The inverter provides five voltage levels according to Eq. (8):

$$v_{io} = k_i \frac{v_{dc}}{2},\tag{8}$$

where V_{io} is the phase-to-middle fictive point voltage, K_i is the switching state variable ($K_i = 1, 1/2, 0, 1/2, -1$), V_{dc} is the DC source voltage, and i is the phase index ($i =$ a, b and c). The five voltage values are shown in Table 1, ($V_{dc}/2, V_{dc}/4, 0, -V_{dc}/4, -V_{dc}/2$).

2.4 Reference current calculation

2.4.1 Self-tuning filter

Song [21], presents in his PhD work a new method for recovering the equivalent transfer function of the integration in the synchronous references frame «SRF».

The output signals $\widehat{x}_{\alpha\beta}(s)$ can be expressed by:

$$\hat{x}_\alpha(s) = \frac{k}{s} \left[x_\alpha(s) - \hat{x}_\alpha(s) \right] - \frac{w_c}{s} \hat{x}_\beta(s)\tag{9}$$

$$\hat{x}_\beta(s) = \frac{k}{s} \left[x_\beta(s) - \hat{x}_\beta(s) \right] - \frac{w_c}{s} \hat{x}_\alpha(s).\tag{10}$$

The block diagram of the STF tuned at the pulsation w_c is depicted in Fig. 7.

2.4.2 Harmonic isolator

The load currents, $i_{La}, i_{Lb},$ and i_{Lc}, of the three-phase three-wire system are transformed into the α–β axis (Fig. 8) as follows:

$$\begin{bmatrix} i_\alpha \\ i_\beta \end{bmatrix} = \sqrt{\frac{2}{3}} \begin{bmatrix} 1 & -\frac{1}{2} & -\frac{1}{2} \\ 0 & \frac{\sqrt{3}}{2} & -\frac{\sqrt{3}}{2} \end{bmatrix} \begin{bmatrix} i_{La} \\ i_{Lb} \\ i_{Lc} \end{bmatrix}. \tag{11}$$

As known, the currents in the α–β axis can be respectively decomposed into DC and AC components by:

$$i_\alpha = \hat{i}_\alpha + \tilde{i}_\alpha \tag{12}$$
$$i_\beta = \hat{i}_\beta + \tilde{i}_\beta. \tag{13}$$

Then, the STF extracts the fundamental components at the pulsation w_c directly from the currents in the α–β axis. Afterward, the α–β harmonic components of the load currents are computed by subtracting the STF input signals from the cor-
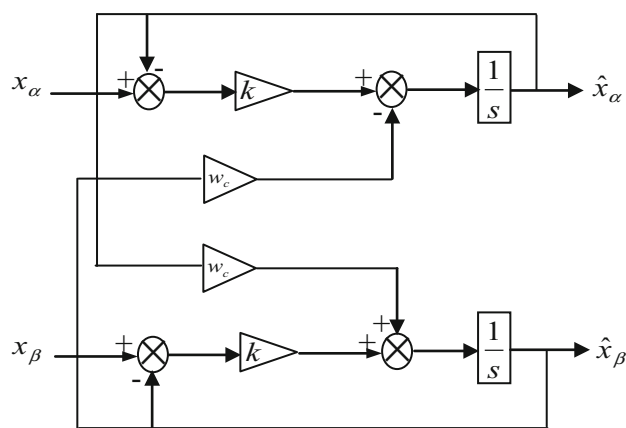
Fig. 7 Self-tuning filter tuned to the pulsation w_c

responding outputs (Fig. 8). The resulting signals are the AC components, $\tilde{i}_\alpha$ and $\tilde{i}_\beta$, which correspond to the harmonic components of the load currents i_{La}, i_{Lb}, and i_{Lc} in the stationary reference frame.

For the source voltage, the three voltages v_{sa}, v_{sb}, and v_{sc} are transformed to the α–β reference frame as follows:

$$\begin{bmatrix} v_\alpha \\ v_\beta \end{bmatrix} = \sqrt{\frac{2}{3}} \begin{bmatrix} 1 & -\frac{1}{2} & -\frac{1}{2} \\ 0 & \frac{\sqrt{3}}{2} & -\frac{\sqrt{3}}{2} \end{bmatrix} \begin{bmatrix} v_{sa} \\ v_{sb} \\ v_{sc} \end{bmatrix}. \tag{14}$$

Then, self-tuning filtering is applied to these α–β voltage components. This filter allows suppressing any harmonic component of the distorted mains voltages and consequently leads to improve the harmonic isolator performance.

After computation of the fundamental component $\hat{v}_{\alpha\beta}$ and harmonic currents $\tilde{i}_{\alpha\beta}$, p and q powers are given as follows:

$$p = i_\alpha \hat{v}_\alpha + i_\beta \hat{v}_\beta \text{ (Instantaneous active power)} \tag{15}$$
$$q = i_\beta \hat{v}_\alpha - i_\alpha \hat{v}_\beta \text{ (Instantaneous reactive power),} \tag{16}$$

where

$$p = \hat{p} + \tilde{p} \tag{17}$$
$$q = \hat{q} + \tilde{q}, \tag{18}$$

where $\hat{p}$, $\hat{q}$ are fundamental components and $\tilde{p}$, $\tilde{q}$ are the alternative components.

The power components $\tilde{p}$ and $\tilde{q}$ related to the same α–β voltages and currents can be written as follows:
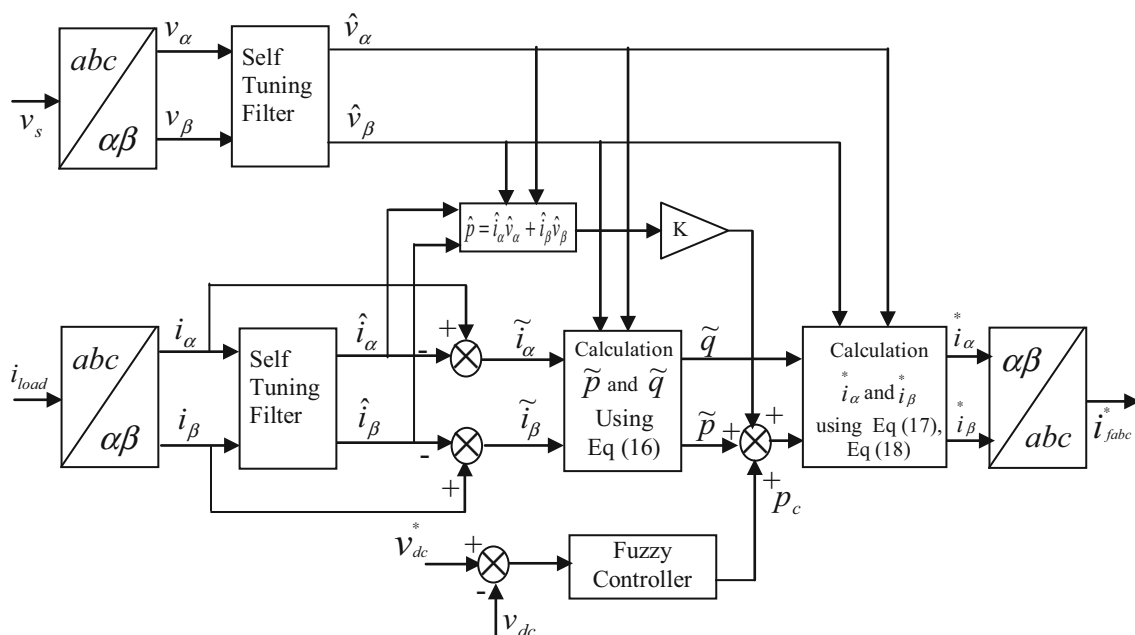

Fig. 8 Block diagram of the proposed harmonic isolator

Table 2 Switching states of one five-level phase leg

Output voltage	T_{i1}	T_{i2}	T_{i3}	T_{i4}	T_{i5}	T_{i6}	T_{i7}	T_{i8}
$V_{dc}/2$	1	1	1	1	0	0	0	0
$V_{dc}/4$	0	1	1	1	1	0	0	0
0	0	0	1	1	1	1	0	0
$-V_{dc}/4$	0	0	0	1	1	1	1	0
$-V_{dc}/2$	0	0	0	0	1	1	1	1

$$\begin{bmatrix} \tilde{p} \\ \tilde{q} \end{bmatrix} = \begin{bmatrix} \hat{v}_\alpha & \hat{v}_\beta \\ -\hat{v}_\beta & \hat{v}_\alpha \end{bmatrix} \begin{bmatrix} \tilde{i}_\alpha \\ \tilde{i}_\beta \end{bmatrix}. \tag{19}$$

After adding the active power required for regulating the DC bus voltage, p_c and a part of active power necessary to feed the load ($p_c + k * \hat{p}$), to the alternative component of the instantaneous real power $\tilde{p}$ (Fig. 8), to compensate power factor, current harmonics, and make the interface between renewable energy sources and the electric grid, injecting a part of the energy necessary to the load and produced by PEM fuel cell power source, the current references in the $\alpha-\beta$ reference frame, $i_{\alpha\beta}^*$, are calculated by:

$$i_\alpha^* = \frac{\hat{v}_\alpha}{\hat{v}_\alpha^2 + \hat{v}_\beta^2}(\tilde{p} + p_c + k * \hat{p}) - \frac{\hat{v}_\beta}{\hat{v}_\alpha^2 + \hat{v}_\beta^2}q \tag{20}$$

$$i_\beta^* = \frac{\hat{v}_\beta}{\hat{v}_\alpha^2 + \hat{v}_\beta^2}(\tilde{p} + p_c + k * \hat{p}) + \frac{\hat{v}_\alpha}{\hat{v}_\alpha^2 + \hat{v}_\beta^2}q. \tag{21}$$

Then, the filter reference currents in the $a-b-c$ coordinates are defined by:

$$\begin{bmatrix} i_{fa}^* \\ i_{fb}^* \\ i_{fc}^* \end{bmatrix} = \sqrt{\frac{2}{3}} \begin{bmatrix} 1 & 0 \\ -1/2 & \sqrt{3}/2 \\ -1/2 & -\sqrt{3}/2 \end{bmatrix} \begin{bmatrix} i_\alpha^* \\ i_\beta^* \end{bmatrix}. \tag{22}$$

2.5 Inverter control using phase distortion PWM

This control implements a fuzzy logic controller which starts from the difference between the injected current (active filter current) and the reference current (identified current) that determines the reference voltage of the inverter (modulating wave). This standard reference voltage is compared with four carrying triangular identical waves. These carrier waves have the same frequency and are arranged on top of each other, with no phase shift, so that they together span from the maximum output voltage to the minimum output voltage [22,23].

The switching states of one five-level phase leg are summarized in Table 2:
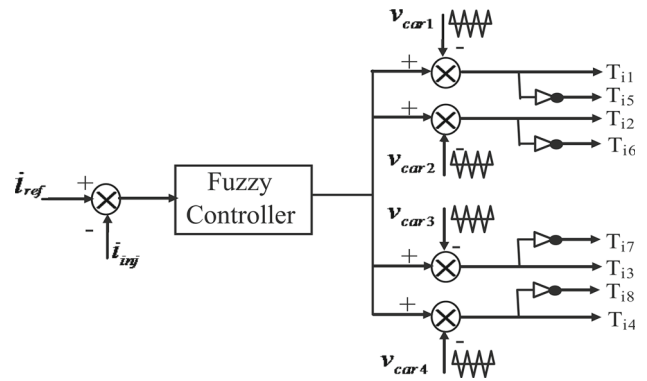
Fig. 9 PWM block diagram of current control

2.6 Active power filter current control

The objective is to get sinusoidal source currents in phase with the supply voltages. This consists of replacing the conventional controllers by fuzzy logic controllers [24]. The establishment of the fuzzy rules is based on the error (e) sign variation, and knowing that (e) is increasing if its derivative (de) is positive, constant i_f (de) is equal to zero, decreasing i_f (de) is negative, positive if ($i_{ref} > i_f$), zero if ($i_{ref} = i_f$), and negative if ($i_{ref} < i_f$). Then the fuzzy rules are summarized as follows:

1. If (e) is zero (ZE), then the command is zero (ZE).
2. If (e) is positive (P), then the command is large positive (LP).
3. If (e) is negative (N), then the command is large negative (LN).
4. If (e) is zero (ZE) and (de) is positive (P), then the command is negative (N).
5. If (e) is zero (ZE) and (de) is negative (N), then the command is positive (P).

General block diagram of currents control is illustrated in Fig. 9.

This system opts for Mamdani's fuzzy inference method, five rules, centroid defuzzification. The conversion of fuzzy values is shown in Fig. 10a–c by the membership function.

2.7 DC capacitor voltages stabilization

In this section, a DC link voltages stabilization system is introduced to balance the four DC input voltages and to avoid NP potential drift and improve the performances of the five-level active power filters. The structure of the bridge balancing is shown in Fig. 11.

If the voltage U_{cx} gets higher then an impose reference U_{ref}, (200 V) the transistor T_x is opened to slow down the charging of C_x. The transistors are controlled as follows:

Fig. 10 a Membership function for current error "e" . **b** Membership function for "de". **c** Membership function for output of the controller

a

b

c
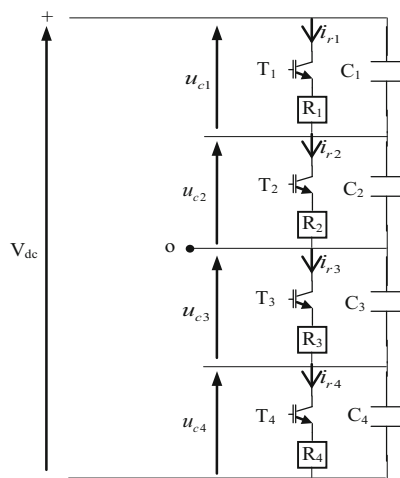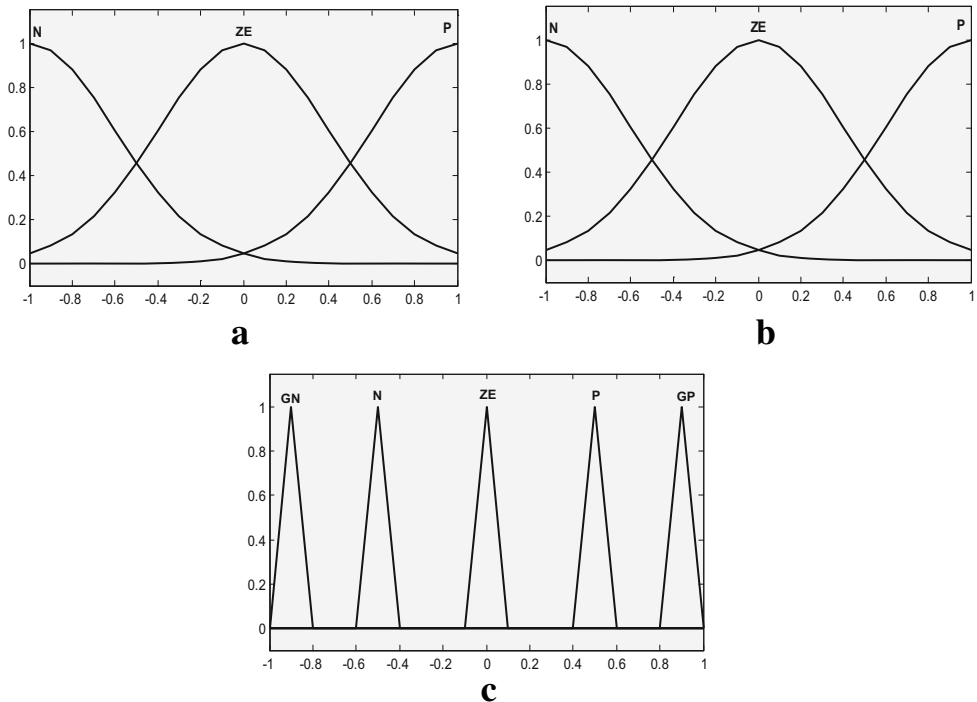
Fig. 11 Structure of the bridge balancing

$U_{Cx} - U_{Cref} = \Delta_x$ with $x = 1, 2, 3, 4.$
If $\Delta_x > 0$, then $F_x = 1$ with $i_{rx} = F_x \frac{U_{Cx}}{R_x}$;
else $F_x = 0.$

2.8 DC capacitor voltage control

In this application, the fuzzy control algorithm is implemented to control the DC capacitor inverter voltage based on DC voltage error $e(t)$ processing and its variation $\Delta e(t)$ to improve the dynamic performance of APF and reduce the total harmonic source current distortion. In the design of a fuzzy control system, the formulation of its rule set plays a

Table 3 Fuzzy control rule table

Δe	e						
	NL	NM	NS	ZE	PS	PM	PL
NL	NL	NL	NL	NL	NM	NS	ZE
NM	NL	NL	NL	NM	NS	ZE	PS
NS	NL	NL	NM	NS	ZE	PS	PM
ZE	NL	NM	NS	ZE	PS	PM	PL
PS	NM	NS	ZE	PS	PM	PL	PL
PM	NS	ZE	PS	PM	PL	PL	PL
PL	NL	NM	NS	ZE	PS	PM	PL

key role in improving the system performance. The rule table contains 49 rules as shown in Table 3, where (LP, MP, SP, ZE, LN, MN, and SN) are linguistic codes (LP: large positive; MP: medium positive; SP: small positive; ZE: zero; LN: large negative; MN: medium negative; SN: small negative).

The conversion of fuzzy values is shown in Fig. 12a–c by the membership function.

3 Results and discussions

Using MATLAB/Simulink with sampling time $Ts = 5\,\mu s$ and ode 45 solver type, the simulation study was carried out for grid-interfaced PEM fuel cell system.

Based on the control schemes for each entity, we deduce the overall scheme of the proposed control system. Figure 13 shows the proposed control system used in simulation.

Fig. 12 **a** Membership
function for voltage error "*e*" . **b**
Membership function for
change in voltage error "Δ*e*". **c**
Membership function for output
of the controller
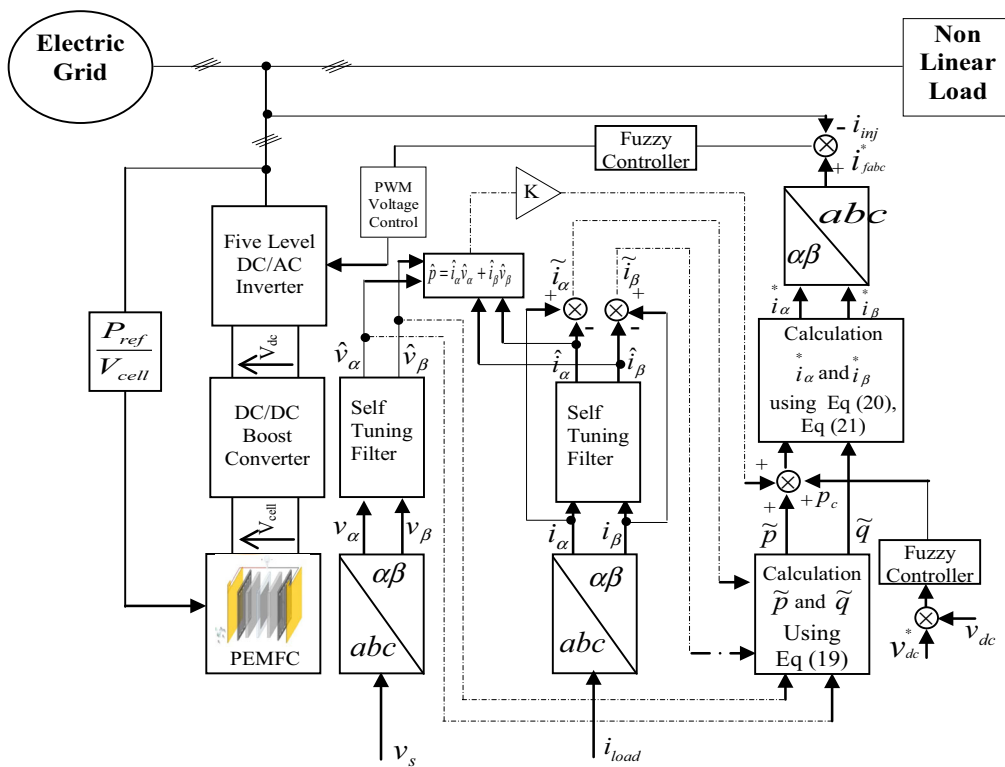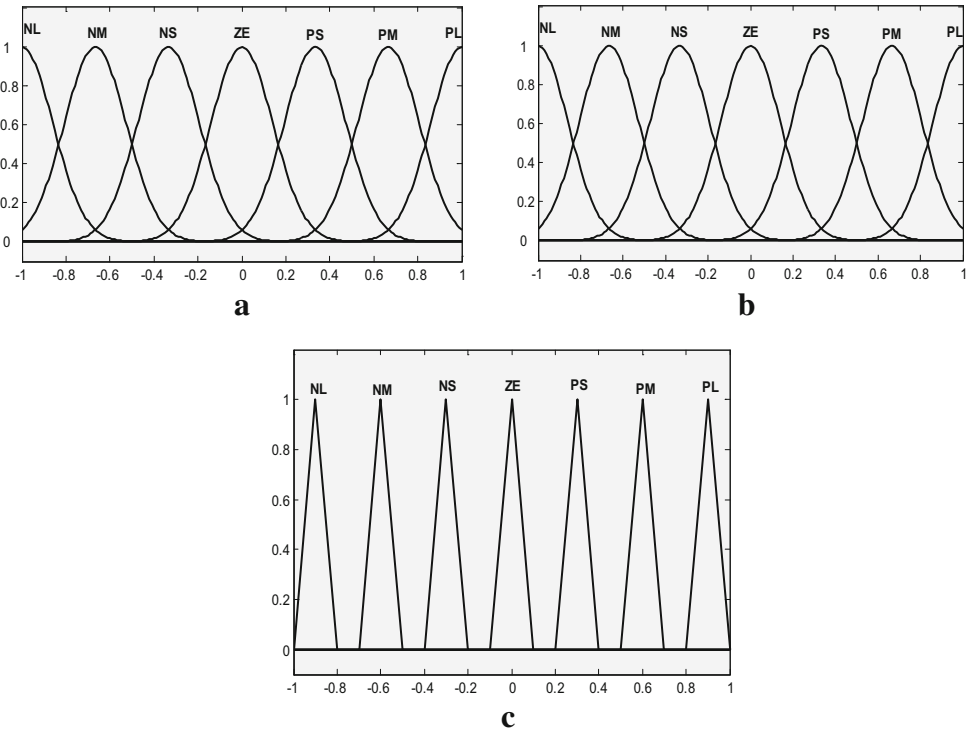
Fig. 13 Overall scheme of the proposed control system
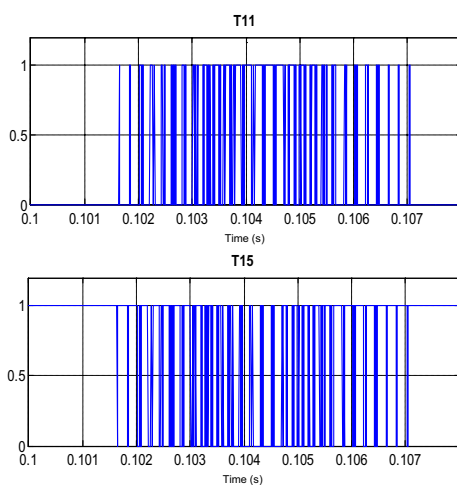
Table 4 Simulation parameters

Electric grid source	
System frequency	60 Hz
System voltage	$230\sqrt{2}V_{\max}$
Impedance (R_s, L_s)	0.5 mΩ, 0.015 mH
FC system model parameters	
Activation current constant (B)	0.04777 (A^{-1})
Activation voltage constant (C)	0.0136 (V)
Conversion factor (CV)	2
Faraday's constant (F)	96,484,600 (C kmol^{-1})
Hydrogen time constant (tH$_2$)	3.37 (s)
Hydrogen valve constant (KH$_2$)	4.22×10^{-5} [kmol (s atm)$^{-1}$]
Hydrogen–oxygen flow ratio (rH-O)	1.168
Kr constant $= N0 /4F$	1.7619×10^{-6} [kmol (s A)$^{-1}$]
N_0 load cell voltage (EO)	0.8 (V)
Number of cells (NO)	680
Oxygen time constant (tO$_2$)	6.74 (s)
Oxygen valve constant (K O$_2$)	2.11×10^{-5} [kmol (s atm)$^{-1}$]
FC internal resistance (Rint)	0.2778 Ω
FC absolute temperature (T)	343 (K)
Universal gas constant (R)	8314.47 [J (kmol K)$^{-1}$]
Utilization factor (U)	0.8
Water time constant (τ H$_2$O)	18.418 (s)
Water valve constant (KH$_2$O)	7.716×10^{-6} [kmol (s atm)$^{-1}$]
3-Leg shunt APF	
DC-link voltage V_{dc}	800 V
DC capacitor C_1, C_2, C_3, C_4	90 mF
Switching frequency	5 kHz
AC side filter (R_f, L_f)	5 mΩ, 0.068 mH
Load	
Inductor L_d	2 mH
Resistor R_d	0.5 Ω
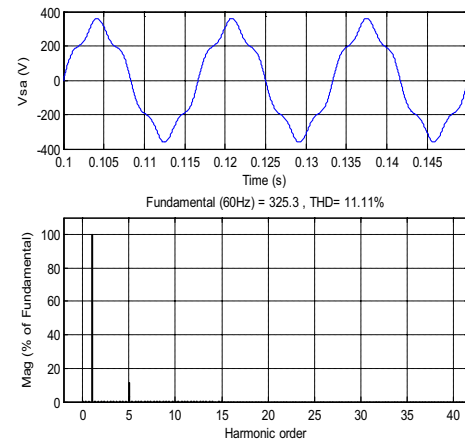
Fig. 15 Supply voltage V_{sa} waveform
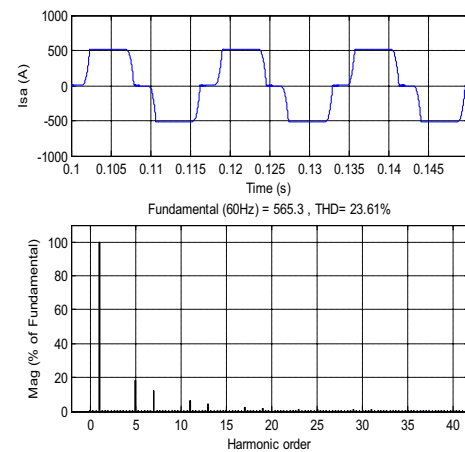
Fig. 16 Supply current I_{sa} waveform without filtering

Fig. 14 Switching pulses of APF arms (T_{11}, T_{15})
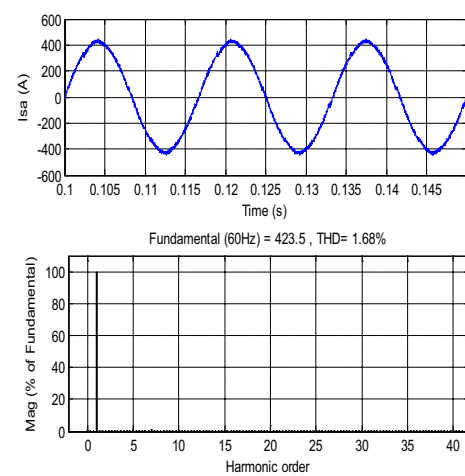
Fig. 17 Supply current I_{sa} waveform with filter
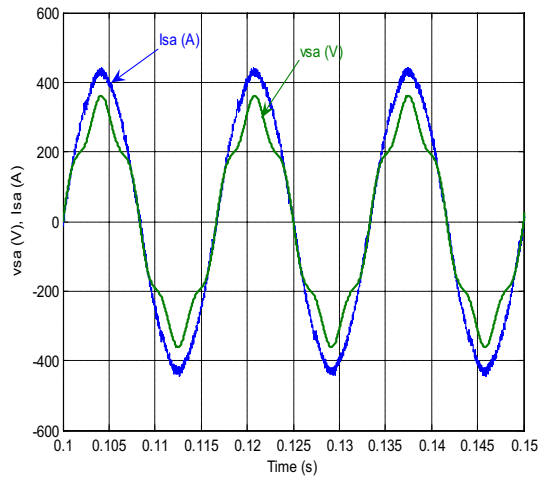
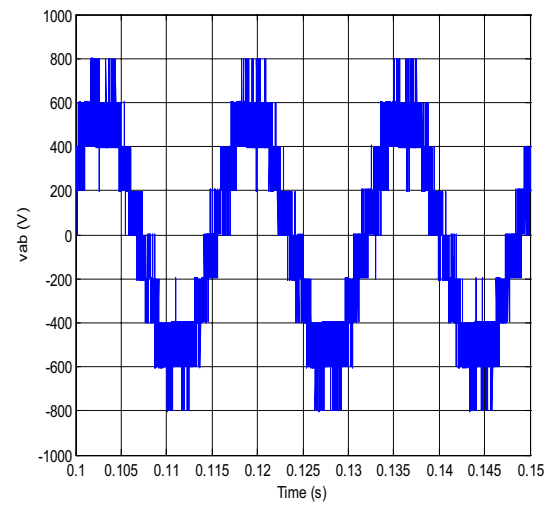**Fig. 18** Power factor correction V_{sa}, I_{sa}
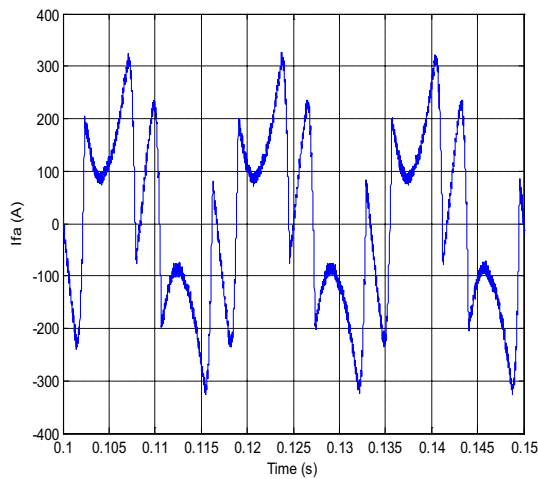
Fig. 19 Active filter current I_{fa}

Fig. 20 APF output voltage V_{ab} (*line* to *line*)

Fig. 21 DC voltage of the condensers V_{dc}

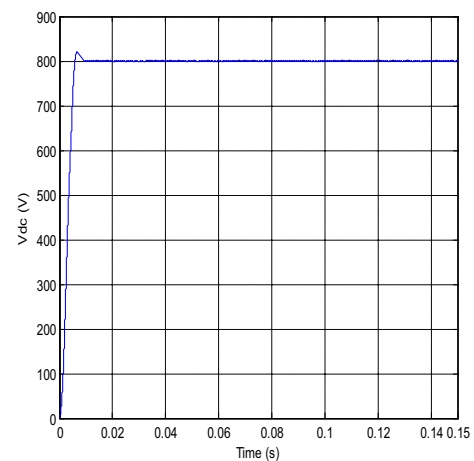Simulation is performed using system parameters presented in Table 4.

The resulting switching signals shown in Fig. 14 illustrate a low frequency commutation process, showing, thus, the advantages of the multilevel inverter.

Figure 15, illustrates that the supply voltage is not sinusoidal and includes a 5th harmonic component (THD = 11.1 %). The total harmonic distortion (THD) of the load current (supply current without filter) is equal to 23.61 % (Fig. 16), whereas, in Fig. 17, the THD of the supply current under this condition is equal to 1.68 % after filtering. Noticeable differences can be found between the fundamental component of the load current (Fig. 16) and the supply current (Fig. 17). It is justified by the successful contribution of the PEM fuel cell to supply simultaneously the load with the electric grid source through the five-level active power filter.

The proposed harmonic isolation and fuzzy control schemes allow harmonic currents and reactive power compensation simultaneously under distorted voltage conditions. The obtained current and voltage waveforms are in phase as illustrated in Fig. 18. Five-level shunt active power filter performances are related to current references quality, self-tuning filters (STF) theory is used for harmonic currents identification and calculation, and the obtained current is shown in Fig. 19. The line to line output voltage V_{ab} is shown in Fig. 20. The five-level active filter with the proposed harmonic isolation and fuzzy control schemes has imposed a sinusoidal source current wave form as illustrated in Fig. 18, and a constant and ripple-free DC voltage in Fig. 21. Figure 22 shows the different voltages obtained by using the stabilization bridge. We can see that the output voltages of the DC side of the five-level active filter (U_{c1}, U_{c2}, U_{c3} and U_{c4}) stabilize around 200 V.

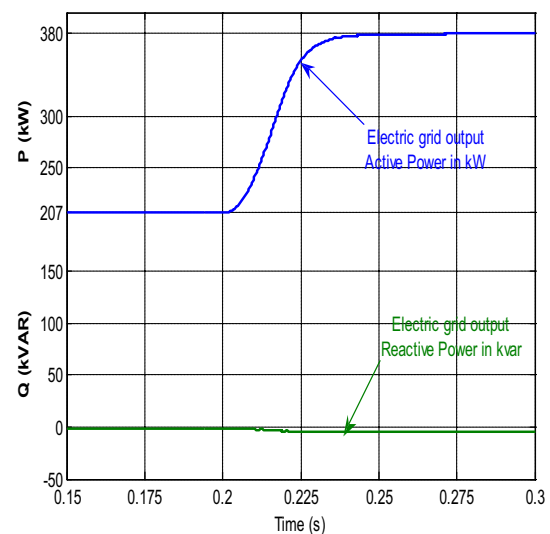To evaluate the dynamic performance of the proposed system, a load change is applied at 0.2 s.

Fig. 22 DC voltages of the five-level APF with clamping bridge: **a** DC voltage U_{c1}, **b** DC voltage U_{c2}, **c** DC voltage U_{c3}, **d** DC voltage U_{c4}
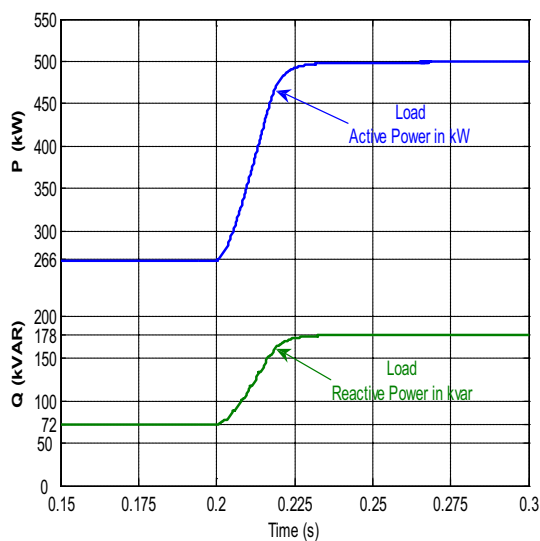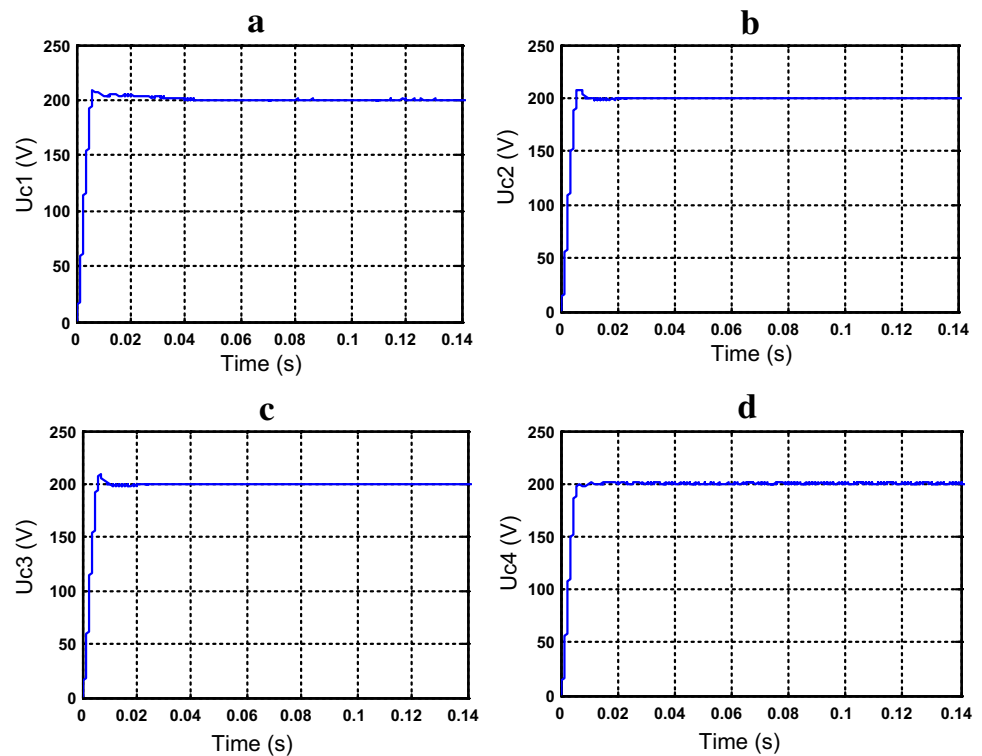
Fig. 23 Load active and reactive powers

Fig. 24 Electric grid output active and reactive powers

The active and reactive power of the load increased, respectively, by about 266 kW and 72 kVAR to 500 kW and 173 kVAR.

Before 0.2 s, it is clear that active and reactive load powers are respectively around 266 kW and 72 kVAR (Fig. 23). In this case (before 0.2 s), the power supplied by the electric grid is of around 207 kW (Fig 24). Therefore, the injected power to the load by the PEM fuel cell through the five-level shunt APF is around 59 kW (Fig. 25). The active filter

also supplies the reactive power required by the load and compensates current harmonics.

From Figs. 26 and 27, it is obvious that the increase in load power increases the FC current, which results in decreased FC output voltage or vice versa.

Figure 28, demonstrates the effect of the DC link voltage for the changes in load current. It is observed that the design of a simple boost converter with hysteresis controller gives
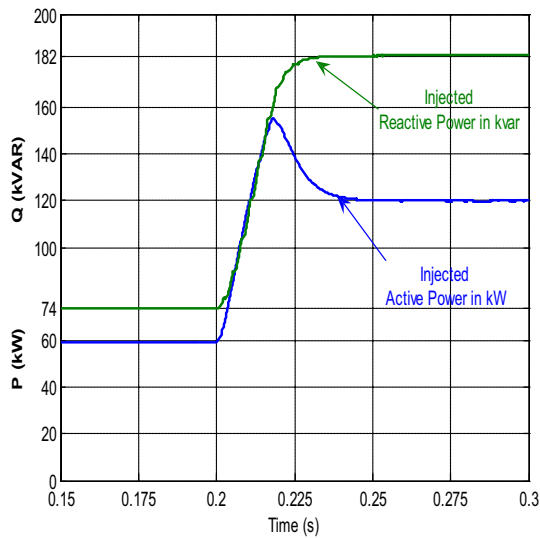
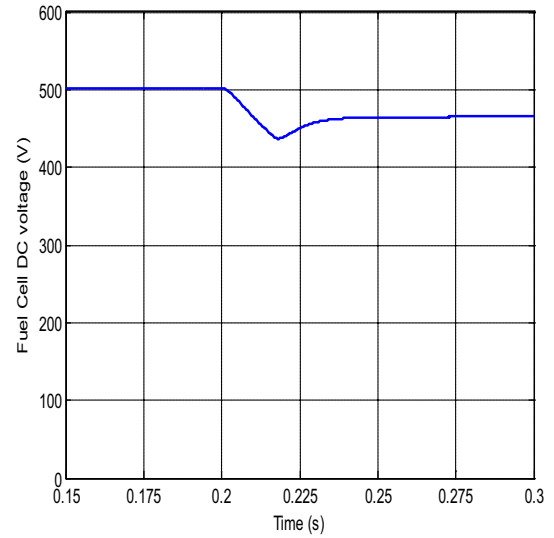**Fig. 25** PEM fuel cell injected with active and reactive powers
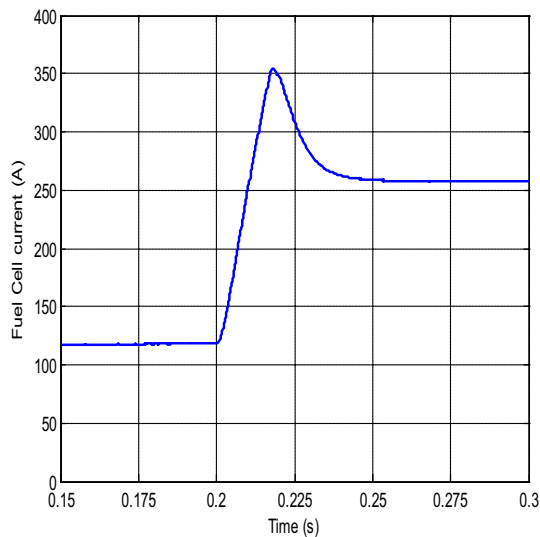

Fig. 27 PEM fuel cell output voltage

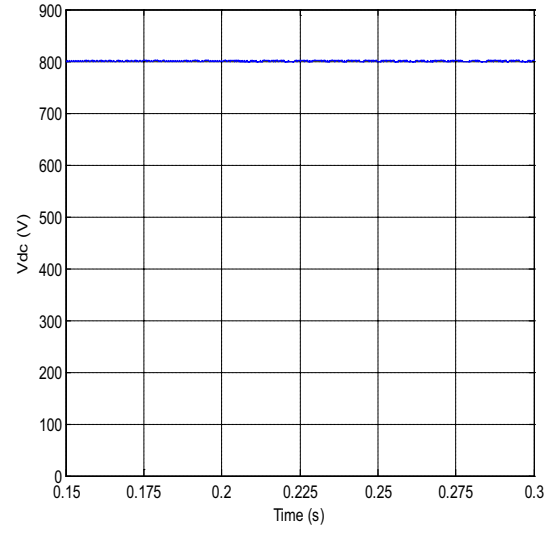**Fig. 26** PEM fuel cell current

Fig. 28 DC link output voltage under changes in load

better performance for changes in load without the use of any storage device.

Figure 29 shows the results under changes in load: (a) load current I_{a1}, (b) supply current I_{sa} waveform and (c) DC voltage V_{dc}.

4 Conclusion

This paper has discussed the use of a proton exchange membrane PEM fuel cell power plant (FCPP) to improve the filtering performance of conventional active power filter, as well as simultaneously contribute with the electric grid to supply the power to the load.

The five-level shunt active power filter is capable of compensating the power factor and current harmonics, and can also make the interface between renewable energy sources (FCPP) and the electric grid, injecting the energy generated by the PEM fuel cell to the load.

This paper has also discussed the control and performance improvement of a shunt active power filter under distorted voltage conditions, using a fuzzy logic controller for a five-level shunt active power filter based on the optimization of the reference current generation and using a modified version of the p–q theory and PDPWM to generate switching signals.

Simulation results have shown high performances in reducing harmonics and power factor correction.

The use of the self-tuning filter leads to satisfactory improvements, since it perfectly extracts the harmonic cur-

Fig. 29 Results under changes in load: **a** load current I_{a1}, **b** supply current I_{sa} waveform, **c** DC voltage V_{dc}
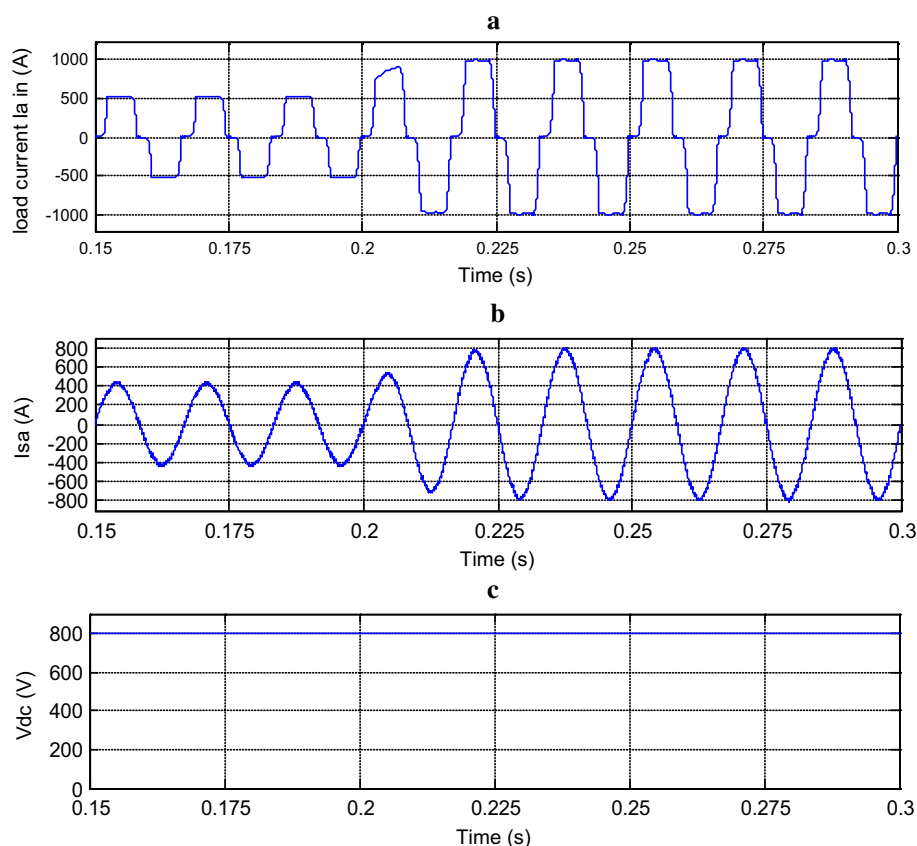
rents under distorted conditions. With the fuzzy logic control, the active filter can be adapted easily to more severe constraints, such as unbalanced conditions.

The five-level APF provides numerous advantages such as improvement of supply current waveform, less harmonic distortion, and possibilities to use it in high power applications.

As a final conclusion, the obtained results show that the PEM fuel cell contributes successfully to supply simultaneously the load with the electric grid and produce a sinusoidal supply current with low harmonic distortion and in phase with the line voltage.

References

1. Noroozian R, Gharehpetian GB (2013) An investigation on combined operation of active power filter with photovoltaic arrays. Electr Power Energy Syst 46(2013):392–399
2. Akagi H (1994) Trend in active power line conditioners. IEEE Trans Power Electron 9:263–268
3. Sangeeta B, Geetha K (2014) Performance of multilevel shunt active filter for smart grid application. Electr Power Energy Syst 63(2014):927–932
4. Chiang H-K, Lin B-R, Yang K-T, Wu K-W (2005) Hybrid active power filter for power quality compensation. IEEE Power Electron Drives Syst 2:949–954
5. Wanfang X, An L, Lina W (2003) Development of hybrid active power filter using intelligent controller. Autom Electr Power Syst 27:49–52
6. Vodyakho O, Kim T, Kwak S (2008) Three-level inverter based active power filter for the three-phase, four-wire system. IEEE power electronics specialists conference, pp 1874–1880
7. Afonso J, Aredes M, Watanabe E, Martins J (2000) Shunt active filter for power quality improvement. International conference UIE 2000—electricity for a sustainable urban development, pp 683–691. Lisboa, Portugal, 1–4 November 2000
8. Abdelkafi A, Krichen L (2014) Energy management optimization of a hybrid power production unit based renewable energies. Electr Power Energy Syst 62(2014):1–9
9. Eid A (2014) Utility integration of PV-wind-fuel cell hybrid distributed generation systems under variable load demands. Electr Power Energy Syst 62(2014):689–699
10. Chang GW, Yeh CM (2005) Optimization-based strategy for shunt active power filter control under non-ideal supply voltages. IEE Electr Power Appl 152:182–190
11. Montero M, Cadaval ER, Gonzalez F (2007) Comparison of control strategies for shunt active power filters in three-phase four-wire systems. IEEE Trans Power Electron 22:229–236
12. Green TC, Marks JH (2005) Control techniques for active power filters. IEE Electr Power Appl 152:369–381
13. Abdusalama M, Poureb P, Karimi S, Saadate S (2009) New digital reference current generation for shunt active power filter under distorted voltage conditions. Electr Power Syst Res 79:759–765
14. Hamadi A, El-Haddad K, Rahmani S, Kankan H (2004) Comparison of fuzzy logic and proportional integral controller of voltage source active filter compensating current harmonics and power factor. IEEE international conference on industrial technology (ICIT), vol 2, pp 645–650

15. Bhat AH, Agarwal P (2007) A fuzzy logic controlled three-phase neutral point clamped bidirectional PFC rectifier. International conference on information and communication technology in electrical sciences (ICTES), pp 238–244

16. Padulles J, Ault GW, McDonald JR (2000) An integrated SOFC plant dynamic model for power systems simulation. J Power Sources 86:495–500

17. El-Sharkh MY, Rahman A, Alam MS, Byrne PC, Sakla AA, Thomas T (2004) Dynamic model for a stand-alone PEM fuel cell power plant for residential application. J Power Sources 139(1–2):199–204

18. Arsov GL (2008) Improved parametric Pspicemodel of a PEM fuel cell. In: 11th International conference on optimization of electrical and electronics equipment, OPTIM 2008, Brasov, Romania, 2008, pp 203–208

19. Cheng KWE, Sutanto D, Ho YL, Law KK (2001) Exploring the power conditioning system for fuel cell. In: 32nd IEEE annual power electronics specialists conference, pp 2197–2202

20. Mohan N, Undeland TM, Robbins WP (2002) Power electronics converters, applications and design, 3rd edn. Wiley, Hoboken. ISBN: 0-471-22693-9

21. Song H-S (2001) Control scheme for PWM converter and phase angle estimation algorithm under voltage unbalanced and/or sag condition. Ph.D in electronic and electrical engineering, Postecch University, Republic of Korea (South)

22. McGrath BP, Holmes DG (2002) Multicarrier PWM strategies for multilevel inverters. IEEE Trans Ind Electron 49(4):858–867

23. Jouanne AV, Dai S, Zhang H (2002) A multilevel inverter approach providing DC-link balancing, ride-through enhancement, and common mode voltage elimination. IEEE Trans Ind Electron 49:739–745

24. Saad S, Zellouma L, Herous L (2008) Comparison of fuzzy logic and proportional controller of shunt active filter compensating current harmonics and power factor. 2nd International conference on electrical engineering design and technology ICEEDT08, pp 8–10, Hammamet, Tunisia

ANTI-WINDUP PROPORTIONAL INTEGRAL STRATEGY FOR SHUNT ACTIVE POWER FILTER INTERFACED BY PHOTOVOLTAIC SYSTEM USING TECHNIQUE OF DIRECT POWER CONTROL

ABDELBASSET KRAMA[1], LAID ZELLOUMA[2], BOUALAGA RABHI[3]

Keywords: Total harmonic distortion (THD), Direct power control, Shunt active power filter (SAPF), Photovoltaic generator, Power quality, Three phase inverter.

This paper focuses on power quality improvement in the distribution network using three phase shunt active power filter, where this later is connected to photovoltaic system. In the present work, a new control method has been presented to eliminate harmonic currents that is caused by nonlinear loads, and to compensate reactive power. This control method has a good accuracy and high efficiency, it bases on direct control of power, rather than conventional one (p-q theory) that relies on current harmonic identification and current control loops. This work proposes to combine a photovoltaic generator with the Dc side of the inverter via boost converter, hence this solution allows to inject the maximum of active power produced by photovoltaic system into the grid in addition to power quality enhancement. The proposed system has been verified by using MATLAB/Simulink and power system. Simulation results demonstrate the effectiveness of the system, where the THD of the source current is reduced to 2.2 %.

1. INTRODUCTION

There are many electrical devices that require high quality of power supply. On the other hand, the number of devices that contain circuits have nonlinear behavior, they cause power quality deterioration and they create, in the distribution networks, non-sinusoidal currents causing high harmonic currents. These result in multiple disagreements such as: increase of line losses, saturation of distribution transformers and interference to adjacent communication systems [1]. These effects can be worse in the case when the voltages or loads are unbalanced [2]. Conventionally, passive filters have been used to eliminate lower order harmonics of the line current, so they reduce the harmonic currents in the distribution network. However, the passive filters present many disadvantages, such as resonances, which are the principal causes of several nuisances, in addition to low performance of the filter.

To overcome the shortcomings of passive power filters and to mitigate the power pollution in networks caused by the nonlinear loads, an active power filter (APF) was established in around 1970's [3]. This work interests in enhancement of main currents and power factor correction, by using an active filter containing a three phase inverter. The source of power that feed the inverter in several researches [1–3] is not an independent voltage source, but a dc-link capacitor voltage, which is charged through the rectifier formed by the diodes connected in antiparallel across the transistors. It is called floating source, in which the dc-link capacitor of shunt active power filter (SAPF) charged and discharged from the grid. In order to maintain this later constant and to provide more electricity to the grid, this work proposes to feed the inverter by one of the cleanest power, which comes from solar energy. In this context, the full system ensure the power quality enhancement and active power injection at the same time, Many researches have been done on active power filter supplied by photovoltaic system; and a lot of them used "p–q theory" for harmonic currents detection and elimination, based on harmonic currents

identification and instantaneous current control loops [4–7]. This proposed control system introduces new control technique that is different from the conventional ones; it is based on direct control of power (DPC), which was proposed by Noguchi *et al.* in 1998. [8] In this paper, the SAPF is supplied by external clean source that is represented by photovoltaic generator (PVG); the studied system allows injecting active power into the grid, compensating line power harmonic and reducing the cost of SAPF. The dc capacitor voltage is regulated and permitted to obtain the reference value of active power by using integral-proportional controller (PI) with an anti-windup. PI controller is calculated to give better performance in time response and system steadiness. The boost converter also controlled to maintain the output voltage of the panel constant and to make the panels provide their maximum power by using sliding mode control. The control of three phase inverter is based on hysteresis comparators with the help of switching table. This approach of control shows significant difference in the term of dynamics, robustness and stability compared to conventional methods.

2. SHUNT ACTIVE POWER FILTER

2.1. THE THEORETICAL PRINCIPLE OF DPC

The idea of the DPC was proposed firstly by Ohnishi *et al.* [9]. He focused on using instantaneous active and reactive power as control variables instead of instantaneous three-phase currents. DPC does not focus on current control loop or unit of PWM, because this method is based on selecting the appropriate voltage vector of the inverter from a switching table, relating to errors of active and reactive power, as well as the angular position of source voltage vector. Thus the choice of the optimum switching state is performed; so that, the error of active power can be limited in a hysteresis band width and the same for the error of reactive power. To improve the performance of DPC, the authors have proposed to divide the vector space into twelve sectors, so we can

───────────────
[1,2] El-Oued University, LEVRES Laboratory, Electrical Engineering Department, P.O. Box 789, El-Oued 39000, Algeria, E-mail: krama.ab@gmail.com
[3] Biskra University, LMSE Laboratory, Electrical Engineering Department, BP. 145, Biskra, Algeria

determine the position of the voltage vector of the source according to this division. In most cases with this technique of control, the dc side voltage is regulated to provide the reference value of the active power. In the state of operation with unity power factor, the reactive power becomes zero. The control strategy of DPC applied to the SAPF is illustrated in (Fig. 1).
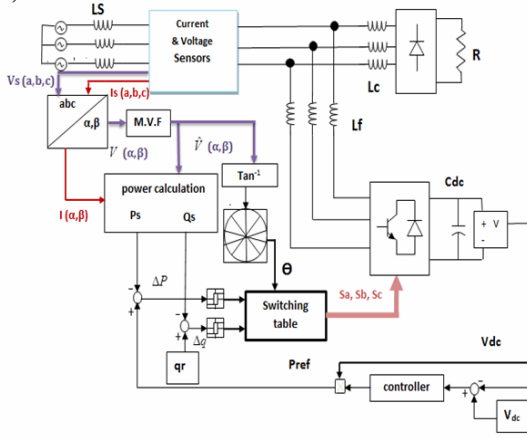

Fig. 1 – General scheme of DPC for SAPF.

2.2. CALCULATION OF INSTANTANEOUS POWERS

To determine the instantaneous active and reactive power, we need to measure the voltage and the current of the source, then they can be calculated by Eq. (1, 2):

$$P_s(t) = V_{sa}i_{sa} + V_{sb}i_{sb} + V_{sc}i_{sc} \qquad (1)$$

$$q_s(t) = -\frac{1}{\sqrt{3}}[(V_{sa} - V_{sb})i_{sa} + (V_{sb} - V_{sc})i_{sb} + \\ + (V_{sc} - V_{sa})i_{sc}. \qquad (2)$$

2.3. SECTOR SELECTION

The influence of each output vector that is provided by SAPF on active and reactive power is very dependent on the real position of the voltage vector of the source. To increase the accuracy and also to avoid the problems encountered at the borders of each vector of control, the plane of the vector space is divided into 12 sectors of 30° for each one (Fig. 2), where the first sector is defined in Eq.(3):

$$-\frac{\pi}{3} < \theta < 0 \qquad (3)$$

The sectors can be obtained by numerical expression as Eq. (4):

$$(n-2) < \frac{\pi}{6} < \theta_n \le (n-1)\frac{\pi}{6}, \qquad (4)$$
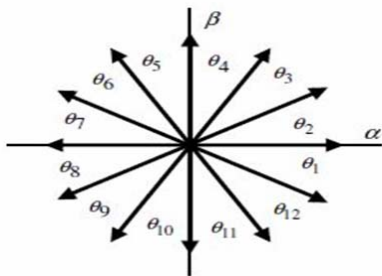
where $n = 1, 2, 3 \ldots 12$.

Fig. 2 – Sectors on stationary coordinates.

The angle is obtained using the inverse tangent function, which is based on the components of the voltage vector on stationary coordinates (α, β), indicated by Eq. (5):

$$\theta = \arctan\frac{V_\alpha}{V_\beta}, \qquad (5)$$

where V_α and V_β are the source voltage on (α, β) frame which are calculated according to Eq. (6):

$$\begin{bmatrix} V_\alpha \\ V_\beta \end{bmatrix} = \sqrt{\frac{2}{3}}\begin{bmatrix} 1 & -\frac{1}{2} & -\frac{1}{2} \\ 0 & \frac{\sqrt{3}}{2} & -\frac{\sqrt{3}}{2} \end{bmatrix}\begin{bmatrix} V_a \\ V_b \\ V_c \end{bmatrix}. \qquad (6)$$

Two-level inverter generates seven voltage vectors for eight different combinations; the calculation of each voltage vector is based on a combination of the respective switching state and the dc bus voltage. By employing (Table 1), the optimum control vector of the inverter, in each instant, can be chosen according to the combination of the digital signals Sp, and Sq and sector number.

Table 1

Switching table

S_p	S_q	θ_1	θ_2	θ_3	θ_4	θ_5	θ_6	θ_7	θ_8	θ_9	θ_{10}	θ_{11}	θ_{12}
1	0	101	111	100	000	110	111	010	000	011	111	001	000
	1	110	111	010	000	011	111	001	000	101	111	100	000
0	0	101	100	100	110	110	010	010	011	011	001	001	101
	1	100	110	110	010	010	011	011	001	001	101	101	100

2.4. SELF TUNING FILTER (STF)

Self tuning filter was proposed firstly by M. Abdusalam *et al.* in their work [10] to extract the direct component of source voltage during distorted conditions. Voltage signal, before and after filtering, can be expressed by Eqs. (7) and (8):

$$\hat{V}_\alpha(s) = \frac{k}{s}[V_\alpha(s) - \hat{V}_\alpha(s)] - \frac{w_c}{s}\hat{V}_\alpha(s) \qquad (7)$$

$$\hat{V}_\beta(s) = \frac{k}{s}[V_\beta(s) - \hat{V}_\beta(s)] + \frac{w_c}{s}\hat{V}_\beta(s), \qquad (8)$$

where W_c is the pulsation of STF.

The block diagram of the STF tuned at the pulsation wc and the frequency response of the STF versus different values of the parameter k are given in [10]. It has been observed that no displacement is introduced by this filter at the system pulsation. It has been also noticed that small value of k increases filter selectivity [11]. Figure 3 represents the block diagram of the self-tuning filter.
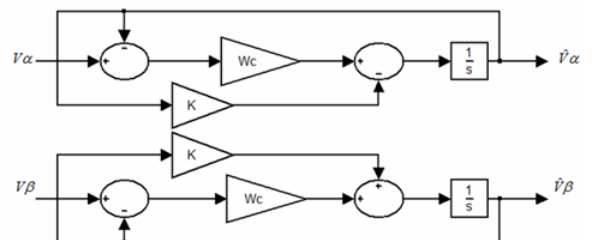

Fig. 3 – Representative scheme of STF.

3. PHOTOVOLTAIC SYSTEM

3.1. MODELING OF SOLAR PV MODULE

The association of a number of photovoltaic cells in series and in parallel provides a photovoltaic generator. The behavior of photovoltaic cell has been extensively studied for more than 25 years. Many articles on modeling modules exist in the literature. The model for a single diode is the most commonly used due to its good results. The equivalent model of a photovoltaic cell can be seen in Fig. 4 [12, 13].

The characteristic (*I–V*) for a PV Cell is described by the nonlinear equation (9) [14, 15].

$$I = I_{pv} - I_0[\exp(\frac{V + R_s.I}{V_t.\alpha}) - 1] - \frac{V + R_s.I}{R_p},$$ (9)
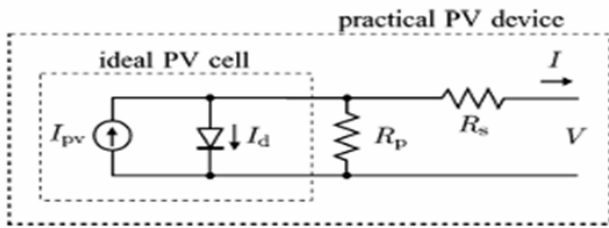
Fig. 4 – Single-diode model of PV cell.

where:

I_{pv} – the current generated by the incident light.
I_0 – the reverse saturation or leakage current of the diode.
$V_t = N_s kT/q$ – is the thermal voltage of the array with.
N_s – number of cells connected in series.
q – the electron charge ($1.60217646 \times 10^{-19}$ C).
k – the Boltzmann constant ($1.3806503 \times 10^{-23}$ J/K).
T – the temperature of the p–n junction in Kelvin.
α – the diode ideality constant.
R_s – the equivalent series resistance.
R_p – the equivalent parallel resistance.

Each module used in the simulation provides 55 W at maximum power point MPP, in Standard Test Conditions mode. Table 1 shows the main information of this module.

Table 1

The main information of proposed PV module

Parameters of the PV module SOLARA SM 220 S/M 55	
Maximum power P_{max}	55W (+/- 10 %)
Maximum power point voltage (V_{mpp})	17.8 V
Open circuit voltage (U_{oc})	21.7 V
Maximum power point current (I_{mpp})	3.1 A
Short circuit current (I_{oc})	3.2 A

3.2. INCREASE AND CONTROL OF OUTPUT VOLTAGE OF PV SYSTEM

To ensure the level of voltage needed to supply the dc-side of SAPF, we proposed to put 4 PV modules connected in series, then raised the output voltage of PV system by using boost converter, this later is controlled by using sliding mode control as observed in Fig 5.
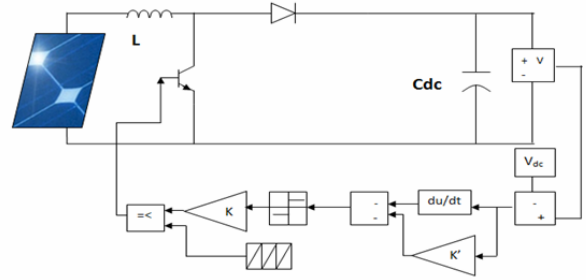

Fig. 5 – Boost converter controlled by sliding mode.

3.3. CONTROL OF DC BUS OF SAPF USING PI CONTROLLER WITH AN ANTI-WINDUP

To maintain the average voltage of dc side at a fixed value, to reduce fluctuation voltage of the dc link capacitor and to compensate the system loss, PI controller is used in dc link voltage control loop. It provides good performance and high efficiency in controlling the system. Voltage control loop diagram can be seen in Fig. 6.
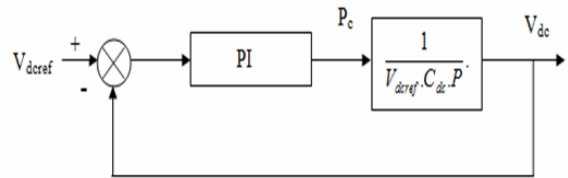

Fig. 6 – Dc bus voltage regulation.

To make the mains current smooth at starting and dumping transient time, A. Chaoui *et al*. in [16] have introduced additionally to the proportional integral (PI) controller an anti-windup compensation, the bloc diagram of PI with anti-windup is shown in Fig. 7.
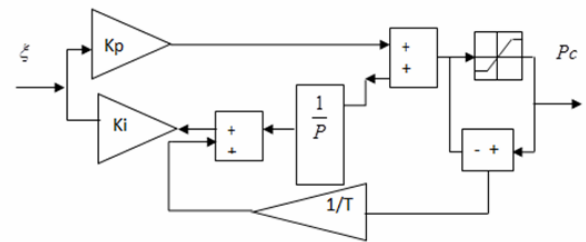

Fig. 7 – PI controller with anti-windup diagram.

4. SIMULATION RESULTS AND DISCUSSION

The proposed PV module is simulated using Matlab/ Simulink, at standard test conditions, the simulated *I–V* and *P–V* characteristics are shown in Fig. 8.
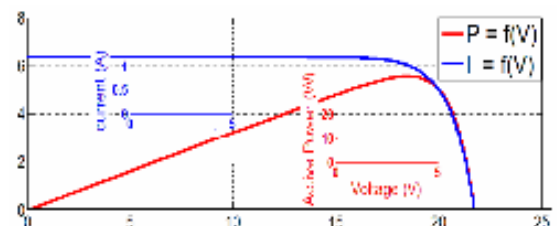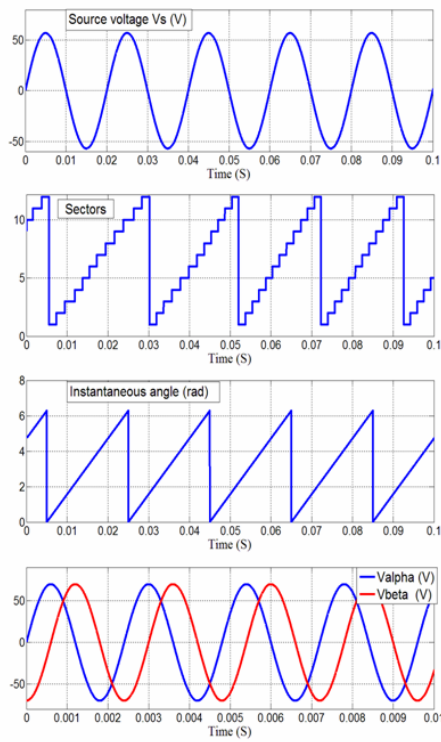

Fig. 8 – Simulated *I–V* and *P–V* characteristics of the panel.

Fig. 9 – Instantaneous source voltage, angle, sector
and voltage position in stationary frame (α, β).

The source current and its spectrum, before connecting the filter, are illustrated in Fig. 10, in addition to active and reactive power. It is noticed that the main current is highly distorted and its THD is equal to 23.15 %.
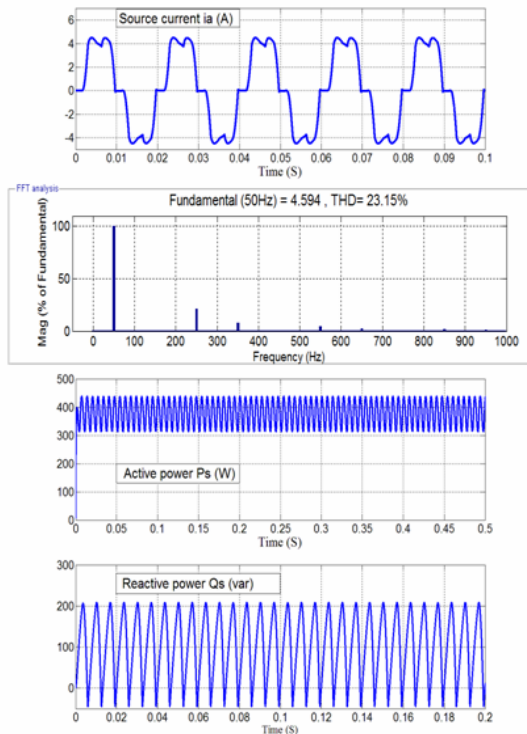

Fig. 10 – Simulation results before filtering.

To evaluate the performance of the proposed system, SAPF connected to PV system, the full system has been modelled and simulated under Matlab/Simulink and power system. Simulation results have been taken under different climatic conditions (variable illumination) as shown, in Fig. 11.

On the other hand, a non-linear load is also changed by varying the value of resistance at the output of the rectifier bridge (load reduction). The simulation results are represented in Fig. 12.

Figure 11 shows simulation results obtained under randomly changes in solar radiation, which are respectively 0 W/m^2, 600 W/m^2, 1000 W/m^2, 400 W/m^2. Firstly, before $t = 0.4$ s, the generated current from PV array remains equal to zero, because the PV array was disconnected from the system, where the source provides the necessary power to the load. Once PV system is connected at $t = 0.4$ s, it injects its maximum power into the grid and the source ensure the remain, although the source current presents variation in amplitude due to the injected current from the PV system , whereas the form remains quasi-sinusoidal during the variations.
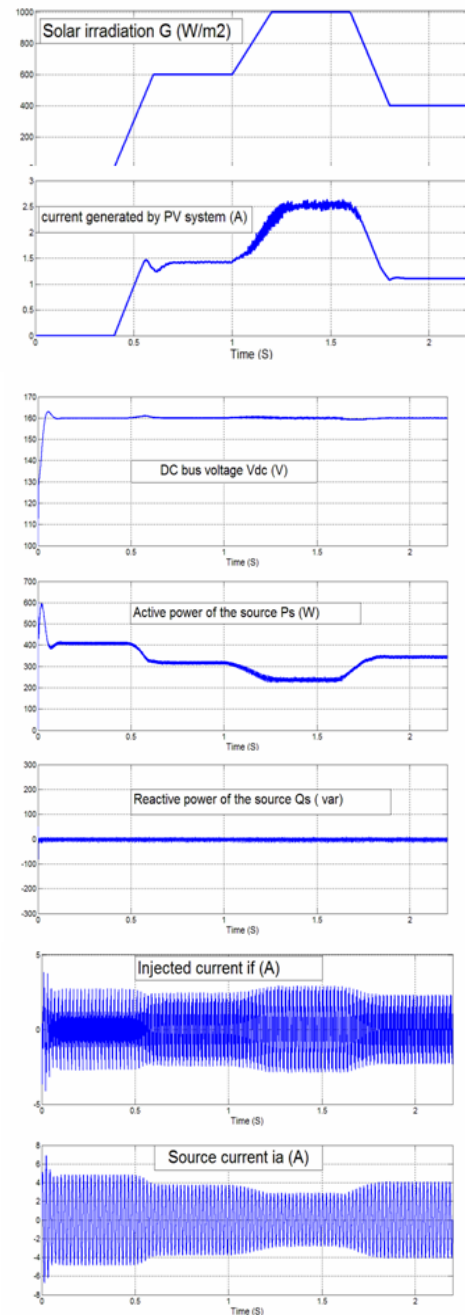

Fig. 11 – Simulation results under varying illumination.

It is observed also that the injected active power is directly influenced by solar radiation, because this later is important

to make the PV generator provide its maximum power, while the reactive energy continues to oscillate around zero to ensure the power factor correction. Regarding the dc bus voltage, it follows its reference and it stays constant all over the experiment with low overshoot at the moment of solar variation.
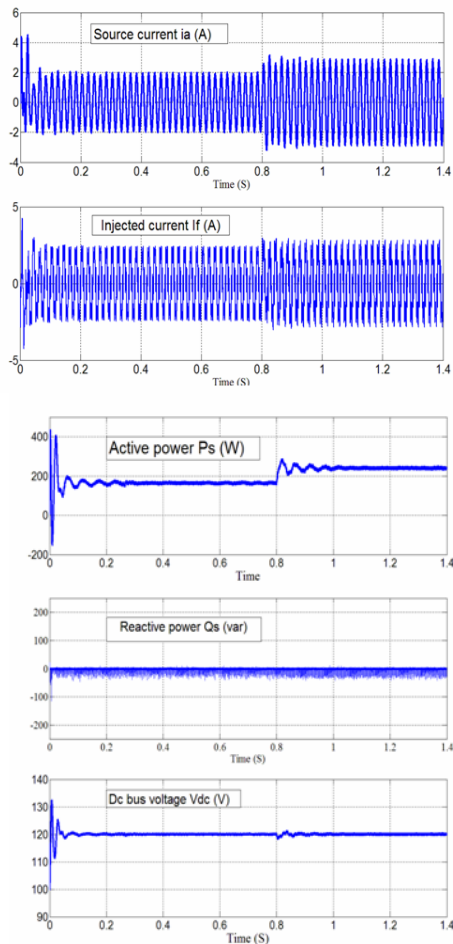

Fig. 12– Simulation results under load variation.

Injected current in the state of absence of PVG $G = 0$ W/m^2 is different from that injected during the presence of PVG, because the first contains only harmonic and reactive current but the second contains harmonic, reactive and active current.

The simulation results during change of the load from 25 Ω to 20 Ω at $t = 0.8$ s are shown in (Fig. 12), it is noticeable that the source current presents significant variation in amplitude (from 2 A to 2.5 A), although the form remains quasi-sinusoidal, where the injected current also increases. It is observed also that the active power undergoes an increase after this variation, which proves that the power consumed by the load is increased, while the reactive power continues to oscillate around zero. Concerning the dc bus voltage, the variation of the load at $t = 0.8$ s causes a low overshoot of dc bus voltage, in that moment the capacitor voltage decreases from the reference value to deliver the needed energy, after that it will follow its reference value.

The source current waveform, after connecting the proposed system, has been analyzed to obtain its THD, It can be deduced that the proposed contains less harmonics in source current as presented in Fig. 13 with a THD equal to 2.2 % after compensation.
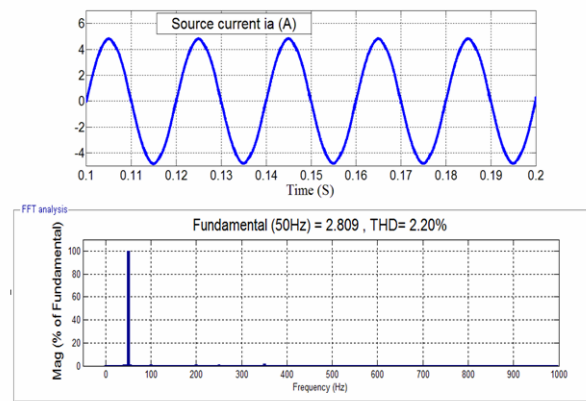

Fig. 13– Source current and its spectrum after filtering.

Simulation results in steady state and in various transient states: under load variation and during variable illumination, thanks to this strategy of control, DPC for grid connected PV system, the system presents very interesting dynamic performance in terms of time response and static state with very acceptable harmonic current distortion (confirms IEEE standars – 519).

4. CONCLUSION

Several traditional solutions for compensation and depollution method have been presented in literature, SAPF considered the best one for harmonics elimination and reactive power compensation.

The simulation results that have been obtained in various cases demonstrate the effectiveness and robustness of the proposed system. We have seen a good signal quality in terms of the total harmonic distortion of main current, THD equal to 2.2 %. That technique of DPC, in addition to its simplicity, better management and control of instantaneous active and reactive power have been achieved.

Finally, the study of the photovoltaic compensation system, which is discussed in this paper, allows obtaining very good performance in injection of active power produced by photovoltaic system to the distribution networks and simultaneously compensating harmonics and reactive power.

REFERENCES

1. M. Bouzidi, A. Benaissa, S. Barkat, *Hybrid direct power/current control using feedback linearization of three-level four-leg voltage source shunt active power filter*, International Journal of Electrical Power & Energy Systems, **61**, pp. 629–646 (2014).
2. I. Nemoianu, R. Ciuceanu, *Aspects of active and reactive powers conservation in three-phase circuits with zero impedance neutral and two nonlinear unbalanced loads,* Rev. Roum. Sci. Techn. – Electrotechn. et Energ., **61**, *4*, pp. 349–354 (2016).
3. M.K. Mishra and K. Karthikeyan, *A Study on Design and Dynamics of Voltage Source Inverter in Current Control Mode to Compensate Unbalanced and Non-linear Loads*, International Conference on Power Electronics Drives and Energy Systems, PEDES 06, New Delhi, 2006.
4. S. Tadjer, I. Habi, *Improvement of the quality of electrical power by a photovoltaic generator connected to the grid*, Rev. Roum. Sci. Techn. – Electrotechn. et Energ., **61**, *1*, pp. 37–41 (2016).
5. B. Exposto, V. Monteiro, J.G. Pinto, D. Pedrosa, A.A.N. Meléndez, J.L. Afonso, *Three-phase current-source shunt active power filter with solar photovoltaic grid interface*, IEEE International Conference on Industrial Technology (ICIT), Seville, 2015, pp. 1211–1215.

6. Y. Bouzelata, E. Kurt, R. Chenni, N. Altin, *Design and simulation of a unified power quality conditioner fed by solar energy*, International Journal of Hydrogen Energy, **40**, *44*, pp. 15267–15277 (2015).

7. R. Belaidi, M. Hatti, A. Haddouche and M.M. Larafi, *Shunt active power filter connected to a photovoltaic array for compensating harmonics and reactive power simultaneously*, Fourth International Conference on Power Engineering, Energy and Electrical Drives (POWERENG), Istanbul, 2013.

8. T. Noguchi, H. Tomiki, S. Kondo, I. Takahashi, *Direct power control of PWM converter without power-source voltage sensors*, IEEE Transactions on Industry Applications, **34**, *3*, pp. 473–479 (1998).

9. T. Ohnishi, *Three phase PWM converter/inverter by means of instantaneous active and reactive power control*, International Conference of the IEEE Industrial Electronics Society (IECON), **1**, pp. 819–8241, Japan, 1991.

10. M. Abdusalam, P. Poure, S. Karimi, S. Saadate, *New digital reference current generation for shunt active power filter under distorted voltage conditions*, Electric Power Systems Research, **79**, *5*, pp. 759–765 (2009).

11. L. Zellouma, B. Rabhi, S. Saad, A. Benaissa, M.F. Benkhoris, *Fuzzy Logic Controller of Five Levels Active Power Filter*, Energy Procedia, **74**, pp. 1015–1025 (2015).

12. M.G. Villalva, J.R. Gazoli, E.R. Filho, *Comprehensive Approach to Modeling and Simulation of Photovoltaic Arrays*, IEEE Transactions on Power Electronics, **24**, *5*, pp. 1198–1208 (2009).

13. A. Attou, A. Massoum, M. Chadli, *comparison study of two tracking methods for photovoltaic systems*, Rev. Roum. Sci. Techn. – Electrotechn. et Energ., **60**, *2*, pp. 205–214 (2015).

14. H.S. Rauschenbach, *Solar Cell Array Design Handbook*, NewYork, Van Nostrand Reinhold, 1980.

15. A. Bellia, Y. Ramdani, F. Moulay, K. Medles, *Irradiance and temperature impact on photovoltaic power by design of experiments*, Rev. Roum. Sci. Techn. – Electrotechn. et Energ., **58**, *3*, pp. 284–294 (2013).

16. A. Chaoui, J-P. Gaubert, F. Krim, *Power quality improvement using DPC controlled three-phase shunt active filter*, Electric Power Systems Research, **80**, *6*, pp. 657–666 (2010).

CrossMark

Design and Experimental Investigation of Predictive Direct Power Control of Three-Phase Shunt Active Filter with Space Vector Modulation using Anti-windup PI Controller Optimized by PSO

Abdelbasset Krama[1] · Laid Zellouma[1] · Amar Benaissa[2] · Boualaga Rabhi[3] · Mansour Bouzidi[4] · Mohamed Fouad Benkhoris[5]

Abstract

This paper presents a robust control scheme for shunt active power filter based on predictive direct power control with space vector modulation. The proposed control strategy solves the problem of variable switching frequency of predictive control strategy, and it offers simple and robust hardware implementation. It uses a discrete model of the system based on time domain to generate the average voltage vector, at each sampling period, with the aim of canceling the errors between the estimated active and reactive power values and their references. Concerning the DC-side voltage of the inverter, anti-windup PI controller is tuned offline using particle swarm optimization algorithm to deliver an optimal performance in DC bus voltage regulation. The overall system has been designed, simulated and validated experimentally; the obtained results in different phases demonstrate the higher performance and the better efficiency of the proposed system in terms of power quality enhancement.

1 Introduction

The widespread use of nonlinear loads in manufacturing activities as well as for domestic reason has caused an undesirable impact on the quality of electric power systems [1]. These nonlinear loads draw non-sinusoidal currents from utility grid that causes harmonic currents. These harmonics introduce many problems such as increasing of line losses, saturation of distribution transformers and poor power factor [2,3]. However, the demand of good power quality is increasing due to the growth of using sensitive devices that require smooth sinusoidal waveforms. As a result, power quality enhancement has become the necessity of the day and it has attracted the interest of many researches. Traditionally, passive filters have been used to suppress current harmonics and to mitigate the power pollution in grid for a long time [1]. However, this kind of filters offers numerous shortcomings such as huge size [4], heavy, and sensitivity to parameters variation which lead to resonance problems [5]. The above-mentioned problems have been effectually relieved by using an active filter which was recognized nearly in 1970s [6]. Shunt active power filter (SAPF) is a flexible solution for harmonic currents mitigation as well as power factor correction. Moreover, it has a perfect ability to adapt with different types of loads [5]. The combination of SAPF is based on voltage/current source inverter that is connected in parallel with nonlinear loads. The inverter generates the needed harmonic components to suppress harmonic currents drawn by nonlin-

✉ Abdelbasset Krama
krama.ab@gmail.com

1 LEVRES Laboratory, Electrical Engineering Department, El-Oued University, 39000 El-Oued, Algeria

2 LAADI Laboratory, Electrical Engineering Department, Djelfa University, 17000 Djelfa, Algeria

3 LMSE Laboratory, Electrical Engineering Department, Biskra University, 07000 Biskra, Algeria

4 Département de l'Electronique et des Communications, Faculté des Nouvelles Technologies d'Information et Communication, Université Kasdi Merbah, 30000 Ouargla, Algeria

5 IREENA-CRTT Laboratory, Ecole Polytech Nantes, University of Nantes, 44600 Saint Nazaire, France

🌐 Springer

ear loads; therefore, it makes the main current sinusoidal and in phase with supply voltage [1–7].

The performance of the SAPF depends mainly on the used control method [8]. Therefore, the control strategy of SAPF is an effective research field and various control strategies have been proposed in the literature [1,9]. The control strategies can be classified in two categories: direct and indirect methods. Direct methods are extensively reported in the literature [10–14]. These methods are based on direct harmonic currents identification stage, so it determines harmonic components to be cancelled by using current sensors at the load side. The most common extraction methods are instantaneous active and reactive power theory (p–q theory) [10–12], synchronous reference frame (SRF) [13,14]. However, the application of such algorithm needs powerful computation process, which results in a relatively slow response time due to the harmonic extraction stage. In addition, the implementation of these direct methods requires additional current sensors at two different sides (to sense the load and filter currents). These two drawbacks make this kind of control more expensive, and it complicates the implementation and loses the precision. In the last few years, indirect control methods for SAPF have attracted the attention of many researchers, and a number of control strategies have been developed such as direct power control (DPC) [15,16] that focuses on predefined switching table to select the appropriate control vector to be applied at the output of the inverter in each sampling period, a predictive direct power control (P-DPC) [17,18] based on cost function minimization and predictive current control [19,20] that uses the currents as a control variables instead of powers as in P-DPC. These three strategies require current sensors only at the main source, they are not interested in load or filter current because it is not based on harmonic currents identification in harmonic elimination stage, but it imposes the grid to provide only the fundamental component (sinusoidal waveform) to the load and the remains (harmonics) are ensured by the inverter. However, these control strategies are more effective than the direct methods but still present non-desired properties such as accuracy of compensation and variable switching frequency which reduce the reliability of power system. To solve this problem, the current research proposes robust control scheme for SAPF based on predictive-DPC with space vector modulation (SVM) [5,21]. The proposed control method offers a perfect ability in harmonic currents mitigation and power factor correction, and it delivers a fixed switching frequency [2,21,22].

Commonly, the control of the DC-side voltage of SAPF is performed using conventional PI controller. However, the optimal parameters of this controller are difficult to obtain by using computing approaches due to nonlinearity and complexity of the system. Therefore, several optimization algorithms have been published in the literature with the aim of solving different application problems such as genetic

algorithms [23], ant colony optimization [24], artificial bee colony [25] and particle swarm optimization (PSO) [26]. Recently, PSO became one of the most useful and most popular algorithms to solve various optimization problems in various fields [27–29]. One of key points behind the PSO is its simplicity and flexibility [30]. However, it is a powerful algorithm [29]. PSO is based on paradigm of swarm intelligence, and it is inspired by social behavior of animals like fish and birds. This level of intelligence is unreachable for any member of the swarm, but with cooperation among these members [31].

In this paper, the parameters of anti-windup PI controller for DC bus voltage have been tuned through particle swarm optimization algorithm considering three different objective functions: Integral Absolute Error (IAE), Integral Square Error (ISE), and Integral Time Absolute Error (ITAE) [32]. The efficiency and performance of the studied system have been examined under simulation using simpower system of Matlab/Simulink environment and investigated in real-time using dSpace board (1104). Simulation and experimental results demonstrate the superiority of the proposed system in steady state performance as compared to some recently published works, whereas the dynamic state is improved after using anti-windup PI optimized by PSO algorithm.

The rest of the paper is planned into five sections as follows: Sect. 2 presents a general configuration of three-phase three-wire SAPF, Sect. 3 explains the basic principle of the proposed control system based on P-DPC-SVM approach and provides its mathematical model. After that, Sect. 4 presents DC bus voltage control based on anti-windup PI controller-based PSO algorithm. Then, in Sect. 5 the simulation and the experimental results are given with analysis and discussion. Lastly, the conclusion is given in Sect. 6.

2 Basic Configuration of SAPF

Generally, the configuration of SAPF relies on four main parts as depicted in Fig. 1: control algorithm, power supply, nonlinear load and voltage source inverter (VSI). The latter takes the role of SAPF, and it aims to mitigate the current harmonic distortion and to delete the phase shift that are caused by nonlinear load. In the present work, the three-phase network is connected to nonlinear load via three inductors. The nonlinear load is constructed from three-phase diode rectifier with resistive load, which is the most common source of harmonic currents. Two-level VSI based on six IGBT switches with a capacitor for energy storage is connected at the point of common coupling (PCC) through inductors (L_f). VSI acts as a controlled source current. It generates the non-fundamental currents that are equal to those consumed by the nonlinear load but in opposite phase to make the grid side free from harmonic currents.

DIRECT SLIDING MODE CONTROL OF DOUBLY FED INDUCTION GENERATOR DRIVEN BY A WIND TURBINE WITH A SVM INVERTER USING SIMULINK

Youcef Bekakra[1,*], Djilani Ben Attous[2], Laid Zellouma[3]

[1,2,3] LEVRES-Research Laboratory, Department of Electrical Engineering, University of El Oued, P.O. Box789, El Oued, Algeria.

*Corresponding author: *E-mail:*
youcef1984@gmail.com, youcef-bekakra@univ-eloued.dz

ABSTRACT

A direct control of Doubly Fed Induction Generator (DFIG) driven by wind turbine fed by a Space Vector Modulation (SVM) with a variable structure control based on a Sliding Mode Controller (SMC) is presented in this paper. Our aim is to make the stator active and reactive power control track their reference variations. The use of the nonlinear sliding mode control gives very good active and reactive power performance when it applies to the DFIG. To improve the quality of energy injected into the electrical grid, we propose the SVM technique which allows the minimizing of stator current harmonics and wide linear modulation range. In addition, we present the implantation, step by step, of the SVM inverter under Matlab/Simulink software. Numerical simulation results and discussion are presented to validate the proposed control strategy. The results show that the SMC with SVM technique give a good quality of energy where the THD of the stator current of DFIG has small value (THD=4.38% <5% according IEEE Std 519-1992).

Keywords

Wind Turbine, Doubly Fed Induction Generator, Sliding Mode Control, Stator Active Power, Stator Reactive Power, Space Vector Modulation, Matlab/Simulink.

1. INTRODUCTION

The use of the wind energy conversion systems (WECS) has been significantly expanding over the last few decades. This is due to the fact that this energy source of production of electricity is emission free [1], [2].

One of the generation systems commercially available in the wind energy market currently is the doubly fed induction generator (DFIG) with its stator winding directly connected to the grid and with its rotor winding connected to the grid through a variable frequency converter.

Vector control technology is used to control the generator, and the rotor of DFIG is connected to an AC excitation of which the frequency, phase, and magnitude can be adjusted. Therefore, constant operating frequency can be achieved at variable wind speeds [3].

This paper adopts the vector transformation control method of stator-oriented magnetic field to realize the decoupling control of the stator active and reactive power using sliding mode control (SMC).

Sliding mode theory, stemmed from the variable structure control family, has been used for the induction motor drive for a long time. It has for long been known for its capabilities in accounting for modeling imprecision and bounded disturbances. It achieves robust control by adding a discontinuous control signal across the sliding surface, satisfying the sliding condition [4].

The power quality problems, such as large values of harmonics, poor power factor and high total harmonic distortion, are usually associated with operation of three-phase AC/DC converters. Negative effects of harmonics, such as failures in computer operation and data transmission, high noise levels in telephone communications, malfunction of sensitive electronic equipment, resonance conditions in power supply network, aging of insulation and additional losses in electrical machines, capacitive bank failures and so on, are well known. To diminish these effects, many countries have issued harmonics limitation standards or recommendations [5].

Traditionally the sinusoidal pulse-width modulation (SPWM) technique is widely used in variable speed drive of induction machine, especially for scalar control where the stator voltage and frequency can be controlled with minimum online computational requirement. In addition, this technique is easy to implement. However, this algorithm has the following drawbacks. This technique gives more total harmonic distortion (THD), this algorithm does not smooth the progress of future development of vector control implementation of ac drive. These drawbacks lead to development of a sophisticated PWM algorithm which is Space Vector Modulation (SVM). This algorithm minimizes the THD as well as loss due to minimize number of commutations in the inverter [6].

This paper presents a numerical simulation study of direct sliding mode control of active and reactive of DFIG fed by SVM inverter for improving the quality of the energy injected into the grid.

The paper is organized as follows. Section II depicts a detailed model of wind turbine and DFIG. Section III presents the field oriented control of DFIG. Section IV gives an overview of sliding mode control and its application on DFIG. Simulation results for 4kW DFIG generation system are presented in section V. At last, conclusions are revealed in section VI.

2. TURBINE MODEL

Normally a wind turbine creates mechanical torque on a rotating shaft, while an electrical generator on the same rotating shaft is controlled to produce an opposing electromagnetic torque. The power equation for the wind turbine is as follows [7], [8]:

$$P_v = \frac{1}{2}\rho S_w v^3 \qquad (1)$$

Where ρ is the air density; S_w is the wind turbine blades swept the area in the wind; v is the wind speed.

The output mechanical power of a wind turbine is:

$$P_m = C_p P_v = \frac{1}{2}C_p \rho S_w v^3 \qquad (2)$$

Where C_p represents the power coefficient.

C_p can be described as [9]:

$$C_p(\beta,\lambda) = (0.5 - 0.0167.(\beta-2)).\sin(\frac{\pi.(\lambda+0.1)}{18.5 - 0.3(\beta-2)}) - 0.00184\,(\lambda-3).(\beta-2) \qquad (3)$$

It is a function of the tip speed ratio λ and the blade pitch angle β in a pitch-controlled wind turbine. λ is defined as the ratio of the tip speed of the turbine blades to wind speed:

$$\lambda = \frac{R.\Omega_t}{v} \qquad (4)$$

Where R is blade radius, Ω_t is the angular speed of the turbine.

The figure 1 shows the relation between C_p, β and λ. The maximum value of C_p ($C_{p\_max} = 0.5$) is achieved for $\beta = 2$ degree and $\lambda_{opt} = 9.2$.
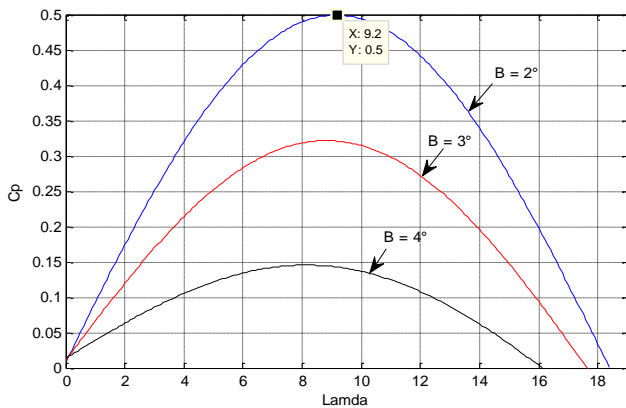
Figure 1. Aerodynamic power coefficient variation C_p against tip speed ratio λ and pitch angle β .

3. DFIG MODEL

The general electrical state model of the induction machine obtained using Park transformation is given by the following equations [10], [11]:

Stator and rotor voltages:

$$\begin{cases} V_{sd} = R_s.i_{sd} + \dfrac{d}{dt}\phi_{sd} - \omega_s.\phi_{sq} \\[2mm] V_{sq} = R_s.i_{sq} + \dfrac{d}{dt}\phi_{sq} + \omega_s.\phi_{sd} \\[2mm] V_{rd} = R_r.i_{rd} + \dfrac{d}{dt}\phi_{rd} - (\omega_s - \omega).\phi_{rq} \\[2mm] V_{rq} = R_r.i_{rq} + \dfrac{d}{dt}\phi_{rq} + (\omega_s - \omega).\phi_{rd} \end{cases} \qquad (5)$$

Stator and rotor fluxes:

$$\begin{cases} \phi_{sd} = L_s.i_{sd} + M.i_{rd} \\[1mm] \phi_{sq} = L_s.i_{sq} + M.i_{rq} \\[1mm] \phi_{rd} = L_r.i_{rd} + M.i_{sd} \\[1mm] \phi_{rq} = L_r.i_{rq} + M.i_{sq} \end{cases} \qquad (6)$$

The electromagnetic torque is given as:

$$C_e = pM\,(i_{rd}.i_{sq} - i_{rq}.i_{sd}) \qquad (7)$$

and its associated motion equation is:

$$C_e - C_r = J\frac{d\Omega}{dt} \qquad (8)$$

The state variable vector is then:

$$X = \begin{bmatrix} i_{sd} & i_{sq} & i_{rd} & i_{rq} \end{bmatrix}^T$$

The state model can then be written as:

$$\dot{X} = A.X + B.U \qquad (9)$$

Where:

A must be an n-by-n matrix, where n is the number of states.

B must be an n-by-m matrix, where m is the number of inputs.

With:

$$\dot{X} = \begin{bmatrix} \dfrac{d}{dt}i_{sd} & \dfrac{d}{dt}i_{sq} & \dfrac{d}{dt}i_{rd} & \dfrac{d}{dt}i_{rq} \end{bmatrix}^T$$

$$U = \begin{bmatrix} V_{sd} & V_{sq} & V_{rd} & V_{rq} \end{bmatrix}^T$$

$$A = \begin{bmatrix} -a_1 & a\omega + \omega_s & a_3 & a_5\omega \\[2mm] -a\omega - \omega_s & -a_1 & -a_5\omega & a_3 \\[2mm] a_4 & -a_6\omega & -a_2 & -\dfrac{\omega}{\sigma} + \omega_s \\[2mm] a_6\omega & a_4 & \dfrac{\omega}{\sigma} - \omega_s & -a_2 \end{bmatrix},$$

$$B = \begin{bmatrix} b_1 & 0 & -b_3 & 0 \\[2mm] 0 & b_1 & 0 & -b_3 \\[2mm] -b_3 & 0 & b_2 & 0 \\[2mm] 0 & -b_3 & 0 & b_2 \end{bmatrix}$$

Where:

$$a = \frac{1-\sigma}{\sigma}, \quad a_1 = \frac{R_s}{\sigma L_s}, \quad a_2 = \frac{R_r}{\sigma L_r}, \quad a_3 = \frac{R_r M}{\sigma L_s L_r},$$

$$, \quad a_5 = \frac{M}{\sigma L_s}, \quad a_6 = \frac{M}{\sigma L_r},$$

$$b_1 = \frac{1}{\sigma L_s}, b_2 = \frac{1}{\sigma L_r}, b_3 = \frac{M}{\sigma L_s L_r}, \sigma = 1 - \frac{M^2}{L_s L_r}$$

4. DFIG FIELD ORIENTED CONTROL

In this section, the DFIM (Doubly Fed Induction Machine) model can be described by the following state equations in the synchronous reference frame whose axis d is aligned with the stator flux vector, ($\phi_{sd} = \phi_s$ and $\phi_{sq} = 0$).

The control of the DFIG must allow a control independent of the active and reactive power by the rotor voltages generated by a SVM inverter.

By neglecting resistances of the stator phases the stator voltage will be expressed by:

$$V_{ds} = 0 \text{ and } V_{qs} = V_s \approx \omega_s . \phi_s \quad (10)$$

We lead to an uncoupled power control; where, the transversal component i_{rq} of the rotor current controls the active power. The reactive power is imposed by the direct component i_{rd} .

$$P_s = -V_s \frac{M}{L_s} i_{rq} \quad (11)$$

$$Q_s = \frac{V_s^2}{\omega_s L_s} - V_s \frac{M}{L_s} i_{rd} \quad (12)$$

The arrangement of the equations gives the expressions of the voltages according to the rotor currents:

$$\begin{cases} V_{rd} = R_r .i_{rd} + \sigma L_r \frac{di_{rd}}{dt} - g\omega_s \sigma L_r i_{rq} \\ V_{rq} = R_r i_{rq} + \sigma L_r \frac{di_{rq}}{dt} + g\frac{M}{L_s} V_s + g\omega_s \sigma L_r i_{rd} \end{cases}$$
$$(13)$$

With:

$$T_r = \frac{L_r}{R_r} ; T_s = \frac{L_s}{R_s} ; \sigma = 1 - \frac{M^2}{L_s . L_r}$$

We can notice in the equations of V_{rd} , (control variable of Q_s) and V_{rq} (control variable of P_s) that these two control variables are coupled. The decoupling is obtained by compensation in order to sure the control of P_s and Q_s , independently. Then, the rotor circuit can be represented in dq frames by the transfer function presented in equation (13).

The inverter connected to the rotor of the DFIG must provide the necessary complement frequency in order to maintain constant the stator frequency despite the variation of the mechanical speed.

The system studied in the present paper is constituted of a DFIG directly connected through the stator windings to the grid, and supplied through the rotor by a static frequency converter as presented in figure 2.
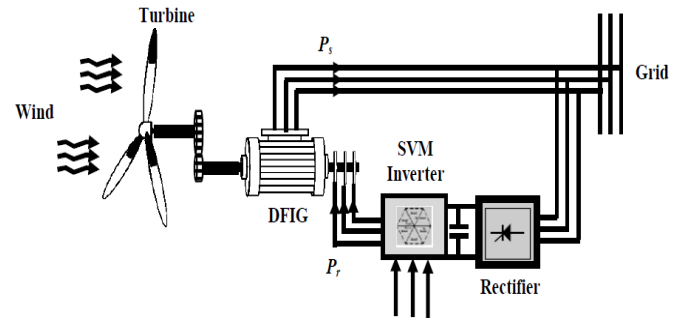

Figure 2. Configuration of a Doubly Fed Induction Generator (DFIG)

5. SLIDING MODE CONTROL

A Sliding Mode Controller (SMC) is a Variable Structure Controller (VSC). Basically, a VSC includes several different continuous functions that can map plant state to a control surface, whereas switching among different functions is determined by plant state represented by a switching function [12].

The design of the control system will be demonstrated for a following nonlinear system [12]:

$$\dot{x} = f(x,t) + B(x,t).u(x,t) \quad (14)$$

Where $x \in \Re^n$ is the state vector, $u \in \Re^m$ is the control vector, $f(x,t) \in \Re^n$, $B(x,t) \in \Re^{n \times m}$.

From the system (14), it possible to define a set S of the state trajectories x such as:

$$S = \{ x(t) , \sigma_s(x,t) = 0 \} \quad (15)$$

Where:

$$\sigma_s(x,t) = [\sigma_{s1}(x,t), \sigma_{s2}(x,t), ..., \sigma_{sm}(x,t)]^T \quad (16)$$

and $[.]^T$ denotes the transposed vector, S and σ_s are called the sliding surface.

To bring the state variable to the sliding surfaces, the following two conditions have to be satisfied:

$$\sigma_s(x,t) = 0, \dot{\sigma}_s(x,t) = 0 \quad (17)$$

The control law satisfies the precedent conditions is presented in the following form:

$$u = u^{eq} + u^n$$
$$u^n = -k_f .\text{sgn}(\sigma_s(x,t)) \quad (18)$$

Where u is the control vector, u^{eq} is the equivalent control vector, u^n is the switching part of the control (the correction factor), k_f is the controller gain. u^{eq} can be obtained by considering the condition for the sliding regimen, $\dot{\sigma}_s(x,t) = 0$.

The equivalent control keeps the state variable on sliding surface, once they reach it.

The sgn function is defined by [13]:

$$sgn(\varphi) = \begin{cases} 1, & if \quad \varphi > 0 \\ 0, & if \quad \varphi = 0 \\ -1, & if \quad \varphi < 0 \end{cases} \quad (19)$$

The controller described by the equation (18) presents high robustness, insensitive to parameter fluctuations and disturbances, but it will have high-frequency switching (chattering phenomena) near the sliding surface due to sgn function involved. These drastic changes of input can be avoided by introducing a boundary layer with width ε. Thus replacing $sgn(\sigma(t))$ by $sat(\sigma(t)/\varepsilon)$ (saturation function), in (18), we have:

$$u = u^{eq} - k_f \cdot sat(\sigma_s(x,t)) \quad (20)$$

Where

$$sat(\varphi) = \begin{cases} sgn(\varphi), & if \quad |\varphi| \geq \varepsilon \\ \varphi, & if \quad |\varphi| < \varepsilon \end{cases} \quad (21)$$

Consider a Lyapunov function [14]:

$$V = \frac{1}{2}\sigma_s^2 \quad (22)$$

From Lyapunov theorem we know that if $\dot{V}$ is negative definite, the system trajectory will be driven and attracted toward the sliding surface and remain sliding on it until the origin is reached asymptotically [7]:

$$\dot{V} = \frac{1}{2}\frac{d}{dt}\sigma_s^2 = \sigma_s \dot{\sigma}_s \leq -\eta|\sigma_s| \quad (23)$$

Where, η is a strictly positive constant.

In this paper, we use the sliding surface proposed par J.J. Slotine,

$$\sigma_s(x,t) = \left(\frac{d}{dt} + \lambda\right)^{n-1} e \quad (24)$$

Where:

$x = \left[x, \dot{x}, ..., x^{n-1}\right]^T$ is the state vector,

$x_d = \left[x^d, \dot{x}^d, ..., x^d\right]^T$ is the desired state vector,

$e = x_d - x = \left[e, \dot{e}, ..., e^{n-1}\right]$ is the error vector, and λ is a positive coefficient, and   is the system order.

Commonly, in DFIG control using sliding mode theory, the surfaces are chosen as functions of the error between the references input signals and the measured signals.

5.1. Active Power Control by SMC

The active power error is defined by:

$$e = P_s^* - P_s \quad (25)$$

For $n = 1$, the active power control equation can be obtained from equation (24) as follow:

$$\sigma_s(P_s) = e = P_s^* - P_s \quad (26)$$

$$\dot{\sigma}_s(P_s) = \dot{P}_s^* - \dot{P}_s \quad (27)$$

Substituting the expression of $\dot{P}_s$ equation (11) in equation (27), we obtain:

$$\dot{\sigma}_s(P_s) = \dot{P}_s^* - \left(-V_s\frac{M}{L_s}\dot{i}_{rq}\right) \quad (28)$$

We draw the expression of the current $\dot{i}_{rq}$ from the voltage equation V_{rq} (Eq. 13):

$$\dot{\sigma}_s(P_s) = \dot{P}_s^* + V_s\frac{M}{L_sL_r.\sigma}\left(V_{rq} - R_r i_{rq}\right) \quad (29)$$

We take:

$$V_{rq} = V_{rq}^{eq} + V_{rq}^{n} \quad (30)$$

During the sliding mode and in permanent regime, we have:

$$\sigma_s(P_s) = 0, \quad \dot{\sigma}_s(P_s) = 0, \quad V_{rq}^n = 0$$

Where the equivalent control is:

$$V_{rq}^{eq} = R_r i_{rq} - \dot{P}_s^*\frac{L_sL_r.\sigma}{V_s M} \quad (31)$$

Therefore, the correction factor is given by:

$$V_{rq}^n = k_{Vrq}sat(\sigma_s(P_s)) \quad (32)$$

k_{Vrq} : positive constant.

5.2. Reactive power control by SMC

The reactive power error is defined by:

$$e = Q_s^* - Q_s \quad (33)$$

For $n = 1$, the reactive power control equation can be obtained from equation (24) as follow:

$$\sigma_s(Q_s) = e = Q_s^* - Q_s \quad (34)$$

$$\dot{\sigma}_s(Q_s) = \dot{Q}_s^* - \dot{Q}_s \quad (35)$$

Substituting the expression of $\dot{Q}_s$ equation (12) in equation (35), we obtain:

$$\dot{\sigma}_s(Q_s) = \dot{Q}_s^* - \left(\frac{V_s^2}{\omega_s L_s} - V_s\frac{M}{L_s}\dot{i}_{rd}\right) \quad (36)$$

We draw the expression of the current $\dot{i}_{rd}$ from the voltage equation V_{rd} (Eq. 13):

$$\dot{\sigma}_s(Q_s) = \dot{Q}_s^* + V_s\frac{M}{L_sL_r\sigma}(V_{rd} - R_r i_{rd}) \quad (37)$$

We take:

$$V_{rd} = V_{rd}^{eq} + V_{rd}^{n} \quad (38)$$

During the sliding mode and in permanent regime, we have:

$$\sigma_s(Q_s) = 0, \dot{\sigma}_s(Q_s) = 0, V_{rd}^n = 0$$

Where the equivalent control is:

$$V_{rd}^{eq} = R_r i_{rd} - \dot{Q}_s^* \frac{L_s L_r . \sigma}{V_s M} \tag{39}$$

Therefore, the correction factor is given by:

$$V_{rd}^n = k_{Vrd} sat(\sigma_s(Q_s)) \tag{40}$$

k_{Vrd} : positive constant.

6. SPACE VECTOR MODULATION (SVM) :

The SVM is identified as an alternative method of determination of switching pulse width and their position. The major advantage of SVM is a degree of freedom of space vector placement in a switching cycle; this technique improves the harmonic performance.

6.1 Realization Steps of the SVM:

Step 1: Determination of reference voltages of V_α, V_β,

Step 2 : Determination of sectors,
Step 3 : Calculate of variables X, Y et Z,
Step 4 : Calculate of t_1 and t_2 for each sector,
Step 5 : Generation of modulate signals t_{aon}, t_{bon} et t_{con},
Step 6 : Generation of series of impulsions T_a, T_b et T_c.

6.2 Blocs of the SVM under Matlab/Simulink:

The simulation of this technique is done through the model represented in the figure 3:
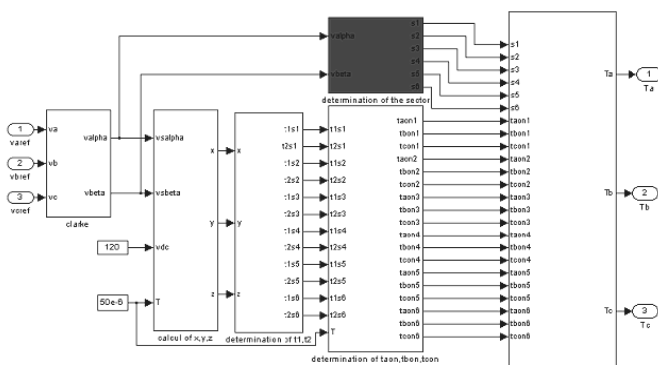
Figure 3. Blocs of the SVM under Matlab/Simulink software

6.2.1 Determination of V_α, V_β :

This bloc is used to project the three phase voltages in the (α, β) reference by using Clarke transformation, as shown in the figure 4.
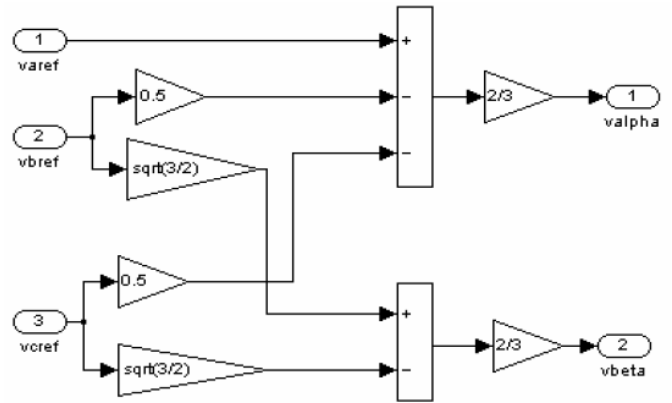
Figure 4 Clarke transformation bloc

6.2.2 Determination of Sectors:

In this section, the sector is determined by a simple method based on the voltages V_α, V_β:

The determination is cited in the table 1, where A_2 is the sign of V_α and A_1 is the sign of V_β.

Where :

If V_α is a negative than $A_2=0$, else $A_2= 1$.

If V_β is a negative than $A_1=0$, else $A_1= 1$.

$A_0 = 1$, if the absolute value of the ratio (V_β / V_α) is bigger than or equal to $(\tan 60° = 1.732)$ otherwise $A_0 = 0$.

This method is used by Panigrahi [15] for the determination of the sector for the Direct Torque Control (DTC).

Table 1. Determination of sectors

A_2	A_1	A_0	Sector
0	0	0	5
0	0	1	4
0	1	0	6
0	1	1	1
1	0	0	3
1	0	1	4
1	1	0	2
1	1	1	1

The sector determination bloc under Matlab/Simulink is presented in the figure 5.
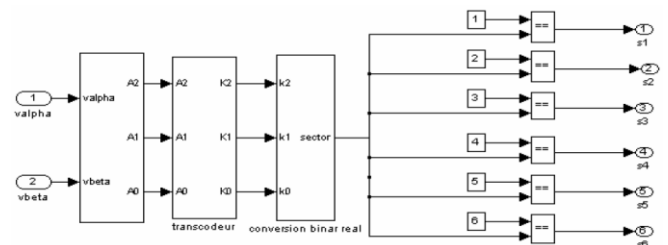

Figure 5. Sector determination bloc

6.2.3 Calculate of Variable X, Y and Z:

The three variables X, Y and Z are given by the following

equations:

$$X = \sqrt{3}\,\frac{T}{V_{dc}}V_\beta \tag{41}$$

$$Y = \frac{\sqrt{3}}{2}\frac{T}{V_{dc}}V_\beta + \frac{3}{2}\frac{T}{V_{dc}}V_\alpha \tag{42}$$

$$Z = \frac{\sqrt{3}}{2}\frac{T}{V_{dc}}V_\beta - \frac{3}{2}\frac{T}{V_{dc}}V_\alpha \tag{43}$$

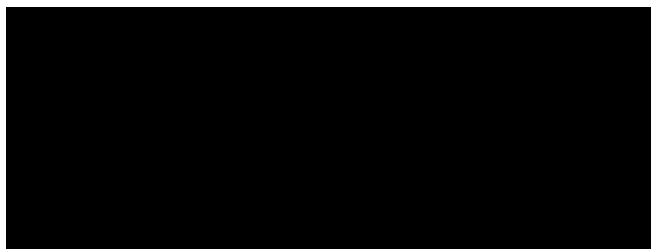The variables X, Y and Z are calculated by the bloc of the figure 6.

Figure 6. Bloc of calculate of X, Y and Z

6.2.4 Calculate of t_1 et t_2 :

The time t_1 and t_2, for each sector according the values of X, Y and Z, are calculated as presented in the table 2.

Tableau 2. Time t_1 and t_2 according X, Y and Z

Sector	1	2	3	4	5	6
t_1	Z	Y	-Z	-X	X	-Y
t_2	Y	-X	X	Z	-Y	-Z

6.2.5 Determination of t_{aon}, t_{bon} and t_{con} :

This bloc generates the modulating signals according to the following formulas:

$$\tag{44}$$

The figure 7 presents the model, under Matlab/Simulink, of each of the six sectors (here, the sector 1).
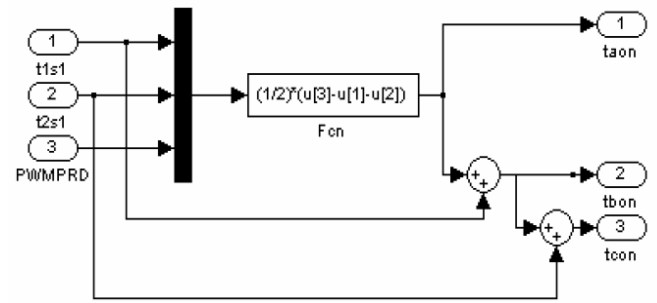
Figure 7. Determination bloc of t_{aon}, t_{bon} and t_{con}

6.2.6 Determination of T_a, T_b et T_c :

This bloc generates the series of impulses which will then be used to produce the control signals of the inverter, following the comparison of a triangular modulating signal with the high frequency carrier. Its model bloc in Matlab/Simulink is presented in the figure 8.
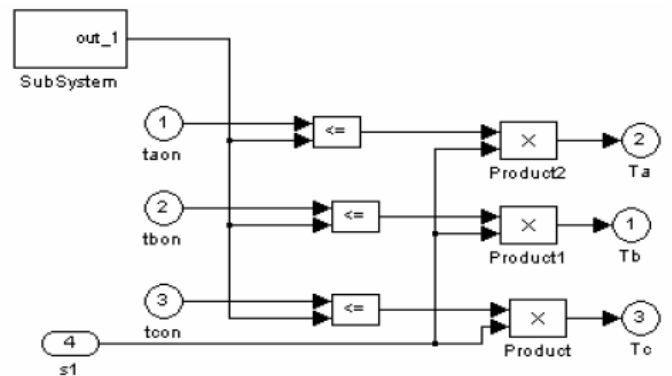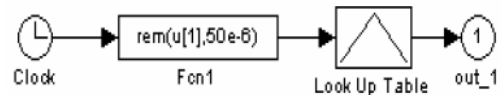

Figure 8. Determination bloc of T_a, T_b et T_c

Figure 9. The SubSystem "out_1"

The t_{xon} signals are arranged in the table 3.

Table 3. The assignment of signals T_a, T_b and T_c

Sector \ Phase	1	2	3	4	5	6
T_a	t_{bon}	t_{aon}	t_{aon}	t_{con}	t_{bon}	t_{con}
T_b	t_{aon}	t_{con}	t_{bon}	t_{bon}	t_{con}	t_{aon}
T_c	t_{con}	t_{bon}	t_{con}	t_{aon}	t_{aon}	t_{bon}

7. Simulation Results:

The DFIG used in this work is a 4 kW, whose nominal parameters are indicated in appendix A.
The control scheme of DFIG using the sliding mode controllers has been presented in figure 10, the blocs (SMC) represent the proposed sliding mode controllers of stator active and reactive

power. The bloc 'DFIG + SVM Inverter' represents the doubly fed induction generator and the space vector modulation inverter.
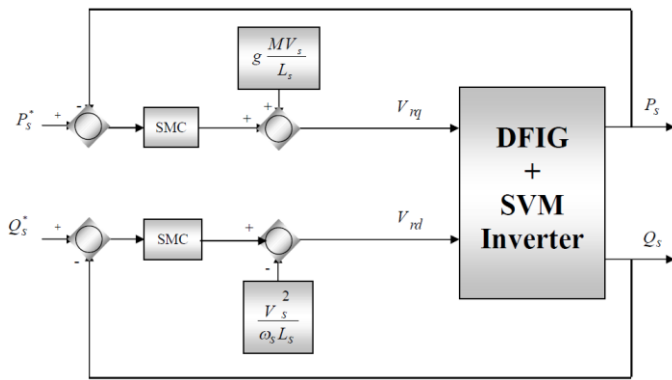

Figure 10. Direct SMC of the DFIG

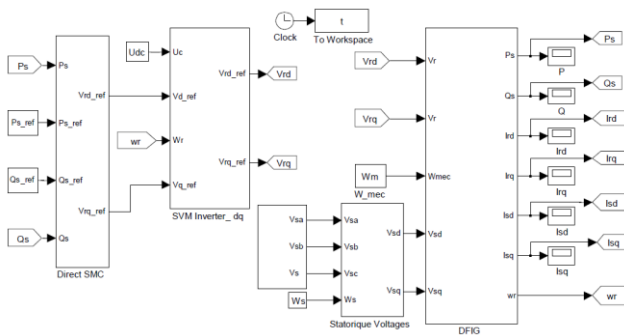The figure 11 presents the implantation of the proposed control under Matlab/Simulink.
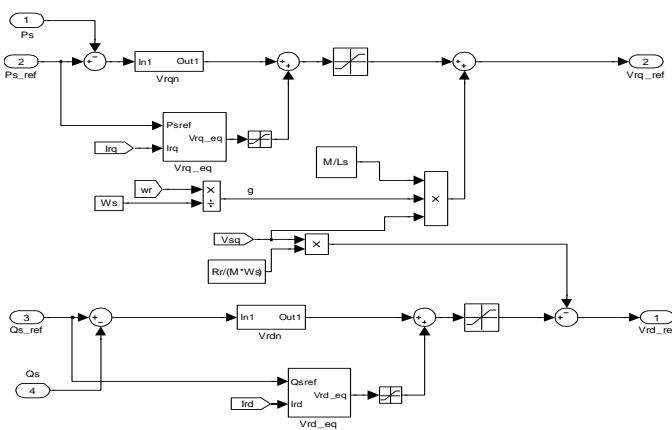

Figure 11. Direct SMC of the DFIG under Matlab/Simulink

Figure 12. The subsystem "Direct SMC"

To verify the feasibility of the proposed control scheme, computer simulations were performed using Matlab/Simulink software.

The bloc diagram was realized and executed on an Intel(R) Core(TM) i3 PC having 2.20 GHz CPU, 4Go RAM.

For verified the robustness of the proposed control, we have proposed a random variable wind speed as shown in figure 13.

Figure 14 shows the turbine rotor speed. Figure 15 presents the power coefficient variation C_p, it is kept around its maximum

value $C_p = 0.5$.

The figure 16.a presents the stator active power and its reference profile injected into the grid. The stator reactive power and its reference profile are presented in figure 16.b. After these figures a very good decoupling obtained between the stator active and reactive power. It is clear that the actual stator active power follows its desired values using the proposed control with the presence of the oscillations produced by the chattering phenomena of the SMC, where the reactive power is maintained to zero to guarantee a unity power factor ($cos(\varphi) = 1$) at the stator side.

Figure 17 shows the DFIG stator current changes versus time and its zoom, it shows good sinusoidal currents, where the amplitude of this current increases when the wind speed increases.

Figure 18 shows the harmonic spectrum of the output phase stator current which obtained by using Fast Fourier Transform (FFT) technique. It can be clearly observed that the stator current has a low Total Harmonic Distortion (THD) where its value is 4.38%, as indicated in the figure 18. Where this value is acceptable according to "IEEE Std 519-1992" which recommended by "*require AC sources that have no more than 5% Total Harmonic Distortion*" [16].
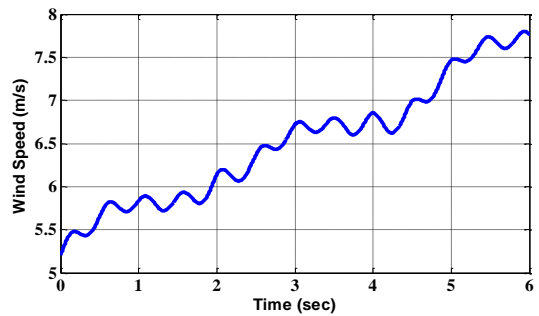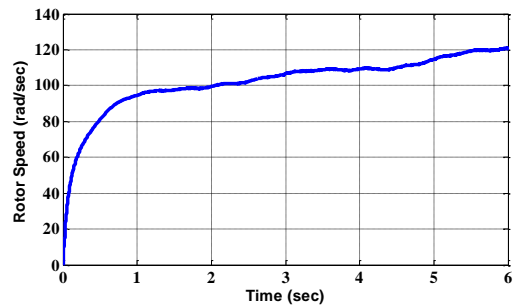

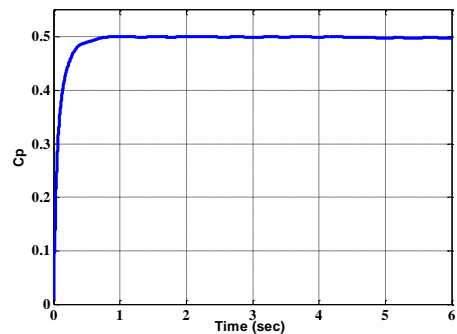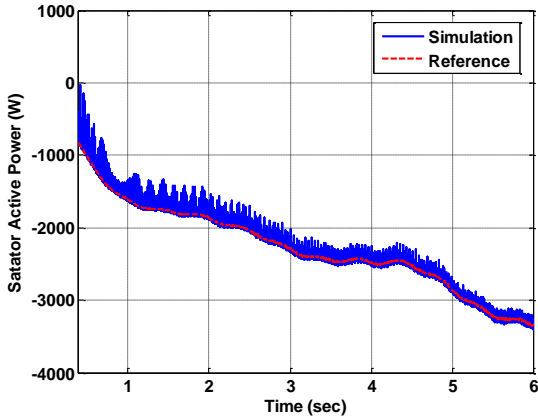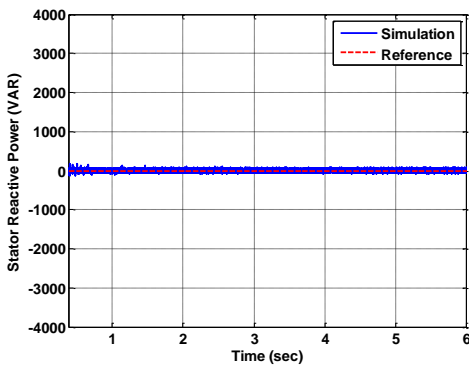**Figure 13. The proposed wind speed**

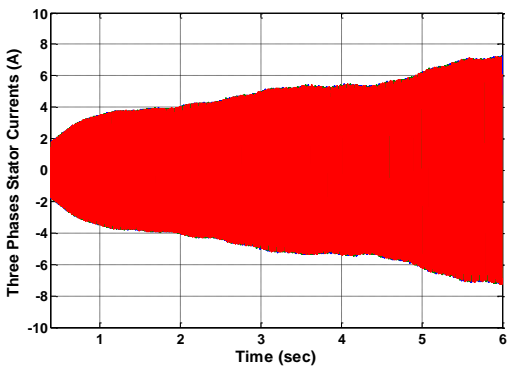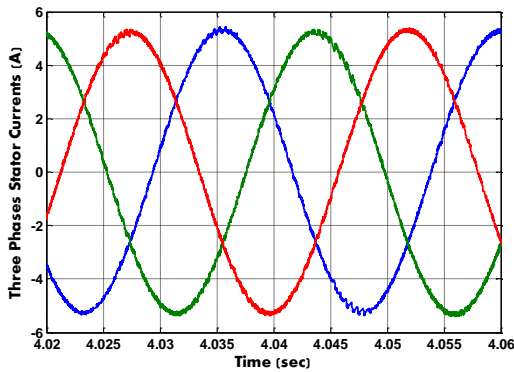**Figure 14. Rotor speed**

Figure 15. Power coefficient *Cp* variation

(a)

(b)

Figure 16. (a) Stator active and (b) reactive power

(a)

(b)

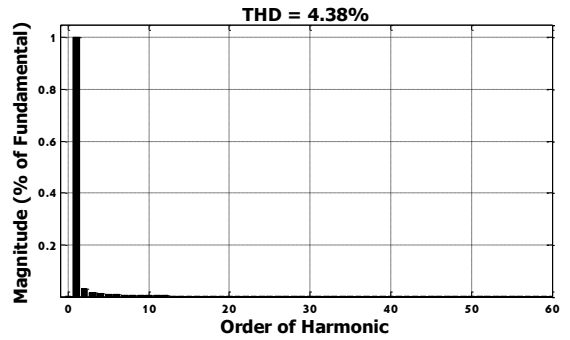**Figure 17. (a) Stator currents with (b) a zoom**

Figure 18. Spectrum of the stator current harmonics

8. CONCLUSION:

The numerical simulation of direct sliding mode control (SMC) for active and reactive power based on a DFIG driven by wind turbine using the space vector modulation (SVM) inverter has been studied and designed with Matlab/Simulink software. The SMC has been used for reference tracking of stator active and reactive power exchanged between the DFIG stator and the electrical grid by the control of the rotor inverter where the simulation results confirm a good dynamic performance and robustness of the proposed control.

In addition, we have used the SVM technique for the inverter control to improve the quality of energy injected into the electrical grid, which this technique allows the minimizing of stator current harmonics and wide linear modulation range where the THD of the stator current has the value 4.38% (<5% according IEEE Std 519-1992).

APPENDIXES

Appendix A. System parameters

DFIG data: Rated values: 4 kW, 220/380 V, 50Hz, 15/8.6 A   Rated parameters: R_s = 1.2 Ω R_r = 1.8 Ω L_s = 0.1554 H L_r = 0. 1568 H M = 0.15 H P = 2   Mechanical constants: J = 0.2 Kg.m^2 f = 0.001 N.m.s/rad
Wind turbine data: R = 3 *m*, G = 5.4, Number of blades =3
Air density value: $\rho = 1.22 Kg / m^3$

Appendix B. Nomenclature

Turbine

Ω_{mec}	mechanical speed of the DFIG
Ω_t	turbine speed
P_m	reference mechanical power
C_p	power coefficient
C_{p_max}	maximum power coefficient
v	wind speed
λ	tip speed ratio
λ_{opt}	optimum tip speed ratio
β	pitch angle
R	blade length
	gear box

DFIG

P_s, Q_s	active and reactive stator power
P_r, Q_r	active and reactive rotor power
V_{sd}, V_{sq}, V_{rd}, V_{rq}	stator and rotor d-q frame voltages
ϕ_{sd}, ϕ_{sq}, ϕ_{rd}, ϕ_{rq}	stator and rotor d-q frame fluxes
i_{sd}, i_{sq}, i_{rd}, i_{rq}	stator and rotor d-q frame currents
R_s, R_r	stator and rotor resistances
L_s, L_r	stator and rotor inductances
M	mutual inductance
σ	leakage factor
T_s, T_r	statoric and rotoric time-constant
Ω	DFIG speed
C_e	electromagnetic torque
C_r	load torque
J	moment of inertia
f	friction coefficient
P	number of pole pairs
ω_s, ω	stator and rotor angular speed
g	slip coefficient

Sliding mode control

S, $\sigma_s(x,t)$	sliding surface
sgn	sign function
	saturation function
x	state vector
x_d	desired state vector

$[.]^T$	transposed vector
	control vector
u^{eq}	equivalent control vector
u^n	switching part of the control
k_f	controller gain
e	error vector
τ	positive coefficient
n	system order
η	positive constant

Subscripts

d, q	synchronous d-q axis
s, r	stator, rotor

Superscripts

" * "	reference value
" . "	derivative value

Acronyms

DFIM	Doubly Fed Induction Machine
DFIG	Doubly Fed Induction Generator
WECS	Wind Energy Conversion System
MPPT	Maximum Power Point Tracking
PWM	Pulse Width Modulation
SVM	Space Vector Modulation
SMC	Sliding Mode Control
THD	Total Harmonic Distortion

REFERENCES

[1] D. Seyoum, M. Rahman, C. Grantham, "Terminal voltage control of a wind turbine driven isolated induction generator using stator oriented field control", Applied Power Electronics Conference and Exposition, APEC '03. Eighteenth Annual IEEE, Vol. 2, February 2003, pp. 846–852.

[2] K. Ghedamsi, D. Aouzellag, EM. Berkouk, "Application of matrix converter for variable speed wind turbine driving a doubly fed induction generator", In: SPEEDAM'06, Italy.

[3] G. Q. Wu, H. J. Ni, G. X. Wu, J. L. Zhou, W. N. Zhu, J. F. Mao, Y. Cao, "On maximum power point tracking control strategy for variable speed constant frequency wind power generation", Journal of Chongqing University (English Edition), Vol. 9, No. 1, 2010, pp. 21–28.

[4] A. Hazzab, B. Ismail Khalil, M. Kamli, M. Rahli, "Adaptive fuzzy PI sliding mode controller for induction motor speed control", International Journal of Emerging Electric Power System, Vol. 4, No. 1, 2005, pp. 1-13.

[5] V. Katic, D. Graovac, "A method of real analysis of AC/DC converter line side harmonics, Electronics and Energetics", Vol. 10, No. 1, 1997, pp. 107-123.

[6] A. Jidin, T. Sutikno, "MATLAB/SIMULINK based analysis of voltage source inverter with space vector modulation", TELKOMNIKA, Vol. 7, No. 1, April 2009, pp. 23-30.

[7]   M. Rahimi, M. Parniani, "Dynamic behavior analysis of doubly-fed induction generator wind turbines-The influence of rotor and speed controller parameters", Int. J. Electric. Power Energy Syst., Vol. 32, No. 5, 2010, pp. 464-477.

[8]   K. Ghedamsi, D. Aouzellag, "Improvement of the performances for wind energy conversions systems", Int. J. Electric. Power Energy Syst., Vol. 32, No. 9, 2010, pp. 936-945.

[9]   E. S. Abdin, W. Xu, "Control design and dynamic performance analysis of wind turbine-induction generator unit", IEEE Trans. On Energy Convers. Vol. 15, No. 1, 2000, pp. 91-96.

[10]   M. Machmoum, F. Poitiers, "Sliding mode control of a variable speed wind energy conversion system with DFIG", International Conference and Exhibition on Ecologic Vehicles and Renewable Energies, MONACO, March 26-29, 2009.

[11]   N. Senthil Kumar, J. Gokulakrishnan, "Impact of FACTS controllers on the stability of power systems connected with doubly fed induction generators", Int. J. Electric. Power Energy Syst., Vol. 33, 2011, pp. 1172-1184.

[12]   Y. BEKAKRA, D. BEN ATTOUS, "A sliding mode speed and flux control of a doubly fed induction machine", IEEE Conference on Electrical and Electronics Engineering, Bursa, Turkey, 2009, pp. 174–178.

[13]   J. Lo, Y. Kuo, "Decoupled fuzzy sliding mode control", IEEE Trans. Fuzzy Syst., Vol. 6, No. 3, 1998, pp. 426-435.

[14]   Y. BEKAKRA, D. BEN ATTOUS, "Comparison between fuzzy sliding mode and traditional IP controllers in a speed control of a doubly fed induction motor", ECTI Transactions on Electrical Eng., Electronics, and Communications, Vol. 10, No. 2, August 2012, pp. 181-189.

[15]   B. P. Panigrahi, D. Prasad, S. SenGuptu, "A simple hardware realization of switching table based direct torque control of induction motor", Electric Power Systems Research, Vol. 77, 2007, pp. 181-190.

[16]   IEEE Std 519-1992, "IEEE recommended practices and requirements for harmonic control in electrical power systems", New York, IEEE Industry Applications Society, ISBN 1-55937-239-7, April 1993, pp. 1-112.

Biographies

Youcef BEKAKRA was born in El-Oued, Algeria in 1984. He received the B.Sc degree in Electrical Engineering from El-Oued University, Algeria in 2007. His MSc degree from El-Oued University in 2010. In 2014, he received his PhD degree in Electrical Engineering from Biskra University, Algeria. His areas of interest are renewable energy, Electrical Drives and Process Control, application of Artificial Intelligence techniques for control and optimize electric power systems. He is member of the LEVRES research Laboratory.

Djilani BEN ATTOUS was born in El-Oued, Algeria in 1959. He received his Engineer degree in Electrotechnics from Polytechnic National Institute Algiers, Algeria in 1984. He got MSc degree in Power Systems from UMIST England in 1987. In 2000, he received his doctorate of state (PhD degree) from Batna University, Algeria. He is currently associate professor at El-Oued University, Algeria in Electrical Engineering. His research interests in Planning and Economic of Electric Energy System, Optimization Theory and its applications and he also investigated questions related with Electrical Drives and Process Control. He is member of the VTRS research Laboratory.

Laid ZELLOUMA was born in El-Oued, Algeria in 1980. He received the B.Sc degree in Electrical Engineering from Biskra University, Algeria in 2004. His MSc degree from Annaba University in 2006. In 2010, he received his PhD degree in Electrical Engineering from Annaba University, Algeria. His areas of interest are renewable energy, Electrical Drives and Process Control. He is member of the LEVRES research Laboratory.

Filtering of Harmonics in DC Traction Substation

Article · June 2017

3 authors:

Yacine Djeghader
Université Mohamed Chérif Messaadia de Souk-Ahras
23 PUBLICATIONS   **73** CITATIONS

SEE PROFILE

Zellouma Laid
El-Oued University
33 PUBLICATIONS   **191** CITATIONS

SEE PROFILE

Chelli Zoubir
Faculty of Science & Technology
13 PUBLICATIONS   **21** CITATIONS

SEE PROFILE

Some of the authors of this publication are also working on these related projects:

Harmonic current identification View project

power quality improvement View project

FILTERING OF HARMONICS IN DC TRACTION SUBSTATION SYSTEM

Y .DJEGHADER[1], L.ZELLOUMA[2]

[1] Department of Electrical Engineering, University of Mohamed-Cherif Messaadia ,Souk Ahras, ALGERIA .
E-mail : djeghaderyacine@yahoo.fr , and yacine.djeghader@univ-soukahras.dz
[1]LEER Laboratory University of Mohamed-Cherif Messaadia ,Souk Ahras, ALGERIA;
[2]Department of Electrical Engineering, University of Echahid Hamma Lakhdar ,El-Oued, ALGERIA.

Z.CHELLI[1]

[1] Department of Electrical Engineering, University of Mohamed-Cherif Messaadia ,Souk Ahras, ALGERIA.
[1]LEER Laboratory University of Mohamed-Cherif Messaadia ,Souk Ahras, ALGERIA;

Abstract: The railways are the most important and modern means of transportation are used to transport a large number of people, and also used in the industrial field to transport heavy weight and raw materials for very long distances. Direct current (DC) electrified railway systems show many power quality problems such as harmonic, reactive power, unbalanced and low power factor. Our study concentrated on the propagation of currents harmonics in the electric network and their filtering solutions. In this article we made a model in Matlab/Simulink of a real DC traction substation which is located in the mineral line Tebessa - Annaba (in east of Algeria), this line transport raw materials such as iron and phosphate. We present in this work to mitigate harmonic currents the passive filtering, using filters (tuned at frequencies 11 and 13) at two different locations before and after the transformer which freedies the DC traction substation. The results of simulations with the proposed solution give the best results with minimum values of total harmonic distortion (THD) in both cases.

Keywords –Electrification, DC Traction Substation, Filtering Harmonics, Power Quality, Passive filter, Railway System.

1. Introduction

Electricity has become the primary source of traction power in modern railways .While the diesel or coal driven trains are still heavily used in some countries , they are often limited to long distance commutation and/or freight transportation [1].

The electric traction system is the most efficient traction system. It offers several benefits over other systems, including quick start and stop, very efficient, pollution free, easy to handle and easy speed control [2]. The DC electric traction system plays again an important role for domain of transportation because of high efficiency, heavy ridership and fast transportation of series DC motor (high initial torque) , and we note that DC train consumes less energy compared to alternating current (AC) unit for operating same service conditions [2-3].

However, the DC electrified railways cause a lot of problems for the power quality such as injecting harmonics (high THD); reactive power , and low power factor issue [4-5]. In this paper we concentrated on filtering of currents harmonics generated by the DC electric traction units in a railway system by using passive filter which installed on different locations of transformer feeding (before , after).

These solutions are cheap, economy and work in the middle and high voltage, eliminate negative sequence current, and also participate in the compensation of the reactive power deficit thus improving the power factor of the power networks [5, 6].

2. Description of DC traction substation

With the development of electrified railway, electric locomotive was applied in railway transportation more and more widely [4]. And they can be harmed security on power system network, production and manufacture badly and more then electrified railway security and reliability in the railway transportation [6-7].

The electrical system studied is DC traction station that exists in the mineral line between the two cities Tebessa and Annaba (eastern Algeria).

The schematic diagram of the system studied is shown in Figure 1.

This series connection of two 6-pulse converter bridges requires two three-phase systems feed by a three winding transformers with star/star/triangle connections (Y/Y/Δ) which are spaced from one another by 30 electrical degrees, that is to say form a 12-pulse rectifier. This grouping of rectifiers has the advantage of eliminating the harmonics (5th and 7th) on the AC side [7-8].

The positive output of the group rectifier (3KV DC) is transmitted along the track via overhead contact (catenary) , and feeds an electric locomotive (3600 horsepower), while the negative output will be connected to the rail (Figure 1). This locomotive consists of six series DC traction motors, each of which is powered by a 750 V voltage through a chopper [8].
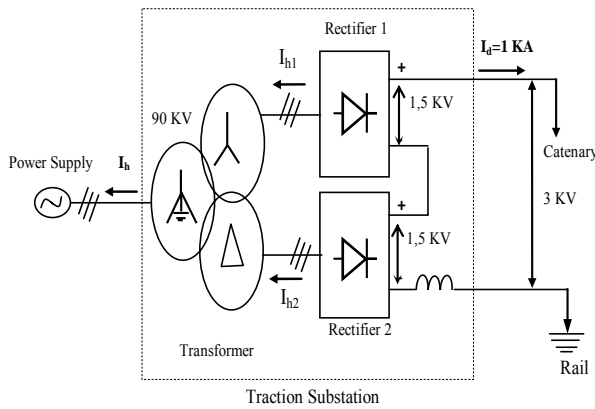
Fig.1. DC traction substation supply

3. Harmonic filtering

We used in this article passive filters which are a classic methods for power quality improvement , consist of series LC tuned for removing a specific harmonic or blocking a bandwidth of severe harmonics of nonlinear loads current [9].

For mitigating the harmonic distortion passive filtering is the simplest conventional solution. The most commonly used passive filter is the single tuned filter. This filter is simple and least expensive as compared with other means for mitigating the harmonic problems [10]. These filters have low impedances for the tuned frequencies such as 11th and 13th (used in our application).

Low cost is a great benefit of these filters. These filters are always connected in parallel across the network [6-10].

3.1. Principle of passive filtering

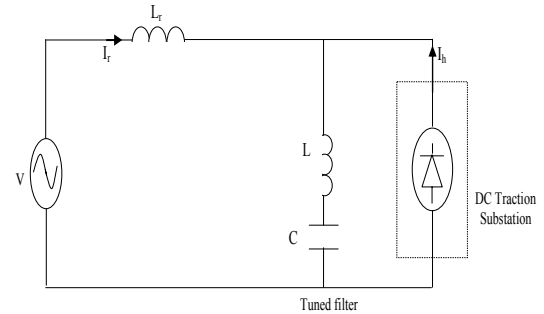The single tuned filter connected to the network is represented in Figure 2.

Fig. 2. Single phase equivalent circuit diagram of a filter connected in parallel on the network

With:
L_r : The inductance of the network
V : Voltage of the line.
I_r : Current of line
I_h : Harmonics currents equivalent to the « DC traction substation ».
L & C: Parameters of passive filter
Impedance of filter branch is given by

$$Z = j\left(L\omega - \frac{1}{C\omega} \right) \qquad (1)$$

ω : angular frequency

Resonant filter is given by the equation (2):

$$L\omega_r = \frac{1}{C\omega_r} \; ; \; and \quad f_r = \frac{1}{2\pi\sqrt{LC}} \qquad (2)$$

The capacitive or inductive reactance which corresponds to the frequency is:
Hence: $\omega_r^2.L.C = 1$

In harmonic regime:

$$X_{Lh} = hX_L \; ; and \quad X_{Ch} = \frac{X_C}{h} \qquad (3)$$

In the case of resonance: $X_{Lh} = X_{Ch}$

$$X_r = L.\omega_r = \frac{1}{C\omega_r} \qquad (4)$$

Therefore:

$$hX_L = \frac{1}{C\omega_r} \qquad (5)$$

$$hX_L = \frac{X_C}{h} \qquad (6)$$

Either: $h^2 = \dfrac{X_C}{X_L}$ (7)

Hence: $h = \sqrt{\dfrac{X_C}{X_L}}$ (8)

But we can express in terms of reactive power "Q" and short-circuit power "S_{cc}". As follows:

$h = \sqrt{\dfrac{S_{cc}}{Q}}$ (9)

With:

h: order harmonic resonance producing parallel

Anti-resonance is given by the following formula:

$\omega_{ar} = 2\pi f_{ar} = \dfrac{1}{\sqrt{(L_r + L)C}}$ (10)

3.2. Use of multiple filters
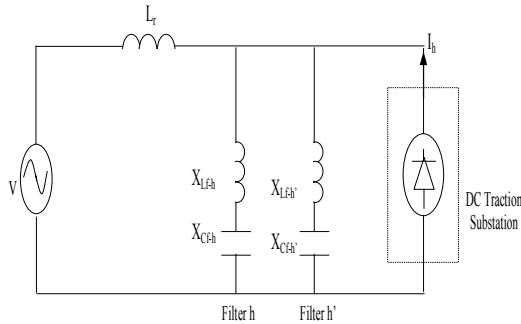
In our work we use two tuned filters to both harmonics h=11 and h'=13

Fig. 3. Equivalent circuit diagram of a tow tuned filters connected

This method requires several conditions to achieve [7]:

$h^2 = \dfrac{X_{Cf-h}}{X_{Lf-h}}$ (11)

$h^{2'} = \dfrac{X_{Cf-h'}}{X_{Lf-h'}}$ (12)

$\dfrac{V^2}{X_{Cf-h} - X_{Lf-h}} + \dfrac{V^2}{X_{Cf-h'} - X_{Lf-h'}} = Q$ (13)

$Z_{f-h}' = \dfrac{h'}{h}.Z_{f-h}$ (14)

After simplification we find the generalized formulas for the use of multiple filters at the same place [7].

$X_{Lf-h} = \dfrac{(h+h').V^2}{(h^2-1).h'Q}$ (15)

$X_{Cf-h} = \dfrac{h^2(h+h').V^2}{(h^2-1).h^2Q}$ (1

$X_{Lf-h'}' = \dfrac{(h+h').V^2}{(h^{2'}-1).hQ}$ (17)

$X_{Cf-h'} = \dfrac{h^{2'}(h+h').V^2}{(h^{2'}-1).hQ}$ (18)

With :

h & h': Order harmonic of filter 11and filter 13.

Q : Reactive power at the filtering place

V : Voltage at the site of filtage

X_{Lf-h} and X_{Cf-h} : Parameters of the filter 11

$X_{Lf-h'}$ and $X_{Cf-h'}$: Parameters of the filter 13

4. Simulation results
4.1. Operation without filtering

We used Power System Toolbox in MATLAB /Simulink ; by affecting the true values (see Annex 1 & 2) for our DC traction substation studied.

In the following figures we present the differents waveforms of the voltages and currents during normal operation of DC traction substation.
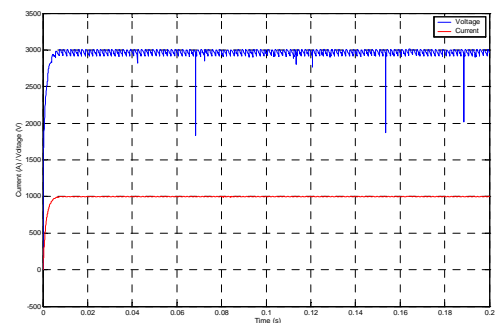

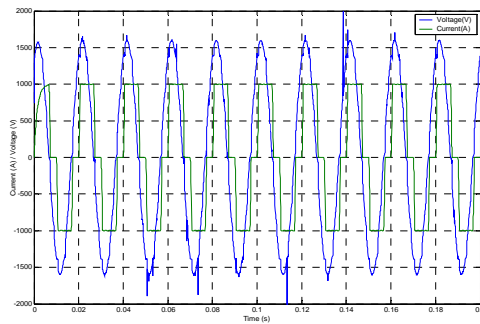Fig. 4. Waveform of the Voltage & Current at the output of group rectifier

Fig. 5. Waveform of the voltage /current absorbed of rectifier (Y/Y)
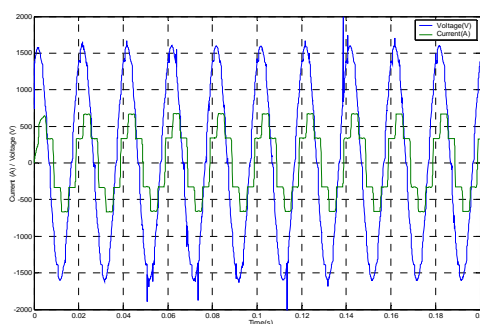

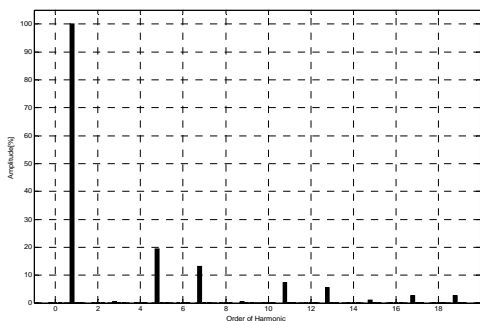Fig. 6. Waveform of the voltage /current absorbed of rectifier (Y/Δ)

Fig. 7. Harmonic Spectrum of current harmonic absorbed by one rectifier
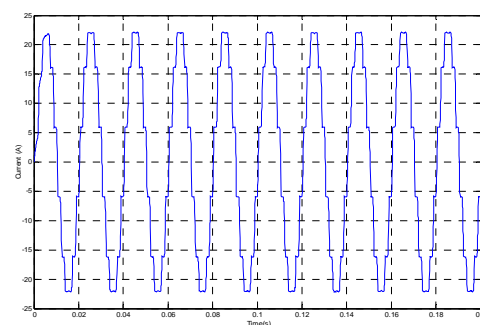

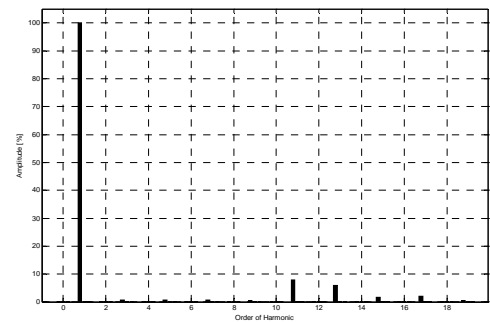Fig. 8. Waveform of the current injected in electric network

Fig. 9. Harmonic Spectrum of current harmonic injected

In figure 7, we see that the current harmonics that exist are of the form $6k \pm 1$ (with k integer), so we can see the existence of 5, 7, 11,13, ..., since the load of pollution is a three-phase rectifier and also marks a high value of **THD = 26.31%.**

From the figure 9 we see the elimination of harmonic of the 5th and 7th order and it returns to the advantage is the use of transformers with three connections Y / Y / Δ (formation of a 12 pulse rectifier), the remaining harmonics are the form $12k \pm 1$ (with integer k) ie, 11,13, ..., the value of **THD = 10.38%** is still higher than the standard, it is for this reason we think of the passive filtering solution with implementations of tuned filters in 11th and 13th before and after the power transformer.

4.2. Operation with filtering

4.2.1. Filtering before transformer (Case 1)

Since the harmonic characteristics that have large amplitudes are 11th and 13th; so the idea is to install two tuned filters corresponding to these harmonics as shown in the following figure 10.
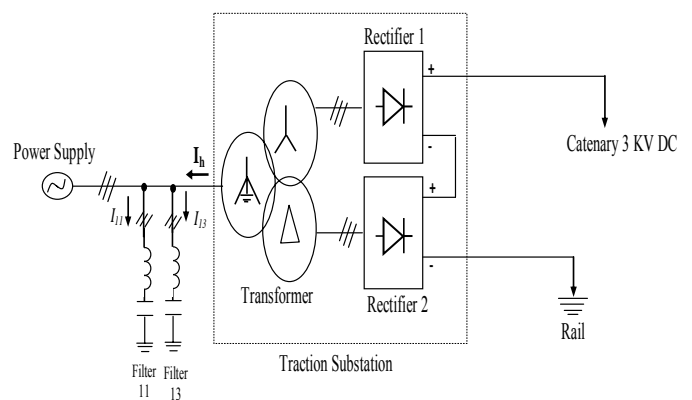

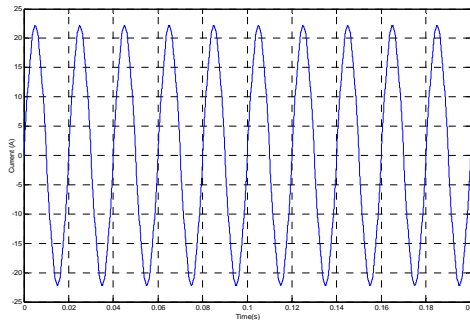Fig. 10. Systems studied with passive filtering (case 1)

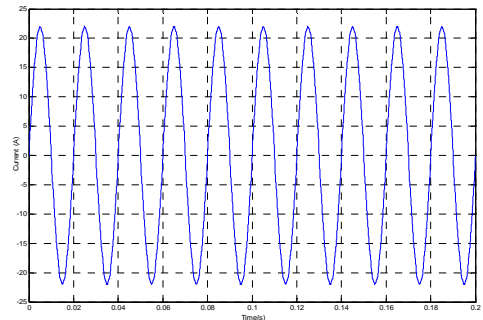Fig. 11. Waveform of the current injected (I_h) in electric network with passive filter (case 1)

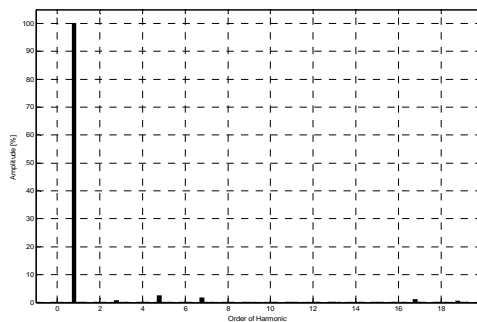Fig. 12. Harmonic Spectrum of current harmonic injected with filtering (case 1)

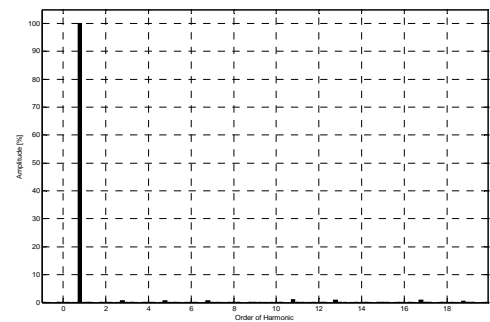Fig. 14. Waveform of the current injected (I_h) in electric network with passive filter (case 2)

Fig. 15. Harmonic Spectrum of current harmonic injected with filtering (case 2)

4.2.2. Filtering after transformer (Case 2)

It is known that 5th and 7th harmonics are theoretically removed before transformer (do not propagate through the electric network); so the idea will be oriented towards eliminating harmonic 11th and 13th with the use of passive filters tuned to these frequencies to just before the three-phase rectifiers as shown in the following figure 13.
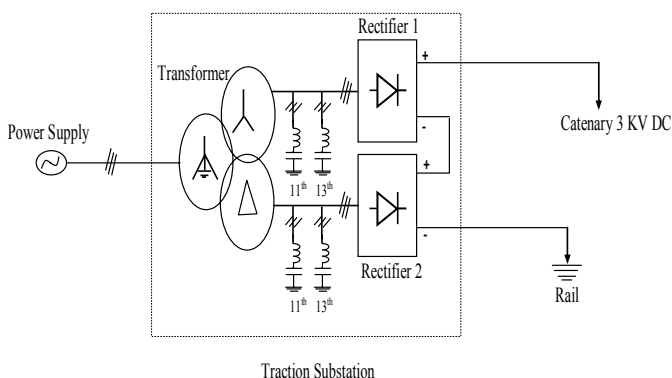

Fig. 13. Systems studied with passive filtering (case 2)

Table 1: Simulation Results

	Without Filtering	**With Filtering**	
		Case 1	**Case 2**
THD (%)	**10.38**	**3.24**	**1.98**
h_5 [%]	0.80	2.48	0.72
h_7 [%]	0.68	1.65	0.62
h_{11} [%]	7.88	0.06	1.03
h_{13} [%]	6.00	0.01	0.83

5. Conclusion

Harmonic disturbances cause damage to power systems and can sometimes be dangerous. This result in overloads, reduced service life and, in some circumstances, can lead to premature failure of electrical and electronic equipment. . In this paper we have used the simplest and most efficient method of attenuating harmonic currents as passive filtering and we have chosen to filter the harmonics 11 and 13 with the use of tuned filters because it is known that the harmonics of Current which propagate in the electrical network, they are with these frequencies.

To achieve this solution in the best way we chose two locations for the installation of these filters (before, and after the transformer that supplies the traction station).

Finally, the simulation results obtained give a minimum value of the current THD injected into the network in the case of filtering after the transformer (medium voltage) and the filtering before the transformer (high voltage).

Annex 1: Characteristic of DC Traction Substation

Coupling transformer	Yn-Dy
Number of tapping points of the tension	0.5 (+ or - 4 to + or - 8% A)
Nominal voltage network side	90 kV
Effective cell side load voltage	1.236 kV
Short circuit voltage	6.7% V
Current cell side	817 A (for the delta winding)
Current cell side	844.4 A (for winding star)
Supports loss (power at rated voltage)	24 kw
Total loss (power at rated voltage)	31.7 kilowatts
Dynamic short-circuit current	0.85 kA
Thermal short circuit current	0.33 kA

Annex 2: Characteristic of the Rectifier Group

| Number of diode in series with the bridge arm.	1
Number of parallel diode bridge arms	4 + 1 = 5
Total number of rectifier diodes	2x30 = 60
Input Rated current (AC side).	577 A
Nominal output current (continuous rating)	1000 A
Actual DC voltage (at the output of the rectifier group)	3310 V
Nominal voltage charge (at the exit of the group)	3240 V
Current DC front (DC side)	16.7 kA
Losses block transformer - rectifier (charging)	38.24 kw
Rated inductance	0.2 mH

References

1. A. Szeląg, T. Maciołek. : *A 3 kV DC electric traction system modernisation for increased speed and trains power demand problems of analysis and synthesis*. In: Przegląd Elektrotechniczny, Vol 89, No. 3a, 2013, p. 21-28.

2. J.Sun, Y.Duan, Y.Xiong, and B. Zhang ; *Study of Reactive Power Compensation for High Speed Railway Design* . In: Energy Procedia, Vol. 17, No.1, 2012, p 414-421.

3. T. Suzuki, H. Hayashiya, T. Yamanoi, and K. Kawahara. : *Application examples of energy saving measures in Japanese DC feeding system* . In: Proc.14th International Power Electronics Conf., Hiroshima, Japan, May 2014, p. 1062-1067.

4. W-A.Jager, M. Huizer, and E. K. H van der Pols. : *Implementation of an active regeneration unit in a traction substation* . In: Proc.16th European Conf. On Power Electronics and Applications, Lappeenranta, Finland, Aug. 2014, p.1-9.

5. M. Popescu and A. Bitoleanu. : *Simulink library for reference current generation in active DC traction substations* . In: International Journal of Electrical, Computer, Energetic, Electronic and Communication Engineering, Vol. 9, No. 8, 2015, p. 578 – 585.

6. Y.Djeghader and L.Zellouma. : *Using Hybrid Power Filter to Mitigate Currents and Voltages Harmonics in Three Phase System* . In: Acta Electrotechnica et Informatica, Vol 15, No. 4, 2015, p 37-43.

7. Y.Djeghader, L. Zellouma,H.Labar, R. Toufouti and Z.Chelli. : *Study and Filtering of Harmonics in a DC Electrified Railway System* . In : Proceedings of the 7th IEEE International Conference on Modelling, Identification and Control, Sousse, TUNISIA, 2015, p.765-770.

8. Archive of the National Company for Railway Transport; Annaba –Algeria-.

9. M. Brenna, F. Foiadelli. : *Analysis of the Filters Installed in the Interconnection Points Between Different Railway Supply Systems* . In: IEEE Transactions on Smart Grid, Vol. 3, No. 1, March 2012, p. 551-558.

10. K.-W. Lao, N. Dai, W.-G. Liu, and M.-C. Wong. : *Hybrid power quality compensator with minimum DC operation voltage design for high-speed traction power systems* . In: IEEE Trans. Power Electron., Vol. 28, No. 4, 2013, p. 2024 - 2036.

Author's Accepted Manuscript

Flatness-based adaptive neurofuzzy control of Induction Generators using output feedback

G. Rigatos, P. Siano, Z. Tir, M. Assad
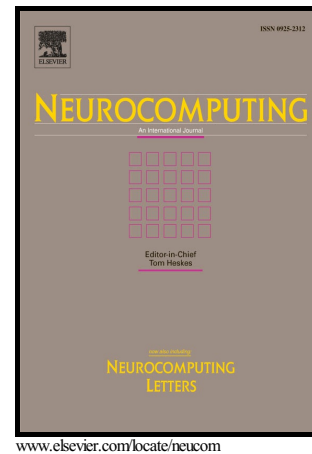
Cite this article as: G. Rigatos, P. Siano, Z. Tir and M. Assad, Flatness-based adaptive neurofuzzy control of Induction Generators using output feedback, *Neurocomputing,* http://dx.doi.org/10.1016/j.neucom.2016.08.040

Flatness-based adaptive neurofuzzy control of Induction Generators using output feedback

G. Rigatos[a]

[a]Unit of Industrial Automation
Industrial Systems Institute
26504, Rion Patras, Greece
e-mail: grigat@ieee.org

Z. Tir[c]

[c]Dept. of Electrical Engineering
University of El-Oued
El-Oued 39000, Algeria
e-mail: tir-zoheir@univ-eloued.dz

P. Siano[b]

[b]Department of Industrial Eng.
University of Salerno
84084 Fisciano, Italy
e-mail: psiano@unisa.it

M. Assad[d]

[d]Department of Electronics
Ouargla University
Ouargla, 3000, Algeria
e-mail: hamida.mohamedassaad@univ-ouargla.dz

Abstract: The functioning of doubly-fed induction generators (DFIGs) under harsh and varying conditions makes their control a non-trivial task. The article proposes an adaptive control approach that is capable of compensating for model uncertainty and parametric changes of the DFIG, as well as for lack of measurements for the DFIG's state vector elements. First it is proven that the DFIG's model is a differentially flat one. This means that all its state variables and its control inputs can be written as differential functions of key state variables which are the so-called flat outputs. Moreover, this implies that the flat output and its derivatives are linearly independent. By exploiting differential flatness properties it is shown that the 6-th order DFIG model can be transformed into the linear canonical form. For the latter description, the new control inputs comprise unknown nonlinear functions which can be identified with the use of neurofuzzy approximators. The estimated dynamics of the generator is used by a feedback controller thus establishing an indirect adaptive control scheme. Moreover, to robustify the control loop a supplementary control term is computed using H-infinity control theory. Another problem that has to be dealt with comes from the inability to measure the complete state vector of the generator. Thus, a state-observer is implemented in the control loop. The stability of the considered observer-based adaptive control approach is proven using Lyapunov analysis. Moreover, the performance of the control scheme is evaluated through simulation experiments.

1 Introduction

The article presents new results on the control of Doubly-fed Induction Generators (DFIGs) with the use of differential flatness theory and adaptive control theory. The control problem of DFIGs is nontrivial because the dynamic model of such electric machines is a multi-variable and nonlinear one. Moreover, under

1

real operating conditions it exhibits parametric variations and is subjected to external perturbations. As a result, empirical model-free control approaches of the PID-type lack stability and robustness, remain functional only round local operating points and in general are proven to be inefficient. DFIG control in stand-lone functioning mode has been analyzed in [1-9]. In particular control schemes exhibiting adaptivity features have been presented in [10-11]. Distributed control of DFIGs and their functioning when interacting with the power grid has been studied in [12-13]. The performance of specific DFIG control schemes under external perturbations has been presented in [14-17]. Moreover, the problem of sensorless control of DFIGs has been studied in [18-20]. Additional results on the use of neuro-fuzzy controllers in induction generators can be found in [21-23] (however stability proofs for such control schemes is not always given). Moreover, results on the use of robust controllers in asynchronous power generators can be found in [24-26]. Such approaches require partial knowledge of the generator's model as well as of the disturbances affecting it. Furthermore, attempts to apply dynamic programming-based techniques for control of power generation systems can be found in [27-28] (again without always providing a stability proof).

To cope with the DFIG control problem, in this article the differential flatness properties of the DFIG model are exploited. It is proven that the rotor's turn speed and the stator's magnetic flux of this electric machine are flat outputs which means that all other state variables and the control inputs of the DFIG can be expressed as differential functions of these outputs [29-36]. Moreover, it is proven that the flat outputs and their derivatives are linearly independent. This comes to complete the proof about the differential flatness of the DFIG model [37-38].

The differential flatness of the DFIG implies also that the transformation of its dynamic model to the linear canonical (Brunovsky) form is possible. After such a transformation the implementation of a stabilizing feedback controller for the generator is enabled. This solution to the control problem would be complete if no model uncertainty and parametric variations of the DFIG existed. Actually, it is assumed that only the order of the DFIG's state-space model is known while its parameters and the specific form of its state-space equations are completely unknown. In the linearized equivalent model of the generator this uncertainty takes the form of unknown functions which appear as part of the system's transformed control inputs. This unknown part of the system's dynamics is identified with the use of neurofuzzy approximators. The estimates of the DFIG's dynamics are used by a state feedback controller thus establishing an indirect adaptive control scheme. The learning procedure for these estimators is defined by the requirement to assure negative definiteness for the system's Lyapunov function [36-37]. Another issue that arises is that the state vector that is fed into the controller is partially measurable, and the missing state vector elements have to be estimated with the use of a state observer. By including such an observer in the control loop an output feedback-based control scheme is established. The stability of the control method is proven through Lyapunov analysis.

The structure of the article is as follows: in Section 2 the complete 6-th order dynamic model of the DFIG is analyzed. In Section 3 it is proven that the dynamic model of the DFIG is a differentially flat one, having as flat outputs the rotor's turn speed and the stator's magnetic flux. In Section 4 the concept of flatness-based adaptive control for multi-input multi-output (MIMO) nonlinear dynamical systems is explained. In Section 5 adaptive neurofuzzy control for the DFIG model is implemented. In Section 6 Lyapunov stability analysis is provided for the adaptive neurofuzzy control scheme of the DFIG. In Section 7 simulation experiments are carried out to evaluate the performance of the DFIG control scheme. Finally, in Section 8 concluding remarks are stated.

2

2 Dynamic model of the DFIG

2.1 The complete sixth-order model of the induction generator

The doubly-fed induction generator (DFIG) is not only the most frequently met technology in wind turbines due to its good performance, but it is also used in many other fields such as hydro-power generation, pumped storage plants and flywheel energy storage systems. The DFIG model is derived from the voltage equations of the stator and rotor. It is assumed that the stator and rotor windings are symmetrical and symmetrically fed. Usually, the saturation of the inductances, iron losses, and bearing friction is neglected. Moreover, the winding resistance is considered to be constant.

This type of wound-rotor machine is connected to the grid by both the rotor and stator side. The DFIG stator can be directly connected to the electric power grid while the rotor is interfaced through back-to-back converters (see Fig. 1). By decoupling the power system's electrical frequency and the rotor mechanical frequency the converter allows a variable speed operation of the wind turbine [37].
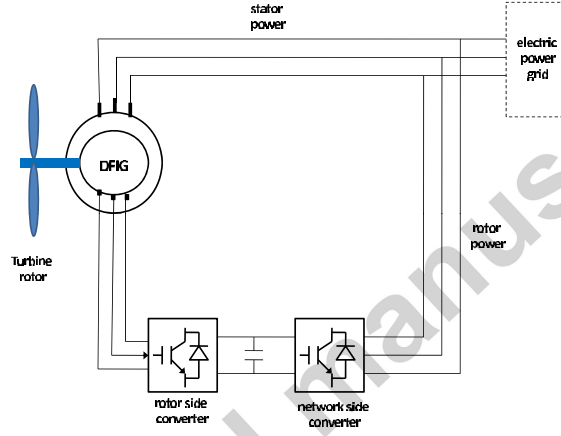

Figure 1: Configuration of a doubly-fed induction generator unit in the power grid

The doubly-fed induction generator is analogous to the induction motor. In an induction motor the stator voltage plays the role of an input variable, while the rotor voltage is a constant (it is usually zero). In case of the doubly-fed induction machine it is very similar but the other way round, with a dual analogy to hold between the stator and rotor parameters of the generator and the motor. This means that the rotor voltage now acts as an input, while the stator voltage depends on the voltage at the bus to which the DFIG is connected (which in the dq reference frame it is a constant parameter) [8],[37].

In a compact form, the doubly-fed induction generator can be described by the following set of equations in the $d - q$ reference frame that rotates at an arbitrary speed denoted as ω_{dq} [3], [37]

$$\frac{d\psi_{s_q}}{dt} = -\frac{1}{\tau_s}\psi_{s_q} - \omega_{dq}\psi_{s_d} + \frac{M}{\tau_s}i_{r_q} + v_{s_q} \tag{1}$$

$$\frac{d\psi_{s_d}}{dt} = \omega_{dq}\psi_{s_q} - \frac{1}{\tau_s}\psi_{s_d} + \frac{M}{\tau_s}i_{r_d} + v_{s_d} \tag{2}$$

$$\frac{di_{r_q}}{dt} = \frac{\beta}{\tau_s}\psi_{s_q} + \beta\omega_r\psi_{s_d} - \gamma_2 i_{r_q} - (\omega_{dq} - \omega_r)i_{r_d} - \beta v_{s_q} + \frac{1}{\sigma L_r}v_{r_q} \tag{3}$$

3

$$\frac{di_{r_d}}{dt} = -\beta\omega_r\psi_{s_q} + \frac{\beta}{\tau_s}\psi_{s_d} + (\omega_{dq} - \omega_r)i_{r_q} - \gamma_2 i_{r_d} - \beta v_{s_d} + \frac{1}{\sigma L_r}v_{r_d} \tag{4}$$

where ψ_{s_q}, ψ_{s_d}, i_{r_q}, i_{r_d} are the stator flux and the rotor currents, v_{s_q}, v_{s_d}, v_{r_q}, v_{r_d} are the stator and rotor voltages, L_s and L_r are the stator and rotor inductances, ω_r is the rotor's angular velocity, M is the magnetizing inductance. Moreover, denoting as R_s and R_r the stator and rotor resistances the following parameters are defined

$$\begin{matrix} \sigma = 1 - \frac{M^2}{L_r L_s} & \beta = \frac{1-\sigma}{M\sigma} & \tau_s = \frac{L_s}{R_s} \\ \tau_r = \frac{L_r}{R_r} & \gamma_2 = \left(\frac{1-\sigma}{\sigma\tau_s} + \frac{1}{\sigma\tau_r}\right) & \end{matrix} \tag{5}$$

The angle of the vectors that describe the magnetic flux $\psi_{s\alpha}$ and ψ_{sb} is first defined for the stator, i.e.

$$\rho = tan^{-1}\left(\frac{\psi_{s_b}}{\psi_{s_a}}\right) \tag{6}$$

The angle between the inertial reference frame and the rotating reference frame is taken to be equal to ρ.

Moreover, it holds that $cos(\rho) = \frac{\psi_{s_a}}{||\psi||}$, $sin(\rho) = \frac{\psi_{s_b}}{||\psi||}$, and $||\psi|| = \sqrt{\psi_{s_\alpha}^2 + \psi_{s_b}^2}$. Therefore, in the rotating $d-q$ frame of the generator, and under the condition of field orientation, there will be only one non-zero component of the magnetic flux ψ_{s_d}, while the component of the flux along the q axis equals 0.

The dynamic model of the doubly-fed induction generator can be also written in state-space equations form by defining the following state variables: $x_1 = \theta$, $x_2 = \omega_r$, $x_3 = \psi_{s_d}$, $x_4 = \psi_{s_q}$, $x_5 = i_{r_d}$ and $x_6 = i_{r_q}$. It holds that

$$\dot{x}_1 = x_2 \tag{7}$$

$$\dot{x}_2 = -\frac{K_m}{J}x_2 - \frac{T_m}{J} + \frac{\eta}{J}(i_{r_q}x_3 - i_{r_d}x_4) \tag{8}$$

$$\dot{x}_3 = -\frac{1}{\tau_s}x_3 + \omega_{dq}x_4 + \frac{M}{\tau_s}x_5 + v_{s_d} \tag{9}$$

$$\dot{x}_4 = -\omega_{dq}x_3 - \frac{1}{\tau_s}x_4 + \frac{M}{\tau_s}x_6 + v_{s_q} \tag{10}$$

$$\dot{x}_5 = -\beta x_2 x_4 + \frac{\beta}{\tau_s}x_3 + (\omega_{dq} - x_2)x_6 - \gamma_2 x_5 + \frac{1}{\sigma L_r}v_{r_d} - \beta v_{s_d} \tag{11}$$

$$\dot{x}_6 = \frac{\beta}{\tau_s}x_4 + \beta x_2 x_3 - (\omega_{dq} - x_2)x_5 - \gamma_2 x_6 + \frac{1}{\sigma L_r}v_{r_q} - \beta v_{s_q} \tag{12}$$

In the above set of equations J is the moment of inertia of the rotor, T_m is the externally applied mechanical torque that makes the turbine rotate, K_m is the friction coefficient, η is a variable that is associated to the number of poles and to the mutual inductance M. Variable η in turn determines the electrical torque T_e which is associated to rotor currents and stator magnetic flux. Eq. (7) to Eq. (12) can be written also in the form

$$\dot{x} = f(x) + g_a(x)v_{r_d} + g_b(x)v_{r_q} \tag{13}$$

where $x = [x_1, x_2, x_3, x_4, x_5, x_6]^T$ and

4

$$f(x) = \begin{pmatrix} x_2 \\ -\frac{K_m}{J}x_2 - \frac{T_m}{J} + \frac{n}{J}(i_{r_q}x_3 - i_{r_d}x_4) \\ -\frac{1}{\tau_s}x_3 + \omega_{dq}x_4 + \frac{M}{\tau_s}x_5 + v_{s_d} \\ -\omega_{dq}x_3 - \frac{1}{\tau_s}x_4 + \frac{M}{\tau_s}x_6 + v_{s_q} \\ -\beta x_2 x_4 + \frac{\beta}{\tau_s}x_3 + (\omega_{dq} - x_2)x_6 - \gamma_2 x_5 - \beta v_{s_d} \\ \frac{\beta}{\tau_s}x_4 + \beta x_2 x_3 - (\omega_{dq} - x_2)x_5 - \gamma_2 x_6 - \beta v_{s_q} \end{pmatrix} \tag{14}$$

$$g_a(x) = \begin{pmatrix} 0 & 0 & 0 & 0 & \frac{1}{\sigma L_r} & 0 \end{pmatrix}^T$$

$$g_b(x) = \begin{pmatrix} 0 & 0 & 0 & 0 & 0 & \frac{1}{\sigma L_r} \end{pmatrix}^T$$

The active and reactive power delivered by the DFIG stator are associated to the real and imaginary part of the power at the stator's terminals, i.e.

$$P_s = Re\{U_s I_s^*\} = v_{s_d} i_{s_d} + v_{s_q} i_{s_q} \tag{15}$$

$$Q_s = Im\{U_s I_s^*\} = v_{s_d} i_{s_q} - v_{s_q} i_{s_d} \tag{16}$$

3 Differential flatness properties of the DFIG

The flat outputs of the system are defined as [37-38]:

$$\begin{aligned} y_1 &= \theta \text{ or } y = x_1 \\ y_2 &= \psi_{s_d}^2 + \psi_{s_q}^2 \text{ or } y_2 = x_3^2 + x_4^2 \end{aligned} \tag{17}$$

It holds that

$$\begin{aligned} \dot{y}_1 &= \omega \text{ or } \dot{y}_1 = x_2 \Rightarrow \\ \ddot{y}_1 &= \dot{\omega} = -\frac{K_m}{J}x_2 - \frac{T_m}{J} + \frac{\eta}{J}(x_6 x_3 - x_5 x_4) \Rightarrow \\ \ddot{y}_1 &= \dot{\omega} = -\frac{K_m}{J}\dot{y}_1 - \frac{T_m}{J} + \frac{\eta}{J}(x_6 x_3 - x_5 x_4) \end{aligned} \tag{18}$$

Deriving the last row of Eq. (18) with respect to time one obtains

$$\begin{aligned} y_1^{(3)} &= -\frac{K_m}{J}\ddot{y}_1 + \frac{\eta}{J}(\dot{x}_6 x_3 + x_6 \dot{x}_3 - \dot{x}_5 x_4 - x_5 \dot{x}_4) \Rightarrow \\ y_1^{(3)} &= -\frac{K_m}{J}\ddot{y}_1 + \frac{\eta}{J}x_3\{[\frac{\beta}{\tau_s}x_4 + \beta x_2 x_3 + (\omega_{dq} - x_2)x_5 - \\ &\quad -\gamma_2 x_6 - \beta v_{s_q}] + \frac{1}{\sigma L_r}u_1\} + \frac{\eta}{J}x_6[-\frac{1}{\tau_s}x_3 + \omega_{dq}x_4 + \frac{M}{\tau_s}x_5 + v_{s_d}] \\ &\quad -\frac{\eta}{J}x_4\{[-\beta x_2 x_4 + \frac{\beta}{\tau_s}x_3 + (\omega_{dq} - x_2)x_6 - \gamma_2 x_5 - \\ &\quad -\beta v_{s_d}] + \frac{1}{\sigma L_r}u_2\} - \frac{\eta}{J}x_5[-\omega_{dq}x_3 - \frac{1}{\tau_s}x_4 + \frac{M}{\tau_s}x_6 + v_{s_q}] \end{aligned} \tag{19}$$

Moreover, about the second flat output it holds

$$\begin{aligned} \dot{y}_2 &= 2x_3\dot{x}_3 + 2x_4\dot{x}_4 \Rightarrow \\ \dot{y}_2 &= 2x_3[-\frac{1}{\tau_s}x_3 + \omega_{dq}x_4 + \frac{M}{\tau_s}x_5 + v_{s_d}] + \\ &\quad +2x_4[-\omega_{dq}x_3 - \frac{1}{\tau_s}x_4 + \frac{M}{\tau_s}x_6 + v_{s_q}] \Rightarrow \end{aligned} \tag{20}$$

Consequently, it holds

$$\begin{aligned} \ddot{y}_2 &= 2\dot{x}_3[-\frac{1}{\tau_s}x_3 + \omega_{dq}x_4 + \frac{M}{\tau_s}x_5 + v_{s_d}] + \\ &\quad +2x_3[-\frac{1}{\tau_s}\dot{x}_3 + \omega_{dq}\dot{x}_4 + \frac{M}{\tau_s}\dot{x}_5] + \\ &\quad 2\dot{x}_4[-\omega_{dq}x_3 - \frac{1}{\tau_s}x_4 + \frac{M}{\tau_s}x_6 + v_{s_q}] + \\ &\quad +2x_4[-\omega_{dq}\dot{x}_3 - \frac{1}{\tau_s}\dot{x}_4 + \frac{M}{\tau_s}\dot{x}_6] \end{aligned} \tag{21}$$

or equivalently

$$
\begin{aligned}
\ddot{y}_2 = {} & 2[-\tfrac{1}{\tau_s}x_3 + \omega_{dq}x_4 + \tfrac{M}{\tau_s}x_5 + v_{s_d}]^2 + \\
& -\tfrac{2}{\tau_s}x_3[-\tfrac{1}{\tau_s}x_3 + \omega_{dq}x_4 + \tfrac{M}{\tau_s}x_5 + v_{s_d}] \\
& -2\omega_{dq}x_3[-\omega_{dq}x_3 - \tfrac{1}{\tau_s}x_4 + \tfrac{M}{\tau_s}x_6 + v_{s_q}] \\
& +\tfrac{2M}{\tau_s}x_3\{[-\beta x_2 x_4 + \tfrac{\beta}{\tau_s}x_3 + (\omega_{dq} - x_2)x_6 - \\
& \qquad -\gamma_2 x_5 - \beta v_{s_d}] + \tfrac{1}{\sigma L_r}u_1\} \\
& +2[-\omega_{dq}x_3 - \tfrac{1}{\tau_s}x_4 + \tfrac{M}{\tau_s}x_6 + v_{s_q}]^2 \\
& -2\omega_{dq}x_4[-\tfrac{1}{\tau_s}x_3 + \omega_{dq}x_4 + \tfrac{M}{\tau_s}x_5 + v_{s_d}] \\
& -\tfrac{2}{\tau_s}x_4[-\omega_{dq}x_3 - \tfrac{1}{\tau_s}x_4 + \tfrac{M}{\tau_s}x_6 + v_{s_q}] \\
& 2x_4\tfrac{M}{\tau_s}\{[\tfrac{\beta}{\tau_s}x_4 + \beta x_2 x_3 + (\omega_{dq} - x_2)x_5 - \\
& \qquad -\gamma_2 x_6 - \beta v_{s_q}] + \tfrac{1}{\sigma L_r}u_2\}
\end{aligned}
\tag{22}
$$

It holds that $x_1 = y_1$, $x_2 = \dot{y}_1$. From the second row of Eq. (17) and considering that the field orientation condition requires $x_4 = \psi_{s_q} = 0$ one obtains that $x_3 = \sqrt{y_2}$. Moreover, from Eq. (18) it holds

$$
\begin{aligned}
\ddot{y}_1 = {} & -\tfrac{K_m}{J}\dot{y}_1 - \tfrac{T_m}{J} + \tfrac{\eta}{J}\sqrt{y_2}x_6 \Rightarrow \\
x_6 = {} & \tfrac{\ddot{y}_1 + \frac{K_m}{J}\dot{y}_1 + \frac{T_m}{J}}{\frac{\eta}{J}\sqrt{y_2}}, \ \ y_2 \neq 0
\end{aligned}
\tag{23}
$$

From Eq. (20) one obtains

$$
\begin{aligned}
\dot{y}_2 = {} & -\tfrac{2}{\tau_s}x_3^2 + \tfrac{2M}{\tau_s}x_3 x_5 + 2v_{s_d}x_3 \Rightarrow \\
\dot{y}_2 + {} & (\tfrac{2}{\tau_s}x_3 - 2v_{s_d})x_3 = \tfrac{2M}{\tau_s}x_3 x_5 \Rightarrow \\
x_5 = {} & \tfrac{\dot{y}_2 + (\frac{2}{\tau_s}\sqrt{y_2} - 2v_{s_d})\sqrt{y_2}}{\frac{2M}{\tau_s}\sqrt{y_2}} \ \ y_2 \neq 0
\end{aligned}
\tag{24}
$$

Therefore, x_5 is also a function of the flat output and of its derivatives. Additionally, by solving the system of Eq. (19) and Eq. (22) with respect to the control inputs u_1 and u_2 one obtains that the control inputs are functions of the flat output and its derivatives. Therefore, the model of the DFIG is a differentially flat one.

Next, to design the flatness-based controller for the DFIG the following transformation of the state variables is introduced: $z_1 = y_1$, $z_2 = \dot{y}_1$, $z_3 = \ddot{y}_1$, $z_4 = y_2$, $z_5 = \dot{y}_2$. Using a notation of variables as in the case of Lie algebra-based linearization it holds [1],[37]

$$
\begin{aligned}
\dot{z}_1 = {} & z_2 \\
\dot{z}_2 = {} & z_3 \\
\dot{z}_3 = {} & L_f^3 h_1(x) + (L_{g_a}L_f^2 h_1(x))u_1 + (L_{g_b}L_f^2 h_1(x))u_2 \\
\dot{z}_4 = {} & z_5 \\
\dot{z}_5 = {} & L_f^2 h_2(x) + (L_{g_a}L_f h_2(x))u_1 + (L_{g_b}L_f h_2(x))u_2
\end{aligned}
\tag{25}
$$

where

$$
\begin{aligned}
L_f^3 h_1(x) = {} & -\tfrac{K_m}{J}[-\tfrac{K_m}{J}x_2 - \tfrac{T_m}{J} + \tfrac{\eta}{J}(x_6 x_3 - x_5 x_4)] \\
& +\tfrac{\eta}{J}x_6[-\tfrac{1}{\tau_s}x_3 + \omega_{dq}x_4 + \tfrac{M}{\tau_s}x_5 + v_{s_d}] \\
& -\tfrac{\eta}{J}x_5[-\omega_{dq}x_3 - \tfrac{1}{\tau_s}x_4 + \tfrac{M}{\tau_s}x_6 + v_{s_q}] \\
& -\tfrac{\eta}{J}x_4[-\beta x_2 x_4 + \tfrac{\beta}{\tau_s}x_3 + (\omega_{dq} - x_2)x_6 - \gamma_2 x_5 - \beta v_{s_d}] \\
& +\tfrac{\eta}{J}x_3[\tfrac{\beta}{\tau_s}x_4 + \beta x_2 x_3 + (\omega_{dq} - x_2)x_5 - \gamma_2 x_6 - \beta v_{s_q}]
\end{aligned}
\tag{26}
$$

$$
L_{g_a}(L_f^2 h_1(x)) = -\tfrac{\eta}{J}\tfrac{1}{\sigma L_r}x_4
\tag{27}
$$

$$
L_{g_b}(L_f^2 h_1(x)) = \tfrac{\eta}{J}\tfrac{1}{\sigma L_r}x_3
\tag{28}
$$

6

and equivalently

$$
\begin{aligned}
L_f^2 h_2(x) = \\
(-\tfrac{4}{\tau_s} x_3 - \tfrac{2M}{\tau_s} x_5 + 2v_{s_d})[-\tfrac{1}{\tau_s} x_3 + \omega_{dq} x_4 + \tfrac{M}{\tau_s} x_5 + v_{s_d}] + \\
(-\tfrac{4}{\tau_s} x_4 + \tfrac{2M}{\tau_s} x_6 + 2v_{s_q})[-\omega_{dq} x_3 - \tfrac{1}{\tau_s} x_4 + \tfrac{M}{\tau_s} x_6 + v_{s_q}] + \\
(\tfrac{2M}{\tau_s} x_3)[-\beta x_2 x_4 + \tfrac{\beta}{\tau_s} x_3 + (\omega_{dq} - x_2) x_6 - \gamma_2 x_5 - \beta v_{s_d}] + \\
(\tfrac{2M}{\tau_s} x_3)[\tfrac{\beta}{\tau_s} x_4 + \beta x_2 x_3 + (\omega_{dq} - x_2) x_5 - \gamma_2 x_6 - \beta v_{s_q}]
\end{aligned}
\tag{29}
$$

$$
L_{g_a}(L_f h_2(x)) = \tfrac{2M}{\tau_s} \tfrac{1}{\sigma L_s} x_3
\tag{30}
$$

$$
L_{g_a}(L_f h_2(x)) = \tfrac{2M}{\tau_s} \tfrac{1}{\sigma L_s} x_4
\tag{31}
$$

Therefore, one obtains the decoupled and linearized representation of the system

$$
\begin{pmatrix} z_1^{(3)} \\ \ddot{z}_4 \end{pmatrix} = \begin{pmatrix} L_f^3 h_1(x) \\ L_f^2 h_2(x) \end{pmatrix} + \begin{pmatrix} L_{g_a} L_f^2 h_1(x) & L_{g_b} L_f^2 h_1(x) \\ L_{g_a} L_f h_2(x) & L_{g_b} L_f h_2(x) \end{pmatrix} \begin{pmatrix} u_1 \\ u_2 \end{pmatrix}
\tag{32}
$$

or equivalently

$$
\begin{pmatrix} z_1^{(3)} \\ \ddot{z}_4 \end{pmatrix} = f_a + \tilde{M} u
\tag{33}
$$

where

$$
f_a = \begin{pmatrix} L_f^3 h_1(x) \\ L_f^2 h_2(x) \end{pmatrix} \qquad \tilde{M} = \begin{pmatrix} L_{g_a} L_f^2 h_1(x) & L_{g_b} L_f^2 h_1(x) \\ L_{g_a} L_f h_2(x) & L_{g_b} L_f h_2(x) \end{pmatrix}
\tag{34}
$$

By defining the control inputs $v_1 = L_f^3 h_1(x) + (L_{g_a} L_f^2 h_1(x))u_1 + (L_{g_b} L_f^2 h_1(x))u_2$ and $v_2 = L_f^2 h_2(x) + (L_{g_a} L_f h_2(x))u_1 + (L_{g_b} L_f h_2(x))u_2$ one can also have the description in the MIMO canonical form

$$
\begin{pmatrix} \dot{z}_1 \\ \dot{z}_2 \\ \dot{z}_3 \\ \dot{z}_4 \\ \dot{z}_5 \end{pmatrix} = \begin{pmatrix} 0 & 1 & 0 & 0 & 0 \\ 0 & 0 & 1 & 0 & 0 \\ 0 & 0 & 0 & 0 & 0 \\ 0 & 0 & 0 & 0 & 1 \\ 0 & 0 & 0 & 0 & 0 \end{pmatrix} \begin{pmatrix} z_1 \\ z_2 \\ z_3 \\ z_4 \\ z_5 \end{pmatrix} + \begin{pmatrix} 0 & 0 \\ 0 & 0 \\ 1 & 0 \\ 0 & 0 \\ 0 & 1 \end{pmatrix} \begin{pmatrix} v_1 \\ v_2 \end{pmatrix}
\tag{35}
$$

The control input for the linearized and decoupled model of the DFIG is chosen as follows

$$
\begin{aligned}
v_1 = z_1^{d(3)} - k_1^{(1)}(\ddot{z}_1 - \ddot{z}_1^d) - k_2^{(1)}(\dot{z}_1 - \dot{z}_1^d) - k_3^{(1)}(z_1 - z_1^d) \\
v_2 = \ddot{z}_4^d - k_1^{(2)}(\dot{z}_4 - \dot{z}_4^d) - k_2^{(2)}(z_4 - z_4^d)
\end{aligned}
\tag{36}
$$

and finally the control input that is applied to the system is

$$
u = \tilde{M}^{-1}(-f_a + v)
\tag{37}
$$

The proposed control scheme can work with the use of measurements from a small number of sensors. That is, there is need to obtain measurements of only $y_1 = \theta$ which is the turn angle of the generator's rotor, and of the magnetic flux $y_2 = \psi_s^2 = \psi_{s_d}^2 + \psi_{s_q}^2$, or due to the orientation of the magnetic field $y_2 = \psi_s^2 = \psi_{s_d}^2$. The stator flux ($\psi_s$) cannot be measured directly from a sensor (e.g. the use of Hall sensor in an electric machine with a rotating part would not be efficient), however the equation that relates stator flux and stator and rotor currents can be used to calculate ψ_s. Thus one has:

$$
\begin{aligned}
\psi_{s_d} = L_s i_{s_d} + M i_{r_d} \\
\psi_{s_q} = 0
\end{aligned}
\tag{38}
$$

which means that by measuring stator and rotor currents one can obtain an indirect measurement of the stator's magnetic flux ψ_{s_d}.

4 Flatness-based adaptive neurofuzzy control

4.1 Transformation of MIMO nonlinear systems into the Brunovsky form

Following the previous procedure, that is after defining the flat outputs of the initial MIMO nonlinear model of the DFIG, and after expressing the system's state variables and control inputs as functions of the flat output and of the associated derivatives, the DFIG is transformed into the Brunovsky canonical form of Eq. (35), or equivalently into the form [1],[36-37]:

$$
\begin{aligned}
&\dot{x}_1 = x_2 \\
&\dot{x}_2 = x_3 \\
&\cdots \\
&\dot{x}_{r_1-1} = x_{r_1} \\
&\dot{x}_{r_1} = f_1(x) + \sum_{j=1}^{p} g_{1_j}(x)u_j + d_1 \qquad
\begin{aligned}
& y_1 = x_1 \\
& y_2 = x_{r_1-1} \\
& \cdots \\
& y_p = x_{n-r_p+1}
\end{aligned} \\
&\dot{x}_{r_1+1} = x_{r_1+2} \\
&\dot{x}_{r_1+2} = x_{r_1+3} \\
&\cdots \\
&\dot{x}_{p-1} = x_p \\
&\dot{x}_p = f_p(x) + \sum_{j=1}^{p} g_{p_j}(x)u_j + d_p
\end{aligned}
\tag{39}
$$

where $x = [x_1, \cdots, x_n]^T$ is the state vector of the transformed system (according to the differential flatness formulation), $u = [u_1, \cdots, u_p]^T$ is the set of control inputs, $y = [y_1, \cdots, y_p]^T$ is the output vector, f_i are the drift functions and $g_{i,j}$, $i,j = 1,2,\cdots,p$ are smooth functions corresponding to the control input gains, while d_j is a variable associated to external disturbances. In holds that $r_1 + r_2 + \cdots + r_p = n$. Having written the initial nonlinear system into the canonical (Brunovsky) form it holds

$$
y_i^{(r_i)} = f_i(x) + \sum_{j=1}^{p} g_{ij}(x)u_j + d_j
\tag{40}
$$

Equivalently, in vector form, one has the following description for the system dynamics

$$
y^{(r)} = f(x) + g(x)u + d
\tag{41}
$$

where the following vectors and matrices are be defined

$$
\begin{aligned}
& y^{(r)} = [y_1^{(r_1)}, \cdots, y_p^{(r_p)}] \\
& f(x) = [f_1(x), \cdots, f_p(x)]^T \\
& g(x) = [g_1(x), \cdots, g_p(x)] \\
& with\ g_i(x) = [g_{1i}(x), \cdots, g_{pi}(x)]^T \\
& A = diag[A_1, \cdots, A_p], \quad B = diag[B_1, \cdots, B_p] \\
& C^T = diag[C_1, \cdots, C_p], \quad d = [d_1, \cdots, d_p]^T
\end{aligned}
\tag{42}
$$

where matrix A has the MIMO canonical form, i.e. with elements

$$A_i = \begin{pmatrix} 0 & 1 & \cdots & 0 \\ 0 & 0 & \cdots & 0 \\ \vdots & \vdots & \ldots & \vdots \\ 0 & 0 & \cdots & 1 \\ 0 & 0 & \cdots & 0 \end{pmatrix}_{r_i \times r_i} \qquad B_i = \begin{pmatrix} 0 \\ 0 \\ \cdots \\ 0 \\ 1 \end{pmatrix}_{r_i \times 1} \qquad C_i^T = \begin{pmatrix} 1 \\ 0 \\ \cdots \\ 0 \\ 0 \end{pmatrix}_{r_i \times 1} \tag{43}$$

Thus, Eq. (40) can be written in state-space form

$$\begin{aligned} \dot{x} &= Ax + B[f(x) + g(x)u + \tilde{d}] \\ y &= C^T x \end{aligned} \tag{44}$$

which can be also written in the equivalent form:

$$\begin{aligned} \dot{x} &= Ax + Bv + B\tilde{d} \\ y &= C^T x \end{aligned} \tag{45}$$

where $v = f(x) + g(x)u$. The reference setpoints for the system's outputs $y_1, \cdots, y_p$ are denoted as $y_{1m}, \cdots, y_{pm}$, thus for the associated tracking errors it holds

$$\begin{aligned} e_1 &= y_1 - y_{1m} \\ e_2 &= y_2 - y_{2m} \\ &\cdots \\ e_p &= y_p - y_{pm} \end{aligned} \tag{46}$$

The error vector of the outputs of the transformed MIMO system is denoted as

$$\begin{aligned} E_1 &= [e_1, \cdots, e_p]^T \\ y_m &= [y_{1m}, \cdots, y_{pm}]^T \\ &\cdots \\ y_m^{(r)} &= [y_{1m}^{(r)}, \cdots, y_{pm}^{(r)}]^T \end{aligned} \tag{47}$$

where $y_{im}^{(r)}$ denotes the r-th order derivative of the i-th reference output of the MIMO dynamical system. Thus, one can also define the following vectors: (i) a vector containing the state variables of the system and the associated derivatives, (ii) a vector containing the reference outputs of the system and the associated derivatives

$$x = [x_1, \cdots, x_1^{r_1 - 1}, \cdots, x_p, \cdots, x_p^{r_p - 1}]^T \tag{48}$$

$$Y_m = [y_{1m}, \cdots, y_{1m}^{r_1 - 1}, \cdots, y_{pm}, \cdots, y_{pm}^{r_p - 1}]^T \tag{49}$$

while in a similar manner one can define a vector containing the tracking error of the system's outputs and the associated derivatives

$$e = Y_m - x = [e_1, \cdots, e_1^{r_1 - 1}, \cdots, e_p, \cdots, e_p^{r_p - 1}]^T \tag{50}$$

It is assumed that matrix $g(x)$ is a nonsingular one, i.e. $g^{-1}(x)$ exists and is bounded for all $x \in U_x$, where $U_x \subset R^n$ is a compact set. In any case, the problem of singularities in matrix $g(x)$ can be handled by appropriately modifying the state feedback-based control input.

The objective of the adaptive neurofuzzy controller, denoted as $u = u(x, e|\theta)$ is: all the signals involved in the controller's design are bounded and it holds that $lim_{t \to \infty} e = 0$, (ii) the H_∞ tracking performance criterion is succeeded for a prescribed attenuation level.

9

In the presence of non-gaussian disturbances w_d, successful tracking of the reference signal is denoted by the H_∞ criterion [9],[37]:

$$\int_0^T e^T Q e \, dt \le \rho^2 \int_0^T w_d{}^T w_d \, dt \tag{51}$$

where ρ is the attenuation level and corresponds to the maximum singular value of the transfer function $G(s)$ of the linearized model associated to Eq. (44) and Eq. (45).

4.2 Control law

The control signal of the MIMO nonlinear DFIG model which has been transformed into the Brunovsky form as described by Eq. (45) contains the unknown nonlinear functions $f(x)$ and $g(x)$. In case that the complete state vector x is measurable these unknown functions can be approximated by

$$\begin{aligned}
\hat{f}(x|\theta_f) &= \Phi_f(x)\theta_f \\
\hat{g}(x|\theta_g) &= \Phi_g(x)\theta_g
\end{aligned} \tag{52}$$

where

$$\Phi_f(x) = (\xi_f^1(x), \xi_f^2(x), \cdots \xi_f^n(x))^T \tag{53}$$

with $\xi_f^i(x), \imath = 1, \cdots, n$ being the vector of kernel functions (e.g. normalized fuzzy Gaussian membership functions), where

$$\xi_f^i(x) = (\phi_f^{i,1}(x), \phi_f^{i,2}(x), \cdots, \phi_f^{i,N}(x)) \tag{54}$$

thus giving

$$\Phi_f(x) = \begin{pmatrix} \phi_f^{1,1}(x) & \phi_f^{1,2}(x) & \cdots & \phi_f^{1,N}(x) \\ \phi_f^{2,1}(x) & \phi_f^{2,2}(x) & \cdots & \phi_f^{2,N}(x) \\ \cdots & \cdots & \cdots & \cdots \\ \phi_f^{n,1}(x) & \phi_f^{n,2}(x) & \cdots & \phi_f^{n,N}(x) \end{pmatrix} \tag{55}$$

while the weights vector is defined as

$$\theta_f{}^T = \left(\theta_f^1, \theta_f^2, \cdots \theta_f^N\right) \tag{56}$$

$j = 1, \cdots, N$ is the number of basis functions that is used to approximate the components of function f which are denoted as $i = 1, \cdots, n$. Thus, one obtains the relation of Eq. (52), i.e. $\hat{f}(x|\theta_f) = \Phi_f(x)\theta_f$.

In a similar manner, for the approximation of function g one has

$$\Phi_g(x) = \left(\xi_g^1(x), \xi_g^2(x), \cdots \xi_g^N(x)\right)^T \tag{57}$$

with $\xi_g^i(x), \imath = 1, \cdots, N$ being the vector of kernel functions (e.g. normalized fuzzy Gaussian membership functions), where

$$\xi_g^i(x) = \left(\phi_g^{i,1}(x), \phi_g^{i,2}(x), \cdots, \phi_g^{i,N}(x)\right) \tag{58}$$

thus giving

$$\Phi_g(x) = \begin{pmatrix} \phi_g^{1,1}(x) & \phi_g^{1,2}(x) & \cdots & \phi_g^{1,N}(x) \\ \phi_g^{2,1}(x) & \phi_g^{2,2}(x) & \cdots & \phi_g^{2,N}(x) \\ \cdots & \cdots & \cdots & \cdots \\ \phi_g^{n,1}(x) & \phi_g^{n,2}(x) & \cdots & \phi_g^{n,N}(x) \end{pmatrix} \tag{59}$$

10

while the weights vector is defined as

$$\theta_g = \left(\theta_g^1, \theta_g^2, \cdots, \theta_g^p\right) \tag{60}$$

where the components of matrix θ_g are defined as

$$\theta_g^j = \left(\theta_{g_1}^j, \theta_{g_2}^j, \cdots \theta_{g_N}^j\right)^T \tag{61}$$

$j = 1, \cdots, p$ is the number of basis functions that is used to approximate the components of function g which are denoted as $i = 1, \cdots, n$. Thus one obtains about matrix $\theta_g \in R^{N \times p}$

$$\theta_g = \begin{pmatrix} \theta_{g_1}^1 & \theta_{g_1}^2 & \cdots & \theta_{g_1}^p \\ \theta_{g_2}^1 & \theta_{g_2}^2 & \cdots & \theta_{g_2}^p \\ \cdots & \cdots & \cdots & \cdots \\ \theta_{g_N}^1 & \theta_{g_N}^2 & \cdots & \theta_{g_N}^p \end{pmatrix} \tag{62}$$

It holds that

$$g = \begin{pmatrix} g_1 \\ g_2 \\ \cdots \\ g_n \end{pmatrix} = \begin{pmatrix} g_1^1 & g_1^2 & \cdots & g_1^p \\ g_2^1 & g_2^2 & \cdots & g_2^p \\ \cdots & \cdots & \cdots & \cdots \\ g_n^1 & g_n^2 & \cdots & g_n^p \end{pmatrix} \tag{63}$$

Using the above, one finally has the relation of Eq. (52), i.e. $\hat{g}(x|\theta_g) = \Phi_g(x)\theta_g$. If the state variables of the system are available for measurement then a state-feedback control law can be formulated as

$$u = \hat{g}^{-1}(x|\theta_g)[-\hat{f}(x|\theta_f) + y_m^{(r)} - K^T e + u_c] \tag{64}$$

where $\hat{f}(x|\theta_f)$ and $\hat{g}(x|\theta_g)$ are neurofuzzy models to approximate $f(x)$ and $g(x)$, respectively. u_c is a supplementary control term, e.g. an H_∞ control term that is used to compensate for the effects of modelling inaccuracies and external disturbances. Moreover, K^T is the feedback gain matrix that assures that the characteristic polynomial of matrix $A - BK^T$ will be a Hurwitz one.

4.3 Estimation of the state vector

The control of the system described by Eq. (41) becomes more complicated when the state vector x of the DFIG is not directly measurable and has to be reconstructed through a state observer. The following definitions are used

- error of the state vector $e = x - x_m$

- error of the estimated state vector $\hat{e} = \hat{x} - x_m$

- observation error $\tilde{e} = e - \hat{e} = (x - x_m) - (\hat{x} - x_m)$

When an observer is used to reconstruct the state vector, the control law of Eq. (64) is written as

$$u = \hat{g}^{-1}(\hat{x}|\theta_g)[-\hat{f}(\hat{x}|\theta_f) + y_m^{(r)} - K^T \hat{e} + u_c] \tag{65}$$

Applying Eq. (65) to the nonlinear system described by Eq. (41), results into

$y^{(r)} = f(x) + g(x)\hat{g}^{-1}(\hat{x})[-\hat{f}(\hat{x}) + y_m^{(r)} - K^T\hat{e} + u_c] + d \Rightarrow y^{(r)} = f(x) + [g(x) - \hat{g}(\hat{x}) + \hat{g}(\hat{x})]\hat{g}^{-1}(\hat{x})[-\hat{f}(\hat{x}) + y_m^{(r)} - K^T\hat{e} + u_c] + d \Rightarrow y^{(r)} = [f(x) - \hat{f}(\hat{x})] + [g(x) - \hat{g}(\hat{x})]u + y_m^{(r)} - K^T\hat{e} + u_c + d.$

It holds $e = x - x_m \Rightarrow y^{(r)} = e^{(r)} + y_m^{(r)}$. Substituting $y^{(r)}$ in the above equation gives

11

$$e^{(r)} + y_m^{(r)} = y_m^{(r)} - K^T\hat{e} + u_c + [f(x) - \hat{f}(\hat{x})]+ \\ +[g(x) - \hat{g}(\hat{x})]u + d \tag{66}$$

and equivalently

$$\dot{e} = Ae - BK^T\hat{e} + Bu_c + B\{[f(x) - \hat{f}(\hat{x})]+ \\ +[g(x) - \hat{g}(\hat{x})]u + \tilde{d}\} \tag{67}$$

$$e_1 = C^T e \tag{68}$$

where $e = [e^1, e^2, \cdots, e^p]^T$ with $e^i = [e_i, \dot{e}_i, \ddot{e}_i, \cdots, e_i^{r_i-1}]^T$, $i = 1, 2, \cdots, p$ and also $\hat{e} = [\hat{e}^1, \hat{e}^2, \cdots, \hat{e}^p]^T$ with $\hat{e}^i = [\hat{e}_i, \dot{\hat{e}}_i, \ddot{\hat{e}}_i, \cdots, \hat{e}_i^{r_i-1}]^T$, $i = 1, 2, \cdots, p$. Matrices A, B and C have been defined in Eq. (43).

A state observer is designed according to Eq. (67) and (68) and is given by [37]:

$$\dot{\hat{e}} = A\hat{e} - BK^T\hat{e} + K_o[e_1 - C^T\hat{e}] \tag{69}$$

$$\hat{e}_1 = C^T\hat{e} \tag{70}$$

The feedback gain matrix is denoted as $K \in R^{n\times p}$. The observation gain matrix is denoted as $K_o \in R^{p\times n}$ and its elements are selected so as to assure the asymptotic elimination of the observation error.

5 Application of flatness-based adaptive neurofuzzy control to the DFIG

5.1 Tracking error dynamics under feedback control

If the state vector in the linearized description of the DFIG of Eq. (25) is constrained into $x = [x_1, x_2, x_3, x_4]^T = [\omega, \dot{\omega}, \psi_{s_d}, \dot{\psi}_{s_d}]^T$, it holds that

$$\ddot{x}_1 = f_1(x) + g_1(x)u \\ \ddot{x}_3 = f_2(x) + g_2(x)u \tag{71}$$

or equivalently

$$\dot{x}_1 = x_2 \\ \dot{x}_2 = f_1(x) + g_1(x)u \\ \dot{x}_3 = x_4 \\ \dot{x}_4 = f_2(x) + g_2(x)u \tag{72}$$

Next, taking into account also the effects of additive disturbances the dynamic model becomes

$$\ddot{x}_1 = f_1(x, t) + g_1(x, t)u + d_1 \\ \ddot{x}_3 = f_2(x, t) + g_2(x, t)u + d_2 \tag{73}$$

$$\begin{pmatrix} \ddot{x}_1 \\ \ddot{x}_3 \end{pmatrix} = \begin{pmatrix} f_1(x, t) \\ f_2(x, t) \end{pmatrix} + \begin{pmatrix} g_1(x, t) \\ g_2(x, t) \end{pmatrix} u + \begin{pmatrix} d_1 \\ d_2 \end{pmatrix} \tag{74}$$

The following control input is defined

$$u = \begin{pmatrix} \hat{g}_1(x, t) \\ \hat{g}_2(x, t) \end{pmatrix}^{-1} \{ \begin{pmatrix} \ddot{x}_1^d \\ \ddot{x}_3^d \end{pmatrix} - \begin{pmatrix} \hat{f}_1(x, t) \\ \hat{f}_2(x, t) \end{pmatrix} - \begin{pmatrix} K_1^T \\ K_2^T \end{pmatrix} e + \begin{pmatrix} u_{c_1} \\ u_{c_2} \end{pmatrix} \} \tag{75}$$

where $[u_{c_1} \ u_{c_2}]^T$ is a robust control term that is used for the compensation of the model's uncertainties as well as of the external disturbances and $K_i^T = [k_1^i, k_2^i, \cdots, k_{n-1}^i, k_n^i]$. Substituting Eq. (75) into Eq. (74) the closed-loop tracking error dynamics is obtained

$$
\begin{pmatrix} \ddot{x}_1 \\ \ddot{x}_3 \end{pmatrix} = \begin{pmatrix} f_1(x,t) \\ f_2(x,t) \end{pmatrix} + \begin{pmatrix} g_1(x,t) \\ g_2(x,t) \end{pmatrix} \begin{pmatrix} \hat{g}_1(x,t) \\ \hat{g}_2(x,t) \end{pmatrix}^{-1} \cdot
$$
$$
\cdot \left\{ \begin{pmatrix} \ddot{x}_1^d \\ \ddot{x}_3^d \end{pmatrix} - \begin{pmatrix} \hat{f}_1(x,t) \\ \hat{f}_2(x,t) \end{pmatrix} - \begin{pmatrix} K_1^T \\ K_2^T \end{pmatrix} e + \begin{pmatrix} u_{c_1} \\ u_{c_2} \end{pmatrix} \right\} + \begin{pmatrix} d_1 \\ d_2 \end{pmatrix}
$$
(76)

Eq. (76) can now be written as

$$
\begin{pmatrix} \ddot{x}_1 \\ \ddot{x}_3 \end{pmatrix} = \begin{pmatrix} f_1(x,t) \\ f_2(x,t) \end{pmatrix} + \left\{ \begin{pmatrix} g_1(x,t) - \hat{g}_1(x,t) \\ g_2(x,t) - \hat{g}_2(x,t) \end{pmatrix} + \begin{pmatrix} \hat{g}_1(x,t) \\ \hat{g}_2(x,t) \end{pmatrix} \right\} \begin{pmatrix} \hat{g}_1(x,t) \\ \hat{g}_2(x,t) \end{pmatrix}^{-1} \cdot
$$
$$
\cdot \left\{ \begin{pmatrix} \ddot{x}_1^d \\ \ddot{x}_3^d \end{pmatrix} - \begin{pmatrix} \hat{f}_1(x,t) \\ \hat{f}_2(x,t) \end{pmatrix} - \begin{pmatrix} K_1^T \\ K_2^T \end{pmatrix} e + \begin{pmatrix} u_{c_1} \\ u_{c_2} \end{pmatrix} \right\} + \begin{pmatrix} d_1 \\ d_2 \end{pmatrix}
$$
(77)

and using Eq. (75) this results into

$$
\begin{pmatrix} \ddot{e}_1 \\ \ddot{e}_3 \end{pmatrix} = \begin{pmatrix} f_1(x,t) - \hat{f}_1(x,t) \\ f_2(x,t) - \hat{f}_2(x,t) \end{pmatrix} + \begin{pmatrix} g_1(x,t) - \hat{g}_1(x,t) \\ g_2(x,t) - \hat{g}_2(x,t) \end{pmatrix} u -
$$
$$
- \begin{pmatrix} K_1^T \\ K_2^T \end{pmatrix} e + \begin{pmatrix} u_{c_1} \\ u_{c_2} \end{pmatrix} + \begin{pmatrix} d_1 \\ d_2 \end{pmatrix}
$$
(78)

The following description for the approximation error is defined

$$
w = \begin{pmatrix} f_1(x,t) - \hat{f}_1(x,t) \\ f_2(x,t) - \hat{f}_2(x,t) \end{pmatrix} + \begin{pmatrix} g_1(x,t) - \hat{g}_1(x,t) \\ g_2(x,t) - \hat{g}_2(x,t) \end{pmatrix} u
$$
(79)

Moreover, the following matrices are defined

$$
A = \begin{pmatrix} 0 & 1 & 0 & 0 \\ 0 & 0 & 0 & 0 \\ 0 & 0 & 0 & 1 \\ 0 & 0 & 0 & 0 \end{pmatrix}, \quad B = \begin{pmatrix} 0 & 0 \\ 1 & 0 \\ 0 & 0 \\ 0 & 1 \end{pmatrix}
$$
(80)

$$
K^T = \begin{pmatrix} K_1^1 & K_2^1 & K_3^1 & K_4^1 \\ K_1^2 & K_2^2 & K_3^2 & K_4^2 \end{pmatrix}
$$

Using matrices A, B, K^T, Eq. (78) is written in the following form

$$
\dot{e} = (A - BK^T)e + Bu_c + B \left\{ \begin{pmatrix} f_1(x,t) - \hat{f}_1(x,t) \\ f_2(x,t) - \hat{f}_2(x,t) \end{pmatrix} + \right.
$$
$$
\left. + \begin{pmatrix} g_1(x,t) - \hat{g}_1(x,t) \\ g_2(x,t) - \hat{g}_2(x,t) \end{pmatrix} u + \tilde{d} \right\}
$$
(81)

When the estimated state vector $\hat{x}$ is used in the feedback control loop, equivalently to Eq. (67) one has

$$
\dot{e} = Ae - BK^T \hat{e} + Bu_c + B \left\{ \begin{pmatrix} f_1(x,t) - \hat{f}_1(\hat{x},t) \\ f_2(x,t) - \hat{f}_2(\hat{x},t) \end{pmatrix} + \right.
$$
$$
\left. + \begin{pmatrix} g_1(x,t) - \hat{g}_1(\hat{x},t) \\ g_2(x,t) - \hat{g}_2(\hat{x},t) \end{pmatrix} u + \tilde{d} \right\}
$$
(82)

13

and considering that the approximation error w is now denoted as

$$w = \begin{pmatrix} f_1(x,t) - \hat{f}_1(\hat{x},t) \\ f_2(x,t) - \hat{f}_2(\hat{x},t) \end{pmatrix} + \begin{pmatrix} g_1(x,t) - \hat{g}_1(\hat{x},t) \\ g_2(x,t) - \hat{g}_2(\hat{x},t) \end{pmatrix} u \tag{83}$$

Eq. (82) can be also written as

$$\dot{e} = Ae - BK^T \hat{e} + Bu_c + Bw + B\tilde{d} \tag{84}$$

The associated state observer will be described again by Eq. (69) and Eq. (70).

5.2 Dynamics of the observation error

The observation error is defined as $\tilde{e} = e - \hat{e} = x - \hat{x}$. Subtracting Eq. (69) from Eq. (67) as well as Eq. (70) from Eq. (68) one gets

$$\dot{e} - \dot{\hat{e}} = A(e - \hat{e}) + Bu_c + B\{[f(x,t) - \hat{f}(\hat{x},t)] + \\ + [g(x,t) - \hat{g}(\hat{x},t)]u + \tilde{d}\} - K_o C^T(e - \hat{e})$$

$$e_1 - \hat{e}_1 = C^T(e - \hat{e})$$

or equivalently

$$\dot{\tilde{e}} = A\tilde{e} + Bu_c + B\{[f(x,t) - \hat{f}(\hat{x},t)] + \\ + [g(x,t) - \hat{g}(\hat{x},t)]u + \tilde{d}\} - K_o C^T \tilde{e}$$

$$\tilde{e}_1 = C^T \tilde{e}$$

which can be written as

$$\dot{\tilde{e}} = (A - K_o C^T)\tilde{e} + Bu_c + B\{[f(x,t) - \hat{f}(\hat{x},t)] + \\ + [g(x,t) - \hat{g}(\hat{x},t)]u + \tilde{d}\} \tag{85}$$

$$\tilde{e}_1 = C^T \tilde{e} \tag{86}$$

or equivalently, it can be written as

$$\dot{\tilde{e}} = (A - K_o C^T)\tilde{e} + Bu_c + Bw + \tilde{d}\} \tag{87}$$

$$\tilde{e}_1 = C^T \tilde{e} \tag{88}$$

5.3 Approximation of functions $f(x,t)$ and $g(x,t)$

Next, the following neurofuzzy approximators of the unknown system dynamics are defined

$$\hat{f}(\hat{x}) = \begin{pmatrix} \hat{f}_1(\hat{x}|\theta_f) \ \hat{x} \in R^{4 \times 1} \ \hat{f}_1(\hat{x}|\theta_f) \ \in \ R^{1 \times 1} \\ \hat{f}_2(\hat{x}|\theta_f) \ \hat{x} \in R^{4 \times 1} \ \hat{f}_2(\hat{x}|\theta_f) \ \in \ R^{1 \times 1} \end{pmatrix} \tag{89}$$
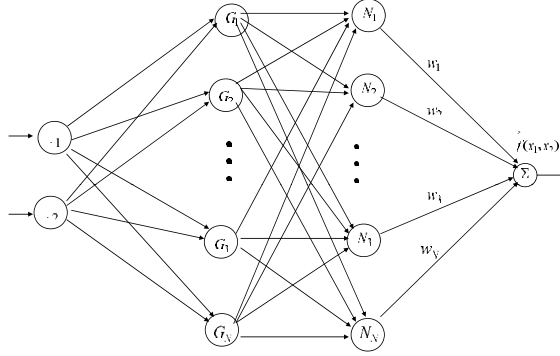
with kernel functions

$$\phi_f^{i,j}(\hat{x}) = \frac{\prod_{j=1}^n \mu_{A_j}^i(\hat{x}_j)}{\sum_{i=1}^N \prod_{j=1}^n \mu_{A_j}^i(\hat{x}_j)} \tag{90}$$

14

where $l = 1, 2$, $\hat{x}$ is the estimate of the state vector and $\mu_{A_j^i}(\hat{x})$ is the i-th membership function associated with the l-th hidden layer node (fuzzy rule), as shown in Fig. 2. Similarly, the following approximators of the unknown system dynamics are defined

$$\hat{g}(\hat{x}) = \begin{pmatrix} \hat{g}_1(\hat{x}|\theta_g) \ \hat{x} \in R^{4 \times 1} \ \hat{g}_1(\hat{x}|\theta_g) \ \in \ R^{1 \times 2} \\ \hat{g}_2(\hat{x}|\theta_g) \ \hat{x} \in R^{4 \times 1} \ \hat{g}_2(\hat{x}|\theta_g) \ \in \ R^{1 \times 2} \end{pmatrix} \tag{91}$$

Figure 2: Neurofuzzy approximator used for estimating the unknown system dynamics

The values of the weights that result in optimal approximation are

$$\theta_f^* = arg \ min_{\theta_f \in M_{\theta_f}} [sup_{\hat{x} \in U_{\hat{x}}} (f(x) - \hat{f}(\hat{x}|\theta_f))] \\ \theta_g^* = arg \ min_{\theta_g \in M_{\theta_g}} [sup_{\hat{x} \in U_{\hat{x}}} (g(x) - \hat{g}(\hat{x}|\theta_g))] \tag{92}$$

where the variation ranges for the weights are defined as

$$M_{\theta_f} = \{\theta_f \in R^h : \ ||\theta_f|| \leq m_{\theta_f}\} \\ M_{\theta_g} = \{\theta_g \in R^h : \ ||\theta_g|| \leq m_{\theta_g}\} \tag{93}$$

The value of the approximation error defined in Eq. (79) that corresponds to the optimal values of the weights vectors θ_f^* and θ_g^* one has

$$w = \left(f(x,t) - \hat{f}(\hat{x}|\theta_f^*)\right) + \left(g(x,t) - \hat{g}(\hat{x}|\theta_g^*)\right) u \tag{94}$$

which is next written as

$$w = \left(f(x,t) - \hat{f}(\hat{x}|\theta_f) + \hat{f}(\hat{x}|\theta_f) - \hat{f}(\hat{x}|\theta_f^*)\right) + \\ + \left(g(x,t) - \hat{g}(\hat{x}|\theta_g) + \hat{g}(\hat{x}|\theta_g) - \hat{g}(\hat{x}|\theta_g^*)\right) u \tag{95}$$

which can be also written in the following form

$$w = \left(w_a + w_b\right) \tag{96}$$

where

$$w_a = \{[f(x,t) - \hat{f}(\hat{x}|\theta_f)] + [g(x,t) - \hat{g}(\hat{x}|\theta_g)]\} u \tag{97}$$

15

$$w_b = \{[\hat{f}(\hat{x}|\theta_f) - \hat{f}(\hat{x}|\theta_f^*)] + [\hat{g}(\hat{x},\theta_g) - \hat{g}(\hat{x}|\theta_g^*)]\}u \tag{98}$$

Moreover, the following weights' error vectors are defined

$$\begin{aligned} \tilde{\theta}_f &= \theta_f - \theta_f^* \\ \tilde{\theta}_g &= \theta_g - \theta_g^* \end{aligned} \tag{99}$$

It is noted that both neural networks and neurofuzzy networks are function approximators using non-orthogonal kernel functions. This is to point out the difference to other approximators using orthogonal basis functions as for instance Fourier series expansions. The distinctive features for neurofuzzy networks are (i) they use as kernel functions in their hidden layer nodes some typical membership functions met in fuzzy logic (for instance Gaussian functions) (ii) the outputs of the hidden layer nodes are normalized so as to sum up to 1 (this is a property of most fuzzy membership functions). On the other hand in neural networks (i) it is possible to have several types of membership functions (e.g. wavelet functions, Gauss-Hermite polynomials, Bezier-Bernstein polynomials, B-splines), (ii) the outputs of the hidden layer nodes are not necessarily normalized. The learning (weights update) in both neural networks and neurofuzzy networks is performed with gradient algorithms of first or higher order.

6 Lyapunov stability analysis

6.1 Design of the Lyapunov function

The adaptation law of the neurofuzzy approximators weights θ_f and θ_g as well as the equation of the supervisory control term u_c are derived from the requirement for negative definiteness of the Lyapunov function

$$V = \tfrac{1}{2}\hat{e}^T P_1 \hat{e} + \tfrac{1}{2}\tilde{e}^T P_2 \tilde{e} + \tfrac{1}{2\gamma_1}\tilde{\theta}_f^T \tilde{\theta}_f + \tfrac{1}{2\gamma_2}tr[\tilde{\theta}_g^T \tilde{\theta}_g] \tag{100}$$

The selection of the Lyapunov function is based on the following principle of indirect adaptive control $\hat{e} : \lim_{t\to\infty} \hat{x}(t) = x_d(t)$ and $\tilde{e} : \lim_{t\to\infty} \hat{x}(t) = x(t)$. This yields $\lim_{t\to\infty} x(t) = x_d(t)$. Substituting Eq. (69), (70) and Eq. (85), (86) into Eq. (100) and differentiating results into

$$\begin{aligned} \dot{V} &= \tfrac{1}{2}\dot{\hat{e}}^T P_1 \hat{e} + \tfrac{1}{2}\hat{e}^T P_1 \dot{\hat{e}} + \tfrac{1}{2}\dot{\tilde{e}}^T P_2 \tilde{e} + \tfrac{1}{2}\tilde{e}^T P_2 \dot{\tilde{e}} + \\ &\quad + \tfrac{1}{\gamma_1}\dot{\tilde{\theta}}_f^T \tilde{\theta}_f + \tfrac{1}{\gamma_2}tr[\dot{\tilde{\theta}}_g^T \tilde{\theta}_g] \Rightarrow \end{aligned} \tag{101}$$

$\dot{V} = \tfrac{1}{2}\{(A - BK^T)\hat{e} + K_o C^T \tilde{e}\}^T P_1 \hat{e} + \tfrac{1}{2}\hat{e}^T P_1\{(A - BK^T)\hat{e} + K_o C^T \tilde{e}\} + \tfrac{1}{2}\{(A - K_o C^T)\tilde{e} + Bu_c + B\tilde{d} + Bw\}^T P_2 \tilde{e} + \tfrac{1}{2}\tilde{e}^T P_2\{(A - K_o C^T)\tilde{e} + Bu_c + Bw + B\tilde{d}\} + \tfrac{1}{\gamma_1}\dot{\tilde{\theta}}_f^T \tilde{\theta}_f + \tfrac{1}{\gamma_2}tr[\dot{\tilde{\theta}}_g^T \tilde{\theta}_g] \Rightarrow$.

$\dot{V} = \tfrac{1}{2}\{\hat{e}^T(A - BK^T)^T + \tilde{e}^T CK_o^T\}P_1 \hat{e} + \tfrac{1}{2}\hat{e}^T P_1\{(A - BK^T)\hat{e} + K_o C^T \tilde{e}\} + \tfrac{1}{2}\{\tilde{e}^T(A - K_o C^T)^T + u_c^T B^T + w^T B^T + \tilde{d}^T B^T\}P_2 \tilde{e} + \tfrac{1}{2}\tilde{e}^T P_2\{(A - K_o C^T)\tilde{e} + Bu_c + Bw + B\tilde{d}\} + \tfrac{1}{\gamma_1}\dot{\tilde{\theta}}_f^T \tilde{\theta}_f + \tfrac{1}{\gamma_2}tr[\dot{\tilde{\theta}}_g^T \tilde{\theta}_g] \Rightarrow$

$\dot{V} = \tfrac{1}{2}\hat{e}^T(A - BK^T)^T P_1 \hat{e} + \tfrac{1}{2}\tilde{e}^T CK_o^T P_1 \hat{e} + \tfrac{1}{2}\hat{e}^T P_1(A - BK^T)\hat{e} + \tfrac{1}{2}\hat{e}^T P_1 K_o C^T \tilde{e} + \tfrac{1}{2}\tilde{e}^T(A - K_o C^T)^T P_2 \tilde{e} + \tfrac{1}{2}(u_c^T + w^T + \tilde{d}^T)B^T P_2 \tilde{e} + \tfrac{1}{2}\tilde{e}^T P_2(A - K_o C^T)\tilde{e} + \tfrac{1}{2}\tilde{e}^T P_2 B(u_c + w + \tilde{d}) + \tfrac{1}{\gamma_1}\dot{\tilde{\theta}}_f^T \tilde{\theta}_f + \tfrac{1}{\gamma_2}tr[\dot{\tilde{\theta}}_g^T \tilde{\theta}_g]$

Assumption 1: For given positive definite matrices Q_1 and Q_2 there exist positive definite matrices P_1 and P_2, which are the solution of the following Riccati equations [36-37]

$$(A - BK^T)^T P_1 + P_1(A - BK^T) + Q_1 = 0 \tag{102}$$

16

$$(A - K_oC^T)^T P_2 + P_2(A - K_oC^T) -$$
$$-P_2 B(\tfrac{2}{r} - \tfrac{1}{\rho^2})B^T P_2 + Q_2 = 0 \qquad (103)$$

The conditions given in Eq. (102) to (103) are related to the requirement that the systems described by Eq. (69), (70) and Eq. (85), (86) are strictly positive real. Substituting Eq. (102) to (103) into $\dot{V}$ yields

$\dot{V} = \tfrac{1}{2}\hat{e}^T\{(A - BK^T)^T P_1 + P_1(A - BK^T)\}\hat{e} + \tilde{e}^T C K_o^T P_1 \hat{e} + \tfrac{1}{2}\tilde{e}^T\{(A - K_oC^T)^T P_2 + P_2(A - K_oC^T)\}\tilde{e} + \tilde{e}^T P_2 B(u_c + w + \tilde{d}) + \tfrac{1}{\gamma_1}\dot{\tilde{\theta}}_f^T\tilde{\theta}_f + \tfrac{1}{\gamma_2}tr[\dot{\tilde{\theta}}_g^T\tilde{\theta}_g]$

that is

$\dot{V} = -\tfrac{1}{2}\hat{e}^T Q_1 \hat{e} + \tilde{e}^T C K_o^T P_1 \hat{e} - \tfrac{1}{2}\tilde{e}^T\{Q_2 - P_2 B(\tfrac{2}{r} - \tfrac{1}{\rho^2})B^T P_2\}\tilde{e} + \tilde{e}^T P_2 B(u_c + w + \tilde{d}) + \tfrac{1}{\gamma_1}\dot{\tilde{\theta}}_f^T\tilde{\theta}_f + \tfrac{1}{\gamma_2}tr[\dot{\tilde{\theta}}_g^T\tilde{\theta}_g]$

The supervisory control u_c is decomposed in two terms, u_a and u_b.

- The control term u_a is given by

$$u_a = -\frac{1}{r}\tilde{e}^T P_2 B + \Delta u_a \qquad (104)$$

where assuming that the measurable elements of vector $\tilde{e}$ are $\{\tilde{e}_1, \tilde{e}_3, \cdots, \tilde{e}_k\}$, the term Δu_a is such that

$$-\tfrac{1}{r}\tilde{e}^T P_2 B + \Delta u_a = -\tfrac{1}{r}\begin{pmatrix} p_{11}\tilde{e}_1 + p_{13}\tilde{e}_3 + \cdots + p_{1k}\tilde{e}_k \\ p_{13}\tilde{e}_1 + p_{33}\tilde{e}_3 + \cdots + p_{3k}\tilde{e}_k \\ \cdots \cdots \cdots \\ p_{1k}\tilde{e}_1 + p_{3k}\tilde{e}_3 + \cdots + p_{kk}\tilde{e}_k \end{pmatrix} \qquad (105)$$

- The control term u_b is given by

$$u_b = -[(P_2B)^T(P_2B)]^{-1}(P_2B)^T C K_o^T P_1 \hat{e} \qquad (106)$$

- u_a is an H_∞ control used for the compensation of the approximation error w and the additive disturbance $\tilde{d}$. Its first component $-\tfrac{1}{r}\tilde{e}^T P_2 B$ has been chosen so as to compensate for the term $\tfrac{1}{r}\tilde{e}^T P_2 B B^T P_2 \tilde{e}$, which appears in the previously computed function about $\dot{V}$. By including also the second component Δu_a, one has that u_a is computed based on the feedback of only the measurable variables $\{\tilde{e}_1, \tilde{e}_3, \cdots, \tilde{e}_k\}$, out of the complete vector $\tilde{e} = [\tilde{e}_1, \tilde{e}_2, \cdots, \tilde{e}_n]$. Eq. (104) is finally rewritten as $u_a = -\tfrac{1}{r}\tilde{e}^T P_2 B + \Delta u_a$.

- u_b is a control used for the compensation of the observation error (the control term u_b has been chosen so as to satisfy the condition $\tilde{e}^T P_2 B u_b = -\tilde{e}^T C K_o^T P_1 \hat{e}$.
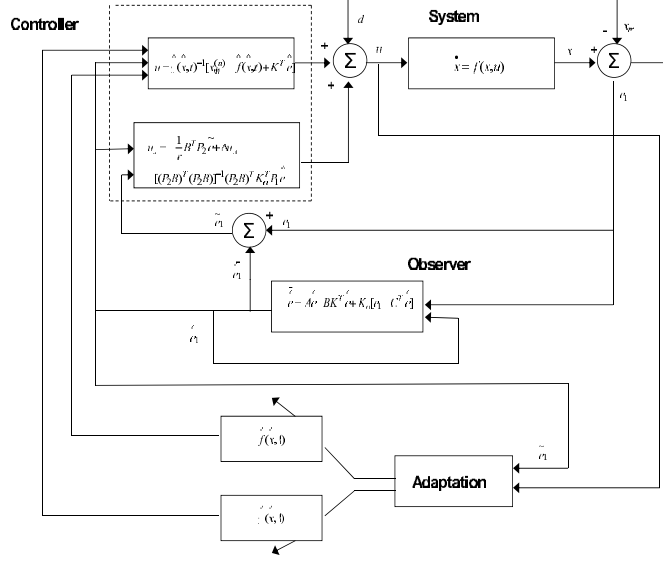
The control scheme is depicted in Fig. 3

Substituting Eq. (104) and (106) in $\dot{V}$ and assuming that Eq. (102) and Eq. (103) hold, one gets

$$\dot{V} = -\tfrac{1}{2}\hat{e}^T Q_1 \hat{e} + \tilde{e}^T C K_o^T P_1 \hat{e} - \tfrac{1}{2}\tilde{e}^T Q_2 \tilde{e} +$$
$$+\tfrac{1}{r}\tilde{e}^T P_2 B B^T P_2 \tilde{e} - \tfrac{1}{2\rho^2}\tilde{e}^T P_2 B B^T P_2 \tilde{e} +$$
$$+\tilde{e}^T P_2 B u_a + \tilde{e}^T P_2 B u_b + \tilde{e}^T P_2 B(w + \tilde{d}) +$$
$$+\tfrac{1}{\gamma_1}\dot{\tilde{\theta}}_f^T\tilde{\theta}_f + \tfrac{1}{\gamma_2}tr[\dot{\tilde{\theta}}_g^T\tilde{\theta}_g] \qquad (107)$$

or equivalently,

17

Figure 3: The proposed H_∞ control scheme

$$\dot{V} = -\frac{1}{2}\hat{e}^T Q_1 \hat{e} - \frac{1}{2}\tilde{e}^T Q_2 \tilde{e} - \frac{1}{2\rho^2}\tilde{e}^T P_2 BB^T P_2 \tilde{e} +$$
$$+\tilde{e}^T P_2 B(w + \tilde{d} + \Delta u_a) + \frac{1}{\gamma_1}\dot{\tilde{\theta}}_f^T \tilde{\theta}_f + \frac{1}{\gamma_2}tr[\dot{\tilde{\theta}}_g^T \tilde{\theta}_g]$$
(108)

It holds that $\dot{\tilde{\theta}}_f = \dot{\theta}_f - \dot{\theta}_f^* = \dot{\theta}_f$ and $\dot{\tilde{\theta}}_g = \dot{\theta}_g - \dot{\theta}_g^* = \dot{\theta}_g$. The following weight adaptation laws are considered:

$$\dot{\theta}_f = -\gamma_1 \Phi(\hat{x})^T B^T P_2 \tilde{e}$$
$$\dot{\theta}_g = -\gamma_2 \Phi(\hat{x})^T B^T P_2 \tilde{e}u^T$$
(109)

where assuming N fuzzy rules and associated kernel functions the matrices dimensions are $\theta_f \in R^{N\times1}$, $\theta_g \in R^{N\times2}$, $\Phi(x) \in R^{2\times N}$, $B \in R^{4\times2}$, $P \in R^{4\times4}$ and $\tilde{e} \in R^{4\times1}$.

The update of θ_f is a gradient type algorithm [39-41]. The update of θ_g is also a gradient type algorithm, where u_c implicitly tunes the adaptation gain γ_2. Substituting Eq. (109) in $\dot{V}$ gives

$\dot{V} = -\frac{1}{2}\hat{e}^T Q_1 \hat{e} - \frac{1}{2}\tilde{e}^T Q_2 \tilde{e} - \frac{1}{2\rho^2}\tilde{e}^T P_2 BB^T P_2 \tilde{e} + B^T P_2 \tilde{e}(w + d + \Delta u_a) + \frac{1}{\gamma_1}(-\gamma_1)\tilde{e}^T P_2 B\Phi(\hat{x})(\theta_f - \theta_f^*) + \frac{1}{\gamma_2}(-\gamma_2)tr[u\tilde{e}^T P_2 B\Phi(\hat{x})(\theta_g - \theta_g^*)]$

or equivalently

$\dot{V} = -\frac{1}{2}\hat{e}^T Q_1 \hat{e} - \frac{1}{2}\tilde{e}^T Q_2 \tilde{e} - \frac{1}{2\rho^2}\tilde{e}^T P_2 BB^T P_2 \tilde{e} + B^T P_2 \tilde{e}(w + \tilde{d} + \Delta u_a) + \frac{1}{\gamma_1}(-\gamma_1)\tilde{e}^T P_2 B\Phi(\hat{x})(\theta_f - \theta_f^*) + \frac{1}{\gamma_2}(-\gamma_2)tr[u\tilde{e}^T P_2 B(\hat{g}(\hat{x}|\theta_g) - \hat{g}(\hat{x}|\theta_g^*)]$

Taking into account that $u \in R^{2\times1}$ and $\tilde{e}^T PB(\hat{g}(x|\theta_g) - \hat{g}(x|\theta_g^*)) \in R^{1\times2}$ it holds

$\dot{V} = -\frac{1}{2}\hat{e}^T Q_1 \hat{e} - \frac{1}{2}\tilde{e}^T Q_2 \tilde{e} - \frac{1}{2\rho^2}\tilde{e}^T P_2 BB^T P_2 \tilde{e} + B^T P_2 \tilde{e}(w + \tilde{d} + \Delta u_a) + \frac{1}{\gamma_1}(-\gamma_1)\tilde{e}^T P_2 B\Phi(\hat{x})(\theta_f - \theta_f^*) + \frac{1}{\gamma_2}(-\gamma_2)tr[\tilde{e}^T P_2 B(\hat{g}(\hat{x}|\theta_g) - \hat{g}(\hat{x}|\theta_g^*))u]$

Since $\tilde{e}^T P_2 B(\hat{g}(\hat{x}|\theta_g) - \hat{g}(\hat{x}|\theta_g^*))u \in R^{1 \times 1}$ it holds

$$
\begin{aligned}
tr(\tilde{e}^T P_2 B(\hat{g}(x|\theta_g) - \hat{g}(x|\theta_g^*)u) = \\
= \tilde{e}^T P_2 B(\hat{g}(x|\theta_g) - \hat{g}(x|\theta_g^*))u
\end{aligned}
\tag{110}
$$

Therefore, one finally obtains

$\dot{V} = -\frac{1}{2}\hat{e}^T Q_1 \hat{e} - \frac{1}{2}\tilde{e}^T Q_2 \tilde{e} - \frac{1}{2\rho^2}\tilde{e}^T P_2 B B^T P_2 \tilde{e} + B^T P_2 \tilde{e}(w + \tilde{d} + \Delta u_a) + \frac{1}{\gamma_1}(-\gamma_1)\tilde{e}^T P_2 B \Phi(\hat{x})(\theta_f - \theta_f^*) + \frac{1}{\gamma_2}(-\gamma_2)\tilde{e}^T P_2 B(\hat{g}(\hat{x}|\theta_g) - \hat{g}(\hat{x}|\theta_g^*))u$

Next, the following approximation error is defined

$$
w_\alpha = [\hat{f}(\hat{x}|\theta_f^*) - \hat{f}(\hat{x}|\theta_f)] + [\hat{g}(\hat{x}|\theta_g^*) - \hat{g}(\hat{x}|\theta_g)]u
\tag{111}
$$

Thus, one obtains

$$
\begin{aligned}
\dot{V} = -\frac{1}{2}\hat{e}^T Q_1 \hat{e} - \frac{1}{2}\tilde{e}^T Q_2 \tilde{e} - \frac{1}{2\rho^2}\tilde{e}^T P_2 B B^T P_2 \tilde{e} + \\
+ B^T P_2 \tilde{e}(w + \tilde{d}) + \tilde{e}^T P_2 B w_\alpha
\end{aligned}
\tag{112}
$$

Denoting the aggregate approximation error and disturbances vector as

$$
w_1 = w + \tilde{d} + w_\alpha + \Delta u_a
\tag{113}
$$

the derivative of the Lyapunov function becomes

$$
\dot{V} = -\frac{1}{2}\hat{e}^T Q_1 \hat{e} - \frac{1}{2}\tilde{e}^T Q_2 \tilde{e} - \frac{1}{2\rho^2}\tilde{e}^T P_2 B B^T P_2 \tilde{e} + \tilde{e}^T P_2 B w_1
\tag{114}
$$

which in turn is written as

$$
\begin{aligned}
\dot{V} = -\frac{1}{2}\hat{e}^T Q_1 \hat{e} - \frac{1}{2}\tilde{e}^T Q_2 \tilde{e} - \frac{1}{2\rho^2}\tilde{e}^T P_2 B B^T P_2 \tilde{e} + \\
+ \frac{1}{2}\tilde{e}^T P B w_1 + \frac{1}{2}w_1^T B^T P_2 \tilde{e}
\end{aligned}
\tag{115}
$$

Lemma: The following inequality holds

$$
\frac{1}{2}\tilde{e}^T P_2 B w_1 + \frac{1}{2}w_1^T B^T P_2 \tilde{e} - \frac{1}{2\rho^2}\tilde{e}^T P_2 B B^T P_2 \tilde{e} \leq \frac{1}{2}\rho^2 w_1^T w_1
\tag{116}
$$

Proof: The binomial $(\rho a - \frac{1}{\rho}b)^2 \geq 0$ is considered. Expanding the left part of the above inequality one gets

$$
\begin{aligned}
\rho^2 a^2 + \frac{1}{\rho^2}b^2 - 2ab \geq 0 \Rightarrow \frac{1}{2}\rho^2 a^2 + \frac{1}{2\rho^2}b^2 - ab \geq 0 \Rightarrow \\
ab - \frac{1}{2\rho^2}b^2 \leq \frac{1}{2}\rho^2 a^2 \Rightarrow \frac{1}{2}ab + \frac{1}{2}ab - \frac{1}{2\rho^2}b^2 \leq \frac{1}{2}\rho^2 a^2
\end{aligned}
\tag{117}
$$

The following substitutions are carried out: $a = w_1$ and $b = \tilde{e}^T P_2 B$ and the previous relation becomes

$$
\frac{1}{2}w_1^T B^T P_2 \tilde{e} + \frac{1}{2}\tilde{e}^T P_2 B w_1 - \frac{1}{2\rho^2}\tilde{e}^T P_2 B B^T P_2 \tilde{e} \leq \frac{1}{2}\rho^2 w_1^T w_1
\tag{118}
$$

The above relation is used in $\dot{V}$, and the right part of the associated inequality is enforced

$$
\dot{V} \leq -\frac{1}{2}\hat{e}^T Q_1 \hat{e} - \frac{1}{2}\tilde{e}^T Q_2 \tilde{e} + \frac{1}{2}\rho^2 w_1^T w_1
\tag{119}
$$

Thus, Eq. (119) can be written as

$$
\dot{V} \leq -\frac{1}{2}E^T Q E + \frac{1}{2}\rho^2 w_1^T w_1
\tag{120}
$$

where

$$E = \begin{pmatrix} \hat{e} \\ \tilde{e} \end{pmatrix}, \quad Q = \begin{pmatrix} Q_1 & 0 \\ 0 & Q_2 \end{pmatrix} = diag[Q_1, Q_2] \tag{121}$$

Hence, the H_∞ performance criterion is derived. For ρ sufficiently small Eq. (119) will be true and the H_∞ tracking criterion will be satisfied. In that case, the integration of $\dot{V}$ from 0 to T gives

$$\int_0^T \dot{V}(t)dt \leq -\frac{1}{2}\int_0^T ||E||^2 dt + \frac{1}{2}\rho^2 \int_0^T ||w_1||^2 dt \Rightarrow$$
$$2V(T) - 2V(0) \leq -\int_0^T ||E||_Q^2 dt + \rho^2 \int_0^T ||w_1||^2 dt \Rightarrow \tag{122}$$
$$2V(T) + \int_0^T ||E||_Q^2 dt \leq 2V(0) + \rho^2 \int_0^T ||w_1||^2 dt$$

It is assumed that there exists a positive constant $M_w > 0$ such that $\int_0^\infty ||w_1||^2 dt \leq M_w$. Therefore for the integral $\int_0^T ||E||_Q^2 dt$ one gets

$$\int_0^\infty ||E||_Q^2 dt \leq 2V(0) + \rho^2 M_w \tag{123}$$

Thus, the integral $\int_0^\infty ||E||_Q^2 dt$ is bounded and according to Barbalat's Lemma

$$\lim_{t \to \infty} E(t) = 0 \Rightarrow$$
$$\lim_{t \to \infty} \hat{e}(t) = 0 \tag{124}$$
$$\lim_{t \to \infty} \tilde{e}(t) = 0$$

Therefore $\lim_{t \to \infty} e(t) = 0$.

7 Simulation tests

The performance of the proposed adaptive neurofuzzy control scheme for the Doubly-fed induction generator, using only output feedback, has been evaluated through simulation experiments. Indicative numerical values for the parameters of the considered doubly-fed induction generator model are given in Table I. The turn speed of the rotor ω was considered to be measurable. Moreover, the magnetic flux of the stator ψ_{s_d} was considered to be computed from measurements of stator and rotor currents, following the procedure that was explained in Section 3. The obtained experimental results are presented in Fig. 4 to Fig. 10. It can be noticed that the proposed control scheme succeeded in all cases fast and accurate tracking of the reference setpoints.

The treated control problem, that is (i) simultaneous estimation of the unknown dynamics of the generator and estimation of the machine's state vector, and (ii) use of this information by an adaptive control scheme, is of elevated difficulty. The provided Lyapunov analysis has come to confirm the stability properties of the control loop. The presented adaptive control method of the DFIG is a model-free one. This means that no prior knowledge about the dynamic model of the generator is needed. Moreover, no knowledge is needed about the mechanical torque exerted on the generator's rotor (e.g. due to wind, steam or water fall). Through the identification procedure that was analyzed in Section 5 it becomes possible to estimate in real-time the unknown dynamical model of the generator and subsequently to use this information in the control loop. Besides, this adaptive control method does not need to measure the complete state vector of the generator and is based only on output feedback. The analyzed adaptive neurofuzzy control approach exhibits robustness to external perturbation thus assuring the reliable functioning of the generator under harsh conditions.

Table I: Ratings of the modeled DFIG	
Rated power	$15.5kW$
Number of Pole pairs	4
Stator Resistance	0.58Ω
Stator Inductance	$13 \cdot mH$
Rotor Resistance	1.30Ω
Rotor Inductance	$3 \cdot mH$
Mutual Inductance	$10 \cdot mH$
Rotor's inertia	$20.0 kg \cdot m^2$

Remark 1: PID control is not the recommended solution to the problem of stabilization and control of the DFIG nonlinear dynamics. The stability analysis of PID control schemes is usually performed considering a locally linearized description of the system's dynamics in the form of a transfer function and by applying next s-frequency domain stability analysis criteria (e.g. analytical computation of phase and gain margin stability conditions, or graphical methods such as the Nyquist, Bode and root-locus diagrams). The validity of such stability analysis methods is only local. The nonlinearities in the system's dynamics imply that multiple linearization points have to be considered and different transfer functions have to be computed at the associated equilibria. The fact that the PID controller parameters are given fixed values, imposes limitations to the disturbance (or model uncertainty) rejection capabilities of the associated control loop. Moreover, the fact that the PID control signal is based on differentiation of the output error makes the control vulnerable to measurement disturbances. For these reasons one cannot ascertain global asymptotic stability features and robustness in PID control schemes and their application to non-trivial and nonlinear control problems should be avoided.

Remark 2: The proposed adaptive fuzzy control scheme for doubly-fed induction generators is shown to satisfy the H-infinity tracking performance criterion which means improved robustness to model uncertainties and external perturbations. Actually, the proposed control method is a model-free one and there is no need for prior knowledge of the parameters' values in the generator's dynamic model. The only necessary information is the order of the model (in the DFIG-case it is a 6-th order model). It is also proven that by selecting the attenuation coefficient ρ in the Riccati equation to be sufficiently small one can always assure that the first derivative of the control loop's Lyapunov function is always upper bounded by zero. The training of the neuro-fuzzy approximator is performed online and aims at identifying the unknown system dynamics. This information is used next to invert the system's dynamics thus implementing an indirect adaptive control scheme. The training of the neuro-fuzzy network is the result of an optimization procedure and actually the learning rates of the associated gradient algorithms are chosen such that the Lyapunov function is always a decreasing one and its convergence to zero is assured.

Remark 3: The considered neuro-fuzzy approximator is a four-layered one and is depicted in Fig. 2. In the input layer, the input patterns (state vectors) to the neural network are aggregated. In the second layer, the input patterns are fed into the Gaussian activation functions and their degree of matching with the centers of these basis functions is concluded. Next, the membership degrees provided by the second layer of the neural network are fed into the third layer of the network, where normalized is performed. This means that the sum of all membership degrees should be equal to 1. Finally at the fourth layer of the approximator, the unknown function describing the DFIG dynamics is computed. The output of the fourth layer is a linear function of the weights connecting it to the preceding layer. These weights can be easily tuned with the use of first order gradient algorithms. The learning rate of the gradient update is chosen according to the Lyapunov stability analysis of the control loop and from the requirement the first order derivative of the Lyapunov function to be always a negative one. This assures that the estimation error of the neuro-fuzzy approximator will be minimized, while global asymptotic stability for the control loop will be also achieved.

Remark 4: The control inputs to the DFIG,denoted as v_{r_d} and v_{r_q} are generated by an AC/DC/AC converter. However there is no particular reason for extending the state-space model of the considered DFIG
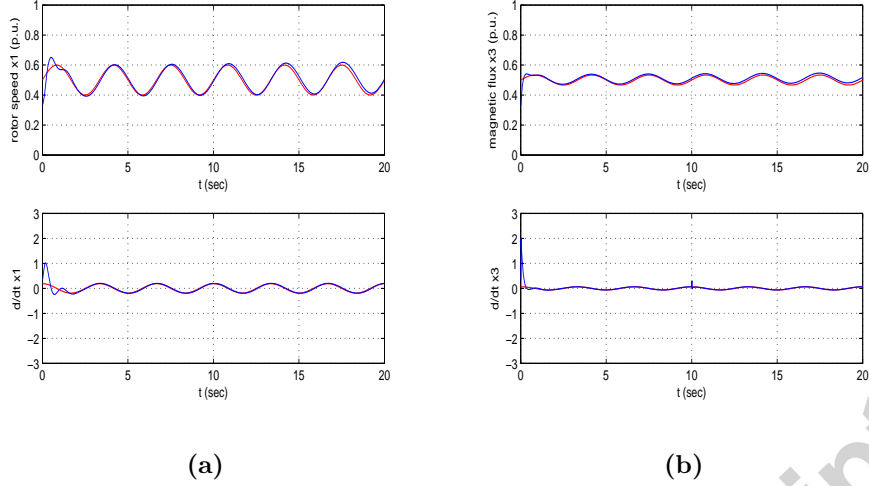
21

(a)   **(b)**

Figure 4: Tracking of setpoint 1 (red lines) from state variables of the DFIG (blue lines): (a) rotor's speed x_1 and its derivative x_2 (b) magnetic flux of the stator x_3 and its derivative x_4.
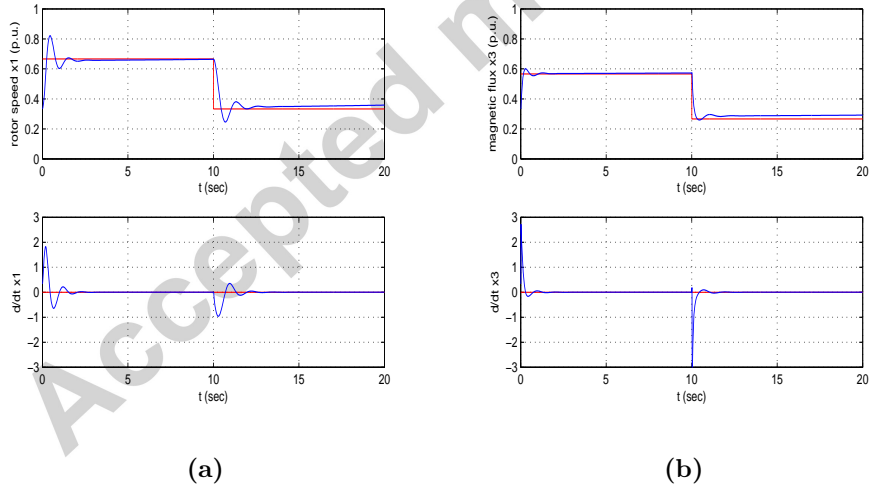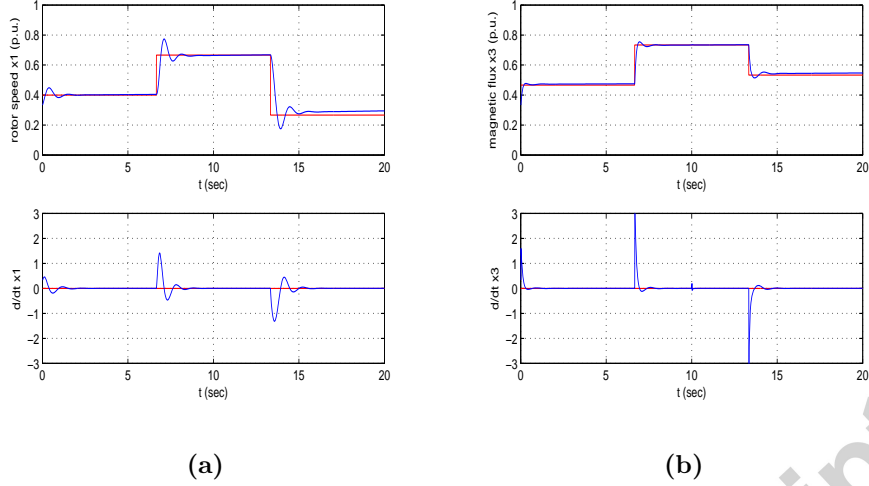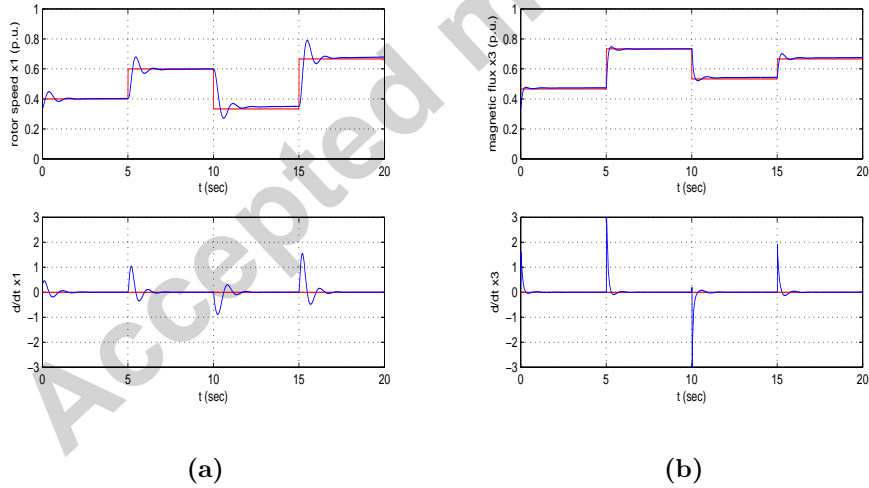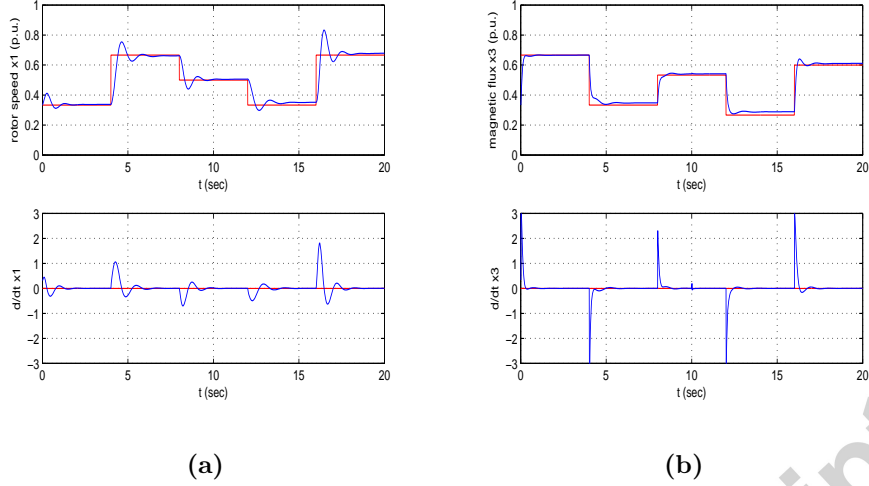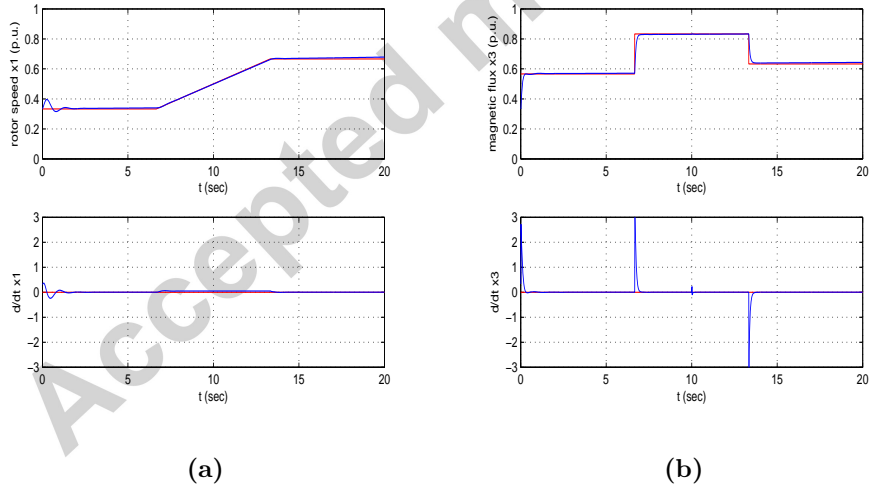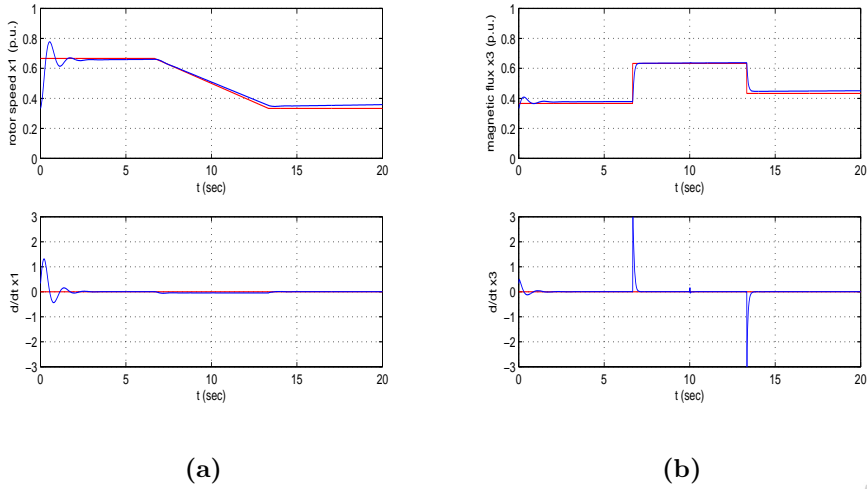

(a)   **(b)**

Figure 5: Tracking of setpoint 2 (red lines) from state variables of the DFIG (blue lines): (a) rotor's speed x_1 and its derivative x_2 (b) magnetic flux of the stator x_3 and its derivative x_4.

22

(a)   (b)

Figure 6: Tracking of setpoint 3 (red lines) from state variables of the DFIG (blue lines): (a) rotor's speed x_1 and its derivative x_2 (b) magnetic flux of the stator x_3 and its derivative x_4.

(a)   (b)

Figure 7: Tracking of setpoint 4 (red lines) from state variables of the DFIG (blue lines): (a) rotor's speed x_1 and its derivative x_2 (b) magnetic flux of the stator x_3 and its derivative x_4.

23

(a)   **(b)**

Figure 8: Tracking of setpoint 5 (red lines) from state variables of the DFIG (blue lines): (a) rotor's speed x_1 and its derivative x_2 (b) magnetic flux of the stator x_3 and its derivative x_4.

(a)   **(b)**

Figure 9: Tracking of setpoint 6 (red lines) from state variables of the DFIG (blue lines): (a) rotor's speed x_1 and its derivative x_2 (b) magnetic flux of the stator x_3 and its derivative x_4.

24

(a)   **(b)**

Figure 10: Tracking of setpoint 7 (red lines) from state variables of the DFIG (blue lines): (a) rotor's speed x_1 and its derivative x_2 (b) magnetic flux of the stator x_3 and its derivative x_4.

control system by including in it the description of the AC/DC/AC converter. The control of AC/DC and DC/AC converters has been extensively analyzed in other publications of the authors and has been treated both with global and with approximate linearization methods. The control input that should be given to the DFIG is the setpoint that the controller of the AC/DC/AC converter has to achieve. On the other side, it should not be overlooked that the proposed adaptive fuzzy control method for the DFIG is a model-free one and there is no need for prior knowledge of the generator's state-space model and of its parameters. Despite the lack of knowledge about the system's dynamics, Lyapunov stability analysis demonstrates that global asymptotic stability is achieved.

Remark 5: The control of the DFIG is finally implemented through an AC/DC/AC converter ([42-49]). This means that the control signal that is computed by the proposed adaptive neurofuzzy control method has to be generated by the aforementioned converter [42-49]. This is a secondary control problem because the control signal for the DFIG becomes the reference setpoint for the converter. In turn the converter's control can be achieved by using nonlinear control methods and applying the PWM (Pulse Width Modulation) technique. Recommended nonlinear control approaches for the converter's dynamics are those based on global linearization (e.g. differential flatness theory), those based on approximate linearization (e.g. nonlinear H-infinity control) and those based on Lyapunov methods (e.g. converter's adaptive neurofuzzy control). These approaches have been extensively analyzed in [50]. Such nonlinear control methods assure that the converter's functioning will remain robust to model uncertainty, parametric changes or external perturbations. According to the above there is no need to examine jointly the control of the converter and of the DFIG. In the same context there is no need to develop a joint state-space model for the generator and the converter. This would make the whole endeavour of adaptive neurofuzzy control of the DFIG unnecessarily complicated because one would have to work with state-space models of elevated dimensionality.

8 Conclusions

The increasing needs in energy supply and the rapid deployment of renewable energy systems has turned control of power generators into a problem of primary importance in the area of control and power engineering. Common model-free control approaches of the PID-type have been proven insufficient for the case of

variable operating conditions of the power generators and their functioning under unmodelled disturbances. The present article has presented a model-free control method for Doubly-fed induction generators which is based on differential flatness theory and on adaptive control theory. In this approach it was assumed that only the order of the DFIG's model was known, whereas its parameters and the differential equations constituting its state-space description were completely unknown. It was proven that the DFIG's model is a differential flat one and by exploiting the differential flatness properties its transformation to the linear canonical form has become possible.

In this new linearized form the DFIG's inputs contained unknown nonlinear functions which describe the system's nonlinear dynamics. These unknown terms were identified with the use of neurofuzzy approximators and the estimated functions' values were fed into a feedback controller, thus implemented an indirect adaptive control scheme. The learning of the approximators was determined by the requirement to have always a negative first-rder derivative for the system's Lyapunov function. To cope with the non-measurable elements in the state vector being fed in the controller a state observer was used in the control loop. To robustify the control loop an additional control term was used, being computed in accordance to H-infinity control theory. The stability of the aggregate control scheme was proven with the use of Lyapunov analysis. Through simulation experiments the excellent performance of this DFIG contol scheme has been confirmed. Taking into account that in real operating conditions one cannot assume knowledge of the generator's exact model and that parametric variations and external perturbations disrupt the generator's functioning, the significance of the proposed model-free control approach becomes apparent.

References

[1] G. Rigatos, P. Siano, N. Zervos and C. Cecati, Control and disturbances compensation for Doubly-Fed Induction Generators using the Derivative-free Nonlinear Kalman Filter, IEEE Transactions on Power Electronics, 2015

[2] G.D. Marques and D.M. Sousa, Stator Flux Active Damping Methods for Field-Oriented Doubly Fed Induction Generator, IEEE Transactions on Energy Conversion, vol. 27, no. 3, pp. 799-806, 2012.

[3] D.G. Forchetti, J.A. Solsona, G.O. Garcia and M.I. Valla, A control strategy for stand-alone wound rotor induction machine, Electric Power Systems Research, Elsevier, vol. 77, pp. 163-169, 2007

[4] A. Gensior, T.M.P. Nguyen, J. Rudolph and H. Guldner, Flatness-based loss optimization and control of a doubly-fed induction generator system, IEEE Transactions on Control Systems Technology, vol. 19, no. 6, pp. 1457-1466, 2011.

[5] B. Boukhezzar and H. Siguerdidjane, Nonlinear control with wind estimation of a DFIG variable speed wind turbine for power capture optimization, Energy Conversion and Management, Elsevier, vol. 50, pp. 885-892, 2009.

[6] R. Pena, R. Cardenas, E. Reyes, J. Clare and P. Wheeler, Control of a Doubly Fed Induction Generator via an Indirect Matrix Converter With Changing DC Voltage, IEEE Transactions on Industrial Electronics, vol. 58, no. 10, pp. 4664-4674, 2011.

[7] V. Calderaro, V. Galdi, A. Piccolo and P. Siano, A fuzzy controller for maximum energy extraction from variable speed wind power generation systems, Electric Power Systems Research, Elsevier, vol. 78, pp. 11091118, 2008.

[8] G. Rigatos and P. Siano, DFIG control using Differential flatness theory and Extended Kalman Filtering, IFAC INCOM 2012, 14th IFAC Intl. Conference on Information Control Problems in Manufacturing, Bucharest, Romania, May 2012.

[9] G. Rigatos and P. Siano, A nonlinear H-infinity feedback control approach for asynchronous generators IEEE ICCEP 2015, 5th International Conference on Clean Electrical Power, Taormina, Sicily, Italy, June, 2015.

[10] S. Abdeddaim, A. Betka, S. Drid, and M. Becherif, Implementation of MRAC controller of a DFIG based variable speed grid, Energy Conversion and Management, Elsevier, vol. 79, pp. 281-288, 2014 connected wind turbine

[11] L. Wang and D. Truong, Stability Enhancement of a Power System With a PMSG-Based and a DFIG-Based Offshore Wind Farm Using a SVC With an Adaptive-Network-Based Fuzzy Inference System, IEEE Transactions on Industrial Electronics, vol. 60, no. 7, 2799-2807 2013

[12] F. Wu, X.P. Zhang, P. Ju and M.J.H. Sterling, Decentralized nonlinear control of wind turbine with doubly-fed induction generator, IEEE Transactions on Power Systems, vol. 23, no. 2, pp. 613-621, 2008.

[13] Y. Xue and N. Tai, System frequency regulation in doubly fed induction generators, Electrical Power and Energy Systems, vol. 43, pp. 977983, 2012.

[14] H. Xu, J. Hu and Y. He, Operation of Wind-Turbine-Driven DFIG Systems Under Distorted Grid Voltage Conditions: Analysis and Experimental Validations, IEEE Transactions on Power Electronics, vol.27, no.5, pp.2354-2366, 2012.

[15] J. Yao, Hui Li, Z. Chen, X. Xia, X.Chen, Q. Li and Y. Liao Enhanced Control of a DFIG-Based Wind-Power Generation System With Series Grid-Side Converter Under Unbalanced Grid Voltage Conditions, IEEE Transactions on Power Electronics, vol. 28, no. 7, pp. 3167-3181, 2013.

[16] J. Yao, H. Li, Z. Chen, X. Xia, X. Q. Li and Y. Liao, Enhanced Control of a DFIG-Based Wind-Power Generation System With Series Grid-Side Converter Under Unbalanced Grid Voltage Conditions, IEEE Transactions on Power Electronics, vol.28,no.7, pp. 3167-3181, 2013.

[17] P. Aguglia, P. Voiarouge, R. Wamkeue and J. Cros, Determination of fault operation dynamical constraints for the design of wind turbine DFIG drives, Mathematics and Computers in Simulation, Elsevier, vol. 81, pp. 252-262, 2010.

[18] D.G. Forchetti, G.O. Garcia and M.I. Valla, Adaptive observer for sensorless control of stand-alone doubly-fed induction generator, IEEE Transactions on Industrial Electronics, vol. 56, no. 10, pp. 4174-4180, 2009.

[19] S. Yang and V. Ajjarapu, A speed-adaptive reduced-order observer for sensorless vector control of doubly-fed induction generator-based variable-speed wind turbines, IEEE Transactions on Energy Conversion, vol. 25, no.3, pp. 891-900, 2010.

[20] S. Peresada, A. Tilli,and A. Tonielli, Power control of a doubly fed induction machine via output feedback, Control Engineering Practice, Elsevier, vol. 12, pp. 4157, 2004.

[21] C.M. Hong, F.S. Cheng and C.H. Chen, Optimal control for variable-speed wind generation systems using General Regression Neural Network, Electric Power and Energy Systems, Elsevier, vol. 60, pp. 14-23, 2014.

[22] H.M. Hasanien and S.M. Muyeen, Speed control of grid-connected switched reluctance generator driven by variable speed wind turbine using adaptive neural network controller, Electric Power Systems Research, Elsevier, vol. 84, pp. 206-213, 2012.

[23] W.M. Lin, C.M. Hong, F.S. Cheng, Design of intelligent controllers for wind generation system with sensorless maximum wind energy control, Energy Conversion and Management, Elsevier, vol. 52, pp. 1086-1096, 2011

[24] E. Kamal and A. Aitouche, Robust fault tolerant control of DFIG wind energy systems with unknown inputs, Renewable Energy, Elsevier, vol. 56, pp. 2-15, 2013.

[25] C. Belfedal, S. Gherbi, M. Sedraoui, S. Moreaua, G. Champenois, T. Allaoui and M.A. Denai, Robust control of doubly fed induction generator for stand-alone applications, Electric Power Systems Research, vol. 80, pp. 230-239, 2010.

[26] D. Qian, S.Tong, H. Liu and X.Liu, Load frequency control by neural-network-based integral sliding-mode for nonlinear power systems with wind turbines, Neurocomputing, Elsevier, vol. 173, pp. 873-885, 2016.

[27] Y. Tang, H.He, Zhen Ni, J.Wen, and X. Sui, Reactive power control of grid-connected wind farm based on adaptive dynamic programming, Neurocomputing, Elsevier, vol. 125, pp. 125-133. 2014.

[28] W.Guo, F. Liu, J. Si, D. He, R. Harley and S. Mei, Approximate dynamic programming based supplementary reactive power control for DFIG wind farm to enhance power system stability, Neurocomputing, Elsevier, vol. 170, pp. 117-127, 2015

[29] J. Rudolph, Flatness Based Control of Distributed Parameter Systems, Examples and Computer Exercises from Various Technological Domains, *Shaker Verlag*, Aachen, 2003.

[30] H. Sira-Ramirez and S. Agrawal, Differentially Flat Systems, Marcel Dekker, New York, 2004.

[31] J. Lévine, On necessary and sufficient conditions for differential flatness, Applicable Algebra in Engineering, Communications and Computing, Springer, vol. 22, no. 1, pp. 47-90, 2011.

[32] M. Fliess and H. Mounier, Tracking control and π-freeness of infinite dimensional linear systems, In: G. Picci and D.S. Gilliam Eds.,Dynamical Systems, Control, Coding and Computer Vision, vol. 258, pp. 41-68, *Birkhaüser*, 1999.

[33] J. Villagra, B. d'Andrea-Novel, H. Mounier and M. Pengov, Flatness-based vehicle steering control strategy with SDRE feedback gains tuned via a sensitivity approach, IEEE Transactions on Control Systems Technology, vol. 15, pp. 554-565, 2007.

[34] S. Bououden, D. Boutat, G. Zheng, J.P. Barbot and F. Kratz, A triangular canonical form for a class of 0-flat nonlinear systems, International Journal of Control, Taylor and Francis, vol. 84, no. 2, pp. 261-269, 2011.

[35] H. Sira-Ramirez and M. Fliess, On the output feedback control of a synchronous generator, 43rd IEEE Conference on Decision and Control Dec. 2004, Bahamas.

[36] G.G. Rigatos, Modelling and control for intelligent industrial systems: adaptive algorithms in robotcs and industrial engineering, Springer, 2011.

[37] G. Rigatos, Nonlinear control and filtering using differential flatness approaches: applications to electromechanical systems, Springer, 2015.

[38] P. Martin and P. Rouchon, Two remarks on induction motors, CESA 96 IMACS Multiconference, vol. 1, pp. 76-79, Lille, France, 1996.

[39] G.G. Rigatos and S.G. Tzafestas, Extended Kalman Filtering for Fuzzy Modelling and Multi-Sensor Fusion, Mathematical and Computer Modelling of Dynamical Systems, *Taylor & Francis*, vol. 13, pp. 251-266, 2007.

[40] M. Basseville and I. Nikiforov, Detection of abrupt changes: Theory and Applications, *Prentice-Hall*, 1993.

[41] G. Rigatos and Q. Zhang, Fuzzy model validation using the local statistical approach, Fuzzy Sets and Systems, Elsevier, vol. 60, no.7, pp. 882-904, 2009.

[42] Z. Chen, J.M. Guerrero, and F. Blaabjerg, A review of the state of the art of power electronics for wind turbines. IEEE Transactions on Power Electronics, vol. 24, no. 8, pp. 1859-1875, 2009.

[43] F. Blaabjerg, M. Liserre and K. Ma, Power electronics converters for wind turbine systems, IEEE Transactions on Industry Applications, vol.48, no. 2, pp. 708-719, 2011.

[44] F. Blaabjerg and Z. Chen, Power electronics for modern wind turbines, Synthesis Lectures on Power Electronics, vol. 1, no. 1, pp. 1-68, 2005.

[45] S.H.,Song, S.I. Kang, N.K. Hahm, Implementation and control of grid connected AC-DC-AC power converter for variable speed wind energy conversion system, In Applied Power Electronics Conference and Exposition, IEEE APEC 2003. Eighteenth Annual IEEE Conference, vol. 1, pp. 154-158). 2003.

[46] V.S.C. Raviraj and P.C. Sen, Comparative study of proportional-integral, sliding mode, and fuzzy logic controllers for power converters. IEEE Transactions on Industry Applications, vol. 33, no 2, pp.518-524, 1997.

[47] T.J. Lee, Input-output linearization and zero-dynamics control of three-phase AC/DC voltage-source converters, IEEE Transactions on Power Electronics, vol. 18, no. 1, pp. 11-22, 2003.

[48] J. Hu, H. Xu and Y. He, Coordinated Control of DFIGs RSC and GSC Under Generalized Unbalanced and Distorted Grid Voltage Conditions, IEEE Transactions on Industrial Electronics, vol. 60, no.7, pp. 2808-2819, 2013

[49] F. Taveiors, L. Barros and F. Costa, Back-to-back converter state-feedback control of DFIG (doubly-fed induction generator)-based wind turbines, Energy, Elsevier, vol. 89, pp. 896-906, 2015

[50] G. Rigatos, Intelligent renewable energy systems: modelling and control, Springer,2017
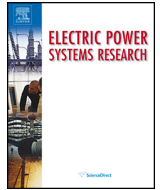
Fuzzy logic based speed control of indirect field oriented controlled Double Star Induction Motors connected in parallel to a single six-phase inverter supply

Zoheir Tir [a,*], Om P. Malik [b,1], Ali M. Eltamaly [c,2]

[a] LEVRES—Research Laboratory, Dept. of Electrical Engineering, University of El Oued, B.P.789, 39000 El Oued, Algeria
[b] Dept of Electrical and Computer Engineering, University of Calgary, Calgary, AB, Canada
[c] Dept of Electric Engineering, Mansoura University, Mansoura, Egypt

A B S T R A C T

Speed control of two Double Star Induction Motors operating in parallel configuration with Indirect Field Oriented Control using a Fuzzy Logic Controller is investigated. The two motors are connected in parallel at the output of a single six-phase PWM based inverter fed from a DC source. Performance of the proposed method under load disturbances is studied through simulations. A comparison of the speed response with the two controllers is presented and analyzed.

© 2016 Elsevier B.V. All rights reserved.

1. Introduction

Use of Double Star Induction Motor (DSIM) drives, especially for high-power applications, has increased considerably over the past 40 years [1–7]. This type of machine is composed of two windings with a 30 electrical degree phase shift. These windings are generally fed by a six-phase inverter supply in variable speed drives [4,5,7–11]. Characteristics, modeling, control and performance of DSIM are extensively covered in [1–3,5,6,8,9,12–16]. The main advantages of this motor are: (1) reduced torque ripple; (2) reduced rotor harmonics as they can be filtered; (3) reduced harmonic content of the DC-link current; and (4) increased reliability as the larger number of phases of this machine allows operation with one or more phases in fault [1–7,11–13,16,17]. With these principal advantages, the drive technique with two Double Star Induction Motors operating in parallel and fed by a single six-phase PWM based inverter can be used in several applications especially

in the field of high power electric/hybrid vehicles, rolling stock traction systems such as locomotive and electric ship propulsion [3,7,14,17,18]. For these applications, the parallel DSIM drive technique can reduce the duplicated components such as inverter, input filter, protection circuit, and help to reduce the cost of the system [19–22].

In recent years, various parallel configurations have been widely proposed for two multi-phase machines drive to feed them from a single inverter [7,18–32]. Among multi-phase machines; five-phase and six-phase machines are more common. A parallel configuration to feed two five-phase motors from a single inverter is suggested in [18,32], and sliding mode control based speed control of two six-phase motors connected in parallel to a single inverter supply is proposed in [7]. These parallel configurations provide decoupled control of flux and torque for each machine and their performance is evaluated experimentally.

Speed control of indirect field oriented controlled DSIMs connected in parallel to a single six-phase inverter supply using Fuzzy Logic Control (FLC) is investigated in this paper. This system is suitable for applications using dual DSIMs with the advantage of compactness, lightness and economy [19–21].

FLC is based on linguistic rules with an IF-THEN general configuration [33]. Its principal advantage resides in the fact that it does

* Corresponding author. Tel.: +00770284829.
  E-mail addresses: tir-zoheir@univ-eloued.dz (Z. Tir), maliko@ucalgary.ca (O.P. Malik), eltamaly@ksu.edu.sa (A.M. Eltamaly).
  [1] Tel: +1 403 220 6178.
  [2] Tel: +00966 14676828.

not need a precise mathematical model of the nonlinear dynamic plant such as an electric machine [34]. It can also handle arbitrarily complex nonlinearity. Moreover, it is robust and as proposed in this paper, the fuzzy output is obtained by 4 fuzzy rules. Robustness of the proposed controller is checked in terms of DSIMs' speed and load variations connected in parallel. Speed performance of the DSIMs with FLC is also compared with that obtained using the commonly employed PI controller.

The paper is organized as follows. System configuration is described in Section 2 with the model of the DSIM given in Section 3. The DSIM field oriented control is described in Section 4 and details of the two controllers (FLC and PI) are given in Section 5 followed by the presentation of results and discussion in Section 6. The conclusions are drawn in Section 7.

2. System configuration

A schematic diagram of the Indirect Field Oriented Control (IFOC) of dual motors connected in parallel to a single six-phase inverter supply is shown in Fig. 1. This method has been adopted in order to avoid the over magnetization of these motors [23]. This method is characterized by the slip angular speed calculation, the stator flux angle calculation and the rotor angular speed calculation. Speeds of the two DSIMs are measured using sensors. The torque reference of each DSIM is calculated from the difference between reference speeds. FLC or PI controllers are used in the speed control loops for the DSIMs as shown in the figure. The other blocks in the figure can be found in the conventional field vector control method, such as [1].

Studies of the drive system in the PWM mode in the middle speed region and in the single pulse mode in the high speed region are performed. The robustness of the proposed method is checked in terms of motor speed and load variations.

3. Modeling of the DSIM

Electrical equations used to model each DSIM in the Park reference frame are [9]:

$$v_{ds1} = R_s i_{ds1}^M + \frac{d\lambda_{ds1}^M}{dt} - \omega_s \lambda_{qs1}^M \tag{1}$$

$$v_{ds2} = R_s i_{ds2}^M + \frac{d\lambda_{ds2}^M}{dt} - \omega_s \lambda_{qs2}^M \tag{2}$$

$$v_{qs1} = R_s i_{qs1}^M + \frac{d\lambda_{qs1}^M}{dt} + \omega_s \lambda_{ds1}^M \tag{3}$$

$$v_{qs2} = R_s i_{qs2}^M + \frac{d\lambda_{qs2}^M}{dt} + \omega_s \lambda_{ds2}^M \tag{4}$$

$$0 = R_r i_{dr}^M + \frac{d\lambda_{dr}^M}{dt} - (\omega_s - \omega_{r-M})\lambda_{qr}^M \tag{5}$$

$$0 = R_r i_{qr}^M + \frac{d\lambda_{qr}^M}{dt} + (\omega_s - \omega_{r-M})\lambda_{dr}^M \tag{6}$$

where the stator and rotor flux linkages are expressed as [9]:

$$\lambda_{ds1} = L_s i_{ds1}^M + L_m \left(i_{ds1}^M + i_{ds2}^M + i_{dr}^M \right) \tag{7}$$

$$\lambda_{ds2} = L_s i_{ds2}^M + L_m \left(i_{ds1}^M + i_{ds2}^M + i_{dr}^M \right) \tag{8}$$

$$\lambda_{qs1} = L_s i_{qs1}^M + L_m \left(i_{qs1}^M + i_{qs2}^M + i_{qr}^M \right) \tag{9}$$

$$\lambda_{qs2} = L_s i_{qs2}^M + L_m \left(i_{qs1}^M + i_{qs2}^M + i_{qr}^M \right) \tag{10}$$

$$\lambda_{dr} = L_r i_{dr}^M + L_m \left(i_{ds1}^M + i_{ds2}^M + i_{dr}^M \right) \tag{11}$$

$$\lambda_{qr} = L_r i_{qr}^M + L_m \left(i_{qs1}^M + i_{qs2}^M + i_{qr}^M \right) \tag{12}$$

The electromagnetic torque of each DSIM can be obtained by:

$$T_{em-M} = P_M \frac{L_m}{L_m + L_r} \left[\left(i_{qs1}^M + i_{qs2}^M \right) \lambda_{dr}^M - \left(i_{ds1}^M + i_{ds2}^M \right) \lambda_{qr}^M \right] \tag{13}$$
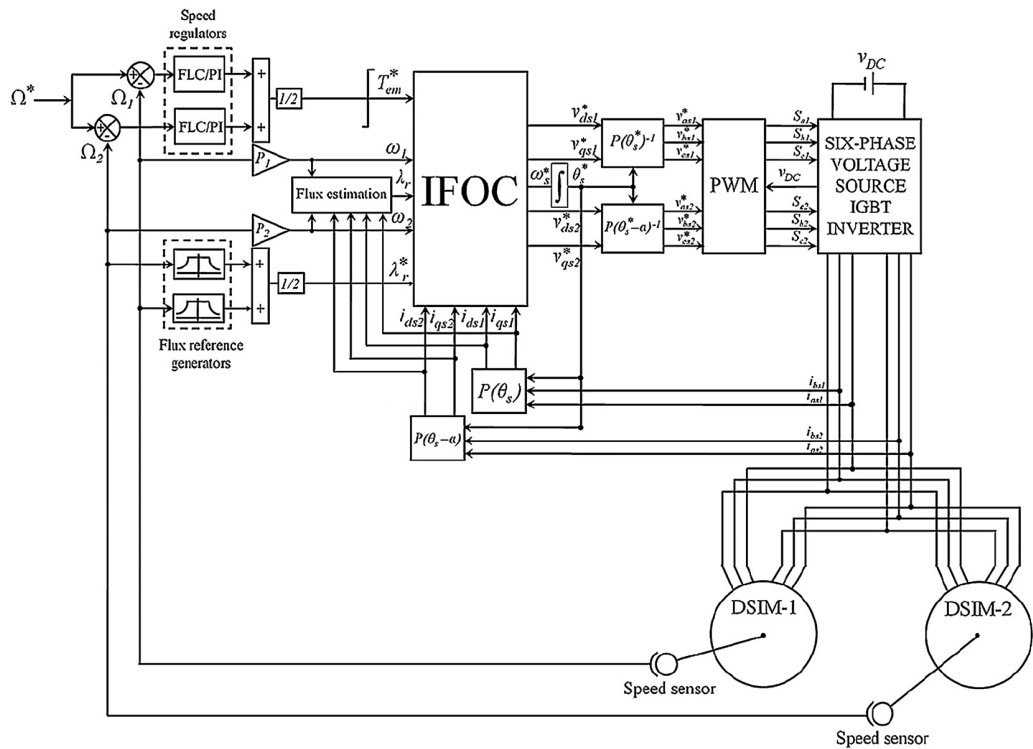

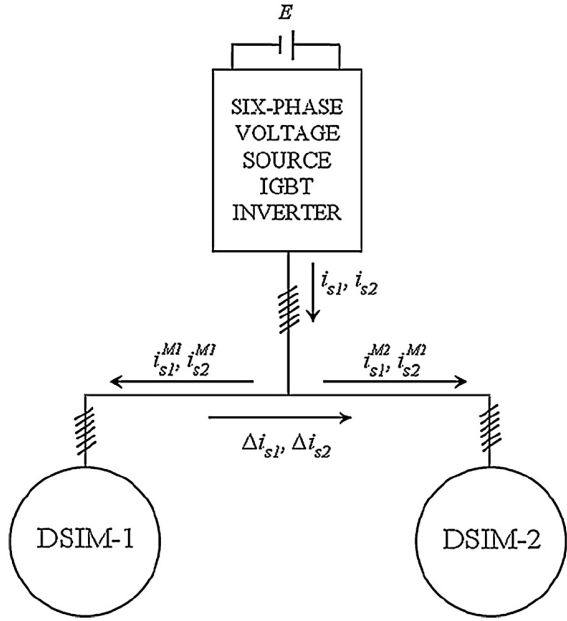**Fig. 1.** Block diagram of the indirect flux oriented control of DSIMs.

Fig. 2. Current flows for parallel connected dual DSIMs.

The mechanical equation of each motor is expressed by:

$$J\frac{d\Omega_M}{dt} + k_f \Omega_M = T_{em-M} - T_{L-M} \tag{14}$$

where ω_s is the synchronous reference frame; L_s and L_r are stator and rotor inductances, respectively; L_m is the resultant magnetizing inductance; P_M is the number of pole pairs; J is the moment of inertia; k_f is the total viscous friction coefficient; T_{L-M} is the load torque; ω_{r-M} is the rotor electrical angular speed; Ω_M is the rotor mechanical angular speed, and M denotes DSIM-1 or DSIM-2.

All these parameters are for each of the two DSIMs.

The currents, i_{s1} and i_{s2}, flowing in each motor can be expressed by i_s which flows equally in both motors, and Δi_{s1} and Δi_{s2} which circulates between the two motors. Currents flowing in the parallel connected DSIMs are shown in Fig. 2 and the relationship of these currents is given below:

$$i_{s1} = i_{s1}^{M1} + i_{s1}^{M2}, \quad i_{s2} = i_{s2}^{M1} + i_{s2}^{M2},$$

$$\Delta i_{s1} = \frac{i_{s1}^{M2} - i_{s1}^{M1}}{2} \quad \text{and} \quad \Delta i_{s2} = \frac{i_{s2}^{M2} - i_{s2}^{M1}}{2}$$

4. Dual DSIMs' field oriented control

4.1. Reference-frame

By choosing the orientation of the rotor flux linkage, the electromagnetic torque and rotor flux linkage will be linked directly to the stator current components. Assuming the rotor flux linkage is aligned with the d-axis [9]:

$$\lambda_{dr} = \lambda_r^* \tag{15}$$

$$\lambda_{qr} = 0 \tag{16}$$

Thus,

$$\lambda_r^* = \frac{\lambda_{r1}^* + \lambda_{r2}^*}{2}$$

where λ_{r1}^* and λ_{r2}^*: Rotor flux linkages of DSIM-1 and DSIM-2, respectively.

Note: The DSIMs' control principle is similar to the well-known rotor IFOC used for the conventional electric machines.

4.2. Control strategy

The reference voltages (v_{ds1}^*, v_{qs1}^*, v_{ds2}^* and v_{qs2}^*) are derived by substituting Eqs. (15) and (16) in Eqs. (1)–(4)

$$v_{ds1}^* = R_s i_{ds1} + L_s \frac{di_{ds1}}{dt} - \omega_s^* \left(L_s i_{qs1} + T_r \lambda_r^* \omega_{sl}^* \right) \tag{17}$$

$$v_{qs1}^* = R_s i_{qs1} + L_s \frac{di_{qs1}}{dt} - \omega_s^* \left(L_s i_{ds1} + \lambda_r^* \right) \tag{18}$$

$$v_{ds2}^* = R_s i_{ds2} + L_s \frac{di_{ds2}}{dt} - \omega_s^* \left(L_s i_{qs2} + T_r \lambda_r^* \omega_{sl}^* \right) \tag{19}$$

$$v_{qs2}^* = R_s i_{qs2} + L_s \frac{di_{qs2}}{dt} - \omega_s^* \left(L_s i_{ds2} + \lambda_r^* \right) \tag{20}$$

where $\quad i_{ds1} = i_{ds1}^{M1} + i_{ds1}^{M2}, \quad i_{qs1} = i_{qs1}^{M1} + i_{qs1}^{M2}, \quad i_{ds2} = i_{ds2}^{M1} + i_{ds2}^{M2}$ and $\quad i_{qs2} = i_{qs2}^{M1} + i_{qs2}^{M2}$

$$T_r = \frac{L_r}{R_r} \tag{21}$$

T_r denotes the rotor time constant.

The component references of stator current and slip speed ω_{sl}^* can be expressed as:

$$\omega_{sl}^* = \frac{R_r L_m}{(L_m + L_r) \lambda_r^*} i_{qs}^* \tag{22}$$

$$i_{ds}^* = \frac{1}{L_m} \lambda_r^* \tag{23}$$

$$i_{qs}^* = \frac{(L_m + L_r)}{P L_m \lambda_r^*} T_{em}^* \tag{24}$$

The d–q axes currents are referred as flux-producing $\left(i_{ds}^* \right)$ and torque-producing $\left(i_{qs}^* \right)$ components of the DSIMs' stator currents, respectively.

To generate the reference voltage vectors (v_{ds1}^*, v_{qs1}^*, v_{ds2}^* and v_{qs2}^*) the PI controller is introduced as shows in Fig. 3.

5. Controller design

5.1. PI controllers

Each DSIM drive has two controllers: the first is the current controller or the inner-loop controller, Fig. 4, and the second is the speed controller or the outer-loop controller, Fig. 5.

The PI controller of the current (i_s), in the inner-loop shown in Fig. 4, is designed first.

Transfer function of the PI controller is:

$$G_c(s) = K_P + \frac{K_i}{s} = K_P \left(1 + \frac{1}{T_i s} \right) = K_P \left(\frac{1 + T_i s}{T_i s} \right) \tag{25}$$

where, K_p and K_i represent, respectively, the proportional and integral gains, and T_i represents the integral time of the current controller.

The transfer function of the system (DSIM) is presently defined as follows:

$$G_s(s) = \frac{i_s}{v_s} = \frac{1}{R_s + s L_s} = \frac{K}{1 + s \tau_s} \tag{26}$$

where $K = 1/R_s$ and $\tau_s = L_s/R_s$ are the system gain and time constant, respectively.

The open-loop transfer function ($G_{ol}(s)$) of the system is:

$$G_{ol}(s) = G_c(s) G_s(s) = K_P \left(\frac{1 + T_i s}{T_i s} \right) \left(\frac{K}{1 + \tau_s s} \right) \tag{27}$$
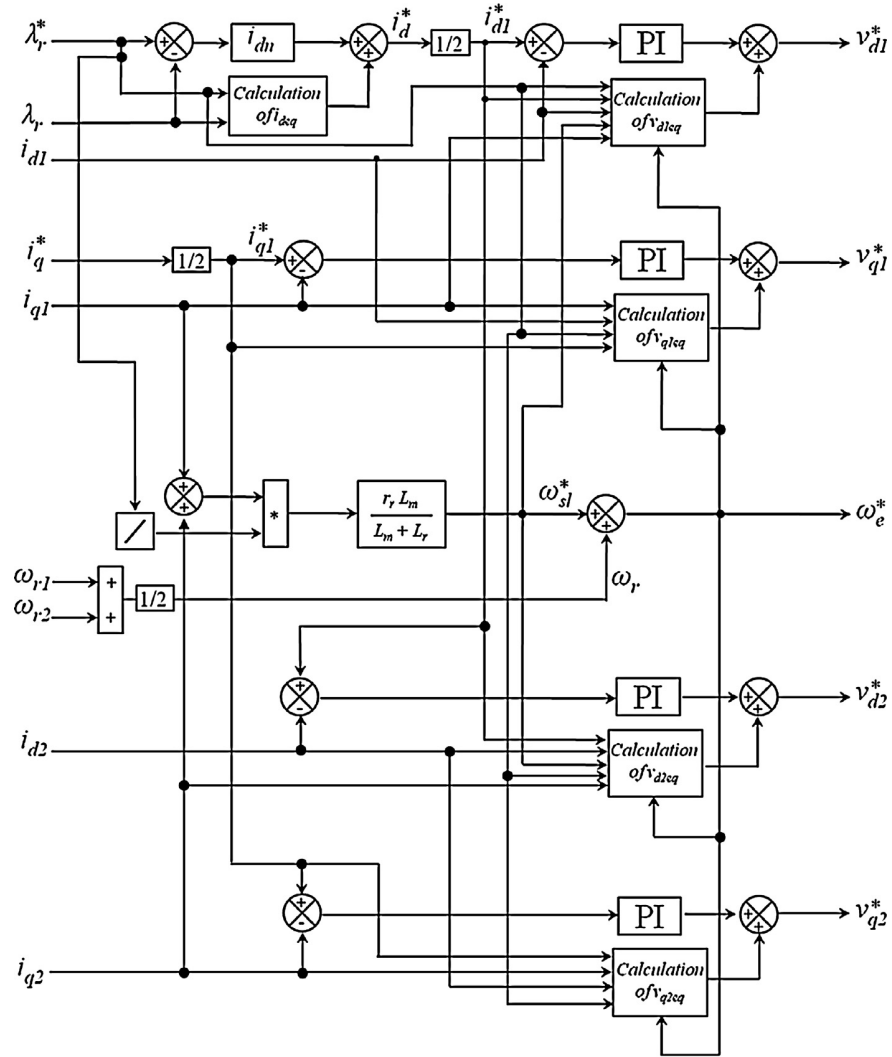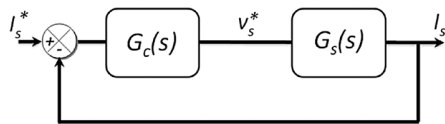
Fig. 3. IFOC of the DSIMs [6].

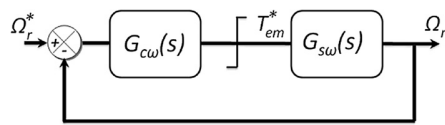**Fig. 4.** Current PI controller block diagram.

Fig. 5. Speed PI controller block diagram.

Let

$$(1 + T_i s) = (1 + \tau_s s) \tag{28}$$

The closed-loop transfer function ($G_{cl}(s)$) of the system is:

$$G_{cl}(s) = \frac{G_{ol}(s)}{1 + G_{ol}(s)} = \frac{1}{1 + (T_i/K_p \cdot K) s} = \frac{1}{1 + T_0 s} \tag{29}$$

where,

$$T_0 = \frac{T_i}{K_p \cdot K} \tag{30}$$

T_0 is the time constant of the closed-loop system.

According to Eqs. (25), (28) and (30), gains of the PI controller are as follows:

$$K_p = \frac{\tau_s}{K T_0} \tag{31}$$

$$K_i = \frac{K_p}{T_i} \tag{32}$$

Note: The value of T_0 is the same as the time constant of the system τ_s, [35].

The PI controller of the speed (ω_s), in the outer-loop shown in Fig. 5, is implemented in the same way as the current controller.

The transfer function of the system (DSIM) is presently defined as follows:

$$G_{s\omega}(s) = \frac{1}{k_f + sJ} = \frac{K_\omega}{1 + s\tau_{s\omega}} \tag{33}$$

where $K_\omega = 1/k_f$ and $\tau_{s\omega} = J/k_f$ are the system gain and time constant, respectively.

Table 1
Parameters of the PI controller.

	K_p	K_i
Speed control loop	13.26 [kg m^2/s]	0.20 [(kg m^2)/s^2]
Currents control loop	11.96 [H/s]	379.92 [H/s^2]
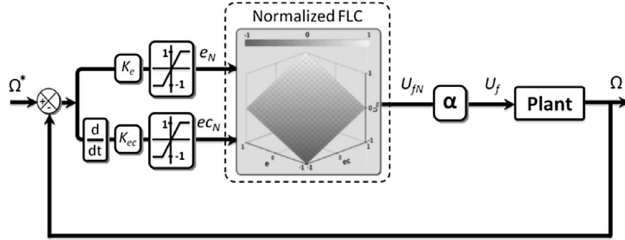
Fig. 6. Fuzzy Logic Controller.
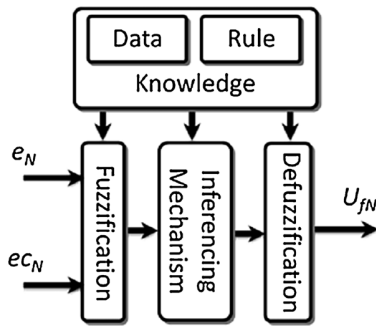
Fig. 7. Block diagram of FLC.

Finally, the gains of the speed controller are calculated as:

$$K_{p\omega} = \frac{\tau_{s\omega}}{K_\omega T_{0\omega}} \tag{34}$$

$$K_{i\omega} = \frac{K_{p\omega}}{T_{i\omega}} \tag{35}$$

Parameters of the PI controllers are given in Table 1.

5.2. Fuzzy Logic Controller

Fuzzy logic theory, based on the strategy of expert knowledge to take decision, was first developed and proposed in [36]. FLC, Fig. 6, is an interesting alternative to the conventional controllers such as PI, which may not yield fully acceptable control performance if the controlled dynamic plant is highly non-linear, uncertain and operates over a wide range [33, 34].

FLC using the product-sum-gravity inference method consists of four blocks: fuzzification, knowledge base, inference mechanism and deffuzification, as shown in Fig. 7 [8].

The input variables of FLC are the error, e_N, and changes in error, ec_N, signals. The output variable is generated from fuzzy rule base and product-sum-gravity method. After the control is computed, defuzzifier is used to obtain the crisp signal.

The speed error and error change signals are defined as:

$$e(k) = \Omega_{\text{ref}}(k) - \Omega(k) \tag{36}$$

$$ec(k) = e(k) - e(k-1) \tag{37}$$

where Ω presents the rotor mechanical angular speed. The corresponding output (U_f) is the torque component T_{em-M}.

The inputs and the output are related as:

$$U_{fN}(t) = f(e(t), ec(t)) \tag{38}$$
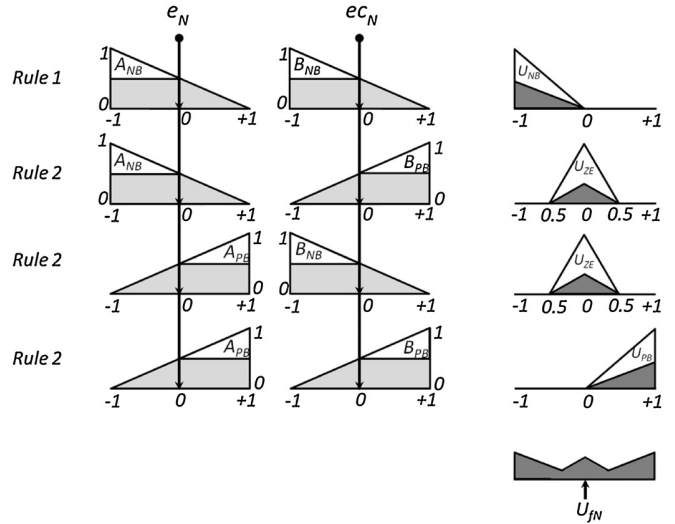
Fig. 8. Product-sum-gravity method.

The relationship between scaling factors and the input and output variables of the controller are as follows:

$$e_N = K_e e, \quad ec_N = K_{ec} ec \quad \text{and} \quad U_f = \alpha U_{fN}$$

The scaling factors (SFs) K_e and K_{ec} are used to normalize the error $e(t)$ and error changes $ec(t)$, respectively. Notice that the normalized inputs, (e, ec), remain within the limits of −1 to +1.

The adequate values of K_e, K_{ec} and α can be calculated as below:

$$K_e = \frac{1}{\Omega_N} = \frac{1}{104} = 0.0096 \quad [\text{s/rd}] \tag{39}$$

$$K_{ec} = \frac{1}{\Delta\Omega_{\max}} = 3e - 4 \quad [\text{s}^2/\text{rd}] \tag{40}$$

where $\Delta\Omega_{\max} = \Omega_k - \Omega_{k-1}$

$$\alpha = U_{f\max} = 1380 \tag{41}$$

The product-sum-gravity method is shown in Fig. 8 [37–40].

The product-sum-gravity method for the following fuzzy rules has the form [33,38–40]:

> If e_N is A_{NB} and ec_N is B_{NB} then U_{fN} is U_{NB}.
> If e_N is A_{PB} and ec_N is B_{PB} then U_{fN} is U_{PB}.
> If e_N is A_{NB} and ec_N is B_{PB} then U_{fN} is U_{ZE}.
> If e_N is A_{PB} and ec_N is B_{NB} then U_{fN} is U_{ZE}.

where A_i, B_i are the membership functions (MFs) of e_N and ec_N, respectively, and U_{fN} is MF of the output variable of the fuzzy controller.

The membership functions used for input and output fuzzy sets are presented in Fig. 9.

The next stage after processing the inputs through knowledge base and inferencing mechanism is that of de-fuzzification. In this paper, the defuzzification method chosen is the center of gravity [8,41]. Therefore, the control output U_{fN} can be calculated as:

$$U_{fN} = \frac{\sum_{k=1}^{4} \mu(U_{fN}(k)) U_{fN}(k)}{\sum_{k=1}^{4} \mu(U_{fN}(k))} \tag{42}$$

where $\mu(U_{fN}(k))$ is the output membership value for kth rule and $U_{fN}(k)$ denotes the output value of FLC.

The linear control surface of output (U_{fN}) of the FLC controller based on only four rules is shown in Fig. 10 with respect to product-sum-gravity (PSG) method [38,42,43].
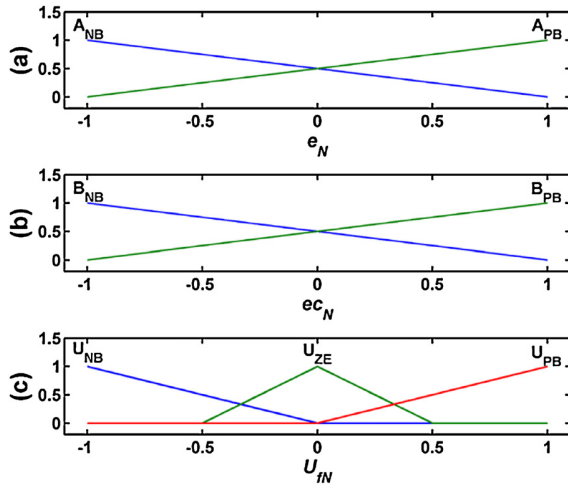
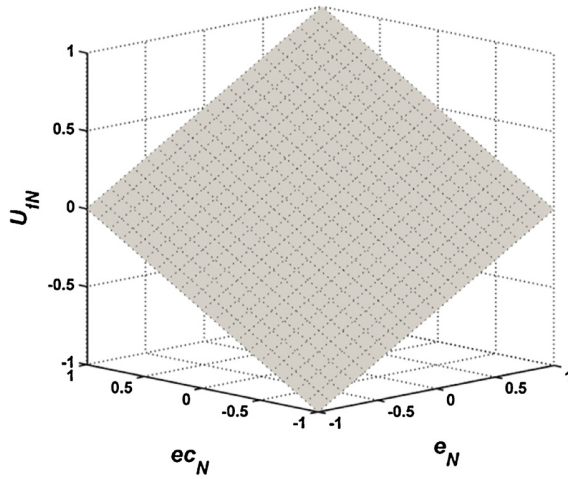Fig. 9. Membership functions for: (a) e_N, (b) ec_N and output U_{fN}.

Fig. 10. Control surface of FLC controller.

Table 2
DSIM parameters used in simulation.

Quantity	Symbol and magnitude
Rated voltage	$V_n = 220$ V
Rated current	$I_n = 6$ A
Rated speed	$N_n = 1000$ rpm
Number of poles	$P = 6$
Rated Frequency	$f = 50$ Hz
Stator resistance	$R_s = 2.03\ \Omega$
Rotor resistance	$R_r = 3\ \Omega$
Stator inductance	$L_s = 0.0147$ H
Rotor inductance	$L_r = 0.0147$ H
Mutual inductance	$L_m = 0.2$ H
Moment of inertia	$J = 0.06$ kg m^2
Coefficient of viscous friction	$k_f = 0.006$ N ms/rd

Fig. 11. Response to a stair of reference speed of DSIM-1.
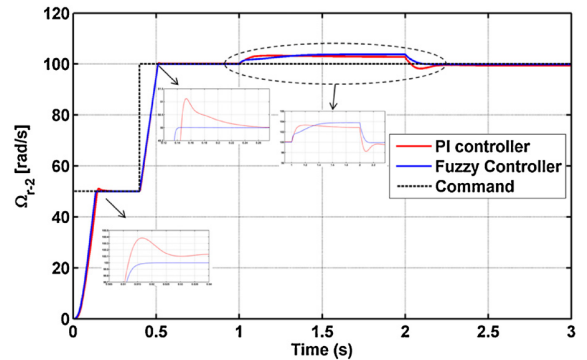
Fig. 12. Response to a stair of reference speed of DSIM-2.

The benefit of using an FLC over a PI or PID controller is that its control surface is modifiable and can provide better performance than PI/PID controller when the system is (i) of a higher order than two, (ii) has oscillatory modes and (iii) has a long dead time [42,43].

6. Simulation results and discussion

In order to show the feasibility of the proposed FLC controller, simulation studies of the drive system based on the DSIMs (Fig. 1) were carried out using MATLAB/Simulink. Each DSIM is rated at 5.5 kW. Parameters used in the simulation studies are shown in Table 2 [14]:

Comparative performance with FLC and PI controllers for tests performed under the same conditions is studied. The response of each DSIM is observed under different operating conditions such as a step change in the command speed or a sudden change in the load.

Results of a set of tests of step changes in speed reference are shown in Figs. 11 and 12 for the two motors. Variation in the reference speed of the machines is chosen as: (t € [0 0.4] sec, $\Omega = 50$ rad/s) and (t € [0.4 3] sec, $\Omega = 100$ rad/s). In these tests the performance of the two controllers is evaluated in terms of speed response. It can be seen that amplitude of transient oscillations of speed is lower with FLC which also has better rejection of

perturbations. The results demonstrate that the FLC controller shows improvement, albeit small, in performance compared to that with the PI controller.

The estimated speeds deviate from the speed references when the conditions of the each DSIM are different. Steady-state errors in speed and electromagnetic torque variations are interrelated due to the motors being connected in parallel and there being coupling terms between the d-q axes of each motor.

Influence of the step changes in load reference on electromagnetic torque of each motor is shown in Figs. 13 and 14.

Finally, the simulation results of the DSIMs connected in parallel associated to IFOC using FLC and PI controllers were also analyzed regarding load torques and speed variations. These results confirm that the FLC controller demonstrates a slightly better performance under changing operating conditions and presents satisfactory performance. Note that in Figs. 11 through 14 the first 0.4 s show the response to change in speed reference and after 1.0 s the response to change in load reference.
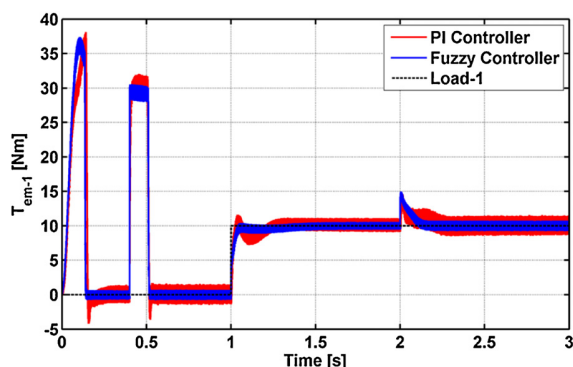
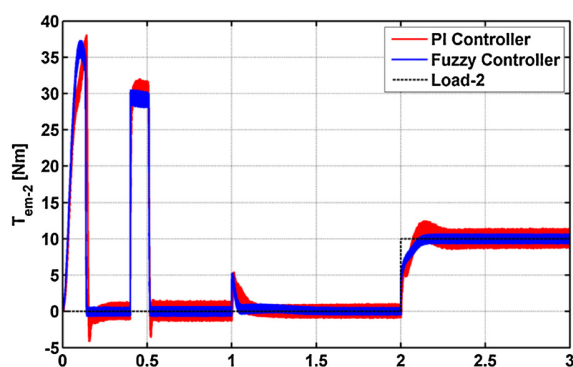**Fig. 13.** Response to step change in load reference for DSIM-1.

Fig. 14. Responses to step change in load reference for DSIM-2.

Table 3
Comparison of performance index.

Controllers	IAE	ISE	ITAE
PI	14.6	1100	1.25
FLC	7.2	270	1.14

Performance with each controller is also analyzed through the use of Integral Squared Error (ISE), Integral Absolute Error (IAE) and Integral Time-weighted Absolute Error (ITAE), and the results described in Table 3 confirm the improved performance with the FLC.

7. Conclusions

Comparison of the performance of two indirect field oriented controlled Double Star Induction Motors connected in parallel to a single six-phase inverter supply using FLC and PI based speed control is presented. It is observed that in terms of speed reference tracking of the dual DSIMs, FLC gives a better performance compared to the PI controller. When the motors' speed is modified, the impact on the electromagnetic torque of the motors is important.

The results presented show that the Fuzzy Logic Control with only four rules can provide an effective solution for devices using DSIMs in parallel such as electric/hybrid vehicles, traction locomotives, rolling stock traction system and electric propulsion ships.

References

[1] R. Bojoi, M. Lazzari, F. Profumo, A. Tenconi, Digital field-oriented control for dual three-phase induction motor drives, IEEE Trans. Ind. Appl. 39 (May/June (3)) (2003) 752–760.

[2] D. Foito, J. Maia, V. Fernao Pires, J.F. Martins, Double three-phase induction machine modeling for internal faults simulation, Electr. Power Compon. Syst. 43 (1) (2015) 1610–1620.

[3] S. Basak, C. Chakraborty, Dual stator winding induction machine: problems, progress, and future scope, IEEE Trans. Ind. Electron. 62 (March (7)) (2015) 4641–4652.

[4] H.S. Che, E. Levi, M. Jones, M.J. Duran, W.P. Hew, N.A. Rahim, Operation of a six-phase induction machine using series-connected machine-side converters, IEEE Trans. Ind. Electron. 61 (March (1)) (2015) 164–176.

[5] G.K. Singh, Multi-phase induction machine drive research—a survey, Electr. Power Sys. Res. 61 (2) (2002) 139–147.

[6] G. Aroquiadassou, A. Cavagnino, H. Henao, A. Boglietti, G.A. Capolino, A new circuit-oriented model for the analysis of six-phase induction machine performances, Electr. Power Syst. Res. 78 (2008) 1798–1805.

[7] N.R. Abjadi, Sliding-mode control of a six-phase series/parallel connected two induction motors drive, ISA Trans. 53 (2014) 1847–1856.

[8] M.A. Abbas, R. Christen, R. Christen, T.M. Jahns, Six-phase voltage source inverter driven induction motor, IEEE Trans. Ind. Appl. IA-20 (April (5)) (1984) 1251–1259.

[9] H. Amimeur, D. Aouzellag, R. Abdessemed, K. Ghedamsi, Sliding mode control of a dual-stator induction generator for wind energy conversion systems, Electr. Power Energ. Syst. 42 (2012) 60–70.

[10] G.K. Singh, K. Nam, S.K. Lim, A simple indirect field-oriented control scheme for multiphase induction machine, IEEE Trans. Ind. Electron. 52 (4) (2005) 1177–1184.

[11] E. Levi, Multiphase electric machines for variable-speed applications, IEEE Trans. Ind. Electron. 55 (May) (2008) 1893–1909.

[12] A.R. Muñoz, T.A. Lipo, Dual stator winding induction machine drive, IEEE Trans. Indus. Appl. 36 (5) (2000) 1369–1379.

[13] K. Marouani, K. Chakou, F. Khoucha, B. Tabbache, A. Kheloui, Observation and measurement of magnetic flux in a dual star induction machine, in: 19th MCCA Conference, Greece, 2011, pp. 289–294.

[14] K. Marouani, L. Baghli, D. Hadiouche, A. Kheloui, A. Rezzoug, A new PWM strategy based on a 24-sector vector space decomposition for a six-phase VSI-fed dual stator induction motor, IEEE Trans. Ind. Electron. 55 (5) (2008) 1910–1920.

[15] E. Levi, R. Bojoi, F. Profumo, H.A. Toliyat, S. Williamson, Multiphase induction motor drives—a technology status review, IET Electr. Power Appl. 1 (4) (2007) 489–516.

[16] A.S. Abdel-Khalik, M.I. Masoud, S. Ahmed, A. Massoud, Calculation of derating factors based on steady-state unbalanced multiphase induction machine model under open phase(s) and optimal winding currents, Electr. Power Syst. Res. 106 (2014) 214–225.

[17] A.S. Abdel-Khalik, M.I. Masoud, B.W. Williams, Vector controlled multiphase induction machine: harmonic injection using optimized constant gains, Electr. Power Syst. Res. 89 (2002) 116–128.

[18] S.N. Vukosavic, M. Jones, E. Levi, D. Dujic, Experimental performance evaluation of a five-phase parallel-connected two-motor drive, in: Proceedings of the 4th IET International Conference on Power Electronics, Machines and Drives (PEMD-UK), Stevenage, Hertfordshire, 2008, pp. 686–690.

[19] Y. Lee, J. Ha, Control method for mono inverter dual parallel surface mounted permanent magnet synchronous machine drive system, IEEE Trans. Ind. Electron. 62 (April (10)) (2015) 6096–6107.

[20] K. Matsuse, H. Kawai, Y. Kouno, J. Oikawa, Characteristics of speed sensorless vector controlled dual induction motor drive connected in parallel fed by a single inverter, IEEE Trans. Ind. Appl. 40 (1) (2004) 153–161.

[21] A. Bouscayrol, M. Pietrzak-David, P. Delarue, R. Peña-Eguiluz, P.E. Vidal, X. Kestelyn, Weighted control of traction drives with parallel-connected AC machines, IEEE Trans. Ind. Electron. 53 (2006) 1799–1806.

[22] S. Ito, T. Moroi, Y. Kubo, K. Matsuse, K. Rajashekara, Independent control of two permanent-magnet synchronous motors fed by a four-leg inverter, IEEE Trans. Ind. Appl. 51 (1) (2015) 753–760.

[23] Y. Matsumoto, S. Ozaki, A. Kawamura, A novel vector control of single-inverter multiple-induction Motor drive for Shinkansen traction system, in: Applied Power Electronics Conference and Exposition, Sixteenth Annual IEEE, vol. 1, 2001, pp. 608–614.

[24] R. Gunabalan, V. Subbiah, Review of speed-sensorless vector control of parallel connected induction motor drive fed by a single inverter, JEE 12 (4) (2012) 73–82.

[25] M. Jones, E. Levi, Series connected quasi-six-phase two-motor drives with independent control, Math. Comput. Simul. 71 (2006) 415–424.

[26] K. Matsuse, Y. Kouno, H. Kawai, S. Yokomizo, A speed-sensorless vector control method of parallel-connected dual induction motor fed by a single inverter, IEEE Trans. Ind. Appl. 38 (6) (2002) 1566–1572.

[27] W. Ruxi, W. Yue, D. Qiang, H. Yanhui, Wang Zhaoan, Study of control methodology for single inverter parallel connected dual induction motors based on the dynamic model, in: Power Electronics Specialists Conference, 2006. PESC'06. 37th IEEE, 2006, pp. 1–7.

[28] J. Nishimura, K. Oka, K. Matsuse, A method of speed sensorless vector control of parallel-connected dual induction motors by a single inverter with a rotor flux control, in: Proceeding of ICEMS'07, Korea, 2007.

[29] R. Gunabalan, V. Subbiah, Speed-sensorless vector control of parallel connected induction motor drive with fuzzy controller, in: IEEE Inter. Conference on CICR'12, 2012.

[30] C.B. Kim, C. Yun, B.K. Yoon, N.S. Cho, W.H. Kwon, Parallel sensorless speed control using flux-axis current for dual SPMSMs fed by a single inverter, J. Electr. Eng. Technol. 10 (3) (2015) 1048–1057.

[31] N.L. Nguyen, M. Fadel, A. Llor, A new approach to predictive torque control with dual parallel PMSM system, in: IEEE Inter. Conference on Industrial Technology (ICIT), 2013.

[32] M. Jones, E. Levi, S.N. Vukosavic, Independent control of two five-phase induction machines connected in parallel to a single inverter supply, in: Proceedings of the 32nd Annual Conference of the IEEE Industrial Electronics Society, Paris, France, 2006, pp. 1257–1262.

[33] Z. Tir, R. Abdessemed, Hybrid fuzzy logic proportional plus conventional integrator-derivation controller of a novel BDFIG for wind energy conversion, JEE 12 (2014) 1–6.

[34] E.H. Mamdani, Application of fuzzy algorithms for control of simple dynamic plant, Proc. IEEE 121 (12) (1974) 1585–1588.

[35] J.M. Retif, Automatique Régulation, Institu INSA de Lyon, Lyon, France, 2008, pp. 148.

[36] L.A. Zadeh, L.A. Zadeh, Fuzzy sets, Inf. Control 8 (1965) 338–353.

[37] K. Hayashi, A. Otsubo, S. Murakami, M. Maeda, Realization of nonlinear and linear PID controls using simplified indirect fuzzy inference method, Fuzzy Sets Syst. 105 (1999) 409–414.

[38] M. Mizumoto, Realization of PID controls by fuzzy control methods, Fuzzy Sets Syst. 70 (1995) 171–182.

[39] W.Z. Qiao, M. Mizumoto, PID type fuzzy controller and parameters adaptive method, Fuzzy Sets Syst. 78 (1996) 23–35.

[40] M. Mizumoto, Product-sum-gravity method = fuzzy singleton-type reasoning method = simplified fuzzy reasoning method, in: Proceedings of the Fifth IEEE International Conference on Fuzzy Systems, vol. 3, 1996, pp. 2098–2102.

[41] E.H. Mamdani, Application of fuzzy logic to approximate reasoning using linguistic synthesis, IEEE Trans. Comput. C-26 (12) (1977) 1182–1191.

[42] Jan Jantzen, A Robustness Study of Fuzzy Control Rules, Technical University of Denmark, Department of Automation, 1998, pp. 31–36.

[43] J. Jantzen, Foundations of Fuzzy Control, Wiley, 2013.

Fuzzy logic field oriented control of double star induction motor drive

Data · October 2016

5 authors, including:

Some of the authors of this publication are also working on these related projects:

Project   converter control View project

Project   Call for Papers: The 1st IEEE International Conference on Communications, Control Systems and Signal Processing CCSSP 2020 View project

CrossMark

ORIGINAL PAPER

Fuzzy logic field oriented control of double star induction motor drive

Zoheir Tir[1] · Youcef Soufi[2] · Mohammad Naser Hashemnia[3] · Om P. Malik[4] ·
Khoudir Marouani[5]

Abstract An indirect field oriented control of a double star induction motor drive with a conventional PI and fuzzy logic controller based on four rules is presented in this paper. To realize a control of this motor, a DC supply and a PWM voltage source inverter (VSI) are introduced. Performance of the proposed control schemes under load disturbances and parameter variations is studied through simulations. The simulation results regarding the speed response with both controllers are presented and discussed.

Keywords Current control · Double star induction motor (DSIM) · Fuzzy logic controller (FLC) · Indirect field

oriented control (IFOC) · PI Controller · Pulse width modulation (PWM) · Speed performance

1 Introduction

Use of the double star induction motor (DSIM) drives, especially for high-power applications, has considerably increased over the past 40 years [1,11]. The principal advantages of these motors are (1) possible reduction of the torque ripple, (2) enabling filter of rotor harmonic currents thus reducing losses, (3) reduction of the harmonics content of the dc-link current and (4) increased reliability and capability of operation under one or more phases fault [1,3,8]. With these advantages, the DSIMs are used in several applications, especially those requiring high power such as electric/hybrid vehicles, locomotive traction and electric ship propulsion [2,11]. The DSIM is composed of windings spatially shifted by 30 electrical degrees. These windings are generally fed by two voltage source inverters (VSIs) for variable speed operation [4,5].

In this paper, two control strategies, PI and fuzzy logic, are considered to adjust the speed of the drive system. The fuzzy logic controller (FLC) is based on the linguistic rules with an IF-THEN general structure, which is the basis of human logic [7]. Its main advantage resides in the fact that it does not require an exact mathematical model of the system, it can handle an arbitrary complex nonlinearity and moreover, it is robust. However, a disadvantage of this control scheme is that the value of fuzzy output is commonly obtained by 49 fuzzy rules, as proposed in [13]. This requires a high-speed microprocessor to obtain good results and makes it an expensive solution. To avoid this problem, a fuzzy logic controller based on only four linguistic rules is proposed in this paper. The robustness of the proposed controller to motor

✉ Zoheir Tir
tir-zoheir@univ-eloued.dz

Youcef Soufi
y_soufi@yahoo.fr

Mohammad Naser Hashemnia
hashemnia@mshdiau.ac.ir

Om P. Malik
maliko@ucalgary.ca

Khoudir Marouani
marouani_khoudir@yahoo.fr

[1] LEVRES-Research Laboratory, Department of Electrical Engineering, University of El Oued, B.P.789, 39000 El Oued, Algeria

[2] Department of Electrical Engineering, University Tebessa, Tebessa, Algeria

[3] Department of Engineering, Islamic Azad University, Mashad, Iran

[4] Department of Electrical and Computer Engineering, University of Calgary, Calgary, AB, Canada

[5] EE-Research Laboratory, Department of Electrical Engineering, Poly. Military School, Algiers, Algeria

Fig. 1 Indirect field-oriented control of DSIM drive Block diagram

parameter variations is verified. The schematic diagram of an indirect field-oriented control (IFOC) drive for DSIM using conventional PI and fuzzy logic controllers is shown in Fig. 1.

This paper is organized as follows: The DSIM model is provided in Sect. 2, and the DSIM IFOC is presented in Sect. 3. Next, the proposed fuzzy logic structure is given in Sect. 4, and the results are presented and discussed in Sect. 5. Finally, conclusions are presented in Sect. 6.

2 Modelling of the DSIM

The electrical equations used to model the DSIM in the Park reference frame are [5]

$$v_{ds1} = R_s i_{ds1} + \frac{d\phi_{ds1}}{dt} - \omega_s \phi_{qs1} \tag{1}$$

$$v_{ds2} = R_s i_{ds2} + \frac{d\phi_{ds2}}{dt} - \omega_s \phi_{qs2} \tag{2}$$

$$v_{qs1} = R_s i_{qs1} + \frac{d\phi_{qs1}}{dt} + \omega_s \phi_{ds1} \tag{3}$$

$$v_{qs2} = R_s i_{qs2} + \frac{d\phi_{qs2}}{dt} + \omega_s \phi_{ds2} \tag{4}$$

$$0 = R_r i_{dr} + \frac{d\phi_{dr}}{dt} - (\omega_s - \omega_r)\phi_{qr} \tag{5}$$

$$0 = R_r i_{qr} + \frac{d\phi_{qr}}{dt} + (\omega_s - \omega_r)\phi_{dr}, \tag{6}$$

where the stators and rotor flux linkages are expressed by [5]:

$$\phi_{ds1} = L_s i_{ds1} + L_m(i_{ds1} + i_{ds2} + i_{dr}) \tag{7}$$

$$\phi_{ds2} = L_s i_{ds2} + L_m(i_{ds1} + i_{ds2} + i_{dr}) \tag{8}$$

$$\phi_{qs1} = L_s i_{qs1} + L_m(i_{qs1} + i_{qs2} + i_{qr}) \tag{9}$$

$$\phi_{qs2} = L_s i_{qs2} + L_m(i_{qs1} + i_{qs2} + i_{qr}) \tag{10}$$

$$\phi_{dr} = L_r i_{dr} + L_m(i_{ds1} + i_{ds2} + i_{dr}) \tag{11}$$

$$\phi_{qr} = L_r i_{qr} + L_m(i_{qs1} + i_{qs2} + i_{qr}), \tag{12}$$

and the electromagnetic torque is [5]:

$$T_{em} = p\frac{L_m}{L_m + L_r}\left[(i_{qs1} + i_{qs2})\phi_{dr} - (i_{ds1} + i_{ds2})\phi_{qr}\right] \tag{13}$$

The mechanical dynamic equation is expressed by [5]

$$J\frac{d\Omega}{dt} + k_f \Omega = T_{em} - T_L, \tag{14}$$

where Ω_s, Ω_r are the synchronous reference frame and rotor electrical angular speeds, respectively; L_s and L_r are the stator and rotor inductances; L_m is the resultant magnetizing inductance; p is the number of pole pairs; J is the moment of inertia; T_L is the load torque and K_f is the total viscous friction coefficient.

3 DSIM field-oriented control

3.1 Reference frame

By adopting a rotor field-oriented control, the electromagnetic torque and rotor field will be linked directly to the stator current components. Assuming the rotor flux is aligned with the d-axis [5],

$$\phi_{\mathrm{dr}} = \phi_r^* \tag{15}$$

$$\phi_{\mathrm{qr}} = 0 \tag{16}$$

The DSIM control principle is similar to the well-known rotor FOC used for the IM.

3.2 Control strategy

The reference voltages (v_{ds1}^*, v_{qs1}^*, v_{ds2}^* and v_{qs2}^*) are derived by substituting (15) and (16) in (1)–(4) [5]:

$$v_{\mathrm{ds1}}^* = R_s i_{\mathrm{ds1}} + L_s \frac{di_{\mathrm{ds1}}}{dt} - \omega_s^*(L_s i_{\mathrm{qs1}} + T_r \varnothing_r^* \omega_{\mathrm{sl}}^*) \tag{17}$$

$$v_{\mathrm{qs1}}^* = R_s i_{\mathrm{qs1}} + L_s \frac{di_{\mathrm{qs1}}}{dt} - \omega_s^*(L_s i_{\mathrm{ds1}} + \varnothing_r^*) \tag{18}$$

$$v_{\mathrm{ds2}}^* = R_s i_{\mathrm{ds2}} + L_s \frac{di_{\mathrm{ds2}}}{dt} - \omega_s^*(L_s i_{\mathrm{qs2}} + T_r \varnothing_r^* \omega_{\mathrm{sl}}^*) \tag{19}$$

$$v_{\mathrm{qs2}}^* = R_s i_{\mathrm{qs2}} + L_s \frac{di_{\mathrm{qs2}}}{dt} - \omega_s^*(L_s i_{\mathrm{ds2}} + \varnothing_r^*), \tag{20}$$

where

$$T_r = \frac{L_r}{R_r} \tag{21}$$

T_r denotes the rotor time constant.

The component references of slip speed ω_{sl}^* and stator current can be expressed as [5]

$$\omega_{\mathrm{sl}}^* = \frac{R_r L_m}{(L_m + L_r)\varnothing_r^*} i_{\mathrm{qs}}^* \tag{22}$$

$$i_{\mathrm{ds}}^* = \frac{1}{L_m} \varnothing_r^* \tag{23}$$

$$i_{\mathrm{qs}}^* = \frac{(L_m + L_r)}{P L_m \varnothing_r^*} T_{\mathrm{em}}^*, \tag{24}$$

where

$$i_{\mathrm{ds}}^* = i_{\mathrm{ds1}}^* + i_{\mathrm{ds2}}^* \tag{25}$$

$$i_{\mathrm{qs}}^* = i_{\mathrm{qs1}}^* + i_{\mathrm{qs2}}^* \tag{26}$$

The d−q axes currents are referred as flux-producing (i_{ds}^*) and torque-producing (i_{qs}^*) components of the stator current, respectively.

To generate two sets of voltage vectors (v_{ds1}^*, v_{qs1}^* and v_{ds2}^*, v_{qs2}^*) two independent pairs of PI or FLC controllers are introduced as shown in Fig. 2.

4 Controller design

4.1 PI conrollers

The DSIM drive has two controllers: the first is the speed controller or the outer-loop controller, Fig. 1, and the second is the current controller or the inner-loop controller, Fig. 2.

The PI controller of the current (i_s), in the inner-loop shown in Fig. 3, is designed first.

Transfer function of the PI controller is

$$G_c(s) = K_P + \frac{K_i}{s} = K_P \left(1 + \frac{1}{T_i s}\right) = K_P \left(\frac{1 + T_i s}{T_i s}\right), \tag{27}$$

where K_p and K_i represent, respectively, the proportional and integral gains, and T_i represents the integral time of the current controller.

The transfer function of the system (DSIM) is presently defined as follows:

$$G_s(s) = \frac{i_s}{v_s} = \frac{1}{R_s + s L_s} = \frac{K}{1 + s \tau_s}, \tag{28}$$

where $K = 1/R_s$ is the system gain and $\tau_s = L_s/R_s$ is the time constant.

The open-loop transfer function ($G_{\mathrm{ol}}(s)$) of the system is:

$$G_{\mathrm{ol}}(s) = G_c(s) G_s(s) = K_P \left(\frac{1 + T_i s}{T_i s}\right) \left(\frac{K}{1 + \tau_s s}\right) \tag{29}$$

Let

$$(1 + T_i s) = (1 + \tau_s s) \tag{30}$$

The closed-loop transfer function ($G_{\mathrm{cl}}(s)$) of the system is

$$G_{\mathrm{cl}}(s) = \frac{G_{\mathrm{ol}}(s)}{1 + G_{\mathrm{ol}}(s)} = \frac{1}{1 + (T_i/K_p \tau_s)s} = \frac{1}{1 + T_0 s}, \tag{31}$$

where

$$T_0 = \frac{T_i}{K_p \tau_s} \tag{32}$$
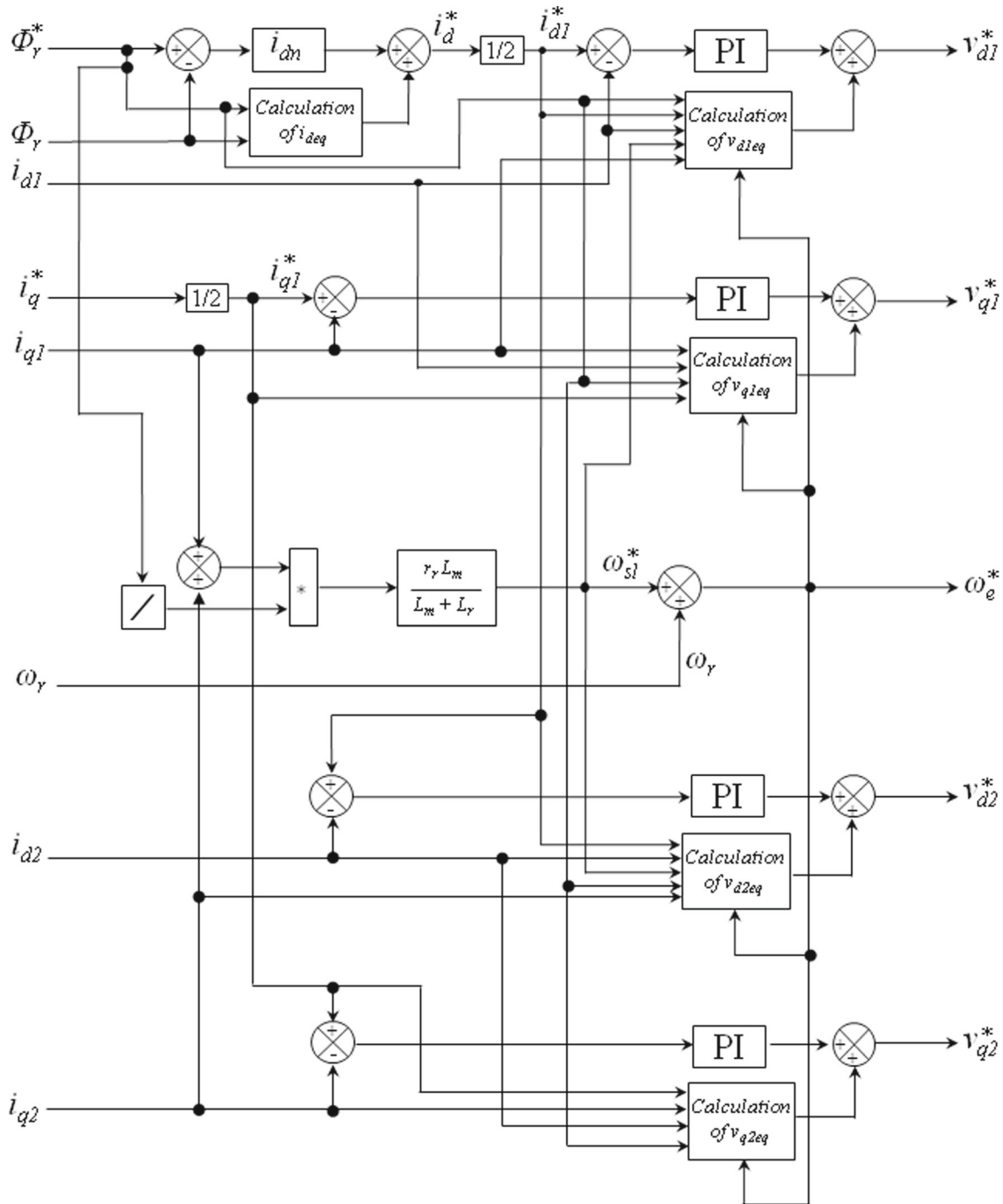
T_0 is the time constant of the closed-loop system.

Fig. 2 IFOC based on PI/FLC controllers [5]

According to (30) and (32), gains of the PI controller are as follows:

$$K_p = \frac{\tau_s}{K T_0} \tag{33}$$

$$K_i = \frac{K_p}{T_i} \tag{34}$$

Note The value of T_0 is of the same as the time constant of the system τ_s [14].

The PI controller of the speed, (ω_s), in the outer-loop shown in Fig. 4, is implemented in the same way as the current controller.

The transfer function of the system (DSIM) is presently defined as follows:

$$G_{s\omega}(s) = \frac{1}{f + sJ} = \frac{K_\omega}{1 + s\tau_{s\omega}}, \tag{35}$$
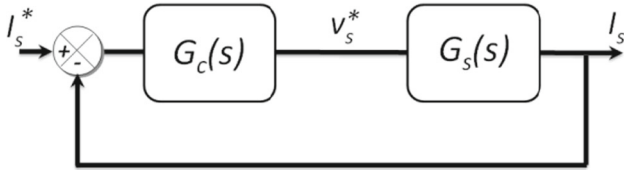
Fig. 3 Current PI controller block diagram
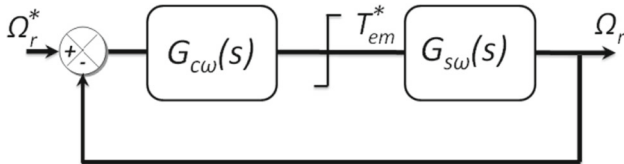
Fig. 4 Speed PI controller block diagram

where $K_\omega = 1/f$ is the system gain and $\tau_{s\omega} = J/f$ is the time constant.

Finally, the gains of the speed controller are calculated as

$$K_{p\omega} = \frac{\tau_{s\omega}}{K_\omega T_{0\omega}} \tag{36}$$

$$K_{i\omega} = \frac{K_{p\omega}}{T_{i\omega}} \tag{37}$$

4.2 Fuzzy logic controller

The fuzzy logic theory is based on the strategy of artificial intelligence and was first proposed in [10]. The FLC seems to be an interesting alternative to the PI controller, which cannot yield good control performances if the controlled system is highly nonlinear and uncertain [11,12]. Block diagram of the FLC is shown in Fig. 5.

The FLC using the product-sum-gravity inference method consists of four blocks: fuzzification, interface, knowledge base and inference, as shown in Fig. 6 [4,9,10].
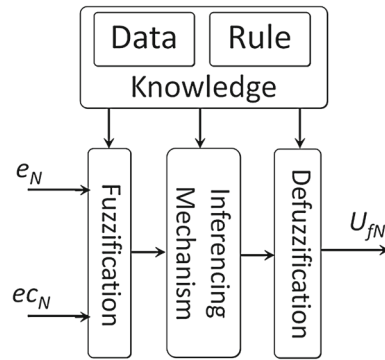
Fig. 6 Block diagram of fuzzy logic controller

The input variables of FLC are the error, $e_N(t)$, and error change, $ec_N(t)$, signals and the output variable is generated from fuzzy rule base. After the defuzzifier, the crisp signal is acquired.

The error and error change signals are defined as

$$e(k) = x_{\text{ref}}(k) - x(k) \tag{38}$$

$$ec_x(k) = e_x(k) - e_x(k-1), \tag{39}$$

where x presents the current components (i_{ds1}, i_{qs1}, i_{ds2} and i_{qs2}) and the speed component Ω_r. The corresponding outputs (U_x) are the voltage components (v_{ds1}, v_{qs1}, v_{ds2} and v_{qs2}) and the torque component T_{em}

The inputs and the output are related as

$$U_x(t) = f(e_{xN}(t), ec_{xN}(t)) \tag{40}$$

The relationship between scaling factors and the input and output variables of the controller are as given below:

$$e_{xN} = K_e e_x, \quad ec_{xN} = K_{ec} e_x \quad \text{and} \quad U_x = \alpha U_{xN}$$
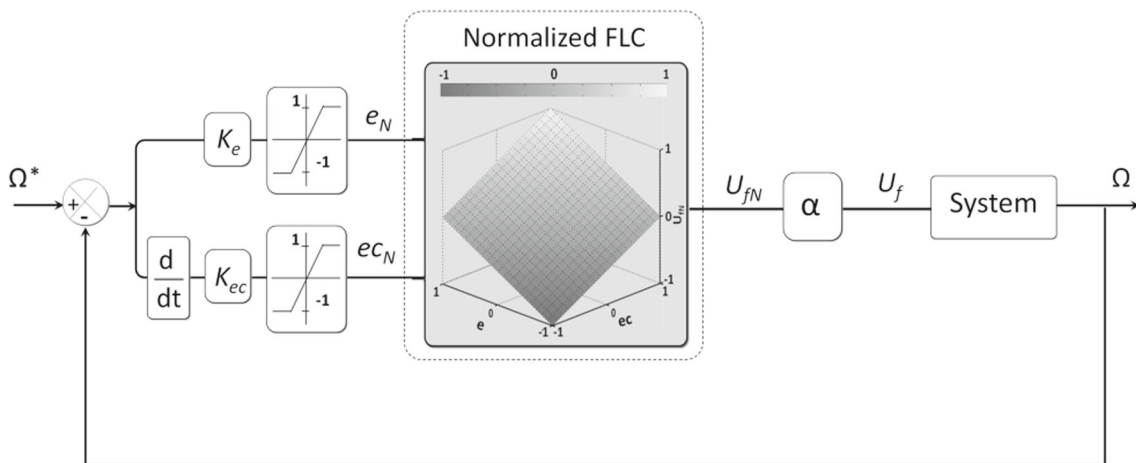
Fig. 5 Fuzzy logic controller block diagram
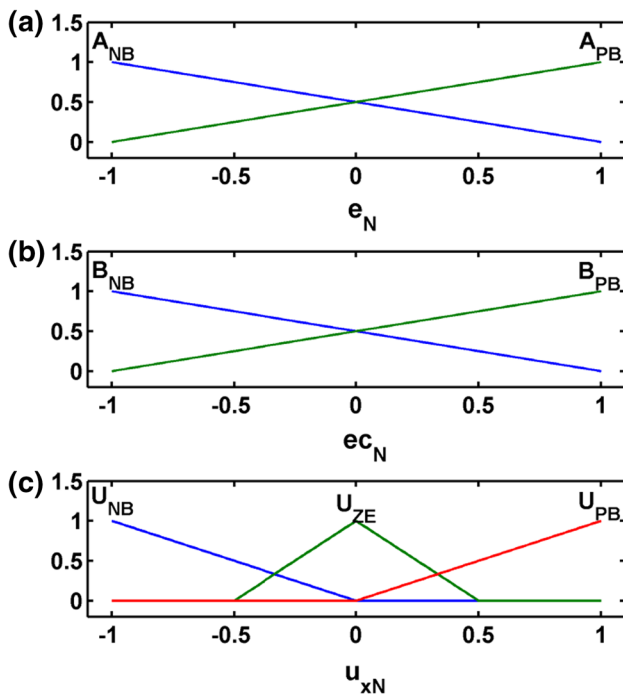
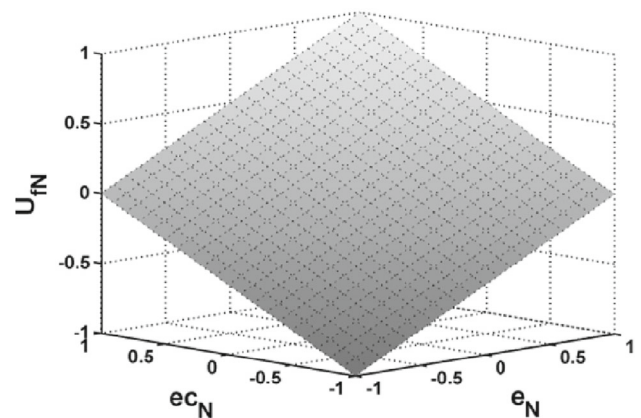**Fig. 7** Membership functions for **a** e_{xN}, **b** ec_{xN} and **c** output U_{xN}

Fig. 8 Control surface of FLC

In this paper, the defuzzification method chosen is the center of gravity [4,9,10]. Therefore, the control output U_{xN} can be calculated as

$$U_{xN} = \frac{\sum_{k=1}^{4} \mu(\Delta x_k)\Delta x_k}{\sum_{k=1}^{4} \mu(\Delta x_k)} \tag{44}$$

The control surface of output U_{xN} is shown in Fig. 8.

5 Simulation results and discussion

In order to show the feasibility of the proposed FLC, simulations of the DSIM drive were carried under Matlab/Simulink environment as shown in Fig. 9. The DSIM is rated at 5.5 kW. These blocks are IFOC, PWM generator, Six-Phases VSI, DSIM and load torque model.

The parameters used in the simulation are based on the laboratory prototype used for experimentation and are given in Table 1 [2]:

A set of tests performed under the same conditions using PI and FLC controllers, respectively, is shown in Fig. 10. The speed response is observed under different operating conditions such as a sudden change in the speed command or a step change in the load.

The first test compares the two controllers in terms of speed response and demonstrates that the FLC has a better performance and is more robust than the PI controller.

Influence of the speed variation on the electromagnetic torque response is shown in Fig. 11. It is seen that transient oscillations occur due to the coupling terms between the d−q axes. The change in the reference speed is chosen as the following: (t ε [0 1] s Ω =40 rad/s), (t ε [1 2] s Ω = 80 rad/s) and (t ε [2 3] s Ω =100 rad/s). It can be seen that the amplitude of transient oscillations is minimized with FLC due to its better rejection of perturbations. Also, this result shows that
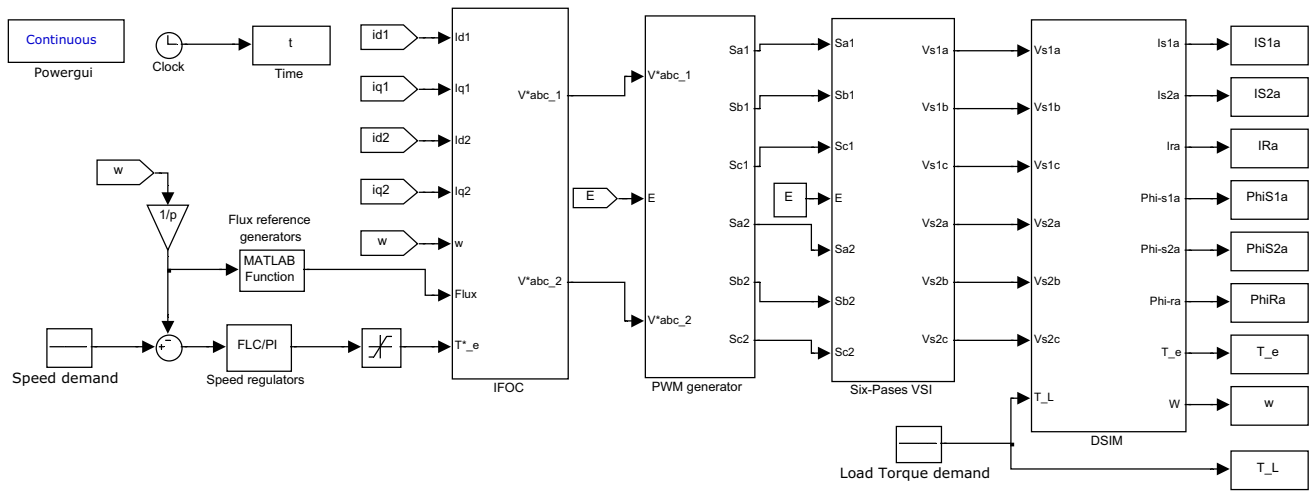
The scaling factors (SFs) K_e and K_{ec} are used to normalize the error $e_x(t)$ and error change $ec_x(t)$, respectively. Notice that the inputs (e_x, ec_x) remain within the limits of −1 to +1 (normalization).

The appropriate values of K_e, K_{ec} and α can be calculated as

$$K_e = \frac{1}{x_{max}} \tag{41}$$

$$K_{ec} = \frac{1}{\Delta x_{max}} \tag{42}$$

$$\alpha = U_{x-max} \tag{43}$$

The fuzzy rules define the output of the controller according to the inputs [4,10]. This can be realized by the following rules:

If e_N is A_{NB} and ec_N is B_{NB} then U_{xN} is U_{NB}.
If e_N is A_{PB} and ec_N is B_{PB} then U_{xN} is U_{PB}.
If e_N is A_{NB} and ec_N is B_{PB} then U_{xN} is U_{ZE}.
If e_N is A_{PB} and ec_N is B_{NB} then U_{xN} is U_{ZE},

where A_i, B_i are the membership functions (MFs) e_N, ec_N, respectively, and U_{xN} is MF of the output variable of the fuzzy controller;

The membership functions used for the input and output fuzzy sets are shown in Fig. 7.

The next stage after processing the inputs through knowledge base and the inferencing mechanism is defuzzification.

Fig. 9 Block diagram of DSIM drive simulation in MATLAB/Simulink

Table 1 Parameters of the simulated motor

Quantity	Symbol and magnitude
Rated voltage	$V_n = 220\,\text{V}$
Rated current	$I_n = 6\,\text{A}$
Rated speed	$N_n = 1000\,\text{rpm}$
Number of poles	$P = 6$
Rated frequency	$f = 50\,\text{Hz}$
Stator resistance	$R_s = 2.03\,\Omega$
Rotor resistance	$R_r = 3\,\Omega$
Stator inductance	$L_s = 0.0147\,\text{H}$
Rotor inductance	$L_r = 0.0147\,\text{H}$
Mutual inductance	$L_m = 0.2\,\text{H}$
Moment of inertia	$J = 0.06\,\text{kg\,m}^2$
Coefficient of viscous friction	$k_f = 0.006\,\text{Nms/rd}$

Fig. 10 Simulated response to step reference speed

the DSIM drive using FLC has good quality and guarantees stability under variable load and speed.

Results of a set of tests showing the impact of DSIM's parameters variations on dynamic/steady-state performances with the two controllers is presented in Fig. 12. The value of the rotor resistance is augmented by 50 %. The DSIM is running at 100 rad/s. The change in the load torque is realized as follows: ([1 2] sec $T_{em}^* = 15\,\text{Nm}$). The results show that parameter variations of the DSIM increase the transient state of both controllers, but the robustness of the FLC to parameter variations is completely verified and is better than that of the PI controller.

Performances of the FLC and PI speed control when the moment of inertia is augmented by 50 % is presented in Fig. 13. It is shown that the FLC presents the same performances obtained with and without moment of inertia variations.

Finally, the simulation results of the IFOC DSIM using PI and FLC controllers are analyzed regarding load torque, speed and inertia moment variations. These results confirm that the FLC controller demonstrates robustness under various operating conditions and shows a very satisfactory performance.

6 Conclusions

Comparative performance of a FLC and a PI control associated with the IFOC of a DSIM is presented in this paper.
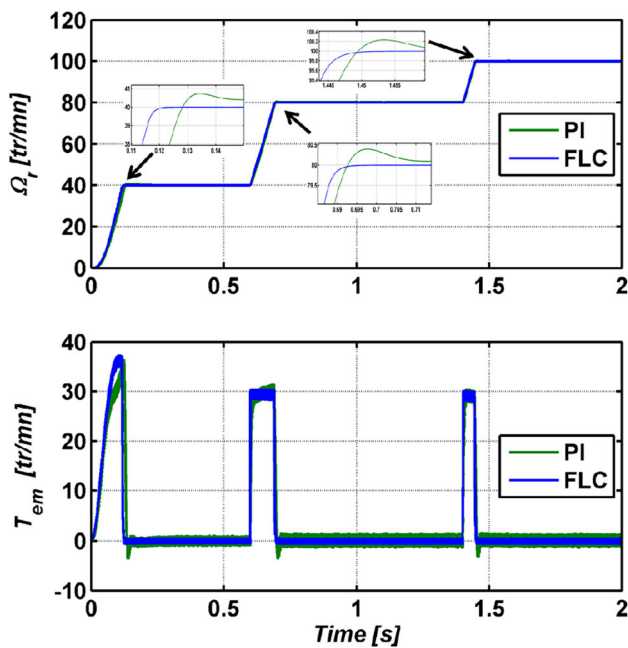
Fig. 11 Simulated response to a stair of reference speed without load

Fig. 13 Simulated response for a stair of reference speed with an increased moment of inertia (J +50 %)

Fig. 12 Simulated response for a step reference speed with an increased rotor resistance (Rr +50 %)

In terms of speed reference tracking with the DSIM, the FLC gives a superior performance compared to the PI controller. Speed variations affect the electromagnetic torque in the PI-controlled drive more than that of FLC-controlled drive. Hence, the FLC drive has better transient response and stability. A robustness test, where the motor parameters are modified, has also been performed. These changes induce

time-response variations with PI controller more that with the FLC controller.

The presented results show that an artificial intelligence control method, such as FLC with only four rules, can be a very attractive solution for devices using DSIM such as electric/hybrid vehicles, traction locomotives and electric propulsion ships. In fact, the majority of the studied DSIM control schemes use classical PI controllers, but the comparison done in this study shows that the limits of this type of controller can have negative effects on the performance of the DSIMs.

The control methodology proposed here can be simply extended to other electric motors. Future work will address the experimental implementation of this proposed control scheme and the design of a speed sensorless controller.

References

1. Bojoi R, Lazzari M, Profumo F, Tenconi A (2003) Digital field-oriented control for dual three-phase induction motor drives. IEEE Trans Ind Appl 39(3):752–760
2. Marouani K, Baghli L, Hadiouche D, Kheloui A, Rezzoug A (2008) A new PWM strategy based on a 24-sector vector space decomposition for a six-phase VSI-Fed dual stator induction motor. IEEE Trans Ind Electr 55(5):1910–1920
3. Marouani K, Chakou K, Khoucha F, Tabbache B, Kheloui A (2011) Observation and measurement of magnetic flux in a dual star induction machine. In: 19th MCCA conference, Greece, June 2011
4. Abbas MA, Christen R, Jahns TM (1984) Six-phase voltage source inverter driven induction motor. IEEE Trans Ind Appl IA–20(5):1251–1259

5. Amimeur H, Aouzellag D, Abdessemed R, Ghedamsia K (2012) Sliding mode control of a dual-stator induction generator for wind energy conversion systems. Electr Power Energy Sys 42:60–70

6. Lekhchine S, Bahib T, Soufi Y (2014) Indirect rotor field oriented control based on fuzzy logic controlled double star induction machine. Electr Power Energy Sys 57:206–211

7. Singh GK, Nam K, Lim SK (2005) A simple indirect field-oriented control scheme for multiphase induction machine. IEEE Trans Ind Electr 52(4):1177–1184

8. Muñoz AR, Lipo TA (2000) Dual stator winding induction machine drive. IEEE Trans Ind Appl 36(5):1369–1379

9. Mamdani EH (1977) Application of fuzzy logic to approximate reasoning using linguistic synthesis. IEEE Trans Comput C-26(12):1182–1191

10. Zadeh LA (1965) Fuzzy sets. Inf Contr 8:338–353

11. Tir Z, Abdessemed R (2014) Hybrid fuzzy logic proportional plus conventional integrator-derivation controller of a novel BDFIG for wind energy conversion. JEE 12:1–6

12. Merabet E, Abdessemed R, Bentouhami L, Bendjedou Y (2011) Speed control of a dual stator windings induction machine using fuzzy logic controller. JEE 9:1–6

13. Lekhchine S, Bahi T, Soufi Y (2014) Indirect rotor field oriented control based on fuzzy logic controlled double star induction machine. Int J Electr Power Energy Sys 57:206–211

14. Retif JM (2008) Automatique régulation. Institu INSA de Lyon, pp 148

Improvement of Power Quality Using Hybrid Power Filter with Fuzzy Logic Controller

Yacine Djeghader

Department of Electrical Engineering, University of Mohamed-Cherif Messaadia of Souk Ahras, P.O. Box 1553, 41000 Souk Ahras, Algeria
Email: djeghaderyacine@yahoo.fr

Laid Zellouma

Department of Electrical Engineering; University of El Oued., Algeria

Abstract—In this paper, we present a Hybrid Power Filter (HPF) which consists of a combined system of Passive Filter (PF) and Series Active Power Filter (SAPF) has been designed by MATLAB/SIMULINK approach for harmonic and reactive power compensation. This filter is a three level PWM voltage source inverter and we use a Fuzzy Logic Controller (FLC) algorithm to control the harmonic voltages. The viability of the proposed algorithm is validated in this work. This combined system of filter is able to compensate the reactive power (showed that source voltage is sinusoidal and in phase with source current), and harmonics (voltage & current) for three phase of the non linear load current proposed with RL load. For the following voltage related problems in the power grid voltage flicker and voltage unbalance in three-phase systems are minimized under norm. The proposed solution has achieved an improvement of power quality in distribution system;

Index Terms—active power filter, shunt passive power filter, power quality improvement, power factor, THD, fuzzy controller

I. INTRODUCTION

Power Quality is defined as the extent to which both the utilization and distribution distresses the electric power system affects the efficacy of electrical equipment. These power harmonics are called electrical pollution which will degrade the quality of the power supply. As a result, filtering process for these harmonics is needed in order to improve the quality of the power supply. Therefore, these harmonics must be mitigating. In order to achieve this, series or parallel configurations or combinations of active and passive filters have been proposed depending on the application type [1], [2]. Conventionally passive filters were used to reduce the Total Harmonic Deduction (THD) and compensate the reactive power. Passive filters were considered to most reliable, cost effective, robust, and can be easily maintained. But they suffer from certain disadvantages like create resonance with the system, they are bulky and the most prominent is that they are tuned for particular harmonic frequency [3].

Since the beginning of the 1980s, active power filters (APFs) have become one of the most habitual compensation methods [4]. A usual APF consists of a three-phase Pulse Width Modulation (PWM) voltage source inverter. The APF can be connected either in parallel or in series with the load. The first one is especially appropriate for the mitigation of harmonics of the loads called harmonic current source. In contrast, the series configuration is suitable for the compensation of loads called harmonic voltage source. However, the costs of shunt active filters are relatively high for large-scale system and are difficult to use in high-voltage grids.

In addition, their compensating performance is better in the harmonic current source load type than in the harmonic voltage source load type [5].

II. HYBRID POWER FILTER TOPOLOGY DESCRIPTIONS AND MODELING

A. Description of the HPF Topology

Fig. 1 shows the topology of the combined system of a series active power filter and shunt passive filter, acting as zero impedance for the fundamental frequency and as high resistor for the harmonics frequencies. The HPF, which is supplied by a low power PWM inverter, is connected in series with the main supply and the non-linear load through the current transformer. The passive filter connected in parallel to the load is used to damp the 5th and the 7th harmonic of V_l because of their high amplitudes.
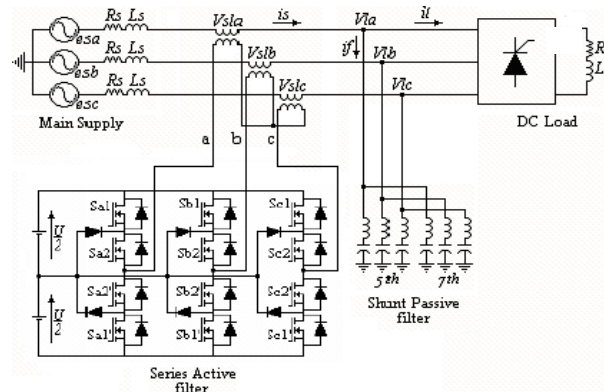

Figure 1. General configuration of a hybrid power filter

The series APF acts as a voltage source and inject a compensating voltage in order to obtain a sinusoidal load voltage. The developments in digital electronics, communications and in process control system have made the loads very sensitive, requiring ideal sinusoidal supply voltage for their operation [5], [6].

B. Modeling

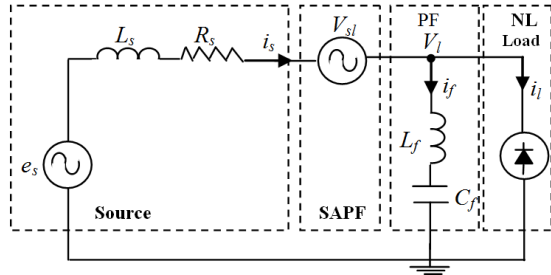Fig. 2 shows the per-phase equivalent scheme of the studied topology.

Figure 2. Per-phase equivalent scheme

where:

e_s, i_s, L_s, R_s: Source voltage, source current, source inductance, and source resistance,

V_s: Line voltage,

V_l, i_l: Load voltage and load current,

V_{sl}: Controllable voltage source representing the series active power filter,

i_f, C_f, L_f: Shunt passive filter current, passive filter capacitance, and passive filter inductance.

This equivalent scheme is modeled by (1) and (2):

$$V_{sl} = V_s - V_l \tag{1}$$

$$i_s = i_f + i_l \tag{2}$$

where:

$$V_s = e_s - (R_s \cdot i_s) - (L_s \, dt/di_s) \tag{3}$$

The voltage error is given by:

$$\Delta V_{sl} = V_{slref} - V_{sl} \tag{4}$$

V_{slref}: is expressed by:

$$V_{slref} = V_{sh} - V_{lh} \tag{5}$$

$$V_{sh} = k \cdot i_{sh} \tag{6}$$

V_{sh}, V_{lh}, i_{sh}: represent, respectively, the harmonic components present in V_s, V_l, and i_s.

k: is a current sensor gain.

C. APF Voltage References Determination

The harmonic component V_{slh} of V_{sl} is defined by:

$$V_{slh} = V_{sl} - V_{slf} \tag{7}$$

First, we extract the p-q components of V_{sl}:

$$\begin{bmatrix} V_{slp} \\ V_{slq} \end{bmatrix} = C_{pq} C_{32} \begin{bmatrix} V_{la} \\ V_{lb} \\ V_{lc} \end{bmatrix} \tag{8}$$

C_{pq}, C_{32} representing the Park matrix and Concordia matrix given respectively by:

$$C_{pq} = \begin{bmatrix} \sin(\omega t) & -\cos(\omega t) \\ -\cos(\omega t) & -\sin(\omega t) \end{bmatrix} \tag{9}$$

$$C_{32} = \sqrt{2/3} \begin{bmatrix} 1 & -1/2 & -1/2 \\ 0 & \sqrt{3}/2 & -\sqrt{3}/2 \end{bmatrix} \tag{10}$$

Next, decomposition of V_{slp} and V_{slq} into continuous components $\overline{V}_{slp}$, $\overline{V}_{slq}$ and alternative components $\widetilde{V}_{slp}$, $\widetilde{V}_{slq}$

$$V_{slp} = \overline{V}_{slp} + \widetilde{V}_{slp} \tag{11}$$

$$V_{slq} = \overline{V}_{slq} + \widetilde{V}_{slq} \tag{12}$$

$\overline{V}_{slp}$, $\overline{V}_{slq}$ are obtained via a second order low-pass filter.

Then, the obtained three-phase fundamental components are presented below:

$$\begin{bmatrix} V_{slfa} \\ V_{slfb} \\ V_{slfc} \end{bmatrix} = C_{23} C_{pq}^{-1} = \begin{bmatrix} \overline{V}_{slp} \\ \overline{V}_{slq} \end{bmatrix} \tag{13}$$

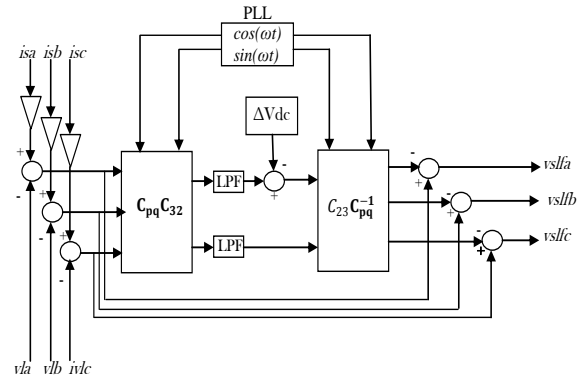Finally, this algorithm can be represented as shown in the block diagram of Fig. 3.

Figure 3. Block diagram of voltages references determination

D. Inverter Control Using PWM

The control method is aimed to control PWM inverter to produce the desired compensation voltage, in the output of series filter. This method is achieved by implementing a fuzzy logic controller [7]-[9] which starts from the difference between the injected voltage (V_{inj}) and the calculated reference voltage (V_{slf}) that determines the reference voltage of the inverter (modulating wave).

This reference voltage is compared with two carrying triangular identical waves shifted one from other by a half period of chopping producing the control signal to control the on-off of the IGBT [10], [11].

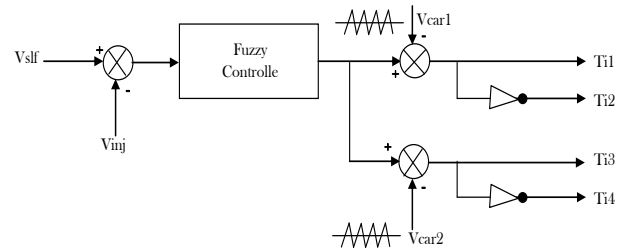Fig. 4 shows the general block diagram of voltage control used.

Figure 4. PWM synoptic block diagram of voltage control

The control of inverter arm constituting the series active filter is summarized in the two following steps.

- Determination of the intermediate signals V_{i1} and V_{i2}.

If error ≥ carrying 1 => $V_{i1} = 1$

I_f error < carrying 1 => $V_{i1} = 0$

If error ≥ carrying 2 => $V_{i2} = 0$

If error < carrying 2 => $V_{i2} = -1$

Determination of control signals of the switches T_{ij} (j = 1, 2, 3, 4).

If $(V_{i1} + V_{i2}) = 1$ => $T_{i1} = 1, T_{i2} = 1, T_{i3} = 0, T_{i4} = 0$

If $(V_{i1} + V_{i2}) = 0$ => $T_{i1} = 0, T_{i2} = 1, T_{i3} = 1, T_{i4} = 0$

If $(V_{i1} + V_{i2}) = -1$ => $T_{i1} = 0, T_{i2} = 0, T_{i3} = 1, T_{i4} = 1$

E. Fuzzy Control Application

The FLC concept was proposed in 1965 that was based on a logical system called fuzzy logic. It is much closer in spirit to human thinking and natural language. FLC was deduced from fuzzy set theory. Fuzzy sets boundaries were undefined, ambiguous and useful for approximate systems design [12], [13]. FLC is used for the HPF in closed loop to control a constant DC voltage, improve the performance and reduce the *THD* of the current.

The (*e*) and its derivation (*de*) are used as inputs for fuzzy process.

Fig. 5 shows the synoptic scheme of fuzzy controller, which possesses two inputs (the error (*e*)).

($e = V_{slf} - V_{inj}$) and its derivative (*de*) and one output (the command (c_{de})). [9]
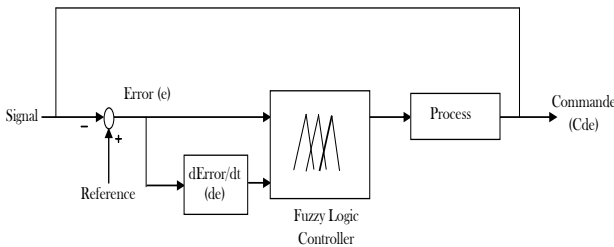
Figure 5. Fuzzy controller synoptic diagram

Mainly, the three main features of FLC are Fuzzification, Fuzzy Inference Mechanism (Knowledge base) and Defuzzification.

Fuzzification: The conversion process of a numerical variable to a linguistic variable.

Rule Elevator: FLC uses linguistic variables as a control gain. The basic operations of FLC requires AND (∩), OR) U (and NOT (~) for evaluation fuzzy set rules.

Defuzzification: The conversion process of linguistic variable to a numerical variable.

Database: stores the definition of the triangular membership function for the fuzzifier and defuzzifier.

Rule Base: stores the linguistic control rules required by rule evaluator. The 25 rules in this proposed controller are shown in Table I, is based on the error (*e*) sign, variation and knowing that (*e*) is increasing if its derivative (*de*) is positive, constant if (*de*) is equal to zero, decreasing if (*de*) is negative, positive if ($V_{slf} > V_{inj}$), zero if ($V_{slf} = V_{inj}$), and negative if ($V_{slf} < V_{inj}$), fuzzy rules are summarized in following table:

TABLE I. RULES BASE OF FUZZY CONTROL

C_{de}		de				
		BN	N	Z	P	BP
e	BN	*BN*	*BN*	*N*	*N*	*Z*
	N	*BN*	*N*	*N*	*Z*	*P*
	Z	*N*	*N*	*Z*	*P*	*P*
	P	*N*	*Z*	*P*	*P*	*BP*
	BP	*Z*	*P*	*P*	*BP*	*BP*

With: (BN): Big negative; (N): Negative; (Z): Zero (P): Positive and (BP): Big positive

Fig. 6 shows the membership Function of FLC used for the error ($e = V_{slf} - V_{inj}$) and its derivative (*de*), and one output (the command (c_{de}))
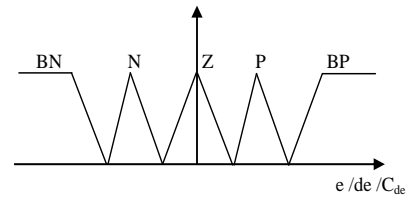

Figure 6. Membership function of FLC used

III. SIMULATION RESULTS

The simulation is carried out using a program working in MATLAB/SIMULINK environment. For non linear load we use a three phase diode rectifier with RL load.

The simulation parameters are shown in the Table II.

TABLE II. SYSTEM PARAMETERS

Source	e_s	230 V
	L_s	5,5 mH
	R_s	3,6 Ω
Load	R	25 Ω
	L	55 mH
Passive filter	L_{f5} ; C_{f5}	13,5 mH ;30 µF
	L_{f7} ; C_{f7}	6,75 mH ;50 µF
Turns Ratio of Coupling Transformer		1:1
Switching Frequency		10 KH
Current sensor gain k		5

A. Without Filtering

In Fig. 7 we present the waveform of the load current, load voltage; and the delay between voltage and current that represents the absorbed reactive power or power factor of the system.
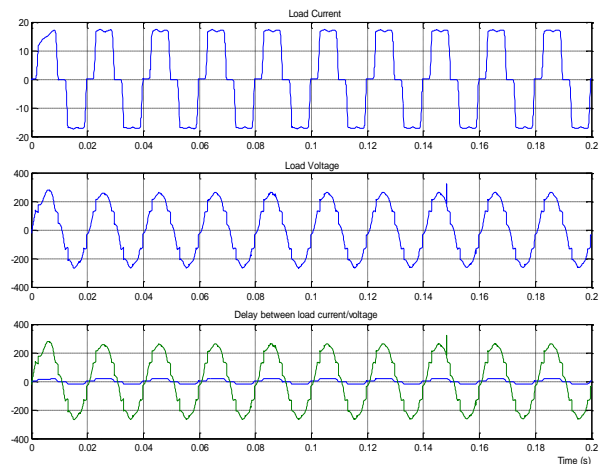

Figure 7. Waveforms of load (current, voltage), and their delay

Fig. 8 shows the waveform of the three voltages on the same graph. In this figure we see that there are disruptive phenomena appear as flicker and voltage imbalance.
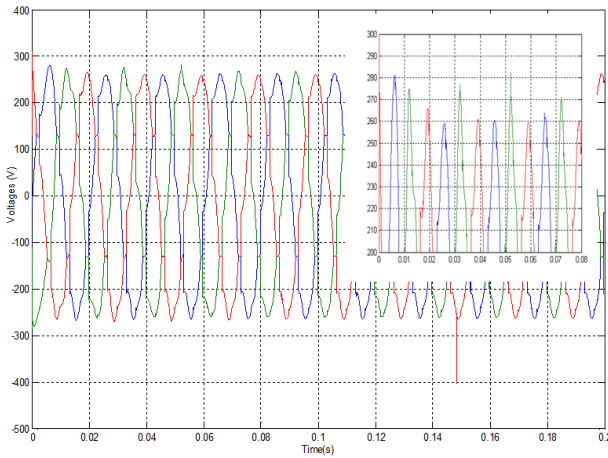

Figure 8. Voltages loads

Fig. 9 shows the harmonic spectrum of current without filtering.
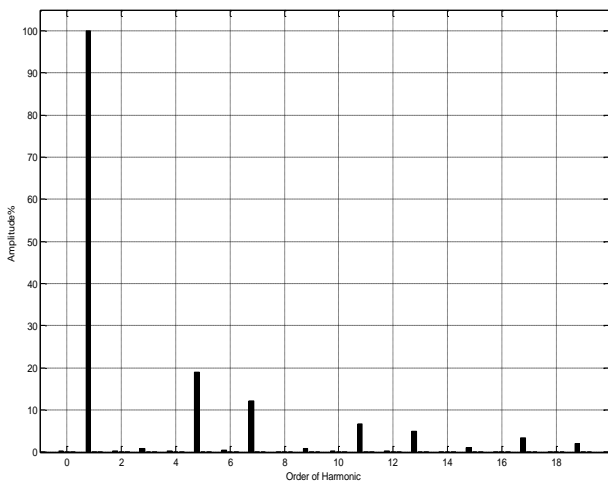

Figure 9. Harmonic spectrum of current

The harmonic spectrum of current shows that the harmonics of order 5, 7, 11, 13 ...; are the most predominant harmonic and have larger amplitudes; because they are harmonics characteristics (following relationship 6K ± 1; k is an integer number); and return to the non linear load used (Three phase rectifier PD3).

B. With Passive Filter (PF) Only

The simulations results with passive filter only are presented in Fig. 10, Fig. 11 and Fig. 12.

Fig. 12 shows the harmonic spectrum of current with passive filter only.

After the use of the passive filtering (two resonant filter to rank harmonics 5 and 7); we clearly see the elimination of the current harmonics of order 5 and 7.
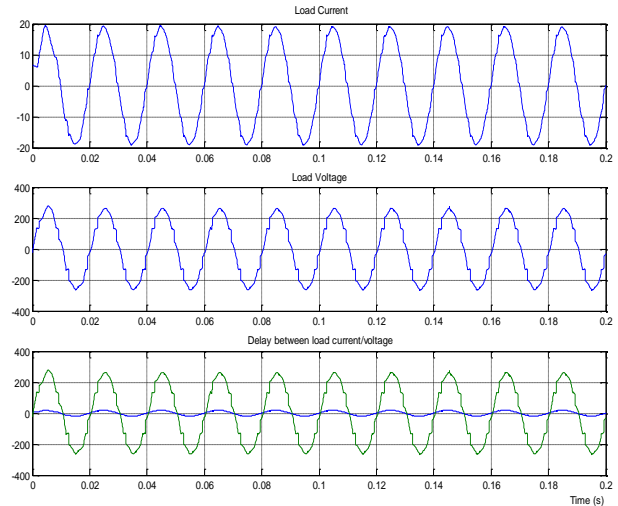
Figure 10. Waveforms of sources (current, voltage), and their delay with PF only
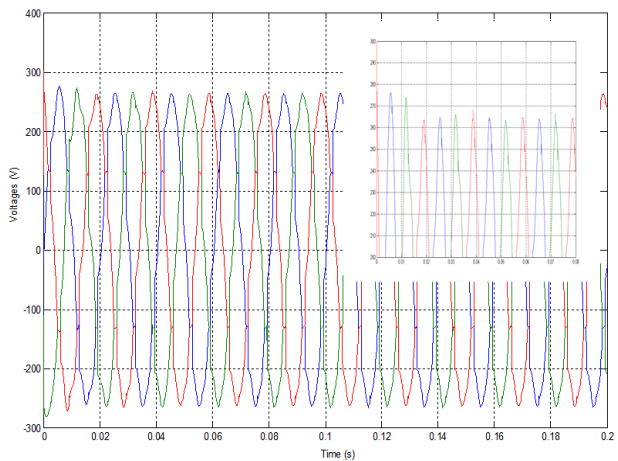
Figure 11. Voltages sources with PF only
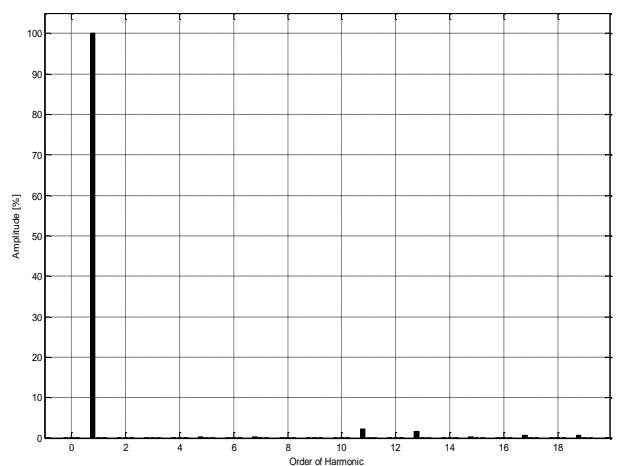
Figure 12. Harmonic Spectrum of current with PF only

C. With Hybrid Power Filter (HPF)

The simulations results after filtering by using hybrid power filter are presented in Fig. 13-Fig. 16.
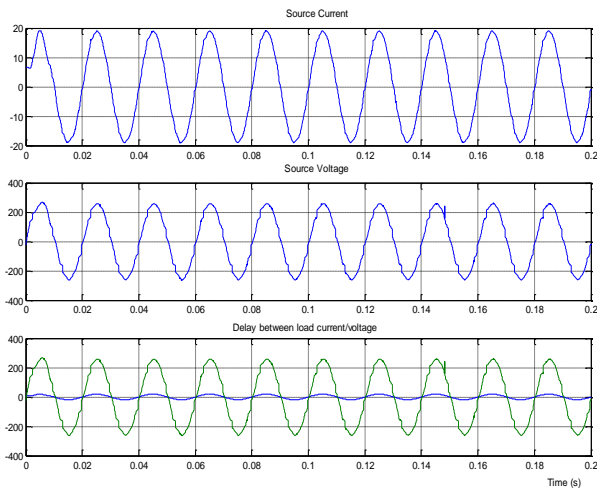
Figure 13. Waveforms of sources (current, voltage), and their delay with HPF
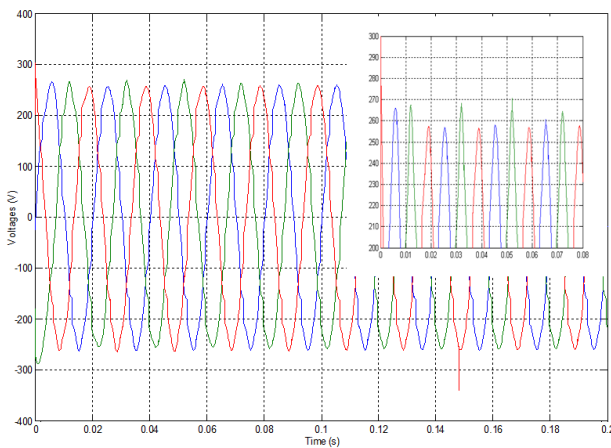
Figure 14. Voltages sources with HPF

Fig. 15 shows the waveform of the injected voltage by the series active series filter.
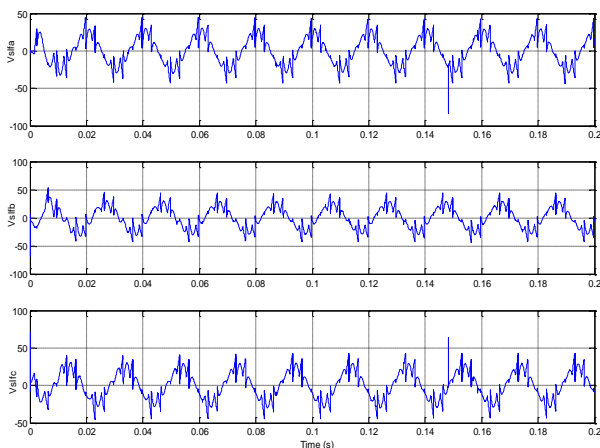

Figure 15. Voltages references of active series filter

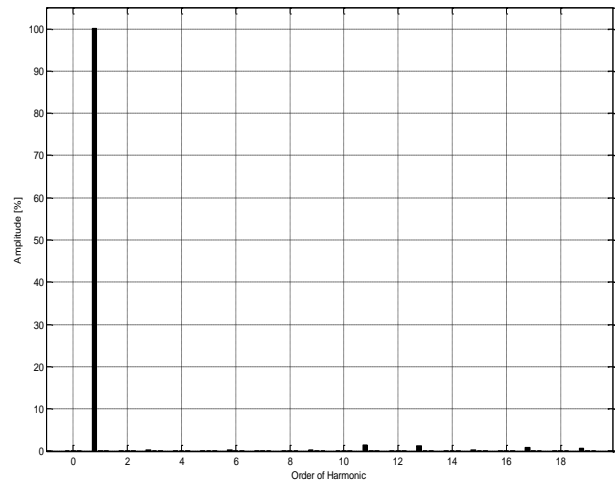Fig. 16 shows the Harmonic Spectrum of current with Hybrid Power filter.

Figure 16. Harmonic spectrum of current with HPF

In Table III and Table IV we present the simulations results before and after filtering for currents and voltages harmonics.

TABLE III. SIMULATION RESULTS OF HARMONICS CURRENTS

Harmonic Currents	Without	With PF Only	With HPF
5	19,00 %	0,26 %	0,19 %
7	12,29 %	0,32 %	0,03 %
11	6,63 %	2,19 %	1,54 %
13	4,93 %	1,74 %	1,27 %
17	3,35 %	0,71 %	0,97 %
19	2,03 %	0,77 %	0,59 %
THDi	**24,46 %**	**3,40 %**	**2,19 %**

TABLE IV. SIMULATION RESULTS OF HARMONICS VOLTAGES

Harmonic Voltages	Without	With PF Only	With HPF
5	1,14 %	0,85 %	0,67 %
7	0,48 %	0,76 %	0,28 %
11	4,08 %	3,42 %	2,42 %
13	3,34 %	2,77 %	1,94 %
17	2,12 %	3,50 %	1,29 %
19	1,88 %	2,03 %	1,07 %
THDv	**7,49 %**	**6,74 %**	**4,27 %**

It summarizes in the Table V; harmonic minimization rate with the use of only passive filtering (PF) and hybrid Power filtering (HPF).

TABLE V. EFFICIENCY OF THE FILTERS USED

	Harmonics Currents		Harmonics Voltages	
	With PF Only	With HPF	With PF Only	With HPF
5	98,63 %	99 %	25,44 %	41,23 %
7	97,4 %	97,67 %	58,33 %	41,67 %
11	68,33 %	76,77 %	16,18 %	40,68 %
13	64,71 %	74,24 %	17,06 %	41,92 %
17	78,81 %	71,04 %	65,09 %	39,15 %
19	62,07 %	70,94 %	7,98 %	43,08 %
THD	86,1 %	**91,05 %**	10,01 %	**36,98 %**

IV. DISCUSSIONS

After the simulation results, we note that with the use of passive filtering (Filter 5 and 7) that there a total elimination of harmonic 5th and 7th which have large amplitudes; The harmonic 5 is reduced from 19% to 0,26% with rate of 98,63%; the harmonic 7 from 12,29% to 0,32% with rate of 97,4% and for the current THD is reduced from 24,46% to 3,40% with rate 86,1% For the voltage THD is reduced from 7, 49% to 6,74% with rate of 10,01%

The obtained results for hybrid filter showed clearly that the use of is better than utilization of passive filter only especially for mitigation of voltages harmonics from 7,49% to 4,27 with rate of 36,98% under norm (5%). and the same for the current THDI from 24,46% to 2,19% (Under Standard) with rate of 91,05% [14].

In Fig. 7 shows the delay between current and source voltage is big but the Fig. 13 illustrates the delay reduction between source current and voltage; i.e. power factor correction when the hybrid filter is connected.

In Fig. 8 we see that it to be disruptive phenomena associated with voltage as imbalance and flicker and after use a Hybrid Filter we note that these phenomena are reduced (Fig. 14) and this because the injected voltage by this filter.

V. CONCLUSION

In this paper we have presented the three-phase hybrid active power filter for compensation of harmonic currents generated by the non-linear load. The fuzzy logic control based HPF for three-phase system is modeled and simulated in MATLAB/SIMULINK environment. The main objective of this research work has been accomplished.

The total harmonic distortion of the supply current and voltage has been decreased at a high level in the simulation. Which is an achievement to meet the IEEE 519 recommended harmonic standard. In fact, not only the harmonics were reduced to an acceptable rate, but also the transient response time was minimized. Moreover, the utility power factor was corrected, unbalanced voltage and flicker is minimized.

REFERENCES

[1] B. Singh, K. Al-Haddad, and A. Chandra, "A review of active filters for power quality improvement," *IEEE Trans. Ind. Electron.*, vol. 46, no. 5, pp. 960–971, Oct. 1999.

[2] H. K. Chiang, B. R. Lin, K. T. Yang, and K. W. Wu, "Hybrid active power filter for power quality compensation," in *Proc. EEEE PEDS*, 2005, pp. 950-954.

[3] B. R. Lin, H. K. Chiang, and C. H. Huang, "Three-phase three level active power filter with a clamped capacitor topology," *IEE Proceedings-Electric Power Applications*, vol. 153, pp. 513–522, July 2006.

[4] R. S. Herrera and P. Salmerón, "Instantaneous reactive power theory: A comparative evaluation of different formulations," *IEEE Trans. Power Del.*, vol. 22, no. 1, pp. 595–604, Jan. 2007.

[5] H. Yang and S. Ren, "A practical series-shunt hybrid active power filter based on fundamental magnetic potential self-balance," *IEEE Trans. Power Del.*, vol. 23, no. 4, pp. 2089–2096, Oct. 2008.

[6] S. George and V. Agarwal, "Optimum control of selective and total harmonic distortion in current and voltage under non sinusoidal conditions," *IEEE Trans. Power Del.*, vol. 23, no. 2, pp. 937–944, Apr. 2008

[7] M. Suresh, A. K. Panda, and S. Yellasiri, "Fuzzy controller based 3phase 4wire shunt active Filter for mitigation of current harmonics with combined p-q and Id-Iq control strategies," *Journal of Energy and Power Engineering*, vol. 3, no. 1, pp. 43-52, 2011.

[8] Y. Djeghader and L. Zellouma, "Using hybrid power filter to mitigate currents and voltages harmonics in three phase system," *Acta Electrotechnica et Informatica*, vol. 15, no. 4, pp. 37-43, 2015.

[9] S. Saad and L. Zellouma, "Fuzzy logic controller for three-level shunt active filter compensating harmonics and reactive power," *Electric Power Systems Research*, vol. 79, pp. 1337–1341, 2009.

[10] B. Ning and Z. Zhang, "Comparison of Total ionizing dose effects for floating and tied body SOI MOSFETs," *International Journal of Electronics and Electrical Engineering*, vol. 1, no. 1, March 2013.

[11] P. Nguyen and M. Han, "The investigation of equivalent harmonic impedances of VSC-based HVDC systems," *International Journal of Electronics and Electrical Engineering*, vol. 4, no. 1, February 2016.

[12] S. Lalouni and D. Rekioua, "Modeling and simulation of a photovoltaic system using fuzzy logic controller," in *Proc. Second International Conference on Developments in e Systems Engineering*, 2009, pp. 23-28.

[13] S. Kerrouche and F. Krim, "Three-phase active power filter based on fuzzy logic controller," *International Journal of Sciences and Techniques of Automatic Control& Computer Engineering*, vol. 3, no. 1, pp. 942-955, July 2009.

[14] Recommended Practices and Requirements for Harmonic Control in Electrical Power Systems, The Institute of Electrical and Electronics Engineers, IEEE Standard 519-1992, 1993.

Dr. Yacine Djeghader was born in 1980 in Annaba, Algeria. He received the BS degree, MS degree and Ph.D. degree in Electrical Engineering from Annaba University, Algeria in 2003, 2006 and 2011 respectively. Presently he is Assistant Professor in Electrical Engineering in Souk Ahras University, Algeria; His fields of interest are Power Quality, Power System, FACTS, Power Electronic.

CrossMark

ORIGINAL ARTICLE

Optimizing of IP speed controller using particle swarm optimization for FOC of an induction motor

Youcef Bekakra[1] · Djilani Ben Attous[1]

Abstract This paper presents a modern approach for speed control of an induction motor (IM) using the particle swarm optimization (PSO) method for determining the optimal parameters, K_p and K_i, of the integral proportional (IP) controller. The use of PSO as an optimization algorithm makes the drive robust, with faster dynamic response, higher accuracy and insensitive to load variation. Comparison between different controllers is achieved, using an IP controller which is tuned by two methods, firstly manually and secondly using the PSO technique. Integral time absolute error, integral absolute error and integral square error performance indices are considered to satisfy the required criteria in output speed of an IM. From the simulation results it is observed that the IP controller designed with PSO yields better results when compared to the traditional method in terms of performance index.

Keywords Induction motor · Field oriented control · Integral proportional (IP) controller · Particle swarm optimization (PSO) · Tuning off-line

✉ Youcef Bekakra
youcef1984@gmail.com; youcef-bekakra@univ-eloued.dz

Djilani Ben Attous
dbenattous@yahoo.com

[1] Faculty of Technology, Department of Electrical Engineering, University of El Oued, P.O. Box 789, El Oued, Algeria

1 Introduction

Field-oriented control (FOC) or vector control of induction machine achieves decoupled torque and flux dynamics leading to independent control of the torque and flux as for a separately excited DC motor. This control strategy can provide the same performance as achieved from a separately excited DC machine. This technique can be performed by two basic methods: direct vector control and indirect vector control. Both direct field-oriented (DFO) and indirect field-oriented (IFO) solutions have been implemented in industrial drives demonstrating performances suitable for a wide spectrum of technological applications (Bousserhane et al. 2006).

However control of IM is complicated due to the fact that in obtaining decoupled control of the torque and flux producing components of the stator phase current, both the magnitude and phase of the stator quantities need to be controlled. In addition, there is no direct access to the rotor quantities, such as rotor fluxes and currents. To overcome these difficulties, high performance vector control algorithms have been developed. These algorithms can decouple the stator phase currents by using only the measured stator current and flux, as well as the rotor speed (Elwer 2006).

In the last decade, various modern control techniques such as adaptive control, variable structure control and intelligent control have been intensively studied for controlling the nonlinear components in power systems. However, these control techniques have few real applications probably due to their complicated structures or the lack of confidence in their stability. Therefore, the conventional IP controllers, because of their simple structures, are still the most commonly used control techniques in

🌀 Springer

power systems, as can be seen in the control of the IM. Unfortunately, tuning the IP controllers is tedious and it might be difficult to tune the IP gains properly due to the nonlinearity and the high complexity of the system (Qiao et al. 2006).

Modern heuristic algorithms are considered as effective tools for nonlinear optimization problems. The algorithms do not require that the objective function has to be differentiable and continuous. A particle swarm optimization (PSO) is one of the modern heuristic algorithms and can be applied to nonlinear and noncontinuous optimization problems with continuous variables. It has been developed through simulation of simplified social models (Naka et al. 2003).

The drive system has one speed IP controller which is tuned using PSO instead of traditional tuning methods; the drive system plays an important role in meeting the other requirements. It should enable the drive to follow any reference speed taking into account the effect of load and speed variation.

Particle swarm optimization (PSO) was first introduced by Kennedy and Eberhart (1995) (Poli et al. 2007). The method is based on the simulation of animal social behaviors such as fish schooling, bird flocking, and swarm theory. Since it is population based and self-adaptive, it has gained an increasing popularity as an efficient alternative to the genetic algorithm (GAs) in solving optimization problems. Moreover, it is shown to be effective in optimizing difficult multidimensional discontinuous problems in a variety of fields. Similar to other population-based optimization method such as the GA, the PSO algorithm starts with random initialization of a population of individuals in the search space. Each particle in the search space is adjusted by its own flying experience and the other particles flying experience to find the global best solution at each generation. Compared with the GA, PSO has memorial ability to let the knowledge of good solutions be retained by all particles, whereas the previous knowledge need not be considered after each evolution in GA. Furthermore, low computation cost, simplicity of implementation, and quick convergence ability make PSO popular in many applications (Lin et al. 2009).

In this paper, we investigate the performance of PSO for optimizing the IP speed controller gains of the Induction Motor (IM) and compared with an IP controller which is tuned manually.

2 Induction machine model

Using the dynamic model of an induction machine as a controlled plant may be expressed in terms of the d-q axes components in a synchronous rotating frame presented in,

the voltage equations in terms of stator current and rotor flux linkage can be restated in matrix form as (Chaari et al. 2007):

$$
\begin{bmatrix} \dfrac{di_{sd}}{dt} \\[2mm] \dfrac{di_{sq}}{dt} \\[2mm] \dfrac{d\phi_{rd}}{dt} \\[2mm] \dfrac{d\phi_{rq}}{dt} \end{bmatrix} =
$$

$$
\begin{bmatrix} -\left(\dfrac{R_s}{\sigma L_s}+\dfrac{1-\sigma}{\sigma T_r}\right) & \omega_s & \dfrac{M}{\sigma L_s L_r T_r} & \dfrac{M\omega_r}{\sigma L_s L_r} \\[3mm] -\omega_s & -\left(\dfrac{R_s}{\sigma L_s}+\dfrac{1-\sigma}{\sigma T_r}\right) & -\dfrac{M\omega_r}{\sigma L_s L_r} & \dfrac{M}{\sigma L_s L_r T_r} \\[3mm] \dfrac{M}{T_r} & 0 & -\dfrac{1}{T_r} & \omega_{sl} \\[3mm] 0 & \dfrac{M}{T_r} & -\omega_{sl} & -\dfrac{1}{T_r} \end{bmatrix}
$$

$$
\times \begin{bmatrix} i_{sd} \\ i_{sq} \\ \phi_{rd} \\ \phi_{rq} \end{bmatrix} + \begin{bmatrix} \dfrac{1}{\sigma L_s} & 0 \\[2mm] 0 & \dfrac{1}{\sigma L_s} \\[2mm] 0 & 0 \\[2mm] 0 & 0 \end{bmatrix} \begin{bmatrix} V_{sd} \\ V_{sq} \end{bmatrix}
$$

$$\tag{1}$$

where $\sigma = 1 - \frac{M^2}{L_s.L_r}$; $T_s = \frac{L_s}{R_s}$; $T_r = \frac{L_r}{R_r}$; $\omega_{sl} = \omega_s - \omega_r$.

The electromagnetic torque and the rotor speed are given by:

$$T_{em} = P\frac{M}{L_r}\left(\phi_{rd}i_{sq} - \phi_{rq}i_{sd}\right) \tag{2}$$

$$\frac{d\omega_r}{\omega_r} = \frac{P}{J}T_{em} - \frac{P}{J}T_l - \frac{f}{J}\omega_r. \tag{3}$$

The position of field rotoric is determined by integration of the stator pulsation, it even reconstituted by the speed of the motor and the rotor pulsation (Mechernene et al. 2008):

$$\theta_s = \int (\omega_r + \omega_{sl})dt = \int \left(P.\Omega + \frac{M.i_{sq}}{T_r\phi_{rd}}\right)dt. \tag{4}$$

2.1 The structure of field oriented control

In the rotor field oriented control scheme, the rotor flux vector is aligned with the d-axis and it imposes the following condition (Ali et al. 2009):

$$\phi_{rd} = \phi_r, \phi_{rq} = 0. \tag{5}$$

Thus by taking into account these new conditions and employing (5) on the (1), the dynamic model of an induction machine became:

$$V_{sd} = \sigma L_s \frac{di_{sd}}{dt} + \left(R_s + \frac{M^2}{T_r L_r} \right) i_{sd} - \omega_s \sigma L_s i_{sq} - \frac{M}{T_r L_r} \phi_r \tag{6}$$

$$V_{sq} = \sigma L_s \frac{di_{sq}}{dt} + \left(R_s + \frac{M^2}{T_r L_r} \right) i_{sq} + \omega_s \sigma L_s i_{sd} + \omega_r \frac{M}{L_r} \phi_r \tag{7}$$

$$\frac{d\phi_r}{dt} = \frac{M}{T_r} i_{sd} - \frac{1}{T_r} \phi_r \tag{8}$$
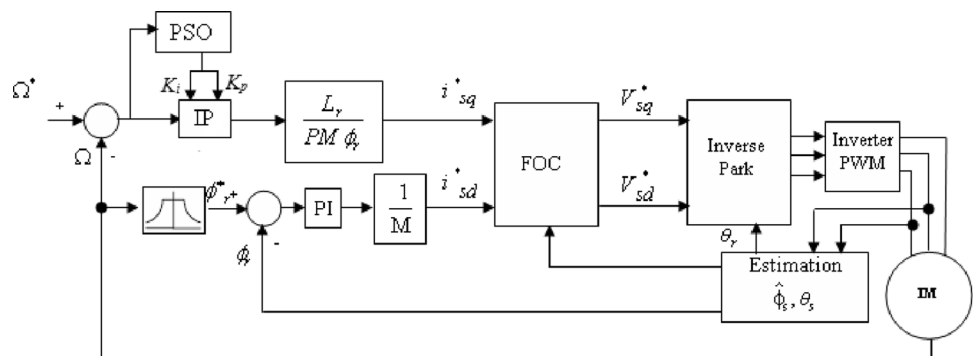
$$T_{em} = P \frac{M}{L_r} \phi_r i_{sq} \tag{9}$$

$$\omega_s = P \cdot \Omega + \frac{M \cdot i_{sq}}{T_r \phi_r}. \tag{10}$$

A block diagram for a direct field oriented controller can be seen in the following section. This design uses a more robust structure known as DFOC.

As can be seen in Fig. 1 these map the three phase stator currents onto a direct and quadrature rotating reference frame that is aligned with the rotor flux. This decouples the torque and flux.

Producing components of the stator currents allows the induction motor to be controlled in much the same way as a separately excited DC machine. Three PI (Proportional Integral) and one IP (Integral Proportional) regulators are used to set the output reference voltages. The IP regulator compares the speed set point with the measured mechanical speed of the rotor and produces the stator current quadrature axis reference, i_{sq}^*. The PI regulator compares the rotor flux set point with the estimate rotor flux and produces the stator current direct axis reference, i_{sd}^*. To operate the motor above its nominal speed a technique known as Field Weakening is used to reduce the rotor flux. The reference currents are compared with the measured stator currents. The error is used by the PI regulators to generate the output stator voltages in the direct and quadrature axes. These are transformed back onto the "a, b and c" axes using the inverse Park transformer to allow the output voltage to be generated directly using PWM.

3 Designing of IP-controller using PSO

The PSO as an optimization tool provides a population-based search procedure in which individuals called particles change their position (state) with time. In a PSO system, particles fly around in a multidimensional search space. During flight, each particle adjusts its position according to its own experience (This value is called P_{best}), and according to the experience of a neighboring particle (This value is called G_{best}), made use of the best position encountered by itself and its neighbor (Lalitha et al. 2010; Bekakra and Attous 2014), as shown in Fig. 2.

This modification can be represented by the concept of velocity. Velocity of each agent can be modified by the following equation:

$$v^{k+1} = w \cdot v_k + c_1 rand * (P_{best} - x^k) + c_2 rand (G_{best} - x^k) \tag{11}$$

Using the above equation, a certain velocity, which gradually gets close to P_{best} and G_{best} can be calculated. The current position (searching point in the solution space) can be modified by the following equation:

$$x^{k+1} = x^k + v^{k+1}, \quad k = 1, 2, \ldots, n \tag{12}$$

where x^k is current searching point, x^{k+1} is modified
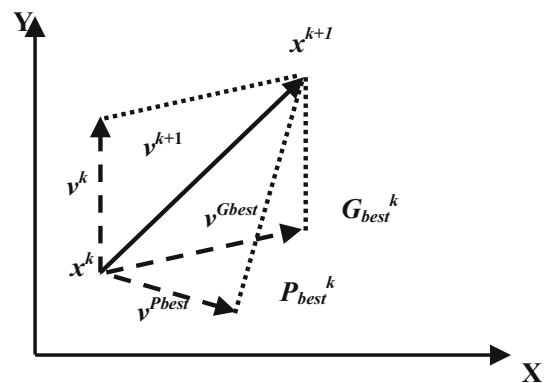
Fig. 2 Concept of a searching point by PSO

Fig. 1 Direct field oriented control of induction motor with PSO

searching point, v^k is current velocity, v^{k+1} is modified velocity. P_{best} is the best solution observed by current particle and G_{best} is the best solution of all particles, w is an inertia weight, c_1 and c_2 are two positive constants, *rand* is a random generated numbers with a range of [0,1].

The following inertia weight is used (Lalitha et al. 2010; Bekakra and Attous 2014):

$$w(k) = w_{max} - \left(\frac{w_{max} - w_{min}}{k_{max}} \right) * k \tag{13}$$

where k_{max}, k is maximum number of iterations and the current number of iterations, respectively. Where, w_{min} and w_{max} are the minimum and maximum weights respectively. Appropriate value ranges for c_1 and c_2 are 1–2, but 2 is the most appropriate in many cases. Appropriate values for w_{min} and w_{max} are 0.4 and 0.9 (Eberhart and Shi 2000) respectively.

The IP-controller is a good controller in the field of machine control, but the problem is the mathematical model of the plant must be known. In order to solve problems in the overall system, several methods have been introduced to tune IP-controller. Our proposed method uses the PSO to optimize the speed IP-controller parameters, the PSO is utilized off-line to determine the controller parameters (K_p and K_i) based on speed error of the IM shown Fig. 1. The performance of the IM varies according to IP controller gains and is judged by the value of *ITAE* (*Integral Time Absolute Error*). The performance index *sum(ITAE)* is chosen as an objective function. The purpose of stochastic algorithms is to minimize the objective function. All particles of the population are decoded for K_p and K_i.

ITAE criterion is widely adopted to evaluate the dynamic performance of the control system (Allaoua et al. 2009). The index *ITAE* is expressed in Eq. (14), as follows:

$$ITAE = \int_0^\infty t \cdot |e(t)| \cdot dt \tag{14}$$

Figure 3 presents the PSO-based approach to find the global maximum value of objective function.

In this paper a time domain criterion is used for evaluating the IP controller. The performance criteria used for comparison between using a IP controller which is tuned by PSO technique and manually. IP controller is including integrated absolute error (*IAE*) and integrated of squared error (*ISE*).

The *IAE* and *ISE* performance criterion formulas are as follows (Allaoua et al. 2009):

$$IAE = \int_0^\infty |e(t)| \cdot dt \tag{15}$$
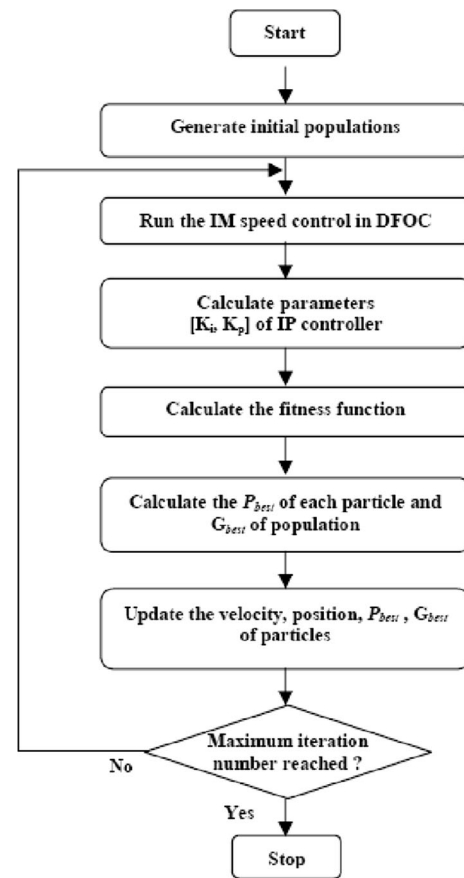
Fig. 3 The flowchart of the PSO-IP control system

$$ISE = \int_0^\infty e^2(t) \cdot dt \tag{16}$$

4 Simulation results

The IM used in this work is a 1.08 KW, whose nominal parameters are indicated in appendix.

The parameters of PSO algorithms are showed in the Table 1.

- After several experiments, we obtained the following "The augmentation of swarm size leads to complicate

Table 1 Parameters of PSO algorithms

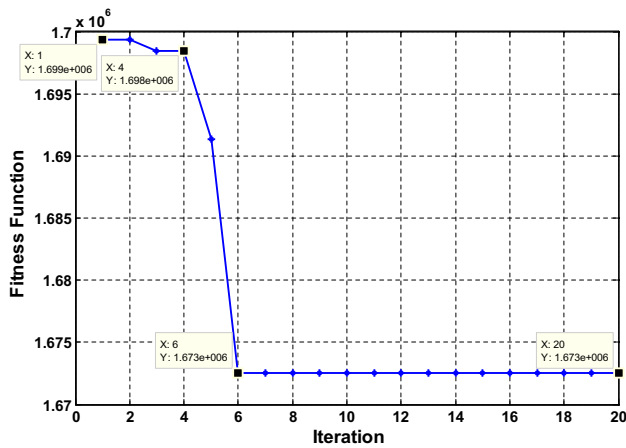|	
Swarm size	15
Number of iteration	20
$c_1 = c_2$	2
w_{max}	0.9
w_{min}	0.4

Fig. 4 The fitness function variation during simulation

the calculation and a prolongation in computing time". In our case swarm size =15 is a good selection.

- In our case, the number of maximum iteration = 20 is satisfying for obtaining good results.

4.1 Load variation

In this test, a cyclic change of different load torque levels are subjected to the motor at certain times and as followings:

$$Time = [0 \quad 0.8 \quad 0.8 \quad 1.1 \quad 1.1 \quad 1.4 \quad 1.4 \quad 1.7 \quad 1.7];$$

$$Torque = [0 \quad 0 \quad 5 \quad 5 \quad 3 \quad 3 \quad -3 \quad -3 \quad 0];$$

After the Fig. 4 the best fitness value is $1.673e + 006$ appeared in iteration number 6. The current positions of the 15 particles of swarm during simulation for the iterations N°01, N°04, N°06 and N°20, are presented in the Fig. 5. These current positions of particles are represented the values of Kp and Ki parameters during the simulation where these parameters are changed in interval [0 20, 0 20].

A comparison between two controllers is achieved using the IP controller which is tuned by two methods, the first is manually and the second uses the PSO technique. The results are shown through Figs. 6, 7, 8 and 9. Figure 6

(a)

(b)

(c)

(d)
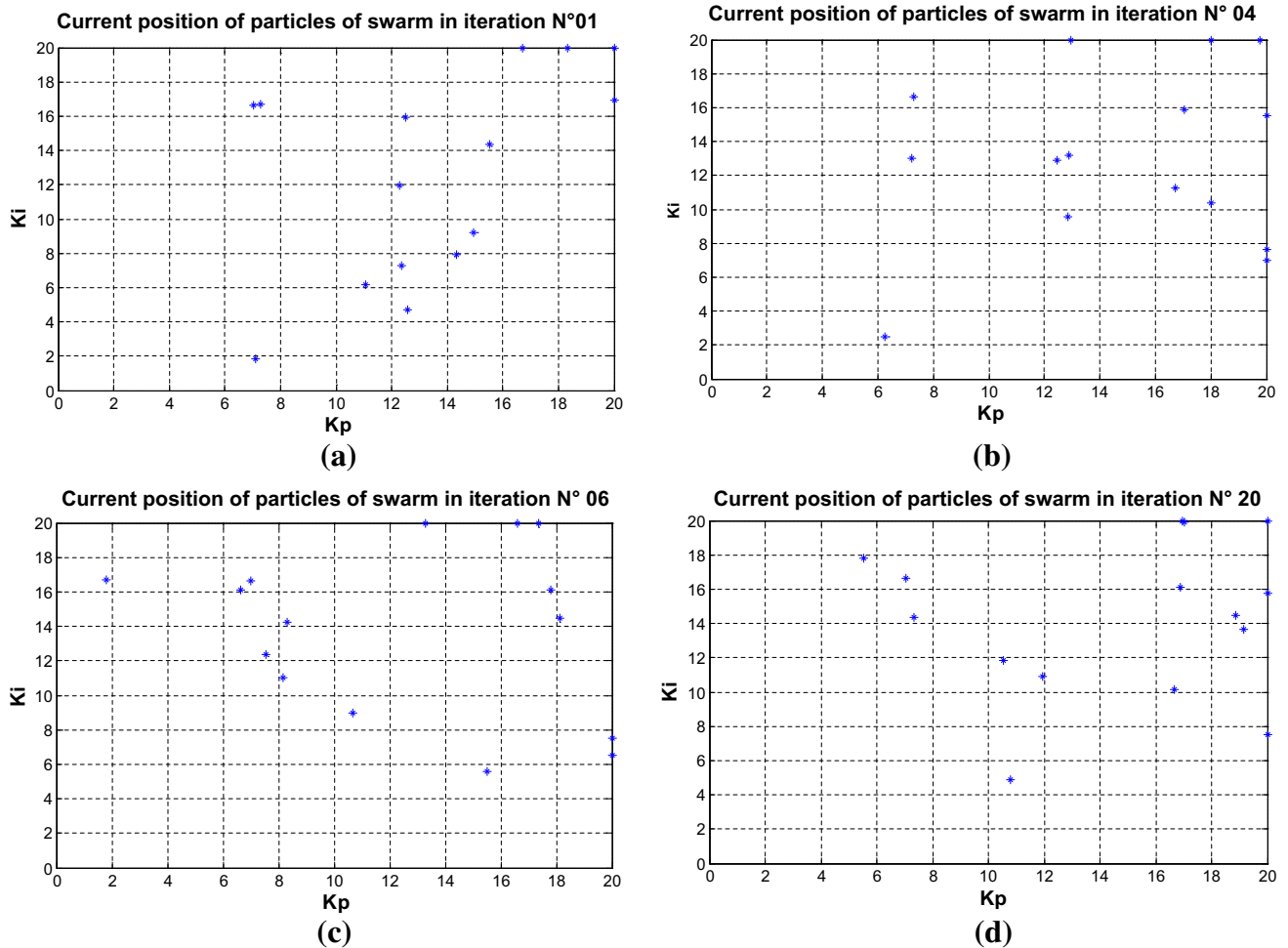
Fig. 5 Current position of particles of swarm during simulation for **a** iteration N°01, **b** iteration N°04, **c** iteration N°06 and **d** iteration N°20
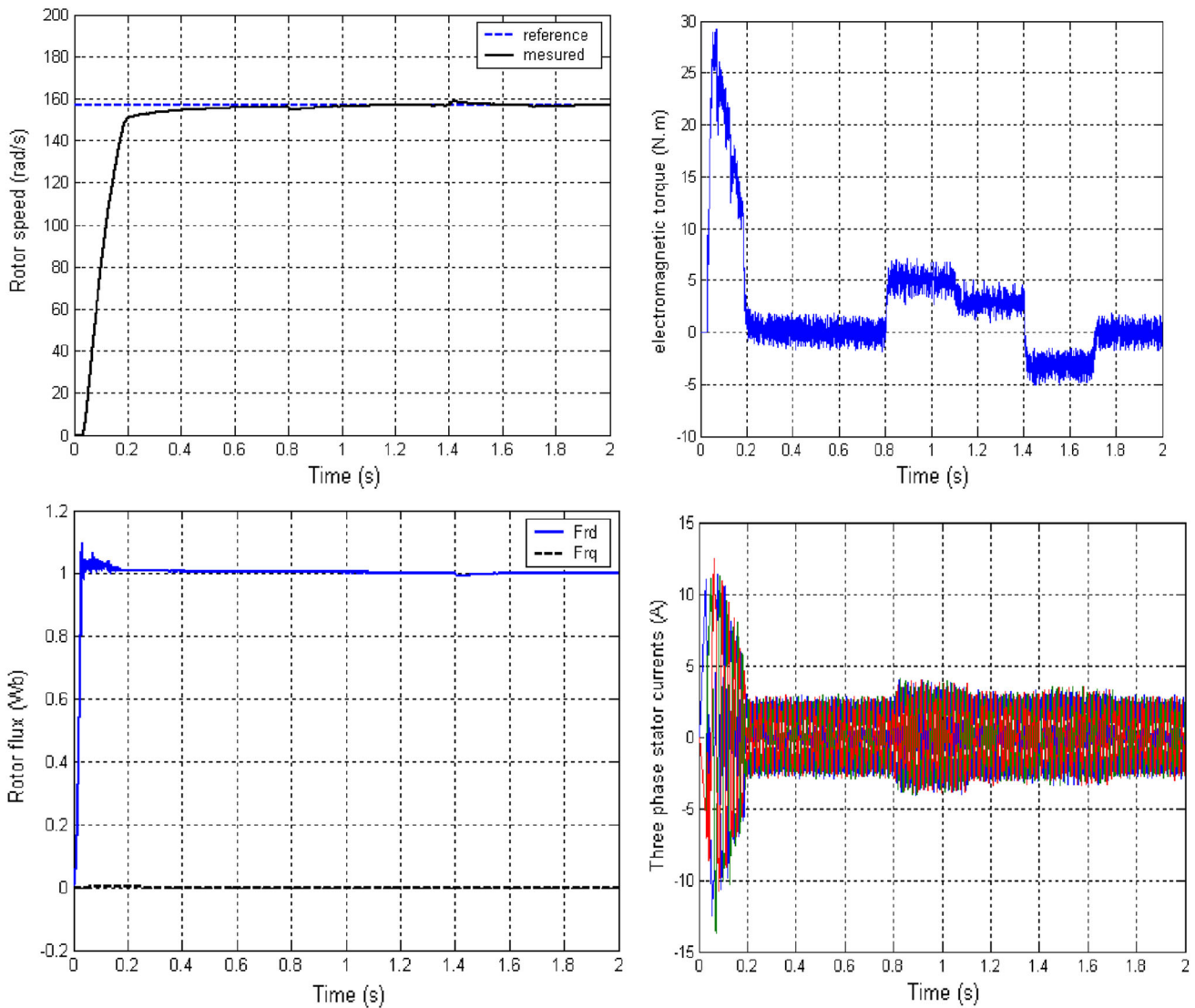
Fig. 6 Results of speed control using the IP controller manual tuning under load variation

shows the speed, electromagnetic torque, rotor flux and the three-phase stator currents response using the IP controller (in speed loop) that is tuned manually. From the figure it is seen that there is a value of steady state error and there is a high overshoot at the loading instant. The motor response using PSO for tuning the IP controller is shown in Fig. 7 and from the figure there is a steady state error and an overshoot smaller than that of Fig. 6 (speed scheme). The response time is also smaller than that of Fig. 6.

In order to compare the performance of PSO-IP regulator with manual-IP regulator in the same test, the Fig. 8 shows the simulated results comparison of traditional IP (manual-IP) and PSO-IP regulators of speed control of IM under load variation. Figure 9 shows a zoom of speed

answer during the starting and the application of the disturbance. The PSO-IP controller based drive system can handle the sudden change in load torque approximately without overshoot and undershoot and steady state error, whereas the manual-IP controller has steady state error and the response is not as fast as compared to PSO-IP controller "as shown in Fig. 9". Thus the proposed controller has been found superior to the conventional IP controller.

A conclusion of the comparison between the two methods is listed in Table 2. From this table, when applying PSO method in the tuning purpose it gives a good static error, it has an overshoot and a response time small than the classical method.
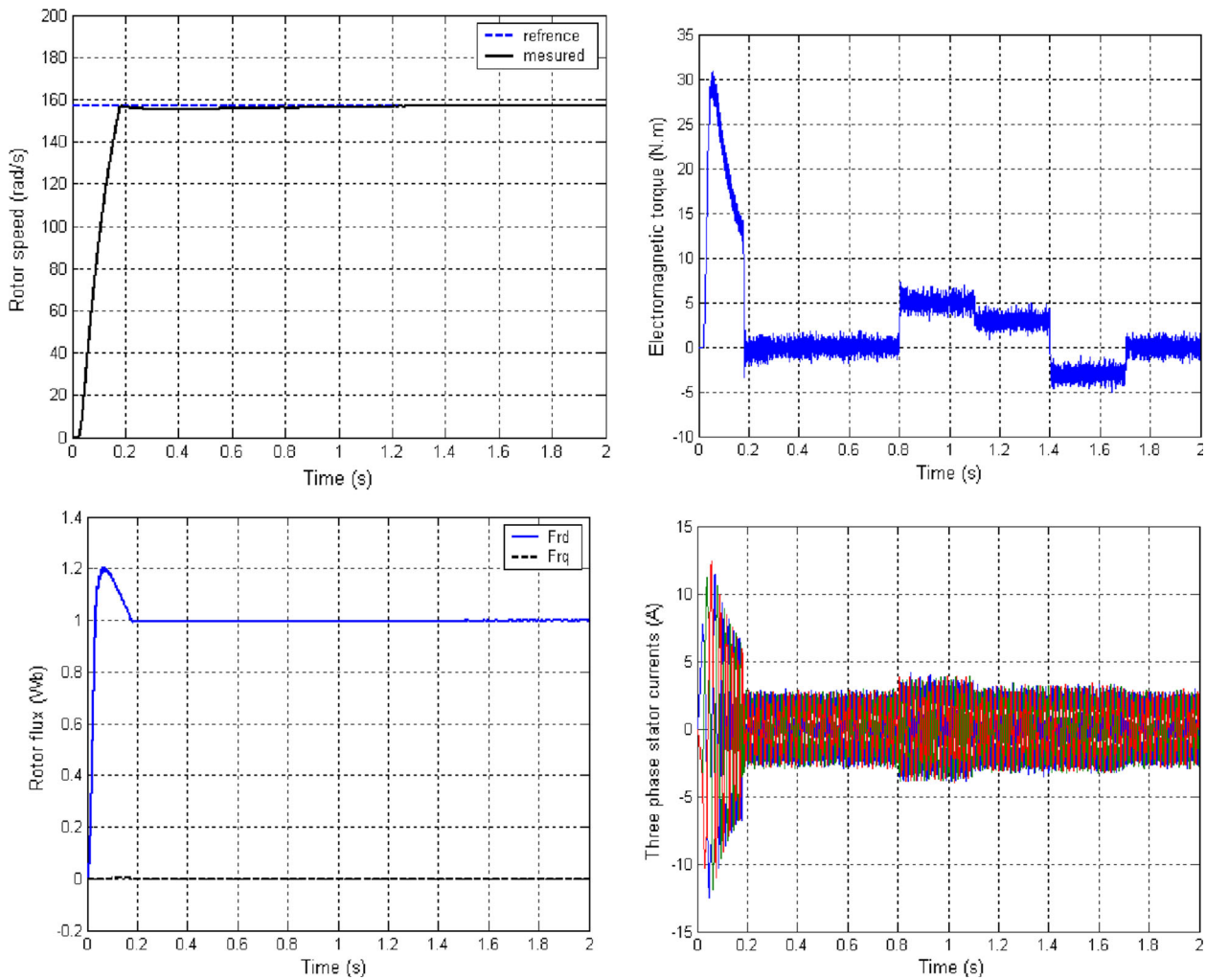
Fig. 7 Results of speed control using the IP controller PSO tuning under load variation
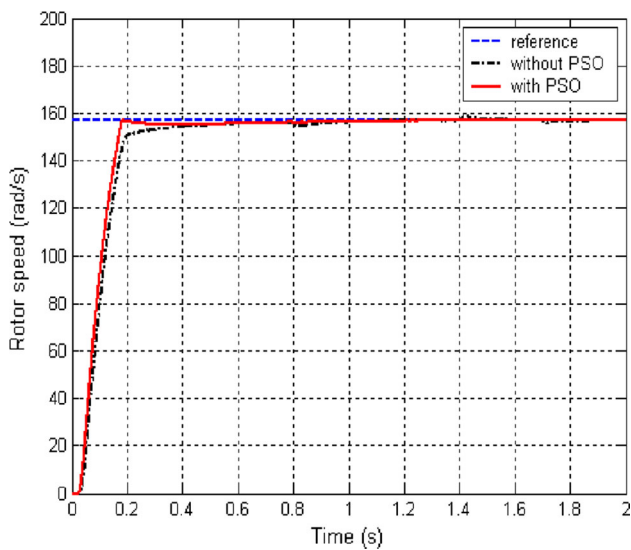
Fig. 8 Simulated results comparison of IP manual tuning and of IP-PSO tuning regulators of speed control under load variation

5 Conclusion

The intelligent IP speed controller uses the PSO algorithm to optimize the IP-parameters instead of the traditional trial and error method. This controller is presented and tested. The Swarm Optimizer is used to adapt the IP controller parameters. A comparison between the different controllers is achieved using the IP controller which is tuned by two methods, the first is manually and the second uses the PSO technique. The results show that the speed response of the traditional IP controller has negligible steady state error. However there is a high overshoot at the loading instant. The motor performance (performance of motor speed) using PSO for tuning the IP controller has a negligible steady state error and also a negligible overshoot and the response time is smaller than the previous case (manual-IP). From the previous simulation results, the PSO succeeds in tuning off-line the IP controller more efficiently
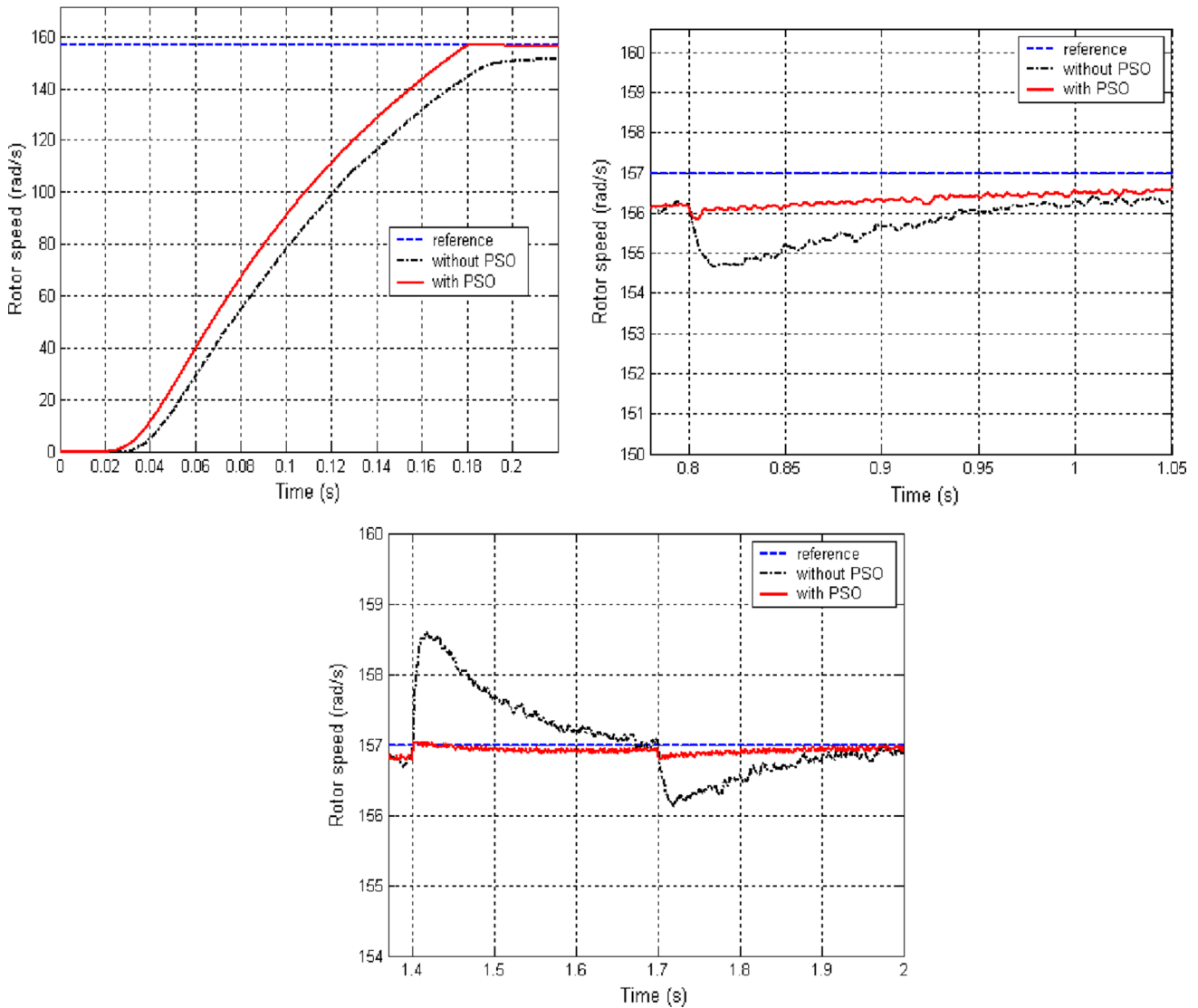
Fig. 9 Zoom of speed answer during the starting and the application of the disturbance

Table 2 Comparison between IP tuned manually and IP tuned by PSO

Controller motor response	IP tuned manually Ki = 8.5; Kp = 2	IP tuned by PSO Ki = 9.8196; Kp = 18.7126
Static error (%)	0.083694	0.0262
Overshoot (%)	1.0196	0.0297
Response time (s)	0.1899	0.1683
IAE	18.79	15.97
ITAE	2.426	1.572
ISE	1983	1747

than the traditional method, and shows a more dynamic response.

Appendix A: Parameters

Rated values: 1.08 Kw; 220/380; 50 Hz; 2.83A/4.91 A, 1500 rpm.

Rated parameters: Rs = 10 Ω, Rr = 6.3 Ω, Ls = 0. 4642 H, Lr = 0. 4612 H, M = 0. 4212 H, P = 2.0, J = 0.01 kg m^2, f = 0.00 N-m/rad.

Appendix B: Nomenclature

V_{sd}, V_{sq} i_{sd}, i_{sq}, ϕ_{rd} and ϕ_{rq} are stator voltage, stator current and rotor flux d-q components in the rotor flux oriented reference frame;

R_s, R_r are the stator and rotor resistances;

L_s, L_r, M are the stator, rotor and mutual inductances;

ω_s, ω_r, ω_{sl} are the synchronous, rotor and slip speed in electrical;

T_{em}, T_l are the electromagnetic torque and the load torque respectively;

P is number of pole pairs;

J, f are the motor inertia and viscous friction coefficient respectively;

IP	Integral proportional;
FOC	Filed oriented control;
PSO	Particle swarm optimization;
IM	Induction motor.

References

Ali AB, Khedher A, Mimouni MF, Dhifaoui R (2009) Torque maximization and sensorless control of induction motor in a flux weakening region. Int J Sci Tech Autom Control Comput Eng IJ-STA 3(1):972–985

Allaoua B, Gasbaoui B, Mebarki B (2009) Setting up PID DC motor speed control alteration parameters using particle swarm optimization strategy. Leonardo Electron J Pract Technol (14):19–32

Bekakra Y, Ben Attous D (2014) Optimal tuning of PI controller using PSO optimization for indirect power control for DFIG based wind turbine with MPPT. Int J Syst Assur Eng Manag 5(3):219–229

Bousserhane IK, Hazzab A, Rahli M, Mazari B, Kamli M (2006) Position control of linear induction motor using an adaptive fuzzy integral—backstepping controller. Serbian J Electr Eng 3(1):1–17

Chaari A, Soltani M, Gossa M (2007) Comparative study between the conventional regulators and fuzzy logic controller: application on the induction machine. Int J Sci Tech Autom Control Comput Eng IJ-STA 1(2):196–212

Eberhart RC, Shi Y (2000) Comparing inertial weights and Constriction factor in particle Swarm optimization. In: Proceeding of the international congress on evaluationing computation, pp 84–88

Elwer AS (2006) A novel technique for tuning PI-controllers in induction motor drive systems for electric vehicle applications. J Power Electron 6(4):322–329

Kennedy J, Eberhart R (1995) Particle swarm optimization. In: Proceedings of IEEE international conference on neural networks, vol 4. Perth, WA, pp 1942-1948

Lalitha MP, Reddy CV, Usha V (2010) Optimal DG placement for minimum real power loss in radial distribution systems using PSO. J Theor Appl Inf Technol 13(2):107–116

Lin FJ, Teng LT, Lin JW, Chen SY (2009) Recurrent functional-link-based fuzzy-neural-network-controlled induction-generator system using improved particle swarm optimization. IEEE Trans Ind Electron 56(5):1557–1577

Mechernene A, Zerikat M, Hachlef M (2008) Fuzzy speed regulation for induction motor associated with field-oriented control. Int J Sci Tech Autom Control Comput Eng IJ-STA 2(2):804–817

Naka S, Genji T, Yura T, Fukuyama Y (2003) A hybrid particle swarm optimization for distribution state estimation. IEEE Trans Power Syst 18(1):60–68

Poli R, Kennedy J, Blackwell T (2007) Particle swarm optimization. Swarm Intell 1(1):33–57

Qiao W, Venayagamoorthy GK, Harley RG (2006) Design of optimal PI controllers for doubly fed induction generators driven by wind turbines using particle swarm optimization. In: IEEE 2006 international joint conference on neural networks, pp 1982–1987

Metadata of the chapter that will be visualized in SpringerLink

Book Title	Renewable Energy for Smart and Sustainable Cities
Series Title	
Chapter Title	Sliding Mode Control of DFIG Driven by Wind Turbine with SVM Inverter
Copyright Year	2019
Copyright HolderName	Springer Nature Switzerland AG

Corresponding Author	Family Name	**Bekakra**
	Particle	
	Given Name	**Youcef**
	Prefix	
	Suffix	
	Role	
	Division	LEVRES-Research Laboratory, Department of Electrical Engineering
	Organization	University of El Oued
	Address	P.O. Box 789, El Oued, Algeria
	Email	youcef-bekakra@univ-eloued.dz

Author	Family Name	**Ben Attous**
	Particle	
	Given Name	**Djilani**
	Prefix	
	Suffix	
	Role	
	Division	LEVRES-Research Laboratory, Department of Electrical Engineering
	Organization	University of El Oued
	Address	P.O. Box 789, El Oued, Algeria
	Email	

Author	Family Name	**Bennadji**
	Particle	
	Given Name	**Hocine**
	Prefix	
	Suffix	
	Role	
	Division	LEVRES-Research Laboratory, Department of Electrical Engineering
	Organization	University of El Oued
	Address	P.O. Box 789, El Oued, Algeria
	Email	

Abstract	In this paper, a direct Sliding Mode Control (SMC) of Doubly Fed Induction Generator (DFIG) driven by wind turbine with Space Vector Modulation (SVM) inverter is presented. The SMC is used to track the stator active and reactive power their references. The SVM inverter is used to improve the quality of the energy generated by DFIG which allows the minimizing of stator current harmonics and wide linear modulation range. Simulation results show that the proposed control give good performance and good quality of the energy where the THD of the stator current of the DFIG has small value.

Sliding Mode Control of DFIG Driven by Wind Turbine with SVM Inverter

Youcef Bekakra[✉], Djilani Ben Attous, and Hocine Bennadji

LEVRES-Research Laboratory, Department of Electrical Engineering,
University of El Oued, P.O. Box 789, El Oued, Algeria
youcef-bekakra@univ-eloued.dz

Abstract. In this paper, a direct Sliding Mode Control (SMC) of Doubly Fed Induction Generator (DFIG) driven by wind turbine with Space Vector Modulation (SVM) inverter is presented. The SMC is used to track the stator active and reactive power their references. The SVM inverter is used to improve the quality of the energy generated by DFIG which allows the minimizing of stator current harmonics and wide linear modulation range. Simulation results show that the proposed control give good performance and good quality of the energy where the THD of the stator current of the DFIG has small value.

Keywords: Doubly Fed Induction Generator · Sliding Mode Control
Wind Turbine · Space Vector Modulation · Total Harmonic Distortion

1 Introduction

One of the generation systems commercially available in the wind energy market currently is the doubly fed induction generator (DFIG) with its stator winding directly connected to the grid and with its rotor winding connected to the grid through a variable frequency converter [1, 2].

Vector control technology is used to control the generator where the rotor of DFIG is connected to an inverter of which the frequency, phase and magnitude can be adjusted. Therefore, constant operating frequency can be achieved at variable wind speeds [3].

This paper adopts the vector control method of stator oriented magnetic field to realize the decoupling control of the stator active and reactive power using sliding mode control (SMC).

The sliding mode theory, derived from the variable structure control family, was used for the induction motor drive for a long time. It performs a robust control by adding a discontinuous control signal across the sliding surface, satisfying the sliding condition [4].

This paper presents a numerical simulation study of direct sliding mode control of active and reactive power of the DFIG fed by SVM inverter to improve the quality of the energy injected into the electrical grid.

2   DFIG Field Oriented Control

The Doubly Fed Induction Machine (DFIM) model can be described by the following state equations in the synchronous reference frame whose axis d is aligned with the stator flux vector, ($\phi_{sd} = \phi_s$ and $\phi_{sq} = 0$) [5, 6].

By neglecting resistances of the stator phases, the stator voltage will be expressed by:

$$V_{ds} = 0 \quad \text{and} \quad V_{qs} = V_s \approx \omega_s \cdot \phi_s \tag{1}$$

The reactive power is imposed by the direct component i_{rd}.

$$P_s = - V_s \frac{M}{L_s} i_{rq} \tag{2}$$

$$Q_s = \frac{V_s^2}{\omega_s L_s} - V_s \frac{M}{L_s} i_{rd} \tag{3}$$

The arrangement of the equations gives the expressions of the voltages according to the rotor currents:

$$\begin{cases} V_{rd} = R_r \cdot i_{rd} + \sigma L_r \frac{di_{rd}}{dt} - g\omega_s \sigma L_r i_{rq} \\ V_{rq} = R_r i_{rq} + \sigma L_r \frac{di_{rq}}{dt} + g\frac{M}{L_s}V_s + g\omega_s \sigma L_r i_{rd} \end{cases} \tag{4}$$

With: $T_r = \frac{L_r}{R_r}$; $T_s = \frac{L_s}{R_s}$; $\sigma = 1 - \frac{M^2}{L_s \cdot L_r}$.

The system studied in the present paper is constituted of a DFIG directly connected through the stator windings to the grid, and supplied through the rotor by a static frequency inverter as presented in Fig. 1.
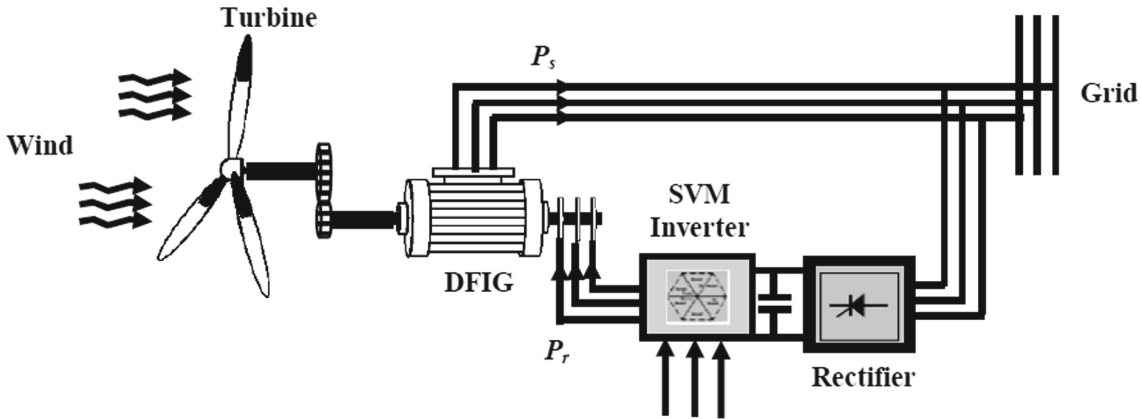
Fig. 1. Configuration of the doubly fed induction generator

3   Sliding Mode Control

3.1   Active Power Control by SMC

The active power error is defined by [4]:

$$e = P_s^* - P_s \tag{5}$$

The surface of active power control equation can be obtained as follow:

$$\sigma_s(P_s) = e = P_s^* - P_s \tag{6}$$

$$\dot{\sigma}_s(P_s) = \dot{P}_s^* - \dot{P}_s \tag{7}$$

Substituting the expression of $\dot{P}_s$ Eq. (2) in Eq. (7), we obtain:

$$\dot{\sigma}_s(P_s) = \dot{P}_s^* - \left(-V_s \frac{M}{L_s} \dot{i}_{rq} \right) \tag{8}$$

We take:

$$V_{rq} = V_{rq}^{eq} + V_{rq}^{n} \tag{9}$$

Where the equivalent control is:

$$V_{rq}^{eq} = R_r i_{rq} - \dot{P}_s^* \frac{L_s L_r . \sigma}{V_s M} \tag{10}$$

Therefore, the correction factor is given by:

$$V_{rq}^{n} = k_{Vrq} sat(\sigma_s(P_s)) \tag{11}$$

k_{Vrq}: positive constant.

3.2   Reactive Power Control by SMC

The reactive power error is defined by [4]:

$$e = Q_s^* - Q_s \tag{12}$$

The surface of reactive power control equation can be obtained as follow:

$$\sigma_s(Q_s) = e = Q_s^* - Q_s \tag{13}$$

$$\dot{\sigma}_s(Q_s) = \dot{Q}_s^* - \dot{Q}_s \tag{14}$$

Substituting the expression of $\dot{Q}_s$ Eq. (3) in Eq. (14), we obtain:

$$\dot{\sigma}_s(Q_s) = \dot{Q}_s^* - \left(\frac{V_s^2}{\omega_s L_s} - V_s \frac{M}{L_s} \dot{i}_{rd} \right) \tag{15}$$

We take:

$$V_{rd} = V_{rd}^{eq} + V_{rd}^n \tag{16}$$

Where the equivalent control is:

$$V_{rd}^{eq} = R_r i_{rd} - \dot{Q}_s^* \frac{L_s L_r \cdot \sigma}{V_s M} \tag{17}$$

Therefore, the correction factor is given by:

$$V_{rd}^n = k_{Vrd} sat(\sigma_s(Q_s)) \tag{18}$$

k_{Vrd}: positive constant.

4   Simulation Results

The DFIG used in this work is a 4 kW, whose nominal parameters are indicated in appendix.

To verify the feasibility of the proposed control scheme, computer simulations were performed using Matlab/Simulink software.

We have proposed a random variable wind speed as shown in Fig. 2 to verified the robustness of the proposed control,
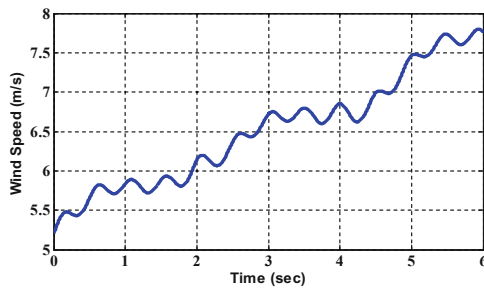
Fig. 2. Proposed wind speed
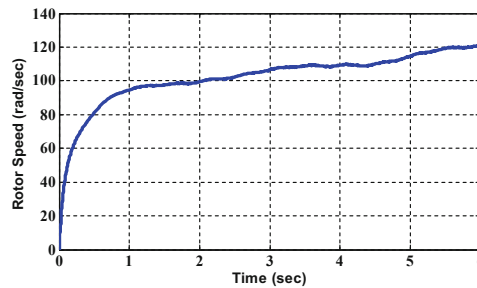
Fig. 3. Rotor speed

Figure 3 shows the turbine rotor speed. Figure 4 presents the power coefficient variation C_p, it is kept around its maximum value $C_p = 0.5$.

Figure 5a presents the stator active power and its reference profile injected into the grid. The stator reactive power and its reference profile are presented in Fig. 5b. After these figures a very good decoupling obtained between the stator active and reactive

power. It is clear that the actual stator active power tracks its desired values using the proposed control with the presence of the oscillations produced by the chattering phenomena of the SMC, where the reactive power is maintained to zero to guarantee a unity power factor ($cos(\phi) = 1$) at the stator side.
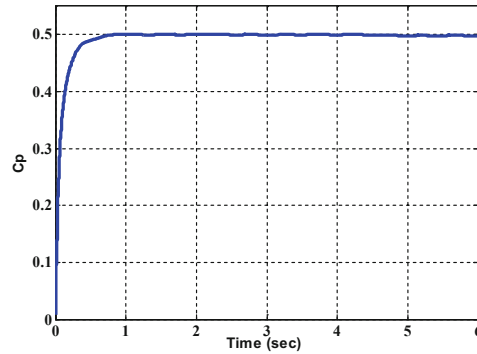
Fig. 4. Power coefficient C_p variation
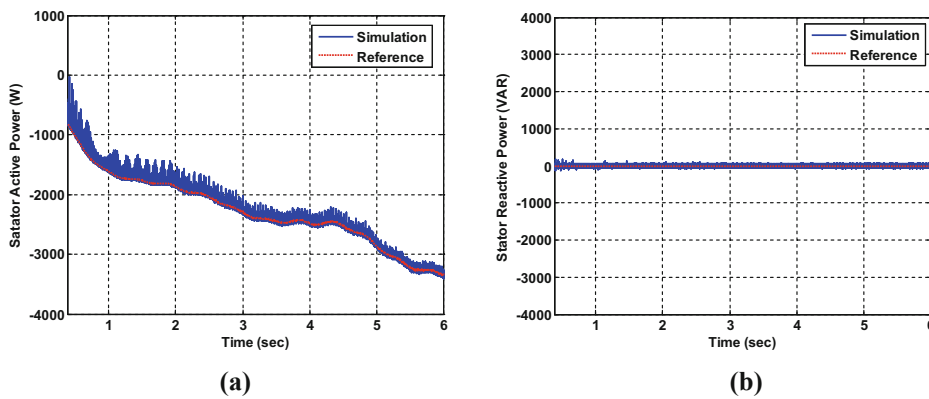
Fig. 5. (a) Stator active and (b) reactive power

Figure 6 shows the DFIG stator current changes versus time and its zoom, it shows good sinusoidal currents, where the amplitude of this current increases when the wind speed increases.

Figure 7 shows the harmonic spectrum of the output phase stator current which obtained by using Fast Fourier Transform (FFT) technique. It can be clearly observed that the stator current has a low Total Harmonic Distortion (THD) where its value is 4.38%, as indicated in the Fig. 7. Where this value is acceptable according to "IEEE Std 519-1992" which recommended by "*require AC sources that have no more than 5% Total Harmonic Distortion*" [7].
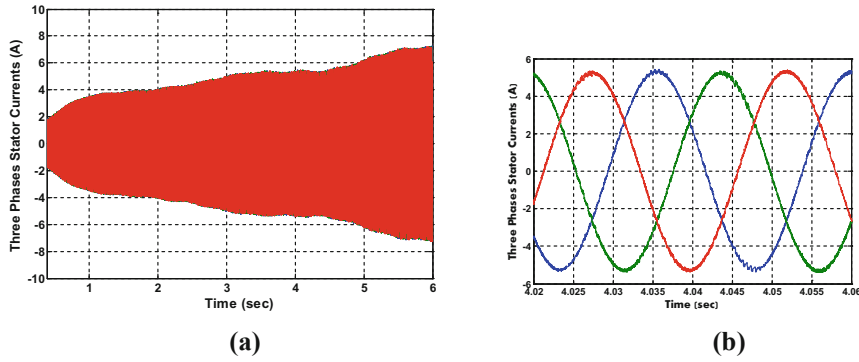
Fig. 6. (a) Stator currents with (b) a zoom
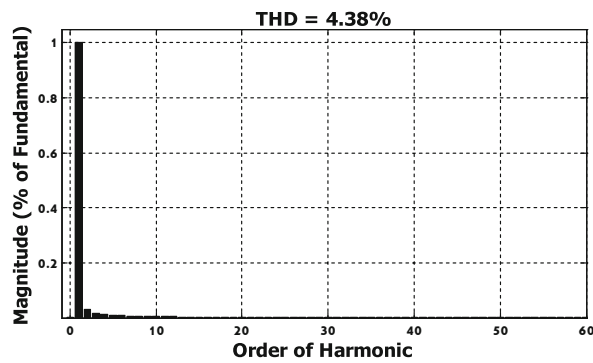
Fig. 7. Spectrum of the stator current harmonics

5   Conclusion

In this paper, a direct sliding mode control (SMC) of active and reactive power based on DFIG driven by wind turbine with space vector modulation (SVM) inverter has been studied and designed in Matlab/Simulink software.

The SMC has been used to track the stator active and reactive power their references. The stator active and reactive powers are exchanged between the stator of the DFIG and the electrical grid by the control of the rotor inverter where the simulation results show good dynamic performances and good robustness of the proposed control.

In addition, SVM technique is used for the inverter control to improve the quality of energy injected into the electrical grid, which this technique allows the minimizing of stator current harmonics and wide linear modulation range where the THD of the stator current has the value 4.38% (<5% according IEEE Std 519-1992).

Appendix

DFIG Data:

R_s = 1.2 Ω, R_r = 1.8 Ω, L_s = 0.1554 H, L_r = 0.1568 H, M = 0.15 H, P = 2, J = 0.2 kg.m^2, f = 0.001 N.m.s/rad.
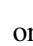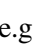
References

1. Ghedamsi, K., Aouzellag, D.: Improvement of the performances for wind energy conversions systems. Int. J. Electr. Power Energy Syst. **32**(9), 936–945 (2010)
2. Kumar, V., Pandey, A.S., Sinha, S.K.: Grid integration and power quality issues of wind and solar energy system: a review. In: International Conference on Emerging Trends in Electrical, Electronics and Sustainable Energy Systems (ICETEESES-16), IEEE, 11–12 March 2016 (2016)
3. Abniki, H., Abolhasani, M., Kargahi, M.E.: Vector control analysis of doubly-fed induction generator in wind farms. Energy Power **3**(2), 18–25 (2013)
4. Bekakra, Y., Ben Attous, D.: DFIG sliding mode control fed by back-to-back PWM converter with dc-link voltage control for variable speed wind turbine. Front. Energy **8**(3), 345–354 (2014)
5. Rahimi, M., Parniani, M.: Dynamic behavior analysis of doubly-fed induction generator wind turbines—the influence of rotor and speed controller parameters. Int. J. Electr. Power Energy Syst. **32**(5), 464–477 (2010)
6. Aydin, E., Polat, A., Ergene, L.T.: Vector control of DFIG in wind power applications and analysis for voltage drop condition. In: 2016 National Conference on Electrical and Electronics and Biomedical Engineering (ELECO) (2016)
7. IEEE Std 519-1992: IEEE recommended practices and requirements for harmonic control in electrical power systems. IEEE Industry Applications Society, New York. ISBN 1-55937-239-7, pp. 1–112 (1993)

MARKED PROOF

Please correct and return this set

Please use the proof correction marks shown below for all alterations and corrections. If you wish to return your proof by fax you should ensure that all amendments are written clearly in dark ink and are made well within the page margins.

Instruction to printer	*Textual mark*	*Marginal mark*
Leave unchanged	··· under matter to remain	
Insert in text the matter indicated in the margin	⋏	New matter followed by or
Delete	/ through single character, rule or underline or ⊢——⊣ through all characters to be deleted	or
Substitute character or substitute part of one or more word(s)	/ through letter or ⊢——⊣ through characters	new character or new characters
Change to italics	— under matter to be changed	
Change to capitals	≡ under matter to be changed	/
Change to small capitals	= under matter to be changed	/
Change to bold type	∿ under matter to be changed	⌣
Change to bold italic	≋ under matter to be changed	≡
Change to lower case	Encircle matter to be changed	=
Change italic to upright type	(As above)	∿
Change bold to non-bold type	(As above)	≋
Insert 'superior' character	/ through character or ⋏ where required	≢ or under character e.g. ⅄ ⅄
Insert 'inferior' character	(As above)	over character e.g. ⅄ ⅄
Insert full stop	(As above)	⋏
Insert comma	(As above)	⋏
Insert single quotation marks	(As above)	or² and/or ⊙ or ,
Insert double quotation marks	(As above)	⅄ or ⅄ and/or ⅄ or ⅄
Insert hyphen	(As above)	⅄ ⅄
Start new paragraph	⌐	⅄ ⅄
No new paragraph	⌒	
Transpose	⎍⎌	⊢ ⌐ ⌒ ⌐
Close up	linking ‿ characters	
Insert or substitute space between characters or words	/ through character or ⋏ where required	⌒
	⏐	
Reduce space between characters or words	between characters or words affected	⅄

USING HYBRID POWER FILTER TO MITIGATE CURRENTS AND VOLTAGES HARMONICS IN THREE PHASE SYSTEM

Y. DJEGHADER*, L.ZELLOUMA**
*Department of Electrical Engineering, University of Souk Ahras ALGERIA; Email: djeghaderyacine@yahoo.fr
**Department of Electrical Engineering, University of El-Oued ALGERIA.

ABSTRACT

This paper describes different power quality problems in distribution systems and their solutions with power electronics based equipment. A hybrid power filter in combined system of shunt passive and series active power filter has been designed and simulate with Matlab/Simulink. This filter is a three level PWM voltage source inverter and we use a fuzzy logic controller algorithm to control the harmonic voltages. The viability of the proposed algorithm is validated in this work. This hybrid power filter is able to compensate the reactive power (showed that source voltage is sinusoidal and in phase with source current), and harmonics (voltage & current) for three phase of the non linear load current proposed with RL and RC load. The proposed solution has achieved an improvement of power quality in distribution system specifically the reduction of currents and voltages harmonics, we see that through the values of THD_I and THD_V that are still below the IEC (61000) standard after filtering.

Keywords: *Active Power Filter, Hybrid Filter, Passive Filter, Power quality, Harmonics; THD; fuzzy controller*

1. INTRODUCTION

The increased severity of harmonic pollution in power networks with the development of power semiconductors and power-electronics application techniques has attracted the attention to develop dynamic and adjustable solutions to the power quality problems. These power harmonics are called electrical pollution which will degrade the quality of the power supply. As a result, filtering process for these harmonics is needed in order to improve the quality of the power supply.

Therefore, these harmonics must be mitigating. In order to achieve this, series or parallel configurations or combinations of active and passive filters have been proposed depending on the application type [1], [2]. Traditionally, a passive *LC* power filter is used to eliminate current harmonics when it is connected in parallel with the load [3]. This compensation equipment has some drawbacks mainly related to the appearance of series or parallel resonances because of which the passive filter cannot provide a complete solution. Since the beginning of the 1980s, active power filters (APFs) have become one of the most habitual compensation methods [4]. A usual APF consists of a three-phase pulse width modulation (PWM) voltage source inverter. The APF can be connected either in parallel or in series with the load. The first one is especially appropriate for the mitigation of harmonics of the loads called harmonic current source. In contrast, the series configuration is suitable for the compensation of loads called harmonic voltage source. However, the costs of shunt active filters are relatively high for large-scale system and are difficult to use in high-voltage grids. In addition, their compensating performance is better in the harmonic current source load type than in the harmonic voltage source load type [7], [8].

2. POWER QUALITIES AND THEIR SOLUTION

Power Quality (PQ) related issues are of most concern nowadays. The widespread use of electronic equipment, such as information technology equipment, power electronics such as adjustable speed drives (ASD), programmable logic controllers (PLC), energy-efficient lighting, led to a complete change of electric loads nature [8]. These loads are simultaneously the major causers and the major victims of power quality problems. Due to their non-linearity, all these loads cause disturbances in the voltage waveform Along with technology advance, the organization of the worldwide economy has evolved towards globalization and the profit margins of many activities tend to decrease. The increased sensitivity of the vast majority of processes (industrial, services and even residential) to PQ problems turns the availability of electric power with quality a crucial factor for competitiveness in every activity sector. There are two approaches to the mitigation of power quality problems. The first approach is called load conditioning, which ensures that the equipment is less sensitive to power disturbances, allowing the operation even under significant voltage distortion. The other solution is to install line conditioning systems that suppress or counteracts the power system disturbances. A flexible and versatile solution to voltage quality problems is offered by active power filters. Currently they are based on PWM converters and connect to low and medium voltage distribution system in shunt or in series. Series active power filters must operate in conjunction with shunt passive filters in order to compensate load current harmonics. Shunt active power filters operate as a controllable current source and series active power filters operates as a controllable voltage source [6], [9]. Both schemes are implemented preferable with voltage source

PWM inverters, with a dc bus having a reactive element such as a capacitor. Active power filters can perform one

or more of the functions required to compensate power systems and improving power quality [7], [11].

3. SERIES APF TOPOLOGY DESCRIPTION AND MODELING

3.1 Description of the APF Topology

Fig.1 shows the topology of the combined SAPF and shunt passive filter (PF), acting as zero impedance for the fundamental frequency and as high resistor for the harmonics frequencies. The APF, which is supplied by a low power PWM inverter, is connected in series with the main supply and the non-linear load through the current transformer. The passive filter connected in parallel to the load is used to damp the 5th and the 7th harmonic of V_l because of their high amplitudes
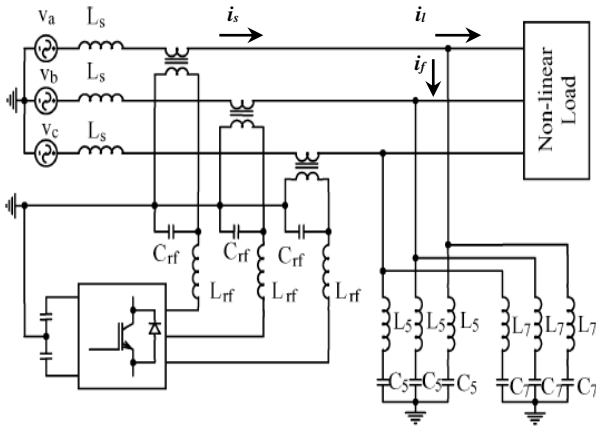
Fig. 1 General Configuration of a combined filter

The series APF acts as a voltage source and inject a compensating voltage in order to obtain a sinusoidal load voltage. The developments in digital electronics, communications and in process control system have made the loads very sensitive, requiring ideal sinusoidal supply voltage for their operation

3.2 Modeling

Fig.2. shows the per-phase equivalent scheme of the studied topology

Fig. 2 Per-phase equivalent scheme.

Where:

e_s, i_s, L_s, R_s: Source voltage, source current, source inductance, and source resistance,

V_s: Line voltage,

V_l, i_l : Load voltage and load current,

V_{sl}: Controllable voltage source representing the series active power filter,

i_f, C_f, L_f: Shunt passive filter current, passive filter capacitance, and passive filter inductance.

This equivalent scheme is modeled by (1) and (2):

$$V_{sl} = V_s - V_l \tag{1}$$

$$i_s = i_f + i_l \tag{2}$$

Where,

$$V_s = e_s - (R_s \cdot i_s) - (L_s \, dt/di_s) \tag{3}$$

The voltage error is given by:

$$\Delta V_{sl} = V_{slref} - V_{sl} \tag{4}$$

V_{slref} : is expressed by:

$$V_{slref} = V_{sh} - V_{lh} \tag{5}$$

$$V_{sh} = k \cdot i_{sh} \tag{6}$$

V_{sh}, V_{lh}, i_{sh}: represent, respectively, the harmonic components present in V_s, V_l, and i_s.

k: is a current sensor gain.

3.3 APF Voltage references determination

The harmonic component V_{slh} of V_{sl} is defined by:

$$V_{slh} = V_{sl} - V_{slf} \tag{7}$$

First, we extract the p-q components of V_{sl}:

$$\begin{bmatrix} V_{slp} \\ V_{slq} \end{bmatrix} = C_{pq} C_{32} \begin{bmatrix} V_{la} \\ V_{lb} \\ V_{lc} \end{bmatrix} \tag{8}$$

C_{pq}, C_{32} representing the Park matrix and Concordia matrix given respectively by:

$$C_{pq} = \begin{bmatrix} \sin(\omega t) & -\cos(\omega t) \\ -\cos(\omega t) & -\sin(\omega t) \end{bmatrix} \tag{9}$$

$$C_{32} = \sqrt{2/3} \begin{bmatrix} 1 & -1/2 & -1/2 \\ 0 & \sqrt{3}/2 & -\sqrt{3}/2 \end{bmatrix} \tag{10}$$

Next, decomposition of V_{slp} and V_{slq} into continuous components $\overline{V}_{slp}, \overline{V}_{slq}$ and alternative components $\widetilde{V}_{slp}, \ \widetilde{V}_{slq}$

$$V_{slp} = \overline{V}_{slp} + \widetilde{V}_{slp} \tag{11}$$

$$V_{slq} = \overline{V}_{slq} + \widetilde{V}_{slq} \tag{12}$$

$\overline{V}_{slp}, \overline{V}_{slq}$ are obtained via a second order low-pass filter.

Then, the obtained three-phase fundamental components are presented below:

$$\begin{bmatrix} V_{slfa} \\ V_{slfb} \\ V_{slfc} \end{bmatrix} = C_{32} C_{pq}^{-1} = \begin{bmatrix} \overline{V}_{slp} \\ \overline{V}_{slq} \end{bmatrix} \tag{13}$$

Finally, this algorithm can be represented as shown in the block diagram of Fig.3.
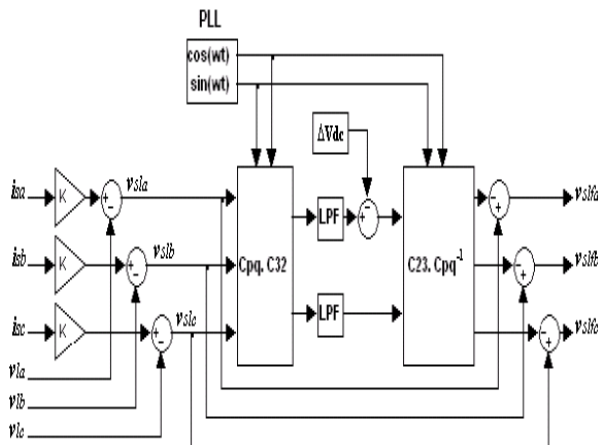
Fig. 3 Block diagram of voltages references determination

3.4 Inverter control using PWM

The control method is aimed to control PWM inverter to produce the desired compensation voltage, in the output of series APF. This method is achieved by implementing a fuzzy logic controller [5-10] which starts from the difference between the injected voltage (V_{inj}) and the calculated reference voltage (V_{slf}) that determines the reference voltage of the inverter (modulating wave). This reference voltage is compared with two carrying triangular identical waves shifted one from other by a half period of chopping producing the control signal to control the on-off of the IGBT. The general block diagram of voltage control is shown in Fig.4.

Fig. 4 PWM synoptic block diagram of voltage control

The control of inverter arm constituting the series active filter is summarized in the two following steps.

- Determination of the intermediate signals V_{i1} and V_{i2}.

If error $\geq$ carrying 1 => $V_{i1} = 1$

If error < carrying 1 => $V_{i1} = 0$

If error $\geq$ carrying 2 => $V_{i2} = 0$

If error < carrying 2 => $V_{i2} = -1$

Determination of control signals of the switches T_{ij} (j = 1, 2, 3, 4).

If $(V_{i1} + V_{i2}) = 1$ => $T_{i1} = 1, T_{i2} = 1, T_{i3} = 0, T_{i4} = 0$

If $(V_{i1} + V_{i2}) = 0$ => $T_{i1} = 0, T_{i2} = 1, T_{i3} = 1, T_{i4} = 0$

If $(V_{i1} + V_{i2}) = -1$ => $T_{i1} = 0, T_{i2} = 0, T_{i3} = 1, T_{i4} = 1$

3.5 Fuzzy Control Application

Fuzzy logic serves to represent uncertain and imprecise knowledge of the system, whereas fuzzy control allows taking a decision even if we can't estimate inputs/outputs only from uncertain predicates. Fig. 5, shows the synoptic scheme of fuzzy controller, which possesses two inputs (the error (e),

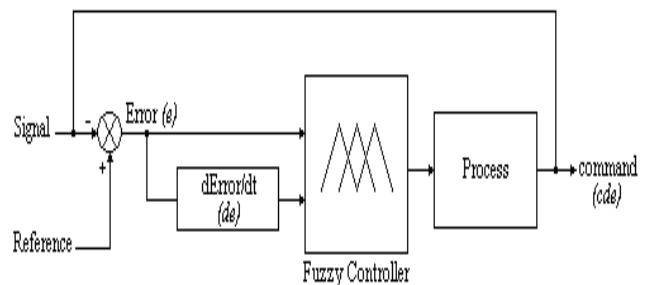($e = V_{slf} - V_{inj}$) and its derivative (de)) and one output (the command (c_{de})). [5]

Fig. 5 Fuzzy controller synoptic diagram
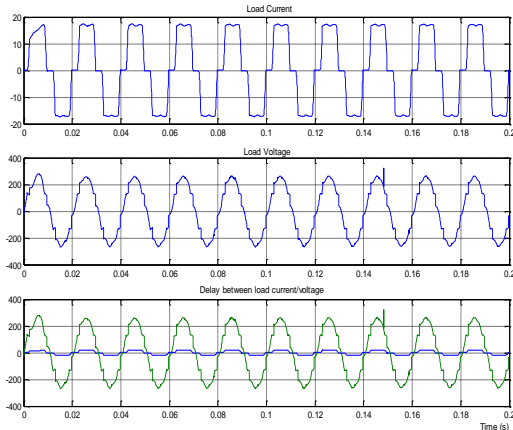
5. SIMULATION RESULTS

The simulation is carried out using a program working in MATLAB/ Simulink environment. For non linear load we use a three phase diode rectifier with RL and RC load

Table 1 System Parameters

Source	e_s	230 V
	L_s	5,5 mH
	R_s	3,6 Ω
Load	R	25 Ω
	L	55 mH
	C	2200µF
Passive filter	L_{f5} ; C_{f5}	13,5 mH ;30 µF
	L_{f7} ; C_{f7}	6,75 mH ;50 µF
Ripple filter	L_{fr} ; C_{fr}	13,5 mH ;50 µF
Turns Ratio of Coupling Transformer		1:1
Switching Frequency		20 KHz

5.1 Simulation Results before Filtering

Simulation Results with RL Load

Fig. 6 Waveforms of load (current, voltage), and their delay for RL
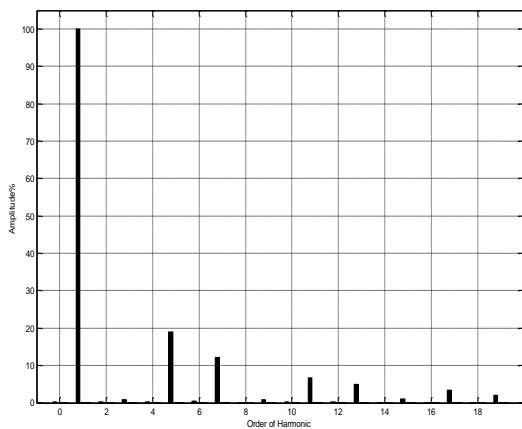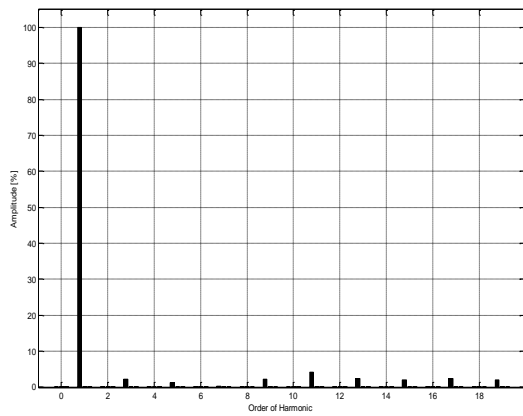

Fig. 7 Harmonic Spectrum of current
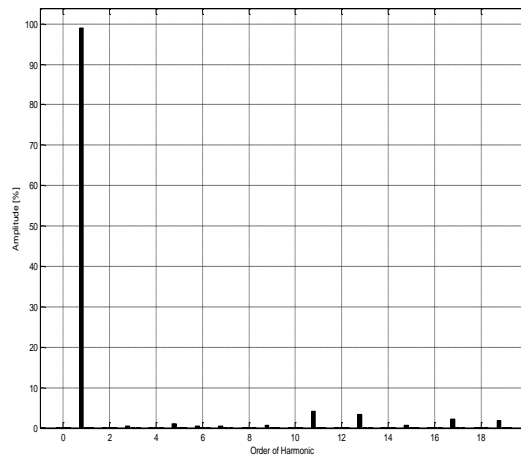
Fig. 8 Harmonic Spectrum of voltage

Simulation Results with RC Load
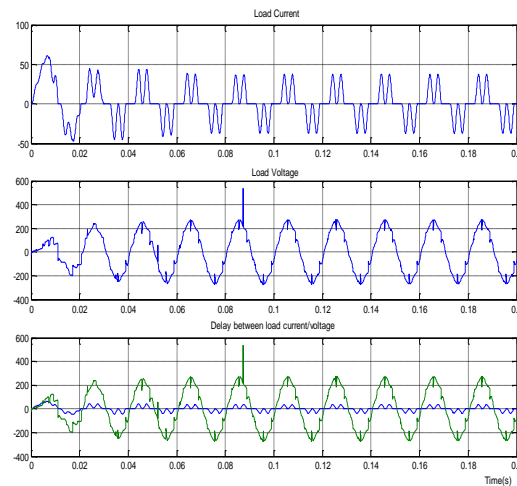
Fig. 9 Waveforms of load (current, voltage), and their delay for RC
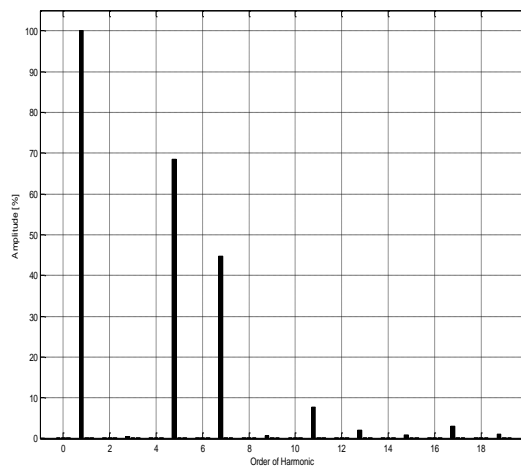
Fig. 10 Harmonic Spectrum of current

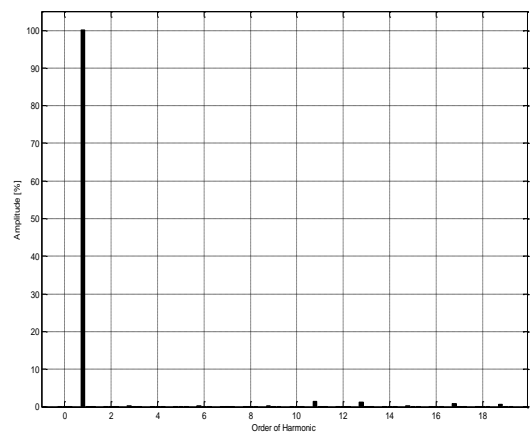**Fig. 11** Harmonic Spectrum of current voltage

5.2 Simulation Results after Filtering

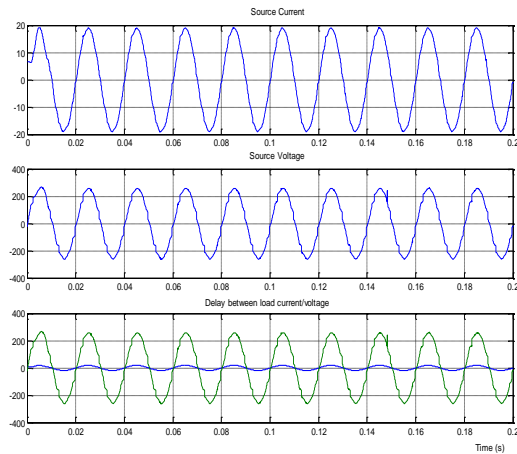Simulation Results with RL Load

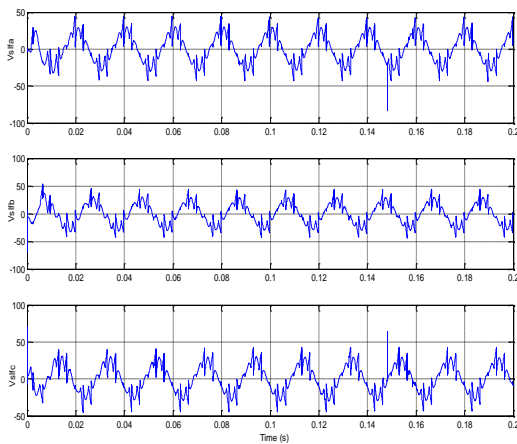**Fig. 12** Waveforms of sources (current, voltage), and their delay HP

Fig. 13 Voltages references of HF for RL load

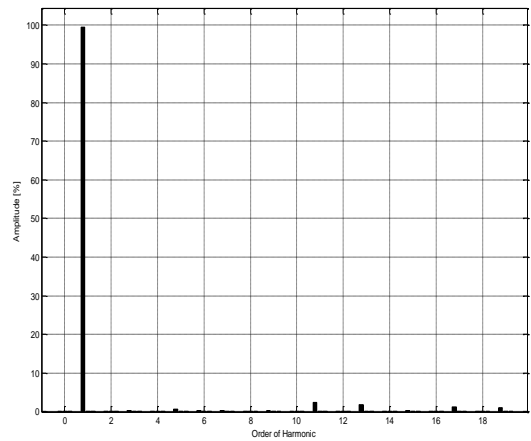
Fig. 14 Harmonic spectrum of current with HP

Fig. 15 Harmonic spectrum of voltage with HP
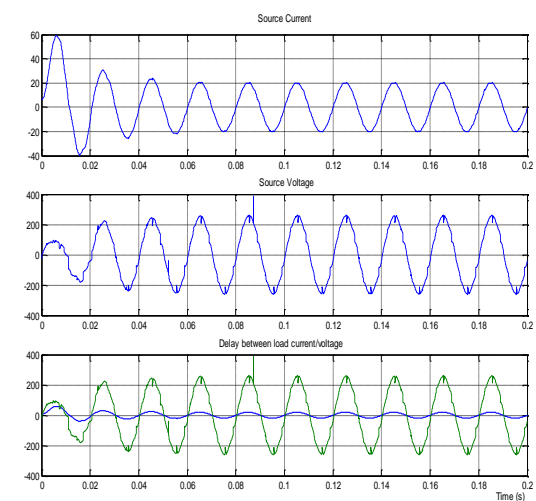
Simulation Results with RC Load

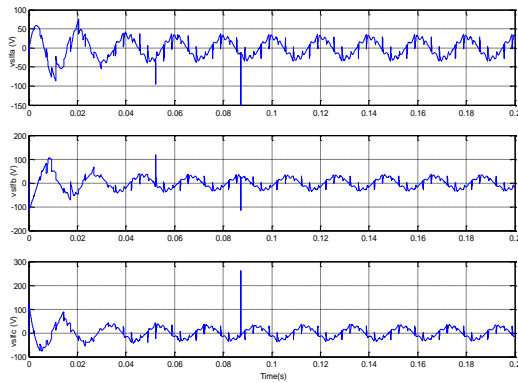**Fig. 16** Waveforms of sources (current, voltage), and their delay
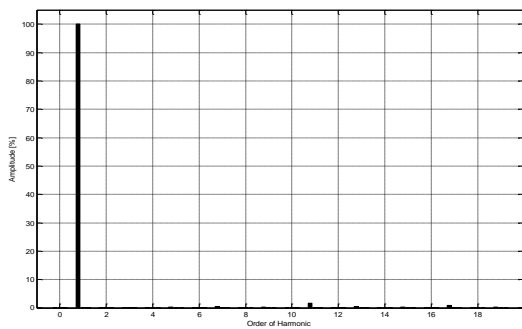
Fig. 17 Voltages references of HF for RC load
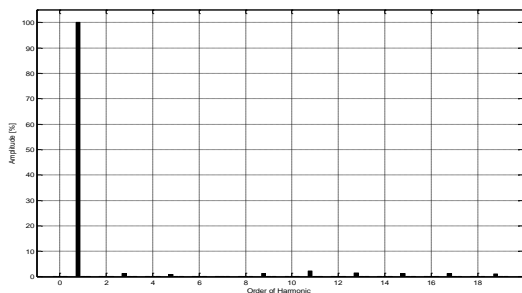

Fig. 18 Harmonic Spectrum of current

Fig19. Harmonic Spectrum of voltage

Table 2 Simulation Results of harmonics currents

Harmonic Currents	RL Load		RC Load	
	Before Filtering	After Filtering	Before Filtering	After Filtering
5	19,00 %	0,19 %	68,54 %	0,32 %
7	12,29 %	0,03 %	44,63 %	0,46 %
11	6,63 %	1,54 %	7,61 %	1,66 %
13	4,93 %	1,27 %	2,07 %	0,52 %
17	3,35 %	0,97 %	2,93 %	0,79 %
19	2,03 %	0,59 %	1,08 %	0,31 %
THDi	**24,46** %	**2,19** %	**81,76%**	**2,03 %**

Table 3 Simulation Results of harmonics voltages

Harmonic Voltages	RL Load		RC Load	
	Before Filtering	After Filtering	Before Filtering	After Filtering
5	1,14 %	0,67 %	1,35 %	0,81 %
7	0,48 %	0,28 %	0,37 %	0,16 %
11	4,08 %	2,42 %	4,19 %	2,33 %
13	3,34 %	1,94 %	2,38 %	1,39 %
17	2,12 %	1,29 %	2,44 %	1,31 %
19	1,88 %	1,07 %	2,00 %	1,17 %
THDv	**7,49 %**	**4,27 %**	**8,12 %**	**4,64 %**

6. CONCLUSION

In this article, we show the advantages of the hybrid power filter which consists of a combination of shunt passive filter and series active filter to improve the power quality especially harmonic mitigation (current and voltage) in three phase system with the use of fuzzy logic controllers.

The results obtained with the use of the hybrid filter (SAPF & PF) have clearly shown that mitigation are important of harmonic current of THD_I from 24,46 % to 2,19% (Under the standard 5%) ; and even for harmonic voltages of THD_V from 7,49 to 4,27 % (Under the standard .In figure 6 shows the delay between the voltage and current source is high but the figure 14 illustrates the reduction in the time between the current and the voltage of the source; ie correcting the power factor when the hybrid filter (SAPF & FP) is connected .

The fuzzy logic controller has improved the performance of the equilibrium state of the series active power filter. The effectiveness of the proposed system is proved by simulation.

REFERENCES

[1] SALMERON - LITRAN: Improvement Of The Electric Power Quality Using Series Active and Shunt Passive Filters, IEEE Trans. On Power Delivery, Vol. 25, N0. 2, APRIL, 2010.

[2] SINGH, B. – AL-HADDAD, K. – CHANDRA, A.: A review of active filters for power quality improvement, *IEEE Trans. Ind. Electron.*, Vol. 46, No. 5, pp. 960–971, Oct. 1999.

[3] CHIANG, H. K. – LIN, B. R. – KAI-TSANG, YANG – KUAN-WEI WU.: Hybrid Active Power Filter for power quality compensation, EEEE PEDS 2005, pp 950-954.

[4] LIN, B.R. – CHIANG, H.K. – HUANG, C. H.: Three-phase three level active power filter with a clamped

capacitor topology, IEE, Electric Power Applications, July 2006, pp. 513 – 522.

[5] SAAD, S. – ZELLOUMA, L.: Fuzzy logic controller for three-level shunt active filter compensating harmonics and reactive power, Elesevier, Electric Power Systems Research 79 (2009) 1337– 1341.

[6] LEE, G. M. – LEE, D. C. SEOK, J. K.: Control of series active power filters compensating for source voltage unbalance and current harmonics, *IEEE Trans. Ind. Electron.*, vol. 51, no. 1, pp. 132–139,Feb. 2004.

[7] HERRERA, R. S. – SALMERÓN, P.: Instantaneous reactive power theory : A comparative evaluation of different formulations, *IEEE Trans. Power Del.*, vol. 22, no. 1, pp. 595–604, Jan. 2007

[8] YANG, H. – REN, S.: A practical series-shunt hybrid active power filter based on fundamental magnetic potential self-balance, *IEEE Trans.Power Del.*, vol. 23, no. 4, pp. 2089–2096, Oct. 2008.

[9] MIKKILI, S. – PANDA, A. K.: Simulation and RTDS Hardware implementation of SHAF for Mitigation of Current Harmonics with pq and Id-Iq Control strategies using PI controller, Engineering, Technology & Applied Science Research, Vol. 1, No. 3, pp. 54-62, 2011

[10] SURESH, M. – PANDA, A. K. – YELLASIRI, S.: Fuzzy controller based 3phase 4wire shunt active Filter for mitigation of current harmonics with combined p-q and Id-Iq control strategies, Journal of Energy and Power Engineering, Vol. 3, No. 1, pp. 43-52, 2011

[11] GEORGE, S. – AGARWAL, V.: Optimum control of selective and total harmonic distortion in current and voltage under nonsinusoidal conditions, *IEEE Trans. Power Del.*, vol. 23, no. 2, pp. 937–944, Aprl 2008

[12] IEEE Standard 519-1992, Recommended Practices and Requirements for Harmonic Control in Electrical Power Systems, The Institute of Electrical and Electronics Engineers, 1993.

BIOGRAPHIES

Dr. Yacine Djeghader
Was born on 05.07.1980 in Annaba -ALGERIA- , he received the B-S degree, M-S degree and Ph.D degree in electrical Engineering with honor from Annaba University, Algeria in 2003, 2006 and 2011 respectively.
Presently: He is Assistant Professor in Electrical Engineering in Souk Ahras University, Algeria;
Field of interest: Power Quality, Power System, FACTS, Power Electronic. *Phone: +213665741133,*
Email: djeghaderyacine@yahoo.fr
yacine.djeghader@univ-soukahras.dz